REVIEW OF THE VKI DOCTORAL RESEARCH

2021 - 2022



von Karman Institute for Fluid Dynamics

Front cover:
Picture of Luca Zampini

©2022 by the von Karman Institute for Fluid Dynamics
Waterloosesteenweg 72, B-1640 Sint-Genesius-Rode
To order: https://www.vki.ac.be

ISBN 978-2-87516-187-1

D/2022/0238/763, T. Magin, Editor-in-Chief

The contents of this book are the property of the von Karman Institute for Fluid Dynamics. No part of this book may be reproduced or distributed in any form of by any means, or stored in a database or retrieval system, without the prior written permission from the Publisher.

PREFACE

The 13th symposium on the doctoral research of the von Karman Institute for Fluid Dynamics took place during the period February 23 to 25, 2022. The doctoral students present the progress of their research work carried out in the three departments: Aeronautics and Aerospace, Environmental and Applied Fluid Dynamics, Turbomachinery and Propulsion. The first-year students have presented a poster on their research plans and some preliminary results, while the most advanced students have proposed a presentation followed by a session of questions.

This event was attended by the faculty of the von Karman Institute, as well as by colleagues from universities and industrial partners. The Symposium is open to external attendees free of charge. In addition to the presentations of the PhD candidates, we had the pleasure to welcome three prominent keynote lecturers who open each day the Symposium:

- Prof. Sina Stapelfeldt, Imperial College, United Kingdom and adjunct professor at the von Karman Institute for Fluid Dynamics, *"Non-Synchronous Vibration Modelling for Modern Axial Compressors,"*
- Prof. Grigorios Dimitriadis, Aeroelasticity and Experimental Aerodynamics (AEA), Department of Aerospace and Mechanical Engineering at the University of Liège and adjunct professor at the von Karman institute for Fluid Dynamics, ","
- Dr. Vincent Moreau, CNRS research fellow at CORIA, France, "High fidelity simulations of turbulent multiphase flows."

This year, the best presentation award has been attributed to Luca Zampini for his research on "One-shot multigrid acceleration of optimisation." The best poster presentation has been awarded to Diana Zaida Felgueiras Luís for her research on "Magnetohydrodynamics enhanced radio blackout mitigation system for space transportation during planetary entries." We would like to congratulate them on their achievement.

This proceedings volume contains 58 papers, which are divided into the following topics: Aerothermochemistry, Aerothermodynamics, Rarefied and Plasma Flows, Aeroacoustics, Liquid Metal and Industrial Flows, Environmental Flows and Safety, Liquid and Solid Propulsion, Shape Optimization, Turbine Aerodynamics and Heat Transfer, Compressor Aerodynamics and Heat Transfer, Instrumentation and Measurement Techniques, Liquid and Solid Propulsion, Shape Optimization.

We would like to emphasize that this publication serves as a tool for communication and aims to enhance exchange between the doctoral candidates, the faculty, and external attendees. The annual publication of their results in proceedings is of crucial importance to the VKI research providing a thorough review of the different activities within the three departments.

As such, the doctoral candidate students play a key role in strengthening the expertise in experimental research, computational methods, and physical modelling. In addition to basic research, works carried out at the von Karman Institute often leads to implementation of real-life industrial applications critical to the fluid dynamics community.

Erica Gallo Romain Hottois PhD Representatives	Thierry Magin Editor-in-Chief	Christelle Debeer Organizer

The contribution of all VKI members who helped with this event is deeply acknowledged in particular the faculty and the communication and marketing team.

TABLE OF CONTENTS

Editorial notes i

Table of contents iii

COMPRESSOR AERODYNAMICS AND HEAT TRANSFER

Gonçalo GRANJAL CRUZ 3
Improvement of measurement accuracy using Bayesian inference – Reduction of instrumentation effort in an axial compressor

Riccardo TORACCHIO 15
Turbulence model assessment for the characterization of highly-loaded compressor stages

TURBINE AERODYNAMICS AND HEAT TRANSFER

Gustavo LOPES 29
An experimental test case for transonic low-pressure turbines - Part 2: Cascade aerodynamics at on- and off-design Reynolds and Mach numbers

Antonino Federico Maria TORRE 41
Numerical traverses of a five-hole probe downstream a transonic turbine vane

Federico BERTELLI 53
On the design and characterization of a turbulence generator for a low-speed cascade rig

Adrien VASSEUR 67
Modeling and exploitation of aerothermal probes in helicopter engines

INSTRUMENTATION AND MEASUREMENT TECHNIQUES

Bart BROUWERS 79
Acoustic attenuation of cohesive sediments (mud) at high ultrasound frequencies

Mizuki OKADA 91
Particle image velocimetry in a high-speed short-duration turbine rig

Muhsin Can AKKURT 101
Thermal investigation of a pipe with heart-shaped dimples using liquid crystal thermography

Tommaso CARLESI 111
Experimental analysis of natural convection in liquid metals

Bora Orcun CAKIR 123
Comparative assessment of image processing techniques for optical flow based Background Oriented Schlieren

SHAPE OPTIMIZATION

Luca ZAMPINI 139
One-shot and multigrid acceleration for industrial shape optimization

Tom DE BRUYN 145
Aero-elastic tailoring of composite turbomachinery blades through gradient-based optimisation: harmonic solvers

Thanh-Son TRAN..... 151
Advance optimization concept for axial compressor

AEROTHERMOCHEMISTRY

Enrico ANFUSO..... 165
An introduction to the role of chemical models in the enthalpy rebuilding procedure of plasma wind tunnels

Michele CAPRIATI..... 173
Multi-fidelity heat flux characterization of a supersonic plasma jet over a catalytic probe

David HENNEAUX 181
Enforcing interface coupling conditions within a high-order sharp interface method: application to viscous compressible gas-liquid flows

Andrea FAGNANI 193
Comprehensive characterization of the aero-thermo-mechanical response of space debris materials to atmospheric entry plasmas

Greyson KALE..... 205
Influence of pressure on the oxidation and nitridation of carbon-based ablators (first-year PhD)

Diana LUIS..... 207
Magnetohydrodynamics enhanced radio blackout mitigation system for space transportation during planetary entries first-year PhD)

Nicolas CORTHOUTS 209
Development of a hybridized discontinuous Galerkin solver for inductively coupled plasma (first-year PhD)

AEROTHERMODYNAMICS

Fabio Miguel PEREIRA MORGADO 213
Multi-fidelity approach for aerodynamic modelling and simulation of uncontrolled atmospheric destructive entry

Ali Can ISPIR..... 223
Simulations of supersonic mixing of alternative fuels for air-breathing engines based on data mining

Daniel Gabor KOVACS 229
Aerothermodynamic investigation of space debris breakup: Experimental characterization of the VKI Longshot Mach 14 contoured nozzle

Ata Onur BASKAYA 243
Influence of ablation on atmospheric entry aerothermodynamics (first-year PhD)

RAREFIED AND PLASMA FLOWS

Louis REBOUL 247
Asymptotic preserving methods for fluid equations

Giuseppe Matteo GANGEMI 261
Towards a high-order fluid simulation of Argon plasma sheath

Pedro JORGE 273
Modeling and estimating measurement uncertainty of VKI's new low density facility

Pietro PARODI 287
Plasma simulation using the implicit particle-in-cell schemes

Firas BEN AMEUR 297
Development of high-order adaptive algorithms for simulating magnetic reconnection processes with uncertainty quantification

Vincent GIANGASPERO 305
Modeling strategy for blackout analysis of re-entry phases in space exploration missions

LIQUID AND SOLID PROPULSION

Domenico FIORINI 315
Transient dynamics of contact angles

Pedro MARQUES 329
Thermo-fluid dynamics of cryogenic liquid storage

AEROACOUSTICS

Kartik VENKATRAMAN 333
Numerical investigation of noise radiated by a H-Darrieus vertical axis wind turbine in the deep stall regime

Manas NERURKAR 341
Modelling of coherent wavepackets in supersonic jets (first-year PhD)

Erica GALLO 343
Experimental and numerical investigation of the noise emitted by maneuvering multicopter drones (first-year PhD)

ENVIRONMENTAL FLOWS AND SAFETY

Pierrette ATIKPO 347
Near-field pollutant dispersion due to explosions

Emmanuel GILLYNS 357
Wind turbine wakes impact on the dynamics of high-voltage cables for fatigue assessment and optimization

Loreline FAUGIER 363
Comparison of numerical results and experimental measures of airflow in a subway station

Baris KALE 373
Multiscale wake modeling and performance assessment of the modified Vestas V27 wind turbine under neutral ABL conditions: a validation study

Benoit FOLOPPE 385
Development of a dynamic wake model accounting for wake advection delays and mesoscale wind transients

Abdelhafidh MOUMEN 395
Particle image velocimetry in the propellant flow : A case study of a.300 blackout weapon

Tom LAURIKS 409
Coarse grid and implicit LES for urban pollutant dispersion

Trond-Ola HAGBO 423
Influence of number of simulated wind directions on pedestrian wind comfort maps

Adithya VEMURI 431
Mesoscale modelling of extreme weather events over Belgian North Sea using WRF-ARW: A multi-event sensitivity analysis

Romain POLETTI 441
On the limits of quasi-steady models for flapping wing aerodynamics

Lorenzo VALLISA 451
Advanced characterization of densified cryogenic hydrogen (first-year PhD)

Rui GONCALVES 453
Aerodynamic and aeroacoustic installation effects of building-integrated wind turbines (first-year PhD)

Tsvetelina IVANOVA 455
Data-driven nowcasting for early detection of high-impact precipitation and lightning strikes on offshore wind turbine blades (first-year PhD)

Romain HOTTOIS 457
Multidisciplinary optimization of noise emission in turbomachinery (first-year PhD)

Jan VAN DEN BERGHE 459
Reconciling engineering models of ejectors with experiments and CFD using physics-informed machine learning (first-year PhD)

LIQUID METALS AND INDUSTRIAL FLOWS

Yohanna HENROTEL 463
Validation of a two-phase flow model for porous media implemented in a numerical code and applied to a plate fin heat exchanger

David BARREIRO-VILLAVERDE 471
Numerical experiments to validate integral film models for jet wiping

Aude LECARDONNEL 481
Experimental characterization of evaporation heat exchangers using low global warming potential fluids

Matilde FIORE 491
Thermal turbulence modelling of liquid metal flows via data-driven techniques

Fabio PINO 505
A journey in the active control of liquid film flows

AERODYNAMICS AND AERONAUTICS

Tomáš LEVÝ 521
HDG solver for time-dependent conservation laws (first-year PhD)

Emilio LOPEZ FIGUEIRAS 523
Passive control of cross-flow by means of small discrete roughness elements (first-year PhD)

COMPRESSOR AERODYNAMICS AND HEAT TRANSFER

Improvement of measurement accuracy using Bayesian inference – Reduction of instrumentation effort in an axial compressor

Gonçalo Granjal Cruz

Turbomachinery and Propulsion Department, von Karman Institute for Fluid Dynamics, Belgium, goncalo.cruz@vki.ac.be

Supervisor: Fabrizio Fontaneto

Associate Professor, Turbomachinery and Propulsion Department, von Karman Institute for Fluid Dynamics, Belgium, fabrizio.fontaneto@vki.ac.be

University Supervisor: Xavier Ottavy

Professor, LMFA - Laboratoire de Mécanique des Fluides et d'Acoustique, École Centrale de Lyon, France, xavier.ottavy@ec-lyon.fr

Abstract

It has become evident that a leap forward in typical testing procedures is required. This project aims at developing a methodology for the performance characterization of turbomachinery components sensitive to instrumentation limitations. The methodology relies on a hybrid approach which consists of coupling experimental and modeling techniques within a Bayesian framework. Results show that flow features can be retrieved with a reduction in the instrumentation effort.

Keywords: experimental, numerical, data assimilation, axial compressors

1. Introduction

In high overall pressure ratio engines, the increased compactness of the core can not be matched by the miniaturization process of measurement devices, inducing a larger blockage and an inevitable variation of the local flow field with a direct impact on the overall performance. This type of effects is also experienced by larger components such as low speed fans where, as a consequence of a flatter characteristic curve, a generally small variation of the flow cross section (i.e. the presence of intrusive instrumentation in the flow field) could lead to a non-negligible shift of the operating point. In general terms, the next generation of turbomachinery components exhibits a larger sensitivity to instrumentation intrusiveness with respect to more classical designs, suggesting that this problematic must be tackled to ensure a reduction of experimental errors. As a consequence of the impractical applicability of non-intrusive experimental techniques (e.g. Particle Image Velocimetry) in industrial rigs, a pragmatic way to reduce the blockage effect is to reduce the instrumentation effort required to assess both the performance and the flow field of a turbomachinery component through the coupling of experimental methods with a data assimilation framework compensating for the limited information available.

This was done by Lou and Key [1; 2] by implementing an optimization algorithm to select optimal probe placing, followed by a multi-wavelet approximation to reconstruct the circumferential flow of the machine, avoiding the common usage of averaging rake measurements to evaluate performance. Seshadri et al.[3] apply a Bayesian treatment to an engine experimental data, in the form of Gaussian Processes (GP)[4], and decompose the posterior uncertainty into the error of the measurements and insufficient sampling, exposing how reducing the latter can lead to optimal sensor placement from a design of experiments perspective.

The trend of leveraging available experiments with data-driven approaches is not limited to turbomachinery. Recently, Sousa et al. [5] implemented a Bayesian inference approach to estimate the inflow boundary conditions for RANS simulations from the exploitation of a reduced number of experimental sensors deployed in an urban environment, showcasing

the possibility of using data assimilation techniques in inverse fluid mechanics problems. An adaptation of the ensemble Kalman filter (EnKF) of Evensen [6; 7], guarantees a straightforward implementation and limited computational cost thanks to its gradient-free nature. The downside of the algorithm lies in the assumption that all the probability distributions (inputs and outputs) are Gaussian, a constraint recently demonstrated to be less stringent than what was initially foreseen [**?**]. Data assimilation techniques can benefit the entire field of fluid mechanics, even in fundamental research [8], by tackling two different problems: The accurate measured experimental data is limited in space and time; and a computational simulation, due to numerical discretization or inaccurate definition on boundary conditions, may not represent the state of the real flow [9].

The present work aims at putting the bases for the development of a hybrid measurement technique that, by exploiting Bayesian inference data-driven techniques, allows the reduction of the instrumentation effort required for the characterization of the performance and flow field of turbomachinery components. By adopting Bayesian statistics within a data-driven framework, the forthcoming measurement technology is believed to be less invasive, cheaper, and of wider validity.

The methodology proposed aims at retrieving missing information over the entire domain just through a few localized experimental measurements supported by a Bayesian framework. The methodology, schemed out in Figure 1, can be summarized as follows. An initial guess of turbomachinery parameters to study (e.g. boundary conditions) is sampled N times and run through a forward model (e.g. CFD), creating a prior database of possible flow combinations. Assimilation with undersampled experimental data is performed with Bayesian data-driven algorithms and a posterior belief of the flow field and the initial parameters is obtained. Convergence and validation criteria are assessed and overall uncertainty quantification of the methodology is computed.

Section 2, briefly describes the test case of this work, a low aspect ratio axial compressor. In Section 3, the Bayesian framework is introduced, followed by the description of the algorithms applied in this work. Section 4 describes the sampling approach used. Section 5 presents the results obtained. Finally, conclusions are drawn on the instrumentation effort reduction, and prospects of the next steps for the methodology are discussed.

2. Test case

The H25 stage (Figure 2) is a low aspect ratio axial compressor stage representative of the last stage of a high pressure compressor. The overall performance is retrieved by combined total pressure - total temperature rakes deployed at measurement planes (MP) 0 and 4, corresponding, respectively, to the inlet and outlet of the test section. The radial traversing of measurement probes is possible in all measurement planes. Azimuthal traversing is only possible in plane 4.

The instrumentation at plane 4 allows a complete sampling of a map (span+pitch) of the probe measured quantities (e.g. total pressure). Sampling this map is time-consuming and, as a consequence, expensive. Additionally, in low aspect ratio stages, an increased influence of the instrumentation on the flow is expected. In parallel, inlet total conditions at plane 0 are estimated from rakes that directly affect the flow that goes into the machine. The present application tackles these specific problems for the design operating point of the machine.

The fully propagated total and static pressure uncertainties are, in the worst case scenario (plane 0), equal to 3.2% and 3% of the dynamic pressure, respectively. The total to total pressure ratio uncertainty budget was estimated to be lower than 1%. The mass flow and the isentropic efficiency uncertainties are 2.1% and 4% for a near-stall operating condition.

The CFD model of the H25 stage, using *NUMECA* FINE Turbo 12.1, has been developed and thoroughly validated by Babin et al. [10]. Fully turbulent steady RANS computations have been performed employing the k-ω SST turbulence model [11] for closure. A mixing plane condition couples the rotor and stator. At the inlet, total quantity profiles and flow angle are employed. The absolute mass flow was imposed at the outlet. The design rotational speed is considered throughout this work.

Changing the values of the above boundary conditions forces the flow field to adapt, leading to multiple operating points on the corrected compressor map that matches the need of the proposed methodology for different numerical flowfields. The boundary conditions range (from stall to choke) used to create the database is depicted in Table 1.

3. Bayesian Inference

From a general standpoint, the present methodology aims at solving the following statement: “Re-

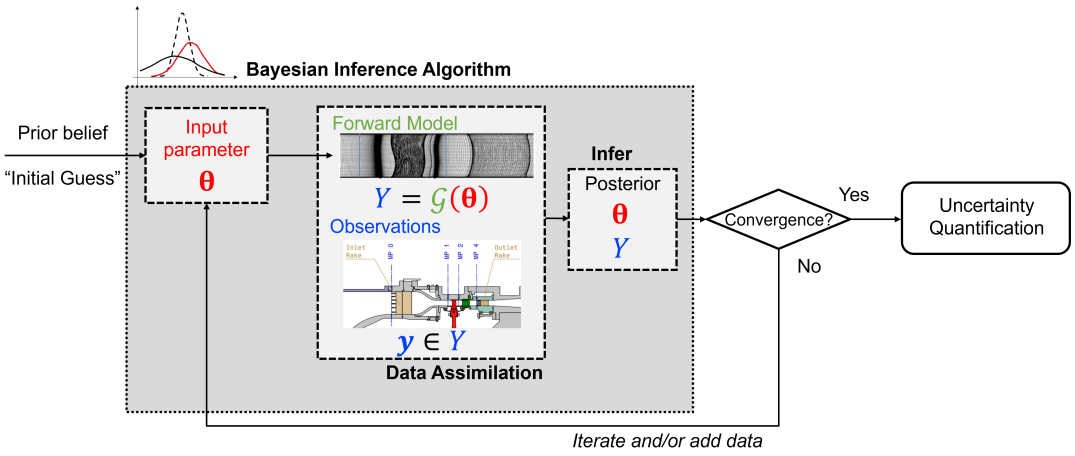

Figure 1: Proposed Bayesian methodology schematic

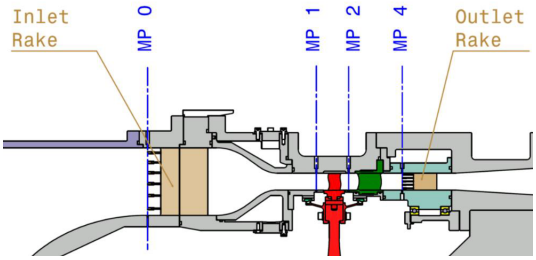

Figure 2: Experimental cross section of the H25 compressor stage

Table 1: H25 Boundary Conditions range

Quantity	Range	Unit
p_{T0}	[93500,10900]	Pa
T_{T0}	[275.15,305.15]	K
$\dot{m}$	[3.9,5.1]	kg/s

trieve missing/unavailable statistical information supported by a model, through the usage of limited experimental observations." This is possible under a Bayesian mathematical framework, which is generally introduced here through Bayes theorem:

$$p(\boldsymbol{\theta}|\mathcal{D}) = \frac{p(\mathcal{D}|\boldsymbol{\theta})p(\boldsymbol{\theta})}{p(\mathcal{D})} \tag{1}$$

where $\boldsymbol{\theta}$ is a generic vector of quantities of interest, defined below depending on the application, and $\mathcal{D}$ is the observed data used for the analysis. $p(\boldsymbol{\theta})$ is the *prior* probability distribution and represents the assumptions on $\boldsymbol{\theta}$ before taking into account the data. The conditional probability $p(\mathcal{D}|\boldsymbol{\theta})$ is called the *likelihood function* and it expresses how probable the data is given the possible values of $\boldsymbol{\theta}$. In practical terms, it will compare the observed data $\mathcal{D}$ with a non-linear model prediction that depends on $\boldsymbol{\theta}$. The term $p(\mathcal{D})$ is a normalization constant that can usually be dropped in practical applications since it does not depend on $\boldsymbol{\theta}$. Hence, through the computation of the *posterior* probability distribution $p(\boldsymbol{\theta}|\mathcal{D})$, the Bayesian framework allows inferences to be made about uncertain parameters $\boldsymbol{\theta}$ based of observed data $\mathcal{D}$. Bayesian inference is analogous to the research methodology. To prior research, one adds observations/experiments and infers new conclusions.

The following subsections introduces algorithms that tackle two types of problems within the Bayesian framework: Inverse and regression problems.

3.1. Ensemble Kalman filter for Inverse problems

An inverse problem aims at estimating parameters $\boldsymbol{\theta}$ from experimental observations $\boldsymbol{y}$ taken from the dataset $\mathcal{D} = \{y_1, y_2, ..., y_i\} \in Y$:

$$\boldsymbol{y} = \mathcal{G}(\boldsymbol{\theta}) + \varepsilon \tag{2}$$

where $\mathcal{G}$ represents a non-linear forward model, mapping parameters $\boldsymbol{\theta}$ to measured observations $\boldsymbol{y} \in Y$. Due to uncertainties in the measurement chain, it is not possible to measure the truth $\boldsymbol{y}^{\dagger}$. The mapping error is assumed to be a Gaussian random variable with zero mean and known covariance $\varepsilon \sim \mathcal{N}(0, \boldsymbol{\Gamma})$. This type of problem is usually ill-posed and requires regularization. In the present algorithm, regularization of the inverse problem is integrated within the prior distribution of the parameters $\boldsymbol{\theta}$.

It is worth noting that while in the generic framework $\boldsymbol{\theta}$, is introduced as a "generic vector of quantities of interest" in the inverse problem framework

$\boldsymbol{\theta}$ becomes a vector of forward model parameters. A common approach for posterior parameter estimation is to use Markov Chain Monte Carlo (MCMC) sampling algorithms. However, this evaluation is typically expensive and requires thousands of forward model $\mathcal{G}$ evaluations.

In this work, the ensemble Kalman Filter for inverse problems [12], described in the appendix, is used to approximate the posterior distribution of the parameters $\boldsymbol{\theta}$. This algorithm is cheaper than MCMC since it requires fewer forward model evaluations. The trade-off of these advantages is a loss of accuracy and the assumption that the distributions are Gaussian. The algorithm uses a state augmentation approach which allows a joint parameter and state estimation. Practically, it infers the parameters $\boldsymbol{\theta}$, solving the inverse problem and unknown states $\boldsymbol{y_*} \in Y$ of the domain that are not measured, estimating the solution of a regression problem.

In the current work, the boundary conditions imposed to the machine, inlet total pressure p_{T0} and temperature T_{T0}, and mass flow $\dot{m}$ are the parameters to infer $\boldsymbol{\theta} = (p_{T0}, T_{T0}, \dot{m})$. Each parameter prior distribution is a uniform distribution sampled with an optimal LHS algorithm, described below, to build the initial ensemble. CFD simulations are performed with the sampled boundary conditions. The measured quantities of interest $\boldsymbol{y}$ presented here are the total pressure p_{T4} at the outlet of the stage (MP4). Of the available measurement locations $\boldsymbol{x_{exp}} = \boldsymbol{(r, pitch)}$ from a complete test, undersampled measurements $\boldsymbol{y}$ are randomly selected. The remaining measurements of the test set are the unknown states $\boldsymbol{y_*}$ that the algorithm infers (in addition to the boundary conditions) and evaluate the algorithm accuracy.

3.2. Gaussian Process Regression

Gaussian Processes (GPs) are a non-parametric method that constructs "Gaussian distributions over functions"[4] rather than in parameters, making GPs a powerful tool for regression problems (predict unknown states $\boldsymbol{y_*}$ from noisy observed states $\boldsymbol{y}$). A Gaussian process defines a multivariate conjugate Gaussian prior over functions for any point in the input space $\mathbf{x}$:

$$p(f \mid \mathbf{x}) = \mathcal{N}(f \mid \boldsymbol{\mu}, \mathbf{K}) \tag{3}$$

where $f(\mathbf{x})$ is multivariate random variable from which noisy observations $\mathbf{y} = f(\mathbf{x}) + \boldsymbol{\epsilon}$ are available with $\boldsymbol{\epsilon} \sim \mathcal{N}\left(\mathbf{0}, \sigma_y^2 \mathbf{I}\right)$. The assumption that the noise follows an independent, identically distributed Gaussian distribution with zero mean and fixed variance is taken. $\boldsymbol{\mu}$ is the prior mean function and is usually assumed to be 0. $\mathbf{K}(\mathbf{x_i}, \mathbf{x_j})$ is a kernel function that defines the joint covariance of the given inputs $\mathbf{x}$. Notice that the GP model takes into account the variance on the random variable $f(\mathbf{x})$ through the covariance $\mathbf{K}(\mathbf{x_i}, \mathbf{x_j})$ that models the underlying system inherent uncertainty. $\mathbf{y}$ and its variance focus on the uncertainty that occurs during observations.

Given the above assumptions and available noisy observations $\mathbf{y}$, the log marginal likelihood function can be derived:

$$\log p(\mathbf{y} \mid \mathbf{x}) = -\frac{1}{2}\log\left(\det\left(\boldsymbol{K} + \sigma_y^2 \boldsymbol{I}\right)\right) - \frac{1}{2}(\mathbf{y} - \boldsymbol{\mu})^\top \left(\boldsymbol{K} + \sigma_y^2 \boldsymbol{I}\right)^{-1} (\mathbf{y} - \boldsymbol{\mu}) - \frac{n}{2}\log(2\pi) \tag{4}$$

Notice the strict dependence of the marginal likelihood in the kernel function $\boldsymbol{K}$. Multiple kernel function families exist in the literature for different function modeling behavior (e.g. smoothness, stationary). In the present work, the kernel function selected is the Matérn kernel:

$$\mathbf{K}\left(\mathbf{x}_i, \mathbf{x}_j\right) = \frac{\sigma_f}{\Gamma(\nu)2^{\nu-1}}\left(\frac{\sqrt{2\nu}}{l}\left(\mathbf{x}_i - \mathbf{x}_j\right)^T\right)^\nu K_\nu\left(\frac{\sqrt{2\nu}}{l}\left(\mathbf{x}_i - \mathbf{x}_j\right)\right) \tag{5}$$

where the l is the length scale and controls the smoothness and σ_f acts as a scaling factor. $\nu = 2.5$ ensures a twice differentiable function. It is of interest to optimize these parameters to fit the available data $\mathbf{y}$. This is achieved by finding the hyperparameters that maximize the log marginal likelihood function above.

Predictions of the unknown states $\boldsymbol{y^*}$ can be obtained by conditioning their input locations $\mathbf{x}_*$ on the previous distributions, giving, through Bayes theorem, a predictive posterior distribution:

$$p\left(\mathbf{y}_* \mid \mathbf{x}_*, \mathbf{x}, \mathbf{y}\right) = \mathcal{N}\left(\mathbf{y}_* \mid \boldsymbol{\mu}_*, \boldsymbol{\Sigma}_*\right) \tag{6}$$

$$\boldsymbol{\mu}_* = \boldsymbol{\mu} + \mathbf{K}(\mathbf{x}, \mathbf{x}_*)(\mathbf{K}(\mathbf{x}, \mathbf{x}) + \sigma_y^2 \mathbf{I})^{-1}(\mathbf{y} - \boldsymbol{\mu}) \tag{7}$$

$$\boldsymbol{\Sigma}_* = \mathbf{K}(\mathbf{x}_*, \mathbf{x}_*) - \mathbf{K}(\mathbf{x}_*, \mathbf{x})(\mathbf{K}(\mathbf{x}, \mathbf{x}) + \sigma_y^2 \mathbf{I})^{-1}\mathbf{K}(\mathbf{x}, \mathbf{x}_*) \tag{8}$$

where $\boldsymbol{\mu}_*$ is the posterior function mean and $\boldsymbol{\Sigma}_*$ its covariance.

A Gaussian Process regression typical approach would usually use as inputs $\mathbf{x} = [\boldsymbol{r}\ \boldsymbol{\theta}]$ with $x_i = (r, \theta)_i$ being a location where a single noisy experimental measurement y_i is available. The unknown states $\boldsymbol{y_*}$ would analogously be the same quantity of interest evaluated at non sampled locations $\mathbf{x}_* = [\boldsymbol{r_*}\ \boldsymbol{\theta_*}]$. This

procedure provides an accurate estimation of the unknowns close to input locations $\mathbf{x}$ but it is known to lose accuracy as the inference moves more than one kernel length scale. Physically, and taking the H25 test case as an example, the quantity of interest is the total pressure at the outlet of the stator, for which undersampled noisy measurements are available. With GP, inference of the non-sampled locations is possible. Losses in accuracy arise in regions where few measurements are available or nonexistent, for example, a typical probe cannot measure the hub boundary layer due to the presence of its stem.

The present proposal is motivated by the coupling of numerical data with measurements in GPs. Instead of mapping the physical input $\mathbf{x} = [\boldsymbol{r}\ \boldsymbol{\theta}]$ domain, multiple RANS simulations (at different operating conditions of the machine) are used as inputs $\mathbf{x}$. Using the example of the total pressure at the compressor outlet, one input $\mathbf{x}_i$ is a j-Dimensional vector containing all the RANS total pressure results evaluated at a grid point $i = (r, \theta)$ where one experimental measurement y_i is available. The GP function mapping of the proposed approach is represented in matrix format below (Eq. 9).

$$f : \mathbf{x} = \begin{bmatrix} p_{T4_{(1,1)}} & \cdots & p_{T4_{(1,j)}} \\ \vdots & & \vdots \\ p_{T4_{(i,1)}} & \cdots & p_{T4_{(i,j)}} \end{bmatrix} \in \mathbb{R}^j \longmapsto \quad \boldsymbol{y} = \begin{bmatrix} p_{T4_1} \\ \vdots \\ p_{T4_i} \end{bmatrix} \in \mathbb{R} \quad (9)$$

A note is made here on the comparison between the two presented approaches. Despite being meant to solve different problems, the Bayesian framework and the Gaussian assumption are shared between them. That can be seen by comparing the update step of the EnKF (Eq. 16) and the posterior function mean (Eq. 7). Despite that, they differ in the thought that describes the underlying process, physical state based versus covariance function, respectively [13]. The presented algorithm to solve inverse problems has a trade-off of low cost, both in terms of the amount of data required and computational time against accuracy for inverse problem parameter estimation. Its formulation also allows inference of unknown states, the same application problem for which Gaussian Processes were presented above. The Inverse Ensemble Kalman filter iteration presents a lower computational cost since it does not require the optimization of model hyperparameters but seems to show a lower performance. If a certain degree of error and uncertainty is acceptable the cheaper option can be viable and provides more information (solving the original inverse problem).

3.3. Performance evaluation

The performance of the algorithm is evaluated using the mean absolute error (MAE) and the root mean squared error (RMSE) between the inferred total pressure results ($\boldsymbol{y}_*$) and the experimental reference ($\boldsymbol{y}^\dagger$) at each grid point, i, for each predicted value, j normalized to a reference inlet pressure value.

$$\mathrm{MAE}_i = \frac{1}{J} \sum_{j=1}^{J} \left| y_{*\,j} - y_j^\dagger \right| \quad (10)$$

$$\mathrm{RMSE}_i = \sqrt{\frac{1}{J} \sum_{j=1}^{J} (y_{*\,j} - y_j^\dagger)^2} \quad (11)$$

4. Sampling

Both of the above sections rely heavily on data and its quality. The EnKF for inverse problems requires an initial ensemble built from sampling the prior distribution of the parameters X that are then run through CFD RANS simulations. Previous analysis [14] showcases the influence of the initial ensemble in the inference results, both in ensemble size and relevance of the parameters sampled. The Gaussian Process approach also requires the previously mentioned simulations to build the functional mapping and infer the unknown states without the risk of extrapolation. To ensure high-quality sampling of the prior parameter distributions and to consequently obtain a complete meaningful database of flow regimes which minimize the number of CFD model evaluations, a design of computer experiments analysis is proposed to define an optimal prior sampling strategy.

Classic design of experiments (DoE) methods, such as central composite, were developed to deal with randomness and non-repeatability in experiments. However, computer simulation codes are deterministic, giving rise to a different DoE framework. Within this framework, static approaches, such as Latin Hypercube Sampling (LHS), aim at achieving a space-filling design before performing any simulation. On the opposite, adaptive algorithms, such as Expected Improvement (EI) [15], adapt to available simulation information to sample in specific regions of interest,

making this type of approach common in optimization problems [16].

For the present work, an optimal LHS strategy is sought. A Latin Hypercube divides the parameter space into J equally sized hypercube bins, where sampling points allocation is random. Multiple optimization procedures can be found in the literature [17] to optimize LHS sampling. An investigation on available optimal LHS techniques that minimize a Centered L2-Discrepancy criterion C_2 (to obtain a uniform sample projection) and a Min-Max Distance Φ_{50} (to good sampling spreading) is performed. The study is presented below in Figure 3. The error bars represent the inherent randomness of the methods obtained by performing 5000 runs of the algorithms. Note that, for both studied criteria, lower values represent a better LHS sampling plan. The enhanced stochastic evolutionary (ESE) algorithm [18] is selected based on the evaluated criteria and reliability in generating an optimal LHS plan.

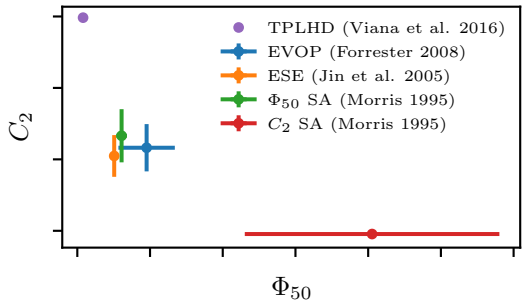

Figure 3: Comparison study of Optimal LHS plans [19; 20; 18; 21] performance evaluated with uniformity and distance criteria: The ESE algorithm gives the best balance between the evaluated criteria

5. Results

The ESE algorithm was used to generate 50 samples to match a multivariate uniform prior distribution of the boundary conditions of Table 1. However, due to numerical convergence issues near stall and chocking limit of the machine (far from the experimental operating range), the following analysis is performed with j=46 CFD simulations. This lead to a loss of a perfect uniform prior, as it can be seen in Figure 4 (in blue), that was considered acceptable since the converged CFD contain stall and chocking flow fields within the experimental operating range of the compressor. The experimental data used throughout this section are randomly sampled from 950 total pressure experimental measurement points over a uniform grid of one span and one-and-half pitch at the outlet of the compressor (MP4). The CFD results are interpolated to match this experimental grid, on which the flow field inference is performed.

5.1. EnKF for Inverse problems

The algorithm posterior result for the operating parameters of the machine, $\boldsymbol{\theta} = (p_{T0}, T_{T0}, \dot{m})$, is presented in Figure 4 with the prior distribution obtained from the LHS plan. The average experimental value is depicted with a red line for comparison and validation. A visual analysis of the histograms shows the Gaussian assumption that is inherent to the algorithm since all posterior histograms tend to a Gaussian distribution. The implicit regularization of the algorithm by the prior distribution is also visible. All posterior distributions lie on the sub spanned space of the prior histogram.

For the total inlet pressure and temperature, the posterior histogram is not centered around the experimental reference, by approximately 3000 Pa and 5 K respectively, which are higher than the reference measurement uncertainty. The mass flow inference shows the best result with a posterior histogram where the high probability matches the experimental test value. Regardless of a wide histogram (high standard deviation) and a bias error in the most probable value for pressure and temperature, these results, within some confidence interval, show the ability of the proposed methodology to infer parameters not observed in the data and for which experimentalists usually rely on rake averaging, recall from Section 2 that these are the quantities (MP0) with higher measurement uncertainty in the machine and that no measurement from the inlet of the machine was used in this approach.

Figure 4 results were obtained with one iteration of the algorithm, a second iteration would use the presented posteriors as priors, resample these priors and then run j CFD simulations again. Synthetic test cases, not shown here, have shown convergence of the inferred parameters but the variance of the posterior seems to be upper bounded to the estimated model error, which might bias the entire inference process. The usage of a more informative prior distribution through the selection of a narrower range for the parameters would highly benefit the inference result. Increasing j, the number of simulations, would also benefit the parameter inference result.

Following the previous analysis about the ability of the methodology to evaluate the operating conditions of the machine and consequently solve an inverse problem, it is of interest to evaluate the capability of the adapted EnKF algorithm to infer the total-

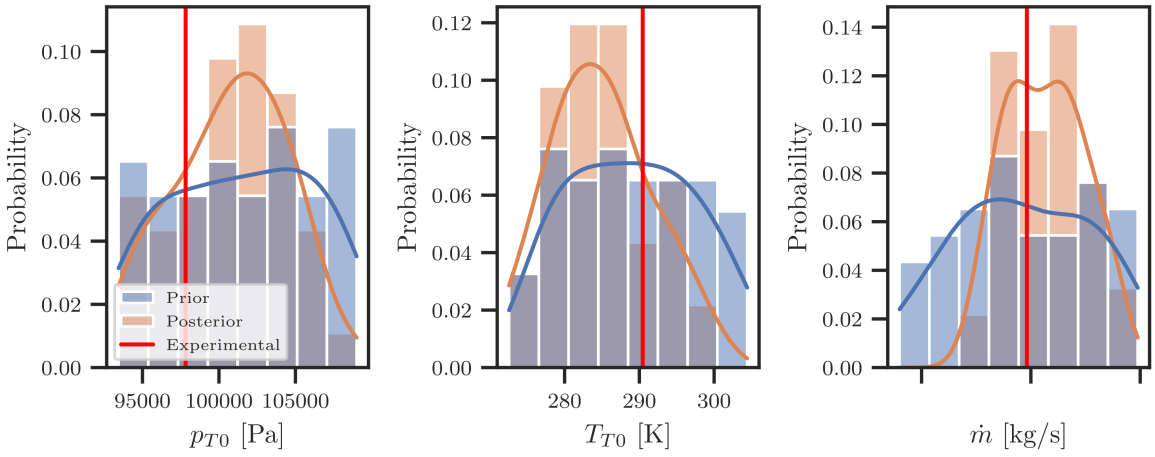

Figure 4: Prior and Posterior histograms of the operating parameters of the H25 compressor stage obtained with the EnKF for inverse problems

to-total pressure map at the outlet of the stage (MP4) to analyze its ability to infer flow features. As a reminder, 350 (33%) of the available 950 experimental measurement points are randomly sampled to be used in the inference, while the other are used for validation.

Figure 5 showcases the complete experimental total pressure map (a) for comparison and the obtained algorithm posterior mean pressure map (b). The assimilated map presents a smooth flow field, unlike previous studies [14] where poor modeling was used. In qualitative term, the map is able to detect coherent flow structures. The blade wake location, around Pitch=1 is an example of that, however there is a clear underestimation of the depth and width of the wake that is then compensated with an overestimated pressure region near the tip. In normalized quantitative terms, an average MAE = 0.00656 is computed. This value is on the order of magnitude of the experimental uncertainty but its still several times higher. Moreover, when one evaluates the algorithm with the quadratic scoring rule, an average RMSE = 0.0489 is obtained. The order of magnitude discrepancy between this two errors measures shows a great variance between the inference predictions. Some areas of the flow are well inferred while others show a high error.

The miss-estimation of the absolute pressure values is a problem that must be understood. An in depth analysis, of the data used and the matrix computations of the algorithm, showed that this is caused by the numerical CFD simulations used since regardless of the variation of the boundary conditions, there always exists a bias on the estimation of the depth of the wake. This bias was tracked down to originate in the rotor-stator interface which is defined in this work with a mixing plane approach.

Consequently, the robustness and sensitivity of the algorithm on this practical test case is studied. Multiple runs of the algorithm are performed to study the influence of the random sampled experimental locations used for assimilation. The percentage of observed data was also varied. Aditionally, more CFD simulations, near the operating limits of the machine, were added to the analysis. Figure 6 shows the algorithm sensitivity through the obtained MAE variance. Adding more CFD simulations, increasing j, and more experimental measurements leads: firstly to a decrease in the average MAE and secondly to a reduction in the experimental sampling influence (lower variance histograms). Despite a reduction in average error, the flow fields obtained, in qualitative terms still show very similar problems to the inferred flow field presented in Figure (b). This means the algorithm, in its current implementation, is limited and biased by numerical model fidelity.

5.2. Gaussian Process Regression

The following results are obtained with the data preprocessed to built the functional mapping proposed above (Eq. 9) where in the training phase $\boldsymbol{x}$ is a matrix concatenated with the RANS simulations evaluted at randomly sampled experimental grid points, and the $\boldsymbol{y}$ is a vector with the mentioned experimental measurements.

The prior and likelihood need to be specified. A prior with a zero mean and squared exponential kernel

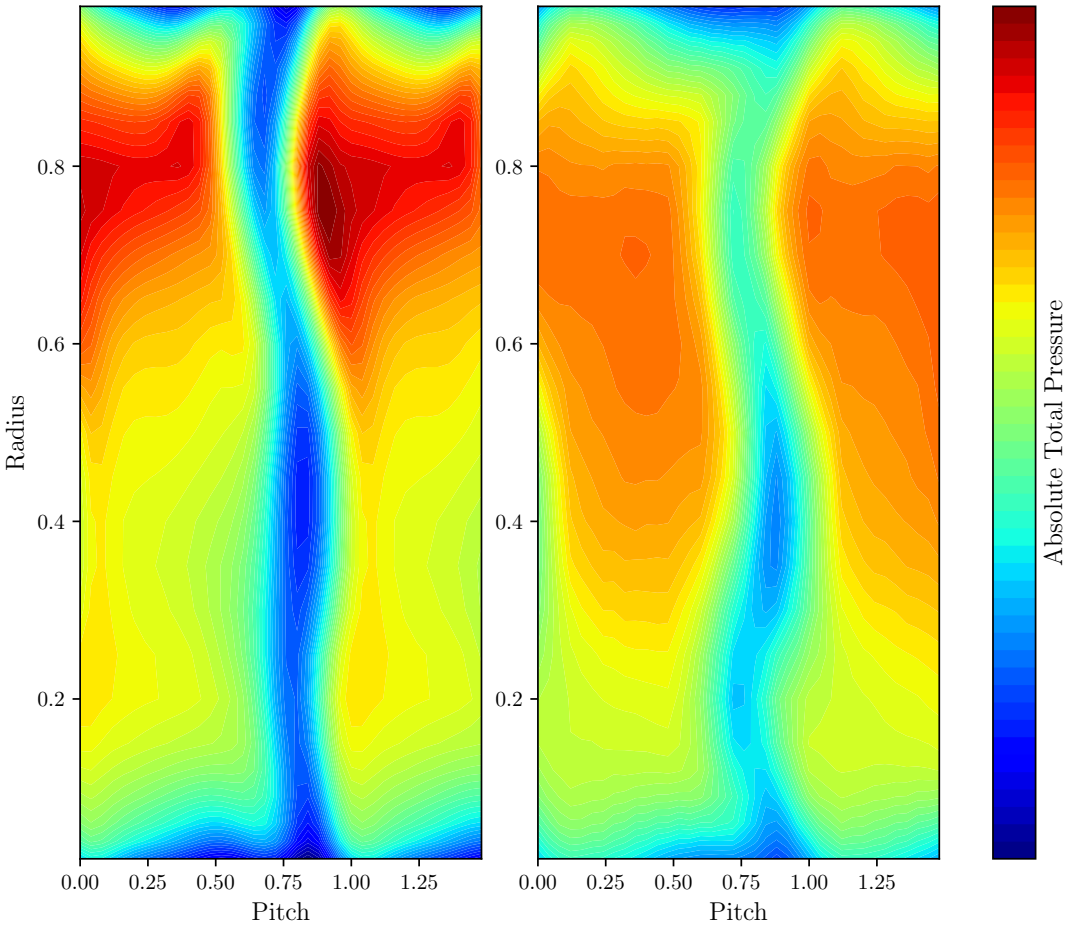

Figure 5: EnKF inference of the total pressure map at the compressor outlet (left) with 33% experimental measurements sampled and experimental fully sampled reference (right): Flow features recovered but over(under)estimated; MAE higher than the experimental uncertainty.

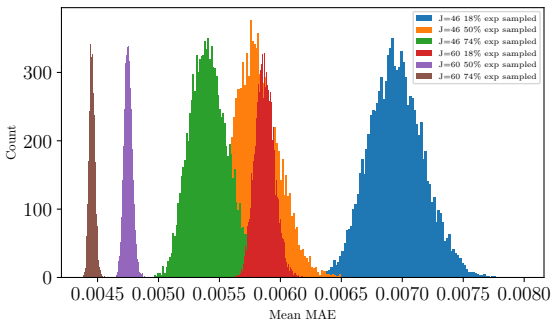

Figure 6: EnKF for inverse problems sensitivity to experimental sampling and ensemble size

(Eq. 5) is selected. The negative of the log marginal likelihood function is minimized with an L-BFGS algorithm to obtain the kernel optimal hyperparameters that match the available data. Predictions are made following the equation 7 obtained from probability theory and Gaussian distribution rules. Notice that this equation holds regardless of the user-defined prior and likelihood. At last, and similarly to the subsection above, the remaining measurements not used to infer predictions are used to evaluate the inference accuracy.

The inferred outlet total pressure map is depicted in Figure **??** (a). The completely sampled experimental reference (b) is plotted in parallel to allow for a visual comparison analysis with the colorbar being shared by both sub-figures. The prediction of the GP shows a smooth flow field that visually matches well with the experimental reference. Important flow features region are well defined. The wake shows a correct

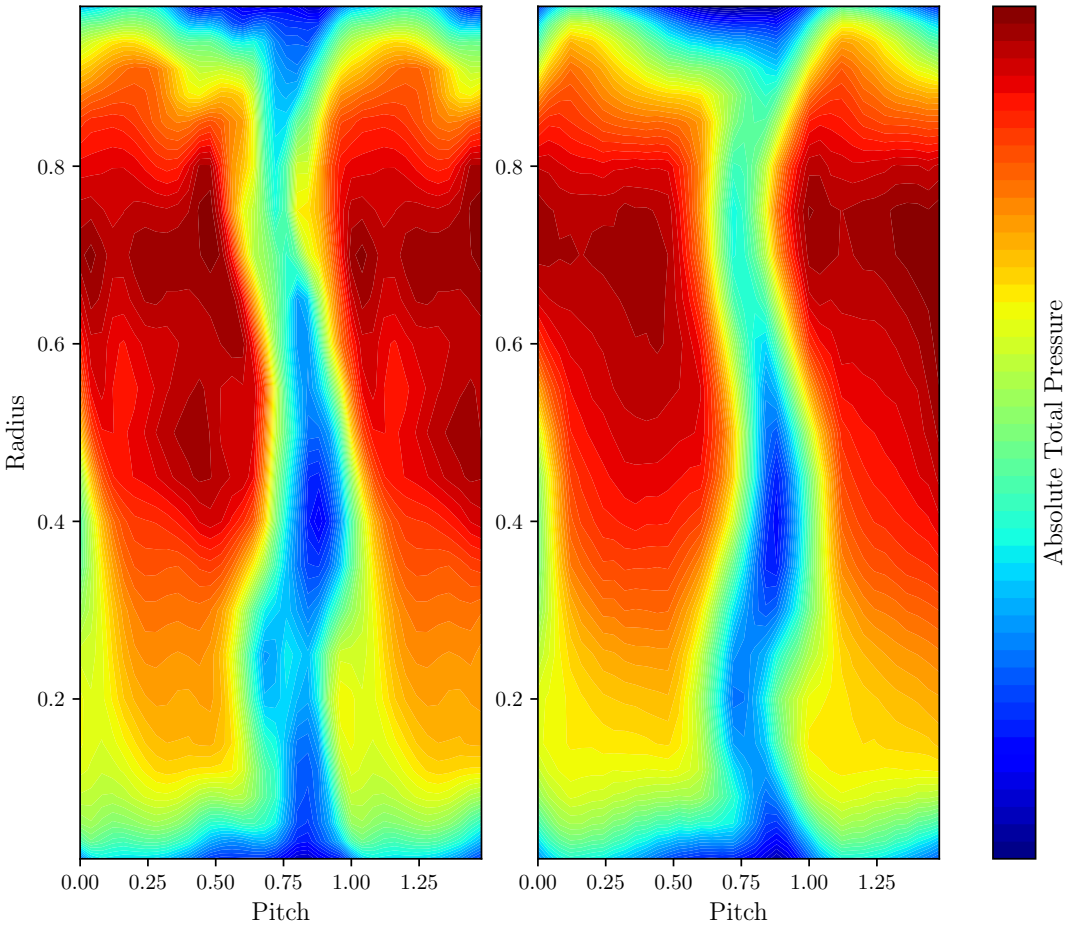

Figure 7: GP inference of the total pressure map at the compressor outlet (left) with 33% experimental measurements sampled and fully sampled experimental reference (right): Overall match of flow features; MAE on the order of magnitude of the experimetnal uncertainty.

depth and width and consequently the span-wise distribution of pressure also agrees with the experimental reference. The inner high pressure area close to the 0.8 radial span is detected despite showing a slightly different shape. This is a important result since this area could be easily missed in experimental tests with sparse sampling. Secondary flows are also visible. The hub secondary flow region is an example of that, with the passage vortex signature more visible in the inferred flow than in the fully sampled experiments. The tip wall secondary flow is also visible but with its pitch-wise direction changed and its size increased.

The error is evaluated in terms of a normalized pressure. An average MAE = 0.00136 is obtained. This absolute value supports the visual analysis performed above and its very close to the uncertainty of the experiments. The average RMSE = 0.00184. This value is still higher than the MAE which means that some flow regions have higher error. Figure 8 (a) present the contour distribution of the MAE. Aditionally, the posterior standard deviation (computed from the diagonal of the covariance matrix [Eq. 8]) is presented in Figure 8 (b). To evaluate the validation and accuracy of the GP, Figure 8 (c) presents a scatter plot of the predictions versus experiments, where each point represents one experimental grid point.

Analysis of the MAE distribution over the flow passage, Figure 8 (a), shows the higher error region to be near the tip secondary flow as expected from visual inspection. Some sparse error ”pockets” are found in the entire span from 0.6 to 0.8 pitch, which is where the main flow and wake interact causing high pressure gradients that are more difficult to infer. Despite presenting a higher error in these regions, the Bayesian

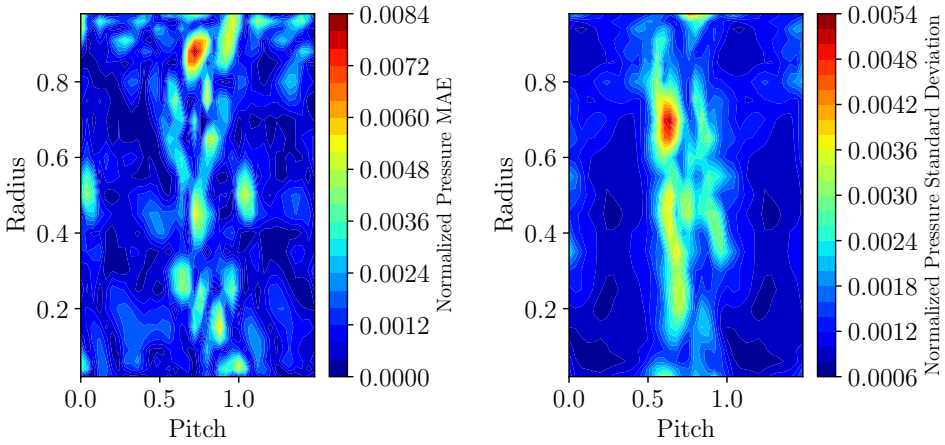

(a) Normalized total pressure Mean Absolute Error (MAE)

(b) Normalized total pressure standard deviation

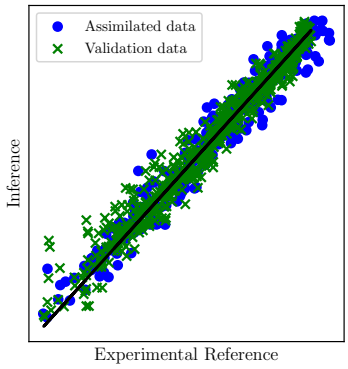

(c) Scatter plot for the total pressure inferred values and experimental reference

Figure 8: GP inference performance evaluation in terms of MAE (a), standard deviation (b) and validation match with experiments (c)

approach taken is aware of its difficulties and as it can be seen in the standard deviation plot of Figure 8 (b), where this region matches the posterior high standard deviation, meaning the region with higher uncertainty.

Finally, Figure 8 (c) presents the scatter plot of the result both for the data used in the assimilation and the one used for validation. Overall a good agreement is obtained. Looking at the assimilated data it is clear that no over-fitting is present. It is also noticeable that the validation data presents an overall higher error specially in the lower part of the plot, where less experimental assimilated data is present. This leads to the discussion on the sensitivity to the randomly sampled experiments that had already been identified with the previous algorithm and plays an even stronger role in GPs where the available data is used to optimized hyperparameters. The optimization process itself is of relevant analysis since it has been noted that the likelihood cost function is not convex and may have multiple minima. Nevertheless, the current GP implementation is able to retrieve physical flow field to a certain confidence level.

6. Conclusion

In this work, the concept of a new hybrid experimental technique methodology, coupling numerical modeling with experimental data through Bayesian data driven algorithms is presented. It aims at reducing the number of required measurements to charac-

terize a machine, leading to lower costs and limited intrusiveness while maintaining high fidelity results.

The methodology was applied to the case of a heavily instrumented research compressor stage with the focus of inferring the operating conditions of the machine without using rake measurements and on the rebuild of the stator outlet total pressure map with undersampled measurements.

The Ensemble Kalman Filter for inverse problems [12] was employed for the assimilation due to its gradient-free, low computational cost and ability to estimate machine parameters and flow fields simultaneously. The algorithm can estimate with some confidence an estimate of the machine operating conditions but shows problems when rebuilding the undersampled pressure map, being biased by the RANS flow features.

Gaussian Processes [4] were employed in the context of a regression problem to tackle the problem of retrieving a high fidelity estimate of the pressure map with highly undersampled random measurements. The increased computation cost of having to perform an hyperparameter optimization is compensated by the physical flow field inferred that presents a good agreement with the experiments used for validation. Nevertheless, both algorithms show an high sensitivity to the randomly selected experimental measurements and in some key regions of the flow the inference error is still higher than standard experimental uncertainty.

Nevertheless, it is worth to notice that there is room for improvement of the proposed methodology to establish it as a hybrid measurement technique at a multi fidelity level. This will be achieved by selecting crucial experimental points to use in the assimilation through a design of experiments optimization study.

References

[1] F. Lou, N. L. Key, Reconstructing compressor non-uniform circumferential flow field from spatially undersampled data – part 1: Methodology and sensitivity analysis, Proceedings of the ASME Turbo Expo GT2020-14867 (2020) 1–12.

[2] F. Lou, D. R. Matthews, N. J. K. Iii, N. L. Key, Reconstructing compressor non-uniform circumferential flow field from spatially undersampled data – part 2 : Pratical application for experiments, Proceedings of the ASME Turbo Expo GT2020-15465 (2020) 1–12.

[3] P. Seshadri, A. Duncan, G. Thorne, G. Parks, M. Girolami, Bayesian assessments of aeroengine performance, arXiv (2020) 1–30I get very lost in his fourier kernel and its priors...

[4] C. E. Rasmussen, Gaussian processes in machine learning, Lecture Notes in Computer Science 3176 (2004) 63–71. doi:10.1007/978-3-540-28650-9.

[5] J. Sousa, C. Gorlé, Computational urban flow predictions with bayesian inference: Validation with field data, Building and Environment 154 (2019) 13–22. doi:10.1016/j.buildenv.2019.02.028.

[6] G. Evensen, Data assimilation: The ensemble kalman filter, Springer Berlin Heidelberg, 2009. doi:10.1007/978-3-642-03711-5.

[7] G. Evensen, The ensemble kalman filter: Theoretical formulation and practical implementation, Ocean Dynamics 53 (2003) 343–367. doi:10.1007/s10236-003-0036-9.

[8] P. C. D. Leoni, A. Mazzino, L. Biferale, Synchronization to big data: Nudging the navier-stokes equations for data assimilation of turbulent flows, Physical Review X 10 (2020) 11023. doi:10.1103/PhysRevX.10.011023.

[9] T. Hayase, Numerical simulation of real-world flows, Fluid Dynamics Research 47 (2015) 51201. doi:10.1088/0169-5983/47/5/051201.
URL http://dx.doi.org/10.1088/0169-5983/47/5/051201

[10] C. Babin, X. Ottavy, M. Dumas, Numerical characterization of a hp compressor stage equipped with a closed shrouded stator cavity, Proceedings of the ASME Turbo Expo GT2020-14908 (2020) 1–13.

[11] F. R. Menter, Two-equation eddy-viscosity turbulence models for engineering applications, AIAA Journal-doi:10.2514/3.12149.

[12] M. A. Iglesias, K. J. Law, A. M. Stuart, Ensemble kalman methods for inverse problems, Inverse Problems 29. doi:10.1088/0266-5611/29/4/045001.

[13] S. Reece, S. Roberts, An introduction to gaussian processes for the kalman filter expert, 13th Conference on Information Fusion, Fusion 2010doi:10.1109/icif.2010.5711863.

[14] G. G. Cruz, C. Babin, X. Ottavy, F. Fontaneto, Bayesian inference of experimental data for axial compressor performance assessment, Vol. 2A-2021, American Society of Mechanical Engineers, 2021. doi:10.1115/GT2021-59200.

[15] M. H. Aissa, T. Verstraete, Metamodel-assisted multidisciplinary design optimization of a radial compressor, International Journal of Turbomachinery, Propulsion and Power 4. doi:10.3390/ijtpp4040035.

[16] T. W. Simpson, J. D. Peplinski, P. N. Koch, J. K. Allen, Metamodels for computer-based engineering design: Survey and recommendations, Engineering with Computers 17 (2001) 129–150. doi:10.1007/PL00007198.

[17] J. N. Fuhg, A. Fau, U. Nackenhorst, State-of-the-Art and Comparative Review of Adaptive Sampling Methods for Kriging, Vol. 28, Springer Netherlands, 2021. doi:10.1007/s11831-020-09474-6.
URL https://doi.org/10.1007/s11831-020-09474-6

[18] R. Jin, W. Chen, A. Sudjianto, An efficient algorithm for constructing optimal design of computer experiments, Journal of Statistical Planning and Inference 134 (2005) 268–287. doi:10.1016/j.jspi.2004.02.014.

[19] F. A. Viana, A tutorial on latin hypercube design of experiments, Quality and Reliability Engineering International 32 (2016) 1975–1985. doi:10.1002/qre.1924.

[20] A. I. J. Forrester, A. Sóbester, A. J. Keane, Engineering Design via Surrogate Modelling, 2008. doi:10.1002/9780470770801.

[21] M. D. Morris, T. J. Mitchell, Exploratory designs for computational experiments, Journal of Statistical Planning and Inference 43 (1995) 381–402. doi:10.1016/0378-3758(94)00035-T.

Appendix 1 - Ensemble Kalman filter for Inverse problems Algorithm

The algorithm is described as it follow. Create an initial ensemble of parameters to infer $\boldsymbol{\theta} = (\theta, ..., \theta_a)$ by sampling j times the prior distributions $p(\boldsymbol{\theta})$:

$$\boldsymbol{\Theta} = (\theta_1, ..., \theta_a)_j^T = \begin{bmatrix} \theta_1^1 & ... & \theta_1^j \\ \vdots & & \vdots \\ \theta_a^1 & ... & \theta_a^j \end{bmatrix} \tag{12}$$

Propagate the initial ensemble $\boldsymbol{\Theta}$ trough the non-linear forward model, $\boldsymbol{G(\theta)}$:

$$\boldsymbol{Y} = (Y(\boldsymbol{x}))_j^T = \begin{bmatrix} Y_1^1 & ... & Y_1^j \\ \vdots & & \vdots \\ Y_x^1 & ... & Y_x^j \end{bmatrix} = \boldsymbol{G}\left(\boldsymbol{\theta}_j\right) + \boldsymbol{q(x)} \tag{13}$$

The output of this operation is a state matrix, $\boldsymbol{Y}$, in which the rows will correspond to the domain output $\boldsymbol{x}$ locations. For example, being the forward model a CFD simulation, the matrix rows will be a certain flow field quantity(e.g.: pressure) evaluated at the $\boldsymbol{x}$ mesh points. Again, the columns correspond to the different j ensemble members, which means different model solutions. The forward model error is assumed to be a multivariate Gaussian distribution with zero mean and an estimated covariance $\boldsymbol{q(x)} \sim \mathcal{N}(0, \boldsymbol{\Gamma_{model}})$.

Since measured observations $\boldsymbol{y}$ are only available in specific positions of the state vector $Y(\boldsymbol{x})_j$, a measurement matrix $\mathcal{M}$, acts as a projector operator on $Y(\boldsymbol{x})_j$ to obtain $\boldsymbol{Y(x_{exp})}$ where the rows correspond to the forward model results at the $\boldsymbol{x_{exp}}$ locations where observations $\boldsymbol{y}$ are available:

$$\boldsymbol{D} = \boldsymbol{d}_j^T = (Y(\boldsymbol{x_{exp}}))_j^T = \mathcal{M}[\boldsymbol{Y}] \tag{14}$$

In parallel, the measured observations matrix, $\boldsymbol{Y_{exp}}$ is built by adding measurement uncertainty ε to the observations $\boldsymbol{y}$.

$$\boldsymbol{Y_{exp}} = \boldsymbol{y}_j^T = \boldsymbol{y} + \boldsymbol{\varepsilon_j} \tag{15}$$

The posterior distribution for both the parameter $\boldsymbol{\theta}$ and state $Y(\boldsymbol{x})$ (observed and unobserved) inference is obtained by updating the corresponding matrices:

$$\begin{pmatrix} \Theta^{n+1} \\ \boldsymbol{Y}^{n+1} \end{pmatrix} = \begin{pmatrix} \Theta^n \\ \boldsymbol{Y}^n \end{pmatrix} + \begin{pmatrix} C_{\boldsymbol{\Theta D}} \\ C_{\boldsymbol{YD}} \end{pmatrix} (C_{\boldsymbol{DD}} + \boldsymbol{\Gamma})^{-1} \left(\boldsymbol{y}_j - \boldsymbol{d}_j^n\right) \tag{16}$$

with the involved covariance matrices calculated as:

$$\begin{aligned} C_{\boldsymbol{\Theta D}} &= \tfrac{1}{J} \textstyle\sum_{j=1}^{J} \boldsymbol{\theta}_j \left(\boldsymbol{d}_j\right)^T - \overline{\boldsymbol{\theta}}\overline{\boldsymbol{d}}^T \\ C_{\boldsymbol{YD}} &= \tfrac{1}{J} \textstyle\sum_{j=1}^{J} Y(\boldsymbol{x})_j \left(\boldsymbol{d}_j\right)^T - \overline{Y(\boldsymbol{x})}\overline{\boldsymbol{d}}^T \\ C_{\boldsymbol{DD}} &= \tfrac{1}{J} \textstyle\sum_{j=1}^{J} \boldsymbol{d}_j \left(\boldsymbol{d}_j\right)^T - \overline{\boldsymbol{d}}\overline{\boldsymbol{d}}^T \end{aligned} \tag{17}$$

where the means represent the average value over the ensemble. The superscript n is added since the algorithm allows the updated result to be iterated on by setting the updated parameter matrix $\boldsymbol{\Theta}$ as the new prior (Eq. 12).

Equation 16 updates both the parameter and the state matrices based on the difference between model predictions and measured observations multiplied by a weight matrix that is computed with the covariance matrices presented in Equation 17. This weight matrix is usually called Kalman gain. Intuitively, this weight balances the model accuracy and the measurement uncertainty. Each ensemble member j is updated independently, allowing the computation of the updated statistical moments on the ensemble.

Turbulence model assessment for the characterization of highly-loaded compressor stages

Riccardo Toracchio

Turbomachinery and Propulsion Department, von Karman Institute for Fluid Dynamics, Belgium, riccardo.toracchio@vki.ac.be

Supervisor: Fabrizio Fontaneto

Associate Professor, Turbomachinery and Propulsion Department, von Karman Institute for Fluid Dynamics, Belgium, fabrizio.fontaneto@vki.ac.be

University Supervisor: Koen Hillewaert

Associate Professor, Aerospace and Mechanical Engineering Department, University of Liège, Belgium, koen.hillewaert@uliege.be

Abstract

The turbulence model still represents a weak point of RANS simulations when dealing with complex turbomachinery flows. This is true especially for models based on the Boussinesq's isotropic eddy viscosity assumption that provide poor performance in a large variety of flow conditions, such as strong adverse pressure gradients and recirculating regions. In presence of large blade loadings the turbulence model can impact severely on the prediction of the low-momentum flow at the end-walls and influence the entire structure of secondary flows in the blade passage, with an important effect on the computed global performance. This paper presents a turbulence model comparison for the characterization of a highly-loaded low-pressure compressor at multiple operating points using 3D RANS simulations. The turbulence models employed are: Spalart-Allamars, Chien k-epsilon and Menter k-omega SST, which are frequently used for the design of axial compressors. The aim is to provide an overview of the implications of using a specific turbulence model, with a clear physical description of their impact on the critical flow features of the machine. Comparisons against experimental results are then used to assess the reliability of the models at design and near-stall conditions. It will be shown that for this type of compressors no single turbulence model is generally better than others and the prediction depends on the operating point analysed, with discrepancies increasing at reduced mass-flow operating conditions.

Keywords: Compressor, turbulence, CFD, secondary flows

1. Introduction

Several studies have been carried out in the past with the aim to characterize three-dimensional separations and secondary flows [1; 2; 3], which are considered the main source of losses in axial compressors, with relevant impact especially when approaching the stability of the machine. The role of the CFD in predicting the impact of these mechanisms has been increasingly important in the last years, up to the point that it is nowadays considered essential during the design process of turbomachinery [4; 5]. At the present state, RANS techniques are the most feasible solution to investigate turbomachinery flows and for compressor design, given still the large limitations of more time consuming approaches (such as LES and DNS) [6; 7]. However, the weakest point of RANS simulations is that the turbulence model adopted impacts severely on the prediction of the secondary flow structures. Turbulence model assessment on transonic axial compressors was performed in [8; 9; 10; 11; 12; 13]. The authors found that limited to the presented application, the SST model provided better performance in separated flow regions, followed by $k-\epsilon$ and Spalart-Allmaras (SA) turbulence models. However, no turbulence model is generally better than others in predicting real and complex flow features [14], especially in compressors develop-

ing large scale structures. The effect of the turbulence model on an axial compressor known to develop large scale vortices, such as tip-leakage and corner vortices, was analyzed in [15]. In the tip region the best prediction was provided by the SST model, while close to the hub it was the $k-$ to have superior performance against experimental results. Linear compressor cascades with highly-loaded blades were analysed in [16; 17; 18]. The $k-\epsilon$ model showed more reliable results, with respect to the SST and Spalart Allmaras, for what concerns the size and the intensity of the hub corner separation. However, these studies highlighted that the performance of the turbulence models is case-by-case dependent, and no general conclusion can be drawn about their reliability and accuracy.

The objective of this paper is to provide a turbulence model assessment for an highly-loaded low-pressure compressor by means of 3D RANS simulations. The models mostly used for the design of turbomachinery are considered: Menter $k-\omega$ SST and Chien $k-\epsilon$ turbulence models. Also results for the Spalart Allmaras model will be briefly described despite no results were available at near-stall conditions. The DREAM compressor, installed in the VKI R4 facility, and representative of the first stage of a modern low pressure compressor, will be used for this purpose. The main idea is to provide a physical explanation to the evolution of secondary flow structures appearing at operating points with reduced mass-flow, while highlighting advantages and drawbacks of the employed turbulence models by means of the validation against the experimental results.

2. Compressor test-rig and instrumentation

2.1. Experimental facility and test section

The VKI R4 facility is a closed-loop high-speed test-rig, composed by a tank used as settling chamber (1), the test section (2), a discharging collector at the compressor outlet (3), a return channel to guide the air back to the reservoir (4), and a throttling valve to run the compressor at different operating conditions (5) (Figure 1). An independent variation of temperature and pressure into the facility is possible by means of the heat exchanger (located upstream of the test compressor) and the closed-loop configuration, allowing to test cruise and take-off aircraft conditions. The test section considered is the DREAM compressor stage: a 1.5 stage, with equal number of inlet guide vanes (IGV) and outlet guide vane (OGV) stators, representative of the first stage of a low-pressure compressor (Figure 2, where the measurement planes are clearly identified).

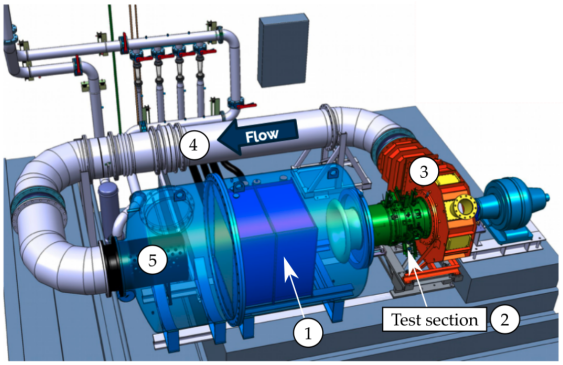

Figure 1: von Karman Institute R4 facility: closed-loop high-speed compressor test rig.

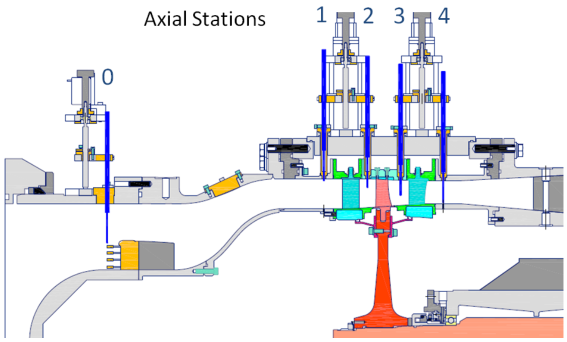

Figure 2: Dream test section.

2.2. Test section instrumentation

Probe traversing is allowed at four circumferential locations (0°, 90°, 180° and 270°) and for each measurement plane, axially located at stage inlet (plane 1), IGV outlet (plane 2), rotor outlet (plane 3) and stage outlet (plane 4). In this way, good resolution measurements of total pressure, temperature, Mach number and flow angles can be performed to properly characterize each location of the machine. For the measurement of the global performance, 4 combined total pressure and total temperature rakes are distributed circumferentially in plane 0, located upstream of plane 1, and in plane 4. A constant rotational speed of the compressor and a variation of the throttling valve position allow to retrieve the compressor map. +/- 0.00053 and 0.7% of the mass-flow at design conditions are the uncertainty respectively associated to the pressure ratio and the mass-flow.

A fast-response pressure probe, employed to obtain the phase-locked-average total pressure maps, is located at the rotor outlet and employed with acquisition frequency of 10Mhz for 10 seconds. It is characterized by resonance frequency of around 300 kHz and uncertainty calibration of +/- 1.8 mbar.

These uncertainty values are presented in a 95% confidence interval and calculated with the ASME method [19]. Further information about the test section instrumentation can be found in [20].

3. Numerical approach

3.1. Numerical setup

Fully-turbulent compressible RANS equations were solved by means of Numeca Fine/Turbo, and spatially discretized with a cell-centered finite volume formulation on a multi-block structured grid. At the inlet the total pressure and temperature retrieved with experiments were imposed, together with the turbulence intensity and viscosity ratio. The mass-flow boundary condition was imposed at the outlet. Air was considered as a calorically perfect gas, and the solid walls as adiabatic. An explicit multi-stage Runge-Kutta method combined with an implicit residual smoothing approach was considered for the time integration to a steady-state condition. Non reflecting boundary conditions with mixing plane approach were employed at the rotor-stator interfaces. For the turbulent closure, the Menter $k-\omega\ SST$, Chien $k-\epsilon$ and Spalart-Allmaras turbulence models were considered. Due to the divergence of the solution at near-stall (NS) conditions, the results for the SA model are only available at design (DE) and middle (MID) operating points. The formulation of the aforementioned models can be found in [21].

3.2. Numerical domain and mesh

3.2.1. Numerical domain

The role of real geometrical features, such as fillets and cavities, was assessed to understand their impact on the global performance and flow field of the machine. Fillets have been integrated into the domain due to their influence on the secondary flows structures and limited impact on mesh size, while the cavities have not been taken into account. Indeed, given their closed geometry on the test facility, they have very limited impact at rotor and stator inlets. Moreover, the rotor tip gap was set to the averaged measured value and hot geometries (i.e. in rotation) were employed. A meridional section and a blade-to-blade cut at 50% of the span of the presented compressor are reported respectively in Figure 3a and 3b.

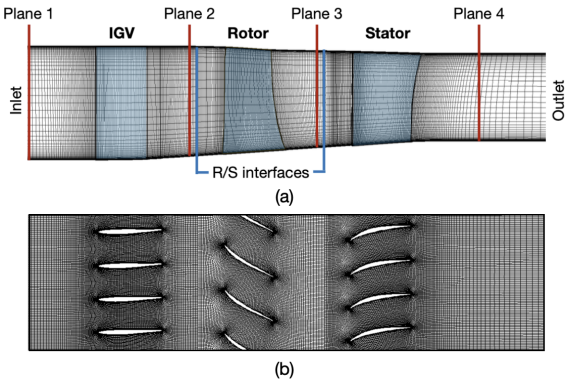

Figure 3: Numerical domain: meridional view (a) and B2B cut 50% span with channel repetition (b) on a coarser mesh.

In the present paper only the 100% speed of the compressor will be investigated.

3.2.2. Mesh quality

Autogrid5 and IGG softwares were used to generate a multi-block structured mesh. An O4H symmetric B2B topology and a OH topology ware considered for every blade row and the rotor tip gap region. For the creation of the hub and shroud fillets a B2B section offset method was considered, with 35 span-wise points and a minimum angle of 25° to guarantee a good distribution and angular deviation of the wall points. 81 cells and 20% constant size cells in the mid-flow gap region were used in the span-wise direction, and skewness level, maximum aspect and expansion ratios were set to provide good quality results. A value of y+ lower than 1.2 was guaranteed everywhere, while expansion ratio and cell width were adjusted to ensure a uniform distribution of cells at the wall.

Global performance and percentage difference of total pressure at the rotor outlet are reported in Figure 4 and Figure 5 considering a coarse, medium and fine mesh solution with 1.2, 9.2 and 73.8 million cells respectively. The fine mesh is here considered as reference case. An isotropic refinement by a factor of 2 was performed in the θ, R and Z directions. The rotor outlet region is considered as the most critical for the phenomena described in the present paper, and for this reason is chosen as location for the comparison. This study was performed with the $k-\omega\ SST$ turbulence model at DE conditions.

The good accuracy level of the medium mesh with respect to the reference, and the reduced computa-

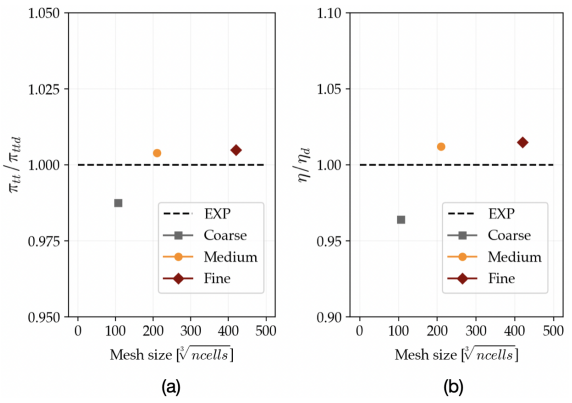

Figure 4: Comparison among mesh levels on the pressure ratio (a) and efficiency (b) of the compressor.

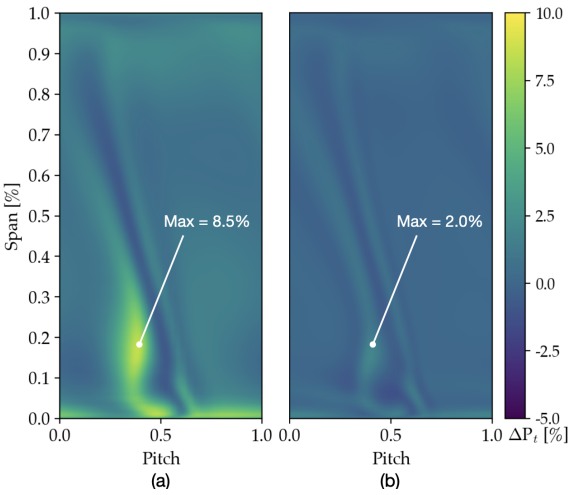

Figure 5: Percentage difference of the coarse mesh (a) and medium mesh (b) with respect to the reference case on the rotor outlet total pressure map.

tional cost, made it suitable to be employed in the simulations. The coarse solution, instead, as shown in Figure 5, presents discrepancies up to 8.5% when compared to the reference case due to the numerical dissipation induced in the recirculating regions of the flow, over-predicting the total pressure reduction.

4. Results

4.1. Overall observations

The large loading of the rotor blade and the high degree of reaction make the rotor a possible region for the development of critical secondary flow structures. In particular, the tested compressor presents a large value of the loading in the hub region, supporting the need of further investigating the development of the flow in this region. Figure 6 shows the skin friction lines on the rotor hub wall.

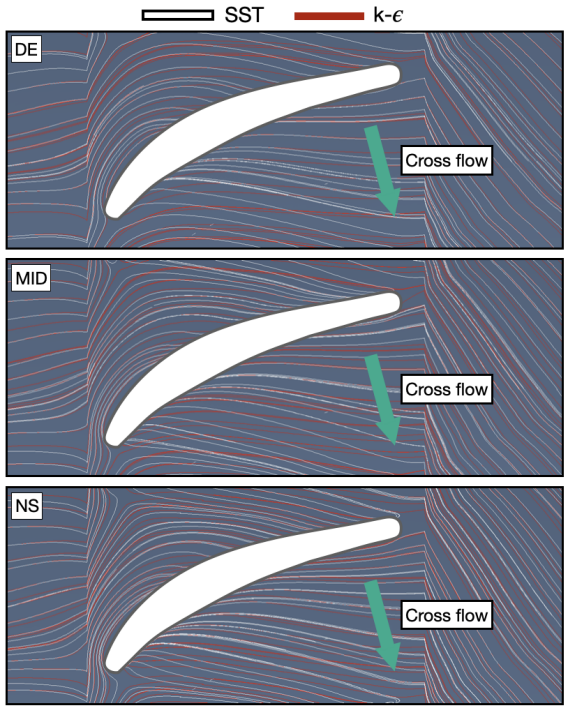

Figure 6: Skin friction lines on the rotor hub wall for SST (white line) and $k-\epsilon$ (red line) models.

From this picture, it is evident that a strong difference is present between the two turbulence models which highly impacts on the flow pattern in the rotor hub region. The SST turbulence model presents, indeed, larger cross-flow in the channel with respect to the $k-\epsilon$, pushing low-momentum flow on the suction side of the adjacent blade and possibly allowing the development of a more critical flow structure in that region. This is further enhanced by the impact of the horseshoe vortex legs in the rear part of the blade, contrarily to the $k-\epsilon$ turbulence model.

Given this evidence, the origin of such behavior and the large-scale effects induced in the entire machine need to be analysed and assessed. The intent is to quantify the differences between the investigated turbulence models and identify the physical quantities driving these secondary mechanisms since their earliest appearance. To do so, the flow quantities at rotor inlet will be firstly observed to understand the influence of inlet conditions on the evolution of the flow field, and then analysing the impact that such flow conditions may have downstream of the rotor blade.

4.2. *Flow conditions at the rotor inlet*

Figure 7a presents the bottom 50% span of the relative flow angle for DE, MID and NS conditions. At reduced mass-flow, discrepancies in the value of the incidence start to appear, and this become visible at MID condition for span lower than 25%. This is even more evident at near-stall condition, where a blockage effect appears in the blade passage that not only impacts the incidence, but also the axial velocity (Figure 7b). This may demonstrate the appearance of a large secondary structure which impacts on the blockage of the passage at NS conditions for the SST turbulence model. However, the skin friction lines around the LE do not reveal any relevant difference as the stagnation point is the same for both models.

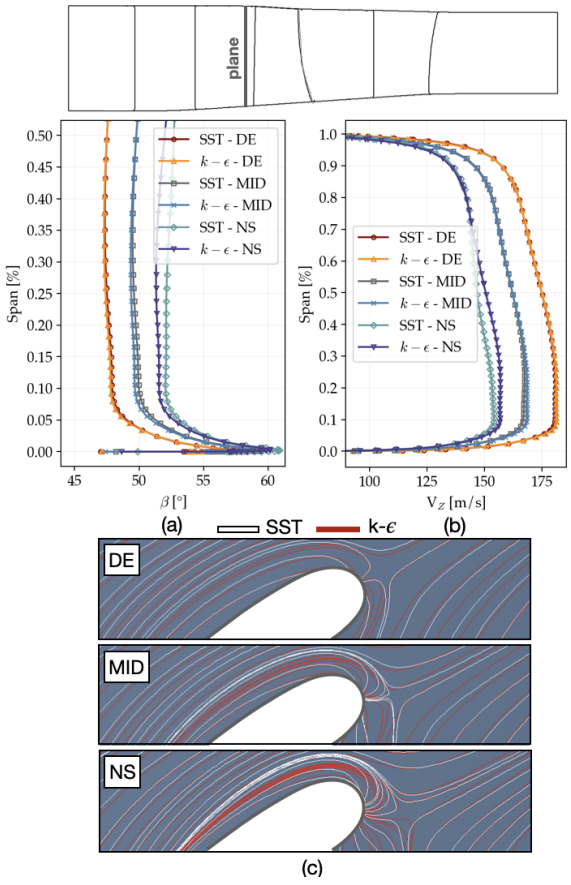

Figure 7: Rotor inlet conditions: relative flow angle (a), axial velocity (b) and hub-wall skin friction lines around the LE (c), at DE, MID AND NS conditions for SST and $k-\epsilon$ turbulence models.

Figure 8 presents the span-wise pitch-averaged distribution of the turbulent viscosity at the inlet and outlet of the rotor, non-dimensionalized with the dynamic viscosity of the flow.

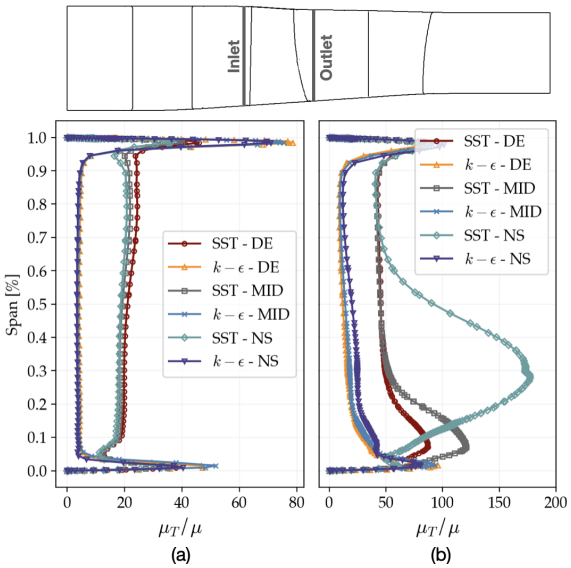

Figure 8: Span-wise distribution of eddy viscosity at rotor inlet (a) and outlet (b).

From the picture two opposite trends appear outside and inside the BL at the rotor inlet. Outside of the boundary-layer, the SST turbulence model presents indeed a larger value of the turbulent viscosity, while into the boundary-layer the trend is inverted. At rotor outlet, an overall increase of the eddy viscosity is visible due to the turbulent action determined by the development of a possible hub corner separation, as expected from a highly-loaded rotor in the hub region. However, the increase of the eddy viscosity from inlet to outlet is much more visible in the SST turbulence model with the variation of the operating point, which could be the trace of a more critical secondary structure developing in that region. The $k-\epsilon$ model, instead, almost does not present at all a variation of eddy viscosity distribution at lower mass-flow.

As a consequence of this behavior, a smaller boundary-layer eddy viscosity and boundary layer dimension for the SST model could therefore possibly reduce the migration of momentum from the mainstream into the boundary layer, decreasing the momentum of the end-wall flow compared to the $k-\epsilon$ model and increasing considerably the cross-flow component. In this way, in the SST model, the end-wall low-momentum flow accumulates on the blade suction side increasing the criticality of possible secondary structures at near-stall conditions. Opposite to this, the larger wall momentum for the $k-\epsilon$ turbulence model would decrease the cross-wise component of the velocity, as already demonstrated with Figure 6.

This difference in the prediction of the eddy viscosity and in the boundary layer height, could be therefore at the origin of the different behavior of the end-wall flow pattern in the rotor hub wall between the two turbulence models.

Moreover, as highlighted in Figure 7, the stagnation point around the leading edge at the hub is the same for the two cases, and therefore the inlet incidence does not play any role in this mechanism.

Anyway, these observation can be considered valid only for the present compressor given the large value of the loading in the hub region. The same conclusions can therefore not be extended to different blade geometries with reduced loading, where the end-wall flow pattern and the evolution of secondary flow structures could assume a less relevant role.

4.3. Impact on large-scale structures

4.3.1. Rotor flow field

The IGV of the present stage was installed to simulate the radial distribution of the flow angle behind a fan and deliver a smooth flow at the rotor inlet, therefore no critical features should take place inside the IGV passage. However, in a highly-loaded rotor blade row, more critical features can appear, such as the tip leakage vortex (TLV) and the hub corner separation, which could lead to flow instabilities and stall inception as mass-flow is reduced [22; 23; 24; 25]. It is therefore worth to detect any possible critical behavior close to the stability limit of the machine looking closer to the casing and hub of the rotor blade.

Figure 9 shows the entropy contour at the rotor casing.

The increased loading at reduced mass-flow induces the streamlines of the tip leakage vortex to become more tangential, with increased entropy gradient across the TLV interface and maximum local entropy. This is visible for both turbulence models. Moreover, at the location of the rotor trailing edge an increase of entropy is representative of a recirculating structure for both turbulence models. However, no clear critical behavior is detected at reduced mass-flow and the flow pattern predicted by the SST and $k-\epsilon$ turbulence models is quite similar for all of the operating conditions.

Figure 10 shows the skin friction lines on the suction side of the rotor blade.

Two flow mechanisms are visible from this picture: a corner separation close to the hub wall and a shock-boundary layer interaction (SBLI) separation in the front part of the blade. The predicted hub corner separation is different for the two models, and the SST

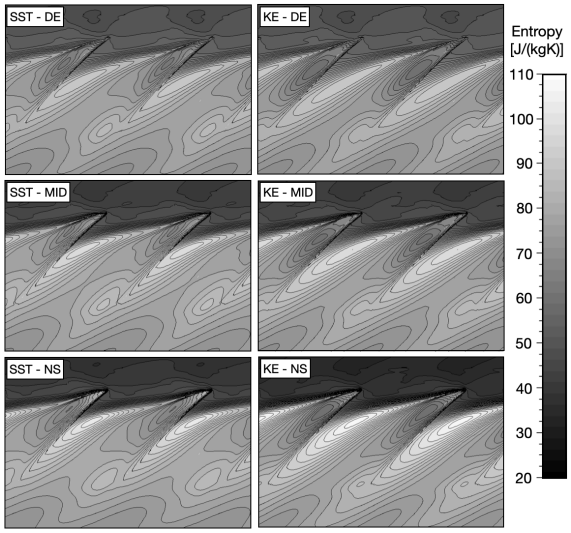

Figure 9: Entropy distribution at casing for SST and $k-\epsilon$ models at DE, MID AND NS conditions.

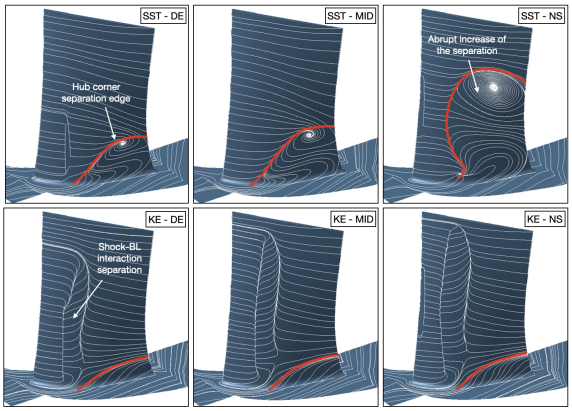

Figure 10: Skin friction lines on rotor blade suction side for SST and $k-\epsilon$ models at DE, MID AND NS conditions.

clearly predicts a larger increase of the corner separation, while for the $k-\epsilon$ this increase is much smoother going form DE to NS. The separation takes place only on the suction side of the blade and on the hub wall the boundary layer keeps attached. The same can be observed in 11, which shows the non-dimensional total pressure map at rotor outlet at near-stall conditions. Concerning the SBLI, only the $k-\epsilon$ model predicts its span-wise and stream-wise variation over the entire operating range of the machine and it assumes larger dimensions with respect to the SST turbulence model. This is a consequence of the reduced eddy viscosity into the main channel for the $k-\epsilon$ model, which reduces the resistance of the boundary-layer to the separation.

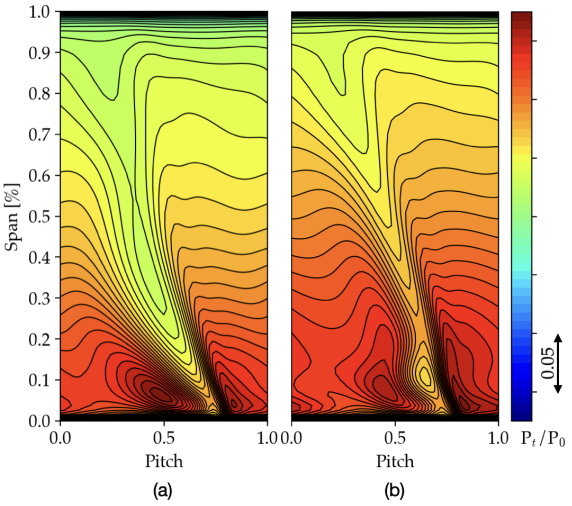

Figure 11: Total pressure map at rotor outlet for SST (a) and $k-\epsilon$ (b) models at near-stall conditions.

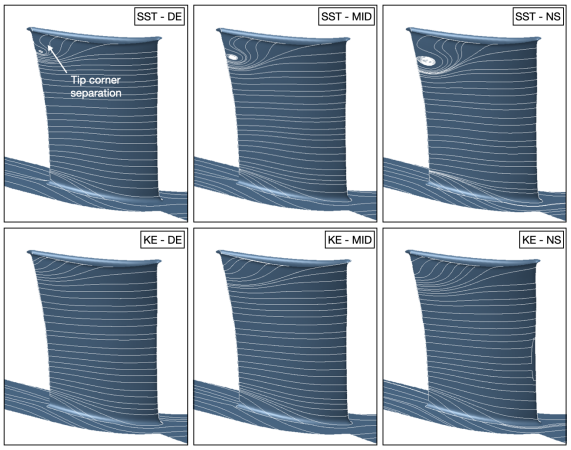

Figure 12: Skin friciton lines on the outlet stator suction side.

It is evident that the reasons behind the different turbulent activity at the rotor outlet are the consequence of a critical development of the rotor hub corner separation for the SST turbulence model. This structure not only reduces the total pressure close to the rotor hub as it happens for the $k-\epsilon$ turbulence model, but involve the entire blade span strongly impacting the losses of the machine (Figure 10). The large loading coefficient of the rotor blade in the hub region (up to 0.75) and the high degree of reaction of the machine (0.86 computed via enthalpy ratios) support this interpretation and the fact that the rotor is prone to develop critical flow structures.

4.3.2. Outlet stator flow field

To check the impact of this structure on the entire flow path of the compressor, the flow pattern on the suction side of the outlet stator is reported in Figure 12.

In the tip region, a corner separation develops but it does not assume the critical behavior of the rotor hub corner one, and it keeps stable all over the operating range of the machine. As expected, the size of the separation increases as mass-flow reduces.

4.3.3. Global performance

It is important to assess the impact of the the detected flow structures on the global performance of the machine. The compressor map non-dimensionalized with respect to the experimental values at design condition, and retrieved with the proposed turbulence models, is shown in Figure 13. The uncertainties linked to the pressure ratio and the mass-flow are reported in the picture (even if the pressure ratio uncertainty is rather small to be visible). The MID operating point is at half operative range with respect to design and near-stall conditions and it is the only point for which an experimental validation does not exist.

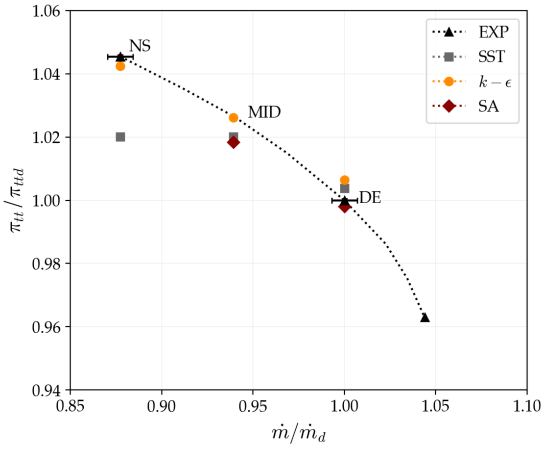

Figure 13: Compressor map obtained by experiments (black) $k-\omega$ SST (grey), $k-\epsilon$ (orange) and SA (red) turbulence models.

At the DE point a difference of 0.62%, 0.38% and 0.2% exists for the pressure ratio predicted by $k-\epsilon$, SST and SA models respectively and the one of the experiments. However, at NS the SST model predicts a totally wrong pressure ratio, as a consequence of the abrupt development of the hub corner separation at reduced mass-flow. The SA model is instead not able to reach the near-stall conditions due to a too strong decrease of the pressure ratio which induces

the simulation to diverge, and only the results at DE and MID operating points are available. This is the reason why only the SST and $k-\epsilon$ turbulence models have been analysed in the paper, as they provide the necessary information to describe possible and different developments of the flow field at NS conditions.

The outcome of this section is that despite the turbulence model impacts on the evolution of the endwall flow pattern and the inlet turbulent quantities all over the operating range of the compressor, at DE condition the overall performance of the compressor is well predicted by both models. However, at reduced mass-flow the turbulence model plays a crucial role as it has a huge impact on the predicted size intensity of the critical flow features, that in this specific case are mainly represented by the hub corner separation.

5. Validation against the experimental results

The reliability of the turbulence model to predict properly flow field and global performance for a specific operating condition is here assessed against the experimental results. As mentioned earlier, only experimental results at design and near-stall operating points are available.

5.1. Span-wise validation at rotor and stator outlets

The comparison of total pressure, temperature and absolute flow angle distributions of the proposed turbulence models against the experimental results is plotted in Figure 14, Figure 15 and Figure 16 in plane 3 (outlet rotor) and plane 4 (outlet of the stage). In these planes, the most important features of the compressor can be observed. The uncertainty for the worst case scenario is reported in the plots.

For the total pressure distributions at rotor outlet, both turbulence models provide results well in agreement with experiments at design conditions, with larger differences in the hub region due to the presence of the corner separation. However at near-stall conditions the results of the $k-\epsilon$ model are better than those of the SST, as expected from the analysis of the compressor map. The TLV evolution, along with the corner separation in the tip region of the stator, determine the differences between experiments and simulations for span location above 60%.

Similar conclusions can be drawn for the total temperature, despite it should be remembered that adiabatic boundary conditions were employed on the solid walls. Indeed, at near-stall conditions the SST model

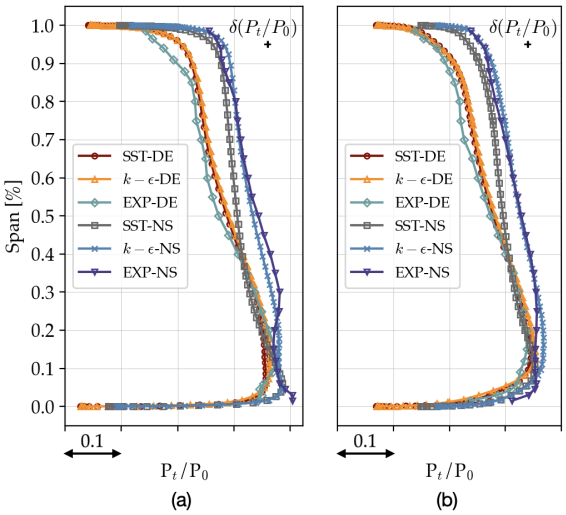

Figure 14: Total pressure predicted by SST and $k-\epsilon$ turbulence models against the experimental results at rotor outlet (a) and stage outlet (b).

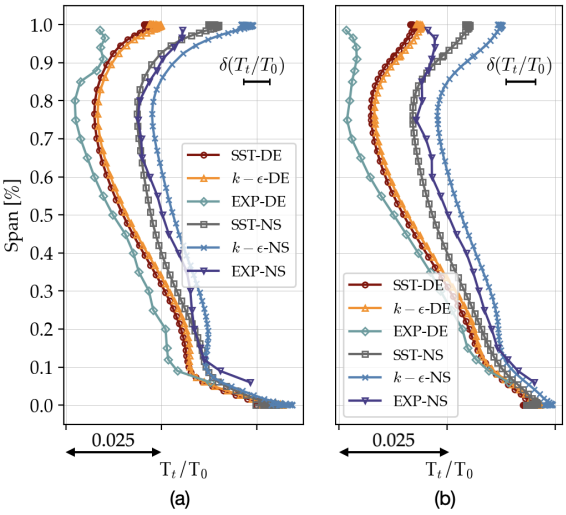

Figure 15: Total temperature predicted by the SST and $k-\epsilon$ turbulence models against the experimental results at rotor outlet (a) and stage outlet (b).

presents better results in the tip region, while the opposite happens on the hub. Both models, at design condition, provide good quality results against the experiments.

For the absolute flow angle at the rotor outlet, the SST model is closer to experiments at near-stall conditions but this depends mainly to the fact that the simulations globally overestimates the flow angle. This is visible also at the stage outlet, where globally the experimental flow angle is 2° smaller than the numerical

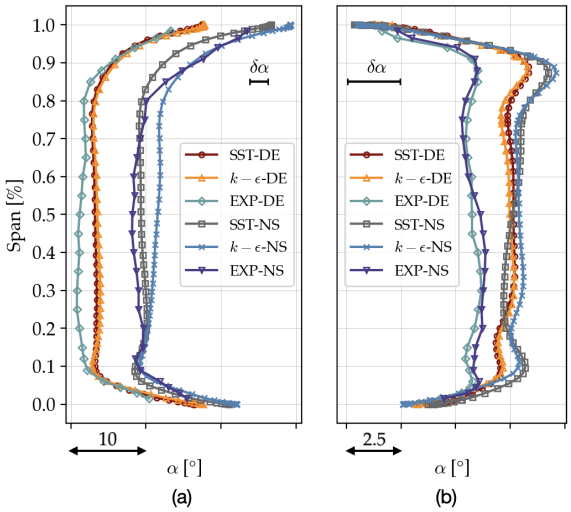

Figure 16: Absolute flow angle predicted by SST and $k-\epsilon$ turbulence models against the experimental results at rotor outlet (a) and stage outlet (b).

one. The reduced $k-\epsilon$ flow angle in plane 3 at 10% span comes from the more axial flow at rotor outlet, as a consequence of the larger end-wall momentum flow, as explained in the previous paragraphs. Moreover, the variation of the operating point impacts largely the flow angle at rotor outlet by an increment of 8° of the flow angle, but the same does not happen at stator outlet, with an angle which keeps constant around 5°.

5.2. 2D validation at rotor outlet

Figures 17 and 18 show a percentage difference of the total pressure at rotor outlet at design and near-stall conditions respectively.

At design conditions (Figure 17), the SST model is more in agreement with the experiments for span lower than 30%. In this region, the maximum percentage difference for the SST model is 3.9%, while for the $k-\epsilon$ model is 5.6%. Close to the tip, instead, they provide similar prediction of the total pressure. At near-stall conditions (Figure 18), the prediction of the two turbulence models is quite similar closer to the hub with a 6.2% difference with respect to experiments, and the SST works properly close to the tip region. However, it completely fails in the prediction of the total pressure at mid-span which is a consequence of the critical development of the separation on the rotor suction side.

6. Conclusions

In the present paper, 3D RANS simulations with the mostly employed turbulence models for the design and analysis of axial compressors were presented, with the intent to assess their influence on the development of the critical flow structures of a highly-loaded compressor. Menter $k-\omega$ SST, Chien $k-\epsilon$, and Spalart Allmaras models were compared, despite for the SA no results were available at NS conditions.

The following conclusions can be drawn from the present analysis:

1. The SST turbulence model develops larger hub cross-flow, which pushes more low-momentum flow toward the suction side of the adjacent blade, enhancing the development of critical flow structures in that region. The opposite behavior is instead visible for the $k-\epsilon$ model. The larger end-wall momentum, indeed, does not allow the horseshoe vortex to impact the rear part of the blade and to accumulate low-momentum flow on the blade corner;
2. The reasons behind such behavior seem to come from the eddy viscosity distribution at the rotor inlet. The lower turbulent viscosity for the SST model in the boundary-layer allows a smaller migration of momentum from the main-flow into the boundary layer with respect to the $k-\epsilon$. This enhances the evolution of tangential cross-flow and critical flow structures on the rotor hub corner.
3. The most critical feature at reduced mass-flow is the separation developing between the rotor suction side and the hub wall. The $k-\epsilon$ turbulence model provides good matching with the experimental global performance, while the SST totally fails this prediction due to the overestimation of the size and intensity of the hub corner separation.
4. The validation against the experimental results shows that no single turbulence model is in general better than the other, and their effectiveness depends on the operating point. At design conditions, the SST model provides better results close to the hub region, while at near-stall operating point it is the $k-\epsilon$ to provide more accurate results. Close to the tip, both models provide results well in agreement with the experiments.

As general outcome, this paper wanted to highlight the effectiveness and weakness of different turbulence models in compressors where the presence of large

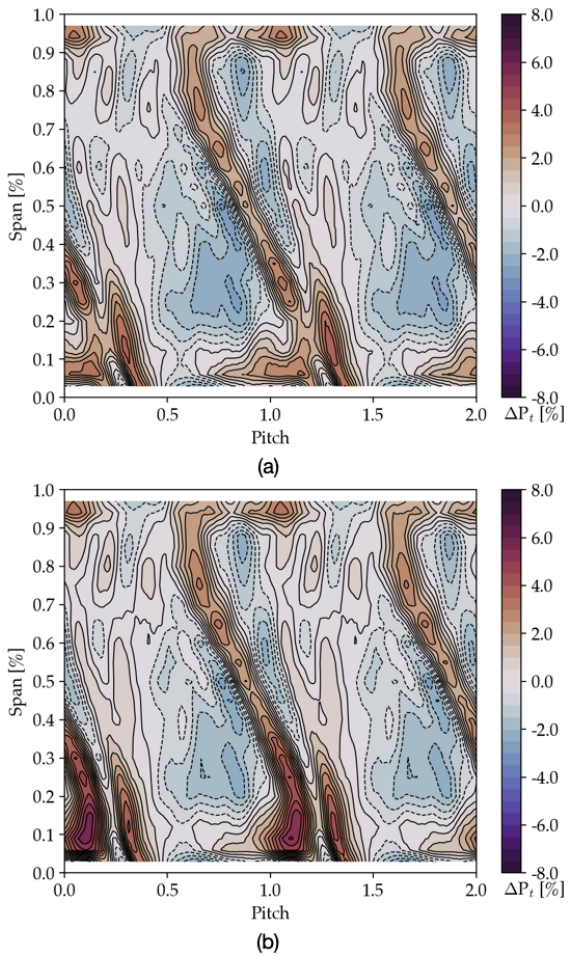

Figure 17: Total pressure percentage difference between SST (a) and $k-\epsilon$ (b) turbulence models against experiments at rotor outlet - DE conditions.

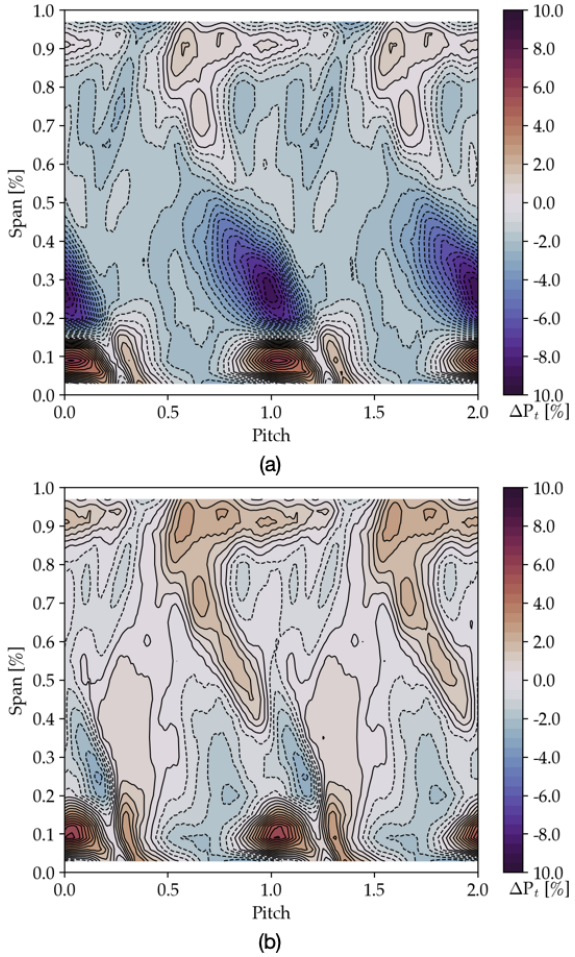

Figure 18: Total pressure percentage difference SST (a) and $k-\epsilon$ (b) turbulence models against experiments at rotor outlet - NS conditions.

scale structures can massively influence the results of a simulation. By doing so, the authors hope to increase awareness about the inherent dangers of relying too much on the results of a single turbulence model to draw conclusions about the evolution of critical flow features and the near-stall behavior of compressors.

Acknowledgments

The authors would like to acknowledge the F.R.S-FNRS for funding the scholarship of Mr. Riccardo Toracchio.

References

[1] Y. Dong, S. J. Gallimore, H. P. Hodson, Three-dimensional flows and loss reduction in axial compressors, Journal of Turbomachinery 109 (3) (1987) 354–361.

[2] J. D. Denton, Loss mechanisms in turbomachines, ASME 93-GT-435 (1993) 1–40.

[3] S. A. Gbadebo, N. A. Cumpsty, T. P. Hynes, Three-dimensional separations in axial compressors, Journal of Turbomachinery 127 (2) (2005) 331–339.

[4] J. D. Denton, W. N. Dawes, Computational fluid dynamics for turbomachinery design, Proceedings of the Institution of Mechanical Engineers, Part C: Journal of Mechanical Engineering Science 213 (2) (1998) 107–124.

[5] R. N. Pinto, A. Afzal, L. V. D'Souza, Z. Ansari, A. D. M. Samee, Computational fluid dynamics in turbomachinery: a review of state of the art, Archives of Computational Methods in Engineering 24 (3) (2017) 467–479.

[6] P. G. Tucker, Trends in turbomachinery turbulence treatments, Progress in Aerospace Sciences 63 (2013) 1–32.

[7] J. Tyacke, N. R. Vadlamani, W. Trojak, , R. Watson, Y. Ma, P. G. Tucker, Turbomachinery simulation challenges and the future, Progress in Aerospace Sciences 110 (2019) 100554.

[8] J. E. Bardina, P. G. Huang, T. J. Coakley, Turbulence modeling validation, testing and development, NASA Technical Memorandum 110446 (1997) 147.

[9] M. R. Simoes, B. J. Montojos, N. R. Moura, J. Su, Validation of turbulence models for simulation of axial flow compressor, in: Proceedings of COBEM, 20th International Congress of Mechanical Engineering, Gramado, RS, Brazil, 2009.
[10] T. Arima, T. Sonoda, M. Shirotori, A. Tamura, K. Kikuchi, A numerical investigation of transonic axial compressor rotor flow using a low-Reynolds-number $k - \epsilon$ turbulence model, Journal of Turbomachinery 121 (1) (1999) 44–58.
[11] F. Ning, L. Xu, Numerical investigation of transonic compressor rotor flow using an implicit 3D flow solver with one-equation Spalart-Allmaras turbulence model, in: Proceeding of ASME Turbo Expo, New Orleans, Louisiana, USA, 2001, 2001-GT-0359.
[12] Y. Song, J. Donghai, D. Xingmin, Z. Fangs, Application and comparison of SST model in numerical simulation of the axial compressors, Journal of Thermal Science 19 (4) (2010) 300–309.
[13] X. He, F. Zhao, M. Vahdati, Evaluation of Spalart-Allmaras turbulence model forms for a transonic axial compressor, in: Proceedings of Global Power and Propulsion Society, GPPS Chania, 2020, gPPS-CH-2020-0013.
[14] M. V. Casey, Validation of turbulence models for turbomachinery flows - a review, Engineering Turbulence Modelling and Experiments *V*, Elsevier Science Ltd (2002) 43–57.
[15] Y. Liu, X. Yiu, B. Liu, Turbulence models assessment for large-scale tip vortices in an axial compressor rotor, Journal of Propulsion and Power 24 (1) (2008) 15–25.
[16] H. Zhang, Y. Wu, Y. Li, Evaluation of RANS turbulence models in simulating the corner separation of a high-speed compressor cascade, Engineering Applications of Computational Fluid Mechanics 9 (1) (2015) 477–489.
[17] L. Yangwe, Y. Hao, L. Yingjie, L. Lipeng, L. Qiushi, Numerical study of corner separation in a linear compressor cascade using various turbulence models, Chinese Journal of Aeronautics 29 (3) (2016) 639–652.
[18] H. Yan, Y. Liu, Q. Li, L. Lu, Turbulence characteristics in corner separation in a highly loaded linear compressor cascade, Aerospace Science and Technology - AESCTE 4378 75 (2018) 139–154.
[19] ANSI, ASME, ANSI/ASME PTC 19.1-2005 measurement uncertainty, American Society of Mechanical Engineers.
[20] G. Dell'Era, N. Habotte, J. Desset, J.-F. Brouckaert, S. Hiernaux., Experimental characterization of stall phenomena in a single-stage low-pressure axial compressor, Journal of Power and Energy 229 (5) (2015) 549–559.
[21] Numeca International, Fine/Turbo theory guide, 13th Edition (2019).
[22] C. Hah, J. Loellbach, Development of hub corner stall and its influence on the performance of axial compressor blade rows, Journal of Turbomachinery 121 (1) (1999) 67–77.
[23] M. Choi, J. H. Baek, S. H. Oh, D. J. Ki, Role of the hub-corner-separation on the rotating stall, 42nd AIAA/ASME/SAE/ASEE Join Propulsion Conference Exhibit - AIAA 2006 (2006) 4462.
[24] S. A. Weichert, Tip clearance flows in axial compressors: stall inception and stability enhancement, PhD Thesis, University of Cambridge, Department of Engineering, Cambridge, MA (September 2011).
[25] M. H. Smith, G. Pullan, S. D. Grimshaw, E. M. Greitzer, Z. S. Spakovszky, The role of tip leakage flow in spyke-type rotating stall inception, in: Proceedings of ASME Turbo Expo, Charlotte, NC, USA, 2017, gT2017-63655.

TURBINE AERODYNAMICS AND HEAT TRANSFER

An experimental test case for transonic low-pressure turbines - Part 2: Cascade aerodynamics at on- and off-design Reynolds and Mach numbers

Gustavo Lopes

Turbomachinery and Propulsion Department, von Karman Institute for Fluid Dynamics, Belgium, gustavo.lopes@vki.ac.be

Supervisor: Sergio Lavagnoli

Associate Professor, Turbomachinery and Propulsion Department, von Karman Institute for Fluid Dynamics, Sint-Genesius-Rode, Belgium, lavagnoli@vki.ac.be

University Supervisor: Koen Hillewaert

Professor, Département d'Aérospatiale et Mécanique, Université de Liège, Liège, Belgium, koen.hillewaert@uliege.be

Abstract

In this work a detailed analysis of the blade aerodynamics and secondary flows in a transonic linear cascade are presented for a range of Mach number from 0.70 to 0.95 and Reynolds number from 65,000 to 120,000. The investigations are performed in the VKI S-1/C transonic linear cascade at engine-representative conditions without unsteady wakes nor purge.

Keywords:
High-speed LPT, Transonic linear cascade, Off-design, Secondary flows

1. Introduction

The Ultra-High By-Pass Ratio Geared Turbofan (GTF) is a key architecture with potential to reduce emissions and noise footprint of the next generation of aviation. As detailed by Kurzke [1], the GTF becomes a more attractive solution for by-pass ratios higher than 10, enabling reduction of specific fuel consumption (SFC), low-pressure turbine (LPT) stage count and weight. The latter can account for as much as 1/3rd of the overall engine weight [2]. Torre et al. [3] performed a thorough investigation of a high-speed LPT in a transonic rotating rig.

Due to the increase in rotational velocity of the low-pressure spool imposed by the gearbox, the LPT operates at transonic exit Mach numbers ($M_{out} > 0.80$) in combination with low-Reynolds numbers encountered during cruising regime [4]. The combination of these flow regimes has been highlighted as one of the main challenges in the development of transonic LPTs for GTFs [5; 6]. Vázquez and Torre [7] pointed out that shock-boundary layer interactions prone to occur in high-speed LPTs can change the transition mechanism and affect the losses.

In conventional LPTs, the profile losses are often predominant over the secondary flow losses due to large aspect ratio encountered in these blades [2]. Hodson and Dominy [8] found the profile and secondary flow losses to be of comparable magnitude in their investigation of a conventional LPT blade operating engine-representative Mach and Reynolds numbers in a linear cascade. In order to design efficient LPT modules, the impact of secondary flows must carefully considered and accurately quantified in the overall turbine loss budget.

Vera et al. [9] investigated the impact of the outlet Mach number on the performance of a LPT linear cascade operating at Reynolds number of 200k. They found the profile loss to be independent of the Mach number up to 0.76, increasing for higher Mach. This was contradicted by Vázquez et al. [10] in their investigation performed in an annular cascade. The increase in losses was attributed to the shift in the velocity peak resultant of increasing the Mach number. They also found decreasing profile losses with increasing Reynolds number. Perdichizzi [11]

investigated the impact of the Mach number on the secondary flow development in a high-pressure turbine (HPT). He found that an increase on the outlet Mach number constrains the secondary flow structures closer to the endwall. A decrease in the under/overturning as well as losses was also found with increasing Mach number.

Hodson and Dominy [12] investigated the impact of the Reynolds number on the secondary flow losses in a LPT linear cascade tested at outlet Mach number close to 0.70 and Reynolds numbers varying between 150k and 600k. They presented an increase in the secondary flow losses with increasing Reynolds number. Duden and Fottner [13] investigated the impact of Mach and Reynolds on the performance of two LPT blades operating and engine-relevant Mach and Reynolds numbers in a linear cascade. Their Reynolds and Mach numbers ranged from 120k to 500k, and 0.30 to 0.80, respectively. They reported a decrease in secondary loss as Mach and Reynolds increased.

In this work the steady aerodynamics of a transonic LPT cascade are investigated at on- and off- design flow. The investigation is performed at engine-representative outlet Mach and Reynolds numbers. The impact of the Mach and Reynolds number on the secondary flows as well as blade performance are achieved by downstream flow traverses and blade surface measurements.

2. EXPERIMENTAL APPARATUS

2.1. The VKI S-1/C High-Speed Linear Cascade

The on- and off-design measurements are performed at engine-scaled conditions in the transonic linear cascade present at the von Karman Institute for Fluid Dynamics. Fig. 1(left) shows the layout of the cascade in the configuration used for the measurements analyzed in this paper. A detailed description of the facility can be found in [14; 15; 16]. Since the current study is aimed at characterizing the test-case baseline, the wake generator bars were not present. The geometry of the tested blade is depicted in Fig. 1(right).

2.2. Experimental Methodology

2.2.1. Blade Measurements

The characterization of the blade steady aerodynamics is obtained by combining measurements performed with two instrumented blades. The location of

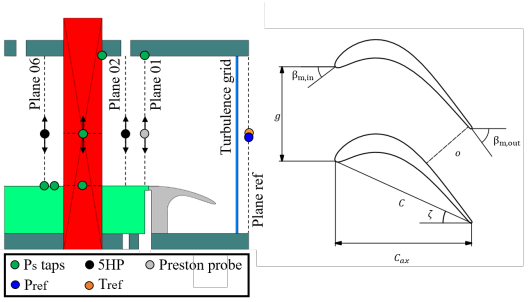

Figure 1: Cascade C1 (left) configuration and (right) geometry

the pressure taps is displaced by traversing the instrumented airfoils by 46 equally spaced spanwise locations starting from the endwall, z/H = 0, until the past midspan, z/H = 0.55.

2.2.2. Downstream Flow Field

The downstream flow field is surveyed with an L-shaped miniaturized five-hole probe at $0.50C_{ax}$ downstream of the central blade trailing edge (Plane 06). The probe is calibrated at atmospheric conditions for a range of yaw (α) and pitch (γ) angles of ±30°at different Mach numbers varying between 0.20 and 0.95. Since the Reynolds number based on the probe head diameter is in the order of 3k downstream of the cascade, the Reynolds dependence on the calibration is assumed negligible [17]. The probe is used in non-nulling mode and the retrieval of the yaw angle, pitch angle, total pressure, static pressure and Mach number is achieved through the calibration coefficients detailed in [18] and an iterative process depicted in [18]. Wall proximity effects affecting the probe measurements are avoided by considering data points that are sampled at least two head diameters away from the endwall (H > 4.4 mm) as recommended in [19]. The error induced by the spatial resolution of the probe ports is reduced by applying the first correction proposed by [20]. A non-uniform grid with refinement in the blade wake and endwall region is used to resolve the high gradients.

3. RESULTS AND DISCUSSION

3.1. Blade Aerodynamics

3.1.1. Isentropic Mach Number Distributions

The profile isentropic Mach number distributions for the investigated flow conditions are displayed in Fig. 2. The Mach number is plotted in function of the distance along the pressure or suction side surface

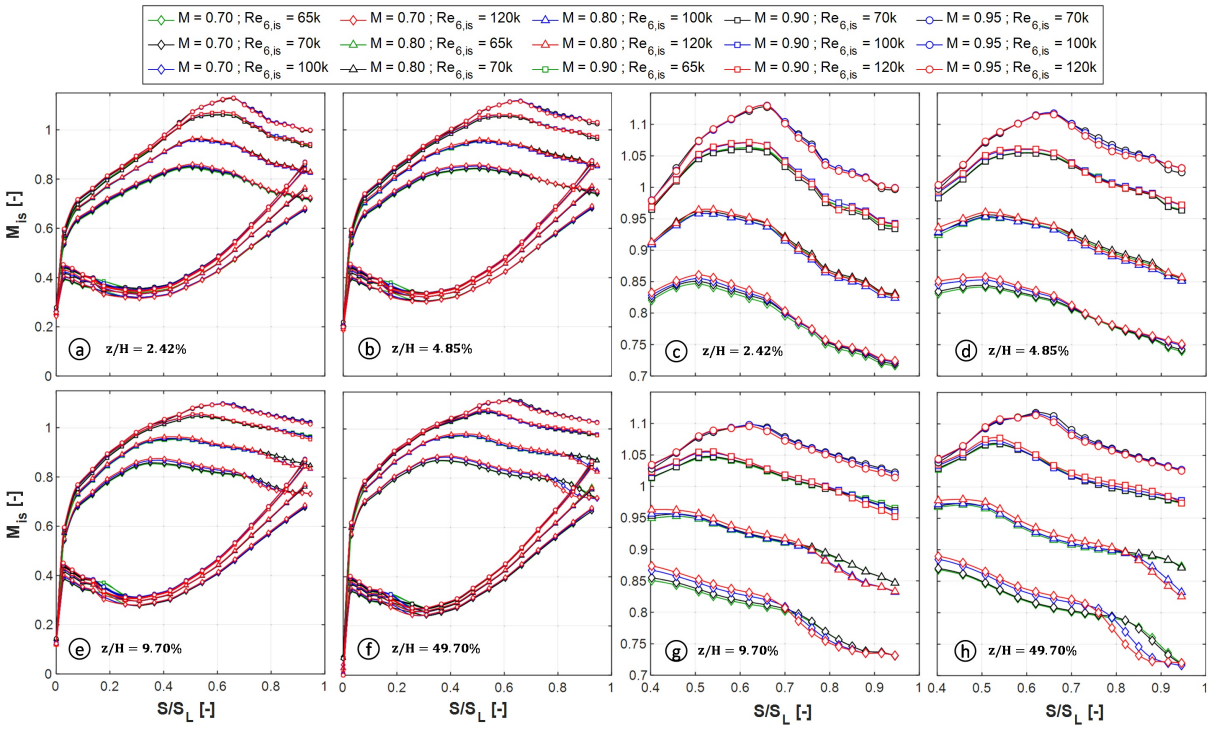

Figure 2: Comparison of (a, b, e, f) PS and SS profile isentropic Mach number distribution and (c, d, g, h) detail of rear part of SS for all investigated flow conditions at different spanwise locations

length, respectively. The distributions at four different span sections (z/H: 0.024, 0.049, 0.097 and 0.50) are presented to assess the impact of secondary flows as the distance to the endwall is reduced. The isentropic Mach number is computed using the blade static pressure and the total pressure outside of the boundary layer upstream of the cascade. All considerations on the blade suction side boundary layer status are drawn based on the analysis of the blade load distributions.

Fig. 2(a), Fig. 2(b), Fig. 2(e) and Fig. 2(f) provide insight on the impact of the outlet Mach on the distributions. An increase in Mach is translated into an increase of the blade loading as well as a shift of the velocity peak towards the TE. As z/H increases from the endwall to midspan, a reduction of the blade M_{is} before the velocity peak is perceptible.

In the two-dimensional flow region represented in Fig. 2(h), the outlet Reynolds number has the greatest impact for exit Mach numbers below 0.90. Distinctive closed separation bubbles are observed in the case of $Re_{6,is}$=100k and 120k for the case of an outlet Mach of 0.70. The location of the separation and reattachment is found at S/S_L ≈0.54 and 0.87, respectively. Flow reattachment for the two lowest Reynolds is predicted to be further downstream at at S/S_L ≈0.92. An increase in the Mach number to 0.80 shifts the separation location, S/S_L ≈0.56, towards the TE for all cases. Even though no reattachment occurs for the cases of $Re_{6,is}$=65k and 70k, for the highest Reynolds cases reattachment occurs at S/S_L ≈0.92. As the exit Mach number is increased past 0.90, the Reynolds effect is extremely weak. For all the investigated Reynolds, the suction side flow undergoes separation at S/S_L ≈0.65 for $M_{6,is}$ = 0.90. For the highest Mach investigated, we speculate that compressibility effects in the form of a weak normal shock standing past the throat region may force separation at S/S_L ≈0.68, making the separation onset insensitive to the Reynolds number.

The effect resultant from the interaction between the secondary flows and the separation/reattachment is visible at z/H=0.097 (Fig. 2(g)). For $M_{6,is}$=0.70, the closed bubble separation location is shifted upstream to S/S_L ≈0.51 comparatively to the case of z/H=0.497 for all Reynolds numbers investigated. The reattachment location is brought upstream due to secondary flow interactions and is shifted downstream as Reynolds decreases, ranging between. S/S_L ≈0.78 and 0.86 for the highest and lowest Reynolds, respectively. The secondary flows have similar effect in

shifting the separation and reattachment locations upstream for $M_{6,is} = 0.80$ even though the flow does not reattach for the cases of $Re_{6,is}$=65k and 70k. The increase in Mach number shifts the separation location downstream to $S/S_L \approx 0.55$ for all Reynolds investigated. In the case of $Re_{6,is}$=100k and 120k, the reattachment is also shifted downstream to $S/S_L \approx 0.87$. As the outlet Mach increases to 0.90, the flow separates and does not reattach for any of the investigated Reynolds numbers. In addition, a shift of the separation location downstream is observed ($S/S_L \approx 0.66$). Lastly, the Reynolds effect is practically eliminated for the highest Mach number of 0.95. For the latter, the location of the separation shifts further downstream ($S/S_L \approx 0.69$) and the flow remains detached from the SS.

3.2. Downstream Flow Field

The secondary flows are characterized according to the secondary flow model of Wang et al. [21]. The model reinforced the work of Sieverding and Van Den Bosche [22] who proved that the pressure side leg of the horseshoe vortex wraps around the passage vortex describing an orbital motion. In addition, a wall induced vortex arises due to the impingement of the passage vortex on the blade SS.

3.2.1. Loss coefficient

The energy loss coefficient, ξ, used in this investigation is defined as:

$$\xi = 1 - \frac{1 - (\frac{P_6}{P_{06}})^{\frac{\gamma-1}{\gamma}}}{1 - (\frac{P_6}{P_{01,fs}})^{\frac{\gamma-1}{\gamma}}} \tag{1}$$

In Eq. 1, the total, P_{06}, and static, P_6, pressures downstream of the cascade are measured locally with the five-hole probe while the freestream inlet total pressure, $P_{01,fs}$, is estimated using a correlation built on experimental data. Fig. 3 presents the contours of energy loss coefficient obtained at on- and off-design conditions. For all cases, a similar topology of the secondary flow structures can be observed.

In the endwall region, two main loss cores are visible. The first one sits at $y/g \approx 0$ and is associated with the SS corner vortex, V_{sc}. Even though the spanwise location cannot be accurately described due to the instrumentation limitations, the corner vortex effect is measured as low as z/H=0.024. The second one is at $y/g \approx 0.15$ and bounded between z/H=0.10 and 0.15 and is related to the interaction of the wall vortex, V_{wip}, with the passage vortex system, V_p. Additionally, a region of low loss coefficient that extends across the suction side near the endwall is attributed to the low-energy fluid of the inlet boundary layer that is convected across the passage due to the crossflow pressure gradient [11]. The magnitude of the loss coefficient of the lower core is higher than the upper one for all investigated flow conditions. For all the investigated Reynolds numbers, an increase in exit Mach number enhances the intensity of the lower loss core. This is also observed by Ella et al. [23].

On the other hand, the overall intensity of the higher loss core is reduced as Mach increases except for the case when it increases from 0.80 to 0.90 at a Reynolds number $Re_{6,is} = 70k$. A small shift in the location of the loss peak of the higher loss core towards the wall and the blade SS occurs as the Mach increases. The effect of the exit Mach number to shift the higher loss core has been also observed and reported by Perdichizzi [23] and Ella et al. [23] in their investigations of high-pressure turbines operating at high subsonic and supersonic outlet Mach numbers. The experimental data suggests that an increase in the Reynolds number reduces the intensity of both loss cores at a constant Mach number. Even though this evidence opposes the findings of Hodson and Dominy [24].

3.2.2. Streamwise vorticity coefficient

The streamwise vorticity coefficient, K_ω, is used to visualize the secondary flow structures and characterize their intensity and motion. The streamwise vorticity coefficient is defined in Eq. 2. The streamwise vorticity as described by Gregory-Smith al. [25] is multiplied by the ratio of the chord to outlet isentropic velocity.

$$K_\omega = \frac{C}{v_{6,is}}(\omega_{ax} cos(\beta_{MS}) + \omega_{tan} sin(\beta_{MS})) \tag{2}$$

The axial vorticity can be directly computed with the five-hole probe data using Equation Eq. 3. Since the downstream measurements were performed on a single plane, the tangential vorticity component, ω_{tan}, is estimated using the Crocco relation as suggested in [26; 27] through Eq. 4.

$$\omega_{ax} = \frac{\partial V_{rad}}{\partial y} - \frac{\partial V_{tan}}{\partial z} \tag{3}$$

$$\omega_{tan} = \frac{1}{V_{ax}}(V_{tan}\omega_{ax} + \frac{a^2}{\gamma}\frac{\partial ln(P_{06})}{\partial z}) \tag{4}$$

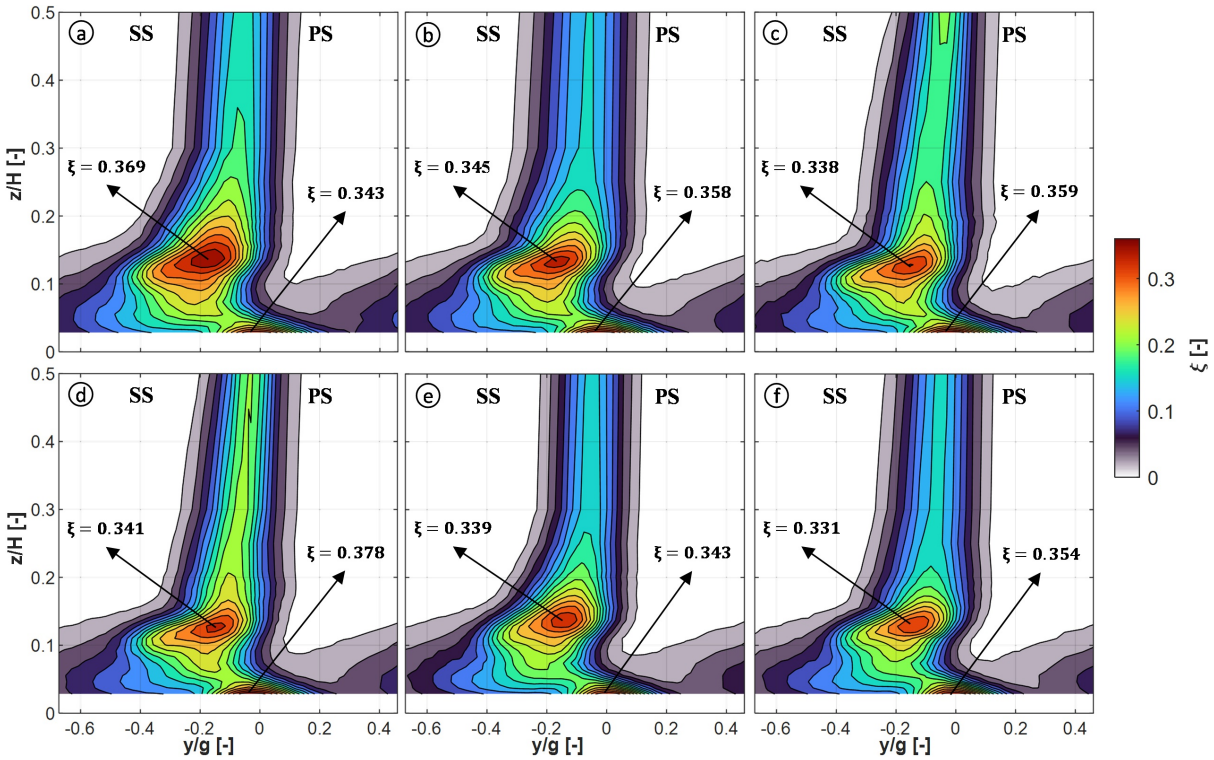

Figure 3: Contours of energy loss coefficient obtained at: (a) $M_{6,is}$ = 0.70 ; $Re_{6,is}$ = 70k, (b) $M_{6,is}$ = 0.80 ; $Re_{6,is}$ = 70k, (c) $M_{6,is}$ = 0.90 ;$Re_{6,is}$ = 70k, (d) $M_{6,is}$ = 0.95 ; $Re_{6,is}$ = 70k, (e) $M_{6,is}$ = 0.80 ; $Re_{6,is}$ = 120k and (f) $M_{6,is}$ = 0.90 ; $Re_{6,is}$ = 120k; (observer looks upstream)

Fig. 4 displays the contours of the streamwise vorticity coefficient obtained for the same flow conditions as investigated for the energy loss coefficient. The blue and red levels denote clockwise and counter-clockwise rotation, respectively. The relative position between the rotating structures and their sense of rotation are also identified with arrows in Fig. 4.

Three major rotating structures are observed. Close to the endwall, the corner vortex, V_{sc}, can be seen rotating clockwise when the observer looks upstream. On the left of the corner vortex and extending from the endwall to z/H = 0.15, the passage vortex system, V_p, rotates counter-clockwise. Lastly, a clockwise rotating structure around z/H = 0.10 is present on the right of the passage vortex and above the corner vortex. As mentioned previously, this is believed to be the wall vortex due to its strong intensity compared to the pressure leg of the horseshoe vortex [21]. Sieverding and Van Den Bosche [22] concluded that the motion of the suction side leg of the horseshoe vortex depends on the turning of the cascade as well as flow conditions. However, for all investigated flow conditions the clockwise rotating structure sits at the same location relative to the passage vortex, suggesting that this structure is in fact the wall vortex due to its insensitivity to the flow conditions.

For a fixed $Re_{6,is}$ = 70$kand$120k, the increase in Mach produces a non-monotonic behavior of the $K_{\omega,V_{sc}}$ intensity. The intensity of $K_{\omega,V_{wip}}$ suffers a monotonic decrease in magnitude as Mach increases from 0.70 to 0.95 for both Reynolds investigated. On the other hand, for fixed $M_{6,is}$ = 0.80and0.90, there is an increase in the $K_{\omega,V_{wip}}$ intensity as Reynolds increases from 70k to 120k. A similar trend is observed by Ella et al. [23].

The streamwise vorticity intensity of the wall vortex vortex increases as the exit Mach number increases from 0.70 to 0.80. However, the trend with Mach number is not sustained, and a slight reduction in intensity is observed as the Mach further increases from 0.80 to 0.90. This trend is observed for both investigated Reynolds numbers. Additionally, for both Reynolds the intensity increases once again as the exit Mach number is increased from 0.90 to 0.95. This is contrary to the findings of Ella et al. [23], who observed a monotonic increase with the outlet Mach.

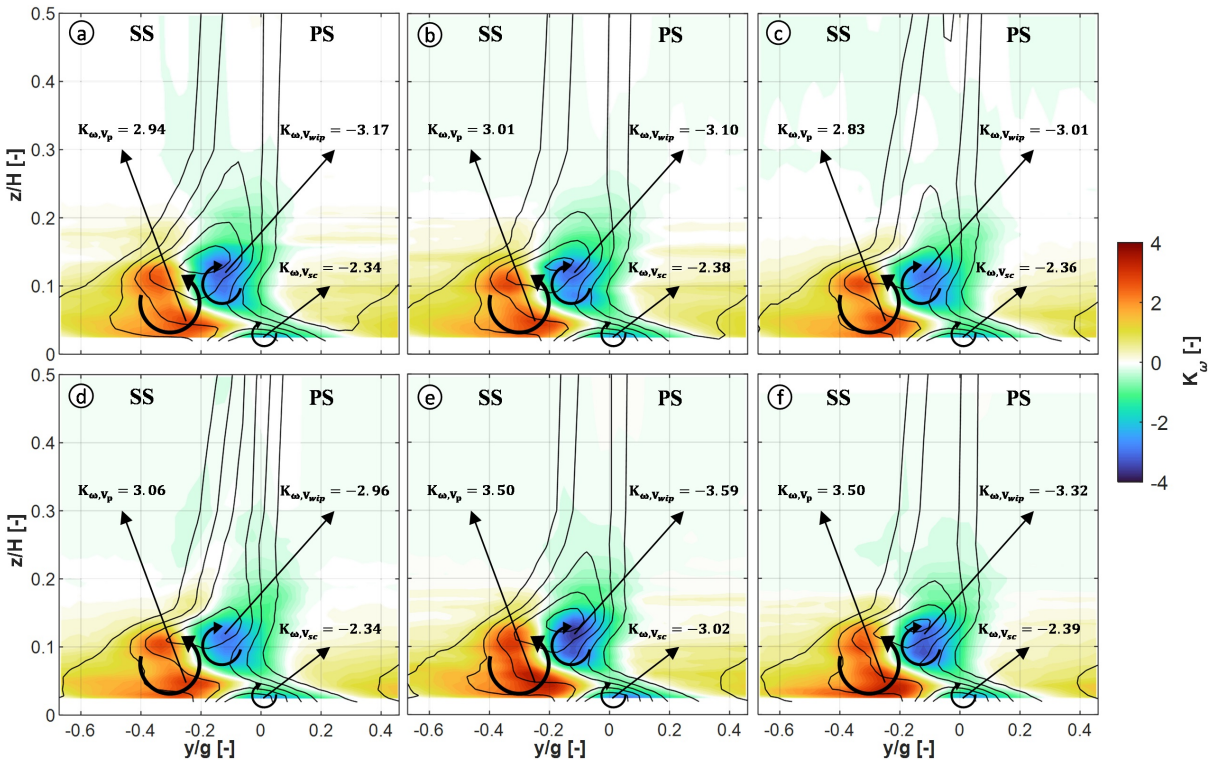

Figure 4: Contours of streamwise vorticity coefficient obtained at: (a) $M_{6,is} = 0.70$; $Re_{6,is} = 70k$, (b) $M_{6,is} = 0.80$; $Re_{6,is} = 70k$, (c) $M_{6,is} = 0.90$; $Re_{6,is} = 70k$, (d) $M_{6,is} = 0.95$; $Re_{6,is} = 70k4$, (e) $M_{6,is} = 0.80$; $Re_{6,is} = 120k$ and (f) $M_{6,is} = 0.90$; $Re_{6,is} = 120$; superimposed with isolines of energy loss coefficient (observer looks upstream)

3.2.3. Pitchwise distributions

The pitchwise distributions of the energy loss coefficient obtained at on- and off-design flow conditions are plotted in Fig. 5. The distributions are displayed for similar blade span locations to the ones used to describe the blade isentropic Mach number distributions.

Fig. 5(a) displays the pitchwise distribution at midspan. The wake width is characterized by the semi-wake width (sww) [28] which is normalized by the TE thickness and plotted in Fig. 6(a) for the investigated cases in the case of z/H=0.50. The area-averaged outlet flow deviation is plotted in Fig. 6(b) to complement the profile performance evaluation. As detailed in the blade aerodynamics sub-section, an open separation occurs when $Re_{6,is} = 70k$ as the Mach increases from 0.70 to 0.80.

The presence of the open separation bubble appears to be associated with an increase of the wake width (Fig. 6(a)). As the Mach further increases to 0.80, the wakes thins out. Finally, a reduction of the wake width occurs as the outlet Mach reaches 0.95. An opposite trend occurs for $Re_{6,is} = 120k$ because of the open separation arising when Mach is increased from 0.80 to 0.90. On the other hand, for $M_{6,is} = 0.90$ there is an increase of the semi-wake width as $Re_{6,is}$ increases. This occurs due to the increase in the wake depth observable for $M_{6,is} = 0.90$.The flow underturning increases monotonically from y/g=-0.70 to -0.90 as the Mach number increases from 0.70 to 0.95, achieving independence when Mach reaches 0.90 in the case of $Re_{6,is} = 70k$ (Figure 12(b)). For a fixed Mach of 0.80 and 0.90, an increase in the Reynolds translates into an increase of the underturning. This is surprising considering that for $M_{6,is} = 0.90$, the increase in Reynolds suppresses the open separation.

At z/H=0.10 (Fig. 5(b)), the loss across the pitch is never null as this region is affected by the losses of the secondary flow structures. The shape of all curves is a consequence of traversing the probe across the passage vortex system followed by the wall vortex. The later has a greater contribution to the losses. For $Re_{6,is} = 70k$, a reduction in the losses is observed as Mach increases. A shift of the curves towards the PS is also present. For $M_{6,is} = 0.90 and 0.95$ the extent of the wall vortex towards the PS is larger than

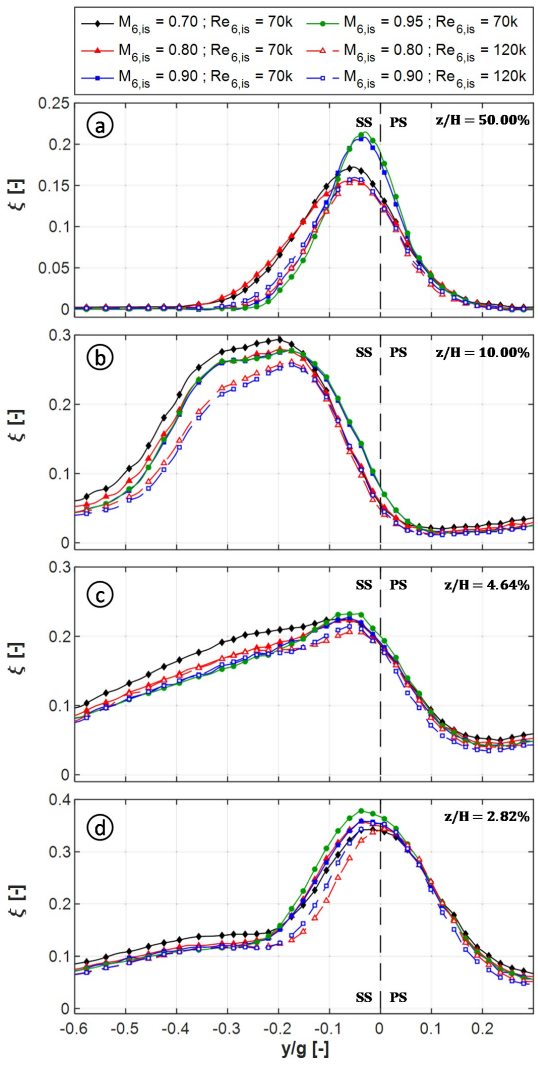

Figure 5: Pitchwise distribution of energy loss coefficient for (a) z/H=0.028, (b) z/H=0.046, (c) z/H=0.10 and (d) z/H=0.50

for the lowest Mach investigated. A decrease of the loss is noticed for $Re_{6,is} = 120k$. The extent of the loss towards the suction side is also decreased. For $Re_{6,is} = 120k$, a decrease of the loss occurs as Mach increases.

As plotted in Fig. 5(c), the impact of the passage vortex is still noticeable when the probe is traversed at z/H=0.046. As the probe is traversed towards the PS, an increase of the loss occurs while approaching the wall vortex. The maximum loss in the passage vortex region is registered for the case of $M_{6,is} = 0.70$ and $Re_{6,is} = 70k$. The loss associated with this region decreases as $M_{6,is}$ is reduced, while the influence of $Re_{6,is}$ is not noticeable. A change takes place when

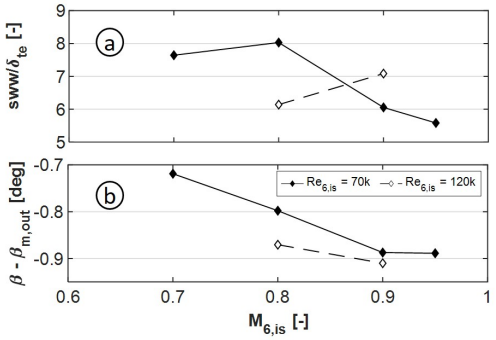

Figure 6: Semi-wake width (a) and area-averaged outlet flow deviation (b) for the investigated flow conditions at z/H=0.50

the probe reaches y/g = -0.20, after which the loss for $Re_{6,is} = 120k$ becomes smaller than for $Re_{6,is} = 70k$. After y/g = -0.10, the highest loss is taken by the case of $M_{6,is} = 0.95$. In addition, after y/g=0, the minimum loss is found to be for the case of $M_{6,is} = 0.90$ and $Re_{6,is} = 120k$.

At z/H=0.028 (Fig. 5(d)), the passage vortex is still responsible for the high loss from y/g = -0.60 to -0.20. However, a region with very high loss caused by the corner vortex is present at y/g=0. The loss induced by the passage vortex is maximum for the case of $M_{6,is} = 0.95$. A shift of the loss peak towards the PS occurs as $M_{6,is}$ is reduced. The overall loss further decreases as $Re_{6,is}$ is reduced.

3.2.4. Pitchwise averaged results

The data obtained with the L-shaped five-hole probe data is averaged along the pitch according to Cumpsty and Horlock [29]. The static pressure is area-averaged, $\bar{P}_6{}^a$ while the total pressure measured by the five-hole probe, $\bar{P}_{06}{}^m$, is mass-averaged. The primary flow direction, $\bar{\beta}_6{}^a$, is computed from the velocity components which are area-averaged to respect continuity. The mass-averaged energy loss coefficient, $\bar{\xi}^m$, and flow deviation, $\Delta\beta_6$, are computed with Eq. 5 and Eq. 6, respectively.

$$\bar{\xi}^m = 1 - \frac{1 - (\frac{\overline{P_6}^a}{\overline{P_{06}}^m})^{\frac{\gamma-1}{\gamma}}}{1 - (\frac{\overline{P_6}^a}{P_{01,fs}})^{\frac{\gamma-1}{\gamma}}} \tag{5}$$

$$\Delta\beta_6 = \overline{\beta_6}^a - \overline{\beta_{6,MS}}^a \tag{6}$$

In the scope of this work, overturning occurs when $\Delta\beta_6 > 0$. The secondary loss coefficient is computed by subtracting the profile loss to the total energy loss

coefficient distribution, $\bar{\xi}^m_{\text{sec}} = \bar{\xi}^m - \bar{\xi}^m_{MS}$ assuming that the profile loss is constant along the spanwise direction [30].

Fig. 7(a) plots the spanwise evolution of $\Delta\beta_6$. As displayed, for $Re_{6,is} = 70k$ the impact of Mach on the $\Delta\beta_6$ is reduced up to z/H=0.10. A first region near the endwall that should be characterized by underturning caused by the corner vortex is not visible since it is too close to the endwall to be captured by the current probe. The first measured region extending from the endwall to $z/H \approx 0.05$ is characterized by overturning induced by passage vortex. A maximum overturning of 6.22° is found for the lowest Mach. After $z/H \approx 0.05$, the wall vortex starts reducing the overturning imposed by the passage vortex and an underturning region arises. In this region, the underturning increases as $M_{6,is}$ decreases. A similar trend is observed by Duden and Fottner [13].

A maximum underturning of 3.68° is found for $M_{6,is} = 0.70$. A migration in the location of the maximum underturning occurs due to the shift of the secondary flow structures closer to the endwall. After z/H=0.15, there is a crossing of the curves for $M_{6,is} = 0.70 and 0.80$, after which they display lower underturning than the curves obtained for $M_{6,is} = 0.90 and 0.95$. Similar trends are observed for $Re_{6,is} = 120k$. The overturning below z/H=0.05 is greater for $M_{6,is} = 0.80$. The maximum measured overturning is 7.07° and 6.48° for $M_{6,is} = 0.80 and 0.90$, respectively. Contrary to the case of $Re_{6,is} = 70k$, the largest value of underturning occurs for the highest Mach. The highest underturning is found to be −3.55° and −3.63° for $M_{6,is} = 0.80 and 0.90$, respectively. A similar shift of the maximum underturning towards the endwall is observed as $M_{6,is}$ increases.

The spanwise distribution of $\bar{\xi}^m_{\text{sec}}$ is displayed in Fig. 5(b). A maximum loss of 0.113 is measured for $M_{6,is} = 0.70$ at the closest measurement point to the endwall (z/H=0.028). For the same location, the maximum loss for the cases of $M_{6,is} = 0.80$ is equal while for 0.90 is lowered compared to the previous case ($\bar{\xi}^m = 0.107$). The loss increases for $M_{6,is} = 0.95$ ($\bar{\xi}^m = 0.110$). As the distance from the endwall is increased, the losses decrease monotonically until the second loss core region is approached starting at around z/H=0.10. As $M_{6,is}$ is increased from 0.70 to 0.95, z/H is found to be 0.13, 0.12 and 0.11, where the latter is the same for $M_{6,is} = 0.90 and 0.95$. On the other hand, the magnitude of the losses does not vary monotonically with Mach number. The highest loss amounting to 0.081 is measured for $M_{6,is} = 0.70$. A decrease occurs for $M_{6,is} = 0.80$, for which the measured loss is 0.072. As Mach increases from 0.80 to 0.90, the loss increases to 0.073. Lastly, the loss increases to 0.074 for $M_{6,is} = 0.95$. The secondary losses are then further reduced as z/H increases. At z/H=0.22 there is a crossing of the loss curves after which the secondary loss behavior is no longer monotonic with the increase in Mach. At z/H=0.30, the secondary loss for the cases of $M_{6,is} = 0.70 and 0.80$ falls to zero. However, for the highest Mach numbers, the secondary losses are still decaying. This suggests that even though the secondary flow structures are squeezed towards the endwall by increasing Mach, the flow displays levels of 3-D features as far as at z/H=0.40.

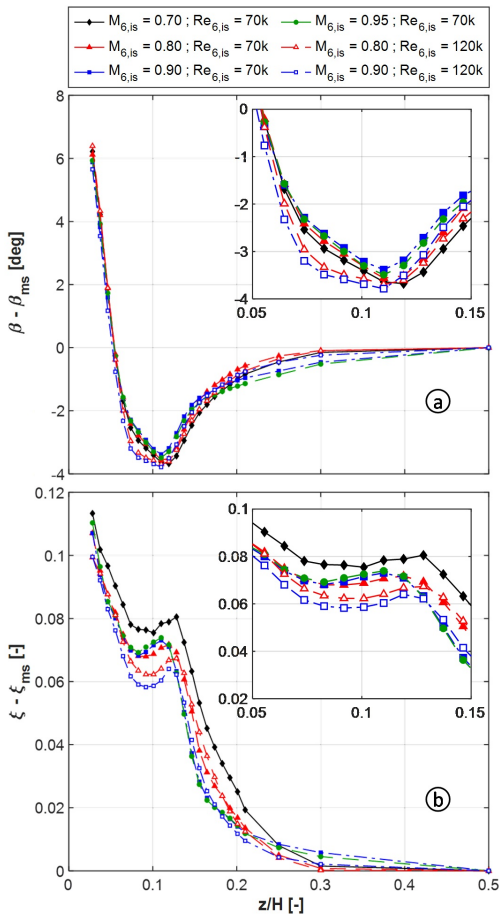

Figure 7: Pitchwise averaged (a) deviation from primary flow direction and (b) energy loss coefficient with zoomed regions

Similar trends occur for $Re_{6,is} = 120k$. For the first measured point near the endwall, the secondary loss is measured to be 0.099 for the cases of $M_{6,is} = 0.80 and 0.90$. In the region of the second loss core, the local maximum loss is found to be at z/H=0.12

and 0.13 for $M_{6,is} = 0.80 and 0.90$, respectively. Loss peaks of 0.067 and 0.064 are measured for $M_{6,is} = 0.80 and 0.90$, respectively. The same crossing in the loss curves apply to this $Re_{6,is}$ case. Fig. 5(a) is also used to characterize the Reynolds effect on the flow deviation and secondary losses. Maximum overturning and underturning values of 6.40° and 3.70° are found for $Re_{6,is} = 120k$, respectively. The Reynolds effect is found to be very small with exception to the region between z/H=0.05 and 0.15 where the underturning found for $Re_{6,is} = 70k$ is lower than for $Re_{6,is} = 120k$. The same trend occurs for the highest Mach number investigated. This effect is attributed to the higher increase of the passage vortex intensity relative to the corner vortex one as the Reynolds number increases Fig. 3. Concerning the losses, for both $M_{6,is}$ investigated, the increase in Reynolds promotes a decrease of the secondary loss near the endwall and in the region of the second loss core. In addition, an apparent shift of the higher loss peak that brings it closer to the endwall takes place.

3.2.5. Planewise averaged results

The breakdown of profile and secondary losses obtained for the on- and off- design investigated flow conditions is presented in Fig. 8. The loss breakdown is performed by subtracting the profile loss coefficient from the total energy loss coefficient as proposed in [30]. For $Re_{6,is} = 70k$, the secondary losses display a non-monotonic behavior as Mach increases. A decrease in the losses as $M_{6,is}$ increases from 0.70 to 0.80 is observed, followed by an increase as $M_{6,is}$ increases from 0.80 to 0.95. An increase in the secondary losses is also observed as $M_{6,is}$ increases from 0.80 to 0.90 for $Re_{6,is} = 120k$. A shift in the secondary floss behavior occurs between the two investigated Reynolds.

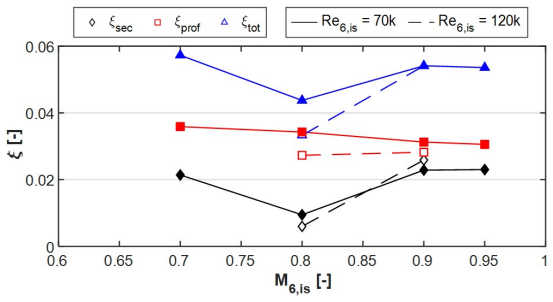

Figure 8: Break-down of cascade averaged losses for the on- and off-investigated flow conditions

For $Re_{6,is} = 70k$, the profile loss experiences a monotonic decrease as $M_{6,is}$ increases in the range of investigated flow conditions. As detailed in the downstream pitchwise distributions, the increase from $M_{6,is} = 0.70 to 0.80$ reduces the wake depth while displaying a similar width which causes a decrease in the profile loss. Even though a further increase from $M_{6,is} = 0.80 to 0.90$ results in a deeper wake, the width is significantly reduced. The fact that the profile loss is computed with a mass-averaging technique is responsible for the reduction of the profile loss. The further decrease as $M_{6,is}$ increases from 0.90 to 0.95 is a consequence the slight difference between the wake width and depth close to the maximum loss region. An opposite trend in observed for $Re_{6,is} = 120k$. The profile losses are decreased as $Re_{6,is}$ increases from 70k to 120k as consequence of suppressing or reducing the displacement of an open separation as detailed in the blade distributions. The reduction is significantly higher for $M_{6,is} = 0.80$ since the separation is clearly suppressed while for $M_{6,is} = 0.90$ the effect is smaller. For $Re_{6,is} = 120k$, an increase of the profile loss takes place as $M_{6,is}$ increases from 0.80 to 0.90 since an apparent separation arises.

The total energy loss coefficient displays similar behavior for $Re_{6,is} = 70k and 120k$ even though only two Mach numbers are investigated for $Re_{6,is} = 120k$. The total loss coefficient is minimum for $M_{6,is} = 0.80$, being inferior for the highest investigated $Re_{6,is}$. The maximum total energy loss is found at $M_{6,is} = 0.70$. An increase of the total pressure loss occurs as $M_{6,is}$ is increased from 0.80 to 0.90 which is then followed by a decrease for the maximum Mach investigated. A $Re_{6,is}$ independence is present for $M_{6,is} = 0.90$.

4. Conclusions

This work provides a comprehensive investigation of the impact of Mach and Reynolds on the performance of a high-speed LPT cascade. The flow is found to be separated for the majority of the flow conditions encountered in high-speed LPTs (M>0.80).

The secondary losses are an important fraction of the total losses, and they seem to become more important at higher Mach numbers, pointing to the fact that it must be accounted in the design of high-speed LPT blades. The effect of Reynolds is smaller than the Mach and a secondary loss minimum is found for an outlet Mach of 0.80. The profile loss decreases at high Mach numbers, suggesting a positive cost-benefit of operating at higher pressure ratio (M = 0.9-0.95) since the Reynolds dependence on the performance can be minimized as well. The impact of the main secondary

flow structures: corner, passage and wall vortices extend to as far as z/H=0.35 ($1.21C_{ax}$).

Acknowledgments

The authors gratefully acknowledge funding of the SPLEEN project by the Clean Sky 2 Joint Undertaking under the European Unions Horizon 2020 research and innovation program under the grant agreement 820883.

References

[1] J. Kurzke, Fundamental Differences Between Conventional and Geared Turbofans, Vol. Volume 1: Aircraft Engine; Ceramics; Coal, Biomass and Alternative Fuels; Controls, Diagnostics and Instrumentation; Education; Electric Power; Awards and Honors of Turbo Expo: Power for Land, Sea, and Air, 2009, _eprint: https://asmedigitalcollection.asme.org/GT/proceedings-pdf/GT2009/48821/145/2763386/145_1.pdf. doi:10.1115/GT2009-59745.
URL https://doi.org/10.1115/GT2009-59745

[2] H. P. Hodson, R. J. Howell, The role of transition in high-lift low-pressure turbines for aeroengines, Progress in Aerospace Sciences 41 (6) (2005) 419–454, publisher: Elsevier.

[3] D. Torre, G. García-Valdecasas, A. Puente, D. Hernández, S. Luque, Design and Testing of a Multi-Stage IP Turbine for Future Geared Turbofans, in: Turbo Expo: Power for Land, Sea, and Air, Vol. 84911, American Society of Mechanical Engineers, 2021, p. V02BT32A007.

[4] J. Hourmouziadis, Aerodynamic design of low pressure turbines, AGARD, Blading Design for Axial Turbomachines 40 p(SEE N 89-27661 22-07).

[5] F. J. Malzacher, J. Gier, F. Lippl, Aerodesign and Testing of an Aeromechanically Highly Loaded LP Turbine, Journal of Turbomachinery 128 (4) (2003) 643–649, _eprint: https://asmedigitalcollection.asme.org/turbomachinery/article-pdf/128/4/643/5941668/643_1.pdf. doi:10.1115/1.2172646.
URL https://doi.org/10.1115/1.2172646

[6] M. Giovannini, F. Rubechini, M. Marconcini, A. Arnone, F. Bertini, Analysis of a LPT Rotor Blade for a Geared Engine: Part I — Aero-Mechanical Design and Validation, Vol. Volume 2B: Turbomachinery of Turbo Expo: Power for Land, Sea, and Air, 2016, _eprint: https://asmedigitalcollection.asme.org/GT/proceedings-pdf/GT2016/49705/V02BT38A053/2429237/v02bt38a053-gt2016-57746.pdf. doi:10.1115/GT2016-57746.
URL https://doi.org/10.1115/GT2016-57746

[7] R. Vázquez, D. Torre, The Effect of Mach Number on the Loss Generation of LP Turbines, in: Turbo Expo: Power for Land, Sea, and Air, Vol. 44748, American Society of Mechanical Engineers, 2012, pp. 1131–1142.

[8] H. P. Hodson, R. G. Dominy, Three-dimensional flow in a low-pressure turbine cascade at its design condition.

[9] M. Vera, H. P. Hodson, R. Vazquez, THE EFFECT OF MACH NUMBER ON LP TURBINEWAKE-BLADE INTERACTION, in: Unsteady Aerodynamics, Aeroacoustics and Aeroelasticity of Turbomachines, Springer, 2006, pp. 203–216.

[10] R. l. Va\' zquez, A. Antoranz, D. Cadrecha, L. Arman anzas, The influence of Reynolds number, Mach number and incidence effects on loss production in low pressure turbine airfoils, in: Turbo Expo: Power for Land, Sea, and Air, Vol. 4241, 2006, pp. 949–960.

[11] A. Perdichizzi, Mach number effects on secondary flow development downstream of a turbine cascade, in: Turbo Expo: Power for Land, Sea, and Air, Vol. 79139, American Society of Mechanical Engineers, 1989, p. V001T01A038.

[12] H. P. Hodson, R. G. Dominy, The off-design performance of a low pressure turbine cascade, in: Turbo Expo: Power for Land, Sea, and Air, Vol. 79283, American Society of Mechanical Engineers, 1986, p. V001T01A077.

[13] A. Duden, L. Fottner, Influence of taper, Reynolds number and Mach number on the secondary flow field of a highly loaded turbine cascade, Proceedings of the Institution of Mechanical Engineers, Part A: Journal of Power and Energy 211 (4) (1997) 309–320, publisher: SAGE Publications Sage UK: London, England.

[14] T. Arts, Aerodynamic performance of two very high lift low pressure turbine airfoils (T106C–T2) at low Reynolds and high Mach numbers, in: 5th European Conference for Aerospace Sciences, Munich, Germany, 2013.

[15] J. Clinckemaillie, L. Fattorini, T. Fontani, C. Nuyts, G. Wain, T. Arts, Aerodynamic performance of a very-high-lift low-pressure turbine airfoil (T106C) at low reynolds and high mach number including the effect of incoming periodic wakes, in: 11 th European Conference on Turbomachinery Fluid dynamics & Thermodynamics, EUROPEAN TURBOMACHINERY SOCIETY, 2015.

[16] J. Michálek, M. Monaldi, T. Arts, Aerodynamic performance of a very high lift low pressure turbine airfoil (T106C) at low Reynolds and high Mach number with effect of free stream turbulence intensity, Journal of Turbomachinery 134 (6), publisher: American Society of Mechanical Engineers Digital Collection.

[17] D. Bohn, Untersuchung zweier verschiedener axialer Überschallverdichterstufen unter besonderer Berücksichtigung der Wechselwirkungen zwischen Luft-und Leitrad, Tech. rep. (1977).

[18] A. L. Treaster, A. M. Yocum, The calibration and application of five-hole probes, Tech. rep., PENNSYLVANIA STATE UNIV UNIVERSITY PARK APPLIED RESEARCH LAB (1978).

[19] F. A. MacMillan, Experiments on Pitot-tubes in shear flow.

[20] P. M. Ligrani, L. R. Baun, B. A. Singer, Spatial resolution and downwash velocity corrections for multiple-hole pressure probes in complex flows, Experiments in Fluids 7 (6) (1989) 424–426.

[21] H.-P. Wang, S. J. Olson, R. J. Goldstein, E. R. Eckert, Flow visualization in a linear turbine cascade of high performance turbine blades.

[22] C. H. Sieverding, P. Van Den Bosche, The use of coloured smoke to visualize secondary flows in a turbine-blade cascade, Journal of Fluid Mechanics 134 (1983) 85–89, publisher: Cambridge University Press.

[23] H. M. Abo El Ella, S. A. Sjolander, T. J. Praisner, Effects of an upstream cavity on the secondary flow in a transonic turbine cascade.

[24] H. P. Hodson, R. G. Dominy, The off-design performance of a low-pressure turbine cascade.

[25] D. G. Gregory-Smith, C. P. Graves, J. A. Walsh, Growth of secondary losses and vorticity in an axial turbine cascade.

[26] F. Taremi, Endwall flows in transonic turbine cascades, PhD Thesis, Carleton University (2013).

[27] M. Yaras, S. A. Sjolander, Development of the tip-leakage flow downstream of a planar cascade of turbine blades: vorticity field.
[28] R. Raj, B. Lakshminarayana, Three dimensional characteristics of turbulent wakes behind rotors of axial flow turbomachinery.
[29] N. A. Cumpsty, J. H. Horlock, Averaging nonuniform flow for a purpose.
[30] S. C. Kacker, U. Okapuu, A mean line prediction method for axial flow turbine efficiency.

Numerical traverses of a five-hole probe downstream a transonic turbine vane

Antonino Federico Maria Torre

Turbomachinery and Propulsion Department, von Karman Institute for Fluid Dynamics, Belgium, antonino.torre@vki.ac.be

Supervisor: Sergio Lavagnoli

Associate Professor, Turbomachinery and Propulsion Department, von Karman Institute for Fluid Dynamics, Belgium, sergio.lavagnoli@vki.ac.be

University Supervisor: Koen Hillewaert

Professor, Department of Aerospace and Mechanics, University of Liège, Belgium, koen.hillewaert@uliege.be

Abstract

This paper presents a numerical investigation on the effect of a miniaturized five-hole probe downstream of a transonic turbine vane. Firstly, the probe numerical calibration is presented, followed by a comparison between the quantities 'measured' by the probe and the undisturbed flow-field of the vanes-only set-up. Finally, the sources of discrepancies are evaluated and a correction is used introduced.

Keywords: Probe intrusiveness, Numerical Simulations, Transonic Low pressure Turbine

1. Introduction

The immersion of the probe inside the wind tunnel generates a local blockage [1] and induces perturbations that fundamentally change the flow-field and affect the aerodynamics of the test article [2]. These effects becomes even more significant when the Mach number approaches transonic values [3]. The interaction between turbomachinery airfoils and directional probes, for example, has a considerable impact on the measured flow quantities. This interaction was numerically studied by Aschenbruck et al. [4] on the last stage of an axial turbine, and Sanders et al. [5] on a high-speed compressor testcase. Both studies showed that the data retrieved by the modeled probe differed from the numerical results obtained from a "clean" testcase without the probe. Boerner et al. [3] compare the experimental measurements of pneumatic five-hole probe with Particle Image Velocimetry (PIV) measurements downstream of a turbine linear cascade. In this study the authors investigate the effect of the Mach number on the interaction between five-hole probe measurements. It was shown that, when approaching sonic conditions, the measured Mach number fail in proximity of the wake. Hoenen et al. [6] studied the effect of the pressure gradients on the pneumatic probe measurements using a five-hole probe downstream of an asymmetric NACA-65 profile located in front of a nozzle. The probe data were compared against the data from a split film probe which were used as the reference data. The trailing edge gradients were shown to have a significant impact on the probe measurements of Mach number and flow angles. The authors showed that a correction applied to account for the spatial distance of the pressure taps could reduce the error in the flow angle measurements. The inaccuracies highlighted by the probes in the presence of pressure gradients are attributed to the fact that probe calibration is generally performed in uniform flow [7]. Total pressure gradients impinging on the multi-hole probe generates a pressure difference between pressure taps that, when using a uniform probe calibration, is erroneously attributed to an incidence effect. Correction procedures have been developed, to overcome these errors [8] [9]. The validation of these procedure was however performed on 2D flow regions only. In this paper the effect of a miniaturized five-hole probe on the flow-field downstream of a transonic low-pressure turbine vane row sector is investigated using numerical simulations. A thorough analysis of the probe-determined data is undertaken

to identify the sources of differences from the results of the undisturbed field. Finally, the fidelity of the probe-determined data in the 2D and 3D flow regions is evaluated.

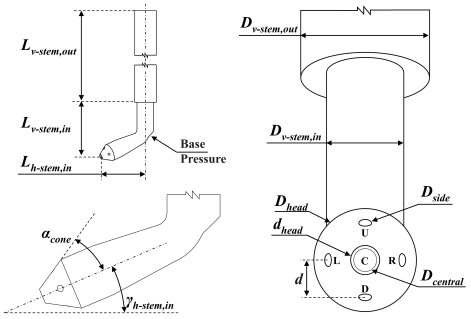

Figure 1: Five-hole probe geometry and key parameters

[Table1] Probe key parameters values

Parameter	Dimension [mm]
d	0.9
dhead	3.2
Dcentral	0.71
Dhead	3.2
Dside	0.4
Dv-stem,in	2.4
Dv-stem,out	4
Lh-stem,in	9.5
Lv-stem,in	10
Lv-stem,out	63.6

2. Numerical Calibration

2.1. Probe Geometry

Fig. 1 shows the geometry of the probe that was used in this study. Key dimensions are marked in the figure and their respective values are reported in Table 1.The probe is of an "L"-shape with conical measurement head characterized by a pre-pitch angle relative to the axial direction to follow the mean pitch angle of the flow so as to limit the calibration range. The head also features five pressure taps drilled normal to the surface of the cone here modeled as patches. The probe also features an additional tap, also modeled as a patch located near the rear end of the vertical stem and is referred to as the base pressure tap. The addition of the base pressure tap enables for a calibration with a higher Mach number sensitivity and thus less measurement error in transonic flows (Boerner and Niehuis [10]).

2.2. Numerical set-up and mesh for calibration

The numerical calibration [11,12] of the probe is performed using the commercial software Numeca FineOpen 8.2. To obtain the calibration coefficients, steady Reynolds-Averaged Navier-Stokes (RANS) simulations were performed using the k-ω SST turbulence model [11]. The spatial discretization employed is a second order central scheme. The fluid domain consists of a cubic volume containing the probe, as shown in figure . 2. The volume top, bottom and side surfaces are set as periodic boundaries and the size of the cube is 100 times the probe diameter. The probe central hole is centered inside the volume and the probe head axis is normal to the domain inlet. The orientation of the probe is not changed throughout the calibration. Various flow yaw and pitch angles are instead achieved by varying the inlet boundary conditions. This calibration procedure was exceptionally convenient because it allowed the use of a single mesh for covering the complete calibration matrix. The unstructured hexahedral mesh was generated using Numeca's HEXPRESSTM 8.2 mesh-generator. Higher refinement is done close to the probe geometry with further refinement in proximity of the hole patches, as shown in figure 2-right. Viscous layers with minimum thickness of 1μm have been applied over the solid surfaces and the hole patches, achieving global y below unity. The mesh of the calibration setup is constituted by approximatively three-million cells.

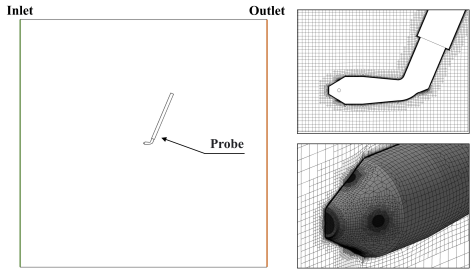

Figure 2: Probe calibration setup and mesh look-up

2.3. Calibration Procedure

The angle and conditions of the flow measured by the probe (figure 3) are obtained by associating the pressure readings of the probe taps to values of yaw, pitch, Mach number and pressures by means of coefficients retrieved through calibration. Experimental calibrations are typically performed in a uniform and well-characterized jet delivered by a nozzle ([12],[13]). Following the same way, a uniform inlet

flow was also used for the numerical calibration performed in this study, the conditions (α, γ, M and P_t) of which are computed by a mass-flow average at the inlet of the domain. The calibration coefficients are calculated using the definitions adopted by Passmann et al. [3] as shown below:

$$K_{yaw} = \frac{P_L - P_R}{P_c - P_{ave}} \tag{1}$$

$$K_{pitch} = \frac{P_D - P_U}{P_C - P_{ave}} \tag{2}$$

$$K_{mach} = \left\{ \frac{2}{\gamma - 1} \left[\left(\frac{P_{ave}}{P_C} \right)^{-\frac{\gamma-1}{\gamma}} - 1 \right] \right\}^{1/2} \tag{3}$$

$$K_{tot} = \frac{P_C - P_{tot}}{P_C - P_{ave}} \tag{4}$$

$$P_{ave} = \frac{P_U + P_D + P_L + P_R}{4} \tag{5}$$

In the above definitions, subscripts C, U, D, L and R correspond to the various taps of the probe, as shown in Figure 1. The value of static pressure P used for each of the taps, is the value of the average static pressure on the respective hole patch. As an alternative to using the average pressure in equation (5), the base pressure can be used in the above definitions to calculate the calibration coefficients so that a higher Mach number sensitivity can be achieved. The calibration was performed for seven pitch angles, from -15°to +15°in steps of 5°, and four yaw angles from 0°to +15°in steps of 5°. To limit the number of simulations, the calibration was performed only on positive yaw angles and was assumed symmetric for the negative yaw angles. The probe was also calibrated for five Mach numbers (0.55, 0.70, 0.8, 0.9 and 0.95), from subsonic to transonic conditions. The flow Mach number was set by maintaining a constant inlet pressure and varying the outlet static pressure thus changing the total-to-static pressure ratio which determines the Mach number. In total, 140 conditions have been used to perform the numerical calibration. The five-hole probe was therefore calibrated at the same turbulence conditions as the ones found downstream of the vane row. These conditions were identified through a separate CFD simulation, discussed later in the paper, which included the vanes. Following the approach described by Main et al. [14], a calibration matrix of coefficients K_{yaw}, K_{pitch} and K_{Mach} is generated at regular steps of α, γ and M. The linear interpolation functions of α, γ, M and K_{tot} have been created on the calibration grid of K_{yaw}, K_{pitch} and K_{Mach}. During the measurements, flow pressures, angles and Mach number are obtained from the interpolant functions by an indexed look-up using coordinates of K_{yaw}, K_{pitch} and K_{Mach} measured by the probe.

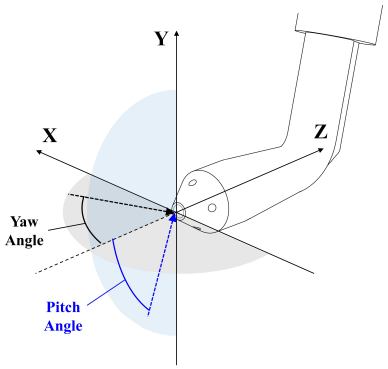

Figure 3: Flow angles on the probe system of reference

Figure 4-Left shows the characteristics total pressure coefficients at Mach number equal to 0.8 using P_{ave} and P_{BP}. Figure 4-Right shows the variation of K_{Mach} with the free stream Mach number. Using P_{BP}, a much higher sensitivity of the Mach number coefficient on every calibration point can be seen, while using P_{ave} results to a flattening of the slope of curve when approaching the sonic condition thus reducing the sensitivity to Mach number and increasing the error in the measurement.

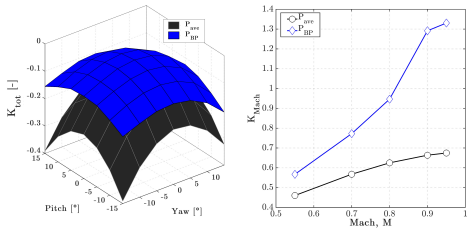

Figure 4: K_{tot} coefficients at M = 0.8 (left) and variation of mach coefficient with flow mach numbers at zero incidence (right) for P_{ave} and P_{BP}

Figure 5 shows the orthogonality maps of the calibrated probe when P_{ave} (left) and P_{BP} (right) are used. The orthogonality maps obtained using P_{ave} do not change with different Mach number. When P_{BP} is used, the maximum and minimum values of yaw and pitch angle coefficients decrease in absolute value, as the Mach number increases. The "shrinking" of the orthogonality map of Figure 5-Right occurs due to a

reduction of the static pressure level during calibration that makes the denominator of Eqs. 1,2 and 4 to increase. This effect implies an unfavorable reduction of pitch and yaw angle sensitivity. For this reason the measurements discussed in the following section will employ the traditional side-holes pressure average (P_{ave}).

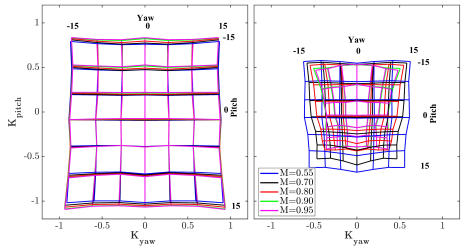

Figure 5: Orthogonality maps for P_{ave} based coefficients (Left) and P_{BP} based coefficients (Right)

3. Effects of the probe-vane interactions on flow-field and probe measurements

3.1. Numerical set-up and mesh

To investigate the effects of probe – vane interactions on the measurements of the five-hole probe two numerical set-ups were simulated, one in which both the vanes and probe are present and one in which only the vanes are present i.e., without probe. Figure 6 shows the numerical set-up for the case where both vanes and probe are present. This set-up consists of two annular-sector domains, a stationary domain containing one vane passage and a rotating domain containing the probe. The probe domain is extended circumferentially for eight vane passages to reduce the periodic propagation of the potential field of the probe, thus resulting in a periodicity between the stationary and the rotating domains equal to 8:1. The inlet of the domain was set to 1.75 axial chords upstream of the vane leading edge where inlet boundary distributions of total pressure, temperature and flow angles are known. The two domains are separated by a stator-rotor interface, located approximatively halfway between the vane trailing edge and Plane 2 where the probe measurements are performed.

[Table2] Vane aerodynamic parameters at undisturbed conditions

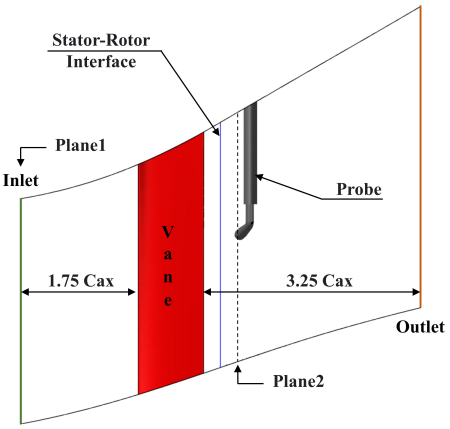

Figure 6: Probe Disturbance setup

Parameter	Value
Reynolds number (Cax), Re	1.67 x 105
Vane exit Mach number, M	0.8
Vane pressure ratio, Pt,in /Pout	1.48
Turbine mass flow rate, (kg/s)	10.5

The probe is located at half axial vane-chord downstream of the vane trailing edge and is traversed in the circumferential direction by imposing a speed of less than 10 rpm to the rotating domain, where the probe is contained, representative of the traversing system's speed to be used in the upcoming experimental campaign. The circumferential traverses are performed at mid- span, to investigate the effect of the vane-probe interactions in the 2D flow region, and near the hub and shroud, to investigate these effects in the 3D flow region. The test case where only the vanes are present (or the no-probe case) provides the "undisturbed" flow-field through the vane row and is used as the reference case to which the results obtained in the vane and probe set-up are compared. The set-up of the vanes-only case is identical to the one where both vanes and probe are present with the only difference that the rotating domain is just a fluid volume with no probe included. The simulation boundary conditions are set such as to obtain for the undisturbed flow-field the aerodynamic conditions reported in Table 2. Figure 7 shows the mesh of the vane and probe domains. The vane domain consists of 1.6 million cells while the rotating domain consists of approximatively nine-million elements. Mesh refinement on the probe is performed in such a way to create consistency with the mesh characteristics used for the numerical calibration setup. Boundary layers are resolved on both domains reaching a y+ ¡ 1.

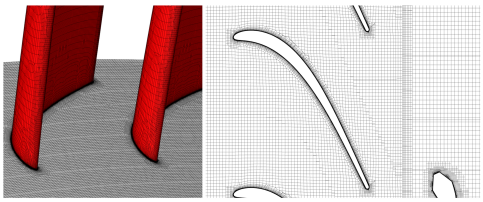

Figure 7: Probe-Vane mesh

3.2. *Effect on the flow-field*

Figure 8a shows the static pressure distribution through the vane and probe domains on an axial-tangential plane at midspan, covering four vane passages in the tangential direction. For these results the probe head was located at mid-span and at mid-pitch between airfoils 0 and 1.

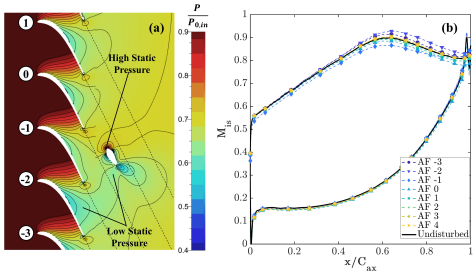

Figure 8: : (a) Static pressure contours across the vane row at midspan and (b) isentropic Mach number distribution on the airfoils at 50% of the span. Results for the probe head located at mid-passage and probe inserted to 50% of the flow-path span

The numerical simulations have been performed using the commercial software Numeca FineOpen 8.2 employing the K-ω SST turbulence model and second order central scheme. The unsteady solutions have been computed using the Non-Linear Harmonic (NLH) approach firstly introduced by He and Ning [15]. This method is particularly advantageous from a computational effort perspective as it allows for a ten-fold reduction in the time to achieve converged solution with respect to the phase-lag solution, whilst producing similar results [16]. The harmonic solution is then reconstructed in time, resulting in 30 circumferential probe positions in one vane passage. The level of accuracy of the solution can be controlled through the number of harmonics propagated between the two domains. A sensitivity analysis (not shown in this paper) was performed and the perturbation of five harmonics of the probe passing frequency was selected to achieve a good balance between computational time and accuracy of the results. A high static pressure region can be seen on the front part of the probe as a result of stagnating flow on the head of the probe. A low pressure region can also be found on the back of the probe due to accelerating flow around the head of the probe. These high- and low-pressure regions affect the flow through the vane passages by altering the static pressure conditions at the outlet of each passage. Treating each passage as a nozzle, any change in the outlet static pressure results in a change of the pressure ratio across the nozzle which in turn causes a change of the mass flow passing through it and a subsequent change of the static pressure distribution in the passages. The high static pressure at the front of the probe decreases the nozzle pressure ratio thus decelerating the flow; this effect occurs in the flow of the two passages around the central vane 0, between vanes -1 and 1. On the contrary, the low static pressure around the probe decreases the nozzle pressure ratio thus accelerating the flow; an effect seen in the lower passages, between vanes -1 and -3. The influence of the probe on the isentropic Mach number distribution on the surface of all eight vanes in the domain, is shown in Figure 8b. In this figure the isentropic Mach number distribution for the "clean" configuration without probe (referred to as "undisturbed" in the figure) is also shown. In general, the influence of the probe on the Mach number distribution around the vanes is limited to the suction side only (negligible effect on the pressure side distributions) and varies between the different vanes. Focusing on the suction side distributions, an acceleration of the flow relative to the undisturbed case can be seen for vanes -2 and -3, and a deceleration for vanes -1 to 1. This is as a result of the acceleration and deceleration of the flow in the respective passages due to the effect of the high- and low-pressure regions of the probe on the flow through the nozzles. The influence of the probe on the flow-field diminishes with circumferential distance away from the probe where, beyond vanes -3 and 1,values march undisturbed case. Figure 9 shows the isentropic Mach number distribution on the surface of the central vane at midspan, for different circumferential positions of the probe when the probe head is located at midspan. The undisturbed vane isentropic Mach number distribution is also shown in the figure for comparison. The presence of the probe results in a reduction of the isentropic Mach number distribution which is particularly evident on the rear of the suction side of the vane. The highest reduction in Mach number ($\Delta M_{max} = 0.02$), and hence the strongest influence of the probe, is shown for the case where the probe is at ($\theta = +0.5$; the location at which the high static

pressure in front of the probe head interacts with the passage formed between the suction side of the central vane and the pressure side of the adjacent vane.

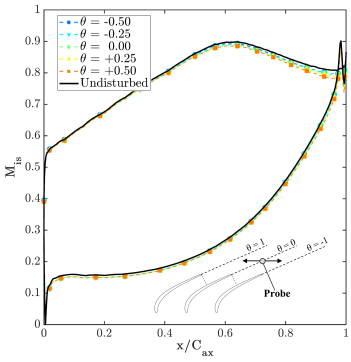

Figure 9: : (a) Static pressure contours across the vane row at midspan and (b) isentropic Mach number distribution on the airfoils at 50% of the span. Results for the probe head located at midpassage and probe inserted to 50% of the flow-path span

3.3. *Effect on the probe measurements in the 2D region*

Figure 10 shows the pitch-wise distributions of (a) normalized total pressure, (b) Mach number, (c) yaw and (d) pitch angles in Plane 2 at 50% span. The distributions of the reference test-case (blue lines) and raw probe measurements (black circle symbols) are included in all of the plots. The probe-determined nondimensional total pressure distribution (Figure 10a) is in excellent agreement with the undisturbed values over most of the vane pitch, except in the wake where the total pressure is underestimated by 0.3% of the inlet total pressure. The Mach number distribution (Figure 10b) is however not very accurately retrieved by the probe. The probe-determined data show an overshoot of the Mach number on the edges of the wake and a strong Mach number reduction with respect to the vane-only case in the wake. These discrepancies are mainly due to the probe not being able to retrieve correctly the static pressure distribution in the flowfield as a result of the short-fallings of the uniform calibration which are discussed in more detail later on in this section. Figure 10c shows the pitch-wise distribution of the yaw angles of the vane-only case and the probe-retrieved data. Data obtained from the vane-only case show a low pitch-wise variation about the mean value of less than ±0.5 degrees. On the contrary, the probe-determined data show a strong variation in the pitch-wise direction resulting in over- and under-estimation of the flow angle with respect to the mean value of ±2 degrees. It is noted that the highest variations are observed close to the strongest total pressure gradients.

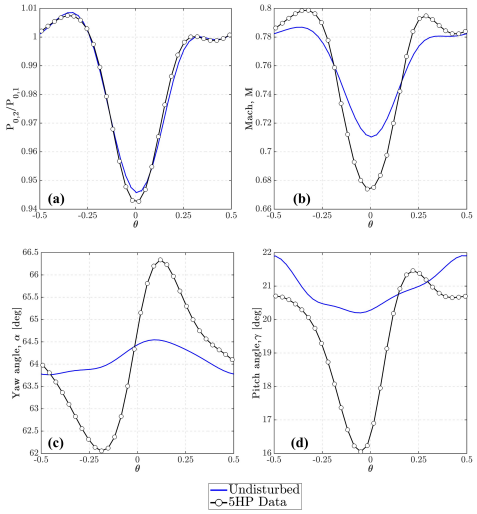

Figure 10: : Midspan pitch-wise distributions of (a) normalized total pressure, (b) mach number, (c) yaw and (d) pitch angles of the vane only case and measurement performed with the five-hole probe

The Pitch angle distributions are shown in Figure 10d. For the vane only case the pitch angle varies of ±1 degrees about the mean value. The probe-determined data show that the pitch angle is underestimated over the majority of the vane passage due to a reduction of the pitch angle of the freestream in proximity of the probe head. This effect is caused by the prominent blockage of the probe stem that deviates the flow downwards. The biggest difference between probe-determined data and vane only flow-field is of 4 degrees at θ = -0.05 with respect to the vane only case.

The discrepancies shown by the quantities of Mach and Yaw and Pitch angles can be attributed to two causes: first the unavoidable distance between the side pressure taps (left to right or up to down) which exposes them in pressure gradients even at zero flow incidence and second the transversal velocity component generated on the probe head when subjected to streamwise velocity (or total pressure) gradients [8].

A two-step correction to compensate for the errors caused by the aforementioned causes was presented by Ligrani et al. [8]. The first step accounts for the local displacement of the side taps on the probe head with respect to the central tap. The second step of the correction is used to compensate for the component of secondary transversal velocity rising when blunt bod-

ies are subjected to gradients in the stream-wise velocity component. The corrected velocity components are given by the following formula.

$$V_y = V_{y,u} + C\ dV_x/dz \tag{6}$$

and

$$V_z = V_{z,u} + C\ dV_x/dz \tag{7}$$

where $V_{y,u}$ and $V_{z,u}$ are the uncorrected components of tangential and radial velocities respectively, V_y and V_z are the corrected components of tangential and radial velocities, V_x is the axial velocity component and C is a coefficient dependent on the probe size. In this study, the value of C used is equal to the 20% of the probe head diameter as determined in the study of Ligrani et al. [8] and confirmed with a similar value (19%) in the work of Chernoray and Hjärne [9]. For the purpose of this study, the two-step correction is performed only in the tangential direction as applying the correction in the radial direction was found to have negligible effects. Another reason for not applying the correction in the radial direction is that the radial interpolation would have caused the loss of information of the already few traversing points in the spanwise direction. For further details on the correction adopted, the reader is recalled to the referenced paper of Ligrani et al. [8]. Figure 11 is a repeat of Figure 10 with the addition of the distributions resulting from the application of the spatial displacement correction (green diamonds) and the complete two-step correction (red squares) to the probe-determined data. As shown in figure 11a, the distributions of the probe-determined non-dimensional total pressure with and without correction are identical, indicating that the effect of the correction is negligible on the measured total pressure value. The Mach number distributions in Figure 11b show that the spatial displacement correction results in a slight improvement in the difference between the probe-determined Mach number distribution and the undisturbed one while the complete two-step correction does not further decrease the aforementioned difference, indicating that the discrepancies in the probe-determined Mach number values are not only caused by secondary transversal velocity effects but also due to changes of the flow-field around the probe that render the uniform calibration somewhat invalid. As it can be seen in Figure 11c, the effect of the two-step correction becomes considerable on the probe-determined yaw angle distribution, with major improvements when accounting for the secondary transversal velocity components. Nevertheless, the corrected data are not able to perfectly retrieve the undisturbed pitch-wise distribution of yaw angles, indicating that in transonic regimes the two-step correction (developed for low-speed applications) underpredicts the effect of the transversal velocity components. The distributions of pitch angles are shown in figure 11d. While the spatial displacement correction is shown to cause negligible improvements in the accuracy of the probe-determined distribution, the two-step correction helps to further decrease the difference from the undisturbed data. Nevertheless, on the pitch angle, the effect of the correction results in minor improvements.

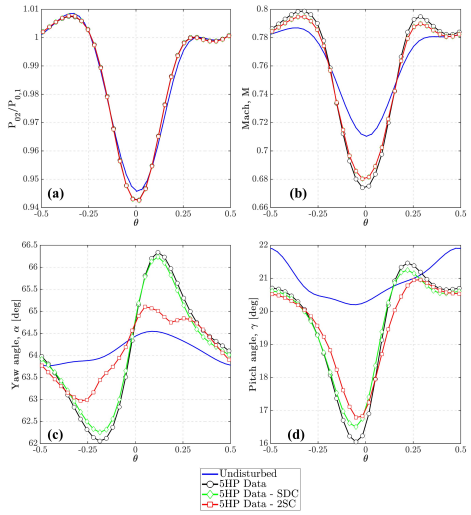

Figure 11: Midspan pitch-wise distributions of (a) normalized total pressure, (b) mach number, (c) yaw and (d) pitch angles of the undisturbed flow field, measurement performed with the five-hole probe and measurement performed with the five-holes probe corrected accounting for pressure taps spatial displacements and velocity gradients.

3.4. Effect on the probe measurements in the 3D region

3.4.1. Effect on the flow-field near the shroud endwall

Figure 12 shows contour plots of the total pressure distribution near the shroud endwall at Plane 2 for the vanes-only (no probe) case and for the case with vanes and probe. For both cases the values in the figures are normalized by the inlet total pressure, P01. The total pressure values, P02, corresponding to the vanes only case are distinguished from the ones corresponding to the vanes and probe case using an asterisk. The total pressure values used for the vanes only case were extracted directly from the simulation and represent

the values obtained in an undisturbed flow-field. The values shown for the case with vanes and probe are the ones retrieved by the probe after the application of the two-step correction and include any disturbances caused by the probe to the flow-field, as in the case of a typical experiment. In both cases the characteristic low total pressure core, as a result of the upper passage vortex of the vanes, is evident. Comparing the two plots it can be seen that the flow-field retrieved by the probe is similar to the one of the vanes only case albeit with lower total pressure values in the passage vortex and with contour lines that appear more stretched in the radial direction.

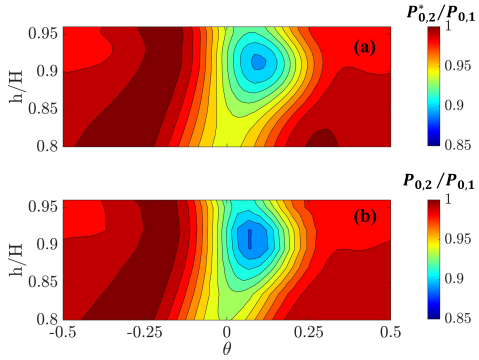

Figure 12: Normalized total pressure distribution near the shroud end-wall at plane 2: (a) flow-field for the vane only case and (b) flow-field retrieved by the probe after two-step correction

The differences between the two cases are better highlighted in the difference plot shown in Figure 13, constructed by simple subtraction the flow-fields of Figures Figure 12a and b. The maximum difference between the flow-filed of the vanes-only case and the probe-retrieved flow-field is equal to ±1.5% of the total inlet pressure. The distribution of the error plot is qualitatively different to the distributions shown in Figure 12, indicating that the differences between the vane-only and probe-retrieved flow fields are partly due to the aforementioned shift of the relative position of the two distributions. A second reason for the difference between the two distribution is the difference in the magnitudes of the total pressure values of the two cases. The underlying cause of these qualitative and quantitative differences between the two flow-fields can either be a fundamental change of the flow-field upstream of the probe due to an influence of the probe on the upstream vane, or an error in the reading of the probe due to the uniform calibration not being able to account for the flow non-uniformities in the measurement set-up. These two effects could not be separated in this study but based on the small effect of the probe on the upstream vane loading shown in Figure 9, it is hypothesized that the primary cause is the inability of the uniform calibration to account for the flow non-uniformities present in the measurement set-up with upstream vanes.

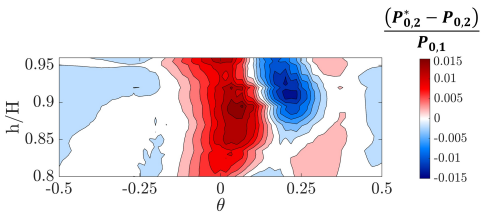

Figure 13: Contour plot of the difference between the normalized total pressure distributions in the flow-field of the vane only case and the flow-field retrieved by the probe.

Figure 14 shows a contour plots of the yaw angle distribution near the shroud end-wall at Plane 2 for (a) the vanes-only case, (b) for the case with vanes and probe when no correction is applied, and (c) for the case with vanes and probe when the two-step correction is applied. As in the preceding plots, yaw angles corresponding to the vanes-only case are distinguished by an asterisk. A region of under-turning (yaw angle smaller than 64o of flow turning expected by vanes) stretching across much of the vane passage can be seen at about 90% span in the vanes-only case as a result of the presence of the upper passage vortex. In the same region, a noticeable difference can be seen for the case of the probe-determined flow-field without correction (Figure 19b). In this case, two adjacent regions of high and low yaw angle can be seen. Upon application of the two-step correction to the probe-determined flow-field the distribution of yaw angle (Figure 19c) shows a much more similar flow-field to the vane only case, demonstrating the benefit of using this correction.

The benefit of using the two-step correction can be better appreciated by looking at the difference plots in Figure 15. When no correction is applied to the probe-retrieved data (Figure 15a), the maximum yaw angle difference between the two cases is ± 5 degrees. When the two-step correction is applied (Figure 15b), the error decreases below ± 1degree from 80-94% of the span and below ± 2.5 degrees above 94% of the span, thus showing the clear benefit of using the correction. The higher error at high span is attributed to probe-endwall interaction effects that are not taken into account by the correction. Despite not shown in this paper, using the two-step correction also im-

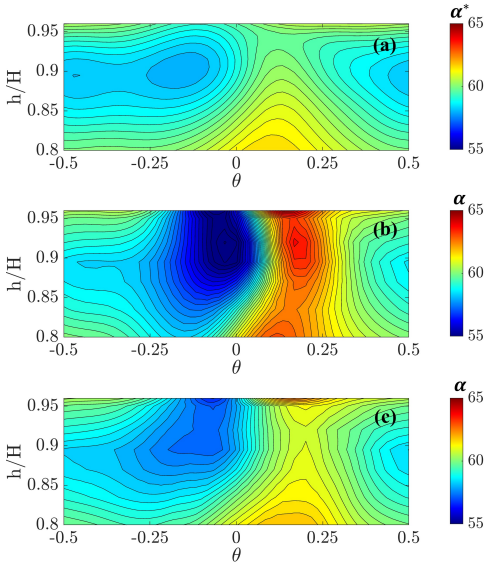

Figure 14: Yaw angle distribution near the shroud end-wall at plane 2: (a) flow-field for the vanes-only case, (b) flow-field retrieved by the probe and (c) flow-field retrieved by the probe after two-step correction

proves the agreement between the probe-determined pitch angle distributions and the ones retrieved in the vanes-only case.

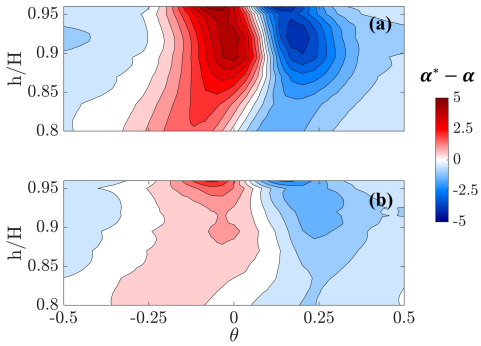

Figure 15: Contour plot of the difference between the yaw angle distributions in the flow-field of the vane only case and the flow-field retrieved by the probe: (a) probe retrieved values without correction and (b) probe retrieved values including two-step correction. plane 2 at the shroud of the flow-path

3.4.2. *Effect on the flow-field near the hub endwall*

Figure 16 shows contour plots of the total pressure distribution near the hub endwall at Plane 2 for the vanes-only case and for the vanes and probe case. In the latter case, the flow-field is the one retrieved by the probe with the two-step correction.

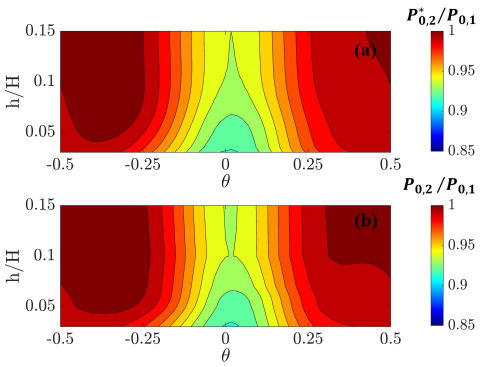

Figure 16: Contours of normalized total pressure in plane 2 at the hub of the flow-path: (a) value for the undisturbed case and (b) probe retrieved values including two-step correction

A vertical region of low total pressure can be seen in the case of vanes-only (Figure 16), corresponding to the wake of the vanes. Surprisingly no evidence of the lower passage vortex can be clearly identified in this figure likely due to the presence of a very weak vortex which remains close to the hub endwall. As it can be seen in Figure 16b, a virtually identical flow-field is retrieved by the probe with the two-step correction albeit with a slight overestimation of the total pressure values. The differences between the two flow-fields can be better visualized by looking at the difference plot in Figure 16. The regions at which the total pressure is overestimated by the probe are found on either side of the wake. The maximum difference between the two flow fields is -1.5% of the inlet total pressure and occurs near the hub enwall on the left side of the wake (pressure side of the vane). This larger discrepancy between the two flow fields is attributed to the probe-proximity error due to a combined effect of the pre-pitch of the probe head relative to the axial direction and the curvature of the hub endwall. The analysis on the yaw angles measured on the hub 3D region is not reported given the similarity to the results obtained at the shroud region (Figures 14 and 15).

3.4.3. *Effect on the pitch-wise averaged distributions*

Figure 18 shows the pitch-wise averaged radial distribution of (a) total pressure, (b) Mach number, (c) yaw and (d) pitch angles. The distributions of the reference test-case (blue lines), raw probe measurements (black circle symbols), and corrected probe data with the two-step approach (red squares) are also included in every plot. In general there is perfect collapse of the data points corresponding to the uncorrected case

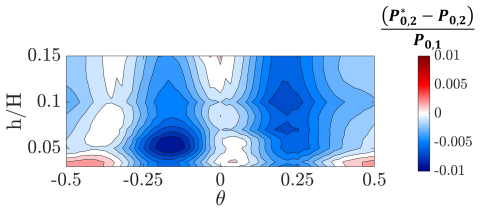

Figure 17: Difference between the normalized total pressure contours at the hub reported in figure 21. Undisturbed case minus probe measured data.

with the ones corresponding to the corrected case. This indicates that the probe effect shown in the previous sections is only localized and that it does not alter the average distributions. Consider first the total pressure distribution shown in Figure 18a. Over the entire span, the maximum difference between the probe-determined and undisturbed flow-field values is ±0.25% of the total inlet pressure. The highest deviations occur in the 3D regions near the hub and shroud where the radial gradients of total pressure are stronger. Figure 18b shows the radial distribution of the pitch-wise averaged Mach number. At midspan and near the shroud region, the probe-determined values show good agreement with the undisturbed values with maximum errors below 0.015. At the hub, higher deviation of the probe-determined quantities are shown due to the probe-endwall interactions. The radial distribution of yaw angles (Figure 18c) shows that the probe-determined values are in good agreement with the undisturbed case. The highest deviation is observed at the hub region, with the error in the probe-determined yaw angles below 1 degree. Lastly,let's now consider the radial distribution of pitch angles (Figure 18d). This deviation is higher at midspan with respect to the tip due to a more conspicuous blockage effect of the probe stem that deviates the flow below the probe, thus causing the reduction of the flow angle "measured" by the probe. Close to the hub, the probe-endwall interactions induces a strong deviation of the probe-determined values in this region.

4. Conclusions

In this study, the effects of vane-probe interactions on the flow-field and probe measurements are analyzed using numerical simulations. The simulations including vane and probe showed that the probe potential field impacts the upstream vane sector causing a variation of the vane loading of three lower (suction

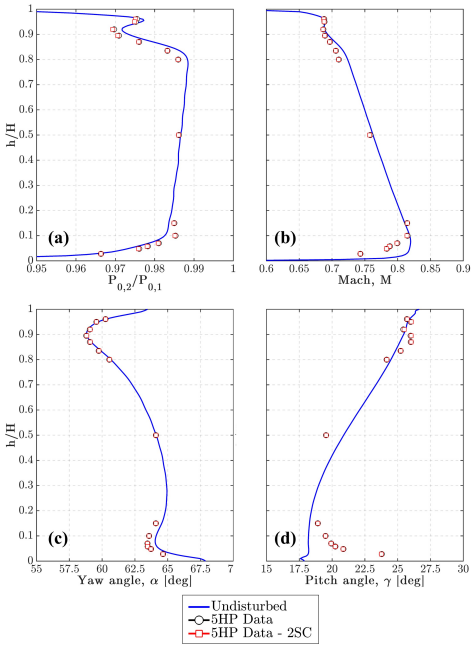

Figure 18: Pitch-wise averaged radial distribution of (a) total pressure, (b) mach number, (c) yaw and (d) pitch angles. Comparison of undisturbed flow-field, probe-measured data and probe data corrected with two-step correction.

side direction) and the first upper (pressure side direction) airfoils. This impact is as a result of a static pressure change downstream of the nozzles which alters the mass flow distribution through the passages and hence the acceleration of the flow over the vane profile. The probe determined quantities have been compared against the 'undisturbed' flow-field to assess the accuracy of the quantities determined by the probe. To compensate for the effect due to velocity gradients, a two-step correction is employed and its effect in the 2D and 3D flow regions is examined. The total pressure distribution is accurately retrieved in the pitch-wise direction except in the wake and passage vortex regions. The correction is shown to be very effective on the "measured" yaw angles both on the 2D and 3D regions, reducing the difference between vane-only and probe-determined data below 1 degree. Finally, the effect on the pitch-wise averaged measured quantities is evaluated. The highest variation between probe-determined data and undisturbed values is found where radial gradients of total pressure are stronger. Furthermore, the two-step correction was shown to have almost negligible impact on the pitch-wise averaged quantities, with the data including the correction being identical to the uncor-

rected raw probe data.

References

[1] J. Wyler, Probe blockage effects in free jets and closed tunnels.

[2] F. Truckenmüller, H. Stetter, Measurement errors with pneumatic probes behind guide vanes in transonic flow-fields, in: 13th Symposium on Measuring Techniques for Transonic and Supersonic Flow in Cascades and Turbomachines. Zürich, Switzerland, 1996.

[3] M. Boerner, M. Bitter, R. Niehuis, On the challenge of five-hole-probe measurements at high subsonic mach numbers in the wake of transonic turbine cascades, Journal of the Global Power and Propulsion Society 2 (2018) 453–464.

[4] J. Aschenbruck, T. Hauptmann, J. Seume, Influence of a multi-hole pressure probe on the flow field in axial-turbines, in: 11 th European Conference on Turbomachinery Fluid dynamics & Thermodynamics, EUROPEAN TURBOMACHINERY SOCIETY, 2015.

[5] C. Sanders, M. Terstegen, M. Hölle, P. Jeschke, H. Schönenborn, T. Fröbel, Numerical studies on the intrusive influence of a five-hole pressure probe in a high-speed axial compressor, in: Turbo Expo: Power for Land, Sea, and Air, Vol. 50787, American Society of Mechanical Engineers, 2017, p. V02AT39A009.

[6] H. T. Hoenen, R. Kunte, P. Waniczek, P. Jeschke, Measuring failures and correction methods for pneumatic multi-hole probes, in: Turbo Expo: Power for Land, Sea, and Air, Vol. 44670, American Society of Mechanical Engineers, 2012, pp. 721–729.

[7] C. Clark, S. Grimshaw, A pneumatic probe for measuring spatial derivatives of stagnation pressure, in: Turbo Expo: Power for Land, Sea, and Air, Vol. 58677, American Society of Mechanical Engineers, 2019, p. V006T05A024.

[8] P. Ligrani, L. Baun, B. Singer, Spatial resolution and downwash velocity corrections for multiple-hole pressure probes in complex flows, Experiments in Fluids 7 (6) (1989) 424–426.

[9] V. Chernoray, J. Hja¨ rne, Improving the accuracy of multihole probe measurements in velocity gradients, in: Turbo Expo: Power for Land, Sea, and Air, Vol. 43123, 2008, pp. 125–134.

[10] M. Boerner, R. Niehuis, Development of an additive manufactured miniaturized wedge probe optimized for 2d transonic wake flow measurements, in: XXIV Biannual Symposium on Measuring Techniques in Turbomachinery; MTT: Prague, Czech Republic, 2018.

[11] F. R. Menter, Two-equation eddy-viscosity turbulence models for engineering applications, AIAA journal 32 (8) (1994) 1598–1605.

[12] T. Yasa, G. Paniagua, Robust procedure for multi-hole probe data processing, Flow Measurement and Instrumentation 26 (2012) 46–54.

[13] B. Hall, T. Povey, The oxford probe: an open access five-hole probe for aerodynamic measurements, Measurement Science and Technology 28 (3) (2017) 035004.

[14] A. Main, C. Day, G. Lock, M. Oldfield, Calibration of a four-hole pyramid probe and area traverse measurements in a short-duration transonic turbine cascade tunnel, Experiments in fluids 21 (4) (1996) 302–311.

[15] L. He, W. Ning, Efficient approach for analysis of unsteady viscous flows in turbomachines, AIAA journal 36 (11) (1998) 2005–2012.

[16] B. R. Green, R. M. Mathison, M. G. Dunn, Comparison of harmonic and time marching unsteady computational fluid dynamics solutions with measurements for a single-stage high-pressure turbine, Journal of Turbomachinery 136 (1) (2014) 011005.

On the design and characterization of a turbulence generator for a low-speed cascade rig

Federico Bertelli

Turbomachinery and Propulsion Department, von Karman Institute for Fluid Dynamics, Belgium,
federico.bertelli@vki.ac.be

Supervisor: Sergio Lavagnoli

Associate Professor, Turbomachinery and Propulsion Department, von Karman Institute for Fluid Dynamics, Belgium,
sergio.lavagnoli@vki.ac.be

University Supervisor: Koen Hillewaert

Professor, Aerospace and Mechanical Engineering, University of Liège, Liège,
koen.hillewaert@uliege.be

Abstract

Quantifying free-stream turbulence effects on the fundamental flow physics of fluid dynamic mechanisms is important for improving physical understanding as well as the predictions of the aerodynamic losses for turbomachinery flows and a wide of other internal and external aerodynamic flows. This paper discusses the development of a turbulence generator that is capable of generating a wide range of turbulence with the peculiarity to set the turbulence intensity levels and yet tune the turbulence scales independently.

Keywords: Turbulence, Turbulence Scales, Active Turbulence Generator, Jet Grid, Low-Speed Wind Tunnel, Low-Speed Cascade Rig, Blade Passage Flow

1. Introduction

The assessment of the aerodynamic performance degradation for turbine passage flows had and continues to have a key role in performance and efficiency predictability. One prominent effect that plagues this predictive capability is the role of turbulence, as it plays a major role in the dynamics of physical processes that are still not fully understood today. In turbine flows, as well as in many other internal and external aerodynamic flows, the time-dependent and multi-scale interactions between turbulence and flow physics represents the main sources of uncertainty both in experiments and CFD simulations, causing significant discrepancies between measurements and predictions of global flow phenomena and entropy generating mechanisms. While the role of free-stream turbulence intensity has been of primary interest to researchers during the past decades, the individual role of turbulence length/time scales on the aerodynamics of turbine passage flows is still scarcely investigated in open literature. The isolated effects of scales are too often brutally ignored or poorly modeled when not considered as a concurrent/dependent effect of the turbulence intensity, as nowadays the turbulence scales are difficult to generate and measure both in experiments and numerical simulations. However, although there have been only few literature evidences in which there has been a systematic variation of turbulence intensity and scales, the results consistently show the importance of both these two parameters on the flow physics of turbine passages. To advance our physical understanding on the role of turbulence as well as the fidelity of the turbulence-modeled CFD predictions, commonly used as standard practice in today's academic and industrial design and optimization processes, this research field needs a boost. The VKI's turbine research group is contributing to fill this knowledge gap, aiming at producing an unprecedented set of both experimental and

numerical measurements to target the precise identification of scales effects on the fundamental physics of the main flow mechanisms characterizing a turbine aerodynamics and the evaluation of their impact on the performance drop. The rationale behind the scope of this paper is to enable the future experimental campaigns in the VKI C-1 low-speed cascade rig with a novel turbulence generator capable to expose turbine flows to a wide range of free-stream turbulence, characterized by values of turbulence scales that can be systematically varied from the intensity levels, so that the effects of these two key parameters are isolated/decoupled and studied independently each other.

The aim of this paper is threefold. First, this paper describes different concepts for generating free-stream turbulence in low-speed wind tunnels, focusing in particular on the only one that provides the authority for the independent control of turbulence scales. Note that there are now a number of different free-stream turbulence generators that have been presented in the open literature that are able to produce a wide range of turbulence intensities without, however, allowing for an independent control of turbulence scales. Second, this paper focuses on the design process of the turbulence jet grid concept developed to generate different combinations of free-stream turbulence with turbulence intensities between 1% to 15% and an independent control of the integral length scale within the range of 5%-20% of the turbine blade chord. Such desired range of turbulence regimes is representative of turbulence values encountered by a broad class of turbine systems as well as a number of other technologies where turbulence-driven flows play a critical role in the definition of efficiency. Third, this paper presents the complete design of the experiment for the measurement campaign that targets the turbulence jet grid characterization in the auxiliary VKI L-12 low-speed test bench, with the main purpose to validate the turbulence generator concept and the generated turbulent flow fields and inform future design iterations for a scaled-up version to install in the VKI C-1 low-speed cascade rig.

The following sections report a review of relevant past studies, a solid understanding of the concepts used to decouple the turbulence scales effects from the intensity, the analysis and development of the turbulence generator, and finally a description of the entire experiment, describing the experimental facility and measurement techniques used for this study together with strategies, methods and procedures to success the tests.

2. Past Studies

On the Role of Turbulence Scales

Past studies have indicated the importance of both turbulence levels and length scales, however, only few experimental works and only for very specific cases have shown the role of turbulence length scales and the related energy spectra on the aerodynamics and heat transfer mechanisms of turbine flow passages. As pointed out by Ames [1], Carullo et al. [2] and Wang et al. [3], free-stream turbulence scales modulate the leading-edge stagnation heat transfer; larger scales interact with the blade leading edge producing small-scale fluctuations associated with more intense convective heat exchanges. Other investigations have observed the effects of free-stream turbulence scales on turbine vanes aerodynamics [4, 5] concluding that the laminar-to-turbulent transition is highly dependent on a variation of the turbulent structures; larger free-stream turbulence scales grow faster within the boundary layer causing an early laminar-to-turbulent transition on the blade suction side. Mahallati et al. [6] show that the spectrum of smaller integral length scales contains the high-frequency content necessary to trigger boundary layer stream-wise streaks and the generation of turbulent spots. Such results are also in agreement with what reported by analysis of aerodynamics and surface heat transfer in flat plate applications [7, 8].

This high coherence between free-stream turbulence length/time scales and the boundary layer response is indicative of the prominent role that the turbulence scales may play on loss generating mechanisms. As pointed out by Folk et al. [9], smaller scales penetrate deeper into the boundary layer causing a rise in dissipation coefficient and in turn of total losses. Also the recent work of Gakhara [10], solicits further research to address the effects of free-stream turbulence scales on the dissipation coefficient in the laminar boundary layer, and on laminar-turbulent transition. In addition, Gakhara [10] suggests to improve our fundamental understanding about the role of free-stream turbulence scales on: the anisotropy of turbulence withing the boundary layer, the extent of penetration of eddies into the boundary layer (and hence, loss generation), the generation and dissipation of mixing-losses in the wake and on the dynamics of vortical structures.

In line with these conclusions, few numerical works [11–13], using turbulence-resolved CFD simulations, emphasize how the transition location and mechanisms on the blade suction side results to be highly

sensitive to free-stream turbulence scales. The authors reported how the turbulence structures affect the turbulent mixing in the boundary layer such that the transition point and length vary, concluding that the response of the boundary layer to the free-stream turbulence levels depends strongly on the turbulence scales.

The interest to investigate experimentally the turbulence scales effects is particularly strong among the CFD community, since, according to Tucker [13], Dick and Kubacki [14] and Tyacke et al. [15], the lack of experimental data prevents attempts to properly model the role of turbulence in CFD simulations. As numerous experiments do not detail the turbulence scales, such values are too often left to guess or become free parameters to adjust, by the CFD users, the match with available experimental data, limiting thus the specification of the turbulence at the inlet CFD domain. In turbulence modeling simulations (RANS/ URANS) too often the length scale (indirectly captured by the turbulence decay behaviour of the turbulence models) is not seen an input to the simulation, but as a parameter to tune the predictions. However, different prescribed turbulence scales at the CFD domain boundaries would result in different dissipation rates with significantly altered the decay of turbulence that, in turn, strongly affect the flow evolution as reported by Babajee and Arts [16] and Bode et al. [17]. The arbitrary choice of the input turbulence scales is not justified, resulting often in turbulence models that do not correctly represents the flow physics (under/over predicted results) and in a severe mismatch with experimental evidence. For these reasons, it is evident the need to focus on a fundamental understanding of the physics behind the role of turbulence scales in internal flows and to align the accuracy of turbulence-modeled simulations with that of experiments.

What this paper wants to address is, therefore, the development of a new turbulence generator that add the possibility to study the role of turbulence scales, putting thus into evidence their isolated effects. To do that, such device has to be able at generating a wide range of turbulence with the peculiarity to set the turbulence intensity levels and yet tune the turbulence scales independently.

Review of Turbulence Generating Techniques

At the state-of-the-art, several methods for generating turbulence, other than the commonly used passive grids [18], have been presented in the literature with most of these techniques appearing in more recent decades. Turbulence generator methods can be broadly classified into wall jets [19], cross-flow injection [8], combustor simulator [1, 20], active grid [21] and jet grid [22–28]. Among these methods, the passive grids, where the generation of vorticity results from the presence of the flow blockage effects, can offer a well-defined experimental conditions, as they are widely used in a variety of experiments. On the other hand, the passive grids allow to cover the target turbulence intensities without, however, being able to control independently the turbulence length scales in the required range (for a fixed design). Wall jets, cross-flow injections and combustor simulator methods are able to achieve high turbulence levels having, however, inherent problem of a non-uniform mean flow field which makes it complex to apply to a turbine passage flow. Indeed, it is difficult for jets in normal or cross-flows direction to penetrate to the centerline of the test section. Although the homogeneity conditions can be improved, these methods are not take into account due to another limiting factor that is the relatively large size of these devices, as the useful space in test section of the cascade rig is limited. The active grid concept makes use of moving elements (rotating rods with agitator wings) to increase the turbulence levels in the flow field, resulting too complex and not suitable for the present project since it does not allow to control the length scales for a fixed turbulence intensity. Finally, the basic idea behind the jet grid concept is to supply momentum in the mainstream flow by using continuously, adjustable and distributed compressed jet injections. Although the main principle is to inject air by distributed jet injections, this concept also bases on the design of a passive grid. Therefore, a variation of the turbulence levels downstream of the grid is due to their combined effect: namely, interactions and mixing between the turbulent bar wakes and jet injections and the blockage effect of the passive grid. The air injections are blown from an auxiliary pressure system into a hollowed passive grid and injected through small injection holes in the upstream or/and downstream direction. On one side, the upstream jets can be used to control the boundary layer separation on the grid bars by reducing the wake width and consequently reducing the effective solidity and the static pressure drop of the grid. On the other side, downstream jets can smooth the downstream flow field (by filling in the bar wakes) for a better flow homogeneity or, if the jets are strong enough, make the bar wakes unstable (due to the additional shear in the jets themselves) to elevate the turbulence level.

Although at the state-of-the-art no information

were available on how to decouple turbulence intensity from the eddy sizes using a jet grid, the operating principle of this turbulence generator was of significant interest to this paper. Indeed, the jet grid concept looked the most promising in terms of generating a broad range of free-stream turbulence parameters showing the authority to be adapted for the independent control of turbulence scales so as to generate turbulent flow fields where the size of turbulent structure can systematically varied from the intensity. For these reasons we began developing this type of turbulence generator on the base of existing designs.

Jet Grids

As presented in literature, a wide range of different turbulence levels result as a consequence of different jet grid designs [22–28]. All these studies served as basis for the present paper to identify the main parameters driving the design of a new jet grid and the generated turbulent flow fields. However, the works by Young et al. [24], Bangert et al. [25] and Nix et al. [27] were of significant interest, since they highlighted three possible methods being able to independently control the length scales at fixed turbulence levels.

Young et al. [24] used a biplanar grid to inject air through evenly spaced holes either in upstream or downstream direction only. The turbulence decay rate, now also a function of the jet injection, is slower compared to a passive grid where the decay heavily depends only on the grid design and flow conditions. As pointed out by the authors, the turbulence level generated by the jet grid is always higher than a passive grid and its value increases as the injection ratio (or upstream or downstream) increases. In particular, with the same injection ratio and at the same downstream distance from the grid, downstream injection shows higher turbulence intensity than upstream. As the downstream injection increases, additional turbulence and shear of the jets themselves become more important resulting thus in an increase of the turbulence level. At higher injection ratio the jets become unstable and higher turbulence levels are observed, concluding that the jet injections penetrate a distance proportional to the relative jets strength. Unlike the downstream injection, upstream jets seem to increase the grid solidity and/or change its "effective position" and, with relatively small injection ratio, cause flow instability with a subsequent increase of the turbulence level and an effect more pronounced as the injection ratio increase. Finally, as the downstream distance from the grid increases, both upstream and downstream injection produce turbulence levels that converge to the same value (5%) but with different integral length scales (2cm vs. 1.5cm respectively). In light of these conclusions, the *method 1* plans to achieve, with a fixed grid position and at long downstream distance, the same turbulence intensity but with different length scales by separately using the turbulence decay of upstream and downstream injection, as shown in Figure.

The research of Bangert et al. [25] developed a method for generating free-stream turbulence with simultaneous upstream and downstream injections. By adjusting the jet grid design and injection ratio, this turbulence generator produced a turbulence intensity up to 20% and an integral length scale within 2.1 cm and 5.5 cm. Although the preliminary experimental characterization showed promise in generating thigh turbulence levels with upstream injection only, this type of designs caused poor flow homogeneity (grater than downstream injection ± 10%) and the final design was based on simultaneous injection. Also in this case, the turbulence levels for the jet grid were much higher that the passive grid and the turbulence decay is slower. The principle behind the *method 2* is base on the displacement of the jet grid in different position. Indeed, as shown in Figure, by fixing the grid geometry and testing different injection ratio, the obtained turbulence decay curves show the same turbulence level at different downstream distances. Therefore, by adjusting the grid position to obtain the same turbulence intensity imply that the resulted length scales are different.

The *method 3* is obtained from the outcomes of Nix et al. [27], where the authors opted for a jointly use of upstream injection to increase the shear stress for elevating the turbulence level, and downstream injection to fill in the wake behind the bars for a better flow uniformity. As shown in Figure, starting from a passive grid configuration, as the injection is activated and increased, a first decreasing of the turbulence intensity is observed, followed by a steady increase with a continue increase of the injection ratio. The first decreasing, in agreement also with the results reported by Boyle et al. [26] and Gad-el-Hak and Corrsin [22], is a result of a fill up of the wakes behind a grid bar and in literature is only reported for large bar diameter where the effects of the boundary layer development is higher. Therefore, with this method it is possible to obtain at the same downstream distance (close to the grid) the same turbulence intensity but different length scales only by adjusting the injection ratio.

In general, most of the literature results about the

influence of the injection ratio on the turbulence parameters trend are in agreement. For a fixed jet grid geometry, the characteristics curve of the turbulence intensity tends to move to higher values of intensity and at higher downstream distance as the injection ratio increases. It means that, with an increment of the injection ratio is possible to obtain higher turbulence intensity but at higher downstream distance. In the other way around if the injection ratio is decreasing the characteristics curve of the turbulence intensity tends to approach the passive grid configuration. Measurements of the integral length scale show that, with growing distance from the grid the smallest eddies dissipate and the integral length scale growth downstream, even more by increasing the injection ratio.

3. Turbulence Jet Grid Development

The purpose of this section is to highlight the step-by-step procedure that was followed to develop the jet grid concept. From an extensive analysis of the literature evidences [22–28], the main parameters that was identified to drive the design was: the geometry and size of the bars, the array setup of the grid, the size and position of the jet holes along the bars, and the ratio and direction of the jet injection. It is important to note that, unlike a passive grid design, nowadays no empirical correlations exist to follow for designing "a priori" a new jet grid, as most of the effects due to the jet injection are strictly correlated to design itself and test conditions. Therefore, only after the experimental characterization will be possible to validate the choices made and iterate on the final design.

The design process of the jet grid has been put into prospective with the target turbulence values that what we want to reproduce for future experimental campaigns in the VKI C-1 low-speed cascade rig, where the test case will be a turbine flow passage with loading representative of a state-of-the-art low-pressure turbine. The desired free-stream turbulence regimes, representative of turbulence values encountered by a broad class of turbine systems, involve turbulence intensities between 1% to 15% and integral length scale within the range of 5%-20% of the turbine blade chord. Bearing in mind both the constraint imposed by the C-1 test section and the target testing conditions, the early-stage of the design process has been dedicated to obtain the best compromise between varying the blade chord length and:

- maximize the size of the turbulence length scales to be generated and consequently improve the measurement resolution,
- maximize the flow periodicity,
- ensure two-dimensional flow conditions at the mid-section of the blades,
- maximize the measurement resolution,
- maximize the pressure rise so that to maximize the pressure differential to be measured.

Indeed, decreasing the blade chord length decreases the size of the turbulence length scales to generate, which are in turn limited by the design constraints of the jet grid. Moreover, smaller turbulence length scales increase the uncertainty of the measurement. Again, to maintain a pitch-to-chord ratio to value representative of modern low-pressure turbine, low blade chord length decreases the cascade pitch for a better flow periodicity (high number of blades) and increases the aspect ratio for an improved distinction between 2D and 3D flow phenomena. On the other hand, to test at the target Reynolds numbers (within the range 50-250k), the pressure rise requested to the facility increases, resulting in the possibility of exceeding the limits imposed by the performance of the C-1 wind tunnel. Moreover, the spatial resolution of the measurement instrumentation has to be improved to capture and to be sensible of smaller turbulence structures. On the contrary, high blade chord length allows the jet grid to easily reproduce higher integral length scales, which results in improved measurement resolution. Increasing the blade chord length reduces also the pressure rise needed to attain the target Reynolds number and allows a better measurement resolution. However, increasing the chord length leads to a poor flow periodicity (low number of blades) and an aspect ratio that may not ensures two-dimensional flow conditions in the midsection of the blades. Indeed, the end-walls flows generate a huge flow recirculation regions on the blade suction surface which may mix with the midsection flow phenomena. From this analysis, the best compromise is identified in a blade chord length of 75 mm, resulting in a target range of integral length scales within 3.5-15 mm, as shown in Figure 1.

Accordingly to this target turbulence range and the compatibility of the jet grid with the VKI C-1 rig, the design process move through a parametric study of the literature evidences, where the geometry and size of the bars have been varied to optimize all possible jet grid design configurations to meet the project-defined

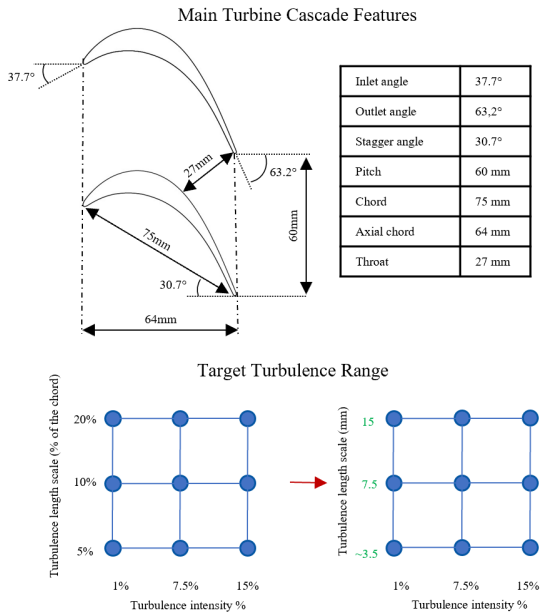

Figure 1: Turbine test case (above) and target turbulence range.

requirements and constraints. The size of the bars has been ranged within from small (5mm) to large (20mm) diameter, whereas the geometry has been varied between a circular and square shape. The choice of the bar shape influences the flow separation and the wake shed downstream of the grid, and consequently his fluid-dynamic solidity and pressure drop. A sharpness of the edges of a square bar shape is less sensitive to variation of the Reynolds numbers and it has a more stationary separation point and wake shape [22], however it produces a more pressure drop with higher turbulence intensity. On the contrary, a circular bar shape generates lower pressure drop and turbulence intensity but, it shows a separation location that depends strongly on the Reynolds number [29], producing more periodic turbulence structure and resulting more inclined to instabilities when the experimental campaigns will vary the Reynolds number. This parametric study can be summarized in the following three steps:

1. the examined bar geometry and shape is found among the literature evidences, seeking to match it with at least one existing jet grid design. The matched design become the baseline on which make the analysis,
2. on the baseline design are applied the methods discussed above that, together with the application of the spatial constraints (some methods involve the displacement of the grid) of the C-1 rig test section, return the turbulence range achievable,
3. following the turbulence parameters trend, resulted by increasing or decreasing the jet injection and/or the bar spacing of the grid, a new scenario is obtained where the baseline design can achieve other turbulence values.

The above steps have been applied for each combination of bar shape and size. When a match with an existing literature designs was not found, an interpolation of data was done to reconstruct the potential turbulence ranges achievable. Note that, while the circular bar shape is commonly used for jet grid design, square bar shape is only used in few experiments. Too few to extract a general trend of the generated turbulence parameters and, therefore, correlations reported by Roach [18] for square passive grids are used to set at least a starting point to predict the turbulence range accessible. The outcomes of this analysis have highlighted that the most promising configurations allowing to cover the target turbulence regimes are three, as reported in Table 1.

	Geometry		*Turbulence Range*	
Conf.	**Shape**	**Size [mm]**	**Intensity**	**Length Scale**
A	Circular	5-7	2-8%	4-10mm
B	Square	5-7	7-15%	4-10mm
C	Circular	9-11	5-11%	8-15mm

Table 1: Promising configurations in terms of bar shape and size.

At this point, the existing jet grid designs has been examined from the point of view of the grid setup. Examination of the experimental evidences shows that a specific design of the grid geometry mainly drives the generated turbulence, as both the pressure losses introduced by the grid and the flow instabilities found downstream scales on the grid array and mesh geometry. Since the turbulence energy generated by a grid is directly related to its design, this study began by fixing the grid array and mesh geometry so as to remove a degree of freedom during the design, focusing thus the study at controlling the turbulence length scales through the only variation of the jet injection and the grid position of the jet grid. By analysing literature evidences, the static pressure drop ΔP of jet grids may be correlated by the equation:

$$\frac{\Delta P}{q} \approx A\left(\frac{\sigma}{1-\sigma}\right)^2 + 2J^2\left(1 + \frac{2}{J} \pm R\right) \qquad (1)$$

where q is the upstream dynamic pressure and σ is the grid solidity. Referring to the Figure 2 the solidity is defined as $\sigma = \frac{A_0 - A}{A_0} = 1 - \beta$, where the porosity β is reported for square-mesh and parallel-mesh array (d is the bar diameter and M the mesh). R is the area ratio, $\frac{A_0}{A_j}$.

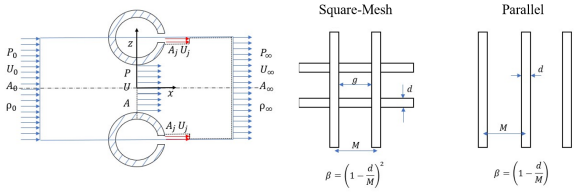

Figure 2: Jet grid representation (left) and grid array setup (right).

When there is not injection ratio, $J = 0$, the equation 1 reduces to $\frac{\Delta P}{q} \approx A\left(\frac{\sigma}{1-\sigma}\right)^2$, as already derived in literature for a passive grid. As reported by Gad-el-Hak and Corrsin [22], an empirical constant, A, multiplied the first term which is function of Reynolds number, Mach number and grid geometry (aerodynamic solidity). Since low pressure drop is given by a parallel-mesh array, the grid is designed based on this setup, choosing in particular an horizontal direction which is coherent with the cascade blade span found in the C-1 low speed rig. In addition, evidences suggest that significant flow instabilities in the wake region of the grid might arise for grid solidity greater than 50%. Since typical values range between $20 - 40\%$, a solidity of around 33% is chosen to allows possible future variations of $\pm 10\%$ without having flow instabilities. Knowing that the solidity is defined as $\sigma = 1 - \beta$, where $\beta = 1 - \frac{d}{M}$ is for parallel-mesh array, this means that the mesh to diameter ratio, $\frac{M}{d}$, is set to 3. Therefore, to match the design constraint of the L-12 test section, the jet grid consists of two configurations of 10 and 6 horizontal-parallel bars for bar diameter of 6 and 10 mm respectively.

Considerable attention has been given to the design of the jet holes, namely, the number, the spacing and the diameter. This because both the flow uniformity of the jet and the jet injection are in function the the jet holes design. As shown in Figure, three different scenario can be arise for the flow uniformity of the jet injections.

In the scenario A, the friction terms due to the inner wall dominate the inertial pressure recovery, which is due to the fact that the flow remaining within the pipe

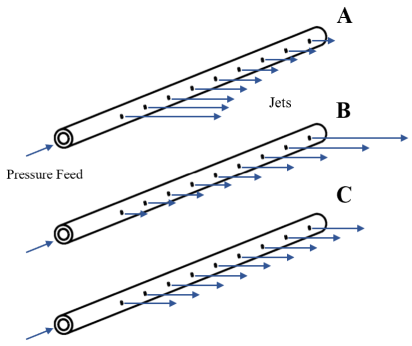

Figure 3: Three possible scenario occurring for the jet injection.

is decelerated along it with a subsequent pressure rise. In this condition, higher flow is biased toward the feed end of the pipe. On the contrary, the scenario B shows as the flow is biased toward the the end of the pipe when the inertial pressure recovery term dominate the friction. To obtain an ideal flow distribution downstream of the grid (scenario C), the inertial pressure recovery and the friction terms have to be balanced. A theoretical models have been used to analysis the perforated pipes.

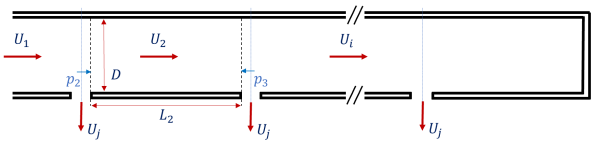

Figure 4: Schematic of the injection pipe.

Referring to the Figure 4, assuming a negligible variation of the density along the injection pipe the pressure rise across a jet hole is:

$$p_{i+1} - p_i = K\rho\left(U_i^2 - U_{i+1}^2\right) \tag{2}$$

where K is the outlet coefficient which considers that the outlet velocity is not totally perpendicular to the pipe, meaning that the pressure variation across the jet holes is only a fraction of an ideal value, $0 < K < 1$. Assuming also an equal distribution of the outlet velocity between n jet holes, $U_i = U_1\left(1 - \frac{i-1}{n}\right)$, the inertial pressure recovery can be written as:

$$p_n - p_1 = K\rho \sum_{i=1}^{n}\left(U_i^2 - U_{i+1}^2\right) = K\rho U_1^2\left(1 - \frac{1}{n^2}\right) \tag{3}$$

Now, by using the Darcy-Weisbach friction factor, f, the pressure loss due to friction between two subsequent jet holes is:

$$p_i - p_{i+1} = \frac{\rho f U_i^2}{2} \frac{L_i}{D} \tag{4}$$

and,

$$p_1 - p_n = \frac{\rho f}{2} \frac{L}{Dn} \sum_{i=1}^{n} U_i^2 = \frac{\rho f}{2} \frac{L U_1^2}{Dn} \sum_{i=1}^{n} \left[\frac{n-(i-1)}{n} \right]^2 \tag{5}$$

Therefore, the balance of the total pressure along the pipe can be written as:

$$\Delta P = \rho U_1^2 \left(\frac{fL}{2D} A - KB \right) \tag{6}$$

where the constant A and B are defined as follow:

$$A = \sum_{i=1}^{n} \frac{1}{n} \left[\frac{n-(i-1)}{n} \right]^2$$
$$B = \left(1 - \frac{1}{n^2} \right)$$

At this point, the goal is to minimize the maldistribution of the jet injections along the pipe. Defining the maldistribution as the percentage variation in jets between the first and last holes, clearly, the pressure variation due to the friction and inertial pressure recovery, ΔP, must be lower than the pressure drop across the holes, ΔP_h, which is defined as $\Delta P_h = \frac{1}{c_d^2} \frac{\rho_h U_h^2}{2}$, where $c_d \approx 0.62$ accounts both for friction and turbulence mechanisms and the approximation of the properties downstream of the orifices. A reasonable value of 5% maldistribution leads to:

$$5\% = 1 - \sqrt{\frac{\Delta P_h - |\Delta P|}{\Delta P_h}} \rightarrow \Delta P_h = 10 \Delta P \tag{7}$$

and substituting all the terms:

$$\frac{\frac{1}{c_d^2} \frac{\rho_h U_h^2}{2}}{\frac{\rho U_1^2}{2} \left| \left[\frac{fL}{D} A - 2KB \right] \right|} = 10 \tag{8}$$

For a number of jet holes greater than 8 the constants A and B are tend to the constant values 0.35 and 1 respectively. The value of K is difficult to assume a priori, however, from literature evidences a value in the order of 0.5 is assumed for discharge manifold. For the expected value of the velocity at the inlet section of the pipe, the Darcy-Weisbach friction factor, f, is assumed ≈ 0.01. The values of $\frac{L}{D}$ are fixed accordingly to the design constraints of the L-12 rig and the bar diameters seen above. Taking into account these approximations, the term $\left| \left[\frac{fL}{D} A - 2KB \right] \right|$ is ≈ 1. Moreover, introducing the definition of the mass flow rate the Equation 8 become:

$$\frac{A_1}{A_h} = \sqrt{10} c_d \sqrt{\frac{\rho_h}{\rho_1}} \tag{9}$$

Referring to the external diameters as reported in Table 1 and assuming a reasonable value for the density ratio across the jet holes, the holes diameter has been computed as 1.1 and 2.1 for bars diameter of 6 mm and 10 mm respectively, resulting in agreement with the existing jet grid designs that report values of the hole-to-diameter ratio ranging between $0.08 - 0.3$. Finally, to match the design constraints of the L-12 test section with the above analysis, the jet holes spacing has been chosen to be 25 mm (the typical values encountered in literature are between $20 - 40$ mm), leading thus to 8 jet holes per bar.

The last analysis is related to the main design parameters: injection ratio and the blowing direction. In reference to the Figure 2, the injection ratio is defined as the ratio of injected mass flow to the mainstream mass flow, $J = \frac{\rho_j A_j U_j}{\rho_0 A_0 U_0}$. The pressurized tubes consist in evenly distributed jet injections, where each tube are connected to a plenum that is pressured by an auxiliary pressure system. In this work, the same type of tube can be integrated in the grid in different ways, namely: for passive grid applications, to inject the flow simultaneous in the upstream and downstream direction [25, 27] or to inject the flow in separated direction at a time [22–24, 26, 28]. This it was thought to characterize the jet grid with respect to possible different uses and to validate the methods described above for the generation of a wide range of turbulence levels. For each of these testing conditions, the plenum to back pressure ratios, P_p/P_{bp}, can be varied to allow both non-choked and choked flow conditions of jets. In the former case, the injection ratio can be set by varying the back pressure of the facility (variation of U_j) or the plenum pressure for the mass flow rate of the injection jets:

$$\dot{m}_j = c_d A_j \sqrt{\gamma \rho_{t1} p_{t1} \left(\frac{2}{\gamma - 1}\right) \left(\frac{p_2}{p_{t1}}\right)^{\frac{\gamma+1}{\gamma}} \left[\left(\frac{p_{t1}}{p_2}\right)^{\frac{\gamma-1}{\gamma}} - 1\right]} \tag{10}$$

where, unless of pressure drops, $P_p \approx p_{t1}$ and $P_{bp} \approx p_2$. In flow condition, the mass flux ratio can be set only by varying the plenum pressure for the mass flow rate of the injection jets:

$$\dot{m}_j = c_d A_j \sqrt{\gamma \rho_{t1} p_{t1} \left(\frac{2}{\gamma + 1}\right)^{\frac{\gamma+1}{\gamma-1}}} \tag{11}$$

Considering the choices made for the jet grid design, the test conditions and, the limitation of the L-12 facility to a 7-bar pressure line, have been computed the plenum pressure needed to meet the target injection ratios. The outcomes are summarized in Table 2, together with all the design parameters.

	Configuration A	***Configuration B***	***Configuration C***
Array Setup	Parallel	Parallel	**Parallel**
Bar Shape	Circular	Square	Circular
Bar outer size	6 mm	6 mm	10 mm
Bar inner size	4 mm	4 mm	8 mm
Bar Spacing M/d	3	3	3
Mesh	18 mm	18 mm	30 mm
Number of bars	10	10	7
Hole diameter	1.1 mm	1.1 mm	2.1 mm
Hole spacing	25 mm	25 mm	25 mm
Number of holes per bar	8	8	8
Intensity range	2 - 8 %	7 - 15 %	5 - 11 %
Length scale range	4 - 10 mm	4 - 10 mm	8 - 15 mm
Pressure supply	1.1 - 5 bar	1.1 - 5 bar	1.1 - 2.5 bar
Injection ratio	1 - 3 %	1 - 3 %	2 - 5 %

Table 2: Summary of the jet grid designs.

4. Design of the Experiment

Experimental facility

The L-12 wind tunnel of the von Karman Institute for Fluid Dynamics is used to characterize the jet grid design and the relative turbulence generation methods. The L-12 rig, reported in Figure 5, is a low speed, open circuit wind tunnel having a contraction ratio of 5.76:1, and a test section designed in plexiglass parts with 0.2m x 0.2m cross section and length of 1 m available. A centrifugal blowing fan is used to push air in the test section with a maximum free-stream velocity of almost 20 m/s with a background turbulence level of about 0.3%. This rig is primarily designed to allow rapid and cost-effective testing of low speed flows, and it is used mainly for laboratory training for boundary layer investigation, three-dimensional velocity measurements, calibration of instrumentation and PIV experiments. The lab is equipped with a 7-bar pressure feed allowing to feed the jet grid. In addition, the L-12 wind tunnel is chosen for its ability to provide easy optical access and modify easily the test sections to accommodate different jet grid designs.

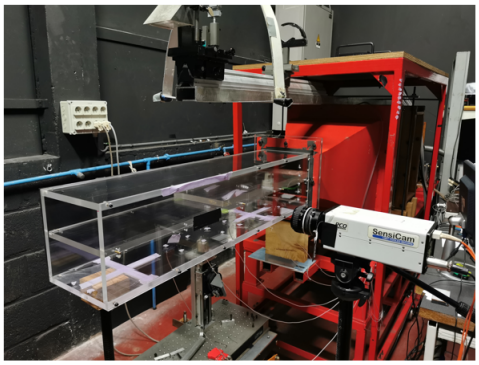

Test Section	20 cm X 20 cm X 100 cm
Maximum Freestream velocity	< 20 m/s
Background Turbulence	0.3 %
Pressure line	7 bar

Figure 5: VKI L-12 low-speed wind tunnel setup.

The idea behind the integration of the jet grid generator concept in the test section is to design an additional section to be added between the end of the contraction and the current test section for two main purposes, namely, to improve the turbulence development and its measurement by increasing the length of the channel and to allow a modular design of the sidewalls to arrange different jet grid configurations. In this sense, the conception of the jet grid was thought as a cassette where the bars, arranged in a horizontal parallel-mesh, are passed in crosswise direction through a slot on the sidewalls of the extension, designed to be compatible with all the jet grid designs. The compatibility is given by coupling the same sidewalls with three couple of supports to assembly different jet grid configurations. Since these slots could be a source of pressure losses/leakage flow, a sealing gasket will be place into a groove designed around the jet grid supports. Similar plexiglass parts of the current test section are used to design those of the extension. Referring to Table 2, except for configuration A and B where, based on literature evidences, the turbulence is supposed to decay in 70 cm, the configuration C needs to be tested in a test section with a channel length of about 110 cm. For this reason, an extension length of about 30

cm is chosen, which is added to the already existing 1 m length. CAD software is employed to digitally support the conception and design of the extension and all the auxiliary parts, as shown in Figure.

The pressure injection into the bars takes place via a pressure line composed by: the 7-bar pressure feed, a plenum and pipelines. The pressure feed will be connected by a pipeline to a plenum chamber that has the main function to equalize the pressure for a more even distribution among the outlets. Indeed, it will be designed relatively large in volume where the air initially resides approximately at rest, and thus has relatively low velocity compared to the outlet pipelines. The contribution to properly design a plenum chamber for an even distribution, and thus to produce a good airflow quality, is often not known. In general, literature reports that the bigger the chamber is the more even the airflow will be. Then, metal sheets are cheap and providing a sufficient plenum chamber is often a simple and cost-effective way to improve air distribution. Gad-el-Hak and Corrsin [22] design a plenum duct with a volume 5 times the volume of the bars, while O'Brien and Van Fossen [23] and Boyle et al. [26] 3 and 2 times respectively. Moreover, open literature reports some guidelines to design a plenum (for air systems): there must be one or more outlet diameter between the inlet and outlet flows, the width of the plenum has to be twice or more the inlet diameter and, the outlet flows have to be on the sides. The plenum will be supplied with compressed air by the pressure feed at gauge pressure: according to the analysis described above, the nominal pressure needed to achieve the target turbulence range between $1.1 - 5$ bar, giving no- and conditions to the jets. To ensure a proper nominal pressure inside the plenum, the pressure feed will be regulated by its own valve and pressure measurements will be performed at the plenum outlets. Each bar is connected by using flexible silicone tubing to the plenum, as is possible throttle and control the flow rate in each bar by squeezing the end of each flexible tube (before entering the hollow bars) with a clamping ring. The bars, made in aluminum, are slightly longer (30 cm) than the test section width (20 cm) so that to allow on one side the air feeding and on the other the measurement through pressure taps.

Jet grid testing are performed to match the conditions found in C-1 cascade rig. At such extent, the main scaling parameter is chosen to be the Reynolds number computed with respect to the grid geometry (bar diameter or mesh). Therefore, the L-12 testing conditions are set ranging the freestream velocity between $5 - 17$ m/s at ambient conditions.

Measurement techniques and planes

The experimental campaign aims to characterize the turbulence downstream of the jet grid as a result of the interactions and mixing between the mainstream flow and jet injections, focusing in particular at controlling the turbulence length scales through the variation of the jet injection and the grid position of the jet grid. The flow features to be characterize are:

Homogeneity and isotropy degree

Homogeneous turbulence is obtained if the property of invariance under spatial translations [30] is satisfied:

$$u_{rms}(\vec{x}_1, t) = u_{rms}(\vec{x}_2, t) \tag{12}$$

In other words, homogeneous turbulence is determined if the turbulent fluctuations are statistically the same at all the points of the flow field. It is often experimentally verified as having relatively constant mean velocity and subsequent constant turbulence intensity profiles, u_{rms}/U , at different traverse planes. In the present experimental campaign, the homogeneity degree should be assessed measuring the streamwise velocity components along different crosswise planes downstream of the jet grid.

Turbulent flows can be considered isotropic if their local statistics of the turbulence fluctuations have the same intensity in all directions [30], i.e. they are invariant under mirroring and axial rotation:

$$u_{rms}(\vec{x}, t) = v_{rms}(\vec{x}, t) = w_{rms}(\vec{x}, t) \tag{13}$$

where v_{rms} and w_{rms} are the root mean square of the velocity fluctuations in crosswise direction with respect to the streamwise direction. Homogeneous and isotropic turbulence (HIT) has same statistical properties in each direction and spatial location. A way to prove the homogeneity of the flow is to show the absence of both turbulent kinetic energy production and transfer among the crosswise fluctuating velocity components, meaning that the flow is shearless (transverse gradients are zero) [31]. Therefore, the ratio w_{rms}/v_{rms} constitutes a measure of the homogeneity degree and a value ideally equal to the unity is expected for homogeneous flows, however value of about 1.2 is found in literature [31]. From the definition, the global isotropy ratio, u_{rms}/v_{rms}, should be the

parameter that defines the change from anisotropic to isotropic flow. Typical values in the range of 1.2-1.4 are found in literature for isotropic flows [32]. Moreover, if the turbulent flow is nearly homogeneous and isotropic then the probability density function should be approximately Gaussian [31], and the PDFs should collapse for different positions in the flows. Therefore, a deviation from a normal probability density function (analysed by means the third and fourth high-order statistics) may be thought as a deviation from the equilibrium itself and thus, the turbulent flow should not be considered neither homogeneous nor isotropic.

Turbulence intensity and length/time scales

Turbulence spectrum is used to characterize turbulence, describing how and how much energy is distributed among eddies of different sizes. On one side is defined the turbulence intensity to quantify how much energy is present in the turbulence and on the other side is defined the length and time scales to quantify the size and frequency of the energy-containing eddies. By measuring at different downstream position from the jet grid both intensity and length/time scales, the turbulence decay can be estimate. To define the level of turbulence in the flow is used:

$$Tu = \frac{\sqrt{\frac{2}{3}k_t}}{U} \tag{14}$$

where the turbulence kinetic energy is defined as: $k_t = \frac{1}{2}(u^2_{rms}+v^2_{rms}+w^2_{rms})$ and U the flow mean velocity. In the case of isotropic flow, turbulence fluctuations have the same intensity in all directions, $k_t = \frac{3}{2}u^2_{rms}$, consequently:

$$Tu = \frac{u_{rms}}{U} \tag{15}$$

To understand the process of energy production and dissipation that occurs in turbulent flow fields must be characterized from the largest (integral) to smallest (Kolmogorov) turbulence scales. The largest eddies are influenced by the geometry and the boundary conditions and they are responsible for the energy transport and mixing. On the contrary, the smallest scales are only influenced by local properties, such as the viscosity and the rate at which the turbulent kinetic energy (TKE) is transported and dissipated in internal energy. Roughly speaking, the integral length scale is used to define the size of the largest eddies in the turbulent flow field. This characteristic length is related to the space correlation coefficient as:

$$L_{ij} = \int_0^\infty R^S_{ij}(\mathbf{r}, t)dr \tag{16}$$

The integral time scale can be computed in the same way by using the time correlation coefficient as:

$$T_{ij} = \int_0^\infty R^T_{ij}(\mathbf{x}, t)dt \tag{17}$$

Considering the most practical methods to compute these quantities:

1. Spatial correlation function can be achieved by using probes array in the flow field. However, the Taylor's hypothesis of frozen turbulence makes possible the relation between the correlation in time and space through a displacement velocity. Then, by measuring with an hot-wire anemometer a velocity component at just one spatial point, the integral length scale is computed multiple the integral time scale by the mean velocity of the flow field: $L_{ij} = U\int_0^\infty R^T_{ij}(\mathbf{x}, t)dt$.
2. The power spectrum obtained from an hot-wire anemometer can be used to extrapolate the value of the power spectrum at zero frequency that results proportional to the integral time scale, $E_{ii}(0) = (u'_i u'_i)/\pi T_{ii}$, and experimentally to the integral length scale, $\Lambda = \left[\frac{E(f)U}{4\overline{u^2}}\right]_{f\to 0}$.

However, one must be careful measuring the integral time and length scales with each of these methods because of their pitfalls. The first method, that makes use of the Taylor's hypothesis and is based on the autocorrelation function, suffers from wide oscillation due to the nature of turbulence. It is clear that, when it is computed a numerical integration of the time correlation, where the autocorrelation function presents negative undershoots around zero, the integration yields to a numerical cancellation and to an erroneous estimation of the time scale and consequently of the integral length scale. Furthermore, while equation to compute the time scales involves the determination of the integral over an infinite domain, the domain of the autocorrelation function from experimental or numerical data is finite, and there is some uncertainty on how best to define the integration domain. However, there are different methodologies presented in literature [33] to compute time scales from the autocorrelation function by using numerical integration: (A) use as the upper limit of the integration the first zero crossing or the first negative minimum of the autocorrelation function, (B) integrate a fit of

the autocorrelation function, (C) integrate the autocorrelation function up to the time when the function reaches the value e^{-1}. The second method is an alternative to compute the turbulence length scale based on the power spectral density function. In theory, methods 1 and 2 are equivalent since the autocorrelation is the transform of the turbulence spectrum. Therefore, the integration and converge problem for the autocorrelation function now is substituted by the form of inaccuracies when dealing with low frequency to compute the spectrum [33]. Typically, the spectrum is extrapolated back to zero frequency by using frequencies above those, corresponding to scales that are physically possible in experiments. Generally, the energy associated to the lower frequency is almost constant and an average of the first frequencies is lead to a reliable estimation of $E(0)$ [34]. Concluding, Lewalle and Ashpis [35] report that the results from methods 1 and 2 are in good agreement, computing around 10% (for the longitudinal integral length scale) to 20% (for the lateral integral length scale) discrepancy. This discrepancy is accounted for by incomplete convergence in the tail of the autocorrelation function and in the low-frequency portion of the turbulence spectrum.

Jet Injection (jet velocity and uniformity)

The air passing through the jet holes can be treated as simple turbulent round free jets since the jet flows into a large space (compared to holes area) being most likely turbulent, carries no additional thermochemical effects (such as density variation, heat release ...) and operates with a simple round nozzle. Measurement of the velocity field at the outlet of the jet holes can be used to provide information useful for the computation of the jet injection and uniformity. Although the hot-wire anemometry technique provides information only at several points, can be used to provide continuous signals of local velocity information as well as information on turbulence properties.

Grid Pressure Loss

The introduction of the jet grid in the main flow field will cause a pressure drop as a function of the design and of the jet injection. Since the pressure drop is defined as the difference in total pressure between two points of a fluid carrying network, the measurement will be done both upstream and downstream of the jet grid, as reported by Nix [27]. On the other hand, Gad-el-Hak and Corrsin [22] characterized the mean drop in static pressure across the grid by experimentally measuring the static pressure at the sidewall both upstream and downstream of the grid. A good pressure distribution (along and among different jet grid bars) is also important to return a good flow uniformity in the channel. Then, by measuring the pressure distribution at different jet holes, in tandem with and jet flow velocity, an estimation of the flow uniformity can be done.

Based on what reported, the test section is instrumented to measure the wind tunnel operating conditions, the jet grid upstream flow, the endwall static pressure distributions, the jet grid downstream flow, the total pressure loss and turbulent flow structures. The instrumentation used for the jet grid characterization are the following:

- Triple hot-wire anemometer. Triple sensor hot-wire from Dantec Dynamics (tungsten wires with diameter of 9 μm and dynamic response of abouth 15 kHz) is traversed in stream- and cross-wise directions at different position both upstream and downstream of the grid. Velocity data from the hot-wire serve to locally characterize: the background turbulence of the wind tunnel, the jet injection and uniformity and, energy spectra and features of turbulence (decay, intensity, length scales, and homogeneity and the isotropy degree),

- Time-resolved particle image velocimeter. Hot-wire measurements are complemented by time-resolved optical PIV measurements in 2D streamwise planes at different downstream distances from the grid to characterize the velocity field and turbulent structures. Two point-correlation PIV and hot-wire measurements is used also to very that Taylor's hypothesis is valid for high turbulence levels.

- Aerodynamic pressure probe. Pitot probe is traversed in crosswise directions to monitor the total and static pressure at both upstream (various axial location from the contraction) and downstream (different planes) section of the jet grid,

- Wall pressure taps. A row of 5 pneumatic taps are positioned upstream and downstream of the grid to monitor the wall static pressure.

As a first step, tests of the wind tunnel performance without the jet grid is performed with the purpose to return a reference value for: background turbulence, mean velocity, total and static pressure. Then, tests are

performed with the jet grid both at the plane of the grid (characterizing the flow uniformity, pressure distribution, jet injection and flow patterns around bars) and downstream (characterizing the turbulent flow fields and the grid pressure drop). The measurement matrix is summarized in Table 3 together with the measurement planes. X indicates the axial location where 0 is the end of the contraction and 130 the end of the test section, S the streamwise plane and C the crosswise planes (y and z directions).

	Plane	***Probe***	Measurement Matrix
W/O Jet grid	Upstream	Triple hot-wire	X= 0 - 10 (Pitch 2cm) S= Centerline
		Pitot probe	X= 5 $C_{y,z}$= 0 - 20 (Pitch 2cm)
		Pressure taps	X=3
W/ Jet grid	Jet grid	PIV	X=10 S= Centerline 2D Planar
		Triple hot-wire	X=10 (in front of jet holes) $C_{y,z}$= 0 - 20 (Pitch 0.5cm)
		Pitot probe	X=10 (in front of jet holes) $C_{y,z}$= 0 - 20 (Pitch 1cm)
		Pressure taps	X= end of the bar
	Downstream	PIV	X=15, 25, 25 S= 2D Planar
		Triple hot-wire	X=20 - 130 S= Pitch x/d=10 $C_{y,z}$= 0 - 20 (Pitch 0.5cm)
		Pitot probe	X=20, 30 $C_{y,z}$= 0 - 20 (Pitch 1cm)
		Pressure taps	X=17

Table 3: Summary of the measurement matrix.

Test matrix

There are three jet grid designs to be characterized and for each of these all the configurations are analysed, namely: passive, active in simultaneous upstream and downstream directions and, active with separated directions at a time. The influence of the injection ratio is tested by varying it between 1.1 – 5 bar.

5. Conclusions

Literature survey highlights the evident need to improve the fundamental understanding of the physics behind the role of turbulence scales on the aerodynamics of bladed-passage flows, so as to better quantify the turbulence effects on the loss generating mechanisms and to align the accuracy of turbulence-modeled simulations with the experiments. A review of the state-of-the-art in turbulence generation has identified several techniques to produce a wide range of turbulence levels, however, only a concept provides the chance for the independent control of turbulence scales: the turbulence jet grid. An extensive analysis of the main jet grid studies return three possible methods allowing to vary the length scales independently from the turbulence intensity as a result of: (1) different injection direction for different turbulence decay, (2) adjusting the injection ratio for different grid positions, (3) continuously variation of the injection ratio with a fixed grid position. In this work, turbulence jet grids capable of ranging from low to high turbulence levels (1-15%) with minimum pressure losses and a low degree of non-uniformity (5%) was successfully designed for a low-speed wind tunnel having a small cross-sectional area. A key feature for the development of this turbulence generator was that the independent control of the integral length scales within the range of 3.5 – 15 mm. The jet grid designs used a horizontal-parallel array of active elements in which non-choked or choked jets are injected in both upstream and downstream directions. Together with the description of the design and scaling parameters, a detailed picture of the future experimental campaign aimed to validate the jet grid designs were documented. The design of the experiment described in detail the experimental facility and the instrumentation used, the measurement techniques, planes and matrix employed and, finally the test matrix planned.

Acknowledgments

This work was sponsored by the von Karman Institute for Fluid Dynamics, monitored by Prof. Sergio Lavagnoli. I would like to thank Prof. Koen Hillewaert at University of Liege for his help and insight into developing the turbulence generator. I would to thank also Prof. Fabrizio Fontaneto, who sponsored the purchase of the instrumentation.

References

[1] Ames, F. E., The Influence of Large-Scale High-Intensity Turbulence on Vane Heat Transfer, ASME Journal of Turbomachinery 119 (1) (1997) 23 – 30.

[2] Carullo, J. S. and Nasir, S. and Cress, R. D. and Ng, W. F. and Thole, K. A. and Zhang, L. J. and Moon, H. K., The Effects of Freestream Turbulence, Turbulence Length Scale, and Exit Reynolds Number on Turbine Blade Heat Transfer in a Transonic Cascade, ASME Journal of Turbomachinery 133 (1) (2011) .

[3] Wang, H. P. and Goldstein, R. J. and Olson, S. J., Effect of High Free-Stream Turbulence With Large Length Scale on Blade Heat/Mass Transfer, ASME Journal of Turbomachinery 121 (2) (1999) 217 – 224.

[4] Butler, R. J. and Byerley, A. R. and Van Treuren, K. and Baughn, J. W., The Effect of Turbulence Intensity and Length Scale on Low-Pressure Turbine Blade Aerodynamics, International Journal of Heat and Fluid Flow 22 (1) (2001) 123 – 133.

[5] Mahallati, A. and Sjolander, S. A., Aerodynamics of a Low-Pressure Turbine Airfoil at Low Reynolds Numbers—Part II: Blade-Wake Interaction, ASME Journal of Turbomachinery 135 (1) (2013) .

[6] Mahallati, A. and McAuliffe, B. R. and Sjolander, S. A. and Praisner, T. J., Aerodynamics of a Low-Pressure Turbine Airfoil at Low Reynolds Numbers—Part I: Steady Flow Measurements, ASME Journal of Turbomachinery 135 (1) (2013) .

[7] Brandt, L. and Schlatter, P. and Henningson, D. S., Transition in Boundary Layer Subject to Free-Stream Turbulence, Journal of Fluid Mechanics 517 (1) (2004) 167 – 198.

[8] Thole, K. A. and Bogard, D. G. and Whan-Tong, J. L., Generating High Freestream Turbulence Levels, Experiments in Fluid 17 (1) (1994) 375 – 380.

[9] Folk, M. and Miller, R. J. and Coull, J. D., The impact of Combustor Turbulence on Turbine Loss Mechanisms, ASME Journal of Turbomachinery 142 (1) (2019) .

[10] Gakhara, K., Effect of Free-Stream Turbulence on Boundary Layer Loss Generation, Ph.D. thesis, Massachusetts Institute of Technology (2020).

[11] R. Pichler, R. D. Sandberg, G. Laskowski, V. Michelassi, High-fidelity simulations of a linear HPT cascade vane subject to varying inlet turbulence, in: ASME Turbo Expo, 2017.

[12] Zhao, Y. and Sandberg, R. D. , By-pass Transition in Boundary Layer Subject to Strong Pressure Gradient and Curvature Effects, Journal of Fluid Mechanics 888 (1) (2020) .

[13] Tucker, P. G., Trends in Turbomachinery Turbulence Treatments, Progress in Aerospace Science 63 (1) (2013) 1 – 32.

[14] Dick, E. and Kubacki, S., Transition Models for Turbomachinery Boundary Layer Flows: A Review, International Journal of Turbomachinery Propulsion and Power 2 (2).

[15] Tyacke, J. and Vadlamani, N. R. and Trojak, W. and Watson, R. and Ma, Y. and Tucker, P. G., Turbomachinery Simulation Challenges and the Future, Progress in Aerospace Science 110 (1) (2010) .

[16] J. Babajee, T. Arts, Investigation of the laminar separation-induced transition with the $\gamma - re_\theta$ transition model on low pressure turbine rotor blades at steady conditions, in: ASME Turbo Expo, 2012.

[17] C. Bode, T. Aufderheide, D. Kozulovic, J. Friedrichs, The effects of turbulence length scale on turbulence and transition prediction in turbomachinery flows, in: ASME Turbo Expo, 2014.

[18] Roach, P. E., The Generation of Nearly Isotropic Turbulence by Means of Grids, International Journal of Heat and Fluid Flow 8 (1) (1986) 82 – 92.

[19] Maciejewki, P. K. and Moffat, R. J., Heat Transfer with Very Hugh Free-stream Turbulence: part II - Analysis of Results, ASME Journal of Heat Transfer 114 (1) (1992) 834 – 839.

[20] J. E. Kingery, F. E. Ames, Stagnation region heat transfer augmentation at very high turbulence levels, in: ASME Turbo Expo, 2015.

[21] Makita, H., Realization of a Large-Scale Turbulence Field in a Small Wind Tunnel, Fluid Dynamics Research 8 (1) (1991) 53 – 64.

[22] Gad-el-Hak, M. and Corrsin, S., Measurements of the Nearly Isotropic Turbulence Behind a Uniform Jet Grid, Journal of Fluid Mechanics 62 (1) (1974) 115 – 143.

[23] J. E. O'Brien, G. J. Van Fossen, The influence of jet-grid turbulence on heat transfer from the stagnation region of a cylinder in crossflow, NASA-TM 87011, NASA (1985).

[24] Young, C. D. and Han, J. C. and Huang, v and Rivir, R. B., Influence of Jet-Grid Turbulence on Flat Plate Turbulent Boundary Layer Flow and Heat Transfer, Journal of Heat Transfer 114 (1) (1974) 65 – 72.

[25] B. A. Bangert, A. Kohli, J. H. Sauer, , K. A. Thole, High freestream turbulence simulation in a scaled-up turbine vane passage, in: ASME Turbo Expo, 1997.

[26] R. J. Boyle, B. L. Lucci, V. G. Verhoff, W. P. Camperchioli, H. La, Aerodynamics of a transitioning turbine stator over a range of reynolds numbers, in: ASME Turbo Expo, 1998.

[27] A. C. Nix, A. C. Smith, T. E. Diller, W. F. Ng, K. A. Thole, High intensity, large length-scale freestream turbulence generation in a transonic turbine cascade, in: ASME Turbo Expo, 2002.

[28] T. Aufderheide, C. Bode, J. Friedrichs, D. Kozulovic, The generation of higher levels of turbulence in a low-speed cascade wind tunnel by pressurized tubes, in: 11th World Congress on COmputational Mechanics, 2014.

[29] J. H. Lienhard, Synopsis of Lift, Drag, and Vortex Frequency Data for Rigid Circular Cylinders, Technical Extension Service 300, Washington State University Pullman (1966).

[30] J. O. Hinze, Turbulence, McGraw-Hill Book Company (1975) 488.

[31] Hearst, R. J., Fractal, Classical, and Active Grid Turbulence: From Production to Decay., Ph.D. thesis, University of Toronto (2015).

[32] Compte-Bellot, G. and Corrsin, S., The Use of a Contraction to Improve the Isotropy of Grid-Generated Turbulence, Journal of Fluid Mechanics 25 (4) (1966) 657 – 682.

[33] Van Fossen, G. J. and Simoneau, R. J. and and Ching, C. Y., Influence of Turbulence Parameters, Reynolds Number, and Body Shape on Stagnation-Region Heat Transfer, Journal of Heat Transfer 117 (3) (1995) 597 – 603.

[34] L. El-Gabry, D. Thurman, , P. E. Poinsatte, Procedure for Determining Turbulence Length Scales Using Hotwire Anemometry, NASA-TM 218403, NASA (2014).

[35] J. Lewalle, D. E. Ashpis, Estimation of Time Scales in Unsteady Flows in a Turbomachinery Rig., NASA-TM 209452, NASA (2004).

Modeling and exploitation of aerothermal probes in helicopter engines

Adrien Vasseur

Aeronautics and Aerospace Department, von Karman Institute for Fluid Dynamics, Belgium and Département Aéronautique et Propulsion, ISAE-SUPAERO, France, adrienvasseur@isae-supaero.fr

Supervisor: Fabrizio Fontaneto

Associate Professor Turbomachinery and Propulsion Department, von Karman Institute for Fluid Dynamics, Belgium, fabrizio.fontaneto@vki.ac.be

University Supervisor: Nicolas Binder

Professor, Head of Turbomachinery and propulsion research group, DAEP, ISAE-SUPAERO, France, nicolas.binder@isae.fr

Industrial Supervisor: Jean-Louis Champion

BEARCAT Project manager, SAFRAN Tech, France, jean-louis.champion@safrangroup.com

Abstract

The flow after the second HP turbine stage of SAFRAN's BEARCAT test engine will take the aerothermal probes far away from their calibration conditions. The relative size of the probe will have a big impact on the flow. These error sources will be investigated numerically and experimentally in this PhD. Hysteresis was shown to not appear in the available conditions.

Keywords: Five hole probes, pressure probes, measure, corrections, turbulence, shear, errors, metrology

1. Introduction

This PhD was launched in support of the creation of the BEARCAT test bench of SAFRAN Tech. It is a heavily-instrumented helicopter engine [1]. Its aim is to provide numerical models with experimental data, to feed and check them. Original measurements will be performed in the combustion chamber and the high pressure turbine region [1]. One of the probes chosen to that extent is a five-hole aerothermal pressure probe.

Five-hole pressure probes are robust probes that give an indirect measure of the flow direction and the Mach number. Adding a temperature reading allows to also get the velocity. As the relationship between flow direction, Mach number and the pressure at the and of each hole is very complex, those probes need to be calibrated. It is usually done in an open jet. The pressures of the five holes are measured at a range of flow conditions and probe orientations. The data is then used, directly or through models, to interpret the set of pressures given by the probe in the unknown flow. The SAFRAN probe studied in this work is depicted in Figure 2.

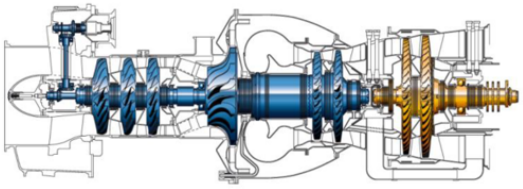

FIGURE 1: CROSS SECTIONAL VIEW OF A MAKILA 2A1 ENGINE

Figure 1: BEARCAT is based on the Makila 2 engine [1]

The use of this probe poses several challenges : it has a significant size in the engine vein, which changes the studied flow, and the flow is very different from the calibration flow which makes the pressure readings harder to interpret correctly.

Figure 3 illustrates several problems encountered:

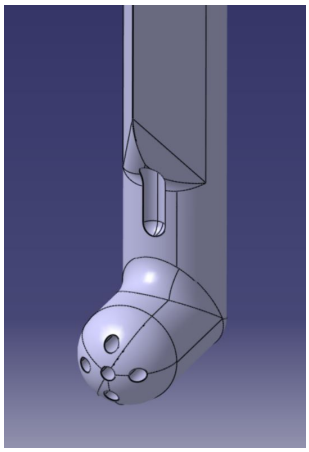

Figure 2: 3D modelling of the probe designed for the BEARCAT project. Above the head is a thermocouple sleeve.

the vein is less than four centimeters high, when the probe has a head diameter of four millimeters. The axial velocity shows strong gradients.

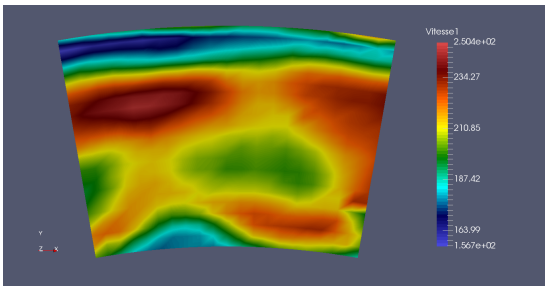

Figure 3: Mean axial velocity field (m/s) at the exit of the second high pressure turbine for 300kW idle engine conditions. BEARCAT data provided by J.-L. CHAMPION

The aim of this PhD is to improve the interpretation of five-hole-probes pressure data sets in engine conditions. The strategy is to identify measurement problems possibly encountered in this kind of set-up, compare and rank them in the BEARCAT context and run experiments and simulations to explore these problems in a unified context with the SAFRAN probe. I will also investigate the possibility of using computational fluid dynamics (CFD) to help with the calibration.

This project is a cooperation between SAFRAN and ISAE-SUPAERO in France and the von Karman Institute (VKI) in Belgium. The experimental campaign will be carried out in VKI and the rest will happen in ISAE-SUPAERO.

2. Bibliographic search

As the specific geometry used by SAFRAN and the flow conditions of interest in this work are hard to find in articles, the bibliographic search as extended to a wide variety of probe shapes, hole numbers and flow conditions. The flow in BEARCAT after the second stage of high pressure turbines can reach Mach 0.6, 1400K and strong turbulence levels. The error sources in the scope of this thesis can be divided in two categories : geometry-related and flow phenomena-related.

2.1. Geometry-related problems

The probe might be of significant size compared to the engine vein it is in. The probe then measures a flow that has been modified by its presence. At the exit of the second high pressure turbine, the probe is as big compared to the vein as a pen is to a post stamp.

The holes of the probe are at a finite distance of each other. When the flow displays strong gradients or the size if the probe is significant compared to the characteristic size of the studied flow, the assumption that the measurement is made on a point becomes wrong. The position of each hole needs to be accounted for [2] [3].

When the probe is closer than three diameters to a wall, a blockage effect occurs that bends the streamlines away from the wall [4]. The probe then measures the flow closer to the wall than its absolute position. Bailey [4] proposes a correction that accounts for this displacement.

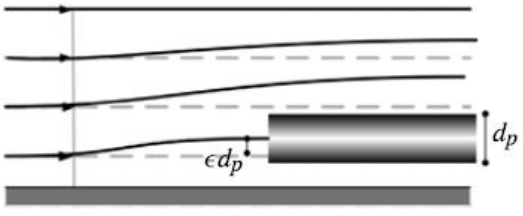

Figure 4: Wall proximity effect. Extracted from [4]

2.2. Flow phenomena-related problems

Crowley [5] in 2013 found a strong hysteresis in the calibration of a five-hole probe. When the probe had a 20° yaw angle, increasing or decreasing velocities

triggered hysteresis in one of the calibration factors. However, the hysteresis disappeared when turbulence intensity reached 1%. The hysteresis in one of the calibration coefficients is reported to reach 30%. The reason is an hysteresis in the behaviour of the recirculation bubble on the probe head [5]. This recirculation can also be responsible of a 5° error in angle measurement and 6% in dynamic pressure if the probe was calibrated in conditions where there was no recirculation bubble according do Dominy [6].

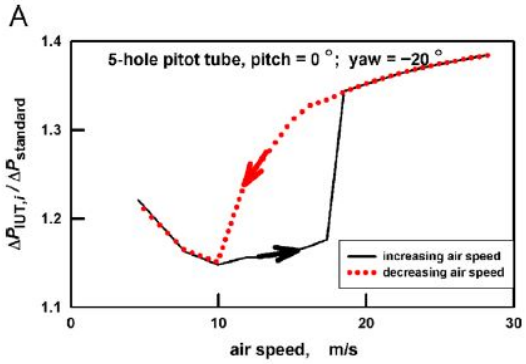

Figure 5: Crowley [5] highlights that the difference between center hole and off-axis holes can display hysteresis

The long tubes in the five-hole probe cause the pressure signal to be the time-averaged value of the pressure at the holes. As the dynamic pressure is a quadratic function of the velocity, turbulence has a increasing effect on the pressure readings. Bailey [4] offers a formula to predict the overestimation of the velocity caused by the turbulence. According to this formula, the error on the velocity is for example 5% for 30% Tu and 0.5% for 10% Tu. Experimental data from the DGEN test bench at ISAE were analysed in this scope. DGEN is a very light turbofan engine produced by Price Induction. The maximum possible overestimation of the velocity due to turbulence in those data was 0.5%. The data is from a little upstream of the fan which makes the turbulence very low.

Turbulence can also affect the measured angle according to Sitaram [3]. A calculation made from his formulas indicates a 0.66% error on pitch angle for 10% Tu. Christiansen [7] reports that turbulence is not a problem for low angles, under 15° in his case. He advises to use the probe in the nulling mode (i.e. the probe is rotated until lateral pressure are the same which makes the angle of the probe the angle reading). Christiansen also reports that the effects of turbulence are worse when the instantaneous velocity direction is out of the linear range of the probe [7].

When in a sheared flow, the probes are subject to a displacement effect. The stagnation line is bent the presence of the probe [4]. The probe at location y_0 is actually measuring the flow at the location $y_0 + \Delta y$, where Δy depends on the shear and the probe geometry [4] [8] and the dimension (2D or 3D) [9]. The shear also is responsible of a change in the measured flow angle [8]. The stagnation streamline arrives on the probe with a non-zero angle and the lateral holes are subject to different flows. Several authors like Hall [9] offer formulas to correct the location of the measured velocity, the angle [8], or the velocity at the measurement location [10]. The problem is illustrated in Figure 6.

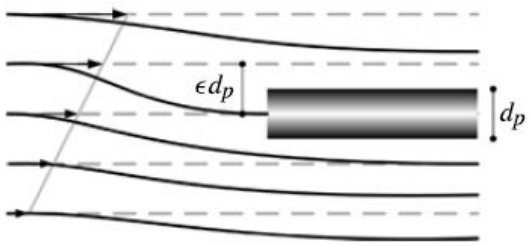

Figure 6: Illustration of the displacement effect. Extracted from [4]

Around unity Mach number the pressure distribution on the probe doesn't change much with the Mach number [11]. It leads to an insensitivity to Mach number changes. This problem can me mitigated by adding a static pressure hole downstream the head for the cobra probe [11]. The uncertainty in Mach number measurement is increased by a factor of five for the five hole probes that Boerned studied [12].

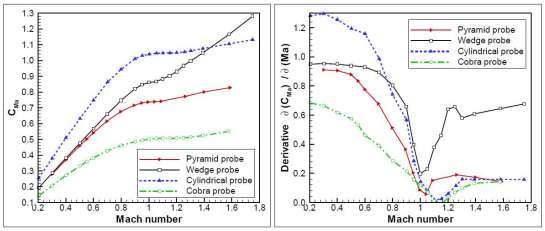

Figure 7: Transsonic insensitivity to the Mach number for different probe geometries. Extracted from [11]

Sitaram [13] reports that the angle measurement is affected by the Mach number. A four hole probe calibrated at a 0.4 Mach number shows a 2.2° standard

error in the measurement of the yaw angle between ±20°. Sitaram doesn't specify wether the Reynolds number has been kept constant between throughout the tests so those errors might also be caused by changes in the Reynolds number.

Reynolds number affects the behaviour of the separation, so it has an importance in the recirculation bubble problems mentioned earlier. In a study of various five hole probe geometries, Dominy [6] noted that for Reynolds numbers higher that 50 000 the yaw coefficient becomes insensitive to yaw between 0 and 4°. Dynamic pressure measurements can display up to a 20% error when the measurement Reynolds number is lower than the calibration Reynolds number [6].

The vortex shedding on the trailing edge of the probe cause pressure fluctuation in the probe holes because of the upstream transmission of pressure information. Liu [14] performed 2D simulations of short oval and trapezoidal probes (see Figure 8) for several Mach number and incidence. He reports that at Mach 0.3 and no incidence, the pressure fluctuation amplitude is between 20 and 25% of the dynamic pressure for both geometries on point *e* and almost zero on *a*. When the probe is at a -12° incidence, it reaches 10% for the oval probe and 5% for the trapezoidal probe. Liu doesn't discuss how the measurements would be affected by this.

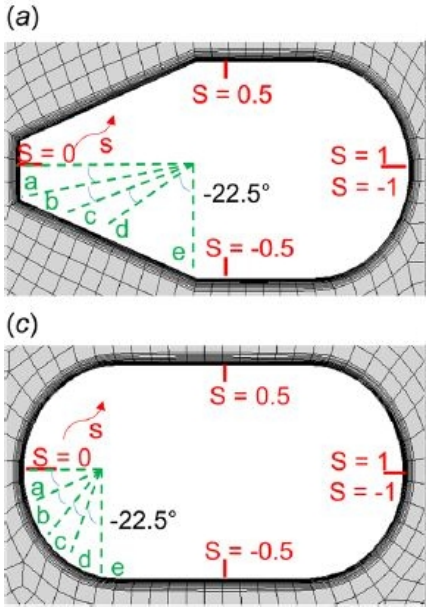

Figure 8: Locations (*a* to *e*) of the pressure signals studied by Liu. Extracted from [14]

Comparable results are to be found in an article by Boufidi [15] that is dealing with a probe with a larger aspect ratio (see Figure 9). She reports that the maximum amplitude of pressure fluctuation in the probe holes is 0.25% of the dynamic pressure. The significant difference between the two articles is probably a consequence of the difference in aspect ratios.

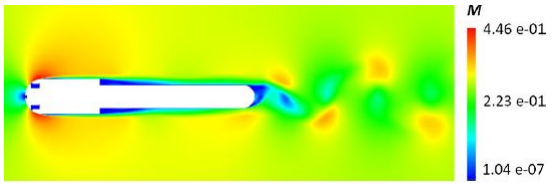

Figure 9: Mach number contour around the probe studied by Boufidi. Extracted from [15]

Ranking the errors in the BEARCAT context is complex, because those errors are often geometry-dependant, interdependant and assessed in flow conditions different from the ones sought. The CFD and experimental work will then also be aimed at understanding in what extent the results found in the bibliographic search are applicable to the SAFRAN probe in BEARCAT.

3. Numerical work

Simulations were first performed on simplified geometries to help with the learning of the CFD tools, and then the 3D SAFRAN probe geometry started to be used.

FineOpen was selected as the CFD software for this thesis, after encountering troubles with elsA and the structured version of Fine. It is a Numeca software that accomodates easily the complex geometry of the probe tanks to hybrid meshes, like the one depicted in Figure 10. The holes are very small and have a sharp inlet, that require a big number of cells.

From 2D simulations ran on different hole geometries and hole boundary conditions, it was observed that they need to have a large aspect ratio and non-slip boundary conditions. In Figure 11, the circulation reaches the end of the shorter hole in slip conditions whereas viscous walls keep high velocities at the entrance of the hole.

3D simulations were performed on the geometry depicted in Figure 2 to simulate a calibration of the probe. The domain shown in was extending 30 diameters from the probe in all direction.

RANS and URANS simulations were run and helped build a inexhaustive calibration map at Mach

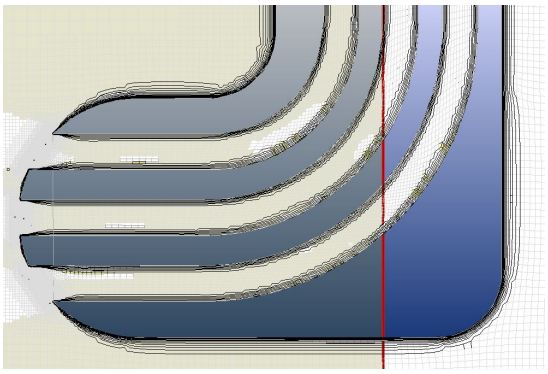

Figure 10: Section of the 3D mesh around the SAFRAN geometry. There are 21 million cells in the whole domain. This mesh was used to compute the calibration coefficients displayed in Figure 13

0.3. At strong incidence, the change of the turbulence model from Spalart-Almaras to $k\omega - SST$ in RANS can change the results by the equivalent of a 0.25° change in the incidence. URANS results at 10° of pitch and yaw are very close to RANS results : the difference in calibration coefficients is equivalent to a negligible 0.04° change in the probe incidence. URANS simulations are thus unnecessary for low incidence simulations. The comparison has yet to be made for high pitch and yaw. The corners of the calibration map stretch as in all the calibration maps found in the literature.

From 3D simulations run with elsA on a simple cylinder in a channel, it was observed that the wake of the cylinder can be asymmetrical when the probe is as far as 10 diameters from a wall. The rule of thumb found in literature about the effects of wall proximity was that it appeared from 3 diameters distance to the wall. This shows that the shape of the flow isn't sufficient to investigate the wall proximity effect, we should also derive the changes in the calibration coefficients caused by that asymmetry.

A. Bilbault, an engineering student of ISAE-SUPAERO, has conducted a numerical study of the effects of the insertion of the SAFRAN probe in a shear flow. He has compared literature formulas for the displacement effect with the displacement of the stagnation streamline observed for the SAFRAN geometry in various shear conditions. One of his findings was that the mast caused a mast-wise displacement of the stagnation streamline up to 0.27 diameters for no shear and shear, whereas the maximum observed shear-wise displacement was 0.11 diameters. A. Bilbault suggested a revised shear effect correction

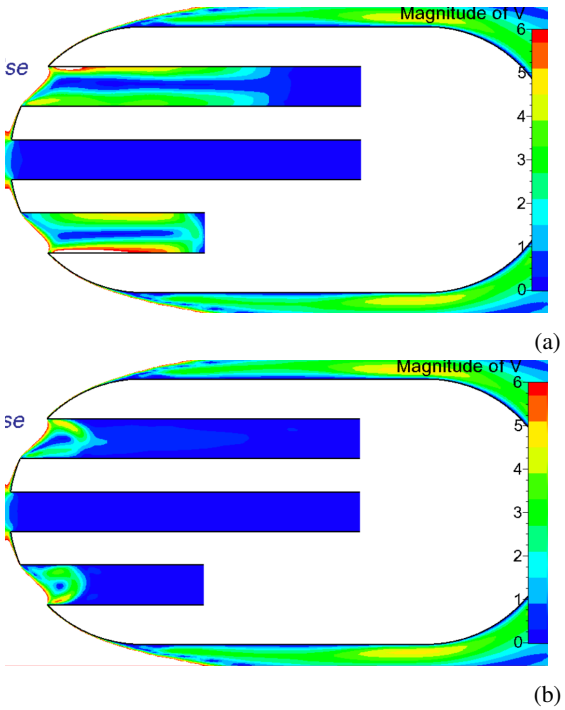

Figure 11: Comparison of $|\vec{V}|$ for slip walls (a) and viscous walls (b)

formula, that includes the mast-wise displacement.

4. Experimental work

The experiments will try to investigate the error sources in simple configurations, independently when possible.

The SAFRAN probe design (L shaped hemispheric head, shown in Figure 2) was simplified for manufacturing purposes. Three heads with diameters of 4mm, 8mm and 16mm were 3D printed, mounted on cylinders and painted black to reduce PIV reflections. All the steps were done in VKI. The different sizes will help change blockage and Reynolds number without changing the Mach number, or keep the same Reynolds number while changing the Mach number.

The probes heads turned out to not be perfectly aligned with the masts, from 1° to 1.3° depending on the probe. The reason is a change in the printed shape during the polymerisation of the resin. This would be very hard to correct thus the angles were measured to incorporate it in the post-processing.

The capability of two different paints to reduce the laser reflections or the brightness of the probes were compared : BLK3.0 and Spectrum black mat spray

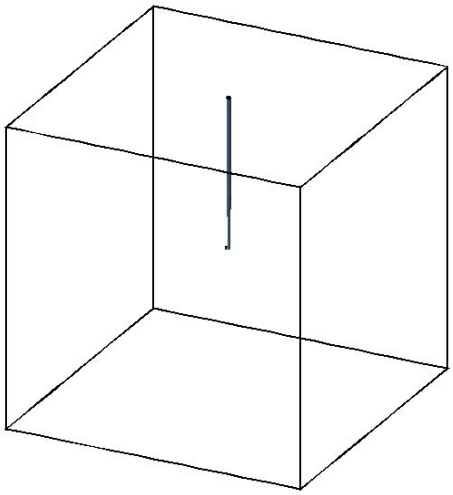

Figure 12: Domain of the calibration simulations

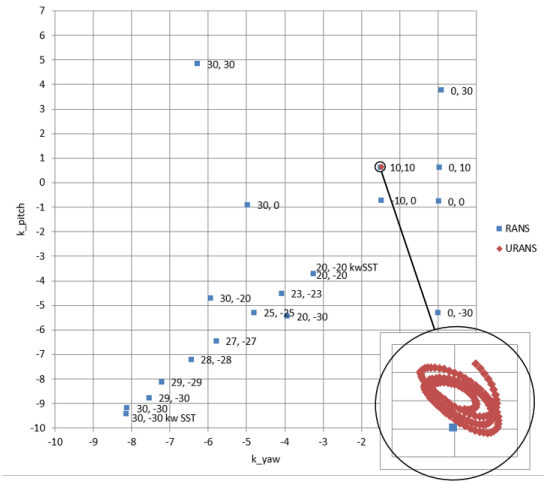

Figure 13: Comparison between RANS calibration coefficients and URANS for 10° of pitch and yaw

paint. Their maximum brightness under the laser light were the same, but the bright zone was smaller for the Spectrum paint. In addition, the BLK3.0 did not resist when the probe was cleaned from PIV seeding oil.

The facility chosen for the experimental campaign is the L12 wind tunnel. It is a very flexible, easy to operate, low mach, ambient temperature and non-pressurized wind tunnel displayed in Figure 18. It is PIV-ready. A new Plexiglas test section was drawn to perform this project's tests. This wind tunnel can produce flow velocities up to 17m/s in the standard $0.04m^2$ test section. The test section is 1m long. The settling chamber is equipped with a total pressure probe. Three Validyne relative pressure sensors measure the total pressure in the settling chamber, the pressure from one probe hole and from one static pressure tap compared to ambient pressure.

A middle plate, obstacles, a turbulent grid and a low section sub-vein can be mounted in the test section. The five hole probe can be inserted just before the exit of the test section to use the developed boundary layers, or just after the converging section to avoid thick boundary layers.

Here is the list of the programmed tests :

- Turbulence effects : a 3D printed grid will produce Tu up to 6.4% ;
- Wall proximity effect : the probe wil interact with a wall mounted in the middle of the test section ;
- Upwind obstacles ;

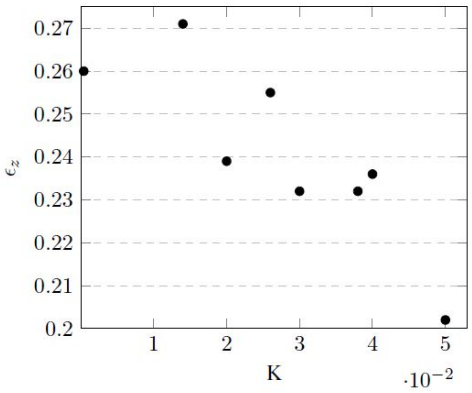

Figure 14: Displacement due to the mast of the probe in [16] as a function of the shear.

- Blockage : the three probe sizes and the small-section sub-vein will help reach a wide range of blockage ;
- Velocity- and angle-related hysteresis ;
- Shear : the probes will be immersed in a boundary layer ;
- Reynolds and Mach number effects ;
- Separation on the head.

The results of the tests will be compared with the results found during the bibliographical search and later to the numerical campaign.

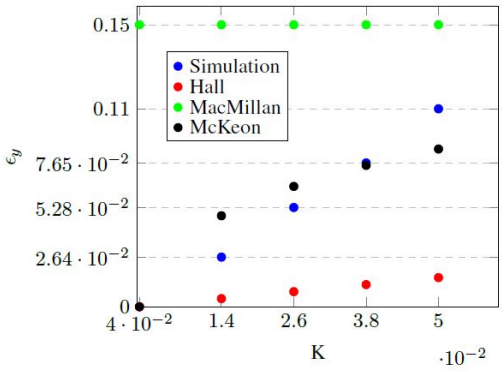

Figure 15: Displacement due to the interaction of the probe and the shear in [16] as a function of the shear.



Figure 16: The three probes without paint

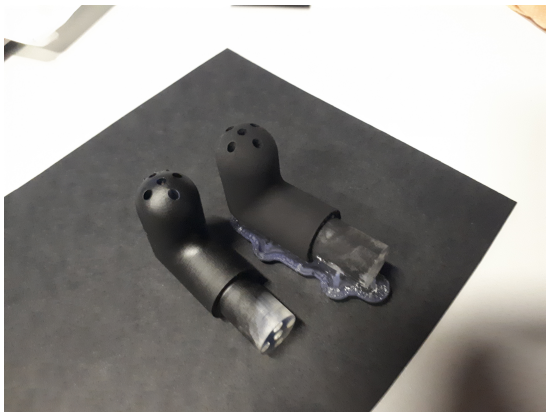

Figure 17: Although the paint from the left appears shinier, it was better suited for the PIV

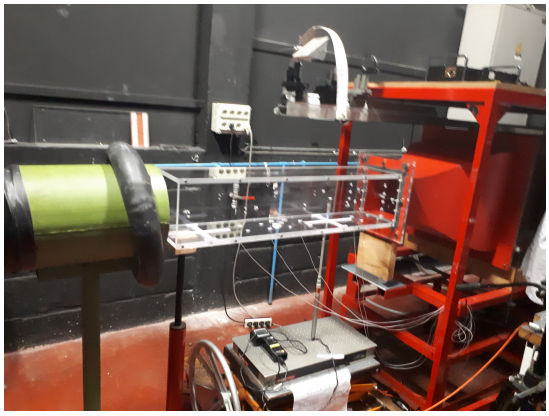

Figure 18: The test section designed for this project mounted on L-12

Tests of the facility were first ran to get familiar with its possibilities and behaviours, to troubleshoot and verify some assumptions about the campaign.

It was found that when the largest probe head, 1.6cm in diameter, is in the center of the test section, which is 10cm away from each wall, rotating it around the mast or around the center of the probe head doesn't change the pressure coefficients. It means the walls are far enough to simplify the tests by not exactly keeping the center of the head in the center of the section. It is consistent with the wall proximity effect threshold of 3 probe diameters mentioned by Bailey [4]. In Figure 19 the yaw pressure coefficient is very similar for each case.

The evolution of the static pressure on the walls was investigated. A simple model of the displacement thickness on a flat plate was used to predict the streamwise evolution of the effective section of the tunnel and predict the static pressure depending of the nature of the boundary layer. Figure 20 shows that the boundary layer at low regime is likely to be laminar, whereas at high regimes it is likely to be fully turbulent.

For the 16m/s case, the velocity is almost 1m/s higher at the end of the test section. PIV will help know the exact velocity around the probe. In experiments without PIV, the ambient pressure will be used as a reference for static pressure.

Special attention to this boundary layer development will have to be paid when using the sub-test section. For low regimes, the boundary layer will fill all the space of this test section and have large effects on the flow.

The hysteresis tests were inspired by the article of Crowley [5]. The largest probe was used to match the

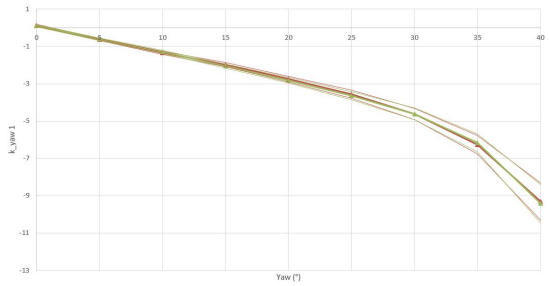

Figure 19: Yaw pressure coefficient for yaw changes made by rotating the probe on its mast axis (blue) or around the center of the head (green). The thin lines are derived from the pressure sensor uncertainties

Reynolds number of 21 000 around mid-velocity of the test section. The velocity was gradually increased to 17m/s, the full power of the facility, and then decreased to zero. The pressure from the left hole and the right hole were regularly measured to plot the yaw pressure coefficient. This was done at a 20° yaw angle, as in [5] and also 40°. A rotation from -60° to 60° of yaw was also performed at 16m/s and 8m/s to check yaw-related hysteresis. As can be seen on Figure 21 there is no evidence of any hysteresis. This is good news for BEARCAT but as this facility doesn't cover the whole range of conditions encountered in BEARCAT, this doens't mean this probe geometry will not be subject at all to hysteresis in the engine. This Figure is to be compared to Figure 5.

5. First conclusions and perspectives

Possible error sources encountered in the BEARCAT test bench were identified. They will be studied with the SAFRAN probe geometry both experimentally and numerically. Although the test facility doesn't produce engine-like conditions, the tests will help understand the phenomena and how they apply to the SAFRAN probe. One experiment has been completed which has shown no sign of hysteresis, and the rest of the experimental campaign is ready to be launched. I will then go back to Toulouse to complete the numerical campaign, process the results and work on the manuscript.

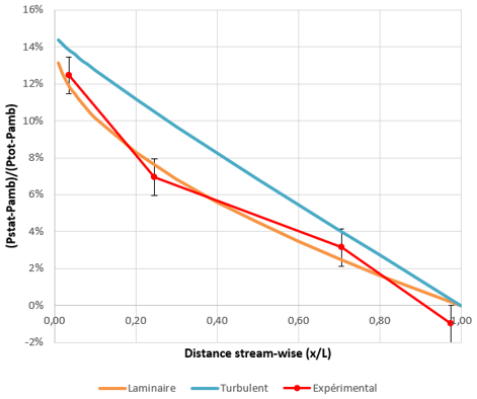

(a)

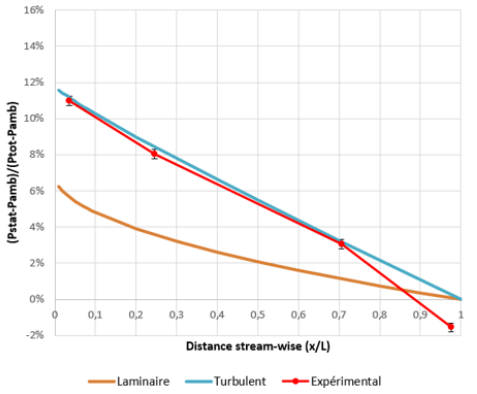

(b)

Figure 20: Evolution of static pressure in the stream-wise direction compared to fully laminar or turbulent boundary layer models, at 4m/s (a) and 16m/s (b)

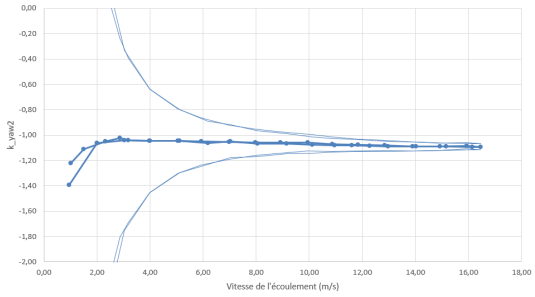

Figure 21: Yaw pressure coefficient for increasing and decreasing velocity. The thin lines are derived from the pressure sensor uncertainties

Acknowledgments

I would like to express my gratitude to SAFRAN and Association nationale de la recherche et de la technologie for the funding of this project and my heartfelt thanks to Nicolas BINDER, Jean-Louis CHAMPION, Fabrizio FONTANETO and Yannick BOUSQUET for the guidance and help.

References

[1] J.-L. Champion, Bearcat: The safran brand new test engine heavily instrumented for accurate comparison with cfd calculations, no. 2020-14295, 2020.

[2] P. Ligrani, B. Singer, L. Baun, Spatial resolution and downwash velocity corrections for multiple-hole pressure probes in complex flows (1989).
URL https://calhoun.nps.edu/handle/10945/40471

[3] N. Sitaram, B. Lakshminarayana, A. Ravindranath, Conventional probes for the relative flow measurement in a turbomachinery rotor blade passage, Journal of Engineering for Power 103 (2) (1981) 406–414. doi:10.1115/1.3230735.

[4] S. C. C. Bailey, M. Hultmark, J. P. Monty, P. H. Alfredsson, M. S. Chong, R. D. Duncan, J. H. M. Fransson, N. Hutchins, I. Marusic, B. J. McKeon, H. M. Nagib, R. Örlü, A. Segalini, A. J. Smits, R. Vinuesa, Obtaining accurate mean velocity measurements in high reynolds number turbulent boundary layers using pitot tubes, Journal of Fluid Mechanics 715 (2013) 642–670. doi:10.1017/jfm.2012.538.

[5] C. Crowley, I. I. Shinder, M. R. Moldover, The effect of turbulence on a multi-hole pitot calibration, Flow Measurement and Instrumentation 33 (2013) 106–109. doi:10.1016/j.flowmeasinst.2013.05.007.

[6] R. G. Dominy, H. P. Hodson, An investigation of factors influencing the calibration of 5-hole probes for 3-d flow measurementsdoi:10.1115/92-GT-216.

[7] T. Christiansen, P. Bradshaw, Effect of turbulence on pressure probes, Journal of Physics E: Scientific Instruments 14 (8) (1981) 992–997. doi:10.1088/0022-3735/14/8/024.

[8] A. Appukuttan, Probe measurement errors caused by shear flows, 2004.

[9] I. M. Hall, The displacement effect of a sphere in a two-dimensional shear flow, Journal of Fluid Mechanics 1 (2) (1956) 142–162. doi:10.1017/S002211205600010X.

[10] K. R. Raju, P. Porey, G. Asawa, Displacement effect in pitot tube measurements in shear flows, Journal of Wind Engineering and Industrial Aerodynamics 66 (2) (1997) 95–105. doi:10.1016/S0167-6105(96)00094-3.

[11] F. Kost, The behaviour of probes in transonic flowfields of turbomachinery, 2009.

[12] M. Boerner, M. Bitter, R. Niehuis, On the challenge of five-hole-probe measurements at high subsonic mach numbers in the wake of transonic turbine cascades, Journal of the Global Power and Propulsion Society 2 (2018) JPRQQM. doi:10.22261/JGPPS.JPRQQM.

[13] N. Sitaram, V. Kumar, V. Pillala, B. Purushothama, B. Prasad, Calibration of multi hole pressure probes for three dimensional flow measurements at high mach numbers, 2015.

[14] Z. Liu, G. Paniagua, Design of directional probes for high-frequency turbine measurements, Journal of Engineering for Gas Turbines and Power 140 (1). doi:10.1115/1.4037640.

[15] E. Boufidi, M. Alati, F. Fontaneto, S. Lavagnoli, Design and testing of a miniaturized five-hole fast response pressure probe with large frequency bandwidth and high angular sensitivity, Journal of Engineering for Gas Turbines and Power 141 (10). doi:10.1115/1.4044660.

[16] A. Bilbault, Obtaining accurate mean velocity measurements on shear flow using five-hole probes, PIR ISAE-SUPAERO.

INSTRUMENTATION AND MEASUREMENT TECHNIQUES

Acoustic attenuation of cohesive sediments (mud) at high ultrasound frequencies

Bart Brouwers

Environmental and Applied Fluid Dynamics Department, von Karman Institute for Fluid Dynamics, Belgium and Flanders Hydraulics Research (FHR), Belgium, Bart.brouwers@mow.vlaanderen.be

Supervisor: Jeroen van Beeck

Professor, Environmental and Applied Fluid Dynamics Department, von Karman Institute for Fluid Dynamics, Belgium, vanbeeck@vki.ac.be

University Supervisor: Evert Lataire

Professor, Department of Civil Engineering, Maritime Technology Division, Ghent University, Belgium, Evert.Lataire@UGent.be

Abstract

Development of ultrasound velocimetry in cohesive sediments (mud), requires knowledge of the acoustic attenuation properties of mud in function of mud density and high ultrasound frequencies (MHz). Conventional experiments using an immersible transducer covering a frequency band of 1 MHz to 5 MHz were therefore conducted. Additional experiments using alternative equipment were also performed to evaluate their reliability.

Keywords: acoustic attenuation, cohesive sediment, mud, high frequency ultrasound

1. Introduction

As the clearance between the keel of a ship and the bottom of a navigation channel greatly influences the controllability of the ship, the passage of large ships trough shallow and confined navigation channels results in specific recommendations for safe navigation. This subject is therefore a specialized discipline in the nautical community. The presence of a mud layer on the bottom of such waters makes the comprehension of the ship's behavior even more challenging. The interactions between ship, water and mud in such situations therefore have been and still are the subject of many nautical research projects [1]. To facilitate such research both CFD models as physical laboratory experiments are used. In these physical experiments the induced flows by a passing ship are of great interest. Although alternative approximations using artificial mud have been used extensively ([2], [3] and [4]) , the ability to perform such tests with real mud is still the preferred option. Nonetheless there are no techniques available today to visualize such flows and measure the flow velocities in mud. In [5] ultrasound speckle tracking is proposed to resolve this deficiency. A first test using a standard medical ultrasound scanner equipped with a linear array set at 7 MHz proved the ability of this technique. Due to the high ultrasound frequency and the attenuation of the ultrasound radiation by the mud, the depth to which flows were recorded was however limited to only a few centimeters. Decreasing the frequency will allow for greater penetration depths, but at the expense of a degradation in speckle image quality. A minimal speckle quality is nonetheless required to allow for the application of image processing algorithms. Further development of this technique therefore comes down to a trade-off between penetration depth and speckle image quality. Optimizing this compromise requires better knowledge of the acoustic attenuation of mud.

In general, ultrasound imaging is performed in the MHz frequency range. When the depth of the object we want to see predominates the resolution at which the object is depicted, e.g. fish spotting, frequencies of 0.7 MHz to 2.0 MHz will suffice [6]. In case the images are produced for diagnostic requiring high resolution, higher frequencies are required at the cost of penetration depth. For medical imaging this can go up to 15 MHz [7]. When speckle images are the objective there is no need to clearly visualize a boundary or interface. Speckle patterns are conceived by the

interferences of multiple backscattered signals which add up or cancel each other out. Hence resolution is replaced in this trade-off by the amount of backscattering, which is determined by the ratio of wavelength of the ultrasound radiation over the size of the scatterers. As determined in [5] the particle size distribution of cohesive sediment from the Port of Zeebrugge indicate an optimal ultrasound frequency range between 1 MHz and 10 MHz to generate speckle patterns. For this research a frequency range of interest is therefore set from 1 MHz to 7 MHz. To the authors knowledge, values for acoustic attenuation of mud in this frequency range are however not documented in existing literature [8], which calls for the need of experiments.

The most straight forward method to measure the attenuation of a medium (solid or liquid) is with the so-called through-transmission technique ([9] and [10]). This technique requires 2 transducers placed opposite to each other where one transducer acts as the transmitter and the other as the receiver (Fig. 1A). In case the properties of liquid are of interest, the 2 transducers are immersed in the liquid. The acoustic attenuation can be deduced by comparing the amplitude received after propagation of the ultrasound wave through the liquid of interest with a received reference signal. The latter is preferably obtained from calibration in water as water has low acoustic attenuation values which in fact can be neglected [11]. The through-transmission demands the 2 transducers to have at least equal center frequencies. Such a pair of transducers were however not available for this research. A technique requiring only a single transducer is the pulse-echo technique ([12] and [13]). Here the transducer acts both as transmitter and receiver (Fig. 1B). Again the transducer is immersed in the liquid of interest, but now an acoustic reflector is placed opposite to the transducer and perpendicular to the wave direction. The emitted ultrasound signal propagates through the liquid, reflects on the acoustic reflector propagates back to the transducer. Relative measurement of the reflection signal amplitude over multiple acquisitions with varying distance between transducer and reflector allows to determine the acoustic attenuation in the liquid.

Immersion of the ultrasound transducers for long periods or in fluids other than clear water can however cause contamination of the sensor surface, influencing the recordings and damaging the transducers [14]. In case of mud this could be caused by the corrosive nature of the seawater present in mud. In such cases an alternative multiple-echo technique can be an

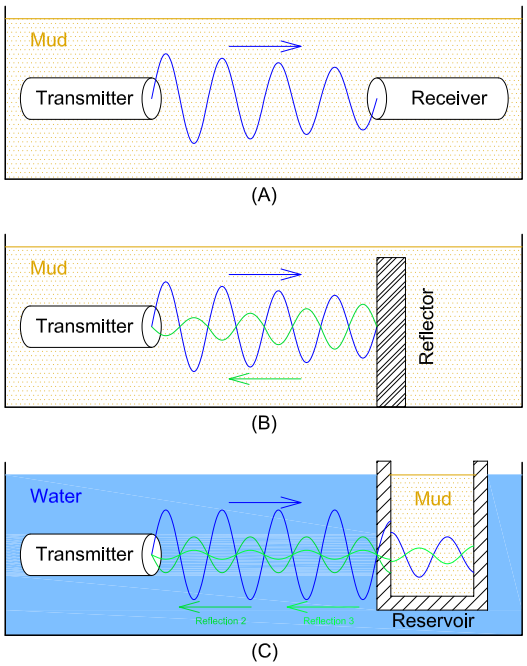

Figure 1: Possible experimental setups using immersible transducers to determine the attenuation of mud. (A) Setup for the through-transmission technique, (B) Setup for the pulse-echo technique, (C) setup for the multiple-echo technique.

option [15]. In this method the liquid of interest is in a secondary reservoir which in turn is immersed together with the transducer in water (Fig. 1C). The attenuation is obtained from comparison between the reflection signals of the two reservoir/liquid interfaces. This method suffers however from great energy losses. Before reaching the liquid of interest, energy is already lost by reflection on the water/reservoir interface and propagation through the reservoir material. Such losses can be compensated by amplifying the signals, however at the cost of accuracy.

The relativity of the pulse – echo measurement technique allows however to simply protect the transducer by inserting it in a thin sheath-shaped rubber. Together with the one-off nature and short duration of the experiments, the (single) pulse – echo technique was therefore preferred for these experiments. To provide future similar research with alternative options, additional experiments using various acoustic equipment were performed. The acoustic equipment used are developed for other applications like on-site marine measurements (Admodus USP pro and AQUAs-

cat 1000R) and medical echography (DiPhAS beamformer platform and FI Toolbox). Nonetheless their output can be used to deduce the acoustic attenuation of mud. The different methods are presented in this paper. All experiments were conducted with the same unique mud samples from the Port of Zeebrugge with differentiating densities of 1.115 g/cm^3, 1.450 g/cm^3 and 1.175 g/cm^3.

Rheological properties of mud are of interest as well for the study of ship, water and mud interactions and multiple other topics ([16] and [17]). Rheological properties can be determined using a rheometer [18], which for practical reasons should be operated in a laboratory. Obtaining the properties from on-site mud layers therefore requires on site sampling and transport towards the lab, which is a laborious operation. Furthermore for continuous monitoring this procedure should be repeated frequently as mud layer properties change over time [19] and are continuously influenced by tidal currents, ship passing and dredging. The ability to perform fast on-site measurement of the rheological properties of mud would therefore be of great interest. In the drilling industry recent research has shown that ultrasonic measurements in non-Newtonian fluids like drilling mud exhibit a non-linear relationship between the acoustic attenuation and rheological properties of the fluids [20]. The results of this paper could help to assess whether or not this relation also holds true for cohesive sediments by providing the values of acoustic attenuation.

2. Reference experiment using an immersible transducer

2.1. Setup and methodology

The experimental setup used to assess the acoustic attenuation of mud is based on the pulse-echo technique (Fig. 1B). In practice the setup was however slightly different as depicted in (Fig. 2). To facilitate the changing distance between transducer and reflector a high precision XYZ gantry stage was used to hold the transducer upright with the emission side facing down in the top layer of the mud. The mud sample was contained in a plastic bucket, positioned underneath the gantry stage. The used transducer is an immersible broadband (fraction bandwidth 50 %) transducer type H5K from General Electric [21]. In mud with density 1.145 kg/m^3 the centre frequency produced by the transducer is around 2.75 MHz. Due to the high attenuation values of mud the ultrasound waves were amplified (gain) using a pre-amp. A gain of 40 dB was applied for all mud samples. Stainless steel was chosen as the material for the acoustic reflector. With a speed of sound in stainless steel of 5800 m/s [9] and a density of 7850 kg/m^3 the acoustic impedance of steel can be calculated using Eq. 1. The same can be done for each mud sample with known density and a speed of sound of 1465 m/s [5]. With the impedance of both media the reflection coefficient of their interface can be determined using Eq. 2.

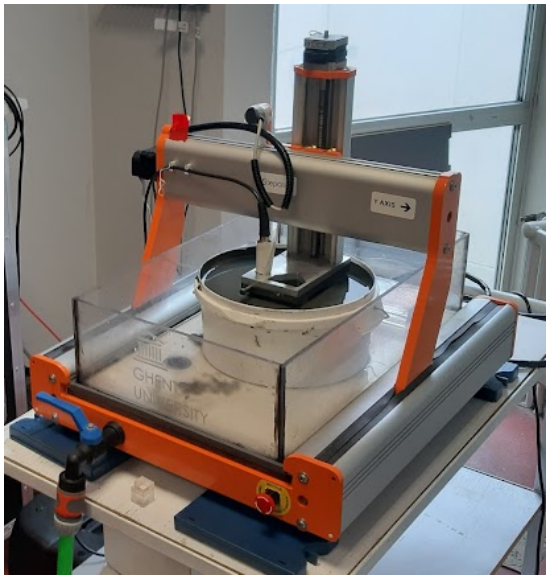

Figure 2: Laboratory setup of the experiments using an immersible transducer. The transducer is clamped by the bracket of the gantry stage, holding it in vertical position sticking with its immersive side in the mud. The transducer is protected with a sheath-shaped rubber. The gantry stage is used for vertical displacement of the transducer. A stainless steel reflector is positioned underneath the transducer at the bottom of the mud bucket.

$$Z_i = c_i.\rho_i \tag{1}$$

Where Z is the is the acoustic impedance $[kg\cdot m^{-2}\cdot s^{-1}]$, c is the speed of sound through the medium $[m\cdot s^{-1}]$, ρ is the density of the medium $[kg\cdot m^{-3}]$ and i the index referring to the medium.

$$r_{ij} = \frac{Z_j - Z_i}{Z_j + Z_i} \tag{2}$$

Where r is the reflection coefficient $[-]$, Z is the acoustic impedance $[kg\cdot m^{-2}\cdot s^{-1}]$ and i and j are the indices referring to the encountered materials or media.

The resulting reflection coefficient of the mud/reflector interface is around 0.93 meaning 93 % of the incoming ultrasound radiation is reflected

back towards the transducer. A plate of 10 *cm* by 10 *cm* and 1 *cm* thickness was placed at the bottom of the mud bucket. Using the XY positioning system of the gantry, the transducer was positioned more or less above the center of the reflector. Adjustment of the distance between transducer and reflector was performed by moving the transducer towards the reflector. For each mud sample this was done in 140 steps, covering a total displacement of 1.315 *cm* (Fig. 3).

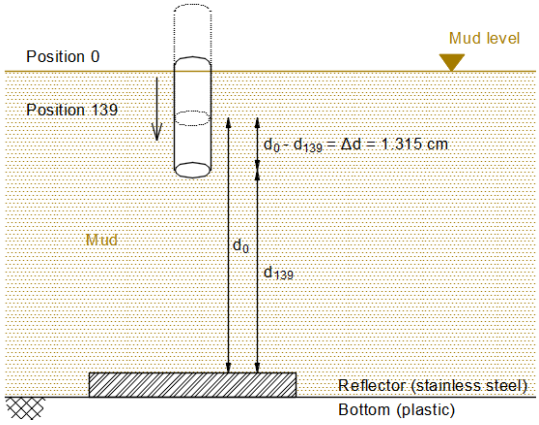

Figure 3: Sketch of the experimental setup depicted in Fig. 2, illustrating the effects of the transducers' displacement

At each step a scan was conducted, recording the amplitude of the reflected signal. The amplitude of the reflected signal can be expressed as:

$$A_R = A_0.P_m.r_{ms}.P_m = A_0.r_{ms}.P_m^2 \tag{3}$$

Where A_R is the amplitude of the reflected signal $[V]$, A_0 is the amplitude of the emitted signal $[V]$, r_{ms} is the reflection coefficient of the mud/stainless steel interface [-] and P_m the propagation loss due to attenuation by the mud $[-]$.

Fig. 1B and Eq. 3 show that loss in amplitude is caused first by attenuation when propagating through the mud towards the reflector P_m. Secondly, energy is lost at the mud/reflector interface. The reflection coefficient r_{ms} shows us that 93 % of the amplitude is reflected back. The remaining 7 % propagates further through the stainless steel and is no longer used. Finally, while propagating back towards the transducer, the reflected signal is attenuated again over the same path as the initial incoming ultrasound wave (P_m). The propagation loss P_m can be expressed with the Beer Lambert Law Eq. 4, [22]:

$$P_m = e^{(-\alpha_{(f)m}.d_m)} \tag{4}$$

Where P_m the propagation loss due to attenuation by the mud $[V]$, $\alpha_{(f)m}$ is the frequency dependent acoustic attenuation of mud $[Np \cdot m^{-1}]$ and d_m the propagation path of the ultrasound wave through mud $[m]$.

2.2. Processing of measurements

The recorded reflection signals are transformed into the frequency domain by Fast Fourier Transformation. This allows to select the reflection signal amplitudes and calculate the acoustic attenuation for each frequency step. For these experiments the frequency band was cut in steps of 0.0125 MHz.

When at rest, the density profile of a mud sample changes over time due to sedimentation [19]. Therefore it can be questioned if a method to determine the acoustic attenuation of a conventional fluid is best suited for mud. Two different ways to cope with this challenge are described and compared in this section. Prior to the experiments the mud was preconditioned by mixing as an attempt to approximate a conventional fluid. The first processing method assumes a homogeneous mud sample allowing for a conventional processing method. Such method is based on relative measurements, making knowledge of the value of some parameters unnecessary. The second approach assumes a non-uniform density profile of the mud sample and processes each scan separately. This however requires additional measurements of the values obsolete for the conventional method, at risk of decreasing reliability due to error propagation.

2.2.1. Conventional method

The reflection signal amplitude of the first position of the transducer is used as a reference ($A_{R,0}$ at $d_{m,0}$). From the ratios with the reflection signal amplitudes recorded at other positions of the transducer ($A_{R,n}$ at $d_{m,n}$) the attenuation of mud can be deduced. A combination of Eq. 3 and Eq. 4 can be rewritten as:

$$\alpha_{(f)m} = \frac{1}{2.(d_{m,n} - d_{m,0})}.\ln\frac{A_{R,0}}{A_{R,n}} \tag{5}$$

Where $\alpha_{(f)m}$ is the frequency dependent acoustic attenuation of the liquid $[Np \cdot m^{-1}]$, d_m the propagation path of the ultrasound wave $[m]$, A_R is the amplitude of the reflected signal $[V]$, index 0 refers to the reference scan and index n to a scan at a different transducers' position $(0 - 139)$.

In practice the logarithm of the ratio of the reflection signal amplitudes recorded at each position of the transducer with the reference signal amplitude is plotted in function of the transducers' displacement

$(d_{m,n} - d_{m,0})$ (Fig. 4). The slope of the linear trendline fitting over these ratios is a measure of the attenuation. Mathematically this procedure corresponds to Eq. 5.

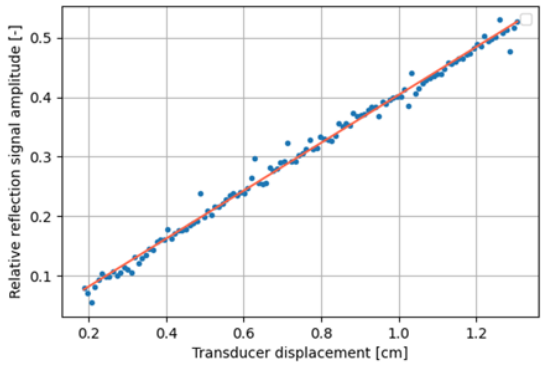

Figure 4: A plot of the logarithms of the relative recordings of the reflection signal amplitude at different positions of the transducer. The slope of the linear trendline fitting the plots is a measure of the acoustic attenuation of mud.

Following this procedure for each frequency step allows to determine the acoustic attenuation in function of frequency over the entire frequency band of the transducer. This was repeated for each mud sample with different density. The results are presented in Fig. 5, showing a more or less linear relation between attenuation and frequency, which is common like for most engineering materials Ono2020.

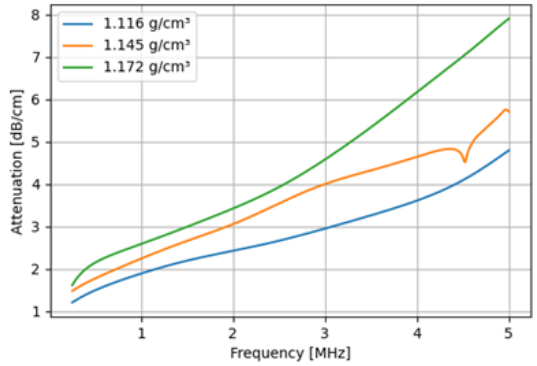

Figure 5: Results for acoustic attenuation in function of ultrasound frequency per mud density. These results were determined using a conventional method for fluids considering mud as a homogeneous fluid.

2.2.2. *Alternative method*

The presented conventional method may be improper because it determines the attenuation over a limited part of the mud sample only. In this case a layer of 1.315 *cm* (Fig. 3). For homogeneous liquids there is no issue there. Mud can however not be considered as a homogeneous fluid. By mixing the mud prior to the experiments an approximation of a homogeneous mud sample can be achieved. Nonetheless as soon as the mud is at rest, sedimentation starts, making mud instantly inhomogeneous [19]. It is therefore recommended to conduct the ultrasonic scanning immediately after the conditioning of the mud. Practically this is however not always possible, casting doubt on whether a limited top layer is representative of the complete mud sample. To verify this possible inaccuracy, an second alternative method to process the recorded reflection signals was performed. The great advantage of the first method is its relative approach, eliminating the need for knowledge of the originally emitted amplitude A_0 and reflection coefficient r_{ms}. Nonetheless with additional experiments in water the values for A_0 can be determined for each frequency. While the speed of sound in mud can be deduced from the scans performed in mud, enabling to verify the estimated value for r_{ms}. Subsequently the propagation loss P_m can be calculated for each scan using Eq. 3 and attenuation $\alpha_{(f)}$ using Eq. 4. Averaging the outcome over the 140 scans for each frequency step results in the curves presented in Fig. 6. The results from this method show an even more linear relationship between attenuation and frequency, at least for frequencies above 1 MHz.

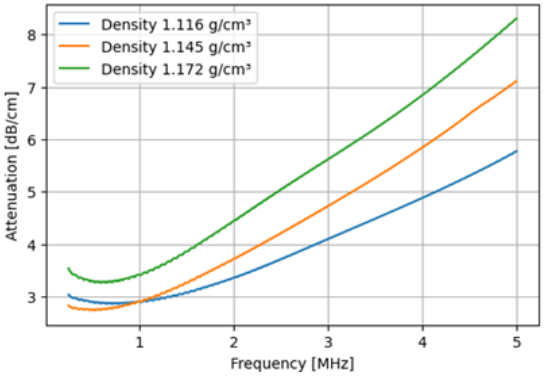

Figure 6: Results for acoustic attenuation in function of ultrasound frequency per mud density. These results were determined using a alternative method for fluids considering mud as a inhomogeneous fluid.

2.3. *Comparison of both methods*

In case of perfect homogeneous mud, the results of both methods should match. This is however not the case as shown in Fig. 5 and Fig. 6. While the

precision of the conventional method can be questions due to the inhomogeneous mud the alternative method suffers from error propagation due to usage of multiple measured values. A reliability analysis was therefore performed for both methods. For the conventional method R^2 values were calculated, indicating how well the trendline fits with the recorded relative amplitudes, Fig. 7. Reliability of the alternative method is evaluated with the standard deviation values of the averaged results, Fig. 8. Both show similar trends with good reliability within and rapidly increasing inaccuracy outside the frequency band of 1.5 MHz to 3.5 MHz. This frequency band corresponds with the fractional bandwidth of 50 % and center frequency of 2.75 MHz as mentioned in Section 2.1.

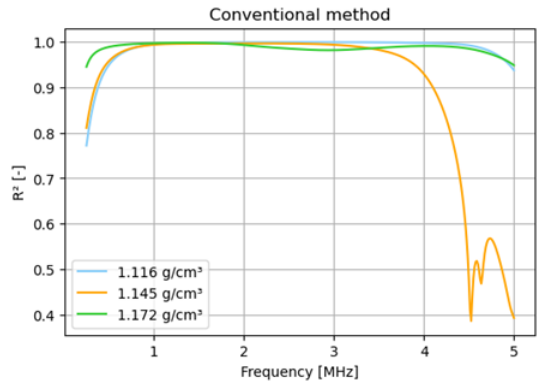

Figure 7: R^2 values plotted in function of frequency representing the reliability of the outcome using the conventional processing method.

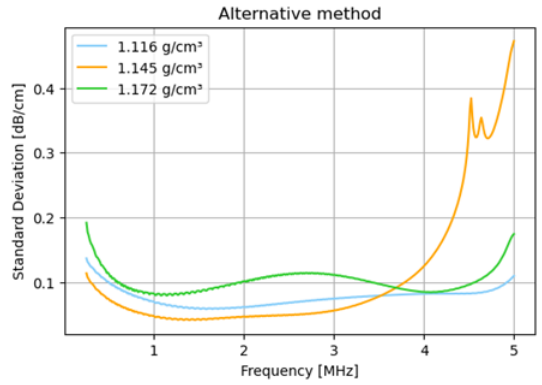

Figure 8: Values of standard deviation plotted in function of frequency representing the reliability of the outcome using the alternative processing method.

2.4. Acoustic attenuation values of mud

To conclude, the average of the 2 methods Fig. 9 is considered to be the best assessment for the acoustic attenuation in function of ultrasound frequency. Highest reliability applies to frequencies within the fractional frequency band.

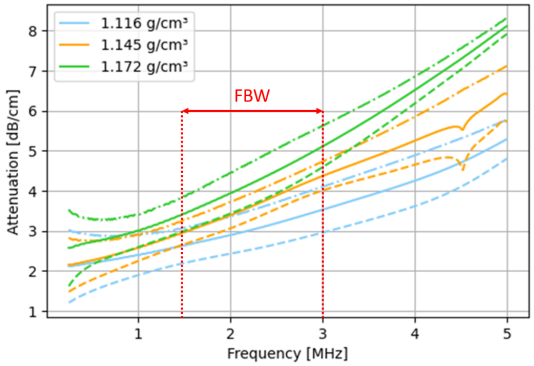

Figure 9: Resulting values for acoustic attenuation of mud in function of ultrasound frequency. The dashed curves represent the results of the conventional processing method. The dashdot curves represent the results of the alternative method. The solid curves represent the results averaged over the two methods. The averaged results are considered to be the best assessment for the acoustic attenuation, especially with the transducers' fractional bandwidth (FBW).

In addition to the relation between acoustic attenuation and frequency, the results show a linear relation between attenuation and density as well. An empirical equation Eq. 6 can therefore be determined expressing the relation between the three properties.

$$\alpha_{(f;\rho)} = (7.035f + 8.831).(\rho_{(m)} - 1) \tag{6}$$

Where $\alpha_{(f;\rho)}$ is the acoustic attenuation $[dB \cdot cm^{-1}]$, f the ultrasound frequency $[MHz]$ and ρ_m the mud density $[g \cdot cm^{-3}]$.

This equation is based only on the results within the fractional bandwidth and provides a good agreement with the averaged curves as depicted in Fig. 10.

3. Alternative experiments using various ultrasound equipment

Immersible transducers and associated equipment are not always directly available for all. Nonetheless, a quick assessment of the acoustic attenuation of a medium can be of great value for a first feasibility study of an experimental setup or new technique. Due to the extensive scope of ultrasound, chances are however there is some type of acoustic equipment more

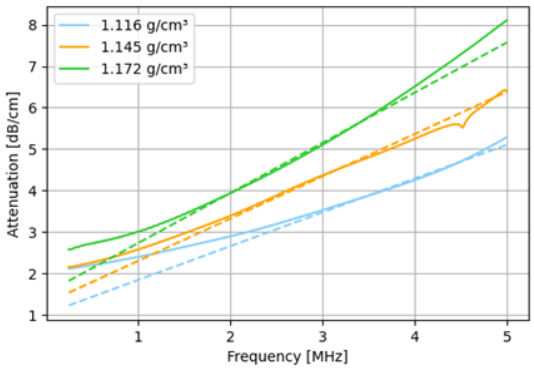

Figure 10: Calculated values of acoustic attenuation using Eq. 6 (dashed curves) compared to measured values of acoustic attenuation (solid curves).

readily available. Although the application of such equipment might be very different, it can still be of use to assess the acoustic attenuation. This was put to the test by performing additional experiments using various acoustic equipment designed for a variety of applications and consequently using different ultrasonic principles. Unless mentioned otherwise all these experiments were conducted in the same mud samples as used with the immersible transducer and preconditioned by mixing. The results are benchmarked against the results presented in Section 2.

3.1. Backscattering based techniques

Insonification of mud within the sound frequency band of 1 MHz to 7 MHz results in Rayleigh scattering of the ultrasound waves [5]. Similar to the pule-echo technique (Fig. 1B) a single transducer can therefore transmit and record the backscattered signals. Based on these recordings the acoustic attenuation can be deduced by the fading of the backscattered intensity with increasing penetration depth. The recording of backscattered signals requires highly sensitive transducers. Ultrasound transducers can be designed in different ways to create specific characteristics such as sensitivity. Customizable features are the piezoelectric element and backing, which both can vary in size and thickness [23]. High ultrasound frequencies require thin piezoelectric elements while width and focus depth of the ultrasound beam are proportional to the element size [24]. The damping capacity of the backing determines the pulse length, which in turn defines the bandwidth of the transducer. High damping resulting in short pulse lengths and consequently wide bandwidths. Low damping produces longer pulse lengths and narrow bandwidths. Narrow bandwidth transducers are considered to be more sensitive compared to broadband transducers which in turn result in a higher axial resolution due to the shorter pulse length[25].

3.1.1. AQUAscat 1000R

The AQUAscat 1000R is a device developed by the Aquatec Group Ltd for on site monitoring of sediment concentration, turbidity and particle size [26] (Fig. 11). It uses multiple ultrasound transducers which act as transmitter and receiver. The device used for this research is equipped with 4 transducers of 0.5 MHz, 1 MHz, 2 MHz and 4 MHz. Because of its intended use the transducers are narrowband transducers [27], making them highly sensitive at the cost of poor axial resolution as elaborated in Section 3.1.



Figure 11: The AQUAscat 1000R, a high frequency acoustic instrument. https://www.aquatecgroup.com/aquascat/aquascat-1000r

To determine the acoustic attenuation of mud, all transducers were submerged in the different mud samples. As attenuation is based on the recordings of the backscattered signals, there should only be sufficient mud in front of the transducers. This to allow for the recording of the decay of the backscattering intensity with penetration depth. A mud layer of 5 cm to 10 cm is considered to be sufficient for the applied ultrasound frequencies. The recordings for each transducer are presented in Fig. 12. They show a clear fading of the backscattered intensity with increasing depth. The slope of the linear trendlines fitting the measurements, are a measure for the attenuation of the ultrasound by mud.

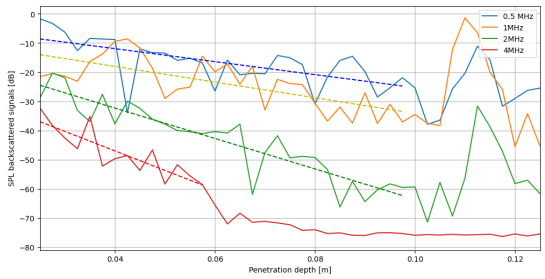

Figure 12: Recordings of each transducer deployed in mud with density 1.116 g/cm^3. The Sound Pressure Levels (SPL) of the received backscattered signals are plotted in function of penetration depth. The dashed trendlines fit the decreasing trend of backscattered SPL representing the attenuation. The peak at approximately 0.115 m is the reflection on the plastic of the bucket.

In total 150 scans were conducted with each transducer in each mud sample, resulting in 150 values for acoustic attenuation per frequency. Final results are obtained by averaging these series of 150 values. The resulting acoustic attenuation values per mud density are presented in Fig. 13.

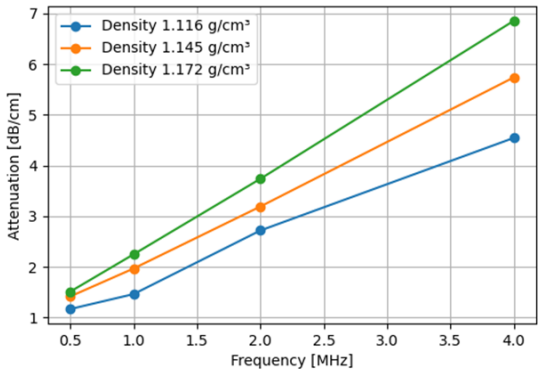

Figure 13: Final results for acoustic attenuation determined with use of the AQUAscat 1000R

3.1.2. Medical ultrasound scanners

Probably the most commonly known application of high frequency ultrasound is that of medical imaging. Two acoustic scanners were therefore used to create B-mode images of mud. The scanners are specifically developed for research purposes, enabling them to cover a broad frequency range. One scanner is the DiPhAS beamformer platform [28], the other the FI Toolbox (Diagnostic Sonar Ltd., Livingston, UK). A flexible linear array, a phased array and a conventional linear array with corresponding centre frequencies of 2.5, 3.5 and 7.5 MHz were used to cover a total frequency band from 1.75 MHz to 6.67 MHz, in steps of approximately 0.5 MHz. In B-mode, or brightness-mode, the amplitude of the received signals is converted into pixel brightness. High amplitudes result in bright pixels and vice versa. Due to the large amount of scatterers many backscattered waves are created, causing them to interfere with each other by adding up or cancelling each other out. In the end this interference results in pictures with a mix of bright and dark pixels, so-called "speckle pattern" images [5], as presented in Fig. 14A. With image processing techniques, pixel brightness profiles can be converted to SPL profiles and plotted in function of penetration depth per pixel column. The decay of the SPL with increasing penetration depth can then be expressed with a linear trendline fitting the SPL plots, Fig. 14B. The slope of the trendline is again a measure of the acoustic attenuation of mud, similar as with the AQUAscat 1000R, Section 3.1.1.

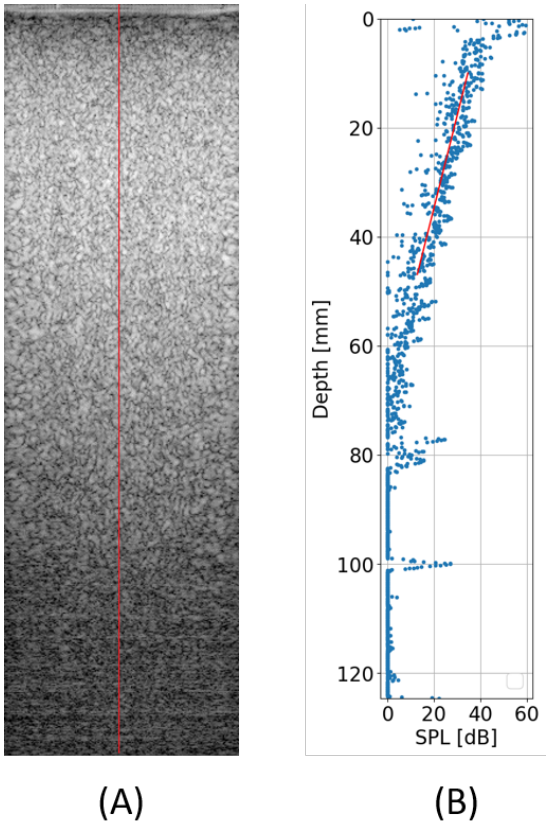

Figure 14: (A) B-mode image of mud resulting in a speckle pattern. (B) SPL plot of the profile indicated with the red line in Fig. 14A. SPL is plotted in function of penetration depth.

This procedure therefore results in a value for acoustic attenuation for each pixel column. As the

picture presented as Fig. 14A has a width of 140 pixels, one picture results in 140 values for the acoustic attenuation. In addition, 20 to 100 images were recorded for each setup of array and mud sample. Processing all these images therefore results in a numerous amount of values for the acoustic attenuation which are averaged for each frequency step and mud density. The resulting acoustic attenuation values per mud density are presented in Fig. 15.

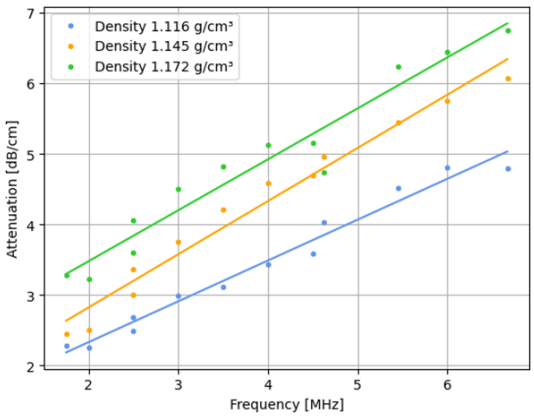

Figure 15: Final results for acoustic attenuation determined with use of medical ultrasound scanners.

3.2. Through-transmission

As elaborated in Section 1, the through-transmission technique is a straight forward technique to assess the attenuation of a liquid. It uses two transducers positioned opposite to each other while submerged in the fluid, (Fig. 1A). One transducer transmits the ultrasound waves while the other transducer acts as the receiver. Based on Eq. 3, the received signals for the through-transmission technique can be expressed as:

$$A_R = A_0.P_m \tag{7}$$

Where A_R is the amplitude of the reflected signal $[V]$, A_0 is the amplitude of the emitted signal $[V]$ and P_m the propagation loss due to attenuation by the mud $[-]$. The received signal when propagated through mud is compared to the signal received when the transducers are submerged in water. The latter is practically equal to A_0 due to the low acoustic attenuation of water [11]. From the ratio with the reference signal in water a value for the propagation loss in mud P_m can therefore be deduced. In turn this allows to determine the acoustic attenuation $\alpha_{(f)}$ using Eq. 4.

3.2.1. Admodus USP pro

The Admodus USP pro is an in-situ measuring probe developed by Synergetik GmbH [29]. It is used in harbours and waterways to determine the density profile of the mud layers at the bottom of navigation channels [30] and [31]. Measurements are made while letting it sink gravitationally into the water and underlying mud layers. Temperature, speed of sound, acoustic impedance and acoustic attenuation are measured, creating a depth profile for each of these properties. For density profiling the measured attenuation values are not used. Its measurement is however already foreseen in case a link is found between attenuation and rheological properties of mud like established for similar fluids [20]. The attenuation is measured using the through-transmission technique. The two transducers used have a centre frequency of 2.25 MHz and a fractional bandwidth of 50 %, corresponding to a bandwidth of 1.69 MHz to 2.81 MHz. The output of the attenuation is however given over a broader frequency band of 1.0 MHz to 3.5 MHz in steps of 0.5 MHz. A survey campaign was performed in February 2019 in the Port of Zeebrugge, where measurements were performed at multiple locations [32]. Values for acoustic attenuation are obtained by averaging these profiles per density. The results are presented in Fig. 16.

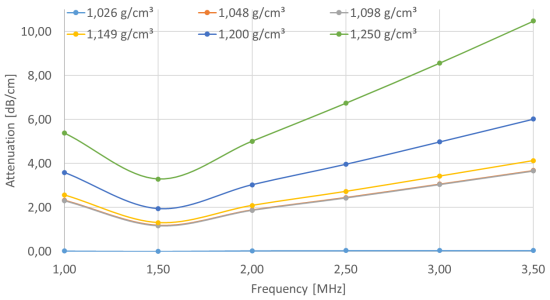

Figure 16: Results for acoustic attenuation from a survey campaign in the Port of Zeebrugge, using the Admodus USP pro.

Again a linear relation is found within the fractional bandwidth of the transducers. Outside the fractional bandwidth this is however deviated from, especially at lower frequencies. Based on the outcome of the other experiments the linear relation seems however clear. Together with 1 MHz being outside the fractional bandwidth of the transducers, the outcome of the Admodus USP pro at this frequency is considered to be incorrect.

3.3. Benchmark of alternative experiment results

Fig. 17 presents all results for acoustic attenuation from the alternative experiments as described in Section 3 together with the reference values provided in Section 2. Only the values for mud density 1.145 g/cm^3 are presented. The ratios and trends between the different curves are however similar for all mud samples.

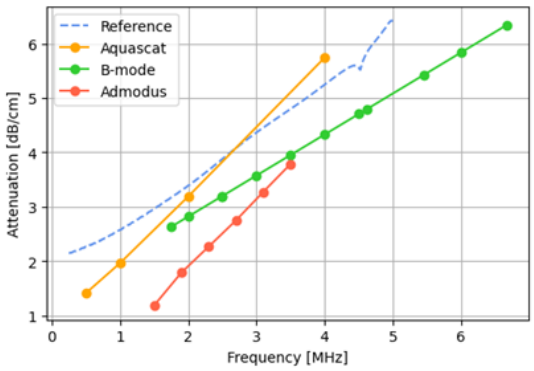

Figure 17: Plot of all results for acoustic attenuation of mud with density 1.145 g/cm^3 for all alternative experiments together with the reference values (blue dashed curve).

Overall the results match up well. Two anomalies however stand out in particular. Firstly, the results of the Admodus USP pro show an underestimation of the acoustic attenuation. These measurements were however performed on-site, in unconditioned mud. The mud therefore can be considered as sedimented or even consolidated, resulting in larger flocs [19]. As particle size distribution has an impact on the acoustic attenuation [33], the lower values provided by the Admodus USP pro confirm the presumed link between acoustic attenuation and rheologic properties as addressed in Section 1.

Secondly, the outcome of the B-mode experiments show a different rate of increase in acoustic attenuation with increasing frequency. This mismatch for the B-mode experiments is probably caused by the design of the transducers. The other devices all have single transducers with large piezoelectric elements. Medical ultrasound scanners however use arrays which consist of many small transducers activated together or in a controlled sequence. While they provide high axial resolution they are less sensitive [25]. Hence they are less suitable for recording small differences in signal amplitudes causing the less steep curve.

4. Conclusion

By means of lab experiments the acoustic attenuation of mud has been determined in function of ultrasound frequency and for different mud densities. Furthermore an empirical formula representing the relation between the three parameters was defined, matching well with the output of the experiments. The generated data will be of use for various topics of mud related research. The main incentive for this paper is the further development of ultrasound speckle tracking in mud. The presented results will assist in determining the optimal operating ultrasound frequency to maximize penetration depth while preserving adequate speckle image quality. In addition, the results can be of use in determining the relation between acoustic attenuation and rheologic properties. In the end this may lead to a technique for on-site monitoring of the rheological properties of mud, which would be of great value for port and waterway authorities.

A known method to determine the acoustic attenuation of fluids was applied in the lab experiments using immersible ultrasound transducers. By using two different methods of processing, it was however shown that mud can't be considered as a common liquid. While the conventional method assumes a homogeneous fluid, this is not applicable for mud due to its changing properties with time. On the other hand, the applied alternative processing method suffers from higher error propagation due to the requirement of results from multiple measurements. The average of the two is therefore considered as the best assessment for now. For similar experiments in the future it is advised to conduct the ultrasound scans while preventing sedimentation of the conditioned mud. This can be achieved for instance by continuous mixing while performing the ultrasonic scans. For this option, the impact of flow velocity on the recordings should however be considered. On a general note, only results for frequencies within the fractional bandwidth should be taken into account as reliability of the measurements deteriorate drastically outside this bandwidth.

A second series of experiments showed that other acoustic devices, developed for various applications, can be used to assess the acoustic attenuation of a liquid as well. A good understanding of the original application of the device and the associated specifications of the transducers is however recommended to fully appreciate the outcome of such measurements.

Acknowledgments

This research is promoted by Flanders Hydraulics Research (FHR) and supported by the Maritime Technology Division of Ghent University in collaboration with the von Karman Institute for Fluid Dynamics (VKI). The author is grateful to these institutions for the opportunity to conduct this research. Additional thanks to prof. Mathias Kersemans, dr. Erik Verboven (Ghent University - Department of Materials, Textiles and Chemical Engineering), prof. Jan D'hooge and dr. Marcus Ingram (KU Leuven - Cardiovascular Imaging and Dynamics Department) for making their lab and equipment available and their advice and assistance while conducting the experiments presented in this paper.

References

[1] G. Delefortrie, M. Vantorre, E. Verzhbitskaya and K. Seynaeve, Evaluation of safety of navigation in muddy areas through real-time maneuvering simulation, Journal of Waterway Port Coastal and Ocean Engineering - ASCE 133 (2) (2007) 125–135.

[2] K. Pouv, A. Besq and S. Guillou, Rheometric study for elaborating transparent model cohesive sediments for local investigations of erosion behaviour, Revue paralia 5 (2012) 1.1–1.14.

[3] K. Pouv, A. Besq, S. Guillou and E. A. Toorman, On the cohesive sediment erosion: A first experimental study of the local processes of transparent model materials, Advances in Water Resources 72 (2014) 71–83.

[4] T. Zaynab, S. Jarny and A. Texier, Rheology and local study of a transparent model cohesive sediment, no. INTERCOH2015: 13th International Conference on Cohesive Sediment Transport Processes, Leuven, Belgium, 2015.

[5] B. Brouwers, J. van Beeck, D. Meire and E. Lataire, Evaluation of known visualization techniques for the application on cohesive sediment layers in experimental fluid dynamics, [Unpublished manuscript]: Flanders Hydraulics Research.

[6] P. H. Dahl, "High-Frequency Underwater Sound," in WILEY ENCYCLOPEDIA OF ELECTRICAL AND ELECTRONICS ENGINEERING, Wiley-Interscience, Hoboken, NJ, USA, 1999.

[7] T. L. Szabo, "Wave Scattering and Imaging," in Diagnostic Ultrasound Imaging: Inside out, Elsevier Academic Press, 2004.

[8] A. D. Pierce, W. L. Siegmann and E. Brown, Analytical Discussion of Past Measurements of Acoustic Attenuation in Mud Sediments and of Possible future Experimental Approaches, no. Proceedings of Meetings on Acoustics, Jacksonville, Florida, USA, 2015.

[9] E. Ginzel and B. Turnbull, Determining Approximate Acoustic Properties of Materials, e-Journal of Nondestructive testing (NDT) 21 (12) (2016)

[10] S. Chaffaï, F. Padilla, G. Berger and P. Laugier, In Vitro Measurement of the Frequency-Dependent Attenuation in Cancellous Bone between 0.2 and 2 MHz, The Journal of the Acoustical Society of America 108 (3) (2000)

[11] W. R. Hendee, E. R. Ritenour, "Ultrasound Waves," in Medical Imaging Physics, Wiley-Liss, New York, USA, 2002.

[12] A. R. Selfridge, Approximate Material Properties in Isotropic Materials, IEEE Transactions on Sonics and Ultrasonics SU-32 (3) (1985) 381–394.

[13] G. Wróbel and S. Pawlak, A Comparison Study of the Pulse-Echo and Through-Transmission Ultrasonics in Glass/Epoxy Composites, Journal of Achievements in Materials and Manufacturing Engineering 22 (6) (2007)

[14] A. Püttmer, N. Hoppe, B. Henning, and P. Hauptmann, Ultrasonic density sensor—analysis of errors due to thin layers of deposits on the sensor surface, Sensors and Actuators A: Physical 76 (1–3) (1999) 122–126.

[15] T. Norisuye, S. Sasa, K. Takeda, M. Kohyama, and Q. Tran-Cong-Miyata, Simultaneous evaluation of ultrasound velocity, attenuation and density of polymer solutions observed by multi-echo ultrasound spectroscopy, Ultrasonics 51 (2) (2011) 215–222.

[16] E. A. Toorman, Modelling the thixotropic behaviour of dense cohesive sediment suspensions, Rheologica Acta 36 (1) (1997) 56–65.

[17] E. A. Toorman, I. Vandebeek, M. Liste Muñoz, M. Heredia, I. Rocabado, J. Vanlede, G. Delefortrie, M. Vantorre and Y. Meersschaut, Drag on an object towed through a fluid mud layer: CFD versus experiment, no. INTERCOH2015: 13th International Conference on Cohesive Sediment Transport Processes, Leuven, Belgium, 2015.

[18] S. Claeys, P. Staelens, J. Vanlede, M. Heredia, T. Van Hoestenberghe, T. Van Oyen and E. A. Toorman, A rheological lab measurement protocol for cohesive sediment, no. INTERCOH2015: 13th International Conference on Cohesive Sediment Transport Processes, Leuven, Belgium, 2015.

[19] E. A. Toorman and J. E. Berlamont, A hindered settling model for the prediction of settling and consolidation of cohesive sediment, Geo-Marine Letters 11 (3–4) (1991) 179–183.

[20] M. H. Jondahl and H. Viumdal, Developing ultrasonic soft sensors to measure rheological properties of non-Newtonian drilling fluids, Tm - Technisches Messen 86 (12) (2019) 744–757.

[21] GE, Ultrasonic Transducers For Flaw Detection and Sizing, Catalog 20117EN, GE Sensing and Inspection Technologies (2008).

[22] A. Ishimaru, Wave propagation and scattering in random media and rough surfaces, Proceedings of the IEEE 79 (10) (1991) 1359–1366.

[23] Olympus, Ultrasonic Transducers, Technical Notes 2019, Olympus Scientific Solutions Americas Corporation (2019).

[24] Ng. Alexander and J. Swanevelder, Resolution in Ultrasound Imaging, Continuing Education in Anaesthesia, Critical Care & Pain 11 (5) (2011) 186–192.

[25] R. Silverman, E. Vinarsky, S. Woods, F. Lizzi and D. Coleman, The effect of transducer bandwidth on ultrasonic image characteristics, Retina (Philadelphia, Pa.) 15 (1) (1995) 37–42.

[26] S. Caine, AQUAscat 1000 User Manual, User Manual 910-0001 1.07, Aquatec Group Ltd (2014).

[27] S. Caine and A. Smerdon, The factors that affect the performance of multiple frequency acoustic backscatter instruments: The evaluation of a commercial ABS system, no. Proceedings of the $2^n d$ International Conference & Exhibition on Underwater Acoustic Measurements: Technologies and Results, FORTH, Heraklion, Greece, 2007.

[28] C. Risser, H. J. Welsch, H. Fonfara, H. Hewener and S. Tretbar, High channel count ultrasound beamformer system with external multiplexer support for ultrafast 3D/4D ultrasound, no. IEEE International Ultrasonics Symposium (IUS), Tours, France, 2016.

[29] F. Schmidt, Operating manual for Admodus USP pro, Operating Manual Version 1.4, Synergetik GmbH (2016).
[30] S. Claeys, B. Dierikx, S. Paul and J. Reenen, Fluid mud density determination in navigational channels, no. Hydro 12 - Taking Care of the Sea, Rotterdam, Netherlands, 2012.
[31] F. M. Y. Plancke, D. Meire, Studie naar meettechnieken voor het onderzoeken van de opbouw van sliblagen in het Deurganckdok: Deelrapport 1 – Bundeling van de belangrijkste resultaten uit 3 masterproeven uitgevoerd op de Universiteit Antwerpen, WL Rapporten 12_160_1 Versie 3.0., Waterbouwkundig Laboratorium (2018).
[32] B. D. M. D. Meire, S. Claeys, F. Mostaert, Evaluatie van meetinstrumenten voor de bepaling van slib karakteristieken: Deelrapport 3: Meetcampagne februari 2019, WL Rapporten 18_059_3 Versie 5.0., Waterbouwkundig Laboratorium (2021).
[33] A. S. Dukhin, P. J. Goetz, Characterization of liquids, nano- and microparticulates, and porous bodies using ultrasound, Elsevier, Amsterdam, Netherlands, 2010.

Particle image velocimetry in a high-speed short-duration turbine rig

Mizuki Okada

Turbomachinery and Propulsion Department, von Karman Institute for Fluid Dynamics, Belgium, mizuki.okada@vki.ac.be

Supervisor: Sergio Lavagnoli

Associate Professor, Turbomachinery and Propulsion Department, von Karman Institute for Fluid Dynamics, Belgium, Sergio.Lavagnoli@vki.ac.be

Advisor: Jorge Pinho

Senior Research Engineer, Turbomachinery and Propulsion Department, von Karman Institute for Fluid Dynamics, Belgium, Jorge.Pinho@vki.ac.be

University Supervisor: Alessandro Parente

Associate Professor, École polytechnique de Bruxelles, Université Libre de Bruxelles, Belgium, Alessandro.Parente@ulb.be

Abstract

This article presents an implementation of a PIV measurement setup into the high-speed short-duration rotating turbine facility of the von Karman Institute. Practical solutions were demonstrated that address various challenges for the effective application of PIV to short-duration test rigs.

Keywords: PIV, High-speed flows, Short-duration, Rotating rig

Introduction

Understanding the unsteady flow fields in turbomachinery is an essential step to improve the performance of the machine. Computational Fluid Dynamics (CFD) is a cost-efficient approach to predict behavior of fluid, however, in the case of turbomachinery flows with complex geometry, the prediction accuracy still needs improvement to be used with confidence. Probe traversing measurement techniques are widely used to generate reliable experimental databases[1], [2], but their instantaneous measurements are spatially sparse and their finite geometry can cause intrusive effects. Particle Image Velocimetry (PIV) is a non-intrusive measurement technique which is developed by numerous researchers and implemented into various applications since it was invented in 80s [3]. For turbomachinery investigations, instantaneous spatial data acquisition with low intrusiveness provides great possibility to analyze the complex three-dimensional flow structures. For planar PIV, the ideal orientation of the optical system is to maintain the light sheet perpendicular to the optical axis of a camera [4], and thus the measurement setup requires two optical accesses (one for the camera view and one for the laser sheet insertion), unless stereoscopic or tomographic system with highly skewed view angles is used [5]. This requirement makes implementation of PIV into turbomachinery test sections challenging due to packed hardware geometries and often limited optical access. Besides, the images are likely to suffer from extreme light reflection issues as the intense laser sheet impacts the metallic surfaces of test section. Furthermore, the large velocity gradients that characterize high-speed turbine flows require carefully designed seeding methods and the use of adapted processing algorithms.

For low subsonic flows (vane exit Mach < 0.6), several authors have presented successful implementations of PIV in both static linear cascades [6], [7], [8], or rotating cascades[9], [10] facilities. There is scarce literature presenting PIV measurements for high-speed testing (vane exit Mach > 0.6) of turbomachinery components, and most of these investigations are lim-

ited to stationary cascade test articles [11], [12], [13], [14]. Yet, PIV measurements conducted in transonic rotating turbine rigs have been reported by [15], [16] as well as in transonic rotating compressor rigs by [17], [18], [5].

Among them, disclosure of PIV study in high-speed and short-duration rotating facilities can only be found in [15] to the best of the authors knowledge. The short-duration blow-down type facility is capable of reproducing engine scaled test condition with relatively cost-effective installation compared to a more onerous continuously-running rig [19] but testing time is severely limited. The use of photographic films for recording in [15] limited the number of images acquired during short testing time, resulted in computation of quasi-steady state flow field from six pairs of images. In past decades a remarkable development of digital image recording and laser systems made high-speed PIV became popular. An experimental study of modern PIV system in short duration test facilities will reveal great potential of its technique and lead development of an efficient whole-field measurement method for turbomachinery flows.

This paper focuses on the implementation of PIV into the high speed short-duration annular turbine rig of von Karman Institute. The optical measurements are performed on a single-stage high pressure turbine (HPT) with a purged stator-rotor hub cavity. The paper presents specific design, operation procedures, and data processing methods for PIV measurements tailored for short-duration testing of fully-featured high-speed turbines.The quality of the measured velocity fields is demonstrated through back-to-back comparison with predictions from mixing-plane RANS calculations of the experimental turbine case.

1. Experimental facility and measurement methodology

1.1. Turbine test rig and test section design

The PIV measurements were performed in the rotating turbine rig of the von Karman Insitute (Fig. 1). The principle of this short-duration turbine rig is the isentropic compression tube [20], the test rig allows HPT tests at engine representative condition in terms of pressure ratio, Mach number and Reynolds number [19]. Cavity purge flow is supplied from a pressure tank isolated from compression tube. For this particular test campaign, the test rig hosted single-stage HPT consists of 34 vanes and 48 rotors, and testing time with current experimental

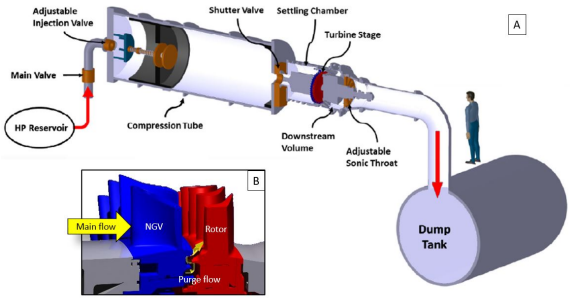

Figure 1: Short-duration compression tube turbine test facility (CT3).

configuration was about 250ms [2]. In addition, the rainbow-rotor configuration [1], [2] was employed for turbine rotor stage, rotor blades were divided into 6 circumferential sectors combining different hub and tip platforms. This experimental methodology allows reduction of number of experiments for such number of investigated sectors. On contrary, a dedicated data reduction technique is required to retrieve sector resolved velocity information.

The nominal flow condition as shown in Table 1 which is representative of engine cruise condition was considered for the present test campaign. The meridional section view of test section with purge flow and seeding supply lines is shown in Fig. 2. Plane 01 is located at half axial chord upstream of the nozzle guide vane (NGV) leading edge and plane 03 is positioned downstream of rotor, approximately 2.5 axial chord downstream of NGV. Pressure and temperature at plane 01 and 03 at midspan were measured by circumferentially distributed probes as well as endwall hub and shroud wall pressure taps, providing reference measurement values to monitor operating conditions. Additional slots at plane 01 and plane 03 were used to introduce seeding probes and laser light sheet endoscope as described in following sections.

1.2. Optical access and light sheet delivery

The main flow path is covered by an internal and external metallic casings as shown in Fig. 2. The internal and external windows mounted on casing are shown in 3(A). The inner surface curvature of internal window was matched to the casing shroud surface. After preliminary tests, it was revealed that every 2 tests the cleaning of windows was required to take acceptable quality images.

In order to allow access for a light sheet to the flow

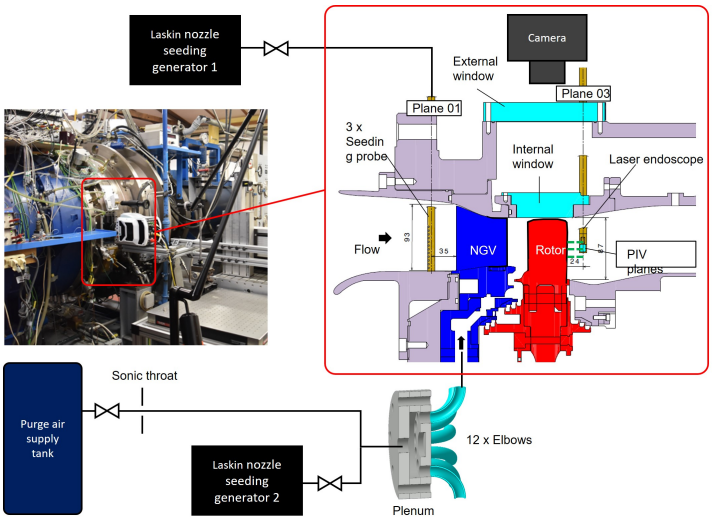

Figure 2: Test section of CT3.

Table 1: Nominal test conditions of Turbine Rig.

Parameter	Value	Units
P_{01}	1037.9	mbar
T_{01}	439.4	K
$P_{01}/P_{s3,hub}$	2.195	-
$P_{01}/P_{s3,tip}$	2.214	-
Re_{03,C_x}	$2.76 \cdot 10^5$	-
$\mathrm{Mach}_{03,rel}$	0.78	-
N_{rot}	5920	rpm
$\dot{m}purge$	1.74% of $\dot{m}_{total}$	-

passage, a laser sheet endoscope of 8mm external diameter was designed and built as shown in Fig. 3 (B, C). The endoscope contains focusing spherical lens (f = 515 mm) at the beam entry side, a 6 mm × 4 mm sheet forming cylindrical lens (f = -5.79 mm) and a 5 mm × 5 mm prism mirror at the tip of the scope. The tip part can be detached in case straight angle light sheet is desired. The endoscope was inserted into the internal casing at downstream of rotor stage, using a slot originally designed for probe measurements [2]. The scope yaw angle and radial position were adjusted by rotating scope and changing the insertion depth. It was revealed that illumination of the blade to blade rotor passage was difficult due to limited access for probes. Consequently, the region of interest was set to tangential plane at rotor blade exit, located between 100 - 115% of rotor axial chord.

The light sheet illuminates not only particles but also other components on its traveling path, such as casing surface and rotor blades. The light reflections on these surfaces, those mostly are metallic, yield significant background noise compared to scattering light from particles. To reduce the light reflection, the rotor blade and casing surface were coated with a black paint.

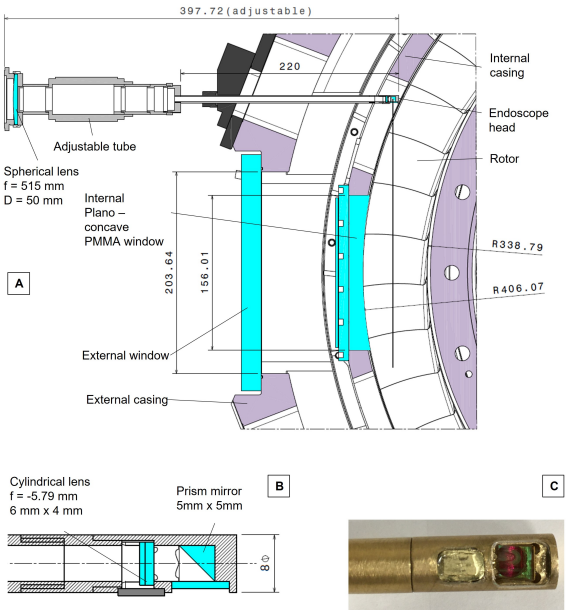

Figure 3: Overview of optical access. A: Test section downstream of rotor row. B: Design of laser endoscope head. C: Picture of laser endoscope head.

1.3. Seeding

1.3.1. Seeding method

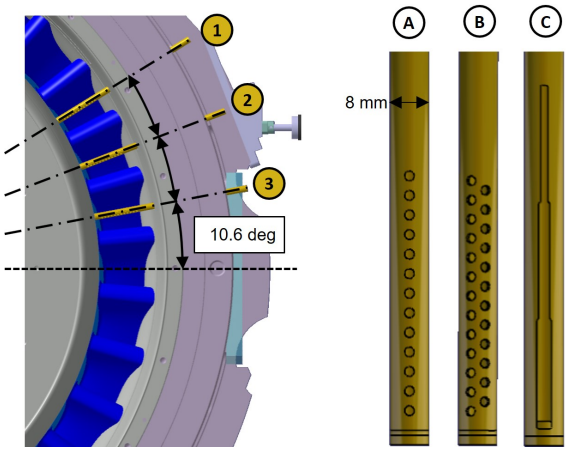

Figure 4: Seeding location and probes for main flow.

Implementing PIV into high-speed and short duration turbomachinery flow raises unique challenges for seeding method. The main difficulty is to seed tracer particles satisfactorily and uniformly in the investigated flow with limited access and time. Besides, particle motion lag with respect to fluid motion must be minimized by careful selection of the particles those have small size and density. Commonly used particles for PIV in high speed turbomachinery are micro scale DEHS oil particles ($d_p = 0.3 - 1.0\ \mu$m) [21], [22]. In this study, 0.9 μm diameter DEHS droplets were generated by laskin nozzle seeding generators (PIVTEC, PIV Part 45 and PIV Part 14). Fig. 2 and Fig. 4 show seeding setup for the experiments. Main flow was seeded through three different seeding probes inserted upstream of NGV row at different circumferential positions. Seeding was also injected into the purge supply line after the sonic throat which is used to measure the mass flow rate of purge air supply from the tank. Typical mass flow rate of seeding injected through the seeding probe B during a test is estimated less than 1% of main flow.

Table 2 shows a comparison of global test condition parameters measured by probes with and without seeding. The difference of parameters due to seeding is within 1% in terms of inlet total pressure P_{01} and stage pressure ratio at both hub and tip. The purge mass flow rate shows larger deviation of 2.4% as repeatability of mass flow control of purge air supply is lower compared to the other two values. The fewer number of tests performed with seeding injection also contributes larger deviation.

Table 2: Seeding effect on test condition.

	P_{01}	Pratio		$\dot{m}_{purge}$
		hub	tip	
Seeding ON/OFF	100.5%	99.0%	99.0%	102.4%
1.96*STD OFF (157tests)	0.7%	0.6%	0.8%	1.9%
1.96*STD ON (27tests)	0.7%	3.0%	3.0%	2.0%

1.3.2. Particle traceability

Once particles were discharged into the flow path, they will be accelerated or decelerated mainly due to the drag force associated with velocity gap between particles and flow medium (slip velocity). The fidelity of seeded particles following the flow is quantified by particle Stokes number STK, defined as the ratio between particle relaxation time and characteristic flow time scale. Practically, the condition $STK < 0.1$ provides an acceptable flow tracing accuracy with errors below 1% [23]. Within the approximation of very low Reynolds number in which drag force can be derived by Stokes's drag law. In high-speed turbomachinery flow, Stokes number introduced above may not be valid as Reynolds number can be much higher than the limit of Stokesian flow regime ($Re_p \leq 0.1$) [24]. A generalized Stokes number in non-Stokesian flow extended to compressible flow was derived by [25].

The various reference lengths are taken as shown in Fig. 5. Fig. 6 shows variation of generalized Stokes number calculated using flow quantities in the test facility. Except at rotor TE, the Stokes number is evaluated to less than 0.1.

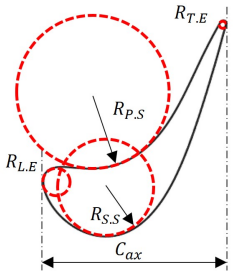

Figure 5: Reference length associated with rotor blade.

1.3.3. Fluorescent particles

In addition to pure DEHS oil droplets, the use of fluorescent dye-doped DEHS droplets was inves-

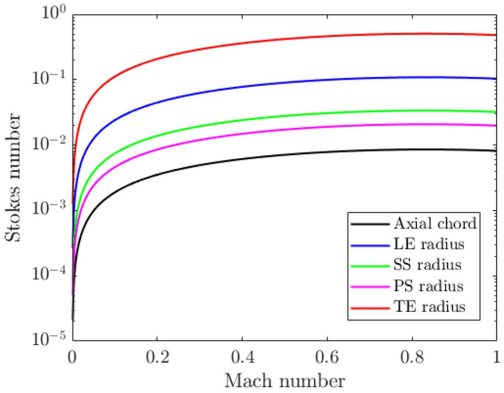

Figure 6: Generalized stokes number with different reference length scale. (DEHS particle with 0.9 μm diameter.)

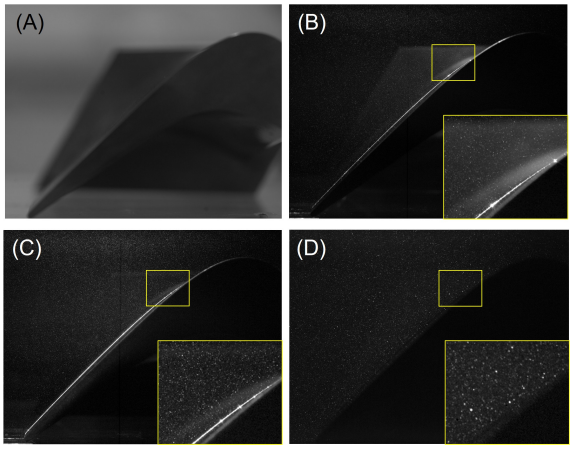

Figure 7: Examples of Mie scattering and fluorescent emission particle images. (A) Field of view (B) Mie scattering image (C) Mie scattering image with black-painted blade (D) Fluorescent emission image

tigated aiming at elimination of undesired reflection on surfaces of objects such as rotor blades and casings. Dye material was selected considering following characteristics: High solubility in DEHS oil, high fluorescent emission efficiency at 527 nm wavelength excitation, availability in commercial market and cost effectiveness.

Suitable dye concentration in a form of sub-micron droplets was investigated by directly comparing signal intensity of fluorescent particle images. The image acquisition was done in the L12 wind tunnel in the VKI employing a high-speed camera (Phantom M310) equipped with OD6 band stop filter (central wavelength: 532 nm, FWHM:10nm) and a high-speed laser system synchronized at 1kHz acquisition frequency. The main flow speed was set to 5.0 m/s. Seeding droplets were generated by PIVPart14 seeding generator using DEHS oil with different dye concentrations. Progressive improvement of fluorescent emission intensity is observed along with the increment of dye concentration. Comparison of particle images taking either Mie scattering or fluorescent emission is presented in Fig. 7. Using fluorescent technique, the reflection on intersection of blade surface and laser sheet is successfully eliminated as well as background illumination. For PIV measurements in CT3, fluorescent particle was tested aside the tests performed with pure DEHS particles. The results is presented later.

1.4. Synchronization and operation sequence

Synchronization of PIV system with the operation of the test rig and the rotor angular position is a crucial part of experiments especially for blow-down type test facilities. A high speed camera, Phantom v2012, and a high speed dual cavity laser system (Quantronix DarwinDuo) were employed. The camera sensor resolution is 1280 $\times$ 800 pixels with 28 μm pixel pitch. The camera was equipped with Nikon AF Micro-Nikkor 60mm f/2.8D lens and was placed as close as possible to the optical window, resulting in approximately 0.56 optical magnification. The camera and the laser were synchronized at 1kHz acquisition frequency (laser output power: 20 - 25 W) by two Stanford digital delay/pulse generators (DG535). The actual separation time of 1.14 μs (at laser input power of 20A) was measured by a fast response photo-diode (Thorlabs DET10A2, 1 ns rise time). The displacement of the rotor blades between the frame separation time is 0.5 % of rotor pitch at nominal rotational speed (5920 RPM).

The test operation sequence is shown in Fig. 8. Rotor angular position was monitored by fast-response diode and its signal was recorded by an acquisition system which also records the signal of reference probes at 1MHz acquisition frequency. Once rotor was spun up to the 90-95% of the nominal speed, laser was launched in prior to the activation of the compression tube. After confirming the power of the laser achieved to the set value, seeding was turned on, then a blow-down sequence was initiated by supplying high-pressure air into the back of the piston in the compression tube. Once the specified tube pressure level was reached, the acquisition systems and the camera were triggered.

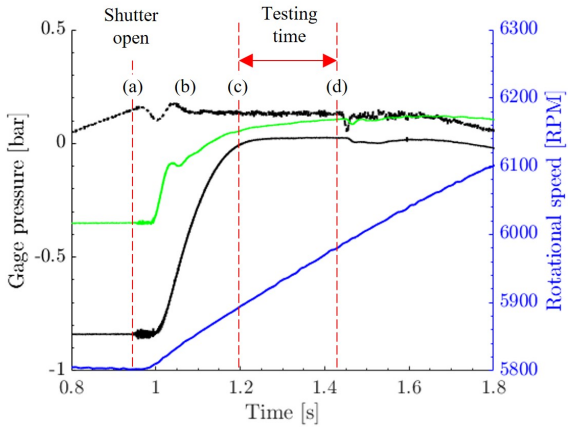

Figure 8: Test sequence with zoomed time scale.

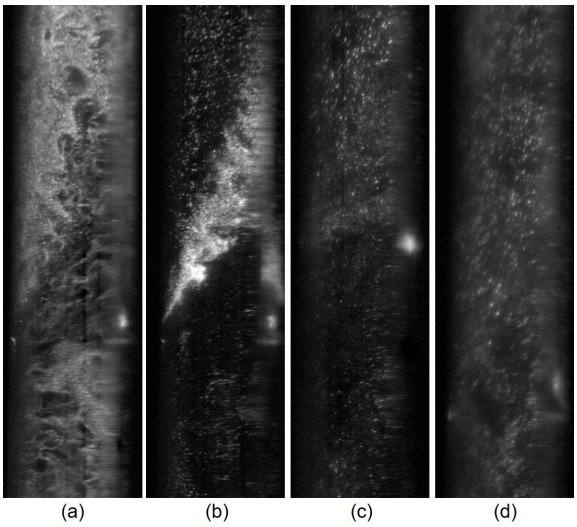

Figure 9: Instantaneous particle images recorded at shutter opening time (a), flow transient (b), steady flow condition (c) and end of the testing time (d)

After preliminary tests, a significant delay was found between the acquisition system and the camera. Dedicated tests were conducted in following procedure in order to quantify this delay because the blade number and its position in each PIV images has to be identified to perform phase locked averaging (PLA). The camera time delay was determined as 527.4μs with standard deviation of 10μs, those corresponds to approximately 250% and 4% of blade passing period (BPP). This means it was compulsory to measure the camera delay in order to identify which blade is in the field of view at each instantaneous moment. However, still, delay ambiguity of 4% of BPP results in unreliable identification of rotor position in images.
To solve this issue, precise rotor position was retrieved by detecting reflection of rotor trailing edge (TE) appears in PIV raw images. A detection algorithm was developed and worked reliably with less than 2% of wrong detection case out of 500 images.

2. Data processing

Instantaneous images acquired at four different time steps during the testing sequence are presented in Figure 9. As the test is initialized, the shutter separating the compression tube from the test section opens (Figure 9a) and the seeding particles priory accumulated in the upstream settling chamber are convected in the test section. As the flow transient occurs (Figure 9b), the particle distribution appears less homogeneous, with a higher seeding concentration denoting the rotor wake and a comparatively lower concentration at the blade suction side, possibly in reason of flow separation effects in this region. Eventually, steady flow conditions are achieved and maintained throughout the testing time (Figure 9c), as the downstream sonic throat operates at choked condition until the end of the test (Figure 9d). A more uniform seeding distribution is observed at instants (c) and (d), while the image sharpness progressively decreases as a results of the accumulation of seeding particles on the wetted surface of the optical window. A selection of image pre-processing algorithms was tested in order to obtain the highest signal-to-noise ratio in the cross-correlation operation, leading to the maximum number of valid vectors presenting a high degree of confidence. As a result of the pre-processing algorithm, more than 10% of the total vectors in close proximity to the rotor trailing edge were converted to valid, at the cost of a minor loss of spurious vectors in other investigation areas.

The commercial software Davis 8.4 was employed for PIV vector calculation. The multi-pass cross-correlation technique was used starting from 128 pixel initial square windows to 32 pixel final square windows. The window overlap was set to 75% for the last pass, resulting in a vector computation every approximately 0.5 mm. The outlier detection was performed by 5 $\times$ 5 median and global max/min filter while no smoothing nor vector interpolation tools were implemented.

2.1. Phase lock averaging (PLA)

The number of images obtained in each test is limited and the rotor position shows significant image-to-

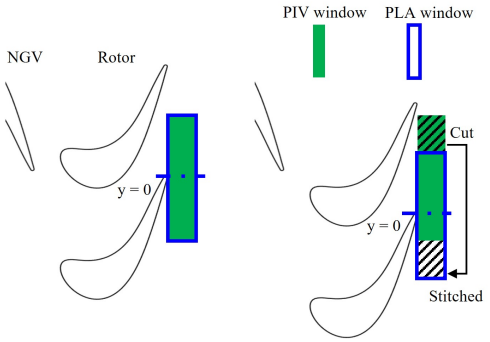

Figure 10: Rotor domain PLA.

image variations as the fixed frequency of the camera does not vary consistently with the rotor acceleration during the testing time (90 rpm over 250 ms). A phase-lock averaging (PLA) technique in the rotor domain was adopted in order to increase the number of velocity fields for averaging and rephase the acquired flow field with respect to the rotor-relative position.
For every computed velocity field, the circumferential coordinate y was rephased in order to align the rotor TE to the field center ($y = 0$), considering periodic boundaries at the peripheral extremities of the averaging domain as shown in Fig. 10. With the deterministic flow unsteadiness averaged in the rotor domain, the flow gradients associated with stationary components such as the upstream NGV are averaged out. This resulting phase resolved information in the rotor domain is directly comparable to the results of RANS flow predictions performed by using the mixing plane approach at the vane-rotor interface.
In order to account for the rainbow rotor configuration adopted in the current test article, a sector-resolved PLA was also performed in the rotor domain, isolating the contributions of the different hub and tip geometries. The computed vector fields were classified into six sector groups using the information on the rotor angular position provided by shaft-mounted optical diodes. In order to exclude sector-to-sector flow interactions and ensure an optimal periodicity of the sector flow field, only the six central passages of each sector were considered in the ensemble averaging operation [2].

3. Results

The main purpose of this study is to demonstrate the feasibility of PIV measurements in a short-duration high speed turbine test rig. In order to simplify the evaluation of PIV performance, axial and tangential velocity components are directly compared against CFD results. The methodology of CFD simulation is described in [2]. PIV measurements presented in this paper were performed at 58% of the rotor span height unless otherwise stated. The average velocity field is retrieved by adding two consecutive tests with same test conditions. This allows to increase the number of instantaneous velocity fields and simultaneously to reduce the standard deviation.

3.1. PLA flow field

Axial and tangential velocity fields from PIV and RANS simulations are presented and compared in Fig. 11. As mentioned in the previous section, image pre-processing is shown to be crucial to properly resolve the velocity defict on the rotor TE. Naturally, this effect is more evident on the axial component of the velocity. In the same figure, both velocity fields from a single sector (Sec2) or multiple sectors (ALL) are compared and detailed.
The standard deviation (STD) of the tangential velocity plotted at 4 different locations (identified in Fig. 11 - Y1, Y2, Y3, Y4) was monitored, the convergence was confirmed after 300 instantaneous PIV data. For sector-resolved PLA (dashed lines), results show that standard deviation is not converged as number of available velocity fields is reduced. Sector-resolved PLA results show velocity fields with more noise due to fewer number of dataset applicable. Still, they represent flow structure visibly, meaning that this technique has potential to exploit sector resolved data if larger number of images are available. For example, to obtain minimum 300 images for proper evaluation of average fields of each sector in current rainbow rotor configuration, repeating 3 - 5 blow down tests with same sampling frequency (1kHz) or performing single measurement at repetition rate higher than 5kHz, or compromise between those two approaches are required.

Finally, comparison of axial (left) and tangential (right) velocity components from PIV and RANS simulation is shown in Fig. 12 (profiles were extracted at $C_{ax} = 1.1$ - dashed line from Fig. 11). Tangential velocity profiles show excellent agreement. On the other hand, axial component globally follows trend, however a noticeable discrepancy is observed. In particular, the rotor wake region and corresponding velocity deficit is reduced in PIV results with respect to RANS calculations. One of the causes is considered to be the error of measurement plane alignment

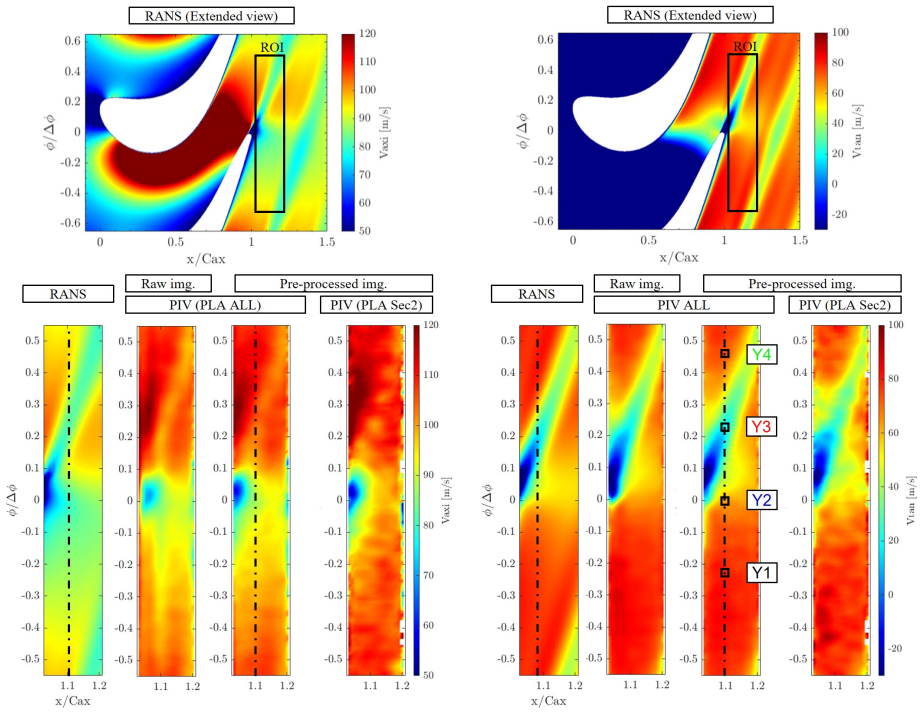

Figure 11: Axial and tangential velocity fields from PIV and RANS simulations. Extended view from RANS calculations of axial velocity and tangential velocity; Comparison between RANS and PIV measurements of axial velocity and tangential velocity using raw and pre-processed images. Both single sector and all sectors data are evaluated.

which is estimated to be ±1 mm corresponding to approximately ±1.5% of the rotor span height. An alignment system with high precision positioning capability will reduce this error. Another cause can be a deviation of PIV ROI plane (tangential plane) from constant radius surface, as the interrogation location on PIV plane departs from a point of tangency. The maximum mismatch of span position is estimated to be 2.8% of rotor span height.

On the other hand, the error can be introduced by estimation of vector through PIV algorithm in discretized interrogation windows. The distribution of wake region has a steep angle with respect to interrogation window grid. In other words, particle displacements are not uniform and their gradient are stronger in axial direction in each interrogation window. Therefore, the PIV velocity result in wake region is spatially filtered resulting in strongly attenuated axial velocity component. Finally, as mentioned in previous section, particle Stokes number is estimated to be above 0.1 at rotor TE, therefore particle may not be able to follow flow faithfully in the vicinity.

3.2. Fluorescent PIV

Tailored fluorescent dye-doped DEHS oil droplets were tested in the PIV measurement campaign. Black tape that has covered the rotor passage was removed during fluorescent PIV measurements as strong light reflection was blocked by the optical notch filter, resulting in the optical access to inter-blade passage. Fig. 13 shows instantaneous fluorescent particle images acquired at different time steps during the test sequence and the instantaneous velocity fields computed from them. The entire rotor passage was not illuminated due to limitation of access for laser sheet probe and curved geometry of rotor blades that blocks penetration of laser sheet. The left image was taken while flow is being established after shutter opens whereas the right image was acquired when the testing time started. Image became less bright and less sharp as time elapses due to the accumulation of seeding particles on the casing window surface and those oil might cause secondary absorption of fluorescent light primarily emitted from particles.

The demonstration of fluorescent PIV technique showed great potential to acquire PIV data at inter-blade passage. Its capability is expected to be en-

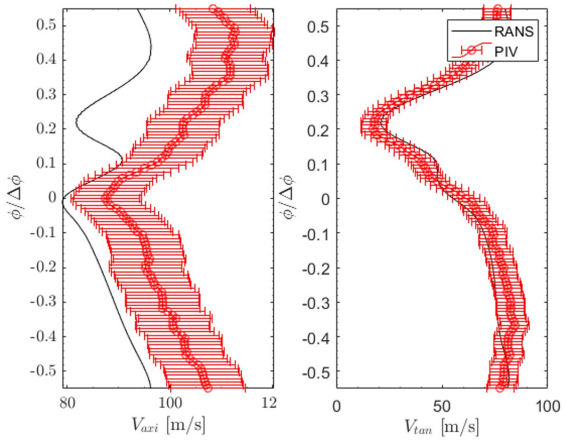

Figure 12: Comparison of velocity profile. PIV vs. RANS. Left: axial velocity. Right: tangential velocity.

hanced by improved seeding method which enables uniform seeding with good concentration in test section without too much accumulation on the casing optical window.

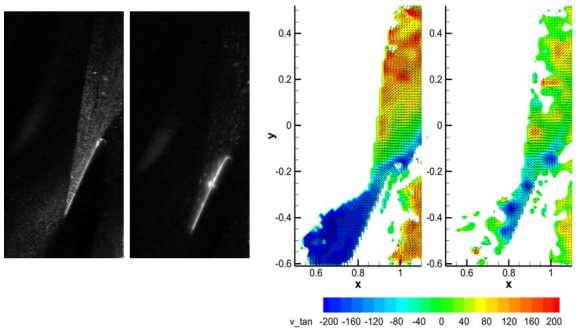

Figure 13: Instantaneous velocity field computed from fluorescent particle images in Fig. **??**. Left: flow transient corresponding to timing (b) in Fig. 8. Right: Steady flow condition corresponding to timing (c)

3.3. Uncertainty analysis

Uncertainty analysis is proposed according to [26]. Considering each parameter are independent, the principle of data reduction equation for a PIV measurement is the systematic uncertainty is given by:

$$\delta V = \sqrt{\left(\frac{\partial V}{\partial Mag}\right)^2 \delta Mag^2 + \left(\frac{\partial V}{\partial \Delta X}\right)^2 \delta \Delta X^2 + \left(\frac{\partial V}{\partial \Delta t}\right)^2 \delta \Delta t^2} \quad (1)$$

where V is estimated flow velocity, M is magnification factor, ΔX and Δt are displacement of particle and separation time between consecutive images, respectively. Partial derivative terms are sensitivity factors of corresponding parameters. The summary of systematic uncertainty is listed in Table. 3.
Random error was estimated at each interrogation window by 95 % confidence interval of mean of all instantaneous velocity field data. Finally, combined uncertainty was calculated at each PLA vector plot. The maximum uncertainty excluding perimeter of ROI is estimated to 7.7 m/s and 6.9 m/s for axial and tangential velocities respectively.

4. Conclusion

Design and implementation of PIV measurement was carried out in the short-duration high-speed turbine test rig equipped with multi-geometry blade rotor in the von Karman Institute for Fluid Dynamics.
Rotor domain PLA technique presented capability of retrieving reliable vector fields those capture deterministic flow structure associated with rotor blade motion regardless original PIV images containing various rotor phases. The results were compared with RANS simulation, while the tangential velocity field provided good agreement, the axial components show discrepancy especially in rotor wake region. Possible causes of mismatch were discussed taking into account errors associated with test setup and errors underlying principle of PIV measurements.
Overall, the study demonstrated a promising potential of PIV measurement in short-duration high-speed turbine test rig. Considering its high spatial resolution and the measurement location which can be very close to the rotating blades, PIV is efficient and powerful measurement tool compared to points measurements which requires much more repeated tests to fill spatial measurement points.

Acknowledgments

The authors would like to acknowledge the Yoshida scholarship foundation for support of this study. We would like to thank Prof. Tony Arts for critical advices during experimental campaign, Argiris Alexopoulos and Sylvain Borrey for their help for installation of equipment and operation of the test facility. In addition, we would like to acknowledge the work of Srinath Srinivasan for investigation of image processing. Finally, our thanks go to Terence Boeyen and Oswald Divers for the manufacturing of the precision instrumentation.

Table 3: Systematic uncertainty

Parameter	Error sources	Source uncertainty		Sensitivity factor		Parameter uncertainty	
Mag	Calibration target resolution	0.025	mm	0.05	1/pixel	0.00125	4*mm/pixel
	Image distortion & Calibration fitting	0.3	pixel	-0.0025	mm/pixel^2	-0.00075	
	Misalignment of calibration target (translation)	1	mm	0.00017	1/pixel	0.00017	
	Misalignment of calibration target (angle)	2	deg	-0.05	mm/pixel	-0.0017	
ΔX	Cross correlation & Sub pixel interpolation	0.05	pixel	1	-	0.05	2*pixel
	Perspective & Out of plane component	0.1	pixel	1	-	0.1	
Δt	Pulse generator & Laser pulse fluctuation	4.0 E-9	s	1	-	4.0E-9	s
V	Magnification	0.0023	mm/pixel	2.0E+06 (@ V = 100 m/s)	pixel/s	4.56	m/s
	Pixel displacement	0.11	pixel	4.4E+04	mm/(pixel·s)	4.93	m/s
	Separation time	4E-9	s	-8.8E+10 (@V=100m/s)	mm/s^2	-0.35	m/s

References

[1] B. Cernat, M. Paty, C. Maesschalck, S. Lavagnoli, Experimental and Numerical Investigation of Optimized Blade Tip Shapes - Part1: Turbine Rainbow Rotor Testing and CFD Methods, no. ASME Turbo Expo, Lillestorm, Norway, 2018.

[2] B. Cernat, J. Pinho, M. Okada S. Lavagnoli, Experimental investigation of a high-speed turbine with rainbow rotor and rim seal purge flow. Part1: Turbine testing and numerical methods, no. ASME Turbo Expo, Rotterdam, 2022.

[3] R. Meynart, Mesure de champs de vitesse dcoulements fluides par analyse de suites d'images obtenues par diusion d'un feuillet lumineux, PhD Thesis, Universite libre de bruxelles, Brussels (Octber 1983).

[4] M. Raffel, Particle Image Velocimetry, Springer, Cham, 2018.

[5] S. Bhattacharya, R. A. Berdanier, P. P. Vlachos, N. L. Key, A New Particle Image Velocimetry Technique for Turbomachinery Applications, Journal of Turbomachinery 138 (12), 124501. doi:10.1115/1.4033672.

[6] J. Woisetschla¨ger, N. Mayrhofer, B. Hampel, H. Lang, W. Sanz, Laser-optical Investigation of Turbine Wake Flow, Experiments in Fluids 34 (2003) 371–378.

[7] R. D. Stieger, D. Hollis, H. P. Hodson, Unsteady Surface Pressures Due to Wake-Induced Transition in a Laminar Separation Bubble on a Low-Pressure Cascade, Journal of Turbomachinery 126 (2004) 544–550.

[8] H. Rehder, A. Dannhauer, Experimental Investigation of Turbine Leakage Flows on the 3D Flow Field and end Wall Heat Transfer, no. ASME Turbo Expo GT2006-90173, 2006.

[9] K. D. Gallier, P. B. Lawless, S. Fleeter, Development of the unsteady flow on a Turbine Rotor Platform Downstream of a Rim Seal, no. ASME Turbo Expo GT2004-53899, 2004.

[10] L. Porreca, Y. I. Yun, A. I. Kalfas, S. J. Song, R. S. Abhari, Investigation of 3D Unsteady Flows in a Two Stage Shrouded Axial Turbine Using Stereoscopic PIV and FRAP, no. ASME Turbo Expo GT2006-90752, 2006.

[11] P. Bryanston-Cross, C.E. Towers, The Application of Particle Image Veiocimetry (PIV) in a Short-Duration Transonic Annular Turbine Cascade, Journal of Turbomachinery 114 (1992) 504–509.

[12] M. Boerner, On the Challenge of Five-hole-probe Measurements at High Subsonic Mach Numbers in the Wake of Transonic Turbine Cascades, Journal of the Global Power and Propulsion Society 2 (2018) 453–464.

[13] S. Chemnitz, R. Niehuis, A Comparison of Turbulence Levels From Particle Image Velocimetry and Constant Temperature Anemometry Downstream of a Low-Pressure Turbine Cascade at High-Speed Flow Conditions, Journal of Turbomachinery 142 (2020) 071008.

[14] D. Inman, D. G. Cuadrado, V. Andreoli, J. Fisher, G. Paniagua, P. A. N. Aye-Addo, L. Bhatnagar, F. Lozano, T. Meyer, M. Bloxham, Particle Image Velocimetry in a High-Pressure Turbine Stage at Aerodynamically Engine Representative Conditions, Journal of Engineering for Gas Turbines and Power 143 (6), 061031. doi:10.1115/1.4049448.

[15] P. Bryanston-Cross, D. Udrea, G. Guenette, A. Epstein, E. d'Hoop, Whole-field visualisation and velocity measurement of an instantaneous transonic turbine flow, in: ICIASF'97 Record. International Congress on Instrumentation in Aerospace Simulation Facilities, 1997, pp. 278–286. doi:10.1109/ICIASF.1997.644690.

[16] E. Gottlich, J. Woisetschlager, Investigation of Vortex Shedding and Wake-Wake Interaction in a Transonic Turbine Stage Using Laser-Doppler-Velocimetry and Particle-Image-Velocimetry, Journal of Turbomachinery 128 178–187.

[17] D. Tisserant, F. A. E. Breugelmans, Rotor Blade-to-Blade Measurements Using Particle Image Velocimetry, Journal of Turbomachinery 119 (2) (1997) 176–181. doi:10.1115/1.2841096.

[18] M. P. Wernet, Development of digital particle imaging velocimetry for use in turbomachinery, Experiments in Fluids 28 (2) (2000) 97–115. doi:10.1007/s003480050015.

[19] G. Paniagua, C. Diverding, T. Arts, Review of the von Karman Institute Compression Tube Facility for Turbine Design, no. ASME Turbo Expo 2013: Turbine Technical Conference and Exposition, American Society of Mechanical Engineers, 2013.

[20] D. Schultz, U. of Oxford, A New Transient Cascade Facility for the Measurement of Heat Transfer Rates, Univ. Oxford Dept. Engineering Science - OUEL Report, University of Oxford.

[21] J. Woisetschläger, R. pecnik, E. Göttlich, Experimental and Numerical Flow Visualization in a Transonic Turbine, Journal of Visualization 11 (1) (2008) 95–102.

[22] S. Chemnitz, R. Niehuis, A Comparison of Turbulence Levels from PIV and CTA Downstream of a Low-Pressure Turbine Cascade at High-speed Flow Conditions, no. ASME Turbo Expo, Phoenix, Arizona, 2019.

[23] J. C.Tropea, A.Yarin, Handbook of Experimental Fluid Mechanics, Springer, 2007. doi:978-3-540-30299-5.

[24] R. Clift, Bubbles, Drops, and Particles, Academic Press, New York, 1978.

[25] R.Israel, D.E.Rosner, Use of a Generalized Stoles Number to Determine the Aerodynamic Capture Efficiency of Non-Stokesian Particles from a Compressible Gas Flow, Aerosol Science and Technology 2:1 (1982) 45–51.

[26] ITTC, Guideline on the Uncertainty Analysis for Particle Image Velocimetry, ITTC Quality System Manual, Recommended Procedures and Guidelines.

Thermal investigation of a pipe with heart-shaped dimples using liquid crystal thermography

Muhsin Can Akkurt

Environmental and Applied Fluid Dynamics, von Karman Institute for Fluid Dynamics, Belgium, muhsin.can.akkurt@vki.ac.be

Supervisor: Delphine Laboureur

Associate Professor, Environmental and Applied Fluid Dynamics Department, von Karman Institute for Fluid Dynamics, Belgium, delphine.laboureur@vki.ac.be

University Supervisor: Kevin M. Van Geem

Professor, Department of Materials, Textiles and Chemical Engineering, Ghent University, Belgium, Kevin.VanGeem@UGent.be

Abstract

The heat transfer improvements and the pressure drop characteristics in a circular channel with heart-shaped dimples were investigated using Liquid Crystals Thermography (LCT). The enhancement factor (EF) distributions were presented at a range of flow regimes of Re=20k-55k and compared with the heat transfer phenomenon in a bare circular channel. The results were also compared with those of the spherical dimpled and ribbed tubes examined previously.

Keywords: dimpled channels, enhancement factor, liquid crystals thermography, infrared thermography

1. Introduction

Steam cracking of hydrocarbons has been widely used in the chemical industry to produce light olefins such as ethylene, propylene and butadiene. The coke layer is formed on the internal walls of the tubular cracking reactors during the process leading to a decrease in heat transfer from furnace to the process gas and an increase in pressure drop as the flow area is reduced [1]. The operations need to be halted for decoking of the reactors when one of these negative effects becomes too big. To improve the process economics, the duration of this production interruption can be decreased by an improvement in wall heat transfer, which reduces the inner wall temperature of the reactor and thus coking formation.

A variety of heat transfer augmentation techniques, as for example rib turbulators, pin fins, dimpled surfaces, are recently employed in channel flows. The mechanism of wall heat transfer improvement in the channels is basically promoting turbulence and disturbing the boundary layer to be separated and reattached downstream the corresponding element [2].

On the other hand, the utilization of these techniques contributes to the rise in the pressure losses in the channels while augmenting the turbulence intensity and the local heat transfer. The pressure penalties have to be kept at minimum levels in the steam cracking reactors since the pressure penalties lead to additional compression power for the heat exchanger and negative effects on the selectivity of the required products in these reactors.

It is stated in many studies that dimpled surfaces provide heat transfer augmentation rates without significant pressure drops. Compared with other techniques, dimples have relatively low friction factors as they do not protrude in the flow field and produce remarkable form drag in the channels [2]. Afanasyev et al. [3] investigated spherical cavities on flat plates and found that the heat transfer is increased by 30-40% without a significant increase in skin friction. Similarly, Virgilio et al. [4] carried out an experimental study to investigate heat transfer enhancement in a channel with spherical dimples. They found that, although the skin friction coefficient of the dimpled channel is twice more than that of a bare tube, it is

half of a tube with discontinuous helixes. In the same study, it is concluded that the use of dimples is a promising method to enhance economic performance in tubular channels such as in chemical reactors, turbines' internal cooling channels, etc.

Furthermore, the effects of the shape and the size of cavities on the flow structures,(therefore on the heat transfer augmentations and pressure losses) have been investigated by several studies. Burgess and Ligrani [5] investigated the effect of the depth of dimples for Reynolds numbers ranging from 9540 to 74800. Experimental results including three different ratios of dimple depth to dimple print diameter showed that the augmentations of Nusselt numbers and friction factor increase as the dimple depth increase at all Reynolds numbers considered. These results were attributed to two main reasons. The vortices and ejected secondary flows become stronger and more intense (i) whereas magnitudes of turbulence production and turbulence transport increase (ii) as the dimple depth increases.

For further performances, the dimple shape optimizations were carried out by several studies in order to maximize the heat transfer whilst keeping the pressure penalties at minimum levels. Chen et al. [6] found by numerical investigation that asymmetric dimple of which deepest point of the spherical indentation is skewed in downstream has considerably higher heat transfer capacity compared to the spherical dimple despite keeping the pressure penalty at the same level. They also emphasized that for further performance developments, other dimple parameters are required to be optimized. Dedeyne et al. [10] carried out an optimization study with multiple design parameters such as width, height and curvature to obtain a dimple geometry that maximizes the performance of the wall modification to be used in steam cracking reactors. In the study, the performance was evaluated with heat transfer improvement, more uniform radial temperature profile, and low pressure drop through nonreactive simulations. It is found that heart-shaped dimples have better performance compared to spherical dimples. Next to this, they stated that the optimized shape can increase the TEF by more than 15% and decrease pressure drop by 20

On the other hand, the numerical studies and the optimization studies in corresponding geometries require experimental verifications providing accurate descriptions so that the simulations can be used to generate and evaluate further designs. Mayo et al. [7] provided well-documented experimental data for both heat transfer and flow field characteristics of turbulent flows in a helically corrugated circular channel using PIV and Liquid Crystals Thermography. They carried out steady state LCT and managed to obtain a detailed enhancement factor (EF) distribution across two consecutive helical ribs. However, the number of studies on heat transfer investigation of circular cooling channels with dimples is highly limited. Virgilio et al. [4] adapted the steady-state LCT to a pipe with spherical dimples to provide spatially resolved experimental data. The authors investigated local heat transfer fields measuring the inner wall temperatures across the entire tube at the flow regime range Re=20k-80k. However, literature still lacks spatially resolved heat transfer distribution on tubes with optimized dimples, such as teardrop, heart-like shapes, due to their complex geometries.

The objective of the current study is to provide spatially resolved heat transfer data to validate a turbulent flow in circular channel with heart-shaped dimples for reliable computations. A detailed EF distributions across three dimples at different locations were obtained at the range of Re=20k-65k. The inner and the outer wall temperatures were obtained using steady-state LCT and infrared camera, respectively. The test tube was scanned with an accuracy of ±0.010 mm to generate the thickness map across the three-dimensional complex cross-sections of the dimples. The map then was matched with the corresponding field of views to define the conductive heat transfer from the inner surfaces followed by the EF. The resulting heat transfer improvements were compared with the spherical dimples investigated by Virgilio et al. [4].

2. Experimental Setup

2.1. Facility

The heat transfer measurements were performed in the low-speed facility that was designed to investigate the heat transfer field in circular channels in the von Karman Institute. The facility is an open circuit operating with air as the working fluid (Fig. 1). The air flow is created in the pipeline with 15cm of inner diameter by a centrifugal fan which is placed at the facility's exit. The fan operates in the suction mode so that the air is pulled towards the test section through the inlet duct to avoid unsteadiness which would occur in the blower mode. The length of the duct is around 20 diameters to ensure obtaining a fully developed turbulent boundary layer before the air enters the test section. The test section, where the experiments are carried out, is made out of a transparent dimpled pipe

mounted on the pipeline. To get access to the pipe's interior surface, it is split into two parts, one smooth and one other dimpled.

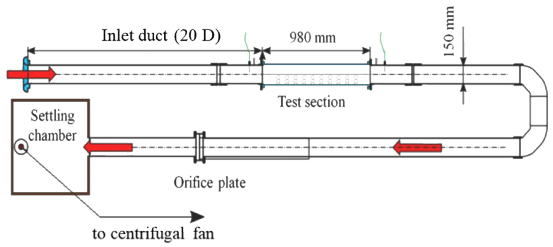

Figure 1: Facility

An orifice flowmeter is placed in the outlet duct mounted to the first section with a U-bend. The orifice flowmeter allows calculating the bulk velocity so that the flow rate can be regulated to set the Re number to a desired value between 20k-80k. Finally, a settling chamber is placed between the outlet duct and the centrifugal fan to dump the fluctuations resulting from the fan.

2.2. *Test section*

The side view of the test section (Fig. 2) shows the configuration used throughout the heat transfer measurements. This configuration allows an SLR camera(Nikon D7100) to record the inner surface temperature while the IR camera simultaneously measures the outer surface temperature for the same region. To avoid any reflections coming from the environment, the test section is surrounded by black painted panels. A rectangular area light source (Pan-70W) is placed parallel to the horizontal on the top of the test section so that the same light temperature can be achieved during both measurements and the calibration process. For the inner wall temperature measurements, around 10 microns of thermo-chromic liquid crystals (LCRHallcrest-SPN100 series) were sprayed on the inner surfaces of the dimpled half. TLCs are the tools that change color in response to temperature variations in range of around 33-55°C. The liquid crystal layer turns from colorless to red at the lowest operating temperature and, as the temperature increases, the color passes through the visible spectrum in succession (orange, yellow, green, blue, violet) before turning colorless again at the highest operating temperature. To improve the color contrast, a layer of black paint (LCRHallcrest-SPB100) is applied to the inner surface on the top of the liquid crystal layer. Similarly, the inner surface of the smooth tube was painted black without applying any liquid crystal layer.

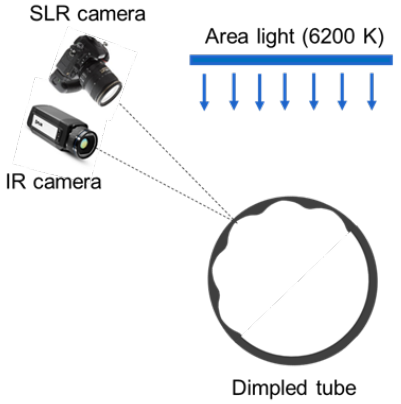

Figure 2: Measurement configuration

To generate heat flux, a transparent conductor film (Holland Shielding Systems, Copper-grid PET) with a transparency of around %85 was glued on the outer surface along the entire length. In this way, the colors scattered by the liquid crystal layer applied on the inner surface can be recorded by the SLR Camera from the outer surface side. A DC voltage is applied to the copper gridded film to generate a uniform heat flux. The cross-section of the dimpled tube is presented along with the schematic view of the layers in Fig. 3.

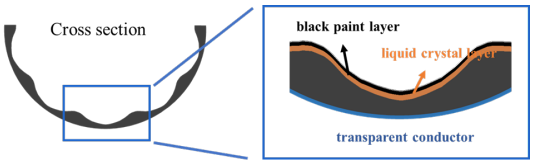

Figure 3: The cross section of the dimpled tube

2.3. *Calibrations*

First of all, two K-type thermocouples to measure the flow temperatures at the inlet, and the outlet of the test section and three K-type thermocouples as reference for the IR camera calibration were calibrated by using an oil bath.

The facility configuration used during the in-situ calibration of the other devices is presented in Fig. 4. Only the dimpled half was mounted to the pipeline with a 45° of rotation which is to be same position as in the measurements. The SLR camera was positioned around 1 meter away from the dimpled surface, at a 45° angle, such that the region of interest (ROI) could be inspected from the outside. The ROI in this

study consists of the area with the dimensions of 8cm in the axial direction and 24° in the azimuthal direction, containing a heart shaped dimple.



Figure 4: Calibration configuration

The infrared camera was installed on the other side of the pipe, with its axis azimuthally aligned with that of the other the SLR camera. The IR camera directly measures the temperature of the inner surface. Thus, the SLR camera can record the colors scattered by the liquid crystals applied, while the IR measures the inner surface temperatures. For the calibration function, the temperature values are taken from three thermocouples located at three different angular positions in the ROI considering that interested surface is curved. The output signal in the IR camera is chosen as the raw intensity unit as it corresponds to raw pixel data without any correction applied for any parameter such as emissivity, relative humidity, distance, etc. All the calibration points are put together to obtain the polynomial fitting for the IR camera calibration.

During the LCT calibration, all the camera parameters are set to the fixed values to be the same as in the measurements. To obtain required depth of field the camera lens is set the aperture f/14. ISO sensitivity is selected as 100 to provide highly saturated colors and therefore minimum uncertainty in the investigation of LC [4]. The white balance is set to 6200K, the same color temperature value as the light source. It is ensured that the IR camera records the same field of view (ROI) as the SLR camera, and 15 image pairs are recorded in the operating temperature range of the liquid crystals, between 33-55°C.

RGB (red-green-blue) intensities in each pixel element in the RGB images recorded by the SLR camera are converted into hue by using the Hollinsworth equation [8]. In this case, hue values depend on both the temperature and the coordinate because the curved surface of the outer wall and the complex surface of the inner wall affect the colors captured by the camera. Therefore, each hue is individually matched with the corresponding pixel in the temperature image recorded by IR the camera. As a result, a particular cubic spline curve consisting of 15 calibration points is obtained for each pixel in the image as shown for several pixels in Fig. 5.

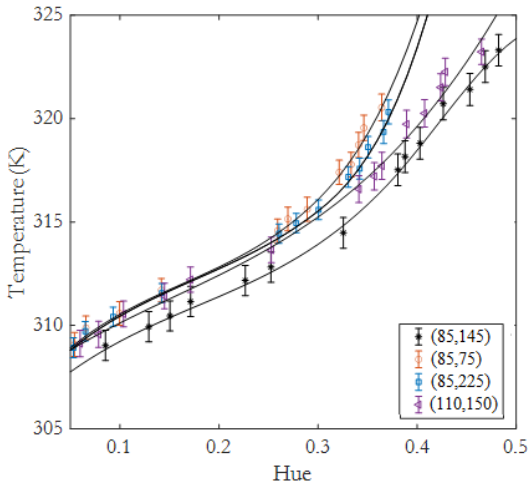

Figure 5: The calibration fits for some pixels

3. Data reduction

3.1. Data acquisition

The recordings of the measurements are taken at the steady state condition in Re=20k, 30k, 55k flow regimes, respectively. Since the voltage required for higher Re numbers may cause minor deformations on the gridded film, further measurements are not possible. The energy required to sustain the steady condition comes from the heat generated by a DC voltage applied to the transparent conductor. The generated energy ($\dot{q}_g$) is then transferred through the pipe by means of the heat conduction ($\dot{q}_{cond}$) as presented in Fig. 6.

However, a part of generated energy is lost due to natural convection from the outer surface to the ambient and the radiation. Applying conservation of energy to a control surface at the outer wall, the balance yields:

$$\dot{q}_g = \dot{q}_{cond} + \dot{q}_{nat.conv} + \dot{q}_{rad} \quad (1)$$

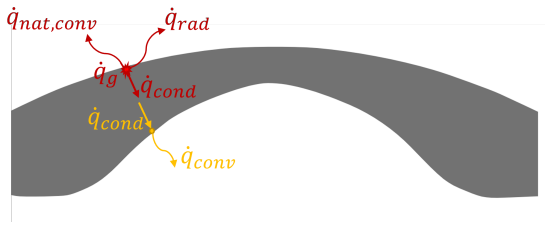

Figure 6: Control surfaces on the walls

The energy carried to the inner wall surface by heat conduction is transferred to the air flow in the channel by means of heat convection. The energy balance for the control surface at the inner wall takes the form

$$\dot{q}_{cond} = \dot{q}_{conv} \tag{2}$$

Once the system reaches steady conditions, IR camera and SLR camera record the same field of view for respectively the outer wall ($T_{w,out}$) and the inner wall ($T_{w,in}$) temperatures. Meanwhile, the air temperatures at the inlet and outlet of the test section are measured by k-type thermocouples located at the center of the pipe to define the bulk velocity (T_b). The heat transfer coefficient, h, for each element (pixels) in the ROI is calculated as:

$$h(x,\theta) = \frac{q_{conv}(x,\theta)}{T_{w,in}(x,\theta) - T_b(x)} \tag{3}$$

where q_{conv} is the convective heat transfer from the inner wall to the air per unit area, and x, and θ are the axial and azimuthal coordinates. T_b is calculated along the axial positions by a linear interpolation between the inlet and outlet temperatures. The convective heat transfer, $q_{conv}(x,\theta)$, is calculated by solving the 3D energy balance (Eq. 2) in both spherical coordinates (for the dimple surface) and cylindrical coordinates (for the smooth surface) as previously suggested [4]. The radial component of heat conduction is calculated for each element with the linear temperature assumption through the pipe. Therefore, the component can be expressed as

$$q_{cond,r} = -k_p(x)\frac{T_{w,out}(x,\theta) - T_{w,in}(x,\theta)}{l(x,\theta)} \tag{4}$$

where l is the pipe thickness, k_p is the conductivity of the pipe. The thickness of the pipe is obtained by scanning of the test section with an accuracy of +/- 0.01 mm and resolution of 0.03mm. The thickness values based on x and θ are then matched with the pixel values to obtain the thickness map throughout the dimple (Fig. 7).

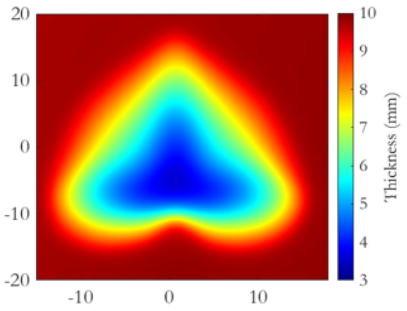

Figure 7: Pipe thickness around the dimple

Nusselt number field is defined as

$$Nu(x,\theta) = \frac{h(x,\theta)D}{k_f} \tag{5}$$

where k_f is the conductivity of the air at the film temperature and D is the pipe diameter.

The comparison of the local Nusselt number over the dimpled ROI with that of the smooth tube, is made through enhancement factor(EF), which is expressed as

$$EF(x,\theta) = \frac{Nu(x,\theta)}{Nu_0} \tag{6}$$

where Nu_0 is estimated using the Dittus-Boelter correlation suggested for fully developed flows in circular channels.

$$Nu_0 = 0.023Re^{0.8}Pr^{0.4} \tag{7}$$

3.2. Uncertainty Analysis

The uncertainty in the measurement of a quantity, which is Nusselt number in this case, can be a combination of systematic(b_{Nu}) and random(s_{Nu}) uncertainty and is expressed as [9]

$$u_{Nu} = \sqrt{{b_{Nu}}^2 + {s_{Nu}}^2} \tag{8}$$

Since many measurements are made to obtain the Nusselt number field, each uncertainty source must be accurately identified. Each source of measured quantities contributes to the uncertainty according to its sensitivity (S) to the Nusselt number. The overall systematic and random uncertainties associated with Nu are then be calculated as:

$$b_{Nu} = \sqrt{\sum_i (S_i b_{Nu,i})^2}, \tag{9}$$

$$s_{Nu} = \sqrt{\sum_i (S_i s_{Nu,i})^2} \tag{10}$$

3.2.1. Inner wall temperature uncertainty

The inner wall temperature is measured by liquid crystals thermography. RGB intensities of each pixel in the image recorded by the SLR camera are converted to the Hue values. Quantization errors for RGB values are expressed taking into account 8-bit resolution of the camera as:

$$b_R = b_G = b_B = \frac{255/2^{8+1}}{\sqrt{3}} \tag{11}$$

Therefore, the systematic error due to camera resolution can be calculated via

$$b_{T_{w,in},RGB} = \sqrt{\left(\frac{\partial H}{\partial R} b_R\right)^2 + \left(\frac{\partial H}{\partial G} b_G\right)^2 + \left(\frac{\partial H}{\partial B} b_B\right)^2} \tag{12}$$

Since all hue values are calibrated with the temperatures recorded by IR Camera, the fitting error between the IR camera signal and the measured temperatures, reading error, thermocouple uncertainties and the uncertainty resulted from the fact that the object signal deviate around the value need to be considered as the systematic uncertainty due to temperature measurement uncertainty by the IR Camera ($s_{T_{w,in},IR}$).

$$s_{T_{w,in},IR} = \sqrt{\left(u_{fitting,IR}\right)^2 + \left(u_{reading,IR}\right)^2 + \left(u_{tc,IR}\right)^2 + \left(u_{sdev,IR}\right)^2} \tag{13}$$

A cubic spline curves are used to fit 15 calibration points to obtain the final temperature values for each pixel, which yield pixel-wise random uncertainty (Eq. 14).

$$s_{T_{w,in},fitting}(x,\theta) = \sqrt{\frac{1}{N-1}\sum_{1}^{N}(T_{w,in,fitting} - T_{w,in,IR})^2} \tag{14}$$

The sensitivity of $T_{w,in}$ is calculated with the partial derivative of Nu number with respect to it as:

$$S_{T_{w,in}} = \frac{\partial Nu}{\partial T_{w,in}} = \frac{\partial Nu}{\partial h}\frac{\partial h}{\partial T_{w,in}} \tag{15}$$

3.2.2. Bulk temperature uncertainty

One of the terms required for the calculation of the heat transfer coefficient is the bulk temperature (T_b). As mentioned before, the temperature at each axial position is obtained by interpolating the temperature values measured at the center of the inlet and outlet pipe. Considering that the difference between these section is around 0.15K, the uncertainty is estimated as the thermocouple measurement uncertainty, 0.13K. The sensitivity of T_b is calculated as:

$$S_{T_b} = \frac{\partial Nu}{\partial T_b} = \frac{\partial Nu}{\partial h}\frac{\partial h}{\partial T_b} \tag{16}$$

3.2.3. Outer wall temperature uncertainty

The outer wall temperature $T_{w,out}$ is measured by IR camera to define the temperature potential in the heat conduction equation (Eq. 4). The uncertainty resulted from IR camera can be calculated as in the inner wall temperature. To define the contributions of its systematic and random uncertainties, the sensitivity of $T_{w,out}$ is calculated as:

$$S_{T_{w,out}} = \frac{\partial Nu}{\partial k_p} = \frac{\partial Nu}{\partial h}\frac{\partial h}{\partial q_{cov}}\frac{\partial q_{cov}}{\partial q_{cond}}\frac{\partial q_{cond}}{\partial T_{w,out}} \tag{17}$$

3.2.4. Pipe thickness uncertainty

Since the heat conduction from the wall is resolved for each pixel element, a thickness map, $l(x,\theta)$), is generated by 3D scanning of the test section. The accuracy of the process, +/-0.01 mm, is considered as the random uncertainty in the thickness whose sensitivity is defined as:

$$S_l = \frac{\partial Nu}{\partial l} = \frac{\partial Nu}{\partial h}\frac{\partial h}{\partial q_{cov}}\frac{\partial q_{cov}}{\partial q_{cond}}\frac{\partial q_{cond}}{\partial l} \tag{18}$$

3.2.5. Overall enfancement factor uncertainty

All the contributions are combined to define the standard uncertainty on Nu number (Eq. 8). The value is calculated pixel-by-pixel since some sources are pixel dependent such as the inner all temperature measurement made by the liquid crystals thermography which is the most dominant source.

The overall uncertainty on Nu number defined at a confidence level to 95% is expressed as ASME PTC 19.1-2005 suggest as:

$$U_{Nu,\%95}(x,\theta) = 2u_{Nu}(x,\theta) \tag{19}$$

Finally, the expanded uncertainty map on EF at the flow regime Re=20k is presented in Fig. 8.

The average EF in the investigated region is around 1.7 with an averaged expanded uncertainty of around 0.15. The maximum levels are located at the trailing edge of the dimple in the symmetry plane, where the deepest point of the dimple is skewed downstream. This is mainly due to the curve fitting uncertainties of the hue values around this complex region as the sharp angle changes make the color observation optically challenging.

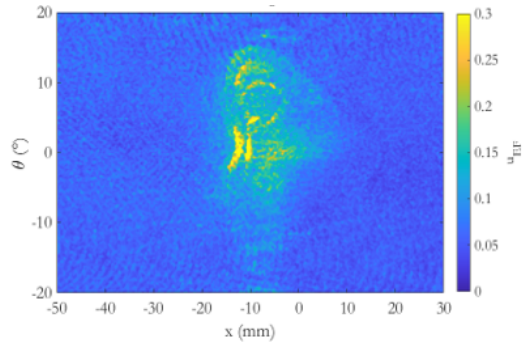

Figure 8: Uncertainty in EF around the region of interest

4. Results

The heat transfer improvement along the dimpled surface and the effects of Re number on this phenomenon are investigated through the enhancement factor distributions in this section. Firstly, the heat transfer phenomenon on the heart-shaped dimpled surface is described by the EF contour on the 9th dimple. To confirm the periodicity, the results are compared with the dimple just upstream. Subsequently, the effect of Reynolds number on the heat transfer from the dimpled surface is investigated. The pressure loss along the heart-shaped dimpled pipe is presented and the friction factors are compared with the other techniques along with the overall performances.

4.1. Heat transfer field on the surface

Fig. 9 shows EF field across the heart-shaped dimple that is located at the center in the 9th row at the flow regime of Re=20k.

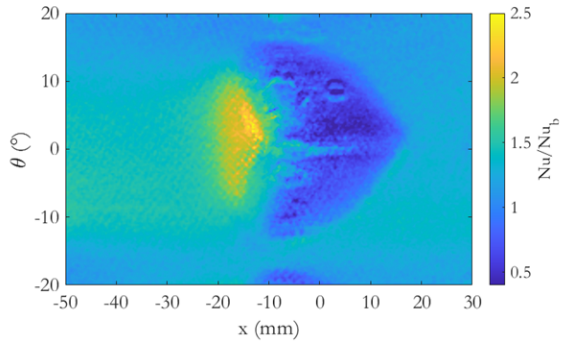

Figure 9: EF field around the heart shape at Re=20k

At the leading edge of the dimple, the separation region results in the EF values lower than unity, which means that the heat transfer rates are lower than that of bare tube.

These values remain below 1 throughout the circulation zone with the minimum value calculated as 0.68. As the flow is moving downstream in the dimple, EF rises above 1 and reaches around 1.64. The highest local heat transfer improvements are occurred at the trailing edge of the dimple, where the boundary layer reattaches to the wall. The maximum is found at the symmetry plane of the shape ($\theta = 0$), equal to 2.48. Behind the dimple, due to the thin boundary layer thickness, EF values are still above 1 and lie in the range of 1.5-2.5.

Detailed EF distribution along the azimuthal and axial planes for both 8th and 9th dimple surfaces are presented in respectively Fig. 10a and Fig. 10b to confirm the flow periodicity.

The figures show that the heat transfer behaviors are quite similar in both fields. All the axial posions agree that the maximum Nusselt numbers are located around the symmetry plane ($\theta = 0$). There is small deviation of the maximum Nusselt number location from the symmetry in both dimples (Fig. 10a). Similarly, Fig. 10a shows that the heat transfer from both dimples is mostly compatible with each other in the other direction as well. However, in Fig. 10b presenting the EF distribution along the symmetry plane shows there is a deviation around the trailing edge where the EF value reaches the maximum values. This is mainly resulted from the fact that EF values around the region are spread over a range due to the highest uncertainty levels.

4.2. The effect of Re number on EF

EF distributions along the axial direction at different angles are presented in Fig. 11a. Although all distributions substantially overlap, the flow regime, Re=20k, provides a slightly lower heat transfer rates for all planes.

The EF range of the asymmetric distributions that took place along all azimuthal locations gets narrower as the angle value increases, ie, as it moves away from the center. All the distributions have the plateaus at the downstream and upstream of the dimple. Compared to other planes, in the symmetry plane ($\theta = 0$), the difference between the heat transfer values in the downstream region and the upstream region of the pit is considerable large (around 1.8 at the downstream, 1.5 at the upstream).

As illustrated in Fig. 11b, each axial position provides similar EF profiles along the azimuthal direction. Re=20k has slightly lower heat transfer rates

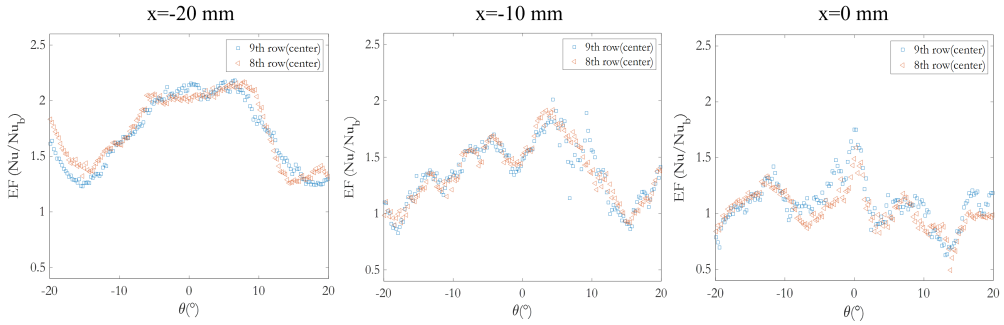

(a) EF distributions along axial direction

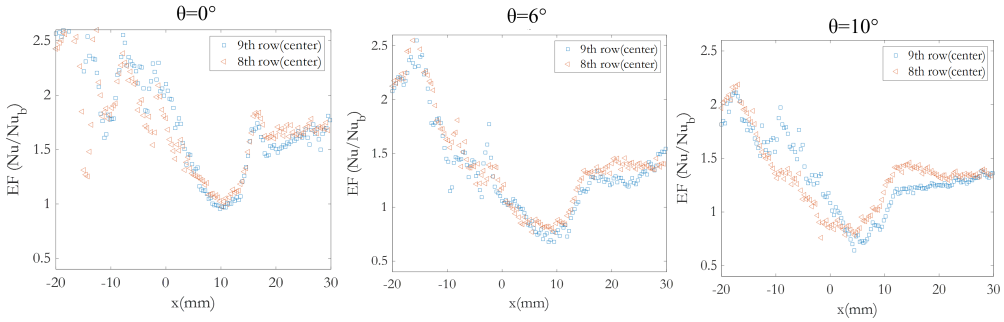

(b) EF distributions along azimuthal direction

Figure 10: Enhancement factor(EF) distributions for the dimples at 8th and 9th rows

compared with the others as it does the previous comparison above. Especially, the deviation of the EF profile is most prominent at x=0 in the region $\theta = -10 + 10$. For all profiles except x=10, the maximum values are located in the center. On contrary, at x=10mm the minimum levels of EF are accumulated around the symmetry plane because the flow is separated near the leading edge in a very narrow span.

4.3. Pressure loss and overall performance

The skin friction coefficients in the heart-shaped dimpled tube in the range of Re number=20k-80k are presented in Fig. 12 along with those of two different ribbed tubes and a tube with spherical dimples.

Dimpled tubes have significantly lower skin friction coefficients than the ribbed tubes while heart-shaped dimples causes slightly lower frictions compared to the spherical dimples. No significant effect of the Re number on the coefficient is observed as in the other techniques.

The Pareto chart in Fig. 13 shows EF values with the corresponding nondimensionalized skin friction coefficients (the value from the bare tube) for the overall performance comparison. Although they cause less pressure drops, heart shaped dimples could not outperform spherical dimples in terms of heat transfer. However, despite substantially reduced pressure penalties, heart shaped dimples provide at least as much heat transfer improvement as the ribbed tubes.

5. Conclusion

Liquid Crystals Thermography was implemented to investigate the heat transfer improvements and the pressure drop characteristics of a heart-shaped dimpled tube. The enhancement factor distributions were presented at a range of flow regime Re=20k-55k to define the thermal performance of the tube. It is found that the EF values are suddenly decreased at the leading at of the dimple and reaches the minimum, 0.57, inside the dimple. The value increases towards the trailing edge and the maximum value, 2.57, is measured at the end of the dimple where the flow reattaches to the wall. The enhancement factor is getting lower and lower as the flow develops. Varying Re number has a slight influence on the heat transfer improvement profiles. Although the general trend of the profiles is quite similar, Re=20k provides less heat transfer than the others, especially around the dimple

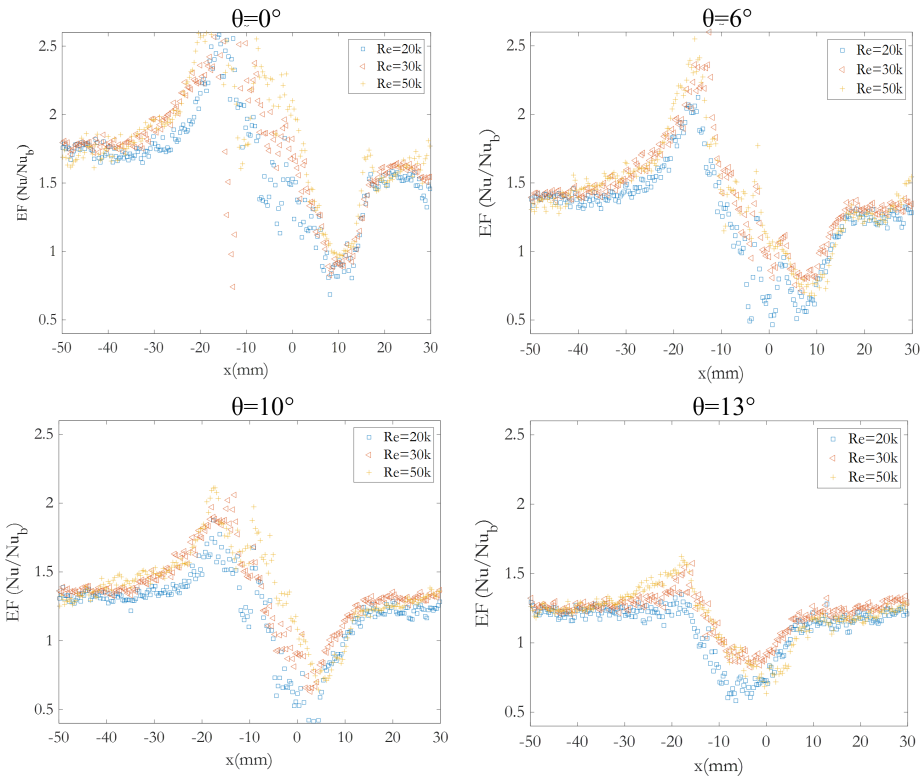

(a) EF distributions along axial direction

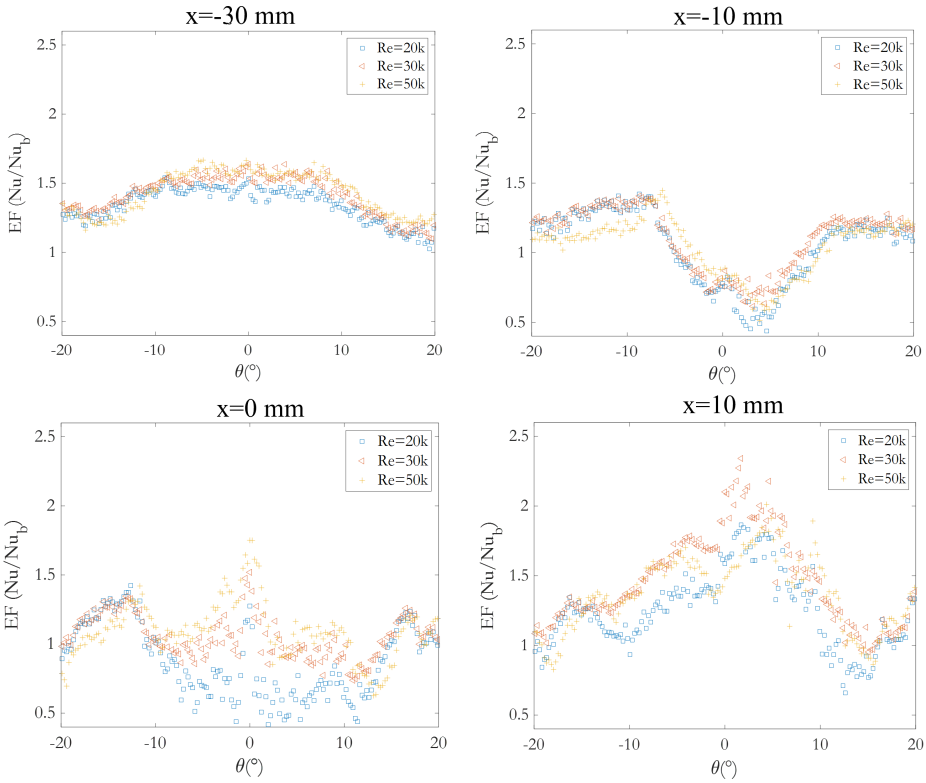

(b) EF distributions along azimuthal direction

Figure 11: Enhancement factor(EF) distributions for the dimples at Re=20k,30k,50k

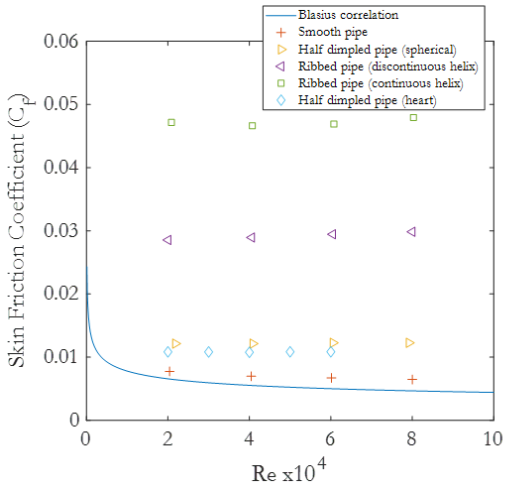

Figure 12: EF field around the heart shape at Re=20k

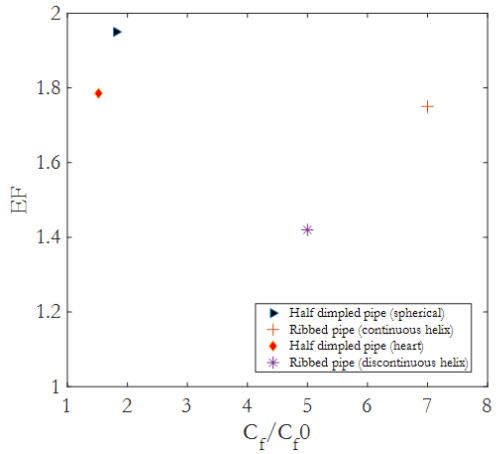

Figure 13: EF field around the heart shape at Re=20k

center. ROI averaged enhancement factors are calculated as 1.6-1.8 in the Re range. In the meantime, pressure drop measurements were performed to be compared with a spherical dimpled channel and two different ribbed channels. The skin friction coefficient was calculated as 0.04, which is the minimum value among the candidates. The experimental results in the flow regime of Re=20k-80k are considered as a useful dataset for the validation of numerical simulations.

References

[1] J. N. Dedeyne, M. Geerts, P. Reyniers, F. Wéry, K. Van Geem and G. Marin, Computational fluid dynamics-based optimization of dimpled steam cracking reactors for reduced CO_2 emissions, Transport Phenomena and Fluid Mechanics 66 (2020) 071702.

[2] P. M. Ligrani, M. M. Oliveira, T. Blaskovich, Comparison of Heat Transfer Augmentation Techniques, AIAA Journal 41 (3).

[3] V. N. Afanasyev, Y. P. Chudnovsky, A. I. Leontiev, P. S. Roganov, Turbulent Flow Friction and Heat Transfer Characteristics for Spherical Cavities on a Flat Plate, Experimental Thermal and Fluid Science 7 (1993) 1–8.

[4] M. Virgilio, J.N. Dedeyne, K.M. Van Geem, G.B. Marin, T. Arts, Dimples in turbulent pipe flows: experimental aerothermal investigation, International Journal of Heat and Mass Transfer 157.

[5] N. K. Burgess and P. M. Ligrani, Effects of dimple depth on channel nusselt numbers and friction factors, Journal of Heat Transfer 127 (2005) 839–847.

[6] Y. Chen, Y.T. Chew, B.C. Khoo, Enhancement of heat transfer in turbulent channel flow over dimpled surface, International Journal of Heat and Mass Transfer 55 (25-26) (2012) 8100–8121.

[7] I. Mayo, B. C. Cernat, M. Virgilio, A. Pappa, and T. Arts, Experimental investigation of the flow and heat transfer in a helically corrugated cooling channel, Journal of Heat Transfer 140 (7) (2018) 071702.

[8] B. Cukurel, C. Selcan, T. Arts, Color theory perception of steady wide band liquid crystal thermometry, Experimental Thermal and Fluid Science 39 (2012) 112–122.

[9] I. Mayo, M. Virgilio, B. C. Cernat, T. Arts, Measurement uncertainty in liquid crystal thermography applied to internal cooling research: Two practical examples, no. Proceeding of ASME Turbo Expo 2018: Turbine Technical Conference and Exposition, 2018.

Experimental analysis of natural convection in liquid metals

Tommaso Carlesi

Environmental and Applied Fluid Dynamics Department, von Karman Institute for Fluid Dynamics, Belgium
Belgian Nuclear Research Centre (SCK CEN), Institute for Advanced Nuclear Systems, Belgium
Electromagnetism and Telecommunication department, Université de Mons, Belgium
tommaso.carlesi@vki.ac.be

Supervisors: Delphine Laboureur and Philippe Planquart

Professor, Environmental and Applied Fluid Dynamics Department, von Karman Institute for Fluid Dynamics, Belgium
delphine.laboureur@vki.ac.be, Chief Project Office, philippe.planquart@vki.ac.be

SCK Supervisors: Julio Pacio and Katrien van Tichelen

Belgian Nuclear Research Centre, Institute for Advanced Nuclear Systems, Belgium
julio.pacio@sckcen.be, katrien.van.tichelen@sckcen.be

University Supervisor: Patrice Mégret

Professor, Electromagnetism and Telecommunication department, Université de Mons, Belgium
patrice.megret@umons.ac.be

Abstract

Turbulent heat fluxes (THFs) in liquid metals are an important factor in the determination of primary coolant temperatures in a nuclear reactor. Measurement of these fluxes is challenging as it requires simultaneous measurement of velocity and temperature fluctuations in an hostile environment. This work reviews and selects suitable techniques and presents the design choices of a natural convection Galinstan (GaInSn) facility.

Keywords: Liquid metals, Galinstan (GaInSn), natural convection, design of experiment, turbulent heat flux.

1. Introduction

This project is contextualized in the framework of the design and construction of the MYRRHA reactor (Multi-purpose hYbrid Research Reactor for High-tech Applications), a pool-type fast-spectrum research reactor under design at SCK CEN (the Belgian nuclear research center). In particular, this work aims at the understanding of the fluid dynamic behavior of its primary coolant, the Lead Bismuth Eutectic (LBE). In the RANS approach, Reynolds averaging of the energy equations results in an additional flux term, the turbulent heat flux (THF) $\overline{q_j^t}$ that appears as in Eq. 1:

$$\overline{q_j^t} = -\rho c_P \overline{T' u_j'} \tag{1}$$

This additional flux term represents the influence of the fluctuations over the averaging time period and strongly influences the temperature distribution inside the reactor. For the design and safety evaluation of MYRRHA, the temperature of the primary coolant must be assessed precisely, both for nominal operation (i.e. forced and mixed convection) and for accidental conditions (i.e. natural convection). This evaluation is performed with a combination of numerical simulations and scaled experiments for proof-of-principle and validation purposes [1]. Nowadays, techniques for the measurement of temperatures and velocities in opaque fluids like LBE allow to acquire data with good accuracy but with a limited spatial and/or temporal resolution. Moreover, no technique is currently available for the simultaneous measurement of these two quantities (i.e. for the THF) and for application in a liquid metal environment (high temperatures, chemical corrosion, ...). In this context, the focus of this Ph.D. is twofold:

- Develop a turbulent heat flux sensor (THFS)

suitable for THF measurements in liquid metals (EPICURUS, ExPerImental teChnique for tURbUlence in liquid metalS)

- Provide reference data for the development and validation of numerical models for THF in liquid metals

In fact, the instruments developed in this Ph.D. will provide unique information on the turbulent heat flux and will quantify the turbulent thermal diffusivity, which is a fundamental term in the modeling of turbulent heat transfer.

Two experimental setups thought for the study of natural and mixed convection are respectively shown in Fig. 1 and Fig. 2. The selected techniques are planned to be tested in both facilities, starting from natural convection.

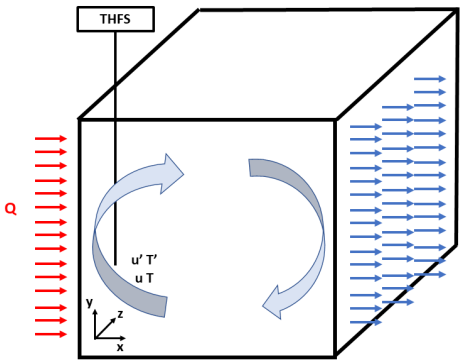

Figure 1: Natural convection setup

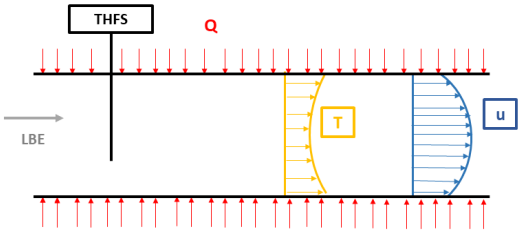

Figure 2: Mixed convection setup

A part of the different flow regimes established and the consequent design dissimilarities, the main difference between the two is the working fluid. While the mixed convection facility will use LBE as in the MYRRHA reactor, the natural convection setup operates with Galinstan (GaInSn), a low melting point liquid metal. Such a choice has been mainly made to ease the setup removing the high temperature challenges in the first stage of the experimental campaign. At the same time, from a thermal hydraulic point of view, the results obtained with GaInSn at ambient temperature are also relevant for LBE at higher temperature as the Prandtl number of the two metals is similar ($Pr_{\text{GaInSn}} = 0.021$ and $Pr_{LBE} = 0.025$). Despite of that, the compatibility with LBE in terms of wetting, corrosion, metal embrittlement, chemical compatibility, temperature etc. are not addressed in this initial test. On the other hand, as shown in Section 2, most of the instrumentation can be adequately coated or otherwise adapted to these conditions and consequently tested in LBE.

The current work is mainly focused on the results obtained from the extensive literature review that leads to a first selection of the suitable techniques. Velocity and temperature measurement techniques are analyzed separately in Section 2.1 and 2.2 and the motivations of the final choice are reported in Section 2.4. Moreover, a detailed description of the natural convection facility in Fig. 1 is reported in Section 3 and the design choices driven by theoretical calculations and numerical studies are motivated.

1.1. Requirements of the sensor

The THFSs must satisfy specific requirements in terms of spatial and temporal resolution, temperature and velocity measurement range and capability of withstanding high temperature and corrosive environment. All these characteristics must be translated in physical specifications that the sensor must meet.

First of all, it is important to understand what it is needed to be measured, therefore the values of the fluctuations that are possible to find in the metals. An overview of these flow features is reported in Fig. 3 where both the natural and forced convection characteristics are explained.

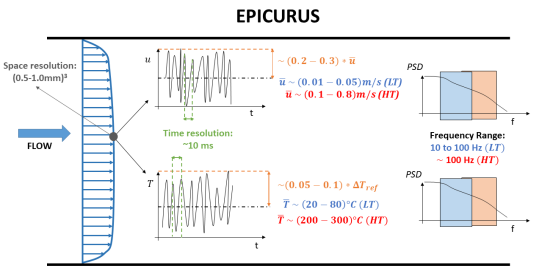

Figure 3: Summary of the EPICURUS-LT requirements.

The expected frequencies for temperature and velocity in LBE are between 10 Hz to 100 Hz for the natural convection regime and higher than 100 Hz for the forced convection regime [2; 3; 4]. This means that, depending on the flow regime chosen for the measurements, the quantity to be measured can change more than 100 times in a second. As a consequence, very strict time response requirements are established for the sensor (ideally lower than 10 ms) to be able to follow the fluctuations even in the fastest case. In general, this will translate into a small dimension of the sensor itself meeting also the constraints given by the spatial resolution. To avoid aliasing effects and alter the frequency content of the signal, it is also advisable to set the target frequency (and therefore the sensor capabilities) at least as double of the frequency of the physical phenomenon. At the same time, an appropriate acquisition system must be chosen. As a rule of thumb, the acquisition frequency should be roughly 10 times higher than the target frequency. A wise choice of commercial systems available on the market should be sufficient in this sense.

Another important feature of the fluctuations to be considered is their amplitude. The amplitudes of the velocity fluctuations are estimated to be as 20 – 30 % of the liquid metal absolute velocity while lower percentages around 10 % are expected for temperature when referred to a conveniently non-dimensionalized temperature [1; 4]. In particular, their relative amplitude seems to be influenced mainly by the Pr number [2; 5], meaning that differences in temperature and flow regime only determine minor changes. In the present case of natural convection expected velocities are in the range of $\mathrm{cm\,s^{-1}}$ [4]. While lower frequencies are usually easier to obtain experimentally, lower velocities are sometimes more complicated due to the higher accuracy and sensitivity required by the sensor. This is also a reason why it is not easy to find instrumentation capable of swiping a wide range of velocities.

The smallest scale of the turbulence that is interesting to measure determines the spatial resolution needed. In terms of instrumentation, this is directly related to the size of the sensor. The Kolmogorov scale has been estimated to be in the order of 10 µm for GaInSn in natural convection [6] and it is reasonable to think that a similar value can be obtained also in the LBE setup. These values are far smaller than the best achievable with experiments. Moreover, it is not meaningful to reach such small scales since no useful information about the dissipation rate could be deduced anyway. For this reason, numerical results and literature studies suggest that the best compromise would be to resolve turbulent structures with a 1 cm dimension meaning that the probes should have a spatial resolution in the order of 0.5 mm to 1 mm.

Moreover, it is important to underline that while the first stage of the experiments will be performed in a low melting point liquid metal (GaInSn), further stages foresee experiments in LBE. The requirements of the two, especially in terms of temperature and corrosion resistance, are generally different. In particular, characteristics like wetting and corrosion (due to chemistry and metal embrittlement) are very much dependent on the liquid metal itself and some materials that are compatible with GaInSn can be not compatible with LBE and vice versa. For this reason, it is difficult to give general specifications in this sense and every choice must be analyzed separately. Since the focus of this paper is on the natural convection setup, only a detailed overview of the compatibility of GaInSn with other materials is reported in Section 3.1.

2. State-of-the-art overview on measurement techniques in liquid metals

This section gives an overview of the state-of-the-art techniques used to measure velocity and temperature in liquid metals. The development of a turbulent heat flux sensor (THFS) will be a direct consequence of the selection of the most suitable instruments currently available since no new sensor will be built during this Ph.D. Therefore, this section analyzes and compares existing instruments through their advantages and disadvantages while used in liquid metals.

2.1. Velocity measurement techniques

In this section standard techniques for the measurement of the velocities in common flows are first analyzed with the idea of being adapted for liquid metals. Because of the opacity of LBE, optical techniques that are in principle capable of reaching the required spatial and temporal resolution with minimal intrusion, are impossible to use (e.g. time resolved PIV).

The use of a **Pitot tube** is possible and presents some advantages in terms of simplicity, accuracy and frequency response. These last two parameters are dependent on the pressure sensor used and accuracies of $5\,\mathrm{mm\,s^{-1}}$ and frequency responses up to 1 kHz have been obtained when combined with piezo-resistive transducers [7]. Unfortunately, high temperatures

complicate the direct use of piezo-resistive elements. The spatial resolution depends again on the probe size and its high intrusivity does not make it a very suitable candidate for the final measurements. Nevertheless, it could be used as a reference in support to other techniques for the measurement of average profiles.

Some attempts have also been made with coated **hot wires/films** [8; 9]. Their high frequency response, usually higher than 10 kHz for common applications, makes them a good choice for turbulent measurements but the special coating needed for liquid metals makes them less sensitive and increases their time response. Probably for these reasons, no literature has been found on their use in turbulent measurements in liquid metals. Moreover, intrusiveness due to the prongs and the support, is another drawback of this technique even if the small size of the sensor allows to get spatial resolution of the order of 0.1 mm. Coatings that are compatible with LBE can be found later in this report in the dedicated chapter. Similar considerations can be made for the hot sphere technique.

One of the most promising solutions seems to be the **Ultrasonic Doppler Velocimetry (UDV)**. Velocity measurements in liquid metals have been already performed successfully using pulsed UDV providing mean and fluctuating quantities [10]. In fact, its spatial resolution can be small enough for the current application whereas previous measurements suggest a frequency response higher than 60 Hz that could be in principle improved for small velocities. The advantage of the Ultrasonic Doppler Velocimetry is its applicability to opaque fluids, its non-intrusive nature and its distributed measurement capabilities (along a whole line corresponding to the axes of the sensor cylinder). The success of the technique in liquid metals is however not consistent and parameters influencing the success are not well understood. Amongst others wetting of the sensor to achieve good acoustic coupling and the need for scatters in the fluid need to be addressed.

Apart of these baseline methods, innovative techniques based on local measurements using the electromagnetic properties of the metal exist. Some of these are intrusive (e.g. **permanent magnet probes PMP**) but they can achieve a high temporal resolution, good accuracy and the possibility to measure a wide range of velocities [11]. As already cited in Section 2.3, acquisitions at 5000 Hz have been performed with this technique [12; 11]. Other novel techniques such as local **Lorentz Force Velocimetry (LFV)** and **Contactless Inductive Flow Tomography (CIFT)** can be considered as alternative methods. While they can allow 3D velocity fields without any perturbation of the flow, they cannot achieve a very high frequency response and also present some problems at very low velocities like the ones that the natural convection flow can show. The susceptibility of all of these probes to electromagnetic interferences must be also taken into account.

2.2. Temperature measurement techniques

Nowadays, temperature measurements in liquid metals are usually performed using **thermocouples** [13; 14]. Their temporal resolution can vary according to the type, allowing to achieve a resolution of the order of few milliseconds (e.g. with the coaxial types). The spatial resolution depends on the size of the sensor itself and it is usually of the order of the millimeter. Thermocouples provide data in a few selected positions and can perturb the flow in a not negligible way. The compatibility of the materials with LBE is also something to be aware of. Despite of that, their robustness, versatility and wide temperature range, far over the LBE operating temperatures (200 °C to 400 °C), make them the most common instrument used in LBE experiments nowadays.

To overcome some of the problems given by the thermocouples, newly developed **distributed temperature sensors based on fiber optics** technology can be used. Their minimal intrusivity and the material that they are composed off (usually glass, sometimes coated with metal) represent the main advantages in respect of the thermocouple. Moreover, they allow in principle to acquire temperatures with an accuracy of about 1 K, achieving a spatial resolution of 5 mm and a frequency response close to 150 Hz [15]. The latter values can be further improved with an accurate choice of size and material of the sensor.

Also fiber-based interferometry or **fiber Bragg gratings (FBGs)** can provide detailed temperature information in multiple locations along the optical fiber. The latter have been used at SCK CEN for the measurement of flow-induced vibrations in LBE at 200 °C. However, both fiber-based techniques still need to be developed for temperature measurements in liquid metals (>200 °C).

2.3. Simultaneous measurement of velocity and temperature

In order to perform a correct measurement of THFs, simultaneous measurement of velocity and temperature fluctuations are required. This is already a difficult task by itself, but the liquid metal environment

imposes additional challenges. Techniques for the individual measurement of velocities and temperatures in liquid metals exist but results of simultaneous measurements of these two quantities in such environment have not been published yet.

Recently, two experiments were successfully performed at low temperature [11; 16]. Because of the complexity of measurements in liquid metals, the first paper [16] uses transparent fluids such as the Helium-Xenon gas mixtures. Whereas these fluids allow a strong decrease in the Prandtl number ($Pr = 0.2$) with respect to the common fluids as water and air, the Prandtl number of LBE, $Pr = 0.025$, is still one order of magnitude lower. This has an impact on the importance of the turbulent heat flux and its modelling approach. In this work, temperature and velocity were measured simultaneously with a frequency of 75 Hz using a double probe combining a hot wire and a thermocouple designed and developed at the VKI. Because of the different thermophysical properties between the gas mixture and a liquid metal, the technique cannot be applied straightforward to the present case. Despite of that, the results still remain relevant. An application more similar to the current project is the turbulent measurement performed in a backward facing step in GaInSn with PMP (Permanent magnet probe) and type K thermocouples [11]. A full turbulent heat flux measurement is considered in principle possible with this technique but it has not been performed yet because the probes were sampled by two different measuring systems and only information about first order statistics were accessible.

2.4. Selection of measurement techniques

Regarding the velocity techniques, the Pitot tube has been considered not suitable for the measurements, mainly for a matter of spatial resolution, that is hard to keep smaller than 1 mm. Moreover, the high surface tension of the liquid metals, could give problems when filling the Pitot tube up to the sensitive part. If the metal is not in direct contact with the sensor, the measurement cannot be considered reliable.

The hot wire and the UDV have been both selected for this experiment. The former has proved to give very good performances when measuring turbulence and applications in liquid metals (even if not very recent) have been found in literature [17]. The intrusiveness given by the support and the prongs can be overcome with an accurate design of the facility and does not really affect the spatial resolution that is instead given by the dimensions of the sensor. In particular, the 90° bent hot film from DANTEC shown in Fig. 4 has been bought.

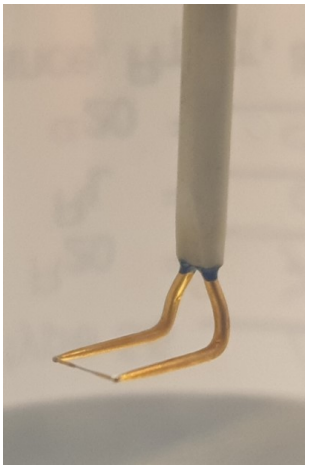

Figure 4: Dantec hot film

Its main characteristic is to have the sensitive part (a nickel film smaller than 1 μm) sputtered around a core in quartz and covered by another quartz layer that insures electrical insulation and protection. Since its maximum operating temperature is considered 150 °C, some problems could arise when applying this technology in LBE. Other coating solutions must be found by that time.

The UDV has proven to be one of the best technique for velocity measurements when optical access is not available. For this reason, its use in liquid metals is strongly supported by many literature studies [18; 19; 20]. Moreover, its maximum spatial resolution is 0.126 mm while its temporal resolution can arrive up to few ms. The main limitations will be given by low velocities and working environment and cannot be precisely predicted before. Despite of that, there is no reason to think that they cannot be overcome.

A final judgement about magnetic technique has not been really formulated. Deeper research is probably needed, even though the most suitable among them seems to be the PMP. The CIFT probably presents too low temporal resolution while the LFV does not give good performances when working at low velocities. None of them is planned to be used in this first stage of the experiments but further research can still be done and implemented.

Regarding temperature measurement techniques, thermocouples have been used in liquid metals for years and often with good results. Despite the difficulty of finding the best type, there is no reason why

they should not be tested in GaInSn and LBE. For GaInSn measurements, a K-type thermocouple with a time response around 30 ms will be tested. For LBE, a sheathed thermocouple with an external diameter of 0.1 mm has been already bought and it will be previously tested also in GaInSn.

FBGs have also been selected for the temperature measurements. Preliminary tests have shown that the time response of bare FBGs is even better than the one of unsheathed standard K-type thermocouples presenting similar dimensions and therefore intrusiveness and spatial resolution. Another big advantage is that, being made of glass, no particular problem should arise in terms of chemical corrosion. Moreover, applications of coated FBGs up to 500 °C is reported in literature.

To conclude, this selection was mainly made keeping in mind the first stage of experiments at low temperature. Despite of that, the above mentioned techniques can also be adapted to LBE to withstand the higher temperatures and the chemical corrosion. Moreover, this selection is still not considered finalized since some techniques can still be evaluated and implemented in the course of the Ph.D.

3. Test section design

In the first experimental campaign, natural convection is chosen as flow regime, not only because the turbulent frequencies are lower and the facility will be easier to operate [21], but mostly because validated turbulent models for natural convection are not available and experimental data for this flow regime are needed more. In literature, mainly two types of heated cavities have been used for natural convection studies:

- differentially heated cell
- Rayleigh-Bénard convection cell

In differentially heated cavities, one vertical side of the cavity is maintained at a constant higher temperature compared to the opposite side, while all other sides of the cavity are adiabatic. In contrast, in Rayleigh-Bénard convection cell, the bottom side of the cavity is maintained at a constant higher temperature compared to the top side. The flow features are slightly different between the two cases and the former setup has been chosen for the current experiment even though less studies are currently available [6]. Referring again to Fig. 1, it is possible to affirm that the temperature difference within the cavity causes a convection loop rotating in the direction from the warmer side towards the colder side [22]. Near the heated and cooled walls, the velocity approaches zero, while the thermal boundary layer is linear since the advection contribution is minimal and the heat is mainly transported by diffusion. Due to the strong mixing, the time-averaged temperature at the bulk is constant and is equal to the average between the controlled temperature sides. The Prandtl (Pr) and Grashof (Gr) numbers control the flow and the turbulence phenomena inside the cavity. In particular, increasing the Gr number promotes instabilities. Previous studies have shown a critical Grashof number of about 1×10^8 where the transition to turbulence in buoyant flows in cavities is expected [2; 23].

The first stage of the experiments will be conducted in a cubic differential heated cavity made of 316L steel with an edge of 60 mm in which natural convection is established through heated/cooled Peltier elements positioned oppositely on each side of the cavity in contact with two copper walls. Two fans are added to avoid overheating. Such a setup is shown in Fig. 5.

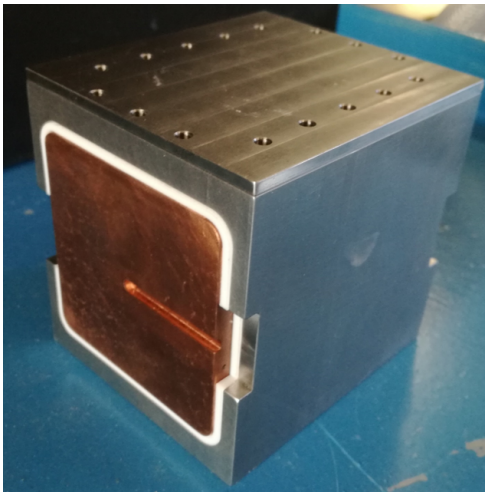

Figure 5: Natural convection setup

3.1. Galinstan

The metal used for this first phase of the project is Galinstan, a low melting point liquid metal (LMPLM). It is liquid at ambient temperature, presenting characteristics similar to mercury but with the big advantage of being not toxic. Thanks to its characteristics, it is more and more used in scientific works concerning liquid metals and electronics [24; 25; 26] and therefore reliable papers have been found addressing its properties [27] and general behaviour [28]. Its ther-

mophysical properties calculated for an average temperature of 50 °C are reported in Table 1[27].

Table 1: Main thermophysical properties of Galinstan

Property	Value
Thermal conductivity	$25.9\,\mathrm{W\,m^{-1}\,K^{-1}}$
Viscosity	1.85 mPa s
Surface tension	$586\,\mathrm{mN\,m^{-1}}$
Density	$6340\,\mathrm{kg\,m^{-3}}$
Specific heat	$296\,\mathrm{J\,kg^{-1}\,K^{-1}}$
Pr	0.021

A major issue with this metal is its fast oxidation that happens even with very low oxygen concentration (below 1ppm 0[28; 29; 30; 31] and in a very short time (below 1 minute) [32]. Too many oxydes can in fact affect the metal properties, the fluid behaviour [30] and ruin the instrumentation so their level must be kept as low as possible. Among the many papers reviewed, the best solution to this problem seem to be obtained with sofisticated gloveboxes capable of keeping oxygen and moisture levels below 1ppm [28; 33]. Mainly because of time and budget limitations, it has been decided to adopt first cheaper and faster solutions trying to deal with the small amount of oxides that could form. This could also be favourable for the UDV technique since the fluid has to be seeded (see Section 2). For this reason, it has been decided to limit as much as possible the contact between GaInSn and air (i.e. oxygen). Some papers underline the effectiveness of a hydrochloric acid vapor used as a cover since in this case the surface oxide is replaced with other alloys (e.g., $GaCl_3$ and $InCl_3$) [24; 31; 34] apparently less intrusive. On the other hand, the toxicity of this gas would negate the primary motivation of replacing mercury with Galinstan. Other works use acidified siloxane oils or electrochemical reduction methods to remove the oxydes and prevent their formation [32; 35]. In this work, the most feasible solution has been identified in using an inert gas layer (Nitrogen) that will cover the top part of the cell and that will shield the metal from the air. On the other hand, this solution will give additional challenges in the design and operation phase (see Section 3.3 and Section 3.4).

Another element to take into account when working in liquid metals is the harsh environment mainly given by high temperature, chemical corrosion and embrittlement phenomena. Working at low temperature usually facilitates the choice of materials since no chemical reactions are triggered or enhanced by this condition. Despite working at low temperature, some incompatibilities between GaInSn and other materials have been highlighted in previous studies. Some insights about this topic are given in this section, mainly to justify some of the design choices made in Section 3.3. Compatibility with stainless steel has been proved up to 200 °C [36]. Since the cell is made of 316L, no major compatibility problems arise for the walls of the cavity. The main issue is the use of copper plates as conductive materials for the heat and cold sides. In fact, it is proven that GaInSn cannot be used with brass, copper and aluminium even at ambient temperature since these materials tend to be corroded, especially for an exposure time in the order of hours [36]. For this reason a coating solution for the plates has been searched. Many works coated the copper with nickel and chromium of different thickness [37; 3]. For instance, layers of 20 µm of NiP_{12} and 2 µm of chromium to prevent the material from dissolving in the GaInSn has been used [37]. After having direct contact with the authors, it has been found that the Nickel layer did not really have any anti-corrosive function but it mainly had the function of intermediate layer between copper and chromium. As a compromise between cost and availability, the coating solution proposed by the University of Namur has been adopted. It consists in a 1 µm carbon coating deposited through magnetron sputtering and the following characteristics mainly lead to its choice.

- Max temperatures reachable: for this application, no more than 100°C should be needed but this coating can withstand up to 400°C.
- Thermal conductivity: the added layer will decrease the thermal conductivity of the copper since it will act as an added thermal resistance. However, due to its small thickness, it has been calculated that the thermal resistance of the layer will be 3 orders of magnitude lower than the one of the copper, therefore giving negligible effects on the heat transfer.
- Roughness: the manifacturing added some roughness to the surface giving a final average roughness of 26 nm. Overall, this can be considered good for the application since higher roughness corresponds to higher probability of enhancing the turbulence.
- Electrical insulation: the chosen solution is not electrically conductive but the current application does not need this property.

- Wettability: previous studies say that wetting is an issue with GaInSn but there is no reason to think that this particular coating should worsen the situation.

To conclude this overview, GaInSn compatibility with some plastics, especially PTFE, is not guaranteed [38] while general plastics that don't contain fluorine can be safely used [36].

All the aspects cited in this section have been taken into account during the design of the facility and the consequent choices will be further discussed in Section 3.3.

3.2. Numerical simulations

In the framework of the Research Master programme 2020-2021 at the VKI, some DNS simulations have been performed in a geometry that reproduces the one used in the natural convection setup [6] with the objective of reaching a better understanding of the turbulent transition in liquid metals. The main outcomes of this research concerns the velocity and temperature fields inside the cell. As shown by Fig. 6, the higher intensities in terms of THFs are concentrated close to the copper plates (i.e. the heated/cooled walls), in particular in the upper right and lower left corner. The same consideration could be done for the temperature fluctuations alone.

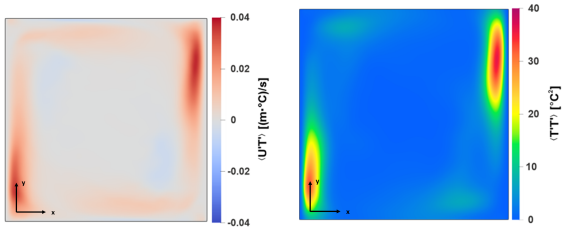

(a) Turbulent heat fluxes (b) Temperature fluctuations

Figure 6: Turbulent fields in the natural convection setup

Detailed recommendations in terms of design and probe placement can be deduced by these figures. In fact, the most interesting zones where the sensors should be placed are close to the walls. Here the turbulent phenomena are more accentuated and the higher amplitudes reached by temperature and velocity will be easier to measure. A summary of the fluctuations characteristics retrieved from the DNS simulation is reported in Table 2.

First of all, it is possible to see that a good agreement is reached between these values and the expected values from literature reported in Section 1.1.

Table 2: Fluctuations characteristics

Variable	Max frequency	Amplitude
Temperature	60 Hz	15 %
Velocity	30 Hz	16 %

The max frequencies for both quantities fall inside the predicted range. The amplitude percentages refer to non-dimensionalized quantities, respectively $(T_{max} - T_{mean})/T_{mean}$ and u_{mean} for temperature and velocity. To be noticed that the velocity fluctuation amplitude as defined above corresponds to the turbulent intensity. In particular, the temperature fluctuation amplitude seems to be slightly higher than expected and of the same order of magnitude of the velocity ones that, on the other hand, is lower than expected.

In further steps of the DNS simulation, some numerical probes have been installed to monitor velocity and temperature and obtain their evolution in time during the whole duration of the simulation. These points are shown in Fig. 7 overlapped with the non-dimensionalized velocity magnitude field in the cell.

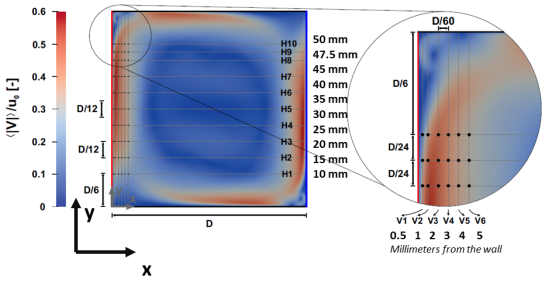

Figure 7: Monitored point location and non-dimensionalized velocity magnitude field in the cell

First of all, it is possible to notice that the velocity field also confirms that the most interesting zone of the flow are located close to the walls and maximum efforts should be made to place there the instrumentation. Furthermore, it is interesting to notice that a total of 60 numerical probes have been placed, focusing in a zone close to the wall, swiping a range of 40 mm in the y direction and up to 5 mm from the wall in the x direction. In order to have a meaningful comparison with experiments, the same monitored points should be kept in the experimental campaign. The practical feasibility of this is discussed in the following sections.

3.3. Design of the cell

Starting from the basic design shown in Fig. 5, some modifications are needed to obtain a full-working setup. Some of them are related to the working fluid needs and are presented in Section 3.1. For instance, the incompatibility between the GaInSn and copper makes the use of a coating layer above the plates necessary. At the same time, working in a low oxygen environment added the need to avoid as much as possible the contact with air and therefore to work in a sealed cavity and controlled environment. As mentioned in Section 3.1, this issue has been solved by covering the metal with a layer of inert gas. The details about the filling procedure of the cavity are reported in Section 3.4.

Once these needs are addressed, the first thing to do is to create the instrumentation accesses in the cavity. A preliminary sketch of their position is reported in Fig. 8.

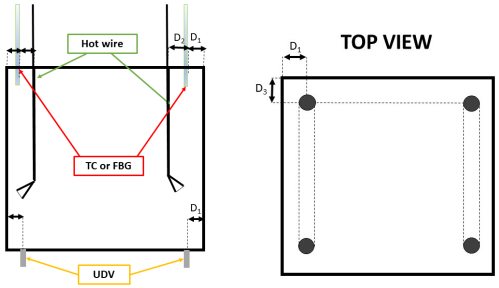

(a) Side view of the instrumentation accesses

(b) Top view of the instrumentation accesses

Figure 8: Sketch of the instrumentation accesses in the cavity

It has been decided to access from the top with the hot wire and the temperature sensor, while the UDV access can be created on the bottom of the cell. Four holes have been made for each sensor so that four different positions can be explored vertically, each one at a distance $D_3 = 15$ mm from the adiabatic walls (Fig. 8 b). The first constraint given by the physics of the THF itself is the fact that temperature and velocity must be measured "at the same point". This is experimentally impossible and previous papers state that a distance of 1.5 mm between the temperature and the velocity sensor is already too large [16]. The 90° bent hot wire used in this work allows to get closer to the temperature sensor without being disturbed by the respective supports up to a distance between 0.5 mm to 1 mm (distance D_2 in Fig. 8a). At the same time, the UDV is placed such that the axes of the cylinder (i.e. the center of the ultrasonic beam) is in correspondence with the temperature sensor tip so that the last meaningful point of the velocity profile measured by the UDV coincides with the point where the temperature sensor acquires. In this case, distances even lower than 0.5 mm between the temperature and the velocity measurements can be obtained but particular attention to interference between the sensors should be given.

The DNS reported in Section 3.2 gave good insights about the best locations for the instrumentation. The first aspect to consider when evaluating numerical results for experiments is whether the suggestions given by the simulations are practically feasible. In fact, given the dimensions of the probes and the limitations of the manufacturing process, it has been impossible to place all the probes in all the 60 locations identified by the DNS. For this reason, it has been decided to select just one distance from the wall (D_1 in Fig. 8) and to move vertically along this distance so that at least 10 vertical locations and 1 horizontal location could be covered. As already mentioned in Section 3.2, the results in Fig. 7 show that the most interesting flow features can be captured close to the wall. Trying to get as close as possible and keeping in mind the constraints given by the instrumentation dimension, the best compromise has been found in a distance $D_1 = 4$ mm. The temperature sensor and the axis of the UDV sensor are therefore aligned in this location while the sensitive part of the hot wire, thanks to its 90° bent, is located at less than 0.5 mm from this axis.

One last important point about instrumentation access is given by the fact that all the accesses must maintain the sealing but at the same time the sensors must be able to move vertically in order to measure along the whole profile. This has been obtained by using nitrile butadiene rubber (NBR) O-rings with specific diameters that guarantee the sealing.

To conclude, an electrical motor is placed on the top of the cell so that the probes can be automatically moved vertically and controlled more precisely. A support in stainless steel is therefore needed to keep all these elements together and to keep the cell raised from the ground level. All these final adjustments lead to the facility shown in Fig. 9.

3.4. Filling procedure

The definition of a detailed filling procedure is currently on going but first insights about it are given in this section. The cell has three different accesses for valves that can be used for gases or liquids. The two on the top are thought to be used respectively for

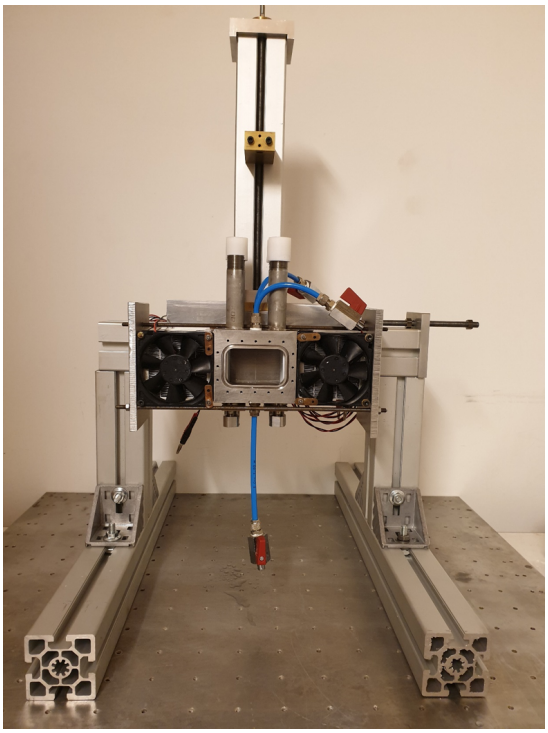

Figure 9: Final experimental setup for GaInSn in natural convection

GaInSn and for the inert gas while the one on the bottom will be used to empty the cavity once that campaign is over. First of all, it is needed to create the low oxygen environment needed. As mentioned in Section 3.1, this issue has been resolved removing the air from the cell and then filling it with Nitrogen. As shown in Fig. 10, this cycle is repeated for at least three times in order to obtain the lowest concentration possible of oxygen.

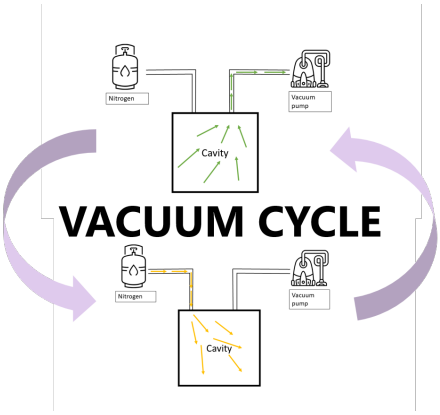

Figure 10: Schematic of the vacuum cycle

After that, GaInSn is introduced from the top. This procedure should be done very slowly since it would be dangerous for the instrumentation if some air bubbles were incorporated in the flow. The quality of the measurements could also be deeply affected. To be noticed that all this procedure should be performed with the instrumentation already inside the cell to be sure to avoid contact with oxygen.

4. Conclusion

This work addresses the issue of measurements of turbulent heat fluxes (THFs) in liquid metals, in particular as a support for the construction and design of the MYRRHA reactor. Despite the use of LBE as primary coolant in MYRRHA, this project considers as working fluid for the first stage of the experimental campaign the Galinstan, a low melting point liquid metal. The work here presented focuses on the preparation of these preliminary tests.

First of all, an overview on the state-of-the-art of the available velocity and temperature measurement techniques is presented. As a consequence of the analysis of advantages and disadvantages of each technique, a first selection has been done. Hot wire and UDV has been selected as the best techniques for velocity measurements, mainly because their spatial and temporal resolution, the strong in-house knowledge and their possibility of being adapted to LBE in further stages of the experimental campaign. Similar reasons lead to the choice of thermocouples and FBGs for temperature measurements.

The second part of this work focuses on the design of the cavity, the natural convection setup chosen for this part of the campaign. Some DNS simulations have been performed in order to find the optimal location for the probes. At the same time, constraints given by the GaInSn characteristics and by manufacturing requirements limited the practical possibilities. The best compromise found has been presented.

Further stages of the project foresee the first experiments performed in the cavity with water. This way the facility will be easier to operate and a good validation test case will be provided. Every issue that might rise will be easier to face and solve in water than in GaInSn. After this phase, the expected experiments in GaInSn will be performed and THFs data in liquid metals will be provided to validate numerical models. The second part of the project will be performed completely in LBE in a mixed convection facility currently under design at SCK CEN.

Nomenclature

Abbreviations and acronyms

GaInSn	Galinstan
HW	Hot wire
LBE	Lead Bismuth Eutectic
LMPLM	Low Melting Point Liquid Metal(s)
MYRRHA	Multi-purpose hYbrid Research Reactor for High-tech Applications
Pr	Prandtl number
RANS	Reynolds averaged Navier-Stokes equations
THF	Turbulent heat flux
THFS	Turbulent heat flux sensor
UDV	Ultrasonic Doppler Velocimetry
VKI	Von Karman Institute

Greek letters

μ	Dynamic viscosity ..... $[\mathrm{kg\,m^{-1}\,s^{-1}}]$
ρ	Density ..... $[\mathrm{kg\,m^{-3}}]$

Roman letters

c_p	Specific heat capacity .... $[\mathrm{J\,kg^{-1}\,K^{-1}}]$
k	Thermal conductivity .... $[\mathrm{W\,m^{-1}\,K^{-1}}]$
$\mathbf{r}$	Spatial coordinate (vector) ..... [m]
$\mathbf{u}$	Fluid velocity (vector) ..... $[\mathrm{m\,s^{-1}}]$

Subscripts

$'$	Turbulent fluctuations

Bibliography

[1] Katrien Van Tichelen, Graham Kennedy, Fabio Mirelli, Alessandro Marino, Antonio Toti, Davide Rozzia, Edoardo Cascioli, Steven Keijers, and Philippe Planquart. Advanced liquid-metal thermal-hydraulic research for MYRRHA. *Nuclear Technology*, 206(2):150–163, 2020.

[2] S. Cioni, S. Ciliberto, and J. Sommeria. Experimental study of high-Rayleigh-number convection in mercury and water. *Dynamics of Atmospheres and Oceans*, 24(1-4):117–127, January 1996.

[3] Tohru Takeshita, Takehiko Segawa, James A. Glazier, and Masaki Sano. Thermal turbulence in mercury. *Phys. Rev. Lett.*, 76:1465–1468, February 1996.

[4] Lilla Koloszár and Matilde Fiore. Assesment of low Prandtl heat transfer and its modeling. Technical Report DEMOCRITOS 3 Deliverable TR22, Von Karman Institute for Fluid Dynamics, 2020.

[5] Janet D. Scheel and Jörg Schumacher. Global and local statistics in turbulent convection at low Prandtl numbers. *Journal of Fluid Mechanics*, 802:147–173, 2016.

[6] Mohammed Alsailani. Numerical simulation of transition in liquid metals. Master's thesis, Von Karman Institute for Fluid Dynamics, 2021.

[7] Sven Eckert, Andreas Cramer, and Gunter Gerbeth. *Magnetohydrodynamics: historical evolution and trends*, chapter Velocity Measurement Techniques for Liquid Metal Flows, pages 275–294. Springer Netherlands, Dordrecht, 2007.

[8] Miklos Sajben. Hot wire anemometer in liquid mercury. *Review of Scientific Instruments*, 36(7):945–949, jul 1965.

[9] Donald Henry White. *An experimental investigation of natural convection heat transfer from vertical flat plates in mercury*. phdthesis, Oregon State Universiry, 1971.

[10] Sven Franke, Sven Eckert, Thomas Gundrum, and Gunter Gerbeth. Channel flow profile measurements at hot liquid metal loops by the Ultrasound Doppler method. In *9th International Symposium on Ultrasonic Doppler Methods for Fluid Mechanics and Fluid Engineering*, 2014.

[11] Thomas Schaub, Frederik Arbeiter, Wolfgang Hering, and Robert Stieglitz. Forced and mixed convection experiments in a confined vertical backward facing step at low-prandtl number. *Experiments in Fluids*, 63(1), dec 2021.

[12] Thomas Schaub, Sascha Wüstling, Joachim Konrad, and Michael Tasler. Design and calibration of permanent magnet probes for the local measurement of velocity and temperature in a liquid metal backward facing step flow. *Experiments in Fluids*, 62(10), sep 2021.

[13] Thomas Schulenberg and Robert Stieglitz. Flow measurement techniques in heavy liquid metals. *Nuclear Engineering and Design*, 240(9):2077–2087, 2010.

[14] Julio Pacio. Accuracy of type K thermocouples for tests in LBE – literature review on drift and calibration requirements. Technical Report SCKCEN 35204407, Belgian Nuclear Research Centre, 2019.

[15] Craig Gerardi, Nathan Bremer, Darius Lisowski, and Stephen Lomperski. Distributed temperature sensor testing in liquid sodium. *Nuclear Engineering and Design*, 312:59–65, February 2017. 16th International Topical Meeting on Nuclear Reactor Thermal Hydraulics.

[16] Sophia Buckingham. *Prandtl number effects in abruptly separated flows: LES and experiments on an unconfined backward facing step flow*. phdthesis, Université catholique de Louvain, August 2018.

[17] David G. Malcolm. *Thermo-anemometry in magnetohydrodynamics*. phdthesis, University of Warwick, 1968.

[18] Marc Dierckx. *Feasibility of ultrasonic inspection techniques for use in the MYRRHA reactor*. phdthesis, Katholieke Universiteit Leuven, 2014.

[19] S. Eckert, S. Franke, T. Gundrum, G. Gerbeth, and J.-C. Willemetz. Applications of Ultrasonic Doppler Velocimetry to flow measurements in hot liquid metals. In *8th International Conference on Electromagnetic Processing of Materials, Oct 2015, Cannes, France*, 2015.

[20] Yoshitaka Ueki, Yuya Noguchi, Juro Yagi, Teruya Tanaka, Takehiko Yokomine, Masaru Hirabayashi, Kuniaki Ara, Tomoaki Kunugi, and Akio Sagara. Ultrasonic Doppler Velocimetry experiment of lead-lithium flow with Oroshhi-2 loop. *Fusion Science and Technology*, pages 1–7, June 2017.

[21] NEA. *Handbook on lead-bismuth eutectic alloy and lead*

properties, materials compatibility, thermal-hydraulics and technologies. Nuclear Energy Agency, 2 edition, 2015.

[22] R. J. Janssen and R. A. W. M. Henkes. Influence of prandtl and number on and instability mechanisms and transition and in a differentially heated square cavity. *Journal of Fluid Mechanics*, 1994.

[23] J. A. Glazier and A. Naert. Evidence against ultrahard thermal turbulence at very high Rayleigh numbers. *Nature*, 398:307–310, 1999.

[24] Yi Chen, Justin L. Wagner, Paul A. Farias, Edward P. DeMauro, and Daniel R. Guildenbecher. Galinstan liquid metal breakup and droplet formation in a shock-induced crossflow. *International Journal of Multiphase Flow*, 106:147–163, 2018.

[25] Michael Knoblauch, Julian M. Hibberd, John C. Gray, and Aart J. E. van Bel. A galinstan expansion femtosyringe for microinjection of eukaryotic organelles and prokaryotes. *Nature Biotechnology*, 17(9):906–909, sep 1999.

[26] Marc Hodes, Rui Zhang, Lisa Steigerwalt Lam, Ross Wilcoxon, and Nate Lower. On the potential of Galinstan-based minichannel and minigap cooling. *IEEE Transactions on Components, Packaging and Manufacturing Technology*, 4(1):46–56, jan 2014.

[27] Yuriy Plevachuk, Vasyl Sklyarchuk, Sven Eckert, Gunter Gerbeth, and Rada Novakovic. Thermophysical properties of the liquid Ga-In-Sn eutectic alloy. *Journal of Chemical & Engineering Data*, 59(3):757–763, March 2014.

[28] Tingyi Liu, Prosenjit Sen, and Chang-Jin Kim. Characterization of nontoxic liquid-metal alloy Galinstan for applications in microdevices. *Journal of Microelectromechanical Systems*, 21(2):443–450, apr 2012.

[29] S.-K. Chen, Y.-M. Chen, and N. E. Todreas. The upgraded Cheng and Todreas correlation for pressure drop in hexagonal wire-wrapped rod bundles. *Nuclear Engineering and Design*, 335:356–373, 2018.

[30] Michael D. Dickey. Emerging applications of liquid metals featuring surface oxides. *ACS Applied Materials & Interfaces*, 6(21):18369–18379, 2014.

[31] Mohamamd Karbalaei Akbari, Francis Verpoort, and Serge Zhuiykov. State-of-the-art surface oxide semiconductors of liquid metals: an emerging platform for development of multifunctional two-dimensional materials. *Jurnal of Materials Chemistry A*, 9:34–73, 2021.

[32] Sarah Holcomb, Michael Brothers, Aaron Diebold, William Thatcher, David Mast, Christopher Tabor, and Jason Heikenfeld. Oxide-free actuation of gallium liquid metal alloys enabled by novel acidified siloxane oils. *Langmuir*, 32(48):12656–12663, 2016.

[33] Jan M. Chabala. Oxide-growth kinetics and fractal-like patterning across liquid gallium surfaces. *Physical Review B*, 46(18):11346–11357, November 1992.

[34] Daeyoung Kim, Peter Thissen, Gloria Viner, Dong-Weon Lee, Wonjae Choi, Yves J. Chabal, and Jeong-Bong (J. B.) Lee. Recovery of nonwetting characteristics by surface modification of gallium-based liquid metal droplets using hydrochloric acid vapor. *ACS Applied Materials & Interfaces*, 5(1):179–185, 2013.

[35] Mohammad Rashed Khan, Collin B. Eaker, Edmond F. Bowden, and Michael D. Dickey. Giant and switchable surface activity of liquid metal via surface oxidation. *Proceedings of the National Academy of Sciences*, 111(39):14047–14051, 2014.

[36] Philip Geddis, Lijun Wu, Andrew McDonald, Steven Chen, and Bruce Clements. Effect of static liquid Galinstan on common metals and non-metals at temperature up to 200 C. *Canadian Journal of Chemistry*, 98:787–798, 2020.

[37] Zacharias Stelzer. *Experimental and numerical study of electrically-driven MHD flow*. phdthesis, ETH Zürich, 2014.

[38] N. B. Morley, J. Burris, L. C. Cadwallader, and M. D. Nornberg. GaInSn usage in the research laboratory. *Review of Scientific Instruments*, 79(5):056107, 2008.

Comparative assessment of image processing techniques for optical flow based Background Oriented Schlieren

Bora Orcun Cakir

Turbomachinery and Propulsion Department, von Karman Institute for Fluid Dynamics, Belgium, bora.orcun.cakir@vki.ac.be

Sergio Lavagnoli

Associate Professor, Turbomachinery and Propulsion Department, von Karman Institute for Fluid Dynamics, Belgium, sergio.lavagnoli@vki.ac.be

Bayindir H. Saracoglu

Research Expert, Turbomachinery and Propulsion Department, von Karman Institute for Fluid Dynamics, Belgium, bayindir.saracoglu@vki.ac.be

Christer Fureby

Professor, Department of Energy Sciences, Lund University, Sweden, christer.fureby@energy.lth.se

Abstract

Computer vision community contributed with various image processing approaches to enhance the quality of optical flow estimations which provides a unique opportunity for quantiative visualizations of desnity varying flows with background oriented Schlieren. Accordingly, their infleunce on the displacement detection procedure is assessed comparatively using synthetic Gaussian density fields in both individually for identification of the relative gains and against the more conventional PIV based cross-correlation technique to showcase the improvement that can be achieved in the image processing stage of BOS with optical flow.

Keywords: Density varying flows, BOS, Optical flow, Computer vision

1. Introduction

Background oriented schlieren imaging (BOS) is of great interest to fluid dynamics researchers enabling quantitative characterization of density varying flows by means of an inexpensive and simple setup that can be utilized for both two and three-dimensional applications [1]. BOS systems perform these measurements by comparing a pair of recorded background images, one undisturbed referred to as the reference and one within the presence of density gradients. The displacement of rays in case of varying refractive indices are reconstructed typically via cross-correlation approaches developed for particle image velocimetry [2]. The corresponding displacement vectors represent the average refractive index variation within the field of view captured by blocks of pixels on the acquired images called interrogation windows (IW) [3]. Therefore, not only the resolution of resulting vector field is limited by the number of pixels within the IWs but also the intensity of the gradient information is prone to oversmoothening due to the averaging effects [4; 5].

Moreover, as the BOS measurements are increasingly employed for the development and validation studies of computational fluid dynamics models [6; 7], the PIV based BOS algorithms become vulnerable to fall short of the corresponding resolution and accuracy requirements. Nevertheless, this problem can be addressed by employing the optical flow (OF) image processing technique which defines the motion of objects within the image plane by means of brightness patterns [8]. The biggest advantage of using OF for BOS can be referred to as its capability to capture the displacement of each pixel which enables one vector-

per-pixel resolution which is proven to go beyond the resolution and accuracy characteristics of PIV algorithms for reconstructing density field information [9]. The only application of OF based BOS in high speed compressible flows is the natural background oriented schlieren application performed through in flight measurements by Heineck et al. [10] where the resolution characteristics in terms of reconstructing supersonic flow structures are demonstrated qualitatively. However, there is no previous attempt to perform quantitative assessments of similar flow behavior with BOS-OF. Considering the complexity of the models exposed to high speed flows, intensity of the localized density gradients and the varying scales of flow structures, BOS-OF provides a great opportunity to recover high fidelity density field data from quantitative visualization of supersonic/hypersonic flows.

2. BOS-OF

2.1. Optical Flow

There exist various approaches within the framework of OF analysis which can be distinguished into two different groups of gradient based and variational algorithms [11]. The common point of these methods is the brightness constancy assumption where the intensity of pixels moving within the image plane are assumed to the constant in both images [12].

$$\begin{aligned} I(x,y,t) &= I(x+\delta x, y+\delta y, t+\delta t) \\ &= I(x,y,t) + I_t + \delta x I_x + \delta y I_y \end{aligned} \quad (1)$$

Following a gradient based approach, the displacement of pixel intensities can be represented as functions of the temporal and spatial pixel intensity gradients. Nevertheless, the underdetermined structure of the resultant governing equation requires a problem closure to obtain a unique solution. Accordingly, Horn and Schunk [13] proposed a solution approach by addition of a regularization term constructed as the L2 norm of the optical velocity gradients enforcing global smoothness. Furthermore, the function to be minimized also included a quadratic penalization of the brightness constancy residuals which further increases the robustness of the algorithm against spurious displacement vectors [14].

$$E(\delta x, \delta y) = \sum \left[\rho_D(I_{t+\delta t} - I_t) + \lambda \rho_S(\nabla \delta x, \nabla \delta y)\right] \quad (2)$$

Upon the introduction of this classical approach, many alternatives and additions are proposed for improving the quality of displacement detection capabilities. Among them, some of the practices include image pre-processing for identifying texture layouts and mitigating illumination effects [15], hierarchical approaches for multi-scale reconstructions [16], various penalty functions for increasing robustness [17] and outlier detection&removal [18]. Although the performance characteristics of these approaches are assessed very comprehensively by Sun et al. [19], the exploration is only made from a computer vision perspective where the objectives and the utilization of optical flow algorithms differ from the experimental measurement technique of background oriented Schlieren.

2.2. BOS background generation

In order to enable capture the complete spatial-frequency spectrum of density gradients with elevated fidelity, a multi-resolution OF analysis approach is employed utilizing the image pyramid procedure introduced by Anandan [20]. In line with the iterative downsampling and warping of images following a coarse-to-fine resolution layout, a multi-scale background image is employed to avoid the short comings of random noise functions often used in BOS applications based on PIV post-processing strategies [1]. Hence, a wavelet noise background pattern proposed by Cook and DeRose [21] is utilized to construct a background image where the scaling factors of the hierarchical optical flow algorithm is matched to capture both large and small scale structures in high accuracy.

3. Image processing configurations

3.1. Image pre-filtering

The gradient based optical flow approaches rely on the local conservation of intensity values between the two images which is violated in many circumstances due to illumination changes, reflections, shadows and various types of noise. Hence, its common practice in OF applications to pre-process the acquired images prior to the detection of displacement vectors by means of various algorithms including smoothing of illuminations gradients and edge identification. Accordingly, many approaches are proposed that either require an estimate of the motion in the image plane and the brightness changes is to be performed simultaneously [22], or employment of image gradients to compose the time varying data term rather than the

intensity values [23]. However, while the former prevented the influence of shading artifacts to be taken into account, the letter suffered from the noisy nature of approximated intensity gradients over the images [24].

3.1.1. ROF texture decomposition

Therefore, Wedel et al. proposed a decomposition method identifying the intensity distributions in two components referred to as the structure and the texture [25]. This is achieved by utilizing the ROF model of variation based image denoising [26] which allowed the modelling of intensity variations due to various illumination artifacts such as shades, reflections and shadows. The intensity map corresponding to the structural part is determined by the ROF denoising in which the eliminated noise is treated to be the textural component. The denoising process acts as a high-pass filter and inherently trims out some of the highly detailed image content that contains artifacts related to sensor noise and sampling are stored in the textural components. Hence, optical flow processing using the structural component alone would eliminate them completely. Nevertheless, the large scale illumination variations due to shadow and shading reflections still persist in the structural component.

3.1.2. Sobel-edge detection

Dealing with illumination artifacts requires the illumination-dependent information within the images to be accounted rather than mapping the images with the assumption of illumination uniformity which is simply violated by the local nature of the artifacts [27]. Hence, similar to the structure-texture image decomposition approach, another alternative of utilizing the residual concept to distinguish the illumination variations due to the motion in the image plane from noisy artifacts is referred to as the Sobel-edge detection scheme [28]. Accordingly, the smoothed version of the original image is obtained employing the Sobel operator [29] as an edge-preserving smoothing filter. The residuals corresponding to the difference between the original image and its smoothed version is treated to be the additive noise while the smoothed version is referred to as the desired image to be processed. Even though the Sobel-Feldman operator is considered to be rather inaccurate among other edge-preserving pre-filters for approximating image gradients, its utilization is rather widespread in practical applications [30; 31].

3.1.3. Laplacian pre-filtering

Contrarily to the separable kernels employed within the Sobel-Feldman operator which induces an inherent independency of the image intensity gradients in horizontal and vertical directions, Laplacian pre-filtering approach utilizes a discrete Laplace operator which provides a measure of the two dimensional uniformity of 2nd order variations of the image intesities [32]. Thus, it determines the filter level based on the sum of spatial intensity differences between a central pixel and its neighboring pixels covering a 3x3 kernel. The corresponding Laplacian identifies the regions where abrupt intensity variations occur in the spatial domain which are referred to as the edges of the objects within the image plane [31]. Nonetheless, owing to the vulnerability of intensity gradients against noise, Laplacian filter is often employed alongside a smoothing filter such as a Gaussian pre-filter prior to the computation of derivative terms [33].

3.1.4. Gaussian pre-filtering

Smoothing an image by using a Gaussian filter (also referred to as the Gaussian blurring) low-pass filters the image to remove any noise associated with high image intensity variations (image derivatives corresponding to the high-frequency content within the images). Accordingly, employing a Gaussian pre-filter also causes the higher detailed structures to be filtered out [34]. It is performed by convoluting the intensity distribution maps of the original with a Gaussian function. Based on the size of the Gaussian function influence (the kernel of pixels) determined by the user provided standard deviation value, the image intensity variations become bounded by the convolution matrix extracted from the Gaussian profiles computed using the neighboring values of each pixel [35]. Gaussian pre-filtering often employed for the resampling process to ensure outliers associated with the high-frequency content within the images do not propagate through the downsampled layers, also known as aliasing [36].

3.2. Penalty functions

Due to the ill-posed nature of the optical flow problem, the underdetermined system of equations derived based on the brightness conservation within the image plane leads to the aperture problem [37]. Hence, gradient based approaches contain additional energy functions to close the system which include a penalization for the displacement vector residuals, enforcing brightness constancy.

3.2.1. Quadratic penalty function

Accordingly, the solution approach proposed by Horn and Schunk [13] included a quadratic function penalizing the displacement vectors corresponding to the deviations from the brightness constancy assumption. Nevertheless, such a definition is associated with two main disadvantages of not allowing any discontinuities in the displacement field and being vulnerable against outliers due to the non-robust nature. Owing to the unbounded formulation of a quadratic function, its influence on the energy function definition and the optimization procedure increase linearly without any limitations [38]. Since, the image gradients are time-averaged between the two images and the images always contain some level of noise, the inevitable deviations from the brightness constancy assumption dominates the extraction of motion in the image plane. Hence, its proposed by various researchers that they shall be replaced with non-quadratic counterparts to drive the optimization problem nonlinear. This is commonly performed by means of employing robust statistical approaches to reduce the weight of the outlier on the optimization process which would also enable an accurate treatment of optical flow discontinuities [39].

3.2.2. Lorentzian penalty function

In this regard, robustness is achieved by allowing the penalty functions, such as Lorentzian, to be more forgiving regarding the outlier scales function [40]. The Lorentzian function allows the penalty definition to be differentiable whose gradients approach to zero asymptotically. Hence, it provides a smoother transition between the outlying displacement vectors and the ones satisfying the brightness constancy assumption [41].

In order to construct the approximation of the energy function in a convex form to benefit the optimization procedure, the complete measurement set defining displacement vectors within the image plane is required to be considered free of outliers. Hence, the influence of outliers is identified by the inflection point of the second derivative of the penalty function. Accordingly, the standard deviation (σ) of a Lorentzian (non-convex by formulation) shall be selected in correlation with the maximum expected residual which would allow the derivatives of the penalty function to be bounded so that a convex form can be ensured. Thus, as the optimization procedure begins, the optical flow field is assumed to be free of any outliers, while they are gradually introduced by lowering the value of σ. Then, the minimization of the energy function can be repeated to allow the optimization process to act in accordance to the updated outlier information. Although this approach is reported to work well in many practical applications, converging to a global minimum can not be guaranteed since the initial approximation of the convex field of disc placement vectors in absence of outliers might be arbitrarily irrelevant with the actual vector field.

3.2.3. Charbonnier penalty function

Although there exits many other alternatives of non-quadratic penalty functions such as Lorentzian where handling of discontinuities and subtle treatment of outlier can be ensured. The definition of non-convex functions require case specific tailoring to confine the energy function within the convex regimes. Nevertheless, well-posedness of the optical flow problem can only be guaranteed with a convex penalty function by nature. Therefore, the use of Charbonnier penalty function is introduced by Bruhn et al. [42]. Thus, by means of utilizing a naturally convex penalization of the deviations within the displacement vector field from the brightness constancy assumption, a unique solution to the minimization of the energy function can be provided while global convergence is always satisfied [43].

3.3. Multiscale reconstruction

The biggest challenges related to the application of optical flow to achieve a high resolution global displacement field originate due to the practical image sequences containing multiple objects in motion within the image plane independently which also induces displacements significantly larger than one pixel. This causes the a global incoherence to occur in terms of the acquired image intensity variations that also contains discontinuities [44]. Hence, as the Taylor series approximation is employed to describe the nonlinear intensity variations based on a brightness constancy assumption, the linearized problem is only valid within the description of TSE. In other words, the derived set of governing equations is only valid for small displacements in absence of any discontinuities. Therefore, additional methods are required to relax the constraints on TSE based formulation of optical flow problem that would allow large displacements within the image plane to be reconstructed accurately [45; 46].

Accordingly, hierarchical algorithms are proposed to separate the computation of displacement vectors based on the scales of optical flow contained within

the processed images [20]. The acquired images are assumed to contain a wide spatial-frequency spectrum where the high amplitude (low spatial-frequency) intensity variations are represented by the large scale motion within the image plane while low amplitude (high spatial-frequency) intensity variation provide the detailed structures over a smaller range. Nevertheless, identification of these scales and separating them accordingly requires a proper control strategy since spatial-frequency decomposition based on the sampling rates of the lower-frequency information would lead to a loss of resolution [47]. Such a proper decomposition of the image intensities leads to a pyramid scheme that is composed of different spatial-frequency channels [48]. The pyramid is generated by consecutive downsampling of the original images by a factor of 2 until a certain resolution level based on the anticipated scale of largest motion is reached. Then, the displacement detection process begins by applying the optical flow at the smallest resolution image (lowest spatial-frequency component) and the displacement field is upsampled to the resolution of the next pyramid level to be subtracted from the image intensity variation by means of unwarping the image. The process is repeated until the pyramid level with the original acquired image resolution is reached.

3.4. Interpolation method and derivatives

As the multi-scale& multi-resolution displacement detection schemes are employed, pyramid levels are adjusted based on the spatial-frequency spectrum of image intensity variations. Hence, the images extract to construct the pyramid levels are generally not harmonics of the downsampled resolution scales which requires interpolations to be used for the non-integer pixel locations while transitioning between different levels of the image pyramid. Accordingly the choice of interpolation function has a great influence not only on the connection between the various spatial-frequency levels which significantly affects the success of a hierarchical algorithm but also on the sub-pixel accuracy of the displacement vectors that would relate to any loss of detail during the displacement detection process. Therefore, apart from convolution based the cubic interpolation [49], bi-linear [50] and spline based bi-cubic [51] interpolation functions can be used. While the use of a bi-linear interpolation function would reveal the importance of the order of accuracy, utilization of a spline based bi-cubic interpolation provides the employment of third order piecewise polynomials rather than 4x4 convolution kernels.

Moreover, numerical implementation of the optical flow approach is based on the computation of derivative terms for both the image intensity variations and displacement vectors which is performed utilizing finite difference (FD) approximation. Hence, the size of the FD kernels can be modified to increase the order of accuracy of the derivative descriptions which might have an impact on the fidelity of the displacement vector fields. Even though the classical formulation uses optimized derivative kernels which provides satisfactory accurate results [52], an alternative method of computing the image derivatives can be obtained by utilizing the spline based interpolation approaches for the warping process of intermediate pyramid stages. Since such an interpolation function would enable the simultaneous computation of image derivatives when the warping between intermediate levels of the pyramid structure is performed, an elevated level of consistency can be established between the warping and derivative computation procedures that would enable a lower energy solution to be achieved.

3.5. Outlier detection

The use median filtering is being introduced in optical flow algorithms to be used for nonlinear local filtering of random noise while preserving high intesity variation amplitudes that are considered to be associated with edges in the image sequences (i.e. structure-texture decomposition)[53]. The median filter identifies the median image intensity value of the pixels within a kernel of user defined size and assigns the central pixel of interest the intensity value of the median of the neighboring kernel [54]. This is performed by scanning the complete image with the median filter windows to prevent outlying signal entries acquired by the cameras in terms of image illumination intensities to be removed.

Employment of a median filter throughout the displacement detection scheme requires consecutive application of the median filter to each of the intermediate flow fields within the hierarchical algorithms which would increase the robustness of the optical flow method by avoiding the presence of outliers. As the median filtering approach alters the energy function to be minimized due to its effect on the outlier treatment, it introduces an additional non-local term to impose a new smoothness assumption within the kernel of its definition [55; 56]. Accordingly, the user defined size of the kernel has a significant influence on the detection and removal of outliers as well as increasing the dependence of each displacement vector on its neighboring elements. Nevertheless, it should

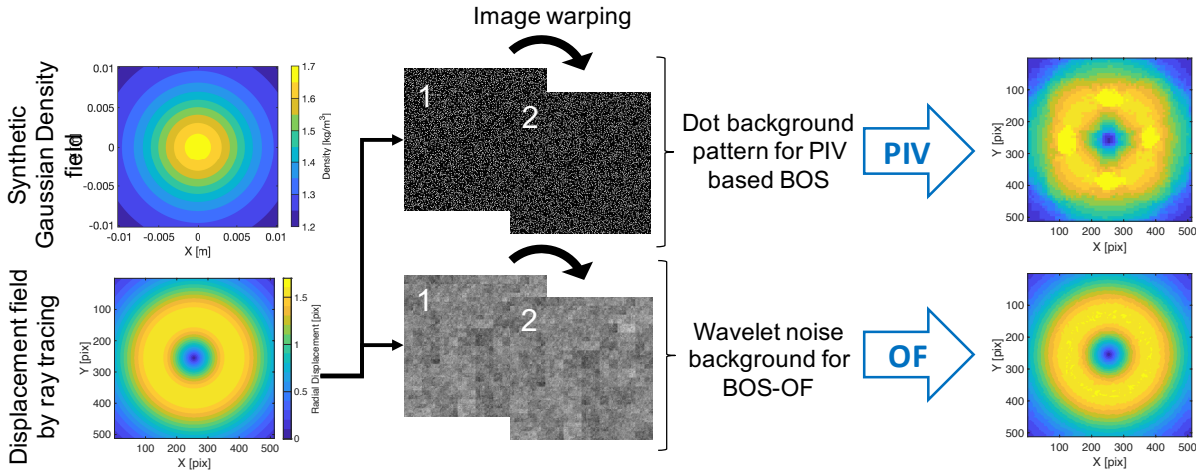

Figure 1: Schematic of the synthetic assessment framework. Density fields based on Gaussian functions are created and ray traced to extract displacement fields. Random dot and wavelet noise patterns are utilized to generate backgrounds that are warped using the synthetic displacement fields. The image pairs with random dot backgrounds are processed with cross-correlation algorithm while ones with wavelet noise backgrounds are processed with optical flow.

be noted that application of the median filter on the images requires proper consideration of certain factors such as filtering around boundary elements which might cause unnecessary cropping images [57].

4. Synthetic assessment

Comparative assessment of the image processing techniques for improving the optical flow reconstruction of displacement vectors within the BOS images is performed with a synthetic density field based on a Gaussian function which provides a wide range of density gradients that translates to low and high magnitudes of displacement vectors [58]. Three different synthetic density fields are created using different values of peak density field ,$\Delta\rho$, and standard deviation of the Gaussian field, σ. For all density fields, the ambient density, ρ_0 is kept constant at 1.225 kg/m3 to represent experimental setups using air. Then, two values of peak density is selected as $\Delta\rho$=0.45 and $\Delta\rho$=0.9, and two values of Gaussian standard deviations are selected to be σ=1/4 and σ=1/8 of the field of view. The BOS images with different background patterns are rendered via ray-tracing based image generation methodology, accounting the realistic experimental features of a BOS setup [59]. Accordingly, the dimensions of the density field is considered to be 10 mm3 and located at 0.25m from the respective background patterns where the image acquisition is assumed to be performed at a 0.5m distance from the background pattern utilizing a 105mm collimating lens which yielded a magnification factor of 40μm/pix.

Accordingly, due to the Superior performance of random dot backgrounds for PIV and wavelet noise backgrounds for OF, each background is selected to be employed for the corresponding displacement detection algorithms respectively. Since the more conventional displacement detection approach of cross-correlation based block matching algorithm to be used as a another metric for the improvements with optical flow based BOS to be assessed, the PIV based BOS is utilized to the best of its capabilities. Thus, for the PIV algorithm a multi-pass approach [60] is used with where the IW sizes and the overlap (OV) between the IWs are altered to obtain the minimum average end-point error (AEPE). As a result, a block shifting based cross-correlation approach is used with 3 iterations where the IW size is consecutively reduced from 32x32 to 8x8 while the OV is determined to be %50. Moreover, the sub-pixel interpolations are enabled to capture the displacement vectors with non-integer magnitudes while both standard deviation based global and median based local filtering approaches are also utilized for outlier removal.

Furthermore, the optical flow approaches with different configurations are initiated based on a baseline setup utilizing classical brightness constancy, no image pre-processing, quadratic penalty function, 6 pyramid levels, 6 warping iterations per level, convo-

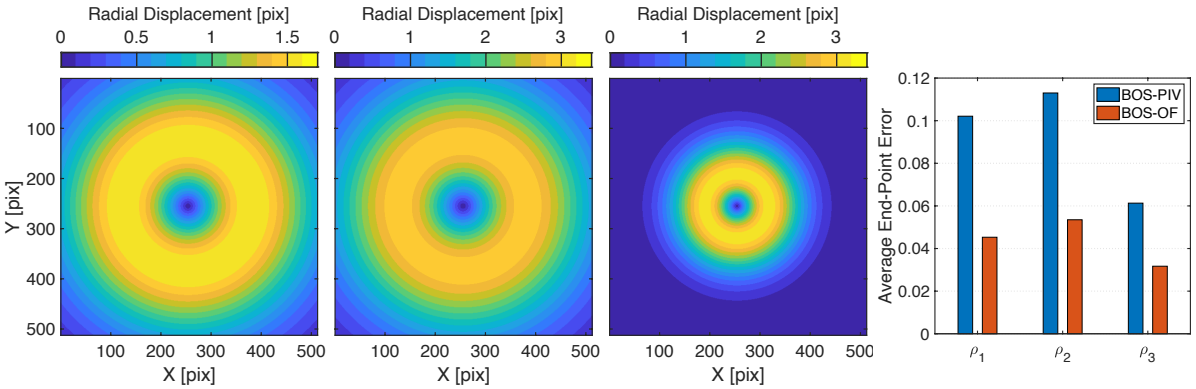

Figure 2: Synthetic displacement fields extracted based on Density Field I (left), Density Field II (left-middle) and Density Field III (right-middle) using the ray tracing approach. The average end-point error values of the displacement fields (right) reconstructed using cross-correlation (BOS-PIV) and optical flow (BOS-OF).

lution based cubic interpolations, 5-point FD stencil and 5x5 median filtering. The regularization parameter for the baseline configuration is first adjusted to obtain the lowest AEPE for each of the density fields to provide a comparable displacement detection fidelity with the PIV based approach [61]. Moreover, for each configuration of various image processing approaches, the corresponding stage of the baseline configuration is modified to incorporate the proposed alternative where the regularisation parameter is kept constant at a lower sub-optimal level to amplify the influence of each configuration induces over the resultant displacement fields. Accordingly, rest of the processing settings are kept constant to confine the comparison to the image processing technique of interest.

4.1. PIV vs OF

BOS measurements over flow fields with refractive index variations inevitably contain sub pixel level displacement vectors which causes a smearing effect on the dot background relating to the loss of brightness intensity of dots (Scarano, 2007). To represent this challenge, the each density field is selected to yield dominant displacement vectors with sub-pixel magnitudes along the vertical and horizontal axes and integer pixel displacement vector magnitudes per each direction along the diagonals of the FOV. While PIV with a random dot background suffers from overestimations along the vertical and horizontal axes, the local brightness constancy assumption of optical flow avoids this problem to interfere with the accuracy of the results. Furthermore, BOS-OF is able to recover both large scale (higher than 1 pixel) and small scale (smaller than 1 pixel) intensity displacements with the employment of a multi-scale background, since the wavelet noise allows a brightness pattern to be tracked rather than dots with constant illumination intensity. This comparison is valid for all three density field where BOS-OF is able to reconstruct the displacement vector with consistently lower AEPE values. The difference in terms of the AEPE values obtained with BOS-PIV and BOS-OF is recorded to be in correlation with the maximum displacement vector magnitude present at the field for constant radius of influence of the Gaussian function. When the standard deviation is reduced to halve the spatial influence domain of the function, the difference is observed to be reduced due to the zero displacement regions around the edges also contributing to the average error computation.

4.2. Image pre-processing

The selected pre-processing methods can be investigated into two main groups of residual based filtering and smoothness based filtering. Accordingly, residual based filters use the image intensity variation maps to identify high amplitudes of intensity derivatives and refer to them as high signal-to-noise ratio objects in the image plane. Then, these are stored in the image plane while the low amplitude variations are associated with random noise to be filtered out from the images prior to processing. Considering that all three density fields, and most of the BOS images, are free of discontinuities the residual based pre-processing approaches of ROF texture decomposition, Laplacian pre-filtering and Sobel-edge detection fail to improve the quality of the images prior to processing. Hence, the low level of displacement vectors, peaking at a

value of 3.4 for the Density Fields I&II, makes it even harder for the filtering approaches to distinguish between the low level intensity variations and the additive noise that is present throughout the synthetically acquired images. Therefore, both approaches cause the images to lose detailed displacement information so when the optical flow is applied, a certain level of detail is lost systematically for all three density fields. This similarity of ROF structure-texture decomposition and Laplacian pre-filtering is also reflected to the processing results using each method.

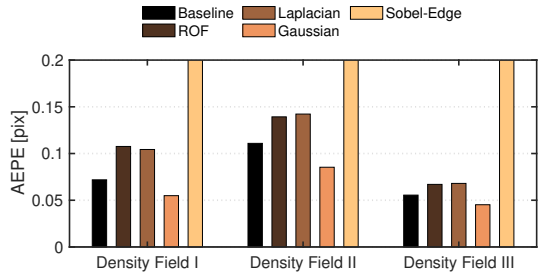

Figure 3: AEPE values of the reconstructed displacement fields with baseline optical flow (no image pre-processing) algorithm and various image processing approaches; ROF structure-texture decomposition, Laplacian pre-filtering, Gaussian pre-filtering and Sobel-Edge detection.

As opposed to residual based pre-filtering algorithms, Gaussian pre-filtering induces an overall smoothness over the images also referred as blurring. Hence, abrupt spatial changes in the image intensity distributions are removed from the images prior to the optical flow processing. This is the major difference between the residual based algorithms such as structure-texture decomposition where the the images are processed with a high-pass filter and the clean images favor high intensity variations to identify objects within the image plane. Whereas, Gaussian pre-filtering acts as a low-pass filter and prevents any discontinuities or large amplitude intensity variations to be removed from the images. Due to the fact that BOS images are free of discontinuities, even over strong density gradients induced by shock waves as proper acquisition of images consider the shock waves to be acquired with multiple pixels, and the synthetic images do not contain any discontinuities, Gaussian pre-filtering in the only approach that improves the image qualities prior to the optical flow processing stage to get rid of the additive noise in the images and yield lower AEPE values.

4.3. Penalty functions

The impact of changing the penalty function definition from a quadratic one to non-linear ones such as the Lorentzian or Charbonnier penalty functions is governed by treatment of the energy function which include a local smoothness consideration penalizing the gradients based on a L1 norm and the residuals that violate the brightness constancy assumption. However, total validity of this assumption cannot be ensured in most of the BOS images due to the realistic effects of illumination variations between the reference wind-off measurements and wind-on measurements with refractive index variations. Hence, due to the unbounded nature of a quadratic function, the influence of residuals representing the deviations from the brightness constancy assumption appear to be overpowering the energy function. This, leads to higher energy solutions of the minimization procedure that is associated with lower accuracy of the optical flow reconstruction.

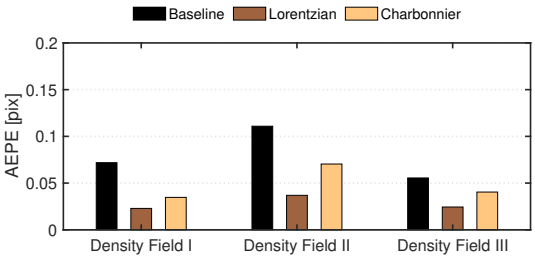

Figure 4: AEPE values of the reconstructed displacement fields with baseline (quadratic penalty function) optical flow algorithm and various penalty functions; Lorentzian and Charbonnier penalty functions.

Nevertheless, non-linear penalty functions solve this issue by not only bounding the actual function value itself based on the residuals but also bounding its derivatives which inherently modifies the optimization procedure to increase the emphasis on the equation set that governs the optical flow rather than the closure model that is required to solve the ill-posed problem. Hence, both Lorentzian and Charbonnier penalty functions allow the influence of the residuals on the governing set of equations to be limited to asymptotic values based on their definition which prevents energy function to grow unbounded and keeps the focus on the optical flow equations which eventually yields higher accuracy on the displacement field reconstruction.

4.4. Multiscale reconstruction

One of the main advantages of employing optical flow is that a multi-resolution and multi-scale reconstruction of motion features within the image plane especially when combined with a background that can provide a complete spatial-frequency spectrum. In this regard, utilizing backgrounds based on a wavelet noise pattern enables features that belong at different levels of the spectrum can be identified simultaneously without any loss of fidelity. Referring to the influence such a methodology has on the displacements induced by the synthetic density field, the difference between the configurations of a hierarchical algorithm is shown to be significant for an accurate optical flow reconstruction. In this regards, the influence of varying pyramid levels for the extraction of multiple spatial resolution scales in investigated over the three synthetic image pairs.

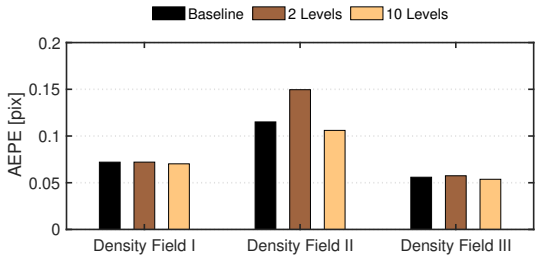

Figure 5: AEPE values of the reconstructed displacement fields with baseline (6 levels) optical flow algorithm and various pyramid levels; 3 levels and 10 levels.

Although for all three image pairs the trend of decreasing AEPE indicating more accurate reconstruction with increasing levels of the pyramid scheme is observed to be persistent. Two major deductions can be made comparing each image pair individually and among each other. First of all, it is obvious that the impact of varying pyramid levels is more profound for the Density Field II. This due to the fact that increased amplitude of the Guassian function without modifying the standard deviation (the measure of the perimeter the Gaussian function is effective) increases the maximum magnitude of displacement fields without altering the spatial domain of influence. Hence, the requirement on a multi layer scheme of a pyramid structure is more dominant for the Density Field II in order to ensure the accuracy is high. On the other hand, as for the Density Field III the standard deviation is lowered while the amplitude is kept constant the resultant displacement field composed an elevated amplitude of the maximum displacement field which is locally concentrated on a small region where the dominance of high spatial-frequency displacements observed. Hence, the influence of multiple scales in terms of resolution has a lower impact on the overall accuracy of the optical flow output.

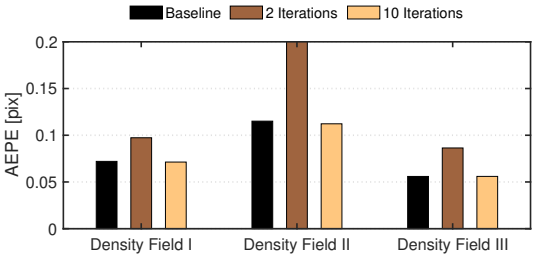

Figure 6: AEPE values of the reconstructed displacement fields with baseline (6 iterations) optical flow algorithm and various pyramid levels; 2 iterations and 10 iterations.

Furthermore, another factor of importance regarding the configuration of a multi-scale reconstruction approach is the intermediate interactions of warping within each level of the pyramid. As the image pyramid is only able to separate the spatial-frequency spectrum to discrete ranges, there are still multiple motion scales contained within each level that are required to be identified simultaneously. Contrarily to the number of pyramid levels, since each image pair and synthetic displacement field contains multiple scales regardless of their range in terms of amplitude, individual warping stages are required to make sure those scales can be captured. Nevertheless, similar to the case with pyramid levels, the effect of varying warping iterations is most profound for Density Field II.

4.5. Interpolation method and derivatives

The reduced accuracy of the bi-linear interpolation method obviously causes a decrease in the accuracy of the optical flow reconstructions which is persistently observed for all three density fields. Mainly in comparison to the baseline computations where the derivative computations are independent of the interpolation procedure, the method of choice only influences the size of the kernels for the interpolation matrix to be created. Hence, by reducing the amount of points switching from a cubic to a linear convolution matrix consistently reduces the amount of information used for the interpolations and relates to loss of sub-pixel displacements between multiple layers of the pyramid structure.

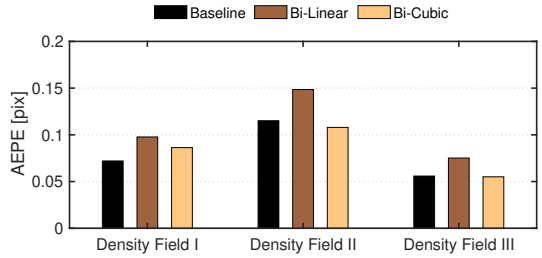

Figure 7: AEPE values of the reconstructed displacement fields with baseline (convolution based cubic) optical flow algorithm and various interpolation methods; convolution based bi-linear and spline based bi-cubic methods.

Comparing the convolution based and spline based cubic interpolation methods, an important result can be identified in comparison to the testing featured for computer vision. For high amplitude displacement vector magnitudes, using a spline based interpolation method indeed becomes more accurate since the increasing signal to noise ratio allows the splines to be constructed more robustly based on the of displacement vectors. However, for low levels of displacement vector magnitudes the signal-to-noise ratio becomes lower which increases the noisy data points to have a greater impact on the spline construction. Thus, the more simplistic approach of using a convolution matrix based on the neighboring intensity values increases the robustness of the sub-pixel interpolations between different levels of the pyramid structure.

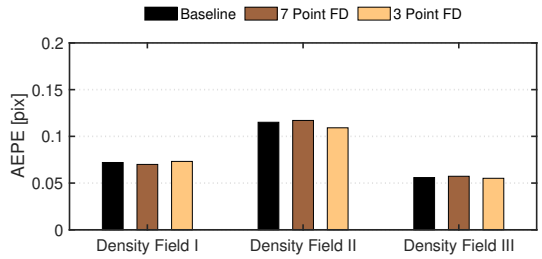

Figure 8: AEPE values of the reconstructed displacement fields with baseline (5-point) optical flow algorithm and various finite difference kernels; 7-point and 3-point.

Furthermore, the computation kernels for derivatives of image intensity variations are based on the finite difference approach where brightness constancy based optical flow reconstructions highly dependent on the accuracy of the derivative computations. In this regard, three levels of approximation accuracy orders are analyzed with baseline having a 5-point stencil, a 3-point stencil corresponding to central differencing approach and a 7-point stencil. With regards to their influence, two outcomes are observed for different density fields. Due to the lower magnitude of intensity variations at the second image of the image pair due to the refractive index variations, increasing the order of FD approximation provides a slight enhancement in the accuracy of the optical flow reconstructions. However, when the displacement vector magnitudes are increased for the Density Fields I & II, the enlarging size of the FD kernels try to induce the elevation of accuracy by incorporating more points into the stencil also increases the dependency of the derivative computations on the neighboring points. Hence, this disrupts the random image intensity distributions obtained with wavelet noise backgrounds and prevents the high amplitude image intensity variations due to the displacements to be lost during the optical flow computation.

4.6. Outlier detection

Presence of a median filter to perform outlier detection and removal allows the spurious displacement vectors to be eliminated throughout the optical flow procedure. This is observed to be favoring a high accuracy reconstruction especially when the median filtering is applied in an integrated fashion throughout the optical flow application at each layer of the multi-resolution scheme.

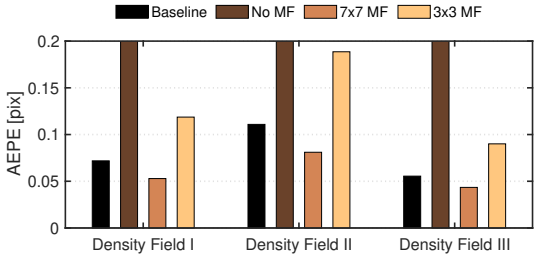

Figure 9: AEPE values of the reconstructed displacement fields with baseline (5x5 kernel) optical flow algorithm and various median filter configurations; no median filtering, 7x7 kernel and 3x3 kernel.

Moreover, the size of the kernel, based on which the filter is constructed, is also crucial for accurate determination of the displacement vector magnitudes. In this regard, expanding the size of the filter improves the quality of the resultant flow field to be more accurate by increasing amount of neighboring information on which the filter is based. Nevertheless, it should

be noted that this is strongly case dependent. In circumstances where high magnitude displacement vectors are present, that are captured within a perimeter of pixels smaller than the median filter size, the filtering approach might treat the displacement vectors to be outliers and remove them. Consequently, the detection of such fine structures might not be possible due to the induced smoothness by the median filtering approach.

5. Conclusion

Since the introduction of optical flow, numerous image processing approaches are introduced in order to elevate the quality of optical flow estimations for characterization of real life motion within the image plane of acquisition. Proposing the use of optical flow for background oriented Schlieren provides a promising possibility go beyond the capabilities of conventional block matching algorithms. Hence, exploration of these image processing techniques reveal a critical point for identification of correct practices that might be followed for high fidelity extraction of flow features in density varying environments. Thus, the various configurations and processing approaches referred in optical flow literature are gathered under 5 main groups and their influence on the displacement field reconstruction is analyzed.

First of all, image pre-processing is found to be a beneficial step for BOS-OF when a low-pass rather than a high-pass filter is selected. This is observed to be due to the absence of discontinuities in BOS imagery which causes the high-pass filters to fail as there is no abrupt intensity variation to identify and blurring effect of Gaussian pre-filter to smooth out the local spurious variations owing to the additive noise. Secondly, the penalty function definitions are observed to have a crucial influence on the success of optical flow processing where non-linear penalty functions allowed the contribution of residuals to be bounded and the brightness constancy relation to dominate the system of equations. Both non-linear penalty function provided a more accurate reconstruction as long as the convexity is ensured manually for the Lorentzian option. Furthermore, multi-scale reconstruction is shown to be the detrimental approach that provides the superior accuracy capabilities of optical flow to be inherited with appropriate multi-resolution backgrounds to ensure the complete spatial-frequency spectrum to be resolved. Moreover, the influence of the interpolation method choice to perform the transition between different levels of the image pyramids is dictated by the accuracy order of the interpolation function while spline based approaches are observed to be more accurate than the convolution based versions for high signal-to-noise ratio images. Finally, outlier treatment is of upmost importance as it is for the conventional PIV based cross-correlation method. The median filtering approach dealing with outliers proved to be essential with increasing size of the filters improving the accuracy of the reconstructions. Nevertheless, it shall be noted that smooth displacement fields extracted from the synthetic density fields are considered to be effective in these results regarding the outlier filtering size.

Acknowledgments

This project has received funding from the European Union's Horizon 2020 research and innovation programme under grant agreement No 101006856.

References

[1] M. Raffel, Background-oriented schlieren (bos) techniques, Experiments in Fluids 56 (3) (2015) 60. doi:10.1007/s00348-015-1927-5.

[2] J. Westerweel, Fundamentals of digital particle image velocimetry, Measurement Science and Technology 8 (12) (1997) 1379–1392. doi:10.1088/0957-0233/8/12/002.

[3] R. D. Keane, R. J. Adrian, Theory of cross-correlation analysis of piv images, Applied Scientific Research 49 (3) (1992) 191–215. doi:10.1007/BF00384623.

[4] G. E. Elsinga, B. W. van Oudheusden, F. Scarano, D. W. Watt, Assessment and application of quantitative schlieren methods: Calibrated color schlieren and background oriented schlieren, Experiments in Fluids 36 (2) (2004) 309–325. doi:10.1007/s00348-003-0724-8.

[5] M. J. Hargather, G. S. Settles, A comparison of three quantitative schlieren techniques, Optics and Lasers in Engineering 50 (1) (2012) 8–17, advances in Flow Visualization. doi:https://doi.org/10.1016/j.optlaseng.2011.05.012.

[6] D. Ramanah, S. Raghunath, D. J. Mee, T. Rösgen, P. A. Jacobs, Background oriented schlieren for flow visualisation in hypersonic impulse facilities, Shock Waves 17 (1) (2007) 65–70. doi:10.1007/s00193-007-0097-7.

[7] T. Kirmse, J. Agocs, A. Schröder, J. Martinez Schramm, S. Karl, K. Hannemann, Application of particle image velocimetry and the background-oriented schlieren technique in the high-enthalpy shock tunnel göttingen, Shock Waves 21 (3) (2011) 233–241. doi:10.1007/s00193-011-0314-2.

[8] E. Davies, Chapter 19 - motion, in: E. Davies (Ed.), Computer and Machine Vision (Fourth Edition), fourth edition Edition, Academic Press, Boston, 2012, pp. 505–522. doi:https://doi.org/10.1016/B978-0-12-386908-1.00019-7.

[9] B. Atcheson, W. Heidrich, I. Ihrke, An evaluation of optical flow algorithms for background oriented schlieren imaging, Experiments in Fluids 46 (3) (2009) 467–476. doi:10.1007/s00348-008-0572-7.

[10] J. T. Heineck, D. W. Banks, N. T. Smith, E. T. Schairer, P. S. Bean, T. Robillos, Background-oriented schlieren imaging of supersonic aircraft in flight, AIAA Journal 59 (1) (2021) 11–21. doi:10.2514/1.J059495.

[11] M. Zhai, X. Xiang, N. Lv, X. Kong, Optical flow and scene flow estimation: A survey, Pattern Recognition 114 (2021) 107861. doi:https://doi.org/10.1016/j.patcog.2021.107861.

[12] J. K. Kearney, W. B. Thompson, D. L. Boley, Optical flow estimation: An error analysis of gradient-based methods with local optimization, IEEE Transactions on Pattern Analysis and Machine Intelligence PAMI-9 (2) (1987) 229–244. doi:10.1109/TPAMI.1987.4767897.

[13] B. K. Horn, B. G. Schunck, Determining optical flow, Artificial Intelligence 17 (1) (1981) 185–203. doi:https://doi.org/10.1016/0004-3702(81)90024-2.

[14] J. L. Barron, D. J. Fleet, S. S. Beauchemin, Performance of optical flow techniques, International Journal of Computer Vision 12 (1) (1994) 43–77. doi:10.1007/BF01420984.

[15] N. Sharmin, R. Brad, Optimal filter estimation for lucas-kanade optical flow, Sensors (Basel, Switzerland) 12 (9) (2012) 12694–12709, pMC3478865[pmcid]. doi:10.3390/s120912694.

[16] S. H. Hwang, S. U. Lee, A hierarchical optical flow estimation algorithm based on the interlevel motion smoothness constraint, Pattern Recognition 26 (6) (1993) 939–952. doi:https://doi.org/10.1016/0031-3203(93)90059-6.

[17] P. Krähenbühl, V. Koltun, Efficient nonlocal regularization for optical flow, in: A. Fitzgibbon, S. Lazebnik, P. Perona, Y. Sato, C. Schmid (Eds.), Computer Vision – ECCV 2012, Springer Berlin Heidelberg, Berlin, Heidelberg, 2012, pp. 356–369.

[18] M. Yang, J. Tao, L. Shi, K. Mu, J. Che, An outlier rejection scheme for optical flow tracking, in: 2011 IEEE International Workshop on Machine Learning for Signal Processing, 2011, pp. 1–4. doi:10.1109/MLSP.2011.6064583.

[19] D. Sun, S. Roth, M. J. Black, A quantitative analysis of current practices in optical flow estimation and the principles behind them, International Journal of Computer Vision 106 (2) (2014) 115–137. doi:10.1007/s11263-013-0644-x.

[20] P. Anandan, A computational framework and an algorithm for the measurement of visual motion, International Journal of Computer Vision 2 (3) (1989) 283–310. doi:10.1007/BF00158167.

[21] R. L. Cook, T. DeRose, Wavelet noise, ACM Trans. Graph. 24 (3) (2005) 803–811. doi:10.1145/1073204.1073264.

[22] H. Haussecker, D. Fleet, Computing optical flow with physical models of brightness variation, IEEE Transactions on Pattern Analysis and Machine Intelligence 23 (6) (2001) 661–673. doi:10.1109/34.927465.

[23] T. Brox, A. Bruhn, N. Papenberg, J. Weickert, High accuracy optical flow estimation based on a theory for warping, in: T. Pajdla, J. Matas (Eds.), Computer Vision - ECCV 2004, Springer Berlin Heidelberg, Berlin, Heidelberg, 2004, pp. 25–36.

[24] H. Spies, H. Scharr, Accurate optical flow in noisy image sequences.

[25] A. Wedel, T. Pock, C. Zach, H. Bischof, D. Cremers, An improved algorithm for tv-l1 optical flow, in: D. Cremers, B. Rosenhahn, A. L. Yuille, F. R. Schmidt (Eds.), Statistical and Geometrical Approaches to Visual Motion Analysis, Springer Berlin Heidelberg, Berlin, Heidelberg, 2009, pp. 23–45.

[26] L. I. Rudin, S. Osher, E. Fatemi, Nonlinear total variation based noise removal algorithms, Physica D: Nonlinear Phenomena 60 (1) (1992) 259–268. doi:https://doi.org/10.1016/0167-2789(92)90242-F.

[27] I. Morales, Y. W. Woo, R. Klette, T. Vaudrey, A study on stereo and motion data accuracy for a moving platform, Tech. rep. (2009).

[28] T. Vaudrey, R. Klette, Residual images remove illumination artifacts!, in: J. Denzler, G. Notni, H. Süße (Eds.), Pattern Recognition, Springer Berlin Heidelberg, Berlin, Heidelberg, 2009, pp. 472–481.

[29] J. W. Woods, Chapter 7 - image enhancement and analysis, in: J. W. Woods (Ed.), Multidimensional Signal, Image, and Video Processing and Coding (Second Edition), second edition Edition, Academic Press, Boston, 2012, pp. 223–256. doi:https://doi.org/10.1016/B978-0-12-381420-3.00007-2.

[30] M. S. Nixon, A. S. Aguado, Chapter 4 - low-level feature extraction (including edge detection), in: M. S. Nixon, A. S. Aguado (Eds.), Feature Extraction Image Processing for Computer Vision (Third Edition), third edition Edition, Academic Press, Oxford, 2012, pp. 137–216. doi:https://doi.org/10.1016/B978-0-12-396549-3.00004-5.

[31] E. Davies, Chapter 5 - edge detection, in: E. Davies (Ed.), Computer Vision (Fifth Edition), fifth edition Edition, Academic Press, 2018, pp. 119–145. doi:https://doi.org/10.1016/B978-0-12-809284-2.00005-8.

[32] V. Lempitsky, C. Rother, S. Roth, A. Blake, Fusion moves for markov random field optimization, IEEE Transactions on Pattern Analysis and Machine Intelligence 32 (8) (2010) 1392–1405. doi:10.1109/TPAMI.2009.143.

[33] H. Kong, H. C. Akakin, S. E. Sarma, A generalized laplacian of gaussian filter for blob detection and its applications, IEEE Transactions on Cybernetics 43 (6) (2013) 1719–1733. doi:10.1109/TSMCB.2012.2228639.

[34] E. S. Gedraite, M. Hadad, Investigation on the effect of a gaussian blur in image filtering and segmentation, in: Proceedings ELMAR-2011, 2011, pp. 393–396.

[35] J. M. Blackledge, Chapter 16 - segmentation and edge detection, in: J. M. Blackledge (Ed.), Digital Image Processing, Woodhead Publishing Series in Electronic and Optical Materials, Woodhead Publishing, 2005, pp. 487–511. doi:https://doi.org/10.1533/9780857099464.4.486.

[36] G. Deng, L. Cahill, An adaptive gaussian filter for noise reduction and edge detection, in: 1993 IEEE Conference Record Nuclear Science Symposium and Medical Imaging Conference, 1993, pp. 1615–1619 vol.3. doi:10.1109/NSSMIC.1993.373563.

[37] B. Galvin, B. McCane, K. L. Novins, D. Mason, S. Mills, Recovering motion fields: An evaluation of eight optical flow algorithms, in: BMVC, 1998.

[38] F. Steinbrücker, T. Pock, D. Cremers, Large displacement optical flow computation withoutwarping, in: 2009 IEEE 12th International Conference on Computer Vision, 2009, pp. 1609–1614. doi:10.1109/ICCV.2009.5459364.

[39] P. Huber, Robust Statistics, Wiley Series in Probability and Statistics - Applied Probability and Statistics Section Series, Wiley, 2004.

[40] M. J. Black, P. Anandan, The robust estimation of multiple motions: Parametric and piecewise-smooth flow fields, Computer Vision and Image Understanding 63 (1) (1996) 75–104. doi:https://doi.org/10.1006/cviu.1996.0006.

[41] O. U. N. Jith, S. A. Ramakanth, R. V. Babu, Optical flow estimation using approximate nearest neighbor field fusion, in: 2014 IEEE International Conference on Acoustics, Speech and Signal Processing (ICASSP), 2014, pp. 673–6577. doi:10.1109/ICASSP.2014.6854871.

[42] A. Bruhn, J. Weickert, C. Schnörr, Lucas/kanade meets

horn/schunck: Combining local and global optic flow methods., International Journal of Computer Vision 61 (3) (2005) 211–231.

[43] A. Delaney, Y. Bresler, Globally convergent edge-preserving regularized reconstruction: an application to limited-angle tomography, IEEE Transactions on Image Processing 7 (2) (1998) 204–221. doi:10.1109/83.660997.

[44] R. Deriche, P. Kornprobst, G. Aubert, Optical-flow estimation while preserving its discontinuities: A variational approach, in: S. Z. Li, D. P. Mital, E. K. Teoh, H. Wang (Eds.), Recent Developments in Computer Vision, Springer Berlin Heidelberg, Berlin, Heidelberg, 1996, pp. 69–80.

[45] P. Beaudet, Rotationally invariant image operators, 1978.

[46] E. H. Adelson, J. R. Bergen, Spatiotemporal energy models for the perception of motion., Journal of the Optical Society of America. A, Optics and image science 2 2 (1985) 284–99.

[47] P. J. Burt, Fast filter transform for image processing, Computer Graphics and Image Processing 16 (1) (1981) 20–51. doi:https://doi.org/10.1016/0146-664X(81)90092-7.

[48] S. Tanimoto, T. Pavlidis, A hierarchical data structure for picture processing, Computer Graphics and Image Processing 4 (2) (1975) 104–119. doi:https://doi.org/10.1016/S0146-664X(75)80003-7.

[49] R. Keys, Cubic convolution interpolation for digital image processing, IEEE Transactions on Acoustics, Speech, and Signal Processing 29 (6) (1981) 1153–1160. doi:10.1109/TASSP.1981.1163711.

[50] E. J. Kirkland, Bilinear Interpolation, Springer US, Boston, MA, 2010, pp. 261–263. doi:10.1007/978-1-4419-6533-2$_1$2.

[51] W. Press, Numerical Recipes in C++: The Art of Scientific Computing, Cambridge University Press, 2009.

[52] J. L. Barron, M. Khurana, Determining optical flow for large motions using parametric models in a hierarchical framework, 2007.

[53] C. Bailer, B. Taetz, D. Stricker, Flow fields: Dense correspondence fields for highly accurate large displacement optical flow estimation, in: Proceedings of the IEEE International Conference on Computer Vision (ICCV), 2015.

[54] M. Ohki, M. E. Zervakis, A. N. Venetsanopoulos, 3-d digital filters, in: C. Leondes (Ed.), Multidimensional Systems: Signal Processing and Modeling Techniques, Vol. 69 of Control and Dynamic Systems, Academic Press, 1995, pp. 49–88. doi:https://doi.org/10.1016/S0090-5267(05)80038-6.

[55] A. Buades, B. Coll, J.-M. Morel, A non-local algorithm for image denoising, in: 2005 IEEE Computer Society Conference on Computer Vision and Pattern Recognition (CVPR'05), Vol. 2, 2005, pp. 60–65 vol. 2. doi:10.1109/CVPR.2005.38.

[56] G. Gilboa, S. Osher, Nonlocal operators with applications to image processing, Multiscale Modeling & Simulation 7 (3) (2009) 1005–1028. doi:10.1137/070698592.

[57] A. C. Bovik, T. S. Huang, D. C. Munson, The effect of median filtering on edge estimation and detection, IEEE Transactions on Pattern Analysis and Machine Intelligence PAMI-9 (2) (1987) 181–194. doi:10.1109/TPAMI.1987.4767894.

[58] L. K. Rajendran, J. Zhang, S. Bhattacharya, S. P. M. Bane, P. P. Vlachos, Uncertainty quantification in density estimation from background-oriented schlieren measurements, Measurement Science and Technology 31 (5) (2020) 054002. doi:10.1088/1361-6501/ab60c8.

[59] L. K. Rajendran, S. P. M. Bane, P. P. Vlachos, PIV/BOS synthetic image generation in variable density environments for error analysis and experiment design, Measurement Science and Technology 30 (8) (2019) 085302. doi:10.1088/1361-6501/ab1ca8.

[60] F. Scarano, Iterative image deformation methods in PIV, Measurement Science and Technology 13 (1) (2001) R1–R19. doi:10.1088/0957-0233/13/1/201.

[61] H.-H. Nagel, W. Enkelmann, An investigation of smoothness constraints for the estimation of displacement vector fields from image sequences, IEEE Transactions on Pattern Analysis and Machine Intelligence PAMI-8 (5) (1986) 565–593. doi:10.1109/TPAMI.1986.4767833.

SHAPE OPTIMIZATION

One-shot and multigrid acceleration for industrial shape optimization

Luca Zampini

Turbomachinery and Propulsion Department, von Karman Institute for Fluid Dynamics, Belgium, luca.zampini@vki.ac.be

Supervisor: Tom Vertraete

Professor, Turbomachinery and Propulsion Department, von Karman Institute for Fluid Dynamics, Belgium, tom.verstraete@vki.ac.be

University Supervisor: Grégory Coussement

Head of department, Department of Fluid Machines, University of Mons, Belgium, gregory.coussement@umons.ac.be

Abstract

The paper is meant as the continuation of a previous research, aiming at optimizing a U-bend passage of a turbine-blade serpentine-cooling channel with the objective to minimise pressure losses. A tri-variate B-spline volume is used to define the volume to be optimised. The position of the external control points are used as design parameters. The grid generation process transforms a Cartesian grid (defined in parametric space) to the physical space using the tri-variate net of control points. This allows the computation of the grid sensitivities with respect to the design variables at a fraction of the cost of a Computational Fluid Dynamics (CFD) iteration, therefore allowing the use of one-shot methods. A steady state, Reynolds-Averaged, density-based Navier-Stokes solver is used to predict the pressure losses at a Reynolds number of 40,000. The sensitivities of the objective function with respect to the control points are computed using a hand-derived adjoint solver and geometry generation system. A one-shot approach is used to simultaneously converge flow, gradient and design, resulting in a rapid design approach with a design time equivalent to approximately 10 normal CFD runs, while still maintaining a CAD representation of the geometry. A large reduction in pressure loss is obtained, and the flow in the optimal geometry is analysed in detail.

Keywords: One-shot, U-Bend

1. Introduction

Internal cooling channels of modern gas turbine blades are a key feature that enables for high Turbine Inlet Temperatures and therefore higher efficiencies. They provide the air for film cooling and simultaneously cool the internal structure as well. A solution to cool down turbine blades with small coolant mass flow is the usage of multiple passages of the coolant by a serpentine layout inside of the blade. A salient feature of such a scheme is the U-bend at the extremities of the straight passages, which requires a flow turning of 180 degrees. These bends are responsible for up to 25% of the total pressure losses of the internal cooling scheme. This total pressure loss reduces the overall efficiency of the gas turbine. Previous literature studies demonstrate the presence of secondary flow structures resulting from an imbalance between the centrifugal and pressure forces along the channel height. Furthermore, it is always highlighted the presence of a separation bubble near the internal wall in the second part of the bend, which is the result of a strong adverse pressure gradient. Additional studies have been devoted towards the reduction of the pressure losses of the U-bend.

The reduced pressure loss reported in the literature is obtained through a laborious approach which is well-established in the engineering environment: modifications are proposed, tested and either accepted or rejected in cycles. Engineers iterate from design to design, building up knowledge, and spending large amounts of time on testing and potentially exploring large numbers of uninteresting design alterations. The main shortcoming of the approaches followed in literature is the limited degree of freedom that can be

given to the shape. Indeed, in order to maintain a feasible degree of evaluations, evolutionary-based algorithms must restrict the number of design shape variables to below 50. This limits the design to mainly 2D geometries extruded in the height direction. On the other hand, gradient-based methods do not exhibit this deterioration, and hence allow much richer design spaces. Additional problems include the need for efficient methods to deform the mesh from one iteration to another, as well as to maintain a link to the Computer Aided Design (CAD) model. In the present work it is used an alternative solution to the mesh deformation problem according to the study in [1]. Tri-variate B-splines are be employed, which define a transformation from a 3-dimensional rectangular computational domain to the U-bend shape while still remaining closely linked to a CAD model. The mesh generation is significantly simplified as trough this approach, since tri-variate B-Splines are intrinsically a volume parametrization. The iso-surfaces of the B-Spline curves, in other words, can be directly used as gridlines for the mesh generation. This leads also to a very fast grid generation process. This in turn allows the use of a one-shot acceleration technique in a Jacobi fashion.
The one-shot acceleration technique hereby proposed aims at solving the optimality condition without following the usual perturb-and-converge procedure used in traditional optimizers. Instead of fully converging the primal and adjoint equations, indeed, the concept of partial convergence is used. The primal and adjoint equations are partially converged in order to provide an estimation of the functional gradient. This allows to sensibly reduce the amount of operations that are required for each traditional optimization step, at the price of reducing the geometrical update. The estimated gradient is then used in an in-hose BFGS optimizer: While the primal and the adjoint solver are converging, the BFGS optimizer marches towards the optimum condition.

2. Methodology

Figure 1 shows a schematic overview of the optimisation method. In the following sections the Figure 1 shows a schematic overview of the optimisation method.

2.1. Geometry

The most commonly used approach to define a geometry in CAD is through boundary patches that are stitched together. This is the most appropriate approach to model complex geometries. However, this approach has significant drawbacks. No direct link is indeed defined between the points lying on the outer surface and point lying inside of the geometry. In other words, there is no automatic transformation from a 3-dimensional computational domain to the internal volume of the geometry. In the present work, the geometry is described directly as a volume rather than a collection of internal volume of the geometry. The main advantage is the easiness in the grid generation process, which becomes significantly easier and computationally more efficient. The volume is obtained through tri-variate B-splines, which are an extension of B-spline surfaces to the thirds dimension. A more exhaustive description of this approach can be found in [1]. Figure 1 shows the mapping from the computational domain to the U-bend, as well as the external control points of the geometry. The skin of the volume is composed of six faces which can be easily expressed as B-spline surfaces by setting the parameters u,v,w respectively to 1 or 0. The skin of the volume is composed of six B-spline marked in black in Figure 2, totalling 180 free control points each with three degrees of freedom, resulting in a total of 540 degrees of freedom. The parameters controlling the shape of the U-bend are the external control points. The internal control points of the tri-variate B-Spline are made dependent from the outside control points. In other words, the surface points are the degrees of freedom and the inner points necessary to describe the volume are obtained by transfinite interpolation.

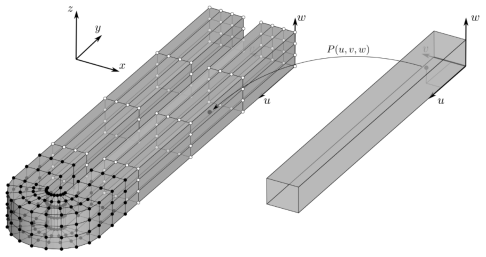

Figure 1: Objective improvement vs one-shot iterations

2.1.1. Grid generation

The use of tri-variate B-splines enables the establishment of a mapping between the computational domain and the U-bend shape. As a result, the generation of a structured mesh is a very straightforward

process. The grid generation requires only the generation of a structured mesh in the computational domain. Then, through the mapping offered by the B-spline mapping, the computational grid in the physicals domain is readily obtained. A suitable boundary layer refinement is also provided. A low-Reynolds turbulence model is used, which allows to correctly predict the secondary flow structures. A grid with 200 × 64 × 64 cells is used in the u,v,w directions respectively, resulting in 819,200 cells.

2.1.2. CFD solver

The Reynolds-Averaged Navier-Stokes equations are solved on multiblock structured grids with a cell-centered finite volume formulation, based on an adaptation of the JT-KIRK scheme. Convective fluxes are computed using Roe's approximate Riemann solver [23] with a MUSCL-type reconstruction of primitive variables for second-order accuracy. Oscillations are supprersed by a Van-Albada type limiter, with the numerical dissipation of the scheme being controlled by the entropy correction of Harten. Viscous fluxes are computed with a central reconstruction of primitive variables for second-order accuracy. The turbulence closure propblem is realised with the negative Spalart Allmaras turbulence model, assuming fully-turbulent flow from the inlet (Re = 40,000, based on the hydraulic diameter.
Geometric multigrid is used to damp the low-frequency spatial modes, thus speeding up the convergence. Diagonally-Implicit time integration is applied on each multigrid level using a GMRES solver with ILU preconditioning. The system matrix used to converge the the system is the first-order Jacobian in ordere to reduce the stiffness of the solver. convergence. The GMRES solver is embedded in a Runge-Kutta multi-stage time integrartion method to damp high-frequency temporal modes.

2.1.3. Adjoint solver

After converging the CFD solver, the pressure loss induced by the U-bend can be readily computed at the domain outlet as

$$J = \int_{S_{out}} \frac{P}{\rho^{\gamma}} \tag{1}$$

The objective function J presented in equation 2 is proportional to the entropy generation, which shall be minimized. It is required to compute the derivative of this objective with respect to every design variable . To compute the derivative with respect to an arbitrary design variable, it is possible to make use of the chain rule:

$$\frac{dJ}{d\alpha} = \frac{\partial J}{\partial \alpha} + \frac{\partial J}{\partial u}\frac{du}{d\alpha} \tag{2}$$

U represent the flow conservative variables. In this problem $\frac{\partial J}{\partial \alpha} = 0$ because J does not explicitly depend on the design variables α. In the present case the outlet is located far away from the zone affected by the design variables, such that this term indeed vanishes. Note, as well, that Equation 2 has to be seen schematically, as the flow variables depend on the position in the domain. In a discretised form u is a large vector containing the flow variables of each grid cell. In the present work, the technique of the discrete adjoint is used. Therefore, only the discrete problem is considered from here on. This leads to the derivation of the discrete adjoint.
The two partial derivatives of J on the right hand side in Equation 2 can be directly computed, while the last total derivative of u can only be computed by looking at the Navier-Stokes equations. We assume that the steady-state governing equations are expressed in a residual form:

$$R(u, \alpha) = 0 \tag{3}$$

This equation relates the flow solution to the design variables and describes how the flow variables change when a design variable is altered. The relation has to still hold for an infinitesimal change to a design variable:

$$\frac{dR}{d\alpha} = \frac{\partial R}{\partial u} + \frac{\partial R}{\partial u}\frac{du}{d\alpha} \tag{4}$$

Equation 4 is a linear system of the unknown $\frac{du}{d\alpha}$, which can be solved using classical linear system solvers. After inserting the result in Equation2, the sensitivity of the design variable α is obtained. It is needed, however, to repeat the process for all other design variables, requiring an expensive linear system solve each time. The computational cost is, as a result, dependent on the number of design variables. By using the adjoint approach, however, it is possible reduce the computational cost to only one linear system solve of the adjoint equation [2]:

$$\left(\frac{dR}{du}\right)^{T} v = \left(\frac{\partial J}{\partial u}\right)^{T} \tag{5}$$

Using the solution v^T to this linear system:

$$\frac{dJ}{d\alpha} = \frac{\partial J}{\partial \alpha} - v^{T}\frac{\partial R}{\partial \alpha} \tag{6}$$

allows to compute the gradient with respect to all design variables with only one linear system solve.
Close examination of Equation 5 reveals that the system matrix on the left hand side is the true Jacobian of the fluxes of the primal CFD solver. The fluxes are obtained using a second order Roe scheme and a central scheme for the viscous fluxes, such that the stencil spans over a large number of neighbouring cells. This leads to a sparse Jacobian, though, with entries that are far off-diagonal. The system is very stiff and difficult to solve with a direct solver and often prohibitive due to memory limitations. Therefore, the adjoint equations 5 are solved with the same iterative time marching method as the primal CFD solver. A further simplification is introduced by a frozen turbulence approach, which assumes the turbulent viscosity to remain invariant to the changes in the geometry.

2.1.4. Calculation of grid sensitivities

The solution of Equation 5 provides the adjoint flow variables v. The computation of $\frac{\partial R}{\partial \alpha}$ is still required in Equation6 to obtain the sensitivities of J with respect to the design variables α. This term expresses how the residual changes under a perturbation of a design variable, through the mechanism of changing each node's coordinates which changes each face normal and area, and each cell volume. It can be computed by a forward approach, i.e., by changing each design variable individually and multiplying the computed term with the adjoint variables v as in Equation 6 to obtain the sensitivities for each design variable. Although in general such a procedure is relatively fast, it needs to be repeated for each design variable and hence becomes less attractive for a large number of design variables. As an alternative, a reverse or adjoint procedure can be used here as well, similar to what has been applied to the CFD solver. The approach hereby followed is the same described in [1]. The chosen approach requires only the evaluation of the basis functions of the tri-variate B-Spline for each grid point, which can be computed in a considerably shorter time compared to one CFD iteration.

2.1.5. Computation of the Design Variable Sensitivities

The sensitivities of the objective function with respect to all control points of the tri-variate B-spline are given by [1].

2.1.6. BFGS update

The gradient calculated in the previous section is provided to an in-house BFGS procedure in order to solve for the KKT optimality condition via quasi-Newton method. The procedure is presented in equation 7, where B_k represents the estimated Hessian, p_k represents the descend direction of the considered iteration k and ∇f is the functional gradient.

$$B_k p_k = -\nabla J(\alpha_k) \tag{7}$$

The estimated Hessian B_k is updated at every iteration using information of the gradient.

2.1.7. One-shot acceleration

The aforementioned convergence scheme is enhanced by a Jacobi-like one-shot acceleration technique. The traditional approach for the solution of the optimality condition follows the perturb-and-observe rationale: the geometry is modified, the flow solution is obtained throught the CFD solver and the adjoint flow field is then calculated through the adjoint solver. The gradient is then calculated in its exact form and an updated geometry is proposed, based on the optimization technique that is chosen: BFGS in this case. The one-shot acceleration technique hereby proposed is instead based on *partial* convergence. The flow field is *partially* converged, as well as the adjoint equation which is *partially* satisfied. This provides an estimated evaluation of the gradient, which is then fed to the BFGS optimizer. The optimizer therefore *continuously* updates the geometry towards the optimal geometry *while* the flow field converges the gradient estimation *continuously* improve.

2.1.8. Results

Figure 2 presents the convergence history of the objective J as a function of the one-shot iteration. In other words, on the x-axis it is presented the continuous geometry update, whereas on the y axis it is reported the convergence of the entropy generation.

Figure 3 shows the evolution of the CFD initial residual as a function of the one-shot iterations. The initial CFD residual is the flow field residual, evaluated from the previous flow field on the current mesh. In other words, it acts as an upper limit to the residual of the current iteration, since the current iteration flow field is calculated performing integration starting form the previous flow field. As it can be observed from figure 3, the residual of the flow field is reducing with the one-shot iterations. In other words, the flow field is converging *while* the performances improve.

Figure 4 shows the evolution of the adjoint initial residual as a function of the one-shot iterations. As it

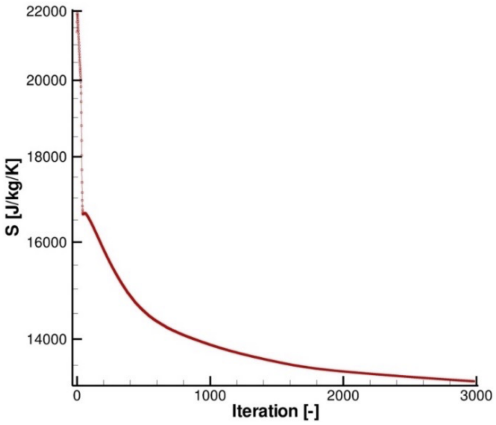

Figure 2: Objective improvement vs one-shot iterations

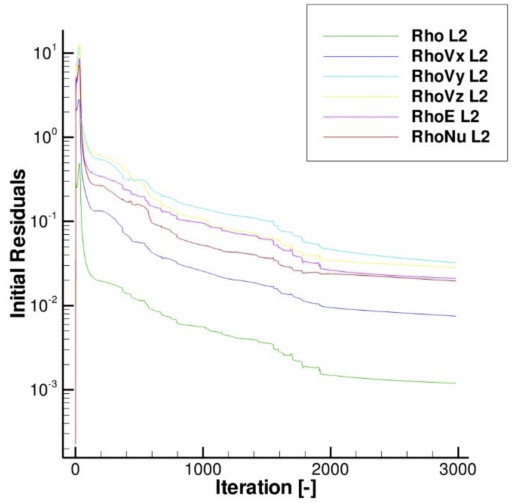

Figure 3: CFD initial residual vs one-shot iterations

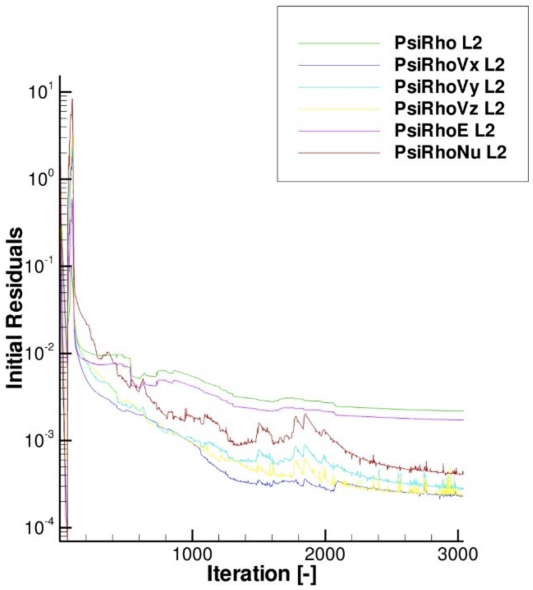

Figure 4: Adjoint initial residual vs one-shot iterations

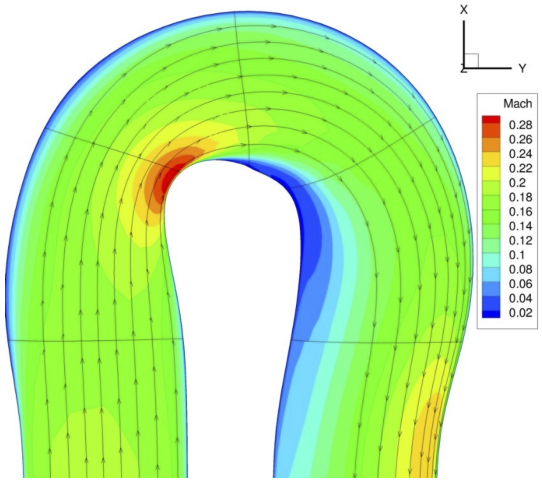

Figure 5: Adjoint initial residual vs one-shot iterations

can be observed from figure 4, also the residual of the adjoint field is reducing with the one-shot iterations.

Figure 5 presents a 2D section of the 3D geometry of the UBend. From the contour of the Mach number and from the streamlines it is possible to observe the effect of the optimizer. The recirculating area in the rear part of the UBend has been reduces and this is the main cause for the loss reduction operated by the optimizer.

3. Conclusion

A one-shot acceleration technique has been successfully implemented in the CADO framework.
A suitably-defined parametrisation method which uses tri-variate B-spline volumes has been used to parametrise the U-Bend geometry. Due to its cheap and robust grid generation process, the method has been embedded in a one-shot optimization framework. This framework allows to optimize the shape *while* the CFD and adjoint solvers are converging. The method has been applied to minimize the entropy gen-

eration of the considered U-bend with 540 degrees of freedom. Gradients of the objective function are calculated through a discrete adjoint technique, and the propagation of the gradients from the adjoint variables to the degrees of freedom has been performed in a reverse way. A reduction of 39% of the objective function was achieved with a significant reduction of the required computational power.

Acknowledgments

Special thanks to Tom Verstraete for the guidance and inspiration. Special thanks also to the FNRS for sponsoring this project.

References

[1] L. M. Tom Vertraete, J.-D. Müller, Adjoint-based design optimisation of an internal cooling channel u-bend for minimised pressure losses, Int. J. Turbomach. Propuls. Power (2017) 202–210.

[2] M. B. Giles, N. A. Pierce, An introduction to the adjoint approach to design, Flow, Turbulence and Combustion 65 (3) (2000) 393–415.

Aero-elastic tailoring of composite turbomachinery blades through gradient-based optimisation: harmonic solvers

Tom De Bruyn

Turbomachinery and Propulsion Department, von Karman Institute for Fluid Dynamics, Belgium, tom.de.bruyn@vki.ac.be

Supervisor: Tom Verstraete[1] and Fabrizio Fontaneto[2]

[1]*Professor, Turbomachinery and Propulsion Department, von Karman Institute for Fluid Dynamics, Belgium, tom.verstraete@vki.ac.be*

[2]*Associate Professor, Turbomachinery and Propulsion Department, von Karman Institute for Fluid Dynamics, Belgium, fabrizio.fontaneto@vki.ac.be*

University Supervisor: Joris Degroote

Professor, Department of Electromechanical, Systems and Metal Engineering, Ghent University, Belgium, joris.degroote@ugent.be

Abstract

As optimisation methods for turbomachinery components become increasingly important to enable further design improvements, such methods should incorporate the interaction between fluid and structure (e.g. flutter) to incorporate mechanical stability of the design during the optimisation. In order to do so however, fluid-domain solvers must consider unsteadiness. Harmonic solvers, describing the unsteadiness as set of harmonic perturbations of the mean flow, achieve this at moderate computational cost.

Keywords: CFD, non-linear harmonics, harmonic balance, optimisation

1. Introduction

Several decades after their introduction, Steady Reynolds-averaged Navier-Stokes (RANS) methods remain the dominant approach to turbomachinery CFD, permitting rapid and relatively inexpensive computation. This is especially true in the context of now prevalent optimisation workflows (as considered in the VKI's in-house turbomachinery optimisation framework *CADO*[1], where up to several hundreds of design evaluations may be required. In such cases, higher fidelity methods become prohibitively expensive. RANS methods however insufficiently capture all physical aspects of interest during the optimisation process. Notably vibrational effects (e.g. flutter, vibrations induced by blade row interaction, ...) are by nature unsteady. These effects are of great importance in turbomachinery component development and directly influenced by typical design variables of the optimisation process, hence they must be included directly.

In order to incorporate unsteadiness without suffering the computational penalty of an unsteady RANS (URANS) computation, an harmonic or frequency-domain method is used to capture most of the unsteadiness at reasonable expense. In order to do so, the solution of the URANS equations for a periodic flow is decomposed into it's temporal Fourier components:

$$U(t, \mathbf{x}) = Re\left[\sum_{k=0}^{\inf} \hat{U}_k(\mathbf{x}) e^{\mathbf{i}k\omega t}\right], \tag{1}$$

where $\omega = 2\pi f$ is the base frequency and U the vector of conservative variables:

$$U = \begin{pmatrix} \rho \\ \rho v_x \\ \rho v_y \\ \rho v_z \\ \rho e \end{pmatrix}. \tag{2}$$

Starting from the unsteady form of the Navier-

Stokes equations:

$$\frac{dU}{dT} + R(U) = 0, \tag{3}$$

where $R(U) = F_c(U) - F_v(U) + Q(U)$ is the steady residual comprising of the convective flux, viscous flux and source term respectively, substitution of (1) leads to:

$$\mathbf{i}k\omega \, Im\left[\sum_{k=0}^{\inf} \hat{U}_k(\mathbf{x}) e^{\mathbf{i}k\omega t}\right] + R(U) = 0. \tag{4}$$

the steady residual R in equation (4) can similarly be decomposed in it's Fourier components:

$$R(U) = Re\left[\sum_{k=0}^{\inf} \hat{R}_k(U) e^{\mathbf{i}k\omega t}\right], \tag{5}$$

Combining equations (4) and (5) and grouping terms by frequency, the unsteady equations can be formulated in the frequency domain:

$$\mathbf{i}k\omega \hat{U}_k(\mathbf{x}) + \hat{R}_k(U) = 0. \tag{6}$$

with $\hat{R}_k$ the k-th harmonic of the steady Navier-stokes Residual R, which depend on all harmonics of the solution U. Writing (6) for all k, one obtains a set of balance equations, leading to the name 'harmonic balance' technique[2].

1.1. Finite harmonics

In practice, a finite number of frequencies is used. As the computational effort inevitably increases with an increased number of included harmonics, the number is a trade-off between performance and the improved accuracy representing relevant unsteadiness as more frequencies are included. When the number of harmonics is truncated, (6) is no longer exact. Indeed the non-linearity of the steady RANS residual $R(U)$ means the solution and residual cannot be represented using the same (finite) set of harmonics.

This can be easily understood from the product of two different harmonic components. The multiplication of two variables $f(t)$ and $g(t)$, described using the same number of harmonics can be written out in full:

$$\begin{aligned} f(t)\, g(t) =& \frac{1}{2}\sum_{k=0}^{K}\left[\hat{F}_k e^{\mathbf{i}k\omega t} + \hat{F}_{-k} e^{-\mathbf{i}k\omega t}\right] * \\ & \frac{1}{2}\sum_{l=0}^{L}\left[\hat{G}_l e^{\mathbf{i}l\omega t} + \hat{G}_{-l} e^{-\mathbf{i}l\omega t}\right] \\ =& \frac{1}{4}\sum_{k=0}^{K}\sum_{l=0}^{L}\Big[\hat{F}_k\hat{G}_l e^{\mathbf{i}(k+l)\omega t} \\ & \hat{F}_k\hat{G}_{-l} e^{\mathbf{i}(k-l)\omega t} \\ & \hat{F}_{-k}\hat{G}_l e^{\mathbf{i}(l-k)\omega t} \\ & \hat{F}_{-k}\hat{G}_{-l} e^{-\mathbf{i}(k+l)\omega t}\Big], \end{aligned} \tag{7}$$

where $\hat{F}_{-k}$ and $\hat{G}_{-l}$ are the complex conjugates of $\hat{F}_k$ and $\hat{G}_l$ respectively. It is clear from (7) that if each of the terms has s up to K harmonic, the product contains harmonics up to the $2K$'th harmonic of the base frequency as well as that a particular harmonic of the solution contribute to the residual for several (other) harmonics.

The non-linearity of the RANS residual thus introduces a coupling between the different harmonics, which - depending on the applied methodology - can be neglected, selectively computed or need to be taken into account to prevent aliasing. Regardless of the methodology, a 'harmonic balance' like (6) always neglects harmonics of the residual of higher order than the choice for the decomposition of the solution. However, as the number of harmonics in the solution is increased the approximation error decreases (as generally higher harmonics have a smaller amplitude in the considered cases).

2. Methodology

Writing the residual term in equation (6) first as a Taylor series around the steady solution $\hat{U}_0$ and applying the Fourier transform afterwards leads to the following expressions for the harmonics of the Residual, with K total harmonics considered:

$$\begin{aligned} \hat{R}_0 &= R(\hat{U}_0) + D_0(\hat{U}_0, ...\hat{U}_K) \\ \hat{R}_k &= R(\hat{U}_0) + \left.\frac{\partial R}{\partial U}\right|_{\hat{U}_0} \hat{U}_K + D_k(\hat{U}_0, ...\hat{U}_K) \quad k \neq 0. \end{aligned} \tag{8}$$

The coupling terms D_k are called the deterministic stresses and contain the interaction between the higher harmonics. As the Taylor series expansion introduces

polynomials of degree higher than one, these terms are non-linear, maintaining the coupling between the harmonics considered above. Linear harmonic (also called time-linearised) methods neglect all deterministic stress terms in (8), retaining only the first, linear term for the higher harmonics [3].

Non-linear harmonic methods [4; 5] include at least the D_0 term modelling the influence of the unsteadiness on the mean flow field. This term is computed from the higher order harmonics and given by (split in a convective and viscous contribution)[6]:

$$D_0(U) = D_{C0} - D_{V0} = \begin{pmatrix} 0 \\ \overline{(\rho \mathbf{v})' v'_x} \\ \overline{(\rho \mathbf{v})' v'_y} \\ \overline{(\rho \mathbf{v})' v'_z} \\ \overline{(\rho H)' \mathbf{v}'} \end{pmatrix} - \begin{pmatrix} 0 \\ 0 \\ 0 \\ 0 \\ \tau' \mathbf{v}' \end{pmatrix}, \qquad (9)$$

where the prime indicates $\rho' = \rho - \hat{\rho}_0$ the unsteady part of the solution. Computation of this term then requires a sum over all harmonics e.g.:

$$\overline{(\rho \mathbf{v})' v'_x} = \frac{1}{4} \sum_{k=1}^{K} \left[\rho \hat{V}_{x_k} \hat{\mathbf{V}}_{-k} + \rho \hat{V}_{x_{-k}} \hat{\mathbf{V}}_k \right]. \qquad (10)$$

the evolution of the higher order harmonics is typically modelled by a transport equation using the time-averaged velocity components, neglecting mutual influence of the harmonics on one another, besides through their effect on the mean flow [4; 6]. Including the coupling is however possible as well, though tedious [7].

As such, this method is formulated exclusively in the frequency domain, avoiding the need for Fourier transformations. This does however render the implementation of boundary conditions, classically formulated in the time domain, somewhat more involved. The major drawback is however the neglecting of the coupling terms for the higher harmonics, reducing the overall accuracy of the method in cases where the unsteadiness is more significant.

2.1. time-spectral method

An attractive alternative approach is not to model the deterministic stresses directly, but rather implicitly incorporate these terms by using the discrete Fourier Transform of the non-linear residual. To do so, the solution U is sampled at at least $2K + 1$ sample points (K the index of the highest considered harmonic), for which the Residual is evaluated, resulting in a set of equations:

$$\mathbf{i} k \omega \hat{U}_k(\mathbf{x}) + \mathscr{F}_k(R(\mathscr{F}^{-1}(\hat{U}))) = 0, \qquad (11)$$

where $\mathscr{F}_k$ is the k-th component of the discrete Fourier transform and $\hat{U}$ is (1) truncated at K, the approximate reconstruction of the flow field [8; 9]. Particular care is needed for these methods to avoid aliasing in the forward and inverse transforms. As discussed in section 1.1, the residual $R(U)$ contains higher harmonics than U itself, which during the forward Fourier transform may produce spurious contributions to the lower harmonics. In order to reduce the effect, Orszag [10] has suggested to sample at $N \geq 3K + 1$ time instances (50% higher than the lower bound of the Shannon-Nyquist theorem), which is sufficient to eliminate aliasing for quadratic functions. As the residual computation is generally rational, it contains infinitely many harmonics, however these contributions are third order in the perturbation amplitude, and hence drop of quickly. It must be noted that (over)sampling comes at a non-negligible cost, as at every time instance a residual evaluation is performed.

The time-spectral method holds several important advantages over the 'classic' linear harmonic approach:

- Coupling between harmonics is implicitly included.
- As the RANS residual is evaluated in the time domain, flux evaluation routines developed for steady computations can be applied without modification. This is particularly advantageous for codes with both a steady and harmonic solver, as a single set of routines can be used.
- The joint use of the time and frequency domain, while necessitating the extra cost of the Fourier transforms, means boundary conditions can be formulated in either.

In some cases (11) is cast into the time-domain, corresponding to a pseudo-spectral discretisation of the time-dependent term in the URANS equations[8]. While this removes the need for the forward Fourier transform, the approximation of the time derivative becomes increasingly inaccurate when few (< 16) sampling points are used. Furthermore, it introduces a further coupling between different harmonics, whereas (6) and (as a result) (11) allow one to solve for every wave number independently.

2.2. phase-shift boundary conditions

In order to limit the computational domain, and therefore computational effort, w.r.t. full-annular simulations, periodic boundary conditions are typically applied to a single blade passage. In most turbomachinery computations, the temporal variation of the solution in the blade passage is induced by a spatial (or spatial and temporal) variation of the inlet or outlet conditions along the domain pitch, rather than a solely temporal one. In these cases, the solution in the adjacent blade passages is not instantaneously equal to the solution in the meshed passage, and periodic boundary conditions need to be adjusted to include a 'phase-shift' between trailing and leading side of the periodic boundary [11].

At any given time t, the solution at the leading edge of the meshed blade passage corresponds to the solution at the trailing edge $2\pi/\omega_R N_B$ seconds into the future, when the rotor has rotated over $1/N_B$ part of a full rotation (N_B being the number of blade passages, ω_R the rotational speed of the machine). Hence,

$$\begin{aligned} U_{LE}(t) &= U_{TE}(t + \frac{2\pi}{\omega_R N_B}) \\ U_{TE}(t) &= U_{LE}(t - \frac{2\pi}{\omega_R N_B}), \end{aligned} \tag{12}$$

where the subscripts TE and LE denote trailing and leading edge respectively. Substituting the frequency domain formulation (1) leads for sampling point t_i of the time-spectral method to

$$\begin{aligned} U_{LE}(t_i) &= Re\left[\sum_{k=0}^{K} \hat{U}_{k,TE}(\mathbf{x}) e^{\mathbf{i}k\omega(t_i + \frac{2\pi}{\omega_R N_B})}\right] \\ U_{TE}(t_i) &= Re\left[\sum_{k=0}^{K} \hat{U}_{k,LE}(\mathbf{x}) e^{\mathbf{i}k\omega(t_i - \frac{2\pi}{\omega_R N_B})}\right]. \end{aligned} \tag{13}$$

The term inside the exponential is typically written as a time-dependent part and a phase-shift:

$$k\omega t_i \pm \frac{k2\pi\omega}{\omega_R N_B} = k\omega t_i \pm \sigma_k, \tag{14}$$

where the shift σ_k only depends on the number of blade passages and the ratio between the perturbation (base)frequency and the rotational speed. E.g. in the case of a single rotating blade row following a stationary row of N_V vanes leads to a spatially periodic inlet condition repeating N_V times along the machine's circumference. In this case $\omega = N_V \omega_R$ and (14) depends solely on the blade ratio.

Note that the definition of a phase-shift is a requirement to unique define an unsteady perturbation, as the same perturbation frequency can be the result of either a temporal or spatial variation of boundary conditions, or a mix of both. Lastly note that generally the temporal shift $2\pi/\omega_R N_B$ does not correspond to the interval between sampling points, showing the strength of the time-spectral method for the formulation of boundary conditions.

2.3. treatment of turbulence

For all aforementioned methods, a common assumption is that turbulence models for RANS can be applied for unsteady flow as well, as with a limited number of harmonics, the time scale of the variation of the mean flow (including the harmonic components, but not turbulence), is still orders of magnitude greater than the time scale of the turbulence. Hence existing methods for RANS turbulence modelling such as the (negative) Spalart-Allmaras model[12] can be used. A common simplification is to assume the effect of the harmonic unsteadiness on the turbulence to be negligible. Under that assumption, the computation of turbulent values (e.g. the Spalart-Allmaras transport quantity) is identical to the treatment for steady flow. The resulting eddy viscosity is used in the computation of all harmonics.

The time-spectral methods offer another approach without the need to express the transport equations in the frequency domain. The same approach used to obtain equation (11) can be applied directly. For the Spalart-Allmaras model used in *CADO* this means expressing the transport quantity as:

$$\rho\tilde{\nu}(t, \mathbf{x}) = Re\left[\sum_{k=0}^{K} \hat{\rho\tilde{\nu}}_k(\mathbf{x}) e^{\mathbf{i}k\omega t}\right], \tag{15}$$

leading to an evolution equation:

$$\mathbf{i}k\omega\hat{\rho\tilde{\nu}}_k(\mathbf{x}) + \mathscr{F}_k(R^{TUR}(\mathscr{F}^{-1}(\hat{U}, \hat{\rho\tilde{\nu}}))) = 0, \tag{16}$$

where to evaluate the turbulence residual both meanflow and turbulence values are brought to the time domain. Hence the solution strategies used for the mean/harmonic flow can straightforwardly be applied to the turbulence model as well.

3. solution strategy

To solve the system of equations (8) or (11) a pseudo-time marching method is used. Hereto, the pseudo-timestep is added to the left-hand side of (6):

$$\frac{d\hat{U}_k}{dt'} + \mathbf{i}k\omega\hat{U}_k(\mathbf{x}) + \hat{R}_k(U) = \frac{d\hat{U}_k}{dt'} + \hat{R}_k^H(U) = 0. \quad (17)$$

Using m to indicate the pseudo-time step, and using

$$\Delta\hat{U}_k^{(m)} = \hat{U}_k^{(m+1)} - \hat{U}_k^{(m)} \quad (18)$$

a theoretical implicit formulation for the numerical update strategy becomes (linearising the residual around the steady component):

$$\left(\frac{1}{\Delta t'} + \mathbf{i}k\omega + \frac{\partial R_k}{\partial U}\right)\Delta\hat{U}_k^{(m)} = -\hat{R}_k(U). \quad (19)$$

In equation (19) different harmonics are generally coupled through the computation of the right-hand side, but also by the jacobian of the linear system. The latter is somewhat problematic, as by using this formulation all harmonics are solved for simultaneously in a linear system of $2K + 1$ equations. As a result the memory requirements increase with the number of harmonics, and quickly become prohibitive for a larger number of harmonics.

Therefore typically the jacobian in the left hand site of (19) is approximated for higher harmonics by the one for the steady computation (e.g. [13]:

$$\left(\frac{1}{\Delta t'} + \mathbf{i}k\omega + \left.\frac{\partial R_0}{\partial U}\right|_{\hat{U}_0^{(m)}}\right)\Delta\hat{U}_k^{(m)} = -\hat{R}_k(U), \quad (20)$$

allowing for the updates of the different harmonics to be solved for sequentially (or in fact in parallel, though in that case read access to the stored system matrix may still be serialised, reducing parallelisation effectiveness). As a result, the system matrix must only be computed once for the update of all harmonics.

4. results

To be completed after the symposium

5. Conclusion

This paper surmises the most commonly used 'harmonic' methods for solving the Reynolds-averaged Navier Stokes (RANS) equations, used when the unsteadiness of the meanflow is periodic and can be accurately represented by small amount of harmonic pertubations. Situated between steady and unsteady RANS solvers, they offer an interesting solution to capture unsteadiness without the - in the context of an optimisation process - prohibitive cost of full annulus URANS. Time-spectral methods are particularly enticing as they can potentially share subroutines with a steady RANS solver, reducing the overal development effort.

Acknowledgments

This PhD research is supported by a fellowship of the Flanders Scientific Research Fund (FWO)

References

[1] L. Mueller, T. Verstraete, Cad integrated multipoint adjoint-based optimization of a turbocharger radial turbine, International Journal of Turbomachinery, Propulsion and Power 2 (3).

[2] C. Frey, G. Ashcroft, H.-P. Kersken, C. Voigt, A harmonic balance technique for multistage turbomachinery applications, 2014. doi:10.1115/GT2014-25230.

[3] G. Dufour, F. Sicot, G. Puigt, C. Liauzun, A. Dugeai, Contrasting the harmonic balance and linearized methods for oscillating-flap simulations, Aiaa Journal - AIAA J 48 (2010) 788–797. doi:10.2514/1.43401.

[4] S. Vilmin, E. Lorrain, C. Hirsch, M. Swoboda, Unsteady flow modeling across the rotor/stator interface using the nonlinear harmonic method, Vol. 6, 2006. doi:10.1115/GT2006-90210.

[5] L. He, W. Ning, Efficient approach for analysis of unsteady viscous flows in turbomachines, Aiaa Journal - AIAA J 36 (1998) 2005–2012. doi:10.2514/2.328.

[6] S. G. Horcas, F. Debrabandere, B. Tartinville, C. Hirsch, G. Coussement, Extension of the non-linear harmonic method for the study of the dynamic aeroelasticity of horizontal axis wind turbines, Journal of Fluids and Structures 73 (2017) 100–124. doi:https://doi.org/10.1016/j.jfluidstructs.2017.06.008.
URL https://www.sciencedirect.com/science/article/pii/S0889974616306302

[7] P. Vasanthakumar, Three dimensional frequency-domain solution method for unsteady turbomachinery flows, Ph.D. thesis, Durham University (2003).
URL http://etheses.dur.ac.uk/3089/

[8] K. C. Hall, J.P. Thomas and W. Clark, Computation of Unsteady Nonlinear flows in Cascades Using a Harmonic Balance Technique, AIAA Journal 40 (5) (2002) 879–886.

[9] McMullen, Matthew Scott and Jameson, Anthony and Alonso, Juan J., The Application of Non-Linear Frequency Domain Methods to the Euler and Navier-Stokes Equations, Ph.D. thesis, Stanford University, Stanford, CA (3 2003).

[10] S. A. Orszag, On the Elimination of Aliasing in Finite-Difference Schemes by Filtering High-Wavenumber Components., Journal of Atmospheric Sciences 28 (6) (1971) 1074–1074. doi:10.1175/1520-0469(1971)028¡1074:OTEOAI¿2.0.CO;2.

[11] L. He, Method of simulating unsteady turbomachinery flows with multiple perturbations, AIAA Journal 30 (1992) 2730–2735. doi:10.2514/3.11291.

[12] S. R. Allmaras, F. T. Johnson, P. R. Spalart, Modifications and clarifications for the implementation of the spalart-allmaras turbulence model, 2011.

[13] G. Ashcroft, C. Frey, H.-P. Kersken, On the development of a harmonic balance method for aeroelastic analysis, in: E. Onate, X. Oliver, A. Huerta (Eds.), 6th. European Conference on Computational Fluid Dynamics - ECFD VI, 2014, pp. 5885–5896.
URL https://elib.dlr.de/90474/

Advance optimization concept for axial compressor

Thanh-Son Tran

Turbomachinery and Propulsion Department, von Karman Institute for Fluid Dynamics, Belgium, TTran@vki.ac.be

Supervisor: Tom Verstraete

Professor, Turbomachinery and Propulsion Department, von Karman Institute for Fluid Dynamics, Belgium, Tom.Verstraete@vki.ac.be

Supervisor: Fabrizio Fontaneto

Associate Professor, Turbomachinery and Propulsion Department, von Karman Institute for Fluid Dynamics, Belgium, Fontaneto@vki.ac.be

University Supervisor: Grégory Coussement

Professor, Service Fluide-Machine, Université de Mons, Belgium, Gregory.Coussement@umons.ac.be

Abstract

Modern low-pressure compressors are required to achieve a high-pressure ratio, good efficiency, and wide operating range within as few stages as possible. To mitigate the rapid boundary-layer growth from a highly loaded blade, one approach consists of restarting the boundary layer by splitting the airfoil. The so-called tandem blade presents several complexities from a large design space that require advanced design consideration.

Keywords: Shape Optimization, Compressor, Adjoint Method

1. Introduction

Aviation has become an essential part of our society and is important for economic, social, and cultural growth. It must therefore face the challenges of the next decades given by climate change. While electric aircraft has lately made promising progress, the bulkiness and the weight of the electric batteries are still limiting factors for the long haul and transatlantic flight and will remain so for the foreseeable future. Airbreathing jet engines have been primarily used in the aviation sector for their proven reliability and range. While being a stronghold of aviation propulsion, many efforts are still made to improve its design. Improved fuel consumption and reduction in emission and noise can also be achieved by increasing the bypass ratio and lowering the fan pressure ratio. Over the past 50 years, a clear trend to increase the bypass ratio has been witnessed which has been the main driver for the increased fuel savings of around 50% [1]. The trend has however reached a plateau that has only recently been surpassed by the introduction of the geared turbofan by Pratt and Whitney. The fan, low pressure compressor, and low-pressure turbine of such an engine can operate at different rotational speeds, enabling a diminution in stage count [2]. The resulting reduction in number of blades helps to decrease the machine weight and bring down the maintenance cost. Today's Low-Pressure Compressors (LPC) are required to achieve high pressure ratio's, good efficiency, and wide operating range within as few stages as possible. The circumferential speed and the flow turning are the two factors that affect the compression ratio. While the former is limited by the rotor blade tip velocity, the flow turning depends directly on the blade aero performance. Conventional single airfoils are required to control the rapid boundary-layer growth due to the high diffusion. One alternative approach consists of distributing the loading over several subsequent airfoil to restart the boundary-layer before an open separation occurs. The design of a two-blade configuration, the so-called tandem blade, presents several difficulties from the large pool of geometry. A systematic evaluation approach is required to avoid time and monetary high expense. [3]

The past decades, however, have seen a large development of optimization algorithms which try to maximize the performance of a design with a minimal intervention from the designer, while using Computational Fluid Dynamics (CFD) to model the fluid flow [4; 5; 6; 7; 8; 9]. Shape optimization has been gradually introduced into the design process for many industries in the aerospace, turbomachinery, and automotive sector. While a myriad of optimization techniques are available, they can be broadly sorted into gradient-free methods and gradient-based methods. Both aim to solve an optimization problem by maximizing or minimizing one or multiple objectives according to imposed constraints by changing the design parameters. Gradient-free methods such as Evolutionary Algorithms (EA) [10; 11] potentially assisted by surrogate models [6] are widely used for their robustness and ability to find global optima but their usage is computationally expensive for applications with large amount of design variables [12]. On the other hand, gradient-based methods aim to compute the direction towards the optimum from a sensitivity analysis, which offers in general a fast convergence rate. The computational cost of computing the gradient can be reduced using the adjoint technique, where the cost is nearly independent from the number of design parameters [13]. This makes gradient-based adjoint optimization methods more attractive as they can handle very large amounts of design parameters, which are expected for turbomachinery applications [14]. Gradient-based methods are however local methods, which cannot find the global optimum in case many local optima are present.

The PhD thesis aims to produce a stator blade for a compact and highly loaded LPC through the use of advanced multi-physics gradient-based optimization techniques. This will be achieved by three key steps:

1. Study of the capabilities and limitations of conventional design through the use of gradient-based optimization techniques.
2. Study of the physics surrounding a two-dimensional tandem blade with an optimization framework capable of handling complex geometry.
3. Study of flow interaction between the three-dimensional flow interaction and the tandem blade configuration through the use of multidisciplinary gradient-based optimization.

In the present work, a three-dimensional transonic rotor blade and two-dimensional single airfoil are explored to develop advance design techniques for a highly loaded compressor. A well established transonic design is first optimized and a discussion on the results is presented. Then an airfoil is fully designed with an optimization approach.

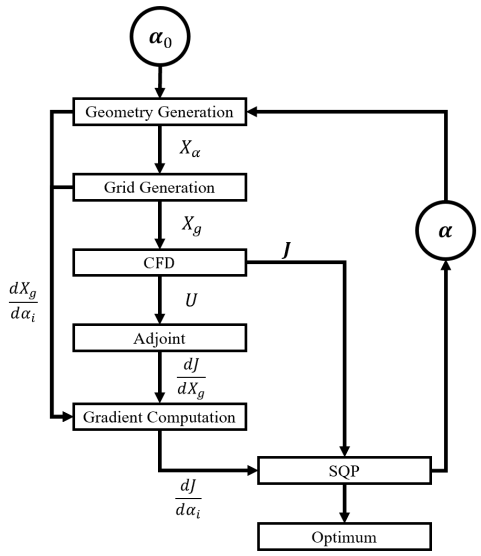

Figure 1: Optimization flowchart description.

2. Highly Loaded Transonic Compressor

2.1. NASA Rotor 37

In the late 70ties, NASA performed a series of tests on different axial compressor stages at the John H. Glenn Research Centre to investigate the efficiency potential of highly loaded compact designs. These machines, such as the NASA stage 37, were intended to cover a range of design parameters typical of jet-engine high-pressure compressor stages [15]. These stages have been representative of advanced air-breathing engines for more than 20 years. Today, the rotor 37, characterized by a rotor tip velocity of 454 m/s, is still often used as a test case to certify many experimental test benches and numerical simulation codes [16; 17]. While for that time advanced design considerations were used to design the rotor 37, the overall design process was based on a trail-and-error principle, which has been around since the invention of the wheel.

2.2. Optimization Framework

The optimization process is composed of several steps presented in Fig. 1. A CAD-based geometry,

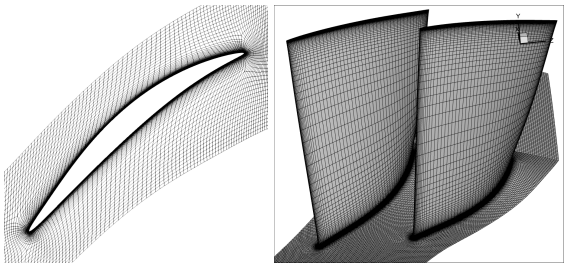

Figure 2: Hub 2D grid (Left) and blade 3D grid (Right).

denoted by a discrete vector X_α which references the surface of the model, is first built from an initial set of design variables α. The grid, X_g, is then generated and passed on to the flow solver, which computes the flow solution, U, and objectives and constraints, J. The sensitivities of the objectives and constraints with respect to the grid, dJ/dX_g, are computed with an adjoint solver. The gradients are assembled using the sensitivities of the grid, objectives, and constraints and they are forwarded to an SQP optimizer. Each step of the optimization process is performed using the CADO software suite developed at the von Karman Institute [18].

2.3. CFD Grid Generation

The computational domain is discretized with a multiblock structured grid [19]. The meridional flow path is subdivided into a zone for the blade and one for the clearance. Both clearance region and near hub endwall region are discretized by a grid point distribution with a boundary layer refinement. Each meridional grid line is converted into a surface of revolution where the ones from the blade region are intersected with the blade. An angle-preserving conformal mapping [20] is used to transform the three-dimensional intersected blade profile (x, y, z) to a two-dimensional plane. Then a two-dimensional grid is applied in the blade-to-blade plane using a multi-block topology, with an O-grid around the blade connected to 4 H-blocks. The result after the elliptic grid smoothing [21] is shown in Fig. 2. The grid points are then brought back to the three-dimensional space where they are regrouped into different grid blocks. The refinement of the grid at the different walls is such to ensure a $y^+ < 4$ at the peak efficiency operating point.

2.4. CFD Computation

The compressible Reynolds Averaged Navier-Stoke (RANS) equations are solved with an implicit time integration scheme accelerated by local time-stepping and multigrid. The flow solver [22] uses a cell-centered finite volume discretization on multiblock structured grid where the fluid is considered as a perfect gas. The viscous fluxes are computed with a central discretization scheme, the Spalart-Allmaras [23] turbulence model is used for the turbulence closure problem assuming a complete turbulent flow from the inlet. The ambient total quantities and flow direction are imposed at the inlet with a dummy cell concept [24], while the static pressure with radial equilibrium is set at the outlet. The CFD is considered converged when a relative decrease of 1.0E-10 is obtained in the density residual.

2.5. Gradient Computation

A gradient-based optimization method requires to compute the gradient of the objective function with respect to the design variables. In the present work, a two-step approach [19] is taken where the sensitivities of the function, $J(U, X_g)$, are first computed with respect to the grid coordinate, X_g, using a discrete adjoint solver [25; 26]. The system given by Eqn. 1 is solved at a similar computational cost compared to the primal solver and is independent from the number of design variables. The sensitivities of the objective function are then computed by Eqn. 2.

$$\left(\frac{dR}{dU}\right)^T \psi = \left(\frac{dJ}{dU}\right)^T \tag{1}$$

$$\frac{dJ}{d\alpha} = \left(\frac{\partial J}{\partial X_g} + \psi^T \frac{\partial R}{\partial X_g}\right) \cdot \underbrace{\frac{dX_g}{d\alpha}}_{\text{C-S}} \tag{2}$$

The sensitivities of the grid coordinate, $dX_g/d\alpha$, with respect to the design variables are calculated instead with a forward approach using a Complex-Step (C-S) method [27]. In contrast to the adjoint method, the cost of such an approach for one single design variable is proportional to the geometry and grid generation cost; it needs to be repeated as many times as there are design variables. As the grid sensitivity analysis can be trivially parallelized while each of them requires less than one tenth of the CFD computational time cost, this approach remains affordable. The process can be distributed to consumer-grade computing machines while the heavy load of the primal and adjoint computations are handled by the main unit.

The computation of the term $\frac{\partial R}{\partial X_g}$ in Eqn. 2 proves to be difficult for the turbulence residual, because

of the dependency on the wall distance. The wall distance of an internal cell depends on the coordinate of the nodes of this cell, but as well on the coordinates of the closest projection of this cell on the nearest wall. This makes the computation of the sensitivities rather involved. An accepted approach is to neglect this term, as it has a lower impact than a frozen turbulence approach [28; 29].

In order to improve the gradient accuracy, another method is developed in the present work. Eqn. 3 demonstrates the split between the forward and reverse process applied to compute the gradient without compromising the accuracy. The difference with respect to Eqn. 2 is that now the dependency of the residual on the design variable α is considered entirely using the complex-step method, enabling to derive through the wall distance computation without added complexity.

$$\frac{dJ}{d\alpha} = \frac{\partial J}{\partial X_g} \overbrace{\frac{dX_g}{d\alpha}}^{\text{C-S}} + \underbrace{\psi^T}_{\text{Adjoint}} \overbrace{\frac{\partial R}{\partial X_g} \frac{dX_g}{d\alpha}}^{\text{C-S}} \tag{3}$$

2.6. Single-Point Aero Optimization

The optimization minimizes the objective, Eqn. 4, to improve the performance of the compressor at near peak total-to-total efficiency. The operating point is set by imposing a constant outlet static pressure throughout the optimization process. A constraint is imposed on the mass flow to keep the operating point within 0.5% of the baseline operating mass flow.

$$\text{Minimize} \quad J \equiv 1 - \frac{\eta_{TT}}{\eta_{TT,ref}} \tag{4}$$

$$Cstr \equiv 0.995 \; < \; \frac{\dot{m}}{\dot{m}_{ref}} \; < \; 1.005 \tag{5}$$

The optimization problem is solved using an in-house developed Sequential Quadratic Programming (SQP) optimizer. Convergence is reached after 26 major iterations where the objective, constraints and gradients are evaluated for a total of 36 CFD (including line searches) and 50 adjoint computations (2 adjoints per major iteration for efficiency and mass flow). The termination criterium of the optimizer is reached when the improvements in total-to-total efficiency, η_{TT}, with respect to the previous iteration is less than 0.001%. A 5.52% η_{TT} increase was finally reached for a 0.4% mass flow decrease, Tab. 1.

Parameters	**Difference** [%]
Total-to-total efficiency, η_{TT}	+ 5.52
Mass flow, $\dot{m}$	- 0.40
Total-to-total pressure ratio, Π_{TT}	+ 4.89

Table 1: Optimization result summary.

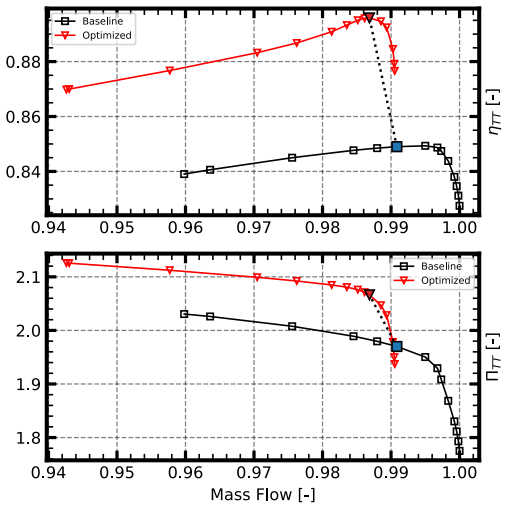

Figure 3: Compressor map.

2.7. Compressor Map

While the overall performance of the optimized design has been increased compared to the baseline, both in terms of η_{TT} and Π_{TT}, a 0.95% decrease in chocking mass flow can be observed on the right side of the compressor map, Fig. 3. This is the result of the tolerance set on the constraint to respect the mass flow at peak efficiency. The range towards the choking condition from the peak efficiency point (red-filled triangle), has been shortened which induces a steep decrease in η_{TT} and Π_{TT}. The optimized η_{TT} distribution also shows a steeper diminution on the left side, which forms a narrow peak near the operating point targeted by the optimization. On the other hand, the Π_{TT} distribution has a similar shape to the baseline but shifted to the left, and with a wider operating range. The following discussion will concentrate on the comparison between the two designs at near peak efficiency shown by the red-filled triangle and the blue-filled square on Fig. 3.

2.8. Blade-To-Blade Flow

On the mid span relative Mach distribution, Fig. 4 (a-b), an attached bow shock is clearly observed

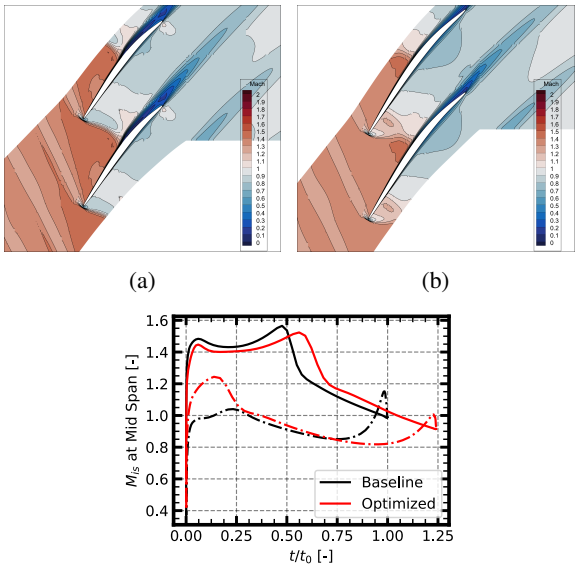

Figure 4: Comparison of M_{rel} at midspan for the baseline (a) and the optimized blade (b). Comparison M_{is} near the hub (c).

at the LE for both baseline and optimized designs. The suction side Mach number prior to the shock is also lower in the optimized design, through a similar mechanism as in the hub passage. The passage shock intensity was reduced from a normal shock to an oblique shock, and the boundary layer thickening through the interaction with the shock is significantly reduced, Fig. 4 (a-b). As the thickness distribution is kept constant during the optimization, these ameliorations lead to less favorable PS velocity distribution. Therefore, the PS performance has been traded-off for a bigger gain on the SS. The optimizer has also increased the chord length (the optimized chord length in Fig. 4 (c) is normalized by the baseline chord) which in turn increases the airfoil solidity. This action is necessary to maintain the same blade loading after reducing the suction side Mach number before the shock. From the flow behavior around the blade, the optimizer has acted on three mechanisms:

1. Decrease of the flow incidence which improves the SS Mach number at the cost of the PS Mach number.
2. Preservation of the blade loading in the optimized design through an increased solidity.
3. Reduction of the passage shock intensity.

2.9. Transverse flow

The overall $V_{\theta,2}$ and $\dot{m}_2$ distribution at 0.1c downstream of the TE, Fig. 5, remain similar to the baseline. The $V_{\theta,2}$ distribution is maintained to keep the same work. A slightly higher mass flow in the main passage of the channel is due to the reduced channel height. Both optimized and baseline design experience a blockage created by the tip leakage vortex. The highest gains in η_{TT} are achieved in the upper half of the passage as the result of the lower shock losses, improved shock-boundary layer interaction, and finally a reduced tip leakage vortex. The radial variation of the relative inlet flow angle is show in Fig. 6 (Left) for a position 0.25c upstream of the leading edge. A similar distribution is obtained except for the hub, where due to the absence of the concave curvature in the optimized design, a higher axial velocity is obtained, resulting in a lower relative flow angle. The optimized blade is however oriented more tangentially, resulting in a lower incidence angle over the full span at peak efficiency, Fig. 6 (Right). The lower incidence leads to a better isentropic Mach number distribution over the blade suction side, as indicated previously, but due to the more tangential blade position, the throat area is reduced, leading to a lower choking mass flow. A reduced margin from the peak efficiency point to choking is then an inevitable result.

3. 2D High Turning Blade

3.1. Preliminary Design

Conventional single airfoils can hardly reach high flow turning due to the rapid boundary-layer growth from high flow diffusion. This study aims to push the conventional design to its limit through the use of gradient-based optimization. Decades of compressor blade design recommend a *De Haller* number, w_1/w_2, above 0.7 to avoid boundary-layer separation. Such criteria can not be satisfied for a reaction blade with a high turning above 45° as shown in Fig. 7. During the conception of the preliminary design, the Lieblein diffusion factor [30] is maintained at a reasonable value by increasing the solidity, while a 50° inlet flow angle is chosen for a fully axial outlet flow. The well-known *NACA-65* thickness distribution [31; 32] is then applied to an arbitrary camberline to create the preliminary shape, Fig. 8. An identical multi-block grid generation process to the NASA rotor 37, Section 2.3, is used to produce the quasi-2D CFD grid. The two-dimensional grid is first generated space with a boundary-layer refinement at the blade

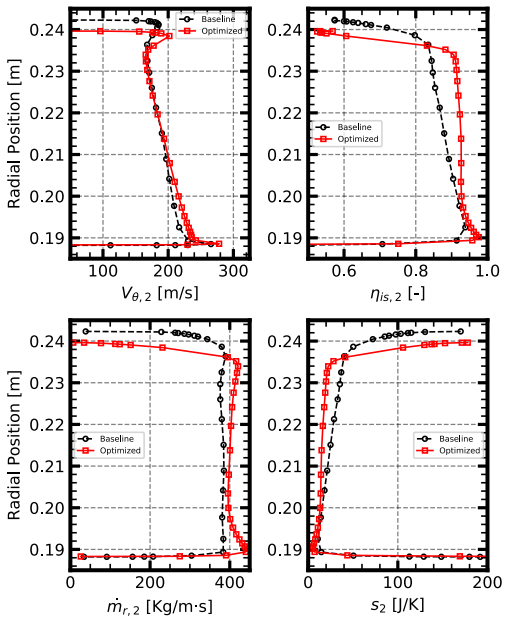

Figure 5: Comparison of $V_{\theta,2}$, $\eta_{is,2}$, $\dot{m}_2$, and s_2, at 0.1c downstream of the TE in the baseline (Black) and optimized design (Red).

wall which is then duplicated to form a spanwise thin three-dimensional fluid domain. The previously explained optimization framework and its core components, Section 2.2, are used to solve the flow, compute the sensitivities, and optimize the design.

Design parameter			
Inlet flow velocity	M_1	0.6	[-]
Inlet flow angle	β_1	50	[°]
Flow turning	θ	50	[°]
Solidity	σ	2	[-]
Reynolds Number	Re	800 000	[-]
Total temperature	T_{01}	340	[K]
Axial chord length	c_h	30	[mm]

Table 2: Summary of the design parameters

3.2. Single-Point Optimization

A total of 9 design variables acting on the airfoil solidity, camberline, and thickness distribution are selected for the optimization process. The SQP optimizer minimizes the objective, Eq. 6, to reduce the pressure loss. The operating point is set by imposing a constant outlet static pressure and a defined inlet flow angle in the flow solver throughout the optimization process. Two constraints, Eq. 7-8, are

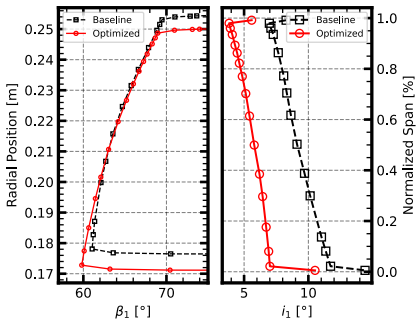

Figure 6: Comparison β_1 (Left) and incidence (Right) at 0.25c upstream in the baseline (Black) and optimized design (Red).

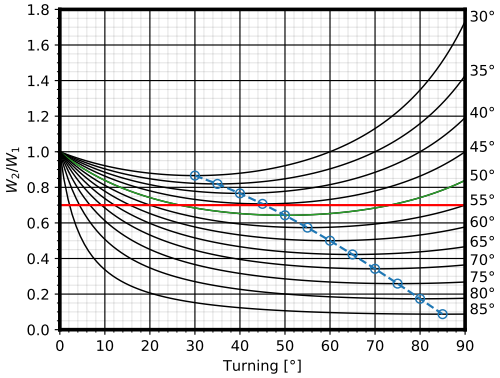

Figure 7: De Haller number with respect to a turning and the inlet flow angle.

imposed on the mass flow and the outlet flow angle to maintain the operating point above the baseline mass flow and a fully axial exit flow.

$$\text{Minimize} \quad J \equiv \frac{\omega}{\omega_{ref}} - 1 \tag{6}$$

$$Cstr1 \equiv 0.995 < \frac{\dot{m}}{\dot{m}_{ref}} \tag{7}$$

$$Cstr2 \equiv \frac{\beta_2}{\beta_{2ref}} < 0 \tag{8}$$

Convergence is reached after 13 iterations and the optimized design, Fig. 8, observes a 37% decrease in pressure loss for a 49.12° flow turning. The blade thickness and solidity have been reduced to respectively decrease the wake width and the flow-wake fraction leading to lesser pressure loss as observed in Fig. 9 (a-b). The optimizer has also chosen to impose a metal blade overturning to compensate for the flow

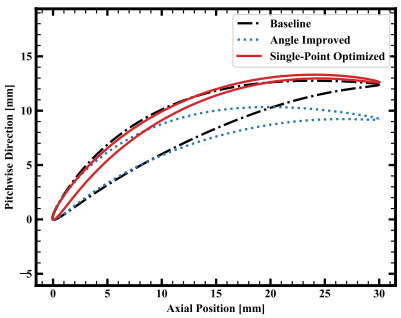

Figure 8: Preliminary baseline, Single-Point optimized and Angle-Improved airfoil geometry.

deviation from the boundary-layer detachment. The optimized design M_{is} distribution, Fig. 9 (c), demonstrates similar features like a controlled diffusion airfoil with a velocity peak in the front part of the SS with a nearly constant velocity on the PS. Nonetheless, neither the preliminary baseline nor the optimized design satisfied the outlet flow angle constraint, and a second baseline design is produced from the same preliminary design through an optimization process aiming at only improving the outlet flow angle. Interestingly, the resulting M_{is} distribution of the angle-improved baseline has a similar SS velocity profile as the first optimized design. The controlled diffusion on the suction side of this design, along with the blade metal-overturning, has contributed to a reduction in boundary-layer separation intensity leading to lower deviation and better flow turning, Fig 12 (a). The angle-improved design is used as a baseline in the following subsection.

3.3. Multi-Point Optimization

The airfoil has been optimized for a single operating point where the off-design performance is uncertain. A multiple operating point strategy is adopted where the objective is computed from several operating point pressure loss quantities. For an equal contribution of the design (OP1) and the 5° positive incidence (OP2) operating point in the objective computation (2-OP), Eqn. 9, the optimizer found an airfoil geometry, Fig. 10, with a thicker LE than the optimized single-point design, a lower curvature on the front part of the SS, and a thin TE to respectively accommodate the incidence variation, reduce the transonic losses in the positive incidence operating point, and decrease the wake pressure loss. The peak velocity of the 2-OP design has been lowered and moved downstream at OP1, Fig. 11. As the velocity

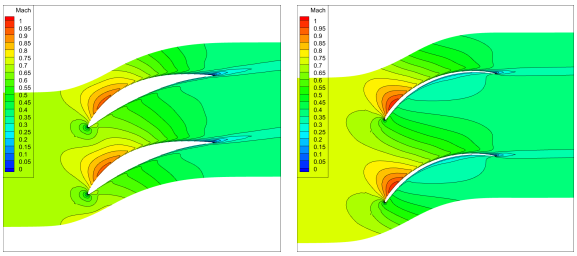

(a) Baseline (b) Single-Point Optimized

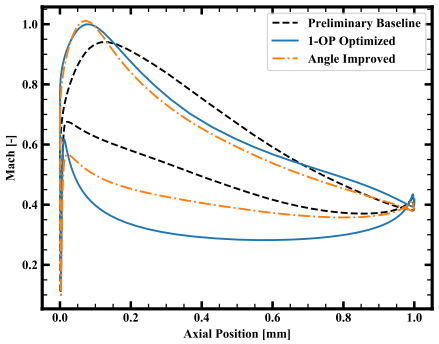

(c) M_{is} distribution

Figure 9: Relative Mach (a-b) and M_{is} distribution (c) at design operating point.

on the SS increases when the airfoil is submitted to a higher inlet flow angle, Fig. 12-13, lowering the peak velocity improves the transonic flow on the blade front at OP2. The flow around the airfoil shows a smoother deceleration from a less curved suction side, Fig. 11, Fig. 13, at OP1. The solidity has also been reduced to improve the flow-wake ratio as previously observed.

Name	Description	Incidence
OP1	Design	0°
OP2	Positive incidence	+5°
OP3	Negative incidence	-5°

Table 3: Summary of the operating points

The three operating point configuration (3-OP) takes into consideration the design (OP1), positive incidence (OP2), and negative incidence (OP3) airfoil performance, with a higher weight on OP1, Eqn. 10. The optimized design has a thicker LE which extends more on the PS than the previous optimization to accommodate OP3, Fig. 10. As more importance was accorded to the OP1, the shape has a higher curvature on the blade front than previously. The SS maximum

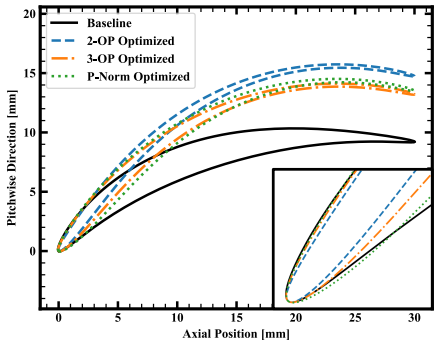

Figure 10: Baseline, 2-OP optimized, 3-OP optimized, P-Norm constrained geometry.

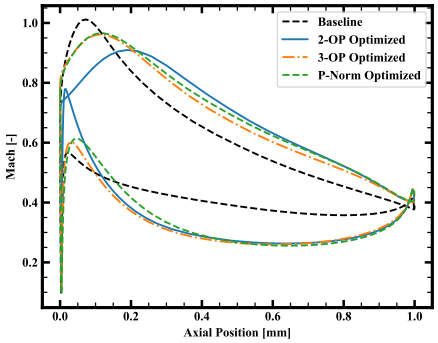

Figure 11: Baseline, 2-OP optimized, 3-OP optimized, P-Norm constrained M_{is} distribution at design operating point.

velocity lies between the baseline and 2-OP peak to improve all three operating points, Fig. 11, Fig. 13. A performance trade-off can be observed between the different optimization configurations, Tab. 4. Adding more operating points with relevant weights allows the airfoil to function better in off-design conditions at the cost of the design point performance. While the optimization method finds an optimum design for a given objective, the choice of operating point and their weighting should be carefully discussed as they directly reflect the designer's choices and intents.

Minimize

$$J_{2OP} \equiv 0.5\frac{\omega_{OP1}}{\omega_{OP1,ref}} + 0.5\frac{\omega_{OP2}}{\omega_{OP2,ref}} - 1 \quad (9)$$

$$J_{3OP} \equiv 0.5\frac{\omega_1}{\omega_{1,ref}} + 0.25\frac{\omega_2}{\omega_{2,ref}} + 0.25\frac{\omega_3}{\omega_{3,ref}} - 1 \quad (10)$$

Constraint

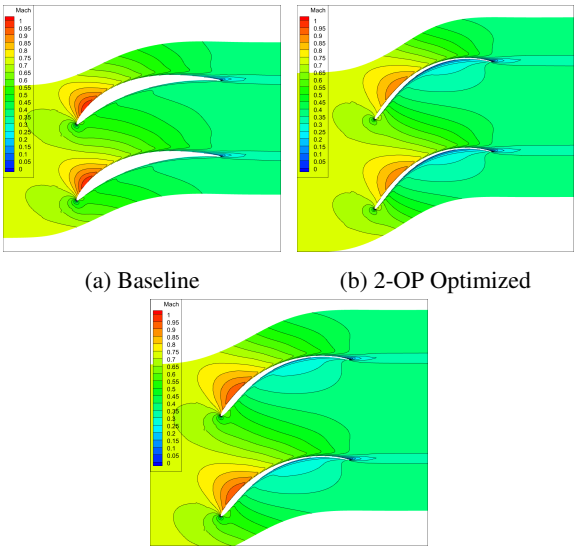

(a) Baseline (b) 2-OP Optimized

(c) 3-OP Optimized

Figure 12: Baseline and the multi-point optimized airfoil relative Mach at design operating point.

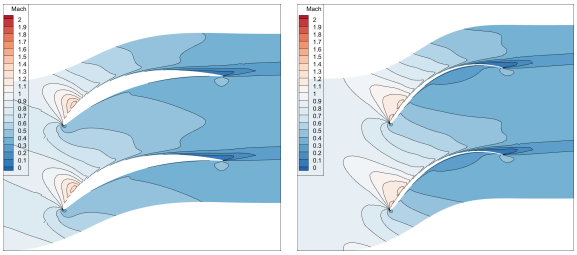

(a) Baseline (b) 2-OP Optimized

Figure 13: Baseline and 2-OP optimized relative Mach at 5° positive incidence.

$$C1 \equiv 0.995 < \frac{\dot{m}_{OP1}}{\dot{m}_{OP1,ref}} \quad (11)$$

$$C2 \equiv \frac{\beta_{2,OP1}}{\beta_{2,OP1,ref}} < 0 \quad (12)$$

Name	Baseline	1-OP	2-OP	3-OP
OP1	0.01183	0.00911	0.01053	0.00949
OP2	0.03522	-	0.02247	0.03138
OP3	0.01375	-	-	0.01053

Table 4: Pressure loss from three multi-point optimization configuration.

3.4. Blade Thickness Constraint

While the multi-point optimization approach has thickened the LE to improve the airfoil performance in off-design conditions, the overall produced airfoil is unrealistically thin. The airfoil may present structural weakness from vortex shedding vibration or foreign object impact. The geometry itself may also be too thin to be manufactured at a reasonable cost.The airfoil thickness problem is approached in this work with the designer's appreciation and experience.

$$C1 \equiv \sqrt[p]{\frac{\sum t_i^p}{n}} > M \tag{13}$$

The airfoil is built from a thickness distribution where one can impose the maximum value to be above a certain value, M. The p-norm is calculated to approximate the maximum value as complex-step sensitivities can not be computed with algorithmic max and min functions. As the mass flow constraint was observed to be inactive in the previous optimizations, it is replaced with the p-norm constraint, Eqn. 8. The three-operating point optimization produced a blade with a thicker LE than the previous optimized design, Fig. 10, with a similar thin shape on the airfoil's second half. Increasing the p-norm constraint will only increase locally the thickness while the TE may be kept slender to reduce the wake losses. A second approach consists of imposing a constraint on the surface area, Eqn. 15, to enforce fair distribution of the thickness along the airfoil.

$$A = \int_0^1 P(u) \times \frac{dP}{du} du \tag{14}$$

$$C1 \equiv \left(A_{ss} - A_{ps}\right) > \epsilon S \tag{15}$$

Several multi-point optimizations were ran with a Surface Constraint (SC) of 25%, 50%, 75% and 100% with respect to the baseline surface, Fig. 14, instead of the p-norm constraint. The optimized geometry with a 50% SC is similar to the p-norm constrained shape with a thinner LE and a slightly thicker second half as intended. The 75% and 100% SC optimizations produced a more reasonable airfoil. The 25% SC case was instead limited by the minimum bound imposed by on each design variables. In contrary to the PS velocity distribution, the SC variation did not drastically impact the SS flow, Fig. 15. Comparably to the

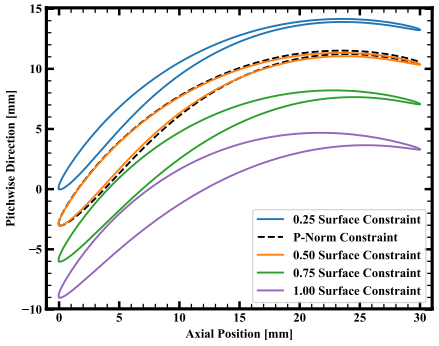

Figure 14: Optimized geometries using different surface constraints.

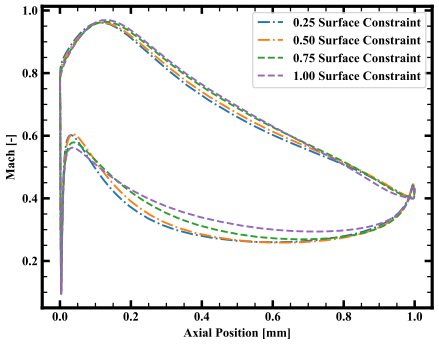

Figure 15: M_{is} distribution of different geometries using different surface constraints at design operating point.

study on the transonic rotor, the optimizer has chosen again to sacrifice more the PS velocity to improve the SS performance. Lower pressure loss at the operating point can be reached with a smaller airfoil surface, Fig. 16, at the cost of a deteriorated off-design performances. The optimizer had to chose between the loss reduction from a thinner blade at design operating point and better off-design from a thicker LE.

4. Conclusion

A high-pressure ratio in conventional low-pressure compressors (LPC) can be achieved by either increasing the circumferential velocity or the flow turning. A three-dimensional transonic rotor blade and a two-dimensional single airfoil are explored to develop a design method for modern LPC through gradient-based optimization. The technique is first implemented for the transonic NASA rotor 37, characterized by a tip velocity of 454 m/s. The CAD-

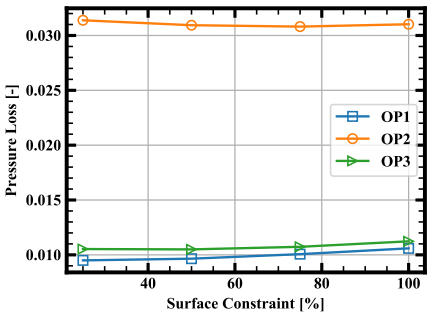

Figure 16: Performance comparison between different surface geometry.

parametrized rotor is given to a gradient-based sequential quadratic program optimizer where the sensitivities are computed with an adjoint method. The optimizer chose to act on the flow incidence to improve the suction side performance at the cost of the pressure side velocity distribution, and reduce the passage shock intensity. Then, a two-dimensional high turning conventional airfoil is entirely designed using an optimization approach. A preliminary airfoil is first drawn from design boundary conditions and correlations. The baseline is then optimized to improve its performance. Several approaches have been taken into consideration during the conception of an optimization technique aiming at producing a coherent airfoil geometry. The resulting method will be then applied to a complex airfoil configuration such as the tandem blade.

References

[1] J. J. Lee, S. P. Lukachko, I. A. Waitz, A. Schafer, Historical and future trends in aircraft performance, cost, and emissions, Annual Review of Energy and the Environment 26 (1) (2001) 167–200, publisher: Annual Reviews 4139 El Camino Way, PO Box 10139, Palo Alto, CA 94303-0139, USA.

[2] A. Peters, Z. S. Spakovszky, W. K. Lord, B. Rose, Ultrashort Nacelles for Low Fan Pressure Ratio Propulsors, Journal of Turbomachinery 137 (2). doi:10.1115/1.4028235.
URL https://doi.org/10.1115/1.4028235

[3] N. L. Sanger, Analytical study of the effects of geometric changes on the flow characteristics of tandem-bladed compressor stators, Tech. rep., National Aeronautics and Space Administration (1971).

[4] C. S. Ahn, K. Y. Kim, Aerodynamic design optimization of a compressor rotor with Navier—Stokes analysis, Proceedings of the Institution of Mechanical Engineers, Part A: Journal of power and energy 217 (2) (2003) 179–183, publisher: SAGE Publications Sage UK: London, England.

[5] E. Benini, Three-dimensional multi-objective design optimization of a transonic compressor rotor, Journal of propulsion and power 20 (3) (2004) 559–565.

[6] A. Samad, K.-Y. Kim, T. Goel, R. T. Haftka, W. Shyy, Multiple surrogate modeling for axial compressor blade shape optimization, Journal of Propulsion and Power 24 (2) (2008) 301–310.

[7] A. Samad, K.-Y. Kim, Shape optimization of an axial compressor blade by multi-objective genetic algorithm, Proceedings of the Institution of Mechanical Engineers, Part A: Journal of Power and Energy 222 (6) (2008) 599–611, publisher: SAGE Publications Sage UK: London, England.

[8] M. C. Duta, S. Shahpar, M. B. Giles, Turbomachinery design optimization using automatic differentiated adjoint code, in: Turbo Expo: Power for Land, Sea, and Air, Vol. 47950, 2007, pp. 1435–1444.

[9] H. Hu, J. Yu, Y. Song, F. Chen, The application of support vector regression and mesh deformation technique in the optimization of transonic compressor design, Aerospace Science and Technology 112 (2021) 106589, publisher: Elsevier.

[10] D. E. Goldberg, J. H. Holland, Genetic algorithms and machine learningPublisher: Kluwer Academic Publishers-Plenum Publishers; Kluwer Academic Publishers ....

[11] E. Zitzler, Evolutionary algorithms for multiobjective optimization: Methods and applications, Vol. 63, Citeseer, 1999.

[12] S. Chen, J. Montgomery, A. Bolufé-Röhler, Measuring the curse of dimensionality and its effects on particle swarm optimization and differential evolution, Applied Intelligence 42 (3) (2015) 514–526, publisher: Springer.

[13] T. Verstraete, Introduction to optimization and multidisciplinary design, VKI, lecture Series 7 (2010) 93.

[14] M. H. Aissa, R. Maffulli, L. Mueller, T. Verstraete, Optimisation of a turbine inlet guide vane by gradient-based and metamodel-assisted methods, International Journal of Computational Fluid Dynamics 33 (6-7) (2019) 302–316, publisher: Taylor & Francis.

[15] L. Reid, R. D. Moore, Design and overall performance of four highly loaded, high speed inlet stages for an advanced high-pressure-ratio core compressor, Tech. rep. (1978).

[16] R. D. Moore, Performance of single-stage axial-flow transonic compressor with rotor and stator aspect ratios of 1.19 and 1.26 respectively, and with design pressure ratio of 2.05, Tech. rep., National Aeronautics and Space Administration (1982).

[17] J. Dunham, CFD Validation for Propulsion System Components (la Validation CFD des organes des propulseurs), Tech. rep., ADVISORY GROUP FOR AEROSPACE RESEARCH AND DEVELOPMENT NEUILLY-SUR-SEINE (FRANCE), section: Technical Reports (May 1998).
URL https://apps.dtic.mil/sti/citations/ADA349027

[18] T. Verstraete, CADO: a computer aided design and optimization tool for turbomachinery applications, in: Proceedings of the 2nd international conference on engineering optimization, Lisbon, Portugal, Vol. 69, 2010, p. 69.

[19] L. Müller, Adjoint-Based Optimization of Turbomachinery with Applications to Axial and Radial TurbinesPublisher: Université libre de Bruxelles.

[20] P. L. Miller IV, J. H. Oliver, D. P. Miller, D. L. Tweedt, BladeCAD: An interactive geometric design tool for turbomachinery blades, Vol. 78729, American Society of Mechanical Engineers, 1996.

[21] J. F. Thompson, A general three-dimensional elliptic grid generation system on a composite block structure, Computer Methods in Applied Mechanics and Engineering 64 (1-3) (1987) 377–411, publisher: Elsevier.

[22] I. Sanchez Torreguitart, T. Verstraete, L. Mueller, Optimization of the LS89 axial turbine profile using a cad and adjoint based approach, International Journal of Turbomachin-

ery, Propulsion and Power 3 (3) (2018) 20, publisher: Multidisciplinary Digital Publishing Institute.
[23] S. R. Allmaras, F. T. Johnson, Modifications and clarifications for the implementation of the Spalart-Allmaras turbulence model, in: Seventh international conference on computational fluid dynamics (ICCFD7), Vol. 1902, Big Island, HI, 2012.
[24] J. Blazek, Computational fluid dynamics: principles and applications, Butterworth-Heinemann, 2015.
[25] O. Pironneau, On optimum design in fluid mechanics, Journal of Fluid Mechanics 64 (1) (1974) 97–110, publisher: Cambridge University Press.
[26] A. Jameson, Aerodynamic design via control theory, Journal of scientific computing 3 (3) (1988) 233–260, publisher: Springer.
[27] J. R. Martins, P. Sturdza, J. J. Alonso, The complex-step derivative approximation, ACM Transactions on Mathematical Software (TOMS) 29 (3) (2003) 245–262, publisher: ACM New York, NY, USA.
[28] C. S. Kim, C. Kim, O. H. Rho, Feasibility study of constant eddy-viscosity assumption in gradient-based design optimization, Journal of Aircraft 40 (6) (2003) 1168–1176.
[29] R. P. Dwight, J. Brezillon, Effect of approximations of the discrete adjoint on gradient-based optimization, AIAA journal 44 (12) (2006) 3022–3031.
[30] S. Lieblein, F. C. Schwenk, R. L. Broderick, Diffusion factor for estimating losses and limiting blade loadings in axial-flow-compressor blade elements, Tech. rep., NATIONAL ADVISORY COMMITTEE FOR AERONAUTICS CLEVELAND OH LEWIS FLIGHT ... (1953).
[31] J. McGlumphy, W.-F. Ng, S. R. Wellborn, S. Kempf, Numerical Investigation of Tandem Airfoils for Subsonic Axial-Flow Compressor Blades, Journal of Turbomachinery 131 (2). doi:10.1115/1.2952366.
URL https://doi.org/10.1115/1.2952366
[32] C. Schluer, M. Böhle, M. Cagna, Numerical investigation of the secondary flows and losses in a high-turning tandem compressor cascade.

AEROTHERMOCHEMISTRY

An introduction to the role of chemical models in the enthalpy rebuilding procedure of plasma wind tunnels

Enrico Anfuso

Aeronautics and Aerospace Department, von Karman Institute for Fluid Dynamics, Belgium, enrico.anfuso@vki.ac.be

Supervisor: Olivier Chazot

Professor, Aeronautics and Aerospace Department, von Karman Institute for Fluid Dynamics, Belgium, olivier.chazot@vki.ac.be

University Supervisor: Aurélie Bellemans

Assistant Professor, Mechanical Engineering Department, Vrije Universiteit Brussel, Belgium, aurelie.bellemans@vub.be

Abstract

The enthalpy rebuilding procedure used at the VKI Plasmatron facility coupled numerical modelings and experimental data. It is based on an iterative procedure to match the experimental data with the numerical counterparts. This work focuses on the heat flux computation and the role played by the chemical models describing the chemical non-equilibrium in the boundary layer region. The analysis assumes a uniform distribution of the parameters of the Arrhenius law used to represent the forward reaction coefficients. Samples of the distributions are input in a boundary layer solver to estimate the heat flux. Results show a strong dependency on the temperature exponent parameter that leads to a bi-modal distribution. The sensitivity analysis ends with the computation of the Sobol indices to quantify the impact of each parameter on the inferred quantity.

Keywords: enthalpy rebuilding, chemical kinetics modelings, Arrhenius law

1. Introduction

Among the different solutions presented to tackle the problem of space debris, the end-of-life disposal through aerothermal demise in atmospheric entry is certainly one of the most effective, especially when dealing with small debris (order of millimeters) compared to solutions such as harpoons, nets, and robotic arms. A meticulous design of the demise process plays a crucial role, and plasma wind tunnels are essential in recreating the same aerothermochemical conditions experienced during atmospheric entry. Testing conditions (e.g., free-stream enthalpy) must be accurately known to replicate a flight scenario [1; 2] but unfortunately, they cannot be directly measured with dedicated probes and must rely on rebuilding procedures [3; 4]. These methodologies rebuild the quantities of interest by matching the experimental data with the numerical counterparts. Accurate and objective uncertainty characterization on the rebuilt quantities needs to include uncertainties stemming from the measurement chain and inadequacies of the selected models.

Chemical models play a key role in providing parameters essential to compute the numerical quantities (e.g., heat flux). As pointed out in [5], these models are affected by large inaccuracies being dated more than 20 years ago and validated with experimental data available at that time from shock tubes, gun tunnels, and ballistic ranges facilities. The impact of the inaccuracies on the characterization of the free-stream enthalpy still suffers a lack of knowledge [3] and a deeper understanding is of paramount importance to reduce the discrepancy existing between experiments and modelings [6].

This work summarizes the state-of-the-art enthalpy determination procedure commonly employed at the von Karman Institute's (VKI) Plasmatron focusing on the role played by chemical models on the heat flux computation, a key parameter in the rebuilding procedure.

Section 2 details the current state-of-the-art about

the chemistry kinetics modelings and their inaccuracies. Section 3 describes the enthalpy rebuilding procedure used at the VKI Plasmatron and the implicated Computational Fluid Dynamics (CFD) codes. Section 4 illustrates the methodology to quantify the role of the chemistry in heat flux estimation. Results are presented in Section 5 while conclusions and future developments in Section 6.

2. Chemical kinetics modelings

Chemical models provide a set of nr chemical reactions and ns species. For each reaction, they deliver a set of parameters required in the computation of the production term of the species mass conservation equations [7]:

$$\dot{\omega}_i = M_i \sum_{j=1}^{nr} \left(\nu''_{j,i} - \nu'_{j,i}\right) \left(k_{f,j} \prod_{k=1}^{nsp} [X_k]^{\nu'_{j,k}} - k_{b,j} \prod_{k=1}^{nsp} [X_k]^{\nu''_{j,k}}\right). \quad (1)$$

M_i refers to the molar mass of the species i, $\nu''_{j,i}$ and $\nu''_{j,i}$ are the stoichiometric coefficients of the reactants and products respectively of the species i in the reaction j, $[X_k]$ the concentrations of the species k, and $k_{f,j}$ $k_{b,j}$ the forward and backward reaction rate coefficients, respectively.

$\dot{\omega}_i$ requires a closure models for $k_{f,j}$ and $k_{b,j}$. However, if on one hand models exists for $k_{f,j}$ as will be detailed in the followings, on the other hand $k_{b,j}$ is computed under the equilibrium assumption through Eq. 2, with $K_{c,j}$ the equilibrium constant provided by Statistical Mechanics.

$$\frac{k_{f,j}}{k_{b,j}} = K_{c,j}(T) \quad (2)$$

Empirical results suggest $k_{f,j}$ being a function of the temperature only following the Arrhenius law (Eq. 3) with $c_{f,j}$ [$\mathrm{cm^3\,s^{-1}\,mol^{-1}}$], $b_{f,j}$ [-] and $e_{f,j}$ [K] constant values stemming from experimental data.

$$k_{f,j} = c_{f,j} T^{b_{f,j}} e^{-e_{f,j}/T} \quad (3)$$

Chemical models differs for the values assigned to $c_{f,j}$, $b_{f,j}$ and $e_{f,j}$ parameters. For instance, Tables 1, 2, 3 summarizes the values provided by by Park et al. [8; 9], Gupta et al. [10] and Dunn&Kang [11] models for an air mixture of $nr = 5$ reactions and $ns = 5$ species (N, O, NO, N_2, O_2).

Table 1: $c_{f,j}$ [$\mathrm{cm^3\,s^{-1}\,mol^{-1}}$] parameters of the Arrhenius law (Eq. 3) provided by Park et. al [8; 9], Gupta et al. [10] and Dunn&Kang [11].

Reaction	M	[8; 9]	[10]	[11]
$N_2 + M \rightarrow 2N + M$	N	3.0×10^{22}	4.15×10^{22}	4.085×10^{22}
	O	3.0×10^{22}	1.92×10^{17}	1.9×10^{17}
	N_2	7.0×10^{21}	1.92×10^{17}	4.7×10^{17}
	O_2	7.0×10^{21}	1.92×10^{17}	1.9×10^{17}
	NO	7.0×10^{21}	1.92×10^{17}	1.9×10^{17}
$O_2 + M \rightarrow 2O + M$	N	1.0×10^{22}	3.61×10^{18}	3.6×10^{18}
	O	1.0×10^{22}	3.61×10^{18}	9.0×10^{19}
	N_2	2.0×10^{21}	3.61×10^{18}	7.2×10^{18}
	O_2	2.0×10^{21}	3.61×10^{18}	3.24×10^{19}
	NO	2.0×10^{21}	3.61×10^{18}	3.6×10^{18}
$NO + M \rightarrow N + O + M$	N	1.1×10^{17}	3.97×10^{20}	7.8×10^{20}
	O	1.1×10^{17}	3.97×10^{20}	7.8×10^{20}
	N_2	5.0×10^{15}	3.97×10^{20}	3.9×10^{20}
	O_2	5.0×10^{15}	3.97×10^{20}	3.9×10^{20}
	NO	1.1×10^{17}	3.97×10^{20}	7.8×10^{20}
$N_2 + O \rightarrow NO + N$	-	5.7×10^{12}	6.75×10^{13}	7.0×10^{13}
$NO + O \rightarrow N + O_2$	-	8.4×10^{12}	3.18×10^{9}	3.2×10^{9}

Cipullo et al. [12] carried out an analysis to quantify the role each of the mentioned models has on the rebuilding procedure employed at the VKI Plasmatron facility. The reference testing conditions are $P_{\mathrm{el}} = 200\,\mathrm{kW}$, $p_{\mathrm{c}} = 1500\,\mathrm{Pa}$, and $\dot{m} = 16\,\mathrm{g\,s^{-1}}$ with P_{el}, p_{c}, $\dot{m}$ the electrical power, chamber static pressure and mass flow rate injected in the torch, respectively. An air mixture of 7 species (5 species plus the ionization of NO in NO^+ and e^-) is considered. Results show that the choice of the gas chemistry model has not a significant impact on the process. However, the pressure in the chamber could significantly affect the results: higher pressure means higher molecular collisions leading to pronounced discrepancies between the models.

Besides the discrepancies, one has to deal with the uncertainties of each parameters. Values in Tables 1, 2, 3 stems from experiments that date back two decades, and carried out in ground facilities available at that time (shock tubes, gun tunnels and ballistic ranges facilities) that differ to the plasma wind tunnels. The quantification of uncertainties affecting the model parameters is a challenging task and hence neglected by the authors, who still rely on the nominal values provided by Park, Gupta, or Dunn&Kang model in CFD codes. However, numerical results can significantly affected by the inaccuracies. For instance, Kim et al. [6] have recently presented a modified version of the 11 species (N, O, NO, N_2, O_2, N^+, O^+, NO^+, N_2^+, O_2^+, e^-) air-mixture [8; 9], based on the results of new state-to-state kinetic calculations and shock tube experimental data, that significantly reduce the discrepancies with

Table 2: $b_{f,j}$ parameters of the Arrhenius law (Eq. 3) provided by Park et al. [8; 9], Gupta et al. [10] and Dunn&Kang [11].

Reaction	M	[8; 9]	[10]	[11]
$N_2 + M \rightarrow 2N + M$	N	-1.6	-1.5	-1.5
	O	-1.6	-0.5	-0.5
	N_2	-1.6	-0.5	-0.5
	O_2	-1.6	-0.5	-0.5
	NO	-1.6	-0.5	-0.5
$O_2 + M \rightarrow 2O + M$	N	-1.5	-1.0	-1.0
	O	-1.5	-1.0	-1.0
	N_2	-1.5	-1.0	-1.0
	O_2	-1.5	-1.0	-1.0
	NO	-1.5	-1.0	-1.0
$NO + M \rightarrow N + O + M$	N	0.0	-1.5	-1.5
	O	0.0	-1.5	-1.5
	N_2	0.0	-1.5	-1.5
	O_2	0.0	-1.5	-1.5
	NO	0.0	-1.5	-1.5
$N_2 + O \rightarrow NO + N$	-	0.42	0.0	0.0
$NO + O \rightarrow N + O_2$	-	0.0	1.0	1.0

Table 3: $e_{f,j}$ [K]parameters of the Arrhenius law (Eq. 3) provided by Park et al. [8; 9], Gupta et al. [10] and Dunn&Kang [11].

Reaction	M	[8; 9]	[10]	[11]
$N_2 + M \rightarrow 2N + M$	N	113 200	113 100	113 000
	O	113 200	113 100	113 000
	N_2	113 200	113 100	113 000
	O_2	113 200	113 100	113 000
	NO	113 200	113 100	113 000
$O_2 + M \rightarrow 2O + M$	N	59 360	59 400	59 500
	O	59 360	59 400	59 500
	N_2	59 360	59 400	59 500
	O_2	59 360	59 400	59 500
	NO	59 360	59 400	59 500
$NO + M \rightarrow N + O + M$	N	75 500	75 600	75 500
	O	75 500	75 600	75 500
	N_2	75 500	75 600	75 500
	O_2	75 500	75 600	75 500
	NO	75 500	75 600	75 500
$N_2 + O \rightarrow NO + N$	-	42 938	37 500	38 000
$NO + O \rightarrow N + O_2$	-	19 400	19 700	19 700

existing flight and ground experimental data.

This article focuses on the impact that the inaccuracies have on the heat flux estimation, which is crucial in the enthalpy rebuilding procedure.

3. The enthalpy rebuilding procedure

The full potential of Plasma Wind Tunnels (PWTs) is unleashed when test conditions correctly reproduce at least the real flight environment around the stagnation point of the aerospace vehicle [13; 14]. The extrapolation from the ground test conditions to flight is commonly achieved employing the Local Heat Transfer Simulation (LHTS) technique [2]. Kolesnikov's works state that, under the assumption of Local Thermochemical Equilibrium (LTE) at the outer edge of the boundary layer, the stagnation point heat flux in flight and in ground are identical, if total enthalpy H, stagnation pressure p, and the velocity gradient β are locally matched: $H_e^t = H_e^f$, $p_e^t = p_e^f$, $\beta_e^t = \beta_e^f$ where the subscript e denotes the boundary layer edge, and the superscripts t and f the test and flight conditions (see Fig. 1), respectively.

While p_e, β_e can be retrieved from dynamic pressure measurements and test probe geometry, the computation of H_e is not straightforward. The standard inverse problem used at the VKI Plasmatron couple experimental data (e.g, Pitot pressure, heat flux) and the numerical counterparts simulated with two steady CFD codes, the Inductively Coupled Plasma (ICP) and the Boundary Layer (BL) solvers. One simulates the plasma jet in the VKI Plasmatron chamber

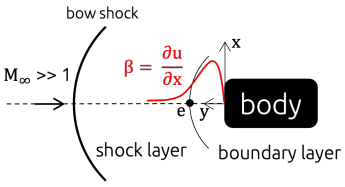

Figure 1: Simplified representation of the bow shock and boundary layer typical of a re-entry body. The red curve represents the gradient of the tangential component (along the $x-$direction) of the velocity.

under the Local Thermo-chemical Equilibrium (LTE) assumption and computes the boundary layer edge quantities. These parameters are then input to the second solver that computes the boundary layer equations around the testing sample under chemical non-equilibrium conditions. Thermodynamic and transport data, as well as the parameters to compute the forward and backward reaction rate coefficients, are inquired through the library PEGASE [15]. The rebuilding process iterates on a thermodynamic variable at the boundary layer edge (e.g., the temperature) until numerical and experimental quantities match (see Fig. 2).

The boundary layer equations are advantageous compared to the full set of Navier-Stokes (NS) equations both in terms of mathematical and numerical complexity. However, they do not provide information about the upstream flow which can be computed solving the full NS equations at the expense of an increasing computational cost. A valid alternative is offered by reducing the complexiting of the

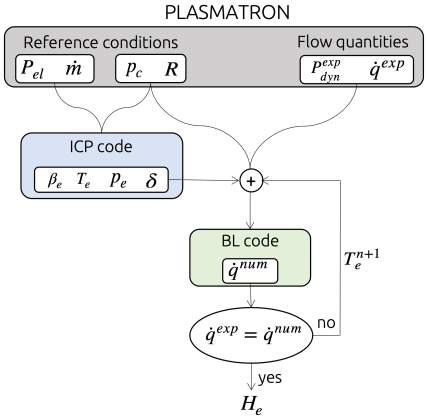

Figure 2: Sketch of the enthalpy rebuilding procedure employed at the VKI Plasmatron facility. The subscript e indicates the boundary layer edge quantities, the superscripts exp, num the experimental and numeral quantities, respectively. δ is the boundary layer thickness and R the radius of the testing probe.

equations focusing in the stagnation line region formulating the Dimensionally Reduced NS Equations (DRNSEs). These are still able to capture the the relevant features of re-entry flows at a reduced computational cost. The VKI owns a stag-line code previously developed by Mufalo et al. [16] able to solve the reacting flow along the stagnation line of spherical body, and to catch relevant flow features around the stagnation point, such as the heat flux. The code can also be extended to non-spherical bodies that can be approximately modeled with an equivalent sphere of radius R_0 [17]. The advantage of NDSEs over the BL equation has recently led to the addition of a new feature that allows inlet conditions to be imposed on the boundary layer edge [18]. The solver is therefore an alternative to the classic boundary layer code. The stag-line code is coupled MUTATION^{++} library [19] for the computation of the thermodynamic and transport properties, as well as it provides the reaction rates of the chemical models.

Chemical models are therefore necessary both in the BL and stag-line solver providing the forward and backward reaction rates coefficients that model the species production(depletion) term in the mass conservation equations. This work focuses on the stag-line code being more accurate in the description of physical phenomena than the BL code, and because coupled with MUTATION^{++} library being more up-to-date and maintained respect to PEGASE.

4. Methodology

The overall objectives of this article is to assess the sensitivity of $c_{f,j}$ [cm^3 s^{-1} mol^{-1}], $b_{f,j}$, $e_{f,j}$ [K] defining the forward reaction rate coefficients on the computed heat flux. From now on the notation is simplified omitting the subscripts f and j, and the SI units. Backward coefficients are then calculated using Eq. 2.

The ICP code provides the boundary layer edge parameters used as inlet conditions in the stag-line solver. The ICP reference condition are $P_{\mathrm{el}} = 75\,\mathrm{kW}$, $p_{\mathrm{c}} = 11\,967\,\mathrm{Pa}$, $\dot{m}= 16\,\mathrm{g\,s^{-1}}$ considering an hemispherical probe of $R = 0.025\,\mathrm{m}$, and an air mixture of 11 species. Simulations were carried out by Sakraker [20] and results, in terms of boundary layer edge quantities, are summarized in Table 4. In this work an air mixture of 5 species is considered that would require a new ICP simulation to exactly assess the BL edge quantities. However, considering the objective of the work and the time required to carry out a new simulation, inlet conditions provided by [20] can be used to carry out the analysis without affecting the sensitivity study. The five species concentration is derived using MUTATION^{++} and assuming LTE condition at the edge. Furthermore, due to the low Mach number of the ICP simulation, the pressure at the edge of the boundary layer can be reasonably approximated to the reference static pressure.

At the wall, temperature and catalytic coefficients for the recombination reactions N + N $\rightarrow$ N2 and O + O $\rightarrow$ O2 are imposed equal to $T_w = 2000\,\mathrm{K}$ and $\gamma = \gamma_{\mathrm{N_2}} = \gamma_{\mathrm{O_2}} = 0.01$, respectively.

Table 4: Inlet conditions impose at the boundary layer edge of the stag-line solver. δ is the BL thickness, β the derivative of tangential component respect to the wall along the tangential direction, u_e the normal component of the velocity respect to the wall.

δ [m]	T_e [K]	P_e [Pa]	β_e [s^{-1}]	u_e [m s^{-1}]
5.43×10^{-3}	5395.06	11 967	1734.24	25.97

Once the inlet (BL edge) and outlet (wall) conditions are defined, the stag-line solver can be solved to compute the heat flux. For simplicity, the procedure is repeated for each reactions separately. The reference model is Park et al. [8; 9].

For instance, let's consider the $N_2 + O \rightarrow NO + N$. The reference parameters are $c = 5.7 \times 10^{12}$, $b = 0.42$, $e = 42\,938$. A uniform distribution is assumed for each parameter of the reaction by setting a lower and upper limit (e.g. $c \in \mathcal{U}$ [10^{10},10^{13}], $b \in \mathcal{U}$ [-1,1],

$e \in \mathcal{U}[41\,000,43\,000]$) while those of the others are kept to the reference values. Samples are drawn from the distributions, each characterized by a set of c, b, and e. Each set is input in MUTATION^{++} providing the parameters to compute the forward reaction coefficient. The stag-line solver resolves the DRNSEs computing the heat flux at the wall. The procedure is repeated a thousand of times employing different samples. The result is the the heat flux distribution related to the $N_2 + O \rightarrow NO + N$ reaction. The sensitivity analysis ends with the computation of the first and total Sobol indices [21; 22] to quantify the role of each parameter (c, b, and e) in the quantity of interest (heat flux). The former indicates the direct contribution of a given input to the output, the latter considers all the effects of a particular input including interactions with other input variables.

The procedure is repeated for all reactions and Table 5 summarizes the distributions of the parameters considered in this work. In case of third body dissociation reactions (e.g. $N_2 + M \rightarrow 2N + M$) the analysis is carried out simultaneously for all the third bodies considered.

Eventually, the heat flux distributions and Sobol indices provide insight to assess which reaction and parameter have the greatest impact on the heat flux computation.

Table 5: Uniform distributions of the parameters c, b, and e considered in this work. M indicates the third body in the dissociation reactions of N, O and NO

Reaction	M	c [cm^3 s^{-1} mol^{-1}]	b	e [K]
$N_2 + M \rightarrow 2N + M$	N	$\mathcal{U}[10^{20},10^{23}]$	$\mathcal{U}$ [-2,0]	$\mathcal{U}$[113 000,113 900]
	O	$\mathcal{U}[10^{20},10^{23}]$	$\mathcal{U}$[-2,0]	$\mathcal{U}$[113 000,113 900]
	N_2	$\mathcal{U}[10^{19},10^{22}]$	$\mathcal{U}$[-2,0]	$\mathcal{U}$[113 000,113 900]
	O_2	$\mathcal{U}[10^{19},10^{22}]$	$\mathcal{U}$[-2,0]	$\mathcal{U}$[113 000,113 900]
	NO	$\mathcal{U}[10^{19},10^{22}]$	$\mathcal{U}$[-2,0]	$\mathcal{U}$[113 000,113 900]
$O_2 + M \rightarrow 2O + M$	N	$\mathcal{U}[10^{20},10^{23}]$	$\mathcal{U}$[-2,0]	$\mathcal{U}$[58 000,60 000]
	O	$\mathcal{U}[10^{20},10^{23}]$	$\mathcal{U}$[-2,0]	$\mathcal{U}$[58 000,60 000]
	N_2	$\mathcal{U}[10^{19},10^{22}]$	$\mathcal{U}$[-2,0]	$\mathcal{U}$[58 000,60 000]
	O_2	$\mathcal{U}[10^{19},10^{22}]$	$\mathcal{U}$[-2,0]	$\mathcal{U}$[58 000,60 000]
	NO	$\mathcal{U}[10^{19},10^{22}]$	$\mathcal{U}$[-2,0]	$\mathcal{U}$[58 000,60 000]
$NO + M \rightarrow N + O + M$	N	$\mathcal{U}[10^{15},10^{19}]$	$\mathcal{U}$[-1,1]	$\mathcal{U}$[74 000,76 000]
	O	$\mathcal{U}[10^{15},10^{19}]$	$\mathcal{U}$[-1,1]	$\mathcal{U}$[74 000,76 000]
	N_2	$\mathcal{U}[10^{14},10^{17}]$	$\mathcal{U}$[-1,1]	$\mathcal{U}$[74 000,76 000]
	O_2	$\mathcal{U}[10^{14},10^{17}]$	$\mathcal{U}$[-1,1]	$\mathcal{U}$[74 000,76 000]
	NO	$\mathcal{U}[10^{15},10^{19}]$	$\mathcal{U}$[-1,1]	$\mathcal{U}$[74 000,76 000]
$N_2 + O \rightarrow NO + N$	-	$\mathcal{U}[10^{10},10^{13}]$	$\mathcal{U}$[-1,1]	U[41 000,43 000]
$NO + O \rightarrow N + O_2$	-	$\mathcal{U}[10^{10},10^{13}]$	$\mathcal{U}$[-1,1]	$\mathcal{U}$[19 000,21 000]

5. Results

Figure 3 shows the Power Density Functions (PDFs) of the heat fluxes for the five reactions considered. The vertical line is the nominal heat flux retrieved using the Park's nominal values of c, b and e in Tables 1, 2 and 3, respectively.

The heat fluxes follow a bimodal distribution featuring two dominant peaks. If, on one hand, one is close to the nominal value ($\approx 86.07\,\mathrm{kW\,m^{-2}}$) with the exception of the the third body dissociation of NO, on the other hand the second one is function of reaction itself. For instance, the third body dissociation of N_2 and O_2 shows a most probable value to ≈ 275.4 and $420\,\mathrm{kW\,m^{-2}}$ while the NO exchange reactions are at ≈ 4.0 and $-8.8\,\mathrm{kW\,m^{-2}}$, with the negative sign denoting a flux outward the wall.

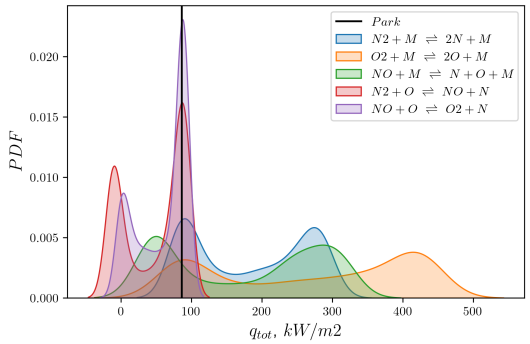

Figure 3: Heat flux distributions obtained sampling the and c, b and e parameters of the Arrhenius law of the forward reactions coefficients from the distribution depicted in Table 5. The black vertical line represents the value obtained using the nominal parameters provided by Park [8; 9] and summarized in Tables 1, 2 and 3.

To understand the bi-modal distributions, it is worth analyzing the heat flux distribution as a function of each parameter. Figure 4 depicts the computation for $N_2 + M \rightarrow 2N + M$ with M = N function of c, b, and e. The c and e present random distributions meaning that the role of the parameters is second-order respect to b, characterized by a nearly monotonic trend. Similar conclusions can be drawn for other reactions and hence not presented.

To better exploit the role of b, a similar analysis is carried out sampling c and e from the distribution in Table 5 and setting b to the Park's nominal value in Table 2. The resulting heat flux distributions are sketched in Figure 5. The PDFs are no longer bimodals with a single peak in the proximity of the reference case. Exceptions are the third-body dissociation reactions of O_2 and NO which shows a nearly uniform distribution and a non-symmetrical unimodal PDF with a slight peak $\approx 200\,\mathrm{kW\,m^{-2}}$, respectively. The impact of the two reactions on the heat flux estimation is hence negligible respect to the other reactions. However, it is worth emphasizing such result is strongly influenced by reference condition considered. At $T_\delta = 5395.06\,\mathrm{K}$, $P_\delta = 11\,967\,\mathrm{Pa}$ the

molar fractions of O_2 ($\mathcal{X}_{O_2} = 8.69 \times 10^{-5}$) and NO ($\mathcal{X}_{NO}$ =3.885 $\times 10^{-3}$) are respectively two and five order of magnitude less than those of the remaining species N ($\mathcal{X}_N$ =0.167), O ($\mathcal{X}_O$ = 0.314), and N_2 ($\mathcal{X}_{N_2}$ = 0.513). New testing conditions must be exploited to further assess the role of these reactions.

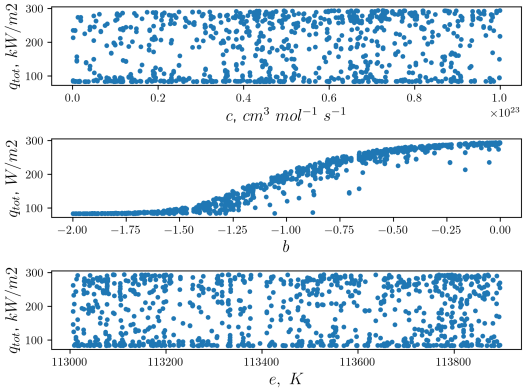

Figure 4: Heat flux distribution respect to the samples of c, b, and e of the reaction $N_2 + M \rightarrow 2N + M$ with M = N.

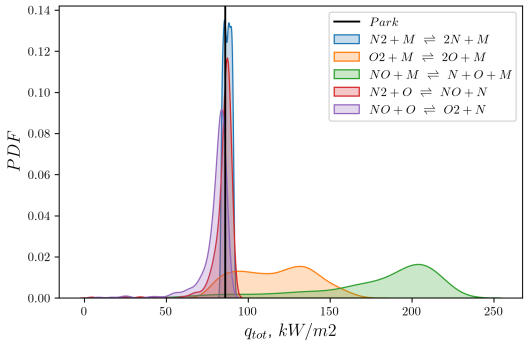

Figure 5: Heat flux distributions obtained sampling the c and e parameters of the Arrhenius law of the forward reactions coefficients from the distribution depicted in Table 5. The b values are set constant equal to the Park's nominal ones. The black vertical line represents the value obtained using the nominal parameters provided by Park [8; 9] and summarized in Tables 1, 2 and 3.

The sensitivity analysis ends with the computation of the first and total Sobol indices. Tables 6 and 7 summarized the indices of each parameters for all the reactions considered. S_{1b} and S_{Tb}, the first and total indices of the b parameter, are several order of magnitude larger than others highlighting the role of the exponent b in the computation. Moreover, S_{1b} and S_{Tb} are also closer each other meaning that b affects the heat flux mainly through direct interactions.

Eventually, the solution employing the Park's model is compared to the those using the Gupta's and Dunn&Kang's. Table 8 summarized the heat fluxes using as reference parameters those presented in Tables 1, 2 and 3. Different models can lead to discrepancies up to 60%. The conclusion has motivates a similar analysis performed by setting the temperate exponent, b, of Gupta's and Dunn&Kang's models equal to the Park's ones. The objective is to assess if the differences in b between the authors are responsible to the discrepancies in the heat fluxes. Table 9 summarized the results. If one one hand, Gupta's and Dunn&Kang's models provide similar results and hence the discrepancies in Table 8 depends on b, on the other hand the heat fluxes differs one order of magnitude respect to the Park's model. The c parameters used by Gupta and Dunn&Kang are very likely responsible for this behaviour: distributions in Table 5 are not broad enough to include values proposed by Gupta and Dunn&Kang and hence, further investigations are fundamental to evaluate the role of the parameter.

Table 6: First Sobol indices of the the three parameters defining the Arrhenius law of the forward reaction rate coefficients.

Reaction	S_{1c}	S_{1b}	S_{1e}
$N_2 + M \rightleftharpoons 2N + M$	0.018	1.069	−0.002
$O_2 + M \rightleftharpoons 2O + M$	−0.007	1.280	0.003
$NO + M \rightleftharpoons N + O + M$	0.064	1.173	0.003
$N_2 + O \rightleftharpoons NO + N$	0.005	0.868	−0.0044
$NO + O \rightleftharpoons N + O_2$	0.116	0.851	−0.004

Table 7: Total Sobol indices of the the three parameters defining the Arrhenius law of the forward reaction rate coefficients.

Reaction	S_{Tc}	S_{Tb}	S_{Te}
$N_2 + M \rightleftharpoons 2N + M$	0.031	0.864	1.4×10^{-4}
$O_2 + M \rightleftharpoons 2O + M$	0.029	1.006	0.002
$NO + M \rightleftharpoons N + O + M$	0.055	1.146	0.001
$N_2 + O \rightleftharpoons NO + N$	0.054	0.900	0.001
$NO + O \rightleftharpoons N + O_2$	0.065	0.824	0.002

Table 8: Heat flux computation using three different chemical models for the parameters of the forward reaction coefficients presented in Tables 1, 2, and 3

	Park et al. [8; 9]	Gupta et al. [10]	Dunn&Kang [11]
q_{tot} [kW m^{-2}]	86.07	36.11	40.75

6. Conclusion

The enthalpy rebuilding in plasma wind tunnels is a complex process coupling experimental data with nu-

Table 9: Heat flux computation using three different chemical models for the parameters of the forward reaction coefficients presented in Tables 1, 2, and 3. The Gupta's and Dunn&Kang's models have been revisited by using the temperature exponent proposed by Park.

	Park	Gupta (modified)	Dunn&Kang (modified)
q_{tot} [kW m^{-2}]	86.07	378.44	377.30

merical modellings. For instance, the procedure employed at the VKI Plasmatron is based on an iterative procedure to match the measured heat flux and the numerical counterpart.

This work aims investigating the role of the chemical models on the simulated heat flux. A CFD code owned by the VKI is used to solve the DRNSEs under thermal equilibrium and chemical non-equilibrium conditions. The codes takes at the inlet the boundary layer edge quantities provided by an ICP solver and the temperature at the wall. The ICP solver reference condition are $P_{\mathrm{el}} = 75\,\mathrm{kW}$, $p_{\mathrm{c}} = 11\,967\,\mathrm{Pa}$, and $\dot{m} = 16\,\mathrm{g\,s^{-1}}$. The boundary layer solver is coupled with the MUTATION^{++} library that provides that the parameters used to describe the forward reaction rate coefficients based on Arrhenius law. Backward rate coefficients are then retrieved from the forward one using the equilibrium constant.

The reference chemical model considers an air mixture of 5 species and 5 reactions. The nominal values of the parameters are presented by Part et al. [8; 9]. A uniform distribution is assumed for each of the three parameters characterising the Arrhenius law. The boundary layer solver is run a thousand of times for each reaction. The parameter mainly affecting the calculation is the temperature exponent that leads to a bimodal distributions of the heat fluxes. First and total Sobol indices are also computed to quantify the impact of each inputs on the heat flux.

Finally, Park's model is compared with those proposed by Gupta et al.. [10] and Dunn&Kang [11]. Discrepancies up to 60% exist in the heat flux estimation. If on one hand the discrepancies between Gupta and Dunn&Kang are due to temperature exponent b, the c parameter is responsible for discrepancies with Park's model.

An ongoing effort is to extend the analysis by considering different test conditions (e.g. at higher pressure promoting the molecular collisions) as well as a more complex air mixture that includes ionized species and free electrons (e.g. 11 species air mixture). Furthermore, broader uniform distributions of c parameter will be analyzed to investigate the discrepancies between the models.

Acknowledgments

The research of E. Anfuso is supported by a doctoral fellowship awarded from the Research Foundation Flanders (FWO, dossier #1SF8822N).

References

[1] P. F. Barbante and O. Chazot, Flight Extrapolation of Plasma Wind Tunnel Stagnation Region Flowfield, Journal of Thermophysics and Heat Transfer 20 (3) (2006) 493–499.

[2] A. Kolesnikov, The concept of local simulation for stagnation point heat transfer in hypersonic flows-applications and validation, in: 21st Aerodynamic Measurement Technology and Ground Testing Conference, 2000, p. 2515.

[3] A. Viladegut, O. Chazot, Empirical modeling of copper catalysis for enthalpy determination in plasma facilities, Journal of Thermophysics and Heat Transfer 34 (1) (2020) 26–36.

[4] B. Helber, Material Response Characterization of Low-density Ablators in Atmospheric Entry Plasmas, Ph.D. thesis, Von Karman Institute for fluid dynamics & Vrije Universiteit Brussel (2016).

[5] J. P. M. Gonzalez, Development of a Chemical Kinematics Model for Inductive Coupled Plasma Simulations, Project Report 1998-36, von Karman Institute for Fluid Dynamics (1998).

[6] J. G. Kim, S. M. Jo, Modification of chemical-kinetic parameters for 11-air species in re-entry flows, International Journal of Heat and Mass Transfer 169 (2021) 120950.

[7] P. A. Gnoffo, Conservation equations and physical models for hypersonic air flows in thermal and chemical nonequilibrium, Vol. 2867, National Aeronautics and Space Administration, Office of Management . . . , 1989.

[8] C. Park, Review of chemical-kinetic problems of future nasa missions. i-earth entries, Journal of Thermophysics and Heat transfer 7 (3) (1993) 385–398.

[9] C. Park, R. L. Jaffe, H. Partridge, Chemical-kinetic parameters of hyperbolic earth entry, Journal of Thermophysics and Heat transfer 15 (1) (2001) 76–90.

[10] R. N. Gupta, J. M. Yos, R. A. Thompson, K.-P. Lee, A review of reaction rates and thermodynamic and transport properties for an 11-species air model for chemical and thermal nonequilibrium calculations to 30000 k, NASA STI/Recon Technical Report N 90 (1990) 27064.

[11] M. G. Dunn, S.-W. Kang, Theoretical and experimental studies of reentry plasmas, Vol. 2232, National Aeronautics and Space Administration Washington, DC, 1973.

[12] A. Cipullo, Helber, F. Panerai, L. Zeni, O. Chazot, Investigation of freestream plasma flow produced by inductively coupled plasma wind tunnel, Journal of Thermophysics and Heat Transfer 28 (3) (2014) 381–393. doi:10.2514/1.T4199.

[13] P. F. Barbante, O. Chazot, Flight extrapolation of plasma wind tunnel stagnation region flowfield, Journal of Thermophysics and Heat Transfer 20 (3) (2006) 493–499.

[14] P. F. Barbante, Heat flux duplication between ground facility and hypersonic flight, Journal of Thermophysics and Heat Transfer 23 (4) (2009) 684–692.

[15] B. Bottin, D. V. Abeele, M. Carbonaro, G. Degrez, G. S. Sarma, Thermodynamic and transport properties for inductive plasma modeling, Journal of thermophysics and heat transfer 13 (3) (1999) 343–350.

[16] A. Munafo, Multi-scale models and computational methods for aerothermodynamics, Ph.D. thesis, Ecole Centrale Paris (2014).

[17] A. Turchi, J. Matesanz Saiz, T. E. Magin, O. Chazot, On the flight extrapolation of stagnation-point ablative material plasma wind tunnel tests, in: Proceedings of 8th European Symposium on Aerothermodynamics for Space Vehicles, Vol. 127, 2015.

[18] P. Schrooyen, A. Turchi, K. Hillewaert, P. Chatelain, T. E. Magin, Two-way coupled simulations of stagnation-point ablation with transient material response, International Journal of Thermal Sciences 134 (2018) 639–652.

[19] J. B. Scoggins, V. Leroy, G. Bellas-Chatzigeorgis, B. Dias, T. E. Magin, Mutation++: Multicomponent thermodynamic and transport properties for ionized gases in c++, SoftwareX 12. doi:10.1016/j.softx.2020.100575.

[20] I. Sakraker, Aerothermodynamics of pre-flight and in-flight testing methodologies for atmospheric entry probes, Ph.D. thesis, Université de Liège, Liège, Belgique (2016).

[21] I. M. Sobol', On sensitivity estimation for nonlinear mathematical models, Matematicheskoe modelirovanie 2 (1) (1990) 112–118.

[22] I. M. Sobol, Global sensitivity indices for nonlinear mathematical models and their monte carlo estimates, Mathematics and computers in simulation 55 (1-3) (2001) 271–280.

Multi-Fidelity heat flux characterization of a Supersonic Plasma Jet over a catalytic probe

Michele Capriati

Aeronautics and Aerospace Department, von Karman Institute for Fluid Dynamics, Belgium, mymail@vki.ac.be

Supervisor: Thierry E. Magin

Professor, Aeronautics and Aerospace Department, von Karman Institute for Fluid Dynamics, Belgium, thierry.magin@vki.ac.be

University Supervisor: Pietro Congedo

Head of the PLATON project-team in CMAP Laboratory (INRIA Saclay Ile-de-France, Ecole Polytechnique), France, pietro.congedo@inria.fr

Abstract

An under-expanded/supersonic air plasma flow over a catalytic probe is numerically simulated. Experimental and modeling uncertainties are propagate exploiting a multi-fidelity surrogate model to estimate confidence intervals of surface heat flux and pressure.

Keywords: Plamsatron, Under-expanded flows, plasma flows, discretization errors, Multi-Fidelity Kriging

1. Introduction

The von Karman Institute Plasmatron facility is used for the characterization of materials exposed to a high-enthalpy plasma environment. It is particularly helpful to predict the behaviour of Thermal Protection Materials (TPMs) for aerospace. In atmospheric entry applications, TPMs protect the vehicle from the extremely demanding aerodynamic conditions to which it is exposed. However, this normally happens at the expenses of the TPM that undergoes thermochemical decomposition and experiences mass loss and shape change. When the local heat transfer simulation constraints are met, the in-flight highly reactive boundary layer developing past the shock can be duplicated on ground by a subsonic plasma flow in the stagnation region. However, differences remain in the heat flux distributions between the hypersonic and subsonic flowfields. In particular, when a typical hemispherical ablative TPM sample is exposed to the subsonic plasma flow, the recession it experiences is almost uniform in space and the shape is preserved. To explore the effects of the shape change of the ablative samples, an experimental campaign has been recently conducted at the VKI using a supersonic plasma. The supersonic condition was achieved by I) mounting a sonic nozzle at the end of the plasma torch, that expands the gas to choked conditions, and II) adequately lowering down the chamber pressure to generate an under-expanded jet and accelerate the flow to the desired regime.

The value of the pressure at the nozzle inlet and in the chamber is experimentally measured and characterized by the uncertainty of the instruments. By contrast, the temperature at the nozzle inlet is not directly measurable and its values needs to be assessed. While in subsonic regime a coupled numerical-experimental approach is well establish, in the new supersonic case a method is sought.

To further increase the complexity, the probe surface is catalytic, promoting the recombination of atomic nitrogen and oxygen present in the gas. Phenomenological approaches allow to model this catalytic behaviour based on a macroscopic probability that a given surface reaction takes place. Also these probabilities need to be assumed, introducing further uncertainty.

In this work, we propose to simulate this experimental campaign using the US3D flow solver and to propagate the above-mentioned sources of uncertainties to characterize the variability of the quantities of inter-

est, *i.e.*, the heat flux and the pressure of the probe. Additionally, an assessment of the numerical error is performed and included in the analysis. It is essential to estimate the numerical precision of the prediction for a given computational budget when the prohibitive computational cost associated to uncertainty quantification analysis prevents the systematic use of the grid-converged mesh.
In fact, to accelerate the building of a surrogate model a hierarchical approach is used, which exploits a lower fidelity model and courser numerical domains.
It was found that the numerical confidence intervals on the quantities of interest overlaps in large area with the experimental values.

2. Experimental Campaign

An experimental campaign was conducted at the von Karman Institute to characterize the response of a material exposed to an air plasma flow. When the flow is subsonic, the sample experiences a quasi-uniform recession. To investigate the effects arising from shape changing, the flow was accelerated to supersonic conditions. To this end, a sonic nozzle was mounted at the exit of the plasma torch to expand the gas to choked conditions. It was chosen a reservoir pressure of 165hPa and a chamber one of 5.5 hPa, resulting in a flow highly under-expanded, as shown in Fig. 1. The Plasmatron was supplied with a power of 600 kW. The sonic nozzle has an exit diameter of 35 mm and the probe is placed at a distance of 75mm from the exit of the nozzle. The probe induces a shock which interacts with the barrel shock generated at the nozzle exit. A calorimeter probe is used to characterize the heat flux and a Pitot probe for the stagnation pressure; they are, respectively 4.48 MW/m2 and 26 hPa. Uncertainty on the heat flux is about the 10% while for pressure measurements is about the 0.25% of the full scale, i.e. 0.5 hPa. Two runs were performed to assess the repeatability of the test. The probes have a nose radius of 25 mm with a 15 mm cylinder.

3. Governing Equations and Numerical Set-up

The gas is a mixture of n_s chemical reacting species in thermal equilibrium. The flow is described by the Navier-Stokes equations:

$$\frac{\partial \rho_\mathrm{i}}{\partial t} + \nabla \cdot (\rho_\mathrm{i}\mathbf{u} + \mathbf{j}_\mathrm{i}) = \dot{\omega}_\mathrm{i}, \quad \forall \mathrm{i} \in S, \tag{1}$$

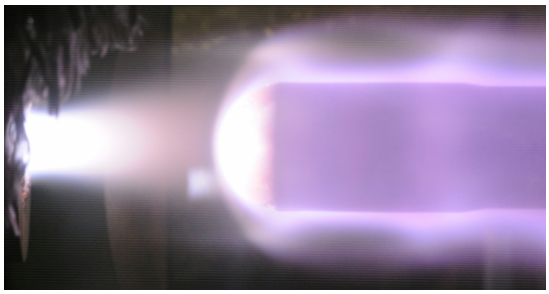

Figure 1: Under-expanded air jet over the catalytic probe.

$$\frac{\partial \rho \mathbf{u}}{\partial t} + \nabla \cdot (\rho \mathbf{u} \cdot \mathbf{u} + p\bar{\bar{\mathrm{I}}} + \bar{\bar{\tau}}) = \mathbf{0}, \tag{2}$$

$$\frac{\partial \rho E}{\partial t} + \nabla \cdot (\rho \mathbf{u} H + \bar{\bar{\tau}}\mathbf{u} + \mathbf{q}) = 0. \tag{3}$$

Symbol S stands for the set of species indices, ρ_i is the partial density of species i, $\mathbf{u}$ is the mass-averaged mixture velocity, $\mathbf{j}_\mathrm{i}$ the diffusion mass flux of species i, $\dot{\omega}_\mathrm{i}$ its chemical production/destruction rate, p, the thermodynamic pressure of the mixture, $\bar{\bar{\tau}}$, the viscous stress tensor, E, the total energy, $H = E + p/\rho$, the total enthalpy, and $\mathbf{q}$, the total heat flux. Thermodynamics properties are obtained using the NASA polynomials [1]. Diffusion mass fluxes are computed using the self-consistent effective binary diffusion models[2], while viscosity and thermal conductivity are computed according to Gupta-Yos mixing rule [3]. Chemical production rates $\dot{\omega}_\mathrm{i}$ for species i are computed using finite-rate chemistry.

3.1. Gas-Surface Interaction

GSI phenomena can be expressed as a boundary condition imposed to the Navier-Stokes equations, when dealing with a chemically reactive surface. It returns to the CFD solver the surface state computed by solving balance equations in an infinitesimal volume containing both the gas and material phases. When the surface temperature is user-defined (isothermal condition), the surface state is defined by means of the species partial densities. For a catalytic material, the surface mass balance for each species i reads:

$$\dot{\omega}_\mathrm{i} = \mathbf{j}_\mathrm{i} \cdot \mathbf{n}, \quad \forall \mathrm{i} \in S. \tag{4}$$

Versor $\mathbf{n}$ is the normal to the surface. It can be computed using phenomenological or finite-rate chemistry models. The different fidelity models for chemical closures are available in MUTATION++ [4; 5]. In this work we used a phenomenological model. The gas state near the interface is obtained by solving the

system 4 using a Newton method and the surface state is returned to the CFD solver.
When the temperature at the wall is unknown, an additional energy balance must be applied. Such a balance is also available in MUTATION++, but was not used in this work.
Phenomenological models were first introduced to describe the catalytic behaviour of a surface in hypersonic simulations [6]. They are widely used in the hypersonic community because of their simplicity, they only require the definition of the probability that a macroscopic reaction takes place:

$$\gamma_{\mathrm{i}}^{rea} = \frac{\mathcal{N}_{\mathrm{i}}^{rea}}{\mathcal{N}_{\mathrm{i}}}, \tag{5}$$

where $\mathcal{N}_{\mathrm{i}}^{rea}$ is the number flux of species i subject to the reaction and $\mathcal{N}_{\mathrm{i}} = n_{\mathrm{i}}\sqrt{k_{\mathrm{b}}T_{\mathrm{s}}/(2\pi m_{\mathrm{i}})}$, the number flux of species i impinging the surface. Symbol k_{b} stands for Boltzmann's constant, T_{s} the surface temperature, and m_{i}, the mass of species i. A fully catalytic behavior is obtained when the probability approaches unity; whereas a non-catalytic behavior is reached when is equal to zero. The chemical production rate reads:

$$\dot{\omega}_{\mathrm{i}}^{\mathrm{s}} = m_{\mathrm{i}}\gamma_{\mathrm{i}}^{rea}\mathcal{N}_{\mathrm{i}}. \tag{6}$$

3.2. US3D flow solver and boundary conditions

US3D is a three-dimensional finite-volume flow solver developed at the University of Minnesota for aerodynamic/hypersonic applications [7]. Numerical fluxes are computed in this work according to the modified Steger-Warming scheme [8] with a MUSCL approach to obtain second-order accuracy. The Data Parallel Line Relaxation (DPLR [9]) ensures rapid convergence to steady-state. US3D is highly scalable and efficient, making it possible to solve very large problems on parallel computers in a cost-effective manner.

The boundary conditions applied to the simulation are the following:

- nozzle inlet: pressure of 165 hPa and tentative temperature; the chemical composition was assumed at equilibrium,
- nozzle surface: isothermal condition, with temperature equal to 1500 K,
- chamber free surface: an inlet condition is prescribed for numerical stability; it is characterized by a small velocity (1m/s), room temperature and a chamber pressure of 5.5 hPa,
- probe: isothermal/catalytic surface with a temperature of 350K and a recombination probability for oxygen equal to 0.12 and for nitrogen to 0.75, as suggested by Bellas [10].

All the other surfaces are characterized by a symmetry boundary condition.

3.3. Numerical domain

The computational domains is represented in Fig. 2: from the left to the right I) exit of plasma torch/nozzle inlet, II) sonic nozzle surface, III) expansion chamber and IV) probe.

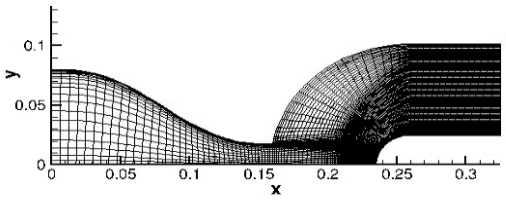

Figure 2: Numerical domain: from the left to the right I) exit of plasma torch/nozzle inlet, II) sonic nozzle surface, III) expansion chamber and IV) probe. Mesh number III on table 1

.

Particular attention was posed to well capture the shock to have reliable results on the probe surface: as one can see in Fig. 3 the grid is aligned to the shock and the cells are stretched in the shock direction.

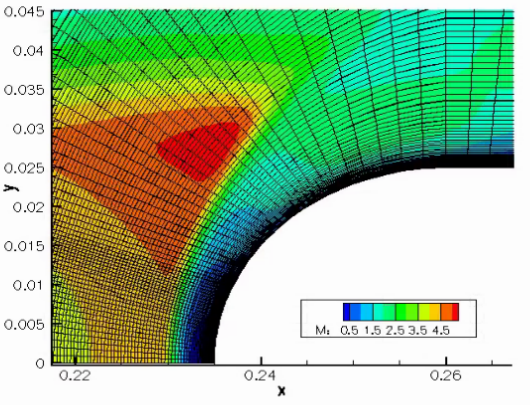

Figure 3: Zoom of the numerical domain: grid aligned to the shock and stretched in the direction of the shock. Mesh number III on table 1

The four grids listed in table 1 are obtained by doubling the number of the nodes in the both the x and y directions starting from the coarsest mesh (IV) to the finest one (I).

Table 1: Used meshes: index, number of cells, length of first cell on the stagnation point (Δy), normalized characteristic mesh, h_i

Tag	cells	$\Delta x[m]$	h_i
I	172224	5E-7	1
II	43056	1E-6	2
III	10764	2E-6	4
IV	2691	4E-6	8

3.4. Numerical error evaluation

The numerical error associated to the discretization of the physical domain can be evaluated by performing a systematic grid refinement [11]. It can be represented by:

$$\epsilon_\phi \approx \delta_\mathrm{RE} = \phi_\mathrm{i} - \phi_0 = \alpha h_\mathrm{i}^p. \tag{7}$$

The quantity ϕ_i is a flow quantity of interest at the grid refinement i, ϕ_0, the estimate of the exact solution, α, a constant to be determined, h_i, the typical cell size and p is the observed order of grid convergence. To represent the density of the grids using a single parameter the numerical grids have to be geometrically similar: grid parameters, such as deviation from orthogonality, skewness, etc. should remain constant.
In most of the application the 'exact' solution of the quantity of interest cannot be analytically computed; in these cases, it can be estimate by minimizing the standard deviation, σ, between the numerical solutions and the fit low:

$$\phi_\mathrm{i} = \phi_0 + \alpha h_\mathrm{i}^p. \tag{8}$$

the minimum number of grids (n_g) required is 4. A positive value of order of convergence (p) implies a monotonic convergence, in contrast a negative value a monotonic divergence.
Eca proposed to compute the uncertainty associated to the numerical prediction [11]:

$$U_\phi(\phi_\mathrm{i}) = \begin{cases} F_\mathrm{s}\epsilon_\phi(\phi_\mathrm{i}) + \sigma + |\phi_\mathrm{i} - \phi_\mathrm{fit}|, & \text{if } \sigma < \Delta_\phi \\ 3\frac{\sigma}{\Delta_\phi}(\epsilon_\phi(\phi_\mathrm{i}) + \sigma + |\phi_\mathrm{i} - \phi_\mathrm{fit}|), & \text{otherwise} \end{cases} \tag{9}$$

where $\Delta\phi = (\phi_\mathrm{i}^\mathrm{max} - \phi_\mathrm{i}^\mathrm{min})/(n_g - 1)$ is a data range parameter and F_s is a safety factor equal to 1.25 if $0.5 < p < 2.1$ and $\sigma < \Delta\phi$, and to 3 otherwise.

4. Uncertainty assessment and construction of a surrogate model

As described in the Introduction, in this work we are interested in proposing a strategy to well define reservoir conditions of the experimental campaign. While total pressure is experimentally accessible, total temperature needs to be estimated.
Following the procedure for characterizing subsonic flows, we propose to use heat flux and pressure measurement to rebuild the reservoir total temperature.
For this reason, uninformative uniform priors are chosen for the rebuilt quantities, namely of ±20% intervals around the nominal values for the reservoir total temperature and for recombination probabilities γ. By contrast, for the reservoir total pressure, intervals were chosen in agreement with the experimental uncertainty. The complete list of uncertainties is resumed in Table 2.

Table 2: Nominal conditions and associated uniform uncertainties for total pressure, p_0, total temperature, T_0, and nitrogen and oxygen recombination probability, γ

Variable	Nominal value	Minimum	Maximum
P_0 [Pa]	16500	16000	17000
T_0 [m/s]	6900	6400	7400
γ_N [-]	0.075	0.06	0.09
γ_O [-]	0.12	0.096	0.144

Kriging interpolation is a well-known and widely-used technique for building a surrogate model; a detailed description of the model can be found in [12; 13; 14; 15].
Depending on the dimension of the uncertainty space and the complexity of the model response, a certain number of training points are needed to build the surrogate model. Even if this number is much lower compared to what a Monte-Carlo analysis would require, the simulations high cost can make this number still prohibitive. In such cases, the uses of multi-fidelity models is appealing. The underlying idea is to combine the solutions of different fidelity:

- low fidelity model: fast, but not very accurate;
- high fidelity model: accurate, but expensive.

A high number of low fidelity simulations can be performed to cover a wide area of the uncertainty space, while retaining few high fidelity simulations to guarantee accuracy in the prediction. In this work we decided to follow the hierarchical approach proposed by Han [16] where the lower fidelity surrogate model is used as a trend to build the higher fidelity one.

Particularly we used 4 different fidelity to describes the flow:

- fidelity α: the flows is solved by using the mesh I of table 1 and employing the US3D solver. The time to converge is around 20 hours. We generated $N_s = 5$ sampling points with the Sobol technique [17] to train the surrogate model, and $N_v = 5$ with a Latin Hypercube strategy [18] for verification purposes.
- fidelity β and γ: the flows is solved by using the mesh III and IV of table 1 and employing the US3D solver. The time to converge is respectively around 15 and 5 minutes. We generated $N_s = 20$ sampling points with the Sobol technique to train the surrogate models.
- fidelity δ: nozzle equations are used to described the expansions, while an in-house 1D solver is used to solve the shock and the boundary layer in a cheap, 1D formulation. It presents several assumptions: I) the expansion is supposed to be adiabatic and isoentropic, II) the chemistry is supposed to be frozen, III) the diameter of the jet boundary is estimated. The time to converge is around 1 minute. We generated $N_s = 80$ sampling points with the Sobol technique to train the surrogate model.

5. Results

The experimental camping, described in section 2, was simulated using the US3D flow solver. A 5 species air mixture was used (N2, O2, NO, N, O), whose reaction rates constant were taken from [19]. Purpose of the numerical analysis is to:

- characterize the numerical error for a given computational budget (number of cells used) and compute the associated uncertainty on a nominal condition;
- predict stagnation point observable on a nominal condition and describe the flow structure: heat flux and stagnation pressure;
- propagating uncertainties.

5.1. Grid convergence

The four numerical grids in table 1 were used to characterize the numerical error for a given computational budget (number of cells) and to compute the associated uncertainty, as described in section 3.4. The value of stagnation point heat flux and pressure and the value of the chocked mass flow is extracted for the four mesh and the convergence analyzed. The behaviour is shown respectively in Fig. 4, 5, and 6. The order of convergence for heat flux and pressure is around 1.55. Such value is below the theoretical value of 2 because of the employment of limiters, which reduce the order of the scheme when a shock is detected to improve numerical stability.
On the same plots the experimental uncertainties are also shown. We can see that the numerical uncertainties are always below the experimental ones, making the mesh I adequate for the analysis.

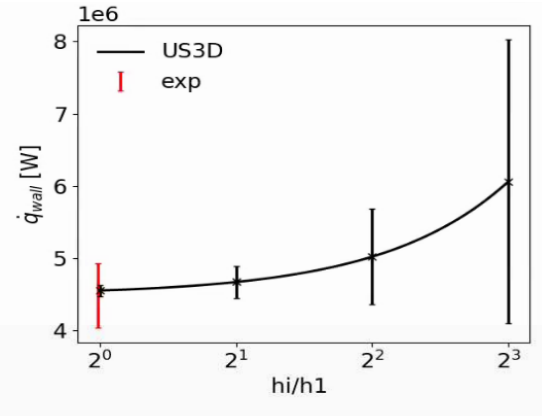

Figure 4: Black: stagnation point heat flux as function of grid refinement, numerical results with cross, fitting with solid line. Red: experimental uncertainty on the same quantity of interest.

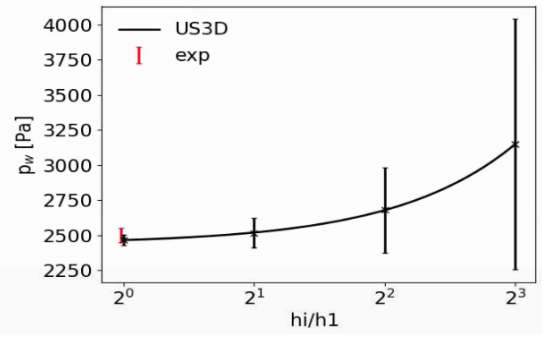

Figure 5: Black: stagnation point pressure as function of grid refinement, numerical results with cross, fitting with solid line. Red: experimental uncertainty on the same quantity of interest.

5.2. Flow Structure

The flowfield solution obtained with the mesh I of table 1 is shown in Fig. 7. The flow is highly

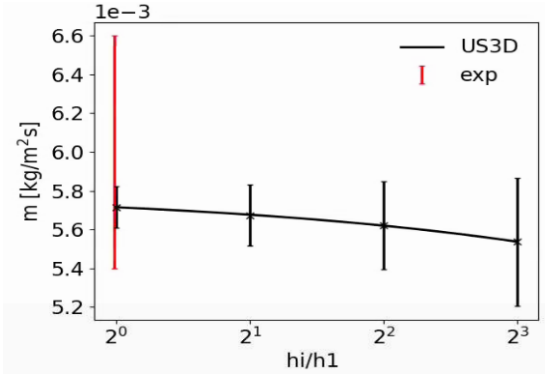

Figure 6: Black: choked mass flux as function of grid refinement, numerical results with cross, fitting with solid line. Red: experimental uncertainty on the same quantity of interest.

under-expanded. In fact, it is characterized by a total pressure ratio, $\eta_0 = p_0/p_{chamber} = 30$; the gas expands in the nozzle to an exit pressure of $\simeq 8000$ Pa, corresponding to an exit pressure ratio, $\eta_{exit} = p_{exit}/p_{chamber} = 15$. Thus, it continues its expansion in the chamber. From the figure, the Prandtl Meyer expansion fan in visible at the nozzle exit, as well as the typical barrel shape shock structure, typical of this configuration. The flow develops until it reaches the probe: a normal shock is generated, it first interacts with the barrel shock; after that the resulting transmitted shock interacts with the jet boundary. After the normal shock the gas undergoes strong velocity gradients to align the streamline to the probe geometry. The probe is positioned relatively close to the nozzle exit and therefore the normal shock prevents the traditional Mach disk to be generated.



Figure 7: Structure of the under-expanded jet: expansion fan, barrel shape shock, and normal shock. Density gradient solution obtain with mesh I in table 1

5.3. Uncertainties propagation

The results obtained by simulating the training points described in section 4 were used to build the multi fidelity surrogate model by using the software UQLab [20]. A surrogate model was also built using the only 5 high fidelity points to underline the improvement in accuracy that occurs when a multi fidelity strategy is adopted. The predictions of the heat flux for nominal values of recombination probability is shown in Fig. 8, as function of reservoir pressure and temperature. To assess the quality of the surrogate model a normalized error is defined as:

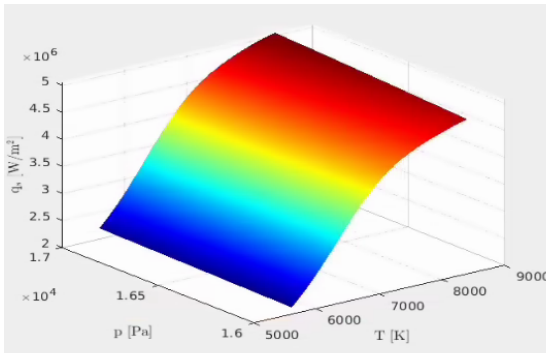

Figure 8: Stagnation point heat flux surrogate models.

$$NRMSE = \sqrt{\frac{\sum_i^{N_v}(Y_{val,i} - Y_{krig,i})^2}{N_v - 1}} \cdot \frac{100}{mean(Y_{krig})}, \tag{10}$$

where $Y_{val,i}$ is the high fidelity response value on the validation points N_v, $Y_{krig,i}$ is the surrogate model response value, and $mean(Y_{krig})$ is the mean of the quantity of interest in the uncertainty space considered, used to normalize the error. As one can see from Fig. 9 the multi fidelity approach allows to gain around one order of magnitude in accuracy for a relatively marginal additional computational cost. Results of the construction are presented for concision for the only heat flux, but the same conclusions can be still drawn for the stagnation point pressure and choked mass flux.

Once the surrogate model is verified through the small validation error, it is possible to exploit it for propagating model/experimental uncertainties. The density functions for stagnation point heat flux, pressure and choked mass flux are plotted in red respectively on Fig. 10, 11, and 12. The experimental results are also shown on the same plot. It is important to note that, the experimental uncertainties overlaps with the confidence intervals of the propagation problem over a wide area. It is thus potentially possible to narrow down the reservoir temperature and pressure to optimal values by exploiting the surrogate model to solve the inverse problem.

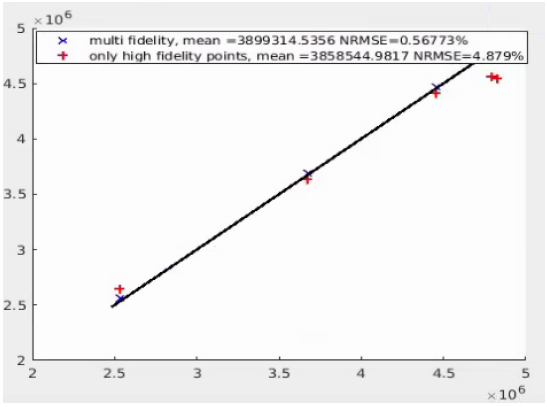

Figure 9: Stagnation point heat flux QQplot. Blue: response of the multi-fidelity model. Red: response of the surrogate model built only on the 5 high fidelity points.

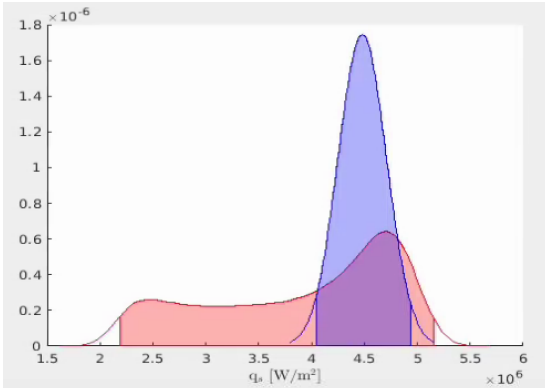

Figure 10: Stagnation point heat flux density probability. Blue: experimental uncertainty. Red: propagation result.

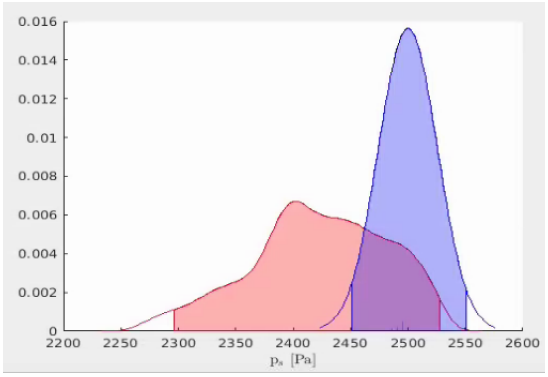

Figure 11: Stagnation point pressure density probability. Blue: experimental uncertainty. Red: propagation result.

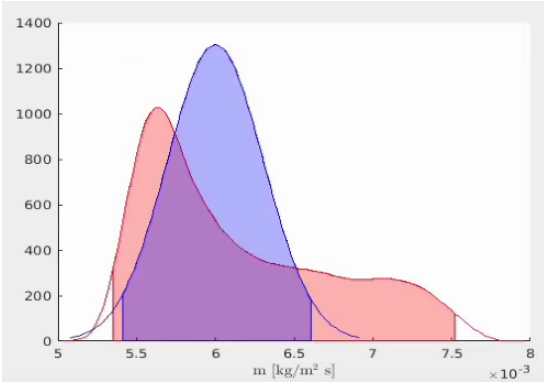

Figure 12: Choked mass flux probability. Blue: experimental uncertainty. Red: propagation result.

6. Conclusion and future work

In this work we numerically characterized an experimental campaign conducted at the von Karman Institute. It consists of a sonic under-expanded plasma jet. From a methodological standpoint, a strategy to build a surrogate model which predicts accurate results for a low computational cost was identify and used. This allows to define a new strategy for flow characterizing. Furthermore, the error on the used numerical grids was estimated, and it turns out to be lower then the experimental uncertainty for each quantity of interest. On the other hand, from an applicable point of view, the surrogate model was used to propagate model/experimental uncertainties, assessing the variability of quantities of interest such us heat flux and pressure. Moreover the flow structure was analyzed.
As future prospective, the surrogate model will be use to invert the problem and to characterize reservoir conditions. While, from a methodology point of view, adaptive sampling technique will be used to further reduce the computational cost.

7. Acknowledgments

* Authors acknowledge the Air Force Office of Scientific Research (AFOSR) for supporting the work under the grant FA9550-18-1-0209.

References

[1] S. Gordon, J. McBride, Thermodynamic Data to 20,000 K For Monatomic Gases, Tech. Rep. 1999-208523, NASA (1999).

[2] J. D. Ramshaw, C. H. Chang, Ambipolar diffusion in two-temperature multicomponent plasmas, Plasma Chemistry and Plasma Processing.

[3] R. Gupta, J. Yos, R. Thompson, K. Lee, A review of reaction rates and thermodynamic and transport properties for an 11-species air model for chemical and thermal nonequilibrium calculations to 30000k, NASA R. P 1232.
URL https://ci.nii.ac.jp/naid/80005467368/en/

[4] J. B. Scoggins, V. Leroy, G. Bellas-Chatzigeorgis, B. Dias, T. E. Magin, Mutation++: Multicomponent thermodynamic and transport properties for ionized gases in c++, SoftwareX 12 (2020) 100575.

[5] G. Chatzigeorgis, A. Viladegut, P. Barbante, O. Chazot, T. Magin, A. Turchi, Development of catalytic and ablative gas-surface interaction models for the simulation of reacting gas mixtures, in: 23rd AIAA Computational Fluid Dynamics Conference, 2017. doi:10.2514/6.2017-4499.

[6] R. Goulard, On catalytic recombination rates in hypersonic stagnation heat transfer, Journal of Jet Propulsion 28 (11) (1958) 737–745.

[7] G. V. Candler, H. B. Johnson, I. Nompelis, V. M. Gidzak, P. K. Subbareddy, M. Barnhardt, Development of the us3d code for advanced compressible and reacting flow simulations, 53rd AIAA Aerospace Sciences Meeting.

[8] J. L. Steger, R. Warming, Flux vector splitting of the inviscid gasdynamic equations with application to finite-difference methods, Journal of Computational Physics 40 (2) (1981) 263–293.

[9] M. J. Wright, G. V. Candler, D. Bose, Data-parallel line relaxation method for the navier-stokes equations, AIAA Journal 36 (9) (1998) 1603–1609.

[10] G. Bellas-Chatzigeorgis", "development of advanced gas-surface interaction models for chemically reacting flows for re-entry conditions", Ph.D. thesis, Politecnico di Milano (2001).

[11] L. Eça, M. Hoekstra, A procedure for the estimation of the numerical uncertainty of cfd calculations based on grid refinement studies, Journal of Computational Physics 262 (2014) 104–130.

[12] G. Matheron, The theory of regionalised variables and its applications, Ph.D. thesis, École Nationale Supérieure des Mines (1971).

[13] N. A. C. Cressie, Statistics for spatial data, John Wiley & Sons, 1993.

[14] S. N. Lophaven, H. B. Nielsen, J. Søndergaard, DACE: a MATLAB kriging toolbox, version 2.0, Tech. rep., Technical University of Denmark (2002).

[15] C. E. Rasmussen, C. K. I. Williams, Gaussian processes for machine learning, The MIT Press, 2006.

[16] Z.-H. Han, S. Görtz, Hierarchical kriging model for variable-fidelity surrogate modeling, AIAA Journal 50 (9) (2012) 1885–1896. arXiv:https://doi.org/10.2514/1.J051354, doi:10.2514/1.J051354.
URL https://doi.org/10.2514/1.J051354

[17] I. Sobol', On the distribution of points in a cube and the approximate evaluation of integrals, USSR Computational Mathematics and Mathematical Physics 7 (4) (1967) 86–112. doi:https://doi.org/10.1016/0041-5553(67)90144-9.
URL https://www.sciencedirect.com/science/article/pii/0041555367901449

[18] M. D. McKay, R. J. Beckman, W. J. Conover, A comparison of three methods for selecting values of input variables in the analysis of output from a computer code, Technometrics 21 (2) (1979) 239 – 245.

[19] C. Park, R. L. Jaffe, H. Partridge, Chemical-kinetic parameters of hyperbolic earth entry, Journal of Thermophysics and Heat Transfer 15 (1) (2001) 76–90.

[20] S. Marelli, B. Sudret, UQLab: A Framework for Uncertainty Quantification in Matlab, pp. 2554–2563. arXiv:https://ascelibrary.org/doi/pdf/10.1061/9780784413609.257, doi:10.1061/9780784413609.257.
URL https://ascelibrary.org/doi/abs/10.1061/9780784413609.257

Enforcing interface coupling conditions within a high-order sharp interface method: application to viscous compressible gas-liquid flows

David Henneaux

Aeronautics and Aerospace Department, von Karman Institute for Fluid Dynamics, Belgium, david.henneaux@vki.ac.be

Supervisor: Thierry Magin

Professor, Aeronautics and Aerospace Department, von Karman Institute for Fluid Dynamics, Belgium, magin@vki.ac.be

University Supervisor: Philippe Chatelain

Professor, Institute of Mechanics, Materials and Civil Engineering (iMMC), UCLouvain, Belgium, philippe.chatelain@uclouvain.be

Abstract

High-order geometrically unfitted sharp interface methods have opened the way to new simulations capabilities in the field of interface problems. One of the main challenges associated to the use of such methods is the consistent enforcement of coupling conditions at the interface. We establish in this work a robust strategy which enables a versatile imposition of interface conditions between two compressible flows. Simple verification test cases demonstrate the potential of the proposed approach while identifying future developments in order to benefit from its high resolution features in complex multi-phase flow situations.

Keywords: Unfitted, Cut-cell, Immersed, Sharp interface, High-order, Discontinuous Galerkin, Two-phase flows, Viscous compressible flows

1. Introduction

Over the past decades, numerous unstructured high-order methods for solving partial differential equations have been developed, theoretically offering increased accuracy for the same computational cost when compared to standard low-order methods. However, there are several obstacles on the road to the systematic adoption of these methods for industrial applications. One of them relates to the preservation of the high-order features for low-regularity solutions, which e.g. occur in two-phase flow problems. To overcome this issue without relying on complex and time-consuming remeshing procedures, an eXtended Discontinuous Galerkin (XDG) method has been implemented in the Argo solver [1; 2], based on the work of [3; 4]. The resulting unfitted-interface discretization is particularly appealing to treat multi-material fluid flow with complex interface dynamics. The challenges associated to such flows are then shifted to the ability of the method to (i) represent and follow the interface, (ii) sharply capture the solution discontinuities, and (iii) enforce the physical coupling conditions between the materials. This work is concerned with the last challenge, i.e. the development of coupling strategies between dissimilar materials in the context of a FEM-type cut-cell method. Of particular interest is the interaction between viscous compressible gas and liquid phases, which finds use in many practical applications. In the context of this PhD, this kind of interactions occur during the ablation of objects re-entering the Earth atmosphere and undergoing melting. Indeed, the molten layer will be sheared by the high-velocity gas and evaporates, which will strongly influence the ablation process of the object. The numerical tool developed in this PhD project aims to provide high-fidelity simulations of the phenomena at stake. One of the essential building blocks of this tool, i.e. the coupling strategy between the gas and the liquid phases, is the subject of the present paper.

The governing balance laws of the problem including the equations in the bulk of each phase and the interfacial jumps are first presented in Sec. 2. Then, the key concepts of the discontinuous Galerkin (DG)

discretization, with a focus on the specification of the numerical fluxes, are recalled in Sec. 3. Starting from those concepts, the XDG method is introduced in Sec. 4 with the emphasis on the interface term appearing in the weak formulation. The way the jumps conditions are imposed through the computation of interfacial fluxes is finally explained in Sec. 5. Some verification test cases showing the performances of the method are presented in Sec. 6 before concluding.

2. Governing equations

2.1. Equations in the bulk of each phase

In the present work, single species equations with constant viscosity, conductivity and heat capacities, with no turbulence model and no source term are considered. Moreover, unsteady effects are not taken into account and the flow is restricted to two dimensions. The two-dimensional stationary compressible Navier-Stokes equations that are solved by the solver in the bulk of each kth-phase can therefore be written, by splitting the convective and the diffusive parts, as

$$\tilde{\nabla} \cdot \left(\underline{\boldsymbol{F}}_k^c(\tilde{\mathbf{u}}_k) \; - \; \underline{\boldsymbol{F}}_k^d(\tilde{\mathbf{u}}_k, \, \tilde{\nabla}\tilde{\mathbf{u}}_k) \right) = \mathbf{0} \, , \tag{1}$$

with the continuous divergence operator in two dimensions defined as

$$\tilde{\nabla} = \left[\frac{\partial .}{\partial x} \, , \; \frac{\partial .}{\partial y} \right] .$$

Note that the notation $\tilde{\bullet}$ indicates exact continuous quantities, making the distinction with the discretized ones introduced later. For the sake of clarity, this notation is only used on the global solution vector $\tilde{\mathbf{u}}$ and its gradient. Moreover, the font $\mathbf{q}$ will identify a vector quantity while $\underline{\boldsymbol{q}}$ will be used for tensors. The conservative variables, the convective fluxes and the diffusive fluxes for phase k are given respectively by

$$\tilde{\mathbf{u}}_k = \begin{bmatrix} \rho_k \\ \rho_k \mathbf{v}_k \\ \rho_k E_k \end{bmatrix} , \quad \underline{\boldsymbol{F}}_k^c(\tilde{\mathbf{u}}_k) = \begin{bmatrix} \rho_k \mathbf{v}_k \\ \rho_k \mathbf{v}_k \otimes \mathbf{v}_k + p_k \underline{\boldsymbol{I}} \\ \rho_k \mathbf{v}_k H_k \end{bmatrix} ,$$
$$\underline{\boldsymbol{F}}_k^d(\tilde{\mathbf{u}}_k, \, \tilde{\nabla}\tilde{\mathbf{u}}_k) = \begin{bmatrix} 0 \\ \underline{\boldsymbol{\tau}}_k \\ \underline{\boldsymbol{\tau}}_k \cdot \mathbf{v}_k - \mathbf{q}_k \end{bmatrix} , \tag{2}$$

in which the density of phase k is noted ρ_k, the velocity vector $\mathbf{v}_k = \left[v_{x,k} \, , \; v_{y,k} \right]$ and the static pressure p_k. The total energy E_k and the total enthalpy H_k per unit mass both include thermal and kinetic contributions

$$E_k = e_k + \frac{\mathbf{v}_k \cdot \mathbf{v}_k}{2} \, , \quad H_k = h_k + \frac{\mathbf{v}_k \cdot \mathbf{v}_k}{2} = e_k + \frac{p_k}{\rho_k} + \frac{\mathbf{v}_k \cdot \mathbf{v}_k}{2} \, , \tag{3}$$

with the specific internal energy e_k and the specific enthalpy h_k. The constitutive equations for the shear stress tensor $\underline{\boldsymbol{\tau}}_k$ and the heat flux $\mathbf{q}_k$ are written as

$$\underline{\boldsymbol{\tau}}_k = \mu_k \left[\tilde{\nabla}\mathbf{v}_k + (\tilde{\nabla}\mathbf{v}_k)^T - \frac{2}{3} \tilde{\nabla} \cdot \mathbf{v}_k \, \underline{\boldsymbol{I}} \right] \, , \quad \mathbf{q}_k = -\lambda \, \tilde{\nabla} T_k \, , \tag{4}$$

following the assumption of a Newtonian fluid and the Fourier law, with the dynamic viscosity μ_k, the thermal conductivity λ_k and the temperature T_k. For the purposes of discretization later, we also introduce the Jacobian of the diffusive fluxes with respect to the solution gradients $\underline{\boldsymbol{G}}(\tilde{\mathbf{u}})$ such that

$$\underline{\boldsymbol{F}}_k^d(\tilde{\mathbf{u}}_k, \, \tilde{\nabla}\tilde{\mathbf{u}}_k) = \underline{\boldsymbol{G}}_k(\tilde{\mathbf{u}}_k) \tilde{\nabla}\tilde{\mathbf{u}}_k \, . \tag{5}$$

To close the system of Eqs. (1), it must be supplemented by constitutive relations relating intensive thermodynamic properties at equilibrium. For this purpose, a stiffened gas model is used for the volumetric and caloric equations of state that unequivocally determine the state of the fluid inside each phase k:

$$\begin{aligned} p_k(\rho_k, T_k) &= \rho_k(\gamma_k - 1) e_k - \gamma_k p_{\infty,k} \, , \\ e_k(\rho_k, T_k) &= C_{v,k} T_k + \frac{p_{\infty,k}}{\rho_k} \, , \end{aligned} \tag{6}$$

where γ_k is the heat capacity ratio, $C_{v,k}$ is the heat capacity at constant volume and $p_{\infty,k}$ models molecular attractive effects and leads to the "stiffened" properties compared to an ideal gas for which $p_\infty = 0$. The larger the value of p_∞, the closer the flow will behave as nearly incompressible. We can note that more advanced equations of state could readily be used instead as the thermodynamic models for both phases are completely decoupled.

2.2. Jumps conditions at the interface coupling both phases

The use of a sharp interface method in this work leads to a so-called local instant formulation requiring the resolution of some jump conditions at the interface. These conditions specify the exchanges of mass, momentum, and energy through the interface and stand as matching conditions between the two phases. They can be derived by writing the balance laws in a control volume around the interface moving with the interface velocity $\mathbf{v}_\Gamma$. Their derivation and the associated assumptions can be found e.g. in [5; 6]. They are written under a generic form as follows:

$$-v_{n,\Gamma} [\![\tilde{\mathbf{u}}]\!]_\Gamma + [\![\underline{\boldsymbol{F}}^c(\tilde{\mathbf{u}}) - \underline{\boldsymbol{F}}^d(\tilde{\mathbf{u}}, \tilde{\nabla}\tilde{\mathbf{u}})]\!]_\Gamma \cdot \mathbf{n}_\Gamma = \tilde{\nabla}_{s,\Gamma} \cdot \underline{\boldsymbol{F}}_\Gamma + \mathbf{S}_\Gamma \, , \tag{7}$$

where $v_{n,\Gamma} = \mathbf{v}_\Gamma \cdot \mathbf{n}_\Gamma$ is the normal interface velocity with the unit normal vector $\mathbf{n}_\Gamma$ pointing outwards from phase $k = 1$ into phase $k = 2$. The jump operator across the interface Γ at a position $\mathbf{x} \in \Gamma$ for some quantity q defined in the bulk of each phase is given by

$$[\![q]\!]_\Gamma = (q_1 - q_2)\,, \quad \text{with} \quad q_k = \lim_{\epsilon \to 0, \epsilon > 0} q(\mathbf{x} \pm \epsilon \mathbf{n}_\Gamma)\,. \tag{8}$$

On the right-hand side of Eq. (7), $\underline{\boldsymbol{F}}_\Gamma$ is the line flux along the interface while $\mathbf{S}_\Gamma$ represents the surface source. Finally, the surface divergence operator is defined as:

$$\tilde{\nabla}_{s,\Gamma} = \tilde{\nabla} - \mathbf{n}_\Gamma(\mathbf{n}_\Gamma \cdot \tilde{\nabla})\,.$$

In this work, we consider that the only contribution to the line fluxes is due to surface tension effects while we keep only a surface source in the energy balance. Then, considering the projections of the momentum jump conditions along the normal $\mathbf{n}_\Gamma$ and the tangent $\mathbf{t}_\Gamma$ to the interface, Eq. (7) can be developed as:

$$\begin{aligned}
-v_{n,\Gamma}[\![\rho]\!]_\Gamma &+ [\![\rho v_n]\!]_\Gamma &&= 0 \\
-v_{n,\Gamma}[\![\rho v_n]\!]_\Gamma &+ [\![\rho v_n^2 + p]\!]_\Gamma &&= \sigma\kappa &&+ [\![\underline{\boldsymbol{\tau}} \cdot \mathbf{n}_\Gamma \cdot \mathbf{n}_\Gamma]\!]_\Gamma \\
-v_{n,\Gamma}[\![\rho v_t]\!]_\Gamma &+ [\![\rho v_n v_t]\!]_\Gamma &&= \nabla_s\sigma \cdot \mathbf{t}_\Gamma &&+ [\![\underline{\boldsymbol{\tau}} \cdot \mathbf{n}_\Gamma \cdot \mathbf{t}_\Gamma]\!]_\Gamma \\
-v_{n,\Gamma}[\![\rho v_n H]\!]_\Gamma &+ [\![\rho v_n v_t]\!]_\Gamma &&= (\sigma\kappa\mathbf{n}_\Gamma + \nabla_s\sigma) \cdot \mathbf{v}_\Gamma &&+ [\![\underline{\boldsymbol{\tau}} \cdot \mathbf{v} \cdot \mathbf{n}_\Gamma]\!]_\Gamma \\
& & & & &- [\![\mathbf{q} \cdot \mathbf{n}_\Gamma]\!]_\Gamma + q_\Gamma
\end{aligned} \tag{9}$$

with the normal and tangent bulk fluid velocities at the interface, $v_n = \mathbf{v} \cdot \mathbf{n}_\Gamma$ and $v_t = \mathbf{v} \cdot \mathbf{t}_\Gamma$, respectively, the surface tension coefficient σ, the interface curvature κ and the interface energy source q_Γ. The set of jumps conditions Eqs. (9) do not constitute sufficient matching conditions to define the problem uniquely. Consequently, they should be supplemented by additional relations. Based on the expression for the entropy production at the interface, the choice is made here to impose the continuity of tangential velocities and temperatures:

$$[\![v_t]\!]_\Gamma = 0\,, \tag{10}$$

$$[\![T]\!]_\Gamma = 0\,. \tag{11}$$

Moreover, for problems involving mass transfer between the phases, a phase transition model is provided to compute the net mass flux $\dot{m}_\Gamma$ across the interface:

$$\dot{m}_\Gamma \coloneqq \rho_k(v_{n,k} - v_{n,\Gamma}) = \dot{m}_\Gamma^{\text{model}}(\tilde{\mathbf{u}}_1, \tilde{\mathbf{u}}_2)\,, \tag{12}$$

where $\dot{m}_\Gamma^{\text{model}}$ is typically a phase transition model derived from kinetic theory and modeling interfacial resistance to mass transfer [7].

In this work, mass transfer phenomena are not taken into account so that $v_{n,1} = v_{n,2} = v_{n,\Gamma}$ and the jumps conditions that will be used in the remaining of this paper are Eqs. (9), Eq. (10) and Eq. (11).

3. Discretization of convective and diffusive fluxes in the discontinous Galerkin method

Before presenting the XDG method and the way the interface conditions are enforced, we first recall some key concepts of the classical DG method that will be useful for the following. As a first approximation, we assume that the continuous physical domain $\tilde{\Omega}$ with boundaries $\tilde{\mathtt{B}}$ can be geometrically discretized into a set of non-overlapping and conforming quadrilateral or triangular elements Ω_m such that $\tilde{\Omega} \approx \Omega = \{\Omega_m\}_{m=1,\dots,N_\Omega}$ and $\tilde{\mathtt{B}} \approx \mathtt{B} = \{\mathtt{B}_b\}_{b=1,\dots,N_\mathtt{B}}$. The set of internal faces is noted as $\mathtt{E} = \{\mathtt{E}_e\}_{e=1,\dots,N_\mathtt{E}}$ with the associated superscripts $\bullet^-$ and $\bullet^+$ identifying the left and right sides of the edge, respectively, depending on its defined orientation. As a second approximation, the exact solution $\tilde{\mathbf{u}}(\mathbf{x})$ must be approximated by a discrete solution $\mathbf{u}(\mathbf{x})$ which belongs to a finite dimensional space. In DG methods, this space is commonly chosen as the space of discontinuous piecewise polynomials of degree p and dimension d, noted $\mathcal{W}_p^d$, defined on the grid Ω:

$$\begin{aligned}
\mathcal{W}_p^d(\Omega) \coloneqq \{\, w \in L^2(\tilde{\Omega}) \;:\; & w\big|_{\Omega_m} \in \mathcal{P}_p^d(\Omega_m) \text{ if } \Omega_m \text{ is a triangle} \\
& \text{or } w\big|_{\Omega_m} \in \mathcal{Q}_p^d(\Omega_m) \text{if } \Omega_m \text{ is a quadrangle} \\
& \forall \Omega_m \in \Omega \,\}\,,
\end{aligned} \tag{13}$$

where $w\big|_{\Omega_m}$ indicates a function whose support is restricted to element Ω_m, L^2 is an Hilbert space on which the L^2-inner product $\int_{\tilde{\Omega}} fg \,\mathrm{d}\mathbf{x}$ is defined, and $\mathcal{P}_p^d$ and $\mathcal{Q}_p^d$ are the spaces of polynomials and tensor product polynomials of degree p. The solution is then expressed in each element as a linear combination between shape functions ϕ_m spanning $\mathcal{W}_p^d$ and nodal expansion weights $\mathbf{U}_{m,n}$

$$\mathbf{u}_m(\mathbf{x}) = \sum_{n=1}^{N_p} \phi_{m,n}(\mathbf{x})\mathbf{U}_{m,n}\,, \tag{14}$$

where the shape functions are chosen here to be Lagrange polynomials of a given order p and the subscript $\bullet_n$ refers to the nth-degrees of freedom on the element.

Going from the strong form Eq. (1) to the weak formulation involves several steps. Following [8], the primal

face-based[1] flux formulation of the problem can then be written as

$$\begin{aligned}\hat{\mathcal{N}}(\mathbf{u},\mathbf{w}) \equiv &\sum_{m=1}^{N_\Omega} \mathcal{V}_m(\mathbf{u}_m,\mathbf{w}_m) \\ &+ \sum_{e=1}^{N_E} \hat{\mathcal{E}}_e(\mathbf{u}_e,\mathbf{w}_e) \\ &+ \sum_{b=1}^{N_B} \hat{\mathcal{B}}_b(\mathbf{u}_b,\mathbf{w}_b) = 0 \quad \forall \mathbf{w} \in \mathcal{W}_p^d\,,\end{aligned} \tag{15}$$

with the test functions $\mathbf{w}$ taken from the same space as the trial functions $\mathbf{u}$. The volume, face and boundary contributions to the global variational formulation $\hat{\mathcal{N}}$ are expressed respectively as:

$$\begin{aligned}\mathcal{V}_m(\mathbf{u}_m,\mathbf{w}_m) = \int_{\Omega_m} [\, &- \underline{\boldsymbol{F}}^c(\mathbf{u}_m) \\ &+ \underline{\boldsymbol{F}}^d(\mathbf{u}_m,\nabla\mathbf{u}_m)\,] : \nabla\mathbf{w}_m \,\mathrm{d}\mathbf{x},\end{aligned} \tag{16}$$

$$\begin{aligned}\hat{\mathcal{E}}_e(\mathbf{u}_e,\mathbf{w}_e) = &\int_{E_e} \left(\hat{\underline{\boldsymbol{F}}}_e^c - \hat{\underline{\boldsymbol{F}}}_e^d\right)\cdot \mathbf{n}_e^+ \,(\mathbf{w}_e^+ - \mathbf{w}_e^-)\,\mathrm{d}s \\ &+ \int_{E_e} [\,(\hat{\mathbf{u}}_e - \mathbf{u}_e^+)(\underline{\boldsymbol{G}}^T(\mathbf{u}_e^+)\nabla\mathbf{w}_e^+) \\ &- (\hat{\mathbf{u}}_e - \mathbf{u}_e^-)(\underline{\boldsymbol{G}}^T(\mathbf{u}_e^-)\nabla\mathbf{w}_e^-)\,]\cdot\mathbf{n}_b^+\,\mathrm{d}s\,,\end{aligned} \tag{17}$$

$$\begin{aligned}\hat{\mathcal{B}}_b(\mathbf{u}_b,\mathbf{w}_b) = &\int_{B_b} \left(\hat{\underline{\boldsymbol{F}}}_b^c - \hat{\underline{\boldsymbol{F}}}_b^d\right)\cdot \mathbf{n}_b^+ \mathbf{w}_b^+\,\mathrm{d}s \\ &+ \int_{B_b} (\hat{\mathbf{u}}_b - \mathbf{u}_b^+)(\underline{\boldsymbol{G}}^T(\mathbf{u}_b^+)\nabla\mathbf{w}_b^+)\cdot\mathbf{n}_b^+\,\mathrm{d}s\,.\end{aligned} \tag{18}$$

Because of the discontinuous solution approximation, the flux terms are not uniquely defined across element faces and must therefore be replaced by numerical flux functions identified by $\hat{\bullet}$ in Eqs. (16, 17, 18). Those fluxes ensure weak inter-elements coupling and should be specified such that the resulting method will satisfy three fundamental properties : conservativity, consistency and stability. The choice of the convective and diffusive numerical fluxes and their link with the above-mentioned properties is detailed below.

3.1. Convective numerical fluxes

The internal interface convective term uses a numerical flux function corresponding to the (approximate) solution of the Riemann problem defined by the jump of the solution along the normal to the face:

$$\hat{\underline{\boldsymbol{F}}}_e^c \cdot \mathbf{n}_e^+ = \mathcal{H}(\mathbf{u}_e^+,\mathbf{u}_e^-,\mathbf{n}_e^+) \quad \text{on } \mathtt{E}\,. \tag{19}$$

To ensure energy stability of the scheme, $\mathcal{H}$ is required to be an E-flux [9]. Moreover, it has to be consistent and conservative. Several approximate Riemann solvers satisfy those conditions. In this work, the SLAU2 Riemann solver is used for its ability to provide accurate solution over a wide range of Mach numbers [10]. The boundary conditions are imposed by providing an appropriate outside solution $\mathbf{u}^{\mathrm{bnd}}(\mathbf{u}_b^+)$ to the Riemann solver:

$$\hat{\underline{\boldsymbol{F}}}_b^c \cdot \mathbf{n}_b^+ = \mathcal{H}(\mathbf{u}_b^+,\mathbf{u}_b^{\mathrm{bnd}},\mathbf{n}_b^+) \quad \text{on } \mathtt{B}\,. \tag{20}$$

3.2. Diffusive numerical fluxes

In contrast to the convective term for which the use of Godunov's schemes is the only reasonable solution, there exists several methods to discretize the diffusive terms. A unified analysis of the different possibilities is given in [11]. The most simple choice would be to specify the numerical fluxes $\hat{\underline{\boldsymbol{F}}}^d$ and $\hat{\mathbf{u}}$ as the mean between left and right states[2]. Although consistent, this formulation is known to be unstable. To stabilize the formulation, we rely on the Interior Penalty (IP) method. The approach extends Nitsche's method for weak Dirichlet boundary conditions imposition to the weak enforcement of solution inter-element continuity. The idea is that instead of a rough and direct imposition, a penalization term $\underline{\boldsymbol{\delta}}$ is consistently added to the discretization to minimize the average interpolation errors between $\mathbf{u}_e^+$ and $\mathbf{u}_e^-$ across element faces and $\mathbf{u}_b^+$ and $\mathbf{u}_b^{\mathrm{bnd}}$ on domain boundaries. The numerical flux function $\hat{\underline{\boldsymbol{F}}}_e^d$ on element faces is then expressed as

$$\hat{\underline{\boldsymbol{F}}}_e^d = \frac{1}{2}\left(\underline{\boldsymbol{F}}^d(\mathbf{u}_e^+,\nabla\mathbf{u}_e^+) + \underline{\boldsymbol{F}}^d(\mathbf{u}_e^-,\nabla\mathbf{u}_e^-)\right) - \underline{\boldsymbol{\delta}}_e(\mathbf{u}_e^+,\mathbf{u}_e^-) \quad \text{on } \mathtt{E}\,, \tag{21}$$

in which the penalization term is expressed as

$$\underline{\boldsymbol{\delta}}_e(\mathbf{u}_e^+,\mathbf{u}_e^-) = \sigma_e(\mathbf{u}_e^+ - \mathbf{u}_e^-)\otimes\mathbf{n}_e^+\,. \tag{22}$$

The value of the stabilisation parameter σ_e determines the stability of the IP method. More precisely, a lower-bound on this parameter must be specified such that the resulting form will be coercive, hence ensuring inf-sup stability of the method. Selecting a too large

[1] The first formulation we come up with when deriving the DG discretization is called the element-based form in which each interior face occurs twice in the sum over all elements. The face-based formulation is obtained from the element-based form by using mean and jump operators and is the one implemented in practice as each interior face occurs only once.

[2] Indeed, in contrast to convective effects which have a "preferred" direction and require upwinding, viscous effects are generally isotropic.

value would however negatively affect the conditioning of the resulting system. An optimal choice of this parameter needs therefore to be derived, at least for the Symmetric SIPG and Incomplete IIPG methods (the IIPG method being the one used in this work, as explained after). In [12], bounds on σ for different element and mesh types are derived from trace inverse inequalities. For two-dimensional triangular and quadrilateral elements, using scalar diffusion coefficients, those are given by

$$\begin{aligned}
\sigma_e &= \max\left(\frac{s\times C_{IP}^{+}}{h^{+}}\,,\ \frac{s\times C_{IP}^{-}}{h^{-}}\right)\cdot\max\left(\beta^{+}\,,\ \beta^{-}\right)\,,\\
C_{IP} &= \begin{cases}(p+1)(p+2)/2 & \text{for 2-D tri}\,,\\ (p+1)^2 & \text{for 2-D quad}\,,\end{cases}\\
h &= \frac{|\Omega_m|}{|\mathtt{E}_e|} = \frac{\text{"Element surface"}}{\text{"Face length"}}\,,\\
\beta &= (2\mu+\lambda/C_v)\,,
\end{aligned} \tag{23}$$

with s, a user-defined safety factor. For the SIPG method (which is not used in this work but deserves some comments), the numerical flux function at the faces on the solution $\hat{\mathbf{u}}_e$ is taken as the mean value

$$\hat{\mathbf{u}}_e = \frac{1}{2}(\mathbf{u}_e^{+}+\mathbf{u}_e^{-}) \quad \text{on } \mathtt{E}\,. \tag{24}$$

Concerning the boundary terms, Neumann boundary conditions are imposed by replacing the average diffusive flux in the first term of $\hat{\underline{\boldsymbol{F}}}^{d}$ by the desired boundary fluxes $\underline{\boldsymbol{F}}^{d,\mathrm{bnd}}$, while Dirichlet boundary conditions are enforced by providing the appropriate outside state $\mathbf{u}_b^{\mathrm{bnd}}$ to the penalty term and replacing the mean solution flux by $\mathbf{u}_b^{\mathrm{bnd}}$:

$$\hat{\underline{\boldsymbol{F}}}_b^{d} = \underline{\boldsymbol{F}}^{d,\mathrm{bnd}}(\mathbf{u}_b^{+},\nabla\mathbf{u}_b^{+}) - \underline{\boldsymbol{\delta}}_b(\mathbf{u}_b^{+},\mathbf{u}_b^{\mathrm{bnd}}) \quad \text{on } \mathtt{B}\,, \tag{25}$$

$$\hat{\mathbf{u}}_b = \mathbf{u}_b^{\mathrm{bnd}} \quad \text{on } \mathtt{B}\,. \tag{26}$$

We note that the penalty parameter σ_b on the boundaries only depend on the interior state. In addition to provide stabilization of the scheme, it can be proved that the specified numerical fluxes are both consistent and conservative [11], as desired.

3.3. Final form of the DG IP discretization in the bulk of each phase

We close this section by presenting the final form of the DG discretized equations in the bulk of each phase before moving to the treatment of the phase interface in the next section. Before doing so, we just define the commonly used mean and jump operators for vector-valued functions $\mathbf{f}$ and tensor-valued functions $\underline{\boldsymbol{f}}$

$$\begin{aligned}
\{\!\{\underline{\boldsymbol{f}}\}\!\} &= \frac{1}{2}(\underline{\boldsymbol{f}}^{+}+\underline{\boldsymbol{f}}^{-}) \ \text{ on } \mathtt{E}\,,\\
[\![\underline{\mathbf{f}}]\!] &= \mathbf{f}^{+}\otimes\mathbf{n}^{+}+\mathbf{f}^{-}\otimes\mathbf{n}^{-} \ \text{ on } \mathtt{E}\,.
\end{aligned} \tag{27}$$

Inserting the numerical fluxes previously defined into the primal flux formulation Eq. (15) and using the trace operators, the final face-based weak formulation of the problem consists in finding $\mathbf{u}\in\mathcal{W}_p^d$ such that

$$\begin{aligned}
\mathcal{N}(\mathbf{u},\mathbf{w}) \equiv &\sum_{m=1}^{N_\Omega}\mathcal{V}_m(\mathbf{u}_m,\mathbf{w}_m)\\
&+\sum_{e=1}^{N_E}\mathcal{E}_e(\mathbf{u}_e,\mathbf{w}_e)\\
&+\sum_{b=1}^{N_B}\mathcal{B}_b(\mathbf{u}_b,\mathbf{w}_b)=0 \quad \forall\mathbf{w}\in\mathcal{W}_p^d\,,
\end{aligned} \tag{28}$$

with the volume contributions Eq. (16) unchanged and the faces and boundaries contributions now specified as

$$\begin{aligned}
\mathcal{E}_e(\mathbf{u}_e,\mathbf{w}_e) = &\int_{E_e}\mathcal{H}(\mathbf{u}_e^{+},\mathbf{u}_e^{+},\mathbf{n}_e^{+})[\![\underline{\mathbf{w}_e}]\!]\cdot\mathbf{n}_e^{+}\\
&-\{\!\{\underline{\boldsymbol{F}}^{d}(\mathbf{u}_e,\nabla\mathbf{u}_e)\}\!\}:[\![\underline{\mathbf{w}_e}]\!]\\
&+\sigma_e[\![\underline{\mathbf{u}_e}]\!]:[\![\underline{\mathbf{w}_e}]\!]\,\mathrm{d}s\\
&-\theta\int_{E_e}\{\!\{\underline{\boldsymbol{G}}^{T}(\mathbf{u}_e)\nabla\mathbf{w}_e\}\!\}:[\![\underline{\mathbf{u}_e}]\!]\,\mathrm{d}s\,,
\end{aligned} \tag{29}$$

$$\begin{aligned}
\mathcal{B}_b(\mathbf{u}_b,\mathbf{w}_b) = &\int_{B_b}\mathcal{H}(\mathbf{u}_b^{+},\mathbf{u}_b^{\mathrm{bnd}},\mathbf{n}_b^{+})\cdot\mathbf{w}_b^{+}\\
&-(\underline{\boldsymbol{F}}^{d,\mathrm{bnd}}(\mathbf{u}_b^{+},\nabla\mathbf{u}_b^{+})\cdot\mathbf{n}_b^{+})\cdot\mathbf{w}_b^{+}\\
&+\sigma_b(\mathbf{u}_b^{+}-\mathbf{u}_b^{\mathrm{bnd}})\cdot\mathbf{w}_b^{+}\,\mathrm{d}s\\
&-\theta\int_{B_b}(\underline{\boldsymbol{G}}^{T}(\mathbf{u}_b^{+})\nabla\mathbf{w}_b^{+}):(\mathbf{u}_b^{+}-\mathbf{u}_b^{\mathrm{bnd}})\otimes\mathbf{n}_b^{+}\,\mathrm{d}s\,.
\end{aligned} \tag{30}$$

It has to be noted that in the present work, the symmetric ($\theta=1$) or non-symmetric ($\theta=-1$) term has not been implemented yet in our solver (i.e. $\theta=0$) so that the method used to produce the results is the Incomplete IP method (IPPG) which remains consistent, conservative and stable but exhibits reduced convergence rates with respect to the L2-norm [13].

4. The eXended DG method to deal with sharp interface problems

As introduced in Sec. 1, this work is motivated by the development of a high-order solver to simulate the

complex interactions between two immiscible phases, a compressible gas and a weakly compressible liquid. To this end, three keys ingredients are needed: (i) a method to capture the interface motion, (ii) a method to handle discontinuous fields, and (iii) a strategy to enforce the physical jumps conditions at the interface. In this work, the phase interface Γ is implicitly represented by the zero iso-0 contour of a level-set function φ, separating the domain in two regions[3] V^1 and V^2, containing phases $k = 1$ and $k = 2$. This can be mathematically stated as

$$\begin{aligned} \Gamma &= \{\mathbf{x} \in \Omega : \varphi(\mathbf{x}) = 0\} \,, \\ V^1 &= \{\mathbf{x} \in \Omega : \varphi(\mathbf{x}) < 0\} \,, \\ V^2 &= \{\mathbf{x} \in \Omega : \varphi(\mathbf{x}) > 0\} \,. \end{aligned} \tag{31}$$

The interface is tracked by advecting the level-set with an extended velocity field provided by the fluid solver. More information can be found in [14].

We then introduce some notations related to the domain and mesh divisions. The set of all elements can be subdivided into three subsets such that

$$\Omega = \left\{\Omega_m^1\right\}_{m=1,...,N_{\Omega^1}} \cup \left\{\Omega_m^2\right\}_{m=1,...,N_{\Omega^2}} \cup \left\{\Omega_m^\Gamma\right\}_{m=1,...,N_{\Omega^\Gamma}} \,, \tag{32}$$

such that Ω^Γ is the set of elements crossed by the level-set iso-0

$$\Omega^\Gamma = \{\Omega_m : \Omega_m \cap \Gamma \neq \varnothing \,,\ \forall m = 1, ..., N_\Omega\} \,, \tag{33}$$

while Ω^k is the set of elements containing a single phase $k = 1$ or $k = 2$

$$\Omega^k = \left\{\Omega_m : \Omega_m \cap V^k \neq \varnothing \,,\ \forall m = 1, ..., N_\Omega\right\} \setminus \Omega^\Gamma \,. \tag{34}$$

The same classification is used to define the set of all cut element faces and boundaries $\mathtt{E}^\Gamma$ and $\mathtt{B}^\Gamma$, as well as the set of all faces and boundaries associated to a single phase k, $\mathtt{E}^k$ and $\mathtt{B}^k$.

In the classical DG framework presented so far, the discretized solution is expressed in each element as the linear combination between some unknowns degrees of freedom (DOFs) and associated polynomial shape functions (Eq. (14)). When dealing with problems where an interface arbitrary cuts a fixed mesh, the presence of important jumps on the quantities and/or their gradients across this interface makes the original discretization inappropriate as a single polynomial interpolant is not able to represent accurately such sharp jumps. Various strategies have been devised to address such kind of interface problems that are ubiquitous in many scientific fields. In this work, we rely on a geometrically unfitted cut/extended DG method, named the eXtended DG (XDG) method, first introduced in [15] and then in [3]. In order to enable independent solution approximations on both sides of the interface and therefore overcome the limitations of the DG method, it is necessary to take into account independent sets of DOFs in every elements crossed by the interface. In other words, we seek a solution among the extended DG functional space

$$\begin{aligned} \mathcal{W}_p^{d,X}(\Omega, \varphi) \coloneqq \{\ & w \in L^2(\tilde{\Omega}) \ : \\ & w\big|_{\Omega_m \cap V^1(\varphi)},\ w\big|_{\Omega_m \cap V^2(\varphi)} \in \mathcal{P}_p^d(\Omega_m) \text{ or } \mathcal{Q}_p^d(\Omega_m) \\ & \forall \Omega_m \in \Omega \ \} \,. \end{aligned} \tag{35}$$

Compared to the DG discretization Eq. (28), the XDG weak form involves the sum over both phases in the elements cut by the interface as well as the addition of an inter-phase term coupling the solutions between both phases. The XDG discretization reads: find $\mathbf{u} \in \mathcal{W}_p^{d,X}$ such that

$$\begin{aligned} \mathcal{N}(\mathbf{u}, \mathbf{w}) &= \mathcal{N}^1(\mathbf{u}_1, \mathbf{w}) + \mathcal{N}^2(\mathbf{u}_2, \mathbf{w}) \\ &\quad + \mathcal{N}^\Gamma(\mathbf{u}_1, \mathbf{u}_2, \mathbf{w}) = 0 \quad \forall \mathbf{w} \in \mathcal{W}_p^{d,X} \,, \end{aligned} \tag{36}$$

with the contributions from the bulk of each phase unchanged compared to the classical DG method, i.e.

$$\begin{aligned} \mathcal{N}^k(\mathbf{u}_k, \mathbf{w}) \equiv & \sum_{m \in \Omega^k} \mathcal{V}_m(\mathbf{u}_{m,k}, \mathbf{w}_m) \\ & + \sum_{e \in \mathtt{E}^k} \mathcal{E}_e(\mathbf{u}_{e,k}, \mathbf{w}_e) \\ & + \sum_{b \in \mathtt{B}^k} \mathcal{B}_b(\mathbf{u}_{b,k}, \mathbf{w}_b) \,, \end{aligned} \tag{37}$$

and the discretization on the cut elements, faces and boundaries given by

$$\begin{aligned} \mathcal{N}^\Gamma(\mathbf{u}_1, \mathbf{u}_2, \mathbf{w}) \equiv \sum_{k \in \{1,2\}} [& \sum_{m \in \Omega^\Gamma} \mathcal{V}_{m,k}^\Gamma(\mathbf{u}_{m,k}, \mathbf{w}_m) \\ & + \sum_{e \in \mathtt{E}^\Gamma} \mathcal{E}_{e,k}^\Gamma(\mathbf{u}_{e,k}, \mathbf{w}_e) \\ & + \sum_{b \in \mathtt{B}^\Gamma} \mathcal{B}_{b,k}^\Gamma(\mathbf{u}_{b,k}, \mathbf{w}_b) \\ & + \sum_{m \in \Omega^\Gamma} \mathcal{I}_{m,k}^\Gamma(\mathbf{u}_{\Gamma_m,1}, \mathbf{u}_{\Gamma_m,2}, \mathbf{w}_m) \ ] \,. \end{aligned} \tag{38}$$

In Eq. (38), the three first contributions are similar to the ones in the bulk of each phase, except the important fact that the integrals of the variational form need

[3] The approach presented here is restricted to the case of two phases, although it would be possible in theory to take into account more.

here to be computed on geometries defined by the intersection of the underlying mesh with the interface. Since we consider two-dimensional computations, the one-dimensional integrals on intersected faces $\mathrm{E}^{\Gamma}_{e,k}$ and boundaries $\mathrm{B}^{\Gamma}_{b,k}$ appearing in Eqs. (29,30) can easily be recast as classical one-dimensional Gaussian quadratures on reference segments. On the other hand, dedicated quadrature techniques are required to evaluate the integrals over the implicitly-defined two-dimensional surfaces $\Omega^{\Gamma}_{m,k}$. To do so, the open-source library *PHG* has been coupled to the solver and provides quadrature rules by recasting the implicitly defined geometry as the graph of an height function [16]. Finally, the additional inter-phase coupling terms can be interpreted as the sum of two distinct but coupled face terms such that

$$\begin{aligned}\hat{\mathcal{I}}^{\Gamma}_{m,k}(\mathbf{u}_{\Gamma_m,1},\mathbf{u}_{\Gamma_m,2},\mathbf{w}_m) = &\int_{\Gamma_m}\left(\hat{\underline{\boldsymbol{F}}}^{c}_{\Gamma,k}-\hat{\underline{\boldsymbol{F}}}^{d}_{\Gamma,k}\right)\cdot\mathbf{n}_{\Gamma,k}\mathbf{w}_m\,\mathrm{d}s\\ &+\int_{\Gamma_m}(\hat{\mathbf{u}}_{\Gamma,k}-\mathbf{u}_{m,k})(\underline{\boldsymbol{G}}^{T}(\mathbf{u}_{m,k})\nabla\mathbf{w}_m)\cdot\mathbf{n}_{\Gamma,k}\,\mathrm{d}s\,,\end{aligned} \tag{39}$$

where

$$\begin{aligned}&\hat{\underline{\boldsymbol{F}}}^{c}_{\Gamma,k}(\mathbf{u}_{\Gamma_m,1},\mathbf{u}_{\Gamma_m,2})\,,\\ &\hat{\underline{\boldsymbol{F}}}^{d}_{\Gamma,k}(\mathbf{u}_{\Gamma_m,1},\nabla\mathbf{u}_{\Gamma_m,1},\mathbf{u}_{\Gamma_m,2},\nabla\mathbf{u}_{\Gamma_m,2}) \quad \text{and}\\ &\hat{\mathbf{u}}_{\Gamma,k}(\mathbf{u}_{\Gamma_m,1},\mathbf{u}_{\Gamma_m,2})\,, \quad k\in\{1,2\}\end{aligned}$$

are numerical flux functions specific to each phase and depending on the solutions on both sides of the interface. The way to specify them is elaborated in the next section but we can already point out the main difference with the bulk face terms: the numerical flux functions are here multi-valued to be able to enforce the desired jumps conditions. Note also that the same quadrature library provides quadrature rules to evaluate the integrals over the interface in Eq. (39).

A crucial element of the XDG method we have to mention is the cell-agglomeration procedure [4]. Since the interface is free to cross the elements of the underlying mesh in any manner, there exist pathological intersection scenarios in which one of the phase occupies only a small volume fraction of the cut element. This results in conditioning issues of the resulting system, intersection-dependent instabilities and suboptimal error estimates [17]. The cell-agglomeration procedure overcomes those issues by 'agglomerating' a non-problematic neighbouring element to the one identified as critical. The detailed description of this technique is out of the scope of this paper but we will see that it has an influence on the results presented later.

5. Enforcement of jumps conditions across the phase interface

This last theoretical section addresses the main novelty of the present work, i.e. the computation of interfacial numerical fluxes in order to couple through complex jumps conditions two general sets of governing equations involving inviscid and viscous effects. Capitalizing on the way the fluxes are specified in the bulk of each phase, the interfacial jumps are weakly imposed into the coupled variational formulation Eq. (36). The key idea of weak constraint imposotion is to relax the strength of imposing the constraints to the benefit of improved accuracy, stability and robustness [17]. These advantages are all the more marked at a phase interface across which huge contrasts in material properties potentially exist. Before detailing the computation of the convective and then diffusive fluxes, we first introduce some notations. The normal to the interface $\mathbf{n}_{\Gamma_m}$ has the same direction as the normal vector emanating from phase 1, $\mathbf{n}_{\Gamma_m,1}$, and is opposite to the normal associated to phase 2:

$$\mathbf{n}_{\Gamma_m} = \mathbf{n}_{\Gamma_m,1} = -\mathbf{n}_{\Gamma_m,2}\,. \tag{40}$$

The 'swapped' phase index k^* is simply defined as

$$k^* = \begin{cases}1 & \text{if } k=2\,,\\ 2 & \text{if } k=1\,.\end{cases} \tag{41}$$

Finally, we associate a tag t_k to each phase given by

$$t_k = \begin{cases}1 & \text{if } k=1\,,\\ -1 & \text{if } k=2\,.\end{cases} \tag{42}$$

5.1. Interface convective numerical fluxes

The specification of the convective fluxes across the interface relies on the concept of multiphase Riemann solvers and reads

$$\hat{\underline{\boldsymbol{F}}}^{c}_{\Gamma,k}\cdot\mathbf{n}_{\Gamma_m,k} = \mathcal{H}_{\Gamma,k}(\mathbf{u}_{\Gamma_m,k},\mathbf{u}_{\Gamma_m,k^*},\mathbf{n}_{\Gamma_m,k}) \quad \text{on } \Gamma\,. \tag{43}$$

The difference with the Riemann solvers used at elements faces is that the multiphase solver considered here returns two distinct fluxes such that the jumps are taken into account. At the same time, waves propagation structure associated to the hyperbolic part of the system is taken into account such as to provide upwinding stablizing the non-linear convective

effects. More precisely, an extension of the single-phase HLLC Riemann solver due to [18] is employed. The different steps are:

1. the solutions in both phases are first projected onto the normal direction to the interface;
2. the Riemann problem is then solved based on the HLLC wave structure: two external shocks waves and an internal contact discontinuity modeling here the phase interface.
   - the propagation speeds of the left and right shock waves, S_L and S_R, are estimated based on the linearization of the Lax curves;
   - the system of equations formed by the Rankine-Hugoniot (R-H) relations across the two shocks and the jumps relations across the phase interface is then solved. This system can be compactly written as:

$$\begin{aligned}
-S_L(\mathbf{u}^*_{n,L} - \mathbf{u}_{n,1}) + \left(\underline{\boldsymbol{F}}^c_1(\mathbf{u}^*_L) - \underline{\boldsymbol{F}}^c_1(\mathbf{u}_1)\right)\cdot\mathbf{n}_\Gamma\cdot\mathbf{n}_\Gamma &= \mathbf{0}\,,\\
-S_R(\mathbf{u}^*_{n,R} - \mathbf{u}_{n,2}) + \left(\underline{\boldsymbol{F}}^c_2(\mathbf{u}^*_R) - \underline{\boldsymbol{F}}^c_2(\mathbf{u}_2)\right)\cdot\mathbf{n}_\Gamma\cdot\mathbf{n}_\Gamma &= \mathbf{0}\,,\\
-v_{\Gamma,n}(\mathbf{u}^*_{n,L} - \mathbf{u}^*_{n,R}) + \left(\underline{\boldsymbol{F}}^c_1(\mathbf{u}^*_L) - \underline{\boldsymbol{F}}^c_2(\mathbf{u}^*_R)\right)\cdot\mathbf{n}_\Gamma\cdot\mathbf{n}_\Gamma &= \nabla_{s,\Gamma}\cdot\underline{\boldsymbol{F}}_\Gamma\cdot\mathbf{n}_\Gamma\,,
\end{aligned} \tag{44}$$

   where $\mathbf{u}^*_{n,L}$ and $\mathbf{u}^*_{n,R}$ are the normal left and right states of the phase interface for which the system is solved;
3. the normal "star" states are then reprojected to the original frame of reference to get $\mathbf{u}^*_L$ and $\mathbf{u}^*_R$;
4. finally the convective numerical fluxes are assembled as

$$\begin{aligned}
\mathcal{H}_{\Gamma,1} &= \underline{\boldsymbol{F}}^c_1(\mathbf{u}_1)\cdot\mathbf{n}_\Gamma + S_L(\mathbf{u}^*_L - \mathbf{u}_1)\,,\\
\mathcal{H}_{\Gamma,2} &= \underline{\boldsymbol{F}}^c_2(\mathbf{u}_2)\cdot\mathbf{n}_\Gamma + S_R(\mathbf{u}^*_R - \mathbf{u}_2)\,.
\end{aligned} \tag{45}$$

   Since the solutions $\mathbf{u}^*_L$ and $\mathbf{u}^*_R$ satisfy the jumps conditions included in the Riemann problem formulation, integrating the fluxes $\mathcal{H}_{\Gamma,1}$ and $\mathcal{H}_{\Gamma,2}$ over the interface will allow to incorporate them into the variational formulation.

5.2. Interface diffusive numerical fluxes

The idea to incorporate the jumps on the the solutions and on the diffusive fluxes is the same: when considering the assembling of the interface term for a given element, the solution, resp. the flux, on the other side of the interface is compensated by the jump condition to correctly account for the intended discontinuity in the solution, resp. the flux. In addition, those combinations between both sides are weighted by a parameter α defined by

$$\begin{aligned}
\alpha_k &= \frac{(q_k)^a}{(q_1)^a + (q_2)^a}\,,\\
\alpha_{k^*} &= 1 - \alpha_k\,,
\end{aligned} \tag{46}$$

where a is a user-defined power taken here as equal to one (which gives the well-known harmonic weighting) and q is a quantity related to the diffusion process. In this work, we select the viscosity or the thermal conductivity as the weighting factor: $q = \mu$ or $q = \lambda$. Based on the previous comments, the diffusive numerical flux functions present in Eq. (39) are specified as follows:

$$\hat{\underline{\boldsymbol{F}}}^d_{\Gamma,k} = \alpha_{k^*}\underline{\boldsymbol{F}}^d_k + \alpha_k\left(\underline{\boldsymbol{F}}^d_{k^*} + \mathbf{J}^{d,\mathrm{Rob}}\otimes\mathbf{n}_{\Gamma_m,k}\right) - \underline{\boldsymbol{\delta}}_{\Gamma,k}\,, \tag{47}$$

$$\underline{\boldsymbol{\delta}}_{\Gamma,k} = \sigma_{\Gamma_m}\left[\mathbf{u}_{\Gamma_m,k} - \left(\mathbf{u}_{\Gamma_m,k^*} + \mathrm{t}_k\mathbf{J}^{d,\mathrm{Dir}}\right)\right]\otimes\mathbf{n}_{\Gamma_m,k}\,, \tag{48}$$

$$\hat{\mathbf{u}}_{\Gamma,k} = (1-\theta\alpha_{k^*})\mathbf{u}_{\Gamma_m,k} + \theta\alpha_{k^*}\left(\mathbf{u}_{\Gamma_m,k^*} + t_k\mathbf{J}^{d,\mathrm{Dir}}\right)\,, \tag{49}$$

where $\mathbf{J}^{d,\mathrm{Rob}}$ incorporate the Robin condition on the jumps and $\mathbf{J}^{d,\mathrm{Dir}}$ contain the Dirichlet jumps conditions on the solution. We can note that the weighting is such that $\hat{\underline{\boldsymbol{F}}}^d_{\Gamma,k}$ is biased to the less viscous/conductive phase while $\hat{\mathbf{u}}_{\Gamma,k}$ is biased to the more viscous/conductive phase. Concerning the penalty parameter in Eq. (48), it takes a similar expression as in the bulk:

$$\begin{aligned}
\sigma_\Gamma &= \max\left(\frac{s\times C_{IP,1}}{\max(h_1,0.3)}\,,\ \frac{s\times C_{IP,2}}{\max(h_2,0.3)}\right)\cdot\max\left(\beta_1\,,\,\beta_2\right)\,,\\
C_{IP,k} &= \begin{cases}(2p+1)(2p+2)/2 & \text{for 2-D tri}\,,\\ (2p+1)^2 & \text{for 2-D quad}\,,\end{cases}\\
h_k &= \frac{|\Omega_{m,k}|}{|\Gamma_m|} = \frac{\text{"Cut element surface"}}{\text{"Interface length"}}\,,\\
\beta_k &= (2\mu_k + \lambda_k/C_{v,k})\,.
\end{aligned} \tag{50}$$

However, the following differences can be mentioned:

- the coefficient C_{IP} is increased to ensure well-posedness of the problem as there exists no strict lower bounds on the penalty parameter for cut elements [3];
- the geometric factor h is here taken as the ratio between the cut surface and the interface length crossing the element. As this factor can become very small, we set its lower limit to a threshold of 0.3.

It remains now to explain how the jumps data $\mathbf{J}^{d,\mathrm{Rob}}$ and $\mathbf{J}^{d,\mathrm{Dir}}$ are assembled, starting with the first.

5.2.1. Non-linear Robin conditions on fluxes

Isolating the diffusive fluxes projected along the normal to the interface in Eq. (9), we find the expression for the Robin jumps vector present in the variational form:

$$\mathbf{J}^{d,\mathrm{Rob}}(\mathbf{u}_1, \nabla\mathbf{u}_1, \mathbf{u}_2, \nabla\mathbf{u}_2) = [\![\mathbf{j}^{\mathrm{Flux}}(\mathbf{u}, \nabla\mathbf{u})]\!]_\Gamma \tag{51}$$

where

$$\mathbf{j}^{\mathrm{Flux}}(\mathbf{u}, \nabla\mathbf{u}) = \begin{bmatrix} 0 \\ \dot{m}_\Gamma v_x + p n_{\Gamma,x} - \sigma\kappa n_{\Gamma,x} - \nabla_{s,x}\sigma \\ \dot{m}_\Gamma v_y + p n_{\Gamma,y} - \sigma\kappa n_{\Gamma,y} - \nabla_{s,y}\sigma \\ \dot{m}_\Gamma E + p(v_x n_{\Gamma,x} + v_y n_{\Gamma,y}) \\ -(\sigma\kappa\mathbf{n}_\Gamma + \nabla_s\sigma \cdot \mathbf{t}_\Gamma) \cdot \mathbf{v}_\Gamma - q_\Gamma \end{bmatrix}. \tag{52}$$

We formulate the following remarks about Eqs. (51,52):

- the original jumps expressed in the coordinate system normal to the interface have been translated into the $x - y$ reference coordinate system as the solver manipulates quantities in this frame;
- the jumps do not explicitly depend on the solution gradients in this case but it may be the case for specific jumps conditions. For example, the imposition of a continuous heat flux across the interface requires to subtract the contribution from the viscous dissipation in $\mathbf{j}^{\mathrm{Flux}}$, which involves velocity gradients;
- as already mentioned, mass transfer is neglected in this work so that the terms multiplied by $\dot{m}_\Gamma$ are removed.

5.2.2. Non-linear Dirichlet conditions on solutions

The enforcement of the jumps on the solution is not as direct as the one on the diffusive fluxes. Indeed, the only conditions on the solution independent of the gradients are Eqs. (10, 11, 12). By combining Eq. (10) and Eq. (12), we obtain jumps on the velocity vector while Eq. (11) gives directly the jump on the temperature:

$$[\![\mathbf{v}]\!]_\Gamma = \dot{m}_\Gamma [\![1/\rho]\!]_\Gamma \mathbf{n}_\Gamma \tag{53}$$

$$[\![T]\!]_\Gamma = 0\,. \tag{54}$$

Thus we have three conditions to be imposed on a solution vector containing four variables (still in two dimensions). Moreover, Eqs. (53, 54) are expressed in terms of the so-called primitive variables $\mathbf{v}$ and T while the solution vector for which we solve the equations may be expressed based on another set of variables, like the conservative ones. The procedure we follow to deal with those difficulties is as follows:

1. the solution vectors in both phases is converted to the primitive type $p - \mathbf{v} - T$: $\mathbf{u}_k \to \mathbf{u}_k^{\mathrm{prim}}$;
2. the second term in Eq. (48) and Eq. (49) which penalizes the solution in phase k towards the desired value is directly assembled in terms of primitive variables:

$$\mathbf{u}\mathbf{J}_k^{\mathrm{prim}} := \mathbf{u}_{\Gamma_m,k^*}^{\mathrm{prim}} + t_k \mathbf{J}_{\mathrm{prim}}^{d,\mathrm{Dir}}\,, \tag{55}$$

   where the jumps on primitive variables include the prescribed jumps on velocities and temperature and the jump on pressure is set to zero in all the cases:

$$\mathbf{J}_{\mathrm{prim}}^{d,\mathrm{Dir}} = [\![\mathbf{j}^{\mathrm{Sol}}(\mathbf{u})]\!]_\Gamma \tag{56}$$

$$\mathbf{j}^{\mathrm{Sol}}(\mathbf{u}) = \begin{bmatrix} 0 \\ \dot{m}_\Gamma(1/\rho) n_{\Gamma,x} \\ \dot{m}_\Gamma(1/\rho) n_{\Gamma,y} \\ 0 \end{bmatrix}; \tag{57}$$

3. the component related to the pressure of the assembled term $\mathbf{u}\mathbf{J}_k^{\mathrm{prim}}$ is then imposed to the value of the pressure in phase k:

$$\mathbf{u}\mathbf{J}_k^{\mathrm{prim}}(0) = p_k\,. \tag{58}$$

   In other words, this allows the pressure to be freely fixed by the other numerical fluxes, as it should be;
4. finally, the assembled term is converted back to the set of working variables: $\mathbf{u}\mathbf{J}_k^{\mathrm{prim}} \to \mathbf{u}\mathbf{J}_k$ and is added in the penalty and symmetric/non-symmetric term of the weak form.

5.3. Summing the interface terms

To conclude this section, it is informative to sum the contributions to the interfacial term from both phases, using the previously introduced jumps operators Eq. (27) (which apply here across the phase interface) and the new weighted average operators defined by

$$\begin{aligned} \{\!\{q\}\!\}_\alpha &= \alpha_1 q_1 + \alpha_2 q_2\,, \\ \{\!\{q\}\!\}_{\alpha^*} &= \alpha_2 q_1 + \alpha_1 q_2\,. \end{aligned} \tag{59}$$

Summing the interface term over both phases, we obtain:

$$\begin{aligned}\sum_{k\in\{1,2\}} \mathcal{I}_{m,k} = \int_{\Gamma_m} & \mathcal{H}_{\Gamma,1}\cdot\mathbf{w}_{m,1} + \mathcal{H}_{\Gamma,2}\cdot\mathbf{w}_{m,2} \\ & - \{\!\{\underline{\boldsymbol{F}}^d\}\!\}_{\alpha^*} : \underline{[\![\mathbf{w}_m]\!]} - \mathbf{J}^{d,\mathrm{Rob}}\cdot\{\!\{\mathbf{w}_m\}\!\}_{\alpha} \\ & + \sigma_{\Gamma_m}\left(\underline{[\![\mathbf{u}_{\Gamma_m}]\!]} : \underline{[\![\mathbf{w}_m]\!]} - \mathbf{J}^{d,\mathrm{Dir}}\cdot\underline{[\![\mathbf{w}_m]\!]}\cdot\mathbf{n}_{\Gamma,m}\right)\mathrm{d}s \\ -\theta\int_{\Gamma_m} & \{\!\{\underline{\boldsymbol{G}}^T\nabla\mathbf{w}_m\}\!\}_{\alpha^*} : \underline{[\![\mathbf{u}_{\Gamma_m}]\!]} \\ & - \mathbf{J}^{d,\mathrm{Dir}}\cdot\{\!\{\underline{\boldsymbol{G}}^T\nabla\mathbf{w}_m\}\!\}_{\alpha^*}\cdot\mathbf{n}_{\Gamma,m}\,\mathrm{d}s\,. \end{aligned} \tag{60}$$

This is very similar to the face term Eq. (29), as expected. However, additional terms are here present to weakly enforce the jumps conditions while across the element faces, the continuity of the solution and the fluxes is implicitly assumed. That is also the reason why the specification of the numerical fluxes is different between the two phases. We insist again here on the fact that the symmetric/non-symmetric term of the IP method has not been implemented yet in the solver, i.e. $\theta = 0$.

6. Verification test cases

In this section, two steady test cases making use of the whole strategy developed in this paper are presented. The test cases do not concern any practical flow configuration at this stage of the present work. However, they are very well suited to meticulously verify the implementation of the discretized equations.

6.1. Steady viscous compressible Couette flow between a gas and a liquid

This test case is about the steady one-dimensional two-phase flow Couette configuration described in [19]. The two phases are a stiff liquid and a perfect gas. Their properties are:

$$\begin{aligned} Cv_l &= 3.229\,, & Cv_g &= 0.708\,, \\ \gamma_l &= 3.0\,, & \gamma_g &= 1.4\,, \\ p_{\infty,l} &= 10^5\,, & p_{\infty,l} &= 0.0\,, \\ \mu_l &= 10.0\,, & \mu_g &= 1.0\,, \\ \lambda_l &= 10.0\,, & \lambda_g &= 1.376\,. \end{aligned} \tag{61}$$

The jumps conditions Eqs. (9) are imposed at the interface with the following parameters:

$$\begin{aligned} \dot{m}_\Gamma &= 0.0\,, & \sigma\kappa &= 0.0\,, \\ [\![T]\!]_\Gamma &= 0.0\,, & [\![\mathbf{v}]\!]_\Gamma &= \mathbf{0.0}\,, \\ q_\Gamma &= 1000.0\,, & \nabla_s\sigma &= [-100.0, 0.0]\,, \end{aligned} \tag{62}$$

The particularity in this case is the imposition of a interfacial heat flux source term and a tangential jump in the viscous stresses.
The solution initialized in the domain is slightly perturbed compared to the exact solution such that we can test the ability of the solver to restore the desired jumps. The solver then iterates until a criterion on the value of the global residual is achieved. A spatial convergence study at polynomial interpolation orders $p = 2, 3, 4$ is presented in Fig. 1 for the the pressure P, axial velocity v_x and temperature T. The first thing to comment is the plateau appearing in all the curves. This is the result of the cell-agglomeration procedure mentioned earlier. Refining the second coarser mesh leads to some intersections between the interface and the mesh that are identified as problematic based on a user-defined threshold. This activates the cell-agglomeration in the flagged elements, which inevitably affects locally the accuracy of the solution, hence the plateau in the convergence curves. After this plateau, the asymptotic convergence rates tend globally to p, or slightly less for some variables, especially at order $p = 4$. The expected theoretical convergence rate is $p + 1$ for the odd interpolation orders and p for even orders[4]. So it seems that the expected order of convergence for $p = 3$ is decreased by one while for the even orders, the effect is less pronounced. This is mainly attributed to the agglomeration strategy as complementary simulations without agglomeration have shown that the theoretical rates are globally recovered.

6.2. Steady 2-D manufactured solution test case with straight interface

The second test case is built from the Method of Manufactured Solution (MMS) [20]. We define a solution in each phase taken as trigonometric functions with free unknown parameters. We then solve symbolically the complete jumps conditions linking the two solutions in order to find the unknowns parameters. Finally, we insert those solutions into the governing equations, using again symbolic derivation, in order to find source terms that are directly provided to the numerical solver. Note that the interface is situated along an inclined plane so that both the x and the y vector components are involved in the jumps. Starting from an initially perturbed solution, the solver should be able to bring the residual to a sufficiently low level.

[4] This is a consequence of the absence of the symmetric/non-symmetric term in the IP method, as explained in [13].

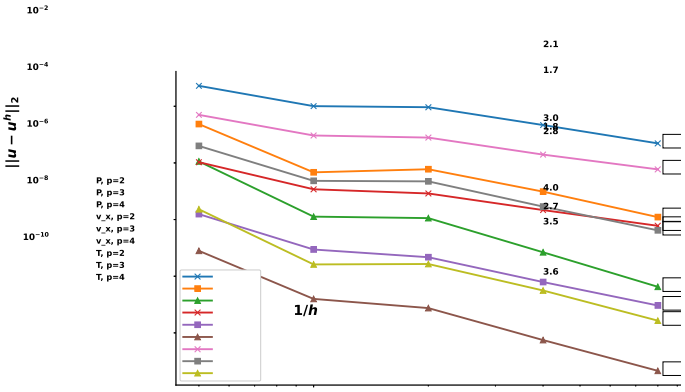

Figure 1: Spatial convergence study on the two-phase Couette flow test case. Errors in L_2-norm between the exact and the numerical solutions as a function of the inverse of the mesh size $1/h$. Asymptotic convergence orders indicated in the boxes.

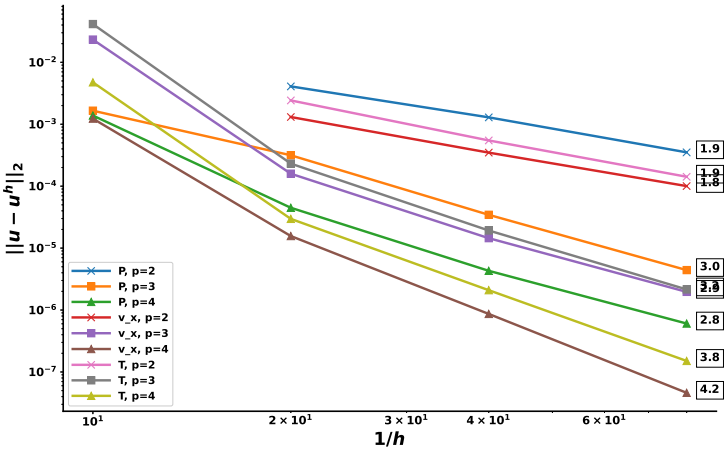

Figure 2: Spatial convergence study on the two-phase manufactured flow test case. Errors in L_2-norm between the exact and the numerical solutions as a function of the inverse of the mesh size $1/h$. Asymptotic convergence orders indicated in the boxes.

This would prove that the jumps conditions, which are implicitly contained in the source terms, are accurately enforced at the interface. The properties of both fluids are the following:

$$\begin{aligned} Cv_1 &= 2.5\,, & Cv_2 &= 2.0\,, \\ \gamma_1 &= 1.4\,, & \gamma_2 &= 1.6\,, \\ p_{\infty,1} &= 0.0\,, & p_{\infty,2} &= 0.0\,, \\ \mu_1 &= 1.0\,, & \mu_2 &= 0.1\,, \\ \lambda_1 &= 1.0\,, & \lambda_2 &= 0.1\,. \end{aligned} \tag{63}$$

The jumps conditions Eqs. (9) are imposed at the interface with the following parameters:

$$\begin{aligned} \dot{m}_\Gamma &= 0.0\,, & \sigma\kappa &= -0.2\,, \\ [\![T]\!]_\Gamma &= 0.0\,, & [\![\mathbf{v}]\!]_\Gamma &= \mathbf{0.0}\,, \\ q_\Gamma &= 1.0\,, & \nabla_s\sigma &= [0.0, 0.0]\,, \end{aligned} \tag{64}$$

A spatial convergence study at polynomial interpolation orders $p = 2, 3, 4$ is presented in Fig. 2 for the the pressure P, axial velocity v_x and temperature T. As for the first test case, we observe a convergence rate limited to p, which could be justified for $p = 2$ and $p = 4$ due to the absence of the symmetric term in the IP formulation, but which is not expected for $p = 3$. Again, simulations without agglomeration reveal that the theoretical order of $p+1$ is retrieved for third order interpolation, except on the pressure variable. This observation would require further investigations.

7. Conclusion

This work presents a strategy to take into account complex non-linear jumps conditions within a high-order sharp interface DG method. Combining the use of multiphase Riemann solvers for the convective part and stabilized weighted interior penalty method for the diffusive part, the solver is able to accurately enforce physical balance conditions between two compressible fluid phases. Although very academic, the test cases treated in this paper demonstrates the order of accuracy with which the jumps conditions can be sharply captured and illustrates the potential of the approach to be applied to more complex and practical situations, such as the one targeted in the framework of this PhD. However, the limitation of the obtained orders of convergence compared to theoretical ones requires some investigations. In particular, the effect of the cell-agglomeration procedure on the accuracy must be better characterized. The direct improvements to be implemented to the method concern the addition of the symmetry term in the IP discretization, the possible addition of other stabilizing terms for the imposition of the Robin conditions based on the approach proposed in [21], the use of tensorial penalty instead of scalar [22], the comparison between different variants of mutliphase Riemann solvers including or not jumps due to viscous fluxes, and the rigorous demonstration of the consistency, stability and conservativity of the proposed weak formulation.

The simulation of moving interface problems involving mass transfer and complex dynamics is the next step to reach.

Acknowledgments

My doctoral work is supported by the Fonds de la Recherche Scientifique (FNRS) of Belgium, under a FRIA grant. I would like to thank Pierre Schrooyen from Cenaero for his continuous and precious help about the methods involved in this work and the implementation strategy into the Argo code.

References

[1] P. Schrooyen, J.-S. Cagnogne, N. Poletz, K. Hillewaert, A high-order extended discontinuous galerkin method for moving immersed interface problem, in: XDMS Conference, Umea, 2017.

[2] P. Schrooyen, L. Arbaoui, J.-S. Cagnone, N. Poletz, K. Hillewaert, A high-order extended discontinuous galerkin method to treat hydrodynamics problems, in: ECCM-ECFD Conference, Glasgow (UK), 2018.

[3] F. Kummer, Extended discontinuous galerkin methods for two-phase flows: the spatial discretization, International Journal for Numerical Methods in Engineering 109 (2) (2017) 259–289.

[4] B. Müller, S. Krämer-Eis, F. Kummer, M. Oberlack, A high-order discontinuous galerkin method for compressible flows with immersed boundaries, Internal Journal For Numerical Methods in Engineering 110 (2017) 3–30.

[5] M. Ishii, T. Hibiki, Thermo-Fluid Dynamics of Two-Phase Flow, 2nd Edition, Springer, 2011.

[6] Y. Z. A. Faghri, Transport Phenomena in Multiphase Systems, Elsevier, 2006.

[7] M. Bond, H. Struchtrup, Mean evaporation and condensation coefficients based on energy dependent condensation probability, Physical Review E 70 (6) (2004) 061605.

[8] R. Hartmann, Numerical analysis of higher order discontinuous galerkin finite element methods, in: D. H. (Ed.), 35th CFD / ADIGMA Course on Very High-Order Discretization Methods, von Karman Institute for Fluid Dynamics, 2008, pp. 1–107.

[9] G. S. Jiang, C.-W. Shu, On a cell entropy inequality for discontinuous galerkin methods, Mathematics of Computation 62 (206) (1994) 531–538.

[10] K. Kitamura, E. Shima, Towards shock-stable and accurate hypersonic heating computations: A new pressure flux for ausm-family schemes, Journal of Computational Physics 245 (2013) 62–83.

[11] D. N. Arnold, F. Brezzi, B. Cockburn, L. D. Marini, Unified analysis of discontinuous galerkin methods for elliptic problems, SIAM journal on numerical analysis 39 (5) (2002) 1749–1779.

[12] K. Hillewaert, Development of the discontinuous galerkin method for high-resolution, large scale cfd and acoustics in industrial geometries, Ph.D. thesis, Université catholique de Louvain (2013).

[13] B. Rivière, Discontinuous Galerkin methods for solving elliptic and parabolic equations: theory and implementation, SIAM, 2008.

[14] D. Henneaux, P. Schrooyen, L. Arbaoui, P. Chatelain, T. E. Magin, A high-order level-set method coupled with an extended discontinuous galerkin method for simulating moving interface problems, in: AIAA AVIATION 2021 FORUM, 2021, p. 2742.

[15] F. Kummer, The bosss discontinuous galerkin solver for incompressible fluid dynamics and an extension to singular equations., Ph.D. thesis, Technische Universität Darmstadt (2012).

[16] T. Cui, W. Leng, H. Liu, L. Zhang, W. Zheng, High-order numerical quadratures in a tetrahedron with an implicitly defined curved interface, ACM Transactions on Mathematical Software (TOMS) 46 (1) (2020) 1–18.

[17] B. Schott, Stabilized cut finite element methods for complex interface coupled flow problems, Ph.D. thesis, Technische Universität München (2017).

[18] S. Fechter, Compressible multi-phase simulation at extreme conditions using a discontinuous galerkin scheme, Ph.D. thesis, Universitat Stuttgart (2015).

[19] S. Peluchon, G. Gallice, L. Mieussens, Development of numerical methods to simulate the melting of a thermal protection system, Journal of Computational Physics 448 (2022) 110753.

[20] K. Salari, P. Knupp, Code verification by the method of manufactured solutions, Tech. rep., Sandia National Lab.(SNL-NM), Albuquerque, NM (United States); Sandia ... (2000).

[21] M. Juntunen, R. Stenberg, Nitsche's method for general boundary conditions, Mathematics of computation 78 (267) (2009) 1353–1374.

[22] R. Hartmann, P. Houston, An optimal order interior penalty discontinuous galerkin discretization of the compressible navier–stokes equations, Journal of Computational Physics 227 (22) (2008) 9670–9685.

Comprehensive characterization of the aero-thermo-mechanical response of space debris materials to atmospheric entry plasmas

Andrea Fagnani

Aeronautics and Aerospace Department, von Karman Institute for Fluid Dynamics, Belgium, andrea.fagnani@vki.ac.be

Supervisor: Olivier Chazot

Head of Department and Professor, Aeronautics and Aerospace Department, von Karman Institute for Fluid Dynamics, Belgium, chazot@vki.ac.be

University Supervisor: Annick Hubin

Professor at Department of Materials and Chemistry, Vrjie Universiteit Brussel, Belgium, annick.hubin@vub.be

Abstract

The number of space debris in Earth's orbit has drastically increased over the last decades, leading to a major concern about future sustainability for the space environment. Moreover, on-ground casualty risk requirements are nowadays imposed by space agencies worldwide, demanding innovative cost-effective strategies to ensure safe disposal of space objects upon uncontrolled re-entry. Combined theoretical, numerical and experimental research is then required to improve our understanding of the complex gas/surface interaction and material response of space debris materials in atmospheric entry flows. In this paper we review the experimental methodology for space debris ground testing in the VKI Plasmatron facility, combining novel techniques with tools inherited from the sound expertise on thermal protection systems testing, and we present preliminary results for quartz and titanium test in air plasma.

Keywords:
Space debris, aerothermochemistry, plasma wind tunnels

1. Introduction

Satellites orbiting Earth offer unrivalled possibilities for research and commercial applications; however, space activities over the last decades have left more than 20000 objects in orbit which are no longer functional, namely, space debris [1]. Their number is predicted to increase exponentially in the future and, due to their hypervelocity motion, collision with existing and new missions can lead to a catastrophic break up, generating even more debris in a cascade effect (Kessler syndrome) [2]. Space debris, mitigation guidelines [3], suggested by the United Nations in 2007, were embraced by the European Commission and implemented by the European Space Agency (ESA) through the Clean Space Initiative. These measures aim at reducing the generation of new debris, limiting the break-up probability, requiring passivation procedures and implementing disposal strategies, such as re-orbiting and de-orbiting at the end-of-life [4]. Moreover, on average over the past decade, an object with mass above 800 kg has re-entered the atmosphere every week [5]. As often witnessed during these events, ground recoveries are the clear testimony of "non-demisability" of some spacecraft components [**?**]. As a result, space agencies and nations have discussed requirements to limit the on-ground casualty risk for future missions. Compliance to this requirement can be safely achieved through controlled re-entry and ground impact over large unpopulated areas. Yet, this solution has major consequences at system level, possibly requiring a full re-design of the spacecraft and leading to higher mass and thus increased mission cost [6]. Among the alternative strategies, the Design for Demise (D4D) refers to all measures taken in the design of a space object to increase the potential

for demise, i.e. complete degradation, upon an uncontrolled re-entry at the end-of-life. The latter, in turn, has the advantage to be cost effective (e.g., no additional propellent is needed) and features less stringent design requirements [7]. Thus, the ultimate goal of the D4D is the ability to correctly predict the complex multi-physical and multi-scale response of space materials to the extreme conditions of atmospheric entry, so as guarantee, at a design level, their complete degradation. Yet, as it will be further detailed later on, this estimation is a complex task and current scientific capabilities do not allow such predictive characterizations [8]. Hence, D4D demands a strong research effort in modeling, numerical simulations and experimental activities.

1.1. Aerothermal phenomena of demising metals and silicates

During atmospheric entry, the bow shock, formed in from of the spacecraft travelling at hypersonic speed produces a high-temperature plasma ($T \approx 10000$ K). If not suitably protected, this interaction causes a series of degradation phenomena, which are technically named as ablation [9]. If the latter proceeds until the entire material mass is consumed, we say that demise occurred. This process can be regarded as a multi-physics gas-surface interaction phenomenon. In particular, aerothermal heating of the material induces melting and formation of gas-liquid and liquid-solid interfaces. The liquid layer can be removed by surface shear forces, imposed by the surrounding flow, or by thermo-chemical phenomena such as evaporation. Injection of vapour into the boundary layer, in turn, affects the aerodynamic heat transfer and the gas-phase chemistry [10], producing a coupled flow-material problem. Additionally, molecular species dissociate due to the extreme temperatures, recombine in the boundary layer and diffuse towards the surface. At the wall, heterogeneous chemistry occurs, including catalysis, nitridation and oxidation. The latter is of paramount importance in the survivability of metallic components, as already documented in the literature [8].

1.2. Ground testing and experimental data demands

The aspiration for a cleaner and more sustainable future for the space environment, allowing to benefit both from its scientific and economical applications, advocates for a revolutionary effort in the design of new demisable systems. Combined theoretical, numerical and experimental research is then required to improve our understanding of the complex gas/surface interaction and material response of space debris materials in atmospheric entry flows.

Ground testing in plasma wind-tunnels is currently the only affordable possibility for both material qualification and validation of material response codes [11]. Due to the multiplicity of the phenomena involved in the space debris demise, however, ground reproduction of a full re-entry scenario seems infeasible. The leading path is then represented by a model development strategy based on consistent wind tunnel experiments. The latter, then, must be able to correctly isolate each critical phenomenon. However, a withstanding challenge in high-enthalpy facilities experimentation is the correct scaling of all the driving physical phenomena [12]. For the specific case of multiphase melting-ablation, this challenge is hardly addressed in the existing literature.

Leveraging on the strong expertise of the VKI in the ground testing of reusable [13] and ablative [9] thermal protection systems, in this work we propose to adapt and improve existing tools and complement them with novel capabilities, chiefly blending numerical models and advanced data processing techniques, to provide a consistent framework to carry out state-of-the-art experimentation on space debris materials. The goal is to improve the ground testing reliability and reducing uncertainties to develop new thermochemical ablation models.

2. Multi-band in situ emittance measurements

Total and spectral emittance measurements are fundamental for characterization and modelling of aerospace materials in re-entry conditions. For instance, the total hemispherical emittance governs the material surface energy balance at high temperatures and it represents a necessary parameter for numerical codes to accurately predict the material response, both for TPS and space debris [14]. In turn, the catalytic efficiency of reusable TPS materials can be measured in ground test facilities by means of a surface energy balance approach, based on the measurement of the material total emittance and surface temperature [15; 16; 17].

On the other hand, spectral or in-band emittance values are useful whenever one wants to perform surface temperature measurements by means of IR radiometry techniques [18]. In this case, emissivity correction must be applied to retrieve the object temperature.

In plasma wind tunnels, infrared radiometry techniques are commonly applied to measure surface temperature and emittance of the test materials. However, the demand for higher accuracy in the experimental data requires accurate modelling of the measurement technique and precise analysis of the test environment. To this purpose, a model of the instrument response is derived and validated. The traditional T^4-ratio methodology for total angular emittance measurements is shown to be affected by non-negligible errors. The optical path emission and transmission are accounted for by solving the radiative transfer equation along the line-of-sight. A Monte Carlo approach allows consistent uncertainty analysis. The methodology is applied for consistent multi-band in situ emittance measurement on test sample materials in the VKI Plasmatron facility.

2.1. *Instrument response model*

A radiation thermometer produces an output signal

$$U = C\left(\int_{\Delta t} \Phi\right), \tag{1}$$

where C is the detector sensitivity curve and $\int_{\Delta t} \Phi$ is the radiant energy detected by the instrument, namely, the integral of the radiant power Φ in the response time Δt. Under common assumptions for IR measurements, we can write the general radiometry measurement formula as

$$\begin{aligned}\tilde{\Phi} = &\int_{\Delta\lambda} \tau_\lambda^{\text{ext}} \tau_\lambda^{\text{atm}} \varepsilon_\lambda \tilde{R}_\lambda^\tau L_\lambda^{\text{BB}}(T_{\text{obj}}) + \\ &+ \int_{\Delta\lambda} \tau_\lambda^{\text{ext}} \tau_\lambda^{\text{atm}} (1-\varepsilon_\lambda) \tilde{R}_\lambda^\tau L_\lambda^{\text{BB}}(T_{\text{amb}}) + \\ &+ \int_{\Delta\lambda} \tau_\lambda^{\text{ext}} \tilde{R}_\lambda^\tau L_\lambda^{\text{atm}},\end{aligned} \tag{2}$$

where τ is the optical path transmittance, ε is the object emittance, R is the detector spectral response and L is the spectral radiance. Once the instrument is calibrated, this can be inverted for the temperature of the target object starting from the measured signal U_{obj}. We call apparent temperature T_{app} the value obtained in this manner, once a set of IR parameters $([\hat{\varepsilon}_{\Delta\lambda}, \hat{\tau}_{\Delta\lambda}^{\text{ext}}, T_{\text{amb}}, \tau_\lambda^{\text{atm}}, L_\lambda^{\text{atm}}]$ is chosen.

2.2. *Validation of the instrument response model with in-band transmittance measurements*

To validate the instrument response model, we measured the in-band transmittance $\hat{\tau}_{\Delta\lambda}^{\text{ext}}$ of 1) a 3 mm thick KRS5 filter and 2) a 2mm thick ZnSe filter and compared to the reference value. The first material was selected for its flat spectral transmission, around 0.7, over a broad spectral range, between 0.5 µm and 40 µm. We recall that, from the IRM with non uniform instrument spectral response, the measured $\hat{\tau}_{\Delta\lambda}^{\text{ext}}$ is equal the actual in-band transmittance $\tau_{\Delta\lambda}$ only if $\tau_\lambda^{\text{ext}}$ is uniform. To this purpose, we placed each instrument in front of the reference blackbody source for calibration. Then, the measurements were repeated inserting the filter in the optical path.

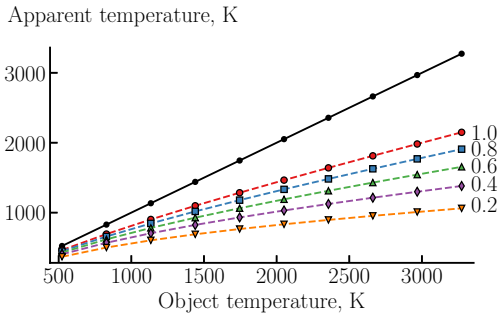

Figure 1: Simulated apparent temperature for $\hat{\tau}_{\Delta\lambda}^{\text{ext}} = 0.5$ and different values of $\hat{\varepsilon}_{\Delta\lambda}$. Black line: bisector. ● $\hat{\varepsilon}_{\Delta\lambda} = 1$, ■ $\hat{\varepsilon}_{\Delta\lambda} = 0.8$, ▲ $\hat{\varepsilon}_{\Delta\lambda} = 0.6$, ◆ $\hat{\varepsilon}_{\Delta\lambda} = 0.4$, ▼ $\hat{\varepsilon}_{\Delta\lambda} = 0.2$.

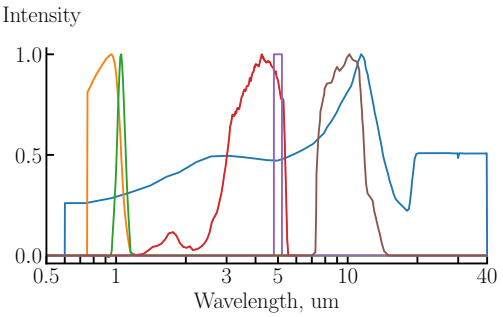

Figure 2: Normalized instrument spectral responses $\tilde{R}_\lambda$. — 0.6 µm – 39 µm, — 0.75 µm – 1.1 µm, — 0.95 µm – 1.1 µm, — 3 µm – 5 µm, — 4.8 µm – 5.2 µm, — 8 µm – 12 µm.

2.3. *Bias of the T^4-ratio method*

A broadband radiometer with spectral sensitivity between 0.6 µm and 39 µm, was introduced to material testing in Plasmatron facility to perform in situ measurements of the total angular emissivity by Panerai [15]. For surface temperatures above 1000 K the largest part of the radiation in included in this spectral band. Neglecting reflected radiation and atmosphere

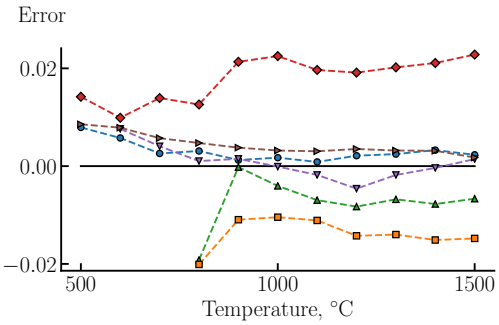

Figure 3: Error of the measured in-band transmittance for the KRS5 filter (nominal value at $\tau_{\Delta\lambda} = 0.7$) with respect to the reference data values. Plot legend: ● 0.6 µm – 39 µm, ■ 0.75 µm – 1.1 µm, ▲ 0.95 µm – 1.1 µm, ◆ 3 µm – 5 µm, ▼ 4.8 µm – 5.2 µm, ▶ 8 µm – 12 µm.

emission, it was claimed that the radiant power received by the radiometer is proportional to the fourth power of the apparent temperature. The total angular emittance was then measured as the

$$\varepsilon_{\text{tot}} \approx \hat{\varepsilon}_{\Delta\lambda} = \frac{\hat{\tau}^{\text{ext}}_{\Delta\lambda}\hat{\varepsilon}_{\Delta\lambda}T^4_{\text{obj}}}{\hat{\tau}^{\text{ext}}_{\Delta\lambda}T^4_{\text{obj}}} = \frac{T^4_{\text{app, meas}}}{T^4_{\text{app, BB}}}. \qquad (3)$$

However the T^4-ratio method is based on the tacit assumption that the instrument responsivity is spectrally uniform. Here we show that this method fails when this is not the case. In fact, under the assumption of uniform transmittance and emittance, neglecting reflections and OP emission, the actual irradiant power received by the radiometer is

$$\tilde{\Phi} = \hat{\tau}^{\text{ext}}_{\Delta\lambda}\hat{\varepsilon}_{\Delta\lambda}\mathcal{A}(T_{\text{obj}}) = \hat{\tau}^{\text{ext}}_{\Delta\lambda}\hat{\varepsilon}_{\Delta\lambda}\int_{\Delta\lambda}\tilde{R}^{\tau}_{\lambda}L^{\text{BB}}_{\lambda}. \qquad (4)$$

If $\tilde{R}^{\tau}_{\lambda}$ is uniform, then this reduces to eq. **??** and the T^4-ratio method can be used. On the other hand, if $\tilde{R}^{\tau}_{\lambda}$ is not uniform, the T^4-ratio method produces a bias in the measured emittance for $\hat{\varepsilon}_{\Delta\lambda} \neq 1$. Exploiting the instrument response model, we can simulate this effect. For a range of object temperatures T_{obj} between 500K and 3000K, the apparent temperature T_{app} is simulated for different values of graybody in-band transmittance $\hat{\varepsilon}_{\Delta\lambda}$. This is then recomputed from eq. 3. Fig. 4(a) shows the error produced by the T^4-ratio method. We can notice that this becomes relevant for low values of $\hat{\varepsilon}_{\Delta\lambda}$ and for high object temperatures. The actual value and trend of the error depends ultimately on $\tilde{R}^{\tau}_{\lambda}$ and it is then instrument dependent. The method is not affected by any error for $\hat{\varepsilon}_{\Delta\lambda} = 1$ since this represents the reference calibration condition. Similarly, the T^4-ratio method can be applied to determine the in-band transmittance $\hat{\tau}^{\text{ext}}_{\Delta\lambda}$, as in the previous section. Fig. 4(b) shows the comparison between the measured error and the simulated value. We can notice that the predicted error follows the trend of the measured. The small discrepancy can be due to the actual response or due to the instrument drift.

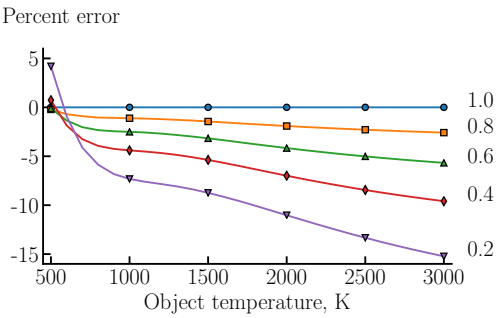

(a)

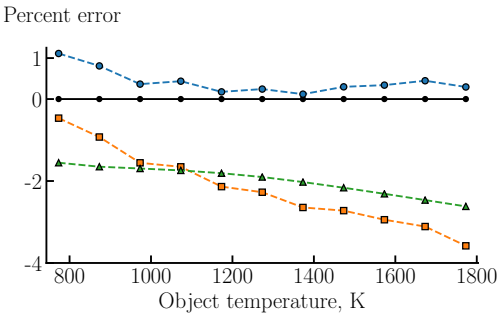

(b)

Figure 4: (a) Simulated percent error of the T^4-ratio method as a function of T_{obj} and $\hat{\varepsilon}_{\Delta\lambda}$ shows large negative errors for high object temperatures and low emittance values. (b) T^4-ratio method applied to the KRS5 filter transmittance measurements of sec. **??** shows increasing error (■) with object temperature. Simulated value (▲) is in noticeable agreement. IRM method (●) demonstrates higher accuracy.

3. Advances in material response simulations

The Material Melting and Ablation program (MMA) was initially developed as a 1D finite-volume simulation code, including melting and ablation models in both Cartesian and spherical coordinates, to predict the response of the material classes of interests for space debris re-entry applications in plasma wind

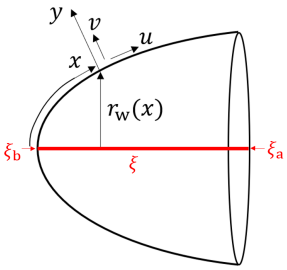

Figure 5: Sketch of the reference frame used to write the liquid layer equations.

tunnel testing. Lacking previous experience on such materials, this revealed a fast and robust approach to guide the design of the test conditions for silicates and metals. Yet, for long duration subsonic tests, we found that the behaviour of the material sample exposed to the plasma flow deviates significantly from the one-dimensional approximation. Aiming at a more precise material response characterization, the code was extended to a two-dimensional axisymmetric formulation. The new solver relies on the finite-element library FreeFem++ **ref** and allows to input heat flux and pressure distributions from CFD codes as boundary conditions, extending the simulated material response far from the stagnation point and accounting for multi-dimensional heat transfer in the material sample.

3.1. Problem

The melting of the material sample is a phase change problem, characterized by discontinuities in the thermophysical properties at material melting temperature. In such case, the integral form of the energy conservation, along with the equation of state expressing the temperature dependence of the enthalpy, contain all the physical information needed to determine the evolution of the phases [19]. The enthalpy method has been used by Dias et al. [20; 21] to investigate meteor ablation and by Fagnani et al. [22] to study erosion of the arc jet electrodes with a shear ablation model initially developed by Bethe and Adams [10].

Considering a domain as represented in Fig. 5, the conservation of energy writes

$$\begin{cases} \frac{d}{dt}\int_\Omega H + \oint_{\partial\Omega} \dot{\mathbf{q}}\cdot\hat{\mathbf{n}} = \dot{s} \\ H(\mathbf{x}, t=0) = H(T_0) \\ \dot{\mathbf{q}}(\mathbf{x},t)\cdot\hat{\mathbf{n}} = 0 \ \text{ on } \ \Gamma_{\text{ad}} \\ \dot{\mathbf{q}}(\mathbf{x},t)\cdot\hat{\mathbf{n}} = \dot{q}_w(t) \ \text{ on } \ \Gamma_{\text{ext}}, \end{cases} \tag{5}$$

where H is the enthalpy per unit volume, $\dot{\mathbf{q}}$ is the heat flux and $\hat{\mathbf{n}}$ is the unit vector and $\mathbf{x}$ is the coordinate vector. We consider an adiabatic boundary condition on Γ_{ad}. A more detailed explanation on the boundary condition on Γ_{ext} is presented later in the next section.

3.2. Numerical approach

The one dimensional version of the code (MMA1D) implements a robust finite volume numerical discretization, where the integral form of the energy conservation is solved for the conservative variable (H) and this allows to treat the discontinuity without numerical issues. The primitive variable (T) is then retrieved by inversion of the function $H(T)$. The generalized (Cartesian and spherical coordinates) 1D finite volume discretization writes

$$\begin{cases} H_j^{n+1} = H_j^n - \frac{\Delta t}{V_j}(A_{j+1/2}\cdot q_{j+1/2} - A_{j-1/2}\cdot q_{j-1/2}) \\ q_{j+1/2} = -\frac{T_{j+1}-T_j}{R_{j+1/2}} \\ R_{j+1/2} = \frac{1}{2}(\frac{\Delta x_{j+1}}{k_{j+1}} + \frac{\Delta x_j}{k_j}) \end{cases} \tag{6}$$

The two-dimensional version of the code (MMA2D), instead, relies on the finite-element library FreeFem++, which requires a weak formulation of the unsteady thermal problem

$$\int_\Omega y(\rho c_p \frac{\partial T}{\partial t}\cdot v) + \int_\Omega y(k\nabla T\cdot\nabla v) - \oint_\Gamma y(k\nabla T\cdot\hat{\mathbf{n}})\cdot v = 0. \tag{7}$$

In this case, since we solve for the primitive variable T, a regularization of the thermo-physical properties, e.g., $h(T)$, should be performed to allow continuity of the first derivative. This is performed with a regularization function as proposed by Dias **ref thesis**. Mesh adaptation is used to refine the domain discretization around the mushy region. Mesh motion is implemented with suitable regularization functions.

3.3. Surface mass and energy balance

Ablation models are similarly implemented in both versions of the code, including evaporation and shear ablation effects. Under common transfer coefficient assumptions [11], the surface energy balance yields

$$\begin{aligned} \dot{q}_{\text{cond}} &= -k\nabla T\cdot\hat{\mathbf{n}} = \\ &= \dot{q}_{\text{conv}} - \dot{q}_{\text{rad}} - \dot{q}_{\text{evap}} = \\ &= \rho_e u_e c_h (h_r^{\text{gp}} - h_w^{\text{gp}}) - \sigma\varepsilon(T_w^4 - T_{\text{amb}}^4) \\ &\quad - \dot{m}_{\text{evap}}(h_w^{\text{gp}} - h_w^{\text{cp}}) \end{aligned} \tag{8}$$

Edge enthalpy and heat transfer coefficients are obtained from CFD simulations on cold wall surfaces.

Evaporation is estimated using $\mathcal{B}'$ tables, which are computed solving the multi-phase equilibrium though the Mutation++ library, providing non-dimensional ablation rates and gas-phase wall enthalpy as a function of the local thermodynamic variables. Assuming equal heat and mass transfer coefficients in the boundary layer, the evaporative mass flux is $\dot{m}_{\text{evap}} = \rho_e u_e c_h \cdot \mathcal{B}'$.

Metallic and silicate materials exposed to high-temperature plasma flows, when subjected to aerodynamic heat transfer, pressure gradients and shear forces, will form a flowing liquid layer. The shear ablation is approximated solving the liquid layer equation in the molten thickness δ, yielding a recession velocity

$$v_{\text{melt}} = \int_0^{\delta} 2 \cdot \Big[\int_0^{y} \Big(\frac{\tau'_w + p''_w(\eta - \delta)}{\mu(\eta)} \Big) d\eta \Big] dy, \quad (9)$$

where τ_w and p_w are the tangential shear stress and pressure. Thus, the ablating mass flux due to the motion of the liquid layer can be estimated as $\dot{m}_{\text{shear}} = \rho_w^{\text{cp}} v_{\text{melt}}$. Once the ablating mass flux $\dot{m} = \dot{m}_{\text{evap}} + \dot{m}_{\text{shear}}$ is computed, one can determine the recession speed as

$$\dot{s}_w = \frac{\dot{m}}{\rho_w^{\text{cp}}}. \quad (10)$$

3.4. Graphite ablation test-case

The 1D and 2D versions of the ablation codes are applied to a reference experimental graphite ablation test case. The *Ch* is extracted from an LTE ICP code CFD simulation, calibrated with reference spectroscopic data, following the method presented by the author in **??**. The same stagnation point value is applied in both codes, while the Ch distribution along the sample external boundary is also imposed in the 2D version. The same $\mathcal{B}'$ tables are used. In Fig. 6(a), we can notice that MMA1D overestimates the surface temperature by almost 200 K with respect to MMA2D, which, in turn, agrees well with the experimental surface temperature. At steady state, the back wall temperature approaches the one on the front surface in the 1D code. The 2D code, instead, agrees with the experimental value until the thermocouple fails, and predicts a more realistic lower value. Despite the different wall temperature, the 1D and 2D codes agree on the predicted recession at stagnation point, as we can observe in Fig. 6(b). This is the result of the diffusion-limited regime for carbon ablation in air, which results in a constant $\mathcal{B}'$ value over a wide range of temperatures. However the simulated recession underestimates the measured values by almost 1 mm at the end of the test. As shown in Fig. 6(c), MMA2D also allows to compare the sample shape change with the measured value. The bias with respect the the measured ablation profile persists far from the stagnation point, but the differential ablation on the sample side is qualitatively predicted. We can conclude that MMA is suitable for a correct order of magnitude estimate of the material response subject to subsonic plasma flow. The 2D version of the code allows a better prediction of the wall temperature and fairly agrees on the sample shape change.

4. Oxidation of titanium in air plasma

Satellites propellant tanks, typically made of high strength metallic liners and possibly reinforced by carbon fiber overwrapping, represent the major concern for spacecraft demisability under uncontrolled re-entry conditions. Grade 5 titanium alloy, including 6% Al and 4%V in weight, is one of the most used materials for such components. The combination of its thermo-physical properties (high melting temperature, relatively high density and heat capacity), with the large geometries of these aerospace structures (up to 1 m diameter), make them hardly demisable under LEO uncontrolled entries, representing some of the highest on-ground risk [23]. In addition, titanium and its alloy elements are highly reactive to oxygen. Hence, oxidation plays a major role in the modelling and prediction of its degradation in atmospheric entry conditions [8]. A various and complex behaviour of titanium oxidation is found in the literature, depending on the specific thermodynamic and atmospheric conditions. Shortcoming of the available literature over the peculiar conditions faced during atmospheric entry drives the challenge of improving the current understanding and modelling of titanium alloys oxidation though plasma wind tunnel testing and post-test surface analysis.

4.1. Literature review of titanium oxidation

TA6V alloys are two-phase ($\alpha + \beta$) alloys which show a high affinity with atmospheric gases (oxygen ,nitrogen, hydrogen). As known, TiO_2 crystallizes mainly in the forms of rutile (tetragonal) and anatase (tetragonal); the former being the most common TiO_2 crystal phase in nature, while the latter is metastable and thus it grows only under a restricted range of conditions [24]. Addition of Al considerably enhances the oxidation behaviour of titanium, by forming a thermodynamically stable and protective $\alpha - Al_2O_3$.

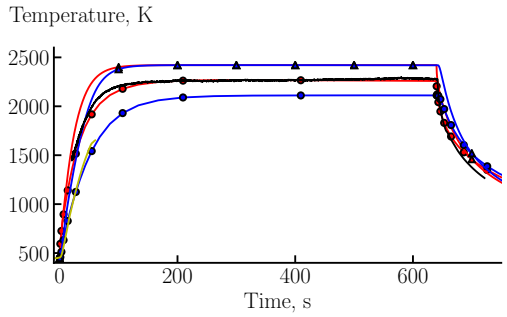

(a)

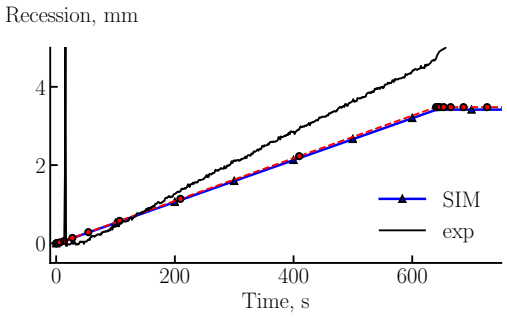

(b)

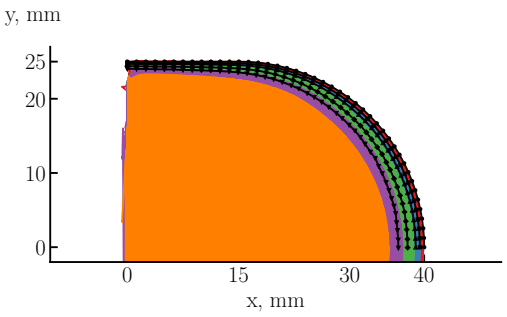

(c)

Figure 6:

However, **(author?)** [25] reported that the presence of V was detrimental for the oxidation resistance at high temperatures. Exposure of titanium and its alloys to any oxygen-containing atmosphere at elevated temperatures leads to formation of an Oxide Layer (OL) on the surface with an Oxygen Diffusion zone (ODZ) beneath it [26]. The high affinity of titanium to oxygen causes formation of a very thin OL on the surface even in air at room temperature. Above 200 °C the thickness of the OL significantly increases. ODZ develops above 400 °C. At temperatures above 600 °C, increase of oxidation rate causes formation of a thicker but defective OL leading to easy penetration of oxygen into the substrate. Oxidation at elevated temperatures (mostly above 800 °C) remarkably degrades the high temperature performance of titanium and its alloys not only as the result of thinning of the material by detachment of thick OL, but also due to formation of wider ODZ.

(author?) [27] found that the oxide scales are characterized by a layered structure. Cross-sectional EDS mapping showed that Ti and Al elements where not uniformly distributed throughout the scale: Al, in particular, was concentrated locally in narrow regions. Different oxide thickness was also observed. XRD analysis revealed the presence of TiO_2, Al_2O_3 and V_2O_5 compounds. Al_2O_3 was observed only in the outer scale, while an increasing concentration of V_2O_5 was observed towards the outer layer. The same authors also report the appearance of cracks and delaminations in vanadium-containing titanium alloys. This was explained by the transition of one titanium oxide into another, i.e, $TiO \rightarrow TiO_2$), which results in a change of the scale density and generates stresses in the layers. Delamination is reported to strongly impede TA6V resistance to oxidation. On the one hand, cracking results in a lower mechanical strength and easier spallation of the oxide layer, while, on the other hand, this also promote faster diffusion of oxygen deeper into the sample.

Several authors report parabolic kinetics between 800 K and 1070 K and a linear kinetics above this temperature.

Oxidation is typically modelled based on the experimental specific weight gain $\Delta W/A$ with respect to the oxidation time t. This is generally represented in the form $\frac{\Delta W}{A} = Kt^{1/n}$ where n is the reaction order ($n = 1$ for linear, $n = 2$ for parabolic) and K is the reaction rate, which, in turn, is commonly represented as a function of temperature as $K = K_0 exp(\frac{-Q}{RT})$,, where K_0 is the frequency factor, Q is the activation energy and T the reaction temperature.

Oxidation of titanium in standard air is well documented in the literature under several thermodynamic conditions. However, this studies are not directly applicable to space debris demise studies since: 1) the studies proposed in the literature on the oxidation of TA6V in air at atmospheric pressure were carried out for temperatures well below the melting one of the alloy(1920–1940 K); 2) oxidation time is typically very long (between 30 min and 4 years) comparatively to

the space debris re-entry duration (around 10 min at most); 3) experimental conditions very far from those encountered in atmospheric entry, in particular no dissociated oxygen in the gas.

Recently some studies on titanium oxidation have been conducted in dissociated air atmosphere in the MESOX facility [8; 28]. This features a solar furnace to heat the material sample with concentrated solar radiation and a microwave plasma generator to produce a dissociated air environment with concentration up to 80% in O.

In particular, **(author?)** [8] showed that the dissociated oxygen atmosphere seemed to promote delamination of the oxide layer, compared to standard air at the same surface temperature and gas pressure. The authors also observed different morphologies of the oxide scales at different oxidation temperatures. Time is reported to affect the oxide characteristics, leading to an adhesive layer for short exposure intervals ($<$ 100 s to an evident delamination for longer times $>$ 100 s. Damaging (cracking, delamination and peeling off) was reported to significantly influence on the oxidation kinetics: an adhesive layer was associated to a parabolic kinetics, due to the slow oxygen in-depth diffusion; a damaged layer, instead, lead to a linear kinetics, due to the faster penetration of oxygen at the deeper scales. A study on the oxide layer thickness time growth was also performed, indicating larger speeds at higher temperature and a possible complex behaviour depending on the delamination. Close to the melting point, different morphologies are also formed due to the interaction of the molten metal with the oxidising surface.

Finally, the authors apply the experimental results on the oxidation dynamics, together with emissivity measurements of the oxidised surface, to the simulation of the atmospheric entry of a TA6V tank

(author?) [28] confirmed the increase in the oxide layer thickness with temperature and reported a weak dependence on pressure between 300 Pa and 2000 Pa. They also confirmed the delamination behaviour of the oxide scale at high temperature and performed mass gain/loss measurements to determine the oxidation kinetics.

4.2. Experimental objective and relevance of the proposed approach

We propose to study the oxidation of titanium samples in the VKI Plasmatron facility. The novelty and relevance of the proposed approach relies partial reproduction of the actual boundary layer of the plasma flow impinging onto the test sample. The LHTS methodology offers a ground to flight scaling approach in the proximity of the stagnation region of the test sample, for a steady condition, if some BL edge and wall quantities are reproduced. Although a re-entering space debris object might be rotating and facing a complex flow environment, this represents at the moment the closest possible replication on ground of the flight environment for a re-entering space object. The calibrated free-stream conditions allow the following ground-to-flight replication: $V_\infty = 6.13$ km s^{-1}, $h = 66.52$ km, $R_\infty = 0.48$ m, which are close to the simulated trajectory of the TA6V tank test case proposed by **(author?)** [8].

Tested samples are stored in a protective argon atmosphere 30 min after testing, until transport to the surface analysis facility (estimated 3 h) to minimize further oxidation and surface contamination.

4.3. Preliminary experimental results

Fig. 7(a) and 7(b) compare the virgin and post-test picture of the sample. A visual inspection shows a complex surface oxidation, showing different colours (black, brown and yellow) which can be correlated to different regions of the sample. Post-test analysis confirms various complex oxide morphologies. The brown layer on the sample side (Fig. 7(c)) shows a porous crystalline structure; the black zone on the sample edge (Fig 7(d)) is characterized by a regular topology. On the sample top, instead, we found overlapping oxide layers with different morphologies: a compact brown layer (Fig. 7(e)) is underlaying a highly porous brittle yellow layer (Fig. 7(f)). This may happen due to the different thermal expansion coefficients of the two layers and can be related to their different composition. A duplex oxide scale was similarly observed on plasma-coated titanium grade 4 samples by **(author?)** [29]. Some topologies of the oxide layers seems to have large porosity, which could increase the oxidation rates, hence mass gain, due to 1) a larger specific surface area, 2) an enhanced in-depth diffusion of oxygen. EDS confirms the presence of the main TA6V alloying elements, together with a large concentration of oxygen, which we can expect to be bound in the forms TiO_2, Al_2O_3 and V_2O_5. XPS analysis will be performed on future test samples to confirm the molecular bonds. EDS, however, shows a non uniform distribution of the elements either among the different zone and within a single zone. Contrary to what was suggested by previous ex-situ analysis, although the oxide layer appeared brittle, no significant

delamination was observed during the test, as testified by the high speed camera frames. However, we must remind that the LHTS ensures the reproduction of the thermochemical boundary layer on the stagnation line, while it does not imply the replication of the flow shear stressed on the surface. Yet, the oxide layer broke easily after sample transportation.

It is of particular relevance to mention that no trace of nitrogen was found on the surface. This would imply a negligible reactivity of the surface with nitrogen, also due to the scarce presence of atomic nitrogen in the boundary layer in the considered conditions.

Acknowledgement

The author would like to acknowledge B. Helber and D. Le Quang for the precious experimental support, B. Dias for the fruitful discussions and teaching about the melting-ablation modelling and K. Baert for the preliminary surface analysis of the titanium sample.

References

[1] H. Klinkrad, Space Debris, Vol. 60 of Springer Praxis Books, Springer Berlin Heidelberg, 2006. doi:10.1007/3-540-37674-7.
URL http://link.springer.com/10.1007/3-540-37674-7

[2] D. J. Kessler, N. L. Johnson, J. C. Liou, M. Matney, Kessler Syndrome-AAS Paper.pdf, Advances in the Astronautical Sciences (2010).
URL https://pdfs.semanticscholar.org/2276/55e022441d1379dfdc395173ed2e776d54ee.pdf

[3] United Nations Office For Outer Space Affairs, Committee on the Peaceful Uses of Outer Space, Space Debris Mitigation Guidelines of the Committee on the Peaceful Uses of Outer Space, United Nations Publication (2010) 1arXiv:SalesNo.E.99.I.17.
URL http://www.unoosa.org/pdf/publications/st{_}space{_}49E.pdf

[4] ESA Space Debris Mitigation WG, ESA Space Debris Mitigation Compliance Verification Guidelines (1.0) (2015) 1–95.

[5] S. Lemmens, Q. Funke, H. Krag, On-ground casualty risk reduction by structural design for demise, Advances in Space Research 55 (11) (2015) 2592–2606. doi:10.1016/j.asr.2015.02.017.
URL http://dx.doi.org/10.1016/j.asr.2015.02.017

[6] S. Heinrich, J. Martin, J. Pouzin, Satellite design for demise thermal characterisation in early re-entry for dismantlement mechanisms, Acta Astronautica 158 (2019) 161–171. doi:10.1016/j.actaastro.2018.03.021.
URL https://doi.org/10.1016/j.actaastro.2018.03.021

[7] P. M. Waswa, M. Elliot, J. A. Hoffman, Spacecraft Design-for-Demise implementation strategy & decision-making methodology for low earth orbit missions, Advances in Space Research 51 (9) (2013) 1627–1637. doi:10.1016/j.asr.2012.11.020.
URL http://dx.doi.org/10.1016/j.asr.2012.11.020

[8] Y. Prévereaud, J. L. Vérant, M. Balat-Pichelin, J. M. Moschetta, Numerical and experimental study of the thermal degradation process during the atmospheric re-entry of a TiAl6V4 tank, Acta Astronautica 122 (2016) 258–286. doi:10.1016/j.actaastro.2016.02.009.
URL http://dx.doi.org/10.1016/j.actaastro.2016.02.009

[9] B. Helber, Material Response Characterization of Low-density Ablators in Atmospheric Entry Plasmas, 2016.

[10] H. A. Bethe, M. C. Adams, A Theory for the Ablation of Glassy Materials, Journal of the Aerospace Sciences 26 (6) (1959) 321–328. doi:10.2514/8.8080.
URL http://arc.aiaa.org/doi/10.2514/8.8080

[11] B. Helber, A. Turchi, J. B. Scoggins, A. Hubin, T. E. Magin, Experimental investigation of ablation and pyrolysis processes of carbon-phenolic ablators in atmospheric entry plasmas, International Journal of Heat and Mass Transfer 100 (2016) 810–824. doi:10.1016/j.ijheatmasstransfer.2016.04.072.
URL http://dx.doi.org/10.1016/j.ijheatmasstransfer.2016.04.072

[12] P. F. Barbante, O. Chazot, Flight extrapolation of plasma wind tunnel stagnation region flowfield, Journal of Thermophysics and Heat Transfer 20 (3) (2006) 493–499. doi:10.2514/1.17185.

[13] D. Vanden Abeele, G. Degrez, Efficient computational model for inductive plasma flows, AIAA journal 38 (2) (2000) 234–242. doi:10.2514/3.14402.

[14] Y. Prevereaud, J. L. Vérant, M. Balat-Pichelin, Orbital debris atmospheric re-entry prediction, Proceedings of the International Astronautical Congress, IAC 3 (January) (2014) 1835–1848.

[15] F. Panerai, O. Chazot, Characterization of gas/surface interactions for ceramic matrix composites in high enthalpy, low pressure air flow, Materials Chemistry and Physics 134 (2-3) (2012) 597–607. doi:10.1016/j.matchemphys.2012.03.036.
URL http://dx.doi.org/10.1016/j.matchemphys.2012.03.036

[16] M. Schüßler, M. Auweter-Kurtz, G. Herdrich, S. Lein, Surface characterization of metallic and ceramic TPS-materials for reusable space vehicles, Acta Astronautica 65 (5-6) (2009) 676–686. doi:10.1016/j.actaastro.2009.01.048.

[17] B. Massuti-Ballester, S. Pidan, G. Herdrich, M. Fertig, Recent catalysis measurements at IRS, Advances in Space Research 56 (4) (2015) 742–765. doi:10.1016/j.asr.2015.04.028.
URL http://dx.doi.org/10.1016/j.asr.2015.04.028

[18] T. Lucatorto, A. Parr, Experimental Methods in the Physical Sciences, 2009. doi:10.1016/s1079-4042(09)04212-x.

[19] V. Alexiades, A. D. Solomon, Mathematical Modeling Of Melting And Freezing Processes, CRC Press, 1992.

[20] B. Dias, F. Bariselli, A. Turchi, A. Frezzotti, P. Chatelain, T. Magin, Development of a melting model for meteors, in: AIP Conference Proceedings, Vol. 1786, 2016, p. 160004. doi:10.1063/1.4967661.
URL http://aip.scitation.org/doi/abs/10.1063/1.4967661

[21] B. Dias, A. Turchi, E. C. Stern, T. E. Magin, A model for meteoroid ablation including melting and vaporization, Icarus 345 (November 2019) (2020) 113710.

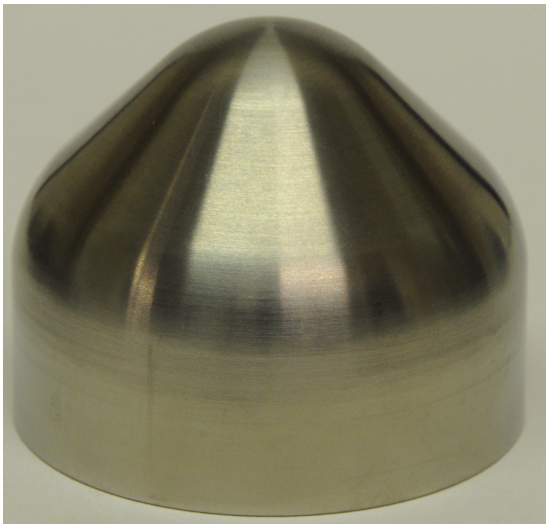

(a)



(b)

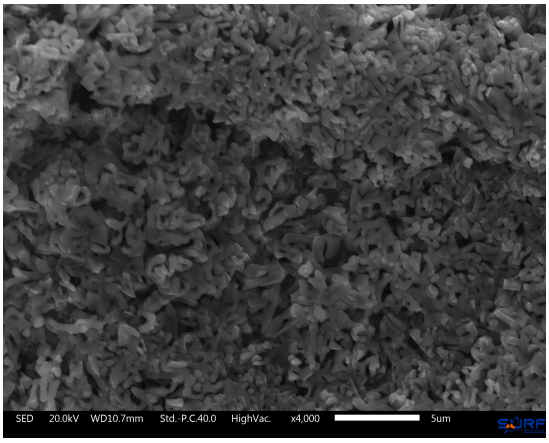

(c)

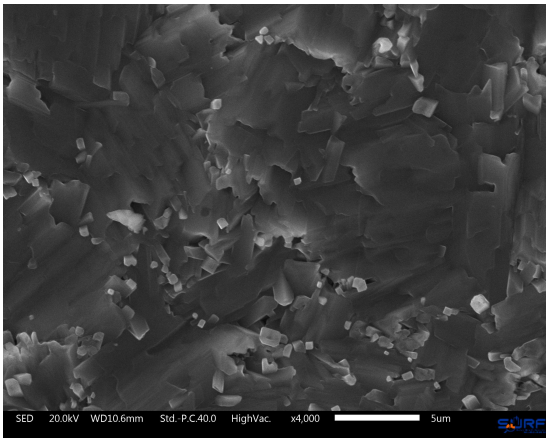

(d)

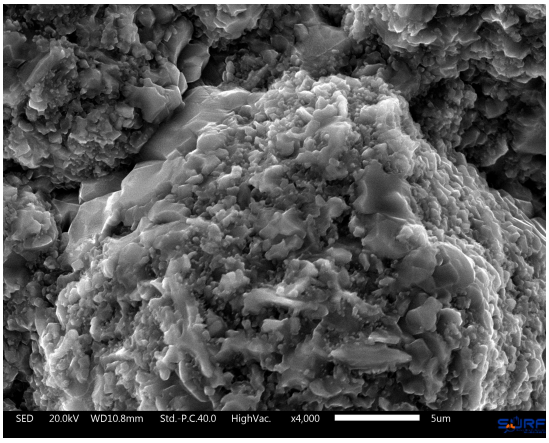

(e)

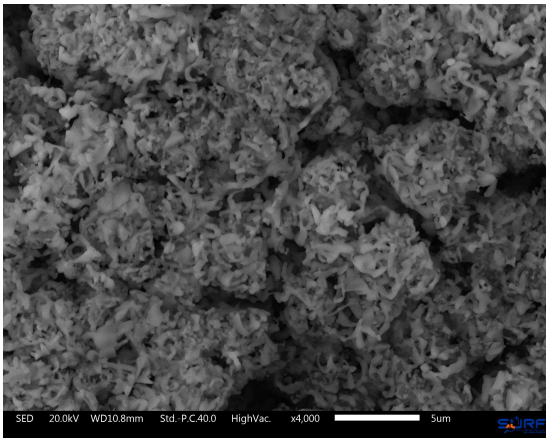

(f)

Figure 7: fig:TiG5-SC50-A

doi:10.1016/j.icarus.2020.113710.
URL https://doi.org/10.1016/j.icarus.2020.113710

[22] A. Fagnani, B. Helber, O. Chazot, Evaluation of Probe-Material Thermal Interaction in Plasma Wind Tunnel Tests by Means of IR Thermography and Thermal Inverse Modelling (2019). doi::10.13009/EUCASS2019-4138TH.

[23] T. Lips, B. Fritsche, R. Kanzler, T. Schleutker, A. Gülhan, B. Bonvoisin, T. Soares, G. Sinnema, About the demisability of propellant tanks during atmospheric re-entry from LEO, Journal of Space Safety Engineering 4 (2) (2017) 99–104. doi:10.1016/j.jsse.2017.07.004.
URL http://dx.doi.org/10.1016/j.jsse.2017.07.004

[24] E. György, A. Pérez Del Pino, G. Sauthier, A. Figueras, F. Alsina, J. Pascual, Structural, morphological and local electric properties of TiO2 thin films grown by pulsed laser deposition, Journal of Physics D: Applied Physics 40 (17) (2007) 5246–5251. doi:10.1088/0022-3727/40/17/035.

[25] Y. Shida, H. Anada, The effect of various ternary additives on the oxidation behavior of TiAl in high-temperature air, Oxidation of Metals 45 (1-2) (1996) 197–219. doi:10.1007/BF01046826.

[26] H. Guleryuz, H. Cimenoglu, Oxidation of Ti-6Al-4V alloy, Journal of Alloys and Compounds 472 (1-2) (2009) 241–246. doi:10.1016/j.jallcom.2008.04.024.

[27] H. Garbacz, M. Lewandowska, Microstructural changes during oxidation of titanium alloys, Materials Chemistry and Physics 81 (2-3) (2003) 542–547. doi:10.1016/S0254-0584(03)00070-1.

[28] M. Balat-Pichelin, J. Annaloro, L. Barka, J. L. Sans, Behavior of TA6V Alloy at High Temperature in Air Plasma Conditions: Part 2—Thermal Diffusivity and Emissivity, Journal of Materials Engineering and Performance 29 (7) (2020) 4606–4616. doi:10.1007/s11665-020-04985-6.
URL https://doi.org/10.1007/s11665-020-04985-6

[29] D. B. Wei, P. Z. Zhang, Z. J. Yao, J. T. Zhou, X. F. Wei, P. Zhou, Cyclic oxidation behavior of plasma surface chromising coating on titanium alloy Ti-6Al-4V, Applied Surface Science 261 (2012) 800–806. doi:10.1016/j.apsusc.2012.08.102.

Influence of pressure on the oxidation and nitridation of carbon-based ablators

Greyson Kale

Aeronautics and Aerospace Department, von Karman Institute for Fluid Dynamics, Belgium, greyson.kale@vki.ac.be

Supervisor: Thierry Magin

Professor, Aeronautics and Aerospace Department, von Karman Institute for Fluid Dynamics, Belgium, magin@vki.ac.be

University Supervisor: Noel Clemens

Professor, Department of Aerospace Engineering and Engineering Mechanics, The University of Texas at Austin, Austin, TX, U.S.A, clemens@mail.utexas.edu

Abstract

As interest in and around ablative thermal protection system (TPS) performance and materials response has re-surged with the Orion program and the rise of private space, work in developing a more holistic understanding of the ablation process has risen commensurately. Thermal protection systems mitigate the extreme heat loading experienced when spacecraft re-enter planetary atmospheres and are typically carbon-based designs that transport energy away from the spacecraft structure via a physical process called ablation.

For carbon-based TPS ablators, the significance of variations in pressure with respect to basic ablative chemical reactivity (oxidation & nitridation) occurring at the surface and in the gas phase is not well understood. Historically, the pressure influence was assumed to be limited, where straightforward empirical expressions for the probability of a oxidation or nitridation reaction proceeding was simply expressed as a constant value, or with a slight dependence on the surface temperature of the material in question. The development of high-fidelity chemistry models seeks to include a pressure dependence, but it is not known whether the approach taken will adequately capture the phenomena seen either in ground test or in flight. Furthermore, the impact of pressure can alter the dynamics of the flowfield itself, driving changes in the state of the chemistry at and above the ablator, which can result in drastic changes to the macroscopic parameters used to evaluate TPS material performance.

This work will take a joint experimental and computational approach working at both the VKI and UT Austin ICP facilities to determine the role of pressure in carbon-based ablation. Experimental work will leverage a number of experimental spectroscopic diagnostic techniques (optical emission spectroscopy, laser induced fluorescence, coherent anti-Stokes Raman spectroscopy) and intrusive ground test facility probes. Numerical work will revolve around the use of pre-established ablative code sets to verify and validate their use against the data obtained in the ground test facilities.

Keywords: ablation, carbon, nitridation, oxidation, pressure.

Magnetohydrodynamics enhanced radio blackout mitigation system for space transportation during planetary entries

Diana Luís

Aeronautics and Aerospace Department, von Karman Institute for Fluid Dynamics, Belgium, diana.luis@vki.ac.be
Signal Theory and Communication Department, Universitat Politècnica de Catalunya, Spain

Alan Viladegut

Research Engineer, Aeronautics and Aerospace Department, von Karman Institute for Fluid Dynamics, Belgium, alan.viladegut@vki.ac.be

Olivier Chazot

Professor, Aeronautics and Aerospace Department, von Karman Institute for Fluid Dynamics, Belgium, chazot@vki.ac.be

Adriano Camps

Professor, Signal Theory and Communication Department, Universitat Politècnica de Catalunya, Spain, adriano.jose.camps@upc.edu

Abstract

Spacecraft enter planetary atmospheres at hypersonic velocities generating shock waves ahead of the vehicle and consequent extreme aerodynamic heating. The high post-shock temperatures dissociate and ionize the gas creating a plasma layer that surrounds the spacecraft. High ionization degrees affect the propagation of the electromagnetic waves emitted by the on-board antennas, leading to a communication blackout for several minutes. This radio blackout occurs when the characteristic frequency of the plasma layer around the vehicle exceeds the radio frequency used for communications. The plasma frequency, f_p, depends on the ionization degree of the gas, and it is related to the electron number density, n_e, by

$$f_p = \frac{1}{2\pi}\sqrt{\frac{q_e^2 n_e}{m_e \epsilon_0}} \approx 9\sqrt{n_e} \qquad (1)$$

where q_e and m_e are, respectively, the electron charge and mass, and ϵ_0 the free space permittivity.

The Horizon 2020 MEESST (Magnetohydrodynamic Enhanced Entry System for Space Transportation) project aims at designing and testing a proof-of-concept magnetic shielding device for mitigation of radio blackout during space entry. As part of the project, this work proposes investigating the effects of the ionized medium on the propagation of the radio signal through the plasma flow in a plasma wind tunnel facility. A representative communication system is being designed to be implemented in the test chamber of the Plasmatron facility at VKI, prior to full characterization in an anechoic chamber at UPC. High resolution optical emission spectroscopy is being conducted for characterization of the electron number densities on the flow and for correlation of the electron densities with the signal propagation and attenuation. The signal propagation results will also serve as validation for numerical computations. In a later stage, a new generation cryogenic cooled magnet will be installed in a probe for testing at the Plasmastron, allowing to study the influence of a magnetic field in the plasma flow and in the signal propagation. This approach will allow investigation of the magnetohydrodynamic window effects, potentially mitigating the blackout phenomenon and opening a communication window in reentry conditions. Finally, an assessment of the extrapolation from ground to flight will be conducted.

Keywords: Atmospheric entry; plasma flow; blackout mitigation; communications; magnetohydrodynamic window.

Development of a hybridized discontinuous Galerkin solver for inductively coupled plasma

Nicolas Corthouts

Aeronautics and Aerospace Department, von Karman Institute for Fluid Dynamics, Belgium, nicolas.corthouts@vki.ac.be

Supervisor: May Georg

Associate Professor, Aeronautics and Aerospace Department, von Karman Institute for Fluid Dynamics, Belgium, georg.may@vki.ac.be

University Supervisor: Hillewaert Koen

Professor, Design of Turbomachines, Université de Liège, Belgium, koen.hillewaert@uliege.be

Abstract

The von Karman Institute for Fluid Dynamics (VKI) houses the most powerful inductively coupled plasma (ICP) wind tunnel in the world : the Plasmatron. With a power of 1.2 MW, the facility produces plasma flows with peak temperatures of 10 000 K. The Plasmatron is an invaluable tool in many applications. For instance, it recreates the conditions in which the demise of space debris occur. It also provides experimental data about thermal protections systems. However, the amount of information it outputs is mostly restrained by the instruments, which usually allow for the collection of specific quantities at defined locations in the facility. On the other hand, numerical solvers provide flow quantities everywhere, allowing the virtual preparation of experiments in new condition without running the risk of damaging the device. In this context, having an accurate ICP solver is an invaluable tool. Existing ICP solvers have many drawbacks: most of them are axisymmetric, making impossible the representation of 3D plasma modes or the simulation of non-axisymmetric nozzles. Another major flaw is the lack of time-accurate ICP solvers, preventing the correct representation of unsteady phenomena, such as the transmission of the ripple part component of the current rectifier directly to the flow. Finally, there exists no high-order ICP solvers. High-order methods have a high spectral accuracy, allowing for a representation of high frequency mode that can occur in the facility. Moreover, high-order methods are better suited for complex geometries, and require less elements than their low-order counterparts for the same accuracy. This feature is important especially in the case of 3D simulations, as it reduces the computational costs. The goal of this work is to provide a 3D, time-accurate and high-order solver to address all of the listed problems. Therefore, the Hybridized Discontinuous Galerkin (HDG) discretization is chosen. Belonging to the family of discontinuous Galerkin methods (DG), HDG methods dramatically improve the computational costs with respect to classic DG by reducing the number of globally coupled degrees of freedom while being embarrassingly parallel. This feature is ideal for large, 3D simulations. The development of the solver will be accompanied by a reformulation of the magnetohydrodynamic equations, usually expressed in axisymmetric, steady-state form for ICP, to take into account temporal and 3D effects. The code will also be parallelized. This project was born from the collaboration of the VKI and the University of Liège, and is financed by the F.N.R.S. through a FRIA fellowship.

Keywords: Discontinuous Galerkin Method, Inductively coupled plasma, 3D, time-accurate.

AEROTHERMODYNAMICS

Multi-fidelity approach for aerodynamic modelling and simulation of uncontrolled atmospheric destructive entry

Fábio Morgado

Aerospace Centre of Excellence, University of Strathclyde, United Kingdom, fabio.pereira-morgado@strath.ac.uk

Supervisor: Thierry Magin

Professor, Aeronautics and Aerospace Department, von Karman Institute for Fluid Dynamics, Belgium, thierry.magin@vki.ac.be

University Supervisor: Marco Fossati

Associate Professor, Aerospace Centre of Excellence, University of Strathclyde, United Kingdom, marco.fossati@strath.ac.uk

Abstract

This paper proposes and showcases a multi-fidelity methodology to the modelling and simulation of destructive atmospheric re-entry of human-made space objects, achieving a favourable trade-off between cost and accuracy. A 6-dof dynamic model is used to determine the motion of the fragments during reentry. A quasi-steady approach to determine the dynamics of the fragments in the instant following the breakup is validated.

Keywords: re-entry, multi-fidelity, fragmentation

1. Introduction

Between the year 2000 and 2020, the number of objects in orbit around the Earth has increased by approximately 82% [1] and forecasts estimate for this number to increase in the forthcoming years, which has been drawing international attention of space sustainability. For a sustainable use of the space environment, it is of utmost importance to guarantee the safe disposal of the objects launched into orbit. After their end of life, in order to avoid the cluttering of space objects in orbit and reduce the chance of in-orbit collisions, they are subjected to a destructive atmospheric re-entry in a controlled or uncontrolled manner, which cause the object to break into several fragments. In order to assess the ground impact risk of such fragments, they need to be properly tracked, thus an accurate prediction of this destructive process has to be assured.

However, the simulation of a multi-body atmospheric re-entry is a complex multi-physics problem that requires the use of multiple coupled physical disciplines. High-fidelity simulations can be performed during the most crucial parts of the re-entry trajectory to better understand the various destructive mechanisms, but they are computationally demanding, and it worsens with the increase in complexity of physical models and numbers of fragments during the demise process. In order to reduce the overall computational power required in simulating the physics, the use of low-fidelity methods is appealing, but can result in high degrees of uncertainty due to the simplified physical model assumptions and geometry treatment.

To overcome this issue, a multi-fidelity based approach is proposed, enabling the use of both low-fidelity and high-fidelity models to compute the aerothermal loads acting on the surface that have impact in the dynamic and demise process of the reentering bodies. The uncertainty of the results is reduced by using the high-fidelity models only for selected time iterations, thus correcting the predictions given by the low-fidelity methods, and during very sensitive time-windows, such as the moments before and after the breakup process. Using this approach, the limited number of calls to the high-fidelity models tend minimize the computational power required for the overall reentry simulation while enabling a good level of confidence in the results.

The paper is structured as follows. After presenting the general structure of TITAN, the paper introduces the methodology and basic formulations underneath

both low and high fidelity aerothermal computations integrated in TITAN, followed by a validation of results with experimental data and a demonstration on the re-entry of an ATV-like cargo.

2. A Multi-Fidelity Approach

TITAN was developed with the objective of efficiently integrating low and high-fidelity re-entry and demise simulation tools. The development of TITAN follows a modular approach with dedicated modules for geometry and meshing, aerothermodynamics, flight dynamics, material thermal response, fragmentation, and ground risk (under-development). These modules can be independently developed by adding multi-fidelity aspects to the workflow and increasing their overall accuracy in the prediction of demise and fragmentation process during atmospheric re-entry of uncontrolled objects. The high-level workflow of the recently developed tool is showcased in Fig. 1.

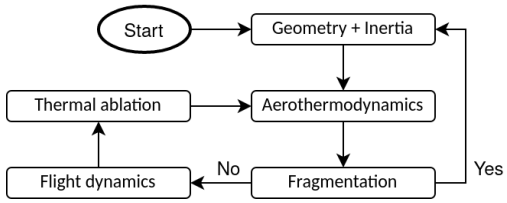

Figure 1: High-level workflow of TITAN.

As a first step, the TITAN tool calls the functions in the Geometry module to generate the surface mesh of the objects that will undergo atmospheric re-entry by importing the user-generated STL files. The use of STL files allow the possibility to generate and simulate complex geometries. TITAN divides the simulated bodies into two groups for representation: primitive bodies (cannot undergo structural fragmentation due to aerothermal loads) and joint bodies (can be fragmented). In this context, it is important to have in mind that primitive bodies do not mean objects basic shapes, as we are using STL files for importing objects. The connection between joint-primitive bodies or primitive-primitive bodies is provided by the user and it allows to dynamically take into account the generation of new objects during the simulation when a fragmentation event occurs. The geometry and mesh module then assembles the multiple STL object files and the surface element properties (area, normal vector, local radius) for the triangular facets and assembled body properties (mass, center of mass, inertia) are then computed in support of re-entry trajectory simulations.

The tool then proceeds to compute the visibility detection of surface elements based on the free-stream flow direction and orientation of the body. Average free-stream properties of the atmosphere are obtained from the US-1976 [2] or the NRLMSISE00 [3] atmospheric database, which contain the information regarding atmospheric temperature and multi-species density as a function of the objects altitude. The aerodynamic and aerothermodynamic loads are then computed on the visible wet facets for the various flow regimes encountered during the atmospheric re-entry. TITAN has the capability to choose between using low-fidelity aerothermal modelling, based on local panel inclination methods, or calling for a high-fidelity CFD solver which enables to obtain a more accurate description of the flow at the vicinity of the objects. A more detailed explanation is provided in section **??**.

An altitude based fragmentation model is implemented for the preliminary use of the tool. When fragmentation altitude is reached, the joints fragment and TITAN introduces into the new fragmented objects into the loop, computing the new inertia and mass properties, together with the new position of the center of mass for each object. The flight dynamics during the re-entry process are computed using a 6DOF trajectory propagator and the trajectories of the several considered objects are followed throughout the re-entry process.

A lumped mass approach is considered to model the thermal response of materials with the computed heat flux in order to update the wall temperature for the individual objects in the assembly. If the computed surface temperature exceeds the melting temperature, the object is assumed to start melting. Then the surface temperature remains constant and the convective heat will be transferred in latent of melting.

3. Aerothermodynamics Modelling

The present multi-fidelity framework enables the computation of aerodynamic and aerothermodynamic loads through selecting fast simplified engineering models or accurate high-fidelity CFD solvers. The low-fidelity models considered allow for the loads computation at the different flow regimes experienced by the bodies during the re-entry process (e.g. rarefied, transitional, slip-flow and continuum regime) using local panel inclination methods. Additionally,

the framework has the capacity of calculating and using local radius information to improve the surface heating prediction.

Regarding the high-fidelity simulation, the surface quantities are computed using the CFD solver SU2-NEMO. The use of CFD solvers require the generation of a numerical grid capable of capturing the flow complexity inside the computational domain. Therefore, before proceeding to the CFD simulation, TITAN calls out GMSH software to automatically generate a grid around the bodies. To achieve a grid convergence solution and to sharply capture the directional flow features, the framework performs anisotropic grid adaptation and the generation of prismatic boundary layers using third-party tools, enabling the physical surface heating predictions. The flowchart for both low-fidelity and high-fidelity aerothermodynamic computation methods is showcased in Fig. 2.

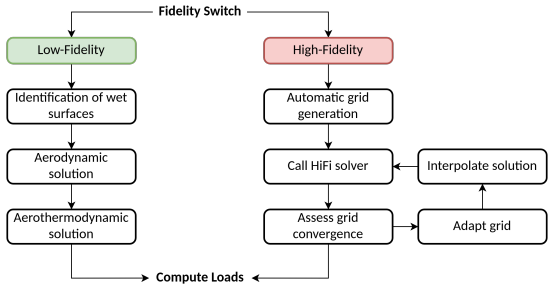

Figure 2: Flowchart of the aerothermal loads computation.

3.1. Low-fidelity Models

The low-fidelity aerodynamics and aerothermodynamics models in TITAN use the local panel inclination methods to enable the modelling of any arbitrary geometry using small triangular facets (STL files). This approach enables the rapid computation of the aerothermal loads acting on the objects during atmospheric re-entry. The pressure and shear stress contribution from each of the facets are computed as a function of local flow inclination angle (θ). The resultant force components are then computed via the integrals distributions over the objects' surface.

A re-entering object experiences different flow regimes, all the way from free-molecular, to transitional and continuum regimes. The aerodynamic contribution in the free molecular regime is evaluated using the analytical model of Schaaf and Chambre's for pressure (C_p) and shear (C_τ) coefficients as described in Eq. 1 and Eq. 2.

$$C_p = \frac{1}{s^2}\left[\frac{2-\sigma_N}{\sqrt{\pi}} s\sin\theta + \frac{\sigma_N}{2}\sqrt{\frac{T_w}{T_\infty}}\right] e^{-(s\sin\theta)^2} + \frac{1}{s^2}\left[(2-\sigma_N)\left((s\sin\theta)^2+\frac{1}{2}\right) + \frac{\sigma_N}{2}\sqrt{\frac{\pi T_w}{T_\infty}}\, s\sin\theta\right] (1+erf(s\sin\theta)) \quad (1)$$

$$C_\tau = -\frac{\sigma_t\cos\theta}{s\sqrt{\pi}}\left[e^{-(s\sin\theta)^2} + \sqrt{\pi}s\sin\theta(1+erf(s\sin\theta))\right] \quad (2)$$

$$s = \frac{V_\infty}{\sqrt{2RT_\infty}}, \quad (3)$$

where σ_N and σ_t are normal and tangential momentum accommodation coefficients. T_∞ is free stream temperature, T_w is the wall temperature, s is the molecular speed ratio given by Eq. 3, and V_∞ is the free stream velocity.

The heat transfer in the free molecular regime is given as a function of the local flow inclination angle in Eq. 4, where α is the energy accommodation coefficient and γ is the specific heat ratio.

$$q = \frac{\alpha\rho_\infty V_\infty^3}{4s^3\sqrt{\pi}}\left[\left(s^2+\frac{\gamma}{\gamma-1}-\frac{\gamma+1}{2(\gamma-1)}(e^{\frac{T_w}{T_\infty}})\right)(e^{-(s\sin\theta)^2} + \sqrt{\pi}s\sin\theta)(1+erf(s\sin\theta)) - \frac{1}{2}(e^{-(s\sin\theta)^2}\right] \quad (4)$$

The aerodynamic contribution in the continuum regime is computed using modified Newtonian theory as given by Eq. 5. C_p is the local pressure coefficient and $C_{p_{max}}$ is the pressure coefficient at the stagnation point. The shear stress contribution in the continuum regime is assumed to be zero, when compared to the pressure contribution. The aerothermodynamic contribution in the continuum regime is obtained by using Van Driest model [4]. Van Driest model estimates sensibly lower heat flux, due to the non-catalytic wall condition, and this model represents the lower boundary. The stagnation point heat transfer for this model is given by Eq. 6, where h_s, h_w are the enthalpy at the stagnation point and the wall, respectively, ρ_s is the density at the stagnation point. (du_e/dx) is the velocity gradient and is given by Eq. 7, where r_N is the effective nose radius. The heat transfer as a function of the local inclination angle, θ, is computed using Eq. 8.

The aerodynamic and aerothermodynamic coefficients in the transition regime are calculated with a local bridging methodology as defined in Ref. [5; 6].

$$C_p = C_{p_{max}} sin^2(\theta) \tag{5}$$

$$q = 0.94(\rho_s \mu_s)^{0.5}(h_s - h_w)\sqrt{\left(\frac{du_e}{dx}\right)_s} \tag{6}$$

$$\sqrt{\left(\frac{du_e}{dx}\right)_s} = \frac{1}{r_N}\sqrt{\frac{2(p_s - p_\infty)}{\rho_s}} \tag{7}$$

$$Q(\theta) = Q_s(0.1 + 0.9\cos\theta) \tag{8}$$

3.2. SU2-NEMO

The open-source SU2 software[1] suite [7] was developed for the analysis of partial differential equations (PDEs) and PDE-constrained systems. The software was written in C++ and Python and promotes code re-usability and flexibility by allowing the construction of high-level object-oriented structures that can be easily integrated with the main code to effortlessly implement new state-of-the-art features. For the accommodation of high-temperature and high-velocity impact in the simulations of chemically-reactive multi-species and non-equilibrium flows, SU2-NEMO (NonEquilibrium MOdels) solver has been developed The solver uses the conventional Navier-Stokes equations with perfect gas model over the classic finite-volume edge-based formulation for the numerical discretization.

The closure of the governing equations for the system of interest is achieved through the linkage of SU2-NEMO and the thermochemistry library Mutation++[2] [8] (Multicomponent Thermodynamic And Transport properties for IONized gases in C++). The library contains efficient algorithms for the computation of the required mixture properties, such as thermodynamic, transport and chemical kinetic gas properties for a wide range of temperatures.

The system of governing equations is obtained through the extension of the Navier-Stokes equations to account for chemically-reacting, nonequilibrium flows [9], using the two-temperature model by Park. The translational and rotational energy mode are assumed to be at equilibrium with one another, and the same assumption is made for the vibrational and electronic energy mode. The system can be described as:

$$\frac{\mathrm{d}\mathbf{U}}{\mathrm{d}t} + \nabla \cdot \mathbf{F^i}(\mathbf{U}) = \nabla \cdot \mathbf{F^v}(\mathbf{U}) + \mathbf{Q}(\mathbf{U}), \tag{9}$$

where $\mathbf{U}$ are the conservative variables, $\mathbf{Q}$ are the source terms, $\mathbf{F^i}$ and $\mathbf{F^v}$ are the inviscid and viscous fluxes, respectively. The vectors are given by

$$\mathbf{U} = \begin{Bmatrix} \rho_1 \\ \vdots \\ \rho_{n_s} \\ \rho\mathbf{u} \\ \rho e \\ \rho e^{\text{v-e}} \end{Bmatrix}, \quad \mathbf{F^i} = \begin{Bmatrix} \rho_1\mathbf{u} \\ \vdots \\ \rho_{n_s}\mathbf{u} \\ \rho\mathbf{u}\otimes\mathbf{u} + p\bar{I} \\ \rho\mathbf{u}h \\ \rho\mathbf{u}e^{\text{v-e}} \end{Bmatrix}, \quad \mathbf{Q} = \begin{Bmatrix} \dot{\omega}_1 \\ \vdots \\ \dot{\omega}_{n_s} \\ 0 \\ 0 \\ \dot{\Omega} \end{Bmatrix},$$

$$\mathbf{F^v} = \begin{Bmatrix} \mathbf{J}_1 \\ \vdots \\ \mathbf{J}_{n_s} \\ \bar{\tau} \\ \bar{\tau}\cdot\mathbf{u} + \sum_s \mathbf{J}_s h_s + \mathbf{q}^{\text{t-r}} + \mathbf{q}^{\text{v-e}} \\ \sum_s \mathbf{J}_s h_s^{\text{v-e}} + \mathbf{q}^{\text{v-e}} \end{Bmatrix}, \tag{10}$$

in which ρ is the density, $\mathbf{u}$ is the velocity vector, p is the static pressure, h is the total enthalpy per unit mass of the mixture, e is the energy per unit mass, $\bar{\tau}$ is the viscous stress tensor, $\mathbf{q}$ is the conduction heat flux, $\mathbf{J}$ is the mass diffusion flux, $\dot{\omega}$ is the net rate of species production, $\dot{\Omega}$ is the source term of vibrational energy and n_s is the number of species in the mixture. The subscript index s stands for the sth chemical species in the mixture and the superscript t-r and v-e stand for the translational-rotational and vibrational-electronic modes, respectively. If the quantity does not have a superscript, it is related to the full mixture. The term $\bar{I}$ denotes the identity matrix.

Individual chemical species are assumed to behave as an ideal gas. Under this assumption, the total pressure of the mixture is defined using Dalton's law as

$$p = \sum_{s=1}^{n_s} p_s, \tag{11}$$

where p_s is the partial pressure of each species. The partial pressure can be determined by using the ideal gas law

$$p_s = \rho_s \frac{R_\mathrm{u}}{M_s} T_\mathrm{tr}, \tag{12}$$

where R_u is the universal gas constant, M_s is the molar mass of species s and T_{tr} is the translational-rotational temperature of the mixture. The total specific energy of the flow is given as the sum of the internal and kinetic energies

[1] https://github.com/su2code/SU2

[2] https://github.com/mutationpp/Mutationpp

$$e = \sum_{s=1}^{n_s} c_s e_s + \frac{1}{2}|\mathbf{u}|^2, \quad (13)$$

where c_s is the mass fraction of species s, $|\mathbf{u}|$ is the magnitude of the flow velocity vector and e_s is the specific internal energy of the species, given by

$$e_s = e_s^{\mathrm{t}}(T_{\mathrm{tr}}) + e_s^{\mathrm{r}}(T_{\mathrm{tr}}) + e_s^{\mathrm{v}}(T_{\mathrm{ve}}) + e_s^{\mathrm{e}}(T_{\mathrm{ve}}) + e_s^0. \quad (14)$$

where e_s^0 is the energy of formation, e_s^t, e_s^r, e_s^v and e_s^e are the translational, rotational, vibrational and electronic energy contribution, respectively. The thermal nonequilibrium calculations are performed using the Rigid-Rotor/Harmonic-Oscillator (RRHO) model.

The ability to simulate slip regimes was recently implemented in SU2-NEMO. The new models allow to simulate moderate rarefied regimes, where the continuum Navier-Stokes equations still hold with the exception of the boundary layer zone. Near the wall, there are insufficient molecular collisions and the velocity and temperature of the gas will not match the velocity and temperature of the surface. The slip conditions are accounted for through the Maxwell velocity slip [10] and Smoluchowski temperature jump [11] equations, given as

$$U_s = \frac{2-\sigma}{\sigma}\lambda\frac{\partial U}{\partial n} + \frac{3}{4}\frac{\mu}{\rho T}\frac{\partial T}{\partial x}, \quad \text{and} \quad (15)$$

$$T - T_w = \frac{2-\alpha}{\alpha}\lambda\frac{2\gamma}{(\gamma+1)Pr}\frac{\partial T}{\partial n} \quad (16)$$

respectively. The Tangential Momentum Accommodation Coefficient (TMAC) σ and Thermal Accomodation Coefficient (TAC) α value account for the physical characteristics of the surface itself. The parameter μ is the flow viscosity, ρ is the mixture density, Pr is the Prandtl number, T is the temperature of the gas, T_w is the temperature of the surface and λ is the mean free path.

4. Quasi-steady analysis of spherical bodies dynamic separation

The use of a quasi-steady approach in the high-fidelity aerothermal model of TITAN allows to account for time-dependent object dynamics without the resource to mesh deformations tools. This aproach assumes a steady flow at each time-step to compute the integrated loads applied at the bodies surface and the bodies dynamics for the given interval of time. Therefore, at each time-step, the grid has to be regenerated to accommodate the new position of the objects. To validate this approach, the simulation of dynamical separation of two spheres in a high-speed flow is conducted and compared with the experimental results of Laurence et al. work [12]. The geometrical properties and spheres density used in this simulation, together with the free-stream conditions are illustrated in table 1.

Table 1: Numerical simulation parameters.

r1 [mm]	25.4
r2 [mm]	12.7
ρ_s [kg/m^3]	1132
M_∞	4
p_∞	1400
ρ_∞	0.07

The initial configuration at t' = 0, where t' is a non-dimensional time computed as $t' = \sqrt{\frac{\rho_\infty}{\rho_s}}t\frac{V_\infty}{r_1}$ has an alignment angle between the sphere centers of -0.1° counterclockwise. At each time iteration, the secondary sphere was limited to move 3 millimeters by adapting the time-step according to the sphere velocity. Three levels of anisotropic mesh adaptation were automatically performed by TITAN at each time step. The last level of grid adaptation for different time intervals can be seen in Fig 3. The purpose of using an adaptation tool in the loop is to obtain grid converged solutions and to sharply capture the directional flow features to accurately predict the loads impact of the shock impingement on the secondary sphere in the body dynamics.

A comparison between the experimental and numerical schlieren is illustrated in Fig. 4 for t' = 0 and t' = 1.66, respectively. The black circles show the experimental spheres position and the red and green contours are the numerical representation of the spheres and shock-wave, respectively. The non-dimensional time is used for both numerical and experimental simulations in order to avoid time deviations. At t' = 0, the spheres are released in the numerical simulation and TITAN is able to correctly predict the position of the secondary sphere at a time of t' = 1.66, as it can be seen in the right sub-figure of Fig. 4.

In Fig. 5 a comparison of force coefficients between the numerical simulation and experiment for both primary and secondary spheres is analysed. Between t' = 0 and t' = 1.5 the force coefficients present a large discrepancy when compared to the experimental data due

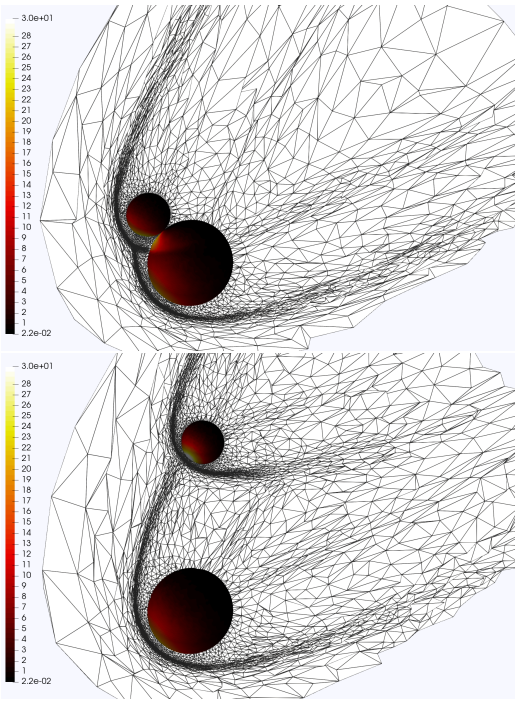

Figure 3: Visualization of the final adapted grid at initial and final time.

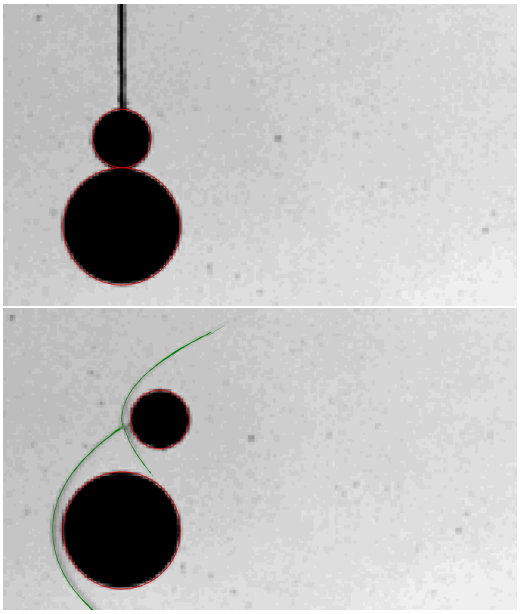

Figure 4: Schlieren results comparison for t' = 0 (left) and t' = 1.66 (right).

to the flow start-up period at the experimental facility. After this period (t' ≥ 1.5), the numerical predictions show a good agreement with the available data for the given time-window.

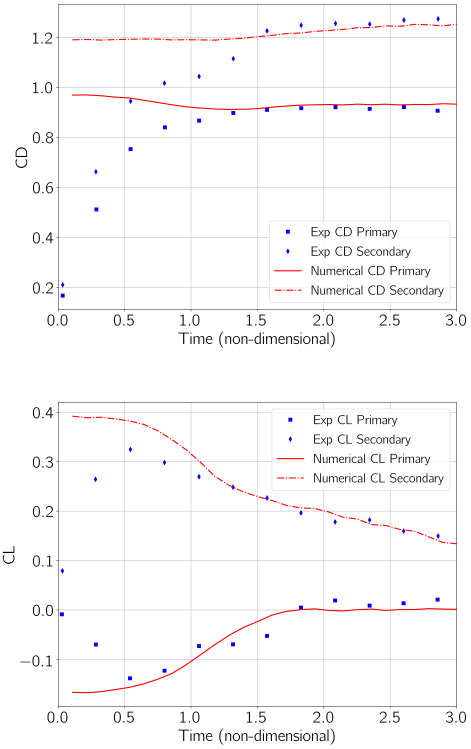

Figure 5: Comparison of Drag coefficient and Lift coefficient with experimental data.

These results suggest that approach is a good alternative to the use of unsteady simulations with immersed boundary methods as a way to accurately predict the dynamics of simulations involving multiple bodies.

5. A conceptual case: ATV-cargo inspired re-entry

To demonstrate the multi-fidelity capabilities of TITAN and assess its impact on the dynamics of the bodies after fragmentation, a simplified conceptual ATV re-entry test-case was conducted for a fully low-fidelity and a multi-fidelity simulation. The fidelity switch in TITAN is set to use high-fidelity models during the instants after fragmentation, set to occur at an altitude of 78 km. For this specific problem, thermal ablation due to high temperatures was not taken into consideration.

The conditions used in this simulation are summarized in Table 2 and the initial simplified ATV geom-

etry before breakup is shown in Fig. 6.

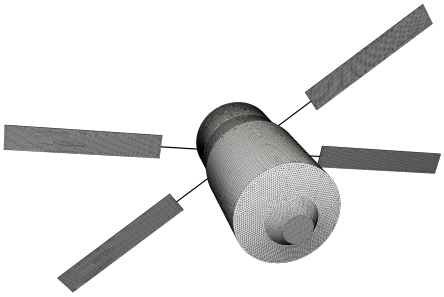

Figure 6: Geometry configuration of the conceptual ATV geometry.

Table 2: Initial trajectory conditions and geometry details.

Altitude [km]	120
Velocity [km/s]	7.57
Flight path angle [°]	-1.45
Initial pitch angle velocity [°/s]	10
Fragmentation trigger altitude [km]	78
Number of facets [x10^3]	160

TITAN uses low-fidelity models to compute the surface loads up until the objects reach the specified breakup altitude. Afterwards, the impact of using low-fidelity and high-fidelity models in the objects dynamics at the instants after fragmentation is assessed in Fig. 7, where the column at the left shows the high-fidelity contours and bodies dynamics and the column at the right shows the low-fidelity results. Each snapshot was taken 30 milliseconds apart. The satellite reached breakup altitude at t = 172 seconds after the re-entry initialization.

For the low-fidelity snapshots, the panels are not affected by the shock incidence and therefore the changes in dynamics are smoother. However, analyzing the high-fidelity snapshots, it is clear that the ATV attitude with respect to the free-stream flow direction leads to the presence of shock impingement at the surface of the top panels, which has a major influence on the dynamic of the bodies. Contrarily, the shock generated by the ATV main body does not affect the bottom panels. For this reason, during the computed time window, the dynamics of the bottom panels are similar for both low- and multi-fidelity approach. The same conclusion can be done by analyzing the evolu-

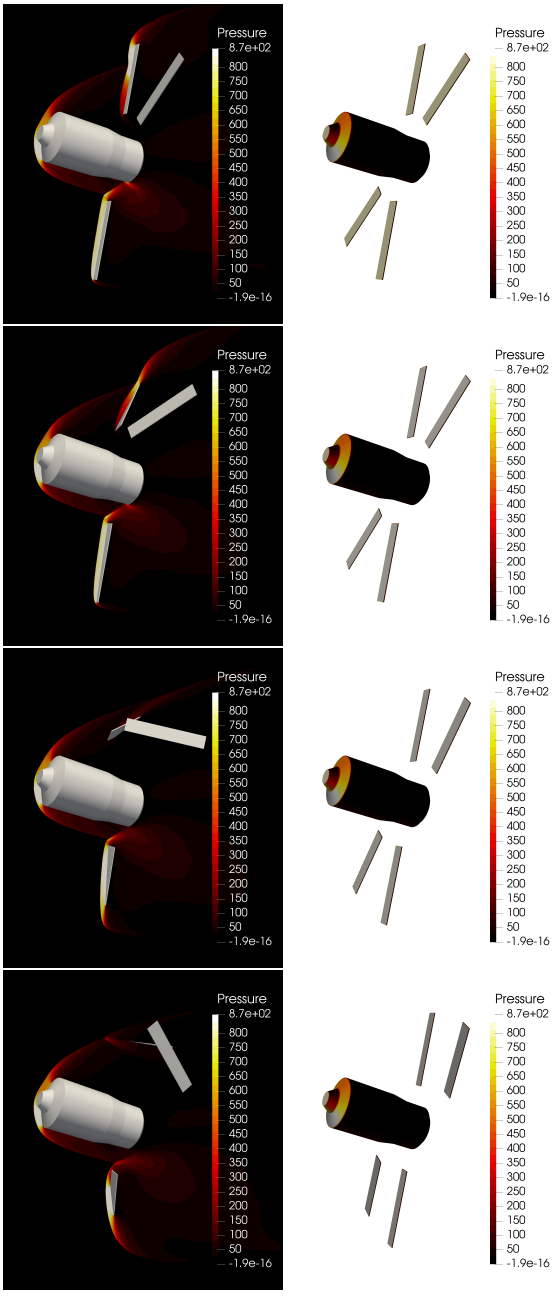

Figure 7: High- (black background) and low-fidelity (white background) ATV snapshots at t = 0, 30, 60 and 90 ms after breakup.

tion of roll, pitch and yaw angles in Fig. 8. The black and blue lines represent the top panels, which show the largest difference due to the shock impingement at breakup and the green and red lines the bottom panels, which present the smallest difference.

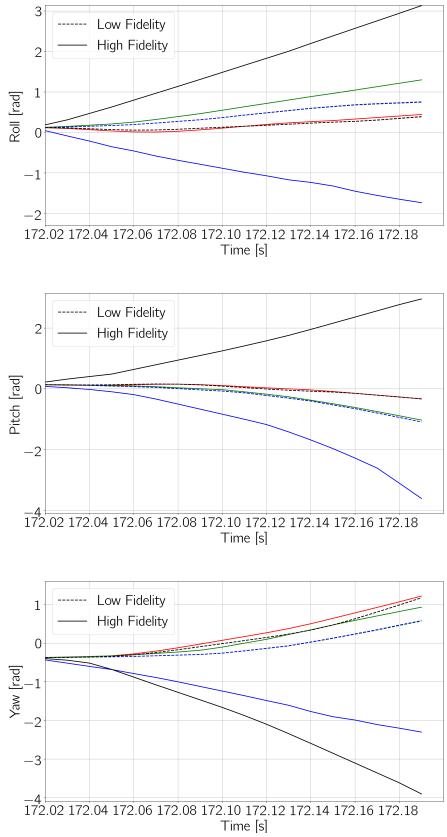

Figure 8: Evolution of roll, pitch and yaw angles of the ATV panels after the breakup instant.

The results presented in this section highlight the importance of using a high-fidelity approach to correctly predict the surface loads at key moments of the re-entry simulation, exemplified in this section as the instant that fragmentation occurs. The use of high-fidelity models for this particular time-window allowed to assess the correct dynamics of the panels due to shock impingement that is not accounted in low-fidelity methods, thus decreasing the simulation uncertainty.

6. Conclusions

The accurate prediction of a destructive re-entry requires the simulation of an unsteady high-speed multi-disciplinary problem. Most of the state-of-the-art tools used to simulate re-entry employ low-fidelity methods to compute the aerothermal loads and structural stress, which can lead to highly inaccurate results due to not accounting for the presence of shock shock interaction and shock impingement, which affects the demise process and bodies dynamics. Simulation accuracy can be increased through the use of high-fidelity tools but these are computationally demanding, and therefore, not suitable for re-entry simulation. For this purpose, the TITAN tool was developed, allowing a multi-fidelity approach during reentry simulation in order to achieve a compromise between accuracy and costs.

The impact and validation of the quasi-steady approach used in the high-fidelity methods for the dynamics prediction is presented for a spherical bodies dynamic separation case at supersonic flow. Using this approach, TITAN regenerates the grid and assumes a steady flow at each time-step. Results showcase the ability of this method to accurately compute the dynamics of the bodies in the following instants after the breakup process. Additionally, a demonstration ATV case is also presented in this work, highlighting the impact of using TITAN multi-fidelity approach for the instants after fragmentation, where the shock impingement on the bodies affect the overall dynamics.

7. Future Work

The future works include the coupling of Sandia laboratory's SPARTA (Stochastic PArallel Rarefied-gas Time-accurate Analyzer) Direct Simulation Monte Carlo solver with the TITAN tool to enable high-fidelity rarefied gas flow simulations. Additionally, a coupling with the ESA's ESTIMATE repository is foreseen, which will enable the use of a library of spacecraft grade materials and their properties as a variation of temperature.

Future plans also include the integration of structural dynamics due to the loads acting at the objects surface. This will be achieved by the inclusion of the open-source FEniCSx tool, which enables the use of Finite Element Methods (FEM) to easily compute the stress, strain and displacements of the structure, crucial to assess when a joint is close to fragment . Preliminary results are shown in Fig. 9.

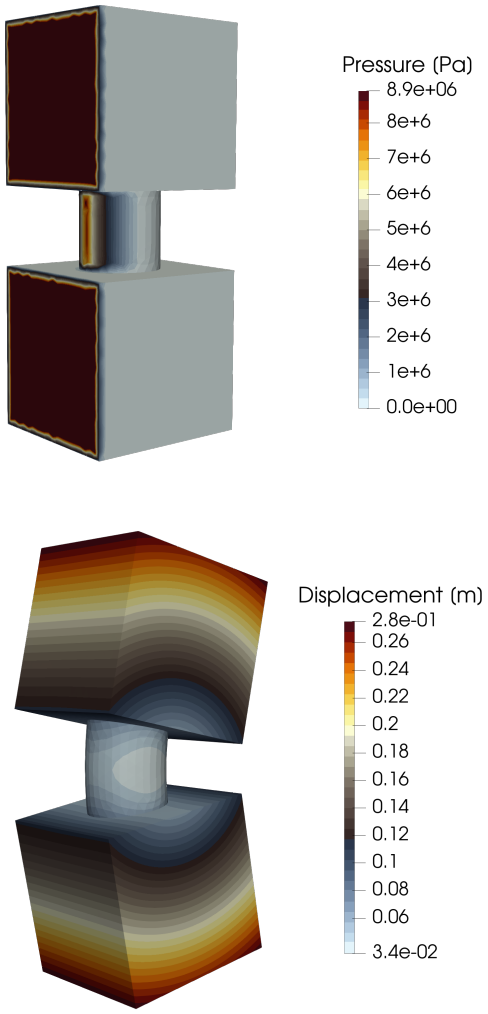

Figure 9: Before and after loads application on the objects surface.

Acknowledgments

This research is partially supported by the EU H2020 MSCA-ETN Stardust-R, grant agreement 813644. The authors wish to acknowledge the support of the European Space Agency through the OSIP MIDGARD project, ESA Contract No. 4000130436/20/NL/MH/ac, 2020-2023. The author also wants to acknowledge the help of Dilaksan Thillaithevan for the work done in the integration of FEniCSx in TITAN.

References

[1] J.-C. Liou, M. Kieffer, A. Drew, A. Sweet, The 2019 u.s. government orbital debris mitigation standard practices, Orbital Debris Quarterly News 24 (1) (2020) 4–8, cited By 9.

[2] U. S. C. on Extension to the Standard Atmosphere, U.S. standard atmosphere, 1976, National Oceanic and Amospheric [sic] Administration : for sale by the Supt. of Docs., U.S. Govt. Print. Off., 1976.

[3] J. M. Picone, A. E. Hedin, D. P. Drob, A. C. Aikin, Nrlmsise-00 empirical model of the atmosphere: Statistical comparisons and scientific issues, Journal of Geophysical Research: Space Physics 107 (A12) SIA 15–1–SIA 15–16. doi:https://doi.org/10.1029/2002JA009430.

[4] E. R. van Driest, The problem of aerodynamic heating, Aeronautical Engineering Review 15, 10 (1956) 26–41.

[5] A. Falchi, V. Renato, E. Minisci, M. Vasile, Fostrad: An advanced open source tool for re-entry analysis, in: 15th Reinventing Space Conference, 2017.

[6] P. Mehta, E. Minisci, M. Vasile, A. C. Walker, M. Brown, An open source hypersonic aerodynamic and aerothermodynamic modelling tool, in: 8th European Symposium on Aerothermodynamics for Space Vehicles, 2015.

[7] T. D. Economon, F. Palacios, S. R. Copeland, T. W. Lukaczyk, J. J. Alonso, Su2: An open-source suite for multiphysics simulation and design, AIAA Journal 54 (3) (2016) 828–846. doi:10.2514/1.J053813.

[8] J. Scoggins, T. Magin, Development of mutation++: Multicomponent thermodynamic and transport properties for ionized plasmas written in c++, 2014. doi:10.2514/6.2014-2966.

[9] P. A. Gnoffo, R. N. Gupta, J. L. Shinn, Conservation equations and physical models for hypersonic air flows in thermal and chemical nonequilibrium, Technical Paper 2867, NASA (Feb. 1989).

[10] J. Clerk Maxwell, On stresses in rarified gases arising from inequalities of temperature, Philosophical Transactions of the Royal Society of London Series I 170 (1879) 231–256.

[11] M. Smolan, Ueber wärmeleitung in verdünnten gasen, Annalen der Physik 300 (2006) 101 – 130. doi:10.1002/andp.18983000110.

[12] S. J. Laurence, N. J. Parziale, R. Deiterding, Dynamical separation of spherical bodies in supersonic flow, Journal of Fluid Mechanics 713 (2012) 159–182. doi:10.1017/jfm.2012.453.

Simulations of supersonic mixing of alternative fuels for air-breathing engines based on data mining

Ali Can Ispir

Aeronautics and Aerospace Department, von Karman Institute for Fluid Dynamics, Belgium, ali.can.ispir@vki.ac.be

Supervisor: Thierry Magin

Professor, Aeronautics and Aerospace Department, von Karman Institute for Fluid Dynamics, Belgium, thierry.magin@vki.ac.be@vki.ac.be

Co-supervisor: Bayindir H. Saracoglu

Research Expert, Turbomachinery and Propulsion Department, von Karman Institute for Fluid Dynamics, Belgium, bayindir.saracoglu@vki.ac.be

University Supervisor: Axel Coussement

Professor, Aero-Thermo-Mechanics, Université Libre de Bruxelles, Belgium, axcousse@ulb.ac.be

Abstract

This doctorate work deals with fuel-air mixing and combustion phenomenon by performing numerical simulations on a multi-strut scramjet combustor. Additionally, some regression techniques are coupled with CFD database to derive surrogate models relevant to the supersonic mixing and combustion physics to be used in conceptual design and performance estimation studies of the hypersonic engine.

Keywords: Artificial neural network, scramjet, fuel-air mixing, supersonic combustion

1. Introduction

As considering the very short residence time of air stream and difficulties in the penetration of two different streams due to high momentum values in scramjet engines, researchers have been attracted to develop several injection strategies in order to have efficient mixing [1]. Among these methods, one technique used commonly in scramjet engine concept is to generate a penetration zone between fuel and air flows along a confined two jet mixing. The fuel flow is injected into the air stream in parallel direction from struts that located at the enter of the combustor. Many parameters associated with geometrical properties of the fuel struts and injectors can play an important role for determining mixing and combustion efficiencies. Sujith et al. performed experimental and numerical studies to investigate the effect of trailing ramp angle on supersonic mixing efficiency with various angles and two configurations [2]. In their findings, the highest total pressure loss was seen in the sample demonstrated best mixing performance. It was noted that vorticity generated by the struts influenced the mixing in a good way nevertheless caused a remarkable loss in the total pressure term. Manna et al. investigated different fuel injection strut arrangements with various combustor inlet flow conditions in order to see their effects on combustion efficiency, thrust, heat release and total pressure loss [3]. The authors concluded that incurred drag losses due to fuel injectors played more significant role on engine performance such as thrust rather than combustion and mixing efficiency. Choubey and Pandey run CFD simulations on DLR scramjet concept for examining the effect of two strut configuration with different angle of attack values of the fuel injectors on aforementioned performance parameters [4]. They found that multi strut configurations had a positive impact on performance parameters while the maximum combustion efficiency and smallest ignition time were provided when injector attack of angles was set as zero. The flight conditions

have an important effect on the engine performance as well as the strut geometries and configurations. Reddy and Venkatasubbaiah performed numerical studies on the same case with Choubey and Randey, and found also that multi strut injector arrangement provides better performance than single strut [5]. They also conducted their works with different flight conditions and noted that increasing of total pressure and temperature with the flight speed led the combustion efficiency to rise. Huang and Yan investigated ram - scram transition mechanism in a strut-based dual-mode scramjet combustor by performing numerical simulations at some cruise speeds of between Mach 4 - 7 [6]. They showed that inlet boundary conditions higher freestream Mach number is beneficial for the fuel - air mixing process. However, they also noted that the mixing efficiency did not vary after the freestream Mach number reaches big enough values.

The numerical investigation of supersonic flow field in both reactive and non-reactive cases require high numerical resolution i.e high computational costs. Recently, surrogate assisted evolutionary algorithms and reduced order models have been widely used in reactive flow applications, they are seen as attractive options to explore supersonic flow field by avoiding expensive computational prices without sacrificing accuracy [7; 8; 9].

In the present work, scramjet operation of a multi-strut injection dual-mode ramjet (DMR) combustor is under investigation to comprehend the physics of supersonic fuel-air mixing and combustion. The 2D supersonic reactive and non-reactive flow field have been solved by Ansys Fluent commercial CFD code. A CFD database has been created by selecting three geometrical design variables which have huge impact on the physics under investigation (strut wedge angle, fuel struts location and strut V-settlement angle). The Artificial neural network regression model was selected to train the dataset and create surrogate i.e. reduce order models (ROM) to be used in low-fidelity performance estimation studies of the hypersonic engine. The general view of the present Ph.D. work is given in fig. 11.

2. Supersonic fuel-air mixing

The cold flow analysis is done to investigate the hydrogen diffusion into the high-speed air stream in the scramjet numerically. The geometrical effects of the multi-strut injection DMR engine on fuel-air mixing process are examined.

2.1. Physical model:

The dual model ramjet (DMR) engine combustor of the Stratofly MR3 aircraft has dorsal orientation and the combustor is 8.4 meter length and lies down between supersonic intake and diverged nozzle sections. The number of 23 fuel struts are located in the entrance of combustor and there are totally 1248 injectors on the struts. The struts are shaped like diamond and injection angle is oriented depending on which side of the middle axis they are in.

The pre-combustion air properties are depends on the flight conditions and the compression along the intake and isolator. The flow and engine geometry data were provided by one of STRATOFLY Horizon 2020 project members that is Italian Aerospace Research Center (CIRA). In present report, the simulations were done for the cruise speed of Mach 8. The air flow enters the combustor with 33.7kPa static pressure and speed of Mach 3.4 in average. The inlet conditions in numerical analysis are defined as inhomogeneous and boundary conditions are provided by aerodynamic 3-dimensional CFD database as shown in fig. 2. The total pressure and temperature of fuel at the injectors is given as 73.4bar and 610K, respectively, and the equivalence ratio is defined as 0.65.

2.2. Numerical method:

In present study, the two-dimensional Reynolds averaged Navier-Stokes (RANS) equations (Eqs. 1 - 3) and k - ω SST turbulence model have been coupled to conduct numerical studies for multi-strut injection DMR engine combustor. Species transport equation based on finite-rate chemistry with multiple species is also used to model hydrogen diffusion as shown in eq. 4. k - ω turbulence model was noted as very effective predictor to resolve the interaction between shock - expansion waves and mixing layer [7]. Compressible real gas Navier-Stokes/Euler equation set which is recommended for variable density, multi-species flows and flows in which the global Mach number is generally higher than about 0.2 [10].

2.2.1. Code validation:

DLR scramjet configuration is chosen for the verification of the numerical model in present study. It is comprised of a rectangular cross section area combustor whose upper wall is diverged with an angle of 3^0 [11]. The fuel is injected into air stream from a wedge-shaped strut that has three injection holes whose diameter is 1mm, is located in the middle axis of the duct, 32 mm length and with an angle of 12^0 as

shown in fig. 4. The the entrance combustor is connected with a Laval nozzle and a length of 298mm. The air is accelerated in this part up to Mach 2 flow conditions in other word, a velocity of 730m/s, a temperature 340K with a pressure of 0.1 MPa. The air flow composes of $Y_{O_2} = 0.23$ and $Y_{N_2} = 0.77$. The injection of the fuel flow from the strut takes place under sonic conditions.

For simplicity, the flow is assumed as uniform and reaches the inlet conditions mentioned above at the end of Laval nozzle. The coordinate system origin is placed in leftmost point on the bottom wall. The x-axis is in the streamwise direction and y-axis is normal to the bottom wall.

As shown in fig. 5, the numerical model is verified by comparing the flow velocity profile along y-axis in different streamwise directions.

2.2.2. Mesh independency analysis:

The computational domain was created in Ansys Meshing software and structured grid is selected for the problem under investigation. Three grid types namely coarse, medium, fine which are comprised of 4.7M, 2.3M and 1.47M number of elements are investigated, respectively. The domain is split up 5 zones for unstructured and structured meshing as seen in fig. 6. The error rate between fine and medium mesh is less than 10 % in all objective functions therefore, the configuration having 2.3M elements was selected.

2.3. Objective functions:

The objective functions for 2-D strut injected scramjet flow field are determined as mixing efficiency along the streamwise direction and total pressure recovery factor.

1. Mixing efficiency: It is given in eq. 5 and reactive molar concentration of oxygen is given with eq. 6. The mixing efficiency is computed in 20 different stations having 10cm interval between each other as can be seen in fig. 1. The slope of the station line varying with the design variable of V-settlement angle for fair calculation and comparison among the data points.
2. Total pressure recovery efficiency: It is given in eq. 7. p_{t1} and p_{t0} are defined as the mass-averaged total pressure at the exit and the entrance of the combustor, respectively.

2.4. Artificial neural network model

Artificial Neural Network (ANN) regression model [12] builds mathematical relations i.e. pattern between the data points with connected nodes called as

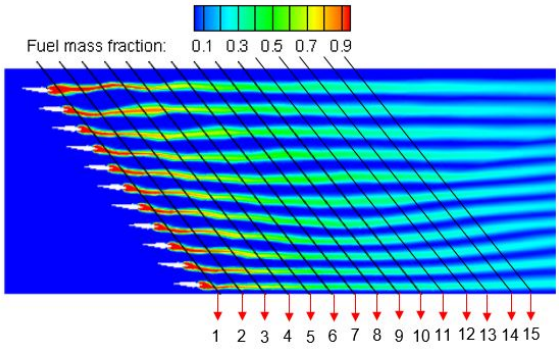

Figure 1: Stations where mixing efficiency is computed.

artificial neurons that represent the simplified model of the neurons in a biological brain. The architecture of ANN is comprised of input, output and hidden layers, learning and training algorithm work with the signals transmitted among these layers [13].

The prediction performance highly depends on neuron and hidden layer numbers. The optimum configuration on the layers for the best prediction differs according to data structure. The manifold assessment is done by computing coefficient of determination and root mean square error values [14] as given in eqs. 8 and 9, respectively.

A dataset including 100 points (determined by Latin hypercube sampling design of experiment method) was generated for supersonic fuel-air mixing investigation. The ANN regression performance was assessed in different mixing efficiency stations for the half of this dataset as seen in fig. 10 and 11.

3. Supersonic combustion

The hot flow simulations are done for assessing the low-fidelity hypersonic engine performance estimation tool. Similarly to cold flow simulations, the methodology is followed by verification of the numerical model, design of experiment (DOE) for the same design variables mentioned in cold flow section, reactive flow simulations in each point of DOE and regression model implementation to get the predicted surface to check the one-dimensional low fidelity engine model accuracy.

3.1. Physical model and numerical method

3.1.1. Physical model:

The physical model of 2D scramjet configuration under investigation in present work is already mentioned in cold flow section. Same boundary conditions

are applied except air inlet of the numerical domain stationed as 1. Pressure-inlet boundary condition is applied; average values of inhomogenous profile of total pressure, total temperature and supersonic gauge pressure along the inlet zone are given as 2451740Pa, 2464.3K and 31000Pa, respectively.

3.1.2. Numerical method:

The 2D and 3D (for the verification case) numerical domains including high-speed turbulent reactive flow field is modeled by Reynolds averaged Navier-Stokes equations [15] in Ansys Fluent Commercial CFD code. k - ω SST turbulence model is selected as highly preferred in the reactive flow problems which the compressibility effects are important [16; 17; 18]. The diffusion flame of hydrogen and air is modeled by progress variable method which is Fluent Generated Manifold and available in Ansys Fluent interface. The turbulent-chemistry interaction is handled by finite rate chemistry. Three combustion models which are available in Ansys-Fluent namely non-premixed combustion, steady diffusion flamelet and Flamelet Generated Manifold, are tested in verification case. The detail chemistry kinetics namely Jachimowski [19] consisting of 33 reactions among 13 species and Zetterval [20] including 25 steps with 12 species, are examined in present work.

Code validation DLR combustor case [11] whose details are mentioned in cold flow section is selected also for hot flow analysis. The comparison includes LES and experimental results. The combustor models mentioned above with a chemistry kinetics which is Zetterval performed in DLR combustor case simulations. The analysis is done in 3D domain with three different grid size which are 8.2M, 4.7M and 1.8M. Temperature and velocity profiles along the y-axis obtained by experimental and LES studies are available in some stations. The compared flow variables profile are given in figs. 7 and 8.

4. Figures

5. Equations

$$\frac{\partial}{\partial t}\rho + \frac{\partial}{\partial x_j}(\rho u_j) = 0 \qquad (1)$$

$$\frac{\partial}{\partial t}(\rho u_i) + \frac{\partial}{\partial x_j}(\rho u_i u_j) = \frac{\partial \tau_{ij}}{\partial x_j} - \frac{\partial P}{\partial x_i} + \rho g_i \qquad (2)$$

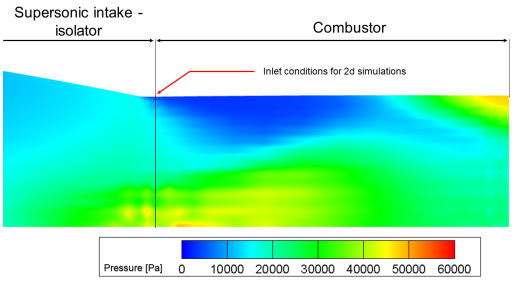

Figure 2: Pressure contour from CFD aerodynamic database of Stratofly MR3 propulsive path for Mach 8 flight conditions.

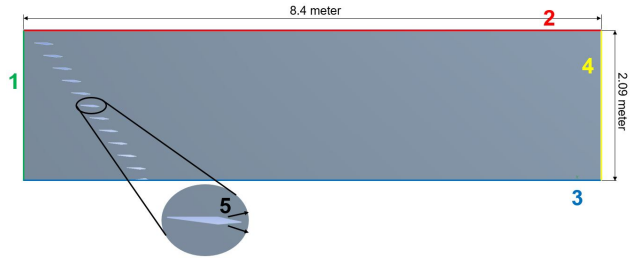

Figure 3: 2D Stratofly combustor domain, boundaries; air inlet (1), wall (2), symmetrical (3), outlet (4), fuel injectors (5)

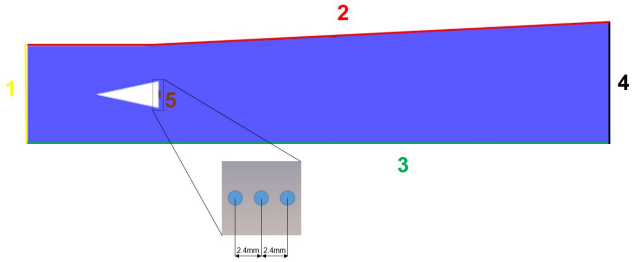

Figure 4: 2D view of DLR combustor case, boundaries; air inlet (1), diverged wall (2), wall (3), outlet (4), fuel injectors (5)

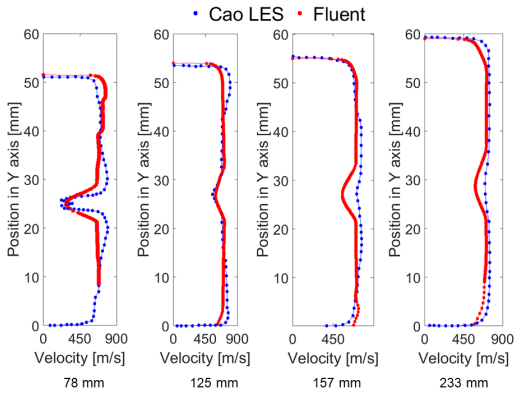

Figure 5: The comparison between results of flow velocity profiles along y-axis in different streamwise directions.

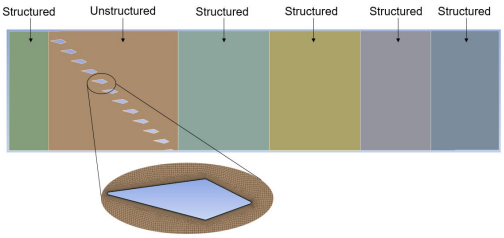

Figure 6: Mesh configuration along the scramjet domain

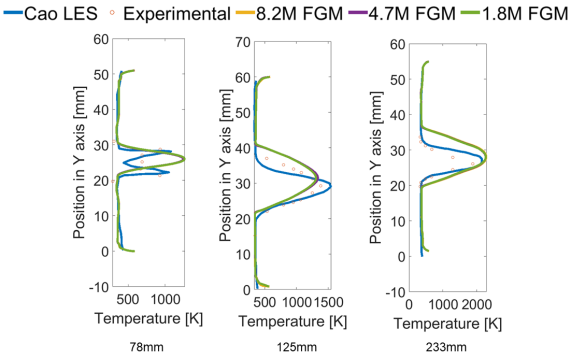

Figure 7: The temperature comparison of combustion models in different stations of the duct and with LES and experimental data [11]

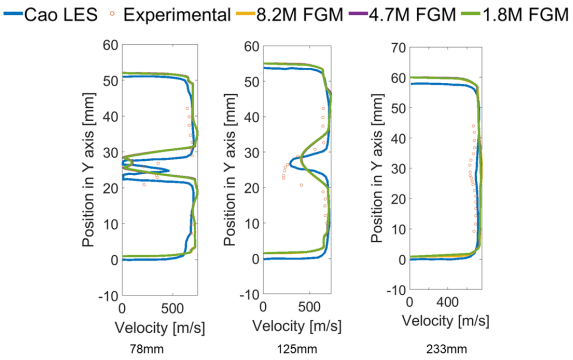

Figure 8: The velocity comparison of combustion models in different stations of the duct and with LES and experimental data [11]

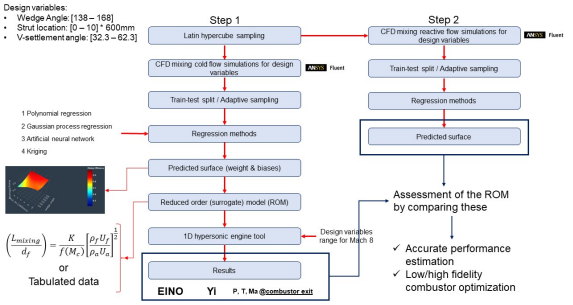

Figure 9: Flow chart of the present doctorate thesis

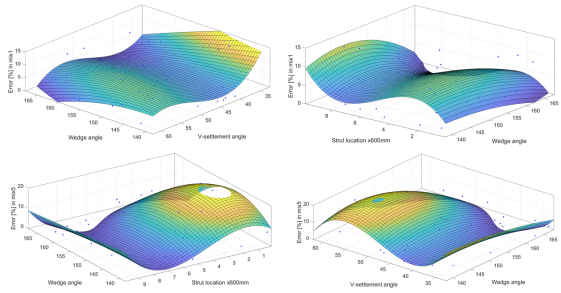

Figure 10: Error rate between predicted and observed mixing efficiency values at first and fifth stations

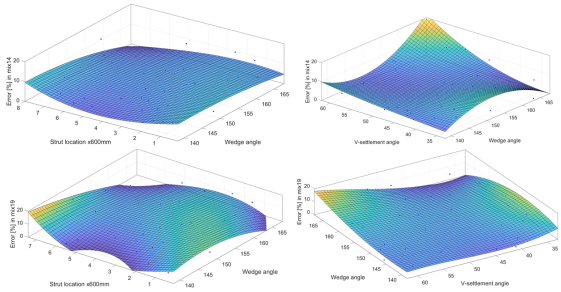

Figure 11: Error rate between predicted and observed mixing efficiency values at fourteenth and nineteenth stations

$$\frac{\partial}{\partial t}(\rho h_s) + \rho\frac{\partial}{\partial t}(\frac{1}{2}\rho u_i u_i) + \rho u_j\frac{\partial}{\partial x_j}(\frac{1}{2}\rho u_i u_i) + \sum_{k=1}^{N} h_{f,i}\omega_k = \frac{\partial P}{\partial t} - \frac{\partial u_i \tau_{ij}}{\partial x_j} + \rho\alpha\frac{\partial^2 h_s}{\partial x_j^2} \tag{3}$$

$$\frac{\partial(\rho Y_i)}{\partial t} + \frac{\partial}{\partial x_j}(\rho Y_i u_j) + \frac{\partial}{\partial x_j}(\rho Y_i D) = \dot{\omega}_i \tag{4}$$

$$\eta_{mix}(x) = 1 - \frac{\int_A C_{O_2,reactive} d\dot{m}|_x}{\dot{m}_{O_2,injected}} \tag{5}$$

$$C_{O_2,reactive} = min(C_{O_2}, \frac{C_{O_2,in} - (C_{O_2,in} - C_{O_2,stoich}).\phi}{C_{H_2,stoich}.\phi}.C_{H_2}) \tag{6}$$

$$\zeta = \frac{p_{t1}}{p_{t0}} \tag{7}$$

$$R^2 = 1 - \frac{\sum_{i=1}^{N}(\phi_{o,i} - \phi_{p,i})^2}{\sum_{i=1}^{N}(\phi_{o,i} - mean(\phi_{o,i}))^2} \tag{8}$$

$$RSME = \sqrt{\frac{1}{N}\sum_{i=1}^{N}(\phi_{o,i} - \phi_{p,i})^2} \qquad (9)$$

6. Conclusion

The present doctorate thesis aims firstly to investigate the supersonic fuel-air mixing process and combustion in a multi-strut injection scramjet engine throughout CFD simulations and secondly by coupling the dataset with machine learning techniques, to develop surrogate i.e. reduce order models (ROMs), relevant to physical phenomenon taking place in the combustor for improving the performance estimation accuracy of the engine.

The verification of the commerical code was completed for both reactive and non-reactive simulations. The half of the dataset determined by Latin hypercube sampling method, was simulated for examining without reaction and ANN was applied to train the dataset.

7. Outlook to final paper

In the final version of the paper, the dataset will be completed for both reactive and non-reactive types of simulation. The surrogate model derived from cold flow simulations will be implemented to the 1d hypersonic engine performance estimation code and the predicted surface obtained from reactive flow simulations will be used to test its accuracy.

References

[1] Z. Gao, C. Lee, Numerical research on mixing characteristics of different injection schemes for supersonic transverse jet, Science China Technological Sciences 54 (4) (2011) 883–893.

[2] S. Sujith, T. Muruganandam, J. Kurian, Effect of trailing ramp angles in strut-based injection in supersonic flow, Journal of Propulsion and Power 29 (1) (2013) 66–78.

[3] P. Manna, R. Behera, D. Chakraborty, Liquid-fueled strut-based scramjet combustor design: a computational fluid dynamics approach, Journal of Propulsion and Power 24 (2) (2008) 274–281.

[4] G. Choubey, K. Pandey, Effect of variation of angle of attack on the performance of two-strut scramjet combustor, international journal of hydrogen energy 41 (26) (2016) 11455–11470.

[5] P. Nithish Reddy, K. Venkatasubbaiah, Numerical investigations on development of scramjet combustor, Journal of Aerospace Engineering 28 (5) (2015) 04014120.

[6] W. Huang, L. Yan, Numerical investigation on the ram–scram transition mechanism in a strut-based dual-mode scramjet combustor, International Journal of Hydrogen Energy 41 (8) (2016) 4799–4807.

[7] W. Huang, Design exploration of three-dimensional transverse jet in a supersonic crossflow based on data mining and multi-objective design optimization approaches, international journal of hydrogen energy 39 (8) (2014) 3914–3925.

[8] G. Aversano, J. C. Parra-Alvarez, B. J. Isaac, S. T. Smith, A. Coussement, O. Gicquel, A. Parente, Pca and kriging for the efficient exploration of consistency regions in uncertainty quantification, Proceedings of the Combustion Institute 37 (4) (2019) 4461–4469.

[9] D. S. Gipe, Surrogate modelling of combustion systems for robust optimized scramjet design.

[10] S. Chakravarthy, U. Goldberg, P. Batten, S. Palaniswamy, Peroomian, 0, CFD++ User Manual, Version 96.

[11] D. Cao, D. Michaels, Confinement and heat-release effects on the mixing region development in a scramjet, AIAA Journal 58 (5) (2020) 2165–2179.

[12] N. Buduma, N. Locascio, Fundamentals of deep learning: Designing next-generation machine intelligence algorithms, " O'Reilly Media, Inc.", 2017.

[13] G. Aversano, G. D'Alessio, A. Coussement, F. Contino, A. Parente, Combination of polynomial chaos and kriging for reduced-order model of reacting flow applications, Results in Engineering 10 (2021) 100223.

[14] K. Zdybał, E. Armstrong, A. Parente, J. C. Sutherland, Pcafold: Python software to generate, analyze and improve pca-derived low-dimensional manifolds, SoftwareX 12 (2020) 100630.

[15] A. Fluent, et al., Ansys fluent theory guide, ANSYS Inc., USA 15317 (2011) 724–746.

[16] X. Song, H. Wang, M. Sun, Z. Cai, C. Liu, J. Yu, Mixing and combustion characteristics in a cavity-based supersonic combustor with different injection schemes, Acta Astronautica 159 (2019) 584–592.

[17] W. Huang, S.-b. Li, L. Yan, Z.-g. Wang, Performance evaluation and parametric analysis on cantilevered ramp injector in supersonic flows, Acta Astronautica 84 (2013) 141–152.

[18] H. Ogawa, Mixing characteristics of inclined fuel injection via various geometries for upstream-fuel-injected scramjets, Journal of Propulsion and Power 31 (6) (2015) 1551–1566.

[19] C. J. Jachimowski, An analytical study of the hydrogen-air reaction mechanism with application to scramjet combustion.

[20] A. Vincent-Randonnier, V. Sabelnikov, A. Ristori, N. Zettervall, C. Fureby, A combined experimental and computational study of the lapcat ii supersonic combustor, in: 22nd AIAA International Space Planes and Hypersonics Systems and Technologies Conference, 2018, p. 5208.

Aerothermodynamic investigation of space debris breakup: Experimental characterization of the VKI Longshot Mach 14 contoured nozzle

Dániel Gábor Kovács

Aeronautics and Aerospace Department, von Karman Institute for Fluid Dynamics, Belgium, / Aerospace and Mechanical Engineering Department, University of Liege, Belgium, daniel.gabor.kovacs@vki.ac.be

Supervisor: Olivier Chazot

Professor and Head of Department, Aeronautics and Aerospace Department, von Karman Institute for Fluid Dynamics, Belgium, chazot@vki.ac.be

Supervisor: Guillaume Grossir

Senior Research Engineer, Aeronautics and Aerospace Department, von Karman Institute for Fluid Dynamics, Belgium, guillaume.grossir@vki.ac.be@vki.ac.be

University Supervisor: Gaëtan Kerschen

Professor of Aerospace Engineering, Aerospace and Mechanical Engineering Department, University of Liege, Belgium, g.kerschen@ulg.ac.be

Abstract

A measurement campaign was conducted in order to commission the new Mach 14 hypersonic nozzle of the VKI Longshot wind tunnel. A probe configuration consisting of a Pitot rake, a reference total pressure probe, a static pressure probe, a heat-flux probe, and an acoustic probe were applied, and tests were performed at similar operating conditions at various streamwise probe positions. The flow characteristics were inferred from the free-stream measurements using an elaborated rebuilding technique. The investigations cover the assessment of: flow uniformity in terms of Pitot pressure, tunnel noise level, core flow diameter, and useful test time.

Keywords: Space debris, Clean Space, re-entry, hypersonic aerodynamics, aerothermodynamics, fragmentation, VKI Longshot, flow characterization

1. Introduction

Nowadays, besides the goal of enabling sustainable and more economical space access, the accumulation of inoperable objects is rising environmental and safety concerns. Various re-entry estimation software is being developed to promote the design of completely demisable spacecraft and hence mitigate the growth of space debris. Such toolkits perform dynamic analysis to compute the states of the re-entering objects, estimate the aerodynamic and aerothermal loads, study the fragmentation, and compute the demise and the ground footprint. These re-entry prediction tools are well suited for single bodies but usually have shortcomings in the analysis of the break-up and dispersion of fragments undergoing mutual interactions due to the complex physics involved. This research aims to deaden the second aspect by supplying Design for Demise tools with data on such unaccounted proximal body interactions.

The first step of this research was to commission the new Mach 14 hypersonic nozzle of the VKI Longshot wind tunnel, which will be used for future experiments. The knowledge of the free-stream flow characteristics, such as the core flow diameter, the flow uniformity, the distribution of the total pressure, the tunnel noise, etc,. is inevitable in any wind tunnel to

ensure the quality of the experimental data and to understand the noise levels and the uncertainty limits.

The new hypersonic contoured nozzle was designed using the HYPNOZE design code [1] which accounts for real gas and viscous effects. After the manufacturing and installation of the nozzle, an experimental campaign was performed to characterize the flow conditions it can provide and to validate the design methodology. This paper gives an overview of the aforementioned measurement campaign and discusses the conclusions obtained. Section 2 introduces the experimental setup and the probes, while Section 3 presents the free-stream rebuilding methodology, and comments on the data obtained. The results of the test campaign are presented in Section 4, Section 5 summarizes the work, and the next steps of this doctoral work are introduced in Section 6.

2. Experimental Tools and Measurement Setup

2.1. Test Matrix

The operating conditions of the VKI Lonsgshot wind tunnel are determined by the compression process of the test gas, which depends on three main independent quantities, the pressure of the driver gas, the pressure of the test gas, and the mass of the piston. The targeted initial conditions were: 34.5 MPa driver gas pressure, 158.6 kPa driven gas pressure, and 2.500 kg piston mass. The test matrix is summarized in Table 1, where one can observe a variation less then ±0.7 % in the driver tube pressure and less then ±0.3 % in the driven tube pressure. The mass of the piston was adjusted within the limit of ±0.1 g. The present runs were all carried out with nitrogen. Five experiments were conducted at four different streamwise Pitot rake locations. A repeat test was conducted at $x = 0.020$ m downstream of the nozzle exit applying a horizontal Pitot rake orientation.

2.2. Probe Alignment and Configurations

The sting mounted set of probes was set in place using a high precision 6-axes positioning mechanism enabling traversing, pitching, yawing and rolling adjustments. For the measurements inside the nozzle, the sting was elongated with a 0.750 m extension. The Pitot rake is equipped with an adapter, enabling the connection of additional supports. The probe configuration is presented in Fig. 1, where ① is the Pitot rake, ② is a reference Pitot probe, ③ is a heat-flux probe, ④ is a static pressure probe, and ⑤ is an acoustic probe. The sensing locations of the probes were aligned in order to be in the same flow-normal plane.

2.3. Probes and Instrumentation

2.3.1. Pitot Rake

A rake of Pitot probes was used to measure the radial flow uniformity, at several streamwise locations. The rake consists of 30 probes with 10 mm spacing between them. Each of them is equipped with a 2 mm external and 1 mm internal diameter, 10 mm long tube, that directs the flow to its own piezoresistive Nova NPP-301A-100A pressure transducer. During this campaign 22 probes (Probe Nr.1-17 and Nr.19-23 due to the failure of Nr.18) were used. The rake was aligned with the vertical and horizontal radius of the nozzle, with the placement of Probe 23 close to the nozzle axis. The calibration of the pitot rake against a reference Ceravac CTR-100 sensor yielded linear pressure-voltage output relationships.

Table 1: Test matrix indicating the position and the alignment of the Pitot rake during the measurement campaign, and the three main parameters influencing the compression process.

Run Nr.	1844.	1846.	1847.	1848.	1849.
Stream-wise position	0.020 m	0.254 m	0.020 m	−0.600 m	−0.875 m
Pitot rake alignment	Vertical	Vertical	Horizontal	Vertical	Vertical
Driver tube pressure	339.47×10^5 Pa	341.40×10^5 Pa	343.04×10^5 Pa	340.95×10^5 Pa	344.17×10^5 Pa
Driven tube pressure	1.5873×10^5 Pa	1.5845×10^5 Pa	1.5811×10^5 Pa	1.5867×10^5 Pa	1.5893×10^5 Pa
Piston mass	2.500 kg				



(a) View from the left side.

(b) View from the right side.

Figure 1: Pictures of the sting supported probe configuration in the VKI Longshot wind tunnel. The Pitot rake is aligned vertically, and the probing position is 0.254 m downstream from the nozzle exit plane.

2.3.2. *Total Pressure Probe*

In addition to the Pitot rake, a standalone Pitot probe was also part of the test configuration. It is illustrated in Fig. 2. The probe is $L = 130\,\text{mm}$ long, and its diameter is $D = 15\,\text{mm}$. A $\varnothing 1\,\text{mm}$ hole is directing the flow into a small cavity, where a fast-response Kulite XCQ-093 absolute pressure sensor is mounted with a housing. For the protection of the transducer, the sensor is placed off-axis, and the nose of the probe is chamfered at an angle of 30 °. Similarly to the pitot rake, this probe was also calibrated against the reference Ceravac CTR-100 sensor, and a linear calibration curve was retrieved.

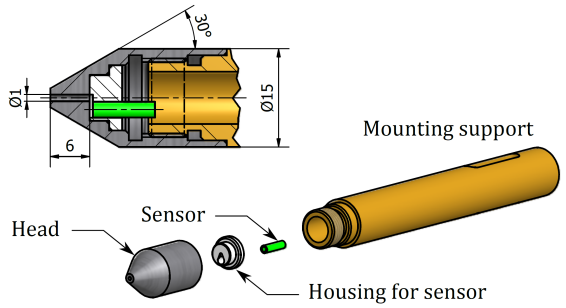

Figure 2: Sketch of the reference Pitot pressure probe [2].

2.3.3. *Heat-flux Probe*

For the measurement of the stagnation point heat-flux, a hemispherical probe presented in Fig. 3 was used. The heat-flux probe has a $D = 15\,\text{mm}$ outer diameter and its length is $L = 130\,\text{mm}$. The sensing component of the probe is an E-type, fast-response coaxial thermocouple (manufactured by the Shock Wave Laboratory of RWTH Aachen University [3]) that is mounted with a chromel insert into the center of the probe head. This is electrically insulated from the mounting support. The sensing junctions of the thermocouple are located along the circumference of the $\varnothing 0.5\,\text{mm}$ circle, which is the boundary between the chromel and the constantan element. Such probes

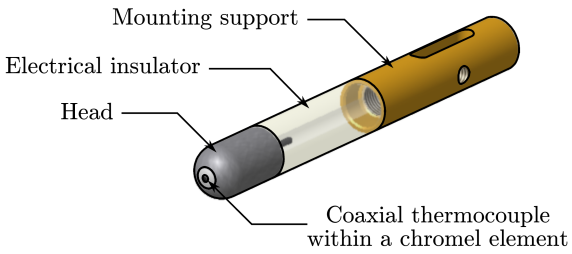

Figure 3: Schematic of the hemispherical heat-flux probe with the indication of its components [2].

allow the computation of the transient stagnation point heat-flux by the integration of the measured temperature history [4] and assuming a one-dimensional heat-flux that penetrates into a uniform, semi-infinite solid of constant thermal properties (ρ, C, k) [4], hence the presence of the chromel insert. Radial effects are corrected for using the approach described in [5]. The thermoelectric voltage generated by the thermocouple is in the order of millivolts, hence the voltage output was amplified by a high precision Flyde FE-351-UA amplifier using a gain of 1000.

2.3.4. Static Pressure Probe

The free-stream static pressure was measured using a Nagamatsu probe designed for the VKI Longshot facility [6]. This slender ($D = 6.6\,\text{mm}$) probe has a contoured nosetip and is equipped with four orifices at $L/D = 24$ which lead to a Kulite XCQ-093-0.35bar piezo-resistive absolute pressure transducer. A schematic of the probe is presented in Fig. 4. Due to the fact that in hypersonic flows the viscous effects promote the development of thick boundary layers, a viscous correction according to [7] is applied on the measured wall pressure p_w to obtain the free-stream static pressure p_∞. The static calibration of the probe was performed against a reference MKS Baratron 626C sensor up to 1600 Pa. Further details of the probe and of the required viscous correction are explained in [8; 6].

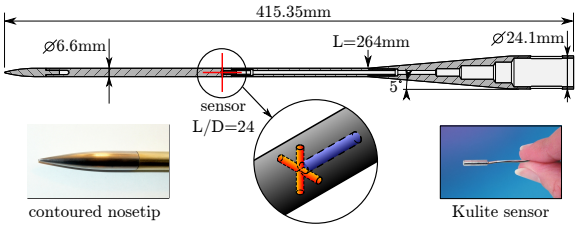

Figure 4: Schematic of the static pressure probe indicating the location of the sensor [2].

2.3.5. Acoustic Probe

An acoustic probe was added to the test configuration to measure the spectra of the pressure fluctuations. A schematic illustrates the probe in Fig. 5. The head of the probe is a truncated 30 ° half angle cone, which merges into a $D = 16\,\text{mm}$ cylinder that connects to the mounting support. A short response time is a strong requirement for the analysis of the fluctuations, therefore, a fast-response PCB 132A31 piezoelectric pressure sensor is flush-mounted to the tip of the probe head. According to the specification of the manufacturer, this configuration ensures a bandwidth up to 1 MHz. The high-impedance charge generated by the sensor is converted to a low-impedance voltage signal using a PCB 482C-2 signal conditioner. The discharge time of the sensor corresponds to a low-frequency cut-off at 11 kHz, given that, the instantaneous pitot pressure will not be measured accurately with this probe. The calibration law issuing from the manufacturer is used.

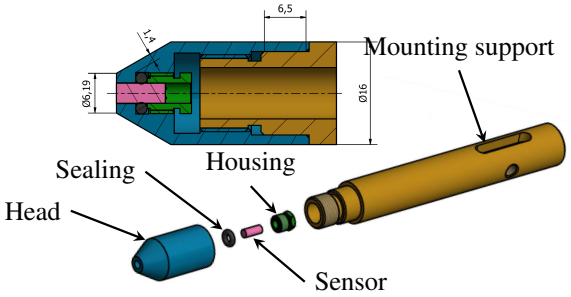

Figure 5: Schematic of the acoustic probe.

2.3.6. Data Acquisition System

The facility is instrumented with a National Instruments PXI-1045 and a PXIe-1073 chassis. The static probe, the total pressure probe and the rake of Pitot probes were connected to the latter one using Wheatstone bridge NI-PXIe-4331 cards and sampled at 102.4 kHz. The heat-flux probe signal was amplified, and recorded using NI-PXI-6123 cards sampling at 500 kHz. The signal of the acoustic probe was acquired at 2.5 MHz using a NI-PXI-6133 card. The data were acquired for 100 ms before and after the beginning of the experiment.

3. Data Reduction

3.1. Rebuilding of the Free-stream Flow Conditions

Former rebuilding techniques for the Longshot tunnel relied [9] on the assumptions of an adiabatic and isentropic nozzle expansion, of a calorically perfect gas in the stagnation point region, and required elaborated equations of state. They were inferring free-stream flow conditions based on the measurement of the upstream reservoir conditions (p_0) and the stagnation point quantities (p_{t_2} and $\dot{q}_w$).

More sophisticated techniques, such as the one described in [10], focus on free-stream diagnostic techniques and do not require the aforementioned assumptions that can lead to poor accuracy. They require the additional measurement of the free-stream static pressure besides the stagnation point pressure and heat-flux. Such a rebuilding technique has been developed for the VKI Longshot facility in [2]. First, the wall pressure (p_w) measured by the static pressure probe is corrected for viscous effects in order to yield the free-stream static pressure (p_∞). Starting from initial guesses for the free-stream temperature (T_∞) and velocity (u_∞), the stagnation point pressure (p_{t_2}) and heat-flux ($\dot{q}_w$) are inferred through the

Rankine-Hugoniot jump relations and the Fay-Riddell equation [11]. High-temperature effects are accounted for while solving shock conservation equations. The computed stagnation quantities are compared to the measured ones, and the free-stream quantities are iterated until convergence is realized.

3.2. Notes on the Experimental Data

The processing of the VKI Longshot experiments starts with the determination of the free-stream flow conditions with the rebuilding technique introduced in Section 3.1. For this calculation, the unevenly acquired data from pressure and temperature probes is resampled with a common frequency. During Run 1846 (vertical profile measurement at $x = 0.254\,\text{m}$ downstream from the nozzle exit) the signal of the heat-flux probe was lost, meaning that the full free-stream rebuilding could not be performed.

To be able to compare the flow characteristics measured during different experiments, the temporal signals must be adjusted to a common reference. In addition to the common time reference, when comparing profiles, one has to account for a delay between the probe signals measured at various streamwise locations, due to the advection time required for the flow to propagate downstream [12]. Therefore, in contrasts to the usual reference (p_{t_2}), the time instant at which the rising reservoir pressure, $p_0(t)$, reaches half of its peak has been used for this purpose. The advection time delay was estimated by the ratio of the instantaneous free-stream flow velocities and the distance between the reservoir pressure sensor and the free-stream probe locations. It must be noted that such estimation assumes constant velocity along the entire nozzle. This is a good approximation in the divergent part of the nozzle where the flow velocity approaches a plateau very quickly, but it breaks down close to the throat and in the convergent section. Due to the absence of the free-stream velocity in case of Run 1846, the advection time was interpolated based on the other experiments.

Regarding the free-stream noise computations, Run 1844 (vertical profile measurement at $x = 0.020\,\text{m}$ downstream from the nozzle exit) was excluded from the analysis because the signal of the acoustic probe was polluted by a large amount of electronic noise.

4. Experimental Results

4.1. Pitot Pressure Profiles

The pressure profiles measured at several streamwise locations are reported in this section. During the evaluation of the profiles, advection times were accounted for in order to compare distributions resulting from similar reservoir conditions. Figure 6 presents the locations of the pitot rake and its individual probes with respect to the nozzle contour, and compares the pitot profiles obtained at various streamwise locations. The presented pressure distributions correspond to $p_0 = 166\,\text{MPa}$ reservoir pressure, which is the designed operational point of this nozzle. The plotted profiles are normalized with the actual mean reservoir pressure, and the contour plot indicates the pitot pressure distribution. A window of 1 ms was used to compute the averaged pitot pressures and their standard deviation $\sigma(p_{t_2})$ which is indicated with error bars. The red markers (referred to as "p_{t_2} *ref.*") are denoting the normalized pitot pressure measured by the reference total pressure probe introduced in Sec. 2.3.2. The nose-tip of this probe was located at the same streamwise location as the rake, halfway between probe Nr.20 and Nr.21, 65.5 mm to the left of the rake's plane. Revolving it's radial distance measured from the nozzle axis, into the plane of the rake, a good match can be observed in the normalized pitot pressures.

The vertical and the horizontal profiles at $x = 0.020\,\text{m}$ downstream of the nozzle exit, show a fair match at the centerline of the nozzle, but they are slightly asymmetrical. Apart from the most upstream measurement, the vertical pitot profiles are generally flat up to half nozzle diameter (measured from the centerline), which indicate a good uniformity in the core flow. The horizontal profile measured at $x = 0.020\,\text{m}$ has a small peak close to the centerline, while the one at $x = -0.875\,\text{m}$ upstream shows a saddle-like behavior. The pitot pressure profile measured at $x = 0.254\,\text{m}$ exhibits a large pressure peak in the vicinity of the boundary layer edge location. This is associated with oblique shock waves induced by the overexpanded nature of the hypersonic nozzle flow for this operating condition at this particular time instant. For subsequent time instants, the oblique shock waves would gradually travel further upstream as a result of the decreasing static pressure within the hypersonic jet (following the reservoir pressure decay) in combination with the increasing pressure within the test chamber (due to the continuous amount of gas being discharged in there). As expected in hypersonic nozzles, a thick boundary layer is present along the wall. Starting from the vicinity of the wall and moving towards the core flow, one can observe that the standard deviation, i.e., the fluctuation of the pitot pressure, is significantly increasing since the probes are exposed to

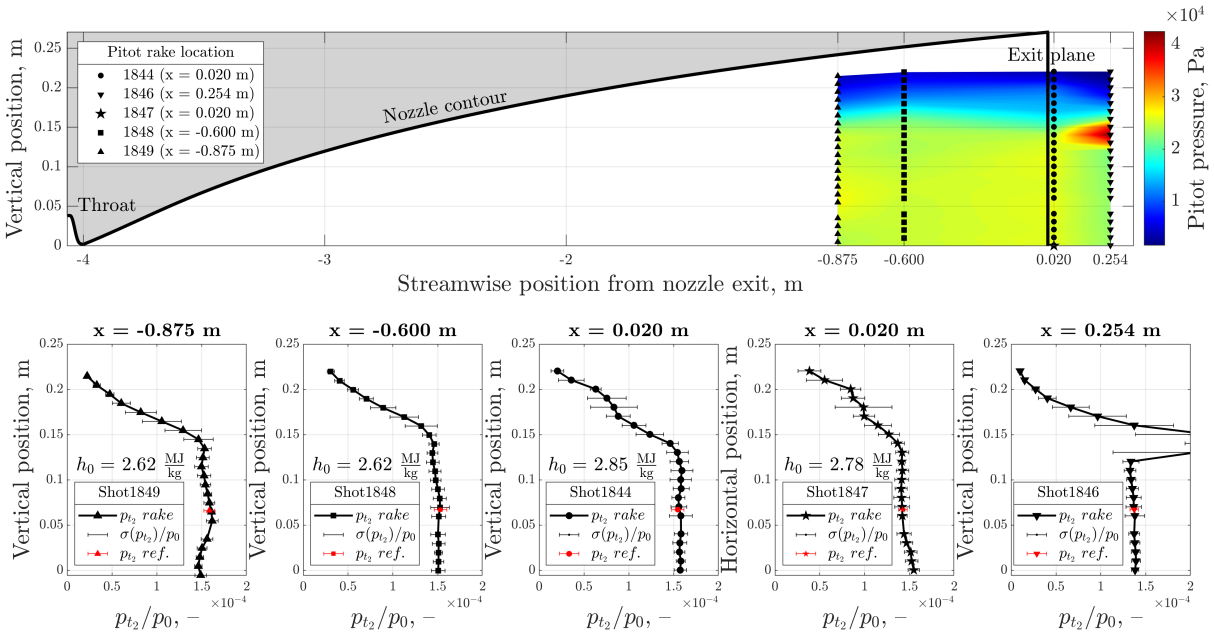

Figure 6: Streamwise and radial locations of the pitot probes during the test campaign, and the normalized pitot pressure profiles that correspond to 166 MPa reservoir condition.

the turbulent fluctuations of the viscous layer. Within the core flow, the standard deviation decreases. Section 4.4 will present a detailed analysis on the free-stream noise levels measured by the acoustic probe.

The evolution of normalized pitot pressure profiles are presented in Fig. 7 at reservoir pressures between $p_0 = 210 - 110$ MPa. The corresponding total specific enthalpies, mean reservoir pressures, and the actual pitot pressures are tabulated in the Appendix of [13]. The lines in Fig. 7 are colored from red to blue depending on the reservoir pressure they correspond to (hence the time instant they were acquired). The vertical axis shows the radial distance between the centerline of the nozzle ($r = 0$) and the probe locations. In the bottom right plot, the temporal variation of the reservoir pressure during each run is indicated. The selected reference time instant $t = 0$ ms refers to the instant for which the reservoir stagnation pressure reaches half of its peak amplitude. This 100 MPa pressure sweep corresponds to an approximately 18 ms time frame. The dotted lines presents p_0 measurements where the wiggles are induced by the cavity line system present in front of the sensor. The continuous lines correspond to exponential curve fits. Time instances when the reservoir pressure is reaching a specific value were identified based on the smoothed curves, and the mean pressure were computed based on the original signals. Similarly to the plot in Fig. 6, a time window of $\Delta t = 1$ ms was used for the computation of the mean pitot pressures and the corresponding mean reservoir pressures.

At $x = -0.875$ m, the pitot profiles at higher reservoir pressures show a good uniformity in the core of the flow and a slightly increasing and then decreasing trend at the edge of the boundary layer. As the pressure is decreasing the profile becomes more and more undulating. A valley of lower pitot pressures is forming close to the centerline and the peak point is moving away from the nozzle axis to approximately 55 mm.

The profiles measured at $x = -0.600$ m are showing a similar behavior as the most upstream ones as the reservoir conditions decay. They remain more homogeneous within the core flow. One can observe that the fluctuations inside the boundary layer are moderate with respect to the profiles measured at other locations. At this axial location, all the profiles seem to commonly have an inflection point around 180 mm.

The vertical profile at $x = 0.020$ m downstream of the nozzle exit presents a very good uniformity inside the core flow until 130 MPa. The horizontal profile has a small peak at the edge of the core, already at high reservoir pressures. The two profiles are showing a fair agreement inside the boundary layer, but

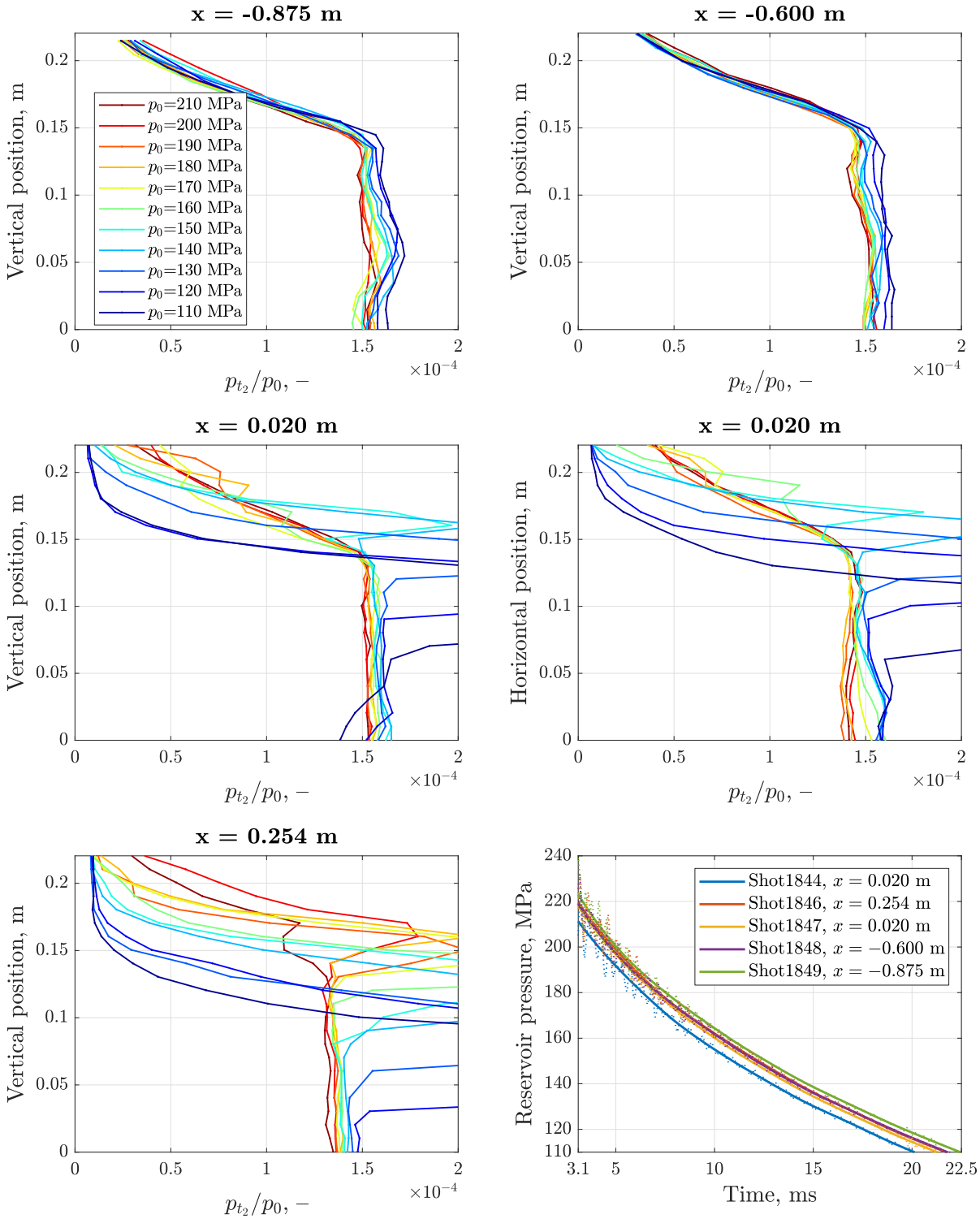

Figure 7: Normalized pitot pressure profiles at different reservoir conditions and the variation of the reservoir pressure in time.

they are asymmetric close to the centerline. It is important to note that the horizontal and vertical profiles were not measured during the same experiment. Attempts were made to synchronize the data by accounting for advection time delays and evaluate the profiles at equal reservoir pressures, but the total enthalpies may still differ. Moreover, this computation is relying on the flow velocity resulting from the full free-stream rebuilding, hence it is also dependent on the enthalpy of the flow. It is visible on both profiles that already at 150 MPa, a peak starts to grow and move from the boundary layer towards the core. Below 130 MPa reservoir pressure, an oblique shock wave induced by the overexpanded structure of the jet is present. It gradually moves upstream the nozzle and is responsible for the larger pressures measured near the edge of the boundary layer and gradually moving towards the nozzle center line.

At the most downstream test location, firmly constant normalized profiles were found in the core flow, similarly to the vertical profile measurement close to the nozzle exit. The process of the jet closure is well visible on the profiles of this streamwise position, and as it can be expected when moving further away from the nozzle exit, the rapid evolution of the profiles indicate limited useful test times.

4.2. Core Flow Uniformity

The variation of the pitot pressures along the nozzle radius were examined according to the method explained later in Section 4.3, and the probes located within the inviscid core were selected. The irregularity is estimated based on these probes, as the ratio of the pitot pressures' standard deviation and the mean pitot pressure. The discrepancies of the core flow were computed for the profiles presented in Fig. 7, and Fig. 8 illustrates the obtained irregularity in percentage. At high reservoir pressures, the irregularity of the profiles were around 2.15 %, which indicates a good uniformity. As the reservoir pressure is decreasing below 170 MPa, one can observe a gently increasing trend in the variation of the pitot pressures. At the same reservoir pressure the hypersonic jet starts to close onto the rake at $x = 0.254$ m downstream from the nozzle exit. Despite the fact that the closure begins around 150 MPa at $x = 0.020$ m, the discrepancies remain around 2.94 %.

4.3. Core Flow Diameter and Useful Test Time

The thick boundary layer that is developing along hypersonic nozzles can represent a significant portion of its diameter. Knowing its dimensions and the available space where we have access to the uniform, inviscid core flow is essential for the planning of aerodynamic experiments, and also for the validation of the code used during the design of the nozzle. When dealing with experimental data, one has to define a robust method for the selection of the points which are consider as part of the core flow.

In the present work, a minimum core radius was set to be 10 mm, i.e., two probes of the pitot rake must be inside this region. First, mean pitot rake profiles were computed for the entire length of the experiment at each 0.1 ms with an averaging window of 1 ms. Then,

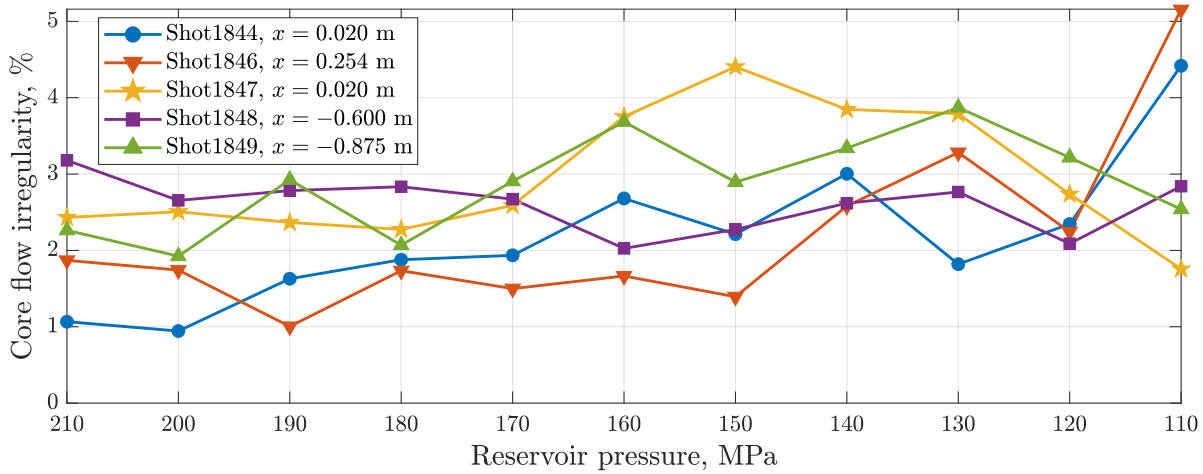

Figure 8: Irregularity of the inviscid core flow at different streamwise locations as a function of the reservoir pressure.

at each evaluated time instance, the pitot profiles were examined starting from the two probes closest to the nozzle axis. A mean pitot pressure was computed based on these probes, and the pressure measured by the adjacent one was compared to it. If the pressure was within the acceptance range (±10 % was used during this computation) the examined probe was considered to be inside the core flow. If the pitot pressure measured by the adjacent probe was out of this range, the search stopped. An interpolation was performed between the last probe of the core region and the first outside, to the point where the pitot pressure is differing with 1 % from the mean value inside the core.

Figure 9 shows the variation of the core flow radius as a function of time. (The $t = 0$ ms time instant corresponds to the half-peak point of the rising reservoir pressure curves. The advection time delays are not accounted for.) As it can be interpreted and as also the results of Section 4.1 showed, testing at $x = 0.254$ m downstream of the nozzle exit yields the shortest useful test time, approximately 6 ms, and a core diameter reduced to 270 mm. Moving upstream, close to the nozzle exit, permits testing inside a core of $D_{\text{core}} = 293$ mm for 10 ms. Performing experiments within a diameter limited to 200 mm is possible for 10 ms and 17 ms respectively, at $x = 0.254$ m and $x = 0.020$ m downstream from the exit. The nozzle was designed [1] in order to reach a maximum core flow diameter at its exit plane, but opposed to that, a slightly larger core (300 mm) was identified at $x = -0.600$ m. The present discrepancy is probably due to the limited accuracy of the inviscid core determination method used in this work, which must be consolidated in the future. Since the diameter of the nozzle is shrinking in the upstream direction, at the expense of moderate test volumes, one could benefit from the elongated test times.

4.4. Tunnel Noise

In the present work, the free-stream noise levels are approximated from the pressure fluctuations sensed by the acoustic probe, i.e., the noise behind the bow shock that forms in front of the probe head. Chaudhry et. al [14; 15] presented a method based on direct numerical simulations for retrieving probe transfer functions which relate the shocked noise levels to the free-stream ones, but such work concerning the present probes remains to be done. The acoustic probe, introduced in Sec. 2.3.5, was placed at a radial location of 116 mm from the center line of the nozzle for all the experiments reported herein. The piezoelectric nature of the PCB132A31 sensor does not entirely eliminate the low frequency content associated with flow transients in spite of its claimed cut-off frequency at 11 kHz. The raw data were therefore offset by their 1000 point moving average in order to focus the analysis on the unsteady part of the signal and exclude the lower frequency content induced by the flow arrival onto the probe.This corresponds to a high-pass filtering with a cut-off frequency of 1.107 kHz. The tunnel noise levels were computed as the ratio of the root mean square (RMS) of the fluctuations and the mean pitot pressure.

$$\text{Noise} = \text{RMS}\left(p'_{t_2}\right) / \overline{p_{t_2}} \tag{1}$$

A time window of $\Delta t = \pm 0.5$ ms was used for the computation, and the noise levels are evaluated at every 0.1 ms. Figure 10 illustrates the variation of the

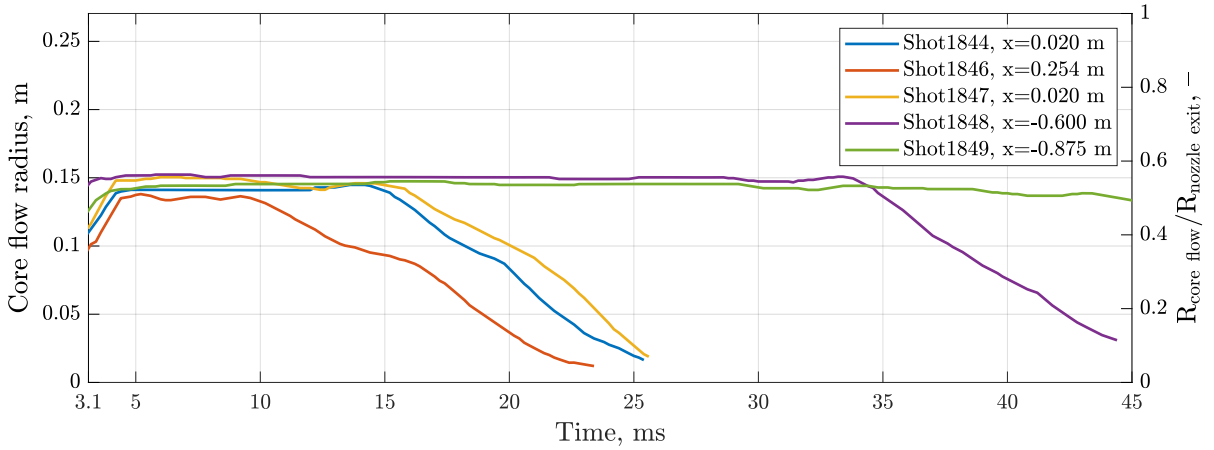

Figure 9: Variation of the core flow radius at several streamwise locations.

noise level in percentage at several streamwise locations. The presented time range is limited to the local useful test times which is limited by large initial transients at arrival of the flow and the closure of the hypersonic jet.

In case of the upstream measurements at $x = -0.600$ m and $x = -0.875$ m, the reference pitot probe and static pressure probe signals indicate that the useful test window reaches up to 38.5 ms and 49 ms respectively, but abrupt fluctuations appeared in the acoustic probe signal around 37.7 ms, which limited the moderately noisy time frame. These fluctuations are probably due the closure of the jet, which is not yet sensed by the other probes since they were located closer to the axis of the nozzle. Moving from downstream of the exit plane upstream into the nozzle yields growing useful test windows. After the significant starting transients at the beginning of the time frame, the noise levels are rapidly fall below 8 %, and are decreasing to 7 %. Regardless of two peaks in the pressure fluctuation at $x = -0.600$ m which yield a short time period of elevated noise, the general level remains between 7-8 %. The mean of the noise levels (indicated as $\overline{\text{Noise}}$) is presented in Table 2. One can observe that the noise levels measured at upstream locations are slightly lower then the downstream ones.

In Fig. 11, the noise levels obtained from an RMS computation for the entire useful test times are plotted against the averaged Reynolds numbers, which are calculated using the local nozzle diameter. As a comparison, the noise levels measured at the Arnold Engineering Development Complex Tunnel No. 9 in [16] at various Mach numbers and Reynolds numbers are also indicated. In the VKI Longshot facility, the noise levels are between 7.3-9.5 %, which is significantly larger then the 3.66-6.24 % measured in the AEDC Tunnel No. 9 at similar Mach numbers. It must be noted, that the AEDC data was acquired at much higher Reynolds numbers and with a significantly larger nozzle. According to the findings of Pate [17], in case of tiny nozzles that have an exit circumference below 305 mm (this corresponds to a diameter of 97 mm), the noise levels are independent of the nozzle dimensions, whereas above this value, they are expected to decrease at increasing nozzle sizes. Lafferty et. al remarked in [16] that the noise levels in Tunnel No. 9 show a logarithmic (linear on this semi-logarithmic plot) decrement with increasing Reynolds numbers. The trendline they obtained ($\%\text{Noise} = -0.0109 \cdot \ln(Re/\text{feet}) + 0.2034$) is also indicated in Fig. 11. Observing the variation of the noise levels measured in the VKI Longshot, it seems to fall closely in line with the AEDC data. Since the Longshot experiments were done at different streamwise locations, such correlation cannot be drawn, but it would be interesting to perform tests at higher Reynolds numbers at the same probe locations, and examine the effect on the noise level. Previous experimental data [12] of the VKI Longshot's Mach 12 Nozzle is also shown in Fig. 11. A cyan diamond is indicating the mean noise level (7.05 %) measured at the exit plane of this nozzle. However the current data-set and the one of [12] were retrieved from different contoured nozzles; one can make a peculiar observation.

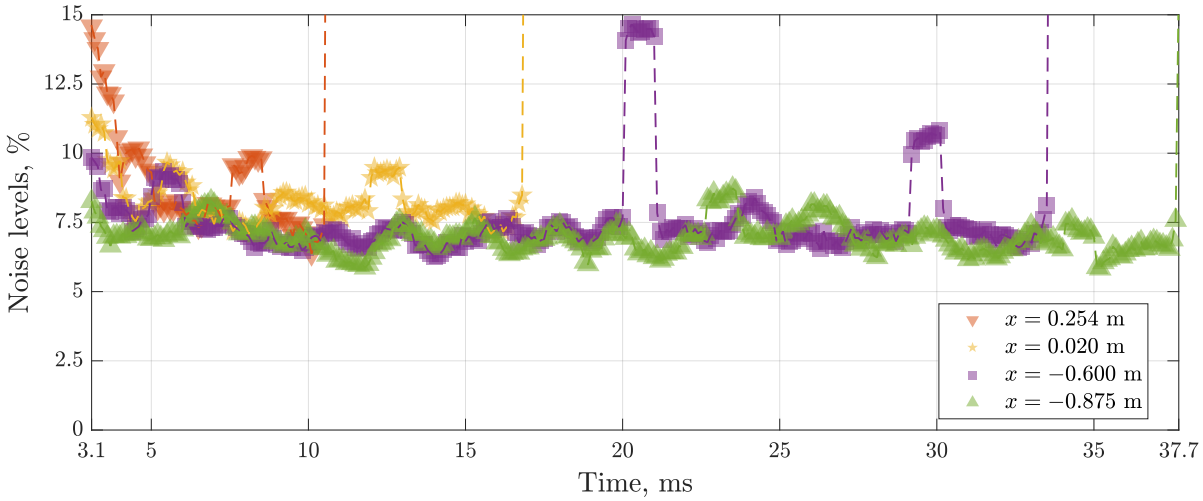

Figure 10: Variation of the noise levels during the useful time frame of the experiments.

The mean of the RMS noise level (8.27 %) measured $x = 0.020$ m downstream of the nozzle exit and the data of [12] form a line with an almost identical slope compared to the Mach 14 trendline of AEDC Tunnel No. 9 [16].

The power spectral density of the pitot pressure fluctuations was computed with Welch's method. Fast Fourier transforms were performed on 512 point, Hamming windowed portions of the dataset, with 256 point overlaps. This yields a frequency resolution of 4.883 kHz. Figure 12 illustrates the power spectral density (PSD) of the pressure fluctuations before the experiments without flow, and during the useful time frame of runs. The frequency axis of the figure is limited to the bandwidth of the sensor, and the PSD is given in Pa^2/Hz and $psia^2/Hz$. The spectra of the two upstream and two downstream experiments are showing a coalescence, and it is clearly visible that the former ones are reaching lower amplitudes. A sharp Z-shaped decay is visible around 300 kHz which is in the range of the sensor's natural frequency. Above 850 kHz, the magnitude of the experiments' spectra approaches the one of the background noise, but this part gives a small contribution to the total fluctuation.

Similarly to [18], the noise levels were also estimated based on the RMS obtained from the frequency spectra by the integration of the PSD. Since the bandwidth of the acoustic probe is limited from 11 kHz to 1 MHz, the integration is performed over this range only. An attempt was made to retrieve the noise content of the lower frequency spectra from the reference pitot probe installed on the side of the rake. Due to the fact that the pressure transducer of this probe is inside a small cavity after a pressure tap, the frequency response is much lower than in the case of flush mounted probes. A conservative estimation based on the Helmholtz resonator model yields a cut-off frequency of 4.955 kHz for this pitot probe. This is bounded from the low frequency range by a high-pass frequency of 453.6 Hz due to the moving average computation used to obtain only the fluctuations. The PSD was computed with Welch's method with the same parameters as the acoustic probe, yielding a frequency resolution of 200 Hz. In order to compute the total noise, the contribution of the probes were summed by integrating their power spectral densities over the respective bandwidths $\left(B_{p_{t_2}}\right.$ and $\left.B_{p'_{t_2}}\right)$, and the square root of the total area was divided by the mean pitot pressure according to:

$$\text{Noise} = \frac{\sqrt{\int_{B_{p_{t_2}}} \text{PSD}\left(p_{t_2}\right)\, df + \int_{B_{p'_{t_2}}} PSD\left(p'_{t_2}\right) df}}{\overline{p_{t_2}}} . \tag{2}$$

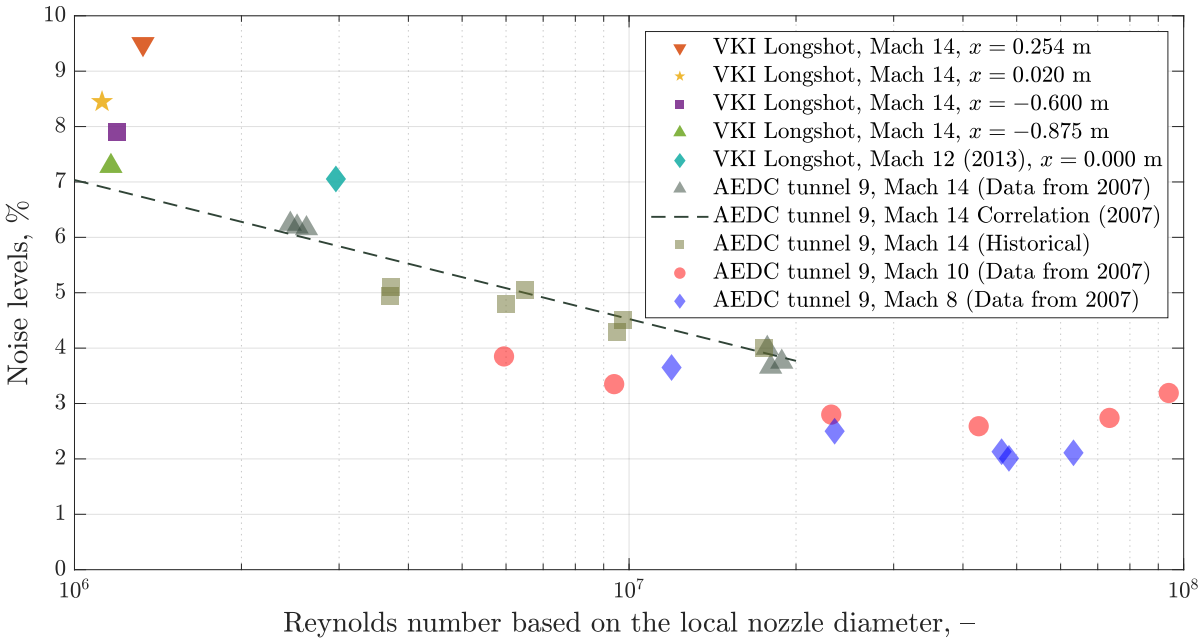

Figure 11: Comparison of the RMS-based noise levels measured in the VKI Longshot facility and in the AEDC Hypervelocity Wind Tunnel No. 9.

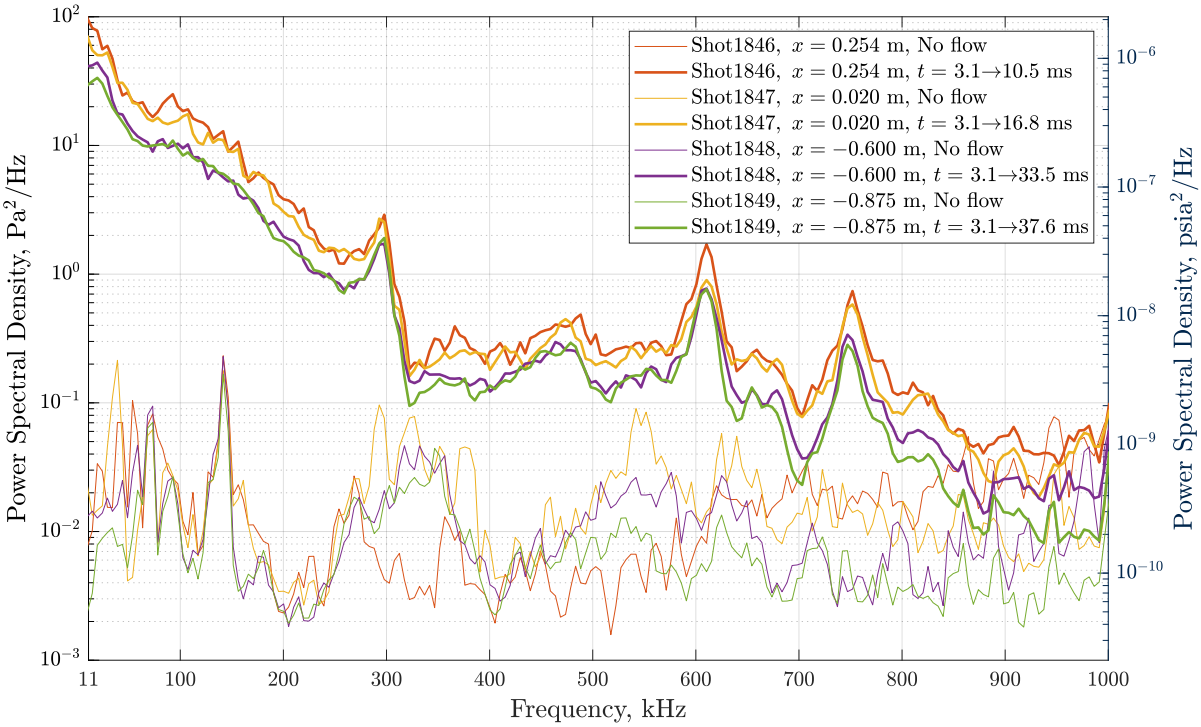

Figure 12: Power spectral density of the pressure fluctuations before and during experiments.

The tunnel noise levels obtained with the two methods are summarized in Table 2. Relying on the PSD-based computation and focusing only on the bandwidth of the acoustic probe yields significantly (0.36-1.70 %) lower noise levels than the RMS-based approach applied to the entire useful time frame. This contrasts the results of [18], where one can observe in a few cases higher noise resulting from the PSD-based computation, and in general, only a slight difference between the two techniques. The PSD-based results of this work are also inferior to the means of the RMS-based noise levels computed for 1 ms time windows, which indicates the presence of notable low-frequency electronic noise contaminating the signal of the acoustic probe. It was observed that the test to test variation between the total noise levels estimated using the PSD is around half or less compared to the RMS approach. The noise computed for the pitot probe are around 4.4 %. Combining the noise from the PSD of the two probes overestimates the full range RMS computations, and yield total noise levels between 8.06-9.21 %.

5. Conclusion

A measurement campaign was conducted in order to commission the new Mach 14 hypersonic nozzle of the VKI Longshot wind tunnel. A probe configuration consisting of a Pitot rake, a reference total pressure probe, a static pressure probe, a heat-flux probe, and an acoustic probe were applied, and tests were performed at similar operating conditions at various streamwise probe positions. Although the experiments were conducted at free-stream Reynolds numbers $Re \approx 2.3 \cdot 10^6$ 1/m, its thorough analysis and the investigation of the Mach number distribution along the nozzle remains to be part of the future work.

The horizontal and vertical pitot profiles measured at $x = 0.020$ m showed a fine agreement within the boundary layer. A good uniformity with irregularities around 2.5 % was observed in the pitot pressure distribution inside the inviscid core of the flow at $x = 0.020$ m and $x = 0.254$ m downstream of the nozzle exit. The results obtained in this work will serve as comparison data and support the numerical modeling of the hypersonic flow inside the nozzle. To verify the symmetry of the pitot profile, supplementary test could be done by centering the rake on the nozzle axis.

Table 2: Tunnel noise levels computed from the RMS-based and the PSD-based calculation.

Test Nr.	**Streamwise location**	**Method**	$\overline{\text{Noise}}$, % RMS(p'_{t_2})	Noise, % RMS(p'_{t_2})	Noise, % PSD(p'_{t_2})	Noise, % PSD(p_{t_2})	Total noise, % PSD(p'_{t_2}, p_{t_2})
		Range	Δt = 1 ms	Entire range	11 kHz – 1 MHz	453.6 Hz – 4.955 kHz	p'_{t_2} and p_{t_2} combined
1846	x = 0.254 m	t = 3.1 – 10.5 ms	8.85	9.49	7.79	4.90	9.21
1847	x = 0.020 m	t = 3.1 – 16.8 ms	8.27	8.45	7.82	4.44	8.99
1848	x = −0.600 m	t = 3.1 – 33.5 ms	7.58	7.90	7.27	4.25	8.43
1849	x = −0.875 m	t = 3.1 – 17.6 ms	6.97	7.28	6.92	4.14	8.06

The investigations verified the presence of a thick boundary layer inside the nozzle, yielding a core flow diameter of D_{core} = 0.293 m for a useful test time of 10 ms at x = 0.020 m, and D_{core} = 0.270 m at x = 0.254 m for 6 ms. The available temporal and spatial test windows are bounded by the initial transients present during the establishment of the flow and the closure of the overexpanded hypersonic jet. The current approach for the estimation of the core flow diameter is based on average pressure computation in the zone close to the nozzle axis, whereas it would be interesting to see the possibility of using a fluctuation based technique that marches from the boundary layer.

Two different techniques, the first relying on time-domain (RMS-based) and the second on frequency domain (PSD-based) computations, were used to estimate the tunnel noise levels. The PSD-based technique has the advantage that it allows to consider only a desired range of frequencies, so one can eliminate the low- and/or high-frequency electronic noise outside of the probe's bandwidth, which can pollute the signal. In line with that, significantly lower noise levels were obtained with the PSD-based method compared to the RMS approach. Moreover, the method allows combining the noise levels measured by different probes, which yielded a total, post-shock noise level of 9 % at 0.020 m downstream of the nozzle exit. It would be interesting to add a second acoustic probe to the test configuration which can capture well lower frequency fluctuations. In future work, it would be beneficial to perform numerical simulations on the probes to estimate their transfer functions, which allow the computation of the free-stream noise levels. In addition to that, performing further experiments at the same streamwise locations using different wind tunnel operating conditions would allow us to investigate the effect of the Reynolds number on the free-stream noise levels.

6. Future Work

In the next part of the present doctoral work, the aerodynamics of a ring that interferes with a cylinder (typical space debris shapes) will be investigated experimentally in the VKI Longshot wind tunnel. The ring model will be initially suspended with thin wires upstream to a transversally mounted cylinder. Upon the arrival of the flow, the support wires rupture, allowing the ring to fly freely and cross the two-dimensional shock generated by a stationary cylinder. The measurement setup consists of three probes (Pitot pressure, static pressure, and heat-flux) and a shadowgraph setup coupled with a high-speed camera.

The design of the test configuration (model and probe arrangement) is based on the useful test times, core flow diameters, and typical dynamic pressure behaviour curve determined in the above flow characterization campaign. The shape of the two-dimensional and three-dimensional bow shock generated by the cylinder and the hemispherical heat-flux probe were estimated based on empirical correlations [19]. The shape of the pitot probe's shock was assumed to be similar to the one of the heat-flux probe, while for the static pressure probe the shock contour computed in [7] was used. The sensing location of the probes will be aligned to the same streamwise location, upstream to the passage of the shock generated by the cylinder. The initial position, attitude, and material of the ring was selected by iterating on these conditions and computing trajectories resulting from them using the dynamic pressure variation retrieved from Shot 1844 and the aerodynamic coefficients presented in [20].

Experiments will be performed at various initial ring positions (with respect to the location of the cylinder) and angles of attack. The free-stream flow conditions are to be computed from the probe data using an elaborate rebuilding technique, and the shadowgraph images will permit the tracking of the ring's

motion and the visualization of the flow. The distortions introduced by the optical system will be corrected, and a pixel to millimeter conversion is to be computed using calibration images and objects. The position and attitude of the ring model are going to be retrieved with a synthetic image fitting algorithm in five degrees of freedom, providing the flight trajectory. The analysis of the trajectory yields the aerodynamic forces and moments, which are to be normalized with the free-stream dynamic pressure to compute the aerodynamic coefficients. A comparison will be presented between the aerodynamic coefficients measured in the post-shock region of the stationary cylinder and the aerodynamic coefficients obtained in the free-stream in previous experiments.

Acknowledgments

This doctoral work is funded by a Ph.D. grant of the von Karman Institute for Fluid Dynamics. Much of the current research has been funded by the ESA Contract No. 4000114170/15/NL/KML and by the Air Force Office of Scientific Research under grant number FA8655-20-1-7024. Special thanks of gratitude must be expressed to Ing. Zdeněk Ilich, Ing. Mikel Spillemaekers, and Ing. Sébastien Paris for their help in conducting the experimental test campaign.

References

[1] G. Grossir, O. Chazot, Design of axisymmetric contoured nozzles for calorically and thermallyimperfect gases using the hypnoze code, in: 2nd International Conference on High-SpeedVehicle Science and Technology, CEAS, Bruges, Belgium, 2022, pp. 1–16, under publication. Conference postponed to 11-15 September, 2022.

[2] G. Grossir, B. Dias, Flow characterization of the vki longshot wind tunnel, in: Flow Characterization and Modeling of Hypersonic Wind Tunnels (STO-AVT 325), von Karman Institute for Fluid Dynamics, STO/NATO, Sint-Genesius-Rode, Belgium, 2018, pp. 1–32.

[3] H. Olivier, Thin film gauges and coaxial thermocouples for measuring transient temperatures, Tech. rep., RWTH Aachen, Shock Wave Laboratory, Aachen, DE (2000).

[4] D. Schultz, T. Jones, Heat-Transfer Measurements in Short-Duration Hypersonic Facilities, no. AGARDograph No. 165, NATO Advisory Group for Aerospace Research and Development, Oxford, UK, 1973.

[5] D. R. Buttsworth, T. V. Jones, Radial conduction effects in transient heat transfer experiments, The Aeronautical Journal of the Royal Aeronautical Society 101 (1997) 209–212.

[6] G. Grossir, S. Paris, P. Rambaud, B. Van Hove, Design of static pressure probes for improved free-stream characterization in hypersonic wind-tunnels, in: 52nd Aerospace Sciences Meeting, American Institute of Aeronautics and Astronautics, Inc., National Harbor, Maryland, USA, 2014, pp. 1–19. doi:10.2514/6.2014-1410.

[7] G. Grossir, Longshot hypersonic wind tunnel flow characterization and boundary layer stability investigations, Phd thesis, von Karman Institute for Fluid Dynamics – Université Libre de Bruxelles (Jul. 2015).

[8] G. Grossir, B. Van Hove, S. Paris, P. Rambaud, O. Chazot, Free-stream static pressure measurements in the longshot hypersonic wind tunnel and sensitivity analysis, Experiments in Fluids (5) (2016) 57–64. doi:10.1007/s00348-016-2137-5.

[9] G. Simeonides, Hypersonic shock wave boundary layer interactions over compression corners, Ph. D. thesis, von Karman Institute for Fluid Dynamics - University of Bristol (April 1992).

[10] H. Olivier, An improved method to determine free stream conditions in hypersonic facilities, Shock Waves 3 (2) (1993) 129–139. doi:10.1007/BF02115892.

[11] J. A. Fay, F. R. Riddell, Theory of stagnation point heat transfer in dissociated air, Journal of the Aerospace Sciences 25 (2) (1958) 73–85. doi:10.2514/8.7517.

[12] G. Grossir, S. Paris, K. Bensassi, P. Rambaud, Experimental characterization of hypersonic nozzle boundary layers and free-stream noise levels, in: 51st AIAA Aerospace Sciences Meeting including the New Horizons Forum and Aerospace Exposition, American Institute of Aeronautics and Astronautics, Inc., 2013, pp. 1–16. doi:10.2514/6.2013-1130.

[13] D. G. Kovács, Z. Ilich, G. Grossir, O. Chazot, Experimental Characterization of the VKI Longshot Mach 14 Contoured Nozzle, in: AIAA SciTech 2022 Forum, American Institute of Aeronautics and Astronautics, 2022, pp. 1–22. doi:10.2514/6.2022-1401.

[14] R. S. Chaudhry, G. V. Candler, Computing measured spectra from hypersonic pitot probes with flow-parallel freestream disturbances, AIAA journaldoi:10.2514/1.J055396.

[15] R. S. Chaudhry, G. V. Candler, K. A. Gray, S. P. Schneider, Computations of Measured Pitot-Probe Spectra using Angled Freestream Disturbances and Comparisons to Experiments, in: AIAA Scitech 2019 Forum, 2019, p. 2149. doi:10.2514/6.2019-2149.

[16] J. F. Lafferty, J. D. Norris, Measurements of Fluctuating Pitot Pressure, "Tunnel Noise", in the AEDC Hypervelocity Wind Tunnel No. 9, in: 2007 U.S. Air Force T&E Days, American Institute of Aeronautics and Astronautics, 2007, pp. 1–11. doi:10.2514/6.2007-1678.

[17] S. R. Pate, Dominance of Radiated Aerodynamic Noise on Boundary-Layer Transition in Supersonic-Hypersonic Wind Tunnels. Theory and Application, Tech. Rep. AEDC-TR-77-107, Arnold Engineering Development Center (Mar. 1978).

[18] A. Bounitch, D. Lewis, J. Lafferty, Improved measurements of" tunnel noise" pressure fluctuations in the AEDC hypervelocity wind tunnel No. 9, in: 49th AIAA Aerospace Sciences Meeting including the New Horizons Forum and Aerospace Exposition, American Institute of Aeronautics and Astronautics, 2011, pp. 1–12. doi:10.2514/6.2011-1200.

[19] F. S. Billig, Shock-Wave Shapes around Spherical- and Cylindrical-Nosed Bodies., Journal of Spacecraft and Rockets 4 (6) (1967) 822–823.

[20] G. Grossir, D. Puorto, Z. Ilich, S. Paris, O. Chazot, S. Rumeau, M. Spel, J. Annaloro, Aerodynamic characterization of space debris in the vki longshot hypersonic tunnel using a free-flight measurement technique, Experiments in Fluids 61 (7) (2020) 163–170. doi:10.1007/s00348-020-02995-7.

Influence of ablation on atmospheric entry aerothermodynamics

Ata Onur Başkaya

Aeronautics and Aerospace Department, von Karman Institute for Fluid Dynamics, Belgium, baskaya@vki.ac.be

Supervisor: Thierry Magin

Professor, Aeronautics and Aerospace Department, von Karman Institute for Fluid Dynamics, Belgium, magin@vki.ac.be

University Supervisor: Stefan Hickel

Professor, Aerodynamics Group, Faculty of Aerospace Engineering, TU Delft, the Netherlands, s.hickel@tudelft.nl

Abstract

During atmospheric entry, the hypersonic flow environment around capsules or space debris is characterized by strong shock waves, complex fluid thermochemistry, and gas-surface interactions (GSI). Such interactions could induce material decomposition and mass loss, referred to as ablation, which alters the shape of the object as the surface recesses. Numerical simulations are crucial in developing a better understanding of hypersonic flows, especially as the simultaneous replication of all aspects of these flows is exceptionally challenging in ground tests. A promising approach for the simulation of complex geometries and deforming objects is the use of immersed boundary methods (IBM) and adaptive mesh refinement (AMR) techniques. These methods offer reliable and efficient mesh generation with minimal user intervention and straightforward mesh adaptation to moving shocks and recessing surfaces, which is a significant advantage over classical body-conforming mesh methods.

A flow solver hosting these capabilities is INCA from TU Delft, which is based on a fully conservative cut-element immersed boundary finite volume method for solving the compressible chemically reacting Navier-Stokes equations. For modelling gas-surface interactions, INCA employs the Mutation++ library of the von Kármán Institute. The current project aims to extend the recent developments within the INCA-Mutation++ coupling to propose a novel approach for high-fidelity flow simulations with accurate physicochemical models. First efforts will consider the realization of surface ablation including recession within the cut-element framework, and the development of a remedy for the common anomaly of fluctuating surface quantities in IBM. Then, the focus will be on demonstrating these developments through relevant test cases and investigating laminar to turbulent transition mechanisms under such conditions.

Keywords: Atmospheric Entry, Aerothermodynamics, Gas-Surface Interactions, Ablation, Immersed Boundary Methods, High-Fidelity Simulations, Transition to Turbulence

RAREFIED AND PLASMA FLOWS

Asymptotic preserving method for Euler-Poisson equations

Louis Reboul

Centre de Mathémtatiques Appliquées (CMAP), École polytechnique, France, louis.reboul@polytechnique.edu

Supervisor: Thierry Magin

Professor, Aeronautics and Aerospace Department, von Karman Institute for Fluid Dynamics, Belgium, magin@vki.ac.be

University Supervisor: Marc Massot

Professor, Centre de Mathématiques Appliquées (CMAP), École polytechnique, France, marc.massot@polytechnique.edu

University Supervisor: Alejandro Alvarez-Laguna

Doctor, Laboratoire de Physique des Plasmas (LPP), École polytechnique, France, anne.bourdon@lpp.polytechnique.fr

University Supervisor: Anne Bourdon

Doctor, Laboratoire de Physique des Plasmas (LPP), École polytechnique, France, anne.bourdon@lpp.polytechnique.fr

Abstract

In low-temperature low-pressure plasmas, the presence of small scales (inverse of electron plasma frequency, Debye length) induces restrictive stability conditions imposed on the mesh size and time step of numerical methods when attempting to simulate plasma discharges including sheaths. While PIC methods are reliable but notoriously costly, the attempt to rely on fluid models such as multi-fluid models including the description of sheaths, in order to alleviate this cost pitfall with classical numerical methods (Finite Volumes) is unsuccessful. Such methods suffer accuracy losses due to those small scales and the stability constraints are extreme. In this work we present a so-called asymptotic preserving method of first order that allows to alleviate stability conditions, as well as recover reasonable accuracy for Euler-Poisson system of equations as a typical example of such multi-fluid hierarchy of models. The configurations range from 1D section of a glow discharge to a 2D section of a plasma column; we assess the numerical strategy in such configurations and show that the method is really well-suited for adaptive mesh refinement based on multiresolution analysis leading to error control.

Keywords: Euler-Poisson system of equations, asymptotic-preserving schemes, plasma discharges

1. Introduction

Plasma discharges are present in numerous applications, ranging from electric propulsion to coating or plasma etching. They consist in low-temperature low-pressure partially-ionized gases where electrons and ions are out of thermal equilibrium, see e.g. [1; 2]. Modeling and simulating such plasmas comes with multiple challenges.

From the modeling perspective it is still not well understood which set of equations best suits the physics at stake in ionized gases. Kinetic models are assumed in the low-temperature plasma community to faithfully capture a wide range of phenomena such as instabilities, but are typically associated to higher and sometimes prohibitive simulation costs as we will detail later. In addition, they do not always allow for interpretations due to their complexity. On the other hand, fluid models directly manipulate macroscopic quantities, such as temperature or pressure, and can yield intuitive comprehension of studied phenomena. Consequently, in multiple instances simple fluid models can be used to understand the onset of instabilities and to derive dispersion relations to characterize those instabilities, see e.g. [3; 4; 5]. However, one of the downsides of fluid models is that they require

additional effort in order to incorporate phenomena that occur at kinetic level, in regimes for which the assumptions that sustain the validity of fluid models no longer hold. A typical example is that of the plasma-wall interaction, where a boundary layer called the sheath forms and can essentially only be described at the level of kinetic scales, see [1; 2]. It is however possible to include to some extent this type of dynamics in fluid models, see e.g. [6].

Whether kinetic or fluid approaches are considered, obtained models involve intricate nonlinear equations that, except for the simplest of applications or in some very specific regimes, cannot be solved analytically. As a result it is necessary to use numerical methods to solve those equations. A popular method in the low-temperature plasma community is the so-called Particle-in-cell approach, that consist in solving the kinetic equations in a stochastic manner involving macro-particles interacting via an electrostatic field, with Monte-Carlo integration of the collision operators (see e.g. [7]). PIC methods have proven to simulate accurately a variety of configurations and phenomena. However, due to the fact that they solve the full particle distribution functions (PDFs), which are functions of both the position and the velocity (six dimensions in 3D), for each species present in the gas, they come at great computational cost. Such level of computational effort becomes intractable for reasonable 3D-configurations (see [8]). An alternative is to use numerical methods that discretize the aforementioned fluid models. We will refers to such methods in what follows with the slightly abusive denomination *fluid numerical methods*. Since they involve macroscopic quantities that only depend on the position, such as the density of particles, their macroscopic velocity or temperature, they have the potential to be used for 3D configurations very efficiently.

Nevertheless, challenges in using fluid numerical methods are not limited at incorporating relevant kinetic effect. Indeed, the nonlinear hyperbolic equations that naturally arise in plasma models introduce the problematic of shocks that can form from smooth initial data in finite time. A well known class of numerical methods that can tackle this issue is that of Finite Volume methods (FVM, see [9; 10]). However coupling theses methods, originally designed for hyperbolic balance laws, with source terms is a nontrivial problem and can become challenging in the case of stiff dynamics. The multi-scale nature of plasma physics precisely induces stiffness in the source terms that stem from electrostatic interactions, namely the Lorentz force applied to charged particles. Electrons have a much smaller mass than that of the other particles (ions and neutrals) present within the gases, meaning their characteristic time scale of evolution is much smaller than the typical period of time during which we wish to observe our macroscopic system. The Debye length, which is the characteristic distance over which electrostatic interactions are screened within the plasma, is also much smaller than the typical size of plasma discharges. One needs to solve those fine time and space scales for the classical numerical methods to be stable and not trigger nonphysical oscillations in simulations. As a result the stability constraints on both the time step Δt and the mesh size Δx are very restrictive which makes the classical fluid methods inefficient, loosing in essence their advantage over kinetic approaches. Moreover, the numerical viscosity introduced in those methods to ensure that the numerical scheme does not trigger spurious oscillations can become excessive in this multi-scale context resulting in results lacking accuracy.

In previous work [11], we showed that it was possible to recover reasonable accuracy using a so-called low-Mach correction applied to classical finite volume methods. Obtained results showed good agreement with PIC simulations and validated both the low-order model that was used as well as the numerical approach. Nonetheless, this correction comes at a significant computational cost. In the present work we introduce an asymptotic-preserving method that both achieves good accuracy in spite of the stiffness of the problem as well as lifts some of the stability constraints, allowing to choose larger time step Δt and mesh size Δx, resulting in a much more efficient method.

So-called *asymptotic-preserving* methods are used to overcome such stability and accuracy difficulties that are encountered for a wide variety of equations featuring small parameters [12; 13; 14; 15; 16; 14; 17; 18; 19; 20]. In the specific case of isothermal Euler-poisson equations, that we will introduce here as our model, several asymptotic-preserving approaches exist in the literature [21; 22]. The method developed in this work distinguishes itself from such approaches by the fact that it does not need to use a modified version of the Poisson equation nor a Lagrangian splitting (details can be found in the main body of the paper), resulting in an easier implementation process, and sets itself in framework that can in theory be extended to higher order of accuracy.

In section 2 we detail the model considered in this work and briefly introduce the notion of asymptotic regime. In section 3 we analyze the limitations of

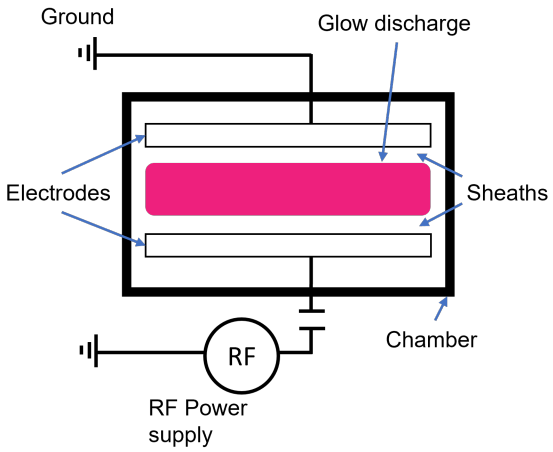

Figure 1: Example of a glow discharge

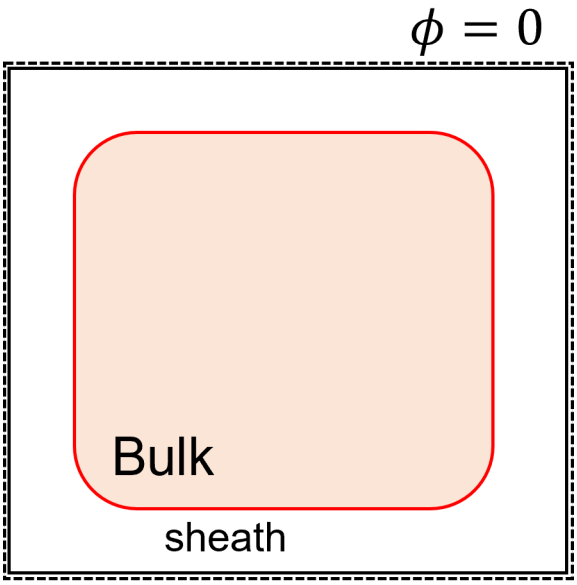

Figure 2: 2D section of a plasma column, with walls set at electric potential $\phi = 0$

classical methods such as the finite volume approach. We describe our new asymptotic-preserving method in section 4 and exhibit its performances in section 5.

2. Model and asymptotic regimes

2.1. Model and assumptions

Typical configurations that we consider in this work are 1D configurations that represent glow discharges (see Figure 1), and 2D configurations corresponding to the section of plasma column (see Figure 2).

Such configurations are representative of the various challenges posed by the small scales identified in the introduction. Indeed the size of the sheath is of the order of the Debye length, much smaller than the macroscopic size of the device, the ratio can be commonly as small as 10^{-4} [1] (disparity of spatial scales). Moreover, within the sheath the macroscopic velocity of electrons becomes comparable to their thermal velocity, which mean their inertia cannot be neglected as is customary and therefore their fast scale of evolution must be incorporated in our modeling efforts (disparity of time scales).

To alleviate our notations and avoid superfluous technical computations we will present the model only the 1D case. However, the method produced in this project has been extended to 2D configurations and 2D numerical results will be presented in section 5.

Our model features two fluids, ions and electrons. The behavior of each fluid is described by collisionless isothermal Euler equations, and the two fluids are coupled by an electric field computed via the Poisson equation. It is possible to derive these equations by integrating the two first moments of kinetic equations on ions and electrons, see for instance [23]. The model reads:

$$\partial_t n_e + \partial_x (n_e u_e) = \nu^{iz} n_e \tag{1a}$$

$$\partial_t (n_e u_e) + \partial_x \left(n_e u_e^2 + p_e\right) = -q_e n_e \partial_x \phi \tag{1b}$$

$$\partial_t n_i + \partial_x (n_i u_i) = \nu^{iz} n_e \tag{1c}$$

$$\partial_t (n_i u_i) + \partial_x \left(n_i u_i^2 + p_i\right) = -q_i n_i \partial_x \phi \tag{1d}$$

$$-\partial_{xx}^2 \phi = \frac{q_e n_e + q_i n_i}{\epsilon_0} \tag{1e}$$

with n_e and n_i the number densities of the fluid of electrons and ions respectively, u_e and u_i the corresponding macroscopic velocities, p_e and p_i the pressure terms, $q_e = -e$ and $q_i = +e$ with e the elementary charge, ϕ the electric potential, ϵ_0 the permittivity of the void and ν^{iz} the ionization rate, computed via for instance the Arrhenius law. The pressure terms are computed via the law of perfect gases:

$$p_e = n_e \mathrm{k_B} T_e, \tag{2}$$

$$p_i = n_i \mathrm{k_B} T_i. \tag{3}$$

where the temperature of electrons T_e and ions T_i are assumed to be constant in this isothermal model, and $\mathrm{k_B}$ stands for the Boltzmann constant. Because they are not central to the asymptotic behaviors that we

consider in the present work, we neglected collisions in this model. It would be possible, however, to readily incorporate the effect of neutral-charge collisions in this approach.

The key aspects of this modeling approach are:

- electron inertia is not neglected, that is we do not make the approximation that $u_e \approx 0$
- quasi-neutrality is not assumed, that is we do not assume that $n_e = n_i$
- fluxes are not assumed to be ambipolar, that is it is not required that $n_e u_e = n_i u_i$
- the plasma is out of thermal equilibrium, that is we do not necessarily have $T_e = T_i$

2.2. Normalized equations

In order to explicitly exhibit the various scales present in this problem we normalize the equations using as reference quantities n_0 the characteristic density of electrons and ions (typically the initial number density of ions averaged over the domain of simulation), L_0 the characteristic macroscopic length of the configuration (for instance the side of the square domain in 2) and T_e the temperature of electrons (assumed constant in our model). From these reference quantities we can derive other characteristic quantities, namely, the Bohm velocity $u_0 = \sqrt{\mathrm{k_B} T_e/m_i}$, that is the velocity at which ions enter the sheath, the characteristic time of evolution of ions in the sheath area $t_0 = L_0/u_0$ and the characteristic electric potential $\phi_0 = \mathrm{k_B} T_e/e$. The normalized set of equations reads:

$$\partial_{\bar{t}} \bar{n}_e + \partial_{\bar{x}} \left(\bar{n}_e \bar{u}_e\right) = \bar{\nu}^{iz} \bar{n}_e \tag{4a}$$

$$\partial_{\bar{t}} \left(\bar{n}_e \bar{u}_e\right) + \partial_{\bar{x}} \left(\bar{n}_e \left(\bar{u}_e^2 + \varepsilon^{-1}\right)\right) = \varepsilon^{-1} \bar{n}_e \partial_{\bar{x}} \bar{\phi} \tag{4b}$$

$$\partial_{\bar{t}} \bar{n}_i + \partial_{\bar{x}} \left(\bar{n}_i \bar{u}_i\right) = \bar{\nu}^{iz} \bar{n}_e \tag{4c}$$

$$\partial_{\bar{t}} \left(\bar{n}_i \bar{u}_i\right) + \partial_{\bar{x}} \left(\bar{n}_i \left(\bar{u}_i^2 + \kappa^{\frac{1}{2}}\right)\right) = -\bar{n}_i \partial_{\bar{x}} \bar{\phi} \tag{4d}$$

$$\partial^2_{\bar{x}\bar{x}} \bar{\phi} = \chi^{-1} \left(\bar{n}_e - \bar{n}_i\right) \tag{4e}$$

with $\varepsilon = m_e/m_i$ is the mass ratio, $\kappa = T_i/T_e$ the temperature ratio, $\chi = \left(\mathrm{k_B} T_e \epsilon_0\right) / \left(e^2 n_0 L_0^2\right) = \lambda_D^2/L_0^2$ the squared Debye length normalized by the scale of our problem, $\bar{\nu}^{iz} = \nu^{iz} t_0$.

Here the Debye length λ_D naturally appeared in our system of equations as a characteristic length linked to to the Poisson equation and electrostatic length. In practice because charged particles tend to move in order to cancel electric fields within the plasma electrostatic interactions are screened over a few times the Debye length. Charge separation can only occur on scales of the order or below the Debye length. As a result the Debye length also corresponds to the characteristic thickness of the sheaths.

2.3. Ionization rate and boundary conditions

In practice $\bar{\nu}^{iz}$ is computed dynamically to compensate for the loss of ions by recombination at the walls, that is to ensure $\partial_{\bar{t}} \int_{\bar{\Omega}} \bar{n}_i \mathrm{d}\bar{V} = 0$, or integrating the ion mass conservation equation (4c):

$$\begin{aligned} \int_{\bar{\Omega}} \bar{\nabla}.\left(\bar{n}_i \bar{\mathbf{u}}_i\right) \mathrm{d}\bar{V} &= \int_{\bar{\Omega}} \bar{n}_e \bar{\nu}^{iz} \mathrm{d}\bar{V} \\ \Leftrightarrow \bar{\nu}^{iz} &= \frac{\int_{\partial\bar{\Omega}} \bar{n}_i \bar{\mathbf{u}}_i \cdot \mathrm{d}\bar{\mathbf{S}}}{\int_{\bar{\Omega}} \bar{n}_e \mathrm{d}\bar{V}}. \end{aligned} \tag{5}$$

The ionization rate can be seen as an eigenvalue of the problem in the sense that not only do we solve for profiles of densities and currents but also for the only possible value of $\bar{\nu}^{iz}$ corresponding to the considered setting. This is usually the case for steady state profiles and is enforce here dynamically to ensure that the ion mass remains constant throughout the simulation.

Regarding the boundary conditions, we assume that the flux of electrons at the wall is the random flux and that electrons have Maxwellian distribution function, which is equivalent to imposing outgoing fluxes of norm $|\bar{n}_e \bar{u}_e| = \bar{n}_e/\sqrt{2\pi\varepsilon}$. This relatively simple boundary condition can be used to incorporate the sheaths into our model [6], although it relies on the rather strong assumption that electrons have a Maxwellian distribution and neglects more complex kinetic phenomena such as secondary electron emission.

2.4. Asymptotic regimes

The presence of the small parameter ε and χ allow to formally define the notion of asymptotic regimes.

The first asymptotic regime that we examine is called low-Mach regime for electrons. It is tied to the mass ratio ε, because the normalized thermal velocity of electron is $\bar{c}_e = \sqrt{\mathrm{k_B} T_e/m_e}/u_0 = 1/\sqrt{\varepsilon}$ and consequently the Mach number of electron reads $M_e = \bar{u}_e/\bar{c}_e = \varepsilon^{-1/2} \bar{u}_e$. Thus in the regime $\varepsilon \to 0$ we have $\bar{u}_e \ll \bar{c}_e = \varepsilon^{-1/2}$ or $M_e \ll 1$, hence the name low-Mach regime. In the limit $\bar{u}_e^2 \ll \varepsilon^{-1}$ equation (4d) leads to the Boltzmann relation:

$$\frac{\partial_{\bar{x}} \bar{n}_e}{\bar{n}_e} = \partial_{\bar{x}} \bar{\phi} \tag{6}$$

In this regime the inertia of electrons is neglected.

The second asymptotic regime that we consider is named quasi-neutral regime. It stems from equation

(4e) in the limit $\chi \to 0$. In this limit we formally have, in order to avoid $\partial^2_{\bar{x}\bar{x}}\bar{\phi} \to \infty$, that necessarily $|\bar{n}_e - \bar{n}_i| \to 0$ or $\bar{n}_e \sim \bar{n}_i$, meaning that the space charge is close to zero and that the gas is consequently nearly neutral.

The main challenge that we are going to address in what follows is that classical numerical schemes, used to produce approximations of the solutions to equations (4), do not naturally preserve these asymptotic limits. In particular, the numerical viscosity that is introduced by classical method in order to ensure the scheme stability becomes unnecessarily large and dramatically reduces the accuracy of the scheme. Moreover, CFL-like stability conditions become more and more restrictive in the regimes where $\varepsilon \to 0$ and $\chi \to 0$. In the next section we detail the method that will stand as the reference classical method as well as the mechanisms responsible for its inaccuracy and inefficiency.

One could be led to believe that it is simply possible to choose either equation (4b) or (6) and to solve or not the Poisson equation (4e) depending on the regime that is considered. However, a first obstacle to this approach is that there exist intermediate regimes, which already contain the difficulties associate to regimes $\varepsilon \to 0$ and $\chi \to 0$ but are not accurately solved using the Boltzmann relation (6) or bypassing the Poisson equation (4e). Another difficulty comes from configurations that feature several regimes. Typically, for the configuration depicted in Figure 2, the approximation $\bar{u}_e \ll \bar{c}_e$ is verified within the bulk of the plasma but breaks down in the vicinity of the walls in the sheath, where we impose via the boundary condition that $|\bar{u}_e| = \bar{c}_e/\sqrt{2\pi}$. Similarly, the assumption that the plasma is quasi-neutral is fairly verified within the bulk but does not hold in the sheath. This will lead to the necessity to devise a scheme that can handle the full scope of the configuration considered in Figure 2.

3. Classical method and limitation

3.1. Presentation of classical methods

For each fluid, electrons and ions, we can rewrite equations (4) under the form:

$$\partial_t \boldsymbol{w} + \partial_x \boldsymbol{f}(\boldsymbol{w}) = \boldsymbol{S}(\boldsymbol{w}) \tag{7}$$

where we have:

$$\boldsymbol{w} = \begin{pmatrix} n \\ nu \end{pmatrix},\ \boldsymbol{f}(\boldsymbol{w}) = \begin{pmatrix} nu \\ nu^2 + nc^2 \end{pmatrix},\ \boldsymbol{S}(\boldsymbol{w}) = \begin{pmatrix} \bar{n}_e \bar{\nu}^{iz} \\ -qn\partial_{\bar{x}}\bar{\phi} \end{pmatrix}$$

with for electrons $c = \varepsilon^{-1/2}$ and $q = -1$ and for ions $c = \kappa^{1/2}$ and $q = +1$. We will refer to equations of the form (7) as hyperbolic systems of conservation laws with source term in the sense that if we were to set $\boldsymbol{S}(\boldsymbol{w}) = 0$ then (7) would become hyperbolic, meaning the jacobian matrix of $\boldsymbol{f}$ only has real eigenvalues and its the set of the corresponding eigenvector forms a full basis of the considered vector space [24].

Our goal is to compute an approximation of the solution on 1D Cartesian mesh spanning a normalized domain $\Omega = [0, 1]$ at some discrete point in time. More precisely we wish to devise $\boldsymbol{w}_j^n$ an approximation of the quantity $\int_{C_j} \boldsymbol{w}(x, t^n)\,\mathrm{d}x$ with $C_j = [x_{j-1/2}, x_{j+1/2}]$, $x_{j+1/2} = j\Delta x$, $1 \le j \le N$, $N \ge 1$, and $t^n = n\Delta t$, $n \ge 1$.

Nonlinear hyperbolic systems of conservation laws are known to potentially generate shocks in finite time from smooth initial data. In order to deal with this specific aspect, it is customary to use Finite Volume Methods [10; 9], which are method specifically designed to avoid triggering spurious numerical oscillations in the vicinity discontinuities by mean of a so-called numerical diffusion, a concept we will detail at the end of the present section. Consequently we use such approach on the left-hand side of equations (4), also referred to, in what follows, as the convective side of the equations.

Nonetheless, equations (4) are not purely hyperbolic, they feature source terms (Lorentz force and ionization terms) and are coupled to the Poisson equation (4e). The coupling with electrostatic forces introduces several stability constraints. First of all, if the source term is treated in a purely explicit manner, the obtained numerical scheme is unconditionally unstable on periodic domains, see [25]. As a result it is required that the mass equations (4a) and (4c) be computed before the Poisson equations (4e).

In order to comply with this constraint, we will compute an approximate solution of Equation (4) using a splitting (see for instance [9; 26; 27]) where first the convective step is conducted:

$$\boldsymbol{w}_j^* = \boldsymbol{w}_j^n - \frac{\Delta t}{\Delta x}\left(F_{j+1/2}^n - F_{j-1/2}^n\right), \tag{8}$$

then the electric potential $\bar{\phi}_j\left(\boldsymbol{w}_j^*\right)$ and the ionization rate $\bar{\nu}^{iz}\left(\boldsymbol{w}_j^*\right)$ are computed respectively with the Poisson equation (4e) and equation (5). Finally the source term step is incorporated to the numerical solution:

$$\boldsymbol{w}_j^{n+1} = \boldsymbol{w}_j^* + \Delta t \boldsymbol{S}\left(\boldsymbol{w}_j^*\right). \tag{9}$$

Regarding the convective step, we use an approximation for the fluxes at the interface of the form $F^n_{j+1/2} = \mathcal{F}\left(\boldsymbol{w}^n_j, \boldsymbol{w}^n_{j+1}\right)$ where we use a modified Lax-Friedrichs (or Rusanov) scheme:

$$\mathcal{F}\left(\boldsymbol{w}_L, \boldsymbol{w}_R\right) = \frac{\boldsymbol{f}\left(\boldsymbol{w}_L\right) + \boldsymbol{f}\left(\boldsymbol{w}_R\right)}{2} - \frac{\lambda_{max}}{2}\left(\boldsymbol{w}_R - \boldsymbol{w}_L\right), \tag{10}$$

with $\lambda_{max} = \max\left(|\bar{u}_L|, |\bar{u}_R|\right) + c$, which is the norm of the maximum eigenvalue that appears in the convective part of the equations.

The Poisson equation is solved using the classical second order approximation:

$$\frac{\bar{\phi}^*_{j+1} - 2\bar{\phi}^*_j + \bar{\phi}^*_{j-1}}{\Delta x} = \chi^{-1}\left(\bar{n}^*_{e_j} - \bar{n}^*_{i_j}\right) \tag{11}$$

Finally the ionization has been computed via the formula:

$$\left(\bar{\nu}^{iz}\right)^* = \frac{\sum_j \bar{n}^n_{i_j}\Delta x - \sum_j \bar{n}^*_{i_j}\Delta x}{\Delta t \sum_j \bar{n}^*_{e_j}\Delta x} \tag{12}$$

that ensures that the mass of ion within the domain Ω remains constant even at numerical level. Since the convective step (8) is conservative this is equivalent to a discrete version of (5).

Regarding boundary conditions, we impose homogeneous Neumann boundary condition (see [10]) on all variables except electron momentum for which we impose a second order discretization of the Dirichlet boundary condition of interest, that is:

$$\frac{(\bar{n}_e\bar{u}_e)_G + (\bar{n}_e\bar{u}_e)_B}{2} \cdot e_n = \bar{n}_{e_B}\sqrt{\frac{1}{2\pi\varepsilon}} \tag{13}$$

where the index G stands for the customarily used ghost cells, that are cells outside of the physical domain entirely defined by the boundary conditions to complete the scheme, with index 0 and $N+1$, and the index B stands for cells within the domain located at its boundaries (index 1 and N), and $e_n = \pm 1$ is the outgoing norm.

3.2. Analysis of the limitations of classical methods

Let us now analyse the main properties of this classical approach.

Firstly, in terms of stability constraints, the convective step requires the condition

$$\frac{\Delta t}{\Delta x} \leq \frac{1}{2\max_j \lambda_{max_{j+1/2}}}, \tag{14}$$

to hold in order to prevent the scheme from producing spurious oscillations around discontinuities (in particular around shocks). This include the value of λ_{max} at the boundary of the domain, that is $\lambda_{max} = \left(1 + 1/\sqrt{2\pi}\right)/\sqrt{\varepsilon}$. Next come the stability condition specific to the coupling with the Poisson equation (4e) (see [25]), namely:

$$\Delta x \leq \sqrt{\chi} = \lambda_D/L_0. \tag{15}$$

Combining these two conditions leads to the constraint:

$$\Delta t \leq \sqrt{\varepsilon\chi} = \bar{\omega}^{-1}_{pe} \tag{16}$$

where $\bar{\omega}_{pe} = \omega_{pe}t_0$ is the normalized electron plasma frequency with $\omega_{pe} = c_e/\lambda_D = \sqrt{\frac{e^2 n_0}{m_e\epsilon_0}}$, that is the characteristic frequency at which electrons oscillate within the plasma. These two constraints can be extremely restrictive, especially when combined together. Typically, for an Argon RF discharge at 1 Pa [1] the macroscopic scale of the device is of the order of a few centimeters while the Debye length λ_D is 1.5×10^{-4} m. The ratio between the mass of ions and that of electrons is 1.36×10^{-5} resulting in a plasma frequency ω_{pe} of 1.77×10^{-10} s^{-1} whereas the characteristic time for the formations of the sheaths for instance is of the order of a few microseconds. Finally, the temperature of ions and electrons are respectively $T_i = 0.05$ eV and $T_e = 2$ eV. All in all this leads to the value for a typical Argon low-pressure inductively coupled discharge: $\varepsilon = 1.36 \times 10^{-5}$, $\kappa = 0.025$, $\lambda_D/L_0 = 3.5 \times 10^{-3}$, hence $\bar{\omega}_{pe} \approx 10^4$ leading to the necessity of conducting tens of thousands of steps in order to simulate only a few microseconds. Consequently, a first objective in devising new methods is to lift, at least to some extent, the stability constraints of the classical methods in order to obtain less time-consuming simulations in regimes where $\varepsilon \to 0$ and $\chi \to 0$.

Secondly, such methods also suffer from accuracy loss the mass ratio and normalized Debye length are small. In order to demonstrate the impact of these asymptotic regimes on the precision of the classical methods we use truncation error analysis, that is we assume the solution is smooth and we inject Taylor-expansions into the approximate fluxes (10):

$$F^n_{j+1/2} = \boldsymbol{f}\left(\boldsymbol{w}^n_{j+1/2}\right) + \frac{\lambda_{max}\Delta x}{2}\partial_x \boldsymbol{w}^n_{j+1/2} + O\left(\Delta x^2\right) \tag{17}$$

Usually this approximation is first order, with its first term, $\left(\boldsymbol{f}\left(\boldsymbol{w}^n_j\right) + \boldsymbol{f}\left(\boldsymbol{w}^n_{j+1}\right)\right)/2$, being a second order approximation of the flux at the interface and its second term, $\lambda_{max}/2\left(\boldsymbol{w}^n_{j+1} - \boldsymbol{w}^n_j\right)$, customarily called numerical diffusion [10; 9], that is there to ensure stability and avoid the development of spurious oscillation and

which scales as Δx, hence going to zero as a first order of Δx. However, within the region of the sheath (see figure Figure 2) we have $\lambda_{max}/2 \sim \bar{c}_e = \sqrt{\varepsilon}$ and $\|\partial_x \boldsymbol{w}^n_{j+1/2}\| \sim n_0/\sqrt{\chi}$. As result, the leading term in the truncation error analysis is of the form $\Delta x/\sqrt{\varepsilon\chi} = \bar{\omega}_{pe}\Delta x$. But we have shown that the normalized plasma frequency $\bar{\omega}_{pe}$ is typically of the order of 10^4, which means that in order to have a negligible leading error term we need at the very least that Δx be of the order of 10^{-6}. This mesh size corresponds to a million cells in 1D and a trillion cells 2D, with a billion time steps. Considering that we have to solve the Poisson equation (4e) at each step, it is unrealistic to apply this method to physical configuration. In practice, this means that only light gases (for instance gases made of protons and electrons) can be simulated. Carefully addressing this accuracy losses in regimes where $\varepsilon \ll 1$ and $\chi \ll 1$ is therefore of paramount importance when designing numerical methods destined to simulate such configurations.

In the next section, we present a class of methods that can maintain both efficiency and accuracy throughout the different asymptotic present in the configuration of interest in our work.

4. Asymptotic-preserving scheme

Asymptotic-preserving (AP) methods can be defined in several ways. A first definition is that the limit of the numerical scheme when the small parameters go to zero is a consistent discretization of the limit of the continuous equation (see [20; 19]). Formally, this means that the scheme automatically switches to a suitable form depending on the regime. Another, more quantitative way to define AP methods is that their CFL conditions should not collapse to zero as small parameter do, and that their truncation error should remain uniformly bounded in all regime (see [14]). This is for instance not the case for the classical methods presented in the previous section, since the time step must be smaller than the inverse electron plasma frequency and since the truncation error scales as a non-negative power of the inverse of the product of the small parameters present in our problem. There exist multiple sets of equations that feature small parameters and for which AP-methods have been developed [12; 13; 15; 16; 17; 18].

In this section we first review briefly existing AP-scheme specifically for the isothermal Euler-Poisson equations (4) and then present a new simpler approach which retains the main advantages of the preexisting approaches, in line with our objective to produce an accurate and efficient method readily available to the low-temperature plasma community.

4.1. Existing asymptotic-preserving strategies

To our knowledge there currently exists only two AP-schemes for the isothermal Euler-Poisson equations (4), namely [21; 22].

We first present the strategy of [22]. The idea behind this scheme stems from the initial consideration that in the regime $\chi \to 0$, equation (4e) becomes singular and leads to $\bar{n}_e = \bar{n}_i$. However, equation (4e) is originally intended to yield the electric potential $\bar{\phi}$. This raises the natural question of how the electric potential is to be derived in this regime? The method used in [22] consists in considering, for smooth enough solutions, an extension of the Poisson equation (4e). We present the steps used to obtain this non-singular equation on the electric potential. First, we differentiate the mass equations (4a) and (4c) with respect to time:

$$\partial^2_{\bar{t}\bar{t}}\bar{n}_e + \partial^2_{\bar{t}\bar{x}}\left(\bar{n}_e\bar{u}_e\right) = \bar{\nu}^{iz}\partial_{\bar{x}}\bar{n}_e, \tag{18a}$$

$$\partial^2_{\bar{t}\bar{t}}\bar{n}_i + \partial^2_{\bar{t}\bar{x}}\left(\bar{n}_i\bar{u}_i\right) = \bar{\nu}^{iz}\partial_{\bar{x}}\bar{n}_e. \tag{18b}$$

Then the momentum equations (4b) and (4d) are differentiated with respect to space:

$$\partial^2_{\bar{x}\bar{t}}\left(\bar{n}_e\bar{u}_e\right) + \partial^2_{\bar{x}\bar{x}}\left(\bar{n}_e\left(\bar{u}_e^2 + \varepsilon^{-1}\right)\right) = \varepsilon^{-1}\partial_{\bar{x}}\left(\bar{n}_e\partial_{\bar{x}}\bar{\phi}\right), \tag{19a}$$

$$\partial^2_{\bar{x}\bar{t}}\left(\bar{n}_i\bar{u}_i\right) + \partial^2_{\bar{x}\bar{x}}\left(\bar{n}_i\left(\bar{u}_i^2 + \kappa^{\frac{1}{2}}\right)\right) = -\partial_{\bar{x}}\left(\bar{n}_i\partial_{\bar{x}}\bar{\phi}\right). \tag{19b}$$

Assuming that the solution are smooth we have $\partial^2_{\bar{t}\bar{x}}\boldsymbol{w} = \partial^2_{\bar{x}\bar{t}}\boldsymbol{w}$ and injecting (18a) into (19a) and (18b) into (19b) and taking the difference of the obtained equations leads to:

$$\begin{aligned}\chi\varepsilon\partial^2_{\bar{t}\bar{t}}\partial^2_{\bar{x}\bar{x}}\bar{\phi} + \partial_{\bar{x}}\left(\left(\bar{n}_e + \varepsilon\bar{n}_i\right)\partial_{\bar{x}}\bar{\phi}\right)\\ - \partial^2_{\bar{x}\bar{x}}\left(\bar{n}_e\left(\varepsilon\bar{u}_e^2 + 1\right) - \varepsilon\bar{n}_i\left(\bar{u}_i^2 + \kappa\right)\right) = 0\end{aligned} \tag{20}$$

This equation on the electric potential $\bar{\phi}$ does not become singular as $\chi \to 0$ or $\varepsilon \to 0$, i.e. we no longer are in the case of a singular perturbation. Solving this equation instead of the classical Poisson equation (4e) leads to an AP-scheme presented in details in [22]. The main properties of this scheme is that it lifts conditions (15) and (16). However, it does not solve the accuracy problem that arises for the classical method in the regime $\varepsilon \to 0$ and requires to solve equation (20) which is second order in time and space. In particular the method has a wide stencil, raising the question of how to properly deal with boundary conditions in our setting.

The second approach that we wish to mention in this brief review is that of [21]. This method used Lagrange splitting that separates the fast dynamics (electron acoustic waves, electrostatic interactions) from the slow dynamics (electron transport and ion dynamics) as well as a low-Mach correction (see for instance [11]) and well balancing techniques to correctly capture steady states (see for instance [28]). This method has the advantage to not only lift the stability constraints (14) and (15), but also to be accurate in the low-Mach regime that is when $\varepsilon \to 0$. However, the method has not yet been used in 2D configurations and there is no obvious way to extend the method to higher orders of accuracy.

In what follow we present a AP-scheme that was design to require less complexity in its implementation than methods from [22; 21] and that uses a framework that should later allow to extend the method to second order.

4.2. New asymptotic-preserving scheme

The core idea of both the schemes [22; 21] is that the flux term $\partial_x \left(\bar{n}_e \bar{u}_e\right)$ in the electron mass equation is, to some extent, treated in an implicit manner, whereas in the classical formulation listed in section 3 only the Poisson equation and the Lorentz force show some level of implicitation. This specific aspect is key to lifting restriction on the range of time steps and mesh sizes acceptable for the method. In devising our new approach we intend to include this feature while trying to keep the scheme as simple as possible, that is avoiding to using Lagrange splitting and avoiding to use a more complex version of the Poisson equation as in [21; 22].

Following the fact that in [21] only the electron fast scales must be made implicit we modify only the structure of the scheme that regards electron dynamic and electrostatic interaction:

$$\frac{\bar{n}_{e_j}^{n+1} - \bar{n}_{e_j}^{n}}{\Delta t} + \left[\partial_{\bar{x}} \left(\bar{n}_e \bar{u}_e\right)\right]_j^{n+1} = 0 \tag{21a}$$

$$\frac{\left(\bar{n}_e \bar{u}_e\right)_j^{n+1} - \left(\bar{n}_e \bar{u}_e\right)_j^{n}}{\Delta t} + \left[\partial_{\bar{x}} \left(\bar{n}_e \left(\bar{u}_e^2 + \varepsilon^{-1}\right)\right)\right]_j^{n} = \varepsilon^{-1} \bar{n}_{e_j}^{n} \left[\partial_{\bar{x}} \bar{\phi}\right]_j^{n+1} \tag{21b}$$

$$\left[\partial_{\bar{x}\bar{x}}^2 \bar{\phi}\right]_j^{n+1} = \chi^{-1} \left(\bar{n}_{e_j}^{n+1} - \bar{n}_{i_j}^{n+1}\right) \tag{21c}$$

The terms in bracket $[\cdot]_j^{n+1}$ must be consistent with time t^{n+1} and position x_j (and analogously the terms $[\cdot]_j^{n+1}$ with time t^n). This approach falls within the framework of Implict-Explicit (ImEx). An exemple of ImEx scheme and of the formalism used here can be found for a simpler set of equations in [15]. The main degree of freedom in designing the scheme lies with the term $\left[\partial_{\bar{x}} \left(\bar{n}_e \bar{u}_e\right)\right]_j^{n+1}$. Descretizing equation (19a) and using the fact that $\partial_{\bar{x}} \left(\bar{n}_e \partial_{\bar{x}} \bar{\phi}\right) = \partial_{\bar{x}} \bar{n}_e \partial_{\bar{x}} \bar{\phi} + \bar{n}_e \partial_{\bar{x}\bar{x}}^2 \bar{\phi}$ we propose the following:

$$\begin{aligned} \left[\partial_{\bar{x}} \left(\bar{n}_e \bar{u}_e\right)\right]_j^{n+1} = {} & \left[\partial_{\bar{x}} \left(\bar{n}_e \bar{u}_e\right)\right]_j^{n} - \Delta t \left[\partial_{\bar{x}\bar{x}}^2 \left(\bar{n}_e \left(\bar{u}_e^2 + \varepsilon^{-1}\right)\right)\right]_j^{n} \\ & + \Delta t \varepsilon^{-1} \left[\partial_{\bar{x}} \bar{n}_e \partial_{\bar{x}} \bar{\phi}\right]_j^{n+1} \\ & + \Delta t \varepsilon^{-1} \bar{n}_{e_j}^{n} \left[\partial_{\bar{x}\bar{x}}^2 \bar{\phi}\right]_j^{n+1} \end{aligned} \tag{22}$$

The guiding principle of this approach is that not all term are made implicit in order to obtain only scalar and linear implicit equations, which have in terms of computational effort the same cost as fully explicit method, while having improved stability properties. In that regards the term $\bar{n}_{e_j}^{n} \left[\partial_{\bar{x}\bar{x}}^2 \bar{\phi}\right]_j^{n+1}$ is linear in $\bar{n}_{e_j}^{n+1}$, satisfying our requirement. The term $\left[\partial_{\bar{x}} \bar{n}_e \partial_{\bar{x}} \bar{\phi}\right]_j^{n+1}$ is strongly nonlinear in the variable of the problem. In order to remove this difficulty we use the Boltzmann relation (6) approximation, following an idea initially developed in a different context by [20]:

$$\left[\partial_{\bar{x}} \bar{n}_e \partial_{\bar{x}} \bar{\phi}\right]_j^{n+1} \approx \bar{n}_{e_j}^{n+1} \left(\left[\partial_{\bar{x}} \bar{\phi}\right]_j^{n}\right)^2 \tag{23}$$

Now equation (21a) reads:

$$\bar{n}_{e_j}^{n+1} + \frac{\Delta t^2}{\varepsilon} \bar{n}_{e_j}^{n+1} \left(\left[\partial_{\bar{x}} \bar{\phi}\right]_j^{n}\right)^2 + \frac{\Delta t^2}{\varepsilon \chi} \bar{n}_{e_j}^{n} \left(\bar{n}_{e_j}^{n+1} - \bar{n}_{i_j}^{n+1}\right) = \bar{n}_{e_j}^{*} \tag{24}$$

where

$$\begin{aligned} \bar{n}_{e_j}^{*} = {} & \bar{n}_{e_j}^{n} - \Delta t \left[\partial_{\bar{x}} \left(\bar{n}_e \bar{u}_e\right)\right]_j^{n} \\ & - \Delta t^2 \left[\partial_{\bar{x}\bar{x}}^2 \left(\bar{n}_e \left(\bar{u}_e^2 + \varepsilon^{-1}\right)\right)\right]_j^{n} \end{aligned} \tag{25}$$

which finally yields:

$$\bar{n}_{e_j}^{n+1} = \alpha \bar{n}_{e_j}^{*} + \beta \bar{n}_{i_j}^{n+1} \tag{26}$$

with

$$\alpha = \frac{\varepsilon \chi}{\varepsilon \chi + \chi \Delta t^2 \left(\left[\partial_{\bar{x}} \bar{\phi}\right]_j^{n}\right)^2 + \Delta t^2 \bar{n}_{e_j}^{n}}, \tag{27a}$$

$$\beta = \frac{\Delta t^2 \bar{n}_{e_j}^{n}}{\varepsilon \chi + \chi \Delta t^2 \left(\left[\partial_{\bar{x}} \bar{\phi}\right]_j^{n}\right)^2 + \Delta t^2 \bar{n}_{e_j}^{n}}. \tag{27b}$$

Let us take a few lines to give some perspective on the structure of equation (26). On the one hand, within the bulk of the plasma, the electric field is extremely limited, that is $\| \left[\partial_{\bar{x}} \bar{\phi}\right]_j^{n} \| \ll 1$, and consequently because we also have $\varepsilon \ll 1$ and $\chi \ll 1$ we obtain that $\alpha \approx 0$

and $\beta \approx 1$, ultimately leading to $\bar{n}_{e_j}^{n+1} \approx \bar{n}_{i_j}^{n+1}$. Thus, the quasi-neutral regime is well-captured by the method. On the other hand, within the sheaths the normalized electric field can scale as the inverse of the normalized Debye length, so that α is no longer negligible as compared to β, allowing the density of electron $\bar{n}_{e_j}^{n+1}$ to collapse in the sheath.

The steps of the complete method are the following:

- The ion density $\bar{n}_{i_j}^{n+1}$ is computed in a similar manner as it would be in the classical scheme from the mass equation (4c).

- The electron density $\bar{n}_{e_j}^{n+1}$ is derived from the formulas (25) and (26).

- The electric potential $\bar{\phi}_j^{n+1}$ and the ionization rate $\left(\bar{\nu}^{iz}\right)^{n+1}$ are computed.

- The ionization source term is added, the momentum equations are used to update the momentum variables with both the convective part and the Lorentz force.

Lastly, we still need to give some definition to the terms $\left[\partial_{\bar{x}}\left(\bar{n}_e\bar{u}_e\right)\right]_j^n$ and $\left[\partial_{\bar{x}\bar{x}}^2\left(\bar{n}_e\left(\bar{u}_e^2+\varepsilon^{-1}\right)\right)\right]_j^n$ in equation (25). Both these terms are computed via classical centered difference. Indeed here, the formula $\bar{n}_{e_j}^*$ already contain some level of "natural" numerical diffusion. It is important not to use finite volume approach with the Rusanov approximation for fluxes in computing $\left[\partial_{\bar{x}}\left(\bar{n}_e\bar{u}_e\right)\right]_j^n$, otherwise the method will not be accurate in the low-Mach regime that is when $\varepsilon \to 0$. This process of choosing the right quantity of numerical diffusion is investigated more in depths for a simpler set of equations in [15]. In particular this choice requires that Δt not be chosen to small. Without a more complete numerical analysis study of the stability properties of the scheme this lower bound to the time step is currently found empirically.

To make a brief comparison with the methods from [21; 22], we emphasize a few points:

- This method, unlike that of [22], does not require a second order in time and space equation be solved, consequently alleviating the process, in particular when non-periodic boundary conditions are considered, such as in configuration in figures Figures 1 and 2. In fact the Poisson equation (4e) is not directly modified allowing for the use of preconditioning techniques to solve the associated discrete linear system (11).

- This method does not involve the Lagrangian splitting that also require significant effort in terms of implementing methods.

- We followed closely in the design of this method the approach of [15], that present second order schemes and consequently we believe this method has the potential to be extended to second order.

In the next section we confirm via numerical simulation that this new AP-scheme does possess the expected stability and accuracy properties.

Methods are implemented in samurai (`https://github.com/hpc-maths/samurai`), a code that provides a new data structure based on intervals and algebra of sets to handle efficiently adaptive mesh refinement (AMR) methods based on a cartesian grid and is versatile enough to handle both AMR and multi-resolution methods.

5. Results

In this section we first demonstrate that the accuracy of the method holds in the regime $\varepsilon \to 0$, then these stability constraints are lifted and finally we provide an example of the 2D configuration.

5.1. Accuracy of the scheme

In Figures 3a to 3c we compare the performances in terms of accuracy of the classical and AP methods. We consider density and current profiles for ions and electrons for a 1D test case corresponding to Figure 1. For this specific test case and more precisely because of its symmetry and the fact that it is 1D, we expect the solution to be ambipolar, that is we expect the ion and electron fluxes to coincide. We can observe in Figure 3a that the classical scheme achieves very poor accuracy as the simulation produces non-physical bumps in the sheath region for the electron momentum. Even when the mesh size is reduced by a factor 8, as presented in Figure 3b, the accuracy achieved by the classical method is not entirely satisfactory, especially considering the additional cost of solving the Poisson equation with eight times the previous number of cells. The AP-scheme however, is naturally much more accurate in this regime where $\varepsilon \ll 1$ and yields results that are consistent with what was expected of the solution [6]. In particular we retrieve that the fluxes are ambipolar in this 1D test case.

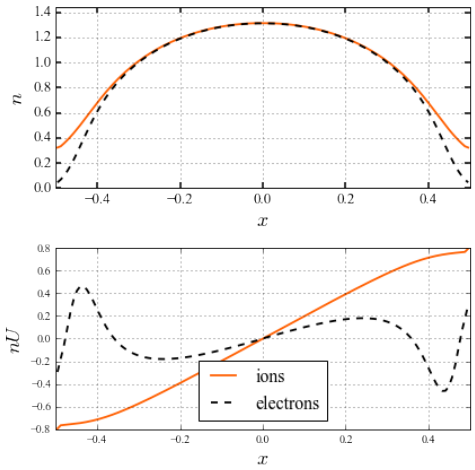

(a) Classical scheme, $\Delta x = 1/128 \approx \lambda_D/(3L_0)$

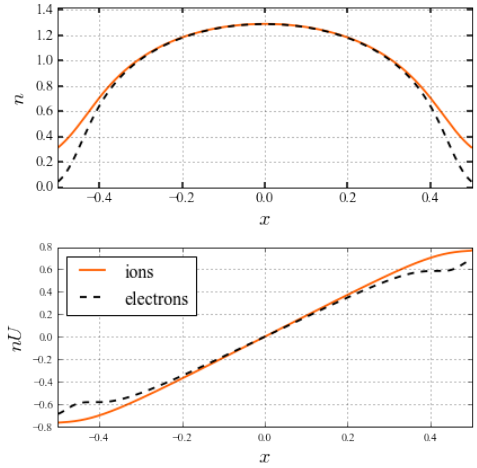

(b) Classical scheme, $\Delta x = 1/1024 \approx \lambda_D/(30L_0)$

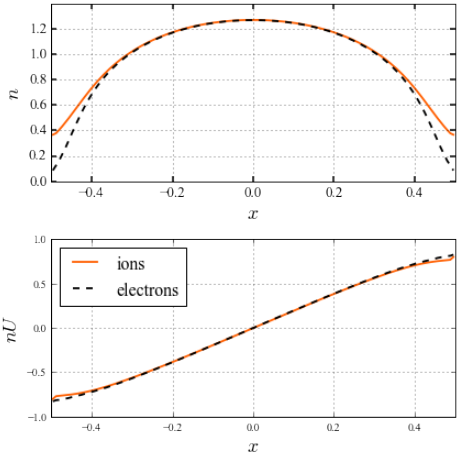

(c) Classical scheme, $\Delta x = 1/128 \approx \lambda_D/(3L_0)$

Figure 3: 1D test case, $\Delta x \leq \lambda_D/L_0$, $\varepsilon = 1/1836$ (H^+), $\lambda_D/L_0 = 0.02$ ($L_0 \approx 3cm$), $\kappa = 0.025$ ($T_i = 300K$), $t_f = 1$ (few μs).

5.2. *Stability of the scheme*

We now present some preliminary results on the compatibility of the method with adaptive mesh refinement techniques, that also allows to validate the extended stability of the method.

In Figures 4a to 4c the solution is represented at various times (close to initial time, at some intermediate time and at the final time with the converged steady state). The mesh is displayed for each of the selected instants. The first point worthy of notice is that throughout the simulation some cells, mostly located at the center of the domain of simulation, are up to three times wider than the Debye length, meaning that neither condition (15) nor condition (16) are respected, but the scheme remains stable as expected and does not generate spurious oscillations, unlike the classical method. The second point that we wish to emphasize is that the multi-resolution seems to be, at least for this preliminary test-case, compatible with the proposed AP-scheme. Here, the adapting the size of the mesh allows us to have a fine mesh in the sheath, which we wish to capture in details, and a coarse in the bulk of the plasma in the center, where the plasma is quasi-neutral and does not require to consider the smallest spatial scales. It is our hope that this approach can be extended macroscopic 3D configurations, such as ionic thrusters, for which the mesh would dynamically adapt and be fine in areas close to the walls in the sheath, as well as around potential instabilities, but be coarse in quasi-neutral area, well-described by the slow time scales and wider space scales of ion dynamics. We expect it will help in such configuration to obtain a gain of several orders of magnitudes in terms of computational cost and allow to consider configurations that are today intractable. As a first step toward that goal, we now present a 2D configuration to which the method was applied.

5.3. *A example of 2D configuration*

As another step to confirm the viability of our approach, we have extended and applied the AP-method to the 2D configuration found in Figure 2. The density and current profiles obtain via simulations using the AP-scheme are displayed in figures Figures 5a and 5b. It is found by comparison with PIC simulations that the results yielded by the AP-scheme are even more accurate than that that were obtained via methods using low-Mach corrections such as the one presented in [11]. It is expected that for heavier gases, such as xenon or argon, for which the correction is even more necessary as ε is smaller and inaccuracies are more

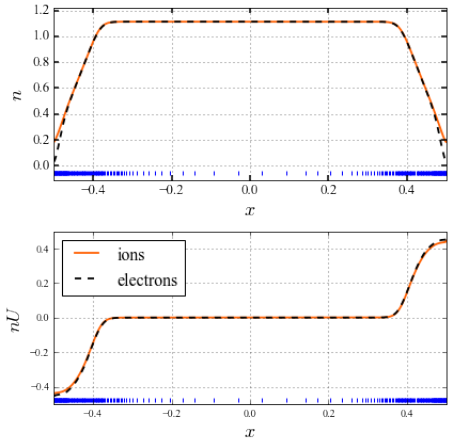

(a) Initial time of the solution.

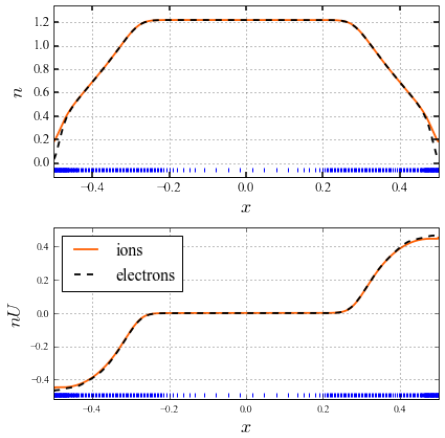

(b) Intermediate regime.

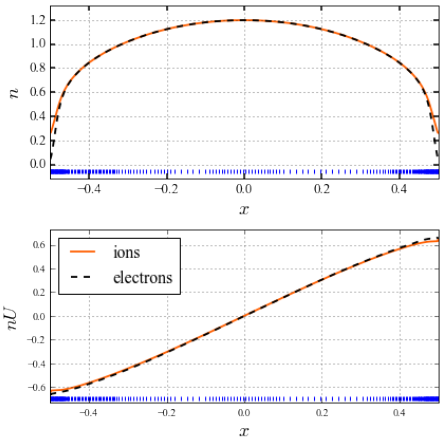

(c) Steady state.

Figure 4: 1D test case, the vertical blue lines correspond to cell centers, $\Delta x > \lambda_D/L_0$ in some part of the configuration, $\varepsilon = 1/1836\,(H^+)$, $\lambda_D/L_0 = 0.002$ ($L_0 \approx 15cm$), $\kappa = 0.025$ ($T_i = 300K$), $t_f = 1$ (few μs).

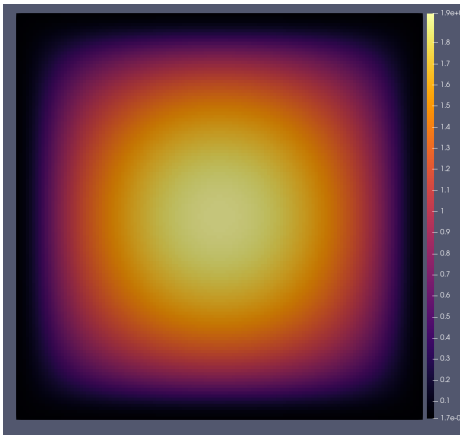

(a) Electron density profile.

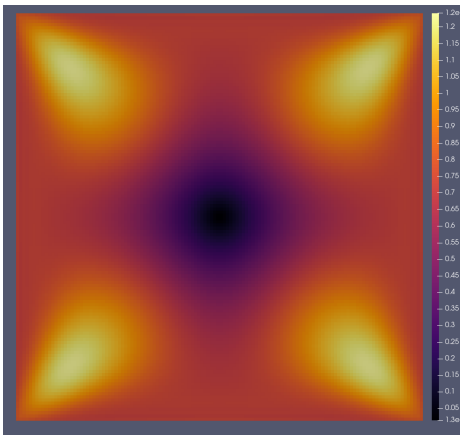

(b) Profile of the norm of the electron current.

Figure 5: 2D test case, the vertical blue lines correspond to cell centers, $\Delta x = 1/128 \leq \lambda_D/L_0$, $\varepsilon = 1/1836$ (H^+), $\lambda_D/L_0 = 0.02$ ($L_0 \approx 3cm$), $\kappa = 0.025$ ($T_i = 300K$), $t_f = 2$ (few μs).

significant, the contrast in terms of the obtained precision will be even more apparent. Regarding the question of stability and of the efficiency of the method, to obtain equivalent accuracy, the AP-scheme presented in this work outperforms the previous low-Mach correction from [11] by up to two orders of magnitude for heavy gases such as argon, since there a factor $\sqrt{\varepsilon}$ that is removed from the CFL condition. Additionally, there is no tuning parameter in this approach, it is automatically consistent at the best of its ability as long as the time step Δt is chosen within the acceptable range of stability. This is a major advantage as compared to most low-Mach corrections that often use cut-off parameters, which have to be chosen respecting a trade off between the desired accuracy and stability restrictions, meaning that in order to obtain more accurate results one must increase the computational cost at constant mesh size.

6. Conclusion

In conclusion we have proposed an approach that in the manner of [21; 22] lifts the constraints (15) and (16) associated to the splitting approach using classical finite volume. However, our approach is notably less complex to implement, and in particular requires no Lagrange splitting or well-balancing technique, nor does it require to modify the Poisson equation, which on fixed cartesian mesh allows for using preconditioning techniques to accelerate the resolution of the associated linear system.

In comparison to other methods that can lead to comparable accuracy in 2D configurations such as that found in Figure 2 or Figures 5a and 5b, the method avoids the use of tuning parameters and can be up to several orders of magnitude faster.

We are now in the process of extending this approach to higher order of accuracy and to combine it with multi-resolution techniques in order to apply it to more complex devices such as electric propulsion.

Acknowledgments

This work is funded by a joint grant by the French Ministry of Defense (via the Agence Innovation Defense, AID) and the Region Île de France (DIM-Math Innov).

References

[1] P. Chabert, N. Braithwaite, Physics of radio-frequency plasmas, Cambridge University Press, 2011.

[2] M. A. Lieberman, A. J. Lichtenberg, Principles of plasma discharges and materials processing, John Wiley & Sons, 2005.

[3] A. Soosaleon, B. Jose, et al., Two stream instability as a source of coronal heating, International Journal of Astronomy and Astrophysics 5 (02) (2015) 61.

[4] R. Lucken, A. Bourdon, M. Lieberman, P. Chabert, Instability-enhanced transport in low temperature magnetized plasma, Physics of Plasmas 26 (7) (2019) 070702.

[5] S. Sadouni, Fluid modeling of transport and instabilities in magnetized low-temperature plasma sources, Ph.D. thesis, École doctorale GEED, https://tel.archives-ouvertes.fr/tel-02978476 (2020).

[6] A. Alvarez-Laguna, T. Magin, M. Massot, A. Bourdon, P. Chabert, Plasma-sheath transition in multi-fluid models with inertial terms under low pressure conditions: Comparison with the classical and kinetic theory, Plasma Sources Science and Technology 29 (2) (2020) 025003.

[7] R. Lucken, Theory and Simulation of Low Pressure Plasma Transport Phenomena, Application to the PEGASES thruster., Ph.D. thesis, École doctorale n^o572 Ondes et Matière (EDOM), https://tel.archives-ouvertes.fr/tel-02435208 (2019).

[8] T. Charoy, J.-P. Boeuf, A. Bourdon, J. A. Carlsson, P. Chabert, B. Cuenot, D. Eremin, L. Garrigues, K. Hara, I. D. Kaganovich, et al., 2d axial-azimuthal particle-in-cell benchmark for low-temperature partially magnetized plasmas, Plasma Sources Science and Technology 28 (10) (2019) 105010.

[9] R. J. LeVeque, et al., Finite volume methods for hyperbolic problems, Vol. 31, Cambridge University Press, 2002.

[10] E. F. Toro, Riemann solvers and numerical methods for fluid dynamics: a practical introduction, Springer Science & Business Media, 2013.

[11] L. Reboul, A. A. Laguna, T. Magin, A. Bourdon, M. Massot, Fluid modeling of low-temperature partially-magnetized plasmas in the presence of sheaths: numerical issues for the simulation of instabilities and comparison with kinetic simulations, von Karman PhD symposium (2021).

[12] G. Albi, G. Dimarco, L. Pareschi, Implicit-explicit multistep methods for hyperbolic systems with multiscale relaxation, SIAM J. Sci. Comput. 42 (4) (2020) A2402–A2435.

[13] C. Berthon, R. Turpault, Asymptotic preserving HLL schemes, Numer. Methods Partial Differ. Equ. 27 (6) (2011) 1396–1422.

[14] C. Buet, B. Després, E. Franck, Design of asymptotic preserving finite volume schemes for the hyperbolic heat equation on unstructured meshes, Numer. Math. 122 (2) (2012) 227–278.

[15] L. Reboul, T. Pichard, M. Massot, Second-order uniformly asymptotic-preserving space-time-imex schemes for hyperbolic balance laws with stiff relaxation, arXiv preprint arXiv:2205.09993.

[16] S. Boscarino, L. Pareschi, G. Russo, Implicit-explicit Runge-Kutta schemes for hyperbolic systems and kinetic equations in the diffusion limit, SIAM J. Sci. Comput. 35 (1) (2013) A22–A51.

[17] L. Gosse, G. Toscani, An asymptotic-preserving well-balanced scheme for the hyperbolic heat equations, C. R. Acad. Sci. Paris 334 (4) (2002) 337–342.

[18] S. Jin, C. D. Levermore, Numerical schemes for hyperbolic conservation laws with stiff relaxation terms, J. Comput. Phys. 126 (2) (1996) 449–467.

[19] S. Jin, Efficient asymptotic-preserving (ap) schemes for some multiscale kinetic equations, SIAM Journal on Scientific Computing 21 (2) (1999) 441–454.

[20] S. Jin, C. D. Levermore, Numerical schemes for hyperbolic

conservation laws with stiff relaxation terms, Journal of computational physics 126 (2) (1996) 449–467.

[21] A. A. Laguna, T. Pichard, T. Magin, P. Chabert, A. Bourdon, M. Massot, An asymptotic preserving well-balanced scheme for the isothermal fluid equations in low-temperature plasmas at low-pressure, Journal of Computational Physics 419 (2020) 109634.

[22] P. Crispel, P. Degond, M.-H. Vignal, An asymptotic preserving scheme for the two-fluid euler–poisson model in the quasineutral limit, Journal of Computational Physics 223 (1) (2007) 208–234.

[23] S. Braginskii, Transport processes in a plasma reviews of plasma physics, Ed. MA Leontovich (New York: Consultants Bureau).

[24] E. Godlewski, P.-A. Raviart, Numerical approximation of hyperbolic systems of conservation laws, Vol. 118, Springer Science & Business Media, 2013.

[25] S. Fabre, Stability analysis of the euler-poisson equations, Journal of Computational Physics 101 (2) (1992) 445–451.

[26] M. P. Duarte, Adaptive numerical methods in time and space for the simulation of multi-scale reaction fronts., Theses, Ecole Centrale Paris (Dec. 2011).
URL `https://tel.archives-ouvertes.fr/tel-00667857`

[27] M. Duarte, Z. Bonaventura, M. Massot, A. Bourdon, A numerical strategy to discretize and solve the poisson equation on dynamically adapted multiresolution grids for time-dependent streamer discharge simulations, Journal of Computational Physics 289 (2015) 129–148.

[28] F. Bouchut, Nonlinear stability of finite Volume Methods for hyperbolic conservation laws: And Well-Balanced schemes for sources, Springer Science & Business Media, 2004.

Towards a high-order fluid simulation of Argon plasma sheath

Giuseppe Matteo Gangemi

Aeronautics and Aerospace Department, von Karman Institute for Fluid Dynamics, Belgium, giuseppe.gangemi@vki.ac.be

Supervisor: Thierry Magin

Professor, Aeronautics and Aerospace Department, von Karman Institute for Fluid Dynamics, Belgium, magin@vki.ac.be

University Supervisor: Koen Hillewaert

Associate Professor, Aerospace Mechanical engineering, Université de Liège, Belgium, koen.hillewaert@uliege.be

University Supervisor: Alejandro Alvarez Laguna

Researcher, Laboratoire de Physique des Plasmas, École Polytechnique, Sorbonne Université, France, alejandro.alvarez-laguna@lpp.polytechnique.fr

Abstract

In a wall-confined environment, the plasma behaviour can be identified by dividing the domain in two main regions: the bulk, where the quasi-neutrality prevails (the charge density is close to zero) and the sheath region near the walls, where positive space charge is built. This phenomenon is due to a higher mobility of electrons, creating an electric potential structure that accelerates the ions towards the surface and repels the electrons. In this work we present the effort carried on in order to obtain high order simulations of a mixture of argon plasma: in particular we present a novel physical model (the multicomponent equations in contrast with the most common multifluid approach) and we show the first results of the application of the Discontinuous Galrkin framework, detailing challenges and solutions adopted. Simulations show encouraging results for future developments involving more complex geometries, more variegated mixtures and more accurate time schemes.

Keywords: plasma, sheath, fluid models, discontinuous galerkin

1. Introduction

Accurate simulation of low temperature plasmas (i.e. plasmas with heavy temperature lower than the one of electrons) is crucial to a wide range of aerospace fields, including electronics applications (such as arcing of components used in platforms newly brought to space [1]), as well as hypersonics (electron transpiration cooling of innovative heat shield for cruise vehicles [2]). These applications vary greatly in terms of conditions (thermal non-equilibrium, pressure and so collisionality degree) and for the nature of the species involved (electrons, neutral and ionized atoms and molecules).
In this introduction we give a brief oversight of the approaches that are used when simulating low temperature plasma physics; for a more detailed treatment we refer to more extensive reviews [3; 4]. Strategies for the numerical simulation of the plasma sheath vary depending on the collisionality of the mixture: most of the work for low-pressure mixtures relies on kinetic approaches, like the Particle-In-Cell-Monte Carlo Collision (PIC-MCC) [5]; these methods provide great level of accuracy in the description of the plasma physics but with high computational cost (with a strong direct dependency on the number of particles involved, i.e. the pressure condition). Fluid modeling of plasmas represent an alternative to kinetic approaches: while describing the behaviour using macroscopic quantities reduces the accuracy and detail of the description of the gas, its computational cost is significantly reduced. Nevertheless coupling the fluid dynamics to the Maxwell's equations results in a strongly multi-scale problem that poses great challenges in the numerical development [6]. Some of

this challenges become predominant in the development of a fluid solver that is able to simulate the interaction of plasmas with solid boundaries: the ability of the solver to capture a smooth transition from the quasi-neutral region to the space-charge boundaries is crucial and, together with the difficulties coming from the presence of faster and slower dynamics in the particle motion, represents one of the main challenges for fluid models nowadays. Recent works have been focused on the development of asymptotic preserving schemes [7], [8], i.e. strategies that are able to tackle those limits in the plasma equations that introduce numerical stiffness in the simulation. We will not touch those new approaches, but they represent interesting future possibilities for this thesis.
In this paper we focus only on a mixture of argon, allowing to neglect for the moment too complex chemical processes and to reduce the number of species involved. More complex mixtures like air plasmas present a greater variety of species: electrons, positive and negative ions, neutrals, atomic and molecular species, that behave in very different way regarding transport phenomena, as well as the coupling between the flow and electromagnetic fields; treatment of these gases is left for future developments.
In this document we present the progress in the development of a high order fluid solver for argon plasma sheath: we focus on the difficulties arising from the nature of the problem and provide solutions to overcome them. The paper is divided as such: Section 2 illustrates briefly the most relevant characteristics of the sheath and introduces the physical quantities of interest for this work; Section 3 introduces the governing equations for both the multifluid and the multicomponent models; Section 4 details the numerical strategies adopted in order to retrieve the profiles shown in Section 5.

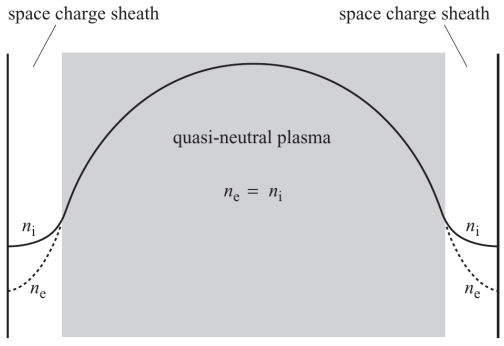

Figure 1: One dimensional DC discharge. [9]

2. Physics of plasma sheaths

The behaviour of plasmas in contact with walls is well described by Chabert & Braithwaite [9]; in order to detail the formation of the sheath and its main features we will take the case of an electropositive gas, i.e. an ionized mixture with only single-charged positive ions and electrons in a background gas of neutral particles of density much larger than those of charge species (as in the argon mixtures treated in this work), confined by walls in a one-dimensional domain (often referred to as a discharge) like the one in Fig.1. This configuration will be the base of the whole simulations in this work.
At the beginning of the experiment we consider a quasi-neutral mixture, i.e. the electron number density is comparable to the ion number density $n_e \sim n_i$. Supposing that this object is not electrically connected to ground (a piece of dielectric or a floating probe), at the boundaries the difference of mean flux between electrons Γ_e and heavy particles Γ_i plays a fundamental role. The current of electrons J_e and ions J_i is given by the following expressions:

$$J_e = -e\Gamma_e = -\frac{1}{4} e n_e \bar{v}_e = -e n_e \sqrt{\frac{k_B T_e}{2\pi m_e}}, \quad (1)$$

$$J_i = e\Gamma_i = \frac{1}{4} e n_i \bar{v}_i = e n_i \sqrt{\frac{k_B T_i}{2\pi m_i}}, \quad (2)$$

with $\bar{v}_k$ the mean velocity of the particle k, T_k its temperature, m_k its mass, n_k its number density and e the elementary charge. Due to the difference of mass of the species involved ($m_i \gg m_e$) we have that:

$$\|J_e\| \gg \|J_i\| \quad (3)$$

and so an higher number of electrons impacts the solid boundary, charging it negatively. This process creates a space-charge region close to the walls that repels the negative species and attracts the positive ones; in the central part of the domain (called “bulk”) the quasi-neutrality condition is preserved.
In Fig.2 we see a representation of the process just described: the formation of the sheath guarantees that, at steady state, the flux of the ions J_i to the wall equals the one of the electrons J_e enforcing continuity of the (zero) currrent from the centre of the domain until the wall. The potential of the wall is called a DC floating potential. Such potential is necessarily more negative than the potential of the plasma because $T_e \gg T_i$ and $me \ll m_i$. However, if the object were conducting, it could be biased by a voltage source and held at any potential with respect to the plasma, provided

an appropriate current from the source were circulating through the plasma. The charged heavy species enter the domain satisfying the Bohm criterion [10], i.e. their velocity must be greater than the ions sound speed (conventionally referred to as "Bohm speed"):

$$u_B = \sqrt{\frac{k_B T_e}{m_i}}. \tag{4}$$

For this reason it is common practice to define the sheath edge as the point where the flux of ions satisfies this requirement; we can then assume that the flux of positive particles entering the space charge region is *supersonic*. On the other hand soundspeed of electrons is much higher (due to their lower mass): for this reason, and because of the short extent of the acceleration region, they reach the wall in a strongly *subsonic* regime.

Riemann et al. in [11] highlighted the importance

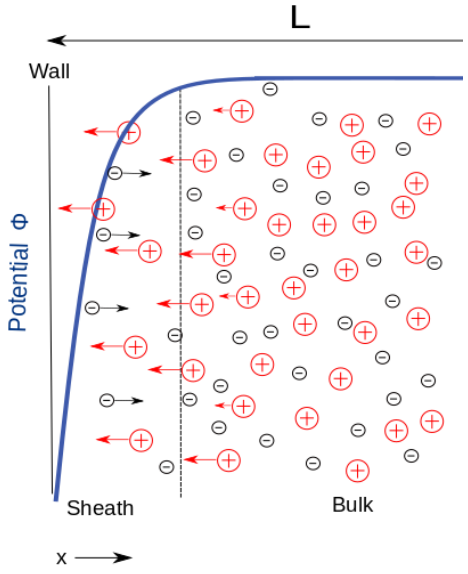

Figure 2: Plasma sheath schematics

of defining a transition zone ("pre-sheath"), where the disturbances in the electrostatic field extend into the quasi-neutral region and accelerate the ions to their sound speed; this region has an intermediate scaling between the sheath one (the Debye length $\lambda_D = (\epsilon_0 k_B T_e) / \left(n_0 e^2 L_0^2\right)$) and the bulk region ($L$). The Debye length can be seen as the ratio of the electron thermal velocity $v_{th,e} = \sqrt{k_B T_e / m_e}$ and the electron plasma frequency ω_e:

$$\lambda_D = \frac{v_{th,e}}{\omega_{pe}}. \tag{5}$$

The electron plasma frequency is an important parameter: being it the fastest response of the the mixture to external disturbances it represents the most relevant physical limitation in terms of stability of (explicit) numerical methods. The ionization frequency for the isothermal discharge is known to be an eigenvalue of the problem [11]: given a geometrical configuration (in our case the only parameter is the width of the discharge L) there is only one value of the ionization frequency that results in a steady-state solution. In this work we follow the iterative strategy proposed in [7]:

$$\nu^{iz} = \frac{\left|\Gamma_i^L + \Gamma_i^R\right|}{\int_L n_e(x)\, dx}, \tag{6}$$

where Γ_i^L, Γ_i^R are, respectively, the flux of the ions to the left and right boundary. With this procedure the value gets updated at every timestep, guaranteeing that the number of particles injected counterbalances the one leaving the domain and that the total number of electrons stays constant.

3. Fluid Models

Fluid models describe the behaviour of the gas by conservation equations of macroscopic quantities derived as velocity moments of the *i-th* particle velocity distribution function (VDF) $f_i(\mathbf{x}, \mathbf{c}_i, t)$. The evolution of this quantity is accounted by means of the famous Boltzmann equation [12]:

$$\frac{\partial f_i}{\partial t} + \mathbf{c}_i \cdot \frac{\partial f_i}{\partial \mathbf{x}} + \frac{\mathbf{F}^{ext}}{m_i} \frac{\partial f_i}{\partial \mathbf{c}_i} = \sum_{j \in \mathcal{S}} \mathcal{J}_{ij}\left(f_i, f_j\right), \tag{7}$$

where $\mathbf{c}_i$ is the *i-th* particle velocity, $\mathbf{x}$ the space coordinate, $\mathbf{F}^{ext} = q_i(\mathbf{E} + \mathbf{c}_i \times \mathbf{B})$ are the external forces (with q_i the particle charge, $\mathbf{E}$ the external electric field and $\mathbf{B}$ the external magnetic field, neglected in the application of interest for the present tractation). The right-hand side of eq. 7 is the collision operator, describing the changes of the distribution function due to the impacts (elastic and inelastic) in the mixture. Detailed description of the modeling of this term is complex and beyond the scope of this document; we refer the interested reader to well-known exhaustive works [12; 13]. In the following subsection we detail the two main family of fluid models: we restrict ourselves to the case of isothermal mixtures. Such a choice has two reasons: the resulting system of equations presents already the numerical challenges that we want to tackle; moreover getting rid of the energy equation(s) allows to neglect, for the present time, the problem of closure of high order terms [14].

3.1. Multifluid models

The governing equations (in normalized form) used to simulate the sheath formation of an argon plasma are the so-called two fluid Euler-Poisson system of equations:

$$\partial_t n_e + \partial_x (n_e u_e) = n_e \nu^{iz}, \tag{8}$$

$$\partial_t n_i + \partial_x (n_i u_i) = n_e \nu^{iz}, \tag{9}$$

$$\partial_t (n_e u_e) + \partial_x \left[n_e \left(u_e^2 + \varepsilon^{-1} \right) \right] = \varepsilon^{-1} n_e \partial_x \phi - n_e u_e \nu_{en}, \tag{10}$$

$$\partial_t (n_i u_i) + \partial_x \left[n_i \left(u_i^2 + \kappa \right) \right] = -n_i \partial_x \phi - n_i u_i \nu_{in}, \tag{11}$$

$$\partial_{xx}^2 \phi = \chi^{-1} (n_e - n_i), \tag{12}$$

where the non-dimensional parameters are defined as:

Electron-ion mass ratio: $\varepsilon = m_e/m_i$,

ion-to-electron temperature: $\kappa = T_i/T_e$,

squared non-dimensional Debye length: $\chi = \dfrac{\lambda_D^2}{L_0^2}$,

dimensionless frequencies: $\nu^{iz} = \bar{\nu}^{iz} t_0$,

$\nu_{kn} = \bar{\nu}_{kn} t_0$.

In this document we rely on the formulation that can be found in [15] : we refer to it for the complete derivation starting from the complete dimensional set. Equations 8-11 represent the fluid dynamic subset, with mass conservation equations for each species (eqs.8,9) and their momentum conservation equations (eqs.10,11); these are coupled to the Poisson equation (eq.12) in order to guarantee charge conservation across the domain. We consider only ionization processes (ν^{iz}) and elastic collisions ($\nu_{kn} = n_n \sigma_{kn} v_{th,k}$, where n_n is the neutral number density, σ_{kn} the cross section, $v_{th,k}$ is the thermal speed of the *k-th* particle). Table 1 shows the typical value of the argon plasma DC discharge (more details in Section 5) in the conditions of interest. Multifluid models are widely used in the plasma physics community: a kinetic derivation relying on the Chapman-Enskog perturbative method can be found in [16]; in the procedure the main assumption is that the number of collision among species of the same type are more common than among different species. This allows the decoupling that leads to momentum conservation equation for each species, with only source terms (the one proportional to the gradient of the electric potential and the one to collisions) to account for the inter-species interactions.

Table 1: Argon discharge conditions

Initial electron number density	n_{e0}	$10^{16}\ \mathrm{m}^{-3}$
Neutral and ion temperature	$T_{n,i}$	0.05 eV
Electron Temperature	T_e	2 eV
Ion-neutral cross section	σ_{in}	$10^{-18}\ \mathrm{m}^2$
Electron-neutral cross section	σ_{en}	$10^{-19}\ \mathrm{m}^2$
Electron-to-ion mass ratio	$\varepsilon = m_e/m_i$	1.36×10^{-5}
Ion-to-electron temperature ratio	$\kappa = T_i/T_e$	0.025
Debye length	λ_D	10^{-4} m
Electron plasma period	ω_{pe}^{-1}	1.77×10^{-10} s
Normalized ion collision rate	ν_{en}	153.8
Normalized electron collision rate	ν_{in}	0.94
Discharge width	L	$100\ \lambda_D$

3.1.1. Boundary conditions

The way the boundary conditions are modeled has a relevant role in the development of a solver that aims at obtaining accurate description of the physics of plasma interaction with solid walls. The multifluid equations have an hyperbolic nature so the quantities to be (or not to be) imposed at the interface have to be chosen accordingly: following [7] we impose the electron flux to both boundaries to be equal to the number of particles crossing the plane with positive velocity component (assuming a maxwellian VDF). In normalized quantities as in eqs.8-12:

$$\Gamma_e^{L,R} = (n_e u_e)^{L,R} = \mp \frac{n_e}{\sqrt{2\pi\varepsilon}}. \tag{13}$$

Electron density has Neumann boundary on both sides; ion quantities (density and momentum) have the same Neumann condition, as the flux of positive charges is assumed supersonic (see Section 2). The electric potential has a Dirichlet condition on both sides $\phi(x = \{0, L\}, t) = 0$.

3.2. Multicomponent models

We show in this section the governing equation under the multicomponent modeling assumption [17]:

$$\partial_t n_e + \partial_x (n_e u) + \partial_x (n_e V_e) = n_e \nu^{iz}, \tag{14}$$

$$\partial_t n_i + \partial_x (n_i u) + \partial_x (n_i V_i) = n_e \nu^{iz}, \tag{15}$$

$$\partial_t (\rho u) + \partial_x \left(\rho u^2 + p \right) = \partial_x \Pi - n q \partial_x \phi, \tag{16}$$

$$\partial_{xx}^2 \phi = \chi^{-1} (n_e - n_i), \tag{17}$$

where u is the bulk velocity of the entire fluid, V_k is the diffusion velocity of the *k-th* species, p the whole fluid pressure and Π the stress tensor. The one dimensional

discharge chosen as testcase of this work (Fig. 1) can be modeled as a pure diffusion problem; assuming $u = 0$ we can get rid of eq.16 and of the term proportional to the bulk velocity in eqs.14, 15:

$$\partial_t n_e + \partial_x (n_e V_e) = n_e \nu^{iz}, \tag{18}$$

$$\partial_t n_i + \partial_x (n_i V_i) = n_e \nu^{iz}, \tag{19}$$

$$\partial^2_{xx}\phi = \chi^{-1}(n_e - n_i), \tag{20}$$

The diffusion velocity for partcle k is modeled under the multicomponent diffusion assumption [18] (adapted under the isothermal assumption):

$$V_k = -\sum_{j\in\mathcal{S}} D_{kj}\left[\frac{T_j}{T_h}\frac{\partial_x n_j}{n} - y_j \sum_{m\in\mathcal{S}} \frac{T_m}{T_h}\frac{\partial_x n_m}{n} + \left(x_j q_j - y_j Q\right)\partial_x\phi\frac{T_e}{T_h}\right] \tag{21}$$

where D_{kj} is the multicomponent diffusion matrix, here computed using Ramshaw approach [19], x_j and y_j are, respectively, the molar and mass fraction and $Q = \sum_{m\in\mathcal{S}} x_m q_m$ the mixture charge. The transport coefficients are obtained using the thermodynamic library Mutation++ [20]. The multicomponent diffusion model allows to couple the diffusion of all the particles at the same time: in order to retrieve a similar behaviour to the one produced by the multifluid equations, we set the mixture at the starting condition and we obtain the physical quantities for the entire mixture; the results proposed in the dedicated section do not consider the dynamics of the neutrals atoms, being it negligible.
A rigorous kinetic derivation of the multicomponent equations can be found in [21].

3.2.1. Boundary conditions

Setting the boundary conditions to the multicomponent modeling presents substantial differences with respect to the multifluid counterpart. Equations 18, 19 present a typical elliptic scaling: following the approach in [22] (but common in literature, see e.g. [23]) we impose Neumann boundary conditions both on electrons and ions. The diffusion flux to the wall of these species is defined as:

$$\Gamma_e^{L,R} = (n_e V_e)^{L,R} = \mp\frac{n_e}{\sqrt{2\pi\varepsilon}}, \tag{22}$$

$$\Gamma_i^{L,R} = (n_i V_i)^{L,R} = \mp n_i\sqrt{\frac{\kappa}{2\pi}} + \Gamma_i^{\phi}, \tag{23}$$

where the additional flux to the wall

$$\Gamma_i^{\phi} = n_i\left(-\sum_{j\in\mathcal{S}} D_{kj}\left(x_j q_j - y_j Q\right)\partial_x\phi\frac{T_e}{T_h}\right) \tag{24}$$

is imposed in order to prevent numerical accumulation of ions at the wall. The boundary condition of the electric potential remains unchanged and has been detailed in Section 3.1.1.

4. Numerical strategies

In this section we detail the numerical approaches, Finite Volumes (**FV**) and Discontinuous Galerkin (**DG**), that have been used to produce the the comparisons in Section 5. The implementation in the Discontinuous Galerkin framework is still on going (Table 2), so the simulations with the multicomponent approach will be presented in future occasions .

Table 2: Recap of the numerical schemes used.

	FV	DG
Multifluid	✓	✓
Multicomponent	✓	✗

In order to detail both the Finite Volume and Discontinuous Galerkin approach we are going to rewrite eqs.8-12 and eqs.18-20 as:

$$\partial_t \mathbf{U} + \partial_x \mathbf{F}(\mathbf{U}) = \mathbf{S}(\mathbf{U}), \tag{25}$$

with:

$$\mathbf{U}^{\mathrm{MF}} = \begin{bmatrix} n_e \\ n_i \\ n_e u_e \\ n_i u_i \\ \phi \end{bmatrix} \quad \mathbf{U}^{\mathrm{MC}} = \begin{bmatrix} n_e \\ n_i \\ \phi \end{bmatrix} \tag{26}$$

and:

$$\mathbf{F}^{\mathrm{MF}} = \begin{bmatrix} n_e u_e \\ n_i u_i \\ n_e\left(u_e^2 + \varepsilon^{-1}\right) \\ n_i\left(u_i^2 + \kappa\right) \\ \partial_x\phi \end{bmatrix} \quad \mathbf{F}^{\mathrm{MC}} = \begin{bmatrix} n_e V_e \\ n_i V_i \\ \partial_x\phi \end{bmatrix} \tag{27}$$

$$\mathbf{S}^{MF} = \begin{bmatrix} n_e\nu^{iz} \\ n_e\nu^{iz} \\ \varepsilon^{-1} n_e\partial_x\phi - n_e u_e \nu_{en} \\ -n_i\partial_x\phi - n_i u_i \nu_{in} \\ \chi^{-1}(n_e - n_i) \end{bmatrix} \quad \mathbf{S}^{MC} = \begin{bmatrix} n_e\nu^{iz} \\ n_e\nu^{iz} \\ \chi^{-1}(n_e - n_i) \end{bmatrix} \tag{28}$$

The use of indices ^{MF} and ^{MC} will be omitted (when not needed)in the rest of the document for the seek of clarity. We do not describe the details of the space discretization of both schemes as their use is wide known and not different from the applications in classic fluid dynamics; on the other hand, next section contains the description of the time integration schemes used, as their choice is fundamental in the development of the solvers.

4.1. Reference solution

As anticipated in Section 3 the multifluid model is the most common in the plasma physics community. For this reason we choose as reference solutions the one obtained using Finite Volumes, with explicit third order Runge-Kutta and Roe numerical flux with third order reconstruction of the solution; the electric potential is obtained by solving the Poisson equation at any timestep using finite differences. The electron plasma frequency imposes strict constraints for explicit schemes but this does not impact too heavily the computational cost of the simulation.

4.2. Finite Volumes - Multicomponent

Implicit methods are needed in order to overcome numerical restrictions on the stability of the simulation; multicomponent models present diffusion terms in the governing law that restrict the timestep according to the von Neumann number condition. This can be overcome by means of implicit methods: here we follow the approach found in [24; 25]. We rewrite eqs.25 as:

$$\alpha\partial_t\mathbf{U} + \partial_x\mathbf{F}\left(\mathbf{U}^{n+1}\right) - \mathbf{S}\left(\mathbf{U}^{n+1}\right) = 0 \tag{29}$$

with:

$$\alpha = \begin{cases} 1 & \text{Fluid Equations} \\ 0 & \text{Poisson} \end{cases}$$

Equation 29 is integrated:

$$\alpha\frac{\partial\mathbf{U}_i}{\partial t}\Delta x_i + \mathbf{F}^{n+1}_{i+\frac{1}{2}} - \mathbf{F}^{n+1}_{i-\frac{1}{2}} - \mathbf{S}^{n+1}_i\Delta x_i = 0 \tag{30}$$

We define the pseudo-steady residual array:

$$\mathbf{H}(\mathbf{U}) = \alpha\frac{\partial\mathbf{U}}{\partial t}\Delta x_i + \mathbf{R}(\mathbf{U}) = 0$$
$$\mathbf{R}(\mathbf{U}) = \mathbf{F}_{i+\frac{1}{2}} - \mathbf{F}_{i-\frac{1}{2}} - \mathbf{S}\Delta x_i$$

and employ a three-point Backward Euler schemes:

$$\mathbf{H}(\mathbf{U}) = \alpha\frac{3\mathbf{U}^{k+1} - 4\mathbf{U}^k + \mathbf{U}^{k-1}}{2\Delta t}\Delta x_i + \mathbf{R} = 0 \tag{31}$$

The jacobian mastrix:

$$\frac{\partial\mathbf{H}}{\partial\mathbf{U}} = \alpha\frac{3}{2\Delta t}\Delta x_i + \frac{\partial\mathbf{R}}{\partial\mathbf{U}}$$

is calculated analytically following [24] through linearization of terms in eq.30. The diffusion term is given by:

$$\mathbf{F}^n_{i+\frac{1}{2}} = \mathbf{A}^n_{i+\frac{1}{2}}\left(\frac{\partial\mathbf{U}}{\partial x}\right)^n_{i+\frac{1}{2}} \tag{32}$$

where the matrix is given in Appendix **??**. The expressions obtained are then linearized around the time-level n as follows:

$$\mathbf{F}^{n+1}_{i+\frac{1}{2}} \simeq \mathbf{F}^n_{i+\frac{1}{2}} + 2\mathbf{A}^n_{i+\frac{1}{2}}\left(\frac{\mathbf{U}^n_{i+1} - \mathbf{U}^n_i}{\Delta x_{i+1} + \Delta x_i}\right) \tag{33}$$

The source term $\mathbf{S}^{n+1}$ is taken as

$$\mathbf{S}^{n+1}_i = \left[n_e\nu^{iz}\right]^{n+1}_i \simeq [n_e]^{n+1}_i\left(\nu^{iz}\right)^n \tag{34}$$

assuming the ionization frequency (calculated as in [7]) as constant in time: this results in a simplified jacobian $\partial\mathbf{S}/\partial\mathbf{U}$ that does not breaks the sparseness of the matrix.
The complete system (31) is approximated then by solving the linear system:

$$\left(\frac{\partial\mathbf{H}}{\partial\mathbf{U}}\right)\mathbf{U}^{n+1} = \mathbf{M}^n_{\mathrm{L}i}\mathbf{U}^{n+1}_{i-1} + \mathbf{M}^n_{\mathrm{C}i}\mathbf{U}^{n+1}_i + \mathbf{M}^n_{\mathrm{R}i}\mathbf{U}^{n+1}_{i+1} = -\mathbf{R}_i \tag{35}$$

with each term calculated as follows:

$$\mathbf{M}_{\mathrm{L}i} = \frac{2\mathbf{A}_{i-1/2}}{(\Delta x_i + \Delta x_{i-1})} \tag{36a}$$

$$\mathbf{M}_{\mathrm{C}i} = \left[\alpha\frac{3}{2\Delta t} - \frac{\partial\mathbf{S}}{\partial\mathbf{U}}\right]\Delta x_i - \frac{2\mathbf{A}_{i-1/2}}{(\Delta x_i + \Delta x_{i-1})} - \frac{2\mathbf{A}_{i+1/2}}{(\Delta x_{i+1} + \Delta x_i)} \tag{36b}$$

$$\mathbf{M}_{\mathrm{R}i} = \frac{2\mathbf{A}_{i+1/2}}{(\Delta x_{i+1} + \Delta x_i)} \tag{36c}$$

$$\mathbf{R}_i = \frac{\left(-4\mathbf{U}^n + \mathbf{U}^{n-1}\right)}{2\Delta t}\Delta x_i + \mathbf{F}^n_{i+\frac{1}{2}} - \mathbf{F}^n_{i-\frac{1}{2}} - \mathbf{S}^n_i \tag{36d}$$

Iterations are performed using a Newton solver until $\|\mathbf{U}^{n+1} - \mathbf{U}^n\| < 10^{-8}$.

4.3. Discontinuous Galerkin - Multifluid

The discretised equations in the DG framework:

$$\sum_e\int_e\varphi_i\varphi_j\partial_t u_j dV - \sum\int_e\partial_x\varphi_i\left(\mathbf{F}_h\right)dV + \sum_e\int_e\varphi_i\mathbf{S}_h dV + \sum_f\int_f\gamma\left(u^+, u^-; \varphi_i^+, \varphi_i^-; \mathbf{n}\right)dS = 0 \tag{37}$$

with e the elements and f the interfaces in the mesh, γ is the numerical flux (with Roe flux used in this work), $\mathbf{n}$ the outward normal from the cell interface and the discretized flux and source terms:

$$\mathbf{F}_h = \mathbf{F}(u_h), \quad \mathbf{S}_h = \mathbf{S}(u_h), \tag{38}$$

The superscript $^{\pm}$ indicate the two sides of the interface considered. Since a shape function φ_i is supported on a single element, this further simplifies to the semi-discrete form

$$M_{ij}\partial_t u_j = \mathbf{R}_i \tag{39}$$

with M_{ij} the mass matrix defined as

$$M_{ij} = \int_e \varphi_i \varphi_j dV \tag{40}$$

with e the common element on which both φ_i and φ_j are defined, and $\mathbf{R}_i$ the (steady) residual associated to shape function φ_i:

$$\mathbf{R}_i = \sum_e \int_e \partial_x \varphi_i (\mathbf{F}_h)\, dV - \sum_e \int_e \varphi_i \mathbf{S}_h dV - \sum_f \int_f \gamma\left(u^+, u^-; \varphi_i^+, \varphi_i^-; \mathbf{n}\right) dS \tag{41}$$

This expression can be reformulated as a set of ordinary differential equations for each of the unknowns, by inverting the mass matrix:

$$\partial_t u_i = M_{ij}^{-1} \mathbf{R}_j \tag{42}$$

The fact that the mass matrix is defined per element allows for its exact inversion. The method used for the time integration of in this work is the fourth-order six-stage Explicit first stage Single Diagonally Implicit Runge-Kutta (ESDIRK64) scheme. Starting from

$$\partial_t u_i = M_{ij}^{-1} \mathbf{R}(\mathbf{u}_j) \tag{43}$$

with M_{ij} being the mass matrix resulting from the DG discretization and $\mathbf{R}$ the residual. The multistage algorithm is then [26]

$$\begin{aligned} u^0 &= u^n \\ u^s &= u^n - \Delta t \sum_{j=1}^{i} a_{ij} \mathbf{M}^{-1} \mathbf{R}(u^j) \\ u^{n+1} &= u_h^s \end{aligned} \tag{44}$$

For a detailed description of the Butcher tableau associated to this scheme the reader must refer to the appendix of [26]. The first stage is explicit as shown in eq.44 with the term $u^0 = u^n$. This is due to the fact that the term Butcher coefficient $a_{11} = 0$ in this methods. Conversely, the last stage updates the solution at the next time. Between these two terms, the scheme is composed of s non-linear problems that has to be solved numerically. The system of s non-linear equations is solved using a classical Newton approach.

5. Results

This section will be divided into two parts: first we study the differences that arise in the simulation of the chosen testcase when we change the physical model adopted (from multifluid to multicomponent) using a finite volumes discretization in both cases; in the second part we mantain the physical equations unchanged (multifluid eqs.8 - 12) and we compare the results of the reference finite volume with the newly developed Discontinuous Galerkin.

5.1. Multifluid vs. Multicomponent

The two physical models have been compared varying the collisionality inside the domain: assuming the majority of (elastic) collisions occurs between charges and neutrals [15], the collision frequency are modified by varying the neutral pressure P_n and retrieving the neutral number density from it $n_n = P_n/k_B T_n$. The test condition adopted can be found in Table 3. Results are shown in Fig.3-4 in terms of number density and electric potential profiles. The matching in low pressure conditions (Fig.3a,3d,4a,4d) is very poor both in the bulk and in the sheath region; the two models show clear how they behave differently as the number of collisions tends to vanish. While the eqs.8-11 present smooth behaviour in the limit $\nu_{en} \to 0, \nu_{in} \to 0$ (the collision term acts only as uniform source term throughout the domain), the same reasoning is not valid for the multicomponent case: the multicomponent diffusion matrix as an inverse proportionality dependency on the collision parameters. For this reason both the profiles tend to a parabolic shape, typical of

Table 3: Collision frequencies.

	P_n	ν_{in}	ν_{en}
Low	1 Pa	2.97×10^{-2}	4×10^{-1}
Intermediate	100 Pa	0.296	3.99
High	1000 Pa	0.888	11.97

a Boltzmann population with temperature T_e. A more detailed analysis of these limits for both models is left for future work; it is important to notice that rarefied gases conditions are out of validity of application of fluid models, as they violate the continuum hypothesis (the smooth behaviour of the multifluid results should not deceive as it is a result of the assumptions made in the kinetic derivation procedure).
Better agreement is expected (and found) increasing the discharge pressure: we notice though how the agreement is slightly poorer in the general in the sheath region (and in general, counter-intuitively, if the 30 Pa solution is compared to the 10 Pa one. Figures 3b, 3e, 3c, 3f). This behaviour is likely a result of the different boundary condition imposed at the wall (that influences the general solution through eq.6): a more accurate analysis of the strategies detailed in Section 3.2.1, but it is important to notice how the multicomponent solution at the wall is influenced by the collisionality of the mixture (eq.23), while the multifluid flux of ions is not.
Figure **??**

5.2. Finite Volumes vs. Discontinuos Galerkin

In this section we present the first results of the comparison between the finite volumes and the discontinuous methods. The starting testcase is a collisionless mixture of argon plasma ($\nu_{en} = 0, \nu_{in} = 0$) and the simulation is advanced to the same degree of convergence for both solvers. The DG simulation was performed with less elements (100 elements compared to 602 for the FV) with fourth order Gauss-Lobatto-Legendre shape functions that allow to retrieve smooth solution under-resolving the Debye length. Results in Fig. 6-7 show great agreement in all the quantities compared.

6. Conclusion

The aim of the present project is to obtain a high order fluid solver that is able to capture the physics underlying the formation of the sheath. In this document we detailed the first steps in this direction.
We propose a novel (for the field) physical model: this approach, even though it introduces stiffer numerical terms, it relies on a rigorous kinetic derivation and will reduce the computational cost and model complexity when we will deal with more complex mixtures (lower number of equations and natural extensions of the terms to multiple species). The comparisons with the reference solution show interesting results but demand further and more detailed analysis.
In the second part we show some preliminary results of the application of high order methods to the case: the Discontinuous Galerkin framework allows to simulate rapidly varying solutions with less fine mesh, by the use of Finite Elements Methods shape functions. Once again results are greatly encouraging.
Further developments will include the extension to more complex mixtures and geometries: we plan to add more detailed chemistry and to simulate air plasmas (hence the difficulty of introducing molecules and negative ions); we will remove the isothermal assumption in order to study the temperature variation in the fluid (and the influence of thermal protection systems on the dynamics of the sheath); more complex geometries will be introduced in order to describe real life testcases.

Appendix

Recalling eq.32 we report here the matrix $\mathbf{A}^n_{i+\frac{1}{2}}$:

$$\mathbf{A}_{i+\frac{1}{2}} = \begin{bmatrix} \mathbf{A}^{f,f}_{N_S \times N_S} & \mathbf{A}^{f,\phi}_{N_S \times 1} \\ \mathbf{0}_{1 \times N_S} & 1 \end{bmatrix} \tag{45}$$

where the block $\mathbf{A}^{f,f}_{N_S \times N_S}$ accounts for the dependency of the flux in eq.29 with respect to the f (*luid*) variables while the block $\mathbf{A}^{f,\phi}_{N_S \times 1}$ accounts for the dependency with respect to the electric potential ϕ. The bottom part results from the simple consideration $\partial^2_{xx}\phi = \partial_x(\partial_x \phi)$ and the acknowledging that there is no dependency on the gradient of the fluid variables in eq.20; the block matrices are in this way defined as (with $i, j \in \mathcal{S}$):

$$\mathbf{A}^{f,f}_{N_S \times N_S} = \left[\mathcal{A}_{ij}\right], \quad \mathcal{A}_{ij} = -\frac{n_i}{n}\left[\sum_{m \in \mathcal{S}} \left(\delta_{jm} - y_m\right) D_{im}\right] \frac{T_j}{T_h} \tag{46}$$

$$\mathbf{A}^{f,\phi}_{N_S \times 1} = \left[\mathcal{A}_i\right], \quad \mathcal{A}_i = -\frac{n_i}{n}\left[\sum_{j \in \mathcal{S}} D_{ij}\left(n_j q_j - y_j Q\right)\right] \frac{T_e}{T_h}, \tag{47}$$

with δ_{jm} the Kronecker delta.

Acknowledgments

For this work the first author thanks the supervisors prof. Thierry Magin, prof. Koen Hillewaert and Dr. Alejandro Alvarez Laguna. For the theoretical and results sections on the Discontinuous Galerkin

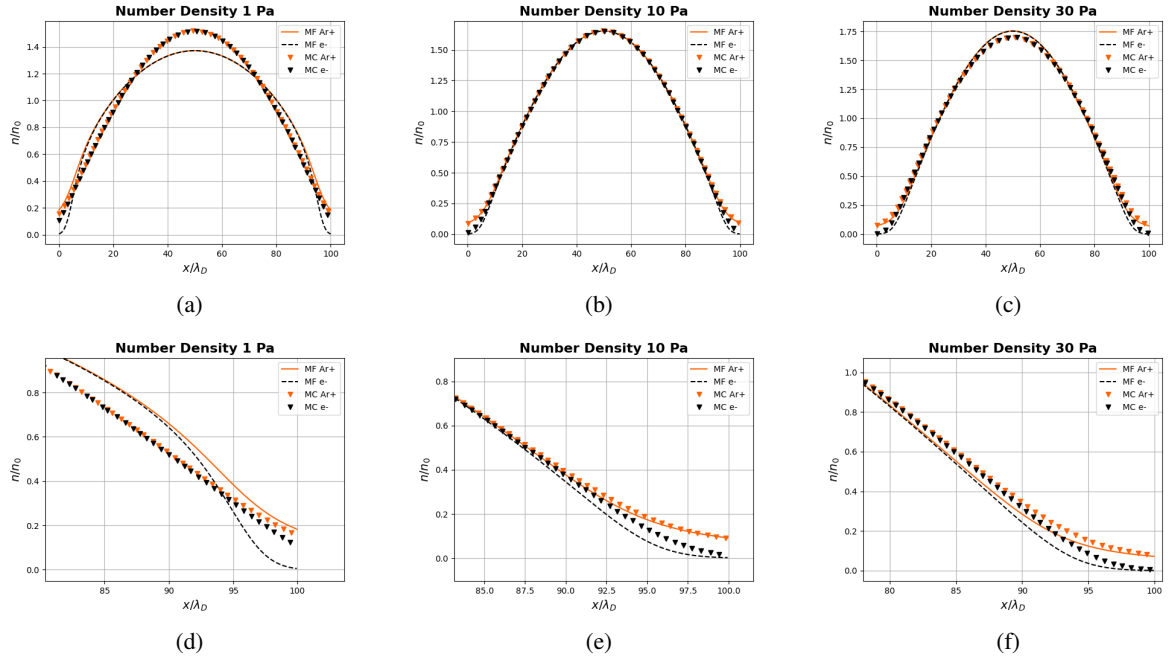

Figure 3: Number density profiles of electrons and ions obtained through multifluid (MF) and multicomponent (MC) modeling.

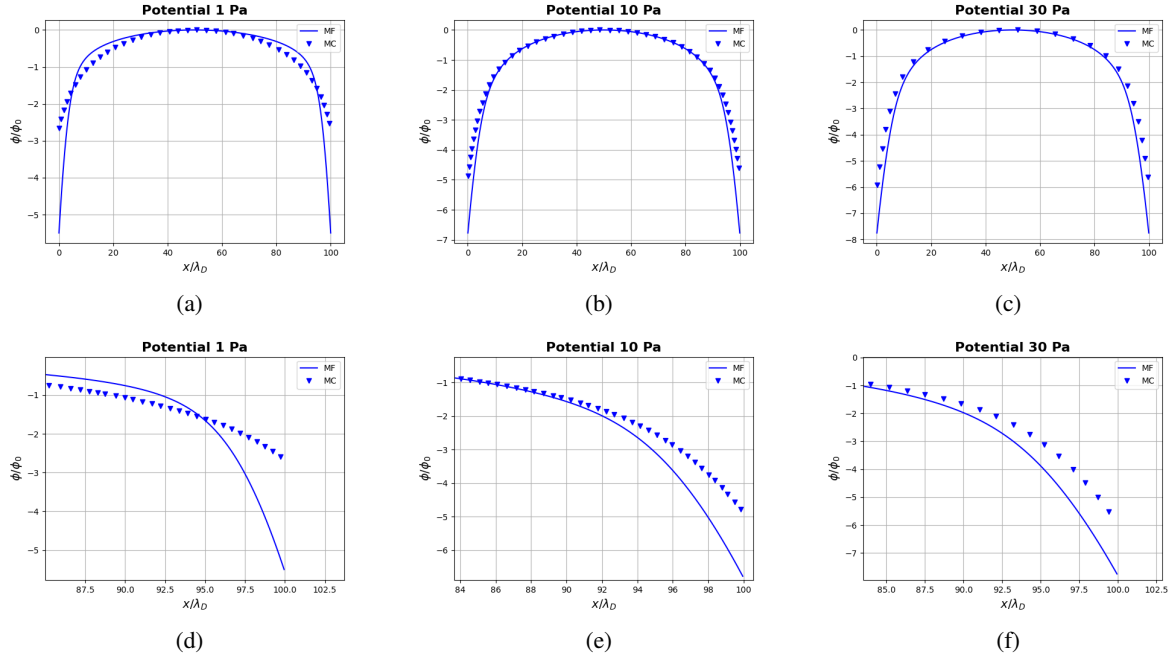

Figure 4: Electric potential profiles obtained through multifluid (MF) and multicomponent (MC) modeling.

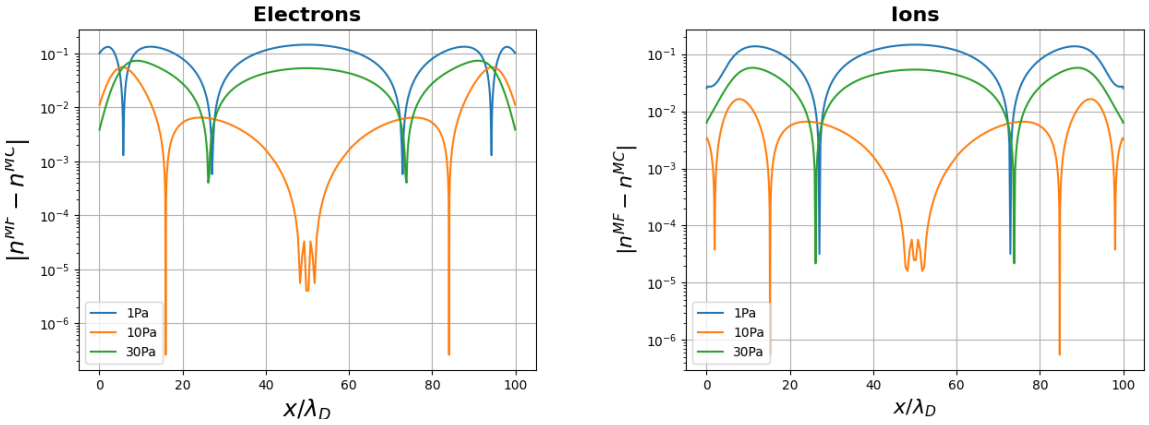

(a) (b)

Figure 5: Logarythmic comparison of the profile obtained at different neutral pressures.

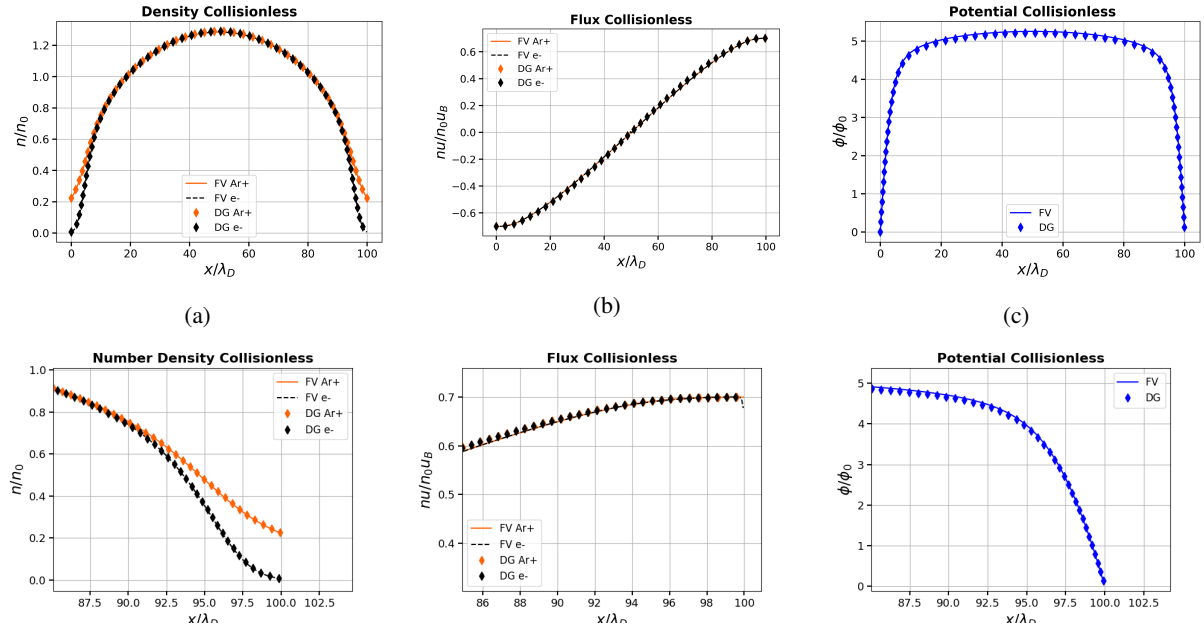

(a) (b) (c)

(d) (e) (f)

Figure 6: Comparison of number density, flux and electric potential profiles for both finite volumes and Discontinuous Galerkin.

Figures/nDensity_noColl_comparison.png

Figure 7: Logarythmic comparison of the profile obtained with the different discretization methods.

we acknowledge the work of Amaury Bilocq, Nayan Levaux and François Custinne. The first author is financed by the Fonds National de Recherche Scientifique (FNRS) through the FRIA grant.

References

[1] M. R. Carruth, J. A. Vaughn, R. T. Bechtel, P. A. Gray, Experimental studies on spacecraft arcing, Journal of Spacecraft and Rockets 30 (3) (1993) 323–327.

[2] L. Uribarri, E. H. Allen, Electron transpiration cooling for hot aerospace surfaces, in: 20th AIAA International Space Planes and Hypersonic Systems and Technologies Conference, International Space Planes and Hypersonic Systems and Technologies Conferences, American Institute of Aeronautics and Astronautics, 2015.

[3] L. L. Alves, A. Bogaerts, Special issue on numerical modelling of low-temperature plasmas for various applications – part i: Review and tutorial papers on numerical modelling approaches, Plasma Processes and Polymers 14 (1690011) (2017) 1–2.

[4] A. Bogaerts, L. L. Alves, Special issue on numerical modelling of low-temperature plasmas for various applications — part ii: Research papers on numerical modelling for various plasma applications 14 (1790041) (2017) 4–5.

[5] L. Garrigues, B. Tezenas du Montcel, G. Fubiani, F. Bertomeu, F. Deluzet, J. Narski, Application of sparse grid combination techniques to low temperature plasmas particle-in-cell simulations. i. capacitively coupled radio frequency discharges, Journal of Applied Physics 129 (15) (2021) 153303.

[6] A. Alvarez Laguna, A. Lani, Y. Maneva, H. Deconinck, S. Poedts, Computational multi-fluid model for partially ionized and magnetized plasma, in: 47th AIAA Plasmadynamics and Lasers Conference, American Institute of Aeronautics and Astronautics, 2016.

[7] A. Alvarez Laguna, T. Pichard, T. Magin, P. Chabert, A. Bourdon, M. Massot, An asymptotic preserving well-balanced scheme for the isothermal fluid equations in low-temperature plasmas at low-pressure, Journal of Computational Physics 419 (109634) (2020) 1–29.

[8] P. Degond, A. Lozinski, J. Narski, C. Negulescu, An asymptotic-preserving method for highly anisotropic elliptic equations based on a micro–macro decomposition, Journal of Computational Physics 231 (7) (2012-04) 2724–2740.

[9] P. Chabert, N. Braithwaite, Physics of Radio-Frequency Plasmas, Cambridge University Press, 2011.

[10] D. Bohm, The characteristics of electrical discharges in magnetic fields, McGraw-Hill, 1949.

[11] K. U. Riemann, J. Seebacher, D. D. Tskhakaya Sr, S. Kuhn, The plasma–sheath matching problem, Plasma Physics and Controlled Fusion 47 (11) (2005) 1949–1970. doi:10.1088/0741-3335/47/11/006.

[12] J. H. Ferziger, H. G. Kaper, Mathematical Theory of Transport Processes in Gases, American Elsevier Publishing Company, 1972.

[13] I. D. Boyd, T. E. Schwartzentruber, Nonequilibrium Gas Dynamics and Molecular Simulation, Cambridge Aerospace Series, Cambridge University Press, 2017.

[14] V. Zhdanov, Transport Processes in Multicomponent Plasma, Vol. 44, Taylor & Francis, 2002.

[15] A. Alvarez Laguna, T. Magin, M. Massot, A. Bourdon, P. Chabert, Plasma-sheath transition in multi-fluid models with inertial terms under low pressure conditions: Comparison with the classical and kinetic theory, Plasma Sources Science and Technology 29 (025003).

[16] M. S. Benilov, A kinetic derivation of multifluid equations for multispecies nonequilibrium mixtures of reacting gases, Physics of Plasmas 3 (4) (1997) 521–528.

[17] V. Giovangigli, Multicomponent Flow Modeling, Birkhäuser, 1998.

[18] T. E. Magin, G. Degrez, Transport algorithms for partially ionized and unmagnetized plasmas, Journal of Computational Physics 198 (2) (2004-08-10) 424–449.

[19] J. D. Ramshaw, C. H. Chang, Ambipolar diffusion in two-temperature multicomponent plasmas, Plasma Chemistry and Plasma Processing 13 (3) (1993) 489–498.

[20] J. B. Scoggins, V. Leroy, G. Bellas-Chatzigeorgis, B. Dias, T. E. Magin, Mutation++: MUlticomponent thermodynamic and transport properties for IONized gases in c++, SoftwareX 12 (2020) 100575.

[21] B. Graille, T. E. Magin, M. Massot, Kinetic theory of plasmas: Translational energy, Mathematical Models and Methods in Applied Sciences 19 (4) (2009) 527–599.

[22] G. Hagelaar, Modelling methods for low-temperature plasmas, Tech. rep., Université Paul Sabatier (2008).

[23] F. J. Artola, A. Loarte, E. Matveeva, J. Havlicek, T. Markovic, J. Adamek, J. Cavalier, L. Kripner, G. T. A. Huijsmans, M. Lehnen, M. Hoelzl, R. Panek, Simulations of COMPASS vertical displacement events with a self-consistent model for halo currents including neutrals and sheath boundary conditions, Plasma Physics and Controlled Fusion 63 (6) (2021) 064004.

[24] A. Munafo, Multi-scale models and computational methods for aerothermodynamics, issue: 2014ECAP0008 (2014).

[25] C. Hirsch, Numerical Computation of Internal and External Flows, second edition Edition, Fundamentals of Computational Fluid Dynamics, Elsevier, 2007.

[26] H. Bijl, M. H. Carpenter, V. N. Vatsa, Time integration schemes for the unsteady navier-stokes equations, Vol. 2612, American Institute of Aeronautics and Astronautics, 2001.

Modeling and estimating measurement uncertainty of VKI's new low density facility

Pedro Jorge

Aeronautics and Aerospace Department, von Karman Institute for Fluid Dynamics, Belgium, pedro.jorge@vki.ac.be

Supervisor: Thierry Magin

Professor, Aeronautics and Aerospace Department, von Karman Institute for Fluid Dynamics, Belgium, magin@vki.ac.be

University Supervisor: Annick Hubin

Professor, Electrochemical and Surface Engineering, Vrije Universiteit Brussel, Belgium, annick.hubin@vub.be

Abstract

The new VKI Low Density Facility(LDF) is a novel experimental facility designed to replicate very low Earth orbit conditions to characterize efficiency parameters of Air Breathing Electric Propulsion(ABEP) intake-collectors. In this work, we present the development of a simple model that allows measuring the collection efficiency from quantities measurable in the facility and evaluate its validity with DSMC simulations. Moreover, we provide an estimate of the measurement uncertainty of the intake efficiency.

Keywords: ABEP, DSMC, TPMC, Uncertainty estimation

1. Introduction

Operation of satellites on Very Low Earth Orbits(VLEO), defined as orbits with altitudes bellow 450 km and as low as 160 km, provides numerous benefits including increased performance of optical and radiometric payloads, reduced costs of vehicle development and launch, as well as lower risk of collision with space debris [1]. On the other hand, VLEO orbits magnify the challenges presented in higher altitude orbits. Firstly, due to the predominance of atomic oxygen, a chemically reactive species, surface erosion poses a challenge to mission lifetime. Secondly, VLEO orbits atmospheric density is increased, causing increased drag that requires frequent compensation. Overcoming the aforementioned challenges can be achieved through the study of VLEO appropriate erosion resistant materials as well as through advances in Air Breathing Electric Propulsion(ABEP) technology. ABEP systems rely on an Air Intake-Collector(AIC) to collect and compress atmospheric gas particles, incoming at the satellite at its orbiting velocity, and direct them to the thruster to be ionized and accelerated in order to generate thrust and provide drag compensation. Therefore, the performance of air intake-collectors is crucial to the feasibility of ABEP technology[2; 3]. Given VLEO's low density and typical satellite dimensions, gas flow inside intake-collectors is free molecular, meaning that collisions between gas particles are rare and flow behavior is dominated by gas-surface collisions. Thus, intake performance as well as overall satellite drag depend heavily on gas surface interaction between atmospheric species and the intake surfaces.

Gas surface interactions in Low Earth Orbit(LEO) have been previously studied by way of flight observations[4; 5; 6] as well as on-ground laboratory testing[7; 8; 9; 6; 10]. Both study types have focused mostly on the study of reactive gas surface interactions, with special focus on the erosion of satellite materials by atomic oxygen. Moreover, most studies of air intake collectors performance are full tests of ABEP systems and provide less focus on intake analysis [11; 12] or are based on numerical simulations[13; 14; 15; 16]. Numerical simulation typically rely on the simple Maxwell model to simulate gas surface interaction between the flow particles and intake surfaces. Therefore, experimental ef-

forts to characterize non-reactive gas-surface interactions and its effects on flow behavior and intake performance are crucial to the progress of VLEO satellite technology. Currently, laboratory investigations are mostly challenged by the difficulty in reproducing orbital flow conditions since most flow sources offer a compromise between producing the correct gas species, appropriate densities and particle velocity. Although written 2 decades ago, Kleiman et al.[17] review of existing facilities still provides relevant insights on the source technologies available today. A noteworthy modern iteration of LEO plasma facilities is the Chamber for Atmospheric and Orbital Space Simulation (CHAOSS) at the University of Colorado Springs. The CHAOSS facility uses a magnetically filtered oxygen plasma source that produces a plume of streaming atomic oxygen ions with orbital energies(5 eV) and low electron temperature[18]. The facility aims to study momentum exchange through gas surface interactions through the use of a nano-Newton thrust stand. Moreover, it allows the study of GSI without the neglect of the effect of solar radiation[19]. As drawbacks, the use of a plasma source results in a non duplication of the chemical composition for lower orbits. Moreover, the facility is composed of a single chamber which makes the qualification of ABEP intake collectors a more challenging task. A more recent facility still under construction, is the Rarefied Orbital Aerodynamics Research facility (ROAR) single chamber wind tunnel at the University of Manchester uses a source based on electron stimulated desorption to generate neutral hyperthermal oxygen atoms[20]. The facility focus on studying gas-surface interactions through scattering experiments although scaled intake geometries tests are also planned[21]. Possible limitations of the facility include it comprising a single chamber and inherent limitations of its flow source such as relative low flux, high beam divergence and energy spread[17].

VKI is currently building a small scale Low Density Facility(LDF) designed to duplicate VLEO conditions and with the immediate purpose of characterizing efficiency parameters of ABEP intake-collectors. The facility comprises two vacuum chambers and features an Inductively Coupled Plasma(ICP) source with magnetic beam control. In this work, we give an high level overview of the facility and present a simplified model for the indirect measurement of performance parameters based on measurable quantities in the LDF. Moreover, we simulate the operation of the LDF by means of Direct Simulation Monte Carlo(DSMC) simulations. The simplified model is confronted against the aforementioned higher fidelity DSMC simulations and its validity assessed. Finally, the simplified model is used to estimate the uncertainty on the measurement of intake collector performance parameters in the LDF based on known instrument uncertainties. The paper is organized as follows: following this introduction, Section 2 presents the main intake performance parameters as well as an high level description of the facility. Section 3 presents the simplified model of gas flow in the chambers as well as the implemented TPMC code that allows closure of the model without the need for detailed simulations. Section 4 presents the results of the 0-D model simulation of the facility and confronts them with the higher fidelity DSMC simulations. Finally, estimates of the uncertainty of intake performance measurements in the low density facility are computed based on Monte Carlo error propagation are provided in Section 5 before the main conclusions of this work are drawn.

2. Intake performance qualification in the Low Density Facility

In this section, we introduce the main parameters that describe intake performance. Moreover, the low density facility design is described and justified according to its main goal of measuring said performance parameters.

2.1. Performance parameters

The main purpose air intake-collectors is to direct the greatest amount of free stream air particles, the effective propellant of ABEP systems, to the electric thruster where particles are ionized and accelerated to provide thrust. The collection efficiency effectively measures the transparency of an intake to the incoming flow and can be defined as the ratio of mass flow rates at the exit and at the inlet of intake collector, as in Eq.1,

$$\eta = \frac{\dot{m}_{out}}{\dot{m}_{\infty}}, \tag{1}$$

where $\dot{m}$ is the mass flow rate and the subscripts *out* and ∞ refer to the outlet and free stream conditions, respectively. However, atmospheric density is too low for proper ignition of typical ion thrusters and the intake-collector is required to provide a degree of flow compression that is sufficient for thruster ignition. The compression ratio quantifies the degree of such compression as is defined as

$$\nu = \frac{n_{out}}{n_{\infty}}, \tag{2}$$

where n is the particle number density. It is often the case that higher collection efficiencies imply a lower compression ratio while the inverse is also true and there needs to be a trade-off between the two quantities. In the next subsection, a description of the facility is provided together with a discussion on the methodology for measuring the performance parameters.

2.2. Low Density Facility overview

The Low Density Facility can be briefly described as being composed by two vacuum chambers connected by a pipe housing the the engineering model of the air intake collector to be tested. The tested intake model size is limited by the pipe diameter of 0.1317 m and length 0.43 m. Figure 1 shows a technical drawing of the facility and its dimensions. The orbital flow conditions are created through a Particle Flow Generator(PFG) which generates particles that traverse the intake and are either rejected back into the main chamber or collected by the secondary chamber.

2.2.1. Pumping system

The facility is comprised of a high vacuum system with enough pumping capacity to allow for free molecular flow conditions with continuous PFG operation. The vacuum pumping system comprises one rotary vane mechanical pump capable of pumping down both vacuum chambers to approximately 10^{-2} mbar, together with one turbomolecular pump on each chamber with enough capacity to reach an ultimate pressure of approximately 10^{-7} mbar with the PFG turned off and approximately 10^{-5} mbar under typical operating conditions. The chamber materials are stainless steel 316 due to its welding, polishing and corrosion resistant properties and are fine glass bead blasted in order to prevent sorption. It is worth to note that the pressure of orbital conditions, approximately 1×10^{-7} mbar, is not duplicated. However, since the flow regime in the facility is free molecular the aerodynamic behavior of the flow should be duplicated as long as gas surface interactions are not modified by facility pressure conditions, for example through different adsorption dynamics at the two pressures.

2.2.2. Flow generation

The particle flow generator is an ICP source with incorporated magnetic beam control and is designed to duplicate orbital flow conditions by providing an adequate ion velocity ($u_{ion} \approx 7600\ \mathrm{m \cdot s^{-1}}$) and temperature ($T_{ion} \approx 1000$ K) as well as a low electron temperature ($T_e \leq 0.5$ eV). The expected source total mass flow rate is 3 sccm while a produced minimum beam ion current of 10 mA is expected. Such ion current is translated into a flux of fast particles that is lower than that expected in orbit. This flux disparity is not problematic since exposure tests are not planned for such facility. Moreover a low flux presents advantages as it allows for a less demanding pumping system.

A disparity between flight and ground testing conditions exists as well regarding the charge state of the particles in the facility. On one hand, Knechtel and Pitts studied gas surface interactions charged nitrogen molecules and argued for little difference in their interactions with surfaces [22] compared with neutral particles. On the other hand, care must be taken so that electric fields present in the facility do not alter the ion trajectory sufficiently for the flow not to be representative of orbital conditions. To this effect, the possibility of electrically biasing the intake is being considered in order to mitigate the creation of electric fields.

2.2.3. Diagnostics

Facility diagnostics are crucial to the measurement of operating test conditions and AIC performance parameters. To this end, both cold-cathode ionization gauges and ceramic capacitance gauges will be installed in each chamber so that the pressure evolution can be monitored in the facility. Thermocouples will be installed to measure both chambers' temperature and a flow meter is installed into the PFG to allow measuring the PFG flow rate. Moreover, a Retarding Field Energy Analyzer(RFEA) and a Faraday probe will be used to measure the current as well as the energy distribution of ions at different positions in the plume and at the entrance of intake. Finally, the chambers include optical ports so that optical access is possible in the plume and near PFG region. To measure the electron temperature and densities the spectral signature in the plasma plume will be measured through a spectrometer and interpreted via detailed collisional radiative models.

Analyzing Eqs. (1) and (2) one understands that while the compression ratio can be directly computed by the measurement of each chamber pressure and temperature to obtain each the local number density, direct measurements of the collection efficiency are not easily realizable with the current diagnostic set up. Indeed, although measuring flow rates of charged particles at the AIC entrance will be performed through a RFEA probe, at the exit of the intake some of

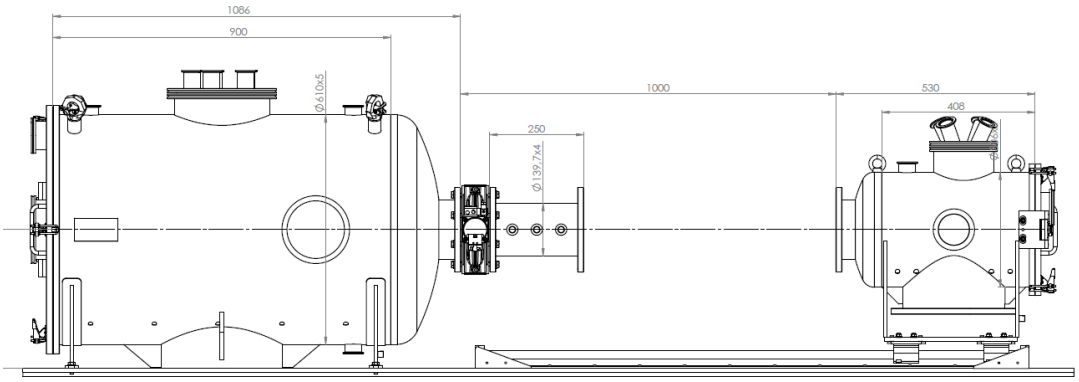

Figure 1: Technical drawing of the Low-Density Facility. Dimensions in mm

these previously charged particles will have been neutralized through either collisions with walls or background gas particles and would therefore not be measured by the probe, resulting in erroneous measurements. On the other hand, measuring fluxes of neutral particles is not trivial in vacuum conditions [23].

In alternative, conductances, a quantity related to collection efficiency, are usually measured by measuring the pressure difference between two vacuum chambers connected by the component to characterize [24]. A components conductance expresses the probability of a particle from one chamber to traverse the component and reach the other chamber. Typically, experiments include one chamber that is fed with a thermalized feed of gas and another that is kept at a lower pressure though the pumping system. Therefore, the net mass exchange is a consequence of the component geometry and can be measured by the pressure difference in each chamber. An analogous test can be performed in the LDF. However, while in typical conductance tests, the flow entering the component at each end is completely thermalized, the same cannot be said in the LDF as the PFG generates a plume of fast particles. Therefore, calculating the collection efficiency from pressure measurements of both chambers is possible but requires an additional modeling layer of the relevant flows that traverse the AIC as well as an extensive characterization of the facility operating conditions. In the next section, we present the development of a simple model that allows measuring the collection efficiency from the available measurable quantities in the facility.

3. Model development

In the previous section, modeling was highlighted as an important feature to infer intake performance parameters from pressure measurements. In this section, we aim to develop a 0-D model with the aim of interpreting measurements in the low density facility.

3.1. 0-D model of the flow in the facility

The 0-D model relies on a simple system of equations based on mass conservation considerations for each chamber as

$$\begin{aligned} V_1 \frac{d}{dt}(n_{c1}) &= \dot{N}_{PFG} + \dot{N}_{2,therm} + \dot{N}_{1,\text{leak}} \\ &\quad - \dot{N}_{P1} - \dot{N}_{1,\text{beam}} - \dot{N}_{1,\text{fast}} - \dot{N}_{1,\text{therm}}, \\ V_2 \frac{d}{dt}(n_{c2}) &= \dot{N}_{1,\text{fast}} + \dot{N}_{1,\text{beam}} + \dot{N}_{1,\text{therm}} + \dot{N}_{2,\text{leak}} \\ &\quad - \dot{N}_{P2} - \dot{N}_{2,\text{therm}}, \end{aligned} \tag{3}$$

where $\dot{N}_i$ represents the the relevant facility particle flow rates in [particles $\cdot\, \text{s}^{-1}$] and the flow rates exchanged through the AIC follow the convention $N_{j,i}$ where j is the flux chamber of origin and i is the flow type. As an example, $\dot{N}_{1,\text{ slow}}$ denotes the flow rate of thermalized particles that flow from chamber 1 to chamber 2. The flow rates taken into account by the model are detailed on Fig. 2.

Provided there is knowledge of the relevant particle flow rates, the system represents a simple initial value problem that can be integrated using a simple ODE integrator. In most test cases, experimental campaigns will focus on steady state operation and the Left Hand Side(LHS) of Eq 3 can be taken as 0. However, experimentally, the problem is the inverse. Chamber quantities are measured and are then related to the flow rates through the intake in order to extract the collection efficiency. The particle number densities variations can be promptly converted into measurable pressures and

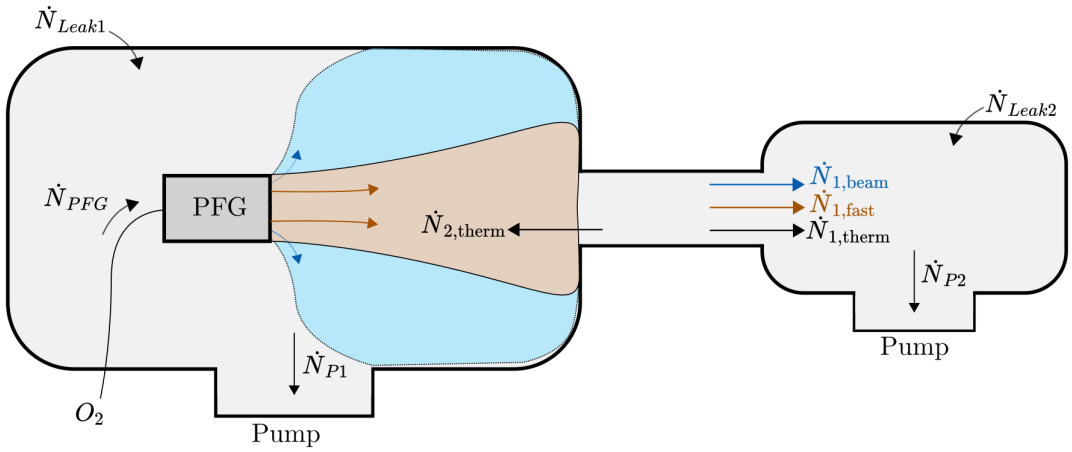

Figure 2: Schematic of the relevant LDF and the relevant fluxes considered in the 0-D model. Blue flow represents the plume of non accelerated particles, orange represents the fast particles accelerated by the PFG while the grey background depicts the background particles in each chamber.

temperatures through the ideal gas equation of state as

$$\frac{d}{dt}\left(p_{ci}\right) = k_b T_{ci} \frac{d}{dt}\left(n_{ci}\right). \tag{4}$$

On orbit, the flow transmitted through the intake arises from the flow of fast particles (relative to the moving satellite) impinging on the intake entrance. However, on ground tests, different flow rates contribute to the mass exchange between chambers. These should be modeled so that one can derive the collection efficiency from the contribution of fast particles only, the ones which duplicate orbital conditions. We can model the terms $\dot{N}_{1,slow}$, $\dot{N}_{2,slow}$, $\dot{N}_{1,beam}$ and $\dot{N}_{1,fast}$ considering that the pressure in the facility is low enough for the free molecular flow assumption to be valid. The slow flow rates through the AIC are given through classical kinetic theory expressions as,

$$\dot{N}_{i,\,\mathrm{slow}} = \frac{n_{ci}}{4} \langle v_i \rangle A_i \tau_{i,\,\mathrm{slow}}\,, \tag{5}$$

where $n_{c,i}$ is the background number density in chamber i , A_i is the entrance AIC area, $\tau_{i,\,\mathrm{slow}}$ is the probability of a particle from chamber i to be transmitted to the other chamber and $\langle v_i \rangle$ is the background mean velocity computed as

$$\langle v_i \rangle = \sqrt{\frac{8 k_b T}{\pi m}}, \tag{6}$$

where k_b is the Boltzmann constant and m is the mass of the gas species.

Regarding $\dot{N}_{1,fast}$, since it is a flow rate related to fast particles produced in the PFG, it is useful to analyze the PFG flow first. The PFG is able to accelerate particles by ionizing an incoming flow rate of gas feed and subsequently accelerating the ionized particles through a potential drop. A fraction of the gas that is fed to the PFG exits without having been ionized, and therefore is not accelerated. This is accounted by the so-called mass utilization efficiency η_{PFG}, and, since only charged particles are accelerated, a significant portion of the flow rate fed to the PFG will exit the PFG without suffering any acceleration. Therefore, the flow rate emitted by the PFG can be analyzed as two different streams. One of the streams is composed of slow particles while another is composed of fast ions which flow through the vacuum chamber. In both streams, a fraction of the particles will reach the intake entrance, f_{beam} and f_{ion}, while the remainder will miss the AIC entrance due to the plume expansion, collide and thermalize with chamber walls and contribute to the increase in background pressure. Therefore, the flow rate of slow particles that reaches the intake from chamber 1 and is transmitted to chamber 2 is computed as,

$$\dot{N}_{1,\mathrm{beam}} = \dot{N}_{\mathrm{PFG}}(1-\eta_{PFG}) f_{\mathrm{beam}} \tau_{1,\mathrm{beam}}. \tag{7}$$

where $\tau_{1,\mathrm{beam}}$ is the probability of a slow beam particle impinging on the AIC entrance to be transmitted to chamber 2. The development of the expression for the flow rate of fast particles that reaches the intake from chamber 1 and is transmitted to chamber 2 is

analogous to that of slow particles,

$$\dot{N}_{1,\text{fast}} = \dot{N}_{\text{PFG}} \eta_{PFG} f_{\text{ion}} \tau_{1,\text{fast}}, \tag{8}$$

where $\tau_{1,\text{fast}}$ is the probability of a fast ion impinging on the AIC entrance to be transmitted to chamber 2. This probability is exactly equivalent to the concept of collection efficiency if the fast ions duplicate the flow experienced on orbit. Therefore, if knowledge of all the other flow rates is obtained, it is possible to invert one of the equations from the system (3) to obtain the collection efficiency, for example

$$\begin{aligned} \dot{N}_{1,\text{fast}} &= \dot{N}_{\text{PFG}} \eta_{PFG} f_{\text{ion}} \tau_{1,\text{fast}} \\ &= \dot{N}_{P2} + \dot{N}_{2,\text{therm}} - \dot{N}_{1,\text{beam}} - \dot{N}_{1,\text{therm}} - \dot{N}_{2,\text{leak}}. \end{aligned} \tag{9}$$

Having developed the expression for the AIC exchange flow rates in Eqs (5) to (8) we notice that most quantities are directly measurable or known. Quantity n_{ci} is computed through pressure and chamber temperature measurements, $\dot{N}_{\text{PFG}}$ is measured through the PFG flow meter and f_{ion} is measured with a Faraday probe. Moreover, the other flow rates can be measured through dedicated tests detailed in Section 5. Therefore, the use of Eq (9) would allow the estimations of the collection efficiency of the intake provided the model assumptions hold (Free molecular flow, uniformly distributed background density). If the free molecular flow assumption is valid, the collection efficiency depends only on the geometry of the intake, the velocity distribution of impinging particles and on the gas-intake wall surface interaction. If estimates of the different flow transmission probabilities of the AIC could be obtained it would be possible have closure of the 0-D model which would allow the simulation of the average pressures in each chamber. A Test Particle Monte Carlo (TPMC) code can provide such estimates and, perhaps more importantly, allow estimations of gas surface interactions (GSI) from the aforementioned experimental measurements. To this effect, we have developed a Python TPMC code that is described in the next section.

3.2. Test Particle Monte Carlo code

A TPMC code is based on the assumption of free molecular flow such that a particle trajectory is independent of other particles, i.e. gas-gas collisions are negligible [25]. Therefore, the TPMC code considers that particle trajectories can only be altered through collisions with walls. Upon colliding with walls, the particles are reflected based on wall laws, known as collision kernels, which are parameterized by accommodation coefficients and define the probability density that an incident particle with velocity $\mathbf{v_i}$ is reflected with velocity $\mathbf{v_r}$[26]. Presently, two collision kernels are implemented, the Maxwell kernel (parameterized by one accommodation coefficient, α) and the CLL kernel (parameterized by two accommodation coefficients, α_n and α_t)[27]. The accommodation coefficients represent the probability of a reflection being diffuse, in the case of the Maxwell kernel, or the degree of accommodation of the normal and tangential kinetic energy., in the case of the CLL kernel.

The simulation starts by sampling initial particle positions and velocities consistent with the flow to be simulated. If one is interested in transmission probabilities of slow particles,$\tau_{1,slow}$, a Maxwellian distribution at the background gas temperature is sampled at the AIC entrance. On the other hand, for the the fast particle transmission probability, $\tau_{1,fast}$, the computation starts by sampling the PFG conditions, e.g. speed ratio and flow temperature, at the PFG exit and propagating the particle trajectories up to the AIC entrance. The fraction of particles that reach the AIC entrance, f_{ion}, from the PFG is directly obtained by counting enough simulated particle trajectories. To compute the transmission probability, the particle trajectories are propagated from the AIC entrance up to either the AIC exit or back to the AIC entrance. It is noteworthy that the TPMC simulations could have as input velocity distributions functions that are obtained experimentally at a specific point. The trajectories could then be propagated from this point with the experimental velocity distribution function therefore providing support in the reconstruction of the experiment.

Moreover, to account for the fact that ground testing is performed at higher than flight background pressures, which can lead to a non-negligible effect in the particle trajectories, Monte Carlo Collisions (MCC) were implemented into the TPMC code. In the case that the background density is significantly higher than the flow density, the background particles are mostly unaffected by the flow particles. However, the opposite statement is not necessarily valid and the behavior of fast ions can be influenced by the background gas particles. Under these circumstances, the background gas is simulated using its density, temperature and mean velocity and the probability of collision between a fast particle with a background gas particle is [28]

$$P_{\text{MCC}} = 1 - \exp\left[-\Delta t \, g \, n_{\text{BG}} \, \sigma_{T,ij}(g)\right], \tag{10}$$

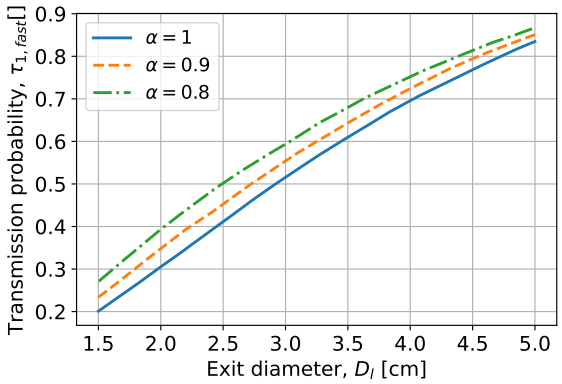

Figure 3: Fast particle transmission probability vs exit diameter and Maxwell accommodation coefficient computed with the TPMC code.

where λ is the background gas mean free path, n_{BG} is the background number density and $\sigma_{T,ij}(g)$ is the collision cross section. For each particle trajectory, the algorithm samples from the specified background properties a particle velocity. In the present case a Maxwellian distribution is assumed for the background particles. In case of collision, the post collision velocity of the fast particle is obtained from either hard or soft sphere scattering and the trajectory propagation is continued. Therefore, for the high speed ratios expected for the particles emitted by the PFG, it is expected that collisions with background particles increase the spread of the beam particles and reduce the beam collimation. This in turn should promote collisions with the walls and reduce the transmission probability of particles.

The TPMC simulation is comprised of a large enough number of particle trajectories which collectively represent the behavior of the flow. The division of the number of particles that reach the AIC exit by the number of particles that reach the AIC entrance represents the transmission probability. Figure 3.2 shows TPMC results of fast particle transmission probabilities for different AIC conical geometries and Maxwell accommodation coefficient. The considered conditions are $S = 10$, $D_{\mathrm{PFG}} = 9$ cm, $L_{\mathrm{PFG}} = 10$ cm, $L = 30$ cm, $D_L = 10$ cm where S defines the speed ratio as

$$S = \frac{V_{bulk}}{\sqrt{\frac{2k_bT}{m}}}. \tag{11}$$

In the next section, we perform simulations of the facility operation using DSMC and the 0-D model in order to evaluate the validity of the simplified conservation model.

4. LDF facility simulation

The flow in the low density facility is simulated using both the 0-D model and DSMC simulations with the same inputs so that the 0-D model results can be verified. For this effect, we will take the values of measured quantities in the facility as the specifications given by components manufacturers i.e., pumping speed and PFG characteristics. Regarding the PFG we assume operation with argon with a mass flow rate of 3 sccm, a mass utilization, $\eta_{PFG} = 5\%$, bulk flow velocity of 7600 $\mathrm{m \cdot s^{-1}}$ and ion and neutral temperature of 1500 K. Regarding the pumping system we assume the manufacturer pumping speed of $S_1 = 2900$ $\mathrm{L \cdot s^{-1}}$ and $S_2 = 2000$ $\mathrm{L \cdot s^{-1}}$ for the main and secondary chambers, respectively. Moreover we consider that the chamber walls, with which gas particles thermalize, are maintained at a constant temperature of 300 K and that leaks in main and secondary chamber are equal to zero. Moreover, simulations are performed with the PFG-AIC distance taken as $d_{PFG} = 0.6$ and 0.2 m. The AIC is taken as either a cylinder with diameter, $D = 0.1317$ m, and length, $L = 0.43$ m, or a cone with the same length but left and right diameters equal to $D_l = 0.1317$ m and $D_r = 0.0479$ m, respectively

4.1. DSMC simulations

The DSMC computations are 3D simulations of the design shown in Fig. 1 performed with the SPARTA DSMC simulator[29]. The PFG is simulated as a source of two distinct particle populations from the same surface. For this purpose, the SPARTA code was modified to allow for this feature. The two streams have the characteristics described in the previous paragraph. The pumps are simulated by attributing a surface transparency that reproduces the pumping speed, assuming a influx of thermalized particles. Transparencies of 0.638 and 0.588 are attributed to the main and secondary chamber pumps respectively. Gas wall collisions are assumed to be diffuse and after collision particle properties are sampled from a wall normal Maxwellian distribution at the wall temperature of 300 K. Finally, gas-gas collisions are taken into account using the VHS cross section provided by [30]. These include Ar-Ar collisions as well as Ar+-Ar collisions, accounting for charge exchange reactions.

The 3-D surface mesh used is shown in Fig. 4. The domain is discretized with a uniformly spaced mesh with spacing $\Delta d = 0.025m$ and refined in the plume, AIC region and chamber surfaces to half the size, $\Delta d_{ref} = 0.0125m$. For comparison, the mean free

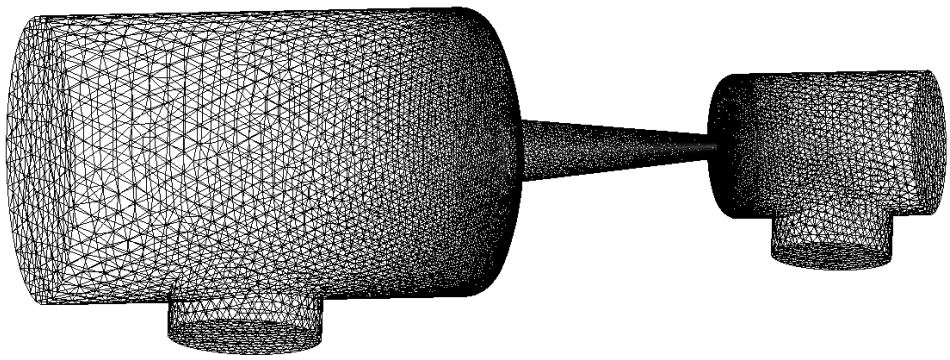

Figure 4: 3-D surface mesh of the low density facility with conical AIC geometry.

path is estimated to be 2 m considering the highest density obtained in simulations and shown in Fig. 5. Moreover, the time step size is chosen to be 1 μs. For reference, the lowest mean collision time in the mixture is the one of CEX reactions estimated as $\tau_{coll,CEX} \approx 25$ ms. The minimum cell crossing time for the refined mesh of $0.0125m$ is estimated as $1.6\,\mu$s. The time step is therefore smaller than both the cell crossing time and a fifth of the minimum collision time[31]. The ratio of physical to simulated particles is chosen to be 10^{10} so that the computational cost is not prohibitively expensive. With the aforementioned ratio, an average of 12 million particles are present in the domain in each time step so that each cell in the simulation has a minimum of 20 particles to provide relevant flow statistics. Results are drawn from grid averages, as in the density, velocity and temperature fields, as well as surfaces at the intake entrance and intake exit where the particle fluxes are computed. For both the computational grid and surfaces of interest, the results are retrieved when steady state is achieved by taking an average over 2000 time steps.

Figure 5 shows the simulated density field considering $L_{PFG} = 0.2$ m for the case of the conical and cylindrical AIC. Due to the low mass utilization efficiency of 5%, the density field is dominated by the neutral plume flowing from the PFG. Nonetheless, it is immediately noticeable that the density fields in each chamber are different due to the different constraints on the chambers mass exchange imposed by the different AIC geometries. Additionally, Fig. 6 shows the distribution of the fraction of CEX neutrals to total fast particles evaluated at the two different PFG-AIC distances for the conical AIC operating conditions. The conical configuration was chosen as it promotes higher background gas densities in the main chamber, and therefore more frequent CEX reaction, when compared to the cylindrical geometry. Estimations of CEX reactions prevalence are important as the available diagnostics of fast particles can only detect the flux of charged particles. If a large fraction of CEX reactions occur and effects due to CEX are not corrected, a flux of neutral fast particles will not be measured. A spatial average of the data of Fig. 6, shows that approximately $P = 10\%$ of the ions emitted by a PFG placed 0.6 m from an AIC undergo CEX reactions before they reach the AIC entrance. To correct for this effect, one should multiply the current measured by the Faraday Probe by $P_{corr} = 1/1 - P$. Moreover, as expected, the CEX effect is less important for lower AIC-PFG distances, as the particles have less time to react. The simulations resulted in an average correction factor of $P = 4\%$. The average correction factors are in agreement with the predictions assuming MCC collisions, Eq. (10), which, assuming a background density of 4.6×10^{17} m^{-3}, yield probabilities of 13.7% and 4.6%, respectively for distances from the PFG of 0.6 m and 0.2 m.

Moreover, the fluxes across the entrance and exit surfaces are evaluated in both normal directions. It is important to point, that even having access to the flux in through each direction of each surface, deriving the transmission probability of fast particles is not trivial. This is due to all types of flow being simulated simultaneously and it being complex to separate the flux due to fast particles from the one due to slow and background particles in post processing statistics. An effective transmission probability that accounts for the three flux sources at the surface (background particles, beam slow particles, fast ions) can be computed through $\tau_{eff} = \dot{m}_{out,exit}/\dot{m}_{in,entrance}$. The results for the different configurations are presented in Table 1. Therefore, even with high fidelity simulations, obtaining the collection efficiency supposes the need

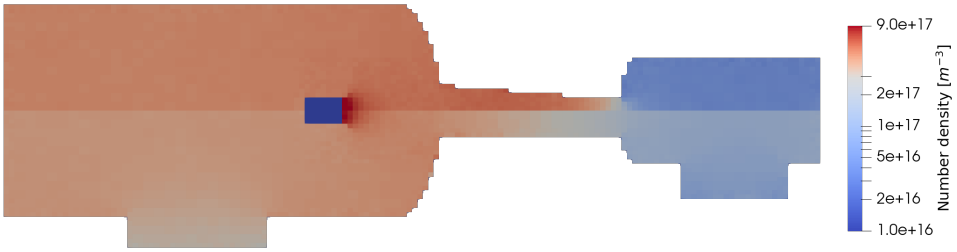

Figure 5: Density field in the LDF for the conical (Top) and cylindrical (Bottom) AIC geometries.

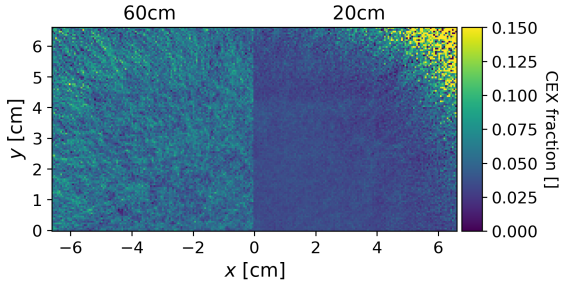

Figure 6: Density of CEX neutrals to total fast particles ratio evaluated at a square section inscribing the intake circular section for different PFG-AIC distances.

of further modeling or of multiple simulations of each stream of particles separately. To this effect, we can evaluate the validity of the 0-D assumption by analyzing the distribution of the background particles density shown in Fig. 7 for the case of the cylindrical AIC 0.2 m from the PFG. It is apparent that the density deviates from the average density in both chambers close to the pump pipe as particles are removed from the simulation if they reach the pump as well as close to the AIC entrance as the particles from the beam that do not reach the AIC entrance are reflected backwards from the chamber walls. However, the biggest deviation appears near the exit of the AIC in chamber 2 due to the beam of particles exiting the AIC. It can be argued that this deviation is not made up of real background particles as the particles exiting the intake have a clear direction bias, although they have thermalized with the intake walls. However, we have no reliable way to filter them out from our statistics and therefore need further confirmation of the 0-D model appropriateness. This is the subject of the next section.

4.2. 0-D model verification

In the present section, we compare the results of the DSMC simulations for the background density as well as effective transmission probability against the results of the 0-D model. We close the 0-D model by computing predictions of quantities otherwise to be measured experimentally. The analytical expression proposed by [32] is used to compute the effective pumping speed of each pump and connecting pipe

$$S_{eff} = \frac{S F_0}{F_0 + S(1/\alpha - 1)}, \tag{12}$$

where $F_0 = \frac{\langle v_i \rangle}{4} \pi R^2$, α is the transparency of the connecting pipe to thermalized flow, and R is the pump orifice radius. The transmission probabilities of the AIC as well as the fraction of ions or neutrals that reach the intake entrance are computed using the TPMC code.

The results for the 4 different configurations are provided in Table 1. As expected, different intake configurations results in substantial differences in chamber pressures, as different constraints are imposed on the mass exchange between the chambers. More transparent configurations (cylinder) result in higher secondary chamber densities due to the higher flow transmission probability. Moreover, the secondary chamber density increases in both configurations when the AIC-PFG distance decreases, as more fast particles reach the intake entrance.

The comparison between the DSMC and 0-D model simulations show an excellent agreement with a maximum error in the density predictions of 2.5%. The agreement justifies the use of the simplified model as a functional relationship to extract the transmission probability from the experimental quantity outputs. In the next section, we will use the 0-D model to estimate the uncertainty of the transmission probability predictions.

5. Measurement uncertainty estimation

Instrument uncertainties can compromise the accuracy of the results obtained with the developed

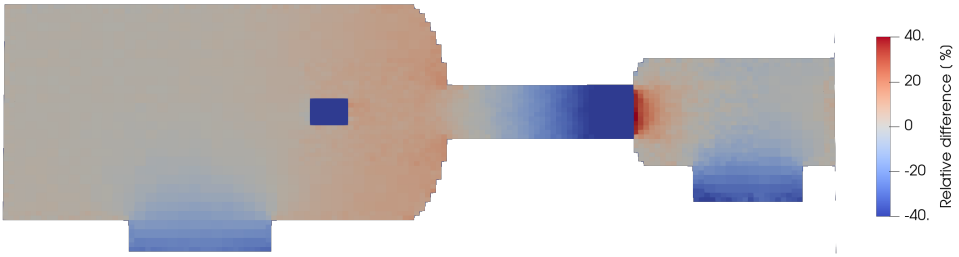

Figure 7: Distribution of the relative difference between the local background density and each average chamber density. The simulation setup comprises a cylindrical AIC and a PFG-AIC distance of $L_{PFG} = 0.2$ m. Intake fields are related to chamber 1 average density

Table 1: Comparison of DSMC and 0-D model results. ϵ denotes the relative difference between DSMC simulations and 0-D model in percentage.

AIC geo.	L_{PFG} [m]	Quantity	DSMC [$m^{-3}/-$]	ϵ [%]
Cone	0.2	n_{c1}	4.6×10^{17}	2.1
		n_{c2}	3.2×10^{16}	1.3
		$\tau_{1,eff}$	0.075	4.1
	0.6	n_{c1}	4.6×10^{17}	0.15
		n_{c2}	2.3×10^{16}	0.25
		$\tau_{1,eff}$	0.065	1.5
Cyl.	0.2	n_{c1}	4.1×10^{17}	−1.8
		n_{c2}	1.1×10^{17}	2.5
		$\tau_{1,eff}$	0.47	3.0
	0.6	n_{c1}	4.2×10^{17}	0.49
		n_{c2}	8.6×10^{16}	0.01
		$\tau_{1,eff}$	0.42	1.1

test plan. The present section aims to estimate typical measurement uncertainties that one can expect with the present experimental configuration. This exploratory analysis is based on the Monte Carlo(MC) error propagation method [33] implemented in a Python script. The technique is used instead of a traditional Taylor series error propagation due the ease in accounting for uncertainty correlation with MC and its capability to detect non symmetric output distributions. In such a method, the propagation of the distributions of input measurements is performed by using the Data Reduction Equation(DRE) to compute the distribution of the output. As detailed in the previous section, the developed 0-D model is a good approximation of facility behavior and will therefore be used as the DRE. Moreover, for algebra simplicity we assume that chamber background gas temperatures are similar and that the leak flow rate is similar in both chambers. Using these assumptions, the DRE to measure facility quantities is obtained by developing Eq (9) as

$$\tau_{1,\,\mathrm{fast}} = \frac{1}{Q_{1,\,\mathrm{fast}}}\left[(P_{c2} - P_{c1})\xi\tau_{1,\,\mathrm{slow}} + S_2 P_{c2} - Q_{\,\mathrm{leak}}\right], \tag{13}$$

where $\xi = 1000A_1\sqrt{\frac{kT}{2\pi m}} = 1000A_2\sqrt{\frac{kT}{2\pi m}}$ and Q denotes throughput with units [$\mathrm{mbar}\cdot\mathrm{L}\cdot\mathrm{s}^{-1}$] and can be obtained from particle flow rates as

$$Q = 10\dot{N}k_bT. \tag{14}$$

The quantities present in Eq. (13) are either directly measurable by the instruments, such as $Q_{1,\,\mathrm{fast}}$, P_{c1} and P_{c2}, or require testing in a slightly different experimental configuration which is the case of Q_{leak}, S_2 and $\tau_{1,\,\mathrm{slow}}$. For the former, the input distribution can be already estimated based on the uncertainty provided by the probe manufacturers. For the later, the respective DRE equations have to be developed. The leak flow rate can be measured by isolating the chambers by closing a valve between both chambers with the PFG off. The pressure can only rise due to leaks so that by monitoring the pressure rise we can estimate the leak flow rate as

$$Q_{i,leak} = \frac{V_{c,i}\Delta P_{c,i}}{\Delta t} \quad i = 1 \text{ or } 2. \tag{15}$$

The secondary pump speed can be measured by closing a valve between both chambers, turning the PFG off, and injecting gas in chamber 2 such that the pressure is equal to the pressure in the full test, with the PFG and valve open. Through the same mass balance equation one can measure S_2 as

$$S_2 = \frac{Q_{injected}|_{S_2} + Q_{leak}}{P_{c2}|_{S_2}}. \tag{16}$$

Although $P_{c2}|_{S_2}$ should equal P_{c2} the subscript represents that the measurements are not done in the same configurations, although performed with the same probe. The same procedure can be applied to the estimation of the background particles transmission probability by opening the valve between the two chambers and keeping the PFG off. Performing a mass balance we obtain

$$\tau_{1,\,\text{slow}} = \frac{1}{\xi}\left(\frac{S_2 P_{c2}|_{\tau_s} - Q_{\,\text{leak}}}{P_{c1}|_{\tau_s} - P_{c2}|_{\tau_s}}\right) \tag{17}$$

At this point, all quantities in Eq (13) have been estimated based on instrument readings for which the uncertainty is know. Table 2 details the uncertainties provided by the manufacturers for a confidence interval of 95%. The standard deviations then equal half the defined uncertainty. We assume for the Faraday probe that a 10% uncertainty is reasonable, based on values provided in the literature [34]. Moreover, multiple measurements are performed with same pressure gauges instruments. Since the operating conditions and the values of the measurements are of the same order of magnitude it is expected that measurements performed by the same probe are correlated. We will further assume that the two probes, one present in the main chamber and another in the secondary chamber, will be calibrated to the same standard such that the systematic uncertainty is correlated between the two probe measurements[35]. Since the pressure gauge repeatability is given as 5% we assume that the remaining error is a systematic bias that we can force to be correlated through imposition of the same calibration.

Table 2: Instrument uncertainties

Probe	Uncertainty [95%*C.I.*]
Pressure gauge	30% Reading
PFG flow meter[sccm]	0.5% Reading + 0.015
Faraday Probe	10% Reading
Thermocouple[K]	0.01

The propagation of the input distributions by sampling 1 millions points from the input distributions for the case of a conical AIC at a distance of 0.2 m from the PFG. The results follow the distribution shown in Fig. 5 with an average collection efficiency value 0.266. The left and right limits for a coverage of 95% are, as a percentage of the average value, 33.6% and 30.8%, respectively and the distribution is slightly skewed. Given the high uncertainty on the pressure measurements the results are encouraging but rely heavily on the fact that part of pressure measurement uncertainties can be imposed to be correlated. This assumption will be evaluated experimentally at a higher pressure range where available probes can be used as a standard and pressure ratios can be measured accurately.

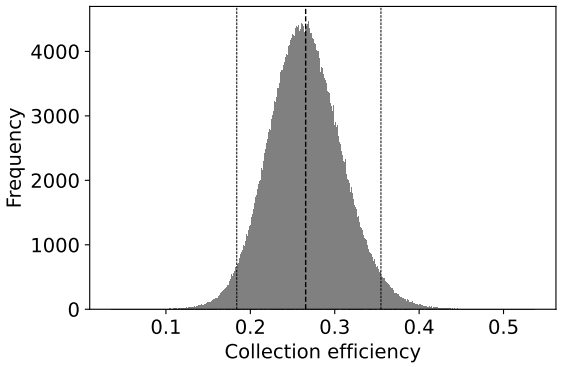

Figure 8: Distribution of Monte Carlo propagation results for the transmission probability using the expanded uncertainties of Table 2. Vertical lines represent the average value, and the limits of a 95% coverage interval.

6. Conclusions

In the present study, VKI's new low density facility is presented with a focus on the methodology for the measurement of ABEP intake efficiency parameters. A model of the facility pressure is developed based on a 0-D mass balance of each chamber and closed with a TPMC code developed in Python. The code provides estimates of the AIC performance parameters under different flow conditions and surface conditions as well as predictions of flow characteristics reaching the AIC.

The facility is then simulated using detailed 3-D DSMC simulations and the results are compared with those of the 0-D model. It is found that the 0-D model predictions of each chamber density as well as the chambers mass exchange agree well with the DSMC simulations. Therefore, the 0-D model assumptions of free molecular flow and uniform background gas density are justified and the model can be used as a DRE for the calculation of the AIC collection efficiency from the experimental measured quantities.

Finally, the 0-D model formulation is used for the propagation of instrument measurement uncertainties through a Monte Carlo procedure. It is shown that

reliable estimates of the collection efficiency can be computed with the current experimental set up if the imposition of correlated pressure gauge systematic uncertainties is successful. The validity of this method will be verified experimentally in future works.

Acknowledgments

This work was supported by a PhD grant from the Portuguese Foundation for Science and Technology (FCT) with number 2020.05450.BD. The author would like to thank Pietro Parodi for his support on the DSMC simulations.

References

[1] N. H. Crisp, P. C. Roberts, S. Livadiotti, V. T. A. Oiko, S. Edmondson, S. Haigh, C. Huyton, L. Sinpetru, K. Smith, S. Worrall, et al., The benefits of very low earth orbit for earth observation missions, Progress in Aerospace Sciences 117 (2020) 100619.

[2] L. A. Singh, M. L. Walker, A review of research in low earth orbit propellant collection, Progress in Aerospace Sciences 75 (2015) 15–25.

[3] P. Zheng, J. Wu, Y. Zhang, B. Wu, A comprehensive review of atmosphere-breathing electric propulsion systems, International Journal of Aerospace Engineering 2020.

[4] B. A. Banks, K. K. de Groh, S. K. Miller, D. L. Waters, Lessons learned from atomic oxygen interaction with spacecraft materials in low earth orbit, in: AIP conference proceedings, Vol. 1087, American Institute of Physics, 2009, pp. 312–325.

[5] K. Moe, G. S. Reiter, Surface-particle-interaction measurements using paddlewheel satellites, Tech. Rep. AD 673 946, DOUGLAS AIRCRAFT CO INC SANTA MONICA CA SPACE SCIENCES DEPT (1968).

[6] I. Harris, A. Chambers, G. Roberts, Preliminary results of an atomic oxygen spaceflight experiment, Materials Letters 31 (3-6) (1997) 321–328.

[7] K. T. Nicholson, T. K. Minton, S. Sibener, Temperature-dependent morphological evolution of hopg graphite upon exposure to hyperthermal o (3p) atoms, Progress in organic coatings 47 (3-4) (2003) 443–447.

[8] T. K. Minton, C. M. Nelson, D. E. Brinza, R. H. Liang, Inelastic and reactive scattering of hyperthermal atomic oxygen from amorphous carbon, JPL Publication 91-34, NASA, Jet Propulsion Laboratory (1991).

[9] J. Zhang, D. J. Garton, T. K. Minton, Reactive and inelastic scattering dynamics of hyperthermal oxygen atoms on a saturated hydrocarbon surface, The Journal of chemical physics 117 (13) (2002) 6239–6251.

[10] C. White, J. Rao, G. Roberts, A. Chambers, K. Lawson, J. Nicholls, The development of carbon-based sensors for the measurement of atomic oxygen, EUROPEAN SPACE AGENCY-PUBLICATIONS-ESA SP 540 (2003) 137–144.

[11] T. Andreussi, G. Cifali, V. Giannetti, A. Piragino, E. Ferrato, A. Rossodivita, M. Andrenucci, J. Longo, L. Walpot, Development and experimental validation of a hall effect thruster ram-ep concept, in: 35th International Electric Propulsion Conference, 2017, pp. 8–12.

[12] M. Tagawa, K. Yokota, K. Nishiyama, H. Kuninaka, Y. Yoshizawa, D. Yamamoto, T. Tsuboi, Experimental study of air breathing ion engine using laser detonation beam source, Journal of Propulsion and Power 29 (3) (2013) 501–506.

[13] F. Romano, T. Binder, G. Herdrich, S. Fasoulas, T. Schönherr, Air-intake design investigation for an air-breathing electric propulsion system, in: 34th International Electric Propulsion Conference, 2015.

[14] S. W. Jackson, R. Marshall, Conceptual design of an air-breathing electric thruster for cubesat applications, Journal of Spacecraft and Rockets 55 (3) (2018) 632–639.

[15] Y. Hisamoto, K. Nishiyama, H. Kuninaka, Design of air intake for air breathing ion engine, in: 63rd International Astronautical Congress, Naples, Italy, 2012.

[16] T. Binder, P. Boldini, F. Romano, G. Herdrich, S. Fasoulas, Transmission probabilities of rarefied flows in the application of atmosphere-breathing electric propulsion, in: AIP Conference Proceedings, Vol. 1786, AIP Publishing LLC, 2016, p. 190011.

[17] J. Kleiman, Z. Iskanderova, Y. Gudimenko, S. Horodetsky, Atomic oxygen beam sources: A critical overview, in: Materials in a Space Environment, Vol. 540, 2003, pp. 313–324.

[18] C. A. Maldonado, A. Ketsdever, L. P. Rand, K. Xie, C. Farnell, J. D. Williams, Characterization of an atomic oxygen plasma source for ground-based simulation of the leo neutral environment, in: 5th AIAA Atmospheric and Space Environments Conference, 2013, p. 2681.

[19] C. Moldonado, T. Lilly, A. Ketsdever, Development of a space simulation facility to study combined effects, in: 4th AIAA Atmospheric and Space Environments Conference, 2012, p. 2941.

[20] V. T. A. Oiko, P. C. Roberts, A. Macario-Rojas, S. Edmondson, S. Haigh, B. Holmes, S. Livadiotti, N. Crisp, K. Smith, L. Sinpetru, et al., Ground-based experimental facility for orbital aerodynamics research: Design, construction and characterisation, in: Proceedings of the International Astronautical Congress, IAC, Vol. 2020, IAF, 2020.

[21] V. Oiko, P. C. Roberts, S. Edmonson, D. García-Almiñana, S. Rodríguez Donaire, M. Sureda Anfres, Design and development of a hyper-thermal atomic oxygen wind tunnel facility, in: Proceedings of the 14th ISMSE & 12th ICPMSE, Biarritz, France, 1 to 5 October 2018, Centre National d'Études Spatiales (CNES), 2018, pp. 1–6.

[22] E. D. Knechtel, W. C. Pitts, Normal and tangential momentum accommodation for earth satellite conditions, Acta Astronautica 18 (1973) 171–184.

[23] D. J. Economou, Fast (tens to hundreds of ev) neutral beams for materials processing, Journal of Physics D: Applied Physics 41 (2) (2008) 024001.

[24] K. Jousten, K. Galda, Handbook of Vacuum Technology, John Wiley & Sons, Ltd, 2016. doi:https://doi.org/10.1002/9783527688265.ch9.

[25] G. Bird, Molecular Gas Dynamics and the Direct Simulation of Gas Flows, no. v. 1 in Molecular Gas Dynamics and the Direct Simulation of Gas Flows, Clarendon Press, 1994.
URL https://books.google.pt/books?id=Bya5QgAACAAJ

[26] S. Livadiotti, N. H. Crisp, P. C. Roberts, S. D. Worrall, V. T. Oiko, S. Edmondson, S. J. Haigh, C. Huyton, K. L. Smith, L. A. Sinpetru, et al., A review of gas-surface interaction models for orbital aerodynamics applications, Progress in Aerospace Sciences 119 (2020) 100675.

[27] R. Lord, Some extensions to the cercignani–lampis gas–surface scattering kernel, Physics of Fluids A: Fluid Dynamics 3 (4) (1991) 706–710.

[28] C. K. Birdsall, Particle-in-cell charged-particle simulations, plus monte carlo collisions with neutral atoms, pic-mcc, IEEE Transactions on plasma science 19 (2) (1991) 65–85.
[29] S. Plimpton, S. Moore, A. Borner, A. Stagg, T. Koehler, J. Torczynski, M. Gallis, Direct simulation monte carlo on petaflop supercomputers and beyond, Physics of Fluids 31 (8) (2019) 086101.
[30] K. Swaminathan-Gopalan, K. A. Stephani, Recommended direct simulation monte carlo collision model parameters for modeling ionized air transport processes, Physics of Fluids 28 (2) (2016) 027101.
[31] D. Gao, C. Zhang, T. E. Schwartzentruber, Particle simulations of planetary probe flows employing automated mesh refinement, Journal of Spacecraft and Rockets 48 (3) (2011) 397–405.
[32] I. Bello, Vacuum and Ultravacuum: Physics and Technology, CRC Press, 2017.
[33] H. W. Coleman, W. G. Steele, Experimentation, validation, and uncertainty analysis for engineers, John Wiley & Sons, 2018.
[34] D. L. Brown, M. L. Walker, J. Szabo, W. Huang, J. E. Foster, Recommended practice for use of faraday probes in electric propulsion testing, Journal of Propulsion and Power 33 (3) (2017) 582–613.
[35] L. Kirkup, R. B. Frenkel, An Introduction to Uncertainty in Measurement: Using the GUM (Guide to the Expression of Uncertainty in Measurement), Cambridge University Press, 2006. doi:10.1017/CBO9780511755538.

Plasma simulation with energy conserving particle-in-cell schemes

Pietro Parodi

Department of Mathematics, KU Leuven, Belgium;
Aeronautics and Aerospace Department, von Karman Institute for Fluid Dynamics, Belgium, pietro.parodi@vki.ac.be

Supervisor: Thierry Magin

Professor, Aeronautics and Aerospace Department, von Karman Institute for Fluid Dynamics, Belgium, magin@vki.ac.be

University Supervisor: Giovanni Lapenta

Professor, Department of Mathematics, KU Leuven, Belgium, giovanni.lapenta@kuleuven.be

Abstract

Simulation of plasmas for applications such as space electric propulsion, nuclear fusion, or heliophysics phenomena, is a complex task because of two reasons: first, the size of interest of the system is usually comparable to the collisional length scale because of the low pressure. The result is that velocity distributions are not always at equilibrium. Secondly, the length and time scales of interest are typically much larger than the natural length and time scales of the plasma, which are dictated by the light electrons. This can make simulations extremely expensive. Using particle methods, in particular the hybrid Particle-in-Cell – Direct Simulation Monte Carlo (PIC-DSMC) method, allows to solve the first problem, since phase space can be efficiently represented using computational particles. In this work, we show how energy conserving semi-implicit PIC schemes can substantially mitigate the second problem. We will show this using representative 1D simulations of a plasma slab expanding into vacuum. Then, we will present an unstructured Finite Element discretization of the energy conserving scheme in 2D.

Keywords: PIC, DSMC, implicit, Air-Breathing Electric Propulsion, Low-Density Facility

1. Introduction

Orbiting platforms for Earth Observation and radio communication may benefit from flying at a lower altitude than traditional platforms [1], in the so-called Very Low Earth Orbit (VLEO), at altitudes below 250 km. At these altitudes, the residual atmosphere causes a drag force on spacecraft, which would make it de-orbit in a matter a days if not compensated with thrust from an engine. If stored propellants are used, spacecraft lifetime is strongly limited by the amount of propellant on board. Recently, studies focused on a concept called Air-Breathing Electric Propulsion [1; 2; 3; 4], which proposes to collect the residual atmospheric molecules through an intake and use them as propellant in an electric thruster.

Ground testing of such propulsion system is a complex task which requires recreating the orbital flow conditions on ground. The low pressure environment can be achieved only in a high-vacuum facility, and the flow of fast particles ($\approx$ 8 km/s) using a plasma source with an appropriate system for ion acceleration, which we call Particle Flow Generator (PFG). The alternative of gasdynamic acceleration in a converging-diverging nozzle has been explored before [5], but generating a flow of sufficient diameter and Mach number does not seem achievable due to the low mass flow rate and pressure required. A Low-Density Facility is being constructed at VKI, where a PFG will generate the flow. Simulation is necessary both for the design of hardware and the experiments, but also for the interpretation of the experimental results. Therefore, our focus is the simulation of the PFG and the plasma flow it produces. The plasma involved in such application has parameters typical of laboratory and electric propulsion plasmas. The Knudsen number, which is the ratio of characteristic dimension and molecular mean free path, is in the range Kn$\approx$ 0.1–10. This means that a high degree of

nonequilibrium is present, but gas phase collisions are still relevant. Electron number density is in the range 10^{13}–10^{17} m^{-3}, with temperatures of the order of 1 eV. Ions are relatively cold, typically below 1000 K. Finally, plasma current densities are low enough that the induced magnetic field is insignificant, meaning that the electrostatic approximation can be safely adopted.

A fluid approach would not be appropriate for the simulation of the plasma in such conditions because of the high degree of translational nonequilibrium. Particle methods, on the other hand, can efficiently represent the six-dimensional *phase space* of 3D particle positions and 3D particle velocities in nonequilibrium. Such methods have been independently developed for collisional gases and for collisionless plasmas, under the names Direct Simulation Monte Carlo (DSMC) [6; 7], and Particle-in-Cell (PIC) [8]. The two methods can be merged in a hybrid PIC-DSMC code, since the underlying assumption of both is that computational particles can represent a large number F_p of real particles. In DSMC, collision events instantaneously change the velocity of particle pairs undergoing the collision at each time step. In PIC, the velocity of charged particles is affected by the electromagnetic field computed on a computational grid, which itself takes into account charged particle currents or densities. We have recently started the development of the PIC-DSMC code Pantera at VKI [9].

Simple electrostatic PIC schemes, like the one previously implemented in Pantera, typically employ an explicit discretization of Poisson's equation. With this scheme, numerical instabilities occur if the cell size does not resolve the physical length scale of the plasma, the (electron) *Debye length* $\lambda_D = \sqrt{\varepsilon_0 k T_e/(n_e q_e^2)}$, and the time step does not resolve the time scale of electron oscillations, the electron plasma frequency $\omega_{pe} = \sqrt{n_e q_e^2/(m_e \varepsilon_0)}$ [8]. Here, ε_0 is the dielectric permittivity of vacuum, k is Boltzmann's constant, T_e and n_e are the electron temperature and number density, and q_e is the electron charge. Unfortunately, the system scales of interest are, in many cases, much larger than the Debye length and the electron plasma period. This can render simulations extremely expensive, especially when two or three spatial dimensions are required. An interesting feature of some recently proposed implicit, energy-conserving schemes, is their ability to avoid the numerical instability called "Finite Grid Instability" in most practical simulation scenarios [10; 11; 12]. This empirical observation was subject of a thorough numerical analysis recently performed by Barnes and Chacón [13]. They reported a previously unidentified stability region when the Mach number for the electrons is less than $O(1)$. According to the authors, this condition is satisfied in plasmas where no significant charge separation is forced. The explicit PIC algorithm currently constitutes the bottleneck for the efficient simulation of plasmas of our interest in Pantera. Therefore, in this work we will concentrate on the applicability of the implicit, energy-conserving scheme to the simulation of plasmas of our interest.

In Section 2, we will introduce the physical model underlying the PIC method, and then present a Finite Element discretization of an explicit and a semi-implicit PIC scheme. Then, in Section 3, we will study the effect of under-resolving physical electron length- and time scales to increase the efficiency of simulations. We will also present a test case for the 2D unstructured discretization of the PIC schemes in the Pantera code.

2. Model and Methods

In this work we will present 1D and 2D simulations using an explicit and a semi-implicit PIC scheme. The 1D explicit scheme follows the classical textbook implementation, detailed in [9]. The 1D implicit scheme is the electrostatic version of the energy-conserving semi-implicit method (ECSIM) of Lapenta, implemented as illustrated in [11]. In this section, we illustrate the Finite Element discretization of the explicit and semi-implicit electrostatic schemes on an unstructured grid.

2.1. Governing equations

We start from the Klimontovich form of the distribution function, where particles are points in phase space. As shown in Eq. (1), Dirac delta functions are used to represent the computational particles.

$$f(\mathbf{x}, \mathbf{v}, t) = \sum_p F_p \, \delta\left[\mathbf{x} - \mathbf{x}_p(t)\right] \, \delta\left[\mathbf{v} - \mathbf{v}_p(t)\right] \qquad (1)$$

Where the sum is performed over all computational particles, which have position $\mathbf{x}_p$, velocity $\mathbf{v}_p$, and macroparticle weight F_p. We want to solve the Boltzmann equation with the Lorentz force term:

$$\frac{\partial f_\alpha}{\partial t} + \mathbf{v}_\alpha \cdot \nabla f_\alpha + \mathbf{a}_\alpha \cdot \nabla_{\mathbf{v}} f_\alpha = \left(\frac{\partial f_\alpha}{\partial t}\right)_{\text{coll}} \qquad (2)$$

Where $\mathbf{a}_\alpha = \frac{q_\alpha}{m_\alpha}\mathbf{E}$ is the acceleration due to Lorentz force. In PIC, we solve for particle trajectories, which

is equivalent to solving Boltzmann's equations with the method of characteristics:

$$\frac{\mathrm{d}\mathbf{v}_p}{\mathrm{d}t} = \frac{q_p}{m_p}\mathbf{E}(\mathbf{x}_p) + \sum_i \Delta\mathbf{v}_{p,i}\,\delta(t - t_i) \tag{3}$$

$$\frac{\mathrm{d}\mathbf{x}_p}{\mathrm{d}t} = \mathbf{v}_p \tag{4}$$

Notice that here, Newton's second law also contains the effect of instantaneous collision events, which change the particle's velocity by $\Delta\mathbf{v}_{p,i}$ at each collision instant t_i.

Fields and particle positions are coupled through Maxwell's equations. Here, we consider the electro-quasi-static limit of Maxwell's equations, where the current induced magnetic field is considered negligible. Maxwell's equations reduce to the following [14]:

$$\nabla \cdot \mathbf{E} = \frac{\rho}{\varepsilon_0} \tag{5}$$

$$\nabla \times \mathbf{E} = 0 \tag{6}$$

$$\frac{\partial \rho}{\partial t} + \nabla \cdot \mathbf{J} = 0 \tag{7}$$

$$\nabla \times \mathbf{B}_1 = \mu_0 \left(\mathbf{J} + \varepsilon_0 \frac{\partial \mathbf{E}}{\partial t} \right) \tag{8}$$

Notice that the curl of the small magnetic field in Ampère's law, Eq. (8), cannot be neglected in the equation, however, it can be neglected when computing the Lorentz force. Here, quantity ρ is the charge density, defined as:

$$\rho = \sum_\alpha \int_{\mathbb{R}^3} q_\alpha f_\alpha \, d\mathbf{v} = \sum_p q_p \delta\left[\mathbf{x} - \mathbf{x}_p(t)\right] \tag{9}$$

And $\mathbf{J}$ is the current density, defined as:

$$\mathbf{J} = \sum_\alpha \int_{\mathbb{R}^3} q_\alpha \mathbf{v} f_\alpha \, d\mathbf{v} = \sum_p q_p \mathbf{v}_p(t)\, \delta\left[\mathbf{x} - \mathbf{x}_p(t)\right] \tag{10}$$

Since the electric field is irrotational, we introduce the scalar potential ϕ, such that $\mathbf{E} = -\nabla\phi$. Then, Eq. (5) can be written as Poisson's equation:

$$\nabla^2 \phi = -\frac{\rho}{\varepsilon_0} \tag{11}$$

The discretization in space and time of a sufficient subset of these equations has been considered many times in literature for the construction of Particle-in-Cell schemes. We will now show an explicit discretization of Poisson's equation (11) and a semi-implicit discretization of the divergence of Eq. (8) using the Finite Element Method.

2.2. *Unstructured explicit discretization of Poisson's equation*

Using first order basis functions Ψ_i for the electric potential, this can be written as:

$$\phi(\mathbf{x}) = \sum_i \phi_i(t)\, \Psi_i(\mathbf{x}) \tag{12}$$

Multiplying Poisson's equation (11) with the basis function and integrating:

$$\int_\Omega \nabla^2 \phi \, \Psi_i \, \mathrm{d}S = -\frac{1}{\varepsilon_0} \int_\Omega \rho \, \Psi_i \, \mathrm{d}S \tag{13}$$

Using the Green-Ostrogradsky theorem:

$$\sum_j \phi_j \int_\Omega \nabla\Psi_j \cdot \nabla\Psi_i \, \mathrm{d}S = \int_{\Gamma_N} g \, \Psi_i \, \mathrm{d}\Gamma + \frac{1}{\varepsilon_0} \int_\Omega \rho \, \Psi_i \, \mathrm{d}S \tag{14}$$

Where $g = \frac{\partial \phi}{\partial \hat{\mathbf{n}}}$ is the Neumann boundary condition on the boundary Γ_N with normal $\hat{\mathbf{n}}$. Then we can write:

$$\sum_j K^{ij} \phi_j = \mathcal{N} + \frac{1}{\varepsilon_0} \sum_p q_p \Psi_i(\mathbf{x}_p) \tag{15}$$

Where we denoted with $\mathcal{N}$ the Neumann boundary term, and with:

$$K^{ij} = \int_\Omega \nabla\Psi_i \cdot \nabla\Psi_j \, dS \tag{16}$$

the integrals of the basis functions. Notice that in 1D, this would be equivalent to the common finite difference discretization with "cloud-in-cell" hat shape functions for the particles. With an explicit discretization in time, this becomes:

$$\sum_j K^{ij} \phi_j^n = \mathcal{N}^n + \frac{1}{\varepsilon_0} \sum_p q_p \Psi_i(\mathbf{x}_p^n) \tag{17}$$

The electric field on the particles can then be written as

$$\mathbf{E}_p^n = \mathbf{E}^n(\mathbf{x}_p^n) = -\sum_i \phi_i^n \, \nabla\Psi(\mathbf{x}_p^n) \tag{18}$$

And particle position is advanced using the leapfrog scheme

$$\mathbf{v}_p^{n+\frac{1}{2}} = \mathbf{v}_p^{n-\frac{1}{2}} + \frac{q_p}{m_p} \mathbf{E}_p^n \Delta t \tag{19}$$

$$\mathbf{x}_p^{n+1} = \mathbf{x}_p^n + \mathbf{v}_p^{n+\frac{1}{2}} \Delta t \tag{20}$$

2.3. Unstructured semi-implicit discretization for energy conservation

We follow the work of Lapenta [11] to obtain a scheme that conserves energy exactly. Since we want to avoid solving for the current-induced magnetic field $\mathbf{B}_1$, we take the divergence of Ampère's equation (8):

$$\nabla \cdot \frac{\partial \mathbf{E}}{\partial t} + \frac{1}{\varepsilon_0} \nabla \cdot \mathbf{J} = 0 \tag{21}$$

Then, we substitute the definition of electric potential:

$$\frac{\partial}{\partial t} \left(\nabla^2 \phi \right) - \frac{1}{\varepsilon_0} \nabla \cdot \mathbf{J} = 0 \tag{22}$$

We discretize this in time, considering the mid-step current as in the original ECsim scheme [11]:

$$\nabla^2 \phi^{n+1} - \nabla^2 \phi^n - \frac{\Delta t}{\varepsilon_0} \nabla \cdot \bar{\mathbf{J}} = 0 \tag{23}$$

Where $\bar{A} = (A^n + A^{n+1})/2$ is a mid-step averaged quantity. We can write:

$$\nabla^2 \bar{\phi}^{n+1} - \nabla^2 \phi^n - \frac{\Delta t}{2\varepsilon_0} \nabla \cdot \bar{\mathbf{J}} = 0 \tag{24}$$

Again, we perform the spatial discretization using the Finite Element method with linear basis functions $\phi(\mathbf{x}, t) = \sum_j \phi_j(t) \Psi_j(\mathbf{x})$, to obtain:

$$\sum_j \bar{\phi}_j \int_\Omega \nabla \Psi_i \cdot \nabla \Psi_j \, dS - \sum_j \phi_j^n \int_\Omega \nabla \Psi_i \cdot \nabla \Psi_j \, dS - \int_{\Gamma_N} \frac{\partial (\bar{\phi} - \phi^n)}{\partial \hat{\mathbf{n}}} \Psi_i \, d\Gamma - \frac{\Delta t}{2\varepsilon_0} \int_\Omega \bar{\mathbf{J}} \cdot \nabla \Psi_i \, dS = 0 \tag{25}$$

Substituting the definition of current, Eq. (10):

$$\sum_c \sum_j \bar{\phi}_j K_c^{ij} - \sum_c \sum_j \phi_j^n K_c^{ij} - \frac{\Delta t}{2\varepsilon_0} \sum_c \sum_{p \in c} q_p \bar{\mathbf{v}}_p \cdot \nabla \Psi_i(\bar{\mathbf{x}}_p) = 0 \tag{26}$$

Where we've dropped the Neumann term for simplicity. This is an implicit equation coupled to the motion of the particles, since the future electric potential depends on the future particle velocities. If the leapfrog particle mover is used, the solution can be obtained by writing explicitly the particle response through mass factors and solving the linear system directly, hence the "semi-implicit" nature. We can then obtain:

$$\sum_c \sum_j \bar{\phi}_j K_c^{ij} + \sum_c \sum_j \bar{\phi}_j K_c^{ij} \frac{\Delta t}{2\varepsilon_0} \sum_{p \in c} \frac{q_p^2 \Delta t}{2 m_p A_\Delta} = \frac{\Delta t}{2\varepsilon_0} \sum_c \sum_{p \in c} q_p \mathbf{v}_p^n \cdot \nabla v_i(\mathbf{x}_p^{n+\frac{1}{2}}) + \sum_c \sum_j \phi_j^n K_c^{ij} \tag{27}$$

We can thus write for each internal node i:

$$\sum_c \left[(1 + M_c) \sum_j \bar{\phi}_j K_c^{ij} \right] = \sum_c \left[\frac{\Delta t}{2\varepsilon_0} J_c^i + \sum_j \phi_j^n K_c^{ij} \right] \tag{28}$$

Where the particle response is contained in:

$$M_c = \frac{\Delta t^2}{4 \varepsilon_0 V_c} \sum_{p \in c} \frac{q_p^2}{m_p} \tag{29}$$

And the current is computed as:

$$J_c^i = \sum_{p \in c} q_p \mathbf{v}_p^n \cdot \nabla \Psi_i(\mathbf{x}_p^{n+\frac{1}{2}}) \tag{30}$$

We show in the appendix that using this scheme, the total energy, defined as:

$$\mathcal{E} = \sum_p m_p \left| \mathbf{v}_p \right|^2 + \frac{1}{2} \varepsilon_0 \int_\Omega |\mathbf{E}|^2 \, dS, \tag{31}$$

is conserved exactly. This leads to the interesting stability properties of this scheme. Notice that charge is not conserved by the scheme we derived. This means that, even if Poisson's equation is satisfied initially, it will not be necessarily satisfied at later time. The reason is the way the current is computed does not account for the real displacement of the charges. Techniques have been devised to decrease this error or eliminate it completely, at the expense of additional complexity and computational cost. See for instance [10].

3. Results

3.1. Cartesian 1D: plasma slab expanding into vacuum

In this section we will compare the explicit and semi-implicit schemes using the test case of 1D expansion of plasma in a periodic domain. The plasma parameters in this test case aim at being representative of those often encountered in electric propulsion.

The domain is discretized using a uniform Cartesian mesh. It is initialized with quasineutral plasma at a density $n = 5 \times 10^{16}$ m^{-3}. Ions are at a temperature $T_i = 300$ K, and electrons are at $T_e = 1$ eV. The physical size of the domain is fixed at 2000 λ_D. For the first cases, 1E and 1I, we start from scale-resolving simulations with 4000 cells, which correspond to cell sizes

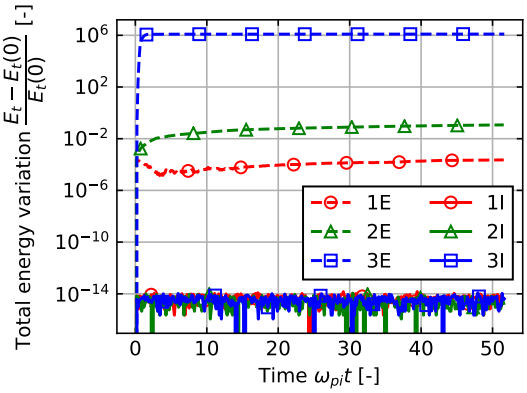

Figure 1: Evolution of the variation of total energy in the simulation for all cases.

of $0.5\lambda_D$. The time step is initially set at a value that resolves the electron plasma frequency ω_{pe}^{-1}, and such that electrons do not cross more than one cell at a time. The latter condition is achieved in practice by imposing $\Delta t < \Delta x/v_{\mathrm{th},e}$, where $v_{\mathrm{th},e} = \sqrt{8kT_e/(\pi m_e)}$ is the thermal velocity of electrons. In all simulations, we use a particle weight of 4×10^9, for a total of 831 136 simulated particles.

First, we show in Figure 1 that the semi-implicit scheme conserves energy to machine precision (or the precision of the direct linear solver), regardless of grid size or time step. Conversely, in all simulations using the explicit scheme, the total energy increases in time. When the Debye length and electron plasma frequency are well resolved (case 1E), the increase can be considered acceptable, especially for short simulations.

Figures 2 and 3 show instantaneous electric field, ion velocity and ion density at instants $\omega_{pi}t = 22.08$ and 51.52. In the figures, we compare the solutions to the two-fluid solution obtained by Mora [15]. The author solved the ion continuity and momentum equations coupled to Poisson's equation and Boltzmann's relation for isothermal electrons. Following [15], results are nondimensionalized using a reference electric field $E_0 = \sqrt{n_0 kT_e/\varepsilon_0}$, the ion acoustic velocity $c_s = \sqrt{kT_e/m_i}$, and the Debye length in the bulk of the plasma, $\lambda_D = \sqrt{\varepsilon_0 kT_e/n_0 q_e^2}$. The results of the explicit and implicit scheme in this case are almost identical, and match very well with the peak electric field, ion front velocity and position predicted by the fluid solution, shown with the dot-dashed lines.

If now we wish to decrease the computational cost, we need to coarsen the grid and increase the time step.

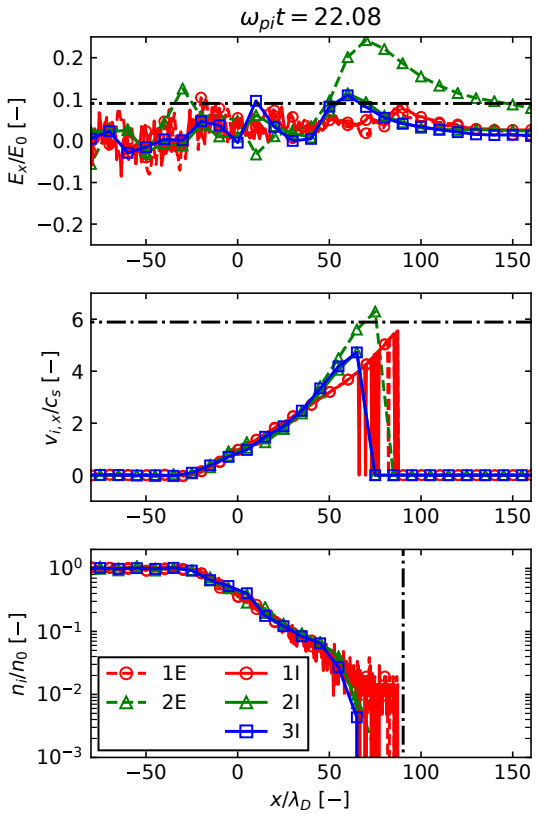

Figure 2: Curves of electric field, ion drift velocity, and ion density for the cases listed in Table 1 at instant $\omega_{pi}t = 22.08$. For case 3E the simulation is numerically unstable and not shown here. The peak electric field, velocity and position of the ion front from the fluid solution of Mora [15] are shown with dot-dashed lines. Quantities $E_0 = \sqrt{n_0 kT_e/\varepsilon_0}$, $c_s = \sqrt{kT_e/m_i}$, and $\lambda_D = \sqrt{\varepsilon_0 kT_e/n_0 q_e^2}$ are used for nondimensionalization.

The latter is typically not possible without the former, since we are bound by the cell crossing constraint:

$$(\omega_{pe}\Delta t) \propto \left(\frac{\Delta x}{\lambda_D}\right) \Big/ \left(\frac{\Delta x}{v_{th,e}\Delta t}\right) \tag{32}$$

As made clear by the expression, often we cannot increase $\omega_{pe}\Delta t$ unless we also increase $\Delta x/\lambda_D$, since the last term cannot be decreased below a certain value.

Therefore, we perform simulations 2E and 2I with a coarsened grid. Since the ambipolar expansion of a plasma occurs on length scales of the order of λ_D, we must address the effect of coarsening the simulation grid on the accuracy of the results. The increased cell size exceeds the stability limit of the explicit scheme (case 2E). In fact, Figure 1 shows that the total energy increases by 12% for this simulation. Figures 2 and 3

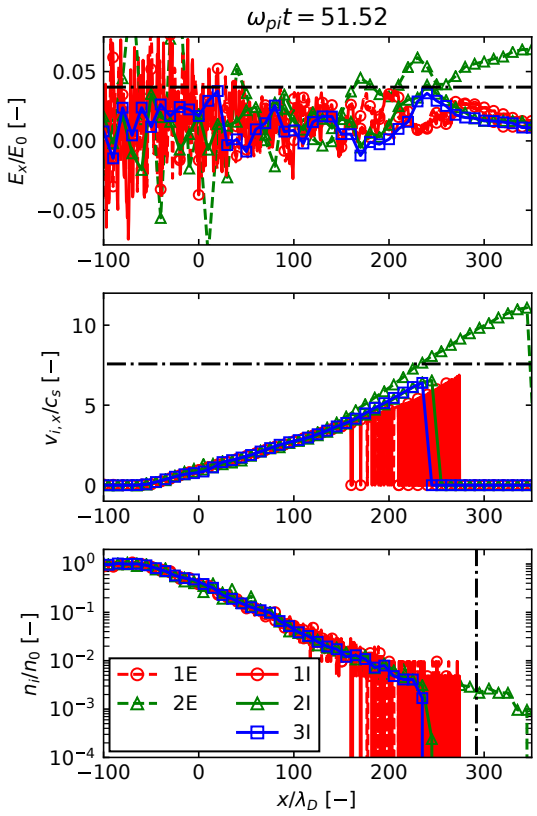

Figure 3: Curves of electric field, ion drift velocity, and ion density for the cases listed in Table 1 at instant $\omega_{pi}t = 51.52$. For case 3E the simulation is numerically unstable and not shown here. The peak electric field, velocity and position of the ion front from the fluid solution of Mora [15] are shown with dot-dashed lines. Quantities $E_0 = \sqrt{n_0 k T_e/\varepsilon_0}$, $c_s = \sqrt{kT_e/m_i}$, and $\lambda_D = \sqrt{\varepsilon_0 k T_e/n_0 q_e^2}$ are used for nondimensionalization.

show an abnormal value of the peak electric field and ion front velocity. These results give a hint to why the explicit scheme is typically used only well within its stability region. The implicit scheme (case 2I) behaves better, with no abnormal electric field peak. The only difference is the position of the ion front, which trails behind the value of the refined simulations and the fluid solution, as can be seen by the density plots. This may be explained by the lack of resolution of the sharp ion front region in the initial instants of the simulation. The effect may be mitigated by a local refinement of the grid at the initial plasma-vacuum interface. Nonetheless, the simulation is stable, and captures well the much more refined solutions.

At this point, we are also free to increase the time step above the electron plasma frequency ω_{pe}, since the cell-crossing constraint is relaxed. As apparent in Figure 1, it is not possible to perform this simulation with the explicit scheme (case 3E) because its stability criteria are not respected. Using the implicit scheme (case 3I), on the other hand, increasing the time step does not degrade the solution with respect to case 2I, in fact the two solutions overlap in Figures 2 and 3. This is probably because, as is often the case, the phenomenon of interest does not depend directly on the electron time scale, but rather on the ion time scale ω_{pi}^{-1} which is much larger and still well resolved. The parameters for all cases are summarized in Table 1.

The phase space solution for cases 1E, 2E, and 3I at time $\omega_{pi}t = 22.08$ can be compared in Figure 4. For clarity, these show the phase space only in correspondence of the expanding plasma, $x \in [-150, 150]\lambda_D$. The velocities are nondimensionalized with the thermal velocities of electrons and ions. Notice that in case 3I (Figure 4c), electrons and ions do not shown any sign of instability. As indicated by the previous plots, a slight difference can be seen in the expanding ion population, where front position and velocity are smaller than in simulation 1E. Remarkably, notice that the expansion region at this instant is resolved using only about 10 cells.

Table 1: Summary of main numerical parameters for the 1D simulations of plasma expansion into vacuum using the explicit and implicit scheme. The wall clock time for the simulations is reported in the last column.

Case	$\Delta x/\lambda_D$ [-]	$\omega_{pe}\Delta t$ [-]	$\frac{\Delta x}{v_{\mathrm{th},e}\Delta t}$ [-]	method	time s
1E	0.5	0.063	5.0	explicit	876
2E	10	0.063	100	explicit	731
3E	10	3.15	2.0	explicit	83
1I	0.5	0.063	5.0	implicit	9363
2I	10	0.063	100	implicit	774
3I	10	3.15	2.0	implicit	98

The simulations were performed on 16 parallel MPI processes on an AMD Ryzen Threadripper 1950X processor. The computational time required for the simulations is shown in Table 1. Generally, the implicit scheme is more demanding for the same set of parameters, since it requires the computation of the mass factors and the factorization of the linear system matrix at each timestep. For the explicit scheme, instead, this factorization is performed only once at the beginning of the simulation. However, the implicit scheme still allows to obtain a sufficiently ac-

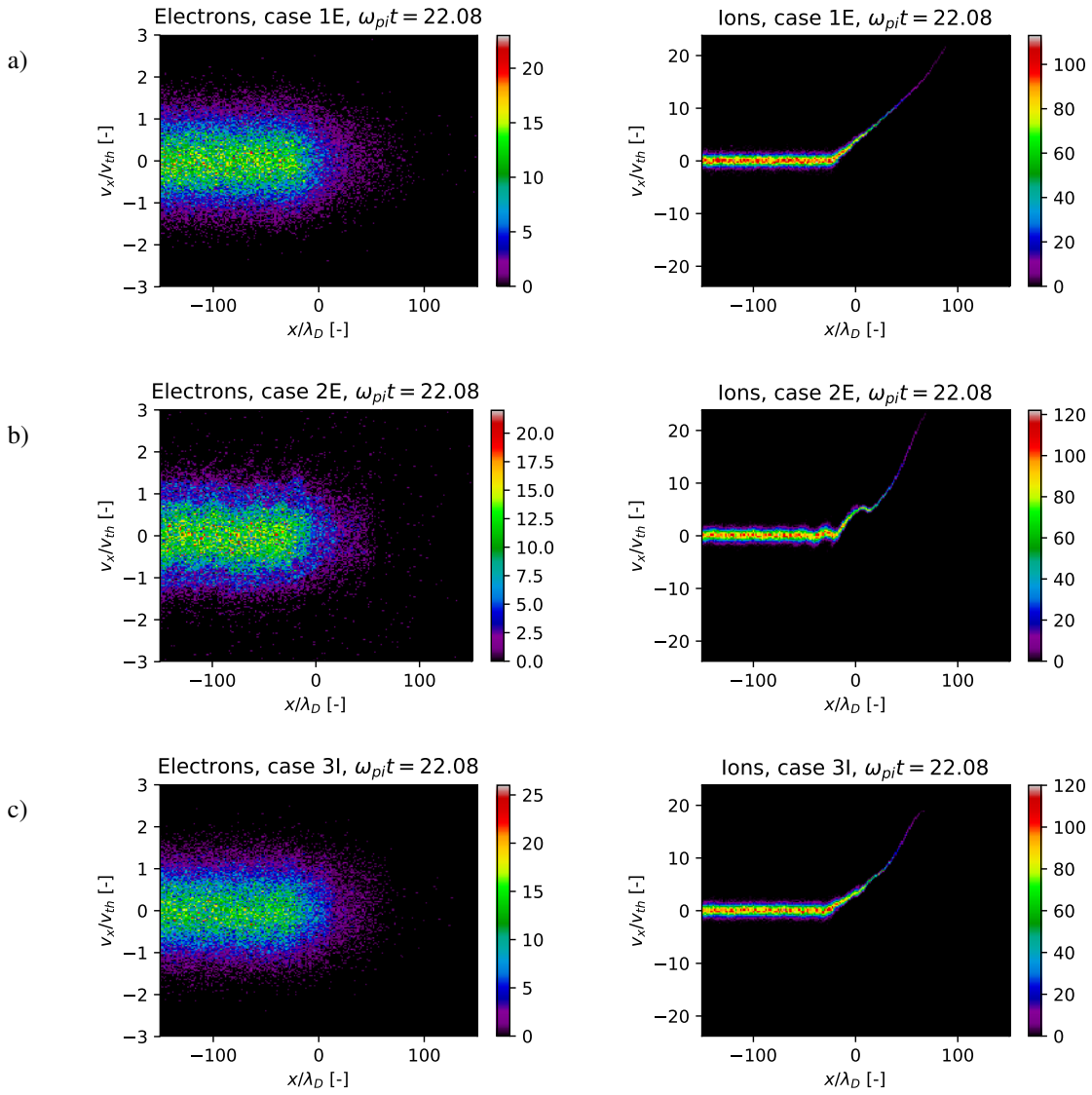

Figure 4: Electron and ion phase space in correspondence of the ion front for cases a) 1E, b) 2E, and c) 3I, at instant $\omega_{pi}t = 22.08$. The velocities are nondimensionalized with the thermal velocities. The plots are obtained as a 2D histogram of position and velocity of all particles in the simulation at this instant. The color scale shows the number of particles in a given interval of the histogram. The first signs of numerical instability are visible in case 2E. Conversely, in case 3I, where the time step is 50 times smaller but the implicit scheme is used, electrons and ions do not shown signs of instability. Case 3I shows a difference in the expanding ion population, where front position and velocity in simulation trail behind those of the well resolved simulation 1E, as already shown in Figure 2. Remarkably, however, the expansion region in case 3I is resolved using only 10 cells.

curate simulation at least 9× faster than the well resolved explicit simulation (case 1E). Notice that here we've kept the number of particles constant, while they could have been reduced proportionally to the number of cells, resulting in a further speedup. This speedup is expected to be exponentially more advantageous for 2D and 3D simulations, as discussed in [10].

The present test cases were limited to a periodic domain. In the following section, we will present the case of a 2D simulation with boundaries and discuss the associated challenges.

3.2. Unstructured 2D: cylindrical Langmuir probe

Given the possible advantages of adopting an energy-conserving implicit scheme, we implemented

the Finite Element discretization illustrated in Section 2.3 in PANTERA. As a test case, we simulate the plasma sheath forming around a cylindrical conductor, remnant of a cyindrical Langmuir probe. The discretized domain is shown in Figure 5. The internal circular edge c represents the conductor. It has a radius $R_1 = 0.25$ m, and has Dirichlet boundary conditions $\phi = \phi_w = 0$. Edges s have Neumann boundary conditions $\partial\phi/\partial\hat{\mathbf{n}} = 0$ and specular reflection for particles. The outer circular edge i has radius $R_2 = 1.5$ m. We inject electrons and argon ions from the outer boundary at $T_e = T_i = 300$ K and $n_e = n_i = n_0 = 5 \times 10^9$ m^{-3}. The Debye length in these conditions is $\lambda_{D_0} = 0.017$ m. The mesh of Figure 5a resolves this length. We perform a simulation using this mesh and the explicit scheme, in order to obtain a reference solution. Then, we perform a simulation with mesh b) using the implicit method. We compare the PIC solutions with the solution to the following system of plasma fluid equations in cylindrical coordinates: ion continuity (33), ion momentum (34), Poisson's equation (35), and Boltzmann's relation for isothermal electrons (36):

$$\frac{\mathrm{d}n_i}{\mathrm{d}r} = -\frac{n_i}{r} - \frac{n_i}{v_i}\frac{\mathrm{d}v_i}{\mathrm{d}r} \tag{33}$$

$$\frac{\mathrm{d}v_i}{\mathrm{d}r} = -\frac{1}{v_i}\frac{q_e}{m_i}\frac{\mathrm{d}\phi}{\mathrm{d}r} \tag{34}$$

$$\frac{\mathrm{d}^2\phi}{\mathrm{d}r^2} + \frac{1}{r}\frac{\mathrm{d}\phi}{\mathrm{d}r} = -\frac{q_e}{\varepsilon_0}(n_i - n_e) \tag{35}$$

$$n_e = n_0 \exp\left[\frac{q_e(\phi - \phi_r)}{kT_e}\right] \tag{36}$$

The equations are integrated with boundary conditions $\phi(R_2) = \phi_r$, $d\phi/dr(R_2) = 0$, $n_i(R_2) = n_e(R_2) = n_0$, and the balance of electron and ion fluxes at the conductor: $1/4 n_e(R_1)\sqrt{8kT_e/(\pi m_e)} = -n_i(R_1)v_i(R_1)$.

The results of these simulations are plotted in Figure 6. The figure shows the values of the species number density, the electric potential, and the radial velocity of ions as function of the radial coordinate. First, we note that the implicit solution is stable and matches well the explicit one, despite the Debye length not being resolved: $\Delta x \approx 2\lambda_{D_0}$ close to the inner boundary, and $\Delta x \approx 10\lambda_{D_0}$ close to the outer boundary. Expectedly, the fluid solution does not match exactly the PIC solutions, especially in terms of density profiles, probably because it does not capture kinetic effects. However, it shows that the size of the sheath, which is the region of charge non-neutrality, is well represented. An excellent agreement is found for the potential drop and ion velocity gain across the sheath. This simulation highlighted the fact that even a local refinement of the mesh for the resolution of the plasma sheath limits the maximum time step that can be achieved. A possible solution to this problem is represented by substepping methods [10; 12], where particles are moved in small steps such that current is correctly deposited on the grid. This, however, would require fully nonlinear convergence of particle and fields.

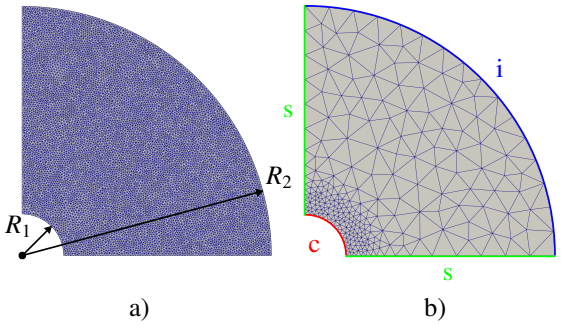

Figure 5: Unstructured meshes used for a) the explicit case, and b) the implicit case. Boundary conditions are indicated with c: conducting wall with fixed potential and particle deletion; s: Neumann condition for the potential and specular reflection for the particles; and i: fixed potential and particle injected at prescribed density and temperature. Mesh a) resolves the Debye length, while b) only resolves macroscopic gradients.

4. Conclusion and Future Work

We have shown the advantages of adopting a semi-implicit PIC scheme for the simulation of plasmas of interest for applications such as electric propulsion. In the representative 1D simulations using both the explicit and the implicit schemes. The latter was able to give reasonably accurate results with a grid 20 times coarser and a time step 50 times larger than what needed by the explicit scheme. We recorded a speed-up of approximately one order of magnitude. In addition, adopting an iterative solver such as GMRES may be more advantageous for the implicit scheme than the direct solver we are currently using, since factorization of the system matrix is computed at each time step.

We have successfully extended PANTERA for the treatment of 2D unstructured meshes, and shown that this discretization retains the properties of the semi-implicit scheme of energy conservation and suppression of the finite grid instability. As future work, we will quantify the charge conservation error for relevant simulations, and explore nonlinearly converged

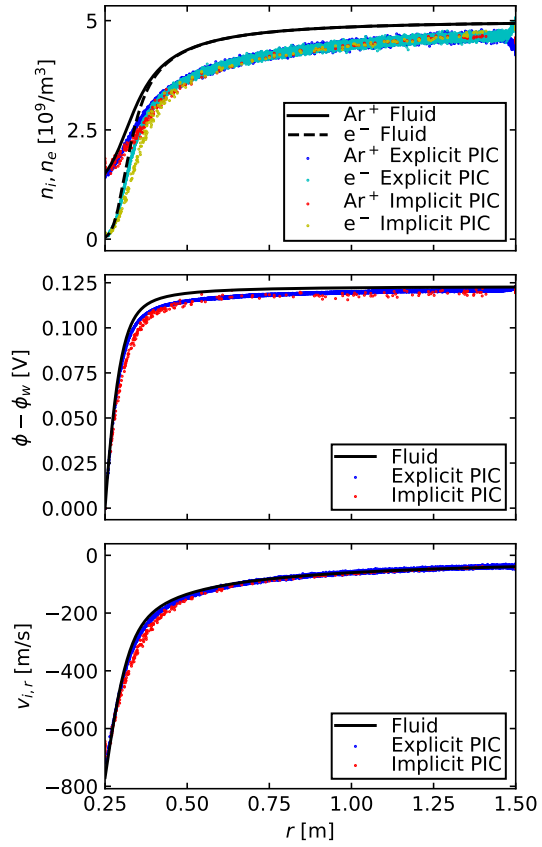

Figure 6: Cylindrical sheath solution using the explicit and the implicit schemes in Pantera and the fluid equations (33)-(36). The panels show the plots of ion and electron number densities n_i, n_e, electric potential ϕ relative to the potential of the inner surface ϕ_w, and ion radial bulk velocity $v_{i,r}$. The points correspond to time-averaged cell or node values.

schemes with particle substepping, which may be advantageous to achieve larger simulation time steps.

5. Acknowledgements

The research of PP is founded by an FWO Strategic Basic PhD fellowship (reference 1S24022N).

References

[1] T. Schönherr, K. Komurasaki, F. Romano, B. Massuti-Ballester, G. Herdrich, Analysis of Atmosphere-Breathing Electric Propulsion, IEEE Transactions on Plasma Science 43 (1) (2015) 287–294.

[2] J. Virgili-Llop, P. Roberts, Z. Hao, L. Ramio, V. Beauplet, Very Low Earth Orbit mission concepts for Earth Observation. Benefits and challenges, in: Reinventing Space Conference, 2014.

[3] T. Andreussi, G. Cifali, V. Giannetti, A. Piragino, E. Ferrato, A. Rossodivita, M. Andrenucci, Development and Experimental Validation of a Hall Effect Thruster RAM-EP Concept, in: 35th International Electric Propulsion Conference, 2017.

[4] M. Tisaev, E. Ferrato, V. Giannetti, C. Paissoni, N. Baresi, A. Fabris, T. Andreussi, 2.

[5] K. Fujita, T. Suzuki, T. Ozawa, Development of a Pilot Model of Hypersonic Rarefied Wind-Tunnel, in: AIP Conference Proceedings, Vol. 1333, 2011, pp. 407–412.

[6] G. A. Bird, Approach to Translational Equilibrium in a Rigid Sphere Gas, The Physics of Fluids 6 (10) (1963) 1518–1519.

[7] G. A. Bird, Molecular Gas Dynamics and the Direct Simulation of Gas Flows, Clarendon Press, 1994.

[8] R. W. Hockney, J. W. Eastwood, Computer Simulation Using Particles, CRC Press, 1988.

[9] P. Parodi, Development of a hybrid PIC–DSMC solver for particle flow generators, Tech. rep., von Karman Institute for Fluid Dynamics (2020).

[10] G. Chen, L. Chacón, D. C. Barnes, An Energy- and Charge-conserving, Implicit, Electrostatic Particle-in-Cell Algorithm, Journal of Computational Physics 230 (18) (2011) 7018–7036.

[11] G. Lapenta, Exactly energy conserving semi-implicit particle in cell formulation, Journal of Computational Physics 334 (2017) 349–366.

[12] D. Eremin, An energy- and charge-conserving electrostatic implicit particle-in-cell algorithm for simulations of collisional bounded plasmas, Journal of Computational Physics 452 (2022) 110934.

[13] D. Barnes, L. Chacón, Finite spatial-grid effects in energy-conserving particle-in-cell algorithms, Computer Physics Communications 258 (2021) 107560.

[14] S. E. Kruger, The Three Quasistatic Limits of the Maxwell Equations, arXiv:1909.11264v2.

[15] P. Mora, Plasma Expansion into a Vacuum, Physical Review Letters 90 (18) (2003) 185002.

Appendix A. Proof of energy conservation for the unstructured discretization

The variation of kinetic energy of the particles in a time step is:

$$\Delta\mathcal{E}_p = \frac{1}{2}\sum_p m_p|\mathbf{v}_p^{n+1}|^2 - \frac{1}{2}\sum_p m_p|\mathbf{v}_p^{n}|^2 \qquad (A.1)$$

While the variation in the energy stored in the electric field is:

$$\Delta\mathcal{E}_f = \frac{1}{2}\varepsilon_0\int_\Omega |\mathbf{E}^{n+1}|^2 dS - \frac{1}{2}\varepsilon_0\int_\Omega |\mathbf{E}^{n}|^2 dS \qquad (A.2)$$

We will now prove that the total energy $\Delta\mathcal{E}_p + \Delta\mathcal{E}_f$ in the simulation is exactly conserved by the unstructured discretization of the ECSIM scheme in a periodic domain. Since $|\mathbf{U}|^2 - |\mathbf{V}|^2 = (\mathbf{U}-\mathbf{V})\cdot(\mathbf{U}+\mathbf{V})$, we can write:

$$\Delta\mathcal{E}_p = \frac{1}{2}\sum_p m_p(\mathbf{v}_p^{n+1} - \mathbf{v}_p^{n})\cdot(2\mathbf{v}_{p,i}^{n+\frac{1}{2}}) \qquad (A.3)$$

Substituting the particle mover, Eq. (19):

$$\Delta\mathcal{E}_p = \frac{1}{2}\sum_p m_p\left(\frac{q_p}{m_p}\bar{\mathbf{E}}_p\Delta t\right)\cdot(2\bar{\mathbf{v}}_p) \tag{A.4}$$

Substituting the definition of electric field as gradient of the potential and how it is applied to the particles, we obtain:

$$\Delta\mathcal{E}_p = \Delta t\sum_p\left(-\sum_j\bar{\phi}_j\nabla v_j(\mathbf{x}_p^{n+\frac{1}{2}})\right)\cdot q_p\bar{\mathbf{v}}_p. \tag{A.5}$$

For the field energy, since:

$$|\mathbf{U}|^2 - |\mathbf{V}|^2 = (\mathbf{U}-\mathbf{V})\cdot(\mathbf{U}+\mathbf{V}), \tag{A.6}$$

we can write:

$$\Delta\mathcal{E}_f = \frac{1}{2}\varepsilon_0\int_\Omega(\mathbf{E}^{n+1}-\mathbf{E}^n)\cdot(2\mathbf{E}^{n+\frac{1}{2}})dS \tag{A.7}$$

Substituting the definition of potential

$$\Delta\mathcal{E}_f = \frac{1}{2}\varepsilon_0\int_\Omega\left(\nabla\phi^{n+1}-\nabla\phi^n\right)\cdot(2\nabla\bar{\phi})dS \tag{A.8}$$

Substituting $\bar{\phi} = (\phi^n+\phi^{n+1})/2$

$$\Delta\mathcal{E}_f = \frac{1}{2}\varepsilon_0\int_\Omega(2\nabla\bar{\phi}-2\nabla\phi^n)\cdot(2\nabla\bar{\phi})dS \tag{A.9}$$

splitting the integral

$$\Delta\mathcal{E}_f = 2\varepsilon_0\int_\Omega\nabla\bar{\phi}\cdot\nabla\bar{\phi}\,dS - 2\varepsilon_0\int_\Omega\nabla\phi^n\cdot\nabla\bar{\phi}_i\,dS \tag{A.10}$$

Using the global basis representation of the potential: $\phi(\mathbf{x}) = \sum_j\phi_j\Psi_j(\mathbf{x})$

$$\Delta\mathcal{E}_f = \sum_j 2\bar{\phi}_j\varepsilon_0\int_\Omega\nabla\bar{\phi}\cdot\nabla\Psi_j\,dS - \sum_j 2\bar{\phi}_j\varepsilon_0\int_\Omega\nabla\phi^n\cdot\nabla\Psi_j\,dS \tag{A.11}$$

Grouping terms

$$\Delta\mathcal{E}_f = \sum_j 2\bar{\phi}_j\varepsilon_0\left(\int_\Omega\nabla\bar{\phi}\cdot\nabla\Psi_j\,dS - \int_\Omega\nabla\phi^n\cdot\nabla\Psi_j\,dS\right) \tag{A.12}$$

Recognize our weak form, Eq. (25), between parentheses:

$$\Delta\mathcal{E}_f = \sum_j\bar{\phi}_j\Delta t\int_\Omega\bar{\mathbf{J}}\cdot\nabla\Psi_j\,dS \tag{A.13}$$

Substitute the definition of particle current

$$\Delta\mathcal{E}_f = \sum_j\bar{\phi}_j\Delta t\sum_p q_p\bar{\mathbf{v}}_p\cdot\nabla\Psi_j(\mathbf{x}_p^{n+\frac{1}{2}}) \tag{A.14}$$

Which by inspection is equal and opposite to the particle energy variation, Eq. (A.5), so that

$$\Delta\mathcal{E} = \Delta\mathcal{E}_p + \Delta\mathcal{E}_f = 0 \tag{A.15}$$

Notice that this is true only when the weak form is applied for all nodes, such as in a periodic domain, or with free boundary conditions with specular particle reflection.

Development of high-order adaptive algorithms for simulating magnetic reconnection processes with uncertainty quantification

Firas Ben Ameur

Aeronautics and Aerospace Department, von Karman Institute for Fluid Dynamics, Belgium, vandenhoeck@vki.ac.be

Supervisor: Andrea Lani

Aeronautics and Aerospace Department, von Karman Institute for Fluid Dynamics, Belgium, lanil@vki.ac.be

University Supervisor: Stefaan Poedts

Professor, Centre for mathematical Plasma-Astrophysics, KU Leuven, Belgium, stefaan.poedts@kuleuven.be

Abstract

The present paper addresses the coupling and further consolidation of an Uncertainty Quantification (UQ) toolkit within the open-source platform COOLFLuiD. A Multi-Level Monte Carlo (MLMC) method used for UQ will construct levels using isotropic p-refinement instead of isotropic h-refinement, therefore requiring, ideally, just one initial "coarse" mesh which will undergo polynomial upgrade for obtaining finer levels. This approach improves the overall computational efficiency of our analysis of the uncertain output, i.e. quantity of interest. In this work, a concise overview of the Flux Reconstruction method and MLMC techniques will be given, followed by some promising results of the uncertainty quantification applied to high-speed flows.

Keywords: High-Order CFD, Hypersonics, Flux Reconstruction, r-refinement, Uncertainty Quantification, Multi-Level Monte Carlo

1. Introduction

The number and complexity of mathematical models used virtually in all areas of science and engineering, to boost our understanding of the real world, is continually increasing. Similarly, the wide variety of the parameters controlling these models is expanding. Uncertainty affects almost all of these parameters. Rigorous quantification of these uncertain parameters is mandatory to define confidence intervals when analyzing the model output, where the outcome of the uncertainty quantification will be used to make engineering decisions. State-of-the-art UQ distinguishes between intrusive and non-intrusive approaches.

Intrusive methods involve the formulation of a stochastic version of the original model (i.e. implying deep modifications in the deterministic Computational Fluid Dynamics (CFD) codes). These methods decompose and provide, respectively, the uncertain variables and the outputs, i.e. Quantities of Interest (QoI), as basis of complete orthogonal polynomials. The Galerkin polynomial chaos is the most well-known intrusive approach[1]. Yet, the implementation of an intrusive method within flow solvers is very demanding and time-consuming, in addition, these methods are generally not well established for complex applications.

Non-intrusive methods treat the deterministic solver as a black-box and simply require a set of simulations for different realizations of the uncertain parameters. We distinguish, among famous methods, polynomial/collocation and Monte Carlo (MC) approaches [2]. The polynomial/collocation methods are efficient for smooth response and moderate number of uncertain parameters, but they lack efficiency for problems whose solutions exhibit sharp gradients and shocks (e.g. Euler and Navier-Stokes equations). (MC)-type methods overcome such deficits, being therefore preferred in his work.

This work will focus on MC-type Forward non-intrusive methods, allowing the propagation of

different sources of uncertainties through a typically large number of simulations to study their effects and obtain numerical data defining the dispersity of the monitored quantities of interests. Since the classic MC method suffers from the *curse of dimension*, multilevel sampling method fortunately exists. Several instances of the multi-level methods will make UQ simulations, involving a large number of the uncertain input parameters and complex, large-scale and high-dimensional systems of partial differential equations (PDEs), affordable to solve [3; 2; 4; 5]. Furthermore, the multilevel sampling method will take the advantage of the use of modern high-order (HO) CFD methods. These HO methods can provide more accuracy "per degree of freedom", potentially making more affordable a UQ analysis where runs on finer meshes would be substituted by runs on relatively coarser meshes but with a higher order of accuracy, therefore reducing mesh generation time. In [6; 7; 8], a state-of-the-art parallel and fully implicit high-order Flux Reconstruction (FR) code has been implemented and used to solve Euler/Navier-Stokes equations, where its structure is extremely modular and can be easily coupled to arbitrary sets of advection-diffusion-reaction PDEs.
Besides, the UQ *Julia* package *MultilevelEstimators* is developed in [9] to carry on forward non-intrusive MC-type simulations of PDEs using multilevel sampling methods. In this work, the *MultilevelEstimators* package is coupled to the COOLFLuiD FR solver for evaluating the effect of different kinds of uncertainties on the selected hypersonic testcases. The statistics of our QoI will be computed based on variance reduction using control variates and a coarse-to-fine hierarchy of models with different levels of accuracy, which will be constructed by means of isotropic p-refinement (i.e. upgrade of solution polynomial order) instead of isotropic h-refinement.

2. The Flux Reconstruction Solver: An oerview:

The FR method was originally developed by Huynh in [10]. It is a compact high-order FE-type method that offers a unifying formulation for various classes of high-order schemes (e.g. nodal Discontinuous Galerkin, Spectral Finite Difference). The formulation of the FR approach proposed by Huynh is applicable to deal with advection-diffusion problems on structured and structured grids [11].
This section presents a brief review of the Flux Reconstruction method in one dimension, including the following main algorithmic steps [6; 7; 8]:

1. Consider solving the one-dimensional advection-diffusion problem within an arbitrary domain Ω, given by:
$$\frac{\partial u}{\partial t} + \frac{\partial f}{\partial x} = 0. \tag{1}$$
In Eq.1, $x \in \Omega = [x_L, x_R]$ is the one dimensional coordinate, t is the time variable, $u(x,t)$ is the conservative variable, and $f = f\left(u, \frac{\partial u}{\partial x}\right)$ is the flux which is a scalar for the 1D case. As the FR method is classified as a FE-type method, the first step of the procedure involves partitioning the spatial domain Ω into a finite number N of non-overlapping, non-empty, open sub-domains Ω'_n such that:
$$\Omega'_n = \{x \mid x_n < x < x_{n+1}\}, \tag{2}$$
where, $x_1 = x_L$ and $x_{N+1} = x_R$
2. The exact solution u of the conservation law 1 is approximated by a continuous function u_n^δ within each element Ω_n. This function u_n^δ corresponds to a polynomial of degree P within Ω_n and is identically zero on $\Omega \setminus \Omega_n$, while being generally discontinuous across elements. The approximate solution polynomial u^δ within the entire domain Ω is constructed as:
$$u^\delta = \sum_1^N u_n^\delta \tag{3}$$
In the same manner, the exact flux f is approximated by a polynomial of degree $P+1$ within each sub-domain Ω_n.
3. Each element Ω_n together with the approximate solution u_n^δ and flux f_n^δ inside, is transformed to a standard reference element $\Omega_S = \{\xi \mid -1 \leq \xi \leq 1\}$, where all computations are performed. The solution u_n^δ within each sub-domain Ω_n can then be obtained by solving the transformed conservation equation (Eq.1) within the reference element Ω_S:
$$\frac{\partial \hat{u}^\delta}{\partial t} + \frac{\partial \hat{f}^\delta}{\partial \xi} = 0 \quad \text{with} \quad \xi \in \Omega_S, \tag{4}$$
where=
   - $\hat{u}^\delta = \hat{u}^\delta(\xi, t) = J_n u_n^\delta(\Theta_n(\xi), t)$,
   - $\hat{f}^\delta = \hat{f}^\delta(\xi, t) = f_n^\delta(\Theta_n(\xi), t)$,

[0] https://github.com/PieterjanRobbe/MultilevelEstimators.jl

- J_n represents the Jacobian of the mapping $\Theta_n(\xi)$.

4. The approximate solution $\hat{u}^\delta$ is defined as a degree P polynomial based on a Lagrange polynomial basis related to the set of $P+1$ distinct solution points ξ_i within Ω_S, where the two endpoints of the standard element Ω_S, i.e. $\xi = -1$ and $\xi = 1$, are referred to as the flux points.
5. This step consists of determining a common interface solution $\hat{u}^{\delta I}$ at the boundaries of the standard element Ω_S, i.e. $\xi = \pm 1$, where the flux points of two neighboring elements coincide.

$$u^{\delta I} = \frac{u^{\delta -} + u^{\delta +}}{2} \tag{5}$$

   where $u^{\delta -}$ and $u^{\delta +}$ are respectively the approximate solutions evaluated at the left and right boundaries.
6. A corrected solution gradient $\hat{q}^\delta$ is computed. $\hat{q}^\delta$ is defined based on two correction functions $g_L(\xi)$ and $g_R(\xi)$ of degree $P+1$ and satisfy the following boundary conditions: [12]

$$\begin{aligned} g_L(-1) &= 1, \qquad g_R(-1) = 0 \\ g_L(1) &= 0, \qquad g_R(1) = 1. \end{aligned} \tag{6}$$

   Furthermore, the correction function for the right boundary $g_R(\xi)$ is defined as the reflection of the correction function $g_L(\xi)$ with respect to the vertical axis in order to ensure symmetry of the correction process $g_L(\xi) = g_R(-\xi)$.
   The corrected solution gradient $\hat{q}^\delta$ is then computed via the following expression:

$$\hat{q}^\delta = \frac{\partial \hat{u}^\delta}{\partial \xi} + (\hat{u}_L^{\delta I} - \hat{u}_L^\delta)\frac{dg_L}{d\xi} + (\hat{u}_R^{\delta I} - \hat{u}_R^\delta)\frac{dg_R}{d\xi}, \tag{7}$$

   where $\hat{u}_L^{\delta I}$ and $\hat{u}_R^{\delta I}$ are the common interface solutions at the left and right boundaries of Ω_S, and $\hat{u}_R^\delta = \hat{u}^\delta(1)$ and $\hat{u}_L^\delta = \hat{u}^\delta(-1)$ are the values of the approximate solution polynomial at the left and right boundaries. The Vincent-Castonguay-Jameson-Huynh (VCJH) scheme, in [13], is used to define the exact polynomial expression of g_L and g_R.
7. On the reference element Ω_S, the approximate discontinuous flux $\hat{f}^{\delta D}(\xi)$ is calculated. Based on $\hat{u}^\delta$ and $\hat{q}^\delta$, the approximate discontinuous flux $\hat{f}^{\delta D}$ is constructed as a polynomial of degree P in the same manner as the approximate solution $\hat{u}^\delta$.
8. The transformed common interface fluxes $\hat{f}^{\delta I}$ at the flux points of the standard element Ω_S, i.e. $\xi = \pm 1$, is calculated. $\hat{f}_L^{\delta I}$ and $\hat{f}_R^{\delta I}$ are denoted as the common interface flux at the left and right end of the standard element, respectively. In the case of the Navier-Stokes equations, it is computed as the sum of a convective and a diffusive term. More details can be found in [7; 8]
9. The flux must be continuous across element boundaries in order to obtain a conservative scheme. Therefore, a correction flux function $\hat{f}^{\delta C}$ is added to the approximate discontinuous flux $\hat{f}^{\delta D}$ in order to obtain a continuous flux $\hat{f}^\delta$. The correction flux $\hat{f}^{\delta C}$ is a polynomial of degree $P+1$ defined as:

$$\hat{f}^{\delta C} = (\hat{f}_L^{\delta I} - \hat{f}_L^{\delta D})h_L(\xi) + (\hat{f}_R^{\delta I} - \hat{f}_R^{\delta D})h_R(\xi), \tag{8}$$

   where $\hat{f}_L^{\delta D} = \hat{f}^{\delta D}(-1)$ and $\hat{f}_R^{\delta D} = \hat{f}^{\delta D}(1)$ are the values of the approximate discontinuous flux at the left and right boundaries. The continuous flux $\hat{f}^\delta$ within the standard element Ω_S is then written as the sum of the approximated discontinuous flux and the correction flux.
10. The divergence of the total flux $\hat{f}^\delta$ at each solution point ξ_i is computed. This step is relatively straightforward as the derivatives of both the Lagrange polynomials and correction functions are exactly known.
11. Finally, a time marching strategy is applied to advance the approximate solution $\hat{u}^\delta$ in time using the following expression:

$$\frac{d\hat{u}_i^\delta}{dt} = -\frac{\partial \hat{f}^\delta}{\partial \xi}(\xi_i). \tag{9}$$

The extension of the 1D philosophy of the FR method to deal with 2D quadrilateral and 3D hexahedral elements is straightforward. To this end, a tensor product basis is defined based on the one-dimensional Lagrange polynomials on the reference element, as shown in [10].

3. Multi-Level Monte Carlo

3.1. Overview

Forward non-intrusive UQ problems consist of propagating uncertainties characterized as random variables into a computational model to quantify the output quantities of interest and study their effects based on statistical indicators (e.g. mean, variance etc...) as Fig.1 shows.

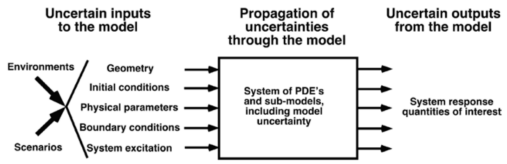

Figure 1: Forward uncertainty propagation

The MLMC method is a clever extension of the standard MC method that relies on a combination of a large number of low cost and accuracy samples and only a few expensive samples, yet with high accuracy. Traditionally, state-of-the-art MLMC uses a Multigrid method, generally based on h-refined hierarchy of meshes. Our MLMC model will benefit from the FR framework and use isotropic p-refinement to construct a coarse-to-fine hierarchy of models. Fig.2 shows the latter hierarchy, where the points inside the cells represented the solution points and the number of the dots next to the cartesian grids represents the number of sampling within each grid.

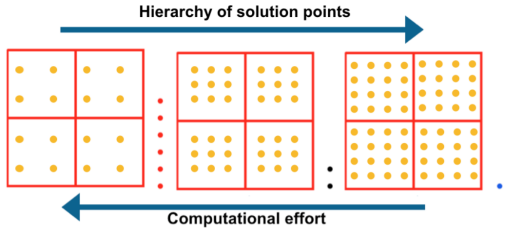

Figure 2: Illustration of the *Levels* used in our MLMC approach. Level 0 (left) – Level 1 (middle) – Level 2 (right)

3.2. MLMC sampling

The classic MC estimator Q for the expected value $\mathbb{E}[Q_L]$ is given by Eq.10:

$$\mathbb{E}[Q_L] \approx Q_{L,N} = \frac{1}{N}\sum_{0}^{N-1} Q_L^{(n)}, \tag{10}$$

where $Q_L^{(n)}$ denotes the nth independent and identically distributed (i.i.d.) sample of the QoI Q_L at level L and N is the number of independent MC samples. For every level l approximation of the QoI, we can construct, by linearity, the following telescoping sum in Eq.11:

$$\mathbb{E}[Q_L(\omega)] = \mathbb{E}[Q_0(\omega)] + \sum_{l=1}^{l=L} \mathbb{E}[Q_l(\omega) - Q_{l-1}(\omega)]. \tag{11}$$

The latter equation can be re-written as

$$\mathbb{E}[Q_L(\omega)] = \sum_{l=0}^{l=L} \mathbb{E}[\Delta Q_l], \tag{12}$$

where, $\Delta Q_l = Q_l - Q_{l-1}$ and $Q_{-1} = 0$.
Using a MC estimator for each term in Eq.12, we obtain the MLMC estimator described in Eq.13:

$$Q_{L,N_l} = \sum_{l=0}^{L} \frac{1}{N_l} \sum_{n=0}^{N_l-1} \Delta Q_l^{(n)}, \tag{13}$$

where $\Delta Q_l^{(n)}$ denotes the nth *i.i.d.* sample of ΔQ_l and N_l is the number of independent samples computed on each level $l \in [0, L]$. Eq.14 gives the variance of the estimator, since the expectations $\mathbb{E}[\Delta Q]$ are estimated independently.

$$\begin{aligned} \mathbb{V}[Q_{L,N_l}] &= \sum_{l=0}^{L} \frac{1}{N_l^2} \sum_{n=0}^{N_l-1} \mathbb{V}[\Delta Q_l] \\ &= \sum_{l=0}^{L} \frac{\mathbb{V}[\Delta Q_l]}{N_l} \end{aligned} \tag{14}$$

MLMC methods are more efficient than the one-level MC since it requires only the computations of the variance of the difference ΔQ_l on higher levels. In spite of the high cost of computing this difference, the variance is smaller, as shown in Eq.15, when a strong positive correlation is found between QoI on level l and $l-1$. Therefore, fewer and fewer samples are required to accurately estimate the expected value $\mathbb{E}[\Delta Q_l]$

$$\begin{aligned} \mathbb{V}[\Delta Q_l] &= \mathbb{V}[Q_l - Q_{l-1}] \\ &= \mathbb{V}[Q_l] + \mathbb{V}[Q_{l-1}] - 2cov(Q_l, Q_{l-1}) \\ &<< \mathbb{V}[Q_l] + \mathbb{V}[Q_{l-1}] \end{aligned} \tag{15}$$

where $cov(Q_l, Q_{l-1})$ is the covariance between Q_l and Q_{l-1}.

4. Implementation

Figure 3 shows our coupling between the UQ Julia package *MultilevelEstimators* and the COOLFluiD solver. The *MultilevelEstimators* package generates the samples, i.e. the uncertain inputs, and assigns the corresponding level. The values of the uncertain inputs as well as the assigned level input the COOLFLuiD solver. The solver generates the result, i.e. the QoI and returns to *MultilevelEstimators* for

analysis. The loop continues until reaching convergence. In *MultilevelEstimators* [9] and in [14], the accuracy of the approximation is controlled via the mean square error (MSE):

$$MSE = \frac{\mathbb{V}[Q_L]}{N} + (\mathbb{E}[Q_L - Q])^2 \tag{16}$$

The convergence criterion is defined as $MSE = O(\epsilon^2)$. In [15], the authors present an error splitting of the MSE as follows: To ensure a MSE of ϵ^2 at most, we need to impose the inequalities present in Inq.17 and Inq.18:

$$\sum_{l=0}^{L} \frac{V_l}{N_l} \leq \theta\epsilon^2, \tag{17}$$

$$(\mathbb{E}[Q_l - Q]))^2 \leq (1-\theta)\epsilon^2. \tag{18}$$

where the splitting parameter $\theta \in [0,1]$. For our simulations, we will choose a constant $\theta = 0.5$.

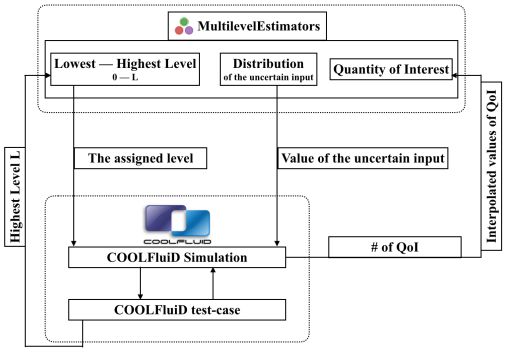

Figure 3: Overview about *MultilevelEstimators* and COOLFluiD coupling

To speed up the process, a parallelization procedure is implemented to reduce the computational time. More precisely, the *MultilevelEstimators* will execute N COOLFluiD simulations with different uncertain values of the input at the same time and in addition, each COOLFluiD simulation will be performed over p cores. Fig.4 illustrates the latter approach.

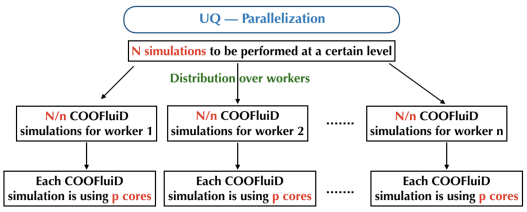

Figure 4: Parallelization strategy

Finally, the MLMC needs nested realizations of the QoI, i.e. fixed distribution of the QoI between the different levels. Nevertheless, the COOLFluiD FR solver employs Gauss-Legendre (GL) distribution for the solution points. The GL is order-dependent and the distribution of the solution points changes in function of the polynomial order. To overcome such problems, an interpolation step is needed to evaluate the QoI at nested positions (coordinates) between all levels (i.e. orders). The key idea is to use the solution point distribution at the highest level, to conserve the level of the accuracy at the highest order, and to evaluate the QoI of the lowest orders at the same point distribution of the highest one. Fig.5 shows the interpolated $P1$ heat flux (HF) solution of the Gnoffo test case[16], evaluated at θ coordinates defined by second order $P2$ Gauss-Legendre distribution. We can notice that the $P2$ and the interpolated $P1$ heat fluxes are evaluated at the same coordinate θ. Fig.6 shows the evaluation of the interpolated $P2$ heat flux at $P4$ Gauss-Legendre θ coordinates distribution.

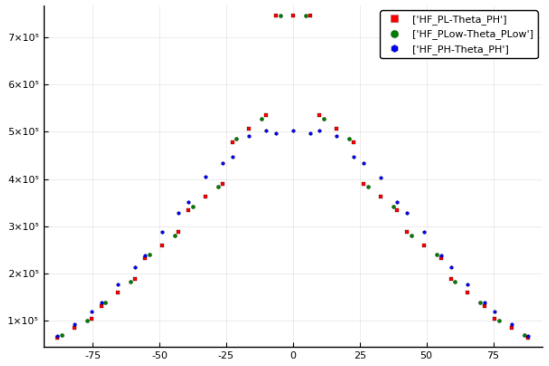

Figure 5: $P1$ HF (circle green) – 1st order interpolation of the $P1$ HF and evaluated at $P2$ θ coordinates (red squares) – $P2$ HF (blue diamonds)

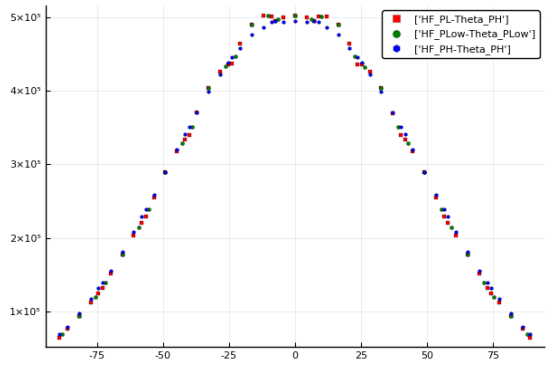

Figure 6: $P2$ HF (circle green) – 2nd order interpolation of the $P2$ HF and evaluated at $P4$ θ coordinates (red squares) – $P4$ HF (blue diamonds)

5. Preliminary Results

Our goal is to compute statistics of a quantity of interest $Q(\omega)$ that can be derived from the solution $\mathbf{u}$ of our PDE model. In particular, we will study the effect of a uniformly distributed wall temperature, denoted T_w, over the heat flux solution of the Cone test case.

5.1. The Deterministic Cone test case

Preliminary results are obtained for the Cone test case that corresponds to Run 35 conditions in [17]. The test case is the flow of nitrogen gas over a 25 half-angle rounded nose cone of radius 1mm. The deterministic test case conditions are presented in Tab.1 and Tab.2, while the test case geometry and the corresponding structured mesh are shown in Fig.7.

Table 1: Cone – Flow characteristics

M_{inf}	$\rho\ [kg/m^3]$	$V_{\text{inf}}[m/s]$	$T_{\text{inf}}[K]$	$T_{wall}[K]$
11.3	0.5515	2713	138.9	296.3

Table 2: Gnoffo – Mesh characteristics

Dimensions	Type	# Elements	Geometric order
2D axisymmetric	Quadrilateral	2000	2 (i.e. curved)
BC 1	BC 2	BC 3	BC 4
Iso-thermal wall	Inlet	Outlet	Mirror

5.2. MLMC Simulations of the Cone test case

Firstly, 3-levels MLMC simulations of the Cone test cases are carried out. The effect of the wall temperature, varying uniformly between $[273.3, 313.3]$, over the heat flux of a specific point on the blunt-body ($x_0 = 0.0252356$[m]). The reader should note that the MLMC levels are mapped to the following (cf. Tab.3), ensuring a p-refined MLMC method.

Table 3: Mapped levels between MLMC and FR

MLMC Level	FR Order	N_{DOF}
0	1	8000
1	2	18000
2	3	32000

where N_{DOF} stands for Number Degrees of freedom, and is computed as : $N_{DOF} = N_{elements} \times (P+1)^2$.

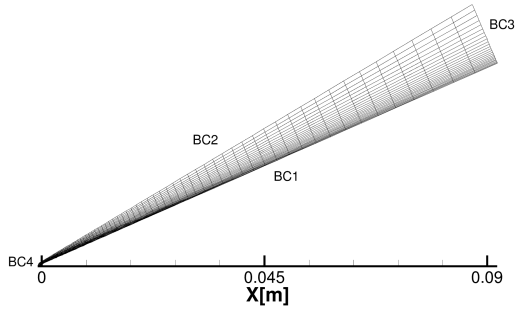

Figure 7: Cone – Mesh Characteristics

The statistical analysis are shown in Fig.8,9 and 10. We observe clearly a decrease of the ΔV_l and N_l when the level increases. The work units of the MLMC method corresponds to 269×17.7 + 14×369.2 + 5×2740 = 23630.1 while the work units for MC is equal to 269×2740=737060. We obtain by using the MLMC method a speedup up to 31.2×.

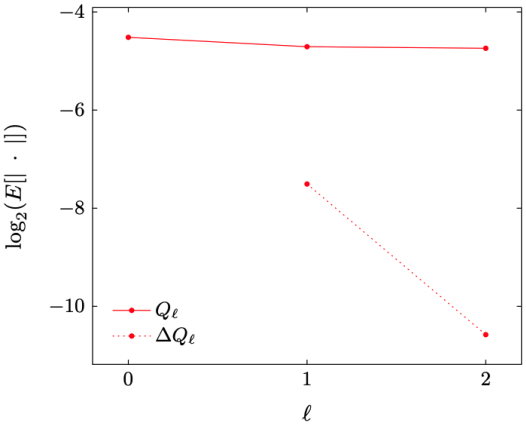

Figure 8: Behaviour of the expected value of x_0

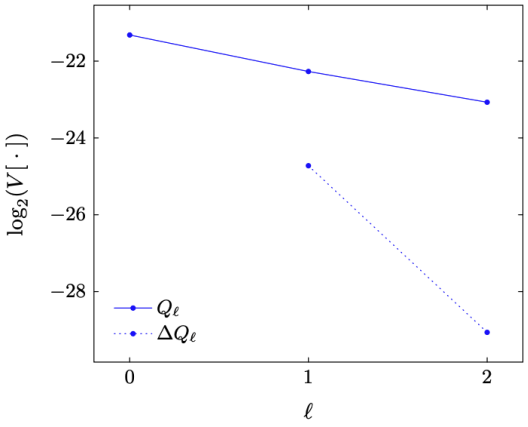

Figure 9: Behaviour of the variance at x_0

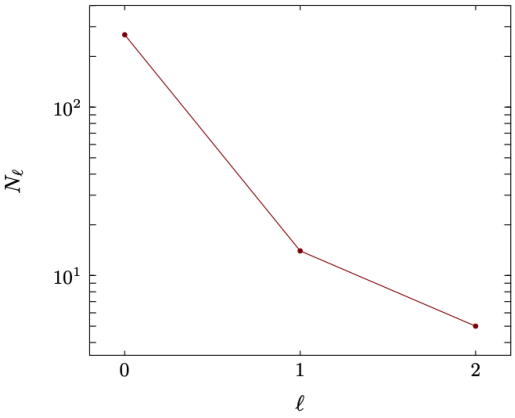

Figure 10: Computed samples N_l over the UQ levels

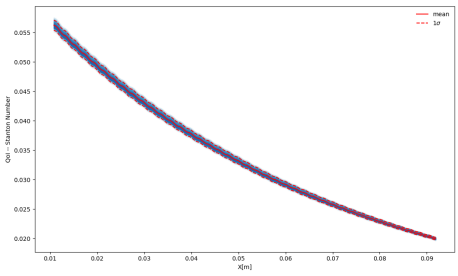

Figure 11: Statistical analysis : mean and standard deviation

Similar analyses are carried out for all points located over the cone with an abscissa x ranging from [0.0108039m, 0.0918783m]. The distributed number of computed samples over the levels 0, 1 and 2 are 206, 37 and 20 respectively. The obtained mean and variance field are shown in Fig.11 and a zoom over the interest region is depicted in Fig.12

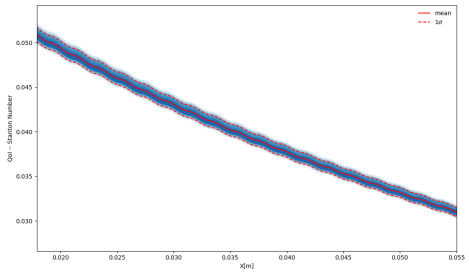

Figure 12: Statistical analysis : mean and standard deviation – zoom over the region of interest

6. Conclusion

The *MultilevelEstimators* Julia package and COOLFluiD solver are successfully coupled. As an additional novelty, the Multi-Level Monte Carlo methods used for UQ constructs levels using p-refinement instead of h-refinement. As future work, we will study the RANS turbulence models by injecting uncertainties over the various parameters of the models (e.g. $k-\omega\ SST$, $\gamma-\alpha$ etc...).

Acknowledgments

- The research of Firas Ben Ameur is supported by SB PhD fellowship 1SC3519N of the FWO.
- Many thanks to Ray Vandenhoeck for providing the deterministic FR-Cone test cases.
- Many thanks to Pieterjan Robbe for his assistance on *MultilevelEstimators* Julia package.

References

[1] O. P. L. Maître, Stochastic spectral methods for uncertainty propagation in computational fluid mechanics models, NATO RTO-VKI Lecture Series.

[2] E. M. Sousa, G. Lin, U. Shumlak, Uncertainty quantification of the gem challenge magnetic reconnection problem using the multilevel monte carlo method, International Journal for Uncertainty Quantification 5 (4).

[3] G. Iaccarino, Introduction to uncertainty representation and propagation, NATO RTO-VKI Lecture Series.

[4] M. Pisaroni, Multilevel monte carlo methods for uncertainty quantification and robust design optimization in aerodynamics, Ph.D. thesis, EPFL (2017).

[5] C. S. T. Barth, S. Mishra, Uq methods for nonlinear conservation laws containing discontinuities, NATO RTO-VKI Lecture Series.

[6] R. Vandenhoeck, A. Lani, Implicit high-order flux reconstruction positivity preserving llav scheme for viscous high-speed flows, in: AIAA Scitech 2019 Forum, San Diego, California, 2019.
[7] R. Vandenhoeck, A. Lani, Implicit high-order flux reconstruction solver for high-speed compressible flows, Computer Physics Communications 242 (2019) 1 – 24. doi:https://doi.org/10.1016/j.cpc.2019.04.015.
[8] F. Ben Ameur, R. Vandenhoeck, A. Lani, High-order flux reconstruction scheme for thermo-chemical nonequilibrium high-speed flows, in: AIAA Scitech 2019 Forum, San Diego, California, 2019.
[9] P. Robbe, Multilevel uncertainty quantification methods for robust design of industrial applications, Ph.D. thesis, KU Leuven (2019).
[10] H. Huynh, A flux reconstruction approach to high-order schemes including discontinuous galerkin methods, AIAA paper 4079 (2007) 2007.
[11] H. Huynh, High-order methods including discontinuous galerkin by reconstructions on triangular meshes, AIAA Paper 44 (2011) 2011.
[12] P. Castonguay, D. M. Williams, P. E. Vincent, M. Lopez, A. Jameson, On the development of a high-order, multi-gpu enabled, compressible viscous flow solver for mixed unstructured grids, AIAA paper 3229 (2011) 2011.
[13] P. Castonguay, P. Vincent, A. Jameson, Application of high-order energy stable flux reconstruction schemes to the euler equations, in: 49th AIAA Aerospace Sciences Meeting, Vol. 686, 2011.
[14] M. B. Giles, Multilevel monte carlo path simulation, Operations research 56 (3) (2008) 607–617.
[15] N. Collier, A.-L. Haji-Ali, F. Nobile, E. Von Schwerin, R. Tempone, A continuation multilevel monte carlo algorithm, BIT Numerical Mathematics 55 (2) (2015) 399–432.
[16] P. Gnoffo, J. White, Computational Aerothermodynamic Simulation Issues on Unstructured Grids, in: 37th AIAA Thermophysics Conference, Fluid Dynamics and Co-located Conferences, American Institute of Aeronautics and Astronautics, 2004.
[17] G. Candler, I. Nompelis, M.-C. Druguet, M. Holden, T. Wadhams, I. Boyd, W.-L. Wang, Cfd validation for hypersonic flight-hypersonic double-cone flow simulations, in: 40th AIAA aerospace sciences meeting & exhibit, 2002, p. 581.

Modeling strategy for blackout analysis of re-entry phases in space exploration missions

Vincent Fitzgerald Giangaspero

Aeronautics and Aerospace Department, von Karman Institute for Fluid Dynamics, Belgium, vincent.giangaspero@vki.ac.be

Advisor: Andrea Lani

Research Expert, Aeronautics and Aerospace Department, von Karman Institute for Fluid Dynamics, Belgium, lani@vki.ac.be

University Supervisor: Stefaan Poedts

Professor, Department of Mathematics, KU Leuven, Belgium, stefaan.poedts@kuleuven.be

Abstract

This works presents the development of a three-dimensional ray tracing solver for the numerical analysis of the communication blackout encountered in atmospheric entry flights. The ray tracing methodology is based on the implementation of the Eikonal system of equation, a fast, efficient and accurate method to analyse interaction of electromagnetic signals and weakly ionised plasmas. The proposed methodology is applied to the atmospheric entry of the ExoMars capsule in Martian environemnt and shows the capability of a three-dimensional approach to analyse real flight configuration.

Keywords: Plasma flows, atmospheric re-entry, CFD, ray tracing, communicaiton blackout, ionization

1. Introduction

The re-entry phase is one of the most challenging phases of a space mission and it's one of the most critical aspects to be considered for the design of a successful space mission. Among the open challenges in the aerospace sector, communication blackout is an important issue for space exploration missions and it is extremely important to develop strategies for ensuring the propagation of telemetry during atmospheric re-entry flights. The methodology proposed in this research is focused on the innovative use of optical ray-tracing analysis to characterize the phenomena of the communications blackout. This will allow to overcome the limits of the current state-of-the-art approaches that are not capable to deliver the information needed to develop blackout mitigation solutions for future space missions.

During the entry phase spacecraft enter a planetary atmosphere at hypersonic speed, typically around 6-10 $km\ s^{-1}$, generating strong shock waves and large aerodynamic heating. When the temperature is high enough to excite the gas molecule internal energy modes up to the point where dissociation and ionization reactions occur, a plasma layer is generated around the vehicle. This plasma interacts with the electromagnetic fields signals from/to the vehicle, disrupting the functionality of the on-board signal transmission systems. Figure 1 shows a sketch representa-

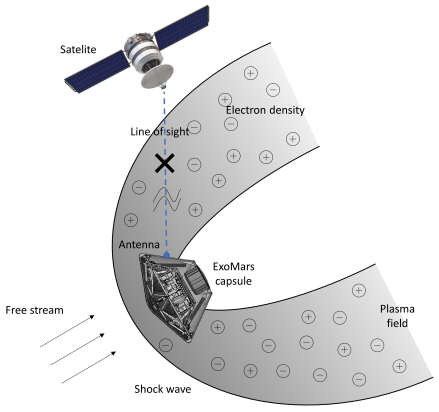

Figure 1: Radio frequency blackout for flow over entry capsule.

tion of the phenomenon.

In general, blackout analysis is composed by two different steps. The first step consist in obtaining plasma density profiles and collision frequencies around the space re-entry vehicle from non-equilibrium hypersonic CFD simulation. The methodology used in this work starts with the numerical simulations of different trajectory points during re-entry missions. The CFD solver needs to be capable to deliver accurate electron density fields, which are needed for the analysis of interaction between electromagnetic waves and plasma, both for air and CO2 mixtures. Then the CFD solutions are used as input solutions to carry on the blackout analysis based on the application of ray-tracing algorithms. The proposed methodology, based on research efforts carried on at the von Karman Institute for Fluid Mechanics over the past years, has been applied to the Martian re-entry of the ExoMars Schiaparelli module in [1] and [2]. This work has been the first study in literature of the ExoMars Schiaparelli blackout period (duration and location on trajectory) by the use of a novel blackout analysis methodology which incorporates a decoupled CFD approach in combination with a ray tracing algorithm based on the application of the Snell's law. The objective of this project is to advance the numerical tools used for the blackout analysis both in terms of CFD accuracy and ray-tracing modeling. This research is taking profit of the collaboration and integration of the work that the COOLFluiD team is carrying on for the recently awarded Future Emerging Technologies (FET), a prestigious 3 years project from the EU Horizon2020 program, with my supervisor Andrea Lani as PI. The project, titled MHD Enhanced Entry System for Space Transportation (MEESST), aims at developing a magnetic shielding technology for next-generation spacecrafts. MEESST will help mitigating surface thermal loads and radio communication blackout during re-entry phases in planetary atmospheres by prototyping an innovative MHD-enabling system based on the latest superconducting technology. All the developments of this PhD project are considered part of the deliverables of the MEESST project [3].

2. Physical modeling of entry plasma

Ray tracing allows for analysing the propagation of EM waves on the basis on the computation of the optical properties of the plasma, which are defined by the refractive index. The optical properties are described by the Appleton-Hartree equation, which has been extensively applied to ionospheric propagation problems [4]. The entry plasma is modeled as an unmagnetised cold plasma, a common assumption for atmospheric entry flows. Under these assumptions, the Appleton-Hartree equation reads:

$$n^2 = (\mu - \imath\chi)^2 = 1 - \frac{X}{1 - \imath Z}, \tag{1}$$

with:

$$\begin{aligned} X &= \mathrm{e}^2 N_\mathrm{e} / \left(\epsilon_0 m_\mathrm{e} \omega^2\right), \\ Z &= \nu_\mathrm{eh} / \omega, \\ \omega &= 2\pi f, \end{aligned} \tag{2}$$

where e denotes the electron charge, N_e the electron number density, ϵ_0 the vacuum permittivity, m_e the electron mass, ν_eh the electron-heavy particle collision frequency, and f for the communication system transmission frequency. The plasma complex refractive index, n, consist of a real part, μ, and an imaginary part, χ. The real part represents the effects of EM waves bending, whereas the imaginary part is related to the absorptivity and is responsible for EM wave attenuation. The effect of neglecting or considering electron collisions in the Appleton-Hartree equation can lead to two different medium characterizations, non-collisional and collisional plasma. Usually the electron plasma frequency is large compared to the electron - heavy particle collision frequency. As repoorted in [2], for CO_2 atmospheric entry the simplification of non-collisional medium is a good approximation to describe plasma characteristics generated by the ionisation level occuring in the entry conditions of the ExoMars capsule. For non-collisional plasma, $Z \sim 0$, meaning $\nu_{eh} \ll \omega$, leading to:

$$n = \mu = \sqrt{1 - X} = \sqrt{1 - \left(\frac{f_p}{f}\right)^2}, \tag{3}$$

with:

$$f_p = \sqrt{k N_e} \tag{4}$$

$$k = e^2 / \left(4\pi^2 \epsilon_0 m_e\right) \tag{5}$$

In this formulation, the refractive index is a real number with values between 0 and 1. The refractive index of the plasma thus becomes a solely a function of the electron plasma frequency f_p and the antenna transmission frequency ω in Hz. Figure 2 shows the electron number density and refractive index distribution computed for the trajectory point c of Table 1.

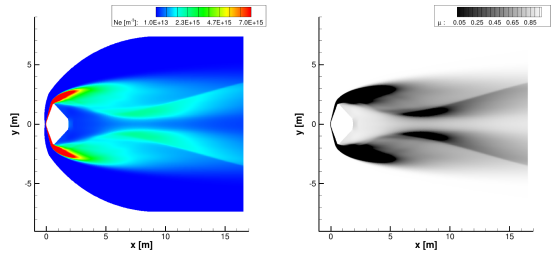

Figure 2: Physical model of entry plasma at 38s entry trajectory. Electron density distribution (left) and refractive index field (right).

3. Eikonal solver

The most important upgrade to the methodology used in this project has been the development and implementation of a new ray-tracing algorithm, the Eikonal equation solver. The previous ray-tracing algorithm, the Snell's law solver, has been proved to be representative of the physical phenomena involving communication blackout [1]. The Snell's law successfully describes the phenomena of interaction between EM waves (in form of rays) and a non homogeneous medium with a varying refractive index field. However, it presents some limitations in terms of physical representation of the phenomena and numerical implementation, both in terms of accuracy and performances. The Snell's Law is the governing equation of geometrical optics, that is a simplified model of EM waves propagation in a medium in form of rays. The simplifying assumptions of geometrical optics include that rays: (i) propagate in straight-line paths as they travel in a homogeneous medium (ii) bend, and in particular circumstances may split in two, at the interface between two dissimilar media (iii) follow curved paths in a medium in which the refractive index changes (iiii) may be absorbed or reflected. It's a general law of physics that can be derived with many different approaches. As of today, there are five different ways to derive Snell's law, that are: Huygens' Principle, Fermat's Principle, Maxwell's equation, Momentum Conservation and Vectorial form [6]. Despite the general validity of the Snell's law, its numerical solution lacks important physical information that characterise the electromagnetic signal and its properties. To overcome this limit, the right approach requires a step back to the more general field of physical (wave) optics. Physical optics is the branch of optics that studies interference, diffraction, polarization, and other phenomena for which the ray approximation of geometric optics is not valid. This is possible with the use of the Eikonal Equation, that is a non-linear partial differential equation that governs wave propagation, directly derived from Maxwell's equation. The Eikonal equation is the direct link between these two branches of optics, physics and geometrical, and it's the theoretical starting point of any physical and advanced ray-tracing method.

The Eikonal equation is an approximate solution of Maxwell's equations in the high-frequency limit [5]. At large frequencies, electric and magnetic fields may be expressed as:

$$E(r) \simeq E_0 e^{-\imath k_0 S(r)} \qquad H(r) \simeq H_0 e^{-\imath k_0 S(r)}, \tag{6}$$

where $S(r)$ is the normalised Eikonal phase function, defining the wave-front surface. Inserting the high frequency fields into Maxwell's equations leads to the Eikonal equation:

$$|\nabla S| = \mu, \tag{7}$$

that defines the relation between the direction of propagation of an EM wave and the refractive index of the medium. The solution of the Eikonal equation yields the ray trajectories. A more convenient, but mathematically equivalent, form of the Eikonal equation may be obtained by writing the former in characteristic form. This may be achieved by introducing the normalized local wave vector $\xi = \nabla S$, that defines the propagation direction of the EM wave, and the position vector $x_i = (x_1, x_2)$. Using the arc-length s along the ray, one arrives at the following system of ordinary differential equations:

$$\begin{aligned} \frac{\partial x_i}{\partial s} &= \frac{\xi_i}{\mu}, \\ \frac{\partial \xi_i}{\partial s} &= \frac{\partial \mu}{\partial x_i}. \end{aligned} \tag{8}$$

The Eikonal approximation is valid as long as medium properties vary slowly over a length-scale of the order of the signal wavelength [5]. In an hypersonic entry plasma, this assumption can be considered valid in the whole wake region.

Thus, the Snell's law can be considered as the local solution of the Eikonal equation at the interface between two medium at different refractive index, in which a straight ray deviates depending on the refractive index discontinuity at the interface. At this stage of the developments, the Eikonal equation is used in the domain of geometric optics to perform the integration of the rays path in the re-entry plasma.

4. 3D Ray Tracing solver

Following the implementation of the 2D version of the Eikonal solver, the next step has been the development of the 3D version of the Eikonal solver. Another advantage of the Eikonal solver lies in the decoupled nature of the ODE system of equation, that requires no particular difficulties for the implementation of the 3D version of the algorithm. In this case, the system of equations reads as follow:

$$\begin{aligned}
\frac{\partial x}{\partial s} &= \frac{\xi_1}{n} \\
\frac{\partial y}{\partial s} &= \frac{\xi_2}{n} \\
\frac{\partial z}{\partial s} &= \frac{\xi_3}{n} \\
\frac{\partial \xi_1}{\partial s} &= \frac{\partial n}{\partial x} \\
\frac{\partial \xi_2}{\partial s} &= \frac{\partial n}{\partial y} \\
\frac{\partial \xi_3}{\partial s} &= \frac{\partial n}{\partial z}
\end{aligned}$$

The system (8) along with prescribed initial conditions allows to predict the ray trajectories determined the refractive index of the plasma and by its gradient. The accuracy of blackout predictions depends on the uncertainty of the electron prediction from CFD simulations and the EM wave propagation method. The second order continuity in plasma frequency of the Eikonal formulation allows to increase ray tracing solution accuracy respect first order ray tracing methods, as used in previous studies [2]. In this work the ray trajectories are computed using an updated version of BORAT, a MATLAB® code developed for the plasma modeling and ray tracing integration. The Ordinary Differential Equations (ODE) system resulted from the Eikonal equation (8) is solved in each step using a Runge-Kutta method (RK4). For a given ray, initial conditions are prescribed in terms of position and angle:

$$\begin{aligned}
x(s)|_{s=0} &= x_0 \\
y(s)|_{s=0} &= y_0 \\
z(s)|_{s=0} &= z_0 \\
\xi_1(s)|_{s=0} &= cos(\theta_0)cos(\alpha_0) \\
\xi_2(s)|_{s=0} &= cos(\theta_0)sin(\alpha_0) \\
\xi_2(s)|_{s=0} &= sin(\theta_0)
\end{aligned}$$

where the angle α_0 is the angle on the plane x-y, and the angle θ_0 is the azimuthal angle respect the positive z axis. Rays integration is completed when either they emerge from the computational domain or if the ray impinges the vehicle surface. The vehicle outer surface is modelled as a metallic solid wall, assuming that the presence of heat shields materials does not affect the refractive property of the body. Thus, a solid reflection boundary condition is imposed when a ray impinges on the vehicle surface. In this case, new initial conditions are imposed to the ray, that will be reshoot from the intersection point. In conclusion, the proposed ray tracing method results in a numerically efficient tool. Each ray is independent and uncoupled respect the other rays, and the solver can be easily parallelized with complexity scale that varies linearly with the number of rays. The main challenge towards the implementation of the 3D version of the code has been the upgrade of the whole code data structure and algorithms to handle three-dimensional conditions. The first tests have been focused on assessing the functionality of the 3D Eikonal solver. In figure 3 two different simplified three-dimensional solution with a converging and diverging beam of rays are shown.

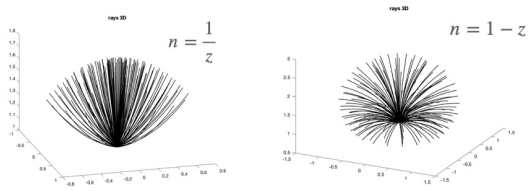

Figure 3: Converging (left) and diverging (right) vertical refractive index field

Figure 4 shows the preliminary tests to complete the implementation of the boundary reflection condition.

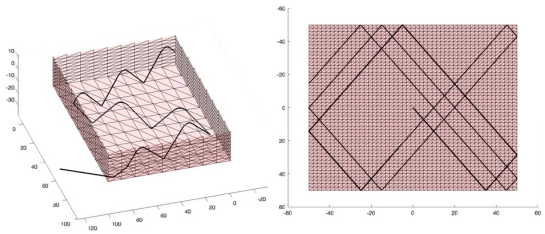

Figure 4: Reflections test on simplified closed box domain

Figure 5 shows the first test of the algorithm for a simplified re-entry case. A cylindrical domain encloses an ARD-like re-entry capsule, on which a beam

of rays is emitted in the vertical direction. A vertical linearly decreasing refractive index field is imposed in the whole domain, bending the rays towards the rear part of the capsule.

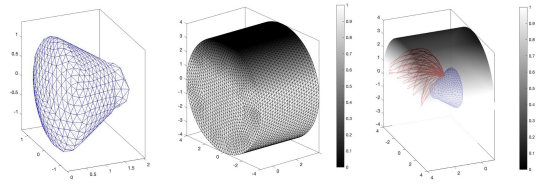

Figure 5: Simplified re-entry benchmark case in vertical decreasing refractive index field

Once all the developments have been successfully tested, the novel 3D Eikonal solver has been used to perform three-dimensional analysis of the ExoMars re-entry trajectory based on the 2D axis-symmetric solution computed with the COOLFluiD ATD solver. The results of this analysis will be presented in the next section.

5. 3D Ray tracing analysis of ExoMars atmospheric entry

The recent developments of the three-dimensional version of the Eikonal solver allowed a fully three-dimensional analysis of the ExoMars re-entry trajectory. These results are based on the 2D axisymmetric CFD solutions. The freestream conditions for the different trajectory points are listed in Table 1. The procedure starts with the interpolation of the 2D solutions on a three-dimensional unstructured meshes suitable for the Borat code. Due to the zero angle of attack flight conditions of the ExoMars spacecraft, in first approximation the 2D axisymmetric solution can be considered representative of the a fully 3D computation.

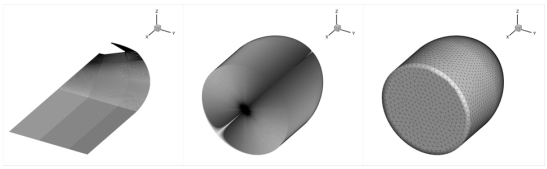

Figure 6: 3D ExoMars solution reconstruction with interpolation from 2D structured solution

This task has been accomplished by the generation of a 6 million cells 3D unstructured tetrahedral mesh, generated with the mesh generation software Gambit. Then the 2D structured solution is interpolated on the new 3D mesh via an inverse distance interpolation algorithm via the use of the software Tecplot v2020R1. Figure 6 shows the intermediate steps of the solution interpolation, and in figure 7 comparison between the two solution is presented.

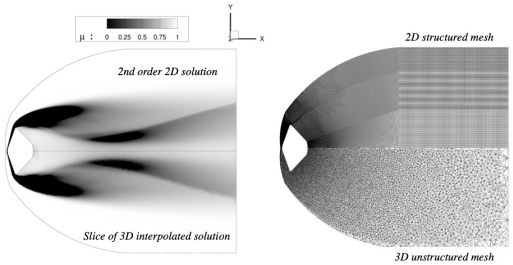

Figure 7: 3D ExoMars solution interpolation comparison on x-y symmetry plane

After the generation of the 3D input solution files via interpolation, the raytracing analysis has been carried on for all the re-entry trajectory point listed in Table 1.

t $[s]$	h $[km]$	ρ_∞ $[kg/m^3]$	V_∞ $[m/s]$	T_∞ $[k]$	M_∞
22	96	6.97 x 10^{-6}	5867	165	28.4
27	91	1.29 x 10^{-5}	5859	155	29.3
38	80	3.72 x 10^{-5}	5856	175	27.5
50	71	1.10 x 10^{-4}	5736	168	27.4
62	63	2.90 x 10^{-4}	5269	169	25.1
73	56	5.82 x 10^{-4}	4516	174	21.2
77	54	7.13 x 10^{-4}	4192	177	19.5
80	52	8.25 x 10^{-4}	3941	180	18.2
85	50	1.01 x 10^{-3}	3532	184	16.1

Table 1: Free stream conditions of ExoMars Schiaparelli at different trajectory points.

For the three-dimensional analysis, the emitting antenna is located on the vertical side of the spacecraft, and the emitted signal is modelled with an omnidirectional beam of 180 rays with a 70 degrees cone aperture respect the normal to the spacecraft.

Figure 8 and 9 show the 3D raytracing solutions. For each solution two different iso-surfaces are highlighted: the first iso-surface (darker in colour and close to the spacecraft body) is the $\mu = 0$ surface, that delimits the zones at high ionisation generated during the blackout and shields the emitted signal from the propagation in the plasma layer. As predicted, its extension varies during the re-entry, reaching its peak at

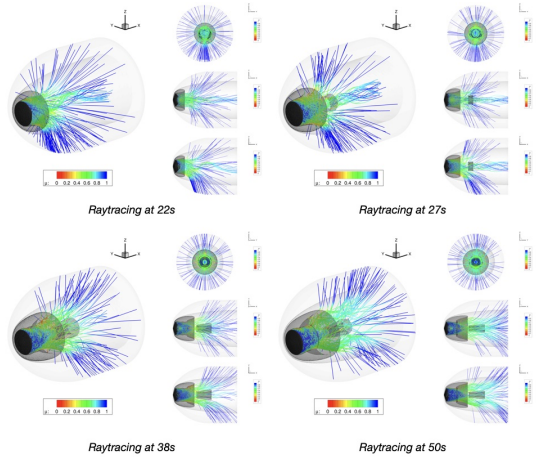

Figure 8: 3D ExoMars raytracing analysis 22-50s re-entry trajectory points

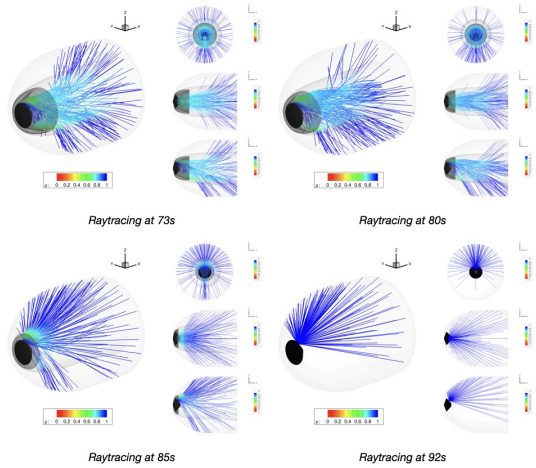

Figure 9: 3D ExoMars raytracing analysis 73-92s re-entry trajectory points

the trajectory points between 38 and 50 s, in which the flight conditions are of complete blackout. On the other hand, the iso-surface at $\mu = 1$ delimits the bow shock surface, from which the plasma layer is generated around the spacecraft. Its extension depends on the Mach number of the flow, and decreases during the re-entry deceleration phase. All rays are coloured depending on the refractive index value of the field encountered in their path. Rays encounter strong reflections near the shoulder of the vehicle and a series of refractions in the wake region. At maximum blackout conditions, the vast majority of the rays are converged in the wake and shielded by the plasma. Brownout phases are characterized by lower ionisation levels of the flow that result in less disruption of the electromagnetic wave signal. In general, the entry plasma wraps the vehicle and forms a shielding cup around it. Because of the reflection at the plasma, the cup has a potential for focussing/defocussing the rays, a fact that may generate directive patterns in certain angular regions. During brownout, not all the electromagnetic waves are fully encapsulated in the plasma layer. In this condition, the presence of plasma redirects the rays, creating communication windows that could possibly be used as alternative communication path. Future works will be focused on the investigation of these alternative communication windows.

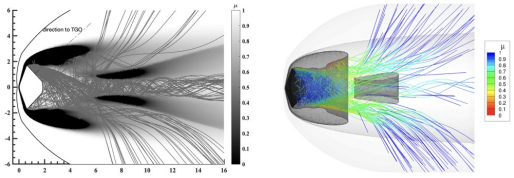

Figure 10: Comparison between 2D raytracing solution (left) and 3D raytracing solution (right) on z-x symmetry plane for the 38s re-entry trajectory point

6. Conclusion

This work presents the application of a ray tracing method for the blackout analysis of the ExoMars Schiaparelli mission. It is based on the application of CFD simulations, performed with the COOLFLuiD aerothermodynamic solver and the PLATO library for non-equilibrium plasmas, in combination with a 3D ray tracing algorithm. Numerical CFD simulation are performed at different entry trajectory points assuming chemical non-equilibrium and thermal equilibrium for a 14 species Martian atmosphere mixture. Results confirm that radio blackout is mostly due to encapsulation of rays by the plasma rather than absorption of the signal. Furthermore, reflection and refraction phenomena can make RF signal rays escape the entry plasma layer. Advanced analysis methods, such as the one presented in this work, allows for properly predicting the emitted signal path in the plasma flow, thus gathering more information on possible alternative communication directions during blackout. This is extremely important for the brownout phases, where, due to lower ionization levels of the flow, the emitted radio waves can possibly reach the receiving spacecraft through refraction and reflection.

Acknowledgments

The research of Vincent Fitzgerald Giangaspero is supported by SB PhD fellowship 1SA8219N of the the Research Foundation - Flanders (FWO).

The resources and services used in this work were provided by the VSC (Flemish Supercomputer Center), funded by the Research Foundation - Flanders (FWO) and the Flemish Government.

References

[1] S. Ramjatan, A. Lani, S. Boccelli, B. Van Hove, Ö. Karatekin, T. Magin, J. Thoemel, Blackout analysis of mars entry missions, Journal of Fluid Mechanics 904.

[2] V. F. Giangaspero, A. Lani, S. Poedts, J. Thoemel, A. Munafò, Radio communication blackout analysis of exomars re-entry mission using raytracing method, in: AIAA Scitech 2021 Forum, 2021, p. 0154.

[3] E. Bögel, M. A. La Rosa Betancourt, M. R. Collier-Wright, Magnetohydrodynamic enhanced entry system for space transportation (meesst) as a key building block for future exploration missions, in: AIAA Propulsion and Energy 2021 Forum, 2021, p. 3272.

[4] K. Davies, Ionospheric radio propagation, Vol. 80, US Department of Commerce, National Bureau of Standards, 1965.

[5] Y. A. Kravtsov, Y. I. Orlov, Geometrical optics of inhomogeneous media, Geometrical Optics of Inhomogeneous Media by Yu. A. Kravtsov.

LIQUID AND SOLID PROPULSION

Transient dynamics of contact angles

Domenico Fiorini

von Karman Institute for Fluid Dynamics, Environmental and Applied Fluid Dynamics Department, Belgium, domenico.fiorini@vki.ac.be

Supervisor: Miguel Alfonso Mendez

Assistant Professor, von Karman Institute for Fluid Dynamics, Environmental and Applied Fluid Dynamics Department, Belgium

University Supervisor: David Seveno

Professor, KU Leuven, Dept. of Materials Engineering, Belgium, david.seveno@kuleuven.be

University CoSupervisor: Johan Steelant

Professor, KU Leuven, Dept. of Mechanical Engineering, Belgium,

ESTEC-ESA, Keplerlaan 1, 2200AG Noordwijk, The Netherlands, Johan.Steelant@esa.int

Abstract

The angle of contact of a gas-liquid interface with a solid surface is a function of the dynamic conditions of the contact line. Although numerous experiments have been performed in simplified conditions, no accurate data exists for the case of low surface tension fluids subjected to impulsive accelerations.
In this work, we investigate the shape of a liquid interface and the corresponding contact angle in accelerating interface conditions. Low surface tension fluids are studied both in ambient and cryogenic conditions with the same experiment configuration.
The results show that traditional models fail to predict the interface shape and its contact angle due to the interface acceleration and contact line history. We propose a new model for a moving interface in axial-symmetric channels and we discuss the impact of the contact angle. We show the relation between the contact angle and the interface shape, as well as the link of the former with the thermodynamic conditions of the interface.

Keywords: Gas-liquid Interfaces, Dynamic Contact Angle, Inverse method, Cryogenic, Space Propulsion

1. Introduction

The curved shape of a gas-liquid interface produces a pressure difference across the interface itself. This is known as capillary pressure and plays a key role in the modeling of the interface motion when the gravity and the capillary forces become comparable Vestad et al. [2004]; Liu et al. [2017]. This is the case of many practical applications such as the imbibition of fluids by porous media Ma et al. [2012], enhanced oil recovery operations Kumar and Fogden [2010], droplet manipulation in microfluidics Willmott et al. [2011, 2010]; Liu et al. [2017] and cryogenic liquid management in space systems White and Troian [2019]; Bellur et al. [2016]; Li et al. [2020]. In the case of the latter, the dynamic contact angle, i.e., the angle formed by the interface at a moving contact line, raised research interest in the last years due to the missing understanding of its role in the motion of the free interface. Classic models miss accurate validation databases and the simulation of the behaviour of cryogenic liquids in space still doesn't reach the level of accuracy required to improve the efficiency of the current space propulsion.

The first definitions of dynamic contact angle can be found in the studies of Blacke, Hoffman and Voinov Blake and Haynes [1969]; Hoffman [1975]; Voinov [1976]. These studies show that the motion of the contact point and the contact angle are strongly correlated and in the case of viscous dominated flow the dynamic contact angle can be computed as a

function of the velocity of the contact line, expressed in dimensionless form by means of the capillary number Blake and Haynes [1969]; Voinov [1976]; Cox [1986]; Petrov and Petrov [1992]; Shikhmurzaev [1993]; De Gennes et al. [1990]; Hoffman [1975]; Tanner [1979]; Jiang et al. [1979]; Bracke et al. [1989]; Kistler [1993]. Both theoretical and empirical correlations were developed in the approximation of steady contact line motion. However, several authors (see Ting and Perlin [1995]; Bian et al. [2003]; Quéré [1997]; Shardt et al. [2014]; Willmott et al. [2020] and references cited therein) have shown that these approaches fail in the presence of inertia and demand new experiments to clarify the influence of the contact line acceleration and the time history of the contact line dynamics (see Ting and Perlin [1995]; Bian et al. [2003]).

Experimental studies on dynamic contact angles emphasize the difficulty to obtain reliable results due to the microscopic nature of the problem and thus the high resolution needed for the optical equipment to visualize the interface. Consequently, the results are often affected by a high uncertainty or by a limited degree of generalization. Petrov and Sedev [1993] consider the dynamic contact angle as "inaccessible" by optical means and attempt to overcome this limit by extrapolating the contact angle from the theoretical quasi-static interface shape fitted to the experimental data. The theoretical interface shape is obtained from the solution of a boundary value problem which Petrov and Sedev [1993] closed by using Dirichlet boundary conditions imposed by the experiment in the form of interface height at given locations.
Maleki et al. [2007] extended the approach of Petrov and Sedev [1993] to a "quasi-steady" approximation where the capillary number is directly involved in the shape of the gas-liquid interface. They found that in the case of receding interfaces a critical capillary number must be defined where the contact angle seemingly jumps to zero and a liquid film is deposed. Voinov and Eggers Voinov [2000]; Eggers [2005b] hypothesized as well the existence of such condition.
The case of an inertia-dominated interfaces has not been yet considered in the framework of the methods described above, which are called Meniscus Profile Methods (MPM). However, interface motion dominated by inertia has already been observed in the work on capillary rise by Quéré [1997], where the dynamics of the contact angle was not considered in the modeling of the interface rise due to the small capillary number expected and hence negligible angle variations.
A similar experiment was performed later on by Shardt et al. [2014], where the dynamics of the contact angle and the possibly non-spherical shape of the meniscus was initially neglected, the authors concludes that better accuracy in modeling the data could be obtained by a more accurate description of the contact angle.
Recent work by Willmott et al. [2020] recognise the importance of the contact angle dynamics in the inertial motion of gas-liquid interfaces in thin capillaries. They distinguish two regimes of motion for the liquid interface. In the viscous dominated regime the interface shape can be effectively described by means of a "quasi-steady" approximation while in the case of the inertia-dominated regime this description is not sufficient. The authors also report that an improved description of the contact angle and the interface in the inertial regime will become increasingly important for microfluidics applications such the liquid uptake by porous materials.

The interplay between macro and microscopic lengths constitutes the main limit to the accuracy of dynamic contact angle measurements, this often implies that important compromises in the resolution of the contact line visualization. This problem become seven more impact-full in the case of perfect wetting fluids such as cryogenic fuels and their substitutes. The interface contact angle approaches values of approximately zero degrees and the classic measurement uncertainty increases dramatically in percentage. Moreover, the extremely low surface tension implies that the dynamic dependence of the contact angle from the contact line velocity changes significantly comparing to the classic viscous oils upon which the most popular correlations are built. In addition to the previous, the study of cryogenic liquid behaviour often imposes strong limits to the spectrum of technique that can be used, due to the difficult accessibility to the experiment imposed by the experimental bench used (e.g. cryostat facilities).

In this paper, we investigate the impact of the dynamic contact angle on the shape of the gas-liquid interface. The chosen configuration is U-tube geometry where an axial-symmetric gas-liquid interface forms on the two sides. The tube radius has been designed to allow an accelerating contact line and the biggest impact of the surface tension on the shape of the liquid interface. We measure the dynamic contact angle by means of a customized Meniscus Profile Method introducing an improved mathematical description of

the interface shape for inertia dominated interfaces in circular tubes. We analyze the results both in terms of interface shape and dynamic contact angle and we propose a new correlation accounting for the acceleration and history of the contact line. Three fluids are considered in this study, distilled water, HFE 7200 and cryogenic liquid nitrogen.
The experimental configuration is described in section 2. The interface parametrization is described in section 3. The regression of both the interface shape and the contact angle correlations was carried out using the optimization strategies described in 3.3 validation is showed in subsection 3.4. The results are presented in section **??**. Conclusions and outlooks are reported in section **??**.

2. Experimental methods

Table 1 shows the relevant properties for the fluids considered in this study. HFE7200 is a synthetic liquid belonging to the family of hydrofluoroethers characterized by small equilibrium contact angles. These liquids are mostly used to simulate the properties of cryogenic space fluids Rausch et al. [2015]. While Water and HFE7200 can be tested in ambient laboratory conditions, tests with liquid nitrogen (LN2) require using the VKI cryostat facility which allows reproducing stable cryogenic conditions in the range 70-80K.

Table 1: Fluids density (ρ), dynamic viscosity (μ) and surface tension (σ) at $p = p_{atm}$

		Water (298K)	HFE7200 (298K)	LN2 (77K)
ρ	kg/m^3	996.66	1423.00	807.69
μ	mPa · s	0.97	0.64	0.16
σ	mN/m	72.01	13.62	8.96

The behavior of the gas-liquid interface is analyzed in a U-shaped quartz tube custom produced by PIERREGLAS (Belgium). The U-tube used at laboratory temperature has internal diameter of 8 mm with axial length 164 mm (figure 1, on the left), the tube used at cryogenic temperature has internal diameter of 7 mm with axial length 164 mm (TBC). The dimensions of the tubes has been optimized for the different fluids to enhance the response to an impulsive acceleration **?**. The setup is divided into two sides A and in the figure 1 connected in a closed-loop by pipes. A fast response valve controls the connection between these sections (BUSCHJOST® Solenoid Valve B43-10 and TRIAD® cryogenic ball valve series 60C respectively for ambient temperature and cryogenic experiment) . Pressure transducers are placed at the entrance of the tube. In the case of experiments at laboratory temperature these were two differential piezo-resistive measuring cells AMS 5812 (ANALOG MICROELECTRONICS®) placed in the left and right side of the tube. In the case of the cryogenic experiment, differential KULITE® transducer was inserted inside the the cryogenic sample space to measure the pressure difference between each side. Complementary, a second KULITE® transducer was inserted externally of the cryostat to measure absolute pressure in side A, while AMS 5812 was placed specularly on side B to measure analogously the absolute pressure of the line. In the case of cryogenic experiment additional LAKESHOREKULITE® silicon diodes DT670B-SD temperature sensors have been placed at the entrance of the Utube (one for each side) to further asses the thermodynamic conditions of the interface. Side A is connected to an input pressure line, while side B is connected to a discharge pressure line. The first experimental campaign concerned only HFE7200 fluid, the tube was kept as-factory-provided protected from external environment until the test, the internal surface of the tube was rinsed with isopropanol solution and let dry before closing all the connections with the laboratory environment. After the tests with HFE7200, the same tube was emptied, dried and prepared for the test with Water using the same procedure . Second experimental campaign concerned only liquid Nitrogen. In this case the tube was prepared analogously to the previous case before being connected to cryostat sample space, afterwords, the tube was never removed for all the duration of the experimental campaign.

Both ambient and cryogenic experiment follow the same test procedure. Initially, the u-tube is filled with the test liquid while the fast response valve is open, connecting the two sides and the two interfaces of the liquid column have the same height. The initial conditions of the experiment are defined by closing the fast response valve and increasing the pressure on side A. This sets the initial level difference between the two interfaces and zero velocity of the interface.

The experiment starts by opening the fast-response valve, and the two liquid interfaces start oscillating around the equilibrium position. The motion of one of the two interfaces is recorded with a high-speed camera SP-12000-CXP4 (STEMMER IMAGING),

acquiring grey-scale images at 300 fps. The interface shape is visualized by a diffused light source on the opposite side of the tube. The active region of the camera is restricted to the central region of 4096x512 pixels in order to achieve the highest acquisition frequency allowed by the camera. The camera mounts a Nikon micro-Nikkor 105mm lens and is positioned to acquire the full motion of the interface while spanning the full tube width, as shown in figure 1 right side.

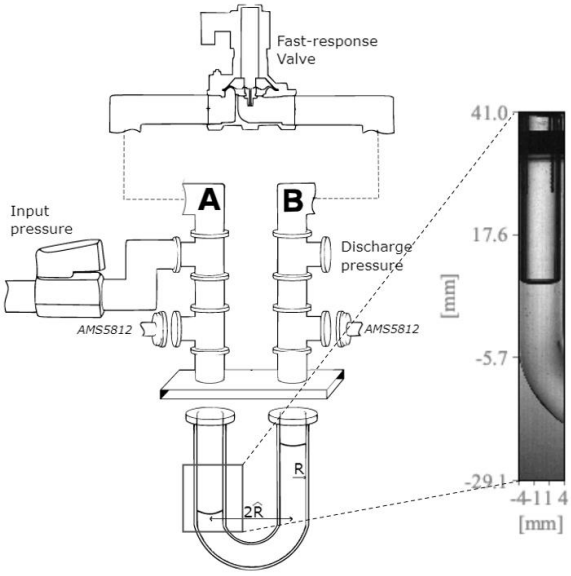

Figure 1: Left: schematic diagram of experimental setup at laboratory conditions. At initial conditions, side A is pressurized and side B is at room pressure, a fast response valve allows for suddenly releasing the pressure difference to begin the dynamic experiment. Right: example of complete image acquired.

2.1. Image analysis

The image processing for the interface detection consists of four main steps, recalled in figure 2. In the first step, the original image (image 2a) is filtered via global noise removal based on n-local means denoising algorithm Buades et al. [2011], followed by a first image recontrasting (image 2b). The second and third steps process each column of the image separately. The gray scale profiles are first filtered using a Savitzky–Golay filter Savitzky and Golay [1964] and the resulting image re-contrasted using directional gray-scale averaging Mendez et al. [2016]. This allows for increasing the gray level intensity in the region of the liquid interface close to the tube walls, which appear darker and slightly blurred compared to the center of the channel.

Preliminary gradient based detection is performed to isolate the region of the interface from the rest of the image (see image 2c) and classic Canny-edge algorithm Canny [1986] is used to accurately determine the shape of the interface at the location of interest (image 2d). The interface is preliminary located with one pixel width and outliers are eliminated based on their distance from the expected interface through successive regression with the curve proposed in the next section (image 2e). Approximately 95% of the possible interface data points are determined in 1.5 second per image (Intel® Core™ i7-4790 CPU @4GHz processor, 32GB of Ram); the remaining pixels do not play a role in the definition of the interface. The final result is shown in figure 2f.

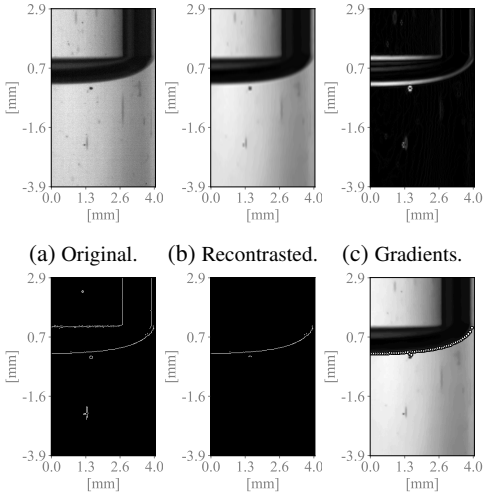

(a) Original. (b) Recontrasted. (c) Gradients.

(d) Edges. (e) Interface. (f) Result.

Figure 2: Sequence of image processing steps implemented to identify the liquid interface

2.2. Optical correction

The circular shape of the tube deforms the image of the meniscus in the radial direction. Consequently, the meniscus generally appears larger than its actual size and the contact point with the solid surface seemingly lies in the region between the inner and outer side of the tube as shown by the red points in figure 4. The non-linear distortion is maximum at the contact point of the meniscus and disappears at the center

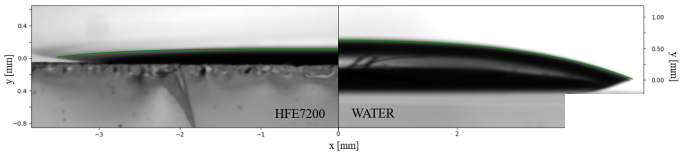

Figure 3: Side view of HFE7200 droplet (left) and water droplet (right) for static contact angle quantification. x =0 coincides with the apex of the droplet while y = 0 corresponds to the positioning of the contact point within the image. The y-axis has a different scale on the left and right side.

of the channel. The distortion can be corrected using analytical relations Darzi and Park [2017] knowing the distance of the camera from the center of the tube and the index of refraction of the materials involved. We validate the procedure by comparing the corrected profiles with the theoretical profile in static conditions at ambient temperature (see eq. 3, section 3.1) as used by Petrov and Sedev [1993]. In static conditions the interface shape is determined by the static contact angle θ_S and the capillary length $l_c = \sqrt{\sigma/\rho g}$. Through regression of the static profiles with the experimental data of static meniscus (see figure 5) we obtain $l_c = 0.98 \pm 0.01\ mm$ and $\theta_s = 8.57° \pm 1.48°$ for HFE7200 and $l_c = 2.72 \pm 0.1\ mm$ and $\theta_s = 22.4° \pm 1.6°$ for distilled water. The capillary length corresponds to the values computed using the fluid properties at the laboratory temperature (25°) respectively being 0.98 mm for HFE7200 and 2.71 mm for distilled water. The static contact angle is compared with side view visualizations of HFE7200 and water droplets (see figure 3) deposited on a flat substrate made of the same quartz material. The sessile droplet measurement yelds $\theta_s = 7.1° \pm 2°$ for HFE7200 and $\theta_s = 20.33° \pm 1°$ for distilled water. We consider the correction procedure valid also for the cryogenic experiment where the capillary length of the fluid oscillates between $AA - BB$, in agreement with the theoretical computation which in the range $74 - 80K$ is comprised between $AA1 - BB1\ mm$. The contact angle values agree within the uncertainty of the measurement and we concluded that the optical correction allows to retrieve the typical parameters of the fluid. The correction is furthermore ensured by the position of the last point of the corrected meniscus (white circles in figure 4) which now lies inside the tube and in the close vicinity of the expected inner surface (vertical white lines in figure 4).

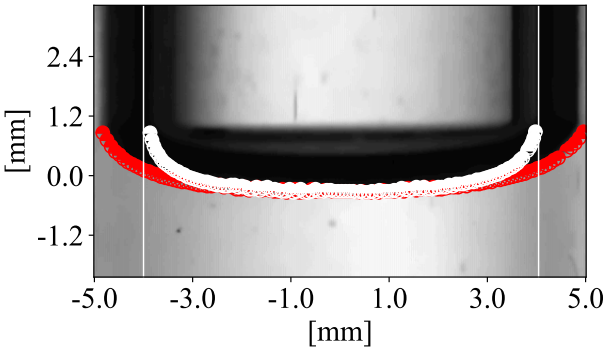

Figure 4: Example image of HFE7200 interface without correction (red circles) and post-correction (white circles). The vertical lines corresponds to the real inner surface of the tube.

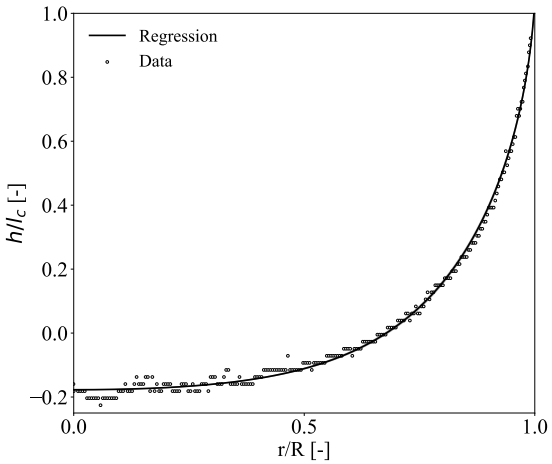

Figure 5: Corrected HFE7200 interface profiles and regression with static interface with $l_c = 0.99mm$ and $\theta_S = 8.6$.

3. Contact angle quantification

In this work, all liquids are expected to wet the inner surface of the quartz tube. Especially, we expect to observe contact angles close to 0° with HFE7200 and LN2. Multiple authors showed that simple Tangent-Line methods (TLM) generally overestimate the contact angle Petrov and Sedev [1993]; Maleki et al. [2007]; Iliev and Pesheva [2011] due to the uncertainty in locating the interface points close to the solid surface, particularly important for the low contact angles investigated in this work. Hence, we aim to improve the accuracy of the measurement by using more points of the interface and the impact that the contact angle has on the shape of the free surface, this technique corresponds to a Meniscus-Profile Method (MPM). We parametrize the interface shape as a function of the contact angle and perform the regression with the experimental interface profiles. The contact angle that allows to optimize the regression correponds to the physical contact angle. The accuracy of the method is guaranteed if the parametrization of the interface represents the actual conditions faced by the interface (e.g. steady or unsteady motion). In the next subsection 3.1, we review two interface parametrizations used by other authors Petrov and Sedev [1993]; Maleki et al. [2007]; Iliev and Pesheva [2011]; Snoeijer and Andreotti [2013] and then in 3.2 we propose a corrective term to account for the impact of inertia on the interface shape.

3.1. Inertial-less modeling

The shape of an axial symmetric interface is here modelled by considering the force balance on a volume element enclosing the interface Landau and Lifshitz [1959].

In static conditions, surface forces and gravity govern the shape of the interface:

$$\sigma \nabla \cdot \mathbf{n} - \rho g h = 0 \tag{1}$$

where the curvature of the interface ($\nabla \cdot n$) in the case of an axial-symmetric meniscus reads as following:

$$\mathbf{n} = \frac{\mathbf{z} - h_r \mathbf{r}}{1 + h_r^2} \qquad \nabla \cdot \mathbf{n} = \frac{-r h_r - r^2 h_{rr}}{r^2 (1 + h_r^2)^{3/2}} \,. \tag{2}$$

To solve Eq. 1 we use Neumann type boundary conditions for half of the interface shape, Dirichlet boundary condition were given instead by other authors Petrov and Sedev [1993] by using the experimental meniscus height at selected locations.

$$\begin{cases} \nabla \cdot \mathbf{n} - l_c^{-2} h = 0 \\ h_r(R, t) = \mathrm{ctg}(\theta(t)) \\ h_r(0, t) = 0 \end{cases} , \tag{3}$$

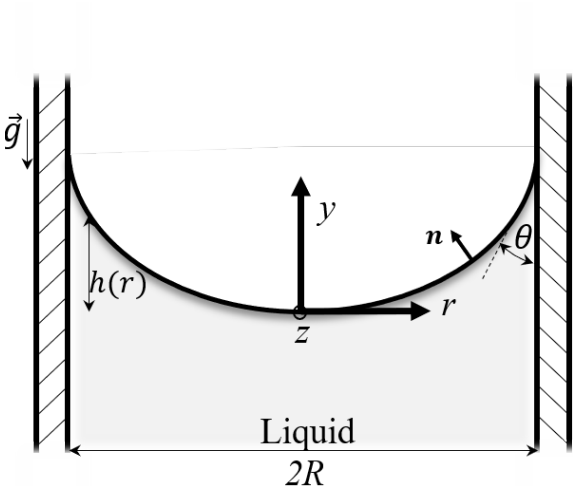

Figure 6: Schematics of the interface model. The origin is located at the interface, in the center of the channel, and moves with it, i.e. h(0,t) = 0 for all times.

with t the time corresponding to specific frame. The system of equations 3 provides a good approximation of the interface shape also for small contact line velocities and hence the model is often called quasi-static Petrov and Sedev [1993]. At low velocities the viscous bending of the interface near the contact line is not visible at the experiment scale and the contact angle is called "apparent" Snoeijer and Andreotti [2013]. The system has a singular point at the center of the channel due to the expression of the curvature in Eq. 2, this does not pose any problem due to the symmetry of the channel. When the capillary number is not negligible, the viscous forces inside the meniscus need to be included in the balance Maleki et al. [2007]; Iliev and Pesheva [2011]. In case of steadily moving contact line with velocity U_{cl} the viscous pressure is generally modeled with the Voinov approximation Voinov [1976]:

$$\Delta p_v = 3 \frac{\mu U_{cl}}{(R - r)} F(\theta) \,, \tag{4}$$

Where $F(\theta)$ is a correction factor Delon et al. [2008] for small angles and can be expressed as $sin(\theta(r))/(\theta(r)^2)$. In case of receding contact line, Voinov's approximation holds until a critical receding capillary number value Voinov [2000]; Eggers [2005a] Ca_c, above which the contact line vanishes and it is impossible to define a contact angle. Considering Eq. 4, the system of equations 4 can be corrected

as follows:

$$\begin{cases} \nabla \cdot \mathbf{n} + l_c^{-2}\, h - 3\frac{Ca}{(R-r)} F(\theta) = 0 \\ h_r(R,t) = \mathrm{ctg}(\theta(R,t)) \\ h_r(0,t) = 0 \end{cases} . \tag{5}$$

This expression is valid for quasi-steady motion of the contact line, where the receding capillary number is above Ca_c and the flow field in the meniscus is dominated by pressure and viscous forces (lubrification approximation). The first Eq. 5 has an additional singular point located at the channel wall due to Voinov's description of the contact line. While the first singularity does not pose any problem due to the symmetry of the channel, the second one limits the validity of Voinov description at a distance l_d from the wall. The exact value of l_d is under debate, however most of the authors Voinov [1976]; Delon et al. [2008]; Maleki et al. [2007] place it in the range $10^{-5} - 10^{-6}$ mm. In the result section **??**, we will refer to the system 3 as gravity-based model and to system 5 as viscous-gravity model.

3.2. Correction for inertia effects

Even if the lubrification approximation remains valid in the vicinity of the contact line for a large range of conditions, at some distances from the solid surface, the inertia of the flow starts to impact significantly the shape of the meniscus. Given the difficulty to estimate a priori the impact of the flow inertia on the meniscus shape, in this work, we assume that its effect can be accounted for with an additional over-pressure term:

$$H_a(r,t) = \rho a_i(Rc_t)\left(1 - e^{-\frac{r-R}{l_i}}\right). \tag{6}$$

The amplitude of the pressure wave corresponds to the product of $a_i(t)$ which is the acceleration of the interface as a function of time t with the characteristic length $c_t R$ which is defined by the free parameter c_t. The shape of the pressure wave is defined by the term under brackets and is designed to be zero near the walls and to saturate in the center of the channel. Among these two extremes, the shape function is characterised by a parameter l_i, describing a sharp or a smooth gradient. The behaviour of the pressure term retrieved by the experiment will be shown in section 4.1. For small interface accelerations, H_a is negligible and the quasi-steady form of the equation is retrieved. Summarizing, the inertia-corrected model has the form:

$$\begin{cases} \nabla \cdot \mathbf{n} - l_c^{-2}\, h - 3\frac{Ca}{(R-r)} F(\theta) + H_a = 0 \\ h_r(R,t) = \mathrm{ctg}(\theta(R,t)) \\ h_r(0,t) = 0 \end{cases} . \tag{7}$$

3.3. Interface regression

An optimization routine is used to solve the regression of the interface shape with the different interface models. The regression aims at finding the best parameters which allow representing the experimental interface shape and hence indirectly retrieving the contact angle of the interface. The inverse problem can be written as nonlinear least square minimization problem, where a function $f(x|\mathbf{w})$, parametrized by the weight vector $\mathbf{w}$, must be fitted to a data-set $\{(x_i, y_i)\}$ with $j \in [1, n_p]$ and n_p the number of points obtained from the image processing algorithm. The weights are thus computed from the minimization of the root-mean-square of the l_2 norm of the Frechét distance vector $(d_\epsilon(x_j, y_j, f(x_j, \mathbf{w}))$with $j \in [1, n_p]$, between data and model prediction:

$$\mathbf{w}\mathrm{argmin}\, J(\mathbf{w}) = \sum_{j=1}^{n_p} \Big(d_\epsilon(x_j, y_j, f(x_j, \mathbf{w}) \Big)^2 \tag{8}$$

Where $d_\epsilon(x_j, y_j, f(x_j, \mathbf{w})$ is the smallest distance between the experimental point j and the model prediction as shown by figure 7.

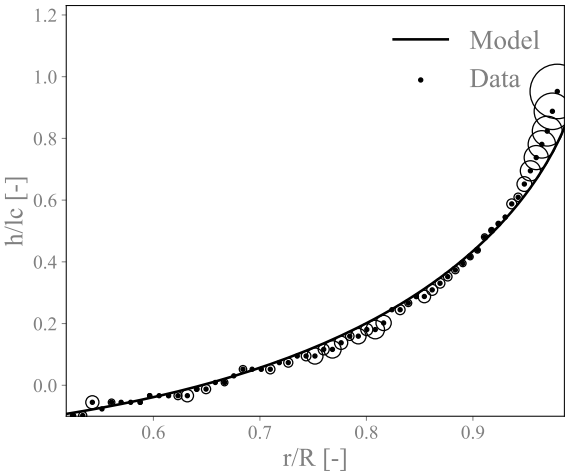

Figure 7: Visualization of the concept of Frechét distance in experimental image. The radius of each hollow circle corresponds to the Frechét distance $d_{\epsilon,j}$ of the data point (filled circle) from the model (solid line). The regression aims at minimizing the root-mean-square of the Frechét distance vector $(d_\epsilon(x_j, y_j, f(x_j, \mathbf{w}))$.

In this work, the optimization was carried out using the Nelder-Mead algorithm Nelder and Mead [1965], implemented in Python library scipy.optimize Virtanen et al. [2020]. Uncertainties are computed by

means of bootstrapping techniques Efron and Tibshirani [1994]. In the interface curve fitting problem, $\mathbf{w} := \theta$ for the gravity based model (Eq. 3) and the viscous gravity model (Eq. 5) and $\mathbf{w} := \theta, c_t, l_i$ for the inertia corrected model (Eq. 7). $(x_i, y_i) := (r_i, h_i)$, and $f(x_i|\mathbf{w}) := h(r_i, \mathbf{w})$ for every image. For each model, we used scipy.integrate Virtanen et al. [2020] implementation for the numerical solution of the boundary value problem by means of collocation algorithm and damped Newton method Ascher et al. [1995]. In the identification of contact angle by means of regression it is worth stressing the importance of choosing the right optimization space for the vector of the weights $\mathbf{w} := \theta, c_t, l_i$ and normalizing all of them within the range $[0, 1]$. Moreover, using the Frechét distance instead of other metrics avoids penalizing curves shapes that approach the wall tangent.

3.4. Validation of the image analysis method

We perform a numerical analysis of the MPM accuracy by generating synthetic images of the interface shape using the inertia-corrected model (Eq. 7). We prescribe a range of possible combinations for the main parameters of the interface, namely Ca, θ, c_t, l_i. For each parameter the minimum and the maximum value are assigned to respect similar conditions as observed within the experiments. We sample 30 random points from each of the vectors of interface parameters and we generate synthetic interfaces $h^*(r_i, Ca, \mathbf{w})$ with r_i located in the range $[-(R-l_m), (R-l_m)]$, where l_m is the smallest distance from the solid surface at which it is still possible to observe the interface. Random noise with standard deviation of $10\mu m$ is superimposed to the synthetic images to simulate an experimental acquisition. We hypothesized three experimental conditions with three different values of $l_m = (1\mu m,\ 10\mu m, 30\ \mu m)$. During the real experiments l_m spaces the interval $[1,\ 3]\ \mu m$ depending on the quality of the edge detection for different interface configurations. The confidence range is calculated by means of bootstrapping technique Efron and Tibshirani [1994] using randomly sampled synthetic interface points for the contact angle measurements and repeating for n = 500 times using different sets of random interface points. Figure 8 compares the imposed contact angle (x-axis) values against the value retrieved by the the contact angle detection algorithm (y-axis). We compare the value retrieved by the MPM with the value obtained by computing the slope of the interface at the nearest point to the solid surface (Tangent Line Method, TLM).

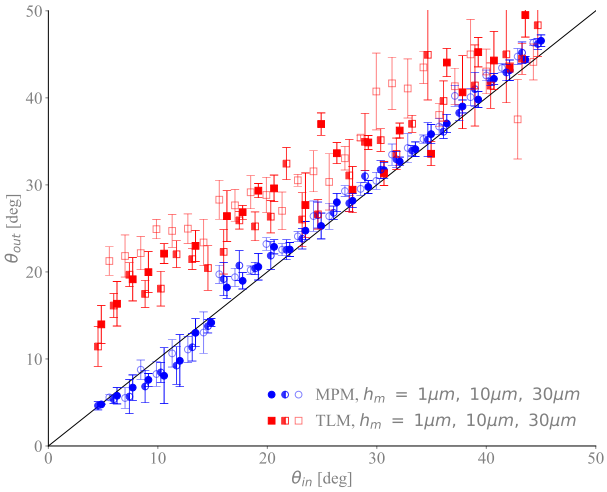

Figure 8: Accuracy comparison between two different methods, MPM (circles) and TLM (squares), for contact angle quantification on synthetic images by using different degree of vicinity to the contact line: $l_m = 1\mu m$ (full symbols), $l_m = 10\mu m$ (left-filled symbols) and $l_m = 30\mu m$ (empty symbols).

Figure 8 shows that TLM generally overestimates the value of the interface contact angle up to value of 30°. Moreover, TLM data show a less clear trend respect to MPM due to the higher sensitivity to the interface conditions far from the solid surface, here randomly generated. Similar behaviour was observed also by Maleki et al. [2007]. On the other hand, the MPM improves greatly the accuracy of the contact angle quantification in the full range of the experimental values, however the ability to correctly identify contact angles below $\approx 10°$ degrees strongly depends on the accurate detection of interface points close to the solid surface. For a coarse resolution of the region near the contact line ($l_m = 10\mu m, 30\mu m$), small contact angles are hardly detectable even by MPM method and the quantification suffers from the bias induced by the inertial conditions of the interface (given by the randomly assigned c_t, l_i) and the capillary number. For the highest resolution ($l_m = 1\mu m$) the difference between the imposed and the retrieved contact angle becomes smaller. It is important to remark that this analysis considered randomly assigned interface parameters, however, in the experiment the interface parameters are not completely independent and the interface model is less prone to encounter challenging contradictory conditions (e.g. small contact angle with large advancing capillary number).

4. Results

This work focuses on the measurement of the dynamic contact angle of a interface unsteadily moving inside a U-tube channel. The average position of the interface oscillates within a range of $\approx 18\ mm$ of axial distance within the tube. The length of the fluid column controls the frequency of the oscillations, which for the experiments presented here is approximately $2\ Hz$ both for HFE7200 , distilled Water and liquid Nitrogen, as shown by the normalized comparison of Figure 17. The two experiments of HFE7200 and LN2 show slightly different behaviours compared with Water: in the former case the motion of the interface is smooth and the damping is low, while for the case of water the damping is higher and the contact line frequently pins to the solid surface during the advancing phase, this is also visible in Figure 17 between $\approx 0.3 sand \approx 0.4$. During the experiment the interface shape deforms and experiences a wide range of shapes especially during the first few seconds as illustrated by the figure 14. For all the cases inertia plays a large role on the interface deformation until close distances to the contact line during the first $\approx$ 0.5 of experiment. For this reason, the experimental quantification of the dynamic contact angle is performed by means of the inverse method (MPM) with inertia correction described in section 3.2. In the following section we will analyse the performance of the MPM using different interface models and in section **??** we will discuss the contact angle results and compare with the classic behaviour expected.

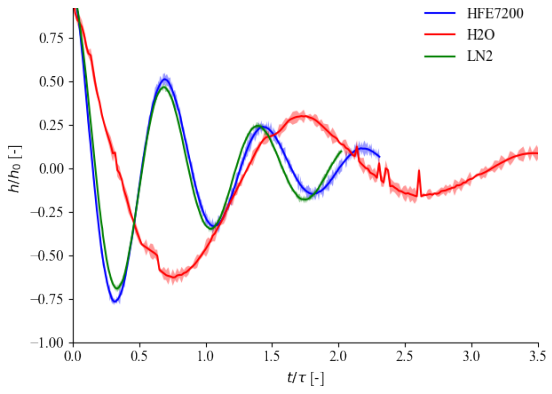

Figure 9: Evolution of the mean interface height (side B))

4.1. Comparison of experimental interfaces with Meniscus Profile Models

The MPM described in section 3.3 requires a model for the interface shape parametrized with the contact angle. We compare three models of increasing complexity: the gravity-based model (Eq. 3), the viscous-gravity model (Eq. 5) and the inertia-corrected model (Eq. 7). Figure 10 and Figure 11 compare the behavior of the three models in one typical experiment in terms of l_2 norm difference between the model prediction and the respective experimental interface profiles. Single point contact angle values where the l_2 norm is superior to the threshold $l_t = 1.5\ mm$ are excluded from the further analysis since the interface shape is considered not well represented by the model. The three models are also compared with the experimental Weber number, computed as $We = \rho v_i^2 (2R)/\sigma$, as a measure of the relative importance of fluid inertia compared with its surface tension.

The inertia-corrected model has the lowest error among the three models during the full duration of the experiment. When the acceleration of the interface decreases, also the gravity-based model and the viscous-gravity model have similar level of agreement with the data. On the other hand, during the inertia dominated regime, these two models disagree significantly with the experiments. Figure 10 shows that the gravity-based model and the viscous gravity model are significantly affected by the oscillations of the interface acceleration. This behavior suggests that even in case of low l_2 error, the results of the MPM based on these models may be biased by the phenomena occurring at the center of the channel. Figure 11 shows that the regression of the three interface models to the experimental data with water behaves similarly to the experiment with HFE in terms of relative magnitude between the three models. We extract three representative conditions from the experiment, namely conditions A-B-C (see Figure 10) corresponding to different interface velocity and acceleration levels, for HFE7200 these corresponds to $A = [0.11\frac{m}{s}; -3.8\frac{m}{s^2}]$, $B = [-0.13\frac{m}{s}; 1.24\frac{m}{s^2}]$, $C = [0.08\frac{m}{s}; -0.34\frac{m}{s^2}]$. Figure 12, 13 and 14 show the comparison with the singular interfaces for the these 3 conditions with the different MPM models. The gravity-based model (Figure 12) and the viscous-gravity model (Figure 13) are unable to give a satisfactory description of the interface shape in the case of interfaces deeply affected by the inertia of the flow (case A). For low accelerations of the interface, we observe that despite similar levels of regression error, the gravity-based model overestimate the slope of the meniscus at the contact point, hence we

can expect higher contact angles respect to the other methods also for low acceleration levels. For Weber numbers below 5 (case B and C) the viscous-gravity model gives similar prediction to the inertia-corrected model hence justifying its application in the case of a quasi-steady assumption.

Figure 15 compares the behaviour of the pressure term introduced by the inertia corrected model with the other terms in the force balance at the interface. In the first instants this term has a large impact on the shape of the interface at the center of the channel. When the acceleration of the interface reduces, also the amplitude of this term decreases. The surface tension term is deeply affected by the amplitude of the inertia term, this is expected since this term is proportional to the curvature of the interface, which in the center of the channel is controlled mainly by the inertia of the flow.

Figure 18 shows the same comparison of Figure 14 (HFE7200) for the case of water. The gradient of the interface shape across the channel is less steep and the range of contact angles is significantly larger than in the case of HFE7200. Despite the similar levels of acceleration, the range of Weber number spaced during the experiment with Water is significantly lower than the case of HFE7200 due to the lower density and higher surface tension. The interface predicted by the inertia-corrected model represents closely the experimental data during the full duration of the experiment, hence validating the same inertia correct model also for the case of interface with higher contact angle. Moreover, similar considerations to the case of HFE7200 can be done regarding the interface predicted by the viscous-gravity and the gravity based model, these comparison are included in the supportive in formations.

Appendix

An appendix, if needed, should appear before the acknowledgments. Avoid section numbering.

Acknowledgments

D. Fiorini is supported by Fonds Wetenschappelijk Onderzoek (FWO), Project number 1S96120N. This work was supported by the ESA Contract No. 4000129315/19/NL/MG. The authors thanks Mathieu Delsipee for its support and contribution in the preparation of the experimental set up and Alessia Simonini for the technical support and the partecipation to the cryogenic experimental campaign.

References

Uri M Ascher, Robert MM Mattheij, and Robert D Russell. *Numerical solution of boundary value problems for ordinary differential equations*. SIAM, 1995.

Kishan Bellur, Vinaykumar Konduru, Manan Kulshrestha, Daanish Tyrewala, Ezequiel Medici, Jeffrey S Allen, Chang Kyoung Choi, Daniel S Hussey, David C Jacobson, Juscelino B Leão, et al. Contact angle measurement of liquid hydrogen (lh2) in stainless steel and aluminum cells. *Journal of Heat Transfer*, 138(2), 2016.

Xiaoqiang Bian, William W Schultz, and Marc Perlin. Liquid slug motion and contact lines in an oscillatory capillary tube. *Journal of Fluid Dynamics (under revision), http://wwwpersonal. umich. edu/schultz/Manuscripts/BianSchultzPerlin. pdf*, 146:151, 2003.

TD Blake and JM Haynes. Kinetics of liquidliquid displacement. *Journal of colloid and interface science*, 30(3):421–423, 1969.

M Bracke, F De Voeght, and P Joos. The kinetics of wetting: the dynamic contact angle. In *Trends in Colloid and Interface Science III*, pages 142–149. Springer, 1989.

Antoni Buades, Bartomeu Coll, and Jean-Michel Morel. Non-local means denoising. *Image Processing On Line*, 1:208–212, 2011.

John Canny. A computational approach to edge detection. *IEEE Transactions on pattern analysis and machine intelligence*, (6): 679–698, 1986.

RG Cox. The dynamics of the spreading of liquids on a solid surface. part 1. viscous flow. *Journal of Fluid Mechanics*, 168: 169–194, 1986.

Milad Darzi and Chanwoo Park. Optical distortion correction of a liquid-gas interface and contact angle in cylindrical tubes. *Physics of Fluids*, 29(5):052004, 2017.

PG De Gennes, X Hua, and P Levinson. Dynamics of wetting: local contact angles. *Journal of fluid mechanics*, 212:55–63, 1990.

Giles Delon, Marc Fermigier, Jacco H Snoeijer, and Bruno Andreotti. Relaxation of a dewetting contact line. part 2. experiments. *Journal of Fluid Mechanics*, 604:55–75, 2008.

Bradley Efron and Robert J Tibshirani. *An introduction to the bootstrap*. CRC press, 1994.

Jens Eggers. Contact line motion for partially wetting fluids. *Physical review E*, 72(6):061605, 2005a.

Jens Eggers. Existence of receding and advancing contact lines. *Physics of Fluids*, 17(8):082106, 2005b.

Richard L Hoffman. A study of the advancing interface. i. interface shape in liquid—gas systems. *Journal of colloid and interface science*, 50(2):228–241, 1975.

Stanimir D Iliev and Nina C Pesheva. Dynamic meniscus profile method for determination of the dynamic contact angle in the wilhelmy geometry. *Colloids and Surfaces A: Physicochemical and Engineering Aspects*, 385(1-3):144–151, 2011.

Tsung-Shann Jiang, OH Soo-Gun, and John C Slattery. Correlation for dynamic contact angle. *Journal of Colloid and Interface Science*, 69(1):74–77, 1979.

STEPHAN F Kistler. Hydrodynamics of wetting. *Wettability*, 6: 311–430, 1993.

Munish Kumar and Andrew Fogden. Patterned wettability of oil and water in porous media. *Langmuir*, 26(6):4036–4047, 2010.

LD Landau and EM Lifshitz. Fluid mechanics pergamon. *New York*, 61, 1959.

Ji-Cheng Li, Hai Lin, Kai Li, Jian-Fu Zhao, and Wen-Rui Hu. Dynamic behavior in a storage tank in reduced gravity using dynamic contact angle method. *Microgravity Science and Technology*, 32(6):1039–1048, 2020.

Yafei Liu, Andrew Hansen, Erica Block, Norman R Morrow, Jeff Squier, and John Oakey. Two-phase displacements in mi-

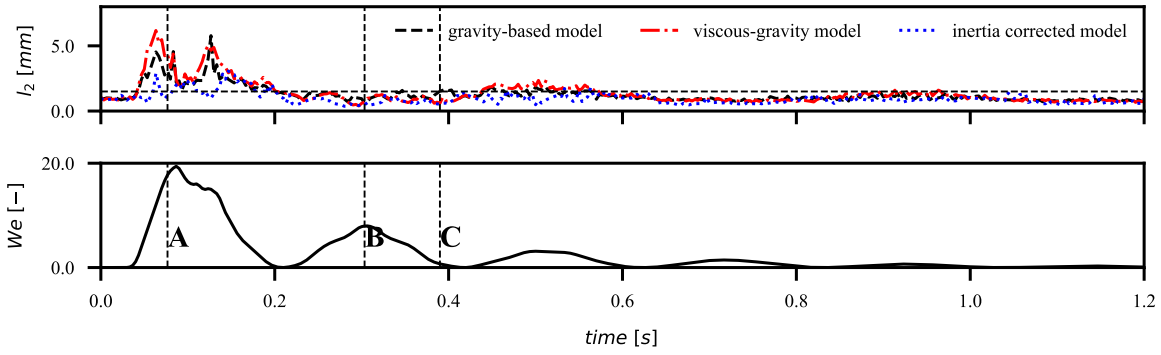

Figure 10: From top to bottom: regression error during the first second of experiment with HFE7200. (top) Comparison between the 3 interface models showing that they have largely different behaviors during the inertia dominated phase. (Bottom) Weber number of the interface. A: Strong inertia dominated conditions, B: Weber number ≈ 5, B: Weber number < 1.

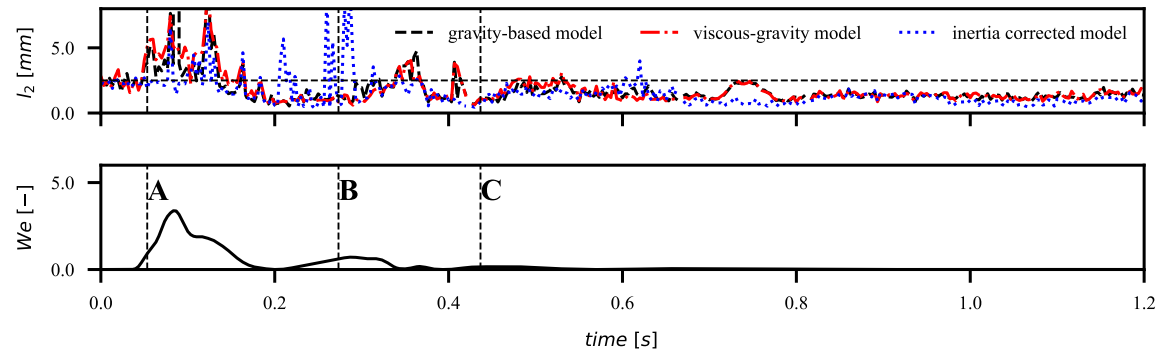

Figure 11: From top to bottom: regression error during the first second of experiment with distilled Water. (top) Three interface models are compared, the three models have largely different performances during the initial highly inertial phase. (Bottom) Acceleration of the interface.

crochannels of triangular cross-section. *Journal of colloid and interface science*, 507:234–241, 2017.

Kun Ma, Rachel Liontas, Charles A Conn, George J Hirasaki, and Sibani Lisa Biswal. Visualization of improved sweep with foam in heterogeneous porous media using microfluidics. *Soft Matter*, 8(41):10669–10675, 2012.

Maniya Maleki, Etienne Reyssat, David Quéré, and Ramin Golestanian. On the landau- levich transition. *Langmuir*, 23(20):10116–10122, 2007.

MA Mendez, L Németh, and Jean-Marie Buchlin. Measurement of liquid film thickness via light absorption and laser tomography. In *EPJ Web of Conferences*, volume 114, page 02072. EDP Sciences, 2016.

John A Nelder and Roger Mead. A simplex method for function minimization. *The computer journal*, 7(4):308–313, 1965.

Jordan G Petrov and Rossen V Sedev. Quasi-static shape of the steady moving meniscus—comparison of the apparent and extrapolated dynamic contact angles. *Colloids and Surfaces A: Physicochemical and Engineering Aspects*, 74(2-3):233–241, 1993.

P Petrov and I Petrov. A combined molecular-hydrodynamic approach to wetting kinetics. *Langmuir*, 8(7):1762–1767, 1992.

David Quéré. Inertial capillarity. *EPL (Europhysics Letters)*, 39(5): 533, 1997.

Michael H Rausch, Lorenz Kretschmer, Stefan Will, Alfred Leipertz, and Andreas P Froba. Density, surface tension, and kinematic viscosity of hydrofluoroethers hfe-7000, hfe-7100, hfe-7200, hfe-7300, and hfe-7500. *Journal of chemical & engineering data*, 60(12):3759–3765, 2015.

Abraham Savitzky and Marcel JE Golay. Smoothing and differentiation of data by simplified least squares procedures. *Analytical chemistry*, 36(8):1627–1639, 1964.

Orest Shardt, Prashant R Waghmare, JJ Derksen, and Sushanta K Mitra. Inertial rise in short capillary tubes. *Rsc Advances*, 4(28): 14781–14785, 2014.

Yu D Shikhmurzaev. The moving contact line on a smooth solid surface. *International Journal of Multiphase Flow*, 19(4):589–610, 1993.

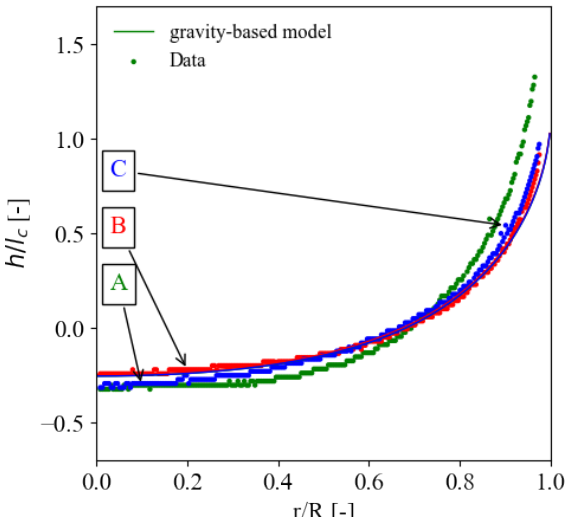

Figure 12: HFE7200. The "Gravity-based model" well describes the condition of low interface acceleration (C), on the other hand, the conditions A and B are impossible to be described by tuning solely the contact angle

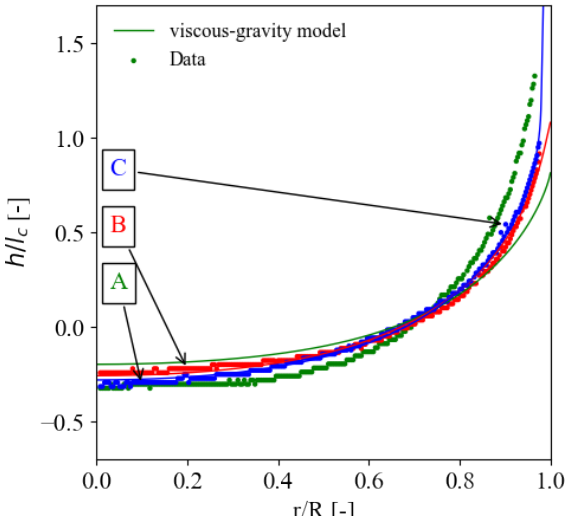

Figure 13: HFE7200. The "Viscous-gravity model" allows a more complete description of the interface, however large interface deformations (case A) are still impossible to be described.

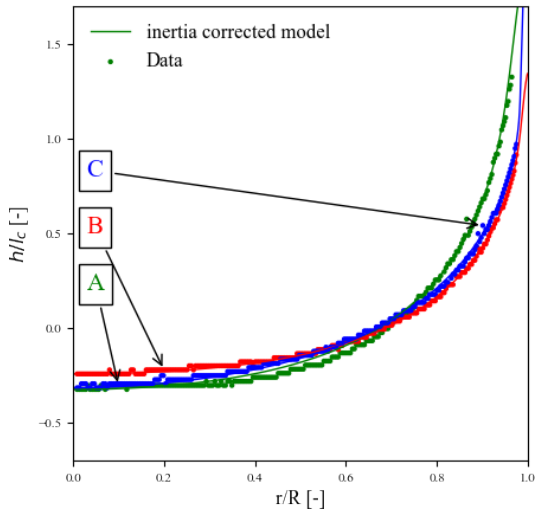

Figure 14: HFE7200. The "Inertia corrected model" allows to decouple the inertial deformation in the central part of the interface from the region close to the contact line, hence providing an overall better agreement with the interface data.

Jacco H Snoeijer and Bruno Andreotti. Moving contact lines: scales, regimes, and dynamical transitions. *Annual review of fluid mechanics*, 45:269–292, 2013.

LH Tanner. The spreading of silicone oil drops on horizontal surfaces. *Journal of Physics D: Applied Physics*, 12(9):1473, 1979.

Chao-Lung Ting and Marc Perlin. Boundary conditions in the vicinity of the contact line at a vertically oscillating upright plate: an experimental investigation. *Journal of Fluid Mechanics*, 295: 263–300, 1995. doi: 10.1017/S0022112095001960.

Tor Vestad, DWM Marr, and J Oakey. Flow control for capillary-pumped microfluidic systems. *Journal of Micromechanics and Microengineering*, 14(11):1503, 2004.

Pauli Virtanen, Ralf Gommers, Travis E. Oliphant, Matt Haberland, Tyler Reddy, David Cournapeau, Evgeni Burovski, Pearu Peterson, Warren Weckesser, Jonathan Bright, Stéfan J. van der Walt, Matthew Brett, Joshua Wilson, K. Jarrod Millman, Nikolay Mayorov, Andrew R. J. Nelson, Eric Jones, Robert Kern, Eric Larson, C J Carey, İlhan Polat, Yu Feng, Eric W. Moore, Jake VanderPlas, Denis Laxalde, Josef Perktold, Robert Cimrman, Ian Henriksen, E. A. Quintero, Charles R. Harris, Anne M. Archibald, Antônio H. Ribeiro, Fabian Pedregosa, Paul van Mulbregt, and SciPy 1.0 Contributors. SciPy 1.0: Fundamental Algorithms for Scientific Computing in Python. *Nature Methods*, 17:261–272, 2020. doi: 10.1038/s41592-019-0686-2.

O.V. Voinov. Hydrodynamics of wetting. *Fluid dynamics*, 11(5): 714–721, 1976.

O.V. Voinov. Wetting: inverse dynamic problem and equations for microscopic parameters. *Journal of colloid and interface science*, 226(1):5–15, 2000.

Nicholas C White and Sandra M Troian. Why capillary flows in slender triangular grooves are so stable against disturbances. *Physical Review Fluids*, 4(5):054003, 2019.

Geoff R Willmott, Chiara Neto, and Shaun C Hendy. An experimental study of interactions between droplets and a nonwetting microfluidic capillary. *Faraday discussions*, 146:233–245, 2010.

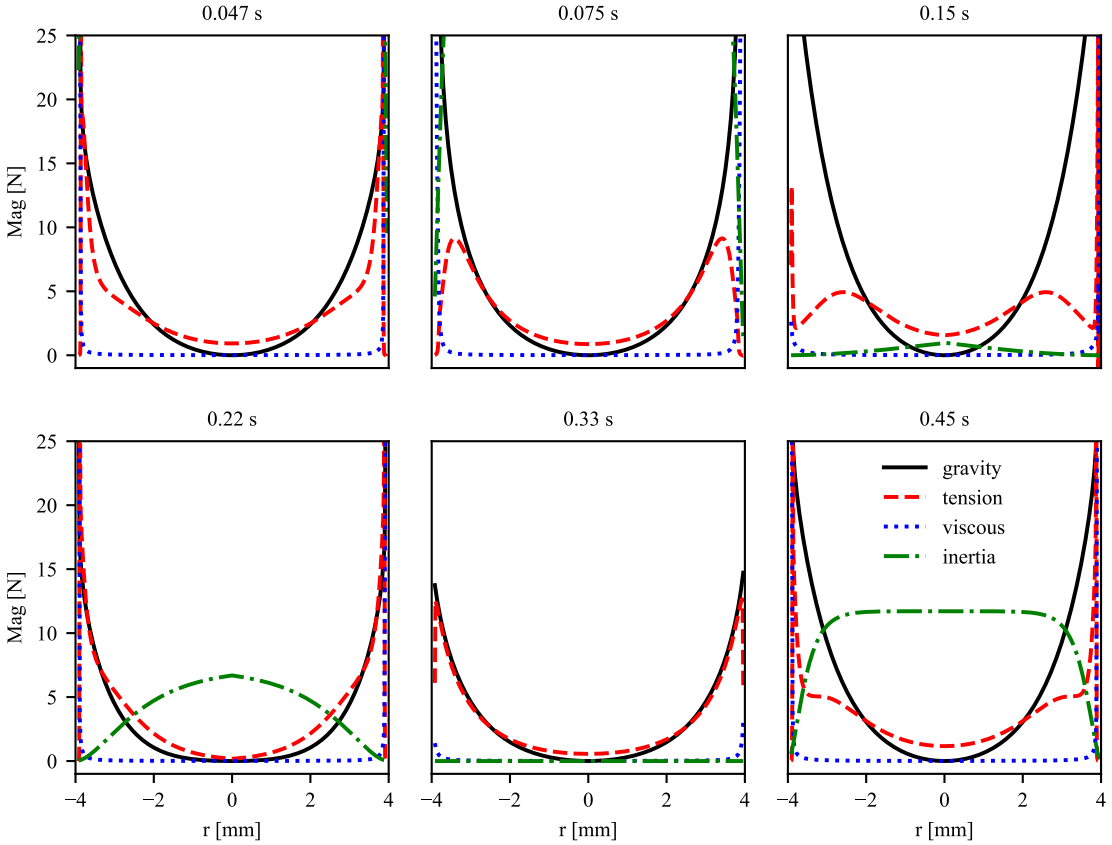

Figure 15: Profiles of the gravity, capillary, viscous, and inertia terms across the channel for different instants of the experiment.

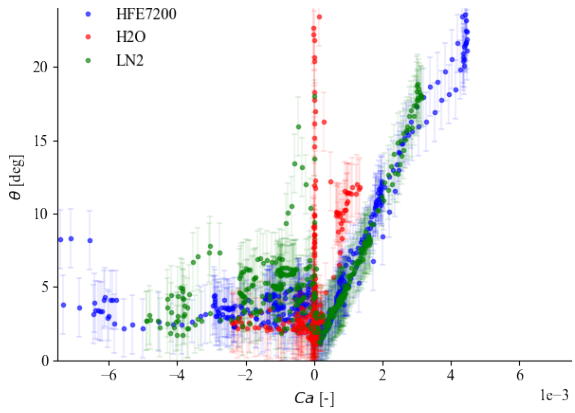

Figure 16: HFE7200. Evolution of the mean interface height (side B)

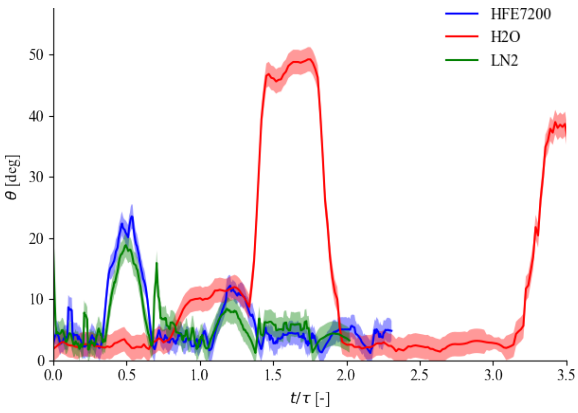

Figure 17: HFE7200. Evolution of the mean interface height (side B)

Geoff R Willmott, Chiara Neto, and Shaun C Hendy. Uptake of water droplets by non-wetting capillaries. *Soft Matter*, 7(6):2357–

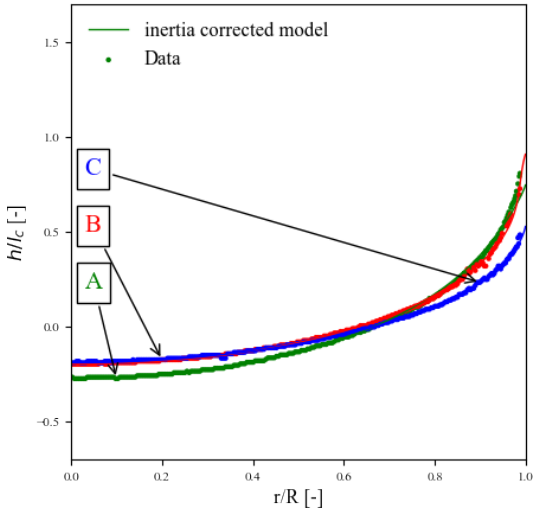

Figure 18: WATER. The ”Inertia corrected model” describes well the interface shape. the normalized height of the meniscus is significantly lower than the case of HFE7200 and the interface is closer to the ideal circular shape.

2363, 2011.

Geoff R Willmott, Alice Briole, and Florence Szczepaniak. Inertial capillary uptake of drops. *Physical Review E*, 101(4):043109, 2020.

Thermo-fluid dynamics of cryogenic liquid storage

Pedro A. Marques

Environmental and Applied Fluid Dynamics Department, von Karman Institute for Fluid Dynamics, Belgium, pedro.marques@vki.ac.be
Transferts, Interfaces et Procédés, Université Libre de Bruxelles, Belgium

Supervisor: Miguel A. Mendez

Assistant Professor, Environmental and Applied Fluid Dynamics Department, von Karman Institute for Fluid Dynamics, Belgium, miguel.alfonso.mendez@vki.ac.be

University Supervisor: Benoit Scheid

Professor, Transferts, Interfaces et Procédés, Physics Fluids, Université Libre de Bruxelles, Belgium, benoit.scheid@ulb.be

Abstract

Reducing greenhouse and pollutant emissions is one of the most severe challenges faced by humankind. Cryogenic fuels such as LNG or LH2 are promising energy sources because the first could be carbon neutral, and the second has potentially no carbon footprint. However, these fuels must be stored and transported in the liquid state to be viable, requiring cryogenic temperatures. Because no insulating system can entirely prevent heat transfer with the surroundings, evaporation in cryogenic tanks is unavoidable. This leads to pressure build-up in the tank that needs to be controlled by venting systems at the cost of significant energy and exergy losses. Furthermore, evaporation or condensation when the storage tank is subject to external acceleration and hence sloshing events causes significant, undesirable, and currently unpredictable pressure fluctuation.

This thesis aims to understand the thermo-fluid dynamics of cryogenic liquid storage by combining modelling, computational fluid dynamics, and experimental techniques in flow configurations of growing complexity. These include the study of evaporation/condensation rates in a partially filled tank in (1) quiescent and initially isothermal conditions, (2) in the presence of an initial thermal stratification, (3) under various sloshing conditions and in (4) microgravity conditions.

These configurations will first be tested at room temperature using a volatile liquid (HFE7200) and later in cryogenic conditions with liquid nitrogen (LN2). 0D and 1D models will drive the experimental and numerical campaigns' design, the post-processing, and the physical interpretation of the results. These will be complemented with 3D CFD accounting for the heat transfer between the fluids and the tank walls and evaporation rates. This work will contribute to deriving and validating modelling strategies that can help design new thermal management systems and, hence, contribute to the race towards de-carbonization.

Keywords: Sloshing, cryogenic, microgravity, boil-off, conjugate-heat-transfer, phase change, CFD

AEROACOUSTICS

Numerical investigation of noise radiated by a H-Darrieus vertical axis wind turbine in the deep stall regime

Kartik Venkatraman

Environment and Applied Fluid Dynamics department, von Karman Institute for Fluid Dynamics, Belgium
kartik.venkatraman@vki.ac.be

Supervisors: Christophe Schram and Julien Christophe

Professor, Environmental and Applied Fluid Dynamics Department, von Karman Institute for Fluid Dynamics, Belgium,
christophe.schram@vki.ac.be

research Expert, Environmental and Applied Fluid Dynamics Department, von Karman Institute for Fluid Dynamics, Belgium,
julien.christophe@vki.ac.be

University Supervisor: Stéphane Moreau

Université de Sherbrooke, Canada, stephane.moreau@usherbrooke.ca

Abstract

The noise radiated by a H-Darrieus wind turbine is investigated at low wind speeds corresponding to the deep stall regime. A three dimensional Lattice Boltzmann Very Large Eddy simulation (LBM-VLES) model is setup using the solver PowerFLOW. The sound pressure level at a given observer position is predicted using a direct propagation method. The noise prediction for both tonal and broadband components shows excellent agreement with experimental data. The flow appears as highly turbulent with the formation of a complex vortex structures shed by the blades along their trajectory. The flow features inside the rotor shed from the upwind phase of rotation and near the tip play a key role in the blade loading during the downwind phase of rotation due to blade-wake interactions, and they also cause a near-wake asymmetry.

Keywords: Darrieus wind turbine, Tip speed ratio, dynamic stall

1. Introduction

The urgent need to tackle climate change has lead to a growing interest in on-site generation, storage and distribution of electricity as a part of futuristic smart city projects. Vertical axis wind turbines (VAWTs) seem to be a promising prospect for on-site power generation on building rooftops and other areas with high wind potential [1]. The flow around VAWTs involves azimuthal variations of angle of attack, blade relative velocity over the rotation and blade-wake interactions. This gives rise to several noise generating mechanisms such as unsteady loading noise at blade passing frequencies, dynamic stall noise and blade vortex interaction noise. These mechanisms are in addition to typical noise mechanisms seen in Horizontal Axis wind turbines (HAWTs) such as trailing-edge noise, leading-edge noise and tip noise. Most of the existing numerical studies for VAWTs have opted for a 2D URANS approach [2; 3; 4]. Several 3D studies also exist, but primarily focused on the aerodynamic performance of VAWTs. Hamada [5] performed both 2D and 3D simulations of VAWT using a sliding mesh technique and found strong 3D effects such as the impact tip vortices, including the interaction with supporting structure and losses at the blade tip, which resulted in power loss. This study aims to address the research gap on numerical investigation of VAWT aeroacoustics for a complete 3D VAWT model at different tip speed ratios, which is the ratio of the blade tip speed to the incoming velocity. It is an extension of the same VAWT model in the previous study presented in Venkatraman *et. al* [6], with the objective of obtaining the noise curve of a VAWT and provide

insight into noise generation mechanisms in a full machine at different operating conditions. The paper is organized as follows: the baseline configuration used in this work is described in Section 2. The basic notions of terms related to VAWT flow physics are analyzed in Section 3. The computational fluid dynamics model is detailed in Section 4. The preliminary results are discussed in Section 5 for the first simulation performed at a tip speed ratio of 0.4, matching Weber's experimental validation database. Finally, the preliminary conclusions are drafted in Section 6.

2. Baseline VAWT Model

Weber *et al.* [7] studied the noise radiated by a 1 : 5 scale H-Darrieus VAWT shown in Fig 1. The model has 3 NACA0018 blades with a chord length of 0.05 m. The height and diameter of the rotor is 0.2 m. Microphone measurements were recorded at the anechoic facility in IPAT, Erlagen at four different azimuthal positions at 1 m distance from the model at midspan. All measurements were carried out with an inflow velocity of 21.28 m/s. The flow conditions corresponded to a chord based Reynolds number Re_c of 28,000 and a rotational speed of 800 rpm. Sound pressure level spectra are provided at a distance of 1 m for validation of the aero-acoustic model.



Figure 1: Model VAWT rotor studied by Weber *et. al* [7; 8].

3. VAWT Flow Physics

The relative velocity experienced by a VAWT blade is the vector sum of the incoming wind velocity U_o and the velocity of the advancing blade $R.\omega$ as shown in Fig 2 and is given by Eq 1. Similarly the geometric angle of attack α experienced by the blades is expressed by Eq 2. Here, both are expressed in terms of the tip speed ratio (TSR) ξ, defined as $U_o/R.\omega$, t is the time. It is the key parameter used to define the different flow regimes for VAWTs.

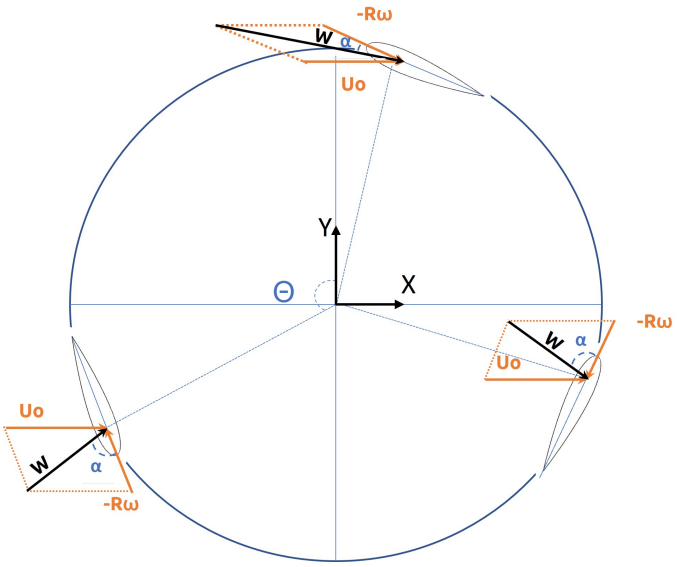

Figure 2: Velocity components for VAWT blades

$$W = |\mathbf{W}| = U_o[1 + \xi^2 - 2\xi\cos(\omega t)]^{1/2} \quad (1)$$

$$\tan(\alpha(t)) = \frac{\sin(\omega t)}{\xi - \cos(\omega t)} \quad (2)$$

At low tip-speed ratios ($\xi < 1$), the blades experience angles of attack as high as 90° and significant dynamic stall. Both the magnitude of relative velocity and the angle of attack experienced by the blades vary of the azimuthal revolution of the blades. As per convention utilized by [9] and shown in Fig 3, the rotation of a Darrieus VAWT can be classified into four different phases. The windward phase between ($315° < \theta < 45°$), upwind phase between ($45° < \theta < 135°$), leeward phase between ($135° < \theta < 225°$), and downwind phase between ($225° < \theta < 315°$). The azimuthal angle θ is defined as angle with respect to the positive y-axis.

4. Computational Fluid Dynamics Model

The Lattice-Boltzmann Method (LBM) is a finite difference solver of the Boltzmann equation on a lattice [10]. The present computations are performed via

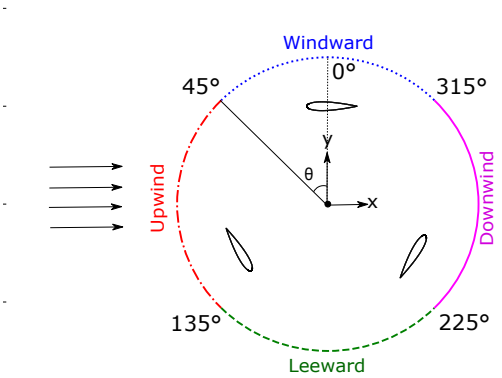

Figure 3: Different phases of VAWT for a counter-clockwise rotation.

the commercial LBM solver PowerFLOW version 6 from 3DS [11]. Fig 4 and Fig 5 show the simulation domain meant to mimic the anechoic environment at IPAT, Erlangen. Cylindrical zones are used to define different levels of grid refinement. The domain size is set to 50 D on all sides, where D is the diameter of the rotor. The domain comprises an inner rotating zone and outer stationary zone. The inner zone contains the wind turbine blades and the supporting structures and forms the body fixed local reference frame. A sliding mesh interface is imposed between the rotor and stator of the domain. The mesh has 135 million voxels, and the surface mesh comprises of 30 million surfels (surface grid elements). The domain is discretized using ten variable refinement (VR) zones. High mesh refinement is defined close to the VAWT blades and supporting structures as seen in Fig 6 zoomed close to the VAWT blade, medium level refinement in the region close to the rotating zone and microphone probes and low refinement further away as seen in Fig 7 for the entire domain. To match the experimental tip speed ratio, the rotational speed is imposed, along with the velocity at the inlet. At the outlet, the ambient static pressure is imposed (101,325 Pa). The rotational speed is set to 800 rpm, for initial validation at TSR 0.4 with the results published by Weber *et. al* [7].

5. Results

A snapshot of the iso-contours of Q-criterion coloured by velocity magnitude is shown in Fig. 8. Complex flow structures are formed around the VAWT. During the upwind phase seen for the blade on the left, the high angle of attack and flow separation results in large structures that formed close to the middle of the blade.

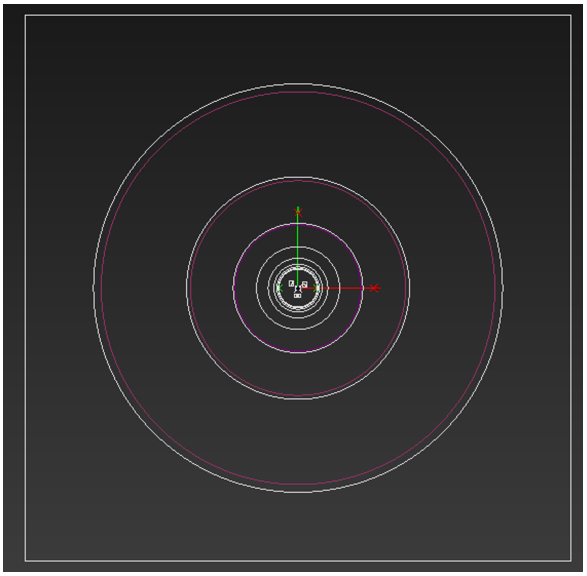

Figure 4: Simulation domain seen from top the top view showing ten cylindrical VR regions.

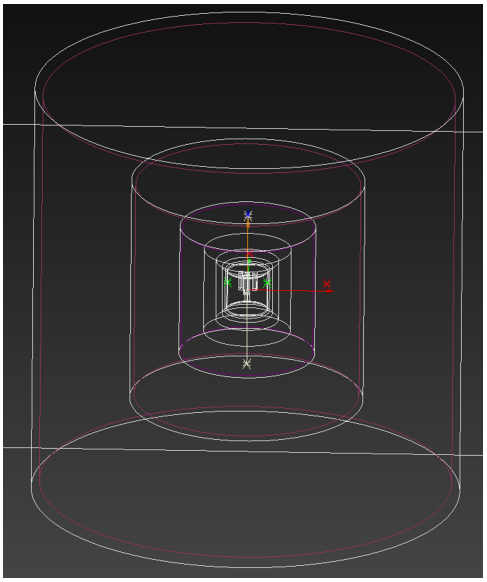

Figure 5: Simulation domain seen from the side view, showing different cylindrical VR regions.

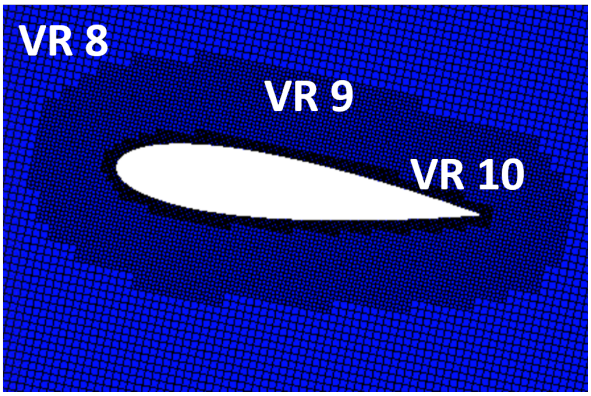

Figure 6: Mesh close to the blade surface.

Tip vortices are also seen near the blade tip and the end plate junction. These anisotropic flow structures interact with the end plate, cylindrical mast and the incoming blades in the downwind phase breaking up into smaller flow structures. This results in an asymmetric wake, with flow structures alternatively populating the windward and leeward side. The significant flow separation induced by the high angles of attack encountered by the blades leads to almost negligible power produced. The instabilities produced in this regime impact the self-starting capability of the turbine [12; 13].

The phase-locked averaged mean velocity contours at the rotor mid span are shown in Figs 9, showing the dynamic stall velocity deficit inside the rotor and near-wake. For each snapshot, the velocity field is averaged over 5 revolutions at the same azimuthal positions. Vortices are shed from both the leading edge and trailing edge. All figures are on the same velocity scale for comparison.

The phase locked averaged mean pressure contours at the rotor mid-span are shown in Figs 10. The interior of the rotor corresponds to a low pressure zone with the inner side of the blades forming the suction side.

For the sound computation, Fig 11 shows the spectra produced from the direct noise probe located 1 m away from the turbine. The cut-off frequency corresponding to the local grid size of 32 mm is around 3 kHz, considering that 3-4 points per wavelength are required to resolve acoustic waves [14]. A good agreement is seen between the numerical prediction and experimental noise spectra, with the tonal peaks captured at the blade passing frequencies and the broadband levels. The difference between simulation and experimental curves at lower frequencies below

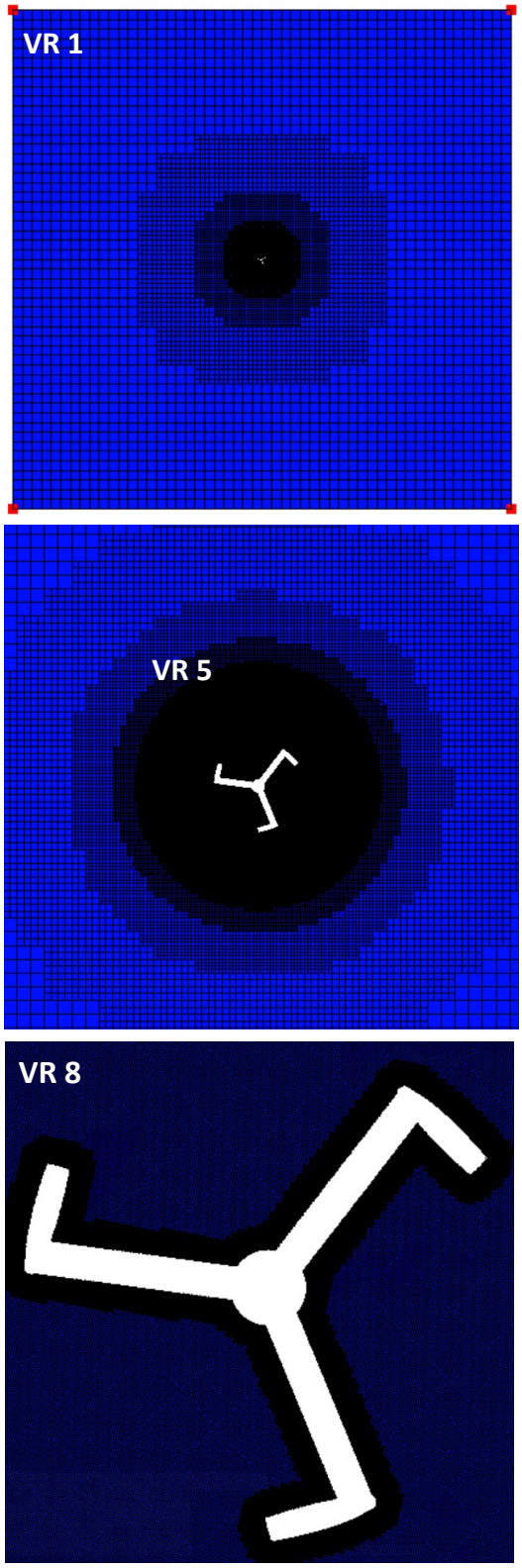

Figure 7: Octree cartesian mesh showing different refinement regions for the whole simulation domain, zoomed close to the rotating region, rotor surface.

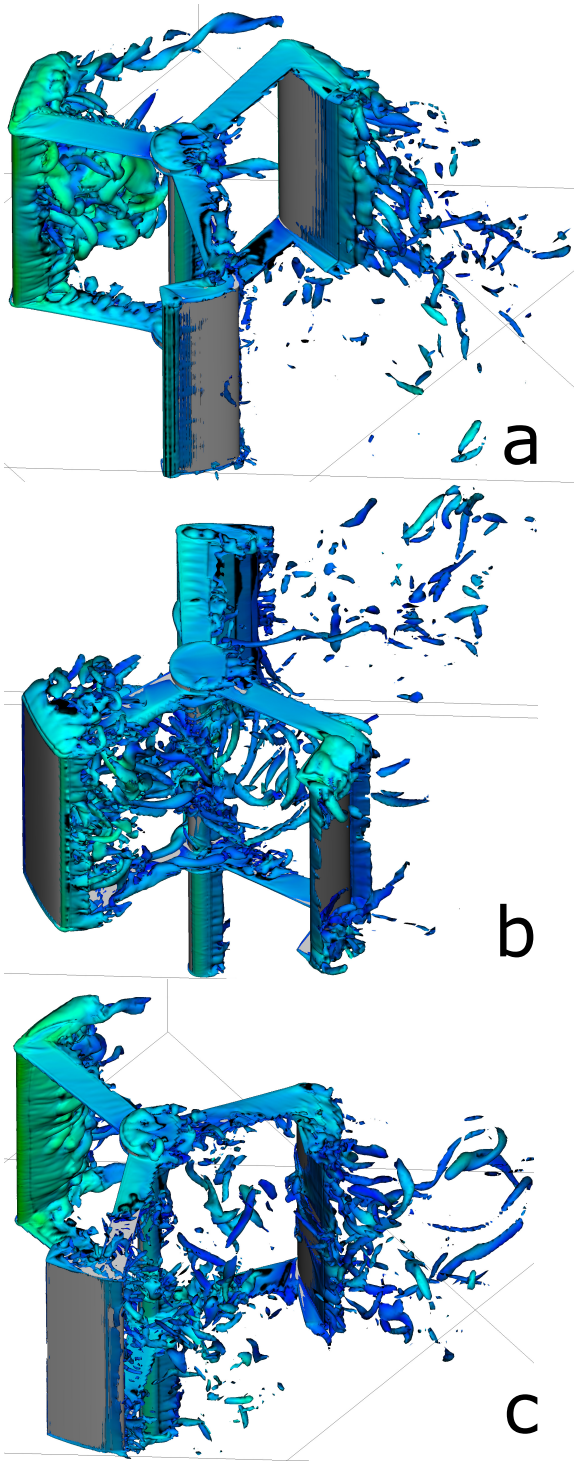

Figure 8: Instantaneous snapshot of iso-contours of Q-criterion for a value of 6000 colored by velocity magnitude at different azimuthal positions.

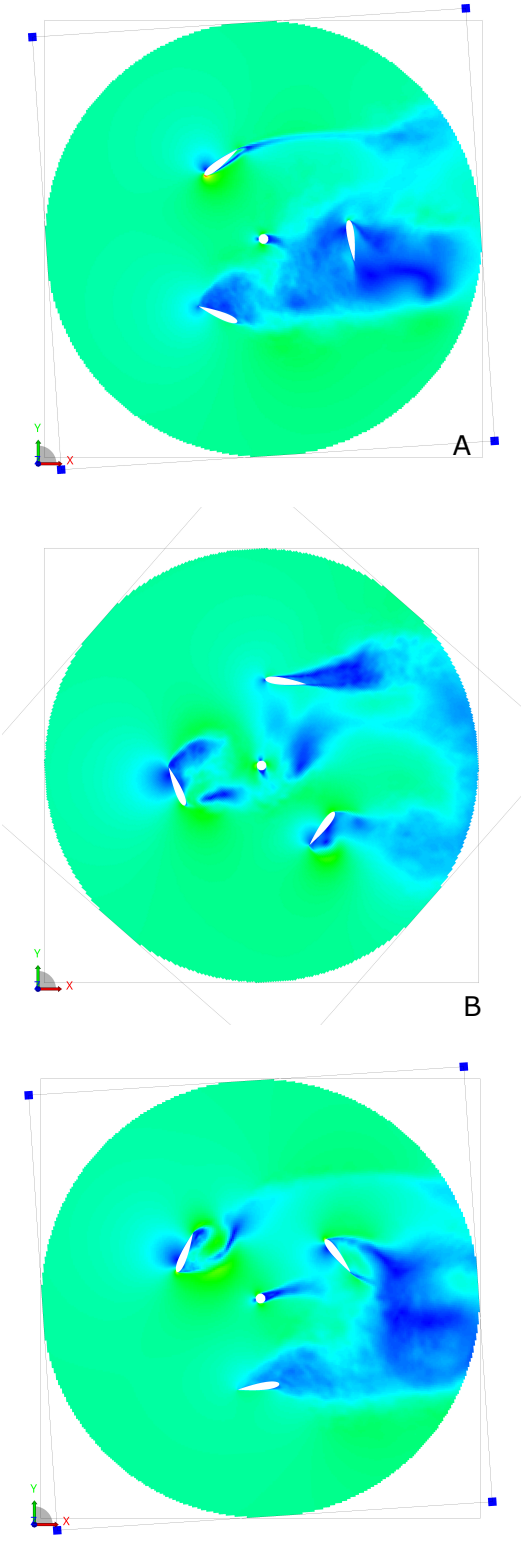

Figure 9: Phase locked averaged mean velocity contour profiles at mid-span at azimuthal positions.

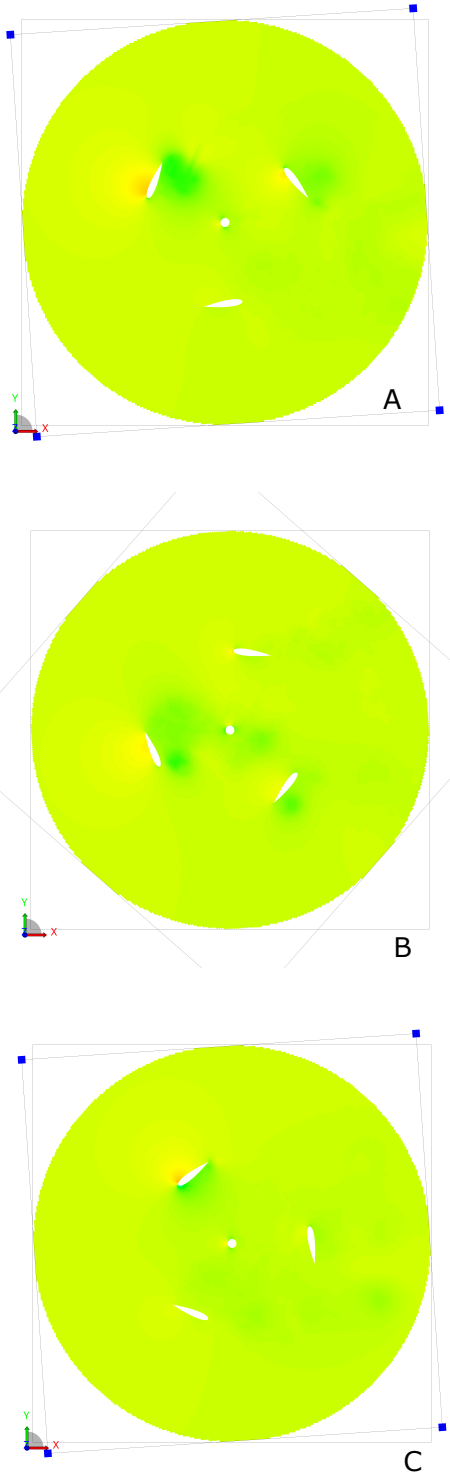

Figure 10: Phase locked averaged mean pressure contour profiles at mid-span at azimuthal positions.

30 Hz is attributed to background noise induced by the open jet in the Erlangen test facility. Blade wake interaction and dynamic stall as seen from the flow structures appear to be the import noise generation mechanisms in this flow regime.

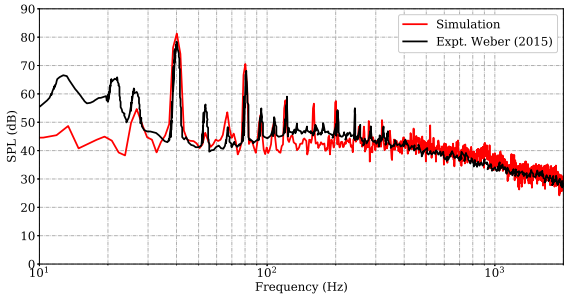

Figure 11: Sound pressure levels at blade azimuth of 0° corresponding to position of microphone 1 in [7] compared with the present simulation results from the direct probe.

6. Conclusions

Noise generated by a vertical axis wind turbine has been simulated in its experimental set-up with LBM using the PoweFLOW solver. The simulated noise spectra has been shown to provide a good agreement with the experimental acoustic far-field pressure at a given microphone position for the tonal and broadband components. Complex flow structures are formed in the deep stall regime, with the presence of important noise generation mechanisms such as dynamic stall noise and blade wake interaction noise. Simulations will be performed for different tip speed ratios to obtain the overall noise curve of the model turbine. As a future work, the sound pressure levels at different observer positions using the Ffowcs Williams and Hawkings (FW-H) analogy is to be computed. An understanding of the contribution of different noise sources to overall noise at different VAWT operating regimes is essential for the development of low noise VAWTs that could be acceptable in the urban environment.

Acknowledgments

The authors acknowledge the European Commission for its financial support through the project H2020-MSCA-ITN-2019 zEPHYR (Grant Agreement No. 860101).

References

[1] H. Riegler, Hawt versus vawt: Small vawts find a clear niche, Refocus 4 (2003) 44–46.

[2] E. Amet, T. Maître, C. Pellone, J. L. Achard, 2d numerical simulations of blade-vortex interaction in a darrieus turbine, J. Fluid Eng. 131 (2009) 111103:1–15.

[3] A. Bianchini, F. Balduzzi, G. Ferrara, L. Ferrari, Dimensionless numbers for the assessment of mesh and timestep requirements in cfd simulations of darrieus wind turbines, Energy 97 (2016) 246–261. doi:10.1016/j.energy.2015.12.111.

[4] F. Balduzzi, M. Zini, A. C. Molina, G. Bartoli, T. De Troyer, M. C. Runacres, G. Ferrara, A. Bianchini, Understanding the aerodynamic behavior and energy conversion capability of small darrieus vertical axis wind turbines in turbulent flows, Energies 13 (11). doi:10.3390/en13112936.
URL https://www.mdpi.com/1996-1073/13/11/2936

[5] K. Hamada, T. Smith, N. Durrani, N. Qin, R. Howell, Unsteady flow simulation and dynamic stall around vertical axis wind turbine blades, Jounral of Wind Engineering 35. doi:10.2514/6.2008-1319.

[6] K. Venkatraman, S. Moreau, J. Christophe, C. Schram, Numerical investigation of the effect of inflow non-uniformity on the noise radiated by a vertical axis wind turbine, in: AIAA AVIATION Forum, 2021, pp. 1–14. doi:10.2514/6.2021-2216.

[7] J. Weber, S. Becker, C. Scheit, J. Grabinger, M. Kaltenbacher, Aeroacoustics of darrieus wind turbine, International Journal of Aeroacoustics 14 (2015) 883–902. doi:10.1260/1475-472X.14.5-6.883.

[8] J. Weber, S. Riedel, J. Prass, A. Renz, S. Becker, J. Franke, Effect of boundary layer tripping on the aeroacoustics of small vertical axis wind turbines, Advanced Engineering Forum 19 (2016) 3–9. doi:10.4028/www.scientific.net/AEF.19.3.

[9] A. Rezaeiha, I. Kalkman, B. Blocken, Cfd simulation of a vertical axis wind turbine operating at a moderate tip speed ratio: Guidelines for minimum domain size and azimuthal increment, Renewable Energy 107 (2017) 373–385. doi:10.1016/j.renene.2017.02.006.

[10] S. Chen, G. D. Doolen, Lattice boltzmann method for fluid flows, Annual review of fluid mechanics 30 (1) (1998) 329–364.

[11] Dassault Systèmes, SIMULIA PowerFLOW User's Guide (2020).

[12] J. Rainbird, E. Ferrer, J. Peiro, J. Graham, Vertical-axis wind turbine start-up modelled with a high-order numerical solver, Springer Tracts in Mechanical Engineering (2015) 37–48.

[13] I. M. Horia Dumitrescu, Vladimir Cardoş, The physics of starting process for vertical axis wind turbines, in: A. M. Esteban Ferrer (Ed.), CFD for Wind and Tidal Offshore Turbines, Springer Tracts in Mechanical Engineering, 2015, Ch. 7, pp. 69–81.

[14] G. Brès, F. Perot, D. Freed, Properties of the lattice boltzmann method for acoustics, 2009. doi:10.2514/6.2009-3395.

Modelling of coherent wavepackets in supersonic jets

Manas Nerurkar

Environmental and Applied Fluid Dynamics Department, von Karman Institute for Fluid Dynamics, Belgium, manas.nerurkar@vki.ac.be

Supervisor: Christophe Schram

Professor, Environmental and Applied Fluid Dynamics Department, von Karman Institute for Fluid Dynamics, Belgium, christophe.schram@vki.ac.be

University Supervisor: Peter Jordan

Professor, PPRIME Institute, CNRS - Université de Poitiers - ENSMA, Poitiers, France, peter.jordan@univ-poitiers.fr

Abstract

In this study, the mechanisms of noise generation pertinent to supersonic jet noise are examined. This study is conducted to develop a low order physical jet noise model, capturing shock interactions with coherent structures; with agreement with high-fidelity simulations, and experimental campaigns. Two nozzles are designed for near-field and far-field experimental campaigns and the acoustic spectrum results for the two configurations are compared. The velocity field and the Nozzle-exit boundary-layer parameters are measured using hot-wire anemometry and particle image velocimetry (PIV) methods, which is also used to measure the turbulence statistics.

Coherent structures are shown to exist in a fully developed high Reynolds turbulent jet. These organised structures are modelled as wavepackets, characterised by spatial amplification and decay. Wavepacket modelling is based on the linearisation of a Navier-Stokes system using the mean field as the base flow. Spectral proper orthogonal decomposition is used, where the flow is decomposed into an orthogonal basis optimally ranked by energy content. Dominant structures are thus educed as the leading modes of the SPOD. These coherent structures are also observed in the nozzle boundary layer, with the most-energetic low-order azimuthal boundary layer structures driving the downstream jet dynamics.

BBSAN arises from the nonlinear interaction between large-scale coherent structures and shocks. The source is assumed to consist of turbulent and shock components. The propagating coherent disturbances closely resemble a Kelvin-Helmholtz instability in the transitional shear layer. These non-linear effects are dominant in the near field, upto several nozzle diameters from the nozzle exit. To investigate the non-linear effects, an array of microphones is set-up in the nearfield of the nozzle in the anaechoic facility JAFAR, at the Von Karman Institute for fluid dynamics.

The near and far-field microphone arrays, coupled with an acoustic analogy could provide a quantitative demonstration of the wavepacket – shock interaction, demonstrating the effect of upstream conditions on BBSAN in supersonic jets, which is the objective of the thesis. Expounding on the understanding that coherent structures in the nozzle drive the noise mechanics downstream, and the wavepacket-shock interactions could help understand shock-cell unsteadiness and development further downstream.

Keywords: Aeroacoustics, Jet-Noise, Coherent Structures, Shock-Cell's

Experimental and numerical investigation of the noise emitted by maneuvering multicopter drones

Erica Gallo

Environmental and Applied Fluid Dynamic Department, von Karman Institute for Fluid Dynamics, Belgium, erica.gallo@vki.ac.be

Supervisor: Christophe Schram

Professor,Environmental and Applied Fluid Dynamic Department, von Karman Institute for Fluid Dynamics, Belgium, christophe.schram@vki.ac.be

University Supervisor: Emanuele Garone

Professor, Department of Control Engineering and System Analysis, Université libre de Bruxelles, Belgium, emanuele.garone@ulb.be

Abstract

Unmanned Aircraft Systems, also known as drones, are nowadays regarded as a promising emerging technology for a wide range of applications including emergency medical service, packaging delivery, or the remote monitoring of hardly accessible industrial facilities such as wind turbines. Regarding the latter, novel structural health monitoring technologies are based on the measurement of the acoustic emissions of the blades using drones equipped with microphone arrays. The aforementioned applications require quiet drone operations, either to ensure community acceptance or to minimize the background noise generated by the drone itself and avoid interference with the structural health monitoring technique. The proposed project is focused on multicopters, and tackles an aspect of the Unmanned Aircraft Systems noise that has received little attention so far, despite being a strong contributor to drone acoustics and annoyance: the transient noise that its either induced during a maneuver or as a result of the flight control attempting to maintain position in a gusty atmosphere. So far, multicopter noise has been mostly characterized for basic flight conditions, such as hover and forward translation. Maneuvers induce more complex unsteady aerodynamic forces and very perceptible changes in the acoustic signature, which represent a challenging characteristic to model and predict. This research aims at identifying the main characteristics involved in the sound generated by a customized quadcopter under maneuvering flight conditions, in steady and turbulent flow conditions. Experimental and numerical work will be carried out for the analysis and prediction of the noise, coupled with flight control strategies for the trajectory definition. The project will be conducted at the von Karman Institute in collaboration with the System and Control Department of the Université Libre de Bruxelles.

Keywords: Multicopter noise, psychoacoustics annoyance, drone flight control, drone maneuvers, propeller aerodynamics

ENVIRONMENTAL FLOWS AND SAFETY

Near – field pollutant dispersion due to explosions

Pierrette Atikpo

Environmental and Applied Fluid Dynamics Department, von Karman Institute for Fluid Dynamics, Belgium,
pierrette.atikpo@vki.ac.be

Mechanical Engineering Department, Royal Military Academy, Belgium,
pierrette.atikpo@mil.be

Major Bart Janssens

Associate Professor, Mechanical Engineering Department, Royal Military Academy, Belgium,
bart.janssens@mil.be

Major David Lecompte

Associate Professor, Head of Military and Protective Engineering Department, Royal Military Academy, Belgium,
david.lecompte@mil.be

Delphine Laboureur

Associate Professor, Environmental and Applied Fluid Dynamics Department, von Karman Institute for Fluid Dynamics, Belgium,
delphine.laboureur@vki.ac.be

Charline Fouchier, PhD

Research Engineer, Environmental and Applied Fluid Dynamics Department, von Karman Institute for Fluid Dynamics, Belgium,
charline.fouchier@vki.ac.be

Abstract

When an explosive is encased in a material that is prone to disintegrate into small particles, these particles are dispersed over a wide area by the explosion and subsequent aerodynamic effects. This situation occurs for example in the case of covered-earth detonation for munitions disposals and dirty bombs. The dispersed particles may have adverse effects on the environment and human health. Thus, accurate models to predict the extent and level of contamination need to be developed. The purpose of this research is to investigate the blast wave, plume evolution and particle dispersion around full–scale buried detonations. Two experiments were carried out. 19 kg TNT and 40 kg TNT equivalent were detonated using World War I explosives. The following instruments were used: blast pencils to measure the blast wave, high speed camera to measure the plume motion, particle counters to measure particle dispersion (particle concentration and number) were placed at 20 m and 30 m from the explosion center. It was observed that a soil volume of 20.7 m^3 attenuated the peak pressure by 95%, positive impulse by 98% and positive impulse duration by 68%, compared to a surface detonation. The plume area increased linearly with time for 1 second. The increase in particle concentration and number lasted for about 7 minutes. The explosion let to 800% and 200% increase in particle number for particle counters placed at 20 m and 30 m respectively. Over 10 m distance between the two counters and within 1.3 minutes duration, particle number decreased by 95%, particle concentrations PM_{10} decreased by 90%, $PM_{2.5}$ by 81% and PM_1 by 59%. Despite the efforts done to record and analyze data around full-scale explosions, it was concluded that to be able to make statistically sound conclusions, more experiments need to be carried out by varying the explosive charge mass, under different environmental and soil conditions.

Keywords: buried detonation, blast wave, plume motion, particle dispersion.

1. Introduction

An explosion is a process resulting from a sudden release of energy [1]. When such energy is released, it activates the adjacent materials through two mechanisms: deflagration and detonation. Deflagration is when the adjacent materials explode because they are warmed above their decomposition temperature. Detonation occurs when adjacent materials explode due to shock pressure forces. A detonation can happen on the ground surface or deep in the ground. When a buried detonation occurs, the shock energy released propagates through the surrounding soil material in all directions and at a very high speed. A big amount of that violent shock energy is used to pulverize and compact the surrounding soil material, thus leading to the attenuation of the shock wave by the time it reaches the surface of the ground. The propagation of the shock wave leads to the motion of the topsoil, crater formation, plume motion and dispersion of small particles over a wide area by subsequent aerodynamic effects. The attenuation of the blast wave and the other phenomena observed during a buried detonation, depend on the depth of burial (DOB), properties of the soil and environmental conditions.

Buried detonation, which is due to the activation of adjacent materials because of shock pressure forces can be used for productive applications such as construction of railways, canals, dams, in mining industry, safe demolition of abandoned buildings and munitions. However, it can also be used for destructive purposes such as in terrorism through covered - earth detonation of dirty bombs. When such bombs are detonated, resulting particles are dispersed over a wide area by the explosion and subsequent aerodynamic effects. The dispersed particles may have adverse effects on the environment and human health. Thus, accurate models to predict the extent and level of contamination need to be developed in order to prevent and mitigate risks associated with them.

Much research has been done in order to understand these phenomena. In 1998, Bergeron et al. [2] performed for the Canadian defense, 20 experiments at reduced scale using 100 g of C4 explosives. The experiments took place in a laboratory and they investigated the impact of depth of burial on the blast wave. Transducers were used to measure in-air shock pressure, Carbon Resistor Gauges and shorting pins were used to measure the in–soil shock pressure and its time of arrival. They concluded that as the depth of burial increases, the in–air pressure decreases while the in–soil pressure increases. They also investigated the velocities of the ejecta and the detonation products by using flash X-ray radiography and high speed camera.

In 2004, Hlady [3] carried out an extensive 200 experiments. His experiments were carried out at small–scale using 25 g of C4 explosives in a controlled environment. He investigated the impact of soil parameters, such as soil type, soil moisture content and density, on blast energy. He used a piston apparatus made of pressure gauges, shaft and piston to measure the blast energy. He concluded that the energy transferred in fine–grained soil is greater than that transferred in coarse–grained soil. He also found that as the soil moisture content increases so does the transferred energy. In order to observe the motion of the topsoil and the plume, he used a high–speed camera.

In 2017, Fouchier et al. [4] studied the effects of explosive powder mass on blast energy and symmetry of explosion. They also investigated the effect of the wind speed on the dispersion of the detonation products. Their experiments were performed in a wind tunnel in laboratory at a gram-scale of Pentaerythritol tetranitrate (PETN) and cyclotrimethylenetrinitramine (RDX) explosive. Two explosive powder masses were used: 10g of a light powder called JetFine 1 and 28g of a heavy powder called Mistron 200. Pressure sensors were used to measure the blast energy, high–speed camera and large–scale Particle Image Velocimetry were used to analyze the plume motion. The study concluded that the increase in the powder mass decreases the blast energy but increases the plume height and as the wind speed increases, the plume height decreases.

Despite the efforts done by researchers to understand and model buried detonation phenomena, most of this research was done at reduce-scaled and in controlled laboratory environments [2], [3], [4]. The current laws and models developed are based on those reduced-scale experiments thus, leading to those phenomena not well characterized and large discrepancies when it comes to modelling and predicting the full–scale phenomena [5], [6], [7].

Thus, the purpose of this research is to investigate blast wave, plume evolution and particle dispersion around full–scale buried detonation in order to provide a better understanding, modeling and evaluation of pollutant dispersion caused by full–scale buried detonation phenomena.

The current research will provide added value to both the scientific and military communities. It will provide data around full-scale explosions to literature.

It will help to better understand explosion phenomena. It will contribute to develop new or improve existing analytical, mathematical and numerical models. It will help the military to predict and mitigate effects of dirty bombs, to better assess threats regarding Chemical, Biological, Radiological and Nuclear (CBRN) agents and to evaluate environmental and health impact of detonations.

2. Methods

2.1. Experimental procedures

2.1.1. Explosive and pit preparation

The experiments took place in DOVO (Belgian Defense Unit in charge of Explosive Ordnance Disposal and Destruction) demolition zone in Poelkapelle, West Flanders (Fig. 1). The explosives used are conventional Word War I abandoned munitions. Fig. 2.

They were collected by DOVO in the fields then brought to the demolition zone, where their shells were cleaned using specialized tools to remove dirt. The purpose of the cleaning is to ensure successful identification confirmation by the X-Ray machine and to facilitate good contact with other explosives when placed together. This to ensure successful detonation. Once the explosive was cleaned, it was then placed in an X-Ray machine to confirm its identification done earlier in the field. The cleaned explosives were then tightly packed inside a rectangular wooden box of dimensions: height = 60 cm, width = 60 cm and length = 80 cm. The explosives were a mixture of Amatol and TNT (Trinitrotoluene). The mass of the explosives is determined using a specialized defense database. Two different explosive masses were used in this experiment: 19 kg TNT and 40 kg TNT equivalent. The geometry of the explosives is mostly cylindrical. The explosive shell is made of cast iron, steel and copper.

While the explosive assembly was placed in the storage zone, a pit was dug in the detonation zone using an excavator. Two pits were used. The first pit was for the 19 kg TNT equivalent. Its geometry was rectangular with the following dimensions: length = 5.4m, width =1.6m, depth =1.4m. The second pit was for the 40kg TNT equivalent. Its geometry is hemispherical with the following dimensions: diameter 1=5.7m, diameter 2=7.4m and depth = 4.5m.

The wooden box containing the explosives was then transported to the detonation zone using a forklift. At the detonation zone, an anti-tank mine made of steel



Figure 1: Poelkapelle demolition zone



Figure 2: World War I explosives

was placed on top of the explosives. 250g TNT equivalent of a cartridge wrapped with a detonating cord was added. A fair amount of soil was then added to keep the whole assembly tightly packed and ensured successful detonation of all the explosives (Fig. 3).

Using a bulldozer, the assembly was carefully placed in the pit and covered with soil up to 1 m (for the 19 kg TNT equivalent) and 2.5 m height (for the 40 kg TNT equivalent) above the ground level. The detonating cord was then connected to an electric detonator which in turn was connected to an electric post at 15 m from the pit (Fig. 4 and Fig. 9).

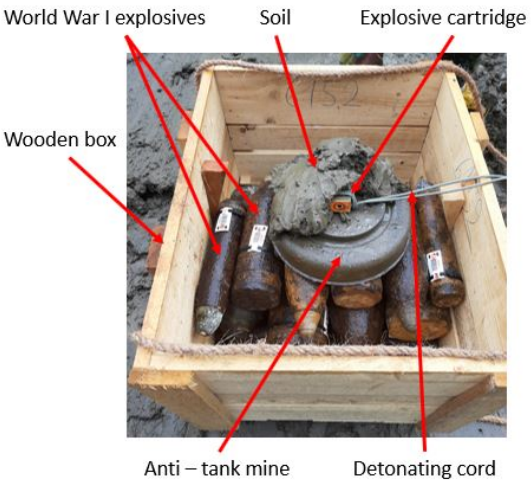

Figure 3: Explosive assembly



Figure 4: Explosive assembly deposition in the pit



Figure 5: Blast pencil



Figure 6: High speed camera

2.1.2. *Measurement instruments*

The three main measurements instruments used were the blast pencil to measure the blast, the high speed camera to measure the plume evolution and the particle counters to measure particle concentration and number.

The blast pencil (Fig. 5) used in this study is a PCB Piezotronics Series 137A20 free field blast pressure probe. It is made of a stable quartz piezoelectric element of sensitivities 1, 10 and 100 mV/psi with full-scale ranges from 0 to 50, 500 or 5000 psi.

The high speed camera used is a Photron Fastcam high speed camera that can offer thousands of frames per seconds depending on the resolutions (Fig. 6).

Two fine dust measurement particle counter brands were used: Fidas Frog Series 3577 (Fig. 7) and GRIMM Model 11-D (Fig. 8). These devices can measure particle number, size and mass or concentration in $\mu g/m^3$. These concentrations based on particle diameters are grouped into classes known as Particulate Matter (PM). They can provide four particulate matters: PM_1 is the concentration of particles whose diameters are less than or equal to 1 μm, $PM_{2.5}$ is the concentration of particles whose diameters are less than or equal to 2 μm, PM_4 is the concentration of particles whose diameters are less than or equal to 4 μm and PM_{10} is the concentration of particles whose diameters are less than or equal to 10 μm. The Fidas Frog particle counter can measure particle size from 0.18 μm to 40 μm and operates with a volume flow rate of 1.4 l/min while the GRIMM particle counter can measure particle size from 0.253 μm to 35.15 μm and operates with a volume flow rate of 1.2 l/min.



Figure 7: Fidas Frog particle counter



Figure 8: GRIMM particle counter

2.1.3. *Measurement instruments set-up*

Once the explosive assembly was placed in the pit and covered with soil, the measurement instruments were then positioned. The blast pencil was placed at 6.5m from the pit center. The GRIMM particle counter was placed at 20 m and the Fidas Frog counter at 30 m from the pit center. The color high speed was placed at 40 m from the pit center (Fig. 9)

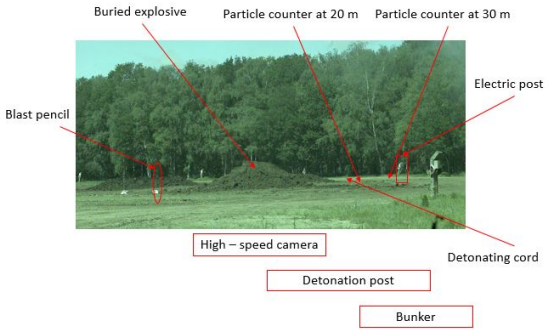

Figure 9: Measurement instruments set-up

2.1.4. *Detonation and data collection*

Once the explosive assembly and pit were ready and the instruments were set up, everyone then left the detonation zone to find refuge in the bunker. The explosive assembly was then detonated from the detonation post by an expert. The high speed camera was activated few seconds before the detonation and the blast pencil was automatically activated by the detonation. During the explosion of the 19 kg TNT equivalent, only the blast was measured and for the 40 kg TNT equivalent only the plume motion and the particle dispersion data were recorded.

Notes:

The entire demolition process, from the collection of the explosives till their demolition, is done exclusively by the experts from DOVO.

During the entire experimental campaign, safety masks, headphones and gloves were worn.

Table 1: Experiments summary

	Experiment 1	Experiment 2
Explosive charge mass	19 kg TNT equivalent	40 kg TNT equivalent
Pit type	Rectangular	Hemispherical
Pit dimensions	l=5.4 m w=1.6 d=1.4 m	d1=5.7 m d2=7.4 m d=4.5 m
Soil height	h=1 m	h=2.5 m
Phenomenon Measured	Blast wave	Plume motion + Particle dispersion
Extracted Data	Peak pressure Positive impulse Duration	Plume area Particle concentration Particle number
Instruments	Blast pencils	High speed camera + Particle counters

2.2. *Methods of analysis*

2.2.1. *Numerical integration and analytical calculations: blast wave parameters*

The recorded blast data for the buried detonation was imported into MATLAB (Fig. 10). Numerical integration was used to calculate the positive impulse. Then simple calculation techniques were used to extract the peak pressure and positive impulse duration. In order to evaluate the impact of the covered earth on the attenuation of the blast, the above recorded peak

pressure, positive impulse and duration were compared with predicted surface detonation of hemispherical explosive of the same mass. Firstly, the standoff distance R was measured. Then the scaled distance Z was calculated as in Eq. 1. Using the metric version of the suitable Kingery – Bulmash blast wave parameters graph (Fig. 11), the peak pressure, positive impulse and positive impulse duration were derived.

$$Z = \frac{R}{W^{1/3}} \tag{1}$$

Z is the scaled distance in $m/kg^{1/3}$, R the standoff distance in m and W the equivalent TNT in kg.

In order to evaluate the amount of soil responsible for the attenuation, the volume of the covered-earth was calculated using the formula in Eq. 2.

$$V = l \cdot w \cdot (d + h) \tag{2}$$

V is the volume in m^3, l is the pit's length in m, w is the pit's width in m, d is the pit's depth in m and h is the height in m of the covered-earth above the ground surface level.

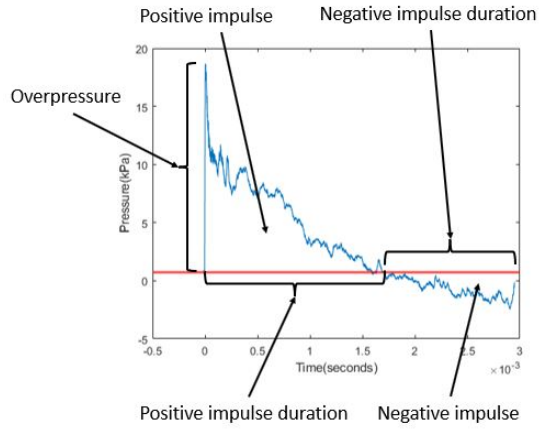

Figure 10: Recorded blast wave

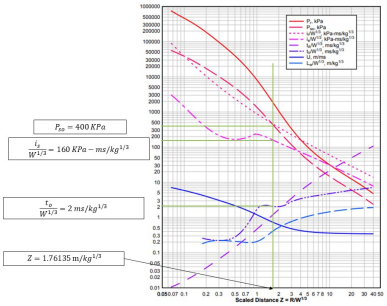

Figure 11: Blast wave parameters calculations [8]

2.2.2. *Image processing: plume motion*

The evolution of the plume was analyzed using image processing techniques in MATLAB. The recorded image was cropped (Fig. 12) to remove unnecessary parts that would complicate the analysis.



Figure 12: Original cropped plume

The cropped image was converted into L*a*b* color space (Fig. 13, Fig. 14 and Fig. 15).

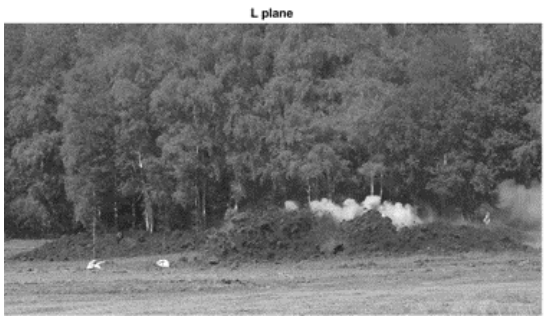

Figure 13: L* channel

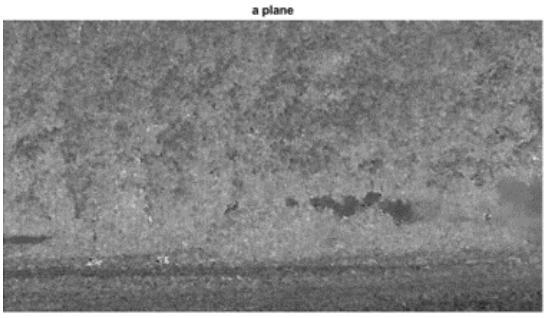

Figure 14: a* channel

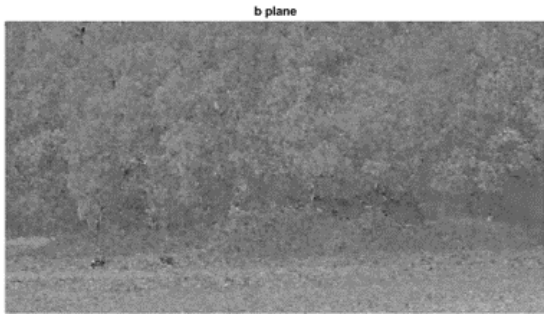

Figure 15: b* channel

This color space mimics better human perception [9]. In this color space, each pixel has value between 0 and 100. The L* stands for Luminance and measures the brightness of the image. The a* channel measures the balance between green and red. The b* channel measures the balance between blue and yellow. The intensities of the plume was then retrieved. The mean intensity of a* and b* channels were calculated. Next, the distance between each pixel and the mean intensity was computed (Fig. 16).

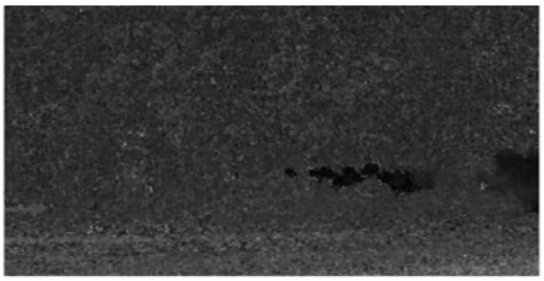

Figure 16: Distance between each pixel and mean intensity

Using the computed distance, the segmentation was created to isolate the plume (Fig. 17). Noises were removed, holes were filled and the segmentation was improved using filters (Fig. 18). Finally, the contour of the segmented cloud was extracted and superimposed on the original plume (Fig. 19). This entire process was repeated for 500 successive images representing 1 second evolution of the plume.



Figure 17: Segmented plume image



Figure 18: Improved segmented plume image



Figure 19: Superimposition of the developed model (yellow) over the original plume

3. Results and Discussions

3.1. Blast wave

Standoff distance $R = 4.7\,m$
Charge equivalent TNT mass $W = 19\,kg$
Scaled distance $Z = 1.76\,m/kg^{1/3}$, using Eq. 1
Pit's dimensions: $length\,l = 5.4\,m$, $width\,w = 1.6\,m$ and $depth\,d = 1.4\,m$.
Soil *height* above ground surface level $h = 1\,m$ Volume V of soil on explosive is $V = 20.7\,m^3$, using Eq. 2
Soil type = clay

In experiment 1, as concluded by Bergeron et al. [2] it was observed that the soil volume of $20.7\,m^3$ considerably attenuated the blast parameters: peak pressure decreased by 95%, positive impulse decreased by 98% and positive impulse duration decreased by 68%, see Table. 2

Table 2: Buried and surface detonation blast parameters

Detonation type	Peak pressure KPa	Positive impulse $KPa.ms$	Duration ms
Buried	18.68	9.6	1.7
Surface	400	426.94	5.34

3.2. Plume motion

The high speed camera (Fig. 6) used in experiment 2 was set to 1024x768 resolution and gave 3500 frames for 7 seconds total duration of the plume motion. However, the analysis shown in this report concerns the plume evolution for just 1 second duration, thus 500 total frames, 2 seconds after the explosion. So the analysis does not provide the plume evolution over the entire 7 seconds recorded video. This was due to some challenges encountered while processing the plume video. In the first 2 seconds after the explosion, the plume and the topsoil were mixed and at late stage of the explosion, the plume started diluting and its color got closer to that of the background and thus making the segmentation of the plume from the background and topsoil complicated and not accurate.

The analyzed 1 second evolution of the plume area was plotted against time (Fig. 20). It was found that the area increased nearly linearly over 1 second duration of the plume evolution in time.

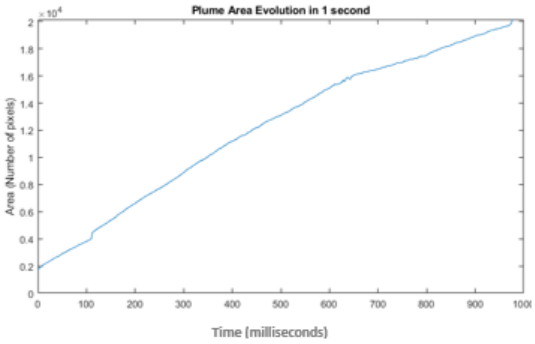

Figure 20: Plume area evolution as function of time

3.3. Particle dispersion

Regarding the particle dispersion, it can be clearly seen that the explosion has a huge impact on the particle number and concentration. Fig. 21 shows that before the explosion, the ambient particle number at 20 m from the explosion center is about 80,000 and that at 30 m is about 11,000. However, 5.7 minutes after the explosion the particle counter placed at 20 m recorded 736,790 maximum particle number, leading to more than 800% increase. At 7 minutes after the explosion, the particle counter placed at 30 m recorded 34,095 maximum particle number, leading to more than 200% increase. The increase in particle number lasted for about 7 minutes as the particle number in both counters got back to their ambient values before the explosion. Over 10 m distance between the two counters, the particle number decreased by 95% in 1.3 minutes.

Fig. 22 to Fig. 24 show the PM concentrations at 20 and 30 m from the explosion center. these figures show that the particle counter at 20 m recorded a maximum PM_{10} of 552.6 $\mu g/m^3$ at 6.9 minutes, $PM_{2.5}$ of 153.9 $\mu g/m^3$ at 5.7 minutes and PM_1 of 54.2 $\mu g/m^3$ at 5.7 minutes. The counter at 30 m recorded a maximum PM_{10} of 55.99 $\mu g/m^3$ at 8 minutes, $PM_{2.5}$ of 29.66 $\mu g/m^3$ at 7 minutes and PM_1 of 22.45 $\mu g/m^3$ at 7 minutes. Over 10 m distance between the two counters and 1.3 minutes interval, the PM_{10} decreased by 90%, $PM_{2.5}$ decreased by 81% and PM_1 decreased by 59%. Same as the particle number, the increase in the PMs concentrations lasted for only about 7 minutes, then got back to their initial values before the explosion.

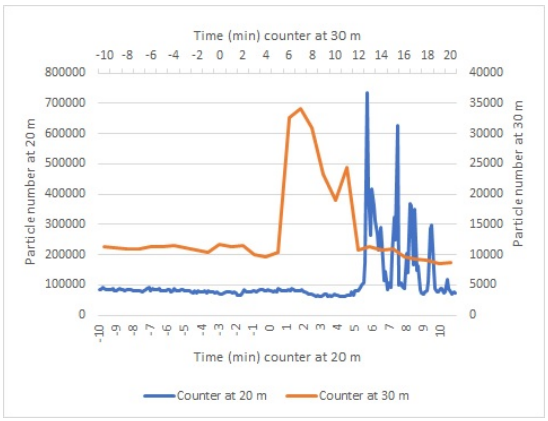

Figure 21: Particle number at 20 m and 30 m

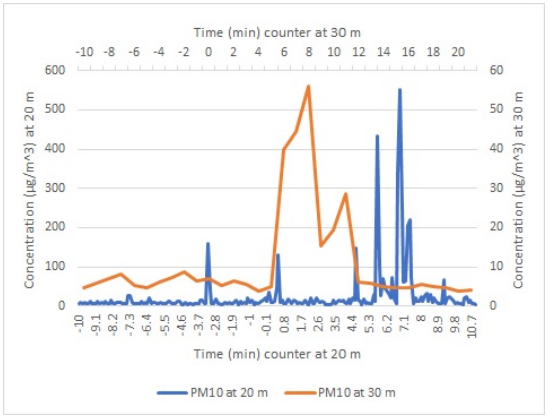

Figure 22: PM_{10} Concentration at 20 m and 30 m

4. Conclusions

Despite the efforts done to record, process and analyze data around full-scale explosions, it was concluded that more experiments with different explosive charge mass under different environmental and soil conditions, need to be carried out in order to derive valid statistically sound conclusions. Regarding the blast, more experiments need to be carried out to investigate the attenuation for different charge mass and soil saturation. Advanced processing techniques need be used in future to analyze the plume evolution over the entire duration of the explosion from the beginning till the end. Plume height and radius also need be investigated. Regarding the particle dispersion, the two different brands of particle counters used could potentially lead to some systematic errors in the analysis. Thus, in future experiments, efforts will be done to either used the same brand particle counters or do an experiment with known input to quantify the difference. Also particle dispersion analysis under different environmental conditions will be carried out.

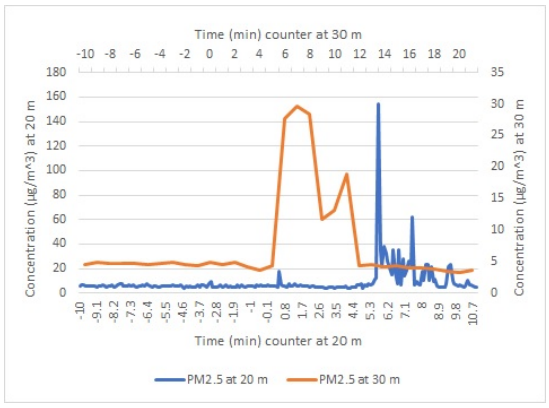

Figure 23: $PM_{2.5}$ Concentration at 20 m and 30 m

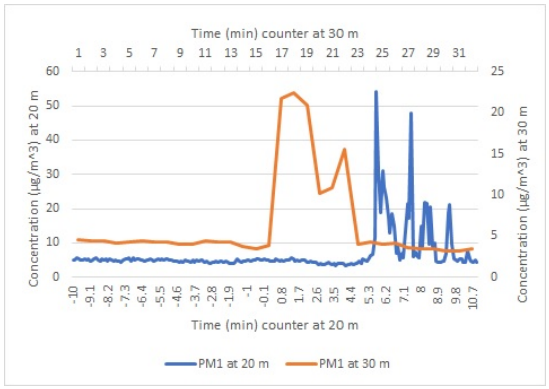

Figure 24: PM_1 Concentration at 20 m and 30 m

References

[1] Kinney, G. F., Graham, K. J. (1985). *Explosive Shocks in Air* (Second). Springer Berlin Heidelberg.

[2] Bergeron, D., Walker, R., Coffey, C. (1998). Detonation of 100 g Anti-personnel Mine Surrogate Charges in Sand: A Test Case for Computer Code Validation. Canada: Defence Research Establishment Suffield.

[3] Hlady, S. L. (2004). Effect of soil parameters on land mine blast. Bad Reichenhall, Germany: Military Aspects of Blast and Shock (MABS).

[4] Fouchier, C., Laboureur, D., Youinou, Y., Lapebie, E., Buchlin, J. M. (2017). Scaled model of the pollutant dispersion driven by a condensed-phase explosion in an urban environment. *International Workshop on Physical Modelling of Flow and Dispersion Phenomena*.

[5] Brown, R. C., Kolb, C. E., Conant, J. A., Zhang, J., Dussault, D. M., Rush, T. L., ... Touma, J. (2004, April). Source Characterization Model (SCM): A Predictive Capability for the Source Terms of Residual Energetic Materials from Burning and/or Detonation Activities. Strategic Environmental Research and Development Program.

[6] Cheeseman, B. A., Wolf, S., Yen, C. F., Skaggs, R. (2006). Blast simulation of explosives buried in saturated sand. *Fragblast*, 10(1–2), 1–8.

[7] Mandal, J., Goel, M. D., Agarwal, A. K. (2021). Surface and Buried Explosions: An Explorative Review with Recent Advances. *Archives of Computational Methods in Engineering*, 28(7), 4815–4835.

[8] Karlos, V., Solomos , G. (2013). Calculation of Blast Loads for Application to Structural Components. European Commission. Joint Research Centre. Institute for the Protection and the Security of the Citizen.

[9] Ly, B. C. K., Dyer, E. B., Feig, J. L., Chien, A. L., Del Bino, S. (2020). Research Techniques Made Simple: Cutaneous Colorimetry: A Reliable Technique for Objective Skin Color Measurement. *Journal of Investigative Dermatology*, 140(1), 3-12.e1.

Wind turbine wakes impact on the dynamics of high-voltage cables for fatigue assessment and optimization

Emmanuel Gillyns

Environmental and Applied Fluid Dynamics, von Karman Institute for Fluid Dynamics, Belgium, emmanuel.gillyns@vki.ac.be

Supervisor: Jeroen van Beeck

Professor, Environmental and Applied Fluid Dynamics, von Karman Institute for Fluid Dynamics, Belgium, vanbeeck@vki.ac.be

University Supervisor: Grégoire Winckelmans

Professor, Institute of Mechanics, Materials and Civil Engineering, UCLouvain, Belgium, gregoire.winckelmans@uclouvain.be

Abstract

The wake of wind turbines is much more turbulent than atmospheric flow. Structures in its wake are heavily affected by this turbulence level. It can easily extend to 10 times the swept diameter, with most recent ones reaching 180 m, leading to a 2 km affected zone. Close-by electrical cables experience premature fatigue due to a coupling yet to be fully understood.

Keywords: wind turbine, wind turbine wake, high voltage cables, galloping, large eddy simulation, actuator line model, atmospheric boundary layer, fluid structure interaction, one-way coupling, fatigue, scale-model wind turbine.

1. Introduction

With the energy sector moving towards renewable energy sources, wind energy becomes essential to produce electricity. Landscapes and even offshore zones gets populated with an ever-increasing number of wind turbines. As such, the wake impacts an increasing number of structures such as building, tower antennas, or overhead electrical cables. This last one will be subject to the present thesis.

The size of a wind turbine is given as the blade swept diameter. In the past few years, this size has been steadily increasing due to higher efficiency of larger wind turbines. To give an order of magnitude, currently the size of the swept diameter of most recently installed wind turbines onshore reaches $\varnothing$180 m [1], and the wake extends to approximately 10 times the swept diameter [2]. This implies that the zone affected by the high level of turbulence in the wake, spans over almost 2 km. The wake inevitably contains high voltage cables carrying the electricity needed for our society, whether it comes directly from the power production of the wind turbine, or due to nearby electricity distribution. This thesis will shine light on the behaviour of such cables in the turbulent structures of the wind turbine wake.

Depending on the inflow conditions and the measurement location, the turbulence intensity present in the wake is observed to be between 10 and 20 % more than the local turbulence intensity (if the wind turbine was not present) [2]. This level of turbulence inevitably affects negatively any structure downstream, and needs to be properly understood. Hanging cables subjected to such conditions will not only be affected by the highly turbulent flow which will degrade its mechanical properties in time, but also can oscillate with the flow and get damaged further by fatigue. The energy spectrum of a turbulent flow spans over several orders of magnitude, with the most energetic part at the largest wavelength. Due to this, the electrical cables can be excited by multiple wavelength and oscillate at their natural frequency, which is a low frequency and high wavelength (order of magnitude of the cable length). Such events are called ”galloping”, and results in extremely large displacements of the cables, inducing fatigue in the material and ul-

timately breakage. Preventing this is therefore crucial, especially with the growing wind turbine installations. Dampers can be used to mitigate this effect, which will be studied in the scope of this work. Due to the extreme cost of high voltage maintenance, it is of utmost importance to be able to predict and mitigate such behaviour.

2. Methodology

Investigating the impact of the wind turbine wake on overhead cables cannot be done full scale experimentally. Performing experiments without controlling the inflow conditions (which is the main factor influencing the wake characteristics) cannot provide the necessary information to characterize the behaviour. Numerically, it is possible to assess any inflow conditions, and be able to simulate the full scale behaviour of the system. Of course, the simulations would have to be validated experimentally which will be done in the controlled environment of a wind tunnel with a scaled down wind turbine.

The dynamics of the cable being time-dependant, the distinctive parts of the wake can excite in different ways the cables. This time dependency requires the fluid simulation of the wake to be coupled with the computation of the cable dynamics. The scale of the cable (typically $\varnothing 4$ cm) being orders of magnitude smaller than the scales of the wind turbine wake (resolved on a mesh in the order of 1 m), the coupling will be a one-way coupling. This means that the wind turbine wake will affect the displacement of the cables, but the cables would be too small to affect significantly the fluid flow.

2.1. Actuator line model

Solving the fluid flow is performed numerically using Large Eddy Simulation (LES), which explicitly resolves the largest scales and models the effect of the smaller scales (smaller than the grid size, known as sub-grid scale). This allows to obtain vastly more accurate solution than Reynolds Averaged Navier Stokes, at a cost orders of magnitude smaller than Direct Numerical Simulation (DNS). Essentially, the turbulent spectrum of the flow is filtered with a low-pass filter, reducing significantly the computational cost. This level of accuracy is essential to be able to capture the relevant scales for coupling the wake to the cable dynamics.

Even though the cost of an LES is vastly reduced compared to a DNS, performing a wall-resolved LES with explicit geometry of the wind turbine blades is currently out of reach with the available computational resources. Modelling of wind turbines is typically done by computing the reactive forces that the blades exert on the flow (lift and drag on the blades, nacelle and tower), and scaling those forces on to the coarser mesh. This method allows to reproduce the same wake behaviour at orders of magnitude lower computational cost compared to explicitly resolving the geometry. Such methods are called Actuator Disk Model (ADM) when the forces are spread on the entire swept disk of the wind turbine blades, or Actuator Line Model (ALM) when they are spread locally around each rotating blades. As expected by the reader, the ALM produces higher resolution results compared to the ADM. Most of the differences are seen in the near wake (approximately in the $3\varnothing$ downstream region), where turbulent structures show coherence, and can couple in very specific ways with the cable dynamics. From industrial sources, namely ELIA (the electricity transmission system operator in Belgium), it has been reported that cases with cables in the near wake already exist, and will most likely continue to grow with the increasing number of wind turbines installed. Obviously, the ALM is therefore required to capture correctly the near-wake region.

For reasons explained in section 3, the code Nek5000 is used for this ALM. Previous implementations of ALM in this code [3; 4] are not openly available, and require to do so, based on the published guidelines.

The working principle of the ALM is to sample the local velocity at the location of the blades, and compute the force of lift and drag at each radial position, and at each timestep. To do so, lookup tables are used based on the aerodynamic profile of the wind turbine blade. Then a Gaussian distribution is used to spread the forces around the lifting line. More details on the Gaussian spreading will be given in the following chapters, as the proposed implementation can allow for much better resolution in the hub region as compared to other implementations [5].

2.2. Experimental comparison of the wind turbine model

As exposed previously, numerical simulations are the chosen way to analyse different types of wind turbine wakes and their effect on the cables with strategies to mitigate the fatigue effect, Numerical results cannot simply be assumed to reflect the physical phenomenon of the real world without comparison with

experiments. As such, the wind turbine wake computed by the LES simulation with the ALM must be compared to experimental wind turbine wake. Full scale experiments are not considered, first because the inflow conditions are not controlled (and therefore extremely difficult to reproduce numerically), and because of the non-disclosed geometry of the wind turbine blades of all accessible wind turbines. Previous research [6] showed that scaled down wind turbines can produce a very similar wake as a full scale one.

A few main dimensionless parameters are used to ensure that the scaling down will produce a representative wake. First, the Tip Speed Ratio (TSR) is the ratio between the incoming flow speed unaffected by the wind turbine (V_0), and the blade tip speed ($V_t = \omega \cdot r$). This TSR ensures the advection speed of the vortex generated by the blade tip, which is the source of the most important turbulent structures of the wake. Then, the thrust coefficient (Ct) is a parameter describing how much force is exerted streamwise opposing the flow, slowing down the flow streamwise. It is responsible for most of the velocity deficit in the wake. Finally the Power coefficient (Cp) describes the amount of power extracted from the inflow due to the rotation of the blades. From the perspective of the wake, it is responsible for the rotation of the wake.

Scaled down experimental wind turbines are designed such that they reproduce the TSR and Ct mostly, as those parameters are the main factors influencing the wake. At smaller scale, the blades operate at much lower Reynolds numbers (Re), therefore the aifoil profiles used must be different from the full-scale wind turbine to prevent boundary layer detachment. As such, low-Reynolds airfoil are used which makes the Cp impossible to match together with the Ct.

Recent study [7] showed that the size of $\varnothing 15\,\mathrm{cm}$ can reproduce a wake within acceptable accuracy, but a larger size would produce a wake with better Re independence. Re independence of the wake, means that operating the miniature wind turbine at different inflow speeds, the wake behaviour remains unchanged. Larger experimental wind turbine would also allow more control over the wind turbine such as variable pitch control. Finally the larger size enables better resolution of the wake measurements, and could even allow for in-blade pressure measurements for comparing with the expected pressure distribution of the airfoil. For all the above reasons, this thesis will include the design and manufacture of a small scale wind turbine that is larger than previously made by researchers.

2.3. LES wall modelling

Similarly to the explicit geometry of the wind turbine being out of scope due to the large computation cost of high Re flow, resolving the wall of an Atmospheric Boundary Layer (ABL) is not currently possible with the computational power available. Indeed, resolving this explicitly would require to mesh all the details of an atmospheric surface (including buildings, trees, grass etc down to the roughness of their surface) which is obviously not considered.

Away from the wall, the flow only sees the effect of the wall roughness elements through the shear stress that is propagated in the wall-normal direction. Therefore a common technique to simulate the roughness of a wall numerically is to contain all of the roughness under-resolved in the first element/cell of the mesh, and to impose a shear stress that is equivalent of resolving it explicitly. This process is called wall modelling, which reduces significantly the computational cost of the LES to a point where an ABL is possible to be simulated.

At the time of writing this paper, no wall model is available in Nek5000. Implementing it is part of the process to have all the tools necessary for the upcoming simulations. The LES wall model implemented by the author for smooth wall proves to provide the correct flow behaviour in a channel flow compared to a DNS. More details will be given in the following chapters, as this implementation of wall modelling outperforms similar LES wall modelling, especially in the non-resolved region. This wall model uses the computed velocity close to the wall (in the resolved region) to calculate the shear stress that needs to be imposed on the wall, with the help of an analytical law of the wall.

Even though such wall model for smooth surface enables to compute flows at much higher Re number, simulating an ABL requires a rough surface wall model. For the range of an ABL limited around a wind turbine, the type of terrain is not changing significantly and can simulated as a constant shear on the entire ground boundary. As opposed to the above mentioned wall model adapting the shear stress based on the resolved flow velocity, this method of setting a constant shear stress is much faster to compute and will be used both for the full scale ABL, as well as the rough terrain wind tunnel.

2.4. LES turbulent inflow generation

As mentioned previously, the wake of a wind turbine heavily depends on the inflow, and particularly

on the turbulence intensity. It is therefore essential to reproduce the correct turbulence level of the flow impacting the wind turbine numerically. In LES, providing turbulent inflow is not trivial, and a number of methods have been developed to fit different needs. The precursor [8] and recycling [9] methods use streamwise periodicity to provide a fully developed flow. A synthetic turbulence generator [10] creates a coherent turbulent inflow with defined mean profile, provided to know the full Reynolds stress tensor, which is usually not the case. Alternatively, the Temperature Perturbation Method (TPM) [11] uses artificial buoyancy to trip a constant inflow to turbulent.

To compare accurately the experimental wind turbine wake to the one produced by the ALM, the inflow of the wind tunnel must be reproduced with the right level of turbulence. The honeycomb upstream of the test section and the fence in the L1 wind tunnel of the von Karman Institute (VKI) produce a high level of turbulence in the test section. This is on purpose to reproduce a scaled down ABL, but is challenging to reproduce numerically. The level of turbulence measured in the test section is higher than what can be simulated in a channel flow numerically because of those elements. For this reason, and because Nek5000 does not contain either one of the above mentioned methods, a new improved method is developed.

In this new method, the mean flow is imposed by using a Recycle and Rescale method (R²M) [REF TO THE R²M]. This alone is not enough to reproduce the level of turbulence of the wind tunnel. For this, a set of forces is triggered upstream of the domain of interest to trip an artificial level of turbulence. These forces are then wrapped in an integral controller to adjust them dynamically and match the experimental turbulence level.

2.5. Cable dynamics coupling and mitigation

With all above numerical tools (ALM, rough wall model for ABL, turbulence generator) validated numerically, the cable dynamics can be couples to the LES simulation to check for their effects. The equations governing the displacements of the cables will be used in a model representing the cables. This model will take into account the force exerted on it by the flow using the drag coefficient of the cable and the local flow velocity. This will accurately simulate the behaviour of the cable for different conditions of the wind turbine.

Meandering of the wake can affect significantly the cables in a way that could not be simulated by a simpler frequency spectrum analysis. This analysis will therefore shine light on this physical phenomenon for the first time.

On these modelled cables, passive devices such as tuned mass dampers will be added as a mitigation to the galloping behaviour. Results from this will provide the necessary data to fully understand the behaviour in multiple conditions.

3. Nek5000 numerical code

The Computational Fluid Dynamics (CFD) code used to for these LES simulations is Nek5000, developed by Argonne National Laboratory. It is an efficient and highly scalable, open source, CFD solver, with advantages such as high order accuracy, reduced cost per degree of freedom, and fast convergence. Such capabilities

4. Actuator line model (ALM)

As mentioned previously, the ALM is computing the forces of lift and drag on each part of the blade, to spread these forces on the coarser mesh. Lift and drag are computed using equations (1, 2) :

$$dL = \frac{1}{2} \cdot \rho \cdot v_r^2 \cdot C_l \cdot c \cdot dr \tag{1}$$

$$dD = \frac{1}{2} \cdot \rho \cdot v_r^2 \cdot C_d \cdot c \cdot dr, \tag{2}$$

with dL : discretized fraction of lift force (N), dD : discretized fraction of drag (N), ρ : fluid flow density (kg/m^3), c : chord length (m), dr : discretized length fraction of radius (m), and finally v_r : relative velocity (m/s).

The relative velocity is the velocity as seen by the airfoil. It is computed based on several quantities as follows :

- V_1 : the local flow velocity perpendicular to the swept disk (when the wind turbine as aligned with the flow, it is the streamwise velocity).

- V_t : the local tangential velocity of the blade element due to the rotation of the blade.

- ϕ : the sum of the twist angle (how the blade twists with respect to the radius) and the pitch angle (base angle to which the blade is fixed to the shaft).

V_t is computed based on the angular velocity ω (rad/s) and radius position r (m) as such : $V_t = \omega \cdot r$.

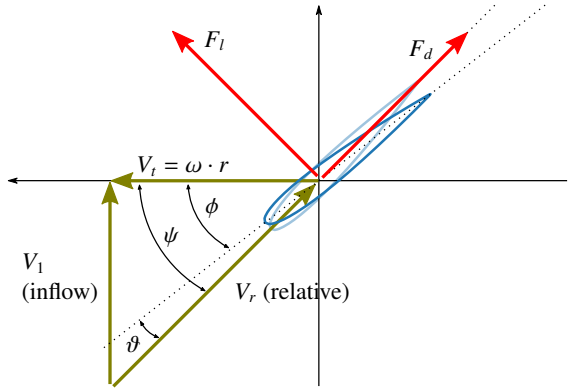

Figure 1: airfoil

The forces of each part of the three 1D-lines representing the blades, should now be redistributed on the coarse mesh. Most implementations use a 3D Gaussian sphere around a number of points along the actuator line. With this method, the resolution (spread of the Gaussian) is related to the number of points on the line, directly linked to the computational cost. With this technique, the resolution in the radial direction is not independent from the resolution around the blades.

Here, we proposes a 2D Gaussian in the direction normal to the radial direction. This has the benefit of the high radial resolution, without compromising on the computational cost. The 2D Gaussian is expressed in equation (3) :

$$f_{(x,y)} = \frac{1}{2\pi\sigma^2} e^{\left[0.5*\left(\frac{d_p}{\sigma}\right)^2\right]}, \tag{3}$$

with σ : spread of the Gaussian function, and d_p the shortest distance from the actuator line to any point in space.

The value of the spread σ can be expressed as a function of the mesh created for the wind turbine [3; 4].

$$\sigma = 2.5 \cdot l/n, \tag{4}$$

whith l : blade length, and n : number of GLL points along the blade.

Not spreading the forces in the radial direction results in a strong gradient of force at the tip of the blade, which can lead to numerical instability if the mesh is not refined enough in this region. To mitigate this issue, a tip spread can be applied to spread the forces at the end of the blade. This tip spread is

$$y = (1 - 1/(1 + np.exp(-slope_exp * (x - offset_exp)))) \tag{5}$$

References

[1] B. Hahn, Turbine size, http://windmonitor.iee.fraunhofer.de/windmonitor_en/3_Onshore/2_technik/4_anlagengroesse/, [Online; accessed 03-February-2022] (2022).

[2] Y.-T. Wu, F. Porté-Agel, Atmospheric turbulence effects on wind-turbine wakes: An LES study, Energies 5 (12) (2012) 5340–5362. doi:10.3390/en5125340.
URL https://doi.org/10.3390%2Fen5125340

[3] W. Jin, Numerical simulation of wind turbine wakes based on actuator line method in nek5000, Master's thesis, KTH Mechanics (1 2013).

[4] E. Kleusberg, Wind turbine simulations, Master's thesis, KTH Mechanics (5 2017).

[5] L. A. Martínez-Tossas, M. J. Churchfield, A. E. Yilmaz, H. Sarlak, P. L. Johnson, J. N. Sørensen, J. Meyers, C. Meneveau, Comparison of four large-eddy simulation research codes and effects of model coefficient and inflow turbulence in actuator-line-based wind turbine modeling, Journal of Renewable and Sustainable Energy 10 (3) (2018) 033301. doi:10.1063/1.5004710.
URL https://doi.org/10.1063%2F1.5004710

[6] M. Bastankhah, F. Porté-Agel, A new miniature wind turbine for wind tunnel experiments. part II: Wake structure and flow dynamics, Energies 10 (7) (2017) 923. doi:10.3390/en10070923.
URL https://doi.org/10.3390%2Fen10070923

[7] N. Coudou, P. Chatelain, L. Bricteux, J. van Beeck, Numerical and experimental investigations of the meandering phenomenon in wind turbine wakes, Ph.D. thesis, UCLouvain and UMons (2021).

[8] W. Munters, C. Meneveau, J. Meyers, Turbulent inflow precursor method with time-varying direction for large-eddy simulations and applications to wind farms, Boundary-Layer Meteorology 159 (2) (2016) 305–328. doi:10.1007/s10546-016-0127-z.
URL https://doi.org/10.1007%2Fs10546-016-0127-z

[9] F. Xiao, M. Dianat, J. J. McGuirk, An LES turbulent inflow generator using a recycling and rescaling method, Flow, Turbulence and Combustion 98 (3) (2016) 663–695. doi:10.1007/s10494-016-9778-6.
URL https://doi.org/10.1007%2Fs10494-016-9778-6

[10] Z.-T. Xie, I. P. Castro, Efficient generation of inflow conditions for large eddy simulation of street-scale flows, Flow, Turbulence and Combustion 81 (3) (2008) 449–470. doi:10.1007/s10494-008-9151-5.

URL https://doi.org/10.1007%2Fs10494-008-9151-5

[11] S. Buckingham, L. Koloszar, Y. Bartosiewicz, G. Winckelmans, Optimized temperature perturbation method to generate turbulent inflow conditions for les/dns simulations, Computers & Fluids 154. doi:10.1016/j.compfluid.2017.05.015.

Comparison of numerical results and experimental measures of airflow in a subway station

Loreline Faugier

Environmental and Applied Fluid Dynamics Department, von Karman Institute for Fluid Dynamics, Belgium, loreline.faugier@vki.ac.be

Supervisor: Delphine Laboureur

Associate Professor, Environmental and Applied Fluid Dynamics Department, von Karman Institute for Fluid Dynamics, Belgium, delphine.laboureur@vki.ac.be

University Supervisor: Walter Bosschaerts & Benoît G. Marinus

Professor, Department of Mechanical Engineering, Royal Military Academy, Belgium, walter.bosschaerts@rma.ac.be

Professor, Department of Mechanical Engineering, Royal Military Academy, Belgium, benoit.marinus@rma.ac.be

University Supervisor: Karim Limam

Professor, Laboratoire des Sciences de l'Ingénieur pour l'Environnement, Université de La Rochelle, France, klimam01@univ-lr.fr

Abstract

This study intends to predict numerically the train-induced wind affecting the climate of subway stations, and to validate these numerical predictions with field tests in an actual station. Elements of the literature mention various sources influencing airflow in the station; the piston wind is one of them, but the weather conditions, the presence of people on the platform, the general air circulation through the tunnel network are also likely to have an influence. Hence, experiments aim to verify of our modeling assumptions, so a validated model could finally be used to calculate different scenarios for trains and with different architectures to improve the comfort and safety of passengers.

One subway station is used as a test case to perform CFD simulations, where the ventilation is only realized by the piston effect caused by the train movement, that is computed numerically. A simplified geometry of the station is used to implement a scenario of a train passing through the station, with dynamic meshing techniques. Experimental measurements in the station, with a hot wire for the air velocity and a LiDAR laser for the metro distance, provide data that can be compared with the corresponding numerical simulation. The similarities and differences between the numerical and experimental results are finally discussed.

Keywords: subway climatology, train, piston effect, CFD, dynamic mesh, hot wire

1. Introduction

1.1. Context

The air quality inside underground public transportation infrastructures faces a growing interest, to maintain a safe and healthy environment for the daily millions of passengers travelling through the subway and transit workers. At rush hours, large numbers of people are brought together under potentially volatile conditions, that is, confined, overcrowded spaces, raising health concerns about the concentration of particulate matter emitted from train brakes or the friction of wheels on the rails, or transmission of infectious diseases communicable through close person-to-person contact, as listed by Gershon *et al.* [1]. Underground stations are also exposed to occasional fire hazard, in which case Modic stresses that smoke control through ventilation is a critical factor to save lives [2]. Recent events have also demonstrated the vulnerability of these indoor environments to possible terror-

ist attacks in the form of toxic chemicals release, such as the infamous Tokyo 1995 event that caused mass casualties [3]. Valuable instruments to study these different phenomenons are the identification and analysis of representative scenarios, allowing to better design and adapt our transportation infrastructures and the many services involved in their operation.

To tackle these topics, a comprehensive understanding of the airflow in subway stations is necessary. Subway station environment is peculiar in terms of climate, as part of the built environment that is open to overground climate and to the underground network formed by the tunnels and the stations. This duality, coupled with the high computational resources required to simulate numerically a moving object through a large domain, makes the elaboration of models a complex subject.

In addition, confidence in such models can only be achieved through coupling with experimental validation. The objective of the present research is therefore to obtain a validated numerical model for air movements in a subway station. The airflow, mainly related to trains passing through the station, is considered and simulated using Computational Fluid Dynamics (CFD) techniques, and the results are compared to the ones obtained through measurements in an actual metro station.

1.2. Previous works

1.2.1. Specificities of subway climate

As Pflitsch *et al.* [4] describe, tunnels and stations of a subway system are a very complex, vertically and horizontally expanding network that has multiple punctual connections to the surface. The air inside a subway station is therefore affected by multiple influences: the natural flows from the outside, the trains that travel at varying and relatively low speed through them and other anthropogenic patterns like passengers' movement and artificial ventilation... In the past three decades, various studies have hence investigated the question of airflow in subway stations.

In a Newcastle upon Tyne complex station, Pflitsch *et al.* [5] undertook measurements at night to assess the different contributions to airflow independently of train operation. With all fans off and doors closed, an airflow velocity of 0.5 m/s to 1.5 m/s was observed on the platforms. This phenomenon is called background airflow, in opposition to the train-induced flow which is observable for only one or two minutes after the passage of a train. Air behaviour in the station is also affected by several factors that differ with the station architecture: presence and operation of escalators, activation of mechanical ventilation, position of the station gates... Fortain [6] has also pointed out source discrimination as a limit to the measurement and modeling of particles in a Parisian subway station at night, including when a train is running. She was able to study independently the activation of the ventilation, the presence of people in the station and the passage of trains, but obtaining reproducible signals is a challenge.

Waymel [7] simulated the mass flow rates through different surfaces of a Parisian subway station after 5 passages of trains in two directions to evaluate thermal comfort of the passengers and found a periodicity related to the train passage frequency appearing in the results. A substantial work of particulate and gas concentration measurements in 10 stations in Barcelona was led by Moreno *et al.* [8], and evidenced the influence of train length, speed, tunnel length and station design on train-induced wind. Monitoring underground particulate concentration in a Parisian station during a week, Walther *et al.* [9] observed that the PM concentration follow closely the frequency of trains, highlighting piston effect and ventilation as key phenomena affecting the dilution mechanism of particles.

1.2.2. Piston effect and its numerical models

Most of the studies including train operation indeed agree on the fact that a major contribution to ventilation in subway stations is performed by the piston wind. This phenomenon appears when a train travels through a narrow tunnel, and the air pushed by the train cannot flow freely around the train as it would in open air; a positive pressure volume is formed at the front, while a negative pressure and highly turbulent region appears behind the train [10]. Those changing pressure differences between the front and back of the train on top of ambient wind cause flows with varying directions and intensities, that are represented schematically on Figure 1. The resulting flow velocities and pressures were monitored at the entrance and the exit of a scaled tunnel by Kim & Kim [11] to better understand the temporal aspect of piston effect. They observed that the pressure difference reaches a maximum when the train reaches its maximum speed. When the train speed stabilises, the pressure difference decreases before becoming constant.

To provide parameters allowing comparison between various cases, velocity can be made comparable using a velocity coefficient $u/u*$, where $u*$ is a reference velocity, in this case the maximum train velocity, *i.e.* the cruise speed of the train in the tunnel before

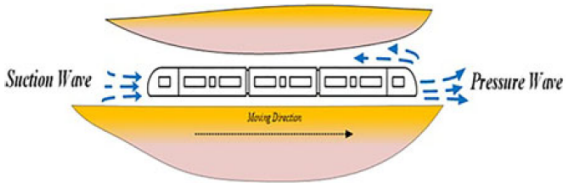

Figure 1: Schematic of airflow generated by the train movement (side view), from [12]

it brakes while arriving in the station. Out of the different parameters influencing the magnitude and the temporal evolution of the piston wind, the blockage ratio β can be used to compare tunnel and station design in a non-dimensional form. It describes the cross-sectional area covered by the train in the tunnel the with the following ratio :

$$\beta = \frac{A_{train}}{A_{tunnel}} \tag{1}$$

Cross *et al.* [13] for instance studied the influence of blockage ratio on tunnel outlet velocities. They observed that during acceleration and deceleration phases, higher blockage ratios translates into steeper and earlier variations in the velocities, and that the maximum attained velocity is higher. During the constant velocity phase, increasing blockage ratio from 0.65 to 0.85 results in an increase of 36% in the outlet velocity.

Through momentum balance equations, Brown [14] gave a developed expression for air velocity in open-air tunnels of different lengths, and calculated that the air velocity in the tunnel can reach about 3 m/s for a train running at 15 m/s speed in a double-track tunnel. Xue *et al.* [15] and Cross *et al.* [13], [10] have used dynamic meshing techniques in CFD models with incompressible Reynolds-averaged Navier-Stokes (RANS) equations to simulate the flow velocities induced by train passing through a station and in a tunnel, respectively. Cross *et al.* [13] validated their results using different versions of the small scale model designed by Kim & Kim [11], and Xue [15] compared the numerical models with flow velocities measurements near the exits – a staircase away from the platform – of a subway station in Shenyang and obtained maximal velocities of 0.8 to 1.4 m/s for a train entering the station at 20.68 m/s. Both obtained a very good agreement between the model and the experiments, but it is hard to draw a link between the studies, as they consider very different architectures.

Despite requiring high computational resources, numerical models allow to visualize and retrieve quantitative data about airflow conditions affecting passengers comfort, health and safety, such as the air velocity distribution on a line along the platform length [16], contaminant dispersion into the station [17] and best location for draught relief shafts [15]. These examples highlight the use of numerical models to study and predict phenomenons that would be impossible, costly or dangerous to observe in real life conditions.

1.2.3. Production of experimental data

In addition to those cited in the previous paragraph, various work include measures at different locations in subway station and their surroundings. Among others, Lin *et al.* [18] compared numerically computed air velocities with experimental results obtained with a hot bulb in the draught relief shafts above a station. Both results were in agreement and the influence of the piston effect on air exchange with the outside atmosphere was shown. To validate their simulations and study the influence of air curtains on piston effect, Khaleghi and Talaee [12] placed their fan-type anemometer probe in a corridor close to the station entrance, separated from the platform by an escalator. But while there has been thorough research concerning airflow in subway tunnels and in a subway station, to the best of the authors' knowledge, few studies offer a direct comparison of numerical and experimental results focusing on how the airflow is perceived by a passenger standing on the platform.

For some studies and depending on the factors of interest, several adaptations of normal operation and schedule of the subway station were made possible for on-site measurements: measurements at night ([19], [20], [21], [6], [5]) with presence of a group of people or of a train executing predefined scenarios ([6]), tracer gas release in the station ([19], [21], [5]) and in the train ([19]), activation or deactivation of mechanical ventilation ([5], [8]), opening or closing the relief shafts ([15]) or the station's gates ([5])... However, the cost of these measures in terms of coordination with public services, staff involved, compliance to procedures, etc, is generally high, and the site is usually available only for a very limited time period. Depending on the case, a limited number of parameters can be controlled, or not, affecting the reproducibility of the results obtained. Since the measurements are always taking place in an already built infrastructure, Pflitsch *et al.* [5] underlined that additional and extensive measurements are needed to account for the

great diversity of architectures and the different factors affecting subway climate. To obtain a comprehensive understanding of airflow in subway underground networks, in situ measurement data are finally useful resource to challenge and validate the numerical models.

2. Methodology

For this study, one metro station in a Belgian major city is taken as a test case. In this parallelepipedic station, there are no corridors, just straight staircases to the outside, and the ventilation is only realized by the piston effect caused by the train movements and temperature-gradient induced wind. The architecture of the station including a part of the tunnel on both sides – 150 m upstream and 100 m downstream – is implemented in a two-dimensional (2D) numerical model (Figure 3). After determinating the appropriate boundary conditions, a transient fluid dynamics simulation with RANS equations is used to model the airflow in the station related to a train arriving, stopping and departing. Validation of the numerical results is sought through experimental measurements of air velocity in the actual metro station.

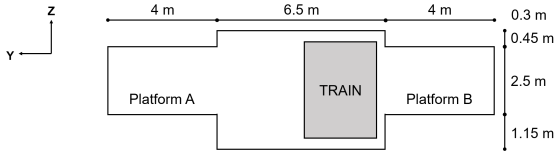

Figure 2: Cross-section of the station geometry

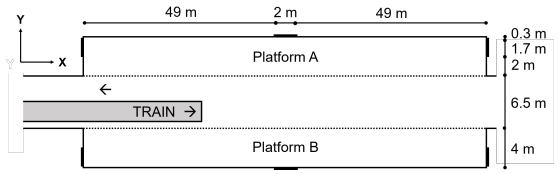

Figure 3: Top view of the station geometry

2.1. Test case

The station is 100 m long and symmetrical with respect to the double-track rails, including one platform on each direction of the metro line, arbitrarily named A and B and forming a cross-shaped cross section detailed in Figure 2. Six exits, three on each side, are separated from the outdoor pressure by a straight staircase. In the vicinity of the station, the tunnels are 4.1 m high and 6.5 m wide on both sides. The train is 90 m long and has a rectangular cross-section of 3.5 m in height and 2.7 m in width. These dimensions give a blockage ratio of 0.35 and 0.20 for the train in the tunnel and in station, respectively. The train speed in the tunnel and at the arrival in the station is 10 m/s, and the corresponding Reynolds number based on the hydraulic diameter of the train in the tunnel is in the order of 10^7.

The base scenario taken for the study is the one of a subway train, arriving at a constant speed of 10.1 m/s through the tunnel. The deceleration is a third order polynomial fitted through the average on-site laser distance measurement (see Section 4.1), as well as the stop duration in the station that lasts 30 seconds. The train is then accelerated at 1.05 m/s^2 for 9.75 seconds, computed from the observed departure time of the train, to reach its cruising speed of 10 m/s when exiting the station.

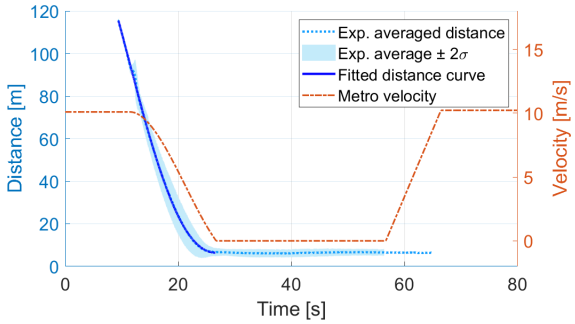

Figure 4: Averaged measured distance with fitted curve and schedule of train run through the station for the UDF

The train is initially positioned in the tunnel, with the front of the train 107 m from the station entrance, i.e the tunnel exit portal. The final position of the train is with the rear of the train 110 m from the station exit, when the train reaches the boundary of the numerical domain. The total travel time and distance are 79.5 s and 253 m, respectively.

2.2. Modeling assumptions

Sections 1.2.1 and 1.2.2 have underlined that on a timescale in the order of a minute, piston wind is the primary force of the airflow from the tunnel, and the turbulence induced on the platform is transient and complex [15]. Therefore, some simplifying assumptions must be made for quantitative analysis:

– In this article, we only evaluate a case where a train is running in one direction of the double-

track tunnel and station at a time, and there is no train arriving or departing in the other direction. This results in two scenarios being studied; the case with a train running on the side of Platform A (resp. Platform B) is called 'A only' (resp. 'B only').

– The train movement is considered to be the only factor affecting the flow field of the station, with background airflow being already present. In most studies indeed, the influences of mechanical ventilation [15], pedestrian behavior or the effect of heating due to people [22] are not considered. The impact of these effects are deemed of lower magnitude than the train-induced airflow, and it is expected that taking a sufficient number of measurements will make these short-term, temporary and irregular phenomena fade in the average.

– A simplified geometry is adopted for the numerical model: structures and objects are removed for similar reasons as those given in the previous point, allowing not only to simplify the meshing process and to decrease the computational power required, but also to make the results more easily comparable to literature and to other station architectures.

Interesting quantities to monitor are the air velocity at given points in the station, at which the experimental measurements are performed.

3. CFD model

3.1. Preliminary study: tunnel length

The measured velocities shown later in Section 4.2 (see Figure 8) will make clear that the flow in the station is already affected several seconds before the train reaches the station entrance. In addition in the CFD model, as the train starts at its beginning position, all of the air surrounding it is stationary, while in reality the airflow around the body would be completely developed as the train has been travelling long enough through the tunnel. The numerical domain far-field limits – in our case, the upstream tunnel length – necessary to ensure a boundary independent solution should hence be studied.

3D numerical simulations of a train travelling through a 1 km long tunnel with varying dimensions (blockage ratios of 0.30, 0.37 and 0.46) and train speeds (from 3.85 m/s to 20.68 m/s), have been conducted in a previously published paper [23]. For all configurations, 30 m of travel through the tunnel were found sufficient to achieve a fully developed flow around the moving train at constant speed. To allow taking into account the effect of piston wind on the platform before the train reaches the station, 200 meters of tunnel upstream and downstream are included in the numerical model of the station.

3.2. Station model

The station architecture described in Section 2.1 is reproduced numerically in a 2D model using a Computer Aided Design (CAD) software. The internal domain of the station is meshed using the integrated mesher of ANSYS Workbench (2020 R2) and solved using the commercial CFD software ANSYS Fluent (2020 R2).

The main meshing features are visible in Figure 5. 175 000 triangular elements were used to capture the geometrical details and allow more flexibility, especially as the train moves through the domain. The cell size in the station is limited to 0.5 m. To better approximate physical results, an area with a cell size of 0.1 m was defined around the tunnel, station and train walls, and an inflation layer was created around these walls with a total thickness of 0.05 m. The enclosure around the train aims to preserve the mesh quality along the train motion; the smaller cells concentrated around the train can provide sufficient resolution in these regions and larger cells located far from the train will to improve computational efficiency [13].

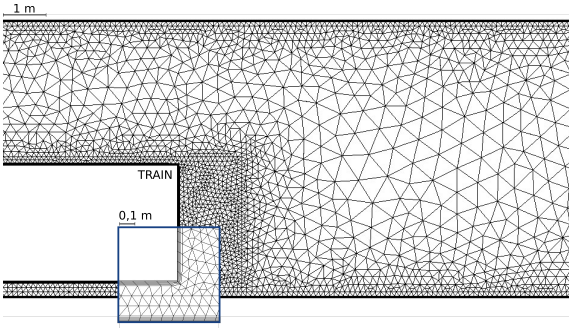

Figure 5: Section of the 2D mesh at t = 0s

The dynamic mesh approach used in this model is similar to Cross' [13], [10] and Xue's [15] ones. The train movement through the station, including deceleration, stop, and acceleration as detailed in Section 2.1 and shown in Figure 4 is controlled by an User-Defined Function (UDF). As the train moves, the fluid calculation area delimited by the station walls and the

train car boundaries changes. The mesh is hence updated by Fluent at each time step of the train motion. In order to permit a correct remeshing process, the displacement of the train between consecutive time steps should not exceed the mesh cell dimensions; a time step of 0.001 seconds is found to be sufficient while the train is moving.

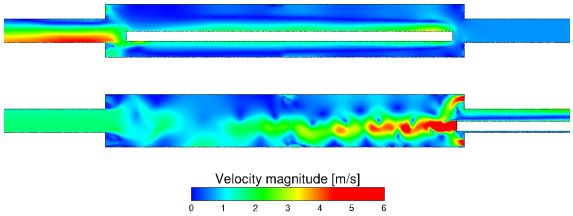

Figure 6: Contours of air velocity in the station at (up) t = 25.5s and (down) t = 68.5s

The airflow is simulated with mass conservation and RANS equations for incompressible, transient flow. The six exits and the tunnel extremities are set to atmospheric pressure inlets/outlets. The k-ε turbulence model is chosen for this high Reynolds number flow, and as it was previously used for the simulation of train-induced airflow where it performed well [11], [15]. The fine near-wall mesh allows to keep mostly $y^+ < 5$ in the laminar regions for the walls far for the subway train; in the more turbulent regions closer to the train, we aim for $30 < y^+ < 300$. To account for this variability and as we are not interested in resolving the flow very close to the wall, the enhanced wall treatment is used. The continuity, momentum, k and ε residual equations are monitored. Additionally, the velocity at various points on the platform is recorded, for later comparison with the experimental measurement points. The symmetry of the station respectively to the train tracks allows, with one simulation, to obtain results for both 'A only' and 'B only' scenarios. Simulating 80 seconds took 10 days, using 80 *Intel Xeon-Gold 6148 (2.4GHz/20 Cores)* cores. The velocity contours of the air into the station as the train ends its arrival phase is available in Figure 6. Detailed results for selected locations will be provided and discussed in Section 5.1.

4. On-site velocity measurements

4.1. Experimental setup

Air velocity measurements, detailed in this section, have been conducted in the station using a hot wire anemometer through a 9-days campaign, equally divided in blocks of 3 days (Tuesday to Thursday) over the course of 3 weeks, at various locations on Platform B as visible on Figure 7, with each measurement day corresponding to a different location. The hot wire (*ComfortSense Mini 54N95* combined with the *54T33* draught prob and a protective cage) was mounted on a wheeled cart and stood approximately 50 centimeters above the platform floor. Different features described below were added to the setup to ensure a certain level of repeatability.

Airflow data is only useful if linked to the train's position in the station. For this aim, 3 short-range HC-SR04 ultrasonic distance sensors on each side (6 in total) were placed along the tracks: one in the tunnel, 100 m upstream the station entrance. The sensors were set with a threshold to record a binary data (presence of train/absence of train), serving as triggers to start the data recording and to detect the defining moments of the train course through the station: 'train approaching station', 'train entering station', 'train leaving', 'train has left'. Additionally, on Platform B side, a LiDAR laser measured the distance between the front of the train from the exit side of the station, allowing precise distance measurements on the whole length of the station.

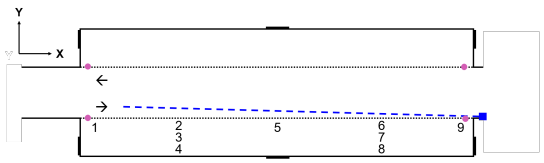

Figure 7: Schematic experimental setup: measurement positions (1 to 9), trigger sensors (pink), and LiDAR laser (blue)

As measurements were taking place during daytime, a condition for the whole setup was that it should absolutely not disturb the train operation or affect the safety of passengers and workers. The measurements probes should hence be kept of a reasonable size and away from the train doors when stopped in the station; cables on the platform were avoided when possible and most of the data was transmitted using HC-12 wireless communication modules and Arduino UNO microcontrollers.

Statistically, it was desired to reach at least 30 measurements per scenario to form sufficiently accurate average velocity curves. Limited time in the station and the subway train's schedule did not allow to achieve this value for Position 1 and Position 4 where

only 11 to 13 datasets per scenario were recorded. On the days corresponding to Positions 4 to 9, the air velocity was recorded several times per day when no train was running, with the aim to account for the background airflow.

4.2. Experimental results

4.2.1. Velocity measurements

The two events 'A only' and 'B only' as described in Section 2.2 were recorded separately. Figure 8 show the raw velocity data for each recording of Position 5 for the 'B only' scenario, along with the distance measured by the laser and the triggers.

To keep the simulation as close as possible from the actual train movement, the averaged distance curve served as an input for the UDF controlling the numerical train velocity (see Section 2.1).

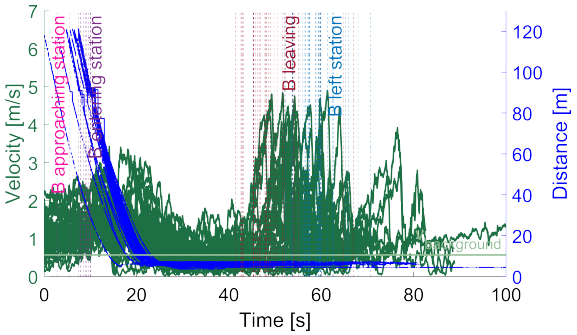

Figure 8: Raw velocity and distance measurements for Position 5 - B only

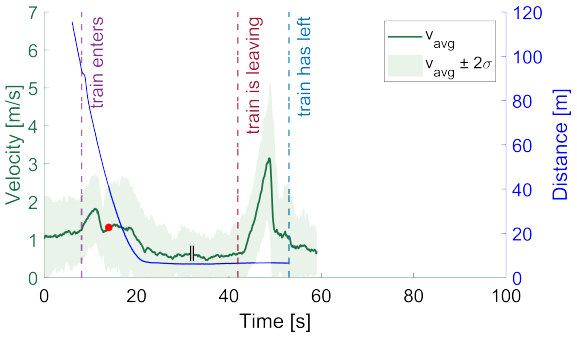

Figure 9: Averaged velocity and distance curves for Position 5 - B only

The velocity results are ensemble averaged based on the activation and deactivation of the trigger sensors for each measurement side: firstly, all the curves were aligned using the 'train enters' trigger, which was necessary as the measurements started at various times throughout the campaign and the train cruise speed could differ. The time a train remained in the station was also varying; as the velocity data was sufficiently constant when the trains remained stopped, part of the stopping time was omitted to align the different curves also on the 'train has left' side. The processed curve corresponding to the raw curves is given in Figure 9.

The average curve is also cut at the end to maintain a sufficient number of measurements to compute a representative average, and it was completed with two corresponding standard deviations (2σ) for a confidence level of 95%. Measurements for additional locations and scenarios are available in Section 5, along with an analysis regarding their correct representation of the station airflow.

4.2.2. Background airflow

Although background airflow was not implemented in the numerical analysis, it was present in the experimental data. To compare both results, an understanding of this phenomenon was essential. Figure 10 shows the average background results measured inside the station, that are also presented with the 95% confidence interval.

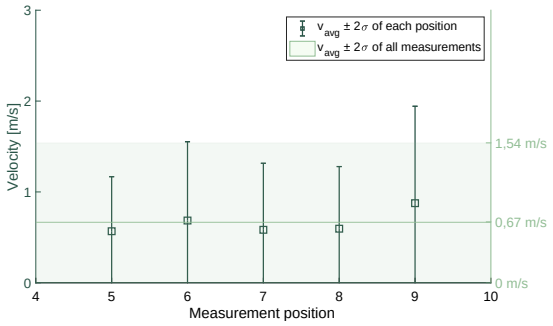

Figure 10: Average background velocity with corresponding two standard deviations

Variations can be attributed to different conditions regarding pressure, temperature and wind velocity, outside the station and in the global underground network. Although the magnitudes are in agreement with the values found by Pflitsch [5] mentioned in Section 1.2.1, the spatially and temporally transient characteristics of this airflow resulted in large variations over the measurements, and the real influence of the background airflow in the experimental results was therefore difficult to distinguish. Additionally, at low flow velocities, the effects of natural convection of heat of

the wire introduce errors in the calibration, and the uncertainties should be red with the measurements.

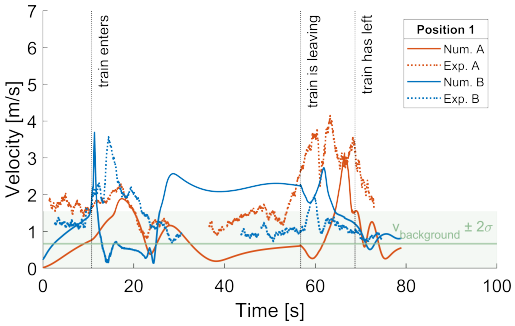

Figure 11: Comparison of airflow velocities at Position 1 for A only and B only

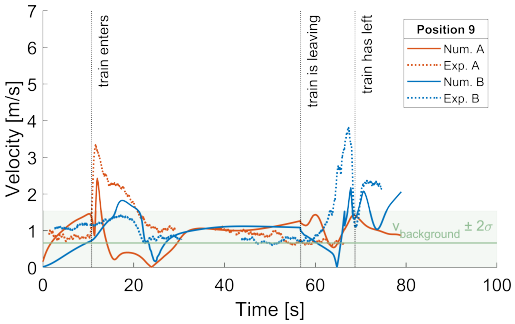

Figure 12: Comparison of airflow velocities at Position 9 for A only and B only

5. Results and discussion

5.1. CFD versus experimental comparison

Figures 11 and 12 visualise the numerically and experimentally obtained velocities at the two extremities of the platform, *i.e.* Positions 1 and 9. Although not in perfect agreement, the general tendency of velocity was clearly visible: first of all, a spike in airflow velocity was observed when a train entered the station. Secondly, non-zero velocities were recorded at standstill for both simulations and on site measurements. Lastly, when a train accelerated, a second peak was formed. The observation of both peaks demonstrated the mechanism of the piston effect.

Although an evident pattern was detected, a few characteristics differed between numerical and experimental results. For all curves, that the timing of both curves were dissimilar as the numerical results seem

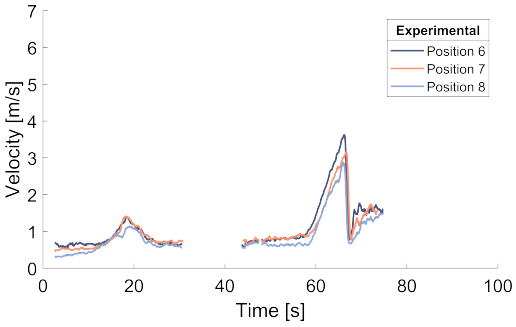

Figure 13: Comparison of experimental airflow velocities at Position 6, 7 and 8 for B only

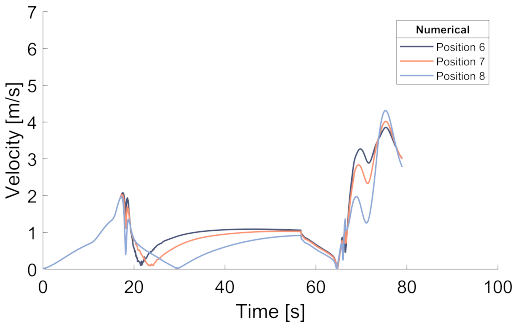

Figure 14: Comparison of numerical airflow velocities at Position 6, 7 and 8 for B only

to be horizontally shifted to the right compared to the experimental average curve.

Besides, in the case of Position 1 for the 'B only', the velocity magnitude during the stop time of the train is clearly out the confidence interval; and for all the numerical curves, the velocity magnitude remains non-negligible during this period even though the background airflow was not simulated. This difference could be explained by the fact that experimentally, the domain of the station exhibits a porosity that does not exist in the numerically. As a consequence, the flows caused by the train keep circulating in the numerical domain, when in reality they have left the station.

5.2. Flow observations

Despite these differences, several qualitative observations can be made based on both numerical and experimental results from Figures 11 and 12.

At Position 1, for the 'A only' scenario, the magnitude of the first peak (for which the measurement point is passed as the train almost reaches its stop position) is clearly smaller compared to the second peak;

whereas for the 'B only' scenario, the first peak (for which the measurement point is passed as the train just entered the station, hence at a higher speed) is larger than the second peak. For Position 9, the opposite happens. This behaviour could be attributed to several effects. Firstly, as explained in Section 1.2.2, Kim and Kim [11] determined that the most extreme pressure difference around a train occurs when a train reached its maximum traveling speed. As the train accelerates while leaving the station, this could result in higher airflow velocities. Secondly, it has also been demonstrated that the piston effect becomes more prominent when the blockage ratio increases [23]. This caused the airflow velocities to increase as well. When a train leaves the station, β increases as the cross-sectional area of the tunnel is smaller than the cross-sectional area of the station. The opposite for the blockage ratio was true when a train entered the station. And lastly, as large turbulent vortices were present behind a train, these provided more mixing of the air and allowed higher velocities to reach the hot wire anemometer, as visible on the velocity contours on Figure 6, and in a detailed view in Figure 15.

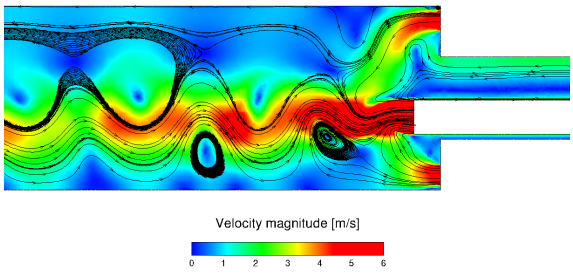

Figure 15: Contours of air velocity and streamtraces in the back of the train at t = 68.5s

Other interesting data to compare are the velocities at the same location on the X axis, but with different distances from the platform wall. For example, Positions 6, 7 and 8 were experimentally and numerically compared in Figures 13 and 14. Both confirmed the reduction of airflow velocity while approaching the wall; similarly, it can also be observed that velocities for 'A only' cases are generally of lower magnitude than for 'B only' cases. This can be attributed to air taking the fastest route from high to low pressure regions. In addition, the velocity difference between the wall and train causes a decreasing velocity profile due to shear stress between airflow layers.

A closer comparison of Figure 6 and of the velocity curves of Figure 12 at the corresponding time demonstrates a sudden drop in airflow when the front or the rear end of the train passed the measurement position. This event, observable for the measurement locations closer from the train exit on both sides, can be explained by the piston effect causing the airflow to change direction. Although the data was not recorded for a sufficiently long time after the train has left the station, it would have been interesting to observe the turbulent effects of the airflow in the station after the train has left the station by measuring for a longer period of time, and if necessary, to extend the length of the tunnel after the station in the simulation.

6. Conclusion

Although the numerical and experimental data were not an exact match, the numerical results lie in the statistical distribution of the experimental results, and can hence be considered as a plausible realization of the flow following the passage of a train in the subway station. Several flow features typical of piston effect could be observed in the station both in the numerical and experimental results:

- a higher velocity magnitude between the observed peaks, that can be correlated with the speed of the train when moving close to the measurement position;
- a decreasing velocity magnitude when measuring moving away from the train;
- abruptly changing magnitudes when the train extremities are passing the measurement location.

To understand fully the different phenomenons related to the passage of trains in a subway station, the continuation of this research could include the study of scenarios with one train arriving on one side as another train is stopped on the other side, as the presence of two trains at the same time in the station will further increase the blockage ratio, and is expected to produce airflows of significantly different intensities. The simulation of the same scenarios in 3D is also necessary to understand better the flow circulation all around the station and to gain knowledge about the wind movements on the platform, especially around the height of a standing person.

Study of different station shapes and architectures would permit the elaboration of reliable models for subway station, and support decision-making to build and adapt fire and contaminant detection systems or

the ventilation system for instance, helping to improve subway networks systems and affecting the overall quality of life of urban communities.

Acknowledgments

The authors would like to acknowledge Isabeau Sabbe and Joren Vanlaere, students from the Vrije Universiteit Brussel, Belgium, for helping to design and conduct the experimental campaign and for their contribution to the CFD model and to the elaboration of graphs in their outstanding master thesis.

References

[1] R. R. M. Gershon, K. A. Qureshi, M. A. Barrera, M. J. Erwin, and F. Goldsmith, Health and Safety Hazards Associated with Subways: A Review, Journal of Urban Health 81 (1).

[2] J. Modic, Fire simulation in road tunnels, Tunnelling and Underground Space Technology 18 (2003) 525–530.

[3] A. T. Tu, Chemical Terrorism: Horrors in Tokyo Subway and in Matsumoto City, Alaken, Inc., 2002.

[4] A. Pflitsch, H. Küsel, C. Storz and M. Brüne, Spatial variability and dynamic changes in air temperature distribution within different subway stations, in: Proceedings of the 15th Conference on Biometeorology/Aerobiology and 16th International Congress of Biometeorology, 2002.

[5] A. Pflitsch , M. Brüne , B. Steiling, M. Killing-Heinze , B. Agnew, M. Irving and J. Lockhart, Air flow measurements in the underground section of a UK light rail system, Applied Thermal Engineering 32 (2012) 22–30.

[6] A. Fortain, Caractérisation des particules en gares souterraines, Ph.D. thesis, Université de La Rochelle (2010).

[7] F. Waymel, Modélisation des effets thermiques et aérauliques dans les stations de métro, Ph.D. thesis, Université de Valenciennes et du Hainaut Cambrésis (2002).

[8] T. Moreno, N. Pérez, C. Reche, V. Martins, E. de Miguel, M. Capdevila, S. Centelles, M.C. Minguillón, F. Amato, A. Alastuey, X. Querol and W. Gibbons, Subway platform air quality: Assessing the influences of tunnel ventilation, train piston effect and station design, Atmospheric Environment 92 (2014) 461–468.

[9] E. Walther and M. Bogdan, A novel approach for the modelling of air quality dynamics in underground railway stations, Transportation Research Part D: Transport and Environment 56 (2017) 33–42.

[10] D. Cross, B. Hughes, D. Ingham and L. Ma, Enhancing the piston effect in underground railway tunnels, Tunnelling and Underground Space Technology 61 (2017) 71–81.

[11] J. Y. Kim and K. Y. Kim, Experimental and numerical analyses of train-induced unsteady tunnel flow in subway, Tunneling and Underground Space Technology 22 (2) (2007) 166–172.

[12] M. Khaleghi and M. R. Talaee, Analysis of unsteady airflow in a subway station influenced by train movement, Science and Technology for the Built Environment 26 (2) (2019) 210–218.

[13] D. Cross, B. Hughes, D. Ingham and L. Ma, A validated numerical investigation of the effects of high blockage ratio and train and tunnel length upon underground railway aerodynamics, Journal of Wind Engineering and Industrial Aerodynamics 146 (2015) 195–206.

[14] W. G. Brown, Basic theory of rapid transit-tunnel ventilation, in: IEEE Railroad Conference Proceedings, Pittsburgh, 1965.

[15] P. Xue, S. You, J. Chao and T. Ye, Numerical investigation of unsteady airflow in subway influenced by piston effect based on dynamic mesh, Tunnelling and Underground Space Technology 40 (2014) 195–206.

[16] l. Jia, P. Huand and L. Yang, Numerical simulation of flow characteristics in a subway station, Heat Transfer–Asian Research 38 (5) (2009) 275–283.

[17] F. E. Camelli, G. Byrne, R. Löhner, Modeling subway air flow using CFD, Tunnelling and Underground Space Technology 43 (2014) 20–31.

[18] C.-J. Lin, Y. K. Chuah, C.-W. Liu, A study on underground tunnel ventilation for piston effects influenced by draught relief shaft in subway system, Applied Thermal Engineering 28 (2008) 372–379.

[19] M. Brüne, J. Spiegel, K. Potje-Kamloth, C. Stein and A. Pflitsch, Tracer gas experiments in subways using an integrated measuring and analysis system for sulfur hexafluoride, Journal of Sensors and Sensor Systems 5 (2016) 381–388.

[20] A. Pflitsch , M. Brüne , M. Killing-Heinze , J. Ringeis , B. Agnew and B. Steiling, Natural Ventilation as a Factor Controlling the Dispersal of Airborne Toxins in Subway Systems in a Disaster Situation, Journal of Transportation Safety & Security 5 (1) (2013) 78–92.

[21] J. Charlton and M. Brune, Towards a dynamic evacuation system: developing methodologies to simulate the evacuation capabilities of subway stations in response to a terrorist attack with CBRNE weapons, in: Proceedings of the 32nd eCAADe Conference, Newcastle upon Tyne, 2009, pp. 109–118.

[22] M. Endregard, B. A. P. Reif, T. Vik and O. Busmundrud, Consequence assessment of indoor dispersion of sarin – A hypothetical scenario, Journal of Hazardous Materials 176 (2010) 381–388.

[23] L. Faugier, B. G. Marinus, W. Bosschaerts, D. Laboureur and K. Limam, CFD model to assess parameters influencing piston wind in a subway tunnel and station, Journal of Physics: Conference Series 2042 (2021) 012076.

Multiscale wake modeling and performance assessment of the modified Vestas V27 wind turbine under neutral ABL conditions: a validation study

Baris Kale

Environmental and Applied Fluid Dynamics Department, von Karman Institute for Fluid Dynamics, Belgium, baris.kale@vki.ac.be

Advisor: Sophia Buckingham

Senior Research Engineer, Environmental and Applied Fluid Dynamics Department, von Karman Institute for Fluid Dynamics, Belgium, sophia.buckingham@vki.ac.be

Supervisor: Jeroen van Beeck

Professor, Environmental and Applied Fluid Dynamics Department, von Karman Institute for Fluid Dynamics, Belgium, vanbeeck@vki.ac.be

University Supervisor: Alvaro Cuerva Tejero

Professor, Aerospace Engineering, Universidad Politécnica de Madrid, Spain, alvaro.cuerva@upm.es

Abstract

A validation study under neutrally-stratified atmospheric boundary layer was carried out using a previously implemented generalized actuator disk model (GAD) into an open-source numerical weather prediction code (i.e., the Weather Research and Forecasting (WRF) model) in order to perform high spatial resolution microscale simulations of atmospheric flows. Large-eddy simulation (LES) is performed to resolve energy-containing eddies of turbulent motions and the GAD model is used to calculate turbine-induced forces distributed over the rotor disk (e.g., thrust, lift and drag). To validate the GAD model, the neutral benchmark in the SWiFT test campaign was chosen for evaluation of the GAD model performance in terms of wake formation and wind turbine response. Weather data is available from a 60 m meteorological tower located 65 m upstream of the turbine, aerodynamic data and downstream wake profiles are available for the Vestas V27 wind turbine thanks to DTU's nacelle-mounted SpinnerLidar [1]. The nonlinear backscatter and anisotropy (NBA) subfilter-scale turbulence closure was chosen for the idealized simulations of the GAD. The surface boundary conditions were specified using the Monin-Obukhov similarity theory and periodic lateral boundary conditions were prescribed for the outer domain. Coarser LES domain was run 15 h to spin-up turbulence consistent with the geostrophic wind, and surface kinematic heat flux of $H_s \approx 2.15$ W m^{-2}. The inner LES domain with the actuator disk was turned on at the beginning of 15 h and was run for 70 minutes.

Keywords: Weather Research and Forecasting model, actuator disk model, large-eddy simulation, SWiFT

1. Introduction

A clean energy revolution is taking place today. Therefore wind energy is of crucial importance as it is one of the free, sustainable, and readily available renewable energy sources worldwide. To capture the wind's power, wind turbines are deployed as clusters within large wind farms; however, turbine wakes developed in the lower part of the atmospheric boundary layer (ABL) are generally affected by momentum exchange, dependent on atmospheric stability. The reduction in wind speed and increased turbulence intensity can significantly influence wind turbine power output, wake velocity deficit, and recovery rate. Past studies have revealed that, at low wind speeds and low turbulence intensities, the wake behind the turbine is often recovered beyond ten rotor diameters. In contrast, in some instances, depending on the atmospheric stability, wake effects can be significant beyond these distances for large turbines [2]. Such issues should be

considered when modeling wind turbine wakes with high-fidelity numerical tools for better wind turbine design, siting, and estimation of transient mechanical loading and power output [3; 4; 5; 6].

The effects of atmospheric stability on wake propagation and wind turbine performance have been widely studied in wind tunnel measurements [7; 8; 9; 10] and field experiments [11; 12; 13; 14]. Wind tunnel experiments and field measurements revealed that the horizontal velocity profiles have a Gaussian-like shape, while vertical profiles are influenced by boundary layer shear. Thermal stratification affects the mean velocity profile in the ABL and the intensity and structure of the turbulence [15]. During daytime conditions for on-shore locations, i.e., unstable or convective conditions typically occur when the ground is hotter than the surrounding air, wind turbine wake attenuates rapidly and begins to meander due to the presence of energy-containing large eddies (i.e., buoyancy forces dominate shear forces). In night-time conditions, i.e., stable conditions typically occur when the ground is radiatively cooler than the air above, the depth of the ABL is shallower than in convective conditions due to the existence of high mechanical turbulence that results in cooling of the surface (i.e., shear forces dominate buoyancy forces), the wake can stretch for much greater downstream distances.

The increase in computational power in the last decades allows for analyzing the interaction between atmospheric turbulence and wakes by utilizing engineering computational fluid dynamics (CFD) tools or numerical weather prediction (NWP) models. However, due to a lack in representing critical atmospheric processes, including cloud formation, solar and terrestrial radiation, and heat transfer between the surface and the atmosphere, NWP models (e.g., the Weather Research and Forecasting (WRF) [16]) are usually favored. The accurate modeling of ABL flow and its interaction with an isolated wind turbine or a set of clustered wind turbines within a large wind farm depends on the proper representation of atmospheric conditions and the correct parameterization of wind turbine dynamics. Mesoscale weather prediction models, which are based on the eddy diffusivity concept and are used to simulate large turbulent structures occurring in atmospheric events, cannot explicitly resolve turbulent transport of momentum and heat and are not capable enough to capture turbine-induced wakes due to their limited spatial and temporal resolutions. One-dimensional parameterizations can represent basic processes occurring in the ABL but do not give information about the small-scale turbulence processes that are important in wind turbine modeling [4]. Moreover, incorporating the mesoscale input into more minor scales, i.e., providing the realistic initial and boundary conditions to microscale models, improves the simulation quality of resolved atmospheric turbulence and flow-turbine interaction.. The turbulence scales of the ABL are of $O(10^3$ m) and $O(10^2$ s), while the length scales in the turbulent boundary layer on the surface of the turbine blades are of $O(10^{-6}$ m) corresponding to the eddy turn-over time scale of $O(1$ s) [17; 18].

Modeling atmospheric turbulence is usually challenging due to the multi-scale nature of the ABL. In general, the mesoscale-microscale coupling is applied to account for these different scales in numerical simulations [19; 17; 20]. However, coupling brings about new challenges such as turbulence downscaling, differences in numerical methods, domain configurations, and sub-filter modeling. Among many techniques used to study wind turbine wakes in smaller scales, large-eddy simulation (LES) is broadly used among researchers [21; 22; 23] since it is more precise than the Reynolds-averaged Navier-Stokes (RANS) simulations [24; 25].

Recent studies on wind energy applications have demonstrated the advantages of LES that permit the accurate reproduction of temporal and spatial turbulence scales in the ABL when performing microscale simulations [4; 5; 26; 6]. Although large-scale turbulent eddies are resolved in large-eddy simulations, the accuracy of LES in atmospheric flow simulations of wind energy applications depends on the parameterization of subfilter-scale (SFS) turbulent stresses and fluxes as well as turbine-induced forces [27; 23]. On the other hand, because the computational cost of a fully-resolved flow field around a wind turbine, including the shed vortices in the wake, is still too expensive since such simulations require too many computational grid points, an appropriate wind turbine parameterization is necessary to represent the forces induced by wind turbines in ABL flows. The earliest and most common approach is the actuator disk model (ADM). A uniform aerodynamic force computed in the vicinity of the wind turbine rotor is smoothed onto the computational grid [28; 21; 22]. However, the resulting force acts only in the axial direction, not including a rotational component. ADM is generalized to overcome such an issue by using the blade-element theory [29] to calculate the lift and drag forces from two-dimensional aerodynamic characteristics using tabulated data of a specific wind turbine and smear them on the rotor disk [22]. It will later

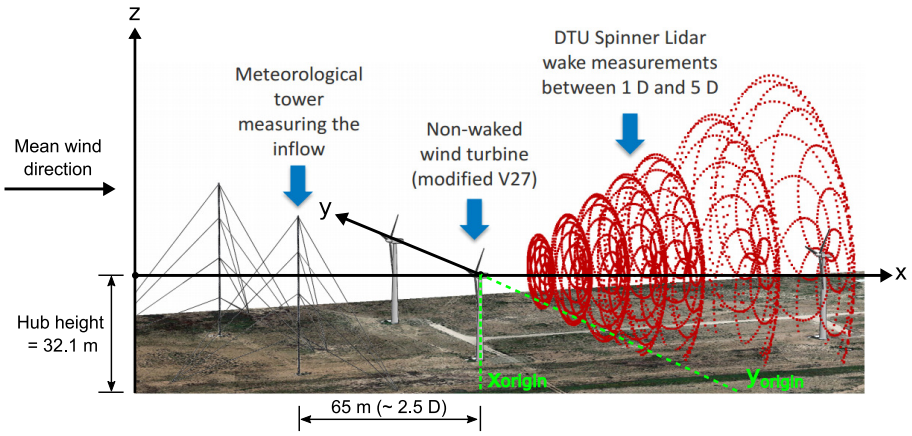

Figure 1: The schematic of the SWiFT facility shows the three V27 wind turbines, the meteorological towers located south of the wind turbines, and one of the DTU SpinnerLidar scanning strategies used for the SWiFT benchmarks (scanning towards the north) [30].

be referred to as the generalized actuator disk (GAD) model.

This work is dedicated to studying how aerodynamic performance and wake are affected for an individual wind turbine operating under a neutrally-stratified atmospheric boundary layer affects aerodynamic performance and wake formation. Specifically, we analyze how neutral ABL conditions affect the turbine's power output. This is achieved by performing a large-eddy simulation in the WRF-LES framework that utilizes the generalized actuator disk model to parameterize the turbine-induced forces (hereinafter referred to as WRF-LES-GAD). Section 2 describes the methodology of the current work, starting from the field campaign, available data, and case studies. After that, it is followed by providing simulation details. Numerical predictions are analyzed and validated by comparing with an upstream meteorological tower, a nacelle-mounted SpinnerLidar [1] and available other LES results reported in [30]. Section 3 presents and discusses the LES results obtained in the given cases. Finally, a summary and conclusions are provided in Sec. 4. Details of the turbulence closure scheme is provided in 2.3.

2. Methodology

2.1. Overview of the SWiFT facility

Sandia National Laboratories' Scaled Wind Farm Technology (SWiFT) facility located in Lubbock, Texas, USA [30], provides the researchers an opportunity to validate their numerical simulations in complex turbulent flows such as wind turbine wakes under varying thermal stratification. Because the SWiFT site is located in flat terrain and is therefore exempt from complex terrain effects (e.g., homogeneous surface cover), atmospheric stability effects become the main driver in the absence of weather phenomena. Although there are three horizontal axis wind turbines at the test site, that are modified versions of Vestas V27, which are variable-speed and variable-pitch turbines, and have a rotor diameter of D = 27 m and hub-height of z_{hub} = 32.1 m, because only one was equipped with a nacelle-mounted lidar, the measurements were performed on this specific turbine (the southeastern turbine in Fig. 1). During the measurement campaign, the others were shut down. The geographical location of the wind turbine is: 33.60795° N, 102.04862° W, and the elevation of the wind turbine base is 1018.0 m.

The inflow measurements to the turbine were collected with a 60 m meteorological mast (hereinafter referred to as met mast) located at 65 m upstream of the turbine when winds come from the south, and wake profiles were scanned toward the north using the Technical University of Denmark (DTU) spinnerLidar [1]. The met tower has sonic and cup anemometers located at heights of 10 m, 18 m, 32 m, 45 m, 58 m, and 18 m, 31.5 m, and 45 m above the ground, respectively. To characterize the atmospheric stability at the site, two barometric pressure sensors, three relative humidity sensors, and three air temperature sensors located between 2.5 m and 56.5 m above the ground were also utilized. All quantities were computed every 10 minutes and sampled at a frequency of 1 Hz: six 10-minute periods for neutral case. Ensemble averages that consider the 10-minute periods

Table 1: Ensemble averages defined for the near-neutral benchmark.

Benchmark	$\overline{U}_\infty$ [m s^{-1}]	$TI = \sigma_u/\overline{U}_\infty$ [%]	$\zeta = z/L$ [-]	u_* [m s^{-1}]	$Q_s = (\overline{w'\theta'_v})_s$ [K m s^{-1}]	z_0 [m]
Neutral	8.7	10.7	0.004	0.45	−0.002	0.005 – 0.05

Note. Inflow conditions were derived from the measurements collected from the upstream met mast. Mean horizontal wind speed and turbulence intensity were computed at hub-height, while stability parameter and friction velocity were computed at 10 m. Near-surface kinematic heat flux was measured at 2 m. Herein, $\overline{U}_\infty$ is the mean horizontal wind speed at freestream, $TI = \sigma_u/\overline{U}_\infty$ is the turbulence intensity computed at the hub-height, $\zeta = z/L$ is the stability parameter calculated at height of z, $L = -u_*^3\theta/\kappa g(\overline{w'\theta'_v})_s$ is the Obukhov length, u_* is the friction velocity, $Q_s = (\overline{w'\theta'_v})_s$ is the near-surface kinematic heat flux, w' is the fluctuating component of vertical velocity, θ'_v is the perturbation virtual potential temperature, and z_0 is the surface roughness.

were defined. Ensemble averages for neutral case are summarized in Table 4.

The data for wind turbine operation were collected with wind speed and direction sensors at the back of the nacelle, a yaw heading sensor, generator power and torque sensors, and a blade-pitch sensor. Four strain gauges located at the blade's root were used to measure the flap and edge moments in the blade coordinate system for load measurements. The calibrated blade pitch was set to −0.75° for the upwind turbine pitch.

Simulation results are also compared with nacelle-mounted DTU spinnerLidar data [1]. It was assumed in the *in-situ* measurements that the beam elevation angle is zero, and the angle between upcoming wind and turbine is approximately zero, meaning that the turbine is always aligned with the upstream flow. As stated in the recent paper of Doubrawa *et al.* [30], the lidar sampling period was approximately set to 30 − 42 s for the neutral case to focus on the spatial evolution of the mean wake. Each scan returns line-of-sight velocity measurements at several points in a rosetta pattern at a desired downstream location [30] (see Fig. 1). Lidar measurements are available at 2, 3, 4, and 5 rotor diameters downstream of the turbine for neutral benchmark. Although wake measurements were available at very close distances, i.e., 1 D, only measurements starting at 2 D were considered due to unclear representation of the near-wake. The origin of the coordinate system is placed onto the nacelle in a fixed frame of reference, as depicted in Fig. 1. For the sake of simplicity, only results for neutrally-stratified ABL conditions are given in this paper.

2.2. Computational framework

We performed large-eddy simulations of idealized atmospheric boundary layers using the open-source Weather Research and Forecasting (WRF) Model v4.3 [16]. The WRF model is a non-hydrostatic, fully compressible solver that solves the Euler and energy equations for high Reynolds number flows. Governing equations are discretized over a staggered Arakawa C-grid, with a terrain-following hydrostatic-pressure coordinate system in the vertical direction, given by $\eta = (p - p_t)/(p_s - p_t)$, where p_t and p_s are the pressure values at the model top and surface, respectively. Therefore, precise derivation of vertical grid spacing is not possible. In addition, default time integration uses a third-order Runge-Kutta scheme, while horizontal and vertical advection schemes are based on fifth- and third-order finite difference approximations. LES mode is activated by turning off the planetary boundary layer scheme option and turning on an appropriate subfilter-scale (SFS) model. Two nested LES domains with flat terrain were utilized to provide homogeneous inflow conditions to the inner domain. The parent domain uses periodic lateral boundaries in both directions, and information is transferred via one-way nesting, meaning that the coarse LES solution updates turbulent boundary conditions for the finer domain. Yet, the parent domain receives no information from its child domain. Homogeneous forcing was prescribed as a vertical sounding profile at the domain inlet, and a uniform flow solution is achieved in the plane across the domain *xy* plane across the domain [31]. Governing equations are solved by applying an implicit filter, which acts as a low-pass filter, to filter out the high wavenumber present in the numerical solution. Therefore, the filter width was automatically set equal to the grid size.

2.2.1. Simulation setup

We utilized two nested domains with periodic lateral boundary conditions prescribed on the coarser bounding domain. The parent domain was run for several hours to develop turbulent flow using specified sounding data for the geostrophic wind and sur-

Table 2: Domain dimensions of the GAD simulations for near-neutral (NBL) benchmark.

Benchmark	Domain	$N_x \times N_y \times N_z$	$\Delta x = \Delta y$ [m]	Δz [m]	L_x [m]	L_y [m]	L_z [m]	Δt [s]
GAD-NBL	Coarse	$201 \times 101 \times 141$	6	2	1200	600	1695.50	0.0625
	Fine	$403 \times 151 \times 141$	2	2	806	300	1695.50	0.0208

Note. N_x, N_y, and N_z stand for the number of grid points whereas $\Delta x, \Delta y$, and Δz represent the spatial grid resolutions in the x, y, and z directions. Note that precise value for Δz cannot be defined due to WRF's terrain-following eta coordinate system in vertical direction. Δt is the computational time-step size, and U_g, V_g are the components of the geostrophic wind in longitudinal and lateral directions. L_x, L_y, and L_z represent physical dimensions of the domain the x, y, and z directions, respectively.

face forcing. Thanks to this spin-up run, one can say that, as anticipated, a turbulent, steady-state ABL flow is achieved on the finer domain. The GAD model is used only on the fine LES nested within.

The horizontal and vertical grid spacing kept constant up to a certain height to minimize the influence of spatial resolution among benchmarks. The domain sizes were chosen to be large enough to develop small-scale structures consistent with the fine grid spacing on the nested domain within $\sim$ 400 m from the domain inlet. Since the test field is located in flat terrain and involves less complexity in terms of atmospheric events, domain size was chosen as small as possible to reduce the computational effort; however, it allows reproducing the turbulent flow before encountering the turbine, and enough downstream space for wake development and quantitative analysis at lidar scanning planes. Besides, the wind turbine simulated here is much smaller than those operating in canonical or utility-scale wind farms. The turbine base was located in the middle of the nested domain, providing enough space for the inflow and wake development. The selection of inlet spacing and turbine location was later validated by comparing LES results with inflow measurements at the met mast location in Sect. 3.1. An abbreviation of NBL is used for near-neutral ABL benchmark. Hereinafter, numerical simulation that incorporates GAD parameterization is abbreviated as a combination of these two terms, for example, GAD-NBL. Domain dimensions for each case are given in Table 2. Coarse domains use horizontal resolutions of $\Delta x = \Delta y = 6$ m, while fine domains use $\Delta x = \Delta y = 2$ m. All cases use vertical resolution, Δz, on both domains approximately equal to Δx on the nested domain. For each case, the values of Δz were kept constant up to a height of 60 m and stretched up to the domain top using a hyperbolic tangential vertical grid stretching algorithm. A Rayleigh damping layer with a coefficient of 0.003 s^{-1} was utilized in the upper part of the inversion layer to damp out spurious vertical motions that would be reflected from the top of the domain. The depth of dampening layer for the NBL benchmark is 690.50 m. A zero vertical motion and zero stress boundary conditions were imposed at the model top. A single-layer capping inversion was applied at 1000 m above the ground to prevent turbulence from reaching the model top [4]. Roughness length was set to $z_0 = 0.014$ m, with a Coriolis forcing of $f = 0.805 \times 10^{-4}$ s^{-1}, representative of wind turbine's geographical location (33.60795° N). Turbulence closure was achieved using the nonlinear backscatter and anisotropy (NBA) model [32]. We chose to use the second variant of the NBA model that solves an additional prognostic equation for SFS turbulence kinetic energy (hereinafter, called NBA-TKE) [33; 34; 35]. Details of the NBA SFS turbulence closure scheme can be found in 2.3. The surface boundary condition was $w = 0$, and Monin-Obukhov similarity theory (MOST) was applied to account for fluxes of momentum and heat [36]. Mean wind and temperature profiles are defined as (e.g., [37]).

$$\begin{aligned} \frac{\partial \overline{u}}{\partial z} &= \frac{u_*}{\kappa z}\Psi_m(\frac{z}{L}), \\ \frac{\partial \overline{\theta_v}}{\partial z} &= \frac{\theta_*}{\kappa z}\Psi_h(\frac{z}{L}), \end{aligned} \tag{1}$$

where $u_* = [\overline{u'w'}^2 + \overline{v'w'}^2]^{1/2}$, $\theta_* = -\overline{w'\theta'}/u_*$ are the surface friction velocity and temperature scale, respectively. $\Psi_m(\zeta)$ and $\Psi_h(\zeta)$ refer to the universal functions for wind speed and temperature (e.g., [38]). Taking thermal stratification into account, the wind speed and potential temperature profiles can be written as

$$\begin{aligned} u(z) &= \frac{u_*}{\kappa}\left[\ln\left(\frac{z}{z_0}\right) - \Psi_m(\frac{z}{L})\right], \\ \theta_v(z) - \theta_v(s) &= \frac{\theta_*}{\kappa}\left[\ln\left(\frac{z}{z_0}\right) - \Psi_h(\frac{z}{L})\right], \end{aligned} \tag{2}$$

where $\theta_v(s)$ is the surface virtual potential temperature, with $\theta_v = \theta(1 + 0.61 q_v)$, where q_v is the water vapor mixing ratio. For dry conditions, $q_v = 0$ and $\theta_v =$

Table 3: Configuration parameters for three different case studies.

Benchmark	u_g, v_g [m s^{-1}]	$(\overline{w'\theta'_v})_s$ [K m s^{-1}]	Cooling rate [K h^{-1}]	z_0 [m]	z_i [m]	Inversion strength [K m^{-1}]	Spin-up time [h]
Neutral	11.70, -3.97	-0.002	0.00	0.014	1000	0.010	15

Note. u_g, v_g denote zonal and meridional components of the geostrophic wind. z_i represents the initial inversion height.

θ, where $\theta = T(p_0/p)^{R/c_p}$. Herein, $p_0 = 1 \times 10^5$ Pa is a reference pressure, R is the universal gas constant for dry air, and c_p is the specific heat of dry air at constant pressure. The surface layer is assumed to be the first vertical layer in the numerical model and parameterizes the equations for surface fluxes mentioned in Eqs. (1) and (2). We used the Revised MM5 Monin-Obukhov scheme to parameterize surface fluxes [39].

The WRF-LES-GAD simulation was initialized using dry atmospheric conditions (i.e., zero vapor mixing ratio, which is the ratio between the mass of water vapor and mass of dry air, was assumed). No radiation, cloud, or land-surface models were utilized. The simulation was initialized with uniform potential temperature profiles up to initial inversion height, and above, an inversion strength of 0.01 K m^{-1} was applied. Potential temperature profile was prescribed to be consistent ensemble average of virtual potential temperature defined in the reference. Moreover, a uniform geostrophic wind profile was applied up to model top. Small perturbations of $[-0.5, +0.5]$ K were added to the initial values of potential temperature below capping inversion to seed turbulence. These perturbations were obtained from a pseudo-random uniform distribution decreasing as a cubic function of height [4; 5].

Since idealized simulations are forced with geostrophic wind and temperature profiles defined prior to the simulation, oscillations in boundary layer structure (e.g., wind and direction profiles in the vertical direction) occur within the first few hours of a simulation. A spin-up LES is necessary to ensure that turbulence in the computational domain is well mixed and numerical solution comes into balance with the geostrophic wind vector. For that reason, a spin-up LES is run for 15 h for the neutral case. Thereafter, the nested domain, including the GAD parameterization, is introduced, and data for model-measurement comparison is saved every 1 min. The nested domain with the GAD model was turned on at the beginning of hour 15 h and run for 1 h and 10 minutes; however, the first 10 minutes were considered as spin-up of the flows within the finer domain, and thus it is not taken into account when analyzing the results.

2.3. *Nonlinear Backscatter and Anisotropy SFS Model*

The Nonlinear Backscatter and Anisotropy (NBA) model [32] was implemented into open-source, community-edition of WRF [40] as an alternative

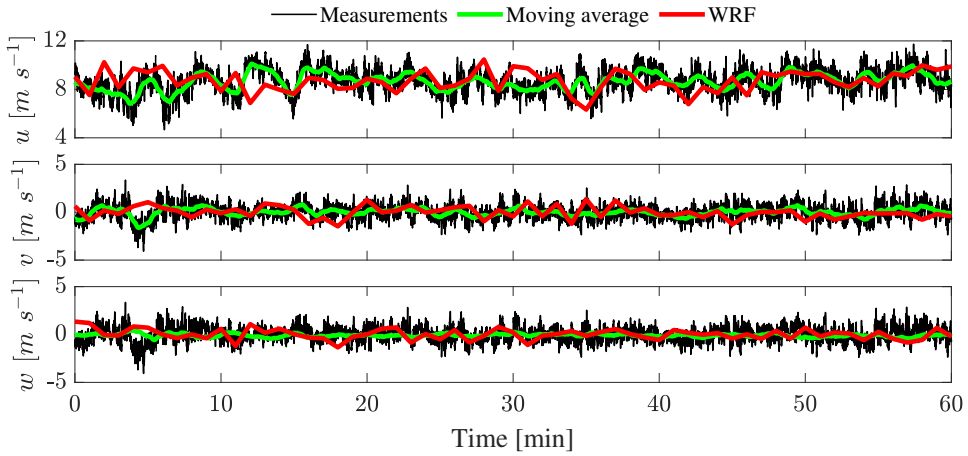

Figure 2: Time series of hub height velocity components from WRF-LES outputs at the met mast location. Black lines show measurement data, while green lines show moving averages over 600 s windows based on the given high-frequency measurement data. Red solid lines depict WRF-LES results.

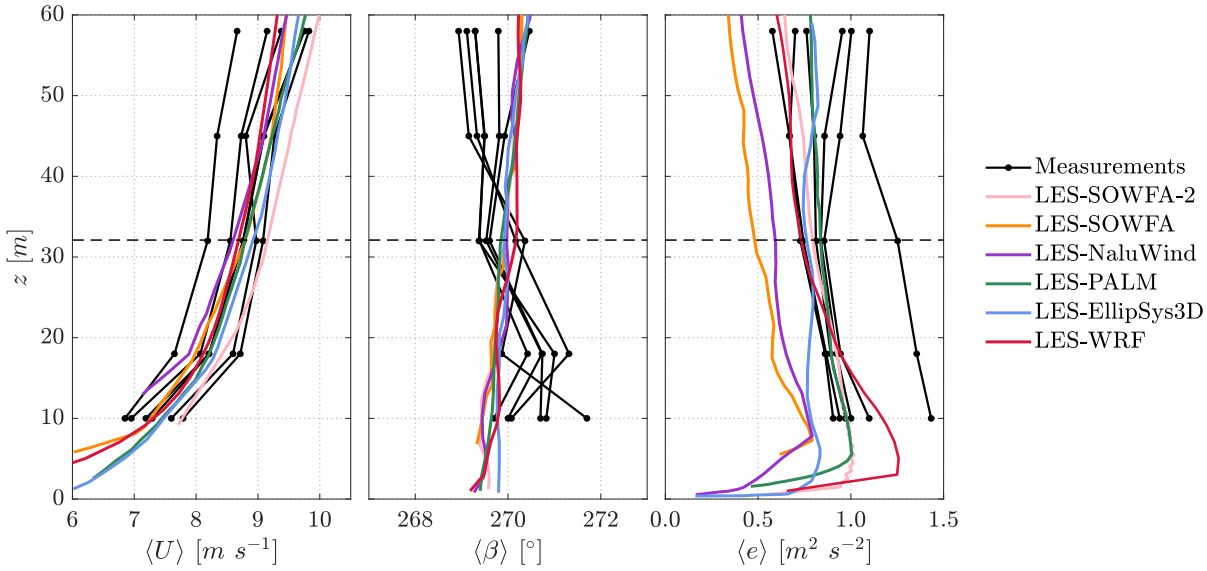

Figure 3: Vertical profiles of temporally- and laterally-averaged atmospheric quantities at the met mast location, horizontal wind speed (left), wind direction (middle), and turbulence kinetic energy (right). Each solid black line represent 10-minute averages of the measurement data, while colored lines are the reference LES results. Horizontal dashed lines depict the wind turbine hub height. $\langle\cdot\rangle$ represents the spatial averaging of the quantity of interest.

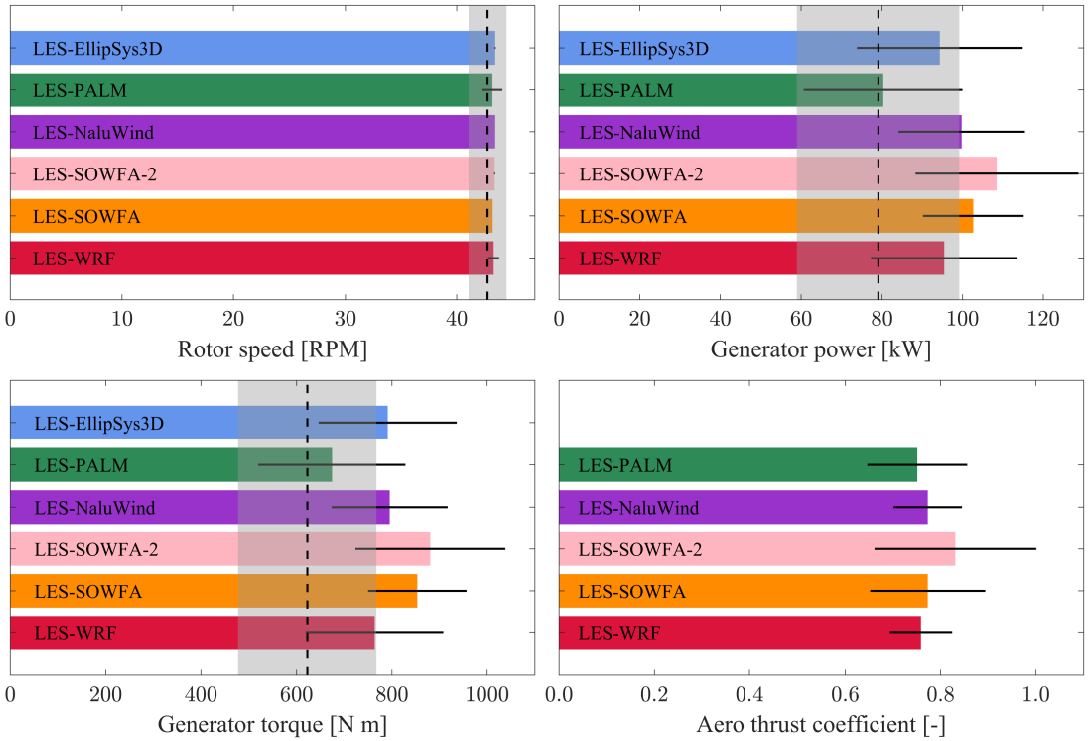

Figure 4: Comparison of mean and standard deviations of wind turbine response quantities, rotor speed (top left), generator power (top right), generator torque (bottom left), and aerodynamic thrust coefficient (bottom right). Vertical black dashed line show the mean of measurements whereas gray shaded region represent the standard deviation. Colored horizontal bars show simulation results and black horizontal lines depict standard deviation.

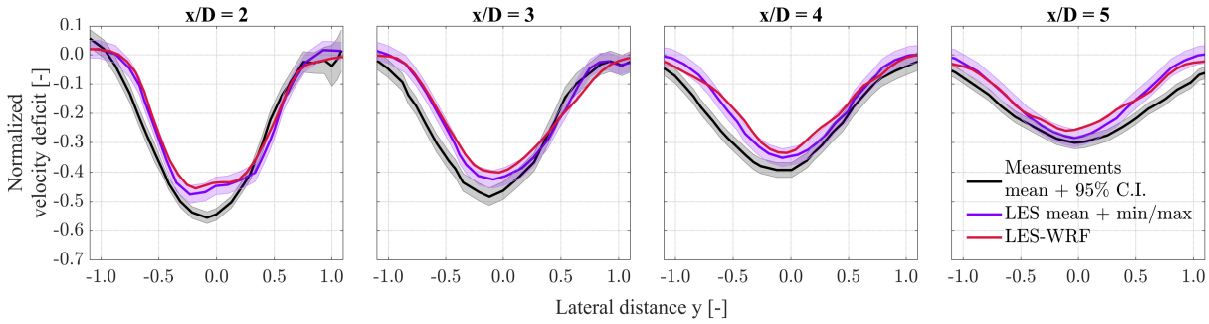

Figure 5: Hub height horizontal normalized velocity deficit profiles averaged in time. Lateral profiles are shown in a fixed frame of reference. Gray shaded region shows the measurements within %95 confidence interval. All LES results are averaged and collapsed into a single mean curve shown in purple within a minimum/maximum region depicted in light magenta.

to the standard eddy-viscosity approach. The NBA model stress tensor can be defined in two ways, one being in terms of strain rate while the second in terms of subfilter-scale TKE. In this study, we use TKE-based NBA model whose stress tensor can be expressed as:

$$M_{ij} = -C_e l\Big\{2\sqrt{e}\tilde{S}_{ij} + \Big(\frac{27}{8\pi}\Big)^{1/3} C_s^{2/3} l\Big[C_1\Big(\tilde{S}_{ik}\tilde{S}_{kj} - \frac{1}{3}\tilde{S}_{mn}\tilde{S}_{mn}\delta_{ij}\Big) + C_2(\tilde{S}_{ik}\tilde{R}_{kj} - \tilde{R}_{ik}\tilde{S}_{kj})\Big]\Big\}. \quad (3)$$

In Eq. (3), $\tilde{S}_{ij} = 0.5(\partial\tilde{u}_i/\partial x_j + \partial\tilde{u}_j/\partial x_i)$ denotes the resolved strain-rate tensor, $\tilde{R}_{ij} = 0.5(\partial\tilde{u}_i/\partial x_j - \partial\tilde{u}_j/\partial x_i)$ is the resolved rotation sensor, with coefficients of $C_s = \sqrt{8(1+C_b)/27\pi^2}$, $C_e = \sqrt[3]{8\pi C_s^4/27}$, $C_1 = C_2 = (8\sqrt{15}C_b)/(7[1+C_b]S_k)$, the skewness parameter, $S_k = 0.5$, and the backscatter coefficient, $C_b = 0.36$. Tildes denote the resolved component of the flow. All constants defined inline are functions of the backscatter coefficient so as to obtain proper normal stresses for sheared homogeneous turbulence. For that reason, the NBA model performs better during stable conditions [5].

3. Results

3.1. Atmospheric inflow calibration

The inflow horizontal wind speed cannot be directly prescribed in WRF-LES; therefore, components of the geostrophic wind should be determined. This is an iterative process and requires a set of simulations that lead to the desired inflow conditions. On the other hand, thanks to high-frequency velocity measurements recorded by a sonic anemometer at hub height, we first compared our LES results with the available sonic data to see how well our WRF-LES results match the observations. Under neutral conditions, we present an analysis of the simulated transient velocity output as time series. The analysis is made by performing moving averages of 600 s windows based on high-frequency samples of measured three-dimensional velocity components. Figure (2) illustrates the time series of u, v, w components of velocity measured at hub height during 1 h simulation after 15 h of spin-up run. Time series of horizontal and vertical velocity components sampled at 1 m intervals are well matched and represent the unsteadiness of the velocity compared to the measurement data. It is important to note that first ten minutes of the WRF-LES-GAD simulation was discarded to ensure horizontally interpolated flow field as well as turbulence are well mixed in the inner domain.

Numerical results are then compared with the given ensemble averages of atmospheric quantities such as horizontal wind speed, surface kinematic heat flux, hub-height turbulence intensity, the standard deviation of velocity components in terms of root mean square errors to assess the accuracy of LES of each case. Lastly, we evaluate how closely the vertical profiles of wind speed, wind direction, turbulence kinetic energy obtained from simulations represent the field measurements and other LES predictions.

3.1.1. Wind speed, wind direction and turbulence kinetic energy

Vertical profiles of wind speed, wind direction, and turbulence kinetic energy are extracted at the met mast location, that is 2.5 rotor diameter upstream of the wind turbine. All profiles are laterally averaged, and mean profiles are obtained by taking the time averages (see Figure (3)). All simulations predict the observed upstream wind speed profile. On the other hand, although all simulations match hub height wind direction, that is $\beta \approx 270°$, all of them fail to predict the negative and positive veer below and above the hub height observed in the measurements. The magnitude of these direction changes is small and negligible. However, large deviations in turbulence kinetic energy were observed through numerical models, e.g., SOWFA and NaluWind. The other models, including WRF-LES, perform better and are able to predict turbulence kinetic energy profiles closely. Model underestimations may be due to not considering the subgrid part of TKE in total turbulence kinetic energy diagnostic. In the WRF-LES model, we plot the total kinetic energy profile that considers contributions of both resolved and sub-grid parts of turbulence.

Table 4: Comparison of ensemble averages with WRF-LES results.

	$\overline{U}_\infty$ [m s^{-1}]	σ_u [m s^{-1}]	σ_v [m s^{-1}]	σ_w [m s^{-1}]	TI [%]
Measurements	8.7	0.93	0.77	0.50	10.7
WRF-LES	8.7	0.89	0.65	0.57	10.2

Note. $\overline{U}_\infty$ is two-dimensional horizontal wind speed at hub height, $\sigma_u, \sigma_v, \sigma_w$ denote the standard deviations of hub height velocity components, and TI depicts the hub height turbulence intensity at met mast location.

Table 4 compares the ensemble averages of measurements and WRF-LES results. A good match is achieved in terms of hub height wind speed and first-order statistics, and thus simulated turbulence intensity is very close to ensemble averaged data, as anticipated.

3.2. Validation of the generalized actuator disk model

Advanced or generalized actuator disk model (GAD) is validated against available field and LES data regarding rotor speed, generator power, generator torque, and aerodynamic thrust coefficient. Since there is no aerodynamic thrust measurement available, WRF-LES-GAD results are compared to LES data. Note that the LES codes parameterize the turbine-induced forces using the actuator line method while an actuator disk model was used to validate in this study. Furthermore, no turbine controller was used in the current study, so the rotational velocity of the wind turbine and blade pitch are interpolated using an operational database specific to Vestas V27. Interpolation was done based on 2-m averages of instantaneous wind speed seen by the rotor at the designated inflow location. The Glauert correction for tip and root losses were used. Nacelle and tower effects were not modeled. Wake deficit profiles obtained at downstream locations of $x/D = 2, 3, 4, 5$ are qualitatively compared with measurements and other LES codes.

3.2.1. Wind turbine response

Figure 4 shows comparisons of different aerodynamic quantities such as rotor speed, generator power, generator torque, and aerodynamic thrust coefficient across simulations and field measurements. All LES codes are in a similar margin, showing fewer deviations in terms of rotor speed; however, only ElliSys3D, PALM, and WRF codes stayed within the standard deviation of the measurements. All LES codes overestimate generator torque, yet the generator torque results of our model lied within the measurement variation margin. Finally, we compared our aerodynamic thrust coefficient prediction with PALM, SOWFA, and NaluWind research codes. All results show similar behavior except for the SOWFA-2 simulations, which have very high variations.

3.2.2. Wake behavior

Time-averaged hub height velocity deficit (vd) profiles at different downstream locations were plotted using Equation (4). For the sake of clarity, the results of LES codes took part in the neutral benchmark were collapsed into a single mean curve showing minimum and maximum deficits while the measurements within 95% confidence interval are shown in Figure (5). As anticipated, the maximum velocity deficit is obtained at $x/D = 2$, that is the closest plane in the wake of the turbine, and wake width is similar to mean observed in LES codes. The wake attenuates slightly faster in WRF-LES than in the other LES codes. One of the reasons for faster wake recovery may be due to WRF's high-order spatial discretization schemes in the horizontal direction. All in all, velocity deficit profiles show very similar behavior, but underestimate measured values.

$$vd(x, y, z, t) = \frac{U(x, y, z, t)}{\overline{U}_\infty(z)} - 1, \tag{4}$$

where $U(x, y, z, t)$ is four-dimensional horizontal wind speed, and $\overline{U}_\infty(z)$ denotes temporal average of

the horizontal wind speed profile in the vertical direction.

4. Conclusion

A validation study was carried out using a generalized actuator disk (GAD) wind turbine parameterization implemented into the Weather Research and Forecasting (WRF) model. Such computationally inexpensive wind turbine parameterization schemes provide more reliable simulation capability in large-eddy simulations of atmospheric pressure flows compared to blade-resolving approaches. Validation of the GAD model was based on the real data recorded during the Scaled Wind Farm Technology (SWiFT) field campaign. Though there were three different benchmarks, namely neutral, unstable, and stable, defined in the SWiFT campaign, only neutral case was studied in the current work. Not only qualitatively but also quantitatively good results were obtained in comparison with the available measurement data and LES codes that use actuator line model. It must be noted that the verification of the actuator disk model in WRF-LES is not straightforward and depends on the aerodynamic properties of the turbine blades and the stability conditions evaluated against corresponding measurement data. Detailed investigations have been performed to evaluate the accuracy and reliability of simulated wake characteristics under different atmospheric stability conditions in extension to this work and will be published in an indexed journal.

Acknowledgments

This research has been performed using computational resources of the von Karman Institute For Fluid Dynamics and has received funding from the European Union's Horizon 2020 research and innovation programme under the Marie Skłodowska-Curie grant agreement No 860101.

References

[1] T. Mikkelsen, N. Angelou, K. Hansen, M. Sjöholm, M. Harris, C. Slinger, P. Hadley, R. Scullion, G. Ellis, G. Vives, A spinner-integrated wind lidar for enhanced wind turbine control, Wind Energy 16 (4) (2013) 625–643.

[2] D. Elliott, J. Barnard, Observations of wind turbine wakes and surface roughness effects on wind flow variability, Solar Energy 45 (5) (1990) 265–283.

[3] J. Meyers, C. Meneveau, Optimal turbine spacing in fully developed wind farm boundary layers, Wind Energy 15 (2) (2012) 305–317.

[4] J. Mirocha, B. Kosovic, M. Aitken, J. Lundquist, Implementation of a generalized actuator disk wind turbine model into the weather research and forecasting model for large-eddy simulation applications, Journal of Renewable and Sustainable Energy 6 (1) (2014) 013104.

[5] N. Marjanovic, J. D. Mirocha, B. Kosović, J. K. Lundquist, F. K. Chow, Implementation of a generalized actuator line model for wind turbine parameterization in the weather research and forecasting model, Journal of Renewable and Sustainable Energy 9 (6) (2017) 063308.

[6] R. S. Arthur, J. D. Mirocha, N. Marjanovic, B. D. Hirth, J. L. Schroeder, S. Wharton, F. K. Chow, Multi-scale simulation of wind farm performance during a frontal passage, Atmosphere 11 (3) (2020) 245.

[7] W. Zhang, C. D. Markfort, F. Porté-Agel, Wind-turbine wakes in a convective boundary layer: A wind-tunnel study, Boundary-layer meteorology 146 (2) (2013) 161–179.

[8] P. Hancock, S. Zhang, F. Pascheke, P. Hayden, Wind tunnel simulation of a wind turbine wake in neutral, stable and unstable wind flow, in: Journal of Physics: Conference Series, Vol. 555, IOP Publishing, 2014, p. 012047.

[9] E. Machefaux, G. C. Larsen, T. Koblitz, N. Troldborg, M. C. Kelly, A. Chougule, K. S. Hansen, J. S. Rodrigo, An experimental and numerical study of the atmospheric stability impact on wind turbine wakes, Wind Energy 19 (10) (2016) 1785–1805.

[10] U. Ciri, G. Petrolo, M. V. Salvetti, S. Leonardi, Large-eddy simulations of two in-line turbines in a wind tunnel with different inflow conditions, Energies 10 (6) (2017) 821.

[11] G. V. Iungo, F. Porté-Agel, Volumetric lidar scanning of wind turbine wakes under convective and neutral atmospheric stability regimes, Journal of Atmospheric and Oceanic Technology 31 (10) (2014) 2035–2048.

[12] R. Menke, N. Vasiljević, K. S. Hansen, A. N. Hahmann, J. Mann, Does the wind turbine wake follow the topography? a multi-lidar study in complex terrain, Wind Energy Science 3 (2) (2018) 681–691.

[13] P. Doubrawa, M. Debnath, P. J. Moriarty, E. Branlard, T. Herges, D. Maniaci, B. Naughton, Benchmarks for model validation based on lidar wake measurements, in: Journal of Physics: Conference Series, Vol. 1256, IOP Publishing, 2019, p. 012024.

[14] A. S. Wise, J. M. Neher, R. S. Arthur, J. D. Mirocha, J. K. Lundquist, F. K. Chow, Meso-to micro-scale modeling of atmospheric stability effects on wind turbine wake behavior in complex terrain, Wind Energy Science Discussions (2021) 1–36.

[15] R. J. Stevens, C. Meneveau, Flow structure and turbulence in wind farms, Annual review of fluid mechanics 49 (2017) 311–339.

[16] W. C. Skamarock, J. B. Klemp, A time-split nonhydrostatic atmospheric model for weather research and forecasting applications, Journal of computational physics 227 (7) (2008) 3465–3485.

[17] H. Gopalan, C. Gundling, K. Brown, B. Roget, J. Sitaraman, J. D. Mirocha, W. O. Miller, A coupled mesoscale–microscale framework for wind resource estimation and farm aerodynamics, Journal of Wind Engineering and Industrial Aerodynamics 132 (2014) 13–26.

[18] F. Porté-Agel, M. Bastankhah, S. Shamsoddin, Wind-turbine and wind-farm flows: a review, Boundary-Layer Meteorology 174 (1) (2020) 1–59.

[19] H. Gopalan, C. Gundling, J. Sitaram, Coupled mesoscale microscale model for wind resource estimation and turbine aerodynamics using an overset grid approach, in: Paper to be pre-

sented at the 51st AIAA Aerospace Sciences Meeting, Dallas, TX, 2013.
[20] P.-A. Joulin, M. L. Mayol, V. Masson, F. Blondel, Q. Rodier, M. Cathelain, C. Lac, The actuator line method in the meteorological les model meso-nh to analyze the horns rev 1 wind farm photo case, Frontiers in Earth Science 7 (2020) 350.
[21] A. Jimenez, A. Crespo, E. Migoya, J. García, Advances in large-eddy simulation of a wind turbine wake, in: Journal of Physics: Conference Series, Vol. 75, IOP Publishing, 2007, p. 012041.
[22] Y.-T. Wu, F. Porté-Agel, Large-eddy simulation of wind-turbine wakes: evaluation of turbine parametrisations, Boundary-layer meteorology 138 (3) (2011) 345–366.
[23] Y.-T. Wu, F. Porté-Agel, Modeling turbine wakes and power losses within a wind farm using les: An application to the horns rev offshore wind farm, Renewable Energy 75 (2015) 945–955.
[24] I. Ammara, C. Leclerc, C. Masson, A viscous three-dimensional differential/actuator-disk method for the aerodynamic analysis of wind farms, J. Sol. Energy Eng. 124 (4) (2002) 345–356.
[25] A. El Kasmi, C. Masson, An extended k–ε model for turbulent flow through horizontal-axis wind turbines, Journal of Wind Engineering and Industrial Aerodynamics 96 (1) (2008) 103–122.
[26] M. J. Churchfield, S. J. Schreck, L. A. Martinez, C. Meneveau, P. R. Spalart, An advanced actuator line method for wind energy applications and beyond, in: 35th Wind Energy Symposium, 2017, p. 1998.
[27] F. Porté-Agel, Y.-T. Wu, H. Lu, R. J. Conzemius, Large-eddy simulation of atmospheric boundary layer flow through wind turbines and wind farms, Journal of Wind Engineering and Industrial Aerodynamics 99 (4) (2011) 154–168.
[28] R. Mikkelsen, et al., Actuator disc methods applied to wind turbines, Ph.D. thesis, PhD thesis, Technical University of Denmark (2003).
[29] H. Glauert, Airplane propellers, in: Aerodynamic theory, Springer, 1935, pp. 169–360.
[30] P. Doubrawa, E. W. Quon, L. A. Martinez-Tossas, K. Shaler, M. Debnath, N. Hamilton, T. G. Herges, D. Maniaci, C. L. Kelley, A. S. Hsieh, et al., Multimodel validation of single wakes in neutral and stratified atmospheric conditions, Wind Energy 23 (11) (2020) 2027–2055.
[31] D. Muñoz-Esparza, B. Kosović, Generation of inflow turbulence in large-eddy simulations of nonneutral atmospheric boundary layers with the cell perturbation method, Monthly Weather Review 146 (6) (2018) 1889–1909.
[32] B. Kosović, Subgrid-scale modelling for the large-eddy simulation of high-reynolds-number boundary layers, Journal of Fluid Mechanics 336 (1997) 151–182.
[33] D. K. Lilly, The representation of small-scale turbulence in numerical simulation experiments, IBM Form (1967) 195–210.
[34] J. W. Deardorff, Stratocumulus-capped mixed layers derived from a three-dimensional model, Boundary-Layer Meteorology 18 (4) (1980) 495–527.
[35] C.-H. Moeng, A large-eddy-simulation model for the study of planetary boundary-layer turbulence, Journal of the Atmospheric Sciences 41 (13) (1984) 2052–2062.
[36] A. S. Monin, A. M. Obukhov, Basic laws of turbulent mixing in the surface layer of the atmosphere, Contrib. Geophys. Inst. Acad. Sci. USSR 151 (163) (1954) e187.
[37] P. S. Arya, Introduction to micrometeorology, Elsevier, 2001.
[38] H. A. Panofsky, Determination of stress from wind and temperature measurements, Quarterly Journal of the Royal Meteorological Society 89 (379) (1963) 85–94.
[39] P. A. Jiménez, J. Dudhia, J. F. González-Rouco, J. Navarro, J. P. Montávez, E. García-Bustamante, A revised scheme for the wrf surface layer formulation, Monthly Weather Review 140 (3) (2012) 898–918.
[40] J. Mirocha, J. Lundquist, B. Kosović, Implementation of a nonlinear subfilter turbulence stress model for large-eddy simulation in the advanced research wrf model, Monthly Weather Review 138 (11) (2010) 4212–4228.

Development of a dynamic wake model accounting for wake advection delays and mesoscale wind transients

Benoit Foloppe

Environmental and Applied Fluid Dynamics Department, von Karman Institute for Fluid Dynamics, Belgium, benoit.foloppe@vki.ac.be

Supervisor: Jeroen van Beeck

Professor, Environmental and Applied Fluid Dynamics Department, von Karman Institute for Fluid Dynamics, Belgium, vanbeeck@vki.ac.be

University Supervisor: Lieven Vandevelde

Professor, Electromechanical and Systems and Metal Engineering Department, Ghent University, Belgium, lieven.vandevelde@ugent.be

Abstract

Currently installed wind turbines are increasingly interacting with the atmospheric boundary layer. Therefore, the research intends to extend the FLORIS framework in order to include wake advection delays between wind turbines, time-varying and spatially heterogeneous wind conditions. The developed model is validated against Large Eddy Simulation and applied to a simulation of the Horns Rev wind farm to show a hysteresis in the wind farm power extraction curve.

Keywords: wake model, advection delay, wind transient, FLORIS, Horns Rev

1. Introduction

Over the last decade, the size and the number of offshore Wind Turbines (WTs) and wind farms are constantly increasing and this growth is expected to continue in the future. With tip height often above 200 meters, currently installed WTs are interacting and impacting massively the atmospheric boundary layer. In the future, wind farms will become even more important contributors to the electrical power system and will require additional flexibility in terms of farm control, ancillary services and response to weather transients [1]. In this view, it is crucial for fast control-oriented models to be informed of such dynamic weather inputs. However, current models are almost always quasi-steady, hence neither exogenous nor internal wind farm dynamics are included. Few tools are currently able to perform wake dynamics simulation while maintaining low computational cost. The FAST.Farm tool [2] is based on the Dynamic Wake Meandering (DWM) model. It is representing the dynamic wake through a collection of wake planes. The main advantages of FAST.Farm lie in the meandering feature and the coupling with FAST to model loads on wind turbines. LongSim [3] has been developed internally by DNV in order to test and evaluate wind farm control algorithms under realistic dynamic wind inflow. Gebraad and van Wingerden [4] developed the FLORIDyn model, which is a dynamic extension of the steady-state FLORIS model [5]. Recently, a revised version of FLORIDyn was released by Becker et al. [6].

In the current work, we develop a new dynamic wake model accounting for wake advection delays and mesoscale wind transients. Similar to FLORIDyn [4, 6], this model is an unsteady extension of FLORIS, and we further refer to the model as UFLORIS. Throughout the paper, we highlight differences and similarities with the recently updated version of FLORIDyn by Becker et al. [6]. We apply the model to an idealized wind direction transient for the Horns Rev wind farm, and compare it to Large Eddy Simulation (LES) data. Section 2 outlines the methodology of extending FLORIS to include dynamic effects. Thereafter, Section 3 presents a validation study with LES data from SOWFA. Next, Section 4 discusses an application to the Horns Rev offshore wind farm subjected to a wind-direction transient. Finally,

Section 5 presents the main conclusions.

2. Methodology

The Flow Redirection and Induction in Steady State (FLORIS) framework [5] has been proven to be an easy to use, easy to tune, computationally inexpensive and powerful wake modelling tool even though lacking dynamical effects. Therefore, an extension of the FLORIS framework is presented in order to include wake advection delays between wind turbines, time-varying and spatially heterogeneous wind conditions. The new dynamical model is inspired by the FLORIDyn model presented in [4] and recently revised in [6]. The so-called Observation Points (OPs) are generated at the rotor centre location as shown in Figure 1. In contrast to [6], only one OP per turbine and per time-step is created. Following a Lagrangian approach, the OPs are convected downstream, along the wake of the wind turbine, defining the wake centerline. OPs are convected with velocities computed at their current location which is another distinguishing feature from [6] where the free stream velocity (U_∞) is used for every OPs. It should be stressed that both formulations are approximations and an improvement could be to use a spatial average of the disturbed (ambient plus wakes) wind velocity as proposed in [2].
In the current paper, we consider cases where the vertical OP displacement is much smaller than the horizontal displacements (computed in following LES and also shown in [7]), justifying the use of a two-dimensional dynamical model at hub height z_t.The first point of the centerline ($p = 1$), of turbine t at time step k, is located at the WT rotor centre, $\mathbf{x_C}(t) = (x_C(t), y_C(t), z_C(t))$, which gives:

$$\mathbf{x_{t,p=,k}} = \mathbf{x_C}(t). \tag{1}$$

The downstream convection of $\mathbf{x_{t,p,k}}$ to $\mathbf{x_{t,p+1,k+1}}$ is defined as

$$\mathbf{x_{t,p+1,k+1}} = \mathbf{x_{t,p,k}} + \mathbf{U_{t,p,k}}\Delta K, \tag{2}$$

where ΔK is the time step. Thus, the previous expression can be simplified to

$$\begin{pmatrix} x_{t,p+1,k+1} \\ y_{t,p+1,k+1} \end{pmatrix} = \begin{pmatrix} x_{t,p,k} \\ y_{t,p,k} \end{pmatrix} + \begin{pmatrix} u_{t,p,k} \\ t,p,k \end{pmatrix} \Delta K. \tag{3}$$

By using matrix notation, the time update laws of OPs are:

$$\begin{bmatrix} x_{t,1,k+1} & y_{t,1,k+1} \\ x_{t,2,k+1} & y_{t,2,k+1} \\ \vdots & \vdots \\ x_{t,N_p,k+1} & y_{t,N_p,k+1} \end{bmatrix} = [A] \begin{bmatrix} x_{t,1,k} & y_{t,1,k} \\ x_{t,2,k} & y_{t,2,k} \\ \vdots & \vdots \\ x_{t,N_p,k} & y_{t,N_p,k} \end{bmatrix} + [B] \begin{bmatrix} x_C(t) & y_C(t) \end{bmatrix} + [A] \begin{bmatrix} u_{t,1,k} & v_{t,1,k} \\ u_{t,2,k} & v_{t,2,k} \\ \vdots & \vdots \\ u_{t,N_p,k} & v_{t,N_p,k} \end{bmatrix} \Delta K, \tag{4}$$

where $[A] = \begin{bmatrix} 0 & & & \emptyset \\ 1 & 0 & & \\ & \ddots & \ddots & \\ \emptyset & & 1 & 0 \end{bmatrix}$, $[B] = \begin{bmatrix} 1 \\ 0 \\ \cdots \\ 0 \end{bmatrix}$ and N_p is the number of OPs.
The local velocity vector $\mathbf{U_{t,p,k}} = (u_{t,p,k}\ v_{t,p,k})$ is obtained with a steady FLORIS evaluation that reflects the background free stream velocity and turbine settings at time index k. It is important to note that N_p is increasing at the beginning of the simulation and thus the computational time is expected to increase during the first part of the simulation and then reach a plateau. It is during this process that the dynamics of WT wake advection delays and background flow field unsteadiness are included. Finally, using the same approach currently implemented for yaw-misalignment wake deflection, the wake is shifted to match the unsteady wake centreline. The discontinuous unsteady wake centreline deflection function is defined as

$$\delta\left(x_{t,p,k} - x_{t,1,k}\right) = \left(y_{t,p,k} - y_{t,1,k}\right), \tag{5}$$

It is representing the difference between the unsteady wake centreline and the steady wake centreline with nominal turbine settings (no yaw-misalignment).
This implementation differentiates from [4] in the fact that the original FLORIS modules, for computing wake velocity, wake turbulence and wake combination, are kept and a new module accounting for the unsteady wake centreline deflection is added. This new model can be improved by considering the variation of the yaw angle and the thrust coefficient along the wake. The α and C_T values are travelling at the same speed as the OPs. Without modifications, during the steady FLORIS evaluation of the local velocity, the current turbine settings are considered to compute the velocity deficit which is no longer correct in this unsteady approach. The velocity deficit module is updated to consider the interpolation of closest α and C_T

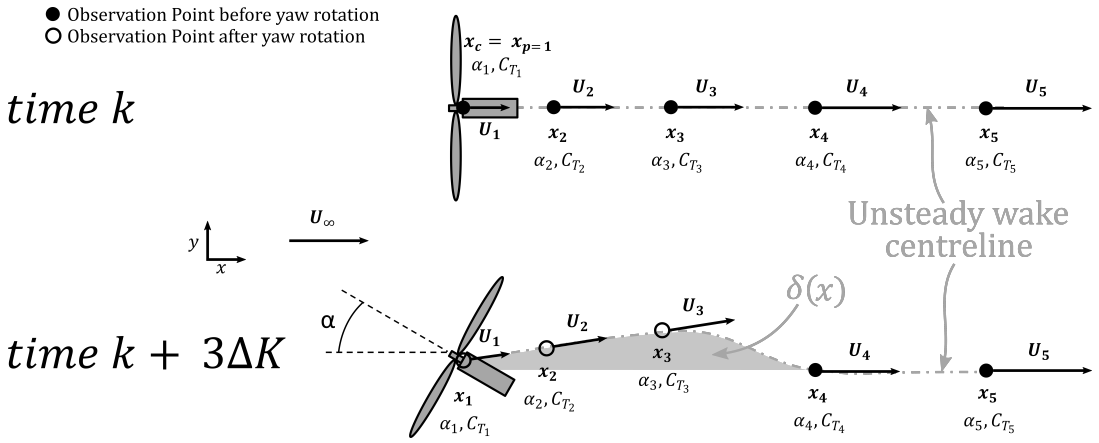

Figure 1: Illustration of the update laws, the unsteady wake centreline deflection function and the $(\alpha; C_T)$ interpolations. Since only one turbine and wake is considered, t indices are omitted in the notation.

values on the centreline as input parameters in the calculation of a local velocity inside the wake. This improvement is hereafter called "UFLORIS corrected". Finally, as a recap, the simulation algorithm is as follows:

- Initialize the simulation
- Create a new OP at the turbine location
- Convect all OPs (Equation 4)
- Compute current local velocities for all OPs (FLORIS call)
- Compute the unsteady wake centreline deflection (Equation 5)
- (optional: Compute the full 2D flow field for visualization)
- Update time $k \rightarrow k+1$, go to step 2.

3. Validation with LES for turbines in unsteady yaw conditions

The developed model is validated against LES by using the SOWFA tool [8]. The validation was conducted for unsteady turbulent inflow conditions, with variable WT control and wake interactions. The simulation shown in Figure 2 is set-up using 5 pairs of NREL 5MW WT represented by an actuator disk model. Turbulent inflow conditions are generated from a periodic precursor domain with dimensions of 3 x 3 kms in the horizontal directions and 1 km in the vertical direction. The resolution is 20 meters in the horizontal directions and goes gradually down to 6 meters in the vertical direction with 4 cells below the rotor and 13 cells across the rotor. The wind is coming from the bottom left at a hub-height velocity of 13 m/s and 6% of turbulence intensity. In the main simulation, the time step is 0.5s. In this simulation, the 5 upstream WTs start with a 30° yaw angle and at T=1000s the turbines start oscillating between 30° and 0° with a period of 600s during 2400s as shown in Figure 3. The WTs are spaced by 7D in downstream, x and y directions. For the UFLORIS simulation, the time step is 10s and the output flow field in Figure 2 Bottom has a resolution of 15m. The wake deficit is computed using a gaussian wake model [9]. The purpose of having 5 pairs of WTs oscillating is to be able to average the obtained results from the turbulent LES and thus obtain a more statistically relevant solution faster.

Figure 2 is showing the comparison between the SOWFA simulation (Top) and the corresponding UFLORIS simulation (Bottom). In the UFLORIS simulation, the turbulence is only considered to compute the wake deficit hence the free stream is set to 13 m/s. Left figures are showing contours of the instantaneous wind speed at the turbine hub height when upstream WTs are facing the wind. In right figures, WTs are experiencing a yaw-misalignment of 30°. The velocity deficit from the UFLORIS is comparing well with the SOWFA results when looking at downstream WT wakes. Bottom figures are also displaying the unsteady wake centrelines for every WT. It can be noticed that when $\alpha = 0$, the wake centreline is crossing the downstream turbine rotor in the right part. However, when $\alpha = 30$, the wake centreline is crossing the

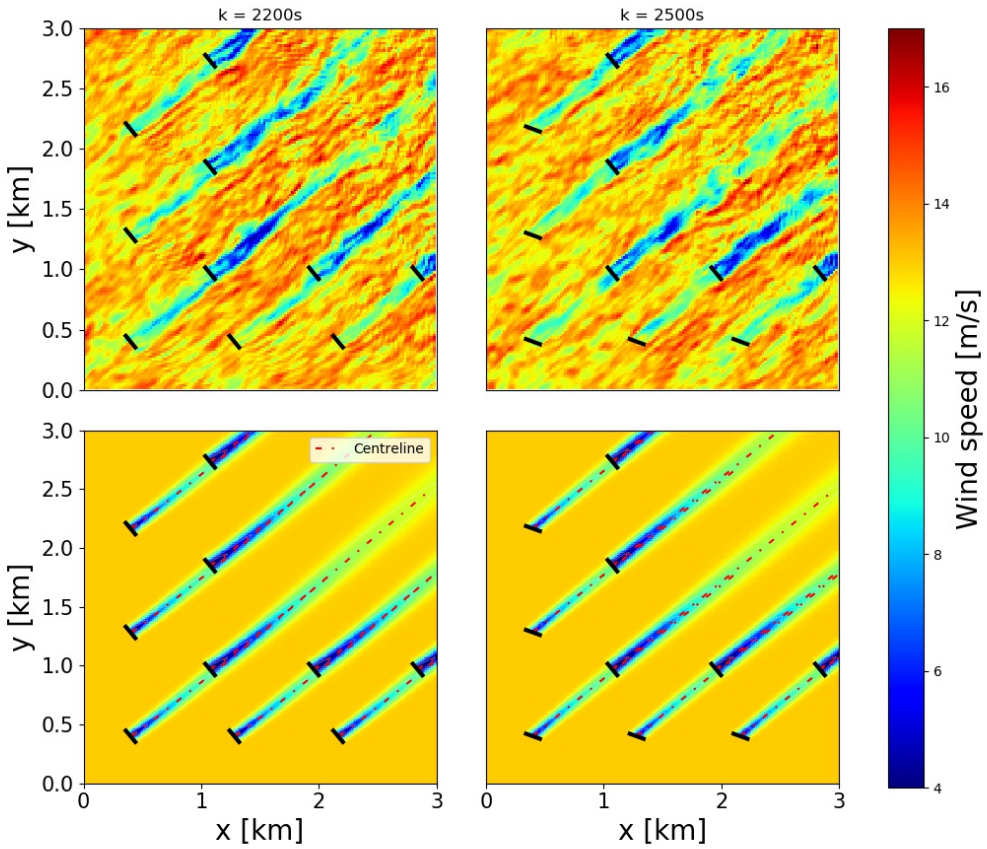

Figure 2: Contours of the instantaneous wind speed at the turbine hub height. Left: $Atk = 2200s$, $\alpha = 0$ for the front WTs. Right: At $k = 2500s$, $\alpha = 30$ for the front WTs. Top: SOWFA. Bottom: UFLORIS.

downstream turbine rotor near the middle. It would be the opposite at steady state. This is showing that the delay between a change in WT setting and its impact on the downstream WT is correctly captured by UFLORIS.

Figure 3 is presenting the averaged power of the five downstream WTs as a function of time (Top). The SOWFA results are filtered with a moving average of 3 minutes in order to remove turbulent fluctuations and facilitate the comparison. On top of the UFLORIS and UFLORIS corrected versions described before, the Quasy-Steady FLORIS (QS FLORIS) simulation is added. It is basically a collection of steady-state computations with varying turbine settings. Therefore, the QS FLORIS power is exactly in phase with the upstream turbine yaw angle. The two UFLORIS simulations show a delay between the change of the yaw angle and its impact on the power. The results are significantly improved compared to QS FLORIS and reducing the absolute error with the filtered SOWFA power (Bottom). The corrected version is located between the black and the red dashed curves as expected. In fact, the decrease in yaw angle is slowing down the convection of OPs. In the uncorrected version, all OPs are instantaneously affected by the change of yaw because there is only one yaw angle parameter for the whole wake. This is leading to a slower displacement of the unsteady wake centreline and then a delayed full wake interaction configuration. In this case, the corrected version is not improving the results but it should be stressed that both UFLORIS simulations are showing a small phase shift compared to the SOWFA

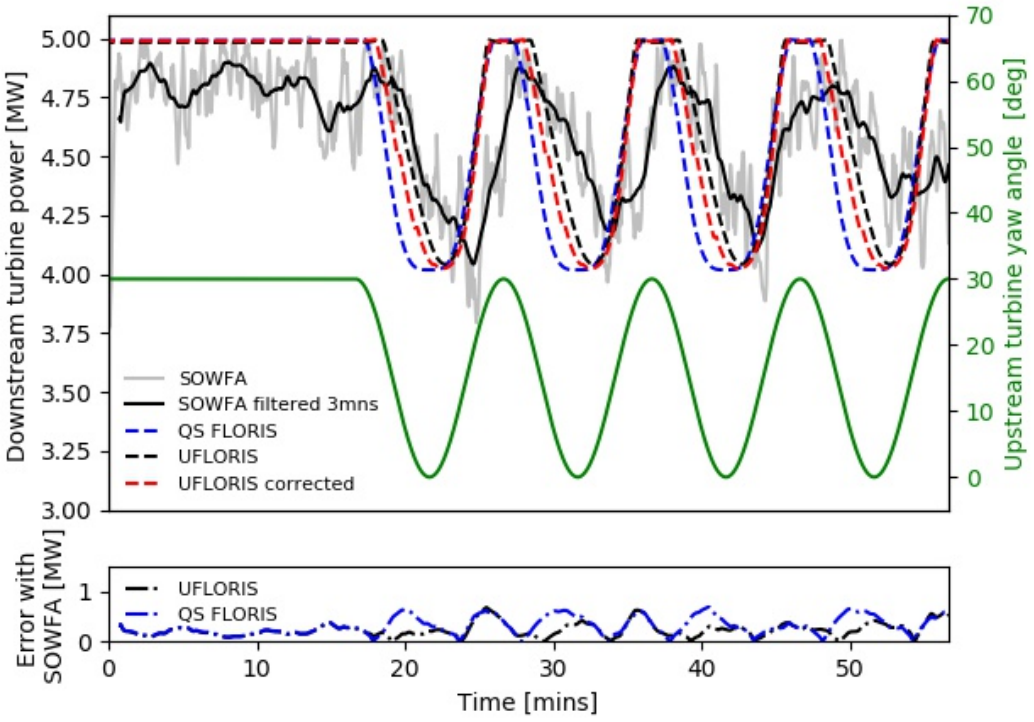

Figure 3: Top: Averaged downstream WT power comparison and upstream WT yaw angle. Bottom: Absolute errors with SOWFA filtered.

power. One possible explanation is the lack of axial induction effect in the wake deficit computation. The axial induction is slowing down the wind upstream of the wind turbine and thus delaying the full wake interaction configuration.

Figure 4 presents a phase-averaged result over each oscillation period. The new red solid line is corresponding to the average of the SOWFA filtered curve in Figure 3. This Figure is also showing that the decrease period is taking more time than the increase (2/3 of the period). It is corresponding to the slowdown of the incoming OPs generated with lower yaw angle. This dynamic behaviour is also observed in both UFLORIS simulations. Note that the discontinuities in the UFLORIS corrected curve are caused by the large time step.

4. Application to Horns Rev subjected to a wind-direction transient

4.1. Mesoscale wind-direction transient

The UFLORIS model is used to simulate the Horns Rev wind farm consisting of 80 Vestas V80-2MW turbines in a rhomboid layout (see Figure 5). A sinusoidally time-varying wind inflow direction ($\theta(k) = 270 - 30sin2k/T$) is applied. The wind is coming from the left at a magnitude of 8 m/s at hub height and around 7.5% of turbulence intensity. The wind direction is oscillating between 240° and 300° while the WT are always facing the wind (no yaw-misalignment). In this first case, the change in wind direction is applied uniformly across the domain, representing a wind direction change generated by a very large-scale effect (or mesoscale effect). It is an ideal test-case to assess this new dynamical wake model because it involves dynamics of wake advection delays in wind farms and dynamical hysteresis effects in power production as shown by LES results in [10].

In Figure 6, results are compared with LES from [10] for three different periods of oscillation ($T_\theta = 1h, 2h, 4h$). First of all, UFLORIS is capable of capturing the power hysteresis in the normalized power curve for both shorter periods. For $T_\theta = 4h$, UFORIS is still capturing an hysteresis while it is not evident in the LES. As expected, results are

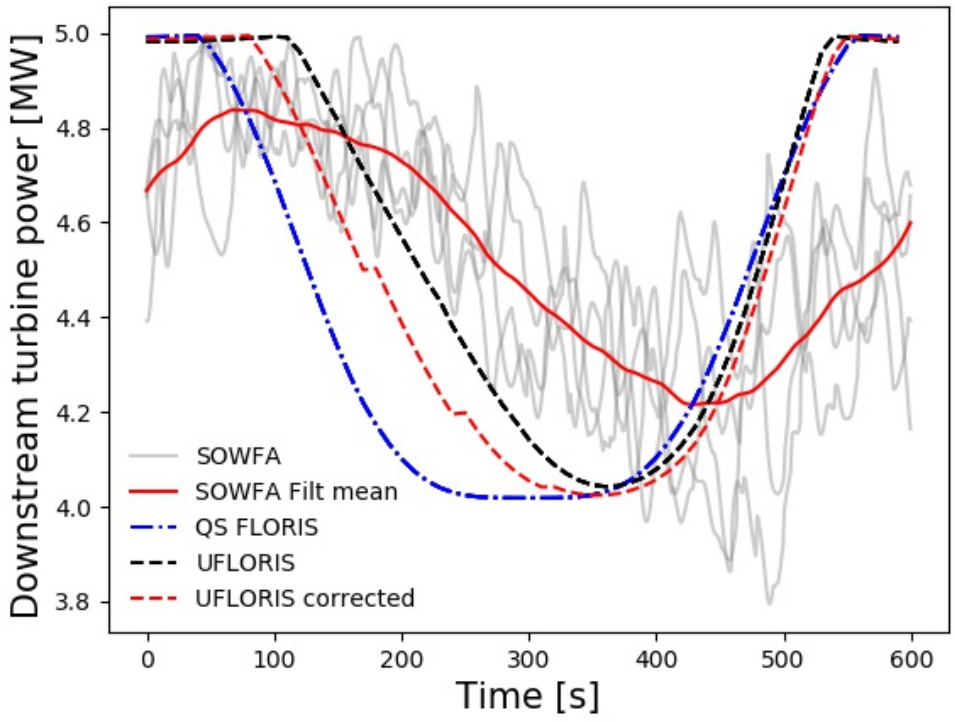

Figure 4: Averaged downstream WT power comparison for the four 600s-periods.

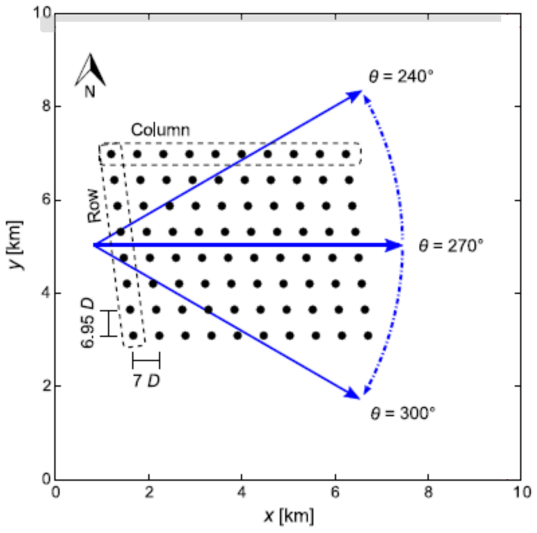

Figure 5: Layout of the Horns Rev wind farm [10].

converging to the steady state solution when the rate of oscillation is decreased. It can be noticed that the starting wind direction is 270° and thus the red curves are starting from the steady state value and then reaching the other unsteady curves. Unlike the LES results, UFLORIS results are not going lower than FLORIS minimum value. Munters et al. hypothesize this effect is due to high-speed channels in between turbine columns in LES steady wind direction simulation [10], an effect which is not captured in our simple wake model. Due to this difference in the steady-state wind farm power between UFLORIS and LES at 270°, the normalization of the UFLORIS results is done with LES at $\theta = 240$. Except for three steady state values around 270°, FLORIS is comparing well with LES. On top of a good estimation of the power minimum locations, UFLORIS is showing good agreement with LES to represent small power variations apart from the middle region ($240 < \theta < 260$ and $280 < \theta < 300$). This shows the high potential of UFLORIS to represent wake dynamic behaviours.

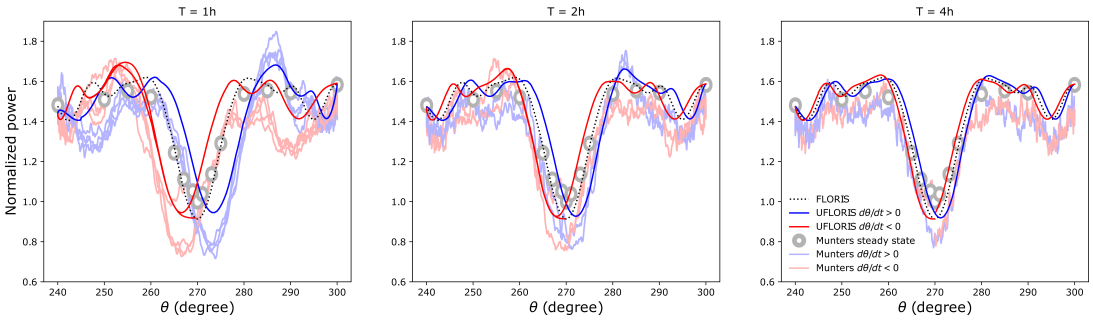

Figure 6: Power variations as a function of wind directions for 3 different oscillation period: $T_\theta = 1h$ (Left), 2h (Middle), 4h (Right). Powers are normalized with steady-state power in LES for $\theta = 240°$. Opaque lines indicate (U)FLORIS results produced in the current paper. Transparent lines are LES results from Munters et al. [10]

4.2. Frontal wind-direction transient

In order to investigate the potential usage of an unsteady wake model, a new type of wind direction change is investigated. While before the wind direction was changing everywhere at the same time, now the wind direction is propagating inside the wind farm. This is representing a small atmospheric-scale effect like a frontal wind passage or a storm. The wind direction is still oscillating as previously defined but it is now corresponding only to the value of the WT at the North-West corner. Then the change propagates through the wind farm at the free-stream velocity of 8 m/s. For this case, the UFLORIS model is not necessary as the heterogenous wind direction can be directly incorporated into the free stream flow field with FLORIS. Thus, frontal direction change is comparable to a QS FLORIS simulation.

In Figure 7, a comparison between the mesoscale (Top) and frontal (Bottom) wind direction definitions is shown for two different time steps corresponding to the minima of UFLORIS in Figure 6 Left: $\theta = 273.6$ at $k = 1870s$ (Left) and $\theta = 266.7$ at $k = 3660s$ (Right). The same period of $T_\theta = 1h$ is used. The arrows are representing local wind directions. For Top figures, only three unsteady wake centrelines are represented in order to avoid overload of the figure but every WT as an associated centreline. It can be seen that the two wind direction change formulations are leading to very different wake deviations inside the wind farm. In the frontal wind figures, WTs on the West part are largely interacting while on the East they are not. Because of this fast wind direction change, strong wake interactions are always limited to subsets of wind turbines, and are rarely present in the entire farm leading to a flatter power curve as shown in Figure 8 blue curve. Figure 8 is also showing that when the rate of oscillation is decreased, frontal results are converging to the steady state solution. Finally, with a period of 4h, the frontal formulation is similar to the mesoscale formulation with a period of 1h.

5. Conclusions

In order to consider wake advection delays and mesoscale wind transients, dynamic wake models are necessary. In this paper, the development of a dynamic wake model is presented and corresponds to a dynamic extension of the steady-state FLORIS. Differences with similar models have been highlighted showing the originality of UFLORIS. Both the validation and the application show the high potential of UFLORIS to represent wake dynamic behaviours. Comparison with LES over the Horns Rev wind farm shows that this new model is able to capture predominant unsteady wake effects but also fine details. Unsteady wake models are opening new possibilities for engineering applications like operational power forecast. Coupled with a weather prediction model, it would be possible to estimate wind-power resources accounting for the influence of synoptic phenomena or to improve current wind farm parametrizations that are commonly used at mesoscale level by informing on sub-grid scale effects. A stand-alone usage is also possible where the flow field is derived from a single measurement location.

Acknowledgements

The authors acknowledge support from the PhairywinD project, funded by the Energy Transition Fund of the Belgian Federal Public Service for Economy, SMEs, and Energy (FOD Economie, KMOs en Energie).

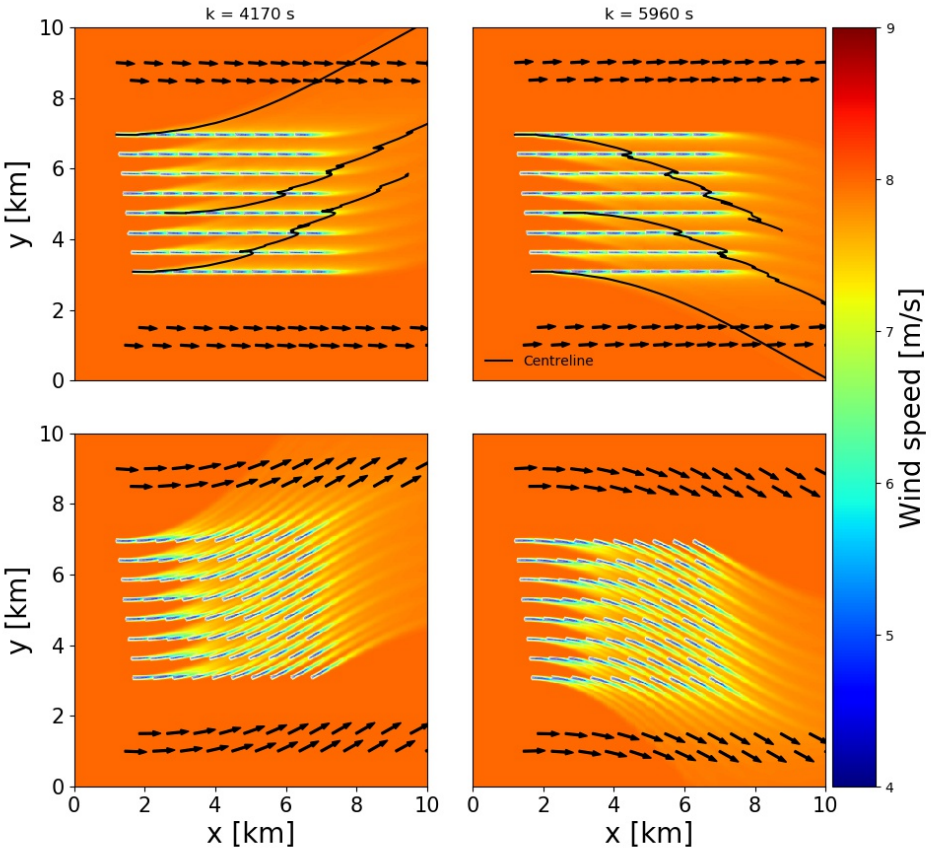

Figure 7: Contours of the instantaneous wind speed at the turbine hub height. Left: At $k = 4170s$, $\theta = 273.6$. Right: At $k = 3660s$, $\theta = 266.7$. Top: Mesoscale wind direction change. Bottom: Frontal wind direction change.

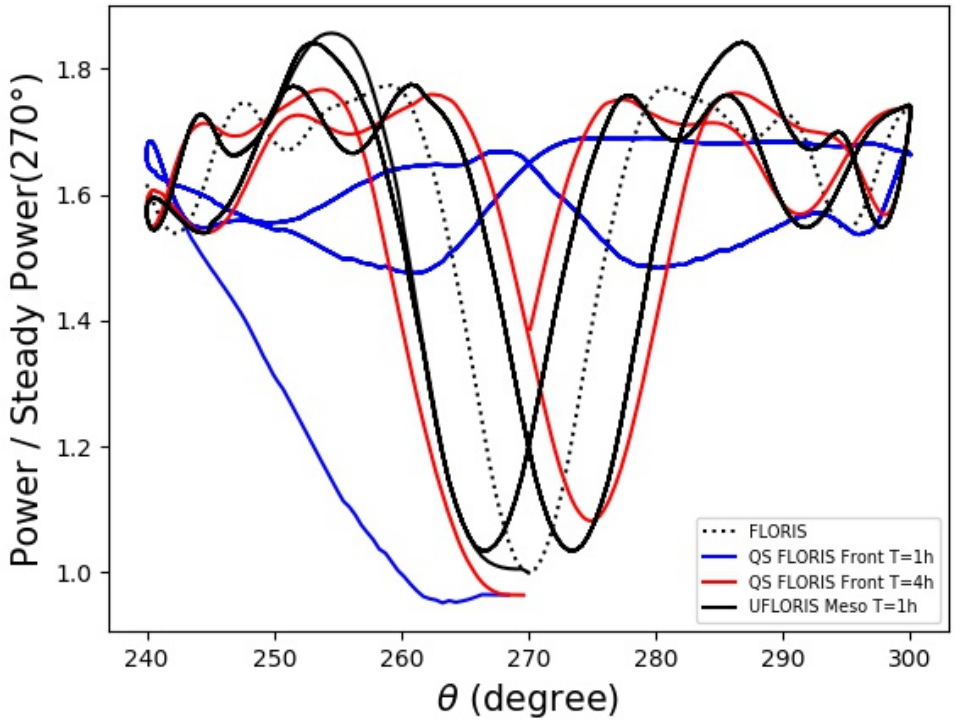

Figure 8: Power variations as a function of wind directions for mesoscale and frontal wind direction change formulations.

References

[1] I. Eguinoa, T. Göçmen, P. B. Garcia-Rosa, K. Das, V. Petrović, K. Kölle, A. Manjock, M. J. Koivisto, M. Smailes, Wind farm flow control oriented to electricity markets and grid integration: Initial perspective analysis, Advanced Control for Applications 3 (3). doi:10.1002/adc2.80.

[2] J. Jonkman, J. Annoni, G. Hayman, B. Jonkman, A. Purkayastha, Development of fast.farm: A new multi-physics engineering tool for wind-farm design and analysis preprint, 35th Wind Energy Symp. (Grapevine Texas).

[3] E. Bossanyi, et al, Description of the reference and the control-oriented wind farm models, cl-windcon deliverable d1.2.
URL https://ec.europa.eu/research/participants/documents/downloadPublic?documentIds=080166e5ba664d11&appId=PPGMS

[4] P. M. O. Gebraad, J. W. van Wingerden, A control-oriented dynamic model for wakes in wind plants, Journal of Physics: Conference Series 524 (2014) 012186. doi:10.1088/1742-6596/524/1/012186.

[5] Floris version 2.4.
URL https://github.com/NREL/floris

[6] M. Becker, B. Ritter, B. Doekemeijer, D. van der Hoek, U. Konigorski, D. Allaerts, J. van Wingerden, The revised floridyn model: Implementation of heterogeneous flow and the gaussian wake preprint, Wind Energy Science Discussions.

[7] J. Bossuyt, R. Scott, N. Ali, R. B. Cal, Quantification of wake shape modulation and deflection for tilt and yaw misaligned wind turbines, Journal of Fluid Mechanics 917. doi:10.1017/jfm.2021.237.

[8] D. Sale, M. Churchfield, P. Bachant, dcsale/sowfa: v1.
URL https://doi.org/10.5281/zenodo.3632051

[9] M. Bastankhah, F. Porté-Agel, A new analytical model for wind-turbine wakes, Renewable Energy 70 (2014) 116–123. doi:10.1016/j.renene.2014.01.002.

[10] W. Munters, C. Meneveau, J. Meyers, Turbulent inflow precursor method with time-varying direction for large-eddy simulations and applications to wind farms, Boundary-Layer Meteorology 159 (2) (2016) 305–328. doi:10.1007/s10546-016-0127-z.

Particle image velocimetry in the propellant flow : A case study of a.300 blackout weapon

Abdelhafidh Moumen

Environmental and Applied Fluid Dynamics Department, Von Karman Institute for Fluid Dynamics, Belgium, abdelhafidh.moumen@gmail.com

Supervisor: Delphine Laboureur

Assistant Professor , Environmental and Applied Fluid Dynamics Department , Von Karman Institute for Fluid Dynamics, Belgium, delphine.laboureur@vki.ac.be

Promotor: Johan Gallant

Professor, Dept of Weapon Systems and Ballistics, Royal Military Academy, Belgium, johan.gallant@dymasec.be

Promotor: Patrick Hendrick

Professor, Laboratory of Aero-Thermo-Mechanics, Université Libre de Bruxelles, Belgium, patrick.hendrick@ulb.ac.be

Abstract

This study is part of ongoing work aiming to improve the understanding of phenomena occurring during the intermediate ballistic phase, such as muzzle flows. Due to the harsh environment, the extremely short duration, and the transient evolution of the intermediate ballistics phase, this flow characterization has been heretofore limited to local and intrusive measurement techniques. Consequently, the quantitative experimental data are limited, so are the number of numerical codes validated in this field. The objective of the present work is to demonstrate the applicability of the Particle Image Velocimetry (PIV) as a quantitative visualization technique in the challenging environment of the propellant flow of a .300 blackout weapon using the naturally present particles in the gas as tracers. To achieve this goal, an experimental setup with four different measurements was installed: (i) PIV system, (ii) classical high-speed schlieren visualization, (iii) optical particle counter, and (vi) projectile velocity measurement. The experimental results demonstrated: (i) The ability of PIV to accurately resolve the main features of the flow as well as the instantaneous velocity fields; (ii) that the structure of this flow is composed of two regions. The first region is located within the underexpanded jet and consists of spatially dispersed particles. The second region, downstream of the Mach disk, is formed by large structures; (iii) that particle tracking velocimetry and cross-correlation algorithms can determine the flow velocity in both regions; (iv) that the combustion products contain sub-micrometric particles which can follow with high fidelity the gas flow.

Keywords: Intermediate ballistics, Particle Imagery Velocimetry, Muzzle flow, Propellant powder, Combustion, Velocity measurement.

1. Introduction

The determination of the muzzle flow field properties is necessary for a better understanding of phenomena occurring in the intermediate ballistics phase (IB) [1]. In addition, the release of propellant gas is accompanied by high momentum and strong blast overpressure, affecting the environment and precision of the weapon system. Therefore, the optimization of the design of muzzle devices and long-range projectiles, as well as the security assessment of personnel and equipment cannot be accomplished without detailed knowledge of muzzle flows.

Muzzle flows generated by the launch of a projectile consist of two distinct but interacting features [2]:

First, one or two precursor flows, essentially composed of still air that initially resides in the barrel expelled outward by a piston effect. When the projectile accelerates in the barrel, it induces compression waves that merge into a normal shock wave. Once it reaches the muzzle exit plane, this shock wave discharges into the open air. It creates then an extremely underexpanded jet encapsulated by an expanding spherical blast wave known as the precursor blast wave. Then, as the projectile base detaches from the barrel, the high-pressure propellant gases, which still contain on average about 40% of their energy, are released into the already disturbed environment. This flow is created by the same mechanism as the precursor flow, resulting in the formation of the main blast wave and the main underexpanded jet. Moreover, the complexity of muzzle flow increases due to the multiphase and reacting characters of the main propellant flow associated with its explosive evolution, as well as the occurrence of flashes and secondary combustion [3]. Due to these complexities, the determination of the quantitative properties of these flows remains limited. This complicates their understanding and their numerical modeling.

An extensive comprehensive literature in the IB field exists [4–8]. However, all publications present the main drawbacks being their qualitative nature and the complexity and limitations of their experimental setups. Optical techniques can form a suitable approach to tackle the lack of quantitative experimental data regarding various quantities of fluids such as density [1] and velocity while being essentially of a nonintrusive nature. For instance, the analysis of the flow velocity profile as a function of time would serve as a valuable reference to validate and improve numerical simulations. There are rather few such references, and the validation of the simulations is mostly limited to the qualitative comparison with shadowgraphy and schlieren images [9–14] resulting in contradictory conclusions [10; 13; 15].

To the author's best knowledge, there has been only one attempt to measure the velocity of exhaust gases at the muzzle [16]. This work was conducted using single-point velocity measurements. To obtain a quantitative description of the entire field, the firing had to be repeated a few dozen times due to short emptying time, making the process very time-consuming and costly. Furthermore, during this study, combustion particles have been used as tracers without any assessment of their tracking capability. Moreover, the implemented technique has only provided measurements of the particles' centerline velocity, which is of minor value in the case of muzzle brake designs, for instance.

The present study explores for the first time the application of Particle Imaging Velocimetry (PIV) [17] as a quantitative visualization technique for muzzle flows. The application of PIV in such flows is considerably challenging due to the presence of important velocity, temperature, and density gradients, and the total lack of control in terms of flow properties, duration, and seeding [18]. Therefore, this paper discusses the feasibility of PIV measurements by using the naturally present particles in the gas as tracers.

Although the first attempt to apply PIV on supersonic flows dates back to 1993 [19], it was not until 2000 that this application proved to be mature and suitable as a modern diagnostics tool in extremely hot, supersonic flow fields ranging from hypersonic flows [20] to combustion environments [21; 22] passing by explosive and shock tube research [23; 24].

Havermann et al. [23] pioneered the use of PIV systems in supersonic flow measurements. They have measured the velocity of shock tunnel freestream and supersonic flows over a wedge and a sphere at Ma = 4.5 and Ma = 6.0, using solid particles of TiO_2 and Al_2O_3 with a nominal size of $0.3\,\mu$m. Balakumar and Adrian [25] performed PIV measurements in the exhaust of small solid rocket engines. They highlighted the difficulty of such a harsh environment, characterized by high temperatures and velocities but concluded that combustion particles are suitable for PIV measurements. They based their assessment only on their diffusion capacity without studying the ability of the particles to follow the gas. In addition, the measurement area was several centimeters downstream of the nozzle exit to avoid measurements inside the underexpanded jet, which is the most difficult part to conduct this type of measurement. Haertig et al. [26] and Arakeri et al. [27] have used high-speed PIV to investigate , the vortex ring formation at an open-ended shock tube. Both have seeded the flow in the driven section with smoke particles having a diameter of $1\,\mu$m. The presented results have permitted a full characterization of the vortex ring formation and properties. Mitchell et al. [28] conducted PIV measurements in core jets with different levels of underexpansion in parallel with high-speed shadowgraphy visualization. They noticed a difference between the theoretically determined tracer relaxation distance and the experimentally observed. They also found that the seeding density varies with the flow density, which constitutes the main reason behind an important discrepancy between the theoretically calculated and the

experimentally measured velocity downstream of the Mach disk (0.7 against 0.4). Scarano [18] has reviewed the challenging technical issues that accompany the application of PIV for the investigation of supersonic and hypersonic flows. He has shown, based on several applications, that these difficulties may be summarized in the evaluation of particles' response and their distribution. Wagner et al. [29] have made time-resolved PIV measurements in the transient flow emanating from a shock tube with and without the presence of a 14 mm cylinder in the test section. They have quantified the velocity and the thickness of the boundary layer along the tube wall. Chen and Liu [30] have emphasized the degree of maturity of PIV by reviewing its applications in combustion measurements. They detailed the state of the art regarding the various tracer particles and the different methods of seeding. Recently, Haghdoost et al. [31] have demonstrated the ability of PIV to investigate the exhaust flow of a Pulse Detonation Combustor (PDC). They have found that TiO_2 particles are the most suitable tracer for this configuration. Their assessment relies on the particles' dispersion and the experimentally determined relaxation time.

The flow condition in the shock tube and PDC configurations [23; 31] can be viewed as equivalent to those that prevail in the barrel of firearms. It must be noted however that there are several fundamental differences regarding the experimental design and the PIV measurement. This is primarily because the formers are initially gas-loaded, unlike weapons where the gas originates from internal combustion. As a matter, in the shock tube, a moving piston compresses the gases until they reach a critical value, leading to the rupture of a burst diaphragm to accelerate and compress the gas in the motor section. Thus, seeding the gas at rest, in the driving section, is straightforward, both in terms of method and the particle specifications. In addition, PDCs allow proper access and seeding of the air before entering the detonation chamber. Furthermore, in both cases, the exhaust gases are significantly more uniform in terms of temperature and composition than the multiphase reactive gas resulting from the combustion of the propellant powder that is encountered in a ballistic environment.

In summary, the implementation of PIV in muzzle flows is subject to a double constraint:

On the one hand, the supersonic velocities of the gases with the presence of discontinuities. Indeed, the muzzle flow originates from a combustion process that initially took place in a closed volume at a high temperature, around 2500°C. Then, at the exit of the barrel, this flow is accelerated to a velocity of about 1300 m/s by the Prandlt-Meyer expansion fan and the extremely underexpanded jet for the configurations considered herein. An additional consideration is the presence of several flow discontinuities, such as the Mach disk.

On the other hand, the complexity of seeding the gases with conventional methods. Although the seeding of dry, homogeneous, non-agglomerated particles is highly recommended for supersonic PIV measurements—which is best provided by dedicated seeding equipment [17]—, the use of these conventional seeding techniques is inappropriate for weapon systems due to the high transient pressure in the combustion chamber: After ignition, the combustion occurs in a closed volume (the projectile is stationary), which results in pressure increase. Once the starting pressure is reached, the projectile progresses through the barrel, but the pressure continues to increase as the amount of gas generated exceeds the volume increment, reaching a maximum pressure of about 150 MPa within 3 ms for the configuration considered in this study. Towards the end of the combustion, this phenomenon is reversed, and the pressure starts to decrease. Then, the seeding pressure is constrained by two factors as follows. From a PIV point of view, it is required that the pressure should be around 1 to 2 MPa higher than the flow pressure [30]. From a ballistic point of view, the seeding pressure should not affect the physics of the flow, i.e., its profile should imitate the bell-shaped one measured in the combustion chamber in terms of amplitude and time reaction (the order of 50 Mpa/ms). Moreover, all things being equal, there is no single pressure curve, but it varies in time and amplitude from shot to shot, i.e., the ballistic dispersion. It would, therefore, be necessary to establish a servo system between the weapon and the seeding device. As we do not have access to such devices and before choosing to engage in the design and manufacturing process of such a system, we investigated the feasibility of PIV measurement based on the naturally existing particle in the gas.

The main objective of this contribution is to demonstrate the feasibility of PIV measurement in the muzzle flow. This aim was accomplished by examining the following questions: (i) Does PIV succeed in resolving the main structures of the muzzle flow? (ii) Are PIV algorithms able to compute particle displacements in this flow (low density and large-scale structures)? (iii) Can the particles that naturally exist in the gas faithfully follow the gas?

This paper is organized as follows: the theory of

particle motion in the flow is detailed in section 2. The experimental setup is presented in section 4. Section 5 discusses the various results of this study in four subsections. The first covers the preliminary observations on the raw PIV images. The second subsection contains the results of the evaluation of the displacement computations of the large structures of the muzzle flow. The results of the response time of naturally existing particles in the gas as well as their distribution are presented in the third and fourth subsections, respectively.

2. The assessment of the particle response across a velocity gradient

The accuracy of PIV measurements assumes the particles' flow-following-fidelity. This assumption becomes critical in supersonic gases where the solid particles have higher densities with respect to the carrier gases. This results in high inertia which may impede their flow-following-fidelity, especially when velocity step changes occur crossing thin regions such as the Mach disk where the gas velocity suddenly drops from supersonic to subsonic. Given the particles' inertia, this sudden fluid deceleration results in a lag between the gas velocity U_f and the particle velocity U_p. In this context, the particle response time τ_p (respectively the particle relaxation distance ξ_p) is the time (respectively the distance) needed for the difference $(U_f - U_p)$ to be reduced by a factor of $1/e$. The response time or distance are crucial indicators of the quality of the measurements [18]. A poor particle response affects the accuracy and the reliability of PIV measurements as it leads to a considerable discrepancy between the gas velocity and the particle velocity ("the measured one") as well as a shifting of the discontinuities' positions, such as shock waves. It is therefore strongly recommended to consider the evaluation of the particle response times before undertaking a flow velocity analysis.

The determination of τ_p is attainable by two methods, analytical and experimental [17]. Both are derived from the equation of motion of a particle in the flow. A thorough discussion of this equation is reported in several papers [32–34], a summarized description is presented here for the sake of completeness. For PIV experiments and when using submicrometer-sized solid particles as tracers in gases, the following assumptions can be adopted. (i) The particle density ρ_p is much higher than the fluid density ρ_f ($\rho_f \ll \rho_p$). (ii) The particles are suspended in a fluid of an infinite extent. (iii) The gravitational and centrifugal forces are neglected. (iv) The force exerted by the fluid on the particles is summarized in the drag force. (v) Given their size, the Reynolds number of the particles $Re_p \ll 1$, so the Stokes' drag law can be applied. Therefore, the equation of motion of a particle in the flow can be greatly simplified:

$$\begin{aligned} \frac{dU_p(t)}{dt} &= -\frac{3}{4} C_D Re_p \frac{\mu}{\rho_p d_p^2} (U_p(t) - U_f(t)) \\ &= -\frac{1}{\tau_p} (U_p(t) - U_f(t)) \end{aligned} \tag{1}$$

where C_D denotes the particle drag coefficient. The Reynolds number is calculated with respect to the velocity lag $(U_p - U_f)$ and the particle diameter d_p. From Eq.1 results that τ_p is only a function of the fluid dynamic viscosity μ, the particle density ρ_p, and the particle diameter d_p. The calculation of τ_p using the analytical formula (Eq.1) is subject to considerable uncertainties related to the determination of ρ_p and d_p [18]. Therefore, it is strongly encouraged to use an experimental procedure wherein τ_p is quantified from the particle's actual behavior when passing through a sharp decrease in velocity, such as a Mach disk [23; 33].

The solution of the differential equation (Eq.1) with an initial condition $U_p(t = 0) = 0$ is

$$U_p(t) = U_f(t) \left(1 - e^{-\frac{t}{\tau_p}}\right) \tag{2}$$

To analyze the velocity of particles through a normal shock wave (Fig. 1), the dimensionless slip velocity U^* is defined as follows:

$$U^*(t) = \frac{U_{pn}(t) - U_{n2}}{U_{n1} - U_{n2}} = e^{\frac{-t}{\tau_p}} \tag{3}$$

where Un_1 and Un_2 denote the normal velocities of the flow upstream and downstream of the shock, and U_{pn} is the particle velocity normal to the shock as a function of time. Eq.3 shows that when a particle passes through a shock wave, it decelerates exponentially, with a decay factor equal to $-t/\tau_p$ to reach the downstream normal velocity of the flow.

If we further integrate this equation, the normal position x_n in a coordinate system relative to the shock wave location can be written as follows:

$$x_n = U_{n2} t + \tau_p (U_{n1} - U_{n2})(1 - U^*) \tag{4}$$

At $t = \tau_p$:

$$x_n = \xi_p = \tau_p [U_{n1} - (U_{n1} - U_{n2}) e^{-1}] \tag{5}$$

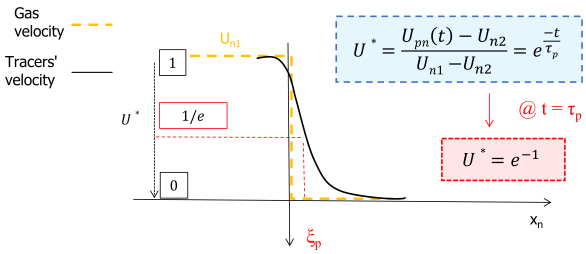

Figure 1: Particle velocity profile across a normal shock

However, the particle response time τ_p alone cannot fully explain the fluid dynamic behavior of the moving particle. The particle Stokes number (St_p) is used to express the particle tracking capability regarding a specific flow configuration:

$$St_p = \frac{\tau_p}{\tau_f} = \frac{\tau_p U_c}{L_c} \tag{6}$$

were τ_f denotes the characteristic time of the flow which is the ratio of its characteristic length L_c to its characteristic velocity U_c. An estimate of the muzzle flow characteristic time is given by $\tau_f = D_j/U_{n1}$, where D_j is the diameter of the underexpanded jet [35; 36]. For low Stokes numbers, i.e., $St_p \ll 1$, the particle is considered to have a high tracking ability and that the slip velocity is negligible. Samimy and Lele [37] analyzed the accuracy of particle tracking using numerical simulations and concluded that for good particle flow fidelity, St_p should not exceed 0.1. This rule is widely adopted for PIV measurements.

3. Experimental setup

The schematic of the experimental setup employed in this study is illustrated in Fig. 2. It consists of four measurement chains; their respective descriptions, as well as the weapon system, are detailed in the subsequent paragraphs.

The visualized muzzle flows are issued from the launch of a .300 Blackout caliber projectile by a Prototypa laboratory weapon model STZA 16$M2$. The propellant powder was Vihtavuori's $N120$ rifle powder [38]. The mass of the propellant powder in the case was $m_{powder} = 0.6$ g which resulted in an average projectile velocity of $V_{proj} = 301$ m/s. The projectile velocity was measured by an infrared double velocity screen placed at a 5 m distance from the muzzle. In addition to the projectile velocity measurements, the device serves as a trigger for both the PIV and the classic schlieren.

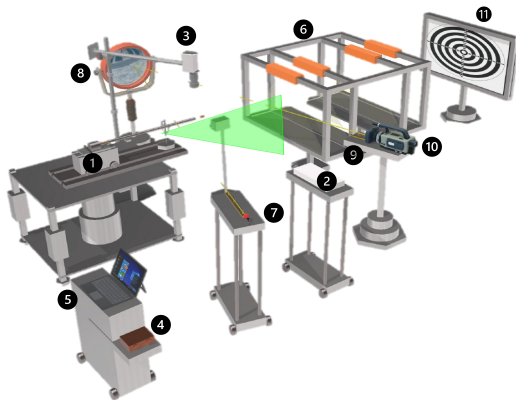

Figure 2: Representation of the experimental setup, 1: weapon system, 2: laser, 3: PIV camera, 4: synchronizer, 5: computer, 6: infrared double velocity screen, 7: light source, 8: parabolic mirror, 9: knife edge, 10: high-speed camera, 11: target.

The 2D PIV system is organized as follows: The muzzle flow was illuminated by a double pulsed Nd:YLF laser type Litron LD30-527 PIV which produces a laser output at $\lambda = 527$ nm (green) with a maximal power of 32.9 mJ/pulse at 1 kHz. It was positioned at a distance $d_L = 1.37$ m from the weapon centerline. Using a cylindrical lens ($f = -20$ mm), the laser beam is converted into a laser sheet that illuminates the horizontal plane passing through the muzzle symmetry axis. This sheet was focused and adjusted so that its minimum thickness was positioned on the muzzle centerline. To avoid laser light reflections, the part of the barrel that was protruding in the laser field was coated with anti-reflective tape. The PIV images were recorded using a Phantom VEO-E-340 L high-speed camera. The viewing direction of the camera was perpendicular to the laser sheet with a standoff distance $d_C = 0.88$ m. A Nikon lens with $f = 50$ mm, mounted with an f-number $f\# = 8$ was set for well-focused particles images and to reduce aero-optical distortion due to temperature and density gradients [39]. The camera was also fitted with a 527 nm band-pass filter with a bandwidth of 10 nm to increase the SNR by filtering out the muzzle flash or any other radiation source. The optical scale factor was $M_f = 5.45$ pix/mm (183.486 μm/pix). The images were recorded at 1.774 kHz in double frame single exposure mode—the maximum rate allowed by the camera—with an exposure time of 280 μs and a pulse separation of $dt = 1.5\,\mu$s. The image size was 1024x800 pixels which gave a field of view (FOV) of

187x128 mm. To synchronize the laser and the camera, a PTU X LaVision High-speed Controller is used.

To assess the particles flow tracking fidelity, the position of the Mach disk (M) should be known with high confidence. Therefore, a single mirror off-axis schlieren system with a 400 mm diameter f = 1.2 m parabolic mirror was implemented [40]. Since the muzzle flow is axisymmetric, the schlieren FOV was designed to be perpendicular to the laser sheet. A high-speed camera type Photron FASTCAM SA-X2 was used during the experiment. This camera was equipped with Nikon lenses with a focal length f = 200 mm and an $f\#$ = 4.5.

The particle size distribution was determined by the GRIMM aerosol spectrometer model 11-D (GRIMM Aerosol Technik GmbH & Co., Ainring, Germany). Based on an optical detection method, this model sizes particles in the range of 0.253 to 35.150 μm and determines their concentration in the number of particles/L. It was programmed for continuous recording throughout the tests with a sampling time of 1 s. In this configuration, the system detects particles ranging in size from 0.253 to 2.982 μm. Its suction head was positioned at a distance d_G = 0.30 m in front of the gun muzzle with a lowering of 0.10 m.

4. Results and discussion

4.1. PIV raw images and preliminary observations

Fig. 3a shows the raw PIV image of the main propellant flow shortly after the projectile cleared the core jet. The direction of firing—the direction of flow—is from left to right, the release of the projectile base from the barrel and its exit plane are considered the origins of the time ($t_{emptying}$) and the length scales, respectively. The PIV has successfully reconstructed the main features of this flow. Qualitatively, these images provide a significant amount of information about the flow structure that is similar to the results of classical schlieren, as well as the BOS visualizations performed by the authors [1]. Indeed, the salient features of the underexpanded jet such as the Prandtl-Meyer expansion fan, the shock bottle, the intercepting shocks, the Mach disk, and the vortex rings are visible. From a point of view of particle density, the flow situation inside the shock bottle corresponds to a low-density case [17]. This was expected because of the low density of the gas and the high velocities in this zone. This is not specific to the use of unburned grains as tracers. Indeed, this low particle density concern is generally encountered in the application of PIV for the underexpanded jets even with gas seeding under much more controlled flow conditions [41].

Then, as the pressure ratio P_e/P_0 increases (P_e is the outlet pressure and P_0 is the ambient pressure), the size of the underexpanded jet increases downstream and then shrinks upstream, conversely [42]. Fig. 3b and Fig. 3c show the flow situation at $t_{emptying}$ = 809.5 μs and $t_{emptying}$ = 1373.1 μs corresponding respectively to the beginning and an advanced stage of the shrinkage where the Mach disk is located at approximately 25 mm from the muzzle. In both cases, regions of the muzzle flow downstream of the underexpanded jet corresponding to high turbulence, delineated by a dashed rectangle in the images, were captured as large structures. These are the two varieties of large structures, labeled $LS\,1$ and $LS\,2$ in Fig. 3b and 3c, observed in all shots. These structures are different from the large structures –also known as speckle patterns– encountered in PIV [17]. In this case, it is essential to ascertain that the cross-correlation algorithms can determine the displacement of these structures.

4.2. Assessment of displacement computations of the muzzle flow large structures: Monte Carlo Simulations

Six Monte Carlo simulations were designed to evaluate the accuracy of the displacement calculation of encountered large scales of type $LS\,1$ and $LS\,2$ using the cross-correlation method, i.e., these simulations aimed to answer the following question: Does the cross-correlation algorithm accurately compute the displacement of these structures?

The first two simulations consisted of randomly sampling a snapshot, termed frame A, with a size of 512x512 pixels from each of the areas labeled $LS\,1$ and $LS\,2$. Then, a second snapshot, frame B, is artificially generated by sliding the frame A in the horizontal direction with a displacement $u_{true} = N$ pixel, with $N = 0.5 : 0.5 : 15$. This operation was repeated 500 times so that for each u-displacement, 500 double frames (a total of 15000 double frames) were generated. Then the displacement fields were calculated using a multi-pass cross-correlation algorithm WiDIM [43] with interrogation window from 128x128 pixels to 32x32 pixels with an overlap factor of 75% was applied. The third simulation is intended to be the reference one where the simulated situations were chosen based on typical PIV recommendations [17]. Thus, for each displacement $u_{true} = N$ pixel, 500 synthetic

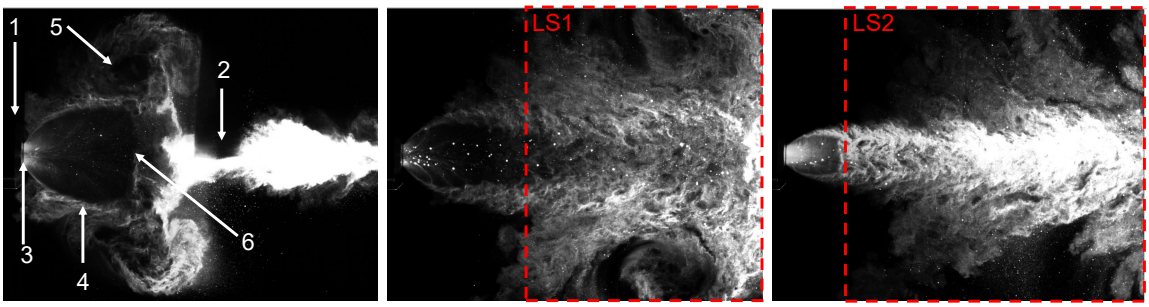

Figure 3: Raw PIV images of the structure of the main propellant released from the launch of the subsonic projectile, $m_{powder} = 0.6$ g, $V_{proj} = 311$ m/s, at (a): $t_{emptying} = 245.8\,\mu$s, (b): $t_{emptying} = 809.5\,\mu$s, (c): $t_{emptying} = 1373.1\,\mu$s. 1: the muzzle, 2: the projectile, 3: Prandtl-Meyer expansion fan, 4: the intercepting shock, 5: the vortex ring, 6: the Mach disk.

double-frame images were generated with 30000 randomly distributed particles whose sizes $d_p = 3 \pm 1$ pixel with a particle density equal to 0.12 ppp.

Then, three other simulations were replicated as above; this time the B images were corrupted by zero-mean white Gaussian noise with a standard deviation equal to 0.001. The displacement fields were calculated using a cross-correlation algorithm according to the specifications described above..

The accuracy of the displacement calculations was evaluated in terms of the total error, δ, defined as follows:

$$\delta = \sqrt{\varepsilon_{bias}{}^2 + \epsilon_{rms}{}^2} \tag{7}$$

where ϵ_{bias} and ε_{rms} are the bias and random error, respectively, and determined as follows:

$$\epsilon_{bias} = \frac{1}{n}\sum_{i=1}^{n} u_{cc} - u_{true} \tag{8}$$

$$\epsilon_{rms} = \frac{1}{n}\sqrt{\sum_{i=1}^{n}(\bar{u_{cc}} - u_{cc})^2} \tag{9}$$

where u_{cc} and $\bar{u_{cc}}$ are the calculated displacement and its mean, respectively, and n is the sample size.

For the noise-free condition, Fig. 4a, the total errors of the computed displacements of the different image types exhibit periodic behaviors with similar minimums δ_{min} but with different shapes, periods T, and maximum δ_{max}. The total error computed for the synthetic images exhibits the classic behavior of a single-pixel triangular waveform with a δ_{min} of about $2 \cdot 10^{-3}$ for integer displacements, and a δ_{max} of about $9 \cdot 10^{-3}$ for semi-integer displacements. The δ

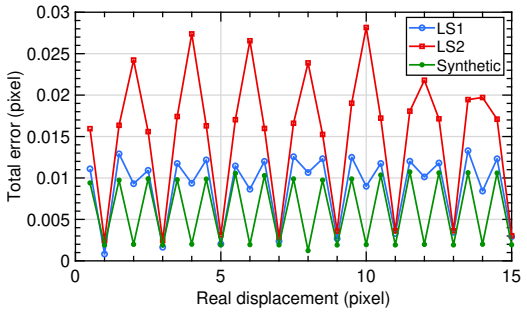

(a)

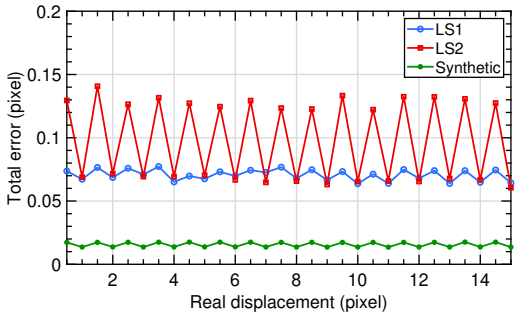

(b)

Figure 4: Accuracy of displacement calculation (total error) of large-scale turbulent patterns ($LS\,1$ and $LS\,2$) embedded in PIV images of muzzle flow using cross-correlation: $LS\,1$ vs. $LS\,2$ vs. synthetic images (a): noise-free and (b): with zero-mean white Gaussian noise with $std = 0.001$.

computed for the $LS\,2$ patterned images also exhibit triangular waveform behavior but with a larger period $T = 2$pixels. In this case, we observe δ_{min} values on odd displacements and δ_{max} values of about 0.025 pixels on even displacements. The δ resulting from the computation of the displacement of the images of the $LS\,1$ type pattern has an M waveform with a period $T = 2$ pixels sharing the same minimum as the previous case and a δ_{max} of about 0.012 pixel at half-integer displacements. Also, in this case, the calculation of even displacements results in relatively high total errors.

Surprisingly, the calculated displacement of the experimental structures showed a maximum total error lower than the minimum total error reported in the literature under controlled PIV conditions, which is of the order of 0.04 pixel [44]. However, classically the error maximum is seen in fractional displacements (subpixel displacements), where the calculated displacement is biased toward an integer displacement [45]. In both cases of the current situation, it is observed that the calculated displacement is also biased towards an odd displacement. This is most likely related to the subpixel estimator algorithm, which is not adapted to this particular structure. Indeed, large structures give rise to rather large peaks of detections in the cross-correlation field as opposed to very narrow peaks that would result from discrete particles, thus complicating the fitting function and the subpixel interpolation.

For corrupted images, Fig. 4b, we observe that the displacement computations of the experimental images are more sensitive to noise than those of the synthetic images and that all total errors exhibit the single-pixel triangular waveform. Indeed, the δ resulting from the $LS\,1$ structure fluctuates slightly around 0.07 pixels. However, although the δ resulting from the $LS\,2$ structure shares the same minimum as that of $LS\,1$, it experiences a δ_{max} around 0.12 pixel at the semi-integer displacements. The total errors from the computation of the displacement of the synthetic images are relatively small, with values lower than 0.02 pixel. Thus, even in this case, where the experimental images have been degraded, the total errors on the determination of the displacement of the large structures oscillate around the famous one-tenth of a pixel bar that is usually reported in the experimental images [44]. We can therefore conclude on the ability of the cross-correlation algorithm to interpret the displacement of turbulent structures and large structures in the muzzle flow occurring downstream of the Mach disk.

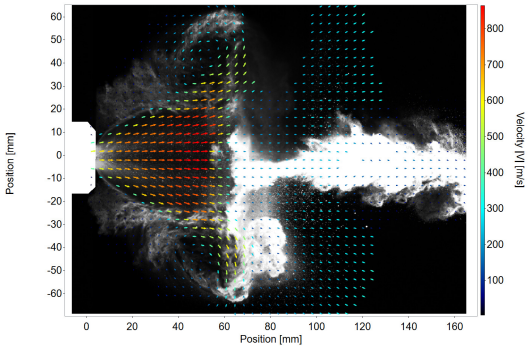

(a) $t_{emptying} = 242.2\,\mu$s, $x_p = 70.5$ mm, $V_{proj} = 284$ m/s

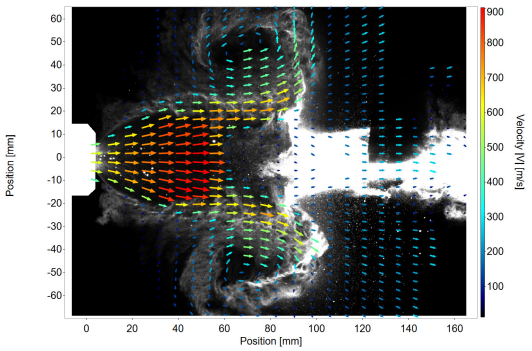

(b) $t_{emptying} = 402.6\,\mu$s, $x_p = 122.5$ mm, $V_{proj} = 293$ m/s

Figure 5: The velocity magnitude field for the muzzle flows determined using the coupled PTV-PIV algorithm. The vector field is subsampled by a factor of two in both directions.

4.3. The response time of the naturally existing particle in the gas

Fig. 5 shows the velocity magnitude fields, computed for two different situations of the emptying process using a hybrid algorithm PIV-PTV [46]. The efficiency of this evaluation approach in the case of high-density gradient and inhomogeneous seeding has been proved [47]. Despite the lack of tracer particles and the high density and velocity gradients, the PTV-PIV coupled algorithm succeeds in computing the particle displacement within the jet core. Both velocity fields are smooth, homogenous, and symmetric. Moreover, the velocity fields reflect the actual physical behavior of the different mechanisms. We can observe that the gas acceleration within the jet core is followed by a sudden deceleration at the Mach disk, that the gas velocities are still supersonic across the intercepting shock and at the slip line resulting from the triple point with the Mach disk and the barrel shock (visible between $x = 60$ and 80 mm in Fig. 5b), as well that

swirling nature at the vortex ring. This agrees with the dynamic behavior of the extremely underexpanded jet [48].

The particle response time has been investigated according to the following workflow: (i) PIV imaging of the muzzle flow at different stages of the emptying process. (ii) Compute the average flow velocity normal to the Mach disk over a width corresponding to the caliber centered on the barrel's axis of symmetry. (iii) Plot the slip velocity $U*$ in a reference frame relative to the Mach disk location determined from the classical schlieren images. (iv) Through a fitting function, determine the response distance ξ_p. (v) Compute the response time τ_p according to Eq. 5. This process was supported by the determination of the particle size distribution in the exhaust gases using an optical particle counter.

Due to the ballistic dispersion and camera limitations, it was not possible to average the recorded PIV images. Thus, each response time determination has been performed based on an instantaneous flow field, all results were statically validated, and experimental reproducibility was ensured.

The comparison of the Mach disk position and shape between the schlieren images and the PIV velocity fields has shown a satisfactory agreement. Nevertheless, the PIV images indicate a slightly higher Mach disk position than its actual position as determined from the schlieren images. This is due to the sudden deceleration of the gas through the shock and the inherent response time required for the particles to gradually reach the gas velocity PIV measurements

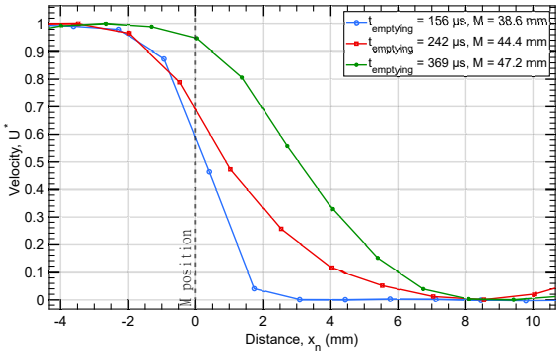

Figure 6: Sample of PIV measurement of the dimensionless slip velocity across the Mach disc along the underexpanded jet centerline.

based on the naturally present particles in the gas revealed that the muzzle flow could not be characterized by a single response time τ_p. Fig. 6 presents three profiles of the particle slip velocity measured across the Mach disk. In all three situations, the velocities U_{n1} and U_{n2} have comparable magnitudes, and the profiles are drawn in a reference system (x_n) relative to the location of the Mach disk determined by schlieren visualization, indicated by a vertical dashed line. Each profile is relative to a specific time of the emptying process ($t_{emptying}$) and therefore three different positions of Mach disk M can be identified. Further analyzing these graphs, a significant change of the shape of these curves as a function of time can be observed. These are visible at the level of the deceleration slopes when passing through the Mach disk. As $t_{emptying}$ progress, the steepness of this slope decreases, thus, the relaxation distance increases. Since the magnitudes of the velocities are of the same magnitude the deceleration process is slowing down as the emptying advances. Fig. 6 also shows that the smallest relaxation distance corresponds to $t_{emptying} = 156\,\mu$s with a Mach disk position $M = 38.6$ mm. This corresponds to the earliest formation of the underexpanded jet unperturbed by the projectile presence. This finding was observed repeatedly and yielded the fastest average particle response time $\tau_p = 1.35\,\mu$s. The results of the average particle response time and Stokes number estimated from N shots are summarized in Table. 1 with the corresponding flow conditions ($t_{emptying}$ and M). It can be seen that the response times τ_p range from $1.35\,\mu$s to $5.10\,\mu$s and increase as a function of $t_{emptying}$. The analysis of these experimental results has led to the splitting of the muzzle flow expansion, as a function of response times, into three phases. Each of these phases are grouping the flow situations that have comparable response times. In terms of Stokes number, it has shown small numbers indicating good flow fidelity of the particles. This is mainly the case when $St_p < 0.1$, which is limited to the first 0.932 ms for the considered ballistic condition. We may therefore conclude that the use of naturally existing particles in the gas as tracers is an appropriate approach for PIV measurement in the muzzle flow, at least during the first phase of emptying where the projectile is still interacting with the combustion gases.

To assess the trend of the relaxation time, namely a rapid response time followed by a gradual slowing down, several aspects need to be discussed. As the relaxation time primarily depends on particle size, it was expected that the fastest response time occurs at the very beginning of the emptying process because, at this stage, the gas is loaded with the smallest and most homogeneous particle size. From a general point

Table 1: Relaxation time and Stokes number for the naturally existing particles in muzzle flow

$t_{emptying}$ (ms)		M (mm)		N° of rounds	τ_p (μs)	St_p
From	To	From	To			
0.154		37		3	1.35	0.03
0.211	0.932	39	51	10	4.09	0.08
		51	32			
1.048	1.660	30	15	8	5.10	0.11
1.936	2.164	13	9.5	4		0.19

of view, the increase in the response time can be explained by technical and physical reasons. The technical aspects consist in the method of evaluating the particle displacements such as the employed cross-correlation algorithm and the size of its interrogation window, as well as the spatial position of the Mach disk within this window, given that the same technique was adopted throughout this investigation, the impact of this parameter can be considered as equal. As for the physical aspects, they are numerous and have a considerable influence on the current flow, the most significant of them are outlined further on.

First, the combustion gas is not homogeneous and contains particles of various sizes, that is the so-called polydispersity. Polydispersity has an important impact on the determination of τ_p. Mitchell et al. [49] have shown that the wide dispersion of the particles' size produces poorer response times. Indeed, larger diameter particles have more intensity in the raw images, and therefore they have a greater influence on the correlation plane. Knowing that these particles move slower than the smaller ones, especially in the case of large velocity gradients, could cause a shift in the peak detection in the correlation plane. It is noteworthy that this weakness is not limited to the use of natural particles, even the most developed seeding methods, including fluidized beds and cyclones, suffer from the same problem and show a high polydispersity that intensifies during the passage across shock waves which, in turn, break up particle agglomerations [49].

Second, the flow conditions influence the particle relaxation process, namely the upstream and downstream velocities, the Mach disk strength, and the state of the post-shock regions. These conditions vary considerably throughout the emptying cycle. For instance, the occurrence of the after-burning process which is a particular phenomenon in intermediate ballistics [50]. It consists of the reinflamation of the unburned particles once in contact with the free air. In fact, this fuel-rich gas with a negative oxygen balance, first experienced heating when crossing the Mach disk, the so-called shock heating, then was supplied with oxygen through a turbulent mixing between the propellant gas plume and the ambient air. These conditions are favorable for the re-ignition of the unburned grains, resulting in a second combustion. This phenomenon has been identified in the studied case, via the BOS visualization [1], as taking place downstream of the Mach disk, leading to an increase in temperature and re-acceleration of the gases, thus modifying the flow post-shock conditions.

Third, the aero-optical distortion is an important physical factor that should not be overlooked, in particular in the presence of large temperature and density gradients. This distortion can cause distorted particle images or even result in ghost particles [39]. The impact of this phenomenon varies according to the angle at which the camera perceives the Mach disk. When the position of the latter changes, the angle of view also changes, which is the case in the muzzle flow since the underexpanded jet grows and then shrinks. The effect of the angle variation was observed in the measured velocity profiles, which in some cases show unphysical oscillations or peaks, whereas in other situations they exhibit a rather smooth shape. These observations are in perfect agreement with those of Elsinga et al. [39].

4.4. Particle distribution

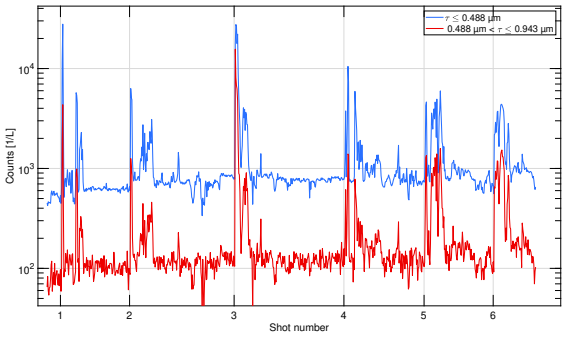

Figure 7: Detection of the concentration of submicrometric-size particles in particles / liter for six successive shots with m_{powder} = 0.6 g.

Fig. 7 displays the particle number concentration, in particles/liter, detected by the aerosol spectrometer. It shows two categories of particle sizes $\tau_p \leq 0.488\,\mu$m and $0.488\,\mu m < \tau_p \leq 0.0.943\,\mu$m for six measurements (shots). We are interested only in this

range of particle sizes as these are the unique size range for which the particles can accurately follow the gas flow. Even though the sampling rate of the employed device is low compared to the time scale of the flow, these results show good detection with excellent repeatability. At each shot, there is an increase in particle concentration. The different peaks within the two categories of interest have approximately the same intensity throughout the six shots. Thus, confirming that the combustion products contain submicron-sized particles that can accurately track the gas velocity, which contradicts Klingebreg's conclusion when he stated that the minimum particle size in the muzzle flow is $1\,\mu m$ [16]. The analysis of the gas composition at each detection peak for 20 shots, showed that the particle size distribution has an obvious consistency. Table. 2 shows the average percentage and standard deviation (STD) of four particle size classes. It can be seen that the combustion gases contain a particle size distribution that covers a range of sizes from the nanoscale to a few microns. This highlights the polydispersity aspect previously discussed. Furthermore, the relatively low STD numbers prove that the gas composition, in terms of particle size, is quite uniform from shot to shot. If we also take into consideration that any particle size larger than $1.821\,\mu m$ is counted in the fourth category while those smaller than $0.253\,\mu\,m$ are considered as inexistent, we can state that the fraction of submicrometer particles in the combustion gases is about 50%.

Table 2: Particle size distribution obtained from 20 tests at the peak detection

$d_p \leq 0.488\,\mu m$	$0.488\,\mu m < d_p \leq 0.943\,\mu m$	$0.943\,\mu m < d_p \leq 1.821\,\mu m$	$d_p > 1.821\,\mu m$
33.44% ± 8.24%	8.76% ± 2.16%	15.72% ± 2.95%	41.87% ± 7.68%

5. Conclusion

In summary, this work has discussed the feasibility of PIV measurements in the IB by measuring the velocity fields of the main propellant flow discharged after firing subsonic .300 Blackout projectiles. The PIV images were captured using naturally present particles in the gas as tracers. The results presented in this paper highlighted the potential and suitability of PIV as a diagnostic tool in the intermediate ballistic phase.

It was shown that the PIV has captured the main features of the main propellant flow consisting mainly of an extremely underexpanded jet and the vortex rings. From a particle-displacement computation standpoint, it has been demonstrated that the coupled PTV-PIV algorithm can overcome the lack of particles inside the shock bottle. Furthermore, based on Monte Carlo simulations, it was proven that the cross-correlation algorithm can accurately evaluate the PIV images formed by the continuous and large structures of the turbulent flow that occurs downstream of the Mach disk.

From a flow tracking standpoint, we have concluded that the combustion products contain submicrometric particles that can accurately follow the gas flow. However, the experimental results have revealed that the muzzle flow cannot be treated as homogeneous; $\tau_p = f(t_{empting})$. Moreover, we have demonstrated that the considered muzzle flow configuration showed good particles' flow-following-fidelity with $St_p < 0.1$, up to $t_{empting} = 0.932\,\mu$s. These results provide a significant first step towards the application of PIV in the IB.

Acknowledgments

The authors would like to acknowledge the team of the Accredited Ballistic Applications Laboratory at the Royal Military Academy for their efforts during the establishment of the experimental setups.

References

[1] A. Moumen, D. Laboureur, J. Gallant, P. Hendrick, On the Application of Background Oriented Schlieren Technique on Ballistics Field (2020).

[2] A. Moumen, J. Grossen, I. Ndindabahizi, J. Gallant, P. Hendrick, Visualization and analysis of muzzle flow fields using the Background-Oriented Schlieren technique, Journal of Visualization (2020-03-30) 1–15.

[3] G. Klingenberg, Gun Muzzle Blast and Flash, Propellants, Explosives, Pyrotechnics 14 (2) (1989-04) 57–68.

[4] G. Klingenberg, J. M. Heimerl, Gun Muzzle Blast and Flash, Vol. 139 of Progress in Astronautics and Aeronautics, Washington, DC : American Institute of Aeronautics and Astronautics, ©1992., 1992-01-01.

[5] G. Klingenberg, Investigation of combustion phenomena associated with the flow of hot propellant gases. III: Experimental survey of the formation and decay of muzzle flow fields and of pressure measurements, Combustion and Flame 29 (1977-01) 289–309.

[6] E. M. Schmidt, D. Shear, Optical Measurements of Muzzle Blast, AIAA Journal 13 (8) (1975-08) 1086–1091.

[7] E. M. Schmidt, Muzzle Blast Pressure Loadings upon Aircraft Surfaces:, Tech. rep., Defense Technical Information Center (1984).

[8] E. M. Schmidt, D. D. Shear, The Flow Field About the Muzzle of An H-16 Rifle, Tech. Rep. AD916646, USA Ballistic Research Laboratory (1974).

[9] E. Chaturvedi, R. K. Dwivedi, Computer aided design and analysis of a tunable muzzle brake, Defence Technology 15 (1) (2019-02) 89–94.

[10] P.-f. Li, Numerical research on adverse effect of muzzle flow formed by muzzle brake considering secondary combustion, Defence Technology (2021) 12.

[11] R. Gopalapillai, H.-D. Kim, T. Setoguchi, S. Matsuo, On the near-field aerodynamics of a projectile launched from a ballistic range, Journal of Mechanical Science and Technology 21 (7) (2007-07) 1129–1138.

[12] D. Cler, CFD Application to Gun Muzzle Blast - A Validation Case Study, in: 41st Aerospace Sciences Meeting and Exhibit, American Institute of Aeronautics and Astronautics, 2003-01-06.

[13] C. K. Muthukumaran, G. Rajesh, H. D. Kim, The Launch Dynamics of Supersonic Projectiles, Journal of Spacecraft and Rockets 50 (6) (2012) 27.

[14] J.-h. Zhang, Y.-g. Yu, X.-w. Zhang, Numerical investigation of a muzzle multiphase flow field using two underwater launch methods, Defence Technology (2021-09) S2214914721001793.

[15] X. Jiang, Z. Chen, B. Fan, H. Li, Numerical simulation of blast flow fields induced by a high-speed projectile, Shock Waves 18 (3) (2008-08) 205–212.

[16] G. Klingenberg, G. Schröder, Investigation of combustion phenomena associated with the flow of hot propellant gases-II: Gas velocity measurements by laser-induced gas breakdown, Combustion and Flame 27 (1976-08) 177–187.

[17] M. Raffel, C. E. Willert, F. Scarano, C. J. Kähler, S. T. Wereley, J. Kompenhans, Particle Image Velocimetry: A Practical Guide, third edition Edition, Springer, 2018.

[18] F. Scarano, Overview of PIV in Supersonic Flows, in: Particle Image Velocimetry, Vol. 112 of Topics in Applied Physics, Springer Berlin Heidelberg, 2008, pp. 445–463.

[19] W. M. Humphreys, Jr., R. A. Rallo, W. W. Hunter, Jr., S. M. Bartram, J. L. Blackshire, Application of particle image velocimetry to Mach 6 flows, in: J. M. Bessem, R. Booij, H. W. H. E. Godefroy, P. J. de Groot, K. K. Prasad, F. F. M. de Mul, E. J. Nijhof (Eds.), Fifth International Conference on Laser Anemometry: Advances and Applications, Vol. 2052, International Society for Optics and Photonics, SPIE, 1993, pp. 519 – 526.

[20] F. F. J. Schrijer, F. Scarano, B. W. van Oudheusden, Application of PIV in a Mach 7 double-ramp flow, Experiments in Fluids 41 (2) (2006-08) 353–363.

[21] A. Stella, G. Guj, J. Kompenhans, M. Raffel, H. Richard, Application of particle image velocimetry to combusting flows: Design considerations and uncertainty assessment, Experiments in Fluids 30 (2) (2001-02-06) 167–180.

[22] H. Weisgerber, R. Martinuzzi, U. Brummund, P. Magre, PIV measurements in a Mach 2 hydrogen-air supersonic combustion, in: 10th AIAA/NAL-NASDA-ISAS International Space Planes and Hypersonic Systems and Technologies Conference, American Institute of Aeronautics and Astronautics, 2001-04-24.

[23] M. Havermann, J. Haertig, C. Rey, A. George, Application of particle image velocimetry to high-speed supersonic flows in a shock tunnel, in: 11th international symposium on application of laser technology to fluid mechanics, Lisbon, Portugal, Citeseer, 2002.

[24] C. M. Jenkins, R. C. Ripley, C.-Y. Wu, Y. Horie, K. Powers, W. H. Wilson, Explosively driven particle fields imaged using a high speed framing camera and particle image velocimetry, International Journal of Multiphase Flow 51 (2013-05) 73–86.

[25] B. J. Balakumar, R. J. Adrian, Particle-image velocimetry measurement in the exhaust of a solid rocket motor, Experiments in Fluids 36 (1) (2004-01-01) 166–175.

[26] J. Haertig, C. Rey, M. Havermann, PIV Measurements of Compressible Vortex Rings Generated by a Shock Tube, in: 13th International Symposium on Application of Laser Techniques to Fluid Mechanics, 2006.

[27] J. H. Arakeri, D. Das, A. Krothapalli, L. Lourenco, Vortex ring formation at the open end of a shock tube: A particle image velocimetry study, Physics of Fluids 16 (4) (2004-04) 1008–1019.

[28] D. Mitchell, D. Honnery, J. Soria, Study of underexpanded supersonic jets with optical techniques, School of Engineering, The University of Queensland, 2007.

[29] J. Wagner, S. Beresh, E. DeMauro, K. Casper, B. Pruett, P. Farias, Time-Resolved PIV in a Shock Tube using a Pulse-Burst Laser, Tech. rep., Sandia National Lab.(SNL-NM), Albuquerque, NM (United States) (2015).

[30] F. Chen, H. Liu, Particle image velocimetry for combustion measurements: Applications and developments, Chinese Journal of Aeronautics 31 (7) (2018-07) 1407–1427.

[31] M. Rezay Haghdoost, D. M. Edgington-Mitchell, C. O. Paschereit, K. Oberleithner, Investigation of the Exhaust Flow of a Pulse Detonation Combustor at different Operating Conditions based on High-Speed Schlieren and PIV, in: AIAA Scitech 2019 Forum, American Institute of Aeronautics and Astronautics, 2019-01-07.

[32] D. Ragni, F. Schrijer, B. W. van Oudheusden, F. Scarano, Particle tracer response across shocks measured by PIV, Experiments in Fluids 50 (1) (2011-01) 53–64.

[33] A. Melling, Tracer particles and seeding for particle image velocimetry, Measurement Science and Technology 8 (12) (1997-12-01) 1406–1416.

[34] G. Tedeschi, H. Gouin, M. Elena, Motion of tracer particles in supersonic flows, Experiments in Fluids 26 (4) (1999-03-05) 288–296.

[35] T. L. de Assunção, Experimental study of underexpanded round jets: Nozzle lip thickness effects and screech closure mechanisms investigation, Ph.D. thesis.

[36] V. Vuorinen, J. Yu, S. Tirunagari, O. Kaario, M. Larmi, C. Duwig, B. J. Boersma, Large-eddy simulation of highly underexpanded transient gas jets, Physics of Fluids 25 (1) (2013-01) 016101.

[37] M. Samimy, S. K. Lele, Motion of particles with inertia in a compressible free shear layer, Physics of Fluids A: Fluid Dynamics 3 (8) (1991-08) 1915–1923.

[38] N120 rifle powder - Vihtavuori (2021).
URL `www.vihtavuori.com/powder/n120-rifle-powder/`

[39] G. E. Elsinga, G. C. Orlicz, Particle imaging through planar shock waves and associated velocimetry errors, Experiments in Fluids 56 (6) (2015-06) 129.

[40] G. S. Settles, Schlieren and Shadowgraph Techniques: Visualizing Phenomena in Transparent Media, softcover reprint of the hardcover 1st edition 2001 Edition, Experimental Fluid Mechanics, Springer, 2001.

[41] C. Chauveau, D. Davidenko, B. Sarh, I. Gökalp, V. Avrashkov, C. Fabre, Piv measurements in an underexpanded hot free jet, in: 13th Int Symp on Applications of Laser Techniques to Fluid Mechanics, 2006, pp. 26–29.

[42] E. Franquet, V. Perrier, S. Gibout, P. Bruel, Free underexpanded jets in a quiescent medium: A review, Progress in Aerospace Sciences 77 (2015-08) 25–53.

[43] F. Scarano, Iterative image deformation methods in PIV, Measurement Science and Technology 13 (1) (2002-01-01) R1–R19.

[44] J. Westerweel, Theoretical analysis of the measurement precision in particle image velocimetry, Experiments in Fluids 29 (7) (2000-12-31) S003–S012.

[45] J. Westerweel, Fundamentals of digital particle image ve-

locimetry, Measurement Science and Technology 8 (12) (1997-12-01) 1379–1392.

[46] A. Stitou, M. Riethmuller, Extension of piv to super resolution using ptv, Measurement Science and Technology 12 (9) (2001) 1398.

[47] C. J. Kähler, S. Scharnowski, C. Cierpka, On the resolution limit of digital particle image velocimetry, Experiments in Fluids 52 (6) (2012-06) 1629–1639.

[48] S. Werner Kieffer, The 1980 eruptions of Mount St. Helens, Washington. Fluid dynamics of the May 18 blast at Mount St. Helens., US Geological Survey Profesional Paper 1250 (1981-01-01) 379–400.

[49] D. Mitchell, D. Honnery, J. Soria, Particle relaxation and its influence on the particle image velocimetry cross-correlation function, Experiments in Fluids 51 (4) (2011-10) 933–947.

[50] G. Klingenberg, J. Heimerl, Gun Muzzle Blast and Flash, Progress in Astronautics and Aeronautics, American Institute of Aeronautics and Astronautics, 1992.

Coarse grid and implicit LES for urban pollutant dispersion

Tom Lauriks

Environmental and Applied Fluid Dynamics Department, University of Antwerp, Belgium, tom.lauriks@uantwerpen.be

Supervisors: Jeroen van Beeck and Wim Munters

Professor, von Karman Institute for Fluid Dynamics, Belgium, jeroen.vanbeeck@vki.ac.be

research Engineer, von Karman Institute for Fluid Dynamics, Belgium, wim.munters@vki.ac.be

University Supervisor: Prof. Siegfried Denys

Bioscience Engineering Department, University of Antwerp, Belgium, siegfried.denys@uantwerpen.be

Abstract

Improving urban air pollution remains important, for which CFD is a powerful tool. However, RANS is insufficiently accurate and LES is too computationally costly. Coarse grid (implicit) LES might remediate this. Dispersion around an array of cuboids was simulated, determining coarse grid (implicit) LES and RANS accuracy, using OpenFOAM. On the finest grid, (implicit) LES was more accurate than RANS.

Keywords: urban pollutant dispersion, computational fluid dynamics (CFD), implicit LES, coarse grid LES

1. Introduction

1.1. CFD modeling of urban air pollution

Both recently and in historical times, urban air pollution has severely affected public health and caused other environmental issues [18]. In some areas in the world, e.g. the Americas and Europe, air pollution levels seem to have decreased in recent years [16, 53, 84]. However, air pollution was in 2020 still identified as the single largest environmental health risk in Europe [17]. For example, in Belgium–a country in Europe–the economic cost of the health problems inflicted by air pollution was estimated as more than 8 billion euro per year [15]. The estimation that the majority of the people in the world is living in urban areas and the still rapidly accelerating urbanization [46], further emphasize this environmental issue. Consequently, research on improving urban air pollution still remains of the utmost importance.

However, the accurate prediction of pollutant dispersion in urban areas is far from straightforward [59, 60, 39]. In current times, computational fluid dynamics (CFD) is considered a powerful tool for the prediction of such dispersion patterns [10, 44, 59]. Nevertheless, CFD still entails important problems and inaccuracies when it is used to model urban wind and dispersion patterns. For example, it is well known that Reynolds-averaged Navier-Stokes (RANS), the faster and simpler approach, is inadequate to study all research topics related to wind flow around buildings (e.g. wind driven rain on buildings [49] and wind loading on buildings [77]). Regarding the focus topic in this paper, pollutant dispersion around buildings, the suitability of RANS in urban dispersion studies is very limited [6, 4]. It is able to fairly accurately simulate dispersion from ground-level sources in densely built urban areas (in general, deviations of the calculated mean concentration from experimental values are less than a factor 2). However, RANS delivers inaccurate results for pollutant dispersion in less densely built urban areas or around isolated buildings (differences between the calculated mean concentration and experimental values of a factor 10 or more are possible). Large eddy simulation (LES), on the other hand, is considerably more accurate than RANS when urban-type flows from wind tunnel experiments are simulated [21]. However, an important problem concerning LES is its large computational cost, which is at least 1 and maybe 2 orders of magnitude larger than for RANS [4]. For example, the calculation time on

1000 processors of an LES model of downtown Oklahoma City took 14 days, resulting in a simulation with a physical time of 31 minutes [21]. This renders LES models useless for practical policy making purposes and very cumbersome, if not even inapplicable, for research purposes. It is hence clear that CFD models with the accuracy of LES and an affordable computational cost, are of great interest to the research field of dispersion in urban environments.
Several strategies to increase the speed of LES can be found in the literature, e.g., hybrid RANS-LES [12], the lattice Boltzmann method [40], and coarse grid LES [3]. The importance of being able to use coarse grids is illustrated by a fact remarked by Boris [8]. When increasing the grid resolution 10 times in each direction, the higher number of cells can be compensated for by increasing the number of CPUs. However, the time step will also be 10 times smaller, which cannot be solved by using more CPUs, resulting in a 10 times longer computation time. Consequently, the way forward to using LES for urban wind and dispersion simulations seems to involve using coarse grids. Exploring the limits of coarse grids for urban dispersion LES is therefore one of the main goals of this paper. Another main goal of this paper, is investigating the capability of implicit LES (ILES) to perform coarse grid urban dispersion simulations, because in the past, this strategy seemed to have performed well.

1.2. Theory of implicit LES

The information in this subsection was retrieved from the book of Grinstein et al. [23], unless indicated otherwise. In ILES, explicit subgrid scale (SGS) models are not applied. The SGS flow features are taken into account implicitly by non-oscillatory finite volume methods (FVMs), such as flux corrected transport (FCT) and total variation diminishing (TVD) algorithms. In these non-oscillatory FVMs, the preservation of monotonicity is implemented mathematically. One of the consequences is that such methods inherently possess an implicit SGS model with desirable properties (see further). Since the ILES approach described in this section makes use of monotone convection algorithms, the method is usually called monotonicity preserving ILES (MILES), or monotone integrated LES.

The starting point to describe methods in CFD, is the governing equations of fluid flow–in this case of constant property Newtonian fluids–which are the continuity and Navier-Stokes equations [68]:

$$\nabla \cdot \boldsymbol{u} = 0 \tag{1}$$

$$\frac{\partial \boldsymbol{u}}{\partial t} + \nabla \cdot (\boldsymbol{u} \otimes \boldsymbol{u}) = -\frac{1}{\rho}\nabla p + \nu \nabla^2 \boldsymbol{u} \tag{2}$$

where $\boldsymbol{u}$ is the fluid velocity, ρ the fluid density, p the pressure, $\nu \equiv \mu/\rho$ the kinematic viscosity, and $\otimes$ the tensor product.

The FVM can be applied to numerically solve Eqs. 1 and 2. In this method, the computational domain, D, is tessellated into a set of non-overlapping control volumes, comprising the entire domain and defining the mesh. Let T be the tessellation, consisting of all control volumes $\Omega_P \in T$. The values of the dependent variables are calculated as control volume average for each $\Omega_P \in T$, and stored at a single location in Ω_P, e.g. the center of Ω_P, $\boldsymbol{x}_P$. If the limit is taken [33] of the divergence theorem [24, 50] and the resulting integral is approximated by a discrete summation, it is possible to write a partially discretized form of Eq. 2:

$$\frac{\partial \boldsymbol{u}_P}{\partial t} + \frac{1}{\delta V_P}\sum_f \left[(\boldsymbol{u} \otimes \boldsymbol{u})_f \, d\boldsymbol{A}_f\right] = -\frac{1}{\rho}(\nabla p)_P + \nu \nabla^2 \boldsymbol{u}_P \tag{3}$$

where subscript P indicates that a variable is evaluated at $\boldsymbol{x}_P$, δV_P is the volume of Ω_P, subscript f indicates that a variable is evaluated at a face of Ω_P, and $d\boldsymbol{A}$ is a face of Ω_P.

In Eqs. 3, in the discretized convection term, the velocity is evaluated at the cell faces, while in the FVM only the cell averages, stored at the cell centers, are known. Hence, in order to obtain a complete numerical method, it must be defined how the velocity is to be "reconstructed" from the cell center data.
In fact, in MILES, monotone reconstruction methods are applied, which means that they do not produce non-physical oscillations:

$$\boldsymbol{u}_f^{\text{hybrid}} = \boldsymbol{u}_f^{\text{linear}} - \left(1 - \Psi_f\right)\left(\boldsymbol{u}_f^{\text{linear}} - \boldsymbol{u}_f^{\text{upwind}}\right) \tag{4}$$

In this equation, $\boldsymbol{u}_f^{\text{hybrid}}$ is the velocity at the face, obtained through weighted contributions of the linear interpolation method and the upwind biased piecewise constant interpolation method. The local blending parameter, $\Psi(\boldsymbol{u}, \boldsymbol{d})$, is mostly referred to as the flux limiter. In this expression, $\boldsymbol{d} = \boldsymbol{x}_N - \boldsymbol{x}_P$ is the vector between the neighboring cell centers, at each side of the face under consideration. The linear interpolation

method is second order accurate and dispersive, while the upwind method is first order accurate and dissipative. The essential target of all flux limiting schemes (e.g. Eq. 4), is producing non-oscillatory solutions.
A numerical scheme that does not produce oscillatory behavior is said to be monotone. Harten [28] showed that monotone schemes are only first order accurate, which is insufficient because of an excessive dissipation. Hence, to obtain the desired combination of sufficient accuracy and no spurious oscillations, weaker conditions have to be enforced.
Relating to weaker conditions, is the concept of TVD. Harten [28] proved that 1) all TVD schemes are monotonicity preserving and 2) all monotone schemes are TVD. Statement 1) means that monotone profiles are preserved during the time evolution of the discrete solution and that overshoots are not created. Sweby [76], subsequently, established bounds for a scheme to be both TVD and second order accurate. The analysis by this author was performed on schemes similar to Eq. 4, where a first and higher order scheme are combined by means of flux limiter Ψ. Besides, the limiter $\Psi = \Psi(r)$ was taken to be a function of the ratio of local consecutive gradients, which for a generic variable ρ can be formulated as: $r = (\rho_k - \rho_{k-1}) / (\rho_{k+1} - \rho_k)$, where the subscripts refer to sequential locations in the discretized domain. The outcome of the analysis is a restriction on $\Psi(r)$:

$$\Psi(r) = \max(0, \min(\Phi r, 1), \min(r, \Phi)), \quad 1 \leq \Phi \leq 2 \tag{5}$$

which is represented graphically in Figure 1. To conclude this paragraph, some commonly applied flux limiters–falling within the second order TVD region–are listed in Table 1 and represented in Figure 1.

A last important aspect, is a modified equation analysis performed by Grinstein et al. [23], of the consequences of applying Eqs. 4. If this equation is substituted into Eqs. 3, it is possible to deduce that additional terms appear in Eqs. 2:

$$\begin{aligned}\frac{\partial \boldsymbol{u}}{\partial t} + \nabla \cdot (\boldsymbol{u} \otimes \boldsymbol{u}) = &-\frac{1}{\rho}\nabla p + \nu \nabla^2 \boldsymbol{u} \\ &+ \nabla \cdot \left(\boldsymbol{C} (\nabla \boldsymbol{u})^T + (\nabla \boldsymbol{u}) \boldsymbol{C}^T - \chi^2 ((\nabla \boldsymbol{u})\, \boldsymbol{d}) \otimes ((\nabla \boldsymbol{u})\, \boldsymbol{d}) \right) \\ &+ \dots\end{aligned} \tag{6}$$

where $\chi = (1 - \Psi)[(1 - l)\beta^+ - l\beta^-]$ and $\boldsymbol{C} = \chi(\boldsymbol{u} \otimes \boldsymbol{d})$, with l and $\beta^{\pm}$ variables related to the linear and upwind interpolation method.

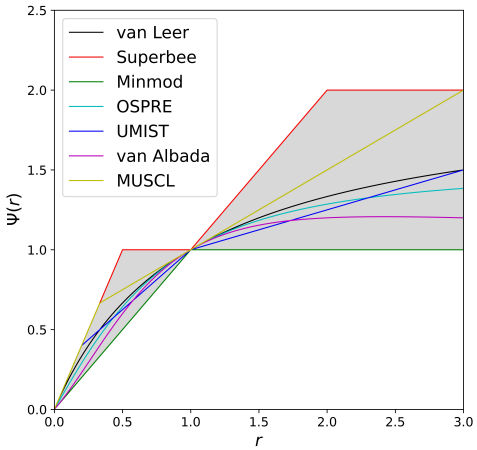

Figure 1: Modified from Sweby [76]. Graphical representation of the region where flux limiting schemes are both TVD and of second order accuracy (shaded area), as a result of the implemented flux limiter $\Psi(r)$. Some commonly applied flux limiters, falling within the second order TVD region, are also represented (see Table 1 for references and mathematical expressions of the limiters).

The last line in Eqs. 6 can be viewed as an implicit SGS model, as a result of the monotonicity preserving interpolation method. It is useful to split its contributions into two components: $\boldsymbol{T}^1 = \boldsymbol{C}(\nabla \boldsymbol{u})^T + (\nabla \boldsymbol{u})\boldsymbol{C}^T$ and $\boldsymbol{T}^2 = \chi^2[(\nabla \boldsymbol{u})\, \boldsymbol{d} \otimes (\nabla \boldsymbol{u})\, \boldsymbol{d}]$. $\boldsymbol{T}^1$ is symmetric and linear in the velocity gradient tensor. It can be interpreted as an implicit version of a general SGS viscosity model in explicit LES [72]. $\boldsymbol{T}^2$ is also symmetric, but it is quadratic in $\nabla \boldsymbol{u}$. It can be viewed as an implicit analogue of a scale-similar model [13, 2]. Hence, an implicit analogue of a mixed model is present. It was already demonstrated that mixed models are able to capture disequilibrium, anisotropic effects, and backscatter [1, 43, 47, 48, 66], making them suitable for complex geometries and marginally resolved flows.

1.3. Applied cases of coarse grid and implicit LES

As explained in Section 1.1, fast LES would be extremely useful for urban dispersion simulations. Also approaching urban dispersion simulations from the viewpoint of computation speed, already in the early 2000s, a well performing ILES code, FAST3D-CT, was used in large scale urban dispersion simulations. Several papers and book chapters were published, in which the application of this code was described [63, 23, 14, 7, 9, 62, 69, 61, 8, 64, 29, 30]. The authors refer to their ILES approach as MILES, as an

Table 1: Examples of available flux limiters, falling within the second order TVD region.

Limiter	Equation
van Leer [81]	$\Psi(r) = \frac{\lvert r\rvert + r}{1+\lvert r\rvert}$
Minmod [71]	$\Psi(r) = \max(0, \min(1, r))$
Superbee [71]	$\Psi(r) = \max(\max(\min(2r, 1), \min(r, 2)), 0)$
OSPRE [83]	$\Psi(r) = 1.5\frac{r^2+r}{r^2+r+1}$
UMIST [42]	$\Psi(r) = \max(0, \min(2r, 0.25 + 0.75r, 0.75 + 0.25r, 2))$
van Albada [80]	$\Psi(r) = \frac{r^2+r}{r^2+1}$
MUSCL [82]	$\Psi(r) = \max(\min(\min(2r, 0.5r + 0.5), 2), 0)$

up-front reminder that monotone methods have an integrated SGS model (see Subsection 1.2). Simulations performed with MILES were fast and accurate.

With regard to the accuracy, the MILES method of the referenced authors was subjected to several validation studies. A simulation of an array of cubes was compared to wind tunnel measurements and showed a good accuracy [23, 63]. For a large scale simulation of Washington DC, it was observed that vortex shedding from a single building in the domain, compared well to vortex shedding from comparable obstacles (square and circular cylinders), as observed in wind tunnel experiments [7, 14]. 98 % agreement probability was observed, when a simulation of an area in Los Angeles was statistically compared to field data [63]. Worse results were obtained for flow over a complex building, where discrepancies were observed in regions of the flow that are more challenging to simulate (building wake) [7, 14]. Validation studies were also performed, where both field and wind tunnel data were used. Regarding a model of Oklahoma city, a comparison was performed of model results to wind tunnel velocity and dispersion data [61]. Mostly, good to excellent agreement was obtained. In the comparison to field data of velocity and dispersion in Oklahoma city, statistically, a good agreement seemed to be obtained, but the number of field experiments was too low to draw firm conclusions. Concerning downtown Hamburg, modeled dispersion results based on the MILES approach were compared to field data. A good agreement was observed [8]. MILES results of that area were also compared to wind tunnel data [29, 64]. With regard to the mean velocity, in general, good agreement with the experiments was obtained above the urban canopy, but inside the urban canopy discrepancies were observed. Concerning energy spectra, integral time scales, and turbulent momentum transport aspects, in general a good agreement with the data was observed.

Concerning simulation speed of the mentioned MILES method, a modeling exercise faster than real time was performed of a contaminant cloud passing over the Pentagon [7]. Moreover, already in 2004, it was claimed that MILES was able to simulate dispersion within urban areas in about one day (time required for one case, using a single wind direction, geometry and domain extent likely being similar to an area of 5.2 square km in downtown Chicago) [9]. This is markedly faster than the earlier mentioned simulation of downtown Oklahoma City (about 9 square km), that took 14 days in 2018 [21]. An important factor that substantially contributed to the speed of MILES, was that all these simulations were performed on coarse grids, where typical grid spacings were 5-10 m [62]. E.g., a grid resolution of 6 m was used to model Washington DC and downtown Chicago [69].

Besides the obtained high speed and accuracy on dispersion simulations around buildings using MILES, other examples can be found that using LES on coarse grids seems possible for some flow and application types and that this possibly involves using ILES. For example, for flow over wings and on the 1D Burgers' equation, ILES performed well on coarse grids [11, 79, 58, 73, 41]. On the other hand, conventional LES performed better on a coarse grid than MILES for a homogeneous turbulence case [20]. For mean pressure distributions over a cube and single buildings, both LES and ILES were very accurate on coarse grids [35]. It was concluded that for this flow type, the flow is mostly dominated by large scale vortexes and that the specifics of the smaller scales are not very important to determine the mean pressure distribution [36]. Besides, flow and heat transfer in an array of surface mounted cubes was simulated [38]. Different SGS models and ILES were compared. Concerning the mean flow features, high accuracy was obtained on coarse grids, both by LES and ILES. As an example of an application for which coarse grids and ILES are not suitable, concerning the mean heat transfer characteristics, ILES performed the worst and displayed the largest sensitivity to the grid resolution.

From the above, it can be concluded that it is possible that both conventional LES and ILES can be accurate for coarse grid urban dispersion simulations, if the concerning flow and application type do not require resolving the finer scales to retrieve a reasonable accuracy. In addition, theoretical indications exist (see

Subsection 1.2) that the MILES version of ILES inherently contains an implicit mixed SGS model, making it suitable for complex geometries and marginally resolved flows. This might be the explanation of the described success of MILES in large scale urban dispersion simulations on coarse grids.

1.4. Research summary

Reducing urban air polution levels still remains imperative, but an accurate prediction of pollutant dispersion in urban areas is far from straightforward. CFD is considered a powerful tool for the prediction of urban wind and dispersion patterns. However, it is well known that the faster RANS method is insufficiently accurate and that LES has a too high computational cost.

A very important strategy to reduce the computational cost of LES is using coarse grids. Luckily, indications exist that urban dispersion cases can be simulated on coarse grids. Moreover, indications exist that ILES (MILES) is a suitable simulation method for marginally resolved flows. Several large scale urban dispersion MILES studies attained high simulation speeds and achieved a good accuracy using coarse grids. These studies were performed using the FAST3D-CT code. Despite this success, no recent similar studies were published, likely due to the fact that FAST3D-CT is not publicly accessible.

In this study, the CEDVAL wind tunnel experiment of flow and dispersion over an array of cuboids was simulated with RANS and LES, to investigate two main goals. The first goal is to determine how coarse the grid can be, so that a wall-modeled LES still significantly outperforms RANS and to determine the resulting computational cost. The second goal is determining whether MILES, as implementable using the standardly available tools in the open source CFD software OpenFOAM, is more accurate than conventional wall-modeled LES. Contrary to the theoretical analysis of MILES in Section 1.2, it is impossible in OpenFOAM to use a flux limiting scheme to retrieve both instances of $\boldsymbol{u}_f$ in Eq. 3 [55], which might result in a significant difference in accuracy as compared to the FAST3D-CT code. However, the rationale for using OpenFOAM, is that it is free and open source, and hence accessible to a large CFD community.

2. CEDVAL wind tunnel experiment

In this research, the CEDVAL wind tunnel experiment of flow and dispersion in a regular and finite array of cuboids (case B1-1, scale 1:200) [25] was simulated (Figure 2 (a)).

An atmospheric boundary layer (ABL) was modeled at a scale of 1:200 in the wind tunnel, making use of modified Standen-Spires [75] and a uniform pattern of LEGO blocks serving as floor roughness. The ABL was measured in the empty wind tunnel across a vertical profile, at the location corresponding to the center of the first building row in the building experiment. The parameters of the ABL in the wind tunnel are: a Reynolds number of 37252, a neutral stratification, a roughness length z_0 of 0.00045 m, and a friction velocity u_* of 0.33393 m/s. (The latter two parameters were determined by log law fitting of the experimental data.) The available variables (Figure 3) are i.a.: the mean longitudinal velocity $\langle u \rangle$ and the following Reynolds stresses: $\langle u'u' \rangle$, $\langle v'v' \rangle$, $\langle w'w' \rangle$, and $\langle u'w' \rangle$.

In the building experiment, a regular array of cuboids was inserted into the wind tunnel. The array consisted of 3 blocks in the spanwise and 7 blocks in the streamwise direction (Figure 2 (a)). Each cuboid had the dimensions 0.125 m, 0.1 m, and 0.15 m, respectively in the height and the streamwise and spanwise direction (Figure 2 (b)). From one of the buildings, a tracer was emitted. In the leeward face of this building, 4 sources were present. The exhaust velocity was between 0.015 and 0.033 [m/s] at each source element. The total area of the sources was 4.6e-4 m^2. The origin of the coordinate system coincided with the center of the bottom face of the source building.

The available measurements are point measurements, performed in several planes. The latter are displayed in Figure 2 (c). 2D flow measurements were performed in 1 horizontal and 4 vertical planes. Concentration data was obtained from 1 horizontal measurement plane. The following variables are available: the velocity [m/s] and the following Reynolds stresses: $\langle u'u' \rangle$, $\langle v'v' \rangle$, $\langle w'w' \rangle$, $\langle u'w' \rangle$, and $\langle u'v' \rangle$ [m^2/s^2]. Concentration is available as dimensionless K-values, where K is defined as:

$$K = \frac{C_{\text{measured}} \langle u \rangle_{\text{ref}} H^2}{C_{\text{source}} Q_{\text{source}}} \tag{7}$$

where C_{measured} is the measured concentration, C_{source} the concentration at the sources, $\langle u \rangle_{\text{ref}}$ the mean longitudinal reference wind speed in the ABL [m/s] measured at a height of $z = 0.66$ m, $H = 0.125$ m the building height, and Q_{source} [m^3/s] the total source volumetric flow rate.

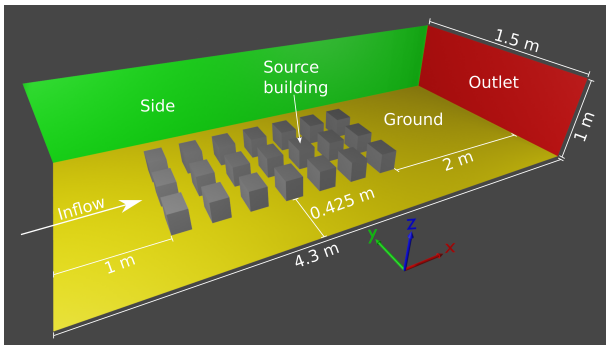

(a) Computational domain of the CEDVAL case. The origin of the coordinate system coincided with the source building bottom face center.

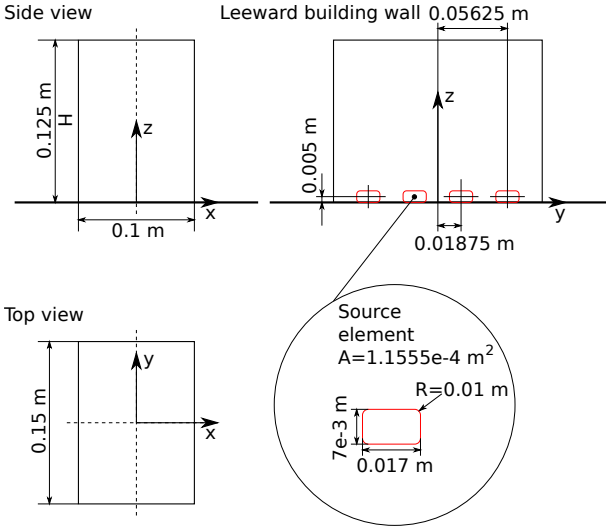

(b) CEDVAL tracer source building dimensions. All buildings had identical dimensions. All spacings between the buildings were 0.1 m.

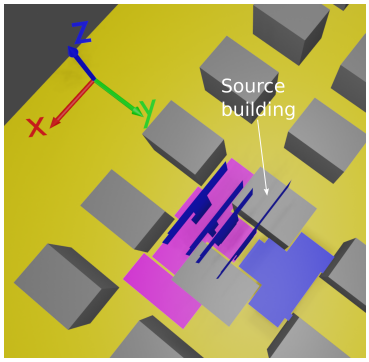

(c) CEDVAL measurement and model sampling locations. Concentration: magenta plane (z = 0.0075 m). Velocity: blue planes (z = 0.0625 m, y = 0 m, y = −0.05 m, y = −0.075 m, and y = −0.125 m).

Figure 2: CEDVAL experiment and computational domain.

3. CFD models of the CEDVAL cuboid array

Considering the two main goals of this study, performing coarse grid simulations and performing MILES with standard OpenFOAM methods (Section 1.4), first an appropriate mesh had to be determined for a wall-modeled LES, i.e. 80 % of the turbulent kinetic energy (TKE) is resolved, except in the near-wall region [68]. From this point, the grid was sequentially coarsened, resulting in a total of 4 grid resolutions. RANS was performed on the same grids as LES. Referring to the second goal, most non-oscillatory FVM schemes in OpenFOAM were tried on the finest mesh, along with conventional LES and coarse direct numerical simulations (CDNS). Conventional LES, CDNS, and the best performing MILES, still need to be applied on the sequentially coarsened grids.

3.1. Governing equations

Simulations were performed with OpenFOAM v2012 [56]. For RANS and LES, respectively, the incompressible LES and unsteady RANS equations were solved, supplemented with a scalar transport equation. In all ILESs and CDNSs, the SGS model was switched off. Unsteady RANS was performed, because in steady RANS, the residuals for the pressure, p, decreased only to 2e-3, which is insufficient [19]. For LES, the WALE SGS model [51] was used, which is suitable for complex geometries and ABL modeling [34]. The cube root of the cell volumes was selected as filter width. For RANS, the realizable $k-\varepsilon$ turbulence model [74] was selected, applying a value of 1.11 for the turbulence model constant σ_ε, as required for ABL modeling [27]. In the scalar transport equation, the standard gradient diffusion hypothesis was applied, with a turbulent Schmidt number, Sc_t, value of 0.75, being the mean of the range (0.2-1.3) in which Sc_t usually varies in atmospheric dispersion [78].

3.2. Computational methods, domain and mesh

The domain dimensions were in accordance with guidelines for urban flow CFD [19], the height and width being the same as in the wind tunnel experiment (Figure 2 (a)), the inflow located 1 m upstream from the buildings (further than $5H$ = 0.625 m, where H is the building height), and the outflow located 2 m downstream from the buildings (further than $15H$ = 1.875 m).

A base mesh was designed to be coarse but at the same time accommodate an appropriate simulation of

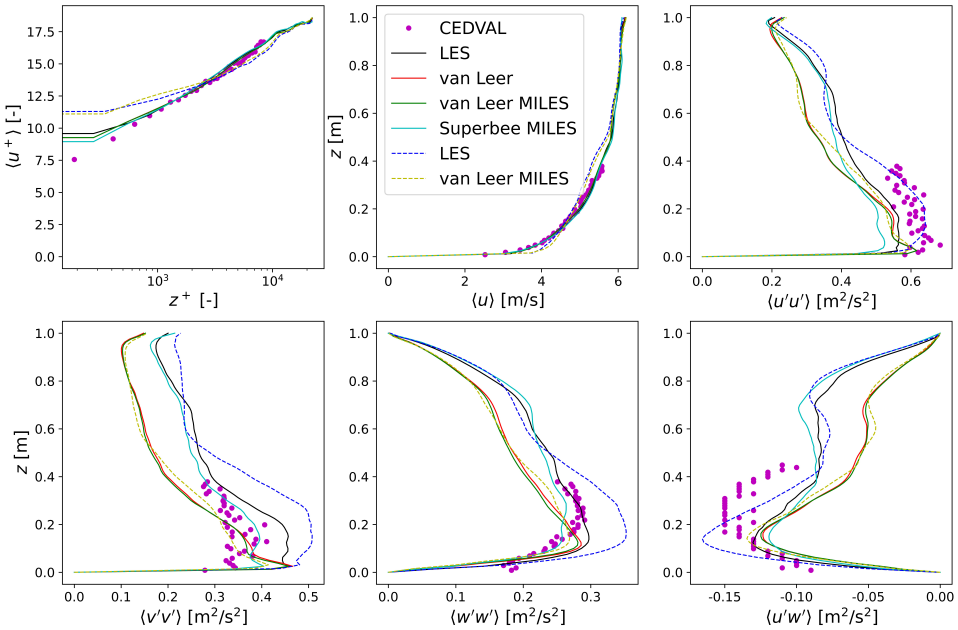

Figure 3: Experimental and LES ABL profiles in the empty wind tunnel and domain, at the target location. Solid lines: ABL mesh resolution of mesh 1 and 2 (Table 2), dashed lines: ABL mesh resolution of mesh 3 and 4. The shown simulations are (see Section 3.4): LES, van Leer scheme with SGS model, MILES with the van Leer Scheme (i.e. without SGS model), and MILES with the Superbee scheme.

the approach flow (ABL) and to be fully orthogonal. For these reasons, the base mesh was constructed, with x, y, and z spacings of 0.02, 0.01, and 0.0125 m respectively, without grading. The corresponding z^+ value in the ABL was 2.8e4. In addition, rescaling these values to full scale, a uniform grid with x, y, and z spacings of 4, 2, and 2.5 m would be obtained. Both this z^+ value and the full scale grid spacings are similar to several examples from the literature that used OpenFOAM or similar codes to simulate an ABL [65, 21, 52, 32, 26, 45]. Using this grid, it was possible to simulate a reasonable ABL (see Section 3.3).

A total of 4 meshes derived from the base mesh was used, where the grid spacing of mesh 1 to 4 increased sequentially from finest to coarsest (Table 2). For mesh 1 (Figure 4 (a)), one refinement, halving the grid spacings in each direction, around the buildings was performed. This allowed the LES to marginally resolve 80 % of the TKE (except in the near-wall region, Figure 4 (b)). Besides, the average z^+ values on the buildings and the streets were approx. 303 and 236, respectively, for the LES. Mesh 2 was the base mesh, where the surfaces of the tracer inlets were refined once. The total surface of the discretized inlets in mesh 1 and 2 was 8.2 % larger than their surface in the wind tunnel. Mesh 3 and 4 were similar to mesh 1 and 2, respectively, except for the ABL grid spacings, which were increased by a factor of 1.25 in each direction (see Table 2).

Table 2: Grid spacings of the used meshes.

	mesh 1	mesh 2
Δx ABL [m]	0.02	0.02
Δy ABL [m]	0.01	0.01
Δz ABL [m]	0.0125	0.0125
refinements around buildings	1	0
refinements of tracer inlets	0	1
	mesh 3	mesh 4
Δx ABL [m]	0.025	0.025
Δy ABL [m]	0.0125	0.0125
Δz ABL [m]	0.015625	0.015625
refinements around buildings	1	0
refinements of tracer inlets	0	1

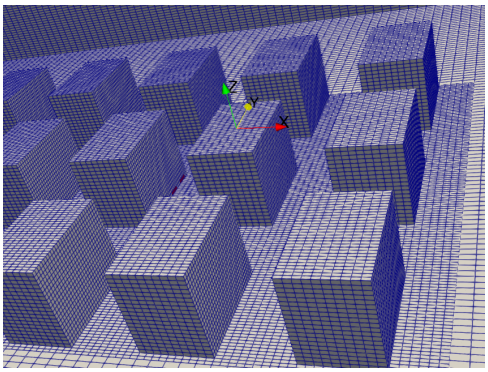

(a) View of the mesh. Red parts: tracer inlets.

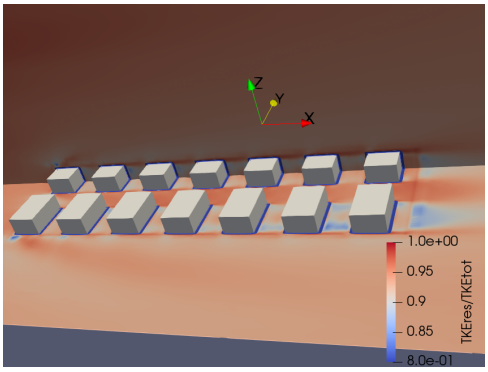

(b) Fraction of resolved TKE in the LES. xy-plane: $z = 0.0625$ m, xz-plane: $y = 0$ m.

Figure 4: Finest mesh (mesh 1, Table 2) of the CEDVAL case.

The LESs were run for 1600 s, with an averaging time of 1200 s, which was observed to be sufficient to reach steady state and obtain statistically converged mean variables. The RANS simulations were run for 600 s, with an averaging time of 200 s, for the same reasons.

3.3. Boundary conditions

A symmetry plane was applied at the top of the domain (Figure 2 (a)). A symmetry plane was also applied at the lateral sides in the RANS model. In the LES model, periodic boundary conditions were applied at the lateral sides. At the outlet, p was set to a constant static pressure and the other variables to zero gradient. At the bottom surface around the buildings, a rough wall function (atmNutkWallFunction) based on the work of Hargreaves and Wright [27] was applied, with $z_0 = 0.00045$ m. At the buildings and the bottom surface between the buildings, a smooth wall function (nutkWallFunction) was applied. At the tracer inlets in the RANS model, the average of the experimental velocity was set (0.024 m/s). In the LES model, the divergence free synthetic eddy method (DFSEM) for turbulence generation [67] was applied to the tracer inlets. The settings applied to this method were: a uniform average velocity of 0.024 m/s and isotropic turbulence with an intensity of 10 %, as performed by Gorlé [22]. A value of 1e-3 kg/m^3 was set for the tracer concentration, at the tracer inlets.

In this research, it was possible to largely avoid the well-known problem of horizontal inhomogeneities in ABL RANS simulations [19, 27, 5], which can also occur in LES when the computationally efficient method of synthetic turbulence generation is applied [37]. In fact, the solution for this problem in LES from the latter authors was applied in this research, where the input parameters of the turbulence generator are changed, so that the correct mean velocity and turbulence profiles are obtained at the location of interest in the domain. By using as input in the DFSEM boundary condition at the inlet, the log law fitted profile of the velocity, the fitted profile of $\langle u'w' \rangle$, and alterations of the fitted profiles of the normal stresses, it was possible to obtain good ABL characteristics at the location of the center of the first building row in the empty domain using the ABL mesh resolution of mesh 1 and 2 (Figure 3). Applying the DFSEM input stresses of the ABL mesh resolution of mesh 1 and 2 to meshes 3 and 4, resulted in worse but still acceptable ABL characteristics.
Concerning the RANS simulations, it was possible to generate a good ABL at the location of interest (Figure 5), using the realizable $k-\varepsilon$ turbulence model, the above mentioned wall function, and the standard ABL inflow boundary conditions available in OpenFOAM. (Further downstream, the profiles started changing substantially.) The available ABL inflow conditions in OpenFOAM impose vertical profiles for modeling a neutral ABL with the $k-\varepsilon$ (or alternatively $k-\omega$) model [57, 70, 27, 85]. The first profile is of the mean streamwise velocity:

$$\langle u \rangle = \frac{u_*}{\kappa} \ln\left(\frac{z + z_0}{z_0}\right) \tag{8}$$

where u_* is the friction velocity and $\kappa \approx 0.41$ is the von Karman constant. The second profile is of the turbulent kinetic energy:

$$k = \frac{u_*^2}{\sqrt{C_\mu}} \sqrt{C_1 \ln\left(\frac{z + z_0}{z_0}\right) + C_2} \tag{9}$$

where C_μ is a constant equal to 0.09, and C_1 and C_2

are fitting constants. The final profile is of the turbulence dissipation rate:

$$\epsilon = \frac{(u_*)^3}{\kappa\,(z+z_0)}\sqrt{C_1 \ln\left(\frac{z+z_0}{z_0}\right) + C_2} \qquad (10)$$

Eq. 9 was fitted to the CEDVAL data (Figure 5) and the values of all constants were set in the model.

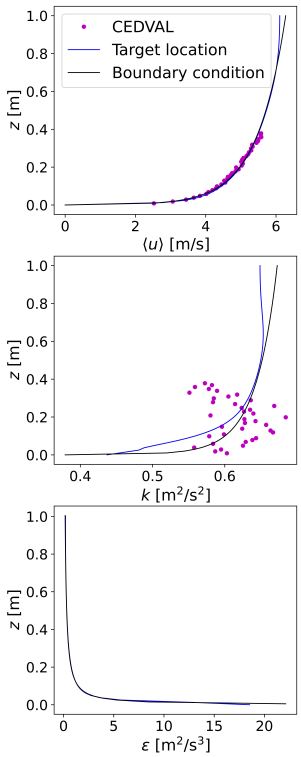

Figure 5: Experimental and RANS ABL profiles at the target location. Simulation: performed on ABL mesh resolution of mesh 1 and 2 (Table 2) and imposed boundary condition also shown.

3.4. Numerical methods

Second order schemes were used for all terms of all equations, except for the convection of the turbulence variables in the RANS simulations and the convection of the velocity in the MILES cases. For the RANS turbulence variables, first order discretization was selected in order to solve convergence problems.
Concerning MILES, the convection of the velocity was discretized with flux limiting schemes (see Section 1.2). A first selection of flux limiting schemes available in OpenFOAM were all the schemes from Figure 1 and Table 1. Their behavior falls completely within the second order TVD region and covers a large area of this region. Using this selection is hence equivalent to calibrating the implicit SGS model [62], since the latter is influenced by the behavior of the flux limiter Ψ (Eq. 6). Other schemes were added to this selection, so that most flux limiting schemes available in OpenFOAM were assessed. All available normalized variable diagram (NVD) schemes, Gamma [31] and SFCD [86], were applied. Lastly, the limitedCubic scheme, that applies a TVD limiter to a centered-cubic scheme [54], was employed. All the flux limiting schemes were applied on mesh 1 (Table 2). Only the most accurate flux limiting scheme will be applied on the coarser meshes. The Gamma, SFCD, van Albada, Minmod, van Leer, limitedCubic, and UMIST schemes caused the simulation to diverge and will not be discussed further.
Both for the RANS and LES models, the upper limit of the residuals was set to 1e-5 for p and to 1e-8 for all other variables.

4. Results and discussion

Only results on mesh 1 are already available. Still, already many line plots can be and were made in the measured locations (see available planes, Figure 2 (c)). The observations below are based on a visual inspection of all these figures. Only a selection of these figures, illustrative for the conclusions, is shown. In the future, single metrics will be calculated for every simulation, in order to unambiguously compare them quantitatively. Besides, the normal stresses were not yet fully converged at the averaging time of 1200 s. They will not yet be discussed. In addition, it was observed that LES and CDNS results in all available measurement locations are identical or very similar. Hence, in the following comparison to MILES and RANS, only LES will be discussed.
Said selection of results can be viewed in Figure 6, where the MILESs are OSPRE, Superbee, and MUSCL. Concerning $\langle u \rangle$ in the zx planes (plot 1), all models results are good and rather close to each other. In the xy plane, $\langle u \rangle$ results are less good (plot 4) and RANS is far off at many locations. The general decreasing order of accuracy in all these planes is: LES, MILES, and RANS.
Concerning $\langle w \rangle$ in the zx planes (plots 2 and 3), again results are less good. In general, the same decreasing order of accuracy seems to hold. It can be noticed that OSPRE is sometimes the least accurate (plot 2) and sometimes the most accurate (plot 3). This highlights the fact that it would be useful to calibrate a single MILES method. Concerning $\langle v \rangle$ in the xy plane (plot

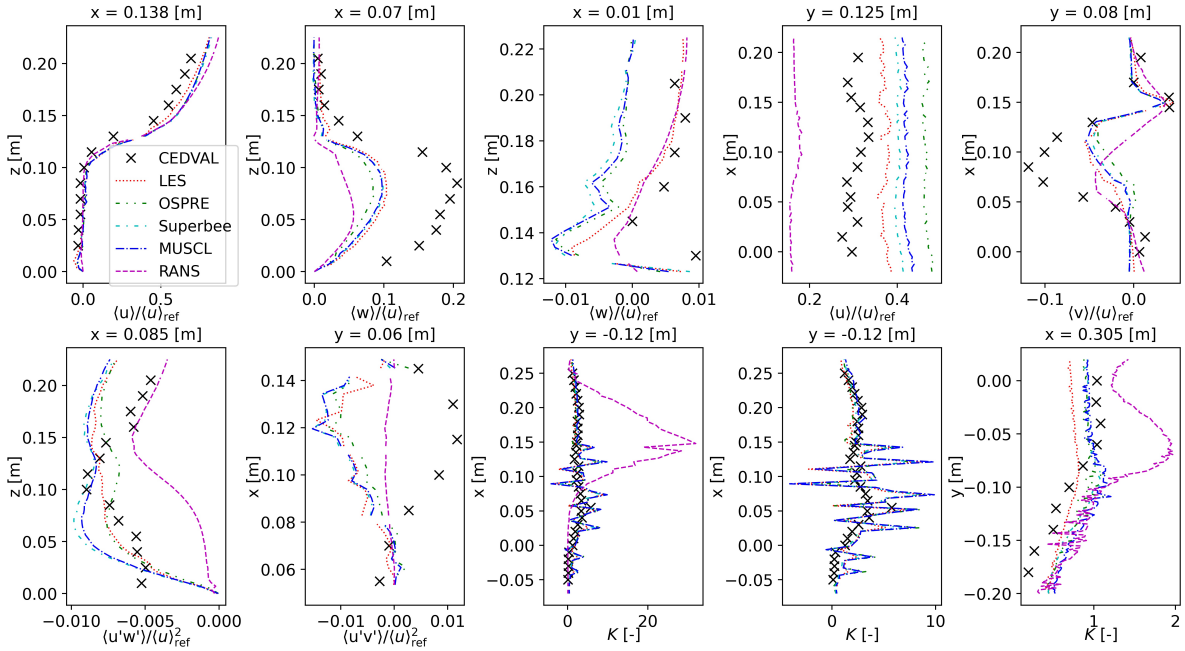

Figure 6: Selection of results on mesh 1. From top left to bottom right, plot 1, 2 and 3: $y = -0.05$, 4, 5, 7: $z = 0.0625$, 6: $y = -0.125$, 8 and 9: close to the source building, and 10: further from the source building.

5), results are again not very accurate. The general decreasing order of accuracy seems to be: LES, RANS, and MILES.

Concerning $\langle u'w' \rangle$ in the xz planes, in the $y = -0.125$ plane (plot 6), it is very remarkable that the stress is simulated better by RANS above the roofs (rooftop height is 0.125 m) and better by the eddy resolving methods below the roofs. This might be the cause of the concentration being simulated very badly by RANS in this region (see further). Concerning $\langle u'v' \rangle$ in the xy plane (plot 7), in general, results are bad. RANS is better than the eddy resolving methods at many locations, but it is still inaccurate.

Concerning the concentration, in the part of the xy plane closest to the source building, RANS is performing very badly in the section besides the source building (plot 8), which might be caused by the bad results for $\langle u'w' \rangle$ there. All eddy resolving methods simulate some locations very well, but need improvements in other locations (plot 9). It is not clear which method performs best. In the part of the xy plane furthest from the source building (plot 10), in general, RANS is performing the worst, but it is much more accurate than in the former region. In general, all results of the eddy resolving methods are good. It is again not clear which method performs best, although it could be possible that MILES is performing slightly better than LES in this region.

In conclusion, on the rather coarse mesh 1, LES in general outperforms RANS concerning the average velocity and stresses. Moreover, it clearly outperforms RANS concerning the concentration. MILES is in general less accurate than LES concerning the average velocity and stresses, but is matching LES closely concerning the concentration. The eddy resolving simulations took approx. 358.7 hours, the RANS simulation 104.7 hours, which is only 3.4 times longer, not 10 times or more as suggested in the literature. These preliminary results might need further improvements, but they are a first indication that coarse grid urban dispersion LES shows an acceptable performance, as compared to RANS. Considering the unstable performance of the MILESs, and their similar or worse results than LES, MILES in OpenFOAM does not seem like an interesting strategy.

Acknowledgments

This work was supported by internal funding of the University of Antwerp.

References

[1] R. Akhavan, A. Ansari, S. Kang, and N. Mangiavacchi. Subgrid-scale interactions in a numerically simulated planar

turbulent jet and implications for modelling. *Journal of Fluid Mechanics*, 408:83–120, 2000.

[2] A. A. Aldama. *Leonard and cross-term approximations in the anisotropically filtered equationsof motion*. 1993. Editors: Galperin, B. and Orszag, S. A.

[3] P. Bauweraerts and J. Meyers. On the Feasibility of Using Large-Eddy Simulations for Real-Time Turbulent-Flow Forecasting in the Atmospheric Boundary Layer. *Boundary-Layer Meteorology*, 171:213–235, 2019.

[4] B. Blocken. LES over RANS in building simulation for outdoor and indoor applications: A foregone conclusion? *Building Simulation*, 2018.

[5] Bert Blocken, Ted Stathopoulos, and Jan Carmeliet. CFD simulation of the atmospheric boundary layer: wall function problems. *Atmospheric Environment*, 2007.

[6] Bert Blocken, Rob Vervoort, and Twan van Hooff. Reduction of outdoor particulate matter concentrations by local removal in semi-enclosed parking garages: A preliminary case study for eindhoven city center. *Journal of Wind Engineering and Industrial Aerodynamics*, 159:80–98, dec 2016. doi: 10.1016/j.jweia.2016.10.008.

[7] J. Boris. The threat of chemical and biological terrorism: Preparing a response. *Computing in Sience & Engineering*, 4:22–32, 2002.

[8] J. Boris. Flux-Corrected Transport looks at forty. *Computers & Fluids*, 84:113–126, 2013.

[9] J. Boris, J. Fulton, K. Obenschain, G. Patnaik, and T. Young. CT-Analyst: Fast and accurate CBR emergency assessment. 2004.

[10] V. Busini and R. Rota. Influence of the shape of mitigation barriers on heavy gas dispersion. *Journal of Loss Prevention in the Process Industries*, 29(13-21):13–21, 2014.

[11] P. Castonguay, C. Liang, and A. Jameson. Simulation of Transitional Flow over Airfoils using the Spectral Difference Method. 2010.

[12] B. Chaouat. *Flow, Turbulence and Combustion*, 99:279—327, 2017.

[13] R. A. Clark, J. H. Ferziger, and W. C. Reynolds. Evaluation of subgrid-scale models using an accurately simulated turbulent flow. *Journal of Fluid Mechanics*, 91:1–16, 1979.

[14] B. Cybyk, J. Boris, T. Young, M. Emery, and S. Cheatham. Simulation of Fluid Dynamics Around Complex Urban Geometries. 2001.

[15] Departement Omgeving. Luchtbeleidsplan 2030. Technical report, Departement Omgeving, 2019.

[16] EEA. Air pollutant emissions data viewer (Gothenburg Protocol, LRTAP Convention) 1990-2017 , 2019. European Environment Agency. Accessed on 25 November 2019.

[17] EEA. Air quality in Europe – 2020 report. Technical report, European Environment Agency, 2020.

[18] D. Fowler, P. Brimblecombe, J. Burrows, M. R. Heal, P. Grennfelt, D. S. Stevenson, A. Jowett, E. Nemitz, M. Coyle, X. J. Lui, Y. H. Chang, G. W. Fuller, M. A. Sutton, Z. Klimont, M. H. Unsworth, and M. Vieno. A chronology of global air quality. *Philosophical Transactions of the Royal Society A-Mathematical Physical and Engineering Sciences*, 378(2183), 2020.

[19] J Franke, A. Hellsten, H. Schlïzen, and B. Carissimo. Best practice guideline for the CFD simulation of flows in the urban environments. Technical report, 2007. COST Action 732.

[20] C. Fureby and F. F. Grinstein. Monotonically integrated large eddy simulation of free shear flows. 1998.

[21] C. García-Sánchez, J. van Beeck, and C. Gorlé. Predictive large eddy simulations for urban flows: Challenges and opportunities. *Building and Environment*, 139:146–156, 2018.

[22] Catherine Gorlé. Dispersion of fine and ultrafine particles in urban environment. Contribution towards an improved modeling methodology for Computational Fluid Dynamics, 2010. PhD thesis.

[23] F. F. Grinstein, L. G. Margolin, and W. J. Rider. *Implicit Large Eddy Simulation. Computing Turbulent Fluid Dynamics*. Cambridge University Press, 2007. ISBN 978-0-511-53974-9.

[24] M. E. Gurtin. *An Introduction to Continuum Mechanics*. 1981.

[25] Hamburg University. CEDVAL at Hamburg University. Compilation of Experimental Data for Validation of Microscale Dispersion Models, 2006. URL `https://mi-pub.cen.uni-hamburg.de/index.php?id=433`. Online, accessed on 11 March 2021.

[26] Y. Han, M. Stoellinger, and J. Naughton. Large eddy simulation for atmospheric boundary layer flow over flat and complex terrains. In *Journal of Physics Conference Series*, volume 753, 2016.

[27] D. M. Hargreaves and N. G. Wright. On the use of the k-ε model in commercial CFD software to model the neutral atmospheric boundary layer. *Journal of Wind Engineering and Industrial Aerodynamics*, 95:355–369, 2007.

[28] A. Harten. High Resolution Schemes for Hyperbolic Conservation Laws. *Journal of Computational Physics*, 49:357–393, 1983.

[29] D. Hertwig, G. Patnaik, and B. Leitl. LES validation of urban flow, part I: flow statistics and frequency distributions . *Environmental Fluid Mechanics*, 17:521–550, 2017.

[30] D. Hertwig, G. Patnaik, and B. Leitl. LES validation of urban flow, part II: eddy statistics and flow structures. *Environmental Fluid Mechanics*, 17:551–578, 2017.

[31] H. Jasak, H. G. Weller, and A. D. Gosman. High resolution NVD differencing scheme for arbitrarily unstructured meshes. *International Journal for Numerical Methods in Fluids*, 31: 431–449, 1999.

[32] P. K. Jha, E. P. N. Duque, J. L. Bashioum, and S. Schmitz. Unraveling the Mysteries of Turbulence Transport in a Wind Farm. *Energies*, 8:6468–6496, 2015.

[33] O. D. Kellogg. *Foundations of Potential Theory. Reprint from the first edition of 1929*. 1929.

[34] M. F. Khaled, A. M. Aly, and A. Elshaer. Computational efficiency of CFD modeling for building engineering: An empty domain study. *Journal of Building Engineering*, 42, 2021.

[35] D. A. Köse and E. Dick. Prediction of the pressure distribution on a cubical building with implicit LES. *Journal of Wind Engineering and Industrial Aerodynamics*, 98:628–649, 2010.

[36] D. A. Köse, D. Fauconnier, and E. Dick. ILES of flow over low-rise buildings: Influence of inflow conditions on the quality of the mean pressure distribution prediction. *Journal of Wind Engineering and Industrial Aerodynamics*, 99:1056–1068, 2011.

[37] G. Lamberti, C. García-Sańchez, J. Sousa, and C. Gorlé. Optimizing turbulent inflow conditions for large-eddy simulations of the atmospheric boundary layer. *Journal of Wind Engineering & Industrial Aerodynamics*, 177:32–44, 2018.

[38] P. Lampitella, R. Mereu, E. Colombo, and F. Inzoli. Large eddy simulation of the flow and heat transfer in a matrix of cubes. 2014.

[39] T. Lauriks, R. Longo, D. Baetens, M. Derudi, A. Parente, A. Bellemans, J. van Beeck, and S. Denys. Application of Improved CFD Modeling for Prediction and Mitigation of Traffic-Related Air Pollution Hotspots in a Realistic Urban Street. *Atmospheric Environment*, 246, 2021.

[40] S. Lenz, M. Schönherr, M. Geier, M. Krafczyk, A. Pasquali, A. Christen, and M. Giometto. Towards real-time simulation of turbulent air flow over a resolved urban canopy using the cumulant lattice Boltzmann method on a GPGPU. *Journal of Wind Engineering and Industrial Aerodynamics*, 189:151–162, 2019.

[41] Y. Li and Z. J. Wang. A priori and a posteriori evaluations of sub-grid scale models for the Burgers' equation. *Computers and Fluids*, 139:92–104, 2016.

[42] F. S. Lien and M. .A Leschziner. Upstream monotonic interpolation for scalar transport with application to complex turbulent flows. *International Journal for Numerical Methods in Fluids*, 19:527–548, 1994.

[43] S. W. Liu, J. Katz, and C. Meneveau. Evolution and modelling of subgrid scales during rapid straining of turbulence. *Journal of Fluid Mechanics*, 387:281–320, 1999.

[44] R. Longo, M. Fürst, A. Bellemans, M. Ferrarotti, M. Derudi, and A. Parente. Cfd dispersion study based on a variable schmidt formulation for flows around different configurations of ground-mounted buildings. *Building and Environment*, 154:336–347, 2019.

[45] A. S. Lopes, J. M. L. M. Palma, and A. Castro F. Simulation of the Askervein flowPart 2: Large-eddy simulations. *Boundary-Layer Meteorology*, 125:85–108, 2007.

[46] W. J. Manning. Urban environment: defining its nature and problems and developing strategies to overcome obstacles to sustainability and quality of life. *Environmental Pollution*, 159(8-9):1963–1964, 2011.

[47] C. Meneveau and J. Katz. Conditional subgrid force and dissipation in locally isotropic and rapidly strained turbulence. In *International Conference on Turbulence*, 1999.

[48] C. Meneveau and J. Katz. Scale-invariance and turbulence models for large-eddy simulation. *Annual Review of Fluid Mechanics*, 32:1–32, 2000.

[49] Peter Moonen, Thijs Defraeye, Viktor Dorer, Bert Blocken, and Jan Carmeliet. Urban Physics: Effect of the micro-climate on comfort, health and energy demand. *Frontiers of Architectural Research*, 1:197–228, 2012.

[50] F. Moukalled, L. Mangani, and M. Darwish. *The Finite Volume Method in Computational Fluid Dynamics. An Advanced Introduction withOpenFOAM® and Matlab®*. 2016.

[51] F. Nicoud and F. Ducros. Subgrid-Scale Stress Modelling Based on the Square of the Velocity Gradient Tensor. *Flow, Turbulence and Combustion*, 62:183–200, 1999.

[52] NREL. NREL / SOWFA-6 / exampleCases / tut.ABLflatTerrain.precursor, 2019. URL `https://github.com/NREL/SOWFA-6/tree/dev/exampleCases/tut.ABLflatTerrain.precursor`. Online, accessed on 20 August 2021.

[53] OECD. Air and GHG emissions, 2019. URL `https://data.oecd.org/air/air-and-ghg-emissions.htm#indicator-chart`. Accessed on 25 November 2019.

[54] OpenFOAM. limitedCubicLimiter< LimiterFunc > Class, 2022. URL `https://www.openfoam.com/documentation/guides/latest/api/classFoam_1_1limitedCubicLimiter.html#details`. Accessed on 26 January 2022.

[55] OpenFOAM. Support, private communications, 2022.

[56] OpenFOAM. OpenFOAM is the free, open source CFD software developed primarily by OpenCFD Ltd since 2004, 2022. URL `https://www.openfoam.com/`. Accessed on 18 January 2022.

[57] OpenFOAM. *atmBoundaryLayer*, 2022.

[58] K. Ou, P. Castonguay, and A. Jameson. 3D Flapping Wing Simulation with High Order Spectral Difference Method on Deformable Mesh. 2011.

[59] A. Parente, R. Longo, and M. Ferrarotti. *CFD boundary conditions, turbulence models and dispersion study for flows around obstacles*. VKI LS 2017-01, 2017. Editors: Benocci, C. and van Beeck, J. P. A. J.

[60] A. Parente, R. Longo, and M. Ferrarotti. *Turbulence model formulation and dispersion modelling for the CFD simulation of flows around obstacles and on complex terrains*. VKI LS 2019-03, 2019. Editor: van Beeck, J. P. A. J.

[61] G. Patnaik and J. Boris. FAST3D-CT: an LES model for urban aerodynamics. 2010.

[62] G. Patnaik, J. P. Boris, F. F. Grinstein, and J. P. Iselin. *Large Scale Urban Simulations with FCT*, pages 105–130. 2005.

[63] G. Patnaik, J. P. Boris, T. R. Young, and F. F. Grinstein. Large scale urban contaminant transport Simulations with miles . *Journal of Fluids Engineering-Transactions of the ASME*, 129:1524–1532, 2007.

[64] G. Patnaik, J. P. Boris, F. F. Grinstein, J. P. Iselin, and D. Hertwig. *Large Scale Urban Simulations with FCT*, pages 91–117. 2012. In: Flux-Corrected Transport. Principles, Algorithms, and Applications. Second Edition.

[65] A. Pelliccioni, P. Monti, C. Gariazzo, and G. Leuzzi. Some characteristics of the urban boundary layer above Rome, Italy, and applicability of Monin-Obukhov similarity. *Environmental Fluid Mechanics*, 12:405–428, 2012.

[66] U. Piomelli, G. N. Coleman, and J. Kim. On the effects of nonequilibrium on the subgrid-scale stresses. *Physics of Fluids*, 9:2740–2748, 1997.

[67] R. Poletto, T. Craft, and A. Revell. A New Divergence Free Synthetic Eddy Method for the Reproduction of Inlet Flow Conditions for LES. *FLow, Turbulence and Combustion*, 91: 519–539, 2013.

[68] B. S. Pope. *Turbulent FLows*. 2000.

[69] J. Pullen, J. P. Boris, T. Young, G. Patnaik, and J. Iselin. A comparison of contaminant plume statistics from a gaussian puff and urban cfd model for two large cities. *Atmospheric Environment*, 39:1049–1068, 2005.

[70] P. J. Richards and R. P. Hoxey. Appropriate boundary conditions for computational wind engineering models using the $k-\varepsilon$ turbulence model. In *Journal of Wind Engineering and Industrial Aerodynamics*, 1993.

[71] P. L. Roe. Some Contributions to the Modelling of Discontinuous Flows. In *Large-scale computations in fluid mechanics*, 1985.

[72] P. Sagaut. *Large Eddy Simulation for Incompressible Flows. An Introduction. Third Edition*. 2006.

[73] S. B. Savaliya, S. P. Kumar, and S. Mittal. Laminar separation bubble on an Eppler 61 airfoil. *International Journal for Numerical Methods in Fluids*, 64:627–652, 2010.

[74] T.-H. Shih, W. W. Liou, A. Shabbir, Z. Yang, and J. Zhu. A new $k-\varepsilon$ eddy viscosity model for high reynolds number turbulent flows. *Computers & Fluids*, 24:227–238, 1995.

[75] N. M. Standen. A spire array for generating thick turbulent shearlayers for neutral wind simulation in wind tunnels. Technical Report LTR-LA-94, National Aeronautical Establishment, 1972.

[76] P. K. Sweby. High Resolution Schemes Using Flux Limiters for Hyperbolic Conservation Laws. *SIAM Journal on Numerical Analysis*, 21:995–1011, 1984.

[77] T. Tamura, K. Nozawa, and K. Kondo. AIJ guide for numerical prediction of wind loads on buildings. *Journal of Wind Engineering and Industrial Aerodynamics*, 96:1974–1984, 2008.

[78] Y. Tominaga and T. Stathopoulos. Turbulent Schmidt numbers for CFD analysis with various types of flowfield. *Atmospheric Environment*, 41:8091–8099, 2007.

[79] A. Uranga, P.-O. Persson, M. Drela, and J. Peraire. Implicit Large Eddy Simulation of Transitional Flows Over Airfoils and Wings. 2009.

[80] G. D. van Albada, B. van Leer, and W. W. Roberts. A Comparative Study of Computational Methods in Cosmic Gas Dynamics. *Astronomy and Astrophysics*, 108:76–84, 1982.

[81] B. van Leer. Towards the ultimate conservative difference scheme. ii. monotonicity and conservation combined in a second-order scheme. *Journal of Computational Physics*, 14: 361–370, 1974.

[82] B. van Leer. Towards the Ultimate Conservative Difference Scheme III. Upstream-Centered Finite-Difference Schemes for Ideal Compressible Flow. *Journal of Computational Physics*, 23:263–275, 1977.

[83] N. P. Waterson and H. Deconinck. A unified approach to the design and application of bounded higher-order convection schemes. In *Proceedings of the Ninth International Conference on Numerical Methods in Laminar and Turbulent Flow*, 1995.

[84] WHO. Ambient (outdoor) air pollution. URL `https://www.who.int/news-room/fact-sheets/detail/ambient-(outdoor)-air-quality-and-health`. Accessed on 11 November 2020.

[85] Y. Yang, M. Gu, S. Chen, and X. Jin. New inflow boundary conditions for modelling the neutral equilibrium atmospheric boundary layer in computational wind engineering. *Journal of Wind Engineering and Industrial Aerodynamics*, 97:88–95, 2009.

[86] H. J. Ziman. Computer Prediction of Chemically Reacting Flows in Stirred Tanks, 1990. PhD thesis.

Influence of number of simulated wind directions on pedestrian wind comfort maps

Trond-Ola Hågbo[1,2]

[1]*Environmental and Applied Fluid Dynamics Department, von Karman Institute for Fluid Dynamics, Belgium, trondola.hagbo@vki.ac.be*

[2]*Department of Mechanical and Structural Engineering and Materials Science, University of Stavanger, Norway*

Supervisor: Jeroen van Beeck

Professor, Environmental and Applied Fluid Dynamics Department, von Karman Institute for Fluid Dynamics, Belgium, jeroen.vanbeeck@vki.ac.be

University Supervisor: Knut Erik Teigen Giljarhus

Associate Professor, Department of Mechanical and Structural Engineering and Materials Science, University of Stavanger, Norway, knut.e.giljarhus@uis.no

Abstract

The construction of a building inevitably changes the microclimate in its vicinity. This article investigates the influence of the number of simulated wind directions on pedestrian wind comfort maps. A neighborhood in Niigata, Japan, was chosen as a case study. The pedestrian wind comfort maps are converging towards a final map as more wind directions are included.

Keywords: Pedestrian wind comfort, RANS, cylindrical domain, inlet/outlet conditions, atmospheric boundary layer.

1. Introduction

Computational fluid dynamics (CFD) has been increasingly applied to solve urban wind engineering problems, such as wind loads on buildings and bridges [1; 2; 3; 4], and pedestrian wind comfort [5; 6; 7; 8]. Knowledge of the wind flow at a given geographic location complements numerous applications in climate modeling, urban planning, environmental modeling, and other applications [9].

Pedestrian wind comfort refers to the mechanical effect of wind on people at ground level. Buildings and other urban structures strongly modify the local wind conditions, and high-rise buildings are especially known for frequently causing high wind velocities at pedestrian level, reducing the experienced pedestrian wind comfort in its vicinity. On some occasions, the strong local wind gusts could even be considered a safety concern.

There is rising concern that uncomfortable and dangerous wind conditions in urban areas will be more common in the future as climate change can cause more frequent extreme weather events [10]. Also, further urbanization in the form of the erection of more high-rise buildings, and a more dense built environment in general, is likely to worsen the wind environment additionally.

These urban wind problems can be addressed by including pedestrian wind comfort studies in city planning processes, and in the design phase prior to the erection of new buildings. The possible negative effect of new buildings on the local wind environment has gained awareness in the past decades. Nowadays, many city authorities request pedestrian wind comfort studies before granting building permits.

A pedestrian wind comfort map illustrates the annual wind conditions experienced at ground level by pedestrians at a site. These maps are produced by combining wind simulations, statistical meteorological data, and a set of defined comfort criteria.

The set of wind simulations used as inputs are to represent the different wind conditions occurring at

the location throughout a year. The setup of the simulations only differs in the wind direction applied at the inlet, which are evenly distributed in the horizontal plane within the set. Wisse et al. [11] argued that 12 wind directions are enough for the analysis of pedestrian wind comfort. 12 wind directions with 30° increments are used in most published journal papers, including [12; 13; 8; 5]. Hågbo et al. [14] instead used the eight cardinal and intercardinal directions. The City of London Corporation recommends that 36 equally spaced wind directions should be used [15], but specify that this number is calibrated for the City of London and may not be appropriate for other areas.

This study aims to investigate the influence of the number of simulated wind directions on pedestrian wind comfort maps. Increasing the number of wind directions will likely result in more accurate maps, but will also raise the computational costs. The required number of wind directions needed to reach a satisfactory accuracy is presumably dependent on the complexity of the urban environment and local meteorological conditions. Other associated uncertainties in the production of the maps, such as the local statistical meteorological data or the simulation's ability to represent the annual local wind conditions, may justify few simulated wind directions.

The number of simulated wind directions used in the production of the pedestrian wind comfort maps in this study is:

1. 4, increments of 90°
2. 8, increments of 45°
3. 16, increments of 22.5°
4. 32, increments of 11.25°
5. 64, increments of 5.625°

The location chosen for this study is a neighborhood in Niigata in Japan, a building complex with simple building shapes. This location is used in the Architectural Institute of Japan (AIJ) benchmark case E, and its geometric model and data from wind tunnel experiments are provided at [16].

CFD is used in the industry today to predict wind velocity levels in urban areas. Regardless of the method's agreement with experiments, it is valuable to investigate the number of wind directions necessary to simulate to obtain a converged pedestrian comfort map. An improved understanding of the influence of the number of simulated wind directions and its associated accuracy in specific cases may help develop more efficient and reliable tools to perform pedestrian wind comfort studies.

This paper is structured as follows. The next chapter describes the methodology in detail, starting with the computational domain and grid, and the numerical setup of the wind simulations. Then the process of producing the aggregated pedestrian wind comfort maps is outlined. Finally, the results are presented and discussed.

2. Methodology

As the accuracy and reliability of CFD simulations can be easily compromised, best practice guidelines (BPGs) have been developed for properly conducting CFD analysis of the wind environment in urban areas. These guidelines are based on the cross-comparison between CFD simulations, wind tunnel experiments, and field measurements on several cases. The BPGs provided by Franke et al. [17] and Tominaga et al. [18] were closely followed to set up the simulations.

2.1. Computational domain

The BPGs have been used as a minimum requirement when sizing the computational domain. The guidelines are based on box-shaped domains only suitable for wind at the inlet to have one specific direction, which is inward parallel to the domain's sidewalls. As the intention of this study was to have a flexible mesh suitable for simulating wind from any horizontal direction, cylindrical domains were used. Therefore, the recommendations of the BPGs had to be applied and adapted to them.

The routine of using a cylindrical computational domain when performing urban wind simulations was introduced by Kastner and Timur [19]. They reported that a cylindrical domain yielded comparable results to a traditional box-shaped domain in terms of accuracy and convergence behavior. Also, Hågbo et al. [14] applied a cylindrical domain in the application of urban wind simulations. Figure 1 presents the computational domain and the dimensions are listed on the right side of the figure.

The BPGs suggest that the top of the domain should be 5 H_{max} from the top of the tallest building. H_{max}, as defined by Franke et al. [20], is the height of the tallest building and is central in sizing the computational domain. As there is no elevation in the terrain patch, the height of the domain is set to 6 H_{max}. Franke et al. [17] suggest a distance of 15 H_{max} downstream of the buildings to the outlet of the domain. As the cylindrical domain is suitable for wind coming in from any direction, the radial distance from the buildings to the domain's sides is set to 15 H_{max}.

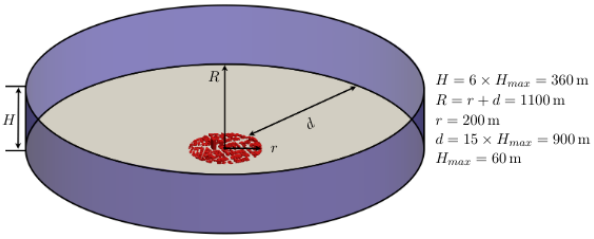

Figure 1: Computational domain, H_{max} is the height of the highest building.

2.2. Computational grids

The computational grid was developed according to the BPGs. The final grid is produced with `snappyHexMesh`, the hex-dominant unstructured mesh generator of OpenFOAM. `snappyHexMesh` requires a base mesh and the triangulated surface geometries it conforms the mesh to fit, here the building model and the terrain model. Hågbo et al. [21] concluded that an unstructured mesh generated with `snappyHexMesh` could be sufficient in urban wind simulations where only the general flow features are of interest.

The base mesh was generated with `blockMesh`, a meshing utility in OpenFOAM suitable for simple structured meshes with grading and curved edges. In the base mesh, the grid is stretched vertically with an overall expansion ratio of three. It means that the width of the top cells is three times the bottom cells.

The grid is refined successively near the terrain and buildings in the final mesh, with eight grid cells between each refinement level. Three refinement levels are used on the terrain patch, while one additional level is applied for the buildings patch.

Figure 2 illustrates the grid structure used inside the domain from the side. The grid consists of about 12.1 million cells.

The height of the cells adjacent to the buildings and on the terrain near the buildings is 0.34 m. On the rest of the terrain the cell height is 0.68 m. These cell heights give the average non-dimensional wall distances y^+ value of about 7.0×10^3 for the building patch and 9.0×10^3 for the terrain patch in the built region.

These are relatively high values that significantly exceed the recommended values of (30 - 500)[17], meaning that the first cell center is well outside the log-law region. However, standard logarithmic wall functions are typically also used in CFD simulations of atmospheric boundary layer wind flow when y^+ is well above the recommended upper limit without reducing the accuracy of the simulated wind velocity field. Examples using y^+ values of the same order of magnitude as in this study include [22; 23; 24; 25].

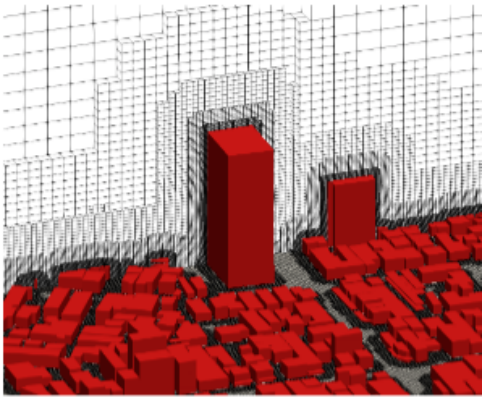

Figure 2: Computational grid structure, partial view from the side.

The high Reynolds number flow studied here makes it challenging to be within the log-law region. The most important reason for using these high y^+ values is that the recommended range is based on smooth walls and would yield unnecessarily small near-wall cells for our rough terrain wall. It should also be noted that the log-law profile is not necessarily valid given the complex geometry of the terrain.

Apart from the y^+-values, the resolution is sufficiently high according to the BPGs as it satisfies the recommendation of a minimum of ten cells per building side and in the passage between buildings, as well as at least three cells from the ground to the elevation height [17; 26; 27]. In this study, the elevation height was set to 2 m above ground level, a reasonable height for pedestrian wind comfort evaluation.

2.3. Simulation setup and other computational parameters

The wind simulations were performed by solving the incompressible, three-dimensional steady Reynolds-averaged Navier-Stokes (RANS) equations with the finite volume method. Turbulent closure was provided by the realizable k-ϵ turbulence model developed by Shih et al. [28] and the SIMPLEC algorithm handled the pressure-velocity coupling ensuring the continuity equation to be satisfied. Second-order discretization schemes were used for the spatial discretization, including the convective terms.

The iterative convergence criteria were that the scaled residuals should drop four orders of magni-

Table 1: Overview of boundary conditions applied.

Patch	Boundary condition type
Sides	Inlet/outlet
Inlet	Atmospheric boundary layer
Outlet	Fixed pressure and zero gradient
Terrain	Rough wall, $z_0 = 3.00\,\mathrm{m}$
Buildings	Smooth wall
Top	Slip

tude for k(turbulent kinetic energy), ϵ(turbulent kinetic energy dissipation rate) and each Cartesian components of U(velocity), as recommended for all flow variables by the BPGs. The convergence criterion for p(pressure) was relaxed to 5.0×10^{-4}. This was done to speed up the simulations, as reaching a residual drop of four orders of magnitude required significantly longer simulation time, and this relaxation of the convergence criterion did not visibly impact the results for velocity magnitude used in this work. These criteria were reached for all simulations presented.

The simulations were conducted using the OpenFOAM (version 6) toolbox, which is an open-source CFD software package [29].

An overview of the boundary conditions (BCs) used is presented in Table 1. Combined inlet/outlet boundary conditions (Robin conditions) are used on the computational domain's sides to allow for wind in any direction. The inlet profiles were set to form a homogeneous atmospheric boundary layer (ABL) with neutral stratified conditions, according to the BPGs. The wind speed at a reference height of 10 m, U_{ref10m}, was set to $5\,\mathrm{m\,s^{-1}}$. At the outlet, outlet conditions were used with constant pressure and zero gradient for the remaining variables. The direction of the flux automatically determines the inlet and outlet regions.

No-slip conditions with wall functions were used for both the terrain and the buildings layer. The logarithmic law for smooth walls was used for the buildings. A rough wall condition was applied for the terrain [30]. The roughness was set to $z_0 = 3.00\,\mathrm{m}$, representing an urban area. The slip condition was applied to the top boundaries.

2.4. Production of pedestrian wind comfort maps

The pedestrian wind comfort maps are produced by combining wind simulations, local statistical meteorological data in the form of a wind rose, and a set of defined comfort criteria. There are numerous sets of wind comfort criteria, and in this study, a version of the Lawson wind comfort criteria [31] is used, see Table 2. The Lawson criteria classify areas with "comfortable" activity types based on their associated accepted average wind speed intervals and exceedance frequency. The calculation of wind comfort criteria was also considered in Blocken et al. [32] and Blocken et al. [5].

Table 2: Pedestrian wind comfort criteria used in study, based on Lawson wind comfort criteria [31].

Wind speed range (m/s)	Exceedance frequency (%)	Activity type	Class number	Color
[0 to 4)	≤ 5	Sitting	1	
[0 to 6)	≤ 5	Standing	2	
[0 to 8)	≤ 5	Strolling	3	
[0 to 10)	≤ 5	Business walking	4	
-	-	Uncomfortable	5	

The procedure of producing pedestrian wind comfort maps in this study is as follows. First, the wind is simulated from 64 evenly distributed horizontal wind directions. A set 4, 8, 16, 32, or all 64, simulations of evenly distributed wind directions are used further in the process.

Then, for each wind direction and wind velocity class in the wind rose, all the computational cells are assigned a wind velocity range class. The wind directions in the simulations correspond to the middle of the sectors in the wind rose. Not all wind speeds are simulated. Instead, a representative wind field for each Lawson category is found by a linear scaling of the simulated wind velocity. To be conservative, the maximum value in each wind speed range is used as the scaling factor. A linear scaling is justified as the wind is well within the turbulent flow regime for all the wind speed intervals under consideration, and hence similar flow distributions are expected. For each category, the frequency of this wind velocity is obtained from the wind rose. The scaled velocity field is then used to identify which Lawson activity type each cell represents, and the total frequency for each activity is accumulated in that cell.

Finally, based on the total exceedance frequency in each cell, the cell is given a comfort value. The comfort of the cells located 2 m above the terrain level is read, and its representing color is projected onto the terrain patch below. The result is a pedestrian wind comfort map.

In this case study, the local wind statistics were arbitrarily chosen such that the wind was set always to be 5 m/s at 10 m height and that all the wind directions are evenly common.

3. Discussion of results

3.1. Validation

The wind tunnel experiments were conducted at a 1/250 scale [33]. A boundary layer with properties similar to an atmospheric boundary layer was generated in the wind tunnel upstream of the test section of dimensions 1.8 m length, 1.8 m width, and 1.8 m height. The vertical profile of the horizontal wind velocity developed to follow a function with a power-law exponent of 0.25 when reaching the test section. Scalar wind velocities at 0.008 m above the wind tunnel floor (2 m above the ground surface in real scale) were measured by multi-point thermistor anemometers.

Figure 3 shows the normalized simulated wind velocity magnitude at 2 m above ground, wind from N (0°). The colored dots are located in the same position as the 80 probes in the wind tunnel experiments, and their color represents the wind velocity magnitude difference, ΔU, between the wind tunnel experiment and the simulation, where ΔU is:

$$\Delta U = U_{\text{exp}} - U_{\text{sim}} \tag{1}$$

Blue-colored dots indicate that the wind velocity magnitude of the simulation is greater than in the wind tunnel experiments, and red-colored dots means that the wind velocity magnitude of the simulation is lower than in the wind tunnel experiments. The experimental values compared against are averaged over time.

The figure clearly shows the expected speed-up effect at ground-level near the side corners of the high-rise building relative to the overall wind direction. The similarly expected wake regions of low wind velocity magnitudes are seen leeward of the buildings. When comparing the wind velocity magnitudes at the probes in the simulations to the results from the wind tunnel experiments from 16 wind directions, we see a slight trend that the simulations are overpredicting the effects of the buildings. More specifically, the simulated values in relatively high wind speed

areas are generally too high compared to wind tunnel results. Likewise, the simulated values are too low compared to wind tunnel results in low wind speed regions. This trend is slightly noticeable in Figure 3, where red dots are somewhat located in blue low-velocity areas, and blue dots in red high-velocity areas. Note that the calculated differences, represented by the colored dots, are highly sensitive to the location of the probes as they are positioned within regions of high flow gradients.

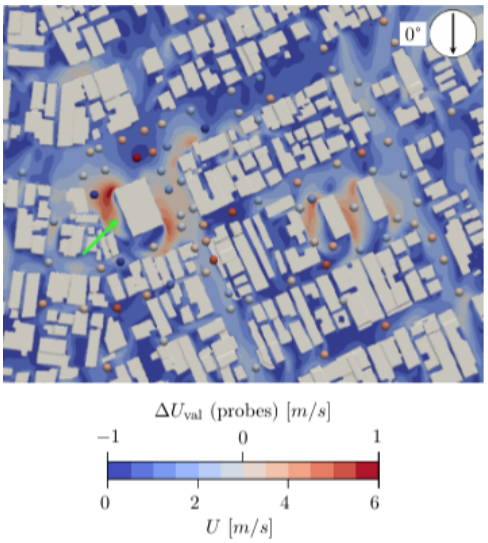

Figure 3: Normalized simulated wind velocity magnitude at 2 m above ground, wind from N (0°). The colored dots represent the wind velocity magnitude difference, ΔU, between the wind tunnel experiment and the simulation at the 80 probes. The experimental values compared against are averaged over time. The black arrow indicates the wind direction at the inlet, and the green arrow points to the high-rise building.

Table 3 lists the average relative difference of wind velocity magnitude, and the Pearson correlation coefficient (PCC), between wind simulations and wind tunnel experiments for 16 wind directions at the 80 probes. The experimental values compared against are averaged over time. It quantifies that the wind velocity magnitude of the simulations is overall lower at ground level than in the wind tunnel experiments. For the 16 wind directions is the average relative difference of wind velocity magnitude in the range from −1 % to −35 %, and the Pearson correlation coefficient in the range 0.71 to 0.84

The overprediction of the extent and significance of the wake regions of low wind velocity magnitudes, and thus the flow reattachment length, leeward of the buildings, agrees with other RANS simulations in the literature. Generally, it is because the transient nature of the flow is difficult to fully represent in time-averaged simulations, leading to less turbulent mixing in the simulations. It is also evident in Table 3 where the negative values of the average relative difference of wind velocity magnitude between wind simulations and wind tunnel experiments are because many of the probes are located within the wake regions in the sim-

Table 3: The average relative difference of wind velocity magnitude, and the Pearson correlation coefficient (PCC), between wind simulations and wind tunnel experiments for 16 wind directions at the 80 probes. The experimental values compared against are averaged over time.

Wind direction (°)	**Average relative difference** (%)	**PCC**
0.0	-11	0.76
22.5	-17	0.77
45.0	-10	0.71
67.5	-10	0.81
90.0	-14	0.78
112.5	-26	0.73
135.0	-35	0.77
157.5	-26	0.81
180.0	-8	0.84
202.5	-4	0.80
225.0	-1	0.78
247.5	-6	0.61
270.0	-7	0.77
292.5	-11	0.79
315.0	-15	0.78
337.05	-13	0.71

ulations.

3.2. Pedestrian wind comfort aggregated map

Figure 4 presents the pedestrian wind comfort maps at 2 m above ground produced using either 4, 8, 16, 32, or 64 evenly distributed horizontal wind directions. Only a section of the computational domain, 100 m in each horizontal direction of the high-rise building, is presented.

Ground areas around the high-rise building, especially near the corners, are classified with the worst ('uncomfortable') or the second-worst ('business walking') wind comfort classification class in all the maps. It is caused by a wind pull-down effect frequently seen near high buildings, particularly ones with sharp corners. The wind is much weaker around the other lower buildings. The areas with frequent high wind are more evenly distributed around the high-rise building as more wind directions are included in the production of the maps, especially compared to the map produced with wind simulations from only 4 wind directions.

The differences in the pedestrian wind comfort maps are best viewed in Figure 5. It gives the classification difference to the reference case, ΔC, where:

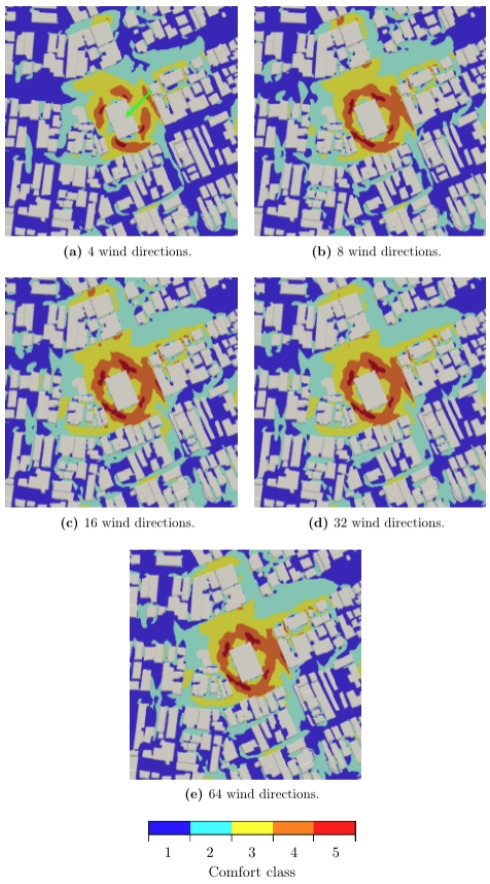

Figure 4: Pedestrian wind comfort maps at 2 m above ground 100 m in each horizontal direction of the high-rise building pointed out by the green arrow.

$$\Delta C = C_i - C_j \tag{2}$$

C_i is the pedestrian wind comfort class classification of a given location using 64 wind directions. And C_j is the classification at the same location using a different number of wind directions. The map produced from the most wind directions, here 64, is likely the most accurate and is used as the reference case.

Negative values, represented by blue, correspond to areas where the reference case has a lower classification number, meaning an improved wind comfort class, than the compared case and vice versa. Notice that there is a relatively big total area in red in the Figure 5a. The reference

case has a higher classification number in these red areas, meaning a worse wind comfort class, than the case using only 4 wind directions.

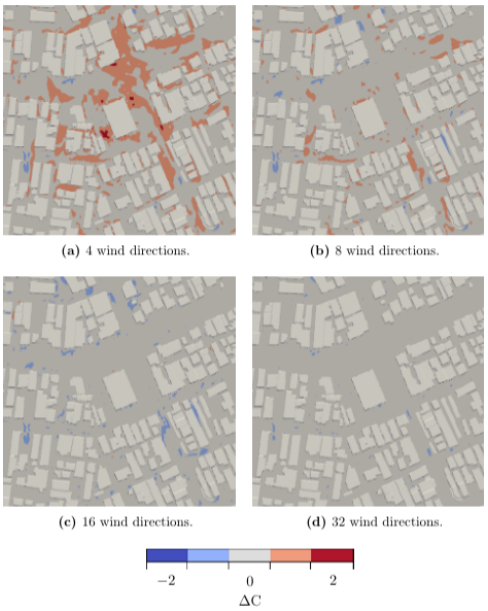

Figure 5: Pedestrian wind comfort classification difference, ΔC, to the map using all 64 wind directions at 2 m above ground 100 m in each horizontal direction of the high-rise building.

Table 4: Area of pedestrian wind comfort classification difference, ΔC, to the map using all 64 wind directions at 2 m above ground 100 m in each horizontal direction of the high-rise building. The building footprint area is excluded. This table provides numbers to the areas seen in Figure 5.

Wind	Comfort class difference (%)		
directions	0	1	2
4	78.66	21.00	0.34
8	91.61	8.39	0.00
16	95.84	4.16	0.00
32	99.01	0.99	0.00

Quantification of the differences is provided in Table 4. It shows the percentage of area classified differently compared to maps using all the 64 simulated wind directions. The total area classified differently from the reference map clearly reduces in size as more wind directions are included.

79 % of the area within 100 m in each horizontal direction of the high-rise building is classified with the same pedestrian wind comfort class as the map produced using 64 wind directions. This number increases to 92 % using 8 wind directions, 96 % using 16 wind directions, and finally 99 % using 32 wind directions. Similar values was observed when including the whole building area of radius 200 m.

4. Conclusion

The simulated wind velocity magnitude at ground level in the urban area is noticeably lower overall than wind tunnel experiments. This is due to the overprediction of the extent of the wake regions of low wind velocity magnitudes leeward of buildings and is in agreement with other RANS simulations in the literature. Transient simulations will likely provide more accurate predictions of the size of the wake regions but at a substantially higher computational cost.

The pedestrian wind comfort maps are converging towards a final map as more wind directions are included. Doubling the numbers of wind directions from 4 to 8 changes the maps significantly, but only a slight variation is observed when doubling the wind direction count from 32 to 64.

It is reasonable to assume that adding more wind directions increases the accuracy of the produced pedestrian wind comfort maps. The extent to which the accuracy is increased is likely dependent on many factors that need further study. It includes the level of urbanization, meaning the urban area's geometrical complexity, and the local meteorological conditions and their variations with the seasons. A greater understanding of the influence of the number of simulated wind directions included may enable more efficient pedestrian wind comfort studies that recognize the associated uncertainties.

Acknowledgments

This research is part of the Future Energy Hub Project funded by The Norwegian Research Council (project no.: 280458), The University of Stavanger, and local industry partners.

References

[1] Tamura T, Nozawa K and Kondo K 2008 *J Wind Eng Ind Aerodyn* **96** 1974 – 1984 4th International Symposium on Computational Wind Engineering (CWE2006)
[2] Huang S, Li Q and Xu S 2007 *J Constr Steel Res* **63** 612 – 627
[3] Montazeri H and Blocken B 2013 *J Built Environ* **60** 137 – 149
[4] Thordal M S, Bennetsen J C and Koss H H H 2019 *J Wind Eng Ind Aerodyn* **186** 155 – 168
[5] Blocken B, Janssen W and van Hooff T 2012 *Environ Model Softw* **30** 15 – 34
[6] 2016 *J Built Environ* **100** 50 – 81
[7] Janssen W, Blocken B and van Hooff T 2013 *J Built Environ* **59** 547 – 562
[8] Blocken B and Persoon J 2009 *J Wind Eng Ind Aerodyn* **97** 255–270
[9] Blocken B 2014 *J Wind Eng Ind Aerodyn* **129** 69–102
[10] National Academies of Sciences E, Medicine *et al.* 2016 *Attribution of extreme weather events in the context of climate change* (National Academies Press)
[11] Wisse J, Krüs H and Willemsen E 2002 "wind comfort assessment by cfd - context and requirements" (Centre Scientifique et Technique du Batiment) pp 154–163
[12] Blocken B, Roels S and Carmeliet J 2004 *J Wind Eng Ind Aerodyn* **92** 849–873
[13] Blocken B and Carmeliet J 2008 *Wind Struct An Int* **11** 51–70
[14] Hågbo T O, Giljarhus K E T and Hjertager B H 2021 *J Wind Eng Ind Aerodyn* **215** 104665
[15] City of London Corporation 2019 Wind microclimate guidelines for developments in the city of london
[16] Architectural Institute of Japan Guidebook for cfd predictions of urban wind environment
[17] Franke J, Hellsten A, Schlünzen H and Carissimo B 2007 *Brussels, COST*
[18] Tominaga Y, Mochida A, Yoshie R, Kataoka H, Nozu T, Yoshikawa M and Shirasawa T 2008 *J Wind Eng Ind Aerodyn* **96** 1749–1761
[19] Kastner P and Dogan T 2020 *J Build Perform Simul* **13** 59–68
[20] Franke J 2006 Recommendations of the cost action c14 on the use of CFD in predicting pedestrian wind environment *The fourth international symposium on computational wind engineering, Yokohama, Japan* (Citeseer) pp 529–532
[21] Hågbo T O, Giljarhus K E T, Qu S and Hjertager B H 2019 *IOP Conf Ser Mat Sci* **700** 012001
[22] van Hooff T, Blocken B and van Harten M 2011 *J Built Environ* **46** 22–37
[23] Blocken B, Stathopoulos T and Carmeliet J 2007 *Atmos Environ* **41** 238–252
[24] van Hooff T and Blocken B 2010 *Environ Model Softw* **25** 51–65
[25] van Hooff T and Blocken B 2010 *J Comp Fluids* **39** 1146–1155
[26] Tominaga Y, Mochida A, Yoshie R, Kataoka H, Nozu T, Yoshikawa M and Shirasawa T 2008 *J Wind Eng Ind Aerodyn* **96** 1749–1761
[27] Yoshie R, Mochida A, Tominaga Y, Kataoka H, Harimoto K, Nozu T and Shirasawa T 2007 *J Wind Eng Ind Aerodyn* **95** 1551–1578
[28] Shih T H, Liou W W, Shabbir A, Yang Z and Zhu J 1995 *J Comp Fluids* **24** 227–238
[29] Weller H G, Tabor G, Jasak H and Fureby C 1998 *Comput Phys* **12** 620–631
[30] Hargreaves D and Wright N G 2007 *J Wind Eng Ind Aerodyn* **95** 355–369
[31] Lawson T 1978 *J Wind Eng Ind Aerodyn* **3** 93–105
[32] Blocken B and Carmeliet J 2004 *J Therm Envel Build Sci* **28** 107–159
[33] Yoshie R, Mochida A, Tominaga Y, Kataoka H, Harimoto K, Nozu T and Shirasawa T 2007 *J Wind Eng Ind Aerodyn* **95** 1551–1578

Mesoscale modelling of extreme weather events over Belgian North Sea using WRF-ARW: A multi-event sensitivity analysis

Adithya Vemuri

Environmental and applied fluid dynamics Department, von Karman Institute for Fluid Dynamics, Belgium, adithya.vemuri@vki.ac.be

Supervisor: Jeroen van Beeck

Professor, Environmental and applied fluid dynamics Department, von Karman Institute for Fluid Dynamics, Belgium, vanbeeck@vki.ac.be

University Supervisor: Jan Helsen

Professor, Mechanical Engineering, Vrije Universiteit Brussel, Belgium, jan.helsen@vub.be

Abstract

The current work describes a multi-event sensitivity analysis of extreme weather events found potentially harmful for the operation of Belgian offshore wind farms using WRF model. The model sensitivities indicate, the combination of physical parameterizations, type of event and turbulence closure techniques to highly influence the predictions. Overall, scale-aware physical parameterizations are observed to exhibit better performance.

Keywords: Mesoscale modelling, extreme weather, Belgian offshore wind, offshore wind energy, Belgian North Sea.

1. Introduction

The simulation of Extreme Weather Events (EWE) in view of offshore wind energy plays an important role in the development, operation and maintenance of commercial wind farms. Over the decades the use of Numerical Weather Prediction (NWP) models to accurately predict weather events in view of wind energy is thoroughly explored by industry and community alike [1; 2]. The current state-of-the-art NWP models such as Weather Research and Forecasting (WRF), North American Mesoscale (NAM), Application of Research to Operations at Mesoscale (AROME), High Resolution Limited Area Model (HIRLAM)-Aire Limitée Adaptation dynamique Développement InterNational (ALADIN) Regional/Mescoscale Operational NWP in Europe (HARMONIE), are capable of providing high-resolution weather predictions for onshore and offshore wind industry. However, the common challenge for NWP models persists, to predict meteorological variables at high-resolution grey-zone scales (1km to 100m) accurately [3]. Literature also establishes NWP models to be highly sensitive to initial boundary conditions, horizontal and vertical grid spacing, location and type of weather event, interactions between physical parameterizations utilized, type of turbulence closure techniques, geospatial domain configuration, etc. For the European continent, Mooney et al. and Stergiou et al. establish the volatility of NWP forecasts using a long-term sensitivity analysis [4; 5].

This study evaluates the model sensitivities of WRF NWP model using a multi-event sensitivity analysis over the Belgian North Sea to establish a general guidance for EWE prediction.

2. Background study and information

This study extends the work that has been performed to generalize WRF model sensitivities for the case of Storm Ciara over the Belgian offshore concession zone, described in Vemuri et al. [6], to multiple extreme weather events. The former study evaluates the WRF model sensitivities: physical parameterizations (planetary boundary layer, cumulus and microphysics), geospatial domain and temporal resolution of initial boundary conditions, against front-row averaged 10min SCADA data from an offshore wind

farm. Simulated precipitation rate is evaluated against radar data from the Royal Meteorological Institute - Belgium (RMI-B). The study concludes, the considered WRF model setups to be highly sensitive producing varying results to the combination of WRF input parameters. Overall the best-suitable WRF model setups included: scale-aware physical parameterizations, large geospatial domains and higher temporal resolution of initial boundary conditions to better qualitatively and quantitatively capture the transience in wind direction and horizontal wind speed. The ensemble average is observed to better capture precipitation rate in comparison to considered WRF model setups.

3. Description of the events

The events selected for this study are based on observed fast changes in wind direction resulting in unfavorable operating conditions for an offshore wind farm located in the Belgian offshore concession zone. The EWE identified follow the methodology defined in Hannesd´ottir et al. [7]. The cases include: Storm Ciara on 10 February 2020, a low pressure system occurring on 24 December 2020 and a cold front on 27 June 2020.

3.1. Storm Ciara

On 10 February 2020 the Belgian offshore coast experienced the extratropical cyclone, Storm Ciara, following heavy rain fall, strong winds and thunderstorms in the local regions surrounding Jabbeke. At 04:40 UTC fast changes in wind direction were recorded by an offshore wind farm. The radar data indicates the presence of a bow-echo over the region, presented in fig. 1. The event is thus identified to be a micro-burst phenomenon [8] following sudden precipitation and fast changes in wind direction.

3.2. Low pressure system

On 24 December 2020, at 02:00 UTC Fast changes in wind direction were observed by an offshore wind farm. A low pressure system was identified over the Belgian offshore concession zone from synoptic maps [9], not presented here for brevity. The observed precipitation rate plots indicate large precipitation cells over the region, presented in Fig. 2 following consistent precipitation and fast changes in wind direction.

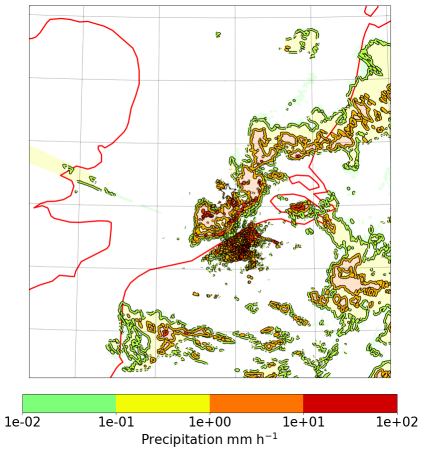

Figure 1: Observed precipitation rate for Storm Ciara on 10 February 2020 at the timestamp 04:40 UTC from RMI-B

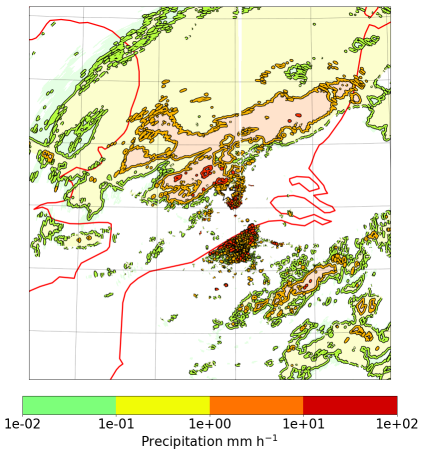

Figure 2: Observed precipitation rate for low pressure system on 24 December 2020 at the timestamp 02:00 UTC from RMI-B

3.3. Cold front

Fast changes in wind direction were observed by an offshore wind farm on 27 June 2020, the synoptic maps indicate the presence of a low pressure region over the British isles, leading a cold front over the Belgian offshore concession zone. The observed radar precipitation rate indicate small precipitation cells, presented in Fig. 3.

4. Methodology and model setup

This study utilizes the community mesoscale modelling framework, WRF version 4.2.2 [10; 11] for simulating the extreme weather events. All simulations are initialized with hourly reanalysis date-set from

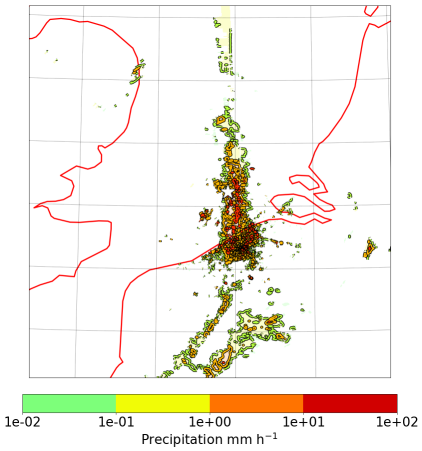

Figure 3: Observed precipitation rate for cold front on 27 June 2020 at the timestamp 15:30 UTC from RMI-B

ERA5 [12], considering a 24 h spin-up period. A timestep of 20 s is considered in this study, the domain configuration is presented in Fig. 4. The summary of model parameters and the combination of simulation runs are presented in table 2. The corresponding parameterizations and references are presented in table 1.

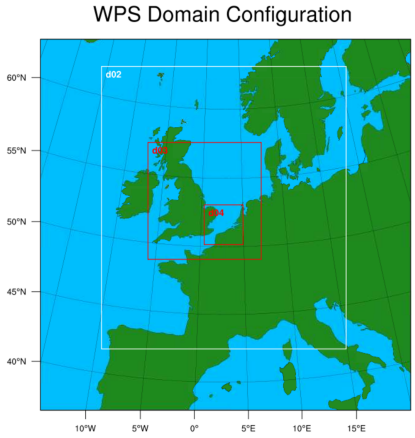

Figure 4: WRF domain configuration considered EWE simulation.

All simulations are evaluated against 10 minute averaged front-row wind direction and horizontal wind speed SCADA data from an offshore wind farm located in the Belgian offshore concession zone. The metrics: Mean Absolute Error (MAE) and Kantorovich distance, per the definition by Wang et al. [24], are considered in this study. MAE and Kantorovich are normalized as, Normalized Euclidean Distance NED $= \sqrt{\text{MAE}^2_{norm.} + \text{Kantorovich}^2_{norm.}}$.

The precipitation rate is compared qualitatively to observed radar reflectively from a dual polarization C-band radar from RMI-B located at Jabbeke, Belgium. The reflectivities are converted to precipitation rate using the Marshall-Palmer relation [25].

5. Results and discussion

The results for individual EWE case are presented in independent subsections. The performance evaluation metrics for each case is presented in assorted tables increasing in fidelity of physical parameterizations. 5 WRF setups are considered under each case study, simulations runs 1 & 2 are the worst-case setups, runs 3 & 4 are the best-case WRF setups identified in Vemuri et al. [6]. Run 5 uses a 3D PBL scheme in place of a 1D PBL in run 4. Precipitation results are qualitatively compared and presented at aforementioned timestamps, for brevity. Similarly, only the ensemble average plots are presented.

5.1. Storm Ciara

The summary of evaluated metrics for respective simulation runs (as described in table 2) are presented in table 3. Considering average NED as the performance evaluation metric, the overall results indicate simulation run 4, considering 1D Shin-Hong scale-aware PBL, scale-aware GF cumulus and Morrison microphysics schemes as the best performer. With the ensemble average performing quantitatively similar to run 4. However, the latter is unable to capture the fast changes in wind direction as observed in SCADA data.

The ensemble average plots for simulated wind direction and horizontal wind speed against SCADA data are presented in Fig. 5 and 6, respectively. The overall trend in wind direction and mean horizontal wind speed for all simulations is found similar to the 10 min SCADA data. The horizontal wind speed for simulation runs 1 and 2 observe an underestimation during the late afternoon period in comparison other simulation setups.

The trend in MAE for simulation runs, as presented in Fig. 7, indicate simulation runs 3 and 4 to produce the lowest wind direction MAE. The horizontal wind speed results indicate no distinguishing results considering only MAE as the evaluation metric.

The qualitative comparison of precipitation is presented in Fig. 8 for simulation runs 1, 4 and 5 against observed radar data. The simulation results are observed to vary strongly with WRF model setups. The

Table 1: Summary of considered WRF physics parameterizations, acronym and references, respectively.

Physics parameterizations		Acronym and reference
Radiation scheme	Rapid Radiative Transfer Model [13]	
Land surface scheme	unified Noah land-surface scheme [14]	
Planetary boundary layer (PBL)	1D MYNN scheme	MYNN [15]
	Shin-Hong 1D scale aware scheme	Shin-Hong [16]
	Zhang 3D scale aware scheme	Zhang [17]
Microphysics	WRF single moment 5 class scheme	WSM5 [18]
	Thompson 6 class scheme	Thompson [19]
	Morrison double moment 6 class scheme	Morrison [20]
Cumulus	Kain-Fritsch scheme	KF [21]
	multi-scale Kain-Fritsch scheme	msKF [22]
	Grell-Freitas scheme	GF [23]

Table 2: A summary of WRF model parameters and simulation runs, considered in this sensitivity study. Scale-aware physics parameterizations are underlined.

Numerical setup	
Nested domains	4
Horizontal resolution	27 km (d01) × 9 km (d02) × 3 km (d03) × 1 km (d04)
Pressure levels	57
Model top pressure	1000 Pa
Time-step	20s
Spin-up	24h
Simulation time	21 h
Boundary conditions	1h ERA5 reanalysis
Physics parameterizations and simulation runs	
Radiation	RRTMG
Land surface	unified Noah land-surface
Simulation run 1	*MYNN / Thompson / KF*
Simulation run 2	*Shin-Hong / WSM5 / KF*
Simulation run 3	*Shin-Hong / Morrison / msKF*
Simulation run 4	*Shin-Hong / Morrison / GF*
Simulation run 5	*Zhang / Morrison / GF*
Simulation run 6	*Ensemble average*

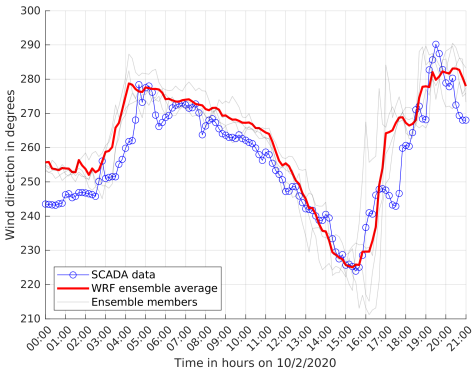

Figure 5: Wind direction plots for SCADA and ensemble average for Storm Ciara on 10 February 2020.

qualitative comparison yields no concrete inferences on the precipitation modelling fidelity in this study.

5.2. *Low pressure system*

The summary of evaluation metrics are presented in table 4. The best case WRF setup considering average NED as the evaluation metric is observed to be simulation run 5, considering 3D Zhang PBL, scale-aware GF cumulus and Morrison microphysical schemes . This particular case study observes the ensemble average to outperform the best-case WRF setup, however, it is unable to capture the fast changes in wind direction as observed in SCADA data (presented in fig. 9).

The ensemble average plots for simulations and SCADA data are presented in fig. 9 and 10, respectively. The wind direction and horizontal wind speed predictions for all simulations is found to reproduce the general transience observed in SCADA data in a similar manner. Albeit, all simulations observed a lag in either wind variables' predictions. With the best-case prediction for simulation run 5.

The comparison of wind direction MAE results, as presented in fig. 11, indicate a trend in better results for the scale-aware simulation setups 4 and 5. However, this distinction is not conclusive considering only MAE as the evaluation meteric for horizontal wind speed.

The qualitative comparison of precipitation rate for all simulations indicate similar performance by all WRF model setups. The case of low pressure system observed large precipitation cells and heavy rainfall. The results for simulation runs 1 and 5 are presented in fig. 12. This qualitative comparison yields no con-

Table 3: Performance metric table for the case study of Storm Ciara on 10 February 2020. Simulations are evaluated against 10-min averaged SCADA data using MAE and Kantorovich distance. Minimum values are underlined.

Simulation run#	Wind direction			Wind speed			Average NED
	MAE	Kantorovich	NED	MAE	Kantorovich	NED	
1	9.83	4.68E+03	1.61	2.85	5.93E+03	2.49	2.05
2	7.50	1.24E+04	2.63	1.76	2.57E+03	1.25	1.94
3	6.06	7.37E+03	1.66	1.87	1.74E+03	1.12	1.39
4	5.87	5.65E+03	1.36	1.80	2.61E+03	1.28	1.32
5	8.77	1.60E+04	3.34	1.84	2.29E+03	1.22	2.28
6	6.26	8.25E+03	1.82	1.70	2.48E+03	1.21	1.51

Table 4: Performance metric table for the case study of low pressure system on 24 December 2020. Simulations are evaluated against 10-min averaged SCADA data using MAE and Kantorovich distance. Minimum values are underlined.

Simulation run#	Wind direction			Wind speed			Average NED
	MAE	Kantorovich	NED	MAE	Kantorovich	NED	
1	16.89	3.20E+04	1.22	2.64	4.24E+03	1.76	1.49
2	20.63	7.33E+04	1.99	2.40	1.69E+03	1.11	1.55
3	18.81	7.00E+04	1.86	2.61	1.67E+03	1.18	1.52
4	16.38	4.23E+04	1.33	2.88	4.85E+03	1.98	1.66
5	11.45	2.49E+04	0.87	2.48	3.63E+03	1.56	1.22
6	15.47	4.14E+04	1.28	2.10	1.86E+03	1.04	1.16

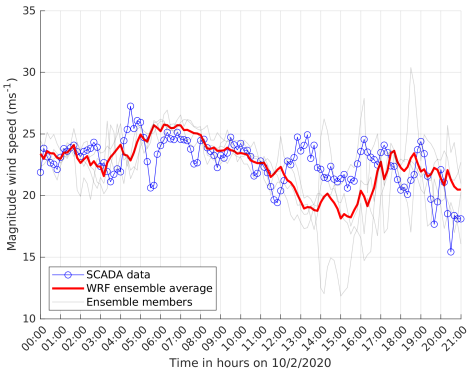

Figure 6: Horizontal wind speed plots for SCADA and ensemble average for Storm Ciara on 10 February 2020.

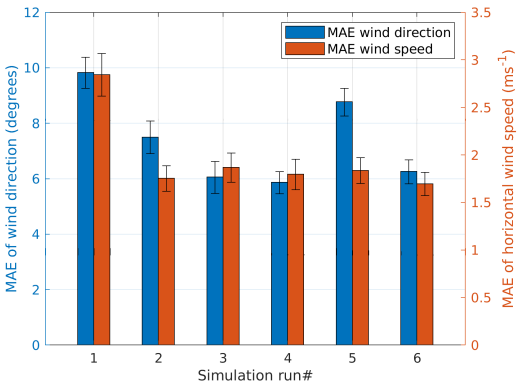

Figure 7: A comparison of wind direction and wind speed MAE for the case of Storm Ciara on 10 February 2020.

crete inferences on the precipitation modelling fidelity in this study.

5.3. Cold front

The summary of evaluation metrics for the case of cold front are presented in table 5. The case in subject is found to be a challenge for all considered WRF setups to adequately predict the fast transience in wind direction observed in SCADA data. Quantitatively simulation run 5 performed better in comparison to other model setups. The ensemble average results are found similar to simulation run 5. However neither simulations were able to capture the fast changes in wind direction.

The ensemble average time series for wind direction and horizontal wind speed plotted against 10 min SCADA data are presented in fig. 13 and 14, respectively. The qualitative comparison of timeseries plots for wind direction indicate a better performance for the scale-aware simulation runs 4 and 5 until the early afternoon period. The fast changes in wind direction observed during 15:00 to 15:30 UTC are severely underestimated by all simulation runs. The horizontal

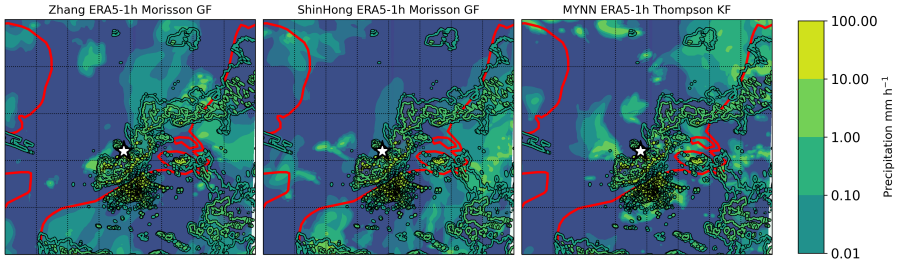

Figure 8: Qualitative comparison of precipitation rate for simulation runs 5, 4 and 1 against observed radar data for the case of Storm Ciara on 10 February 2020.

Table 5: Performance metric table for the case study of cold front on 27 June 2020. Simulations are evaluated against 10-min averaged SCADA data using MAE and Kantorovich distance. Minimum values are underlined.

Simulation run#	Wind direction			Wind speed			Average NED
	MAE	Kantorovich	NED	MAE	Kantorovich	NED	
1	18.33	5.82E+04	1.57	1.98	3.38E+03	1.00	1.29
2	23.51	7.88E+04	2.08	2.53	6.03E+03	1.47	1.78
3	24.38	4.27E+04	1.61	2.77	8.24E+03	1.82	1.71
4	16.30	3.87E+04	1.20	2.59	6.13E+03	1.50	1.35
5	11.82	2.69E+04	0.86	2.36	6.16E+03	1.44	1.15
6	14.91	4.35E+04	1.22	2.20	5.28E+03	1.28	1.25

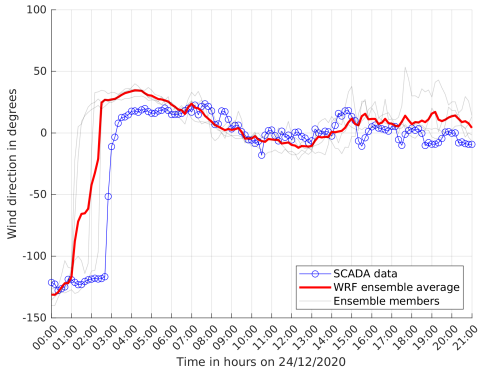

Figure 9: Wind direction plots for SCADA and ensemble average for low pressure system on 24 December 2020.

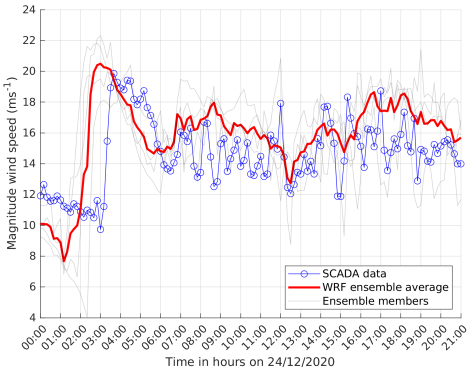

Figure 10: Horizontal wind speed plots for SCADA and ensemble average for low pressure system on 24 December 2020.

wind speed on the 27 June 2020 observed a steady day-long ramp. The considered WRF setups captured the general trend in the ramp however, underestimated the magnitude of wind speed.

The comparison of wind direction MAE results as presented in fig. 15 observed better results for simulation runs 4 and 5, with the ensemble average performing similar to the aforementioned runs. The horizontal wind speed MAE observed better results for simulation run 1 with similar performance for ensemble average.

The qualitative comparison of precipitation rate versus observed radar data indicate very similar performance by all considered model setups. The case of cold front observed little to no precipitation during the time period of interest, 15:00 to 15:30 UTC. The results for simulation runs 1 and 5 are presented in Fig. 16.

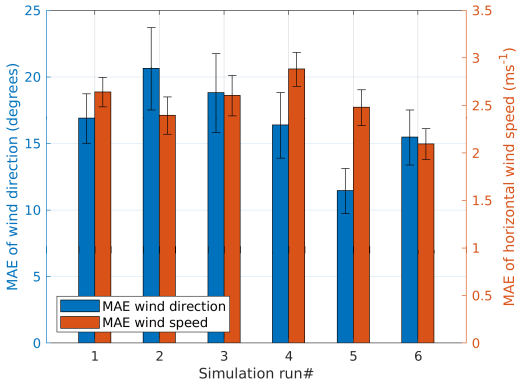

Figure 11: A comparison of wind direction and wind speed MAE for the case of low pressure system on 24 December 2020.

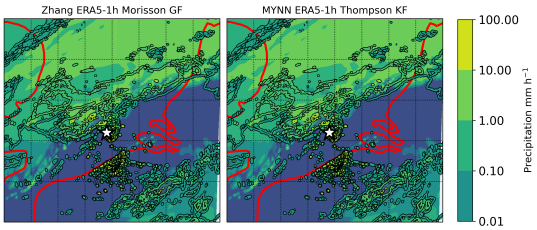

Figure 12: Qualitative comparison of precipitation rate for simulation runs 5 and 1 against observed radar data for the case of low pressure system on 24 December 2020.

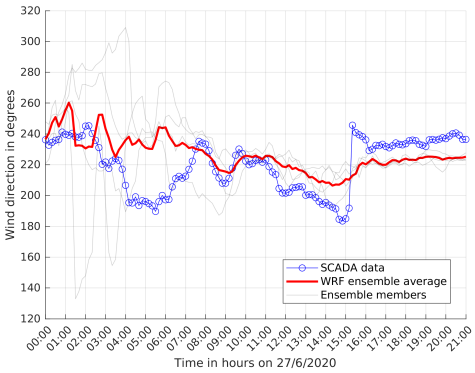

Figure 13: Wind direction plots for SCADA and ensemble average for cold front on 27 June 2020.

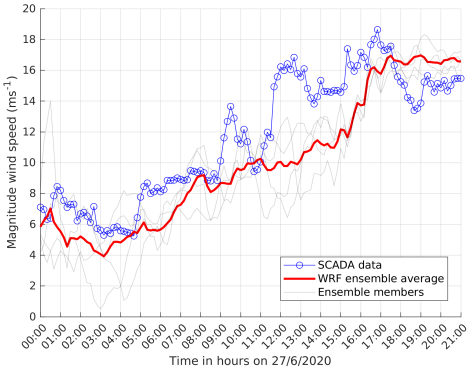

Figure 14: Horizontal wind speed plots for SCADA and ensemble average for cold front on 27 June 2020.

6. Conclusions and recommendations

This study describes a multi-event sensitivity analysis for the Belgian offshore concession zone using the WRF NWP model. 3 EWE identified to be potentially harmful for the operation of Belgian offshore wind farms are utilized as case studies. Considered EWE include: Storm Ciara on 10 February 2020, low pressure system on 24 December 2020 and cold front on 27 June 2020. The WRF model version 4.2.2 is utilized for this study. A total of 5 model setups are considered in this work consisting, scale-aware and non-scale-aware physical parameterizations. The model setups are evaluated quantitatively and qualitatively against 10min SCADA data and qualitatively against radar data from RMI-B. The statistical metrics mean absolute error and Kantorovich distance are utilized, later normalized as NED.

Model sensitivities are found to be highly sensitive producing varying results to the type of event, PBL, cumulus and microphysical parameterizations considered. Accurately capturing the fast transience in wind direction observed in SCADA data posed a challenge for all WRF simulations. In the case of cold front, all setups highly underestimated the wind direction changes. Overall, a betterment in evaluation metrics and timeseries plots is observed for model setups considering scale-aware physical parameterizations. With the overall better performer being simulation run 5, considering scale-aware Zhang 3D PBL, scale-aware GF cumulus and Morrison microphysical parameterizations. Albeit with some challenges, run 5 overestimates the wind direction in the case of Storm Ciara in comparison to the better performing scale-aware run 4. Model sensitivities focusing on Zhang 3D PBL in view of cumulus and microphysics could throw light for this case. The ensemble average estimates quantitatively perform better for the case of low pressure system, however, the fast transience in wind direction, present in SCADA data are better captured by simulation runs 4 & 5. A qualitative comparison of timeseries plots, for other cases, observe similar results concerning the ensemble average. Concluding,

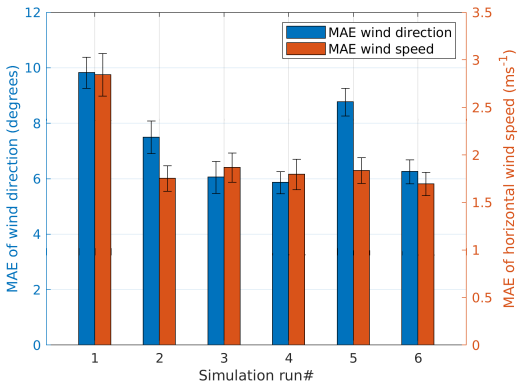

Figure 15: A comparison of wind direction and wind speed MAE for the case of cold front on 27 June 2020.

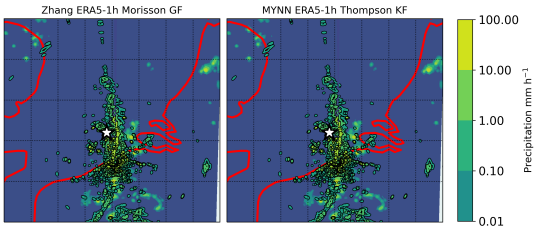

Figure 16: Qualitative comparison of precipitation rate for simulation runs 5 and 1 against observed radar data for the case of cold front on 27 June 2020.

a single model setup to effectively capture different EWE is likely infeasible given the current state-of-the-art of physical parameterizations. Scale-aware physical parameterizations exhibit a promising approach and perform better qualitatively and quantitatively in most cases. The qualitative comparison for precipitation disallowed this study to yield any concrete inferences considering the WRF setups.

Acknowledgments

This work has received funding from the Flemish Government through the Agency for Innovation and Entrepreneurship (Vlaams Agentschap Innoveren en Ondernemen, VLAIO) through the cSBO project SeaFD in the context of the MaDurOS program for Material Durability for Off-Shore of the cluster on Strategic Initiative for Materials in Flanders (SIM). Furthermore, the authors acknowledge VLAIO funding through the RAINBOW project in the context of SIM and the Blue Cluster. The authors thank the Royal Meteorological Institute of Belgium for providing RADAR reflectivity data from the dual-polarization C-band RADAR, located in Jabbeke at the Belgian North Sea coast. Adithya Vemuri thanks Pieter-Jan Daems from Vrije Universiteit Brussel for sharing details on identified extreme weather events.

References

[1] P. Bauer, A. Thorpe, G. Brunet, The quiet revolution of numerical weather prediction, Nature 525 (7567) (2015) 47–55.

[2] J. Dudhia, A history of mesoscale model development, Asia-Pacific Journal of Atmospheric Sciences 50 (1) (2014) 121–131.

[3] S.-Y. Hong, J. Dudhia, Next-generation numerical weather prediction: Bridging parameterization, explicit clouds, and large eddies, Bulletin of the American Meteorological Society 93 (1) (2012) ES6–ES9.

[4] I. Stergiou, E. Tagaris, R.-E. P. Sotiropoulou, Sensitivity assessment of wrf parameterizations over europe, in: Multidisciplinary digital publishing institute proceedings, Vol. 1, 2017, p. 119.

[5] P. Mooney, F. Mulligan, R. Fealy, Evaluation of the sensitivity of the weather research and forecasting model to parameterization schemes for regional climates of europe over the period 1990–95, Journal of Climate 26 (3) (2013) 1002–1017.

[6] A. Vemuri, S. Buckingham, W. Munters, J. Helsen, J. van Beeck, Sensitivity analysis of mesoscale simulations to physics parameterizations: a case study of storm ciara over the belgian north sea using wrf-arw, Wind Energ. Sci. Discuss. [preprint] https://doi.org/10.5194/wes-2021-137, in review.

[7] Á. Hannesdóttir, M. Kelly, Detection and characterization of extreme wind speed ramps, Wind Energy Science 4 (3) (2019) 385–396.

[8] T. T. Fujita, Manual of downburst identification for project nimrod., SMRP Res. Paper, 156 104.

[9] R. Floors, Wetterzentrale.de.

[10] W. C. Skamarock, J. B. Klemp, J. Dudhia, D. O. Gill, Z. Liu, J. Berner, W. Wang, J. G. Powers, M. G. Duda, D. M. Barker, et al., A description of the advanced research wrf model version 4, National Center for Atmospheric Research: Boulder, CO, USA (2019) 145.

[11] J. G. Powers, J. B. Klemp, W. C. Skamarock, C. A. Davis, J. Dudhia, D. O. Gill, J. L. Coen, D. J. Gochis, R. Ahmadov, S. E. Peckham, et al., The weather research and forecasting model: Overview, system efforts, and future directions, Bulletin of the American Meteorological Society 98 (8) (2017) 1717–1737.

[12] H. Hersbach, B. Bell, P. Berrisford, S. Hirahara, A. Horányi, J. Muñoz-Sabater, J. Nicolas, C. Peubey, R. Radu, D. Schepers, et al., The era5 global reanalysis, Quarterly Journal of the Royal Meteorological Society 146 (730) (2020) 1999–2049.

[13] E. J. Mlawer, S. J. Taubman, P. D. Brown, M. J. Iacono, S. A. Clough, Radiative transfer for inhomogeneous atmospheres: Rrtm, a validated correlated-k model for the longwave, Journal of Geophysical Research: Atmospheres 102 (D14) (1997) 16663–16682.

[14] M. Tewari, F. Chen, W. Wang, J. Dudhia, M. LeMone, K. Mitchell, M. Ek, G. Gayno, J. Wegiel, R. Cuenca, et al., Implementation and verification of the unified noah land surface model in the wrf model, in: 20th conference on weather analysis and forecasting/16th conference on numerical weather prediction, Vol. 1115, 2004.

[15] M. Nakanishi, H. Niino, Development of an improved turbulence closure model for the atmospheric boundary layer,

Journal of the Meteorological Society of Japan. Ser. II 87 (5) (2009) 895–912.
[16] H. H. Shin, S.-Y. Hong, Representation of the subgrid-scale turbulent transport in convective boundary layers at gray-zone resolutions, Monthly Weather Review 143 (1) (2015) 250–271.
[17] X. Zhang, J.-W. Bao, B. Chen, E. D. Grell, A three-dimensional scale-adaptive turbulent kinetic energy scheme in the wrf-arw model, Monthly Weather Review 146 (7) (2018) 2023–2045.
[18] S.-Y. Hong, J. Dudhia, S.-H. Chen, A revised approach to ice microphysical processes for the bulk parameterization of clouds and precipitation, Monthly weather review 132 (1) (2004) 103–120.
[19] G. Thompson, P. R. Field, R. M. Rasmussen, W. D. Hall, Explicit forecasts of winter precipitation using an improved bulk microphysics scheme. part ii: Implementation of a new snow parameterization, Monthly Weather Review 136 (12) (2008) 5095–5115.
[20] H. Morrison, G. Thompson, V. Tatarskii, Impact of cloud microphysics on the development of trailing stratiform precipitation in a simulated squall line: Comparison of one-and two-moment schemes, Monthly weather review 137 (3) (2009) 991–1007.
[21] J. S. Kain, The kain–fritsch convective parameterization: an update, Journal of applied meteorology 43 (1) (2004) 170–181.
[22] Y. Zheng, K. Alapaty, J. A. Herwehe, A. D. Del Genio, D. Niyogi, Improving high-resolution weather forecasts using the weather research and forecasting (wrf) model with an updated kain–fritsch scheme, Monthly Weather Review 144 (3) (2016) 833–860.
[23] G. A. Grell, S. R. Freitas, A scale and aerosol aware stochastic convective parameterization for weather and air quality modeling, Atmospheric Chemistry and Physics 14 (10) (2014) 5233–5250.
[24] Y. Wang, S. Basu, Utilizing the kantorovich metric for the validation of optical turbulence predictions, Optics letters 41 (17) (2016) 4008–4011.
[25] J. S. Marshall, The distribution of raindrops with size, J. meteor. 5 (1948) 165–166.

On the limits of quasi-steady models for flapping wing aerodynamics

Romain Poletti

Environmental and Applied Fluid Dynamics Department, von Karman Institute for Fluid Dynamics, Belgium, romain.poletti@vki.ac.be

Supervisor: Jeroen van Beeck

Professor, Environmental and Applied Fluid Dynamics Department, von Karman Institute for Fluid Dynamics, Belgium, jeroen.vanbeeck@vki.ac.be

University Supervisor: Joris Degroote

Professor, Department of Electromechanical, Systems and Metal Engineering, Ghent University, Belgium, joris.degroote@UGent.be

Abstract

Flapping wings micro air vehicles have the potential to replace quadcopters in hazardous missions. The control of flapping drones is fraught with challenges since the wings must handle complex unsteady flows. This article details and compares two models of flapping aerodynamics: a quasi-steady model and a CFD environment. The limits of the quasi-steady model are shown and perspectives for improvement are discussed.

Keywords: flapping wings, unsteady aerodynamics, quasi-steady model, Computational Fluid dynamics, overset method

1. Introduction

Millions of years of evolution have shaped and optimized the outstanding flight capabilities of natural flyers. Birds and insects stably hover, catch preys in the blink of an eye and glide for hours continuously morphing their wings as a function of the flight requirements. Their unique features have inspired engineers throughout the centuries. Leonardo Da Vinci's flight machine and the Wright brothers' airplane are two remarkable examples of bird bio-mimicry.

More recently, Flapping Wings Micro Air Vehicles (FWMAVs) take inspiration from insects and hummingbirds to reproduce their high manoeuvrability, stable hovering and good adaptability to various wind conditions. The FWMAVs fly at low Reynolds number, from 10 to 10^4, at which they reach better aerodynamic performance and efficiency than standard quadcopters. The hand-sized flapping drones could then be crucial in demanding operations such as rescue in confined and hazardous environment, surveillance or even environmental monitoring.

The Nano Hummingbird from DARPA [1], the Delfly from Delft university [2] and the Robobee from Harvard university [3] are pioneer prototypes. Nevertheless, they are still far from extracting nature's full potential. Numerous challenges still arise in the design and control stages [4]. From an electromechanical perspective, micro drones must find a balance between weight and material robustness to both maximize the flight endurance and withstand extreme environment conditions. Moreover, the embedded electronics and actuators must be further miniaturized to match insect dimensions and operability.

The optimization of flight control is also particularly challenging. The FWMAVs must adapt its wing motion to avoid obstacles, cancel gust perturbations, take-off rapidly, stably hover, etc. The complexity of this multiple point optimization is directly inherited by the complex aerodynamics characterised by highly unsteady vortical flows. A complete understanding and modelling of the flapping aerodynamics is still missing.

Experiments, simplified models (SM) and Computational Fluid Dynamics simulations (CFD) are the three methods to study the flow physics. The three tools select a different trade-off between accuracy and rapidity that makes them separately, ineffective to optimize flapping strategies in different flight scenarios.

The present research proposes a comprehensive, multi-disciplinary, numerical environment to teach a bio-inspired drone how to learn and continuously optimize its flapping strategies. The framework combines three disciplines: simplified models, CFD and optimization theory (figure 1).

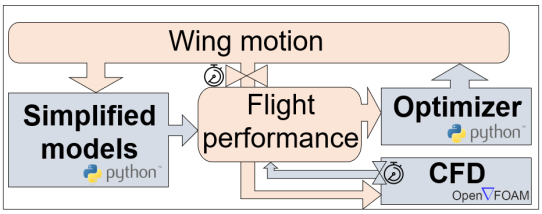

Figure 1: Simulation methodology to optimize the aerodynamic performance of flapping wing motions

First, the simplified model represents the flapping aerodynamics based on fundamental theories, quasi-steady assumptions and calibrated empirical constants. The model cheaply estimates the flapping performance of given wing motions and continuously feeds it to an optimizer. The optimizer leverages on gradient-based and gradient-free methods. It learns, by trial and error and experience, the best flapping strategies driven by various objectives and constraints in different conditions. At last, the optimization loop sparsely calls high fidelity CFD simulations for two purposes: to verify and analyze the flow details of few optimized strategies as well as to improve the simplified models thanks to data regression techniques.

The first year of this PhD was devoted to learn and develop the three tools of figure 1. This article illustrates this journey for a simple wing shape, following motions representative of the hovering regime. The report puts particular emphasis on the SM and the CFD environment, it aims to:

- Detail their working principles
- Compare their aerodynamic predictions and highlight the limits of the simplified models.

Section 2 describes the important notations of flapping wing kinematics. A motion parametrization and a simple wing geometry are defined to evaluate the simplified model and CFD in section 6. Section 3 describes the fundamentals of flapping aerodynamics and sow the seeds for section 4. The latter details the simplified model that strongly relies on flapping aerodynamic peculiarities. Section 5 defines the CFD environment and details the overset method needed to fit the grid to the wing motion. Section 6 compares then the aerodynamic forces computed by the SM and CFD for the test case defined in section 2. Finally, section 7 discusses perspectives to improve the simplified models.

2. Flapping wing kinematics

Depending on the flight regime and their morphology, flying species move their wings differently. The wing motion generally combines three degrees of freedom[1] (figure 2):

1. The flapping $\dot{\phi}$ defines the azimuthal rotation of the wings along the axis $\hat{z}$ in the stroke plane. For each period T, a dorsal to ventral sweep (the downstroke phase) precedes the ventral to dorsal upstroke phase.
2. The pitching motion $\dot{\alpha}$ defines the rotation along the feather axis. In other words, the pitching motion varies the geometric angle of attack α. The angle of attack is zero when the chord is aligned with $\hat{z}$.
3. The deviation motion $\dot{\theta}$ models the elevation rate of the wing tip with respect to the stoke plane.

The present study focuses on the hovering regime in still air for which deviation angles θ are often ignored. Natural flyers essentially flap their wings in a horizontal stroke plane and the small deviation angles contribute negligibly to the total force production [5]. Inspired by [6], the two degrees of freedom motion is parametrized with:

$$\phi(t) = \frac{A_\phi}{sin^{-1}K_\phi} sin^{-1}(K_\phi sin(2\pi t + \phi_0)) \quad (1)$$

$$\alpha(t) = \frac{A_\alpha}{tanhK_\alpha} tanh(K_\alpha sin(2\pi t)) \quad (2)$$

Equation 1 and 2 are popular in the literature since the sole parameters K_ϕ and K_α modulate the motion shape (figure 3). The increase of K_ϕ changes the flapping function from a smooth harmonic to a triangular shape while K_α transforms the pitching from a harmonic function to a square wave. The high K_ϕ/K_α case mimics more closely the wing motion of hovering flyers [7]. They almost maintain a constant angle of attack and a constant flapping velocity during most of the cycle. At the end of each stroke, they rapidly flip their wings during phases called supination and

[1] Additional parameters complete the parametrization when the wing flexibility is considered

pronation in order to always keep angles of attack that generate positive lift. The influence of different motion shape is analysed in section 6.

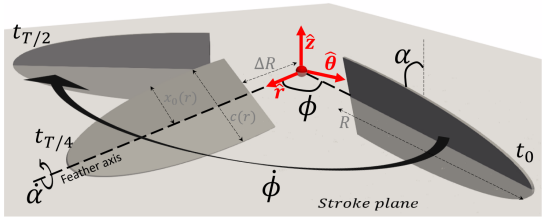

Figure 2: Flapping wing test case with its main notations highlighted during downstroke

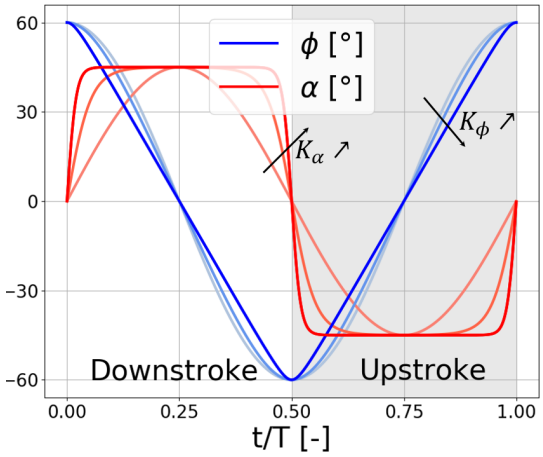

Figure 3: Flapping and pitching motion parametrized by equation 1 and 2

Wing geometry. In this article, the drone body is ignored and basic wing shapes are considered. The shape choice matters less for flapping flight than for standard fixed wings due to the aerodynamic phenomena detailed in section 3.
This report studies a thin, semi-ellipsoid wing defined in [8] and summarized in table 1. Three dimensionless numbers, namely the Reynolds number, the Rossby number and the aspect ratio are also provided. The dimensions fall in the range of typical hummingbirds and MAVs [1].

c	R	ΔR	Re	Ro	AR
1.5	5	2.2	4000	2.97	3.25

Table 1: Semi-ellipsoid dimensions [mm] and its dimensionless numbers

The test case benefits from reference data of aerodynamic forces that will be used for preliminary validation of the SM and CFD environment (section 6).

3. Fundamentals of flapping aerodynamics

Until the end of the 90's, pioneers struggled to justify how flapping species manage to fly. Ellington draw a decisive conclusion from his research on various insects [9]: the lift predicted by quasi-steady model is not capable to balance an insect weight. Standard aerodynamics theories ignore dynamic phenomena triggered by flapping wings. Progresses in experimental measurements and CFD have allowed to identify 5 main aerodynamic mechanisms that can enhance the lift production during classical hovering motion (figure 3, case with high K_ϕ and K_α).

The absence of stall. At the beginning of each stroke, the wing flaps with a high acceleration $\ddot{\phi}$ and a high angle of attack α. Those conditions favour the flow separation at the leading edge and the formation of a strong leading edge vortex [10]. This LEV stops growing and remains attached to the wing during most of the stroke thanks to the spanwise flow induced by the flapping motion [10]. The attached LEV allows the wing to provide a high downward momentum to the flow and is the dominant contributor to the lift and drag.

Kramer effect. When the wing rapidly flips at the end of the strokes, the Kutta condition tends to be broken [10]. Indeed, the stagnation points move towards the leading edge and strong pressure gradients appear at the trailing edge. Fortunately, the viscous nature of the flow resists those unstable gradients and brings the stagnation points back to the trailing edge. From a mathematical perspective, the wing generates an additional circulation to counter-balance the effect of its rotation. This rotational circulation contributes to the total aerodynamic forces.

Added mass. When a wing accelerates, it must also set the surrounding air in motion. This added mass creates a non-circulatory, reaction force that is analogous to an inertial term: it resists the velocity changes of the wing.

Wing-wake interactions. At the beginning of a stroke, the wing crosses the vorticity shed in the wake during the previous stroke. Depending on the wing trajectory [11], the wing can experience higher velocity field and

hence increase its peak lift at the end of stroke reversal. This unsteady effect is also called wake-capture since the wing can recover a part of the energy left in the wake.

Clap and fling. The clap corresponds to the instants where the wings contact each other while fling defines the moments when the wings get away from each other. Both mechanisms increase the net circulation and more details are given in [10] as this article considers only one flapping wing.

4. Simplified models

Compared to CFD, the simplified models benefit from low prediction times at the expense of less accurate aerodynamic predictions. The authors of [12] have classified the simplified models in three categories: steady-state, quasi-steady and unsteady (from lower to higher prediction time or lower to higher accuracy).

The steady-state approach assumes constant aerodynamic forces during the complete cycle. Notorious models derive from the actuator disk theory [13] and the Prandtl lifting line theory [14]. The quasi-steady approach treats each wing position as an instantaneous steady-state. The models differs from the quasi-steady approach used for fixed wings [15]. The unsteady approach takes into account unsteady vorticity and so, acknowledges that part of the flow history influences the instantaneous forces. For example, Ansari [16] derived an unsteady model from potential flow theory.

Currently, the vast majority of the literature that studies the control of flapping wings employs quasi-steady (QS) models [17]. The approach benefits from lower computation time and better applicability than unsteady models [12]. The quasi-steady approach is also chosen for this study and implemented in Python. The model is borrowed from [8] which improves the original implementation defined in [15]. The model breaks down the total aerodynamic force into independent contributions that correspond to the aerodynamic phenomena described in section 3:

$$F(t) = F_{tr} + F_{rot} + F_a \tag{3}$$

where F_{tr} refers to the translation/flapping motion, F_{rot} to the wing pitching and so the Kramer effect, and F_a to the added mass. The QS force doesn't consider the wing-wake interaction since the phenomena is unsteady by nature [11]. This simplification is analysed in section 6.

The three forces are derived with the Blade-Element Theory. The BET divides the wing into infinitesimally thin, independent chord strips. A force, function of the radial position r though the linear velocity and acceleration of the wing, is computed on each strip. The total force integrates all the piecewise contributions along the span R.

Translational force. The instantaneous translational lift is[2]:

$$L_{tr} = K_{tr}(AR, Ro) \cdot 0.5\rho\dot{\phi}^2(t) C_{L_{tr}} \int_0^R c(r) r^2 dr \tag{4}$$

which comes from the lift formula $L = 0.5\rho U(r)^2 c(r) R C_L$ where the wing velocity U is function of the radial position and where the lift coefficient $C_{L_{tr}}$ takes into account the leading edge vortex attached to the wing (section 3). In [8], the authors define its expression thanks to regressions made on dedicated CFD simulations that isolate the LEV influence on rectangular wings. The coefficient $C_{L_{tr}}$ is function of the Reynolds number and the angle of attack:

$$C_{L_{tr}} = [1.966 - 3.94 Re^{-0.429}] sin(2\alpha) \tag{5}$$

The authors have also modelled the influence of the wing planform and the Rossby number with correction factors represented by $K_{tr}(AR, Ro)$ in equation 4.

Rotational force. The rotational lift that arises during the pitching of the wing is:

$$L_r = K_r(\hat{x}_0) \cdot [\rho C_r \dot{\phi}(t) \dot{\alpha} \int_0^R c^2 r dr] \cdot sin(\alpha) \tag{6}$$

The author of [18] proofs equation 6 in the case of fluttering wings, which is analogous to the wing pitching. The derivation relies on the Kutta-Joukowski theory and thin airfoil theory for small angles of attack. Following the same methodology than for the translational coefficient, the rotation coefficient C_r is found by regression on dedicated CFD at different Reynolds numbers. $K(\hat{x}_0)$ models the influence of the feather axis location along the chord length (mid-chord in this study: $\hat{x}_0 = 0.5$).

[2] drag is almost identical and omitted for brevity

Added mass. The added mass force is defined as:

$$L_a(t) = K_a(AR, Re) \cdot \frac{\pi}{4}\rho \, [\ddot{\phi}(t) sin\alpha(t) \int_0^R c^2(r) r dr + \ddot{\alpha}_r(t) \int_0^R c^2(r) x_m dr] \cdot sin\alpha \tag{7}$$

The mass of air that acts on the wing is limited to a cylinder of diameter equal to the chord length $m = \frac{\pi}{4}\rho c^2 R$. The mass is then multiplied by the wing acceleration.The complete derivation of expression 7 is given in [19].

5. CFD

CFD is a high fidelity alternative to predict the aerodynamic forces of flapping motions. As shown in figure 1, CFD simulations will be sparsely used to analyse the flow physics of optimized wing motions, to guide the optimization algorithms to wing motions unexplored by the simplified models and finally to improve the SM thanks to data-driven techniques (section 7). CFD simulations are performed with the open-source software OpenFOAM. The central piece of the CFD environment is the dynamic mesh technique that must adapt the grid to follow the wing motion.

5.1. The overset method

OpenFOAM proposes four main dynamic mesh techniques: the morphing-remeshing meshes, the sliding meshes, the Immersed Boundary Method (IBM) and the overset method [20]. The latter can handle any complex motion (unlike the deforming mesh and the sliding interface techniques) and can accurately compute fields everywhere, even close to moving walls of complex geometries (unlike the IBM). However, the overset method suffers generally from a higher computation time, requires a tedious setting of its numerical parameters and can not model the deformation of bodies.

The overset method decomposes the domain into multiple independent grids [21]. For a flapping wing, a small grid called the component is fitted around the wing and is overlapped on a larger grid, the background (figure 4). The component grid follows the wing motion inside the background grid.

Transfer of flow variables couple the two grids. Figure 5 summarises the inter-grid communication for

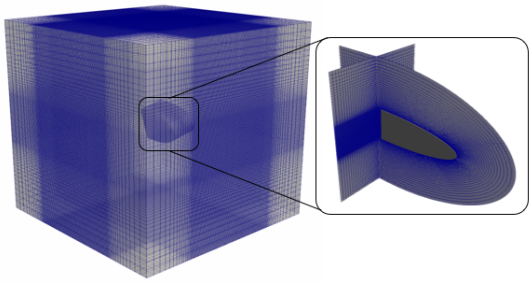

Figure 4: Typical component and background grid of the overset method for a flapping wing

the simplest tilted airfoil. Each cell gets a role, updated at each time step. Blue activated cells solve the flow equations, red holes are inactive cells of the background that overlap with the airfoil and, green interpolated cells receive information from neighbour cells of the other grid system.

Most the background grid cells are activated cells. A light gray area below the component grid border highlights a special kind of those activated cells. They transfer some of their computed fields to set the boundary conditions of the component grid (green cells). The component grid solves then the flow equation towards the airfoil where a gray shaded area is also present. Those cells transfer their fields to the neighbours of the holes (green cells). The information transfer in each direction is done thanks to numerical interpolation schemes such as the inverse distance method, the least square method or even high order schemes [22].

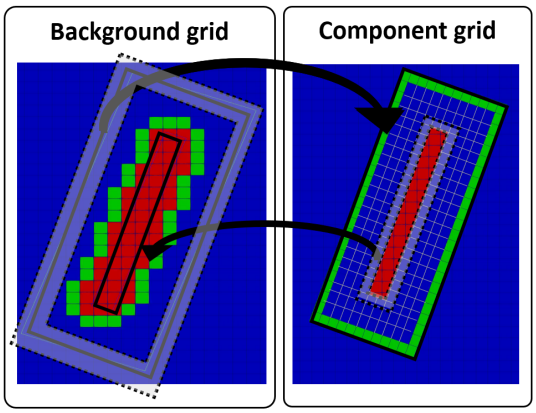

Figure 5: Summary of the inter-grid communication implemented by the overset method

The main inaccuracies of the method originate from the interpolation diffusion as well the violation of the

mass and momentum conservation, also due to the field interpolation [21]. Three 2D test cases check the overset accuracy (figure 6). The first two cases consider a standing airfoil which experiences an incoming horizontal flow at velocity U_x. The first case has an uniform grid while the second case uses the overset method with a standing wing. Regarding the third case, the airfoil moves in still air from left to right at the same horizontal velocity U_x. For the three cases, all the other numerical and physical parameters are identical (unsteady, laminar flow, second order schemes, etc). If numerics were infinitely accurate, the same flow field should be observed in the three test cases.

Figure 7 analyses the dimensionless drag for Re = 500. After a transitory phase, the three drags match quantitatively well. For a well-designed grid, with similar cell size in the interpolated area of both grids, the error due to the inter-grid interpolation doesn't affect significantly the drag.

During the simulation of the third test case, the role of the cells can switch between activated, interpolated and unactivated. For sufficiently small time steps, this doesn't affect significantly the drag accuracy nor numerical stability as the drag of the dynamic overset simulation closely fits the one of the static overset simulation. Finally, the conservation errors are also negligible since the domain is not closed.

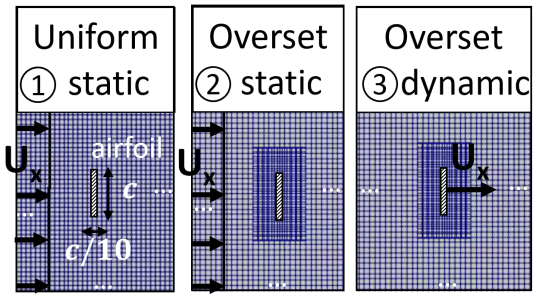

Figure 6: Layout of three test cases: an airfoil meshed with uniform grid (left) and overset grid (centre and right)

5.2. *Baseline simulation setting*

In order to simulate the test case defined on figure 2, a baseline overset mesh is defined (figure 4). Small cells capture the boundary layer near the wing wall and expand towards the overset interface. The background grid keeps the maximum cell size of the component grid and expands it towards the domain boundaries. This reduces interpolation error and keeps a reasonable number of cells (around 3M). Near the wing,

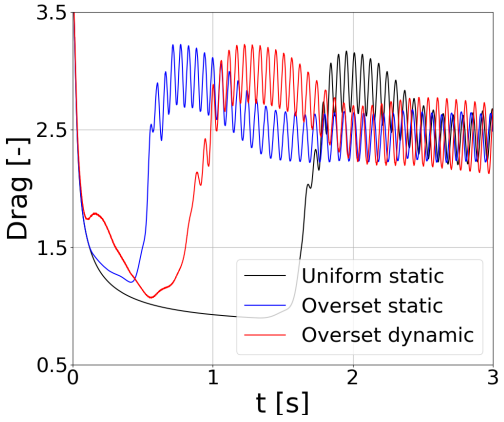

Figure 7: Evolution of the dimensionless drag computed for the three airfoil cases of figure 6

the fluid is dragged at very low Reynolds number, laying in the early turbulent regime (but assumed laminar as verified in [8]). The unsteady overPimpleDyMFoam from OpenFOAM v2012 solves the flow.

6. Result comparison and analysis

6.1. *Harmonic motion*

The baseline case of this report is:

- Harmonic motions for the flapping and pitching (figure 3): $K_\phi = 0.01$ and $K_\alpha = 0.01$ in equation 1 and 2
- Flapping and pitching amplitudes: $A_\phi = 60°$ and $A_\alpha = 45°$
- Frequency: $f = 20\ [Hz]$

Figure 8 and 9 show the lift and drag for one flapping cycle. The fifth flapping cycle is represented to eliminate the transient from one cycle to another [23]. The three traces are computed by Lee's CFD [8] (black), the overset OpenFOAM simulation (red) and the presented simplified model [8] (blue).

First of all, Lee's CFD fits closely the OpenFOAM simulations. This confers confidence in the validity of the overset OpenFOAM environment. Indeed, Lee performed its simulation on a different software (Ansys) with a different dynamic mesh technique (sliding interface). Moreover, Lee has compared part of its simulations with experiments [8].

Secondly, good agreements are also observed between the simplified models and the CFD. Both lifts

follow a similar sinusoidal motion and have a mean difference below 5 percent (the CFD's lift peaks slightly later than the SM). During the first half of the downstroke, the lift rises while both $|\dot{\phi}|$ and α increases (α peaks at 45°). This motion favours the formation of a strong and stable LEV on the wing top surface supported by a low-pressure bubble (section 3). The Q criterion and streamlines confirm this trend on figure 10. $|\dot{\phi}|$ and α follow the opposite tendency during the second quarter. The wing slows down, goes vertical again (α peaks at 0°) and the LEV detaches near the end of the period. The upstroke phase is symmetric to the downstroke such that the lift trace is similar for the two strokes.

The drag computed by the SM and CFD also agrees qualitatively well even if the drag from the CFD oscillates more at the beginning of the strokes. The wing-wake interaction explains this behaviour (section 3 and figure 11). At the beginning of a stroke, the wing moves back in the vortices that were shed during the previous stroke (figure 10). Overall, the wing-wake interaction lightly influences the forces since vorticity is progressively shed during the entire second half of the stroke. For certain dynamic pitch motions, the wing can use the shed LEV to significantly enhance lift at the beginning of the strokes.

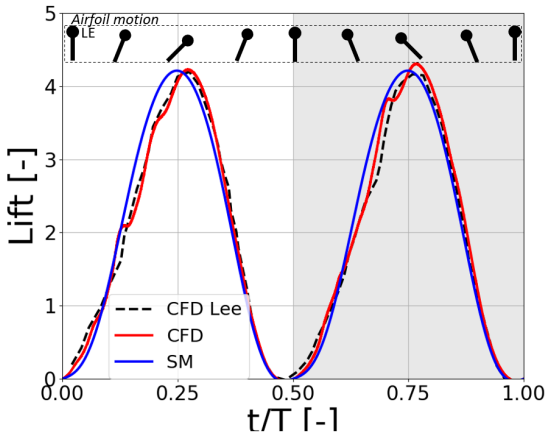

Figure 8: Dimensionless lift computed by the simplified model (SM), the OpenFOAM simulation (CFD) and the Ansys simulation of Lee [8] for a harmonic wing motion

6.2. *Towards realistic wing motions*

Hummingbirds and insects do not hover with smooth harmonic wing motions. The flapping motion is complex [24] but can be coarsely approximated with the parametrization 1 and 2 modulated by K_ϕ and K_α (figure 3).

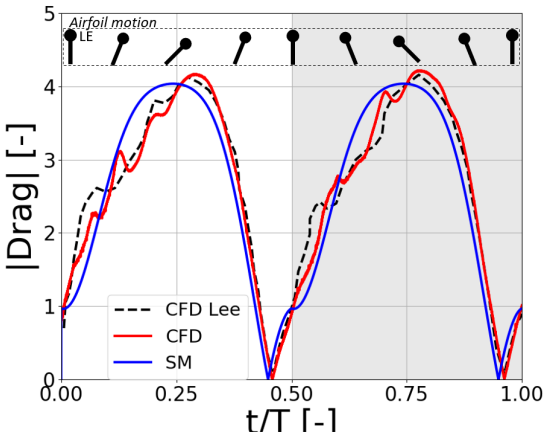

Figure 9: Dimensionless drag computed by the simplified model (SM), the OpenFOAM simulation (CFD) and the Ansys simulation of Lee [8] for a harmonic wing motion

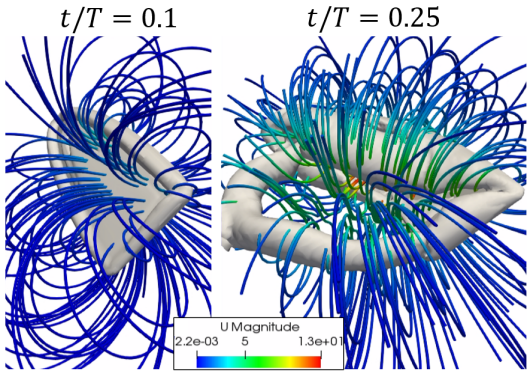

Figure 10: Growth of the LEV during the first half of the downstroke highlighted by the Q-criterion field and streamlines

Figure 12 studies the lift of three motion types. The flapping and pitching amplitudes as well as the frequency are kept the same as for the harmonic test case. The reader should compare the dashed lines (SM) with the solid ones (CFD), color by color (different (K_ϕ, K_α) sets). By increasing K_ϕ and K_α, the motion gets more dynamic and the discrepancies between SM and CFD tend to increase. For example, the CFD computes first a large peak lift which oscillates and then stabilises to the SM predictions at mid-stroke. This transient behaviour directly originates from the LEV stability. Q-criterion fields show that the strong acceleration (of pitching and flapping) sheds part of the LEV during the early stage of the stroke which then reattaches in the same stroke. As described in section 4, the QS model is calibrated for attached vorticity and hence fails to capture those lift oscillations. A similar analysis could be conducted for the drag.

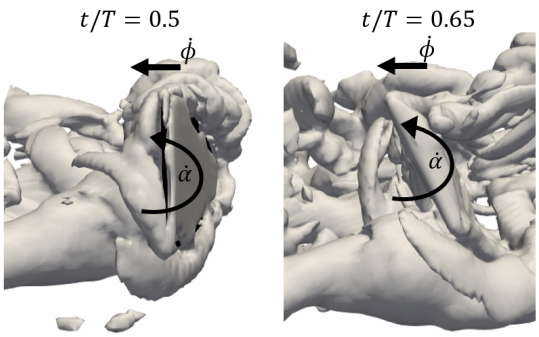

Figure 11: Wing-wake interaction at the beginning of the upstroke evidenced by the Q-criterion field

Figure 13 focuses again on the harmonic motion but varies the maximum angle of attack reached at mid-stroke. For recall, $\alpha = 0°$ designates a vertical wing. The increase of A_α generates oscillations in the drag trace near the mid stroke for both models. Those oscillations come, once again, from the LEV. As seen on equation 5, the translational lift coefficient is function of $sin(2\alpha)$. Hence when $\alpha(t) > 45°$, the lift (and also the drag) can decrease even if the flapping velocity still increases. The SM poorly predicts the amplitude and phase of those oscillations.

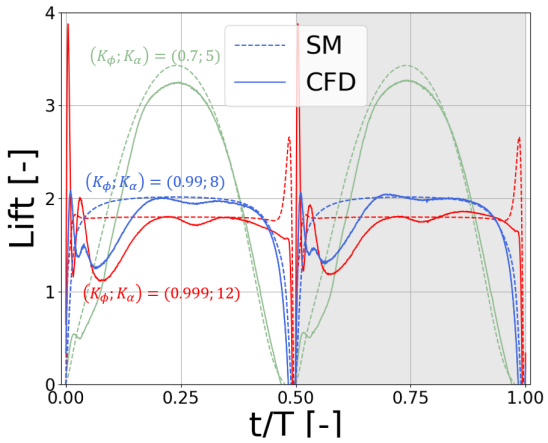

Figure 12: Influence of the motion type on lift. Dashed lines: SM, solid lines: CFD computed with three sets of (K_ϕ, K_α)

7. Discussion

Previous section showed the good adequacy of simplified models in the force predictions of smooth wing movements. The main discrepancies come from the wing-wake interaction, not predicted by the QS

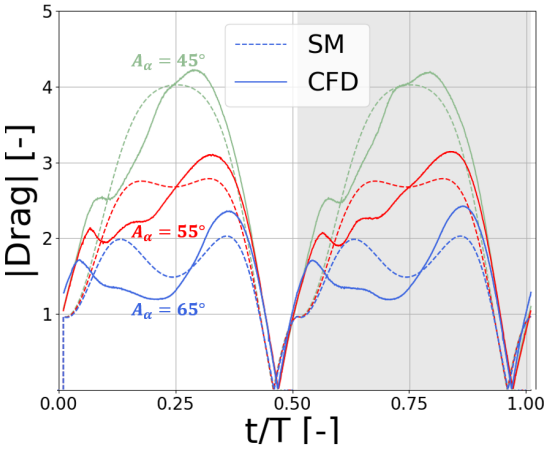

Figure 13: Influence of the maximum angle of attack A_α on drag. Dashed lines: SM, solid lines: CFD computed for with three different A_α

model. Most of the literature also ignores this effect though some works have attempted to include it [25].

When the motion gets more dynamic, the fits between SM and CFD remain qualitatively good but deteriorate in the highly unsteady phases of the strokes.

The simplified model breaks down the total force in three aerodynamic contributions. The translational force models the LEV influence and is the main contributor to lift. However, as reported in [8] and [12], the force is derived with quasi-steady assumptions and hence can not account for the shedding of vorticity. The model is not suited to simulate any flight scenario.

Lately, new data-driven models have gained popularity. For example, the authors of [26] and [27] have derived CFD-data driven models. They first generate a large data base of aerodynamic forces from various wing motions in representative flight regimes (hovering, forward flight, etc). Then, they use regression techniques to calibrate the empirical coefficients of a QS model. The objective of the procedure is to obtain a fast, accurate and robust QS model. While their model extrapolates well with CFD cases not seen during training, the authors of [28] stated that QS models could never capture the complete dynamical system of the aerodynamic forces. Based on multiple experiments with a rectangular wing, they define a gaussian process state-space model that maps the wing motion with the instantaneous forces. The authors claimed to achieve better performance than CFD data driven aerodynamic models.

To extend the present study, the three force contributions will be estimated from CFD simulations and compared back with the SM predictions (equation 4,

6 and 7). The model limits of each term will be highlighted and data driven techniques will be explored to improve the accuracy and universality of the QS model terms. This is crucial in this project to drive the optimizer towards real optimized wing motions in different control scenarios (figure 1).

8. Conclusion

The design and the control of bio-inspired flapping drones has became an active research area over the last two decades. This project aims to teach a bio-inspired drones how to continuously optimize its flapping strategies as a function of the flight requirements. A multi-disciplinary, numerical environment is proposed: it combines a simplified model (SM), a high-fidelity CFD environment and an optimizer. The SM is semi-empirical and based on quasi-steady assumptions [8] while the CFD environment uses the overset method with laminar flow. This article has compared the aerodynamic forces computed by both models for different flapping and pitching motions that simplify the hovering regime. SM fits well CFD simulations for low dynamic wing motions but fails to capture the strong transient phases of highly dynamic wing motions. Data-driven models and state space models are promising alternatives to improve quasi-steady models. They will be explored in this project in collaboration with a research master student.

Nevertheless, the simplified model provides sufficiently good aerodynamic predictions to be used by a wing motion optimizer in its preliminary stages. The latter relies on a flight dynamic model: it controls the drone trajectory, to maximise flight objectives and satisfy constraints, by continuously adapting the flapping strategies. The next chapter of this PhD will evaluate different optimization algorithms such as sequential least programming and reinforcement learning. The flapping strategies will be analysed with CFD for different optimization criteria and compared with real birds to gradually uncover millions of years of evolution.

References

[1] M. Keennon, K. Klingebiel, H. Won, Development of the nano hummingbird: A tailless flapping wing micro air vehicle, in: 50th AIAA aerospace sciences meeting including the new horizons forum and aerospace exposition, 2012, p. 588.

[2] G. De Croon, M. Perçin, B. Remes, R. Ruijsink, C. De Wagter, The delfly, Dordrecht: Springer Netherlands. doi 10 (2016) 978–94.

[3] K. Y. Ma, P. Chirarattananon, S. B. Fuller, R. J. Wood, Controlled flight of a biologically inspired, insect-scale robot, Science 340 (6132) (2013) 603–607.

[4] N. Haider, A. Shahzad, M. N. Mumtaz Qadri, S. I. Ali Shah, Recent progress in flapping wings for micro aerial vehicle applications, Proceedings of the Institution of Mechanical Engineers, Part C: Journal of Mechanical Engineering Science 235 (2) (2021) 245–264.

[5] Y. Bayiz, M. Ghanaatpishe, H. Fathy, B. Cheng, Hovering efficiency comparison of rotary and flapping flight for rigid rectangular wings via dimensionless multi-objective optimization, Bioinspiration & biomimetics 13 (4) (2018) 046002.

[6] G. J. Berman, Z. J. Wang, Energy-minimizing kinematics in hovering insect flight, Journal of Fluid Mechanics 582 (2007) 153–168.

[7] M. H. Dickinson, F.-O. Lehmann, S. P. Sane, Wing rotation and the aerodynamic basis of insect flight, Science 284 (5422) (1999) 1954–1960.

[8] Y. Lee, K.-B. Lua, T. Lim, K. Yeo, A quasi-steady aerodynamic model for flapping flight with improved adaptability, Bioinspiration & biomimetics 11 (3) (2016) 036005.

[9] C. Ellington, Unsteady aerodynamics of insect flight., in: Symposia of the society for experimental biology, Vol. 49, 1995, pp. 109–129.

[10] S. P. Sane, The aerodynamics of insect flight, Journal of experimental biology 206 (23) (2003) 4191–4208.

[11] D. D. Chin, D. Lentink, Flapping wing aerodynamics: from insects to vertebrates, Journal of Experimental Biology 219 (7) (2016) 920–932.

[12] H. Xuan, J. Hu, Y. Yu, J. Zhang, Recent progress in aerodynamic modeling methods for flapping flight, AIP Advances 10 (2) (2020) 020701.

[13] C. P. Ellington, The aerodynamics of hovering insect flight. v. a vortex theory, Philosophical Transactions of the Royal Society of London. B, Biological Sciences 305 (1122) (1984) 115–144.

[14] M. R. Nabawy, W. J. Crowthe, A quasi-steady lifting line theory for insect-like hovering flight, PloS one 10 (8) (2015) e0134972.

[15] S. P. Sane, M. H. Dickinson, The aerodynamic effects of wing rotation and a revised quasi-steady model of flapping flight, Journal of experimental biology 205 (8) (2002) 1087–1096.

[16] S. Ansari, R. Żbikowski, K. Knowles, Non-linear unsteady aerodynamic model for insect-like flapping wings in the hover. part 1: methodology and analysis, Proceedings of the Institution of Mechanical Engineers, Part G: Journal of Aerospace Engineering 220 (2) (2006) 61–83.

[17] F. Fei, Z. Tu, Y. Yang, J. Zhang, X. Deng, Flappy hummingbird: An open source dynamic simulation of flapping wing robots and animals, in: 2019 International Conference on Robotics and Automation (ICRA), IEEE, 2019, pp. 9223–9229.

[18] Y. C. Fung, An introduction to the theory of aeroelasticity, Courier Dover Publications, 2008.

[19] Q. Truong, Q. Nguyen, V. Truong, H. Park, D. Byun, N. Goo, A modified blade element theory for estimation of forces generated by a beetle-mimicking flapping wing system, Bioinspiration & biomimetics 6 (3) (2011) 036008.

[20] J. L. Steger, F. C. Dougherty, J. A. Benek, A chimera grid scheme.

[21] H. Hadzic, Development and application of finite volume method for the computation of flows around moving bodies on unstructured, overlapping grids, Technische Universität Hamburg, 2006.

[22] D. D. Chandar, B. Boppana, V. Kumar, A comparative study

of different overset grid solvers between openfoam, starccm+ and ansys-fluent, in: 2018 AIAA Aerospace Sciences Meeting, 2018, p. 1564.
[23] C. Badrya, Cfd/quasi-steady coupled trim analysis of diptera-type flapping wing mav in steady flight, Ph.D. thesis, University of Maryland, College Park (2016).
[24] J. Song, H. Luo, T. L. Hedrick, Three-dimensional flow and lift characteristics of a hovering ruby-throated hummingbird, Journal of The Royal Society Interface 11 (98) (2014) 20140541.
[25] J. Hu, H. Xuan, Y. Yu, J. Zhang, Improved quasi-steady aerodynamic model with the consideration of wake capture, AIAA Journal 58 (5) (2020) 2339–2346.
[26] X. Cai, D. Kolomenskiy, T. Nakata, H. Liu, A cfd data-driven aerodynamic model for fast and precise prediction of flapping aerodynamics in various flight velocities, Journal of Fluid Mechanics 915.
[27] H. Zheng, F. Xie, T. Ji, Y. Zheng, Kinematic parameter optimization of a flapping ellipsoid wing based on the data-informed self-adaptive quasi-steady model, Physics of Fluids 32 (4) (2020) 041904.
[28] Y. E. Bayiz, B. Cheng, State-space aerodynamic model reveals high force control authority and predictability in flapping flight, Journal of the Royal Society Interface 18 (181) (2021) 20210222.

Advanced characterization of densified cryogenic hydrogen

Lorenzo Vallisa

Environmental and Applied Fluid Dynamics, von Karman Institute for Fluid Dynamics, Belgium, lorenzo.vallisa@vki.ac.be

Supervisor: Delphine Laboureur

Associate Professor, Environmental and Applied Fluid Dynamics, von Karman Institute for Fluid Dynamics, Belgium, delphine.laboureur@vki.ac.be

University Supervisor: Michel De Paepe

Professor, Department of Electromechanical, Systems and Metal Engineering, Ghent University, Belgium, michel.depaepe@ugent.be

Abstract

Hydrogen has lately drawn the attention of politics and industry for being one among the most powerful fuels and highly suitable source for clean energy production. Academic fundamental research is crucial for providing solutions to the many technological challenges posed by the role of hydrogen in our energy transition. This PhD project is part of a group of research activities in the context of the Be-Hyfe program, a Belgian based network of expertise with the main goal of supporting industry in their technical challenges related to hydrogen RD.

Among the fields being investigated, one of the most critical is indeed the process of hydrogen storage, whose capability can be strongly enhanced by densifying hydrogen to its slush state, a multi-phase mixture of vapour, liquid and solid crystals.

The research activity of this PhD aims at tackling some of the issues connected with the thermodynamic stability of the slush state. Hydrogen crystals can in fact melt under the effect of convective fluxes and heat transport mechanism happening inside the tank they are stored into. This gives rise to a multi-physics scenario, in which the phase change process needs to be modelled accurately and cannot prescind from the arbitrary geometrical configuration each crystal particle might have. The innovative approach of this research is in the attempt of describing moving particle's boundaries to account not only for thermally dependent geometries, but also for collisional phenomena between complex shaped particles. The work will be organised mainly in two parts: a first part concerned with the numerical modelling, in a which an Immersed Boundary Method solver will be implemented to capture the delicate fluid-particle dynamics. The solver will be then coupled to an Overset Grid method to allow for an Arbitrary Euler Lagrangian formulation that will benefit from an overall increased computational efficiency. To handle complex geometries a NURBS algorithm will be implemented in the numerical model and employed as well in the second part of the project, where experimental data produced with the CryMe cryostat facility at VKI need to be post-processed for the final validation step.

Keywords: Multi-phase, phase change, complex geometry, NURBS, Immersed Boundary Method

Aerodynamic and aeroacoustic installation effects of building-integrated wind turbines

Rui Gonçalves

Environmental and Applied Fluid Dynamics Department, von Karman Institute for Fluid Dynamics, Belgium, rui.goncalves@vki.ac.be

Supervisor: Christophe Schram

Professor, Environmental and Applied Fluid Dynamics Department, von Karman Institute for Fluid Dynamics, Belgium, christophe.schram@vki.ac.be

University Supervisor: Leandro de Santana

Assistant Professor, Engineering Fluid Dynamics, University of Twente, the Netherlands, leandro.desantana@utwente.nl

Abstract

Large cities require a large amount of energy to function, however these are mostly powered by electricity produced abroad.

Building Integrated Wind Turbine (BIWT) are a solution that allows residents inside urban centers to own production of electricity to offset their own needs and consumption.

This is achieved by coupling wind turbines (can be horizontal or vertical) with the building, in order to take advantage of the available wind potential, usually found at higher altitudes (undisturbed by the urban canopy layer).

The aeroacoustic noise produced by wind turbines is known to cause annoyance, being the great disadvantage and obstacle of its installation in urban centers.

Defining the appropriate position and configuration for the turbines is a method to increase the system's performance and reduce noise and vibrations, required to comply with regulations and contain the discomfort.

The diffuser augmented wind turbine is a configuration that delays the flow separation downstream of the rotor. The effect allows capturing airflow from a greater area with the same rotor size, improving the power coefficient (Cp). Other advantages such as a wider range of operation curve with maximum Cp and possible noise reduction due to the introduction of the casing can be observed.

CFD will be used to study the effects of installing a diffuser on a turbine in a free flow state, and also to understand the advantages and disadvantages of using a duct/diffuser-augmented wind turbine configuration through a building.

Keywords: Aeroacoustics, Wind Turbine, Wind Turbine Noise, Building Integrated Wind Turbine, Diffuser Augmented Wind Turbine, Ducted Acoustics, CFD.

Data-driven nowcasting for early detection of high-impact precipitation and lightning strikes on offshore wind turbine blades

Tsvetelina Ivanova

Environmental and Applied Fluid Dynamics Department, von Karman Institute for Fluid Dynamics, Belgium, tsvetelina.ivanova@vki.ac.be

Supervisors: Pr. Jeroen van Beeck, Dr. Sophia Buckingham, Dr .Wim Munters

Environmental and Applied Fluid Dynamics Department, von Karman Institute for Fluid Dynamics, Belgium, vanbeeck@vki.ac.be

University Supervisor: Jan Helsen

Professor, Department of Mechanical Engineering, Vrije Universiteit Brussel, Belgium, Jan.Helsen@vub.be

Abstract

This PhD topic is in the framework of project RAINBOW on optimized prediction and decision support for rain erosion and lightning-driven degradation of wind turbine blades. The objective is to design a comprehensive and accurate forecasting system for extreme weather conditions across a wide range of time scales by combining numerical weather prediction (NWP) and machine learning methods. The time scales span from minutes to several days ahead.

The climate system is chaotic and for different initial conditions, numerical weather forecasts often strongly deviate from one another. Therefore, the Weather Research and Forecasting model (WRF) will be optimized for predicting local weather conditions via data assimilation of wind farm observations in the Belgian North Sea. This procedure will provide forecast uncertainty quantification that can serve when building an ensemble-based probabilistic prediction system. As a consequence, decision support in the wind farms can be improved.

The unification in a comprehensive forecasting system will be performed depending on the time scales. Forecasting on days-ahead predictions will be mainly based on high-resolution NWP outputs. The limitations of physics-based NWP models in the hourly-scale will be overcome by combining these with observation-based (data-driven) nowcasts that can progressively take over as time shortens towards minute-scale. The predicted weather features will be translated from forecasting and nowcasting information into risk and look-up-tables of wind maps. These maps will be associated with extreme weather conditions aiming to alert wind farm owners and maintenance services. Thus, risk management and decision-making strategies will allow for safer maintenance operations, and for more efficient wind power extraction.

Keywords: numerical weather prediction, data assimilation, nowcasting, wind energy, atmospheric flows

Multidisciplinary optimization of noise emission in turbomachinery

Romain Hottois

Turbomachinery and Propulsion Department, von Karman Institute for Fluid Dynamics, Belgium, romain.hottois@vki.ac.be

Supervisor: Tom Verstraete

Professor, Turbomachinery and Propulsion Department, von Karman Institute for Fluid Dynamics, Belgium, tom.verstraete@vki.ac.be

University Supervisor: Grégory Coussement

Professor, Fluides-Machines Department, UMONS, Belgium, gregory.coussement@umons.ac.be

Abstract

Noise mitigation has become an inescapable problem for aerial transportation, be it for achieving higher efficiencies, or for electrification in Urban Air Mobility (UAM). The past decades have seen a significant improvement in the accuracy of noise predictions through simulations, which now allow to include aeroacoustic considerations into the design process. Recent studies show that combining the Harmonic Balance (HB) method for calculating the noise sources, combined with a state-of-the-art Ffowcs-Williams and Hawkings (FW-H) analogy to compute the noise propagation, allows to resolve the acoustic field in the frequency domain at a reduced computational cost. This type of hybrid approach is particularly well suited for predicting tonal noise in rotating machines. In parallel, efficient adjoint-based shape optimization algorithms, for which the cost is nearly independent of the number of design variables, have been developed and are now routinely used in industry for aerodynamic shape optimization. This research project aims at developing numerical tools for noise prediction and to apply them in an aeroacoustics shape optimization of turbomachinery components for novel propulsion technologies. The key ingredients are the implementation of a HB – FW-H hybrid noise prediction model and the gradient computation for the design improvement by means of the adjoint method. Gradient-based multidisciplinary optimization will be performed on several industrial test cases (e.g., axial fan, open rotor configurations, UAM propeller, ...). The success of the present work will be assessed by its ability to accurately predict aerodynamic noise levels and gradients, and to optimize geometries from an aeroacoustics point of view. Eventually, multi-physics optimization with structural constraints will also be considered to include the most relevant physical aspects into the design process.

Keywords: Aeroacoustics, Design optimization, Adjoint-based method, Turbomachinery

Reconciling engineering models of ejectors with experiments and CFD using physics-informed machine learning

Jan Van den Berghe

Environmental and Applied Fluid Dynamics Department, von Karman Institute for Fluid Dynamics, Belgium, jan.vandenberghe@vki.ac.be

Supervisor: Miguel Alfonso Mendez

Assistant Professor, Environmental and Applied Fluid Dynamics Department, von Karman Institute for Fluid Dynamics, Belgium, miguel.alfonso.mendez@vki.ac.be

University Supervisor: Yann Bartosiewicz

Professor, Thermodynamics and Fluid Dynamics Department, Université catholique de Louvain, Belgium, yann.bartosiewicz@uclouvain.be

Keywords: ejector modelling, engineering models, closure modelling, physics-informed machine learning

1. Abstract

Ejectors are devices for mixing, compression or aspiration having no moving parts, with applications in refrigeration, aeronautics and more. Their design is primarily based on 0D lumped parameter models because Computational Fluid Dynamics (CFD) is too expensive for optimization. However, lumped parameter models are based on integral balances and require closure parameters, usually computed from empirical correlations with a limited range of validity. Moreover, these models do not provide sufficient local information for the ejector's design optimization.

This thesis aims to bridge the gap between the CFD and 0D models by introducing a new family of self-calibrating 1D models using physics-informed machine learning. The ejector will be modelled as a combination of two 1D flows which exchange mass, momentum and energy through mixing coefficients that depend on the stream-wise evolution of the flow. The models will be time-dependent and implemented in a dedicated numerical solver.

Artificial Neural Networks (ANN) will be used to learn the closure functions for the mixing coefficients. Two approaches will be investigated: Physics-Separated (PS) and Physics-Integrated (PI). PS is classic supervised learning and thus requires a pre-processed database with inputs (flow quantities) and outputs (mixing coefficients). PI will couple the ANN regression with the physical model, integrating the sensitivity of the physics into the learning algorithm and thus enabling online self-calibration.

Two experimental campaigns are foreseen, covering the steady and the unsteady operation of an ejector. CFD will complement the experimental work by providing insights into the ejector's physics, cross-sectional averaged quantities in both streams, and thus training data for the ANN closure model.

The new family of self-calibrating 1D ejector models will allow for a compromise between 0D models and CFD and thus provide a valuable tool for design optimization of these important devices.

LIQUID METALS AND INDUSTRIAL FLOWS

Validation of a two-phase flow model for porous media implemented in a numerical code and applied to a plate fin heat exchanger

Yohanna Henrotel

TEMISTh Marignane, France, yohanna.henrotel@temisth.com

Supervisor: Damien Serret, Joseph Jabbour

Head of RD, TEMISTh Marignane, France, damien.serret@temisth.com

University Supervisor: Olivier Le Metayer

Professor, Mechanical Engineering Energy, Aix-Marseille University - IUSTI / UMR CNRS 7343, France, olivier.le metayer@univ-amu.fr

Abstract

Porous media have been widely used in industrial applications such as car radiator, electronic cooling, geothermal system, and others. Channels with high fins density can be considered as a porous media represented by a porous matrix. It is defined by its specific transport properties. That means that it is not resolved explicitly but represented by a volumetric porous zone where a volume-averaged pressure gradient drag term is applied to the Navier–Stokes momentum equation. Porous media in heat exchanger industry is mostly used to gain on computational power, a compromise between classic local CFD, which is the most precise but costly and empirical correlation, which are simple but imprecise and limited by geometries. This paper will be testing a porous two-phase code in industrial HX condition and comparing it to recommended empirical correlations.

Keywords: CFD, Porous media, Heat exchanger, Heat transfer, Mass transfer, Multiphase flow

1. Introduction

A heat exchanger is a widely used device that exchanges heat between two fluids or gas. The design of heat exchangers can be a complicated problem if it takes into account not only heat-transfer analysis alone, but the cost of fabrication and installation among other things. Although cost is an important consideration, size and footprint are usually the dominant factors in choosing a design.

Often the heat exchanger is designed using empirical correlations. Yet, one of the most dynamically improving research field is the Computational Fluid Dynamics (CFD), which is a good alternative of the expensive and time demanding experimental test measurements. Meanwhile the simulation methods often are not just a more cost efficient solution than experimental measurements, but even provide more details and information about a given problem. Analytical approaches permit to calculate average values, but not the local values. Meanwhile, the CFD calculationpermits to calculate the local values, but this method can be very expansive for complex products.

Likewise, there are commercial software to calculate not only CFD, but also the stress analysis and optimization calculation. It means ispossible to use one model for all types of simulation with need to design product.

Although numerous semi-empirical correlations are available in the literature for estimating the convection coefficient of tube bundles with solid fins, the values predicted by such correlations rarely agree with one another, and in some cases can differ by as much as 30%. A compromise between empirical correlations and full CFD modeling in the case of heat exchangers, is the porous media approach, where for example the finned tube bundles in a heat exchanger are represented by a porous matrix, which is defined by its porosity, permeability, and the form drag coefficient. The porosity is equal to the tube bundle volumetric void fraction and the permeability is calculated by using correlations.

This paper focuses on the validation of a two-phase flow model for porous media implemented in a numerical code and applied to a plate fin heat exchanger.

2. State of the art

Multiple developments were made surrounding the numerical modelization of heat exchangers with porous media. A first work by [1] to develop a scientific procedure for optimization of heat exchanger geometry. As a part of this program an integral numerical code for modeling of heat exchangers was constructed. The numerical code is based on Volume Averaging Technique (VAT) for a porous media flow, which was presented by Whitaker [2]. Treating the Heat exchanger core as porous medium is a way to make code fast and suitable for the surface optimization calculations. The heat exchanger internal structure, in form of isothermal tubes and is treated as a homogenous porous media. The local values of drag and heat transfer coefficients that were needed to close the transport equations were taken from [3]. The resulting partial differential equations were discretized using the conservation properties of the finite volume method (FVM). The resulting system of semilinear equations was then solved with a preconditioned conjugate gradient method. In this paper he calculated values of drag and heat transfer coefficients show excellent agreement with published data.

A multi-scale model for two-phase simulation of multi-stream plate-fin heat exchangers was developed in [4]. Important features in a multi-stream HX simulation, such as phase change phenomena, multi-component mixtures, multiple streams, transversal, lateral and longitudinal conduction, non-uniformity of inlet flow, variable fluid properties, and heat leakage are simultaneously considered in this model.

The following assumption are considered: Steady-state operation, the temperature variation along the thickness of plates is negligible, the mass flow distributions are known and do not vary in the flow direction and the conduction heat transfer through the fluid is neglected in comparison with the heat conduction within the solid. Porous approach was not used in this study and each domain and sub-domain of the exchanger was discretized in computational elements governing equations are derived separately, and thermal interactionsare addressed by their common boundary conditions.

Another case was simulated by Pozhilov and al. [5], for the heat and mass transfer in a 3D model of a loop heat pipe evaporator. This simulation included the model of Reynolds-averaged Navier–Stokes equations describing the flow in the liquid and vapor regions, Darcy's law for filtration modeling in the wicks (porous structure) and the energy equation with an accurate coupling of connected sub-domains that includes the effects of evaporation on interfaces between the porous and vapor regions.

In [5] and [1] local thermal equilibrium is assumed, meaning that at the interface, fluid and porous structure are at the same temperature. Unless one is working with higher velocity flows (3m/s for air) [6] this assumption usually gives unrealistic prediction and thermal-non equilibrium is mostly used when investigating phase change flows.

In [7], a CFD model using a commercial software is developed for better understanding the transport phenomena, especially the phase change, in a plate-fin heat exchanger used for gas refining. The flow channels, ducts and passes of the cold box, are considered in the computational geometry. The porous media technique is introduced in the computational domain due to the excessive increase in the number of computational grids when the fins accounted for in the numerical domain. A flash calculations (FC) technique is coupled with CFD in evaluation of chemical species in the cold box by a user defined function. This study examines the importance of local thermal equilibrium between the porous medium and fluid flow without mass transfer, local thermal equilibrium between the porous medium and fluid flow with mass transfer (LTE), and local thermal non equilibrium between the porous medium and fluid flow with mass transfer (LTNE).

3. Model description

3.1. Multi-phase model

The implemented model is from Baer & Nunziato (1986) and has 7 equations, for phase-separated compressible flows and each phase obeys its own thermodynamics.

$$\frac{\delta \alpha_1}{\delta t} + \vec{u_1}.\vec{\nabla}\alpha_1 = 0 \tag{1}$$

$$\frac{\delta (\alpha\rho)_1}{\delta t} + \vec{\nabla}.(\alpha\rho\vec{u})_1 = 0 \tag{2}$$

$$\frac{\delta(\alpha\rho)_2}{\delta t} + \vec{\nabla}.(\alpha\rho\vec{u})_2 = 0 \tag{3}$$

$$\frac{\delta(\alpha\rho\vec{u})_1}{\delta t} + \vec{\nabla}.(\alpha(\rho\vec{u}\vec{u} + P\overrightarrow{I}))_1 = P_1\vec{\nabla}\alpha_1 \tag{4}$$

$$\frac{\delta(\alpha\rho\vec{u})_2}{\delta t} + \vec{\nabla}.(\alpha(\rho\vec{u}\vec{u} + P\overrightarrow{I}))_2 = P_1\vec{\nabla}\alpha_1 \tag{5}$$

$$\frac{\delta(\alpha\rho E)_1}{\delta t} + \vec{\nabla}.(\alpha(\rho E + P))_1 = P_1\vec{u_1}\vec{\nabla}\alpha_1 \tag{6}$$

$$\frac{\delta(\alpha\rho E)_2}{\delta t} + \vec{\nabla}.(\alpha(\rho E + P))_2 = P_1\vec{u_1}\vec{\nabla}\alpha_1 \tag{7}$$

Each phase has its own state equation to close its system, the ideal gas law for the vapor phase and Tate-Tamman law for the liquid phase. Several simplifying hypothesis are applied to this model. Pressure equilibrium between phases is considered (μ tends towards infinite) as well as thermal equilibrium (H_T tends towards infinite) in an homogeneous mixture. No velocity slip between phases is considered (λ tends towards infinite) and chemical potential are at non-equilibrium ($\dot{m} = \rho v(g_1 - g_2)$ translate the mass transer, with v the the equilibrium velocity of chemical potential) which implies a finite rate mass transfer. The final system yields:

$$\frac{\delta\alpha_1}{\delta t} + \vec{u_1}.\vec{\nabla}\alpha_1 = \mu(P_1 - P_2) - \frac{\dot{m}}{\rho_1} \tag{8}$$

$$\frac{\delta(\alpha\rho)_1}{\delta t} + \vec{\nabla}.(\alpha\rho\vec{u})_1 = -\dot{m} \tag{9}$$

$$\begin{aligned}\frac{\delta(\alpha\rho\vec{u})_2}{\delta t} + \vec{\nabla}.(\alpha(\rho\vec{u}\vec{u} + P\overrightarrow{I}))_2 \\ = P_1\vec{\nabla}\alpha_1 + \lambda(\vec{u_2} - \vec{u_1}) - \dot{m}\vec{u_1}\end{aligned} \tag{10}$$

$$\begin{aligned}\frac{\delta(\alpha\rho E)_2}{\delta t} + \vec{\nabla}.(\alpha(\rho E + P))_2 \\ = P_1\vec{u_1}\vec{\nabla}\alpha_1 - \mu P_1(P_1 - P_2) \\ +\lambda\vec{u_1}(\vec{u_2} - \vec{u_1}) + H_T(T_2 - T_1) - \dot{m}H_1\end{aligned} \tag{11}$$

It is to this final model that source terms like the flow law defining the porous media will be applied.

3.2. Porous model

In the porous domain, the pressure losses are defined by the Darcy-Forchheimer law, for the ΔP in the x-direction it yields:

$$\frac{\Delta P}{\Delta x} = -\frac{\mu}{k}u - \frac{\rho}{k_1}u^2 \tag{12}$$

With k the permeability and k_1 the inertial permeability, the permeability of a porous material is its capacity to let a fluid pass through it. A good permeability therefore implies a good porosity, but the opposite is not necessarily true, it has been shown to be intrinsic to the solid matrix of the porous medium and therefore only a function of its topology and its associated geometric properties.
The first characteristic of a porous medium is its porosity: this is the ratio between the volume not containing solids and the total volume of the medium V:

$$\epsilon = \frac{V_f}{V} \tag{13}$$

The heat transfer in the porous media is treated with a local thermal non-equilibrium with the following thermal aspects:
Conduction in the solid matrix:

$$(1 - \epsilon)(\rho Cp)_s\frac{\delta T_s}{\delta t} = \vec{\nabla}.(k_s^{eff}\nabla T_s) \tag{14}$$

Conduction in the fluid volume:

$$\epsilon(\rho Cp)_f\frac{\delta T_f}{\delta t} = \vec{\nabla}.(k_f^{eff}\nabla T_f) \tag{15}$$

Heat transfer between fluid and solid:

$$\pm h_{sf}\alpha_{sf}(T_s - T_f) \tag{16}$$

3.3. Phase change model

Local phase change rate is finite as chemical potential relaxation is not considered. The thermodynamic state at the liquid-vapor interface is assumed to be at saturation (saturation pressure and temperature at the interface), with:

$$\frac{\delta\rho Y_1}{\delta t} = -\dot{m} \tag{17}$$

$$\dot{m} = \frac{(h_{T2} + h_{T1})(T - T_{sat})}{L_{VL}} \tag{18}$$

Where $L_{VL} = f(T_{sat})$ and $T_{sat} = f(P)$ and $h_{Tk} = H_{Tk}A_I$

4. Test case description

Validation through correlations of each physics in the code:

- Single phase heat transfer (analytic solution for the base), with and without a porous domain.
- Two-phase (Evaporation and condensation) heat transfer, with and without a porous domain.

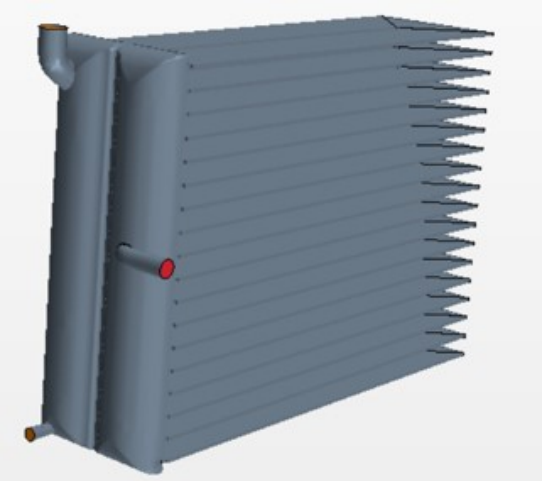

Figure 1: CAD view of the GRU HX

4.1. Geometry

The channel chosen for the testing is a representative one of Liebherrs evaporator as the code aim is to simulate this type of heat exchanger. The test channel have the following dimenssions:

Table 1: Test channel geometry

length mm	height mm	width mm
296.5	2.4136	49.5

The channel 2D model in the code is meshed with a Cartesian mesh of 20 cells in the y-direction (height) and 200 cells in the x-direction (length).

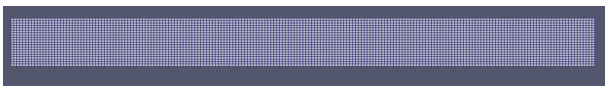

Figure 2: Meshed test channel

4.2. Fluid and solid properties

The working fluid is water at 10^5Pa with the following properties for both phases:

Table 2: Water properties gas and liquid

	λ (W/mK)	μ Pa.s	Cp (J/kg.K)	γ -
Liquid	0.6	10^{-3}	4180	1.33
Gas	0.03	10^{-5}	2000	1.3

The porous properties of the finned channel, with $S\,p_{porous}$ the specific porous surface alone, and $S\,p_{base}$ the specific base surface alone:

Table 3: Porous properties

ϵ -	β (m^{-1})	k (m^2)	$S\,p_{porous}$ (m^2/m^3)	$S\,p_{base}$ (m^2/m^3)
0.86	78	$7.6\,10^{-8}$	2.64	1.74

4.3. Boundary conditions

The boundary conditions applied at the inlet and outlet are respectively a uniform velocity condition (v=0.014m/s) and a pressure condition (P=10^{-5}). In the case without mass transfer the inlet temperature in 293K and in the case including phase-change the inlet temperature in 392K. The inlet mass fraction of liquid is set to 1 for every case. A uniform heat flux of $1000W/m^2$ is applied at the north and south boundary of the 2D model.

5. Empirical correlations

5.1. Single phase heat transfer correlation

The Nusselt of a single phase flow between two plate admit an analytical solution in the case of a set temperature or heat flux.
Temperature:

$$Nu = 7.54 \tag{19}$$

Heat Flux:

$$Nu = 8.24 \tag{20}$$

5.2. Single phase porous correlations

Wieting and Joshi correlations are recommended for pressure loss on channels of this type with offsets fins by the Echtherm software.
With fins geometrical characteristics:
- h : fin height
- s : fins spacing
- δ : fin witdth

Hydraulic diameter for offset fins is defined by:

$$Dh = 2\frac{sh}{s+h} \tag{21}$$

Wieting correlation [8] is based on 22 tested geometries. For the pressure losses, with j the colburn factor and f the fanning friction factor, is the following:

$$j = 0.424(\frac{L}{Dh})^{-0.322}(\frac{\delta}{h})^{0.089}Re^{-0.368} \tag{22}$$

$$f = 1.136(\frac{L}{Dh})^{-0.781}(\frac{\delta}{h})^{0.534}Re^{-0.198} \quad (23)$$

For roughly the same configuration, Joshi and Webb, after carrying out a momentum and energy balance on an elementary model, suggest the following correlations based on 21 tested geometries:

$$j = 0.21(\frac{L}{Dh})^{-0.24}(\frac{\delta}{Dh})^{0.02}Re^{-0.4} \quad (24)$$

$$f = 1.12(\frac{L}{Dh})^{-0.65}(\frac{\delta}{Dh})^{0.17}Re^{-0.36} \quad (25)$$

5.3. Two phase heat transfer correlation

To determine the heat transfer coefficient (HTC) in phase changing cases the Shah correlation [9]for two-phase flows is used, with h_{tp} being the two-phase heat transfer coefficient and h_l the liquide single phase one:

$$\phi = h_{tp}/h_l \quad (26)$$

The N parameter is defined as follow: For vertical tubes at all values of Fr and for horizontal tubes with $Fr_l \geq 0.04$.

$$N = Co \quad (27)$$

For horizontal tube with $Fr_l \leq 0.04$,

$$N = 0.38Fr_l^{-0.3}Co \quad (28)$$

with,

$$Co = (\frac{1}{x} - 1)^{0.8}(\frac{\rho_g}{\rho_l})^{0.5} \quad (29)$$

For N ≥ 1.0:

$$\begin{aligned} \phi_{nb} &= 230Bo^{0.5} \quad , Bo > 0.3 * 10^{-4} \\ \phi_{nb} &= 1 + 46Bo^{0.5} \quad , Bo < 0.3 * 10^{-4} \\ \phi_{cb} &= \tfrac{1.8}{N^{0.8}} \end{aligned} \quad (30)$$

ϕ is the larger of ϕ_{nb} and ϕ_{cb}.
For 0.1 ≤ N ≤ 1.0 :

$$\phi_{bs} = FBo^{0.5}exp^{2.47N^{-0.1}} \quad (31)$$

ϕ_{cb} is calculated using the same equation as before, ϕ is again the larger of ϕ_{bs} and ϕ_{cb}.

For N ≤ 0.1 :

$$\phi_{bs} = FBo^{0.5}exp^{2.47N^{-0.15}} \quad (32)$$

ϕ is again the larger of ϕ_{bs} and ϕ_{cb}. The F constant is as follows:

$$\begin{aligned} Bo &\geq 11 * 10^{-4} \quad , F = 14.7 \\ Bo &\leq 11 * 10^{-4} \quad , F = 15.42 \end{aligned} \quad (33)$$

5.4. Two phase porous correlation

As no slip velocity between phases is considered, the homogeneous flow model is assumed in the gas and liquid two-phase mixture . The properties of the two-phase mixture are calculated with the gas quality and the properties of liquid and gas fluids. The two-phase frictional pressure drop based on the homogenous flow model is expressed by:

$$\frac{dP}{dz} = f\frac{2G^2}{\rho D} \quad (34)$$

Where G is the mass flow rate, D is the hydraulic diameter, ρ is the density of the two-phase mixture, and f is the two-phase frictional factor. The two-phase frictional pressure drop is calculated by the Churchill (1977) [10] correlation with the two-phase flow Reynolds number as:

$$f = 8\left[(\frac{8}{Re})^{12} + \frac{1}{(A+B)^{3/2}}\right]^{1/12} \quad (35)$$

With

$$A = \left[2.457ln\left[\frac{1}{(\frac{7}{Re})^{0.9} + 0.27\frac{\epsilon}{D}}\right]\right]^{16} \quad (36)$$

$$B = (\frac{37530}{Re})^{16} \quad (37)$$

6. Results

The simulation results are presented bellow and compared to the introduced correlation in 5. Observation will be discussed in 7

6.1. Single-phase heat transfer and pressure loss

The heat transfer coefficient without porous domain is calculated and compared to the exact solution in the case of a set heat flux applied uniformly to a surface.

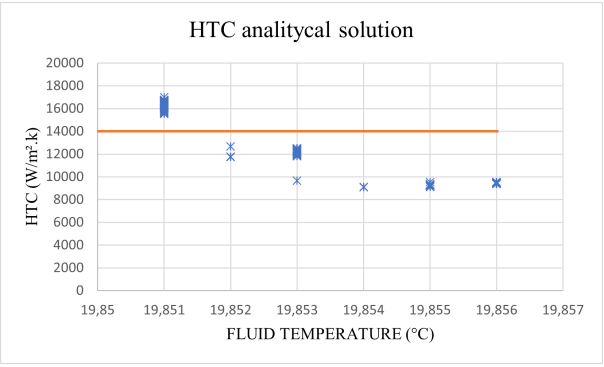

Figure 3: HTC without porous function of fluid temperature with analitycal solution (orange)

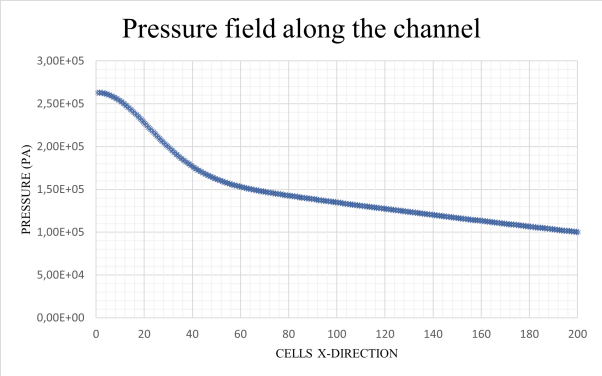

Figure 4: Pressure profile along the channel

In figure 4 the pressure evolution along the channel is ploted and the pressure drop is compared in Table 4 Pressure drop is calculated from the middle of the domain to the end on x/2 to only consider the linear part of the pressure losses, it is the double to account for the whole channel.

Table 4: Pressure drop comparison to correlation

	Code	Wieting	Joshi
ΔP	$1.03\,10^5$	$1.16\,10^5$	$1.21\,10^5$
ERROR	0%	12.3%	17.1%



Figure 5: Pressure profile in the channel

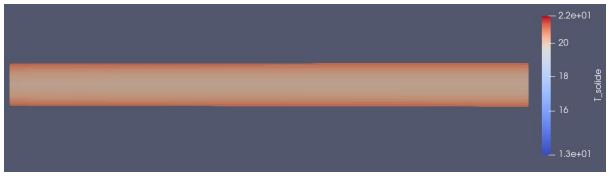

Figure 6: Temperature profile in the porous matrix

Figures 5 and 6 shows an example of the obtained value fields with the code for the pressure field and the temperature field in the solid porous matrix.

6.2. *Two-phase heat transfer and pressure loss*

Figure 7 shows the pressure profile in the test channel for the two-phase (boiling) flow case. Pressure drop is calculated on the linear part of the profile, as in the preceding case. It is of $0.4\,10^5$ Pa When the empirical correlation yields $0.56\,10^5$ Pa.

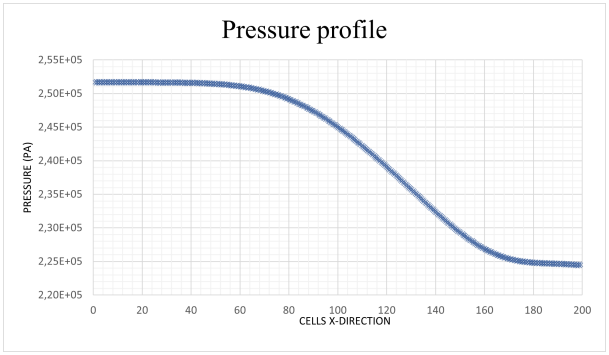

Figure 7: Pressure profile along the channel

Figures 8, 9 and 10 shows the heat transfer function of the mass fraction of liquid, the simulation was carried out on the non porous case (ϵ=1), on the HX channel (ϵ=0.86) and on an additional case with a porosity of 0.9.
On each plot the empirical correlation result is plotted for the liquid mass fraction of 0.95, 0.9 and 0.85. Figure 11 shows the temperature profil in the solid matrix in boiling flow conditions.

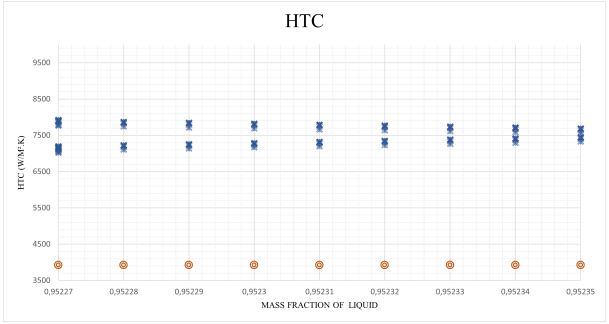

Figure 8: HTC function of mass fraction of liquid for ϵ=0.86

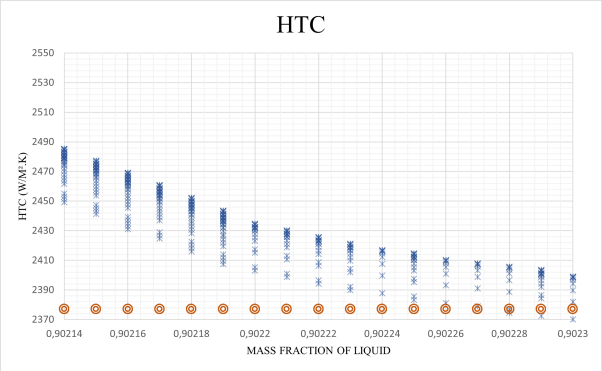

Figure 9: HTC function of mass fraction of liquid for ϵ=0.9

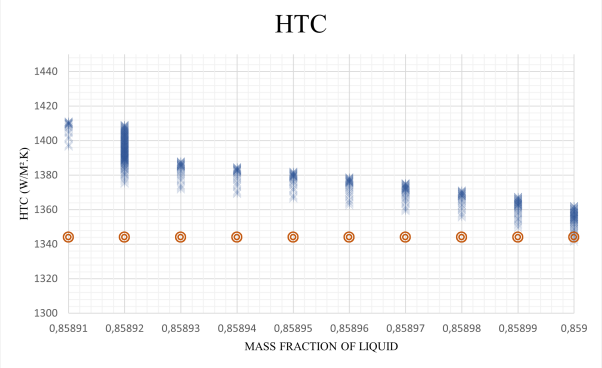

Figure 10: HTC function of mass fraction of liquid for ϵ=1



Figure 11: Temperature profile in the solid for ϵ=0.86

7. Discussions

On the heat transfer coefficient one can see that it tend to decrease with the mass fraction of liquid. Which is in agreement with what is found in literature, before 90% of vapor rate, gas mixture intensifies the transfer. Overall the evolution of the liquid mass fraction in low over the length of this sole channel to conclude on the evolution of the coefficient as a function of the vapour rate, but the order of magnitude at the same fraction is in agreement with the literature. On the pressure drops we observe almost the same gap with the correlation on the results, if the pressure correlations show less important deviation than that of exchange coefficient it remains very dependent on the geometry what induces systematically errors in the different configurations. The entry effects mean that the pressure drop cannot be evaluated directly between the inlet and the outlet, but by considering the second half of the channel in twice its size to be able to compare the linear pressure drop with the correlation, it is observed that it tends to be underestimated.

8. Conclusion

Error from correlation are within the range of acceptable for two-phase flows, for example in [11] multiple boiling flows correlation were reviewed and the MEA ranged from 59.4% to 28.1%. For single-phase flow the heat transfer coefficient is off the same order of magnitude as the one given by the Nusselt exact solution.

Acknowledgments

This project has received funding from the Clean Sky2 Joint Undertaking (JU) under grant agreement No 886698. The JU receives support from the European Union's Horizon 2020 research and innovation programme and the Clean Sky 2 JU members other than the Union. This paper reflects only the author's view and that the JU is not responsible for any use that may be made of the information it contains. It is observed that overall the code tend to

References

[1] A. Horvat, I. Catton, Development of an integral computer code for simulation of heat exchangers.

[2] S. Whitaker, The equations of motion in porous media, Chemical Engineering Science 21 (3) (1966) 291–300.

[3] A. Zukauskas, R. Ulinskas, Heat transfer in tube banks in crossflow.

[4] R. Niroomand, M. Saidi, S. Hannani, A general multiscale modeling framework for two-phase simulation of multistream plate-fin heat exchangers, International Journal of Heat and Mass Transfer 156 (2020) 119730.

[5] A. A. Pozhilov, D. K. Zaitsev, E. M. Smirnov, A. A. Smirnovsky, Numerical simulation of heat and mass transfer in a 3d model of a loop heat pipe evaporator, St. Petersburg Polytechnical University Journal: Physics and Mathematics 3 (3) (2017) 210–217.

[6] Z. Faizurrahmany, Brief overview on local thermal non-equilibrium modeling of heat and mass transfer in open porous materials, Academic Journal of Civil Engineering 37 (1) (2019) 374–377.

[7] A. Zargoushi, F. Talebi, S. Hosseini, Cfd modeling of industrial cold box with plate-fin heat exchanger: Focusing on phase change phenomenon, International Journal of Heat and Mass Transfer 147 (2020) 118936.

[8] A. R. Wieting, Empirical correlations for heat transfer and flow friction characteristics of rectangular offset-fin plate-fin heat exchangers.

[9] R. K. Shah, Classification of heat exchangers., Tech. Rep. (eds.), Washington, U.S.A., Hemisphere Publishing Corp., 1983, p.9-14. (ISBN 0-89116-254-2) (1983). doi:10.1002/9780470172605.ch1.

[10] S. W. Churchill, Comprehensive correlating equations for heat, mass and momentum transfer in fully developed flow in smooth tubes, Industrial & Engineering Chemistry Fundamentals 16 (1) (1977) 109–116.

[11] S.-M. Kim, I. Mudawar, Review of databases and predictive methods for heat transfer in condensing and boiling mini/micro-channel flows, International Journal of Heat and Mass Transfer 77 (2014) 627–652.

Numerical experiments to validate integral film models for jet wiping

David Barreiro-Villaverde

CITIC Research, Spain, david.barreiro1@udc.es

Environmental and Applied Fluid Dynamics, von Karman Institute for Fluid Dynamics, Belgium, david.barreiro@vki.ac.be

Supervisor: Miguel A. Mendez

Assistant Professor, Environmental and Applied Fluid Dynamics, von Karman Institute for Fluid Dynamics, Belgium, miguel.alfonso.mendez@vki.ac.be

University Supervisor: Marcos Lema[1], Anne Gosset[2]

[1]*Professor, Centro de Investigacions Tecnolóxicas (CITIC), University of A Coruña, Spain, marcos.lema@udc.es*

[2]*Professor, Technological Research Center (CIT), University of A Coruña, Spain, anne.gosset@udc.es*

Abstract

This work aims at validating integral film formulations for the application in jet wiping, a contactless metering technique used in hot-dip galvanization to control the coating thickness by means of planar gas jets. We perform Computational Fluid Dynamics (CFD) simulations with a validated numerical model that combines the Volume of Fluid (VOF) and Large Eddy Simulation (LES) methods to analyse an air-water wiping configuration particularly interesting due to its similarity with the one in industrial galvanization. The data extracted from the high fidelity simulations is injected in the integral film model to compare the coating layer evolution predicted by these two approaches. The results reinforce the future perspectives of the integral models for the design of flow control strategies in galvanization.

Keywords: jet wiping, liquid metals, numerical simulations, integral models, two-phase interaction

1. Introduction

The hot dip galvanization is an industrial process designed to protect steel products from corrosion. A ferrous substrate is withdrawn vertically from a coating bath with molten zinc, dragging a coating layer on its surface. The jet wiping is a crucial part of the process in which the coating film is impinged with turbulent planar gas jets, as sketched in Fig. 1. The final film thickness is reduced and the excess of liquid is forced to reverse direction, inducing a *runback flow*. The momentum transfer between the gas jet and the film takes place through the stream-wise pressure gradient $\partial_x p_g(x)$ and shear stress $\tau_g(x)$ at the interface, often referred to as wiping actuators. Their wiping strength depends on several process parameters, which include the nozzle slot opening (d), its distance to the substrate (Z), the stagnation pressure in the nozzle (ΔP_N, which leads to a jet exit velocity U_J) and the substrate speed (U_p). The relevant fluid properties are the gas and the liquid densities (ρ_g, ρ_l) and viscosities (μ_g,μ_l) as well as the gas-liquid surface tension (σ).

Despite being the most widely used technique in galvanization, some unsteady phenomena restrict the operational windows in industrial lines: the violent breakup of the run-back flow (splashing) and the non-uniformities in the final coating (undulations). This article is mostly focused on the latter, originated from the unsteady interaction between the impinging jet and the coating film as first proposed in the experimental work of Gosset *et al.*[1] and Mendez *et al.*[2].

High fidelity numerical simulations have been applied to investigate the jet wiping process[3; 4; 5]. The first extensive validation with experimental data has been accomplished in Barreiro-Villaverde *et al.*[6] using a numerical model that combines the Volume of Fluid (VOF) and Large Eddy Simulation (LES) meth-

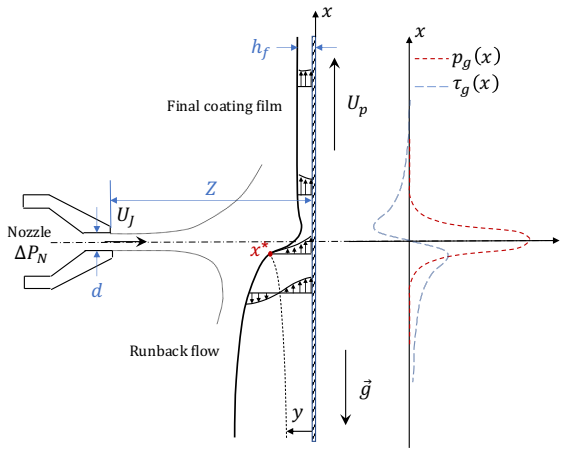

Figure 1: Schematic of the jet wiping process, recalling the main operating parameters. The substrate moves upwards at a speed U_p. The average final film thickness is denoted h_f, and the wiping point, at which the surface flow reverses direction, x^*. The pressure and shear stress distributions produced by the impinging jet at the film interface are denoted $P_g(x)$ and $\tau_g(x)$, respectively, and their typical shape is represented on the right hand side.

ods. The multiscale Proper Orthogonal Decomposition (mPOD)[7] and correlation analysis of the results proved that the undulations result from the unsteady wiping efficiency of the gas jet caused by the periodical formation of waves in the run-back flow. Nevertheless, the computational cost of these simulations is yet prohibitive to reproduce the industrial galvanization.

Alternatively, integral film models based on the long-wavelength approximation and several assumptions on the film flow can be used to investigate the film dynamics. Different models have been implemented in the last 50 years to estimate the average coating thickness in the galvanizing lines[8; 9], to analyse the intrinsic stability of the coating film[10], or to analyse the response of the film to several jet perturbations[11]. An integral film model that includes the role of inertia, transition to turbulence, and the Weighted Integral Boundary Layer (WIBL) model for the velocity profiles has been developed at the von Karman Institute by Mendez *et al.*[12]. This film solver, referred to as BLEW (Boundary LayEr Wiping), has been recently extended to a three-dimensional formulation in the framework of the Research Master thesis of Ivanova[13].

This work aims at validating the 3D integral film solver BLEW as a tool to develop and assess more sophisticated flow control algorithms oriented to mitigate undulation in jet wiping [14]. The previous computations using dipropylene glycol are not suitable for this purpose because the stream-wise and cross-stream scales are comparable according to the scaling laws. Therefore, we carefully design and simulate three air-water wiping configurations whose thickness and flow rate are introduced in BLEW for validation. To this end, we compare the film dynamics predicted by the CFD and by BLEW in terms of the mean thickness, wave amplitude and frequency spectra at three different locations in the final film.

The manuscript is structured as follows. Section 2 recalls the dimensionless numbers involved in jet wiping and explains the motivation of using water for the liquid film. Section 3 describes the numerical details of the CFD simulations and the derivation of the integral film model. Section 4 presents the results obtained using these two approaches, emphasizing the differences with respect to the wiping of dipropylene glycol and the validation of the film model. Finally, Section 5 summarizes the conclusions of this article and the future perspectives of the project.

2. Dimensionless analysis

This section introduces the most representative dimensionless variables in the jet wiping process with a two-fold objective. First, to show to which extent the laboratory conditions investigated in [6] using dipropylene as working liquid are representative of the industrial galvanization. Second, to demonstrate why the air-water combination is of particular interest, especially for the validation of integral film models.

The average film thickness can be scaled with several liquid and gas flow quantities, although the scaling laws do not hold for the undulation characteristics due to the coupling between the gas jet and liquid film [1; 2]. On the liquid side: the final film Reynolds number $Re_f = U_p h_f/\nu_l$ represents the ratio between inertia and viscous forces, the Capillary number $Ca = \mu_l U_p/\sigma$ represents the ratio between viscous and surface tension forces, the Kapitza number $Ka = \sigma/\rho_l g^{1/3}\nu^{4/3}$ represents the ratio between the role of surface tension and viscosity in the damping of the undulation, and the film parameter $\epsilon = Ca^{1/3}$ represents the cross-stream to stream-wise length scales ratio in the film according to the Skhadov scaling recalled in Section 3.2. On the gas side: the equivalent gas jet Reynolds number $Re_j = U_j d/\nu_g$, the wiping number $\Pi_g = \Delta P_N d/\rho_l g Z^2$ represents the wiping

Table 1: Dimensionless numbers for a test case using dipropylene glycol in Barreiro-Villaverde *et al.*[6], one of the proposed test cases with water, and a reference test case with zinc in industrial galvanization characterized by $\Delta P_N = 20$ kPa, $U_p = 1$ m/s, $Z = 12$ mm and $d = 1.2$ mm.

	Dipropylene	Water	Galvanization
Re_l	7.4	320	478
Re_f	2.1	28	18
Ca	0.80	0.014	0.0037
Ka	4.8	3400	16440
ϵ	0.93	0.24	0.15
Re_j	2380	2830	14370
Π_g	0.16	1.02	2.45
$\hat{\nabla} p_g$	5.6	36.4	87.6
$\hat{\tau}_g$	0.3	3.7	7.2

strength, and the dimensionless pressure gradient and shear stress represent the maximum value of the wiping actuators obtained from empirical correlations and scaled with the Shkadov reference quantities.

Three wiping configurations are compared in terms of these dimensionless numbers in Table 1, showing that the wiping using dipropylene is far from the industrial case in terms of both liquid and gas flows, and improved similarity can be reached with water: the film flow is completely laminar and mostly dominated by viscosity since Ca and Ka are of the order one, unlike in industrial galvanization where the wave damping is dominated by surface tension and the film can be turbulent. The film parameter ϵ is well below the unity as in galvanization, and therefore more suitable for the validation of integral models. Finally, in terms of the jet parameters, we are still far from the industrial galvanization lines (compressible flow and Re_j up to 20000), although this could be seen as an advantage because we are capable to reach similar wiping numbers Π_g at a fraction of its computational cost.

3. Numerical methodology

This section presents the three different test cases investigated and the details of each of the two approaches applied to study the jet wiping process in this article: the high fidelity CFD model and the integral model, in Section 3.1 and Section 3.2 respectively.

The substrate is assumed to be flat, and withdrawn from a bath of isothermal coating. The working liquid is water, with density $\rho_l = 1000$ kg/m^3, dynamic viscosity $\mu_l = 0.001$ Pa·s and surface tension $\sigma = 0.0728$ N/m. The gas is air, with density $\rho_g = 1.2$ kg/m^3, dynamic viscosity $\mu_g = 1.776 \times 10^{-5}$ Pa·s. The coating liquid dragged by the substrate is impinged by a slot air jet, with a nozzle opening $d = 1$ mm and stand-off distance $Z = 10$ mm, corresponding to normalized distance $\hat{Z} = Z/d = 10$. Two nozzle pressures are tested: $\Delta P_N = 1$ and $1,5$ kPa. The three configurations are summarized in Table 2.

Table 2: Conditions of the three analyzed test cases, in terms of plate speed U_p, nozzle pressure ΔP_N, wiping number $\Pi_g = \Delta P_N d/(\rho_l g Z^2)$ and film Reynolds number $Re_f = U_p h_f/\nu_l$, where h_f is the mean final thickness.

Case #	U_p [m/s]	ΔP_N [Pa]	Π_g [-]	Re_f
1	1	1000	1.02	28
2	1.5	1000	1.02	54
3	1	1500	1.53	22

The domain used for computations is represented in Fig. 2. It includes the coating bath, the moving flat substrate emerging from it, and a portion of the slot nozzle. The domain spans 50 *mm* in the direction of the moving substrate (x) at both sides of the jet impingement, 20 mm in addition to the stand-off distance Z_n in the jet axis direction (y), and 20 *mm* in the span-wise direction (z). The boundaries open to atmosphere are modelled as outlet conditions with a reference pressure set to 0. The solid boundaries are defined as walls, and the gas jet flow is established through an inlet condition with a prescribed stagnation pressure ΔP_N.

The discretization of the numerical domain is particularly challenging due to the multiscale and three-dimensionality nature of the jet wiping process. The mesh must capture the small scales inside the nozzle and the large scale vortices at the two sides of the gas jet; as well as the strong velocity gradients in the vicinity of the interface (y) and in the shear layers of the gas jet (x).

The structured mesh designed in *blockMesh* consists of 14M hexahedral cells. The width of the first cell in the direction perpendicular to strip is $2\mu m$, which means that we have approximately 10 cells in the final film. The mesh size in the stream-wise direction is $\Delta x = 50\mu m$, which ensures approximately 200 cells per wavelength assuming an undulation fre-

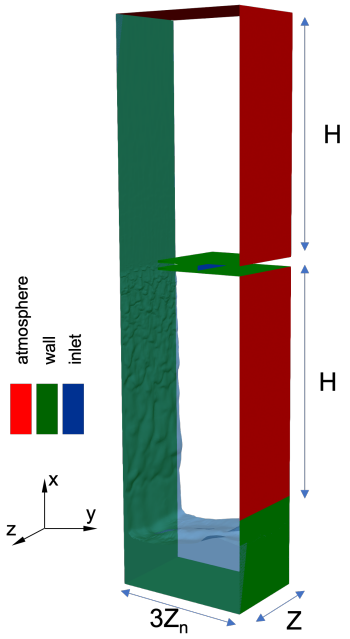

Figure 2: Sketch of the computational domain. The boundaries are categorized in colours as described in the legend and the front and back patches are set as cyclic. The length $H = 50\ mm$ refers to the simulated length in the stream-wise of the film, $Z = 20\ mm$ the distance in the span-wise, and Z_n the stand-off distance.

quency of 100 Hz and a substrate speed of $U_p = 1m/s$. The mesh size in the span-wise direction is $\Delta z = 250\mu m$, which corresponds to 20 cells per wavelength based on the detected transverse modulation of the undulations. The mesh sensitivity is briefly discussed later on in Section 4.1, but from a technical point of view, the combination of the mesh aspect ratio and the interface compression rate have been found to be critical for the stability of the computations.

3.1. CFD simulations

The numerical simulations are carried out using a combination of Large Eddy Simulation (LES) for the gas flow turbulence modeling, and the Volume of Fluid (VOF) method to account for the two-phase flow nature of the problem. The VOF method is based on the transport of a color function which represents the liquid volume fraction α in each computational cell. This function is equal to 1 when this is filled with liquid, and 0 when it is filled with gas. The gas-liquid interface is located in the cells where $0 < \alpha < 1$. The local fluid properties ϕ are computed as a weighted average of the properties of the liquid (ϕ_l) and the gas (ϕ_g), depending on α:

$$\phi = \phi_l \alpha + \phi_g (1 - \alpha) \tag{1}$$

Starting from the conservation equations for an incompressible, immsicible two-phase flow with single fluid formulation:

$$\nabla \cdot \mathbf{U} = 0 \tag{2a}$$

$$\frac{\partial (\rho \mathbf{U})}{\partial t} + \nabla \cdot (\rho \mathbf{U} \otimes \mathbf{U}) = -\nabla p + \rho \mathbf{g} + \nabla \cdot [2\mu \mathbf{S}] + S_\sigma \tag{2b}$$

where $\mathbf{U} = (U, V, W)$ is the velocity, p the pressure, μ the dynamic viscosity, $\mathbf{S} = (\nabla \mathbf{U} + \nabla^T \mathbf{U})/2$ is the strain rate tensor and S_σ is the term accounting for the Laplace pressure due to surface tension at the interface, computed using the continuum surface force (CSF) model. These equations are combined with a transport equation for the volume fraction α:

$$\frac{\partial \alpha}{\partial t} + \nabla \cdot (\alpha \mathbf{U}) = 0 \tag{3}$$

The computations in this work are performed using the *interFoam* solver from OpenFoam[15], which implements an algebraic VOF formulation. To limit the numerical diffusion of the interface, an artificial relative velocity term $U_r = U_l - U_g$ is defined in order to compress the gas-liquid boundary, where U_g is the velocity of the gas and U_l the velocity of the liquid at the interface. The major benefit of this method is its low computational cost and simple implementation. For the flux corrected transport scheme, the algorithm implemented in *interFoam* is known as the Multidimensional Universal Limiter with Explicit Solution solver (MULES [15]), which adjusts the compression by means of the face fluxes and a user-defined parameter C_α to guarantee boundeness and stability [16].

The LES consists in the filtering of the turbulence scales based on the grid scale [17]. The scales smaller than the grid (sub-grid scales) are modeled as they are supposed to have a universal and isotropic behaviour. The larger scales are more case-dependent and crucial in the global mechanism we are interested in, so their accurate resolution is of capital importance. The Smagorinsky model used for the computations is based on the Boussinesq approximation, in which the turbulent eddy viscosity μ_t reads:

$$\mu_t = \rho(C_s \Delta x_{cell})^2 |\mathbf{S}| \tag{4}$$

where C_s is the Smagorinsky model constant, set to 0.158 (usual values are in the range 0.1-0.2), Δx_{cell} is the cell size and $|\mathbf{S}| = \sqrt{2\mathbf{S} : \mathbf{S}}$ is Frobenious norm of the the strain rate tensor.

3.2. Integral model for the liquid film

This section presents the general aspects of BLEW, the integral film model used for the validation. In this model, the Navier-Stokes (NS) equations are integrated across the film thickness, thus formulating the problem in terms of the thickness $h(x,t)$ and volumetric flow rate in the stream-wise $q_x(x,t) = \int_0^{h(t)} u(x,y,t)dy$ and span-wise directions $q_z(x,t) = \int_0^{h(t)} w(x,y,t)dy$. This integration is simplified by scaling the NS equation using a long-wave assumption, i.e. the reference length in the stream-wise direction $[x]$ is assumed to be much larger than the reference thickness $[h]$. The ratio between these two scales leads to a small parameter $\varepsilon = [h]/[x]$ which can be used to weight the contribution of each term of the equation. The long-wave formulation results in the assumption that the pressure gradient across the film thickness $\partial_y p$ is negligible, hence the velocity field within the liquid film is governed by a set of boundary layer like equations. The nondimensionalization and integration of these equations, considering the relevant boundary conditions at the wall and at the interface, yields the following system of PDEs:

$$\partial_{\hat{t}}\hat{h} + \partial_{\hat{x}}\hat{q}_x + \partial_{\hat{z}}\hat{q}_z = 0 \tag{5a}$$

$$\varepsilon Re\Big(\partial_{\hat{t}}\hat{q}_x + \partial_{\hat{x}}\mathcal{F}_{\hat{x}} + \partial_{\hat{z}}\mathcal{F}_{\hat{x}\hat{z}}\Big) = \hat{h}\Big(-\partial_{\hat{x}}\hat{p}_g + \partial_{\hat{x}\hat{x}\hat{x}}\hat{h} + \partial_{\hat{x}\hat{z}\hat{z}}\hat{h} + 1\Big) + \hat{\tau}_{g,\hat{x}} + \hat{\tau}_{w,\hat{x}} \tag{5b}$$

$$\varepsilon Re\Big(\partial_{\hat{t}}\hat{q}_z + \partial_{\hat{x}}\mathcal{F}_{\hat{x}\hat{z}} + \partial_{\hat{z}}\mathcal{F}_{\hat{z}}\Big) = \hat{h}\Big(-\partial_{\hat{z}}\hat{p}_g + \partial_{\hat{z}\hat{z}\hat{z}}\hat{h} + \partial_{\hat{z}\hat{x}\hat{x}}\hat{h}\Big) + \hat{\tau}_{g,\hat{z}} + \hat{\tau}_{w,\hat{z}} \tag{5c}$$

where $Re = [h]U_p/\nu = (U_p^3/g\nu)^{1/2}$ is the film Reynolds number; $\mathcal{F}_{\hat{x}} = \int_0^{\hat{h}(\hat{t})} \hat{u}^2 dy$, $\mathcal{F}_{\hat{x}\hat{z}} = \int_0^{\hat{h}(\hat{t})} \hat{u}\hat{w}dy$ and $\mathcal{F}_{\hat{z}} = \int_0^{\hat{h}(\hat{t})} \hat{w}^2 dy$ are the integral advection terms, $\tau_{g,\hat{x}}$ and $\tau_{g,\hat{z}}$ are the interface shear stresses due to the gas and $\tau_{w,\hat{x}} = -\partial_{\hat{y}}\hat{u}|_{\hat{y}=0}$ and $\tau_{w,\hat{z}} = -\partial_{\hat{y}}\hat{w}|_{\hat{y}=0}$ are the wall shear stresses. The hats in Eq. 5 denote dimensionless variables (e.g. $\hat{h} = h/[h]$), scaled with respect to the reference quantities $[\phi]$ in Table 3. This choice of reference scales leads to the definition of the film parameter as $\varepsilon = Ca^{1/3}$ with $Ca = U_p\mu_l/\sigma$ the Capillary number. This scaling is obtained by keeping the surface tension term to leading order even if $\varepsilon \to 0$. In the literature of falling liquid films[18; 19], this is known as the Skhadov scaling[20; 21].

Table 3: Reference quantities [ ] for the Shkadov scaling, for which $\varepsilon = Ca^{1/3}$, with $Ca = \mu_l U_p/\sigma$ the Capillary number.

Reference	Definition	Expression
$[h]$	$(\nu_l [u]/g)^{1/2}$	$(\nu_l U_p/g)^{1/2}$
$[x]$	$[h]/\varepsilon$	$[h]\, Ca^{-1/3}$
$[u]$	U_p	U_p
$[v]$	εU_p	$U_p\, Ca^{1/3}$
$[p]$	$\rho_l\, g\, [x]$	$\rho_l\, g\, [h]\, Ca^{-1/3}$
$[\tau]$	$\mu_l [u]/[h]$	$(\mu_l \rho_l\, g\, U_p)^{1/2}$
$[t]$	$[x]/[u]$	$(\nu_l/U_s\, g)^{1/2}\, Ca^{-1/3}$

The derivation and the closure of Eq. 5 build on three assumptions, herein briefly described: 1) the long-wavelength formulation, 2) the one-way coupling, 3) self-similarity. The long-wave assumption finds a theoretical justification only if $\varepsilon = Ca^{1/3} \ll 1$. The one-way coupling formulation make the pressure gradient and the shear stress in Eq. 5 independent from the liquid film dynamics ($\hat{h}$, $\hat{q_x}$ and $\hat{q_z}$). The simplest formulation consists then in modeling these terms via empirical correlations derived for the case of gas jet impinging on a dry wall. Finally, the hypothesis of self-similarity is needed to close the system as both the advection and the wall shear stress term require some assumptions on the velocity field $\hat{u}(x,y,t)$ and $\hat{w}(x,y,t)$. The simplest assumption postulates a parabolic dependency and self similarity across the film. For a more extensive description of these models, the reader is referred to Mendez *et al.*[22].

4. Results

This section presents the results obtained using the two approaches described in Section 3. First, the verification and overview of the high fidelity simulations is developed in Section 4.1. Second, the validation of the integral film model is presented in Section 4.2.

4.1. CFD simulations

The VOF-LES model has been already validated with experimental data for different wiping conditions [6]. Nevertheless, we start by verifying some aspects of the numerical configuration to assess the resolution of the liquid film and the gas jet flows.

For the liquid film, we compare for one simulation the average thickness of the final film computed as in Eq. 6 with the predicted using the 0-D model [9], the simplest wiping analytical model that provides the mean final thickness as a function of the wiping parameters. The plot in Fig. 3 shows an excellent agreement between these two quantities.

$$\overline{h}_f(t_i) = \frac{1}{n_t n_z} \sum_{i=max(1,i-k+1)}^{n_t} \sum_{j=1}^{n_z} h(x = 50mm, z_j, t_i) \quad (6)$$

, where $k = 1000(= 0.1s)$ is the length of the averaging window and the time t_0 corresponds to the instant at which the flow is fully established.

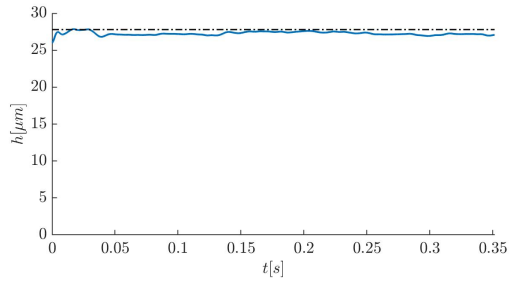

Figure 3: Comparison between the moving average final film computed with Eq.6 on the CFD simulation versus the mean final thickness predicted by the 0-D model.

The verification of the gas jet flow is more complex because it also involves the modelling of the unresolved scales. A single phase simulation of the gas jet impinging on a dry flat plate is performed to elude any impact of the liquid on the gas flow. Fig. 4 compares the average pressure at the wall from the simulations with empirical correlations [23]. The comparison is very satisfactory, but the slopes of the profile are slightly different probably due to the uncertainty of the nozzle geometry and turbulent quantities at the inlet. Nevertheless, we do not expect a significant impact on the wiping.

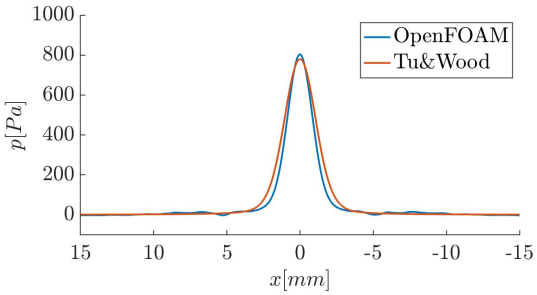

Figure 4: Time averaged pressure profile from the empirical correlations [23] and from the CFD computations.

Finally, the ratio between the resolved and the total turbulent kinetic energy is assessed using Eq. 7 from [24]:

$$LES_{idx} = \frac{1}{1 + \alpha_\nu \left(\frac{\nu_t}{\nu}\right)^n} \quad (7)$$

, where $\alpha_\nu = 0,05$ and $n = 0,53$.

According to this index, the resolved turbulent kinetic energy is higher than 90% in all the domain, and we can consider the mesh sufficiently fine since as suggested in [25], a good LES computation should resolved at least the 80% of the flow.

For the analysis of the results, we will focus on the liquid film side since the jet Reynolds number Re_j does not significantly change compared to the previous numerical campaign as pointed out in Section 2. Fig. 5 shows a qualitative comparison of the film patterns produced using dipropylene glycol (right) and water (left). The previous computations correspond to a weak wiping regime in which the run-back flow is not fully developed and the waves are periodically formed due to the non-stationary balance between the viscous effects that push the liquid towards the final film, and the combined action of gravity and gas shear stress that forces part of the film to return to the coating bath. On the other hand, the wiping with water is sufficiently strong to develop a fully-developed run-back flow whose wave patterns resemble the ones on an unstable falling liquid film.

The volume fraction fields α are post-processed in the range $x \in [-15, 50]mm$, $z \in [0, 20]mm$ and $y \in [0, 1]mm$ to obtain the spatio-temporal thickness evolution $h(x, z, t)$. An exemplary of the film patterns is depicted in Fig. 6 for the final film (top) and run-back flow (bottom). The undulations are fundamen-

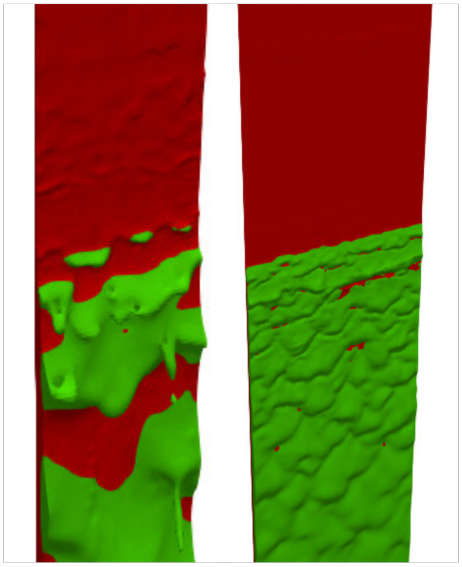

Figure 5: Comparison of the film patterns observed in the runback flow for the wiping on dipropylene glycol (left) and water (right) in [6]. The film is coloured in red for the cells $u_x > 0$ and in green for $u_x < 0$.

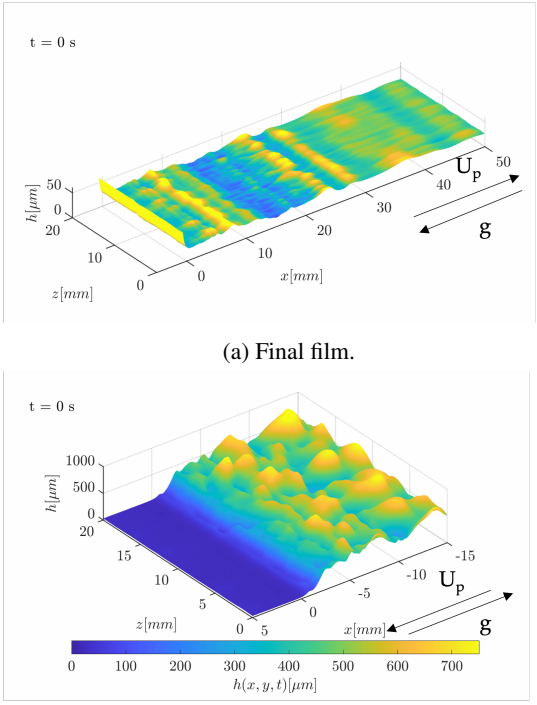

(a) Final film.

(b) Run-back flow.

Figure 6: Snapshot of the undulation patterns obtained in the CFD simulation (top) and integral film solver (bottom). Please, note that the x-axis is reversed between the two images.

tally two-dimensional as observed with dipropylene glycol and slightly modulated in the transverse direction.

The run-back flow exhibits much more different structures. The waves are two-dimensional but rapidly turned to three dimensional structures that interact between each other while they flow back to the bath, similar to the intrinsically developed waves in falling films at comparable Re_f [26].

4.2. *Integral model for the film flow*

The high fidelity data obtained in the simulations with water is now used to feed the integral model for the validation of BLEW with CFD. The comparison is restricted to the final film flow because the goal is to use the tool to develop more sophisticated flow control strategies to mitigate undulation once it is developed in the wiping.

The domain for the film solver is highlighted in Fig. 7. The inlet is located at $x = 0$ in the jet axis, where Dirichlet boundary conditions are prescribed for the thickness $h(x = 0, z, t)$ and the flow rates in the streamwise $q_x(x = 0, z, t)$ and spanwise $q_z(x = 0, z, t)$ directions. The wiping actuators, namely the pressure gradients $\partial_x p(x, z, t)$ $\partial_z p(x, z, t)$ and shear stresses $\tau_x p(x, z, t)$ $\tau_z p(x, z, t)$, are extracted from the CFD simulations. All quantities must be interpolated in time and space due to the largely different scales used in the solvers, and filtered to avoid numerical instabilities in the solver due to the noise in the original signal.

Fig. 8a compares the instantaneous thickness distributions obtained with the CFD simulations (OpenFOAM) and with the film solver (BLEW). The qualitative agreement is remarkable: the large-scale undulations –of major interest in industry– and the transverse modulation are well captured by the simplified model. The temporal evolution of the film thickness at different positions with both approaches is illustrated in Fig. 8b, in which one can see that the curves start to differ at $x \approx 25$ mm. The reason is that, for $x > 20$ mm the CFD mesh features larger cell width in the streamwise direction to keep a reasonable cell count, increasing the numerical diffusion and artificially damping the undulations. In this sense, the film solver seems to be more convenient for the purpose of analysing the downstream evolution of the undulations because we can afford finer meshes that limit the numerical diffusion.

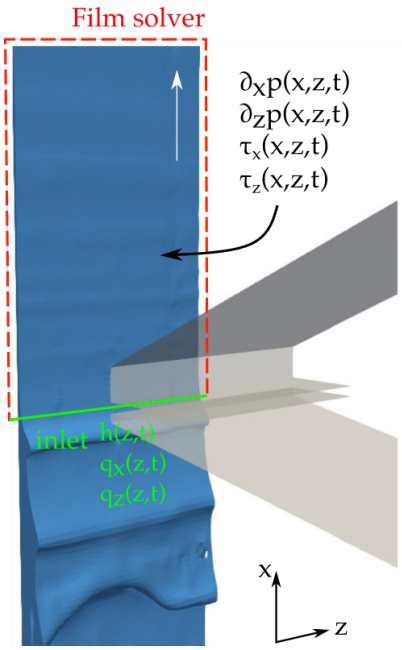

Figure 7: Representation of the domain and boundary conditions in the film solver.

5. Conclusions

We have performed numerical simulations of an air-water wiping configuration that features improved similarity conditions with respect to industrial galvanization.

The inputs of the integral model (film thickness and flow rates at the inlet, and wiping effect of the jet) are extracted from the high-fidelity simulations. The final film dynamics predicted with the film model is compared to the one in the CFD simulations with very good agreement. The long-wavelength undulations, of great concern in industry, are perfectly captured with this integral model.

Therefore, the integral film model BLEW has been validated to investigate the evolution of three-dimensional waves in jet wiping. These results are very important for the future application of BLEW on research to develop flow control strategies to mitigate the undulations in jet wiping.

Acknowledgments

D.Barreiro-Villaverde is financially supported by Xunta de Galicia with the pre-doctoral grant "Programa de axudas á etapa predoutoral" (ED481A-2020/018) and the research project is founded by

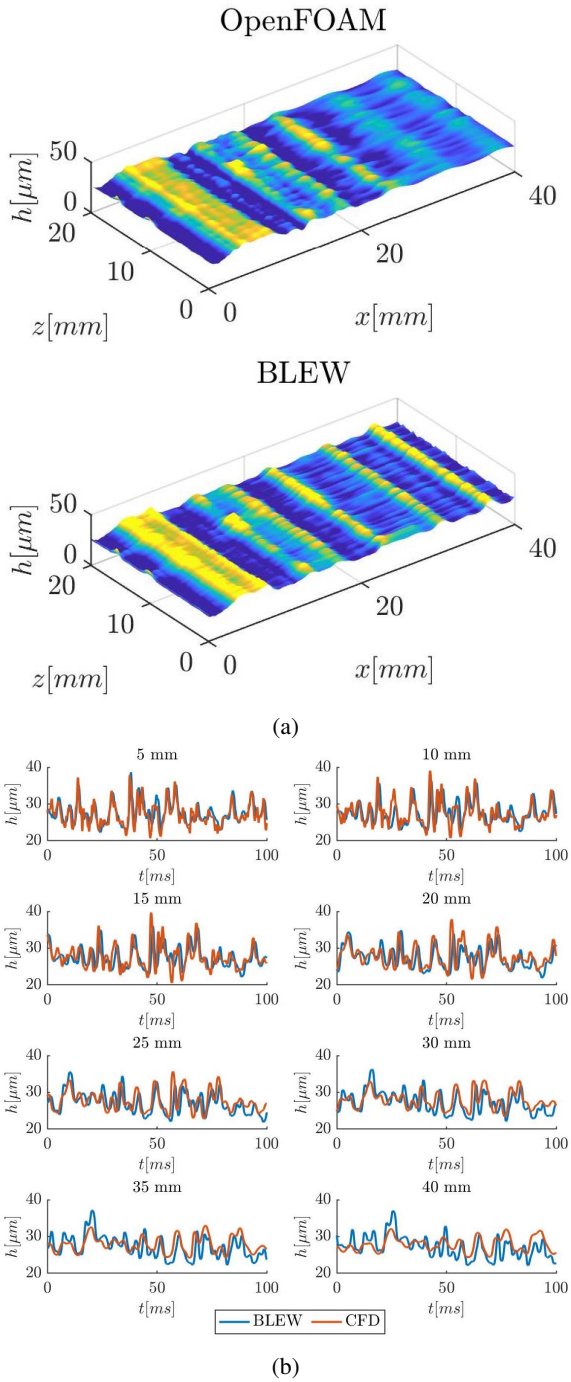

Figure 8: (a) Snapshot of the undulation patterns obtained in the CFD simulation (OpenFOAM) and integral model (BLEW), and (b) temporal evolution of the film thickness at z=10 mm for 8 different locations in x.

Arcelor-Mittal. The authors also wish to thank the "Red Española de Supercomputación" for the attribution of special computational resources at FinisTerrae II (CESGA) (FI-2021-3-0012).

References

[1] A. Gosset, M. A. Mendez, J. M. Buchlin, An experimental analysis of the stability of the jet wiping process: Part I – Characterization of the coating uniformity, Experimental Thermal and Fluid Science 103 (2019) 51–65. doi:10.1016/j.expthermflusci.2018.12.029.

[2] M. A. Mendez, A. Gosset, J. M. Buchlin, Experimental analysis of the stability of the jet wiping process, part II: Multiscale modal analysis of the gas jet-liquid film interaction, Experimental Thermal and Fluid Science 106 (2019) 48–67. doi:10.1016/j.expthermflusci.2019.03.004.

[3] C. Pfeiler, W. Eßl, G. Reiss, W. Ecker, C. K. Riener, G. Angeli, LES-VOF Simulation and POD Analysis of the Gas-Jet Wiping Process in Continuous Galvanizing Lines, steel research international (9) 1600507. doi:10.1002/srin.201700362.

[4] K. Myrillas, P. Rambaud, J. M. Mataigne, P. Gardin, S. Vincent, J. M. Buchlin, Numerical modeling of gas-jet wiping process, Chemical Engineering and Processing: Process Intensification 68 (2013) 26–31. doi:10.1016/j.cep.2012.10.004.

[5] W. Aniszewski, Y. Saade, S. Zaleski, S. Popinet, Planar jet stripping of liquid coatings: Numerical studies, International Journal of Multiphase Flow 103399doi:https://doi.org/10.1016/j.ijmultiphaseflow.2020.103399.

[6] D. Barreiro-Villaverde, A. Gosset, M. Mendez, On the dynamics of jet wiping: Numerical simulations and modal analysis, Physics of Fluids 33 (6). doi:10.1063/5.0051451.

[7] M. A. Mendez, M. Balabane, J. M. Buchlin, Multiscale proper orthogonal decomposition of complex fluid flows, Journal of Fluid Mechanics 870 (2019) 988–1036. doi:10.1017/jfm.2019.212.

[8] J. A. Thornton, H. F. Graff, An analytical description of the jet finishing process for hot-dip metallic coatings on strip, Metallurgical Transactions B (4) 607–618. doi:10.1007/BF02698594.

[9] J. M. Buchlin, Modelling of gas jet wiping in Thin Liquid Films and Coating Processes, in: VKI Lecture Series, Rhode-Saint-Genese, 1997.

[10] G. C. Hocking, W. L. Sweatman, A. D. Fitt, C. Breward, Deformations during jet-stripping in the galvanizing process, Journal of Engineering Mathematics (1-3) 297–306. doi:10.1007/s10665-010-9394-8.

[11] A. D. Johnstone, B. Kosasih, L. Q. Phan, A. Dixon, W. Renshaw, Coating Film Profiles Generated by Fluctuating Location of the Wiping Pressure and Shear Stress, ISIJ International (2) 319–325. doi:10.2355/isijinternational.ISIJINT-2018-413.

[12] M. Mendez, A. Gosset, B. Scheid, M. Balabane, J.-M. Buchlin, Dynamics of the jet wiping process via integral models, Journal of Fluid Mechanics 911 (2021) A47. doi:10.1017/jfm.2020.1075.

[13] T. Ivanova, F. Pino, Physics-based and data-driven modeling of non-linear waves in liquid films, Research master thesis, von Karman Institute.

[14] F. Pino, M. Mendez, B. Scheid, Prospects in machine learning-based flow control for liquid metal coating, 2021.

[15] S. Márquez Damián, An Extended Mixture Model for the Simultaneous Treatment of Short and Long Scale Interfaces, Ph.D. thesis, Universidad Nacional del Litoral (nov).

[16] S. S. Deshpande, L. Anumolu, M. F. Trujillo, Evaluating the performance of the two-phase flow solver interFoam, Computational Science & Discovery 5 (1) (2012) 014016. doi:10.1088/1749-4699/5/1/014016.

[17] P. Sagaut, Large Eddy Simulation for Incompressible Flows: An Introduction, 3rd Edition, Springer, 2005.

[18] S. Kalliadasis, C. Ruyer-Quil, B. Scheid, M. G. Velarde, Falling Liquid Films, Springer London, 2012. doi:10.1007/978-1-84882-367-9.

[19] M. A. Mendez, B. Scheid, J. M. Buchlin, Low Kapitza falling liquid films, Chemical Engineering Science 170. doi:10.1016/j.ces.2016.12.050.

[20] V. Y. Shkadov, Wave-flow theory for a thin viscous liquid layer, Fluid Dynamics 3 (2). doi:10.1007/BF01013543.

[21] V. Y. Shkadov, Wave formation on surface of viscous liquid due to tangential stress, Fluid Dynamics 5 (3). doi:10.1007/BF01019285.

[22] M. A. Mendez, D. Hess, B. B. Watz, J. M. Buchlin, Multiscale proper orthogonal decomposition (mPOD) of TR-PIV data-a case study on stationary and transient cylinder wake flows, Measurement Science and Technology 31 (9). doi:10.1088/1361-6501/ab82be.

[23] C. V. Tu, D. H. Wood, Wall pressure and shear stress measurements beneath an impinging jet, Experimental Thermal and Fluid Science 13 (4) (1996) 364–373. doi:10.1016/S0894-1777(96)00093-3.

[24] I. B. Celik, Z. N. Cehreli, I. Yavuz, Index of resolution quality for large eddy simulations, in: Journal of Fluids Engineering, Transactions of the ASME, Vol. 127, 2005. doi:10.1115/1.1990201.

[25] S. B. Pope, Turbulent Flows, Cambridge University Press. doi:10.1017/CBO9780511840531.

[26] E. A. Demekhin, E. N. Kalaidin, S. Kalliadasis, S. Y. Vlaskin, Three-dimensional localized coherent structures of surface turbulence. I. Scenarios of two-dimensional-three-dimensional transition, Physics of Fluids (11) 114103. doi:10.1063/1.2793148.

Experimental characterization of evaporation heat exchangers using low global warming potential fluids

Aude Lecardonnel

Environmental and Applied Fluid Dynamics Department, von Karman Institute for Fluid Dynamics, Belgium, aude.lecardonnel@vki.ac.be

Supervisor: Delphine Laboureur

Associate Professor, Environmental and Applied Fluid Dynamics Department, von Karman Institute for Fluid Dynamics, Belgium, delphine.laboureur@vki.ac.be

University Supervisor: Piero Colonna

Full Professor, Chair of Propulsion and Power, Delft University of Technology, The Netherlands, P.Colonna@tudelft.nl

Abstract

The present work aims at presenting the selection of the most appropriate measurement techniques that will be used to study the two-phase flow distribution of an air/water mixture inside the channels of an adiabatic heat exchanger. The first results for the calibration and the use of these techniques are also presented.

Keywords: Gas-liquid two-phase flow, multiphase flow metering, experimental

1. Introduction

Vapor cycle systems are closed loops that can be used for equipment cooling and environmental control purposes such as air conditioning. They are composed of several key components (compressor, condenser, expansion valve,...), among which evaporators are continuously subjects of research to improve their efficiency by reducing their volume and increasing their overall aerothermal performances. One straightforward way to improve the heat exchange is to improve the flow distribution among the different channels of the evaporator. Indeed, flow misditribution of the inlet two-phase fluid can cause up to 30% of thermal losses [1].Commonly, high Global Warming Potential (GWP) refrigerants like R134a are used as fluids [2] [3] [4], meaning that their behavior, when it comes to flow distribution in the header and channels, is well characterized and rather predictable. However, their use is already strictly regulated for domestic use or other industrial applications. Eventhough it does not yet apply for the aeronautical field, research is currently undergoing in this industry to explore the low GWP refrigerants in order to reduce the environmental impact of aircrafts. The present work is part of the exPerimental And Numerical mulTiscale mulTiphasic Heat ExchangeR (PANTTHER) Clean Sky 2 project, which will aim at studying and characterizing the behavior of the low GWP refrigerants like R1234ze for which research works focused mainly so far on simpler geometries [5] [6], as well as improving the flow distribution in the evaporator header. The Von Karman Institute is in charge of the experimental approach. To do so, two experimental test benches will be constructed: one transparent adiabatic to develop and validate the methods for the distribution improvement and the measurement techniques chosen, and a full-scale diabatic one. One fundamental objective of this work will also be the better understanding and prediction of the flow patterns transitions in two-phase flows. This paper deals with the first adiabatic test facility.

During the first year of the project, the main parameters influencing the flow maldistribution were gathered and analyzed, to decide whether they could be expected to have a major or minor impact. It was also noticed that most studies in the literature focus on one specific parameter or sometimes a couple of them, but very few studies exist about the impact of a combination of several parameters. Thereby, in a

second time, the adiabatic test bench was designed to be able to reach this objective. Besides, the required air and water flow conditions were calculated to be in flow similarity with a low GWP refrigerant by mean of three two-phase flow variables, but also to take into account the project requirements in terms of mass flow rates and maximum dimensions. In a third time, a literature review about the multiphase flow metering was achieved, to select the appropriate two-phase flow measurement techniques required for the monitoring of the mass-flow rates, the void fraction, the quality and the pressure at several locations of the facility. This work will be firstly presented in the section 2, as well as the main correlations cited in the literature for the prediction of the pressure and the void fraction. The experimental results obtained so far are shown in the section 4 and discussed.

2. Literature review

To be able to measure accurately the flow distribution among the channels, a strong literature review was achieved in a first time about the existing measurement techniques suited for a two-phase flow. Due to the complexity of a flow involving two phases, selecting the most appropriate combination of techniques is not an easy task. In a second time, due to the selection of a void fraction measurement technique through differential pressure measurement, the main predictive correlations for the pressure drops in a two-phase flow were gathered.

2.1. Multiphase flow metering

Multiphase flow metering can be defined as a mean to obtain, through a combination of instruments, the flow rates of the two individual phases. Depending on the mass flow rates of the gas and the liquid phase, the structure of the flow will be different. However, it should be noted that the instruments used for multiphase flow metering are very sensitive to the flow patterns in the channel, and this is the main reason why two-phase flow measurements are so difficult to perform [7; 8]. Since no instrument is able to determine both individual flow rates, several devices have to be combined. In multiphase flow metering, the instruments can measure five basic parameters: density, velocity, momentum, void fraction and mass flow. Since various devices exist for each category, only the most relevant for the present project will be presented in the next sections.

2.1.1. Coriolis flowmeter

To measure both the density and the total mass flow at the same time, a Coriolis flow meter can be used [9; 7]. The Coriolis flow meter consists in using a bent pipe that is vibrating at his resonant frequency. If a fluid is flowing inside the pipe, its inertia alternately reinforces and resists the oscillations that are imposed in the tube to cause the twist. The tube distortions, evaluated electronically by optimally located sensors, will allow to directly determine the mass flow rate by measuring the phase shift between the sensors. In addition, the resonance frequency at which the tube is vibrating depends on the tube geometry, material, but also mass of the medium vibrating in the tube. Therefore, monitoring the change in the resonance frequency of the pipe will allow the determination of the fluid density.

2.1.2. Venturi flowmeter

Venturi flowmeter are also often found in studies for two-phase flow metering of the total mass-flow in which case a correlation has to be used to estimate the total density of the flow [10; 11], and is a type of head flowmeter, which is based on the Bernoulli equation. The flow meter consists in placing a restriction in the flow, which will increase the velocity and decrease the static pressure. The total mass flow is obtained in a two phase flow, the same way as in a single phase flow, meaning that the flow rate is determined through the measurement of the pressure difference upstream the venturi and in the throat ΔP, providing the diameter ratio β, discharge coefficient C, the compressibility and thermal expansion factors contained in K are known [12].

$$\dot{m_{TP}} = \frac{C}{\sqrt{1-\beta^4}} K \sqrt{2\Delta P \rho_{TP}} = K_{geo} \sqrt{\Delta P \rho_{TP}} \quad (1)$$

The two-phase flow density is then approximated by multiple correlations that have been developed since the 90's. These correlations are usually based on a weighted average of the vapor and liquid phase densities and on the quality. Hence, the values of the coefficients can be easily adapted to fit the results from a specific design and different fluids [13]. The correlations that will be used for comparison with the measurement data in the section 4 are listed in the table 1.

These venturi flowmeters are very often coupled in the literature with void fraction meter such as capacitance probe [12] for two main reasons. The first one is because the void fraction is used in the calculation

Table 1: Venturi correlations

Correlation name	Equation
Homogeneous [14]	$\dot{m_{TP}} = K_{geo}\sqrt{\Delta P / \left(\frac{x}{\rho_v} + \frac{1-x}{\rho_l}\right)}$
Chisholm [15]	$\dot{m_{TP}} = K_{geo}\sqrt{\Delta P \rho_l} / \left[(1-x)\sqrt{1 + \frac{C}{X} + \frac{1}{X^2}}\right]$ with $X = \sqrt{\rho_v/\rho_l}\frac{(1-x)}{x}$ and $C = (\rho_v/\rho_l)^{0.25} + (\rho_l/\rho_v)^{0.25}$ when $X < 1$ and $C = (\rho_v/\rho_l)^{0.5} + (\rho_l/\rho_v)^{0.5}$ when $X \geq 1$
Zhang et al. [16]	$\dot{m_{TP}} = K_{geo}\sqrt{\Delta P \rho_l} / \sqrt{\left[x^{1.25+0.25x^{1/3}}\right]\left(\frac{\rho_l}{\rho_v} - 1\right) + 1}$
Zhang et al. [17]	$\dot{m_{TP}} = K_{geo}\sqrt{\Delta P \rho_l} / \sqrt{c\left(\frac{\alpha}{1-\alpha}\right)^n \left(\frac{\rho_l}{\rho_v}\right)^m + 1}$ $= c'\left(\frac{\alpha}{1-\alpha}\right)\left(\frac{\rho_v}{\rho_l}\right)^H = \frac{\sqrt{\Delta P_l}}{\sqrt{\Delta P_g}}$ with c, n, m, c' and H which are flow pattern depending constants and are equal to 0.50, 0.95, 0.02, 0.51 and 0.65 respectively for bubbly and slug patterns
Murdock [18]	$\dot{m_{TP}} = K_{geo}\sqrt{\Delta P} / \left(\frac{x}{\sqrt{\rho_v}} + M\frac{1-x}{\sqrt{\rho_l}}\right)$ with M=1.26
Lin [19]	$\dot{m_{TP}} = K_{geo}\sqrt{\Delta P} / \left(\frac{x}{\sqrt{\rho_v}} + \theta\frac{1-x}{\sqrt{\rho_l}}\right)$ With $\theta = 1.48625 - 9.26541\left(\frac{\rho_v}{\rho_l}\right) + 44.6954\left(\frac{\rho_v}{\rho_l}\right)^2 - 60.6150\left(\frac{\rho_v}{\rho_l}\right)^3$ $-5.12966\left(\frac{\rho_v}{\rho_l}\right)^4 - 26.5743\left(\frac{\rho_v}{\rho_l}\right)^5$
Philipps [20]	$\dot{m_{TP}} = K_{geo}\sqrt{\Delta P} / \left(\frac{x}{\sqrt{\rho_v}} + M\frac{1-x}{\sqrt{\rho_l}}\right)$ with M=1.5
James [21]	$\dot{m_{TP}} = K_{geo}\sqrt{\Delta P} / \left(\frac{x^n}{\sqrt{\rho_v}} + \frac{(1-x)^n}{\sqrt{\rho_l}}\right)$ with n=1.5
Collins [22]	$\dot{m_{TP}} = K_{geo}\sqrt{\Delta P} / \left(a\frac{x}{\sqrt{\rho_v}} + b\frac{1-x}{\sqrt{\rho_l}} + c\frac{\sqrt{x(1-x)}^{1/4}}{\sqrt{\rho_l \rho_v}}\right)$ with a,b, and c to be defined experimentally

of the quality, required for the correlations as stated above. These two quantities are related by mean of a calibration. The second on is because the calibration of the venturi depends on the flow patterns, which can be retrieved from the data clustering of the void fraction meter signal as will be explained in the section 2.1.5.

2.1.3. Capacitance probe

The capacitance probes are the most widely used for the determination of the void fraction, but their output signals can also be used for flow pattern identification. These instruments are also referred as impedance probes in the literature. The impedance probe is a volume-averaged void fraction meter. The working principle is based on the fact that the impedance between two electrodes facing each other on a channel can be related to the change of conductivity or capacitivity in the medium, and thus to the void fraction, through a calibration curve. Many designs exist for the electrodes, whether of concave shapes (Fig. 1, parallel symmetrical or asymmetrical plate shapes, or helicoidal [23]. The number of electrodes can also differ from only two (a low-potential one and a high-potential one), up to eight alternating between a high and low potential electrodes and creating a rotating field. A major issue of this probe is that it can be very sensitive to the flow pattern inside the channel for some designs, while for other the influence seems to be minor, especially when at least 6 electrodes are used [12; 7]. If the flow regime is found to influence the output signal, several calibration curves will have to be obtained, at least one for the annular and the stratified flow patterns, and ideally one for each pattern.

2.1.4. Dual optical probe

Another void fraction measuring instrument that can be cited is the optical probe, that is part of a wider section of intrusive measurement techniques named

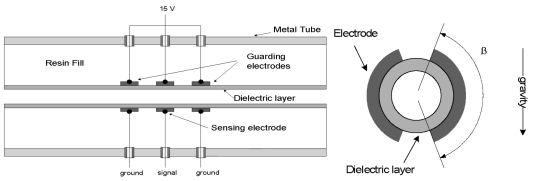

Figure 1: Concave capacitance probe design [24]

needle probes which are mainly found for liquid/gas applications [25]. The working principle of this instrument relies on the change of refractive index in the measured medium, between the liquid and the gaseous phase. Light is emitted in the sensor until the end of the probe tip located inside the channel. Whether the sensor is surrounded by gas or liquid, the light will be reflected (due to the low optical index or the gaseous phase) and thus send back to the acquisition system to be converted into an electrical signal or not reflected (Fig. 2). Hence, this is a very local void fraction measurement which does not require any prior calibration.

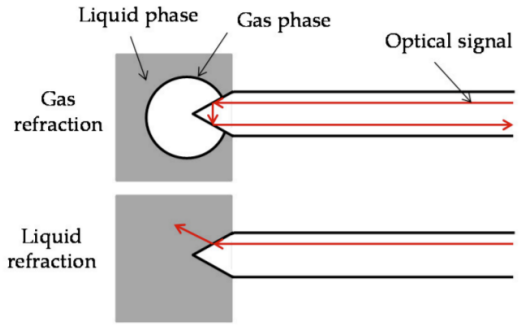

Figure 2: Optical probe principle [25]

2.1.5. *Flow pattern identification*

The most common way to characterize the flow pattern in a channel was originally by visualizations [8]. However, since this method depends upon the appreciation of an operator, it is thus very subjective, and there is a lack of clear and quantitative criteria to discriminate the flow regimes transitions. Over the last three decades, more and more studies tend to determine the flow patterns based on the data clustering or classification of probe signals, in an attempt to obtain more objective and reliable experimental data and thus to be able to model more precisely the flow transitions. Most of the studies employ signals coming from capacitance/conductance probes and from differential or absolute pressure taps measurements [26; 27; 28; 29]. The flow regimes are often determined by analysing the Power Spectral Density or the Probability Density Function of the signal. This method relies on the principle that each pattern has a "flow regime signature" [8] (Fig. 3), which means that for each regime, the combination of the fluctuations and of the average value of the signal is specific. The data clustering or classification of signals has been proven over the last decades to be able to predict efficiently the flow patterns. Besides, it is now supported by a numerous amount of studies in the literature [25].

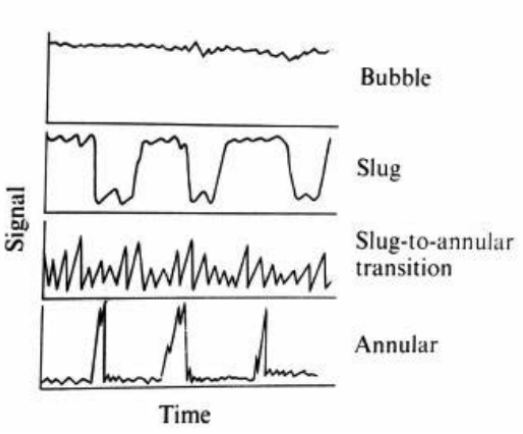

Figure 3: Flow regime signature examples [8]

2.2. *Pressure drops and void fraction correlations*

Like for any other system, it is important to be able to predict the pressure drops as well the heat transfer that will be created by the boiling two-phase flow in the evaporator for three main reasons: to know the pump power required, to verify that the global pressure drops do not exceed a certain limitation usually fixed ahead of the sizing process and on the other hand to verify that the minimum required heat transferred from one fluid to the other one is reached. Several model exist for the pressure drops [30; 31]that are either based on a homogeneous assumption (meaning zero slip condition: both phase flow at the same velocity), or on a separated flow assumption. The main models that can be found in the literature: Lockhart - Martinelli [32], Chisholm [33], Friedel [34] and Müller-Steinhagen and Heck [35].

However, the pressure drops correlations are highly depending on the flow patterns. The range of flow conditions and especially of flow patterns for which the correlations are accurate is not well documented by their authors, making the choice of the most suitable correlation difficult.

To be able to predict the pressure drops, the void fraction has to be either measured or predicted also thanks to a correlation. Márquez-Torres et al. [36] realized a great review of 63 void fraction correlations that they compared with 11 895 experimental points to determine if one single equation could predict all the corresponding void fractions. Their work led to the conclusion that none of the existing correlation was sufficient to accurately predict the void fraction over a wide range of operating conditions. They also presented a very interesting schematic summary of the best correlation to calculate the void fraction knowing the pipe orientation and the flow pattern studied or the fluid viscosity.

3. Experimental facility

A rather common experimental facility was constructed at the Von Karman Institute (VKI) to test (Fig. 4), select and calibrate the appropriate instruments to be used for a more complex test bench. The void fraction was measured in a 29.7mm smooth pipe diameter. The fluid studied consisted in a two-phase flow of an air-water mixture. A quality of up to 0.23 was reached as well as a void fraction of 0.8. The mass flow rate of water ranged from 0 to 12 L/min while the flow rate of air covered the range from 0 to 0.0235kg/s. A schematic of the set-up can be found on the figure 4. Water is pumped from a tank by a centrifugal pump (Wilo) and its flow rate is measured by mean of electromagnetic flowmeter (Fuji Electric). A 15-bar compressed air line is connected to the facility and its pressure is then decreased to 0.5-0.8 bar. The air flow rate is measured thanks to a thermal massflow sensor (CS Instruments). Air and water are mixed and then sent to a 60 pipe diameters straight length to ensure a fully developed flow at the inlet of the test section, which consists in a 1m long horizontal smooth pipe made of Plexiglass and of 20mm diameter, on which a capacitance probe is mounted for the "void fraction line", and in a 1m long horizontal plexiglass smooth pipe of 10mm diameter and connected the venturi flowmeter for the "venturi line". Visualizations of the flow patterns in the test section are achieved by mean a high-speed camera (Dantec). Two taps distanced by 1.5m from each other are connected to two pressure membrane sensors (Valydine) to monitor the pressure inside the pipe and to retrieve the void fraction. The air-water mixture is further sent to a Coriolis flowmeter (Yokogawa) to obtain the total mass flow rate and to the dual optical probe. The tests were carried at a very low overpressure above the atmospheric pressure.

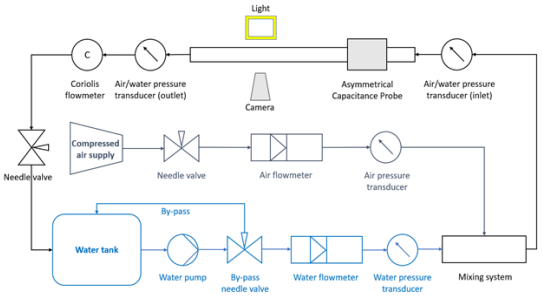

Figure 4: Facility for the calibration and test of the different instruments

The second step was to understand how to measure the flow distribution among all the channels and which quantity needed to be evaluated to do so. Based on the literature study several measurement techniques were found to be relevant: capacitance probe for the void fraction measurement, coupled with a venturi flow meter calibrated by mean of a Coriolis flowmeter, flow pattern recognition based on pressure signal data clustering [12; 13] and a dual otpical probe to be able to relate the void fraction and the quality. The Venturi was designed at the VKI and based on the standard NFENISO5167-4 that defines how to calculate all the characteristic dimensions. Concerning the capacitance probe design, two leads were followed. The first one consisted in selecting a design from the literature that was sufficiently documented to be able to run electrostatic simulations, and designed for a mixture of air and water. The concave design from the work of Caniere et al. [24] was selected. The second solution was to test a capacitance probe designed at the VKI by a former PhD [37] for air and water with asymmetric parallel plates.

The optical probe was manufactured by the company RBI and equipped of two 30 microns tips of Sapphire, which enables also the obtention of the bubble size and velocity. The last void fraction calculation to be tested is derived from the pressure measurements [38].

4. Results

4.1. Flow patterns

Firstly, the flow patterns obtained in the 20mm diameter line were compared with the predictions of the flow map of Lin et al. [39] for almost the same pipe diameter.

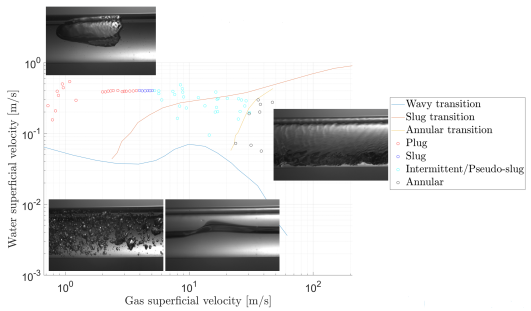

Figure 5: Flow regimes compared with the transition predictions from Lin et al. [39]

It appears from the figure 5 that the flow patterns obtained by visualizations and from observations of the high-speed camera images fitted very well the flow map of Lin et al. appart for the intermittent/pseudo-slug regime that was found to start at earlier vapor velocity.

Secondly, the pressure drops obtained from the two taps and for tests from different days were measured and analyzed (Fig. 6).

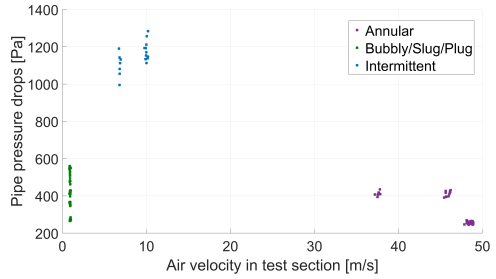

Figure 6: Pressure drops as a function of air velocity in the test section

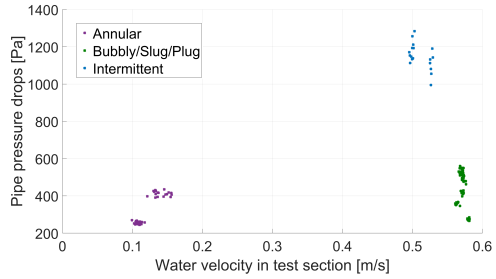

Figure 7: Pressure drops as a function of water velocity in the test section

It can be straightforwardly understood from the graph why the choice of a predictive correlation can be difficult and why a unique correlation can hardly cover all the flow patterns.

4.2. *Dual optical probe*

To evaluate the void fraction, measurements using a dual optical probe were achieved as explained in the section 3, and were compared with several correlations available in the literature. The results from this experimental campaign are presented in the figure 8.

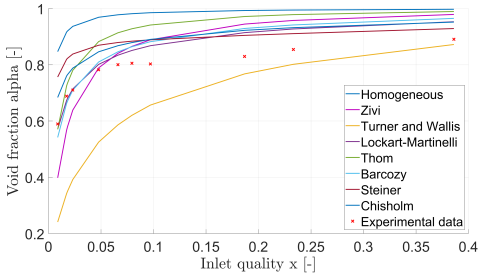

Figure 8: Void fraction measurements by mean of a dual optical probe and comparison with model predictions

It can be seen that the void fraction is well predicted by two distinct correlations depending on the flow regimes. At low quality, and thus for bubbly or plug flow regimes, the Barcozy correlation [40] is the best fitting of the results. At higher quality, and for slug to intermittent or annular flow patterns, the results are in between the Wallis and the Zivi predictions [41; 42].

However, most correlations can be summarized in a common equation defined by Butterworth [13].

$$\alpha = \left[1 + k_0 \left(\frac{1-x}{x}\right)^{k_1} \left(\frac{\rho_v}{\rho_l}^{k_2}\right) \left(\frac{\mu_l}{\mu_v}\right)^{k_3}\right]^{-1} \tag{2}$$

where x is the quality, ρ_l and ρ_v are the liquid and vapor densities, μ_l and μ_v are the liquid and vapor viscosities and k_0, k_1, k_2 and k_3 are the fitting parameters. The experimental data were fitted using this relationship and the result is presented in the figure 9 as well as the different coefficients.

The fitting by the Butterworth correlation gives a good result and the coefficients will be used later on in the project to obtain the quality, knowing the void fraction that will be provided by the capacitance probe.

4.3. *Venturi flowmeter*

The final results obtained so far concern the 10mm diameter line in which the venturi is implemented.

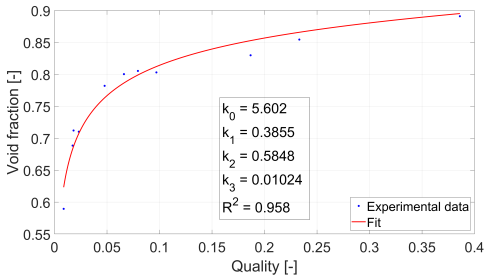

Figure 9: Void fraction measurements by mean of a dual optical probe fitted by the Butterworth correlation

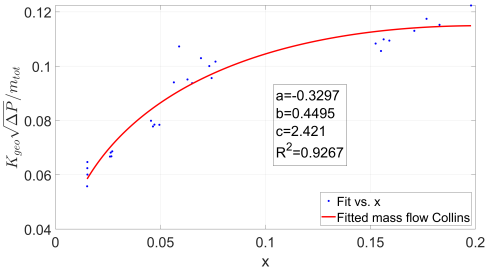

Figure 11: $K_{geo}\sqrt{\Delta P}/m_{tot}$ fitted by the Collins correlation [22] as the function of the quality x

The discharge coefficient C of the venturi (Eq. 1) was evaluated by mean of a water single-phase flow measurement and is found to be worth around 0.925 ±0.1 (due to the diameter throat uncertainties), which is, eventhough a bit low, a reasonnable value according to the literature [43]. Several correlations gathered from the literature review and presented in the section 2.1.2 were used to calculate the mass-flow rate in the venturi from the pressure drop measurements. The results are compared with the total mass flow rate obtained from the Coriolis flow meter.

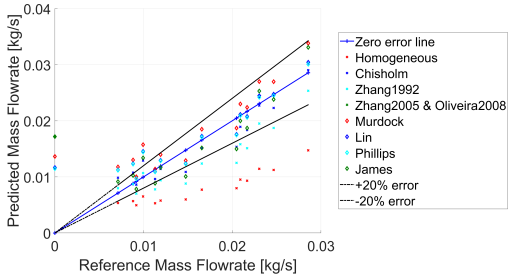

Figure 10: Coriolis mass-flow rates compared with Venturi mass flow rates obtained with several correlations

It can be seen that the Chisholm [44] correlation gives very promising results, while the Murdock [18] and James [14] give reasonable results but not over the whole range. However, these two correlations as well as the one from Collins [22], rely on coefficients that can be modified and fitted to specific data but also for each flow pattern as done by Meng et al. [13].

The same work on the present data is shown in the figure 11 as long with the coefficients obtained when the Collins correlation is used for the fitting.

The flow patterns below a quality value of 0.1 comprise the Plug/Slug/Intermittent, while above 0.1, only the annular pattern is found. It can be noticed that the fitting of the results gives good results, but that two trends exist in the two groups of flow patterns. Thus, the two groups could be fitted separately but it would also be interesting to fill the gap between a quality of 0.075 and 0.15 to verify if the values of the coefficients are also valid in that zone.

5. Conclusion

The full characterization of a two phase flow through the measurement of the main parameters is a complex task due to the diversity of the instruments and their possible combination. A literature review of the relevant probes for the present study is presented, as well as the main correlations that will be used for the comparison. The experimental results obtained with an air/water mixture flow are presented and a new correlation for a 30mm diameter pipe between the void fraction and the inlet quality is given. The designed Venturi flowmeter is found to be a relevant instrument for air/water mass flow rate measurements and the calibration curve obtained from the adaptation of existing correlations is presented.

Acknowledgments

This project has received funding from the Clean Sky2 Joint Undertaking (JU) under grant agreement No 886698. The JU receives support from the European Union's Horizon 2020 research and innovation programme and the Clean Sky 2 JU members other than the Union. This paper reflects only the author's view and that the JU is not responsible for any use that may be made of the information it contains. The author wishes to thank Pr. Delphine Laboureur from von Karman Institute and Pr. Piero Colonna for their supervision and guidance.

References

[1] J. M. Choi and W. V. Payne and P. A. Domanski, Effects of non-uniform refrigerant and air flow distributions on finned-tube evaporator performance, International Congress of Refrigeration, Washington, DC (2003) 1–8.

[2] P. Fei and P. Hrnjak, Adiabatic Developing Two-Phase Refrigerant Flow in Manifolds of Heat Exchangers, Air Condtioning and Refrigeration Center TR-225.

[3] Y. Zou and P. S. Hrnjak, Effects of fluid properties on two-phase flow and refrigerant distribution in the vertical header of a reversible microchannels heat exchanger, Applied Thermal Engineering 70 (2014) 966–976.

[4] N. -H. Kim and D. -Y. Kim and H. -W. Byun, Effect of inlet configuration on the refrigerant distribution in a parallel flow minichannel heat exchanger, International Journal of Refrigerant 34 (2011) 1209–1221.

[5] A. Diani and S. Mancin and L. Rossetto, R1234ze(E) flow boiling inside a 3.4 mm ID microfin tube, International Journal of Refrigeration 47 (2014) 105–119.

[6] M. A. Kedzierski and K.-J. Park, Horizontal Convective Boiling of R134a, R1234yf/R134a, and R1234ze(E) within a Micro-Fin Tube with Extensive Measurement and Analysis Details, NIST Technical Note 1807.

[7] G. Falcone, G. F. Hewitt, C. Alimonti, Multiphase Flow Metering - Pinciple and Applications, Elsevier, 2010.

[8] C. Bertani, M. De Salve, M. Malandrone, G. Monni, B. Panella, State-of-art and selection of techniques in multiphase flow measurement, Report RdS/2010/67, Torino.

[9] B. Schweber, Coriolis flowmeters, part 2: The principle.

[10] R. T. H. Machadao, Multiphase flow in venturi: an experimental and theoretical study.

[11] L. Moura, C. Marvillet, et al., Measurement of two-phase mass flow rate and quality using venturi and void fraction meters, American Society of Mechanical Engineers, Fluids Engineering Division (Publication) FED.

[12] J. L. G. Oliveira, et al., Medição de vazão de escoamentos bifásicos utilizando tubo de venturi ou placa de orifício associados a um sensor de fração de vazio com campo elétrico girante.

[13] Z. Meng, Z. Huang, B. Wang, H. Ji, H. Li, Y. Yan, Air–water two-phase flow measurement using a venturi meter and an electrical resistance tomography sensor, Flow Measurement and Instrumentation 21 (3) (2010) 268–276.

[14] Z. Lin, S. Wang, D. Wang, Gas-liquid two-phase flow and boiling heat transfer, Xi'an: Xi'an Jiaotong.

[15] D. Chisholm, Research note: two-phase flow through sharp-edged orifices, Journal of Mechanical Engineering Science 19 (3) (1977) 128–130.

[16] H. Zhang, S. Lu, G. Yu, An investigation of two-phase flow measurement with orifices for low-quality mixtures, International journal of multiphase flow 18 (1) (1992) 149–155.

[17] Z. Hong-jian, Y. Wei-ting, H. Zhi-yao, Investigation of oil-air two-phase mass flow rate measurement using venturi and void fraction sensor, Journal of Zhejiang University-SCIENCE A 6 (6) (2005) 601–606.

[18] J. Murdock, Two-phase flow measurement with orifices.

[19] Z. Lin, Two-phase flow measurements with sharp-edged orifices, International Journal of Multiphase Flow 8 (6) (1982) 683–693.

[20] R. N. Steven, Wet gas metering with a horizontally mounted venturi meter, Flow measurement and Instrumentation 12 (5-6) (2002) 361–372.

[21] R. James, Metering of steam-water two-phase flow by sharp-edged orifices, Proceedings of the Institution of Mechanical Engineers 180 (1) (1965) 549–572.

[22] D. Collins, M. Gacesa, Measurement of steam quality in two-phase upflow with venturimeters and orifice plates.

[23] Y. Sakamoto, T. Sato, H. Kobayashi, Development study of a capacitance void fraction sensor using asymmetrical electrode plates, Journal of fluid science and technology 11 (2) (2016) JFST0008–JFST0008.

[24] H. Canière, C. T'Joen, A. Willockx, M. De Paepe, Capacitance sensor design for refrigerant two-phase flow characterization, in: AIP Conference Proceedings, Vol. 914, American Institute of Physics, 2007, pp. 178–183.

[25] Á. R. Gardenghi, D. G. Chagas, G. Scagnolatto, R. M. Oliveira, C. B. Tibiriçá, et al., Overview of void fraction measurement techniques, databases and correlations for two-phase flow in small diameter channels, Fluids 5 (4) (2020) 216.

[26] H. Canière, B. Bauwens, C. T'Joen, M. De Paepe, Probabilistic mapping of adiabatic horizontal two-phase flow by capacitance signal feature clustering, International Journal of Multiphase Flow 35 (7) (2009) 650–660.

[27] D. Barnea, O. Shoham, Y. Taitel, A. Dukler, Flow pattern transition for gas-liquid flow in horizontal and inclined pipes. comparison of experimental data with theory, International Journal of Multiphase Flow 6 (3) (1980) 217–225.

[28] S. Lin, PRESSURE FLUCTUATION AND FLOW REGIMES OF AIR-WATER FLOW IN A SMALL TUBE, Experimental Heat Transfer 14 (2001) 135–144.

[29] N. K. Tutu, Pressure fluctuations and flow pattern recognition in vertical two phase gas-liquid flows, Int. J. Multiphase Flow;(United Kingdom) 8 (4).

[30] U. Soupremanien, Ecoulements diphasiques aux petites échelles - Application au refroidissement d'une Pile à Combustible (PEMFC), Ph.D. thesis, Mécanique des fluides [physics.class-ph]. Grenoble INP, France (2010).

[31] J. R. Thome, Encyclopedia of Two-Phase Heat Transfer and Flow I: Fundamentals and Methods (A 4-Volume Set), World Scientific, 2015.

[32] R. W. Lockhart, Proposed correlation of data for isothermal two-phase, two-component flow in pipes, Chem. Eng. Prog. 45 (1949) 39–48.

[33] D. Chisholm, Pressure gradients due to friction during the flow of evaporating two-phase mixtures in smooth tubes and channels, International Journal of Heat and Mass Transfer 16 (2) (1973) 347–358.

[34] L. Friedel, Improved pressure drop correlation for horizontal and vertical two-phase pipe flow, in: European Two-phase Flow Group Meeting, Ispra, Italy, 1976.

[35] H. Müller-Steinhagen, K. Heck, A simple friction pressure drop correlation for two-phase flow in pipes, Chemical Engineering and Processing: Process Intensification 20 (6) (1986) 297–308.

[36] L. Márquez-Torres, J. Ochoa-Pineda, P. Pico, J. P. Valdés, D. Becerra, A. Pinilla, E. Pereyra, N. Ratkovich, Comparison of 63 different void fraction correlations for different flow patterns, pipe inclinations, and liquid viscosities, SN Applied Sciences 2 (10) (2020) 1–24.

[37] M. Scelzo, Experimental and numerical investigation of slurry flows in pipelines: a contribution towards slush propellants for future rockets' engines.

[38] J. Jia and A. Babatunde and A. Wang, Void fraction measurement of gas-liquid two-phase flow from differential pressure, Flow Measurement and Instrumentation 41 (2015) 75–80.

[39] P. Lin, T. Hanratty, Effect of pipe diameter on flow patterns for air-water flow in horizontal pipes, International journal of

multiphase flow 13 (4) (1987) 549–563.
[40] C. Baroczy, Systematic correlation for two-phase pressure drop., in: Chem. Eng. Progr., Symp. Ser., 62: No. 64, 232-49 (1966)., Atomics International, Canoga Park, Calif., 1966.
[41] S. Zivi, Estimation of steady-state steam void-fraction by means of the principle of minimum entropy production.
[42] J. Turner, G. Wallis, Two-phase flow and boiling heat transfer. the separate-cylinders model of two-phase flow. interim report, Tech. rep., Thayer School of Engineering, Dartmouth Coll., Hanover, NH (1965).
[43] A. H. Hasan, G. Lucas, Experimental and theoretical study of the gas–water two phase flow through a conductance multiphase venturi meter in vertical annular (wet gas) flow, Nuclear Engineering and Design 241 (6) (2011) 1998–2005.
[44] D. Chisholm, Two phase flow through sharp-edged orifices, research note, J. Mech. Eng. Sci 19 (1977) 127–129.

Thermal turbulence modelling of liquid metal flows via data-driven techniques

Matilde Fiore

Environmental and Applied Fluid Dynamics Department, von Karman Institute for Fluid Dynamics, Belgium, matilde.fiore@vki.ac.be

Supervisor: Lilla Koloszar

Research Engineer, Environmental and Applied Fluid Dynamics Department, von Karman Institute for Fluid Dynamics, Belgium, lilla.koloszar@vki.ac.be

Supervisor: Miguel Alfonso Mendez

Assistant Professor, Environmental and Applied Fluid Dynamics Department, von Karman Institute for Fluid Dynamics, Belgium, miguel.alfonso.mendez@vki.ac.be

Supervisor: Jeroen van Beeck

Dean of Faculty, Environmental and Applied Fluid Dynamics Department, von Karman Institute for Fluid Dynamics, Belgium, vanbeeck@vki.ac.be

University Supervisor: Yann Bartosiewicz

Professor, Mechanical Engineering Department, Universite catholique de Louvain UCL, Belgium, yann.bartosiewicz@uclouvain.be

Abstract

Liquid metals play a central role in new generation liquid metal cooled nuclear reactors, for which numerical investigations require the use of an appropriate thermal turbulence model for low Prandtl number fluids. Given the limitations of traditional modelling approaches and the increasing availability of high-fidelity data for this class of fluids, we propose a Machine Learning strategy for the modelling of the turbulent heat flux. Two different modelling approaches are proposed in the framework of this project: the first consists of a data-driven Algebraic Heat Flux Model (AHFM), while the second seeks to extend a Differential Transport Heat Flux Model (DTHFM) to low Prandtl number fluids. The modelling developments are constrained by physical and mathematical properties promoting robustness and realizability. Field inversion and artificial neural networks are the main tools applied to generate the closures. The validation against data for flows of academic interest shows that the methodology is promising.

Keywords: Prandtl number, heat flux, turbulence modelling, ANN

1. Introduction

Heat transfer in liquid metals is fundamental in many engineering applications, including high-performance cooling systems in new generation nuclear reactors. For such systems, the thermal hydraulics conditions establishing during normal operation and transients must be carefully analyzed for economic and safety reasons.

The numerical approach is often preferred to the experimental one, due to the severe operating conditions of these flows, their metal opaqueness and chemical aggressiveness. However, current thermal turbulence modelling should advance to get reliable predictions for these kind of flows, since the low Prandtl numbers of liquid metals make the similarity between momentum and thermal field less justified. Hence, traditional modelling concepts, as the Reynolds' analogy [1], seem not recommended to accurately simulate these flows, as shown in a number of available works on this topic [2; 3; 4].

The increasing availability of high-fidelity data

opens the way to Machine Learning techniques to develop more accurate thermal models for low Prandtl number flows. In particular, Artificial Neural Networks (ANNs) earned increasing popularity in the field of turbulence modelling [5; 6; 7; 8; 9] by solving high-dimensional and highly non-linear regression problems and generalizing well outside the conditions employed for the training. Classical feed-forward neural networks provide pointwise input-output mappings that can be used to construct sophisticated algebraic closures. Algebraic turbulence models are appealing for their simplicity, numerical stability and easy calibration. Several networks configurations can be found in literature acting as algebraic closures for the Reynolds stresses [5; 6; 9; 7] or the turbulent heat flux [8]. To ensure the generality and the applicability of the formulations, fundamental properties need to be embedded into the data-driven mathematical structure. Examples of these properties are the invariance under rotation [10] required by any consistent tensorial or vectorial modelled quantity, or the positiveness of the Reynolds stresses [7] guaranteeing their realizability.

Regardless of the amount of training data and the number of constraints enforced into the model structure, the performances of the algebraic closures are limited by their inherent locality and the absence of historical effects [11]. Such limitations seem critical at low Prandtl numbers, as the significant thermal diffusion make the single-point approach less justified. Differential models introduce historical and non-local effects, though their calibration with data-driven techniques is challenged by the need of integrating the transport equation each time a sample model is tested. To face this issue, Duraisamy and coworkers [12; 13] and Diez [14] proposed a methodology based on inference and regression steps. During the inference step, the distribution of the modelled coefficients or parameters is estimated for the whole database by solving the PDEs-constrained optimization problem. Then, the collected data are used as reference to apply supervised learning techniques (e.g. Gaussian processes, ANNs) to end up with the functional form of the modelled quantities.

This paper presents the status of development of data-driven thermal turbulence models for low Prandtl fluids. After a brief description of the reference database given in section 2, section 3 presents the developed data-driven AHFM and its performance and limitations detected in the *a priori* and *a posteriori* validation. Section 4 introduces the data-driven DHFM that is being built with the aid of field inversion and artificial neural networks. In particular, first results related to the inference phase are presented and discussed.

2. Training database

The database used for the thermal turbulence modelling consists of DNS datasets related to different forced convection flows at various Re and Pr numbers. The details of the datasets are summarized in Table 1. Most of these databases concern standard, quasi two-dimensional flow configurations simulated at various Reynolds and Prandtl numbers and with different thermal boundary conditions. In particular, the databases of Kawamura et al. [15], Tiselji et al. [16] and Bricteux et al. [17; 18] consist of DNS simulations of non-isothermal turbulent channel flow at Reynolds number ranging from $Re_\tau = 180$ to 2000 and Prandtl number from 0.01 to 0.71. Li et al. [19] provided the DNS data of a non-isothermal turbulent boundary layer flow simulation at Re_θ=800, and Prandtl numbers of 0.71 and 0.2.

Beside these academic flows, additional three-dimensional flow configurations were used for training and test the current model to promote its robustness to real world applications. Specifically, the database of Oder et al. [20] refers to a three-dimensional confined backward facing step flow at $Re_b = 3200$ and with an expansion ratio of 2.25. The forced convective heat transfer for this flow configuration was simulated at Prandtl numbers of 0.1 and 0.005, which is typical of sodium. Angeli et al. [21] provided data related to convective heat transfer around cylindrical rods arranged in bundles. This flow reaches a $Re_\tau = 550$ in the lattice subchannels and the $Pr = 0.031$ is considered as representative of liquid Lead-Bismuth Eutectic (LBE).

3. Algebraic Heat Flux Model (AHFM)

3.1. Mathematical model

The algebraic model for the turbulent heat flux $\overline{\mathbf{u}\theta}$ is based on a generalised gradient hypothesis for which the heat flux is written as the product of a dispersion tensor $\mathbf{D}$ with the mean temperature gradient:

$$\overline{\mathbf{u}\theta} = -\mathbf{D}\nabla T, \quad \mathbf{D} = f\left(\mathbf{b}, \mathbf{S}, \mathbf{\Omega}, \|\nabla T\|, k, \epsilon, k_\theta, \epsilon_\theta, \alpha, \nu\right). \tag{1}$$

Table 1: Available DNS databases for forced convection at different *Re* and *Pr* numbers

Author and Ref.	Flow Configuration	Reynolds number*	Prandtl number	Usage
Kawamura et al.[15]	Channel flow	Re_τ=180-640	0.025-0.71	training/test
Li et al. [19]	Turbulent Boundary Layer	Re_θ=830	0.2, 0.71	training/test
Tiselj et al. [16]	Channel flow	Re_τ=180-590	0.01	training/test
Oder et al. [20]	Backward-Facing Step	Re_b=3200	0.1,0.005	training/test
Angeli et al. [21]	Rode Bundle Flow	Re_τ =550	0.031	test
Bricteux et al. [17; 18]	Channel flow	Re_τ =180-2000	0.01-0.025	test

* The complete definition of the Reynolds number for each flow configuration can be found in the related references.

where **b**, **S** and **Ω** are given by

$$b_{ij} = \frac{\overline{u_i u_j}}{k} - \frac{2}{3}\delta_{ij}, S_{ij} = \frac{1}{2}\left(\frac{\partial U_i}{\partial x_j} + \frac{\partial U_j}{\partial x_i}\right), \qquad \Omega_{ij} = \frac{1}{2}\left(\frac{\partial U_i}{\partial x_j} - \frac{\partial U_j}{\partial x_i}\right). \tag{2}$$

and the reader is referred to the nomenclature for the definition of the other parameters. The modelling of tensor **D** is aided by the introduction of physical and mathematical constraints that are convenient to get a general and realizable formulation. In particular, we seek to construct a model which satisfies invariance under rotation and which is consistent with the second law of thermodynamics.

The property of invariance under rotation requires to restrict the functional tensorial form indicated in eq. (1) to all the possible linear mappings from **D** to a finite basis of independent tensors that can be formed from polynomials of tensors **b**, **S** and **Ω**. In practice, this constraint restricts the parameters of the nonlinear regression problem to isotropic variables, i.e. quantities that are invariant under any rotation of the coordinate system. The consistency with the second law of thermodynamics requires that the real part of the eigenvalues of **D** are positive, to prevent conditions of reverse heat flux.

The above conditions were integrated into the model structure by applying the tensor representation theory [22] under the assumption of quasi two-dimensional flow. This hypothesis allows to restrict the basis of independent tensors and invariants for the given set of parameters (eq.(1)), whose number would significantly increase in the more general, three-dimensional case. The Buckingham theorem was then applied to the set of independent scalar variables. These steps led to the following definition of **D**:

$$\mathbf{D} = \left[(\mathbf{A} + \mathbf{A}^T)(\mathbf{A}^T + \mathbf{A}) + \frac{k}{\epsilon^{0.5}}(\mathbf{W} - \mathbf{W}^T)\right], \tag{3}$$

where **A** and **W** are written as linear combinations of the basis tensors $\mathbf{T}^i$ indicated in the second column of Table 2 :

$$\mathbf{A} = \sum_{i=1}^{n} a_i \mathbf{T}^i, \qquad \mathbf{W} = \sum_{i=1}^{n} w_i \mathbf{T}^i, \tag{4}$$

and a_i and w_i are arbitrary functions of the invariant dimensionless groups in first column of Table 2:

$$a_i = f_i(\pi_i, Re_t, Pr), \qquad w_i = g_i(\pi_i, Re_t, Pr). \tag{5}$$

This mathematical structure ensures that the model satisfies rotational invariance and realizability by construction, regardless of the particular functional form assumed for the coefficients a_i and w_i.

3.2. Structure of the neural network, training and corrections

The coefficients a_i and w_i of the expansion series introduced by eq.(4) are modelled by an artificial neural network developed in Pytorch[1]. The structure of the ANN is depicted in Figure 1: the network consists of two input layers for the invariant basis and the molecular Prandtl number, respectively. Six and one hidden layers are set for the first and the second branches of the network, respectively. The layers have 100 units each with rectified linear unit and hyperbolic tangent activation functions. The two branches of the network merge through a multiplication of the outputs performed in the final layer. Then, the turbulent heat flux is calculated following eq. (4), (3) and (1).

[1] See https://pytorch.org/

Table 2: Basis tensors and invariants.

Invariant Basis	Tensor Basis
$\pi_1 = \frac{k^2}{\epsilon^2}\{\mathbf{S}^2\}$, $\pi_2 = \frac{k^2}{\epsilon^2}\{\mathbf{\Omega}^2\}$, $\pi_3 = \frac{1}{\{\mathbf{b}\}}$, $\pi_4 = \frac{k}{\epsilon}\{\mathbf{bS}\}$, $\pi_5 = \{\mathbf{b}_2\}$, $\pi_6 = \{\mathbf{bS\Omega}\}$, $\pi_7 = \frac{\|\nabla T\|}{\sqrt{k_\theta}}\frac{k^{3/2}}{\epsilon}$, $\pi_8 = \frac{k_\theta \epsilon}{k \epsilon_\theta}$, $Re_t = \frac{k^2}{\epsilon\nu}$, $Pr = \frac{\nu}{\alpha}$	$\mathbf{T_1} = \frac{k}{\epsilon^{1/2}}\mathbf{I}$, $\mathbf{T_2} = \frac{k}{\epsilon^{1/2}}\mathbf{b}$, $\mathbf{T_3} = \frac{k^2}{\epsilon^{3/2}}\mathbf{S}$, $\mathbf{T_4} = \frac{k^2}{\epsilon^{3/2}}\mathbf{\Omega}$, $\mathbf{T_5} = \frac{k^2}{\epsilon^{3/2}}\mathbf{bS}$, $\mathbf{T_6} = \frac{k^2}{\epsilon^{3/2}}\mathbf{b\Omega}$, $\mathbf{T_7} = \frac{k^3}{\epsilon^{5/2}}\mathbf{S\Omega}$, $\mathbf{T_8} = \frac{k^3}{\epsilon^{5/2}}\mathbf{bS\Omega}$

The loss function employed for the training promotes the smoothness of the predicted heat flux[2] by taking into account the error made in terms of heat flux derivatives:

$$\mathcal{J} = \frac{1}{N}\left(\sum_{i=1}^{N}\sum_{j=1}^{3}\left(\hat{q}_{i,j} - q_{i,j}\right)^2\right) + \frac{\lambda}{N}\left(\sum_{i=1}^{N}\sum_{j,k=1}^{3}\left|\frac{\partial \hat{q}_{i,j}}{\partial x_k} - \frac{\partial q_{i,j}}{\partial x_k}\right|\Delta x_k\right), \tag{6}$$

where $i \in [1, \dots N]$ is the index spanning across the N data points contained in each mini-batch, $q_{i,j} = \overline{u_j\theta}$ is the prediction of the ANN and $\hat{q}_{i,j}$ is the corresponding flux provided by DNS data. Both values $q_{i,j}$ and $\hat{q}_{i,j}$ are normalized with respect to the maximum DNS value achieved in each flow configuration. The hyperparameter λ was empirically set to 10.

Since the developed AHFM is gradient based by definition (eq. (1)) it has troubles to handle regions of vanishing thermal gradients, where the formulation becomes ill-posed. A particular training strategy based on noise addition was applied to mitigate this issue. Moreover, the predicted dispersion tensor is corrected a posteriori to prevent extremely large values of $\mathbf{D}$ in the zones where the temperature gradient tends to zero. We refer the reader to a previous work [23] for further details about the training procedure and the corrections applied after the training.

3.3. Results

The validation of the data-driven model consisted in an *a priori* validation (the model is directly applied to the high-fidelity data excluded from the training) and an *a posteriori* validation (the model is integrated into the CFD solver and applied to close the energy equation). Figure 2 shows the heat flux predicted by the model when applied to training and test data related to non-isothermal turbulent channel flow at various Reynolds and Prandtl numbers. The ANN accurately fits the DNS data in this wide range of Prandtl numbers, also matching the correct near-wall behaviour for both the components of the turbulent heat flux. The accuracy of the predictions is similar for both training and test data, showing that the network does not overfit the training data.

The data-driven AHFM was also used to predict the turbulent heat flux over the DNS data of the rode bundle flow [21], which was not used for the model training. The turbulent heat flux predictions in the x and y directions are depicted in Figure 3. The data driven model underestimates the peak values achieved by the heat flux in the gaps by around 10%, though its distribution agrees very well with the DNS counterpart.

In the *a posteriori validation*, the data-driven AHFM was implemented in OpenFoam and applied in combination with two different momentum turbulence closures, i.e. the Elliptic Blendin Reynolds Stress Model (EBRSM) developed by Manceau [24] and the Launder-Sharma k-ϵ model. Figure 4 compares the wall-normal heat fluxes obtained by simulating non-isothermal turbulent channel flows up to $Re_\tau = 2000$ with the data-driven AHFM combined with the EBRSM. Note that, even if the network was trained up to $Re_\tau = 640$ at $Pr = 0.025$ and up to $Re_\tau = 590$ at $Pr = 0.01$, the model is able to extrapolate very well at higher Re_τ and accurately reproduces the correct heat fluxes at $Re_\tau = 2000$. These generalisation properties are very important for the practical applicability of the formulation, as industrial problems usually involve much higher Reynolds numbers than those encountered in the current training database.

Figure 5 depicts the temperature field obtained with the simulation of the non-isothermal turbulent channel flow at $Re_\tau = 395$ and $Pr = 0.025$[3]. The results are compared with the ones obtained with other thermal turbulence closures [25; 26; 27] for low Prandtl number fluids. Figure 5 also compares the results obtained

[2]The smoothness of the heat flux field is an important requirement, as this quantity enters the averaged energy equation through its divergence.

[3]Note that these conditions were excluded from the training for a meaningful validation.

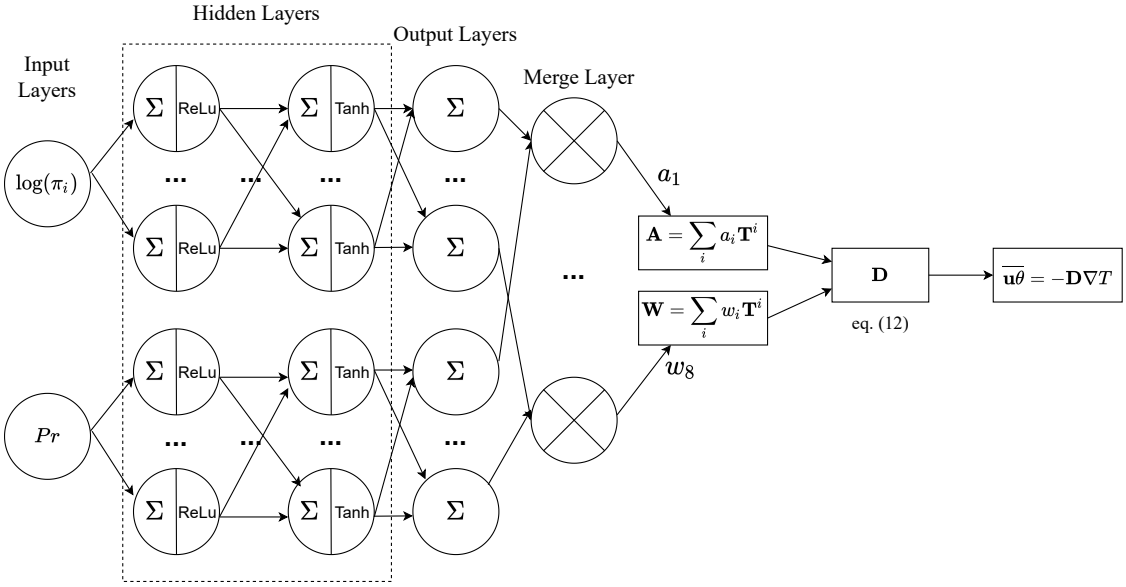

Figure 1: Structure of the artificial neural network used to predict the turbulent heat flux (AHFM) as a function of the molecular Prandtl number and the basis of invariants indicated in Table 2.

by coupling the model with the EBRSM (Figure 5a) and the Launder-Sharma k-ϵ (Figure 5b). When the thermal models are combined with the EBRSM as momentum closure, the temperature field computed with the data-driven AHFM is more accurate than the ones obtained with the other thermal models. On the other hand, if the ANN is coupled with the k-ϵ model, it gives the least accurate temperature predictions. This behaviour is expected, since the model was trained over a *frozen* momentum field taken from the DNS data. The resulting model is in fact significantly sensitive to the anisotropic part of the Reynolds stresses, which is roughly represented by the Boussinesq approximation. For further details, the reader is referred to Ref. [23] where the data-driven AHFM is interpreted with the Integrated Gradient Method [28] to explain such a sensitivity.

4. Differential Transport Heat Flux Model (DTHFM)

This section presents the current status of development of the data-driven DTHFM. In particular, we present the field inversion technique applied to infer the values of the unknown model parameters. The collected data will be used in future to train an ANN that will support the second order thermal turbulence model.

4.1. Mathematical model

The development of the DTHFM starts from a baseline formulation developed by Dehoux et al. [29] which is based on the elliptic blending concept. The transport equations for the turbulent heat flux components are expressed as:

$$\frac{D\overline{u_i\theta}}{Dt} = \left(-\overline{u_iu_j}\frac{\partial T}{\partial x_j} - \overline{u_j\theta}\frac{\partial U_i}{\partial x_j}\right) + D_{i\theta} + T_{i\theta} + \beta_1\phi_{i\theta} - \beta_2\epsilon_{i\theta}. \quad (7)$$

where the expressions for the molecular diffusion ($D_{i\theta}$) turbulent transport ($T_{i\theta}$), redistribution ($\phi_{i\theta}$) and dissipation ($\epsilon_{i\theta}$) terms are given in [29], and the parameters β_1 and β_2 are herein introduced to extend the baseline model to low Prandtl number fluids. The choice of correcting the terms $\phi_{i\theta}$ and $\epsilon_{i\theta}$ is justified by the analysis of the budget terms provided by some DNS databases [15; 19], for which the redistribution and dissipation terms significantly change their ratio in the whole balance by passing from near unity to low Prandtl number fluids.

4.2. Field inversion

The parameters β_1 and β_2 need to be inferred for the available test cases to improve the predictions in terms of heat flux. This requires to solve a constrained

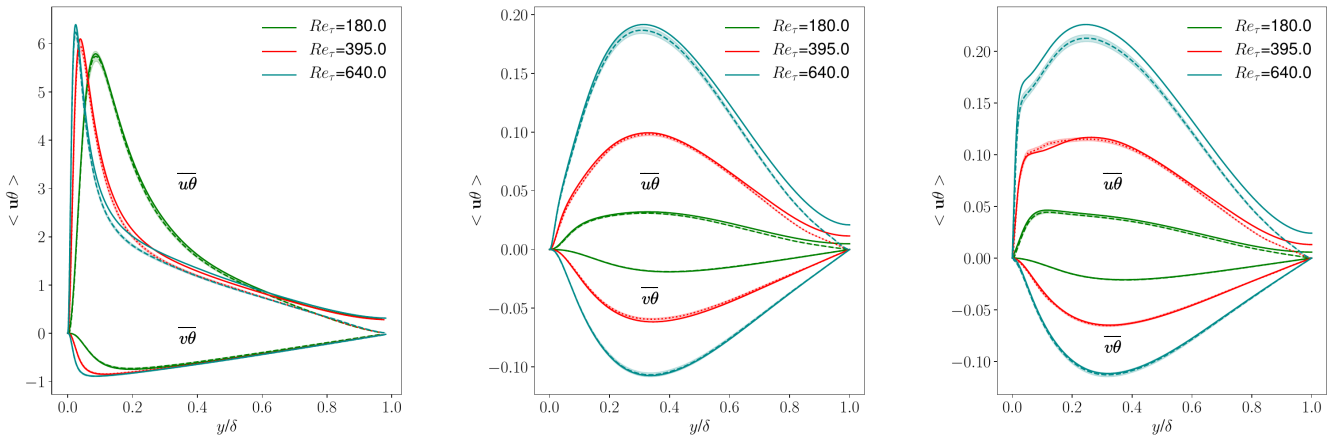

(a) $Pr = 0.71$ (b) $Pr = 0.025$ (c) $Pr = 0.01$

Figure 2: Streamwise and wall-normal components of the turbulent heat flux predicted by the AHFM after the training. Predictions in the training range and validation range are depicted with dashed and dotted lines, respectively. Shaded areas represent the uncertainty ranges of the heat flux predictions estimated with dropout. DNS data [15] are indicated with solid lines.

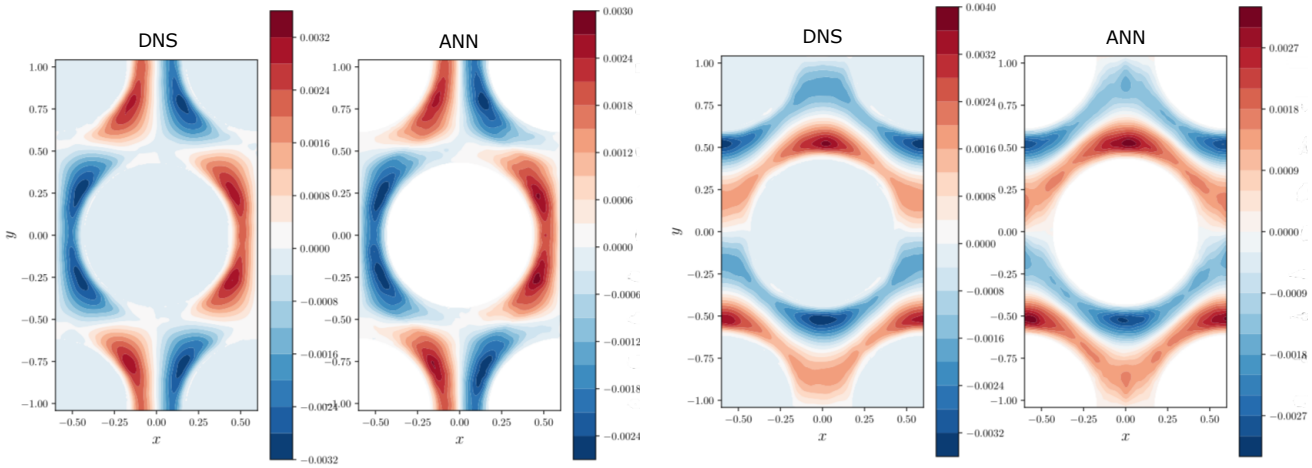

(a) $\overline{u\theta}$ (b) $\overline{v\theta}$

Figure 3: Contours of the x and y components of the turbulent heat flux in case of rode bundle flow at $Pr = 0.031$. Comparison of the AHFM predictions with the corresponding DNS data [21].

optimization problem for $\boldsymbol{\beta} = [\beta_1, \beta_2]$:

$$\boldsymbol{\beta}_{opt} = argmin\mathcal{J}, \tag{8}$$

$$\mathcal{J} = \frac{1}{2}\left((\hat{\mathbf{q}} - \mathbf{q}(\beta))^T \mathbf{C}_m^{-1}(\hat{\mathbf{q}} - \mathbf{q}(\beta)) + (\boldsymbol{\beta} - \mathbf{1})^T \mathbf{C}_\beta^{-1}(\boldsymbol{\beta} - \mathbf{1})\right), \tag{9}$$

where $\hat{\mathbf{q}}$ is the reference heat flux given by the DNS data and $\mathbf{q}(\boldsymbol{\beta})$ is the heat flux obtained by integrating the differential model given by eq. (4). The constraint imposed enforces the residual $\mathcal{R}$ of the heat flux transport equations to be zero:

$$\mathcal{R}(\mathbf{q}(\boldsymbol{\beta}), \boldsymbol{\beta}) = 0. \tag{10}$$

The first term on the right-hand side of eq.(9) indicates the mean squared error made on the heat flux, while the second is a regularization term that tends to limit

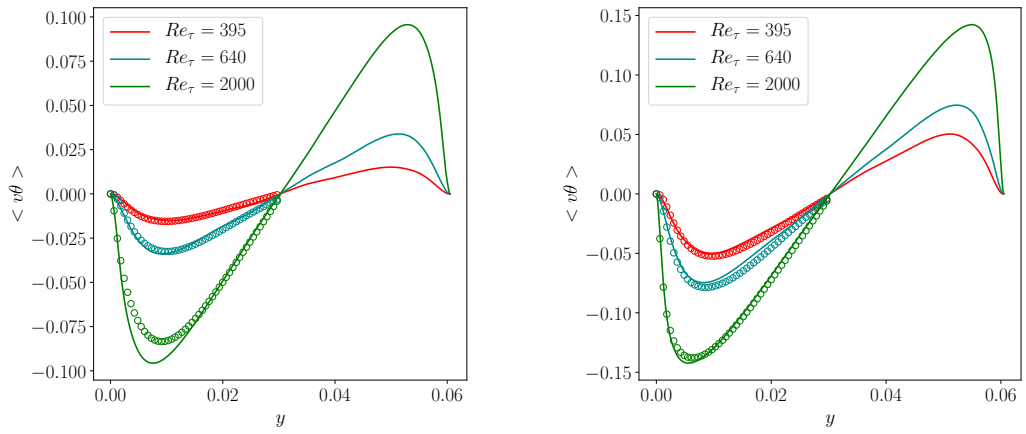

(a) $Pr = 0.01$ (b) $Pr = 0.025$

Figure 4: Comparison of the wall-normal heat flux computed with the data-driven AHFM with the corresponding DNS [15] and LES data [18] for simulations of non-isothermal turbulent channel flows at Re_τ up to 2000.

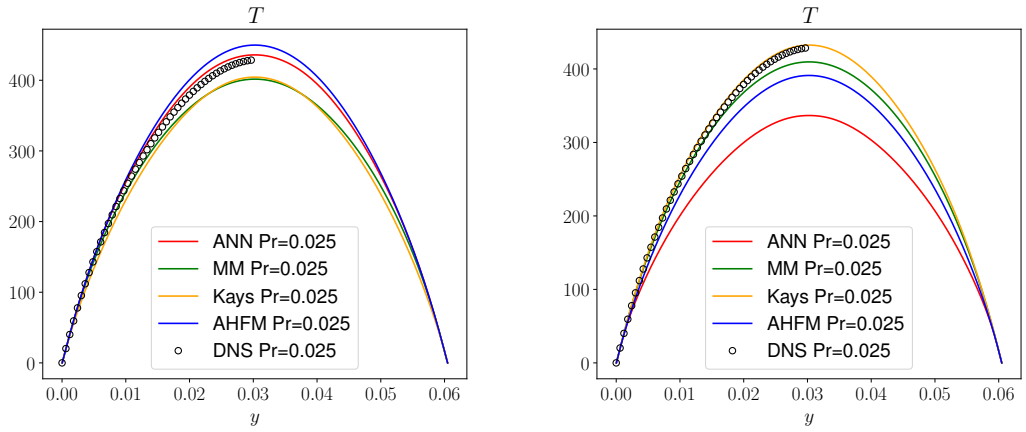

(a) EBRSM (b) Launder-Sharma $k - \epsilon$

Figure 5: Comparison of the temperature profiles obtained with the data-driven AHFM and other thermal turbulence closures [27; 26; 25] for a non-isothermal turbulent channel flow at $Re_\tau = 395$ and $Pr = 0.025$. The thermal models are combined with the EBRSM [24] and the Launder-Sharma $k - \epsilon$ model.

the magnitude of the correction. In a Bayesian perspective, the matrices $\mathbf{C}_m$ and $\mathbf{C}_\beta$ can be interpreted as observational and prior covariance matrices, respectively, as done in Ref. [12]. Eq. (10) enforces the residuals of the heat flux transport equations (eq.(7)) to be zero.

As the dimensionality of the optimization problem scales with the number of mesh points, the adjoint method [30] is applied to compute the gradients to reduce the computational efforts. Hence, the gradient is computed as:

$$\frac{d\mathcal{J}}{d\boldsymbol{\beta}} = \frac{\partial \mathcal{J}}{\partial \boldsymbol{\beta}} + \psi^T \frac{\partial \mathcal{R}}{\partial \boldsymbol{\beta}}, \tag{11}$$

with

$$\left(\frac{\partial \mathcal{R}}{\partial \mathbf{q}}\right)^T \psi = -\left(\frac{\partial \mathcal{J}}{\partial \mathbf{q}}\right)^T. \tag{12}$$

The partial derivatives $\frac{\partial \mathcal{R}}{\partial \mathbf{q}}$ and $\frac{\partial \mathcal{R}}{\partial \boldsymbol{\beta}}$ are computed ana-

lytically after having discretized the derivatives of the operating variables (β_1, β_2, $\overline{u\theta}$, $\overline{v\theta}$) with finite differencing. Several gradient-based optimization methods are applied to solve the above minimization problem, i.e. the BFGS [31], the Truncated Newton method (TNC) [32], the Conjugate Gradient method (CG) [33] and the Bold Drive Method with added momentum (BDM) [34].

After having optimized the distributions of β_1 and β_2, the uncertainty ranges for these parameters are estimated by assuming that the probability distributions of the reference data ($\hat{\mathbf{q}}$) and the optimized parameters ($\boldsymbol{\beta}$) are Gaussian. Hence, the posterior covariance matrix is computed as:

$$\mathbf{C}_{\beta,post} = \mathbf{H}^{-1} + \mathbf{C}_{\beta}, \tag{13}$$

where a first order approximation is used to compute the Hessian matrix $\mathbf{H}$:

$$\mathbf{H} = \left(\frac{\partial \mathcal{J}}{\partial \mathbf{q}}\frac{\partial \mathbf{q}}{\partial \boldsymbol{\beta}}\right)\left(\frac{\partial \mathcal{J}}{\partial \mathbf{q}}\frac{\partial \mathbf{q}}{\partial \boldsymbol{\beta}}\right)^{T}. \tag{14}$$

Following the same approach presented in [12], the uncertainty ranges are then constructed by sampling from the posterior distribution:

$$\mathbf{R}\mathbf{R}^{T} = \mathbf{C}_{\beta,post}, \tag{15}$$

$$\boldsymbol{\beta} = \boldsymbol{\beta}_{opt} + \mathbf{R} \cdot \mathcal{N}(0,1). \tag{16}$$

The uncertainty ranges obtained are qualitative, rather than quantitative, since the matrices $\mathbf{C}_m$ and $\mathbf{C}_\beta$ are unknown. Herein, the covariance matrices are assumed diagonal $\mathbf{C}_m = \sigma_m^2\mathbf{I}$ and $\mathbf{C}_\beta = \sigma_\beta^2\mathbf{I}$, with σ_m and σ_β given by 0.001 and 0.5, respectively.

4.3. Results

Figure 6 shows the decay of the cost function given by eq. (9) for several cases of non-isothermal turbulent channel flow at several Re_τ and Prandtl numbers of 0.71, 0.025 and 0.01. Among the different optimizers, the Conjugate Gradient (CG) and the Bold Driven (BDM) methods achieved the lowest value of the cost function. The distributions of the parameters β_1 and β_2 over the channel width and their uncertainty ranges are presented in figures 7 and 8. The correction is more significant at $Pr = 0.025$ and 0.01 than for $Pr = 0.71$. This was expected, as the original model [29] was validated for near unity Prandtl numbers. The distribution of the uncertainty ranges show that, for β_1, the uncertainty is minimum in the logarithmic region of the boundary layer ($y^+ > 10$). Very close to the wall and the near centerline, the uncertainty in β_1 is higher as the redistribution term $\phi_{i\theta}$ tends to zero. For β_2, the minimum uncertainty is reached in the viscous sublayer ($1 < y^+ < 10$) where the dissipation term $\epsilon_{i\theta}$ is the dominant term in the overall balance. These considerations indicate the low sensitivity of $\overline{v\theta}$ to the values of β_1 and β_2 in a wide portion of the channel width, and suggest to modify the current parametrization to increase the sensitivity and reduce the uncertainties. Figure 7 also shows that the β_1 peaks move to higher y^+ when the Prandtl number changes from 0.71 to 0.025 and 0.01. This is in agreement with the thickening of the thermal boundary layer at low Prandtl number.

Figure 9 indicates the improvements in terms of wall-normal heat flux achieved by solving the inverse problem. While small improvements are reached at $Pr = 0.71$, for $Pr = 0.025$ and 0.01 the agreement is considerably higher than with the base model.

The DNS budgets at $Re_\tau = 640$ and $Pr = 0.025$ are compared with the budgets given by the original model and the model optimized with Field Inversion (Figure 10). There is still inconsistency between the DNS data and the original model regarding the term $\phi_{i\theta} - \epsilon_{i\theta}$. However, the optimization improves the agreement of this term with the DNS data very close to the wall.

5. Conclusion

Data-driven approaches were applied to leverage the high-fidelity data available for low Prandtl number fluids to construct more accurate thermal models. An algebraic mathematical structure was primarily preferred for its simplicity, stability and limited computational effort. The data-driven AHFM was capable to accurately fit the DNS data in a wide range of Prandtl numbers and to generalize well outside the range of data used for the training. On the other hand, the data-driven formulation showed to be significantly sensitive to the modelling of the Reynolds stresses, and the model looses its accuracy when combined with momentum models based on the Boussinesq approximation. Also, the generalized gradient assumption at the basis of the AHFM makes the model ill-posed in the vanishing gradient regions, thus requiring corrections during and after the training. The algebraic mathematical structure also neglects historical and non-local effects that seem important for this class of fluids.

These considerations led to the development of a DTHFM starting from a baseline formulation validated for at unity Prandtl numbers. The first step

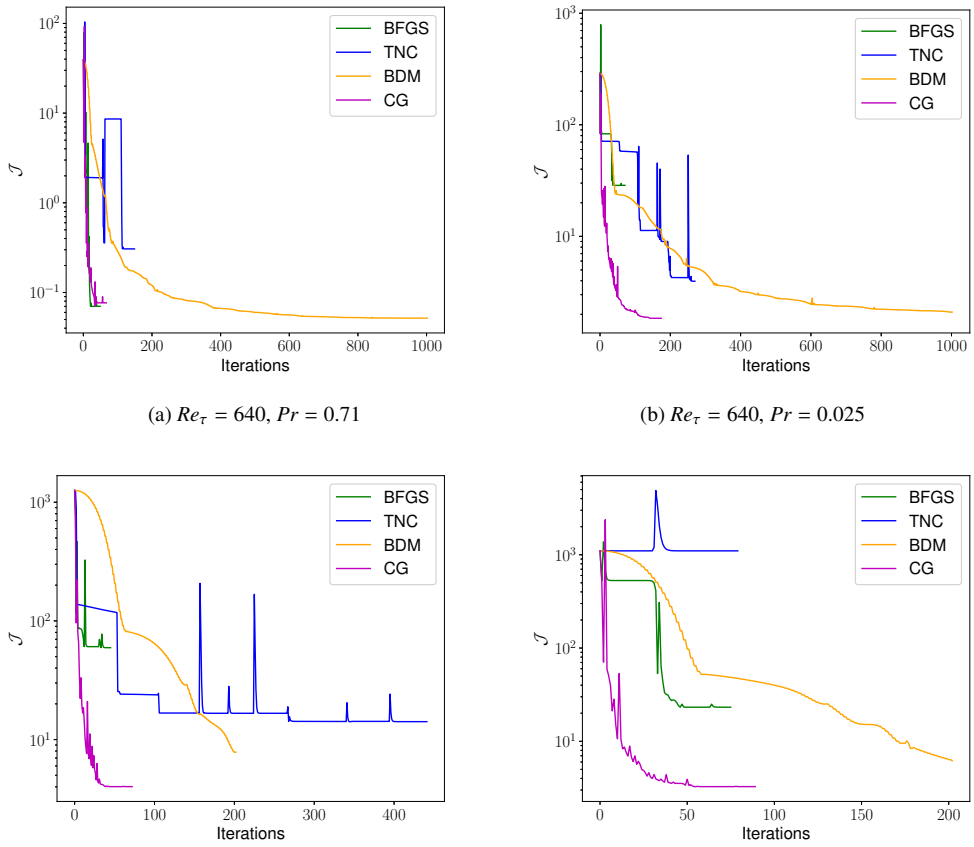

(a) $Re_\tau = 640$, $Pr = 0.71$

(b) $Re_\tau = 640$, $Pr = 0.025$

(c) $Re_\tau = 590$, $Pr = 0.01$

(d) $Re_\tau = 395$, $Pr = 0.01$

Figure 6: Decay of the cost function (9) with several optimizers in case of non-isothermal turbulent channel flow at different Re and Pr numbers.

of the methodology consisted in inferring the values of two correction coefficients for simple channel flow configurations by solving the inverse problem. The inferred correction parameters proved to be effective to improve the agreement with the reference data at low Prandtl numbers. However, the retrieved uncertainty distributions and the disagreement in terms of singular budget terms suggest to improve the parametrization to increase the reliability of the optimized field. This would ease the following regression phase, where the collected results will be used as target to train a neural network model.

Nomenclature

$\mathbf{U}$	[m/s]	Mean velocity
T	[K]	Mean Temperature
k	[m^2/s^2]	Turbulent kinetic energy
ϵ	[m^2/s^3]	Turbulent dissipation rate
k_θ	[K^2]	Thermal variance
ϵ_θ	[K^2/s]	Thermal dissipation rate
$\overline{\mathbf{uu}}$	[m^2/s^2]	Reynolds stress
$\overline{\mathbf{u}\theta}$	[mK/s]	Turbulent heat flux
$\mathbf{g}$	[m/s^2]	Gravity vector
ν	[m^2/s]	Molecular viscosity
α	[m^2/s]	Molecular diffusivity
δ	[m]	Half channel width
$\boldsymbol{D}_\theta$	[m K /s^2]	Molecular diffusion term
$\boldsymbol{T}_\theta$	[m K /s^2]	Turbulent diffusion term
$\boldsymbol{\phi}_\theta$	[m K /s^2]	Redistribution term
$\boldsymbol{\epsilon}_\theta$	[m K /s^2]	Dissipation term

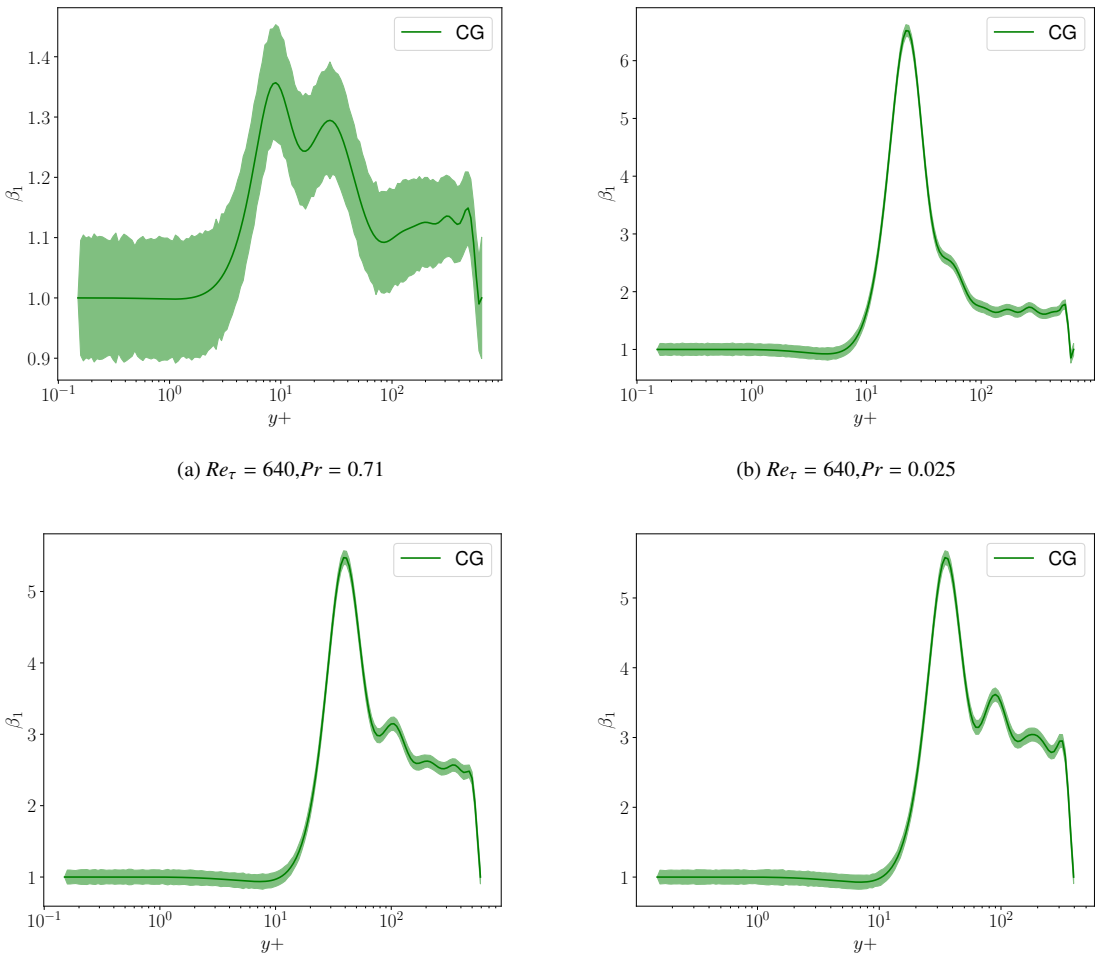

(a) $Re_\tau = 640, Pr = 0.71$

(b) $Re_\tau = 640, Pr = 0.025$

(c) $Re_\tau = 590, Pr = 0.01$

(d) $Re_\tau = 395, Pr = 0.01$

Figure 7: Inferred distributions of β_1 over the channel width for several Re and Pr numbers. Shaded areas indicate the estimated uncertainty ranges.

Acknowledgments

M. Fiore is supported by a F.R.S.-FNRS FRIA grant and gratefully acknowledges Prof. Iztok Tiselj, Prof. Diego Angeli, Dr. Matthieu Duponcheel and Dr. Jure Oder for providing their datasets, as well as Dr. Clyde Fare from IBM for his valuable suggestions during the course of this work.

References

[1] C. J. Geankoplis, Transport processes and separation process principles:(includes unit operations), Prentice Hall Professional Technical Reference, 2003.

[2] Z. Ge, J. Liu, P. Zhao, X. Nie, M. Ye, Investigation on the applicability of turbulent-prandtl-number models in bare rod bundles for heavy liquid metals, Nuclear Engineering and Design 314 (2017) 198–206.

[3] A. Shams, A. De Santis, L. Koloszar, A. V. Ortiz, C. Narayanan, Status and perspectives of turbulent heat transfer modelling in low-prandtl number fluids, Nuclear Engineering and Design 353 (2019) 110220.

[4] M. Ziefuß, A. Mehdizadeh, A comprehensive assessment of the reynolds analogy in predicting heat transfer in turbulent wall-bounded shear flows, International Journal of Heat and Fluid Flow 81 (2020) 108527.

[5] J. Ling, A. Kurzawski, J. Templeton, Reynolds averaged turbulence modelling using deep neural networks with embedded invariance, Journal of Fluid Mechanics 807 (2016) 155–166.

[6] N. Geneva, N. Zabaras, Quantifying model form uncertainty in reynolds-averaged turbulence models with bayesian

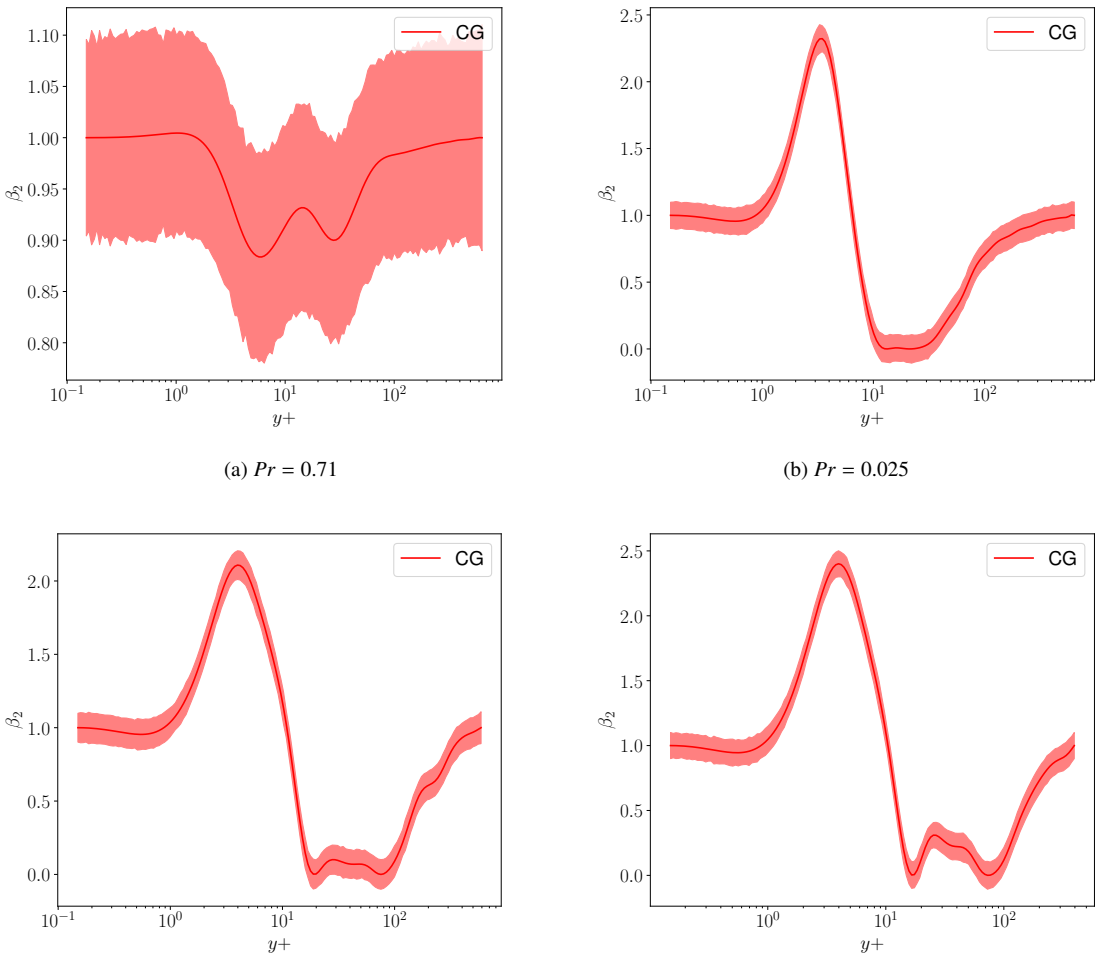

(a) Pr = 0.71

(b) Pr = 0.025

(c) Pr = 0.025

(d) Pr = 0.025

Figure 8: Inferred distributions of β_2 over the channel width for several Re and Pr numbers. Shaded areas indicate the estimated uncertainty ranges.

deep neural networks, Journal of Computational Physics 383 (2019) 125–147.

[7] C. Sotgiu, B. Weigand, K. Semmler, P. Wellinger, Towards a general data-driven explicit algebraic reynolds stress prediction framework, International Journal of Heat and Fluid Flow 79 (2019) 108454.

[8] C. Sotgiu, B. Weigand, K. Semmler, A turbulent heat flux prediction framework based on tensor representation theory and machine learning, International Communications in Heat and Mass Transfer 95 (2018) 74–79.

[9] C. Jiang, J. Mi, S. Laima, H. Li, A novel algebraic stress model with machine-learning-assisted parameterization, Energies 13 (1) (2020) 258.

[10] J. Ling, R. Jones, J. Templeton, Machine learning strategies for systems with invariance properties, Journal of Computational Physics 318 (2016) 22–35.

[11] A. Johansson, Engineering turbulence models and their development, with emphasis on explicit algebraic reynolds stress models, in: Theories of turbulence, Springer, 2002, pp. 253–300.

[12] E. J. Parish, K. Duraisamy, A paradigm for data-driven predictive modeling using field inversion and machine learning, Journal of Computational Physics 305 (2016) 758–774.

[13] B. D. Tracey, K. Duraisamy, J. J. Alonso, A machine learning strategy to assist turbulence model development, in: 53rd AIAA aerospace sciences meeting, 2015, p. 1287.

[14] R. Diez Sanhueza, Machine learning for rans turbulence modelling of variable property flows.

[15] H. Kawamura, H. Abe, K. Shingai, DNS of turbulence and heat transport in a channel flow with different Reynolds and Prandtl numbers and boundary conditions, Turbulence, Heat and Mass Transfer 3 (2000) 15–32.

[16] I. Tiselj, R. Bergant, B. Mavko, I. Bajsic, G. Hetsroni, DNS of turbulent heat transfer in channel flow with heat conduction in the solid wall, J. Heat Transfer 123 (5) (2001) 849–857.

[17] L. Bricteux, M. Duponcheel, G. Winckelmans, I. Tiselj,

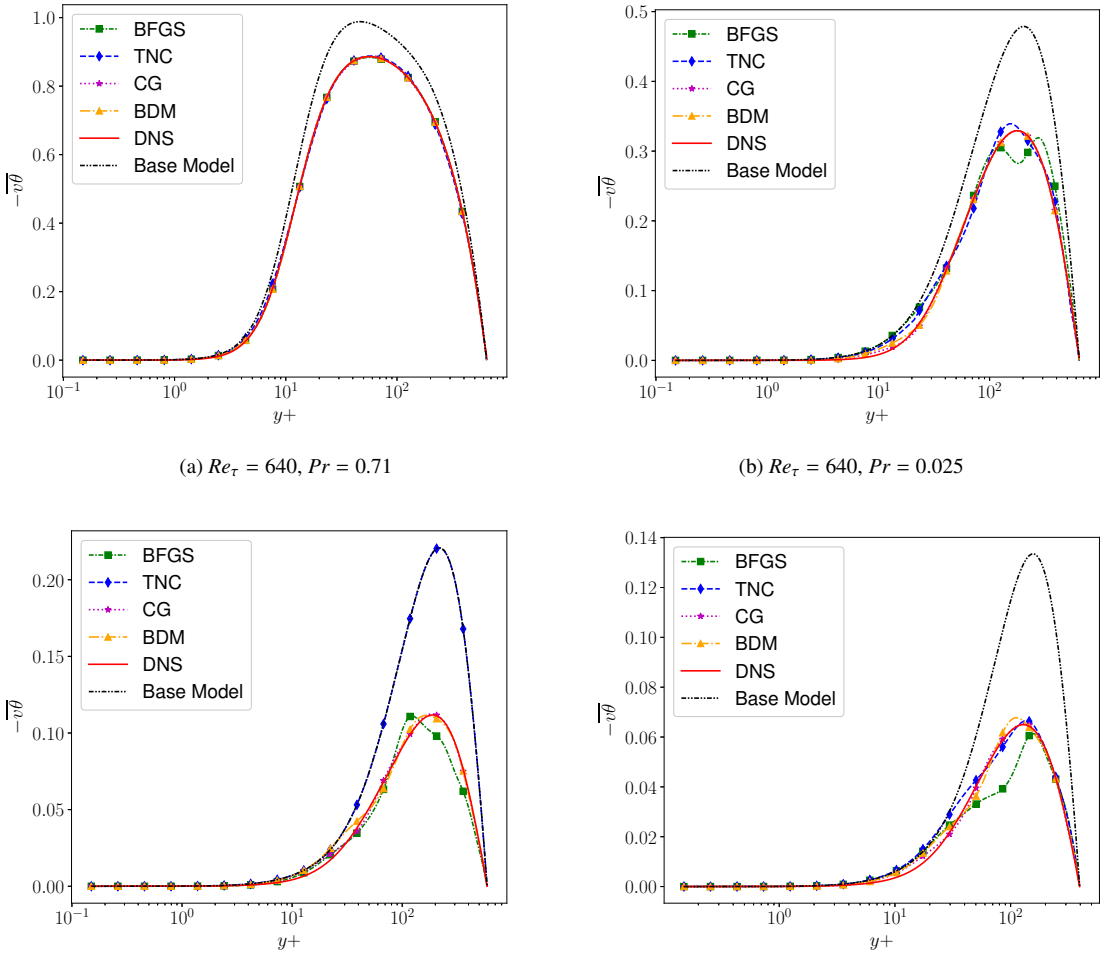

(a) $Re_\tau = 640$, $Pr = 0.71$

(b) $Re_\tau = 640$, $Pr = 0.025$

(c) $Re_\tau = 590$, $Pr = 0.01$

(d) $Re_\tau = 395$, $Pr = 0.01$

Figure 9: Wall-normal components of the turbulent heat flux computed with the baseline DTHFM [29] and the optimized versions obtained with the different optimizers. Comparison with the corresponding DNS data [15; 16].

Y. Bartosiewicz, Direct and large eddy simulation of turbulent heat transfer at very low Prandtl number: Application to lead–bismuth flows, Nuclear engineering and design 246 (2012) 91–97.

[18] M. Duponcheel, L. Bricteux, M. Manconi, G. Winckelmans, Y. Bartosiewicz, Assessment of rans and improved near-wall modeling for forced convection at low prandtl numbers based on les up to reτ= 2000, International Journal of Heat and Mass Transfer 75 (2014) 470–482.

[19] Q. Li, P. Schlatter, L. Brandt, D. S. Henningson, DNS of a spatially developing turbulent boundary layer with passive scalar transport, International Journal of Heat and Fluid Flow 30 (5) (2009) 916–929.

[20] J. Oder, A. Shams, L. Cizelj, I. Tiselj, Direct numerical simulation of low-Prandtl fluid flow over a confined backward facing step, International Journal of Heat and Mass Transfer 142 (2019) 118436.

[21] D. Angeli, A. Fregni, E. Stalio, Direct numerical simulation of turbulent forced and mixed convection of LBE in a bundle of heated rods with P/D= 1.4, Nuclear Engineering and Design 355 (2019) 110320.

[22] A. Spencer, R. Rivlin, The Theory of Matrix Polynomials and its Application to the Mechanics of Isotropic Continua, in: Collected Papers of RS Rivlin, Springer, 1997, pp. 1071–1098.

[23] M. Fiore, L. Koloszar, M. A. Mendez, M. Duponcheel, Y. Bartosiewicz, Physics-constrained machine learning for thermal turbulence modelling at low prandtl numbers, arXiv preprint arXiv:2201.06301.

[24] R. Manceau, An improved version of the elliptic blending model application to non-rotating and rotating channel flows, in: Fourth International Symposium on Turbulence and Shear Flow Phenomena, Begel House Inc., 2005.

[25] A. Shams, F. Roelofs, E. Baglietto, S. Lardeau, S. Kenjeres, Assessment and calibration of an algebraic turbulent heat flux model for low-Prandtl fluids, International Journal of Heat

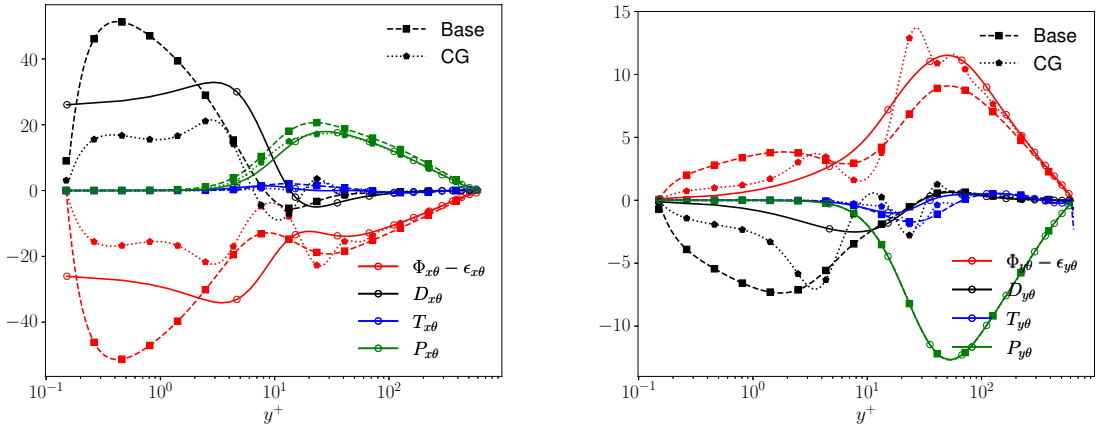

(a) Streamwise budgets

(b) Wall-normal budgets

Figure 10: Distribution of the budget terms over the channel width ($Re_\tau = 640$, $Pr = 0.025$) obtained with the DTHFM [29] and the model optimized with the CG method. Comparison with the corresponding DNS data [15].

and Mass Transfer 79 (2014) 589–601.

[26] W. M. Kays, Turbulent Prandtl number. Where are we?, ASME Transactions Journal of Heat Transfer 116 (1994) 284–295.

[27] S. Manservisi, F. Menghini, A CFD four parameter heat transfer turbulence model for engineering applications in heavy liquid metals, International Journal of Heat and Mass Transfer 69 (2014) 312–326.

[28] M. Sundararajan, A. Taly, Q. Yan, Axiomatic attribution for deep networks, arXiv preprint arXiv:1703.01365.

[29] F. Dehoux, S. Benhamadouche, R. Manceau, An elliptic blending differential flux model for natural, mixed and forced convection, International Journal of Heat and Fluid Flow 63 (2017) 190–204.

[30] M. B. Giles, M. C. Duta, J.-D. Muller, N. A. Pierce, Algorithm developments for discrete adjoint methods, AIAA journal 41 (2) (2003) 198–205.

[31] J. E. Dennis, Jr, J. J. Moré, Quasi-newton methods, motivation and theory, SIAM review 19 (1) (1977) 46–89.

[32] J. Martens, et al., Deep learning via hessian-free optimization., in: ICML, Vol. 27, 2010, pp. 735–742.

[33] G. W. Stewart, Conjugate direction methods for solving systems of linear equations, Numerische Mathematik 21 (4) (1973) 285–297.

[34] R. Battiti, Accelerated backpropagation learning: Two optimization methods, Complex Syst 3.

A journey in the active control of liquid film flows

Fabio Pino

Environmental and Applied Fluid Dynamics Department, von Karman Institute for Fluid Dynamics, Belgium, fabio.pino@vki.ac.be

Supervisor: Miguel Alfonso Mendez

Assistant Professor, Environmental and Applied Fluid Dynamics Department, von Karman Institute for Fluid Dynamics, Belgium, miguel.alfonso.mendez@vki.ac.be

University Supervisor: Benoit Scheid

Professor, Transfers, Interfaces and Processes (TIPs) laboratory, Université libre de Bruxelles, Belgium, benoit.scheid@ulb.ac.be

Abstract

The undulation control is pivotal in the hot-dip galvanizing process. To find an optimal control law, we investigated machine learning control techniques on a simplified test case and to limit the computational efforts, we implemented a reduced order model, based on which e performed a preliminary analysis of the nonlinear liquid film stability to characterize which would be the best actuators' location.

Keywords: liquid film, flow control, metal coating, modelling, machine learning, reinforcement learning

1. Introduction

Liquid coating is a widely used technique in many industrial processes nowadays, with many engineering and scientific challenges [1]. This process consists in applying a liquid layer over a solid substrate to protect it from external elements or to give it specific mechanical or thermic properties. In the hot-dip galvanizing process, a metal strip is dip and withdrawn from a bath of molten zinc to create a thin anti-corrosion protective layer. To be industrially attractive, the coating process needs a control system capable of removing the excess liquid. This is usually achieved with the jet-wiping technique [2]. A gas jet impinges on the free surface and via some geometric and fluid dynamics parameters, the user can control the final coating thickness. Although being easily handled and economically profitable, in certain conditions the liquid film can trigger jet oscillations, which combine with inertia to generate undulation patterns in the final zinc coating. These reduces the final product quality and hence they limit the range of operating conditions [3]. One of the possible solution to this problem would consist in using an active feedback regulator which interact with the system via gas-jets following a control law which defines the best action to take in the light of information coming from sensors, Fig.1. In its most abstract formulation, the (flow) control problem is essentially a functional optimization problem constrained by the (fluid) systems' dynamics [4; 5]. The goal is to find a control function that minimizes (or maximizes) a cost (or reward) functional which measures the wave attenuation.

The control problems can be classified as white, grey or black depending on how much knowledge about the system is used to solve the optimization, [6]: the whiter the approach, the more the control relies on the analytical description of the system to be controlled.

Due to their outstanding performances along with robustness and simplicity of implementation, the black box approach are nowadays in the limelights in the flow control community. Indeed, instead of relying on the governing equation, these methods use only input-output relations in the search for the optimal control law. The popularity of these heuristic approaches has been growing considerably in the last decade, promoted by the popularization of machine learning tools, the development of new algorithms, and the increase in available computational power.

Machine learning[7; 8; 9] is a subset of Artificial

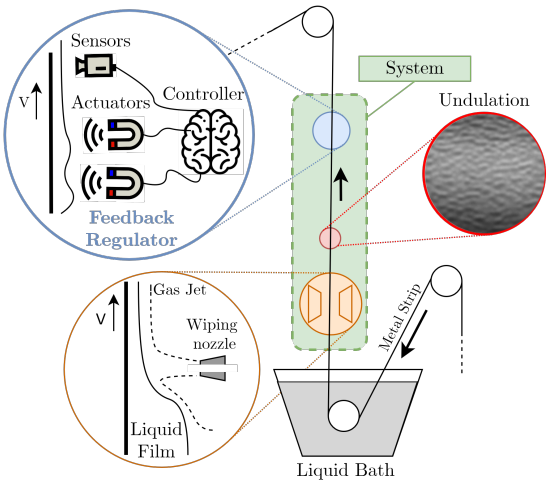

Figure 1: Representation of the hot-dip galvanizing process via jet wiping, the undulation instability resulting in wavy patters in the final coating, and position of the envisaged feedback regulation to cope with this issue

Intelligence which combines optimization and statistics to "learn" (i.e. calibrate) models from data (i.e. experience). These models can be general enough to describe any (nonlinear) function without requiring prior knowledge and can be encoded in various forms: examples are parametric models such as Radial Basis Function (RBFs[10]) expansions or Artificial Neural Networks (ANNs[11]), or tree structures of analytic expressions such as in Genetic Programming (GP[12]). The process by which these models are "fitted" to (or "learned" from) data is an optimization in one of its many forms[13]: continuous or discrete, global or local, stochastic or deterministic. Within the flow control literature, at the time of writing, the two most prominent model-free control techniques from the machine learning literature are Genetic Programming[12] and Reinforcement Learning[14]. Both are tested, and analysed in this article.

Reinforcement Learning (RL) is one of the three main machine learning paradigms and encompasses learning algorithms collecting data "online" in a close loop, trial and error process. In Deep RL (DRL), the control law (known as policy) is modelled by an ANN which needs to be trained.

Genetic Programming (GP) is an evolutionary computational technique developed by Koza[12] as a new paradigm for automatic programming and machine learning[15; 16].

We also include simpler black-box optimization methods. Within this category, we include model-free control methods in which the control action is predefined and prescribed by a few parameters (e.g. PID), we here focus on more sample efficient alternatives: the Bayesian Optimization (BO) and the LiPschitz global Optimization technique (LIPO).

Before attacking the undulation problem, we assessed these techniques on a simplified test case, the control of nonlinear travelling waves described by the 1D Burgers' equation, due to its representativeness of advection-diffusion problems characteristics.

In view of the implementation of these machine learning techniques to the undulation problem, we created a virtual environment based on a reduced order model (ROM) of the process. Indeed, attacking the problem through CFD simulations would have a too big computational cost, reduced-order modelling allows reducing the number of variable keeping the main dynamical characteristics of the process.

One approach for the construction of this ROM is by integral boundary layer (IBL) models, which proves to be especially useful in industrial processes [17]. The dynamics of the liquid film flow is described in terms of film thickness and flow rates on the stream-wise and span-wise directions, as opposed to the Navier Stokes equations where the film thickness, velocity and pressure fields along with the free surface position must be computed. We extend the 2D models in [17] to a 3D configuration similar to the model by [18], here generalized to account for the substrate motion as well as the presence of shear stress and pressure gradient.

The rest of the article is structured as follows. Section 2 introduce the formulation of the optimal control problem, and it bridges its main concept with the machine learning based approach. Section 4 report the derivation and implementation of the 3D integral model along with its linear stability analysis for a 2D perturbation. Then, in section 4 we give some details about the implemented machine learning based algorithms. Section 5 details the vis-cous Burgers equations control problem. Finally, sec-tion 6 show the results of the viscous Burgers test case and of the numerical and theoretical stability analysis.

2. From optimal control to machine learning

This section briefly presents the framework of the optimal control problem, reinforcement learning and global optimization methods. We refer the reader to the literature [14; 19; 4; 5] for more details. We introduce the optimal control problem in 2.1, and we focus on model-free learning based control in 2.2.

2.1. Methods from Optimal Control Theory

An optimal control problem consists in finding a *control action* $\mathbf{a}(t)$, within a feasible set $\mathcal{A}$, which optimizes a functional measuring our ability to keep a flow (*plant* in control theory and *environment* in reinforcement learning) close to the desired states or conditions. The functional is usually a cost to minimize in control theory and a payoff to maximize in reinforcement learning. We focus on the second and denote the reward function as $R(\mathbf{a})$. The optimization is constrained by the plant/environment's dynamic:

$$\max_{\mathbf{a}(t)\in\mathcal{A}} \quad R(\mathbf{a}) = \phi(\mathbf{s}(T)) + \int_0^T \mathcal{L}(\mathbf{s}(\tau), \mathbf{a}(\tau), \tau)\, d\tau,$$
$$\text{s.t.} \quad \begin{cases} \dot{\mathbf{s}}(t) &= \mathbf{f}(\mathbf{s}(t), \mathbf{a}(t), t) \quad t \in (0, T] \\ \mathbf{s}(0) &= \mathbf{s}_0 \end{cases}, \tag{1}$$

where $\mathbf{f} : \mathbb{R}^{n_s} \times \mathbb{R}^{n_a} \to \mathbb{R}^{n_s}$ is the vector field in the phase space of the dynamical system, $\mathbf{s} \in \mathbb{R}^{n_s}$ is the system's *state* vector evolving along a *trajectory*, $\mathbf{a} \in \mathbb{R}^{n_a}$ is the action/actuation, taken by a *controller* in control theory and an *agent* in reinforcement learning.

The functional $R(\mathbf{a})$ comprise a *running cost* (or Lagrangian) $\mathcal{L} : \mathbb{R}^{n_a} \times \mathbb{R}^{n_s} \to \mathbb{R}$, which accounts for the system's states evolution, and a *terminal cost* (or Mayer term) $\phi : \mathbb{R}^{n_s} \to \mathbb{R}$, which depends on the final state condition. Optimal control problems with this cost functional form are known as Bolza problem[4; 19; 5].

The actions/actuation are selected by the agent/controller following a *control law* or *policy* $\pi : \mathbb{R}^{n_s} \to \mathbb{R}^{n_a}$:

$$\mathbf{a}(t) = \pi(\mathbf{s}(t), t) \in \mathbb{R}^{n_a}. \tag{2}$$

Note that the system might not be fully observable, and hence the policy would generally depend on some observation $\mathbf{y} = O(\mathbf{s}(t)) \in \mathbb{R}^{n_o}$, with $n_o \ll n_s$, rather than the state itself. However, as we later focus on black-box methods, this clarification is unessential.

Identifying the best policy $\mathbf{a}^*(t) = \pi^*(\mathbf{s}(t), t)$ is the goal of optimal control theory and reinforcement learning alike. When the agent/controller acts according to π^*, the state evolves along the optimal trajectory $\mathbf{s}^*(t)$.

2.2. Model Free Control and Machine Learning

In the context of machine learning control, the equations governing the system are unknown, and the controller is designed relying only on input/output relations. As shown in Figure 2, the dynamics of the system $\mathbf{f}(\mathbf{s}, \mathbf{a}, t)$, as well as the performance measures $R(\mathbf{a})$, are embedded into an unknown black-box and the algorithm looks for an optimal control/policy through an iterative trial and error process.

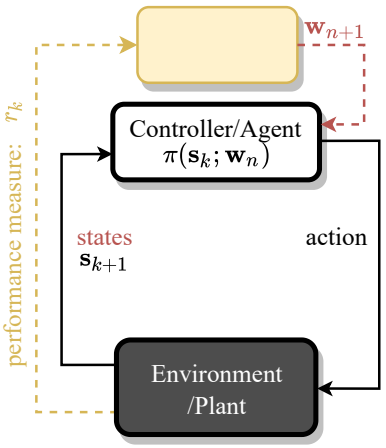

Figure 2: General setting for a machine learning-based control problem: the learning algorithm improves the agent/control performances by interacting with the environment/plant. The agent/controller acts according to a parametric law and receives feedback on its actions. The control problem is an optimization of the weights to maximize a function of actions and states.

We uniformly discretize the time interval $t \in [0, T]$ in (1) as $t_k = k\Delta t$, leading to $N = T/\Delta t + 1$ points indexed as $k = 0, \dots N$ and we introduce the notation $\mathbf{s}_k = \mathbf{s}(t_k)$. Although it is impossible to predict the response of the system to an action, i.e. $\mathbf{s}_{k+1} = \mathbf{f}(\mathbf{s}_k, \mathbf{a}^\pi_k, k)$, it is possible to collect a sequence of states $\mathbf{S} := \{\mathbf{s}_1, \mathbf{s}_2 \dots \mathbf{s}_N\}$ while taking a sequence of actions $\mathbf{A}^\pi := \{\mathbf{a}_1, \mathbf{a}_2 \dots \mathbf{a}_N\}$.

Moreover, one can give a reward $\mathcal{L}(\mathbf{s}_k, \mathbf{a}_k, k)$ to each state-action pair as a function of time (index). In an episodic approach, each set of N interactions with the system is an *episode*, at the end of which it is possible to compute a discrete version of the performance measures $R(\mathbf{a})$ in (1):

$$R(\mathbf{A}^\pi) = \phi(\mathbf{s}_N) + \sum_{k=1}^{N} \mathcal{L}(\mathbf{s}_k, \mathbf{a}^\pi_k, k). \tag{3}$$

In the RL literature, this is known as cumulative reward, and the Lagrangian takes the form $\mathcal{L}(\mathbf{s}_k, \mathbf{a}^\pi_k, k) = \gamma^k r(\mathbf{s}_k, \mathbf{a}^\pi_k) = \gamma^k r^\pi_k$, where $\gamma \in [0, 1]$ is a discount factor which prioritize immediate over future rewards. In a deterministic policy, the sequence of actions is taken from a parametric function which we denote $\mathbf{a}^\pi = \pi(\mathbf{s}; \mathbf{w})$. In a stochastic policy, the parametric function outputs the parameters of the distribution

(e.g mean and standard deviation in a Gaussian) from which the actions will be sampled. In both cases, the vector $\mathbf{w} \in \mathbb{R}^{n_w}$ is unknown and must be *learned*. By mapping the action space $\mathcal{A}$ onto a finite weight space $\mathbf{w} \in \mathbb{R}^{n_w}$, the variational problem of maximizing $R(\mathbf{a}(t))$ reduces to the optimization problem of maximizing $R(\mathbf{w})$.

Although there is no guarantee that the optimal control law/policy can be found, it is possible to define a value function that gives the minimal cost/maximum reward achievable by a controller/agent following π, from $\mathbf{s}_t$ to $\mathbf{s}_T$ under the policy π:

$$\begin{aligned}\mathbf{V}^{\pi}(\mathbf{s}_t) =& \phi(\mathbf{s}_N) + \sum_{k=t}^{N} \mathcal{L}_r(\mathbf{s}_k, \mathbf{a}_k^{\pi}, k) \\ =& \phi(\mathbf{s}_N) + \sum_{k=t}^{N} \gamma^{k-t} r_k = r_k + \gamma \mathbf{V}^{\pi}(\mathbf{s}_{t+1})\,.\end{aligned} \tag{4}$$

One thus has $R(\mathbf{A}^{\pi}) = \mathbf{V}^{\pi}(\mathbf{s}_1)$. Moreover, one might occasionally let the environment/controller act *off-policy* and thus take an action $\mathbf{a}_k$ rather than $\mathbf{a}_k^{\pi}$. Then, it is worth defining the value of a state-action pair $(\mathbf{s}_t, \mathbf{a}_t)$ under policy π as:

$$\begin{aligned}\mathbf{Q}^{\pi}(\mathbf{s}_t, \mathbf{a}_t) =& \phi_r(\mathbf{s}_N) + r(\mathbf{s}_k, \mathbf{a}_k) + \sum_{k=t+1}^{N} \mathcal{L}_r(\mathbf{s}_k, \mathbf{a}_k^{\pi}, k) \\ =& r(\mathbf{s}_k, \mathbf{a}_k) + \gamma \mathbf{V}^{\pi}(\mathbf{s}_{t+1})\,.\end{aligned} \tag{5}$$

This function, known as Q-function, measures the reward that can be obtained if a 'de-tour' from the current policy is taken at time k, the action $\mathbf{a}_k$ is taken instead of $\mathbf{a}_k^{\pi}$, and the policy π is followed *afterwards*. It is therefore possible to define the *advantage* of such exploration as

$$\mathbf{A}^{\pi}(\mathbf{s}_t, \mathbf{a}_t) = r(\mathbf{s}_t, \mathbf{a}_t) - r(\mathbf{s}_k, \mathbf{a}^{\pi}{}_k) = \mathbf{Q}^{\pi}(\mathbf{s}_t, \mathbf{a}_t) - \mathbf{V}^{\pi}(\mathbf{s}_t)\,. \tag{6}$$

If the optimal policy is followed, the advantage is zero. It is worth noticing that all the definitions (4), (5),(6) assume that the system is deterministic. This is somewhat uncommon in the literature of RL, where the environment is considered stochastic and modelled as a Markov Decision Process (MDP)[14]. All systems considered in this work are deterministic; hence, treatment in a stochastic framework is unnecessary. For a deterministic system one has $V^{\pi}(\mathbf{s}_t) = Q(\mathbf{s_t}, \mathbf{a}_k^{\pi})$. We briefly reconsider the stochastic approach in the description of the DDPG in 4.3.

Control methods based on Machine learning differ in the form of the policy parametrization $\mathbf{a} = \pi(\mathbf{s}_t, \mathbf{w})$ and, most importantly, in how they use data to compensate for the lack of solid theoretical tools.

Some machine learning tools –borrowing from the RL literature– could be classified as *actor-only*. These methods focus on the policy parametrization and seek to maximize $R(\mathbf{A}(\mathbf{w}))$ regardless of the physical constraints $\dot{\mathbf{s}}(t) - \mathbf{f}(s(t), \mathbf{a}(t), t) = 0$ in (1). Actor-only methods are essentially optimizers coupled with a (possibly adaptive) policy parametrization. Like all optimizers, these can be global and gradient-free or local and gradient-based, and might use surrogate functions to approximate the function $R(\mathbf{w})$. Within this last category, we consider the BO and LIPO in section 4.1. Among the gradient-free, actor-only methods, the most classic approach is the GP, briefly described in Section 4.2. Among the gradient-based, actor-only methods, one finds RL algorithms such as REINFORCE[20], which use a gradient descent/ascent approach with a probabilistic estimation based on the policy gradient theorem[14].

Other machine learning tools – borrowing again from RL literature, can be classified as "critic only". These methods take an indirect path, and aims at estimating the state-action value function $Q^{\pi}(\mathbf{s}, \mathbf{a})$ so that the best policy is simply the greedy $a_t = \arg\max_{\mathbf{a} \in \mathcal{A}} Q^{\pi}(\mathbf{s}, \mathbf{a})$. The most classic example of this approach is deep Q learning[21].

Modern RL algorithms are actor-critic, i.e. combine both approaches. The DDPG algorithm implemented in this work falls within this category and is described in Section 4.3.

3. IBL model in 3D for a moving substrate

In both the falling film (FF) and in the moving substrate case (MS) problems, the integral boundary layer (IBL) models can be derived from the Navier-Stokes equations, scaled according to the reference quantities in Mendez *et al*[17] and retaining only terms up to $O(\varepsilon)$. This results in the boundary layer equations:

$$\partial_{\hat{x}}\hat{u} + \partial_{\hat{y}}\hat{v} + \partial_{\hat{z}}\hat{w} = 0, \tag{7a}$$

$$\delta(\partial_{\hat{t}}\hat{u} + \hat{u}\partial_{\hat{x}}\hat{u} + \hat{v}\partial_{\hat{y}}\hat{u} + \hat{w}\partial_{\hat{z}}\hat{u}) = -\partial_{\hat{x}}\hat{p}_x\partial^2_{\hat{y}\hat{y}}\hat{u} + 1, \tag{7b}$$

$$\partial_{\hat{y}}\hat{p}_y = 0, \tag{7c}$$

$$\delta(\partial_{\hat{t}}\hat{w} + \hat{u}\partial_{\hat{x}}\hat{w} + \hat{v}\partial_{\hat{y}}\hat{w} + \hat{w}\partial_{\hat{z}}\hat{w}) = -\partial_{\hat{z}}\hat{p}_z + \partial^2_{\hat{y}\hat{y}}\hat{w}, \tag{7d}$$

where (7a) is the continuity equation, and (7b), (7c), (7d) are the momentum equations along $\hat{x}$, $\hat{y}$, and $\hat{z}$

respectively. The dimensionless kinematic boundary conditions at the wall and at the interface are

$$\vec{\hat{v}}\big|_{\hat{y}=0} = (\hat{u},\hat{v},\hat{w})\big|_{\hat{y}=0} = (\alpha,0,0), \tag{8a}$$

$$\hat{v}\big|_{\hat{y}=\hat{h}} = \partial_{\hat{t}}\hat{h} + \hat{u}\partial_{\hat{x}}\hat{h} + \hat{w}\partial_{\hat{z}}\hat{h}, \tag{8b}$$

where $\alpha = 0$ for the FF problem and $\alpha = -1$ for the MS problem. This parameter is introduced to link the derivation of the two models, but it is worth stressing that these problems have different scaling laws. At $O(\varepsilon)$, the dynamic boundary conditions formulating the force balance at the free surface is:

$$\hat{p}_l\big|_{\hat{y}=\hat{h}} = \hat{p}_g - (\partial_{\hat{x}\hat{x}}\hat{h} + \partial_{\hat{z}\hat{z}}\hat{h}), \tag{9a}$$

$$\partial_{\hat{y}}\hat{u}\big|_{\hat{y}=\hat{h}} = \hat{\tau}_{g,x}, \tag{9b}$$

$$\partial_{\hat{y}}\hat{w}\big|_{\hat{y}=\hat{h}} = \hat{\tau}_{g,z}, \tag{9c}$$

where $\hat{\tau}_{g,x}$ and $\hat{\tau}_{g,z}$ are the shear stress components along x and z respectively.

To derive the integral model, We integrate (7) along y assuming a self-similar parabolic velocity profile for both the stream-wise $\hat{u}$ and the span-wise $\hat{w}$ velocity components, as introduced by [22]. The three coefficients required to describe these velocity profiles are functions of the local flow rates and thickness, and can be derived from the boundary conditions and from the flow rate definitions. The main hypothesis under this assumption is that the balance of viscosity and gravity is not significantly altered by inertia and surface tension.

The integration results in a system of nonlinear partial differential equations for the liquid film height $\hat{h}$, the stream-wise $\hat{q}_x$ and span-wise $\hat{q}_z$ flow rates. In conservative form, this reads:

$$\partial_{\hat{t}}\vec{U} + \nabla\cdot\mathbf{F} = \vec{S}, \tag{10}$$

with the state vector consisting of the liquid film height and the volumetric flow rates, $\vec{U} = (\hat{h},\hat{q}_x,\hat{q}_z)^{\mathrm{T}}$.

The source vector is denoted by $\vec{S} = (S_1,S_2,S_3)^{\mathrm{T}}$, and reads

$$\vec{S} = \begin{pmatrix} 0 \\ \frac{1}{\delta}\Big[\hat{h}\Big(-\partial_{\hat{x}}\hat{p}_x + \partial_{\hat{x}\hat{x}\hat{x}}\hat{h} + \partial_{\hat{x}\hat{z}\hat{z}}\hat{h} + 1\Big) + \Delta\hat{\tau}_x\Big] \\ \frac{1}{\delta}\Big[\hat{h}\Big(-\partial_{\hat{z}}\hat{p}_z + \partial_{\hat{z}\hat{z}\hat{z}}\hat{h} + \partial_{\hat{z}\hat{x}\hat{x}}\hat{h}\Big) + \Delta\hat{\tau}_z\Big] \end{pmatrix} \tag{11}$$

where the terms with third derivatives of $\hat{h}$ correspond to the capillary pressure gradients and the terms $\Delta\hat{\tau}_x = \hat{\tau}_{g,x} + \hat{\tau}_{w,x}$ and $\Delta\hat{\tau}_z = \hat{\tau}_{g,z} + \hat{\tau}_{w,z}$ result from the integration of the viscous term in (7b) and (7d). These represent the difference in shear stress betWeen the interface (terms $\hat{\tau}_{g,x}$ and $\hat{\tau}_{g,z}$) and the wall (terms $\hat{\tau}_{w,x}$ and $\hat{\tau}_{w,z}$). The shear stress at the wall, using the self-similar assumption for the velocity profiles, reads:

$$\hat{\tau}_{w,x} = \frac{1}{2}\hat{\tau}_{g,x} - \frac{3\hat{q}_x}{\hat{h}^2} - \alpha\frac{3}{\hat{h}} \tag{12a}$$

$$\hat{\tau}_{w,z} = \frac{1}{2}\hat{\tau}_{g,z} - \frac{3\hat{q}_z}{\hat{h}^2} \tag{12b}$$

The flux matrix $\mathbf{F}$ in (10) is

$$\mathbf{F} = \begin{pmatrix} F_{11} & F_{12} & F_{13} \\ F_{21} & F_{22} & F_{23} \end{pmatrix} = \\ = \begin{pmatrix} \hat{q}_x & \int_0^{\hat{h}}\hat{u}^2 d\hat{y} & \int_0^{\hat{h}}\hat{u}\hat{w}d\hat{y} \\ \hat{q}_z & \int_0^{\hat{h}}\hat{u}\hat{w}d\hat{y} & \int_0^{\hat{h}}\hat{w}^2 d\hat{y} \end{pmatrix}, \tag{13}$$

and it has the following components:

$$F_{11} = \int_0^{\hat{h}}\hat{u}d\hat{y} =: \hat{q}_x \tag{14a}$$

$$F_{21} = \int_0^{\hat{h}}\hat{w}d\hat{y} =: \hat{q}_z \tag{14b}$$

$$F_{12} = \frac{1}{120\hat{h}}\Big(144\hat{q}_x^2 + 6\hat{\tau}_{g,x}\hat{h}^2\hat{q}_x + \hat{\tau}_{g,x}\hat{h}^4 + \\ -\alpha(48\hat{h}\hat{q}_x + 6\hat{\tau}_{g,x}\hat{h}^3 + 24\hat{h}^2)\Big) \tag{14c}$$

$$F_{22} = \frac{1}{120\hat{h}}\Big(144\hat{q}_x\hat{q}_z + 3\hat{\tau}_{g,x}\hat{h}^2\hat{q}_z + 3\hat{\tau}_{g,z}\hat{h}^2\hat{q}_x + \\ +\hat{\tau}_{g,x}\hat{\tau}_{g,z}\hat{h}^4 - \alpha(24\hat{h}\hat{q}_z + 3\hat{\tau}_{g,z}\hat{h}^3)\Big) \tag{14d}$$

$$F_{13} = F_{22} \tag{14e}$$

$$F_{23} = \frac{144\hat{q}_z^2 + 6\hat{\tau}_{g,z}\hat{h}^2\hat{q}_z + \hat{\tau}_{g,z}^2\hat{h}^4}{120\hat{h}} \tag{14f}$$

This model recovers the 3D model for falling liquid films by [18], if $\alpha = 0$, $\partial_{\hat{x}}\hat{p}_x = \partial_{\hat{x}}\hat{p}_z = 0$, $\hat{\tau}_{g,x} = \hat{\tau}_{g,z} = 0$ and its two-dimensional version by [23] if also $\hat{q}_z = 0$ and $\partial_z \to 0$. Moreover, the model recovers the 2D liquid film model in jet wiping by [17], if $\alpha = -1$, $\hat{q}_z = 0$, $\hat{\tau}_{g,z} = 0$ and $\partial_z \to 0$. If only $\alpha = -1$ is introduced in system (10), this model is the first 3D formulation of an integral boundary layer model for the jet wiping process in the literature.

4. Implemented Algorithms

4.1. Optimization via BO and LIPO

Let the policy be described by a predefined function $\mathbf{a} = \pi(\mathbf{s}_t, \mathbf{w}^\pi) \in \mathbb{R}^{n_a}$, defined by a set of weights $\mathbf{w}^\pi \in \mathcal{W} \subseteq \mathbb{R}^{n_w}$. This function could be a linear mapping, a user-defined nonlinear function, or any other parametric model from machine learning (r.g. RBFs or ANNs). We assume in this section that this model depends on a relatively small number of parameters (say $n_w \sim O(10)$).

For a given set of weights, the policy defines the behaviour of the agent/controller and the cumulative reward at each episode can be computed from (3). In a stochastic system, the cumulative reward varies even if the same set of weights is considered: in this case, we shall repeat the evaluation of a set of weights multiple times and average the results. In both cases, the problem is now an optimization, in which every episode gives an evaluation of a "black-box" function $R(\mathbf{w})$ (or its expectation over a number of episodes). Because this function might be expensive, we focus on efficient optimizers. Other methods are illustrated by Maceda *et al* [24].

4.1.1. Bayesian Optimization (BO)

The first ingredient of BO is a regression tool that derives a surrogate model of the function to optimize. Among several options, the classic BO uses a Gaussian Process (GPr) as surrogate function. Let $\mathbf{W}^* := \{\mathbf{w}_1, \mathbf{w}_2 \dots \mathbf{w}_{n_*}\}$ be a set of n_* *tested* weights and $\mathbf{R}^* := \{R_1, R_2 \dots R_{n_*}\}$ the associated cumulative rewards. The GPr offers a probabilistic model that computes the probability of a certain reward given the observations $(\mathbf{W}^*, \mathbf{R}^*)$, i.e. $p(R(\mathbf{w})|\mathbf{W}^*, \mathbf{R}^*)$. In a GPr, this is

$$p(R(\mathbf{w})|\mathbf{R}^*, \mathbf{W}^*) = \mathcal{N}(\boldsymbol{\mu}, \boldsymbol{\Sigma}), \tag{15}$$

where $\mathcal{N}$ denotes a a Gaussian distribution with expected function $\boldsymbol{\mu}$ and covariance function $\boldsymbol{\Sigma}$. In a Bayesian framework, eq (15) is interpreted as a posterior distribution, conditioned to the observations $(\mathbf{W}^*, \mathbf{R}^*)$. A Gaussian process is a distribution over functions whose smoothness is defined by the covariance function, computed using a kernel function. Given a set of data $(\mathbf{w}^*, \mathbf{R}^*)$, this allows for building a continuous function to estimate both the reward of a possible candidate and the uncertainties associated with it.

Let us assume we are interested in evaluating (15) on a set of n_E *new* samples $\mathbf{W} := \{\mathbf{w}_1, \mathbf{w}_2 \dots \mathbf{w}_{n_E}\}$ and let us denote as $\mathbf{R} := \{R_1, R_2 \dots R_{n_E}\}$ the random variables with the possible outcomes. Assuming that the possible candidate solutions belong to the same Gaussian process (usually assumed to have zero mean[25]) as the observed data $(\mathbf{W}^*, \mathbf{R}^*)$, we have:

$$\begin{pmatrix} \mathbf{R}^* \\ \mathbf{R} \end{pmatrix} \sim \mathcal{N}\left(\mathbf{0}, \begin{pmatrix} \mathbf{K}_{**} & \mathbf{K}_* \\ \mathbf{K}_*^T & \mathbf{K} \end{pmatrix}\right), \tag{16}$$

where $\mathbf{K}_{**} = \kappa(\mathbf{W}^*, \mathbf{W}^*) \in \mathbb{R}^{n_* \times n_*}$, $\mathbf{K}_* = \kappa(\mathbf{W}, \mathbf{W}^*) \in \mathbb{R}^{n_e \times n_*}$, $\mathbf{K} = \kappa(\mathbf{W}, \mathbf{W}) \in \mathbb{R}^{n_E \times n_E}$ and κ a kernel function.

The prediction in (15) can be build using standard rules for conditioning multivariate Gaussian, and the functions $\boldsymbol{\mu}$ and $\boldsymbol{\Sigma}$ in (15) becomes a vector $\boldsymbol{\mu}_*$ and a matrix $\boldsymbol{\Sigma}_*$:

$$\boldsymbol{\mu}_* = \mathbf{K}_*^T \mathbf{K}_R^{-1} \mathbf{R}^* \quad \in \mathbb{R}^{n_E} \tag{17}$$

$$\boldsymbol{\Sigma}_* = \mathbf{K} - \mathbf{K}_*^T \mathbf{K}_R^{-1} \mathbf{K}_* \quad \in \mathbb{R}^{n_E \times n_E}, \tag{18}$$

$$\boldsymbol{\mu}_* = \mathbf{K}_*^T \mathbf{K}^{-1} \mathbf{R}^* \quad \in \mathbb{R}^{n_E} \tag{19}$$

$$\boldsymbol{\Sigma}_* = \mathbf{K} - \mathbf{K}_*^T \mathbf{K}_R^{-1} \mathbf{K}_* \quad \in \mathbb{R}^{n_E \times n_E}, \tag{20}$$

where $\mathbf{K}_R = \mathbf{K}_{**} + \sigma_R^2 \mathbf{I}$, with σ_R^2 the expected variance in the sampled data and $\mathbf{I}$ the identity matrix of appropriate size. The main advantage of BO is that the function approximation is sequential, and new predictions improve the approximation of the reward function (i.e. the surrogate model) episode after episode. This makes the GPr- based BO one of the most popular black-box optimization methods for expensive cost functions. Nevertheless, many variants exist and are continuously proposed in the growing field of Hyperparameter Optimization (HPO)[26].

Moreover, in perspective towards possible future hybridization, it is worth noticing that Gaussian processes implemented in classic BO are generic function approximators (like ANNs) and could be used, for example, to attempt approximating the value functions in (4) and (5). On thus enters the realm of Bayesian Reinforcement learning[27], which, to the authors' knowledge, is fairly unexplored in fluid dynamics.

The second ingredient of BO is a function suggesting where to sample next. Many variants exist[28], each providing their exploration/exploitation balance. In BO, the exploration seeks to sample in regions of large uncertainty, while exploration seeks to sample at the best location according to the current function approximation. The most classic function, used in this study, is the expected improvement, defined as[25]

$$\mathrm{EI}(\mathbf{x}) = \begin{cases} (\Delta - \xi)\Phi(Z) + \sigma(\mathbf{w})\phi(Z) & \text{if } \sigma(\mathbf{w}) > 0 \\ 0 & \text{if } \sigma(\mathbf{x}) = 0 \end{cases} \tag{21}$$

with $\Delta = \mu(\mathbf{w}) - R(\mathbf{w}^+)$ and $\mathbf{w}^+ =_{\mathbf{w}} \tilde{R}(\mathbf{w})$ the best sample so far, $\Phi(Z)$ the cumulative distribution (CDF) and $\phi(Z)$ the probability density (PDF) of a standard Gaussian and

$$Z = \begin{cases} \frac{\Delta - \xi}{\sigma(\mathbf{w})} & \text{if } \sigma(\mathbf{w}) > 0 \\ 0 & \text{if } \sigma(\mathbf{w}) = 0 \end{cases}. \tag{22}$$

Eq (21) balances the desire to sample in regions where $\mu(\mathbf{w})$ is closer to $R(\mathbf{w}^+)$ (hence large and positive Δ) versus sampling in regions where $\sigma(\mathbf{w})$ is large. The parameter ξ sets a threshold over the minimal expected improvement that justifies the exploration.

Finally, the method requires the definition of the kernel function and its hyper-parameters, as well as an estimate of σ_y. In this work, the GPr based BO was implemented using the Python API *scikit-optimize*[29]. The selected kernel function was a Mater kernel with $\nu = 5/2$ (see Chapter 4 from Rasmussen and Williams[25]) which reads:

$$\kappa(\mathbf{x}, \mathbf{x}') = \kappa(r) = \Big(1 + \frac{\sqrt{5}r}{l} + \frac{5r^2}{3l^2}\Big)\exp\Big(-\frac{\sqrt{5}r}{l}\Big), \tag{23}$$

where $r = \|\mathbf{x} - \mathbf{x}'\|_2$ and l the length scale of the process. In general, the performances of the BO strongly depends on the choice of these parameters and their estimation implies knowledge of the cost function, particularly its smoothness or the possible presence of noise. If the computational cost of evaluating an episode is not too large, it is worth running a first exploratory analysis and test the Gaussian process regression on the collected data with various parameters.

4.1.2. LIPschitz global Optimization (LIPO)

Like BO, LIPO relies on a surrogate model to select the next sampling points [30]. However, LIPO's surrogate function is the much simpler upper bound approximation $U(\mathbf{w})$ of the cost function $R(\mathbf{w})$ [31]. In the DLIB implementation by King[32], used in this work, this is given by:

$$U(\mathbf{w}) = \min_{i=1\ldots t} (R(\mathbf{w}_i) + \sqrt{\sigma_i + (\mathbf{w} - \mathbf{w}_i)^T K (\mathbf{w} - \mathbf{w}_i)}), \tag{24}$$

where $\mathbf{w}_i$ are the sampled parameters, σ_i are coefficients which account for discontinuities and stochasticity in the objective function, and K is a diagonal matrix that contains the Lipschitz constants k_i for the different dimensions of the input vector. We recall that a function $R(\mathbf{w}) : \mathcal{W} \subseteq \mathbb{R}^{n_w} \to \mathbb{R}$ is a Lipschitz function if there exists a constant C such that:

$$\|R(\mathbf{w}_1) - R(\mathbf{w}_2)\| \leq C\|\mathbf{w}_1 - \mathbf{w}_2\|, \quad \forall\ \mathbf{w}_1, \mathbf{w}_2 \in \mathcal{W}, \tag{25}$$

where $\|\cdot\|$ is the Euclidean norm on $\mathbb{R}^{n_w}$. The Lipshitz constant k of $R(\mathbf{w})$ is the smallest C that satisfies the above condition [33]. In other terms, this is an estimate of the largest possible slope of the function $R(\mathbf{w})$. The values of K and σ_i are found by solving the optimization problem:

$$\begin{aligned} \min_{K,\sigma} \quad & \|K\|_F^2 + 10^6 \sum_{i=1}^{t} \sigma_i^2 \\ \text{s.t.} \quad & U(\mathbf{w}_i) \geq R(\mathbf{w}_i), \quad \forall i \in [1 \cdots t] \\ & \sigma_i \geq 0, \quad \forall i \in [1 \cdots t] \\ & K_{i,j} \geq 0, \quad \forall i, j \in [1 \cdots d] \\ & \mathrm{K} = \{k_1, k_2, \cdots, k_{n_w}\}, \end{aligned} \tag{26}$$

where 10^6 is a penalty factor and $\|\cdot\|_F$ is the Frobenius norm.

To compensate for the poor convergence of LIPO in the area around local optima, the algorithm alternates between a global and a local search. If the iteration number is even, it selects the new weights by means of the maximum upper bounding position (MaxLIPO):

$$\mathbf{w}_{k+1} =_{\mathbf{w}} (U(\mathbf{w})), \tag{27}$$

otherwise, it relies on a Trust Region (TR) method [34] based on a quadratic approximation of $R(\mathbf{w})$ around the best weights obtained so far $\mathbf{w}^*$, i.e:

$$\begin{aligned} \mathbf{w}_{k+1} = \arg\max_{\mathbf{w}} \overbrace{\Big(\mathbf{w}^* + g(\mathbf{w}^*)^T\mathbf{w} + \frac{1}{2}\mathbf{w}^T\mathbf{H}(\mathbf{w}^*)\mathbf{w}\Big)}^{m(\mathbf{w};\mathbf{w}^*)} \\ \text{s.t.}\ \|\mathbf{w}_{k+1}\| < d(\mathbf{w}^*) \end{aligned} \tag{28}$$

where $g(\mathbf{w}^*)$ is the approximation of the gradient at $\mathbf{w}^*$ ($g(\mathbf{w}^*) \approx \nabla R(\mathbf{w}^*)$)), $\mathbf{H}(\mathbf{w}^*)$ is the approximation of the Hessian matrix $(\mathbf{H}(\mathbf{w}^*))_{ij} \approx \frac{\partial^2 R(\mathbf{w}^*)}{\partial \mathbf{w}_i \partial \mathbf{w}_j}$ and $d(\mathbf{w}^*)$ is the radius of the trust region. If the TR-method converges to a local optimum with an accuracy smaller than ϵ:

$$|R(\mathbf{w}_k) - R(\mathbf{w}^*)| < \varepsilon, \quad \forall\ \mathbf{w}_k, \tag{29}$$

the optimization goes on with the global search method, until it finds a better optimum.

4.2. Genetic Programming

In a Genetic Programming (GP) approach to optimal control, the policy $\mathbf{a} = \pi(\mathbf{s}; \mathbf{w})$ is encoded in the form of a syntax tree. The optimal parameters $\mathbf{w}^*$ are not scalar quantities but lists of numbers and functions which can include arithmetic operations, mathematical functions, Boolean operations, conditional operations or iterative operations. An example of a syntax tree representation of a function is shown in Figure 3.

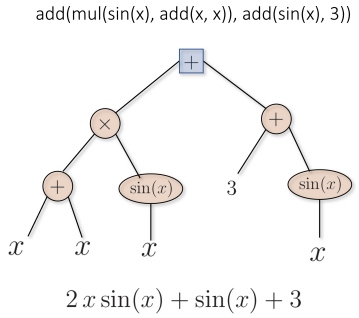

Figure 3: Syntax tree representation of the function $2x\sin(x) + \sin(x) + 3$. This tree has a root '+' and a depth of two. The nodes are denoted with orange circles while the last entries are leafs.

A tree (or *program* in GP terminology) is composed of a root that branches out into nodes (containing functions or operations) throughout various levels. The number of levels defines the *depth* of the tree, and the last nodes are called *terminals* or *leaves*. These contain the input variables or constants. Any combination of branches below the root is called *sub-tree* and can generate a tree if the node becomes a root.

Syntax trees allow encoding complex functions by growing into large structures. The flexible nature of GP allows this architecture to adapt during the training: the user does not provide a parametrization of the policy but a *primitive set*, i.e. the pool of allowed functions, the maximum depth of the tree, and set the parameters of the training algorithm. Then, the GP operates on a population of possible candidate solutions (individuals) and evolves it over various steps (generations) using genetic operations in the search for the optimal tree. Classic operations include elitism, replication, cross-over and mutations, as in Genetic Algorithm Optimization[35].

The implementation of GP in this work was carried out in the **D**istributed **E**volutionary **A**lgorithms in **P**ython (DEAP)[36] framework. This is an open-source Python library allowing for the implementation of various evolutionary strategies. In this work, we focus on the (μ, λ) algorithm, which we here briefly describe for completeness. The reader is referred to the literature[15; 16; 37; 38] for many other possible implementations of this method.

We used a primitive set of four elementary operations $(+, -, /, \times)$ and four functions $(\exp, \log, \sin, \cos)$. The initial population of individuals varied between $n_I = 30$ and $n_I = 50$ candidates depending on the test case and the maximum depth tree was set to 17. In all test cases, the population was initialized using a classic "half-half" approach, whereby half the population is initialized with the *full method* and the rest with the *growth method*. In the full method, the trees are generated with a predefined depth and then filled randomly with nodes and leafs. In the growth method, trees are randomly filled from the roots: because nodes filled with variables or constant are terminals, this approach generates trees of variable depth.

4.3. Reinforcement Learning via DDPG

The Deep Deterministic Policy gradient (DDPG) by Lillicrap *et al* [39] is an off-policy actor-critic algorithm using an ANN to learn the policy and an ANN to learn the Q function. In what follows, we call Π-network the first (i.e. the actor) and Q-network the second (i.e. the critic).

The DDP combines the DPG by Silver *et al*[40] and the Deep Q learning (DQN) by Mnih *et al*[21; 41].

The policy encoded in the Π network is deterministic and acts according to the set of weights and biases $\mathbf{w}^\pi$, i.e. $\mathbf{a} = \pi(\mathbf{s}_t; \mathbf{w}^\pi)$. The environment is assumed to be stochastic and modelled as a MDP. Therefore, (5) must be modified to introduce an expectation operator:

$$Q^\pi(\mathbf{s}_t, \mathbf{a}_t) = \mathbb{E}_{\mathbf{s}_t, \mathbf{s}_{t+1} \sim E}\left[r(\mathbf{s}_t, \mathbf{a}_t) + \gamma Q^\pi(\mathbf{s}_{t+1}, \mathbf{a}^\pi_{t+1})\right], \quad (30)$$

where the policy is intertwined in the action state relation, i.e. $Q^\pi(\mathbf{s}_{t+1}, \mathbf{a}_{t+1}) = Q^\pi(\mathbf{s}_{t+1}, \mathbf{a}^\pi(\mathbf{s}_{t+1}))$ and having used the shorthand notation $\mathbf{a}^\pi_{t+1} = \pi(\mathbf{s}_{t+1}; \mathbf{w}^\pi)$. Because the expectation operator in (30) solely depends on the environment (E in the expectation operator), it is possible to decouple the problem of learning the policy π from the problem of learning the function $Q^\pi(\mathbf{s}_t, \mathbf{a}_t)$. Concretely, let $Q(\mathbf{s}_t, \mathbf{a}_t; \mathbf{w}^Q)$ denote the prediction of Q function by the Q network, defined with weights and biases $\mathbf{w}^Q$ and let $\mathcal{T}$ denote a set of N transitions $(\mathbf{s}_t, \mathbf{a}_t, \mathbf{s}_{t+1}, r_{t+1})$ collected through (any) policy $\mathbf{a}_t = \beta(\mathbf{s}_t)$. The performances of the Q-network can be measured as

$$J^Q(\mathbf{w}^Q) = \mathbb{E}_{\mathbf{s}_t, \mathbf{a}_t, \mathbf{r}_t \sim \mathcal{T}}\left[\left(Q(\mathbf{s}_t, \mathbf{a}_t; \mathbf{w}^Q) - y_t\right)^2\right], \quad (31)$$

where

$$y_t = r(\mathbf{s}_t, \mathbf{a}_t) + \gamma Q(\mathbf{s}_{t+1}, \mathbf{a}_{t+1}; \mathbf{w}^Q)\,. \tag{32}$$

In words, equation (31) measures how closely the prediction of the Q network satisfies the discrete Bellman equation (5). The training of the Q network can be carried out using standard stochastic gradient descent methods using the back-propagation algorithm[42] to evaluate the gradient $\partial_{\mathbf{w}^Q} J^Q$.

The training of the Q-network gives the off-policy flavour to the DDPG because it is carried out with an exploratory policy that largely differs from the policy that will be finally selected. Nevertheless, because the training of the Q-network is notoriously unstable, Mnih *et al*[21; 41] introduced the use of a *replay buffer* to leverage accumulated experience (previous transitions) and a *target network* to under-relax the update of the weights during the training. Both the computation of the cost function in (31) and its gradient are performed over a randomly chosen batch of transitions $\mathcal{T}$ in the replay buffer R.

The DDPG combines the Q-network prediction with a policy gradient approach to train the Π-network. This is inherited from the DPG by Silver *et al*[40], who have shown that, given

$$J^\pi(\mathbf{w}^\pi) = \mathbb{E}_{\mathbf{s}_t \sim E, \mathbf{a}_t \sim \pi}\big[(r(\mathbf{s}_t, \mathbf{a}_t))\big] \tag{33}$$

the expected return from the initial condition, the gradient with respect to the weights in the Π network is:

$$\partial_{\mathbf{w}^\pi} J^\pi = \mathbb{E}_{\mathbf{s}_t \sim E, \mathbf{a}_t \sim \pi}\big[\partial_{\mathbf{a}} Q(\mathbf{s}_t, \mathbf{a}_t; \mathbf{w}^Q)\, \partial_{\mathbf{w}^\pi} \pi(\mathbf{s}_t; \mathbf{w}^\pi)\big]\,. \tag{34}$$

Both $\partial_{\mathbf{a}} Q(\mathbf{s}_t, \mathbf{a}_t; \mathbf{w}^Q)$ and $\partial_{\mathbf{w}^\pi} \pi(\mathbf{s}_t; \mathbf{w}^\pi)$ can be evaluated via back-propagation, on the Q network and the Π network respectively. The main extension of DDPG over DPG is the use of DQN for the estimation of the Q function.

In this work, we implement the DDPG using Keras API in Python with three minor modifications to the original algorithm. The first is a clear separation between the exploration and the exploitation phases. In particular, we introduce a number of exploratory episodes $n_{Ex} < n_{Ep}$ and the action is computed as

$$\mathbf{a}(\mathbf{s}_t) = \mathbf{a}(\mathbf{s}_t; \mathbf{w}^\pi) + \eta(\text{ep})\mathcal{E}(t; \theta, \sigma)\,, \tag{35}$$

where $\mathcal{E}(t; \theta, \sigma)$ is an exploratory random process. This could be the time-correlated Ornstein-Uhlenbeck[43] noise or white noise, depending on the test case at hand, as detailed in the next sections. The transition from exploration to exploitation is governed by the parameter η ep, which is taken as $\eta(\text{ep}) = 1$ if $\text{ep} < n_{Ex}$ where $d^{\text{ep}-n_{Ex}}$ if $\text{ep} > n_{Ex}$. This decaying term for $\text{ep} > n_{Ep}$ progressively reduces the exploration and the coefficient d controls how rapidly this is done.

The second modification is in the selection of the transitions from the replay buffer R that are used to compute the gradient $\partial_{\mathbf{w}^Q} J^Q$. While the original implementation selects these randomly, we implement a simple version of the prioritized experience replay from Schaul *et al* [44]. The idea is to prioritize, while sampling from the replay buffer, those transitions which have lead to the largest improvement in the network performances. These can be measured in terms of Temporal Difference Error (or TD-Error):

$$\delta = r_t + \gamma Q(\mathbf{s}_{i+1}, \mathbf{a}^\pi_{t+1}; \mathbf{w}^Q) - Q(\mathbf{s}_i, a_i; \mathbf{w}^Q)\,. \tag{36}$$

Intuitively, this quantity measures how much a transition was *unexpected*. As discussed by Schaul *et al* [44], it can be shown that this increases the learning rate of the algorithm towards the steepest gradients $\partial_{\mathbf{w}^Q} J^Q$, and helps overcoming local minima. Ranking the transitions in decreasing order of TD error δ, the sampling is performed following a triangular distribution which assigns the highest probability $p(n)$ to the transition with the largest TD error δ.

The third modification, extensively discussed in previous works on reinforcement learning for flow control[45; 46; 47], is the implementation of a moving average of the actions. In other words, a given action is performed for K consecutive interactions with the environment, which in our work corresponds to the time step of the simulations.

5. The viscous Burgers's equation control problem

We consider Burger's equation because it offers a simple 1D problem combining nonlinear advection and diffusion. The problem set is:

$$\begin{aligned} \partial_t u + u\partial_x u &= \nu \partial_{xx} u + f(x,t) + c(x,t), \\ u(x,0) &= u_0 \\ \partial_x u(0,t) &= \partial_x u(L,t) = 0 \end{aligned} \tag{37}$$

where $(x,t) \in (0,L)\times(0,T]$ with $L = 20$ and $T = 15$ is the episode length, $\nu = 0.9$ is the kinematic viscosity, $f(x,t)$ is a disturbance term and $c(x,t)$ is the control

function. These are both Gaussian functions in space, modulated by a time varying amplitude:

$$f(x,t) = A \sin(2\pi f_p t) \cdot \mathcal{N}(x - x_f, \sigma), \quad (38)$$

$$c(x,t) = a(t) \cdot \mathcal{N}(x - x_a, \sigma), \quad (39)$$

taking $A = 100$ and $f_p = 0.5$ for the disturbance's amplitude and frequencies and denoting as $a(t)$ the action function provided by the controller. The disturbance and the controller action are centered at $x_f = 6.6$ and $x_c = 13.2$ respectively and have $\sigma = 0.2$. The uncontrolled system produces a set of nonlinear waves propagating in both directions at approximately constant velocities.

The objective of the controller is to neutralize the waves downstream the control location, i.e. for $x > x_c$. The controller is informed by three observations, located at $x = 8, 9, 10$. The action is then computed as

$$a(t) = w_0\, u(8,t) + w_1\, u(9,t) + w_2\, u(10,t)\,. \quad (40)$$

The controller's performance is measured by the reward function:

$$r(t) = -\left(\ell_2(u_t)_{\Omega_r} + \alpha \cdot a(t)^2\right) \quad (41)$$

where $\ell_2(\cdot)_{\Omega_r}$ is the Euclidean norm of the displacement u_t at time step t over a portion of the domain $\Omega_r = \{x \in \mathbb{R} | 15.4 \leq x \leq 16.4\}$ called reward area, α is a penalty coefficient and a_t is the value of the control action selected by the controller. The cumulative reward is computed with a discount factor $\gamma = 1$while the penalty in the actions was set to $\alpha = 10$. Figure 4 shows the evolution of the uncontrolled system in a contour plot in the space-time domain, recalling the location of perturbation, action, observation and reward area.

Eq.(37) was solved using a Crank–Nicolson's method. The Neumann boundary conditions are enforced using ghost cells and the system is solved at each time step via the banded matrix solver *solve_banded* from the python library *scipy*. The mesh consists of $n_x = 1000$ points and the time stepping is $\Delta t = 0.01$, thus leading to $n_t = 1500$ steps per episode.

6. Results

6.1. Viscous Burgers' equation test case

We present here the outcomes of the different control algorithms in terms of learning curves and control actions for the viscous Burgers' equation test case.

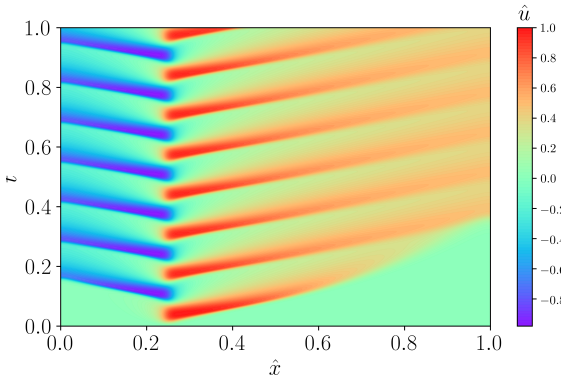

Figure 4: Contour plot of the spatio-temporal evolution of u in (37) for the uncontrolled problem, i.e $c(x,t) = 0$. The perturbation is centred at $x = 6.6$ (red continuous line) while the control law is centred at $x = 13.2$. The dashed black lines visualize the location of the observation points, while the region within the white dash-dotted line is used to evaluate the controller performance.

Given the heuristic nature of these control strategies, we ran several training sessions for each, using different seeding values for the random number generator. We define as *learning curve*, the upper bound of the cumulative reward $R(\mathbf{w})$ in (3) obtained *at each episode* within the various training sessions. Moreover, we define as *learning variance*, the variance of the global reward between the various training sessions *at each episode*. We considered ten training sessions for all environments and for all control strategies. For the GP, each iteration involves n_p episodes, with n_p the number of individuals in the population.

Table 1 collects the final best cumulative reward for each control method together with the confidence interval, while figures 5 and 6 show the learning curve and the learning variance over ten training sessions.

$\cdot 10^3$	**LIPO**	**BO**
Best Reward	-**7.26** ±0.93	-**7.10** ±0.32
	GP	**DDPG**
Best Reward	-**12.06** ±12.25	-**6.88** ±0.58

Table 1: Mean optimal cost function (bold) and confidence interval (over 10 training sessions with different random number generator seeds) obtained ad the end of the training for the viscous Burgers' equation control problem.

DDPG achieved the best overall performance, with a low variance, whereas GP performed worse in both maximum reward and variance. The performances of LIPO and BO are comparable. For the LIPO, the evo-

lution of the learning variance is initially growing, as the algorithm selects the weights of the second and third episode randomly. This leads to a worse surrogate model which needs to collect some more samples (from episode 3 to 10) to improve its performances.

For this test case, the GPr-based surrogate model of the reward function used by the BO proves to be particularly successful, as the improvements in the cumulative rewards are visible right from the first iterations. The GP is run for 20 generations with an initial population of 10 individuals, which explains the stair-like evolution of the reward function.

The optimal control laws found by BO and LIPO have similar weights (with differences of the order $O(10^{-2})$.), although the BO has much lower variance among the training sessions. Figure 8 shows the best control law derived by the four controller, together with the forcing term. The linear control laws of BO and LIPO are characterized by two main periods, one that seeks to cancel the incoming wave and the second that accounts for the upward propagation of the control action, due to the viscous dissipation. This mechanism challenges the closed-loop approach by the simple linear law used by the LIPO and BO, because actions performed at a given time are fed back into the observations after a certain time. An open-loop strategy (for example introducing a constant term in the policy) could help the controllers in this case, but it is not available to the LIPO and BO's linear policy.

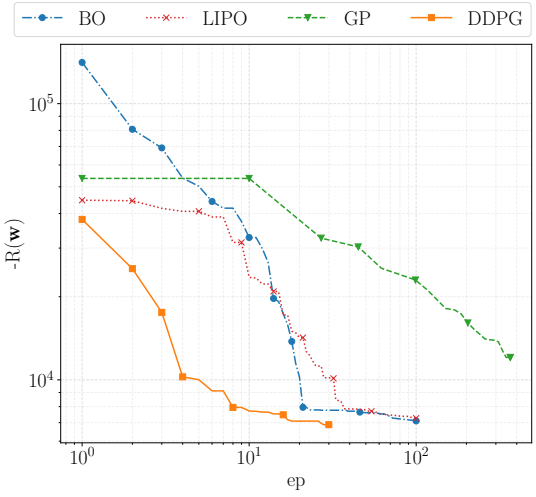

Figure 5: Evolution of the cost function, for the viscous Burgers test case, as a function of the number of episodes during the training phase.

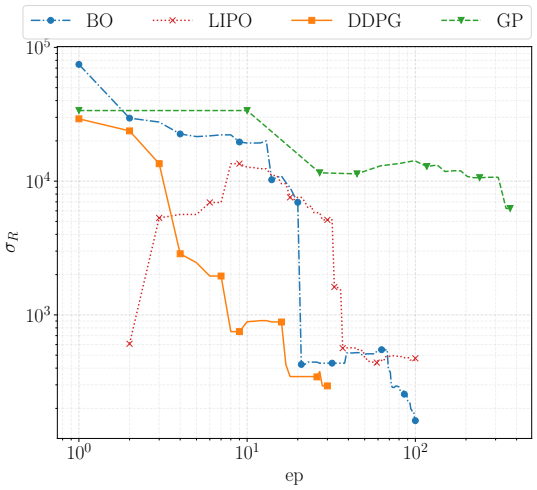

Figure 6: Evolution of the uncertainty liked to the cost function, for the viscous Burgers test case, as a function of the number of episodes during the training phase.

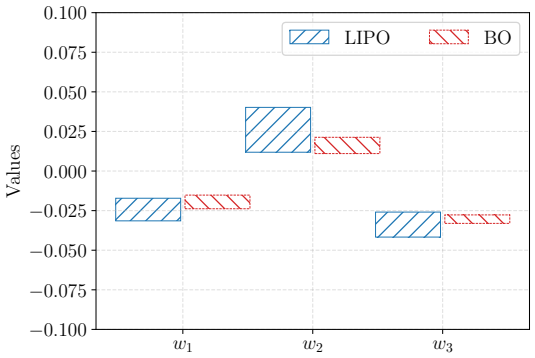

Figure 7: Weight linear combination Burgers' equation

By contrast, the control actions found by GP and DDPG, hinging on non-linearities, allows for breaking this feedback mechanics. Both the expression tree formalism of the GP and the ANN representation of the policy in the DDPG allows for producing a constant and enable open-loop control if needed. Accordingly, the results of GP and DDPG have completely different behaviour from the linear controllers. The GP takes only negative actions, and this prevents waves travelling upstream. The DDPG also avoids upstream travelling waves by taking nearly constant actions (i.e. almost open-loop) and leveraging more on the viscous dissipation of the system.

Despite the large differences in the control method, all methods succeeds in cancelling the travelling waves.

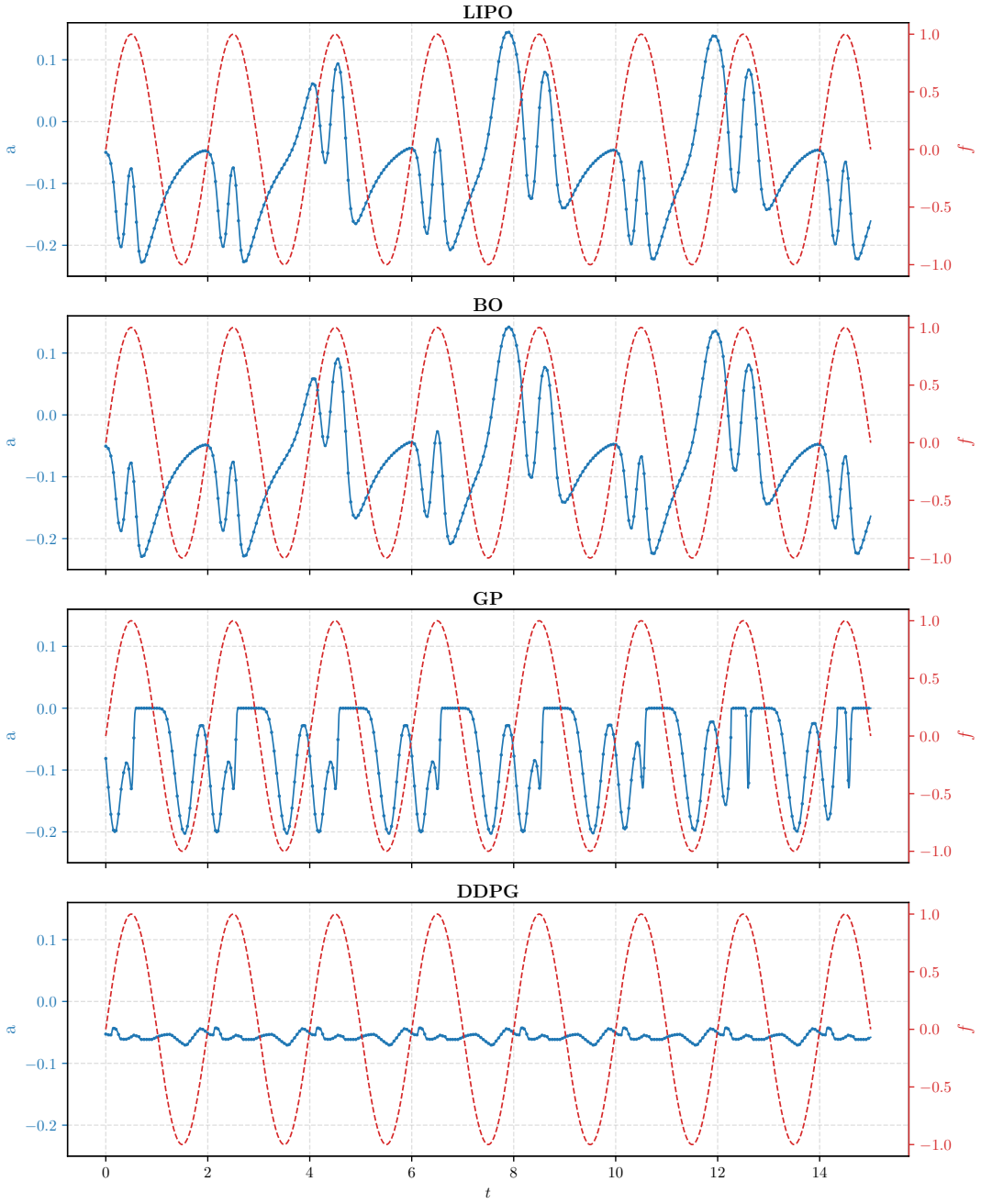

Figure 8: Comparison of the control actions derived by the four machine learning methods. The action for each control methods are shown in blue (left axis) while the curves in dashed red show the evolution of the introduced perturbation (term $A\sin(2\pi f_p t)$ in (**??**)).

6.2. Analysis of 3D waves

In order to investigate the span-wise wave propagation on a moving substrate, we performed 3D simulations. Figure 9 shows a snapshot of the liquid interface subject to a 3D perturbation with its corresponding contour plot. Contrary to what happens in, e.g., shallow water flows, the wave propagation is not isotropic, but strongly biased in the direction of the substrate.

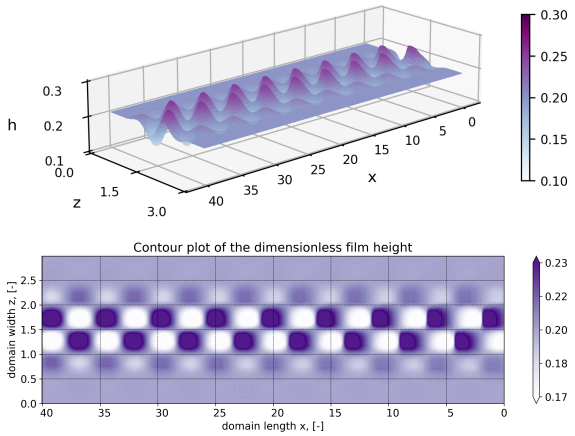

Figure 9: Dimensionless liquid film height (top) and its contour plot (bottom) evolved on a 3D wave along a moving substrate. The substrate moves against the direction of gravity, which is $\hat{x} \to \infty$. The disturbances are introduced on the left, at $\hat{x} = 40$.

7. Conclusion

All the machine learning based techniques used on a simple 1D viscous Burgers' control problem were capable of controlling the system within a limited number of episodes. By means of the 3D wave analysis performed on the derived reduced order model, we understood that the influence region of a disturbance is limited to a narrow are of the liquid film. This information will be of paramount important for the application of the control methods to the 3D undulation problem and to the optimal placement of the control jets.

Acknowledgments

I would like to express my deepest appreciation to my supervisor Prof. Miguel Alfonso Mendez whose valuable assistance and support were crucial to obtain these achievements. I would like to extend my gratitude to Prof. Benoit Scheid; Tsvetelina Ivanova e Lorenzo Schena.

References

[1] S. F. Kistler, P. M. Schweizer, Liquid film coating: scientific principles and their technological implications, Springer, 1997.

[2] A. Gosset, J.-M. Buchlin, Jet wiping in hot-dip galvanization.

[3] M. Mendez, A. Gosset, J.-M. Buchlin, Experimental analysis of the stability of the jet wiping process, part ii: Multiscale modal analysis of the gas jet-liquid film interaction, Experimental Thermal and Fluid Science 106 (2019) 48–67.

[4] R. F. Stengel, Optimal control and estimation, Courier Corporation, 1994.

[5] D. E. Kirk, Optimal control theory: an introduction, Courier Corporation, 2004.

[6] N. Wiener, Cybernetics: or the Control and Communication in the Animal and the Machine, MIT Press, Boston, 1948.

[7] Y. S. Abu-Mostafa, M. Magdon-Ismail, H.-T. Lin, Learning from Data, AMLBook, 2012.

[8] F. M. M. Vladimir Cherkassky, Learning from Data, John Wiley & Sons, 2008.

[9] S. L. Brunton, B. R. Noack, P. Koumoutsakos, Machine learning for fluid mechanics, Annual Review of Fluid Mechanics 52 (2020) 477–508.

[10] G. E. Fasshauer, Meshfree Approximation Methods with Matlab, WORLD SCIENTIFIC, 2007. doi:10.1142/6437.

[11] I. Goodfellow, Y. Bengio, A. Courville, Deep Learning, the MIT Press, 2016.

[12] J. Koza, Genetic programming as a means for programming computers by natural selection, Statistics and Computing 4 (2). doi:10.1007/bf00175355.

[13] S. Sun, Z. Cao, H. Zhu, J. Zhao, A survey of optimization methods from a machine learning perspectivearXiv:http://arxiv.org/abs/1906.06821v2.

[14] R. S. Sutton, A. G. Barto, Reinforcement learning: An introduction, MIT press, 2018.

[15] W. Banzhaf, P. Nordin, R. E. Keller, Genetic Programming: An Introduction, MORGAN KAUFMANN PUBL INC, 1997.

[16] L. Vanneschi, R. Poli, Genetic Programming — Introduction, Applications, Theory and Open Issues, Springer Berlin Heidelberg, Berlin, Heidelberg, 2012, pp. 709–739. doi:10.1007/978-3-540-92910-9$_2$4.

[17] M. Mendez, A. Gosset, B. Scheid, M. Balabane, J.-M. Buchlin, Dynamics of the jet wiping process via integral models, Journal of Fluid Mechanics 911. doi:10.1017/jfm.2020.1075.
URL `https://doi.org/10.1017/jfm.2020.1075`

[18] E. A. Demekhin, E. N. Kalaidin, Three-dimensional localized coherent structures of surface turbulence. i. scenarios of two-dimensional–three-dimensional transition, Physics of Fluids 19 (114103).

[19] L. C. Evans, An introduction to mathematical optimal control theory, lecture notes (February 1983).

[20] R. J. Williams, Simple statistical gradient-following algorithms for connectionist reinforcement learning, Machine Learning 8 (3-4) (1992) 229–256. doi:10.1007/bf00992696.

[21] V. Mnih, K. Kavukcuoglu, D. Silver, A. Graves, I. Antonoglou, D. Wierstra, M. Riedmiller, Playing atari with deep reinforcement learningarXiv:http://arxiv.org/abs/1312.5602v1.

[22] E. Demekhin, V. Shkadov, Three-dimensional waves in a liquid flowing down a wall, Fluid Dynamics 19 (1984) 689–695. doi:10.1007/BF01093533.

[23] V. Y. Shkadov, Wave flow regimes of a thin layer of viscous fluid subject to gravity, Fluid Dynamics 2 (1) (1970) 29–34. doi:10.1007/bf01024797.

[24] G. Y. C. Maceda, B. R. Noack, F. Lusseyran, M. Morzynski, L. Pastur, N. Deng, Taming the fluidic pinball with artificial intelligence control, in: European Fluid Mechanics Conference, 2018.

[25] C. E. Rasmussen, Gaussian processes in machine learning, in: Summer school on machine learning, Springer, 2003, pp. 63–71.

[26] J. Bergstra, D. Yamins, D. Cox, Making a science of model search: Hyperparameter optimization in hundreds of dimensions for vision architectures, in: ICML, 2013.

[27] M. Ghavamzadeh, S. Mannor, J. Pineau, A. Tamar, Convex optimization: Algorithms and complexity, Foundations and Trends® in Machine Learning 8 (5-6) (2015) 359–483. doi:10.1561/2200000049.

[28] P. I. Frazier, A tutorial on bayesian optimization-arXiv:http://arxiv.org/abs/1807.02811v1.
[29] T. Head, M. Kumar, H. Nahrstaedt, G. Louppe, I. Shcherbatyi, scikit-optimize/scikit-optimize (2020). doi:10.5281/ZENODO.1157319.
[30] C. Malherbe, N. Vayatis, Global optimization of lipschitz functions, in: International Conference on Machine Learning, PMLR, 2017, pp. 2314–2323.
[31] M. O. Ahmed, S. Vaswani, M. Schmidt, Combining bayesian optimization and lipschitz optimization, Machine Learning 109 (1) (2020) 79–102. doi:10.1007/s10994-019-05833-y.
[32] D. E. King, Dlib-ml: A machine learning toolkit, Journal of Machine Learning Research 10 (2009) 1755–1758.
[33] K. R. Davidson, A. P. Donsig, Real analysis and applications: theory in practice, Springer Science & Business Media, 2009, pg. 70.
[34] M. J. Powell, The newuoa software for unconstrained optimization without derivatives, in: Large-scale nonlinear optimization, Springer, 2006, pp. 255–297.
[35] R. L. Haupt, S. Ellen Haupt, Practical genetic algorithms.
[36] F.-A. Fortin, F.-M. De Rainville, M.-A. Gardner, M. Parizeau, C. Gagné, DEAP: Evolutionary algorithms made easy, Journal of Machine Learning Research 13 (2012) 2171–2175.
[37] J. Kober, J. Peters, Reinforcement learning in robotics: A survey, in: Springer Tracts in Advanced Robotics, Springer International Publishing, 2014, pp. 9–67. doi:10.1007/978-3-319-03194-1_2.
[38] T. Duriez, S. L. Brunton, B. R. Noack, Machine learning control-taming nonlinear dynamics and turbulence, Springer, 2017.
[39] T. P. Lillicrap, J. J. Hunt, A. Pritzel, N. Heess, T. Erez, Y. Tassa, D. Silver, D. Wierstra, Continuous control with deep reinforcement learningarXiv:http://arxiv.org/abs/1509.02971v6.
[40] D. Silver, G. Lever, N. Heess, T. Degris, D. Wierstra, M. Riedmiller, Deterministic policy gradient algorithms, in: Proceedings of the 31st International Conference on International Conference on Machine Learning - Volume 32, ICML'14, JMLR.org, 2014, p. I–387–I–395.
[41] V. Mnih, K. Kavukcuoglu, D. Silver, A. A. Rusu, J. Veness, M. G. Bellemare, A. Graves, M. Riedmiller, A. K. Fidjeland, G. Ostrovski, S. Petersen, C. Beattie, A. Sadik, I. Antonoglou, H. King, D. Kumaran, D. Wierstra, S. Legg, D. Hassabis, Human-level control through deep reinforcement learning, Nature 518 (7540) (2015) 529–533. doi:10.1038/nature14236.
[42] H. J. Kelley, Gradient theory of optimal flight paths, Ars Journal 30 (10) (1960) 947–954.
[43] G. E. Uhlenbeck, L. S. Ornstein, On the theory of the brownian motion, Physical Review 36 (5) (1930) 823–841. doi:10.1103/physrev.36.823.
[44] T. Schaul, J. Quan, I. Antonoglou, D. Silver, Prioritized experience replayarXiv:http://arxiv.org/abs/1511.05952v4.
[45] J. Rabault, A. Kuhnle, Accelerating deep reinforcement learning strategies of flow control through a multi-environment approach, Physics of Fluids 31 (9) (2019) 094105. doi:10.1063/1.5116415.
[46] H. Tang, J. Rabault, A. Kuhnle, Y. Wang, T. Wang, Robust active flow control over a range of Reynolds numbers using an artificial neural network trained through deep reinforcement learning, Physics of Fluids 32 (5) (2020) 053605. arXiv:2004.12417, doi:10.1063/5.0006492.
[47] J. Rabault, F. Ren, W. Zhang, H. Tang, H. Xu, Deep reinforcement learning in fluid mechanics: A promising method for both active flow control and shape optimization, Journal of Hydrodynamics 32 (2) (2020) 234–246. doi:10.1007/s42241-020-0028-y.

AERODYNAMICS AND AERONAUTICS

HDG solver for time-dependent conservation laws

Tomáš Levý

Aeronautics and Aerospace Department, von Karman Institute for Fluid Dynamics, Belgium, tomas.levy@vki.ac.be

Supervisor: Georg May

Associate Professor, Aeronautics and Aerospace Department, von Karman Institute for Fluid Dynamics, Belgium, georg.may@vki.ac.be

University Supervisor: Jan Vimmr

Associate Professor, Department of Mechanics, Faculty of Applied Sciences, University of West Bohemia in Pilsen, Czech Republic, jvimmr@kme.zcu.cz

Abstract

High-order methods are of great interest for problems of computational fluid dynamics because of their potential in delivering higher accuracy of the numerical solution at lower cost than conventional low order methods. One such method is hybridized discontinuous Galerkin (HDG) method which benefits from lower number of globally coupled degrees of freedom compared to standard discontinuous Galerkin (DG) method. In this work we are interested in further development of existing HDG solver which has been introduced for solving steady state problems. The main focus is on extension of the solver for generic time-dependent balance laws of convection-diffusion-reaction type. The ultimate goal of this research is to extend the solver for large eddy simulations of complex turbulent flows where high-order methods have proven beneficial for the case of implicit filtering of the Navier-Stokes equations.

The hybridized formulation allows to reduce computational cost when solving given problem by introducing additional variables at the element interfaces. The globally coupled degrees of freedom then lie on the mesh skeleton only as opposed to the mesh elements in DG. The remaining degrees of freedom are then recovered locally in element-by-element fashion. Applying the HDG method to an unsteady convection-diffusion-reaction equation leads to a differential-algebraic system of equations representing a stiff problem. The use of explicit methods for time integration is therefore not possible and it is necessary to apply implicit methods. In order to minimize the number of time steps needed to perform for the desired accuracy of the numerical solution at final time we aim to high-order methods also in time. So far, two families of methods has been implemented. These are Backward Differentiation Formulas (BDF) and Diagonally Implicit Runge-Kutta (DIRK) methods. The DIRK methods are often designed such that they include an embedded method of lower order which can serve as another estimate of the solution in given time step without additional computational effort. Based on the norm of the difference of these two solutions a time step control algorithm can be employed in order to keep the local error below a prescribed tolerance.

Previous research has been focused on the use of anisotropic mesh adaptation algorithms and it is desirable to utilize this technique also for the time-dependent problems. An essential pitfall is then the transfer of the numerical solution from initial to adapted mesh. Current solution transfer algorithm is based on L^2 projection of the initial solution to each element of the new mesh which results in conservative interpolation of the solution.

Besides basic scalar advection-diffusion-reaction problems, the implemented methods are verified and tested with well-known test cases for Euler (isentropic vortex, shock-vortex interaction) and Navier-Stokes (flow past cylinder) equations.

Keywords: hybridized discontinuous Galerkin, time-accurate solver, backward differentiation formulae, diagonally implicit Runge-Kutta method, anisotropic mesh adaptation

Passive control of cross-flow by means of small discrete roughness elements

Emilio López Figueiras

Aeronautics and Aerospace Department, von Karman Institute for Fluid Dynamics, Belgium, emilio.lopez.figueiras@vki.ac.be

Supervisor: Fabio Pinna

Senior Research Engineer, Aeronautics and Aerospace Department, von Karman Institute for Fluid Dynamics, Belgium, fabio.pinna@vki.ac.be

Supervisor: Christophe Schram

Professor, Environmental and Applied Fluid Dynamics Department, von Karman Institute for Fluid Dynamics, Belgium, christophe.schram@vki.ac.be

University Supervisor: Axel Coussement

Professor, Aerothermomechanics Department, Université Libre de Bruxelles, Belgium, axel.coussement@ulb.be

Abstract

In swept wings, widespread among commercial aviation, the flow transition from laminar to turbulent flow is triggered and dominated by the apparition of the cross-flow instability, where the adverse pressure gradient and the curvature of the inviscid streamlines create a secondary, unstable flow perpendicular to the main flow direction within the boundary layer.

Hence, for the prediction and delay of the transition in such wings, it is important to characterise the receptivity mechanisms that generate the perturbations leading to turbulent flows. Past studies have shown that free stream disturbances and surface roughness near the leading edge are the only mechanisms involved and that the former is the main transition trigger in low disturbance conditions like free flight. However, the knowledge concerning the receptivity processes in cross-flow is still limited in the most common flow conditions with high Reynolds numbers, where multiple transition unstable modes are present and which are more computationally expensive to simulate.

This project aims to numerically model the cross-flow instability in order to have a better insight about the transition phenomena.

The geometries to study will cover a blunt flat plate case with elliptical leading edge and an infinite wing. The base flows will be computed with high order DNS or spectral element methods and the roughness elements will be modelled as inhomogeneous boundary conditions or added via adjoint solutions.

From these models it is expected to obtain valuable conclusions about roughness as a receptivity mechanism, studying its role in the flow stability of the flat plate and how different roughness configurations can model the growth of disturbances; or as a passive control device, implementing arrays of discrete elements placed near the leading edge to delay the transition to turbulent flow in a wing.

Keywords: Flow Stability, Transition, Cross-flow, Receptivity, Roughness.